STATE OF CALIFORNIA DEPARTMENT OF TRANSPORTATION

TECHNICAL REPORT DOCUMENTATION PAGE

TR0003 (REV. 10/98)

1. REPORT NUMBER	2. GOVERNMENT ASSOCIATION NUMBER	3. RECIPIENT'S CATALOG NUMBER
CA 17-2425		

4. TITLE AND SUBTITLE Shake Table Studies of Soil-Abutment-Structure Interaction in Skewed Bridges	5. REPORT DATE July 2017 6. PERFORMING ORGANIZATION CODE UNR
7. AUTHOR(S) Bahareh Abdollahi, M. Saiid Saiidi, Raj Siddharthan, Sherif Elfass	8. PERFORMING ORGANIZATION REPORT NO. UNR/CA17-2425
9. PERFORMING ORGANIZATION NAME AND ADDRESS Department of Civil and Environmental Engineering, MS 258 University of Nevada, Reno 1664 N. Virginia Street Reno, NV 89557	10. WORK UNIT NUMBER 11. CONTRACT OR GRANT NUMBER 65A0468
12. SPONSORING AGENCY AND ADDRESS California Department of Transportation Engineering Service Center 1801 30th Street, MS 9-2/5i Sacramento CA 95816 California Department of Transportation Division of Research and Innovation, MS-83 1227 O Street Sacramento CA 95814	13. TYPE OF REPORT AND PERIOD COVERED Final Report 6/1/2012 – 5/31/2016 14. SPONSORING AGENCY CODE 913

15. SUPPLEMENTAL NOTES

Prepared in cooperation with the State of California Department of Transportation.

16. ABSTRACT

Soil-abutment-structure interaction could affect the seismic response of bridges considerably. Skew angle might significantly influence the mobilized passive resistance of the backfill soil and the behavior of soil-abutment system due to the large induced in-plane rotations and translation of the superstructure, coupled with variations in stiffness and strength of backfill soil in skewed abutments. The current Seismic Design Criteria of the California Department of Transportation (Caltrans) does not include any special consideration for the skew angle effect on the passive capacity of soil-abutment systems. Previous experiments on skewed abutments were undertaken on abutments that were restrained against rotation with prescribed uniform displacements tested by gradually increasing lateral loads under static conditions, with no dynamic effect simulated. The effects of abutment rotation, impact on the abutment wall and dynamic earthquake forces were not studied.

The overall objective of the current study was to investigate experimentally and analytically the effect of skew angle on the abutment soil response under realistic dynamic earthquake loading and develop recommendations on modeling of skewed abutments for application in bridge seismic design.

The experimental study was focused on soil-abutment-structure interaction in skewed bridges under dynamic loading based on large-scale shake table tests at the University of Nevada, Reno. Three 5.5-ft high abutment walls at three skew angles of 0º, 30º, and 45º with a projected width of 10 ft in the direction of motion were impacted by a bridge superstructure and pushed in the longitudinal direction of the bridge into a 25 ft long by 19 ft wide engineered backfill soil embankment in a stationary timber box. The abutment walls were allowed to rotate to further simulate actual bridge abutments realistically. The bridge superstructure was represented by a concrete bridge block supported on elastomeric bearings that simulated the stiffness of the substructure and a mass that accounted for similitude effect. The skew angle of the bridge block was changed in different experiments to match the angle of the abutment wall. The bridge block was supported on a shake table. The 1994 Northridge Sylmar earthquake record was simulated in the table with successively increasing amplitudes. A large number of transducers of different types were used to monitor the bridge block and the abutment response under the simulated lateral dynamic loading. The experiments verified that skewed bridges tend to rotate in the direction of reducing the skew angle. This corresponds to impacting abutment at the obtuse corner and unseating of superstructure at the acute corner. The test results showed that the passive capacity, heaves, and accelerations of soil were reduced by increasing the skew angle although the abutment wall width increased when a higher skew was simulated. The distribution of backfill pressure across the abutment was primarily dependent on direction of the abutment wall rotation while the maximum pressure, heaves and accelerations occurred at the obtuse corner of the bridge block.

Analytical studies were performed by developing FLAC3D models of the shake table tests in the current study. The analytical models simulated the abutment wall and backfill under the static uniform and non-uniform displacement loading on the wall. Results from the analytical studies indicated that the backfill passive capacity was reduced when the abutment rotation was accounted for. The displacement contours from the analytical models that simulated the abutment wall rotation were similar to those obtained in the shake table tests. Design recommendations were developed by evaluating the most recent available models estimating the passive force-displacement relationships of the abutments considering the effect of skew.

17. KEY WORDS	18. DISTRIBUTION STATEMENT	
Abutment, Skew, Seismic, Shake Table, Dynamic, Nonlinear, Lateral, Backfill, Passive Capacity	No restrictions. This document is available to the public through the National Technical Information Service, Springfield, VA 22161	
19. SECURITY CLASSIFICATION (of this report)	20. NUMBER OF PAGES	21. PRICE
Unclassified	837	

DISCLAIMER STATEMENT

Report No. CCEER 17-04

SHAKE TABLE STUDIES OF SOIL-ABUTMENT-STRUCTURE INTERACTION IN SKEWED BRIDGES

Bahareh Abdollahi
Mehdi “Saiid” Saiidi
Raj Siddharthan
Sherif Elfass

A report sponsored by the California Department of Transportation

---

Center for Civil Engineering Earthquake Research

University of Nevada, Reno
Department of Civil and Environmental Engineering, MS 258
1664 N. Virginia St.
Reno, NV 89557

July 2017

ABSTRACT

Soil-abutment-structure interaction could affect the seismic response of bridges considerably. Skew angle might significantly influence the mobilized passive resistance of the backfill soil and the behavior of soil-abutment system due to the large induced in-plane rotations and translation of the superstructure, coupled with variations in stiffness and strength of backfill soil in skewed abutments. The current Seismic Design Criteria of the California Department of Transportation (Caltrans) does not include any special consideration for the skew angle effect on the passive capacity of soil-abutment systems. Previous experiments on skewed abutments were undertaken on abutments that were restrained against rotation with prescribed uniform displacements tested by gradually increasing lateral loads under static conditions, with no dynamic effect simulated. The effects of abutment rotation, impact on the abutment wall and dynamic earthquake forces were not studied.

The overall objective of the current study was to investigate experimentally and analytically the effect of skew angle on the abutment soil response under realistic dynamic earthquake loading and develop recommendations on modeling of skewed abutments for application in bridge seismic design.

The experimental study was focused on soil-abutment-structure interaction in skewed bridges under dynamic loading based on large-scale shake table tests at the University of Nevada, Reno. Three 5.5-ft high abutment walls at three skew angles of 0º, 30º, and 45º with a projected width of 10 ft in the direction of motion were impacted by a bridge superstructure and pushed in the longitudinal direction of the bridge into a 25 ft long by 19 ft wide engineered backfill soil embankment in a stationary timber box. The abutment walls were allowed to rotate to further simulate actual bridge abutments realistically. The bridge superstructure was represented by a concrete bridge block supported on elastomeric bearings that simulated the stiffness of the substructure and a mass that accounted for similitude effect. The skew angle of the bridge block was changed in different experiments to match the angle of the abutment wall. The bridge block was supported on a shake table. The 1994 Northridge Sylmar earthquake record was simulated in the table with successively increasing amplitudes. A large number of transducers of different types were used to monitor the bridge block and the abutment response under the simulated lateral dynamic loading. The experiments verified that skewed bridges tend to rotate in the direction of reducing the skew angle. This corresponds to impacting abutment at the obtuse corner and unseating of superstructure at the acute corner. The test results showed that the passive capacity, heaves, and accelerations of soil were reduced by increasing the skew angle although the abutment wall width increased when a higher skew was simulated. The distribution of backfill pressure across the abutment was primarily dependent on direction of the abutment wall rotation while the maximum pressure, heaves and accelerations occurred at the obtuse corner of the bridge block.

Analytical studies were performed by developing FLAC3D models of the shake table tests in the current study. The analytical models simulated the abutment wall and backfill under the static uniform and non-uniform displacement loading on the wall. Results from the analytical studies indicated that the backfill passive capacity was reduced when the abutment rotation was accounted for. The displacement contours from the analytical models that simulated the abutment wall rotation were similar to those obtained in the shake table tests. Design recommendations were developed by evaluating the most recent available models estimating the passive force-displacement relationships of the abutments considering the effect of skew.

ACKNOWLEDGEMENTS

The research presented in this document was funded by the California Department of Transportation (Caltrans) through grant No. 65-A0468. However, the statements and findings presented in this document are those of the authors and do not necessarily represent the Caltrans views. The advice and support of Caltrans research program manager, Mr. Peter Lee, are highly appreciated. The authors would like to greatly acknowledge the Caltrans technical monitor, Dr. Anoosh Shamsabadi, for his pioneering researches on the subject and his continuous feedback and comments.

Continuous cooperation and helpful support of the UNR Earthquake Engineering Laboratory personnel, Dr. Patrick Laplace, Eng. Chad Lyttle, Eng. Todd Lyttle, and Eng. Mark Latin is greatly acknowledged. The valuable assistance of the UNR students, Mojtaba Alian, Francesco Zuniga, Colton Schaefer, Osvaldo Arias, and Guillermo Munoz in the course of the study is appreciated.

This report is based on a Ph.D. dissertation by the first author supervised by the other authors.

TABLE OF CONTENTS

LIST OF TABLES

LIST OF FIGURES

1. INTRODUCTION

1.1. Background

Soil-abutment-structure interaction could affect the seismic response of bridges considerably. Skew angle might significantly influence the mobilized passive resistance of the backfill soil and the behavior of soil-abutment system due to the large induced in-plane rotations and translation of the superstructure, coupled with difference in behavior of backfill soil in skewed abutments. The current Seismic Design Criteria (SDC, 2013) of the California Department of Transportation (Caltrans) does not give any special consideration to the skew angle effect on the passive capacity of soil-abutment systems. Effect of skew angle would be important for bridges under seismic forces and skewed integral abutments subjected to thermal expansion.

The Federal Highway Administration (FHWA) report (Yen et al., 2011) presented post-earthquake investigations on the Chilean (2010) earthquake. The most commonly observed damage to bridges was due to the unseating or translational movement of the superstructure. The Las Mercedes overpass with a slight skew experienced significant in-plane rotation during the earthquake that resulted in unseating of exterior girders at both abutments (Figure 1-1). The reason could be that the rotational (or torsional) vibration mode of the bridge was excited under the ground motion, or the rotational component of the ground motion was significant. Examples of collapsed skewed bridges as a results of unseating are Miraflores bridge (20° skew, Figure 1-2), Lo Echevers bridge (33° skew, Figure 1-3), and Quilicura railway overcrossing (45° skew, Figure 1-4). Some old non-skewed abutments in straight bridges designed based on Pre Mid-1990s Chile Design Practice (Figure 1-5) performed well in the Chilean earthquake (Kawashima, 2010).

Sanford and Elgaaly (1993) installed pressure cells and temperature sensors on a 20° skewed bridge with integral abutments in Maine. They monitored the backfill pressures during 33 months to determine the effects of thermal stresses in a skewed bridge. They observed the pressure near the obtuse corner was three times the pressure on the opposite side at the acute corner when the bridge was moved into the backfill due to temperature expansion. They stated that the skew angle effect was minimized over time due to the larger permanent deformation of the backfill on the obtuse side compared to that on the acute side as shown in Figure 1-6. The researchers concluded that the larger permanent deformation on the obtuse corner occurred as a result of counterclockwise rotation of the superstructure. They proposed a passive soil pressure distribution in which the Rankine active pressure and passive pressure was used on the acute and obtuse corners of the bridge, respectively. The observed soil pressure distribution was different from other studies (e.g. Kavianijopari, 2011) that suggested the passive pressure is higher at the acute corner than at the obtuse corner due to the larger volume of soil at the acute corner

A comprehensive review of the state-of-the-art on abutment studies is presented in the next chapter. Some key studies are briefly discussed herein as a background to the current study. Prior to the start of the current study, the only available experimental data on seismic performance of skewed abutments was from the small-scale laboratory tests on 2-ft high abutments (Jessee, 2012) at the Brigham Young University (BYU). The research in this area was followed by large-scale field tests on 5.5-ft high abutments at the BYU. These studies have all shown that there is a significant reduction of abutment passive resistance due to the skew (Marsh, 2013; Franke, 2013; Palmer, 2013; Smith, 2014; Wagstaff, 2016). The results from these studies are discussed in Chapter 2. All these experiments were undertaken by gradually increasing the lateral load under static conditions, with no dynamic effect simulated. Therefore, there was a major gap in the literature on studies of skewed abutment under dynamic loading that simulates earthquakes to properly accounts for high damping of the soil.

Another issue in all the previous abutment tests is that it was assumed there is always full contact between the superstructure end diaphragm and the abutment under lateral loading resulting in a uniform load transfer across the width of the abutment. The abutment wall elements in these tests did not rotate about a vertical axis because of the test setup. In reality, however, the superstructure tends to undergo in-plane rotation that results in changing contact point between the superstructure and the abutment and rotation of the abutment wall about vertical axis. Tests of bridge models have shown that uneven contacts (only partial contact) may occur between the abutment and superstructure, which could lead to significant in-plane rotations and unseating of the superstructure (Nelson et al., 2007). There has been a lack of information about the effect of non-uniform contact between the superstructure and the abutment that could result in abutment rotation.

The current study was focused on structure-soil-abutment interaction in skewed bridges under dynamic loading based on large-scale shake table tests at the University of Nevada, Reno. The dynamic loading simulated ground motion accelerations recorded in past earthquakes to obtain a realistic response that includes soil damping effect. The abutment walls were allowed to rotate to further simulate actual bridge abutments realistically.

1.2. Objectives and scope

The overall objective of the current study was to investigate experimentally and analytically the effect of skew angles on the abutment soil response under realistic dynamic earthquake loading and develop recommendations on modeling of skewed abutments for application in bridge research and design. Three 5.5-ft high abutment walls at three skew angles of 0º, 30º, and 45º with a projected width of 10 ft in the longitudinal direction of the bridge were subjected to impact loading by a bridge block superstructure and pushed into a 25 ft long by 19 ft wide engineered backfill soil in a stationary timber box.

The objectives of the experimental studies were to investigate the bridge block and backwall response including accelerations and displacements of the wall and the bridge block, and the backfill response including the soil pressure, accelerations, displacements, and failure mechanism as a function of the earthquake intensity and the skew angle. The number of instrumentation data channels varied from 250 to 270, depending on skew angle. The abutment height was 5.5 ft, which is considered to be full scale, but the width was 10 ft, which was close to the width of abutment wall models in previous experiments.

The objectives of the analytical studies were to evaluate the applicability of available software and soil constitutive models to reproducing the test data obtained from previous abutment tests and modeling the soil-abutment system in the current shake table tests.

The back fill material in all the shake-table tests was clean sand, with shear strength properties similar to the backfills in the previous abutment tests. The shake-table motions were simulated only in the longitudinal direction of the bridge, and the effect of vertical and bi-directional motions was not evaluated. To keep the scope of the study within the budget and time constraints of the project, the analytical studies were focused on only static analysis of the soil-abutment test model even though the shake table tests were dynamic.

1.3. Organization of dissertation

Chapter 1, “Introduction”, presents an introductory report on the significance, main objectives, and scope of the current experimental and analytical studies.

Chapter 2, “Literature Review”, presents a comprehensive state-of-the-art literature review on experimental and analytical studies on soil-abutment interaction. The objective is to highlight lessons learned in the past skewed abutments studies.

Chapter 3, “Preliminary Analytical Studies”, presents analytical studies using PLAXIS and FLAC3D software to evaluate their applicability to modeling soil-abutment systems based on comparing the analytical results with the experimental data from the non-skewed abutment tests at the University of California Los Angeles (UCLA).

Chapter 4, "Analytical Studies for Preliminary Design of Shake Table Tests", summarizes pre-test analytical studies on simulating the shake table test model using OpenSees. The studies resulted in a preliminary design of the test model and the shake table testing protocol.

Chapter 5, "Test Model Design and Construction", discusses the final details of the shake table test model components and stages of construction, instrumentation, and testing.

Chapter 6, "Shake Table Testing Program and Experimental Results", presents the measured response of the test model components and discusses the main findings from the experiments.

Chapter 7, "Interpretation of Experimental Results", presents an interpretation of the experimental results focusing on the study of the skew angle effect on the key response of the soil-abutment test model and comparing with experimental data on the skewed abutments available in the literature.

Chapter 8, "Analytical Studies and Design Recommendations", presents analytical studies on the shake table test models using FLAC3D. The studies resulted in design recommendations regarding the force-displacement relationships of the skewed abutments.

Chapter 9, "Summary and Conclusions", presents a summary of the experimental and analytical studies on the soil-abutment-structure response with conclusions and design recommendations regarding the skewed abutments behavior and modeling.

Appendix A to D provide detailed information and drawings regarding design and construction of the test models, the highlights of which were presented in Chapter 5.

Appendix E and F present detailed experimental data on natural period of the test model bridge block and soil acceleration histories discussed in Chapter 6.

Appendix G presents detailed data on the interpretation of the experimental results including estimated soil pressure distribution and passive force histories that were presented in Chapter 7.

2. LITERATURE REVIEW

2.1. Introduction

This chapter presents a state-of-the-art literature review on modeling soil-abutment interaction under lateral loading. Passive earth pressure theories that are applicable to soil-abutment interaction are described and the load-deflection relationships of soil-abutment systems are summarized. Large-scale experimental tests that modeled the soil-abutment interaction are described and the corresponding measured data are interpreted. This is followed by review of analytical studies performed on simulating the behavior of soil-abutment systems. Finally, a brief summary of the findings from this literature review is summarized and recommendations are made to address the gaps in the literature.

2.2. Passive earth pressure theories

An overview of some of the prominent methods to analyze the passive behavior of abutment walls is provided in this section. These methods are used to estimate the passive soil capacity.

2.2.1. Coulomb method

One of the earliest methods for estimating the earth pressure against the walls was developed by Coulomb (1776). As shown in Figure 2-1, Coulomb assumed the soil failure to occur in the form of a wedge undergoing translation as a rigid body along a shear plane. This theory accounts for both internal friction and friction at the wall-soil interface. Based on the limit equilibrium method, passive pressure resultant force is calculated for cohesionless soil as

$$P_P = \frac{1}{2} K_P \gamma H^2 \tag{2-1}$$

where P_P is the passive earth pressure resultant force, K_P is the coefficient of passive earth pressure according to the following equation, γ is the unit weight of the backfill soil, and H is the height of the wall.

$$K_P = \frac{\cos^2(\emptyset + \theta)}{\cos^2\theta \cos(\delta - \theta)\left[1 - \sqrt{\dfrac{\sin(\phi + \delta)\sin(\phi + \beta)}{\cos(\delta - \theta)\cos(\beta - \theta)}}\right]^2} \tag{2-2}$$

where δ is the friction angle between wall and backfill material, β is the embankment slope angle, θ is the wall inclination angle, and ϕ is the internal friction angle of the soil. In the case of zero friction at the wall-soil interface (δ=0), θ=0, and β=0, the passive pressure coefficient is

$$K_P = \frac{1 + \sin\phi}{1 - \sin\phi} = \tan^2(45 + \frac{\phi}{2}) \tag{2-3}$$

2.2.2. Rankine method

The Rankine (1857) method is a special case of the conditions by Coulomb. Rankine method is also based on the limit equilibrium approach with a planar failure surface. The Rankine theory assumes that there is no friction at the wall-soil interface (δ=0) and direction of earth pressure is parallel to the backfill slope. Thus, the coefficient of passive earth pressure is calculated by

$$K_P = \cos\beta \frac{\cos\beta + \sqrt{[\cos^2\beta - \cos^2\phi]}}{\cos\beta - \sqrt{[\cos^2\beta - \cos^2\phi]}} \tag{2-4}$$

where β is the embankment slope angle and ϕ is the internal friction angle of the soil. For β=0, the same simplified equation as the Coulomb's equation applies.

The Rankine method results in identical values of passive pressure coefficient for both positive and negative backfill slope. Trenching and Shoring Manual of California Department of Transportation (Caltrans) suggests that Rankine method should not be used for sloping ground.

The effect of soil cohesion is not explicitly incorporated neither in Coulomb nor Rankine methods. Rankine's theory is modified to determine the earth pressure for cohesive soil using the Mohr Circle formulation, as in the following equation.

$$P_P = \frac{1}{2} K_P \gamma H^2 + 2c\sqrt{K_P} H \qquad (2\text{-}5)$$

2.2.3. Passive trial wedge method

This method is an iterative method to determine the earth pressure for sloping ground with an irregular backfill condition (Figure 2-2). The failure plane angle, α_n, is varied until the minimum value of passive earth pressure is computed using Eq. (2-6). This equation is based on the limit equilibrium approach for a general soil wedge. It is assumed that the soil wedge moves upward along the failure plane and wall surface to mobilize the passive pressure.

$$P_P = \frac{W_n[\tan(\alpha_n + \emptyset)] + cL_c[\sin\alpha_n \tan(\alpha_n + \emptyset) + \cos\alpha_n] + C_a L_a[\tan(\alpha_n + \emptyset)}{[1 - \tan(\delta + \omega)\tan(\alpha_n + \emptyset)]\cos(\delta + \omega)} \qquad (2\text{-}6)$$

where W_n is the weight of soil wedge plus the relevant surcharge loads within the failure mass, α_n is the failure plane angle with respect to horizontal line, δ is the friction angle between wall and backfill material, ω is the wall inclination angle, ϕ is the internal friction angle of the soil, c is the soil cohesion, L_c is the failure plane length, and L_a is the effective wall-soil interface length.

2.2.4. Composite log-spiral method

Terzaghi (1943) extended the Coulomb theory to accommodate a failure surface geometry consisting of log-spiral and linear parts as shown in Figure 2-3. Log-spiral earth pressure forces can be computed by charts and tables that are available in textbooks and manuals. Another approach is to calculate the passive force by a trial and error log-spiral graphical process based on the assumption that a surface traction makes an angle of ϕ with the tangent to the spiral surface and the lines of the surface traction pass through the center of spiral.

The passive earth pressure based on log-spiral method is significantly more accurate than those predicted by Coulomb or Rankine theories. The Rankine and Coulomb theories tend to underestimate and overestimate the passive capacity, respectively.

Figure 2-3 shows the geometry of log-spiral composite failure plane. The logarithmic spiral part of failure surface is governed by height of the wall, location of center of the log-spiral arc, and internal friction angle of soil. The log-spiral portion of failure plane is defined by the following equation.

$$R = R_0 e^{\theta \tan\emptyset} \qquad (2\text{-}7)$$

The linear portion of failure surface is tangent to the curve at the intersection point between the two parts. The location of center of log-spiral curve is defined based on the angle θ_m. Either force equilibrium or moment equilibrium method may be used to calculate the passive earth pressure force.

2.2.4.1. Force equilibrium procedure

The value of θ_m can be obtained from the geometry of composite failure surface. The log-spiral surface starts with the angle α_w at the bottom of the wall, with a positive value when it is above the horizontal axis and with a negative value when it is below the horizontal axis.

$$\alpha_w = \left(45 - \frac{\emptyset}{2}\right) - \alpha_p \qquad (2\text{-}8)$$

where α_p is defined using the following equation.

$$\alpha_p = \frac{1}{2}\tan^{-1}\left[\frac{2K(\tan\delta)}{K-1}\right] \tag{2-9}$$

where δ is the friction angle of wall-soil interface that varies from zero to its full value (δ=δ_{ult}), and K is the ratio of horizontal stress to vertical stress.

$$K = \frac{A1 + A2}{A3} \tag{2-10}$$

Where

$$A1 = 1 + \sin^2\emptyset + \frac{C}{\sigma_z}\sin 2\emptyset \tag{2-11}$$

$$A2 = 2\cos\emptyset\left(\sqrt{\left(\tan\emptyset + \frac{C}{\sigma_z}\right)^2 + \tan^2\delta\left[4\left(\left(\frac{C}{\sigma_z}\right)^2 + \frac{C}{\sigma_z}\tan\emptyset\right) - 1\right]}\right) \tag{2-12}$$

$$A3 = \cos^2\emptyset + 4\tan^2\delta \tag{2-13}$$

$$\sigma_z = \gamma H \tag{2-14}$$

The value of θ_m is obtained from the following equation:

$$\theta_m = \alpha_1 - \alpha_w \tag{2-15}$$

where α_1 is the failure angle of slice 1 (Figure 2-4). The geometry of failure surface is established using the above equations. Then the failure mass is divided into slices as shown in Figure 2-4. The horizontal passive force, P_h, is finally calculated by summation of forces in the vertical and horizontal direction for all the slices.

$$P_h = \frac{\sum_{i=1}^{n} \mathrm{d}E}{[1 - \tan\delta\tan(\alpha_w + \emptyset)]} \tag{2-16}$$

where

$$\mathrm{d}E = \frac{W\tan(\alpha + \emptyset) + (C)(L)[\sin\alpha\tan(\alpha + \emptyset) + \cos\alpha]}{1 - \tan\delta\tan(\alpha + \emptyset)} \tag{2-17}$$

The horizontal passive pressure coefficient, K_{ph}, is obtained by dividing the resisting force P_h by $0.5\gamma H^2$ as shown in the following equation:

$$K_{ph} = \frac{2P_h}{\gamma H^2} \tag{2-18}$$

2.2.4.2. Moment equilibrium procedure

The passive force can be determined from summation of moments about the center of log-spiral failure surface. This is done in two steps and is solved by method of superposition of forces acting on the soil free body associated with weight and the soil free body associated with cohesion, respectively. Considering the weight of free body diagram shown in Figure 2-5, the passive earth pressure due to weight (E_w) is calculated by the following equation.

$$E_w = \frac{(W_{ABDF})(L_2) + (P_R)(L_3)}{L_1} \tag{2-19}$$

Considering the cohesion of free body diagram shown in Figure 2-6, the passive earth pressure due to cohesion (E_c) is calculated by the following equation:

$$E_C = \frac{M_c + (P_c)(L_5)}{L_4} \tag{2-20}$$

where Mc is the moment due to cohesion for log-spiral section:

$$M_c = \frac{C + P_c}{\tan\emptyset}(R^2 - R_0^2) \tag{2-21}$$

And for cohesive soil with zero friction angle:

$$M_c = (C)(\theta)(R^2) \tag{2-22}$$

The total passive force is obtained by summation of passive forces due to weight and cohesion.

$$P_P = E_w + E_c \tag{2-23}$$

However, this approach may not provide a unique solution to the problem since only one trial surface is examined. The final value of passive force is determined for several trial failure surfaces as shown in Figure 2-7 until the minimum value of P_P is obtained for the critical failure surface. The same procedure is used for Coulomb, Rankine and trial wedge methods to determine the minimum passive earth pressure for different trial failure surfaces.

For cohesionless soil, the passive force may be calculated from Figure 2-8. The initial passive pressure coefficient is determined based on the values of ϕ and β/ϕ. The reduction factor R is obtained based on the values of ϕ and δ/ϕ. The reduction factor is applied to the initial passive force to calculate the final passive force.

2.2.5. Non-composite log-spiral method

This method assumes that a single log-spiral curve represents the entire failure surface, as shown in Figure 2-9. Similar to the composite log-spiral method, the force and moment equilibrium procedures are used to determine the passive force. The difference is that the soil body is not divided into log-spiral zone and Rankine zone in this method.

2.2.5.1. Force equilibrium procedure

The formulation is similar to the force equilibrium procedure for composite log-spiral failure surface, since Rankine zone is treated as a single slice in that method. For the non-composite log-spiral failure method, the entire mass above the failure surface is divided into slices and thus, Eq. 15 and Eq. 17 are still valid to calculate the passive earth pressure.

2.2.5.2. Moment equilibrium procedure

Some modifications are made to the moment equilibrium procedure for the composite log-spiral failure surface by removing the Rankine components from the equations. For the passive force associated with the weight (Figure 2-9), the passive force is calculated by the following equation.

$$E_w = \frac{(W_{ABD})(L_2)}{L_1} \tag{2-24}$$

For the passive force due to cohesion of soil body as shown in Figure 2-10, the associated passive force is calculated by the following equation.

$$E_c = \frac{M_c}{L_4} \tag{2-25}$$

The passive pressure coefficients for different methods are provided in Trenching and Shoring Manual by Caltrans in Figures 4-40 to 4-46 for zero slope backfills. For sloping backfill, the earth pressure coefficient is determined using Figure 2-8.

Table 2-1 shows the values of passive earth pressure coefficient for zero slope backfill for the different methods discussed in previous sections. For the soil-wall interface with friction less than 1/3 of the backfill soil friction angle, the value of passive earth pressure coefficient does not change significantly. However, for higher value of soil-wall interface friction angle, the log-spiral method should be applied.

2.2.6. Mononobe-Okabe method

This method is an extension of Coulomb earth pressure theory by including a horizontal force on the backfill soil to represent seismic loading. Figure 2-11 shows the schematic seismic lateral forces according to this method. The effect of vertical acceleration is usually neglected in practice. The reason is that the vertical acceleration is generally out of phase with the horizontal acceleration and has different frequency characteristics. Therefore, it is not necessary to superimpose the effect of vertical acceleration with the horizontal acceleration.

Seismic passive earth pressure is computed according to the following equation.

$$P_{PE} = \frac{1}{2}\gamma H^2(1 - k_v)K_{PE} \tag{2-26}$$

where P_{PE} is the seismic passive earth pressure, K_{PE} is the coefficient of seismic passive earth pressure according to the following equation, k_v is the vertical acceleration coefficient, γ is the unit weight of the backfill soil, and H is the height of the wall.

$$K_{PE} = \frac{\cos^2(\phi - \theta + \omega)}{\cos\theta\cos^2\omega\cos(\delta - \omega + \theta)\left[1 - \sqrt{\frac{\sin(\phi + \delta)\sin(\phi - \theta + \beta)}{\cos(\delta - \omega + \theta)\cos(\beta - \omega)}}\right]^2} \tag{2-27}$$

where δ is the friction angle between wall and backfill material, β is the embankment slope angle, ω is the wall inclination angle, ϕ is the internal friction angle of the soil, and θ is the seismic inertial angle by the following equation:

$$\theta = \tan^{-1}\frac{k_h}{1 - k_v} \tag{2-28}$$

where k_v and k_h are vertical and horizontal acceleration coefficients, respectively.

According to NCHRP report by Anderson et al. (2008), all walls need not be analyzed for seismic loading. Table 2-2 shows conditions under which seismic analysis is not necessary for free standing earth retaining structures unless the foundation is susceptible to liquefaction. These conditions are defined based on the site-adjusted peak ground acceleration and the backfill slope.

2.3. Force-displacement relationships of wall-soil systems

This section provides an overview of available methods to estimate the passive behavior of abutment walls with respect to the wall displacement up to the passive capacity of soil-abutment system (i.e., passive force-displacement relationship).

2.3.1. Hyperbolic stress-strain relationships

The basic form of the hyperbolic model can be expressed by the following equation:

$$P = \frac{y}{A + By} \tag{2-29}$$

where *P* is the lateral force acting on retaining wall corresponding to lateral deflection *y*, and *A* and *B* are the constants of the hyperbolic model.

According to Duncan & Mokwa (2001), the passive earth pressure force per unit width of the wall includes three parameters: the component due to soil weight and internal friction, the component due to soil cohesion, and the component due to surcharge. They introduced the use of a hyperbolic equation for lateral load-deflection of retaining structures. The parameters describing their model are shown in Figure 2-12 and are used in the following equation:

$$P = \frac{y}{\frac{1}{K_{max}} + R_f\frac{y}{P_{ult}}} \tag{2-30}$$

where *P* is the load at any displacement *y*, P_{ult} is the ultimate passive force by log-spiral method, K_{max} is the initial stiffness corresponding to the initial slope of the load deflection curve. The failure ratio, R_f, is defined as the ratio between the actual failure force and the hyperbolic ultimate force, which is an asymptotic value that is approached as *y* approaches infinity. For soil stress-strain curves, R_f is always smaller than 1 and varies from 0.5 to 0.9 for most soils.

2.3.2. Log-spiral hyperbolic (LSH) method

The log-spiral method of Terzaghi (1943) can be extended using the method of slices to calculate the passive pressure resistance. Shamsabadi et al. (2007) employed a limit equilibrium method using the mobilized logarithmic-spiral failure surfaces coupled with a modified hyperbolic soil stress-strain relationship. This model referred to as LSH model, estimates the nonlinear force-displacement relationship of abutment as a function of wall displacement and soil backfill material properties. A hyperbolic stress-strain relationship was modified to develop the mobilized backfill shear strength parameters (c, ϕ) as a function of strain.

The hyperbolic soil model by Duncan & Chang (1970) is defined as below and shown in Figure 2-13.

$$(\sigma_1 - \sigma_3)_i = \frac{\varepsilon_i}{\dfrac{1}{E_0} + \dfrac{\varepsilon_i}{(\sigma_1 - \sigma_3)_{ult}}} \qquad \text{(2-31)}$$

$(\sigma_1 - \sigma_3)_i$ is the intermediate deviatoric stress, $(\sigma_1 - \sigma_3)_{ult}$ is the ultimate deviatoric stress at failure, ε_i is the strain level and E_0 is the initial tangent modulus.

The modified hyperbolic stress-strain relationship is expressed as below

$$SL(\varepsilon_i) = \frac{(\sigma_1 - \sigma_3)_i}{(\sigma_1 - \sigma_3)_f} = \frac{\varepsilon_i}{\dfrac{\varepsilon_{50}}{R_f} + \left(2 - \dfrac{1}{R_f}\right)\varepsilon_i} \qquad \text{(2-32)}$$

where SL is the deviatoric stress ratio, ε_{50} is the strain corresponding to 50% of failure strength and R_f is the failure ratio defined by the following equation. By introducing ε_{50}, the above modified equation avoids the need for determination of E_0.

$$R_f = \frac{(\sigma_1 - \sigma_3)_f}{(\sigma_1 - \sigma_3)_{ult}} \qquad \text{(2-33)}$$

Figure 2-14 shows the mobilized logarithmic-spiral failure surface including the geometry and acting forces. Summation of the forces of the slices yields the mobilized horizontal passive capacity associated with the mobilized failure surface *i* as

$$F_{ih} = \frac{\sum_{j=1}^{n} \Delta E_{ij}}{1 - \tan\delta_{iw}\tan(\alpha_{iw} + \phi_i)} \qquad \text{(2-34)}$$

where ΔE_{ij} is the horizontal component resulting from interslice forces E_{ij} and $E_{(i+1)j}$ acting at the sides of slice j, E_{ij} is the intermediate mobilized force of slice, δ_{iw} is the intermediate mobilized wall-soil interface friction angle, $\alpha_{iw} = \theta_{i1} + \alpha_{i1}$ is the intermediate mobilized inclination of failure plane at wall-soil interface (from horizontal line), and ϕ_i is the intermediate mobilized soil interface friction angle.

The local horizontal displacement of slice *j* associated with the mobilized failure surface *i* is as follows:

$$\Delta y_{ij} = \Delta z_{ij}\frac{\gamma_{ij}}{2} = \Delta z_{ij}\frac{1}{2}\varepsilon_{ij}(1+\nu)\sin 2\alpha_{ij} \qquad \text{(2-35)}$$

where γ_{ij} is the shear strain in the slice, ε_{ij} is the axial strain in the slice and ν is the Poisson's ratio of the soil.

The displacement of the entire mobilized logarithmic-spiral failure surface is the summation of horizontal displacements of all slices.

$$y_i = \sum_{j=1}^{n} \Delta y_{ij} \qquad \text{(2-36)}$$

The LSH model was evaluated by Shamsabadi et al. (2007) by comparing its results with the results from eight experimental nonlinear force-deformation full-scale tests, centrifuge model tests, and small-scale laboratory tests of abutments and pile caps with different backfills.

Shamsabadi et al. (2007) developed the following modified hyperbolic equation, as a function of soil stiffness, maximum abutment force, and maximum displacement to be used in seismic bridge design.

$$F(y_i) = \frac{F_{ult}(2K_{50}y_{max} - F_{ult})y_i}{F_{ult}y_{max} + 2(K_{50}y_{max} - F_{ult})y_i} \quad (2\text{-}37)$$

where F_{ult} is the maximum abutment force (per unit width of the backwall) developed at displacement y_{max}, $K_{50} = F_{ult}/(2y_{50})$ is the average abutment stiffness, and y_{50} is the displacement at half of the maximum abutment force. These parameters of hyperbolic force-displacement (HFD) relationship are shown in Figure 2-15.

The HFD parameters were derived for each of eight experimental tests and the results of HFD model were compared with the test data. Furthermore, some values were suggested for HFD parameters to develop the nonlinear force-displacement curves for compacted abutment backfills when geotechnical data is not available.

Shamsabadi et al. (2010) extended the LSH analyses to determine the load-deflection relationships for walls of different heights. The HFD relationship developed by Shamsabdi et al. (2007) was extended to determine backbone curves for cohesive (clayey silt) and granular (silty sand) backfills as expressed below.

$$F(y) = \frac{8y}{1+3y} H^{1.5} (kips, in.) \text{ for granular backfill} \quad (2\text{-}38)$$

$$F(y) = \frac{8y}{1+1.3y} H (kips, in.) \text{ for cohesive backfill} \quad (2\text{-}39)$$

2.3.3. Caltrans Seismic Design Criteria

The current Caltrans method is originally based on the test results of large-scale abutments performed at University of California, Davis (UCD) (Maroney et al. (1994) and Romstad et al., 1995). Caltrans Seismic Design Criteria (SDC) 2010 suggests an initial abutment longitudinal stiffness of $K_i \approx 50\ kip/in$ per foot of the wall width for embankment fill material meeting the requirements of Caltrans Standard Specifications. For embankment fill material not meeting the requirements of Caltrans Standard Specifications, the initial stiffness is taken as $K_i \approx 25\ kip/in$ per foot of the wall width. The initial stiffness should be adjusted proportional to the backwall or diaphragm height as

$$K_{abut}(kip/in) = K_i \times w \times \left(\frac{h}{5.5\ ft}\right) \quad \text{U.S. units} \quad (2\text{-}40)$$

where w is the projected width of backwall or diaphragm for seat and diaphragm abutments, respectively (see Figure 2-16 and Figure 2-17 for effective abutment dimensions), h=h_{bw} is the effective height of seat), h=h_{dia}^{*} is the effective height of diaphragm abutment if the diaphragm is not designed for full soil pressure, and h= h_{dia}^{**} is the effective height of diaphragm abutment if the diaphragm is designed for full soil pressure (Figure 2-16). For seat-type abutments, the effective abutment wall stiffness should account for the expansion hinge gaps as shown in Figure 2-18.

The passive resisting pressure increases linearly with the displacement as shown in Figure 2-18. The ultimate capacity of the abutment is given by the following equation in which the maximum passive resistance of 5 ksf and the height proportionality factor are based on the ultimate static force developed in large-scale abutment tests at UCD.

$$P_{abut} = A_e \times 5.0\ ksf \times \left(\frac{h_{bw}\ or\ h_{dia}}{5.5\ ft}\right) \quad (\text{ft, Kips}) \quad (2\text{-}41)$$

where A_e is the effective abutment wall area:

$$A_e = \begin{cases} h_{bw} \times w_{bw} & \text{for seat abutments} \\ h_{dia} \times w_{dia} & \text{for diaphragm abutments} \end{cases} \tag{2-42}$$

where h_{bw} is the effective height of seat abutment, $h_{dia} = h_{dia}^{*}$ is the effective height of diaphragm abutment if the diaphragm is not designed for full soil pressure, $h_{dia} = h_{dia}^{**}$ is the effective height of diaphragm abutment if the diaphragm is designed for full soil pressure, w_{bw} and w_{dia} are the effective abutment widths corrected for skew for seat and diaphragm abutments, respectively (Figure 2-16 and Figure 2-17).

2.4. Experimental studies of non-skewed abutments

2.4.1. Maroney et al. (1994) and Romstad et al. (1995)

Maroney et al. (1994) tested two one-half end diaphragm abutments to failure at UCD and monitored their behavior to assess the validity of the assumptions often used in bridge design. According to Caltrans 1989, the initial lateral abutment stiffness was estimated as the sum of backwall stiffness and the lateral pile stiffness, using a passive wall-soil stiffness of 200 kips/in/linear foot of backwall and a pile stiffness of 40 kips/in/pile for standard 45 and 70 ton piles. Ultimate strength capacities of abutment were normally assumed to be limited to a maximum soil stress under dynamic loading of 7.7 ksf. This was based on the static shear strength of typical embankment material to be 5 ksf multiplied by (1/0.65) to account for strength increase due to higher strain rate of earthquake loading.

Two different abutment heights (5.5 ft for west abutment, and 6.75 ft for east abutment) were tested by pushing against each other, as shown in Figure 2-19. The backfill soils used behind the abutments were Yolo Loam (clayey soil) and sand for west and east abutments, respectively. Longitudinal test up to a superstructure displacement of approximately 1 in. was conducted on the smaller abutment under load control. The smaller abutment was tested to failure longitudinally under displacement control using the larger abutment as the reaction frame. Subsequently, load test was performed on the larger abutment to failure under load control in the transverse direction. Figure 2-20 and Figure 2-21 show the corresponding results of the tests.

The results of west abutment (smaller abutment) test with compacted Yolo Loam clay were further discussed by Maroney et al. (1994) and Romstad et al. (1995) (Figure 2-22). The failure surface defined a wedge length that was nearly two times the abutment height Figure 2-23).

According to Maroney et al. (1994), the loads carried by the piles were removed from the load-displacement of total system of west abutment, based on experimental load-deformation data for free and fixed head piles by Griggs (1993). Then the reduced stiffness values were normalized by 10 ft width of abutment and multiplied by 8/5.5 to adjust for the backwall height, as shown in Figure 2-24. The data points in this figure showed that abutment stiffness of 200 kip/in/ft previously used in Caltrans design equations was too high when compared to test results. However, the abutment stiffness could be equal to 200 kip/in/ft only at very small displacements.

The measured ultimate strength was 325 kips compared to the one predicted based on the free body diagram of soil wedge, which was 366 kips. These values compared well with Caltrans estimate of 5*10*5.5=275 kips.

The above-mentioned studies by Maroney et al. (1994) and Romstad et al. (1995) form the basis for the revised abutment-related design considerations in the current Caltrans, SDC 2010.

2.4.2. Duncan & Mokwa (2001)

Duncan & Mokwa (2001) tested an anchor block of dimensions 3.5 ft high, 6.3 ft wide, and 3.0 ft thick at Virginia Tech (Figure 2-25). The block was pushed first against natural soil consisting of hard sandy silt and sandy clay and then against compacted gravel backfill. Prior to the second test, the natural soil was excavated to a depth of 3.5 ft for a distance of 7.5 ft from the block face extending 1.5 ft beyond each edge of the anchor block. The actuator pushing against the anchor block reacted against a pile group with a concrete cap. The failure zone in the soil was not confined laterally and hence was three dimensional in geometry. For the first test performed in the natural soil, a scarp parallel to the wall face was observed at a distance of about 6.0 ft from the anchor block. During the second test, a failure surface developed 7.0 ft from the anchor block face in the loading direction.

The test data were compared to the results computed using three theories of Coulomb, Rankine, and log-spiral methods, with and without correction for 3D end effects. The log-spiral theory considering 3D effects correction resulted in the best agreement with the experimental results. 3D effect correction was done based on Ovesen-Brinch Hansen method (Ovensen, 1964 and Brinch Hansen, 1966). The ultimate passive resistance computed as a result of 3D effects is higher than that those computed from conventional theory. Figure 2-26 displays the comparison between the measured and calculated passive loads of two tests based on log-spiral theory corrected for 3D effects. The correlation between the experimental and analytical data was favorable.

2.4.3. Rollins & Sparks (2002)

Rollins & Sparks (2002) tested a pile cap of 9ft×9ft and 4 ft deep as shown in Figure 2-27. The cap was supported by a 9-pile group in saturated low plasticity silts and clays and backfilled with compacted gravel in the loading direction.

Resistance was provided by friction at the base of the cap, pile-soil-pile interaction, and passive resistance of the backfill. The ultimate passive resistance was computed based on methods of log-spiral, Coulomb, Rankine and Caltrans (1988) accounting for an effective width beyond the edges of pile cap. The method proposed by Ovensen & Stromann (1972) was used to calculate the effective width that was larger than the actual width of the pile cap. Log-spiral method provided the best agreement with test results. The Rankine method underestimated the resistance by a factor of approximately 3.5. Coulomb method overestimated the capacity by a factor of 2 due to high wall friction. The Caltrans method gave an equivalent coefficient of passive pressure that was 65% higher than the Rankine estimate, but only one-half of the log-spiral value. Therefore, the Caltrans method was still found to be conservative. Figure 2-28 shows the load-displacement curve for different components and the total system. For the case of passive resistance, the load was calculated using the log-spiral method. The displacement to fully mobilize the passive resistance was about 6% of the cap height, which is larger than that reported in other studies. This was attributed to the underlying clay layer.

2.4.4. Rollins & Cole (2006)

Rollins & Cole (2006) performed full-scale static and cyclic tests on a 10ft×17ft pile cap with a height of 3.67 ft on a pile group driven in cohesive soil. The pile cap was placed on a 3×4 group of 12 in. diameter steel pipe piles, as shown in Figure 2-29. The tests were designed to investigate the passive resistance of the pile cap in four different types of backfill including clean sand with small amount of silt, silty sand, fine gravel and coarse gravel.

Seven tests were performed including four cyclic tests for different backfill soils, two tests without the backfill, and one test with a trench excavated between the pile cap and the backfill soil.

For clean sand, fine gravel, and coarse gravel tests, the passive resistance was fully mobilized at displacements between 3.0 and 3.5% of the pile cap height. The silty sand tests required higher wall displacement equal to 5.2% of the cap height to fully mobilize the passive resistance, which could be explained by the significantly higher fines content in comparison to the other backfill types. Figure 2-30 shows the observed cracking and bending of polystyrene columns along with the sliding surface based on log-spiral theory, which were generally in good agreement.

The passive force-deflection curves were derived by subtracting the resistance provided by the pile cap without backfill from the total force-deflection curve. Figure 2-31 depicts the measured backbone curves of passive resistance versus deflection for each backfill test along with the reload curves for several deflection increments. The general shape of the first-cycle passive resistance curves is similar for clean sand and silty sand tests with an initial linear slope. Very little passive force is developed until the closure of the gap between the pile cap and backfill upon reloading, but the passive force substantially increases afterwards. For fine gravel and coarse gravel tests, the initial portion of the curve is concave upward and changes more gradually before transition into backbone curve.

2.4.5. Nelson et al. (2007) and Saiidi et al. (2012)

Nelson et al. (2007) tested a quarter-scale 4-span bridge under bidirectional earthquakes along with the application of hydraulic actuators to simulate the abutment movements. Figure 2-32 shows an overview of the bridge model. There was no soil used in the model. Shear keys were not included in the model since they are sacrificial elements under moderate and strong motions. Figure 2-33 shows the abutment system of the test model. Results showed that damage was concentrated in plastic hinge regions of column, while bent caps and superstructure remained elastic. The shortest bent failed but still continued to carry vertical loads.

To determine the effect of coupling between the transverse and longitudinal direction, bent top particle movements relative to the tables were examined. The dominant direction of movement was toward the east for Bent1 and toward the west for Bent3, due to significant in-plane rotation during high-amplitude runs (Figure 2-34).

A new indicator of coupling was introduced as the ratio of OA over OB which is 0.7 for circular movements (Figure 2-35 (a)). Results showed that the degree of coupling between the longitudinal and transverse motions was relatively high for all bents, which indicates the response of the bents was biaxial Figure 2-35 (b).

Despite zero skew angle, the superstructure-abutment interaction led to locking of superstructure end and large in-plane rotations that caused significant residual displacement. Residual displacements were observed starting form Run 5 for Bent1 and Bent3. This trend continued for higher amplitude runs showing the in-plane rotation of superstructure. The in-plane rotation was found to increase exponentially with PGA in different runs (Figure 2-36).

The hysteresis loops depicted in Figure 2-37 are highly asymmetric with Bent 1 mostly oscillating in the positive direction and Bent3 in the negative direction due to large in-plane rotation.

2.4.6. Stewart et al. (2007) and Lemnitzer et al. (2009)

Stewart et al. (2007) performed a full-scale cyclic load test at UCLA on a 15 ft by 3 ft abutment wall with the height of 8.5 ft. The height of the wall in contact with the soil was 5.5 ft. The purpose of test was to simulate the seat-type abutment. The backwall was pushed horizontally into the 16-ft wide backfill with 95% compacted silty sand between the wingwalls. The abutment wingwalls were constructed using smooth plywood. Plastic sheeting was used at the interior surface of plywood to minimize the friction along the wingwalls and simulate a plane strain condition. The natural clayey soil at the site was excavated so that the failure surface would be entirely within the backfill. This test was later reported by Lemnitzer et al. (2009) in which Figure 2-38 shows the plan view and the cross section of test specimen.

The first step of the test was to push the wall with no backfill to establish the load-deflection relationship associated with the base friction. Subsequently, backfill was placed and testing was continued. Unloading was controlled to maintain the positive contact between the backfill and the wall (Figure 2-39).

The contribution of the backfill to the overall measured horizontal loads was estimated by comparing the response of the wall with and without the backfill soil. The lateral resistance of the test without backfill reached a peak value of 40 kips at a displacement level of 0.4 in. and dropped to approximately 30 kips at a displacement of 1 in. (Figure 2-40). This was consistent with the expected base resistance based on the shear strength of natural clayey soil under the wall.

The deformed wedges started to develop within the upper soil layer and extended deeper and away from the bottom of the backwall. The first and the second crack were formed at approximately 14 ft and 17 ft behind the wall, respectively. The final failure surface was formed from the bottom of abutment and intersected the backfill surface 17 ft from the wall at approximately 3 times the height of backwall (Figure 2-41).

The test data were compared with the estimated load-deflection relationship using several models as shown in Figure 2-42. Both hyperbolic model of Duncan & Mokwa (2001) and LSH model of Shamsabadi et al. (2005, 2007) predicted the shape of backbone curve. Duncan & Mokwa model overestimated the passive capacity, while LSH model could well predict the passive capacity. There are two elastic-plastic load-deflection curves in the figure. The first followed the current Caltrans SDC 2006 at that time (K=20 kip/in/ft, maximum passive pressure=5 ksf), based on the effective abutment height of 5.5 ft. This significantly underestimated the abutment stiffness because it was derived based on previous tests using clayey backfill (Romney et al., 1994 and Romstad et al., 1995). The second elastic-plastic curve was drawn using K=50 kip/in/ft with the same maximum passive pressure of 5.0 ksf and showed a better fit to the measured data.

2.4.7. Bozorgzadeh (2007) and Bozorgzadeh et al. (2008)

Bozorgzadeh (2007) tested a half scale bridge abutment at the UCSD. The dimensions of the model were 15.5 ft wide by 7.5 ft high and 1.5 ft thick (Figure 2-43). However, the backfilled abutment height was changed in different tests (Table 2-3). The wall was constructed integrally with two wingwalls that laterally confined the backfill. The backfill was sloped from the base of the wall, which forced the failure surface to occur at the transition between the backfill and natural soil. The backfill consisted of clayey sand and silty sand. The wall was pushed with five hydraulic actuators reacting against a movable reaction wall consisting of four concrete reaction blocks post-tensioned to a deep pile foundation.

The goal of the experimental program was to examine the effects of different parameters on longitudinal stiffness and capacity of abutments including the structure backfill soil type, backfill height, restraining the vertical movement of wall and pre-existing weak planes or cut slopes (Table 2-3).

The wall was restrained from any rotational movement. In Test 1, the wall was also restrained vertically by the proper configuration of actuators. The actuators in the other tests allowed the vertical movement of abutment wall to simulate a backwall that has sheared off from stemwall in seat-type abutments. The height of backfill was increased to 7.5 ft in Test 3. Also, the excavated area prior to placement of backfill was extended to a larger area. In Test 4, the backwall height was changed to 5.5 ft with a large excavation area (Figure 2-44). The second phase of research was conducted on a seat-type abutment system with a backwall separated from the stemwall and wingwalls. This test simulated a large-scale prototype abutment (Figure 2-44 and Figure 2-45).

Bozorgzadeh et al. (2008) reported that the failure mechanism in Test 1 was different from that of other tests due to the restraining of the vertical movement. Test 1 was stopped after 4 in. displacement due to reaching the maximum capacity of two actuators. In Test 1, the abutment capacity degraded under cyclic loading. The permanent displacement at the end of each half cycle showed the plastic behavior of backfill soil. In Tests 2, 3, 4 and system test, the abutment force-displacement behavior reached a peak point and then started degrading. In those tests, an inflection point occurred at approximately two times the displacement at maximum capacity. The force-displacement results shown in Figure 2-46 indicated a substantial post-peak softening behavior in all tests except for Test 1. It was concluded that the passive resistance of the structure backfill was controlled by the soil shear strength and the interface friction angle. Furthermore, it was found that the vertical movement of the wall had a significant effect on post-peak behavior of abutments.

2.4.8. Heiner et al. (2008) and Rollins et al. (2010)

Heiner et al. (2008) performed the first large-scale tests to evaluate the passive force-deflection curves for abutments with mechanically stabilized earth (MSE) wingwalls. The abutment wall was simulated with a pile supported concrete cap 5.58 ft high, 11 ft wide, and 15 ft long backfilled to a height of 5.5 ft. As a reference point, a test with backfill extending beyond the pile cap abutment was also conducted. The backfill in this case was unconfined. The backfill for both tests consisted of clean compacted sand. The MSE wall panels were 12 ft by 5 ft and 6 in. and the MSE wall on either side of the cap was 5.5 ft tall and 24 ft long. For the unconfined backfill, the area behind the cap was excavated about 1.5 ft below the bottom of cap for a distance of 8 ft and then sloped at 1V:3.5H at an elevation equal to the bottom of pile cap. The excavation extended 5 ft beyond the width of the pile cap to allow for 3D end effects of failure wedge. Figure 2-47 and Figure 2-48 depict plan and elevation views of the tests for MSE wall confined backfill and unconfined backfill, respectively.

The pile cap was loaded using hydraulic actuators in approximately 0.25 in increments of pile cap deflection. Heiner et al. (2008) and Rollins et al. (2010) reported that for the MSE wall confined backfill, parallel cracking occurred within 4 ft of the pile cap face as well as perpendicular cracking from 4 to 22 ft from the cap pile face. The walls moved outward engaging the grid reinforcement allowing cracks to occur parallel to the MSE walls. For the unconfined backfill without the MSE walls, radial cracks beginning near the corners of the pile cap were formed up to a distance of about 4 ft from the pile cap face. This indicated the 3D end effect resulting in an effective failure surface width of 18 to 19 ft. Although significant difference was observed between the widths of the effective soil wedge, the maximum vertical heave for both tests was about 1.25 in and occurred 6 ft from the pile cap face near the center. The crack pattern for the unconfined backfill is typical of a three-dimensional failure, while the one for the backfill with MSE wingwalls is more typical of a two-dimensional failure in a plane strain condition (Figure 2-49).

Figure 2-50 shows the total and passive force-displacement curves for both backfills. At the maximum deflection of the unconfined backfill of 2.5 in., the total resistance provided by the pile cap and backfill with MSE walls was 80% of that provided by the pile cap with unconfined backfill. The passive resistance for each test was computed by subtracting the resistance provided by the pile cap system without backfill from the total resistance. At the ultimate state, the MSE wall confined backfill developed 76% of the passive resistance provided by the backfill without wingwalls. The increased passive force for the unconfined backfill was due to the increased effective width of the pile cap. The ultimate passive resistance occurred at pile cap deflections of 4.2% and 3.8% of the wall height for the MSE-confined and unconfined backfills, respectively. These measured values were greater than the range of 3.0 to 3.5% for the full-scale lateral pile cap tests in dense sands and gravels reported by Heiner et al. (2008).

The measured ultimate passive force was compared with different models of Rankine, Coulomb, log-spiral, hyperbolic, and Caltrans. For the MSE wall confined backfill, the cap width was 11 ft. However, the effective width of unconfined backfill was computed equal to 19.6 ft, using the correction method of Brinch Hansen (1996), which accounts for 3D shear effects at the ends of cap. Table 2-4 shows the calculated forces reported by Heiner et al. (2008). The log-spiral methods with the allowance for shearing beyond the edge of the cap provided excellent estimates of passive force for the unconfined backfill. However, it underestimated the passive force for the backfill with MSE wingwalls by 36% because it did not account for confinement effects provided by MSE walls. The higher passive force could be adequately accounted for by using a higher plane strain friction angle of 42.6º rather that the triaxial friction angel of 39º. The

Caltrans method provided an excellent estimate of the ultimate passive resistance for MSE-confined backfill, but underestimated the ultimate passive resistance for the unconfined backfill since it does not account for 3D shearing effects at the edges of the pile cap.

Passive force-displacement curves were calculated using hyperbolic method (Duncan & Mokwa, 2001 and the Caltrans method (Caltrans, 2001) to compare with the measured curves. Figure 2-51 and Figure 2-52 show the computed and measured passive force-deflection curves for the unconfined backfill and the MSE confined backfill. The Caltrans method using an initial stiffness of 20 kips/in per foot of width underestimated the initial stiffness by a factor of 2. The hyperbolic model provided a reasonable estimate of the initial stiffness in both cases as well as a reasonable fit to the curve for the unconfined backfill. Neither method could match the overall shape of the measured response due to flattening of the measured curve, possibly caused by cyclic loading especially for the MSE-confined backfill.

2.4.9. Wilson & Elgamal (2008), Wilson (2009) and Wilson & Elgamal (2010)

Wilson & Elgamal (2008), Wilson (2009), and Wilson & Elgamal (2010) performed large-scale tests of densely compacted sand with 7% silt content behind a test wall to derive the passive earth pressure load-displacement curves and calibrate their FE model. The first test was conducted in a dry condition of 20 days after construction, while the second test was conducted 3 days after construction. Figure 2-53 and Figure 2-54 show the schematic and field test setup.

The passive resistance increased until the peak point at displacement of 2.7% and 3% of backfill height and then decreased to a residual level of 55% and 65% of the peak value at a lateral displacement of 8% of backfill height for Test 1 and Test 2, respectively (Figure 2-55).

Due to the low wall-soil friction, a triangular failure wedge shape was observed. Test 1 resulted in higher passive resistance at a lower displacement. Test 1 curve showed a sharp peak followed by a rapid reduction in passive resistance, while Test 2 showed a more rounded peak with a gradual degradation of passive resistance. The distance of observed surface scarp from the wall was less than 16.4 ft m and about 13 ft in Test 1 and Test 2. Shear strength characteristics were measured according to the test results and force equilibrium for the failure wedge. The estimated in-situ shear strength characteristics of Test 2 backfill showed a lower Φ and higher c than the drier backfill of Test 1.

The measured peak passive resistances in Tests 1 and 2 were compared to the earth pressure theories of Rankine, Coulomb and Log-Spiral. Using the in-situ shear strength characteristics, both Coulomb, and log-spiral theories resulted in very good prediction with a slight underestimation of the peak passive resistance. Rankine theory underestimated the peak passive resistance in all cases.

Finally, as shown in Figure 2-56, FE model which was calibrated based on the experimental results of Test 2 was used to provide force-displacement curves for a larger abutment with a higher soil-wall friction. The low δ is representative of relatively light structures with vertical movement during passive loading. In a larger abutment or one supported on piles, vertical movement may be restrained. Results for two additional backfill soils of SM (silty sand) and SC (Clayey sand) are displayed in the figure to show the potential range of variation for a relatively soft and stiff response. These two curves are based on the results of laboratory tests on soils used in abutment backfills (Earth Mechanics, Inc, 2005).

2.5. Experimental studies of skewed abutments

2.5.1. Jessee (2012), Rollins & Jessee (2012), and Jessee & Rollins (2013)

Rollins & Jessee (2012) performed experimental tests on abutment-soil system with 4 different skew angles to investigate the passive force-deflection curves for skewed bridges. Tests were performed on a wall 4.1 ft wide 2 ft high with skew angles of 0º, 15º, 30º, and 45º and backfill of dense compacted sand. The sand was compacted to reach an average relative compaction greater than 95%. The sand backfill was extended 1 ft below the base of the wall to allow for a possible log-spiral failure surface. The backfill was 10 to 13 ft long and 4.2 ft wide, slightly exceeding the width of the wall (Figure 2-57).

Figure 2-58 shows the measured curves of passive force versus backwall displacement for different skew angles. There were two or three identical tests for each skew angle. The figure indicates that as the skew angle increased, the passive force decreased significantly with 50% reduction at skew angle of 30º, while the initial stiffness remained unchanged. Reduced passive force in skewed abutments would be important for bridges under seismic forces or integral abutments subjected to thermal expansion. The passive force reduction may be due to the fact that a smaller part of the backfill soil is mobilized. Other factors may also contribute to the reduced force. Additional large-scale tests and calibrated numerical analyses are required to properly explain the causes of the reduced capacity.

The shape of passive force-deflection curve transitioned from a hyperbolic shape to a bilinear shape in skewed abutments. As the skew angle increased, the passive force showed a longer plateau where the force remained constant or gradually increased before the peak and abruptly decreased to a residual value. However, the horizontal displacement necessary to develop the peak passive force was still between 2 to 4% of the wall height and did not change consistently with skew angle. The curves show a reduction in passive force to a residual value at displacement of 4 to 6% of the wall height. While passive force reduction after the peak value was expected for the dense sand backfill, it was observed to be more abrupt for higher skew angles. The post peak residual strength ranged from 53 to 72% of the peak value with an average of 60%.

The peak passive force for each skew angle was divided by the peak value at zero skew, introducing a reduction factor as a function of skew angle as shown in Figure 2-59. Normalized data from analytical studies of skewed abutments reported by Shamsabadi et al. (2006) are also depicted in this figure and follow the same trend line. Although the trend line shows a good match with the data, however, the provided test data are limited. Furthermore, the test data are based on 2 ft high backwall which is a relatively small dimension. Large scale dynamic tests are required to address the effect of skew angle on passive force reduction.

The distance of the failure surface from the wall for the zero skew case was nearly constant across the width of sand box. However, for other skew angles, the failure surface showed a skew across the width as shown in Figure 2-60. The skewed failure surface appears to be parallel to the abutment, but no specific correlation between the angles of failure surface and abutment wall was reported by the authors. The length of failure surface behind the middle of wall ranged from 5.9 ft to 8.5 ft with an average of 7 ft.

The passive force-deflection curves computed using the computer program PYCAP and ABUT developed by Duncan & Mokwa (2001) and Shamsabadi et al. (2007). The measured and computed curves for the non-skewed case are shown in Figure 2-61. The agreement between the measured and calculated curves was very good up to the peak, but none of the methods could duplicate the post-peak decrease in passive force.

2.5.2. Marsh (2013) and Marsh et al. (2013)

The BYU large-scale field tests were performed at a test site near the Salt Lake City Airport. The test set up is shown in Figure 2-62 and Figure 2-63. The abutment was 11 ft wide and 5.5 high with a dense compacted sand backfill.

The measured passive force-displacement curves are presented in Figure 2-64. The peak passive capacity was 73% and 58% of the non-skew capacity for the 15° and 30° skew angles, respectively. The force reduction factors were similar to those of the laboratory tests by Rollins & Jessee (2012) and consistent with the reduction curve they proposed. The peak passive forces occurred at the displacement of approximately 3 to 5% of the backfill height.

Figure 2-65 shows heave contours of the backfill. The maximum heaves occurred at the corners of the abutment in the 0° and 15° skew cases. The failure mechanism was different in the

30° skew abutment in which the maximum heave occurred at a distance of approximately 4 ft from the acute corner of the pile cap. Figure 2-66 shows the failure plane in the colored sand columns in the non-skew case.

2.5.3. Franke (2013)

The large-scale abutment test set up at BYU described in the previous section was used by Franke (2013) in which the mechanically stabilized earth (MSE) wingwalls confined the backfill as shown in Figure 2-67.

Figure 2-68 presents the measured passive force-displacement relationships of the abutments. The peak passive capacity was 62% and 49% of the non-skew capacity for the 15° and 30° skew cases, respectively. These force reductions were comparable to those found by previous tests at BYU (Sections 2.5.1 and 2.5.2) and fit skew reduction curve proposed by Rollins & Jessee (2012). The peak capacity occurred at a displacement of approximately 5% and 3% of the wall height in the non-skew and skewed cases, respectively. The hyperbolic force-displacement curves by Duncan & Mokwa (2001) and Shamsabadi et al. (2007) were in good agreement with the experimental results. Figure 2-69 shows the heave contours in which the maximum heaves in the skewed cases occurred at the acute corner.

2.5.4. Palmer (2013) and Rollins et al. (2015)

The previous skewed abutment tests of small-scale (Sections 2.5.1) and large-scale (Sections 2.5.2 and 2.5.3) were performed with the abutment width-to-height ratios of 2.0. The ratio is usually much higher in real bridges. Therefore, Palmer (2013) and Rollins et al. (2015) performed tests using the same large scale pile cap of 11 ft wide and 5.5 ft high but the backfill height was lowered to 3 ft. This configuration changed the abutment width-to-height ratio from 2.0 to 3.7.

Figure 2-70 shows the passive force-displacement relationships. It was concluded that regardless of the higher width-to-height ratio, the passive forces decreased significantly as the skew angle was increased. The results from this study also fit the skew reduction curve by Rollins & Jessee (2012). The peak passive force occurred at the displacement of 3.5% and 2.75% of the backfill height for the non-skew and skew cases, respectively.

2.5.5. Smith (2014)

Two large-scale experiments were performed at BYU on the 0° and 45° skew abutments with a set up that was similar to the previous field tests (Section 2.5.2 to 2.5.4) but with reinforced concrete wingwalls. Figure 2-71 shows the test set up for the 45° skew angle. The backfill was sloped (2H:1V) beyond the abutment width.

Figure 2-72 shows the measured passive force-displacement curves for the 0° and 45° skew angles. The non-skew passive resistance was achieved at large displacement of nearly 6% of the abutment height that was different from the previous tests of abutments with wingwalls (Bozorgzadeh et al., 2008) in which the peak passive force occurred at displacement of 2 to 3% of the backwall height.

Figure 2-73 presents the capacity reduction factor of the skew abutments obtained in this study and the previous studies that fit the capacity reduction curve proposed by Rollins & Jessee (2012). The capacity reduction factor for the 45° skew angle was higher than those in the previous tests. The higher soil confinement at the obtuse corner corresponded to higher friction compared to that at the acute corner. The researcher concluded that the soil near the obtuse corner moved almost as a rigid block and simulated a skew angle of approximately 35° rather than 45° (corresponding to a capacity reduction factor of 0.46).

Figure 2-74 shows the heave contours of the backfill confined with reinforced concrete wingwalls of this study with those for the backfill configurations of unconfined and confined with MSE wingwalls. The maximum heave for the confined backfill of the non-skewed case in this study was 2.3 in. at 4 ft from the abutment face. The maximum heave for the 45° skew abutment was 1.4 in. at approximately 6 ft from the abutment face. The surface cracks near the obtuse corner showed that the rigid block of soil extended to the wingwall mid-point at 3 ft from the obtuse corner. The failure surface location was reported at approximately 14 ft from the abutment face with shear cracks associated with a heave of 0.5 to 0.75 in.

2.5.6. Wagstaff (2016)

The previous studies on the skewed abutments were focused on sand or gravel backfill material. The objective of this research was to study the passive force-displacement relationships of the skewed abutments with a backfill consisting of controlled low-strength material (CLSM). This self-leveling and self-consolidating cementitious material may work as a cost effective alternative to the conventional aggregate backfills and could save time.

The researcher performed two tests on the abutments with the skew angles of 0° and 30°. Figure 2-75 shows the test set up. The abutments were represented by reinforced concrete blocks connected to an actuator. The blocks were 4.125 ft wide and 2 ft high and placed on 11 in. high wooden support. One-in. diameter steel rollers were placed on top of the wooden support to reduce the friction between the support and the abutment. The backfill was 4.25 ft wide, 8 ft long, and 3 ft deep. The abutment and the backfill dimensions were similar to those in the laboratory test by Jessee (2012) except for the backfill length.

Figure 2-76 shows the force displacement relationships for the 0° and 30° skew cases. The displacement corresponding to the peak passive force was approximately 2% and 0.75% of the abutment height for the 0° and 30° skew cases, respectively. The displacement corresponding to the peak passive force using conventional backfill materials were 3-5% of the abutment height. The smaller displacements in the CLSM backfill was attributed to the brittle nature of this material and higher modulus compared to the conventional materials.

Figure 2-77 shows the failure planes of the backfill in the 30° skew abutment. The shape of the failure plane was similar to that in the non-skew case. A triangular wedge of the backfill seemed to move with the backwall as a rigid block. The researcher concluded that the CLSM trapped against the obtuse corner of the abutment (Figure 2-78) since the shear resistance along the abutment was much higher that the applied transverse force (P_T). Therefore, the backfill at the obtuse corner acted as an extension of the abutment and led to an effective skew angle close to zero. The failure plane occurred at approximately 6 ft from the abutment center in both cases. Figure 2-79 shows the heave contours of the backfill. Very small heaves at the obtuse corner of the 30° skewed abutment verified the researcher's explanation of the soil rigid body movement at that location.

2.6. Analytical studies of non-skewed abutments

2.6.1. Zadeh & Saiidi (2007)

Zadeh & Saiidi (2007) performed pre-test analytical studies focusing on the development of a 4-span bridge model using OpenSees, which was based on a ¼-scale 4-span bridge that was later tested at the UNR. The bridge had 4 spans with three, 2-coulmn bents and roller supports at the abutments. The column heights varied among the piers to make an asymmetric model with respect to the transverse axis. An analytical model was developed for a 2-span bridge previously tested on the UNR shake tables. The accuracy of the 2-span bridge analytical model in prediction of measured response would give an indication on how accurate the model would be for the 4-span bridge model. The 2-span bridge analytical model predicted the measured response with reasonable accuracy. The calculated displacements showed good correlation with the measured data for the entire range of amplitudes with the analytical model underestimating the measured peak displacement by 12%.

For the 4-span bridge, the force deformation relationship of abutments was derived based on the formulation proposed by Shamsabadi et al. (2005). A tensile stiffness was also defined for the backwall representing the friction force at the backwall base when it moves toward the deck equal to 10% of the soil compressive strength. Three models were used to study bridge-abutment interaction. The first model represented a bridge with no abutment interaction. In the second model, the abutment soil was represented by a nonlinear spring with the specified backwall stiffness. The spring stiffness was assigned to a zero length element to connect the backwall to a fixed point. A uniaxial elastic gap element was placed between the deck and the backwall spring to model the gap. The third model represented the actual bridge test set up with the abutment springs replaced by the actuators at the end.

Figure 2-80 shows a maximum separation of 3.4 in. between the right abutment and bridge deck recorded at about 5 seconds. No gap closure was seen after about 7 seconds and the gap size was remained close to its initial value with no significant permanent displacements.

The force transmitted between the deck and the abutment at gap closure was taken as the force in gap element. Figure 2-81 shows the instant force transmission between the deck and abutment at the times they were in contact. Figure 2-82 presents the actuator force in Model 2 and Model 3.

2.6.2. Shamsabadi et al. (2007)

The log-spiral hyperbolic (LSH) model of Shamsabadi et al. (2007) estimated the nonlinear force-displacement capacity of abutment as a function of wall displacement and soil backfill material properties. The LSH model was evaluated by comparing its results with eight experimental nonlinear force-deformation results from full-scale tests, centrifuge model tests and small-scale laboratory tests of abutments, and pile caps in different structure backfills.

This model was implemented in 3D nonlinear seismic soil-abutment interaction analyses of a simple two-span bridge using SAP 2000. The abutment-soil interface model consisted of a longitudinal nonlinear spring in series with a longitudinal gap element as shown in Figure 2-83. The spring element represented the nonlinear resistance of backfill and was assigned the hyperbolic stress-strain relationship.

Two input ground motions with different dynamic characteristics were used in the analyses to observe their effect on the abutment response. The analyses were focused on the effects of ground motions with high velocity pulses on the overall bridge response. The selected records were Northridge (Rinaldi) record with a large asymmetric velocity pulse of 61.7 in./sec resulting from near-fault effect and Kobe (Takarazu) record with a smaller velocity pulse of approximately 35.4 in./sec.

Figure 2-84 shows the displacement response of the bridge deck relative to the abutments. The peak relative displacement increased with the peak velocity increase. For the Rinaldi record, the bridge deck had a maximum large displacement of about 15 in. but a negligible permanent residual displacement at the end of the record. For Kobe record, the deck experienced a maximum displacement of about 5.1 in. with a significant residual displacement of 2.4 in. at the end of excitation. The asymmetric Rinaldi motion caused the right abutment to reach its capacity. However, under the Kobe motion neither abutment forces reached the capacity (Figure 2-85). The Rinaldi motion led to a substantial residual displacement at the right abutment and much smaller displacement at the left abutment. In contrast, the abutment residual displacements under the Kobe motion were relatively small and comparable.

Figure 2-85 presents the hysteretic force-displacement responses. The loading and unloading features reflect different dynamic characteristics of input motions. The right abutment reached the ultimate capacity at approximately 5.1 in. of deck displacement under the Rinaldi motion, while the ultimate capacities were not reached during Kobe excitation.

2.6.3. Elgamal et al. (2008)

Elgamal et al. (2008) investigated the overall response of Humboldt Bay Bridge (HBB) based on their bridge-foundation-ground model using OpenSees program. HBB is 1082.7 ft long, 32.8 ft wide, and 39.4 ft high. It is a 9-span superstructure consisting of 4 precast prestressed concrete I-girders and cast-in-place concrete slabs.

Different types of elements used in OpenSees include 3D linear elastic beam-column elements for main longitudinal I-girders and transverse braced I-beams, 3D fiber-section forced-based beam-column elements with nonlinear fiber materials for piers and piles, 4-node linear elastic shell elements for deck, and 8-node Hexahedra solid elements for soil. Soil domain depicted in Figure 2-86 was 2132.5 ft long, 495.4 ft wide, and 244.4 ft deep. Figure 2-87 shows the residual deformation of the entire system, in which the arrows indicate the directions of soil flow, heave, settlement and lateral displacement.

2.6.4. Shamsabadi et al. (2010)

Shamsabadi et al. (2010) evaluated two numerical models using data from full-scale abutment tests at the University of California, Los Angeles (UCLA) and the University of California, Davis (UCD). The first model was the log-spiral hyperbolic (LSH) model introduced by Shamsabadi et al. (2007). The second model used two- and three- dimensional FE analyses performed by PLAXIS. For FE analyses, hardening soil (HS) model available in PLAXIS was used. Figure 2-88 shows the 2D and 3D simulation of UCLA test by PLAXIS program and the calculated passive failure surfaces.

Figure 2-89 and Figure 2-90 compare the measured data and the results of simulation using LSH and finite element modeling for UCLA test and UCD test, respectively.

After validating LSH and FE simulations with the test results, the LSH analyses were extended to determine the load-deflection relationships for walls of different heights. A simple hyperbolic force-displacement (HFD) relationship developed by Shamsabdi et al. (2007) was extended to predict the backbone curves for cohesive (clayey silt) and granular (silty sand) backfills. Finally, they used the EHFD (extended hyperbolic force-displacement) equations to compare with other test data.

However, the proposed EHFD model applies only to the backfill materials that are not significantly different from those used in UCLA and UCD tests. The variation of HFD curves with parameters controlling the backfill shear strength (soil type, compacted density, water content, etc.) is the subject of ongoing work. Furthermore, nonlinear dynamic analyses of bridges would require simulation of unloading/reloading behavior of backfill soil, gapping between the backwall and backfill, wingwalls, shear keys and abutment piles, which were not considered in this study.

2.6.5. Ebrahimpour et al. (2011)

Ebrahimpour et al. (2011) developed an analytical model to simulate the interaction between the bridge and abutment based on the experimental results of the conventional 4-span bridge tested at the UNR. This quarter-scale four-span bridge was tested under biaxial horizontal motions. The ground motions were applied in seven test runs with increasing amplitudes based on the Northridge record. Emphasis was placed on the abutment-deck interaction, localized damping and the resulting residual bent displacement. The model accounted for changes in the abutment gap thickness as a result of each earthquake run.

The interaction between the deck and abutment was modeled using a ZerolengthContact3D element (Figure 2-92). This node-to-node frictional contact element is capable of developing normal and tangential (friction) forces that follow the Mohr-Coulomb law. Initially, one contact element was used at each end. Using one contact element did not account for the rotations that the abutment experienced during experiments. Further, one contact element did not fully represent the change in gap distances at each corner. Therefore, a revised version of abutment model was used in which each abutment was modeled with two rigid links and two contact elements (Figure 2-92).

The analytical and experimental transverse bent displacements matched better than a model without the abutment friction, but the measured residual displacements were larger than the calculated displacements in the last 3 tests as shown in Figure 2-93 and Figure 2-94. Having friction at all corners reduced the calculated residual displacements.

Sensitivity analyses were performed to improve the calculated results, which included changing the contact element normal and tangential penalty values, changing the pinging factors of hysteretic material of column bond-slip elements, and replacing concrete material model. No definite conclusions could be obtained. Therefore, a friction sensitivity analysis was conducted with seven cases of having friction at the corners. For active corners, friction coefficients of 0.1, 0.3, 0.5, 0.7 and 0.9 were used. There seemed to be a pattern when comparing the average SRSS values of one case to that of another case. The least values of average SRSS was for when the friction was applied at both NE and SW corners (Figure 2-95). However, due to high variability of simulated residual displacements, it was difficult to identify the exact set of friction values with the best estimation of displacements. Also, a small change in friction coefficient value resulted in significantly different results, especially for the last three tests.

Changing the damping in contact elements was not possible. The other option was changing the damping of elements representing the support blocks attached to the abutment and longitudinal actuators. By increasing the damping of support blocks and slightly decreasing damping of superstructure, the average SRSS response was slightly improved as displayed in Figure 2-96.

2.6.6. Carvajal Uribe (2011)

Carvajal Uribe (2011) developed a simple dynamic mass-spring-dashpot for integral abutment bridges (IABs) considering interaction of “near and far field” approach embankments with the bridge. The near field is assumed as a part of approach embankment in which the soil deformation is influenced by the abutment displacement. This part extends up to a distance of approximately 3 times the abutment height. The near field adds stiffness to the abutment due to the backfill soil stiffness and also connects the seismic response of far field embankment to the bridge. The far field is a part of approach embankment that is not affected by the abutment displacement or by the bridge seismic response. Interaction of far field with near field and bridge structure is called embankment-abutment-structure interaction (EASI). Four different analysis approaches to calculate the seismeic response of bridge structure were described by Carvajal Uribe (2011).

Response history analysis with continum soil models (Figure 2-97) are rearely used in engineering practice due to high demand of computational and human resources.

Response history analysis with frame-spring-dashpot model (Figure 2-98) requires that the applied input motions represent the seismic response of approach embankments in the far field. The input motions are obtained by separately modeling the embankments with specialized software for soil response analysis. The seismic response is calculated in the form of acceleration records along the embankment height. This method is rarely used in practice due to large amount of input motions which is time-consuming and not applicable to commercial software used in bridge design. Therefore, the seismic response of the embankment in the far field is commonly neglected.

Pseudo-Static analysis with frame models (Figure 2-99) is the most common technique used by bridge designers. This method requires a design spectrum and the fundamental period of the bridge. The lateral earth pressure of the backfill soil is usually determined by the Mononobe-Okabe method, which underestimates the soil pressure in moderate and high seismicity regions.

Pseudo-Static analysis with frame-spring model (Figure 2-100) is a more refined method to calculate the seismic demand by replacing the backfill and foundation with springs. However, this method neglects the far field embankments response.

The objective of the research was to provide bridge engineers with an accurate and simple dynamic model to calculate seismic demands of IABs considering embankment-abutment-structure interaction.

An analytical model (Figure 2-101) was developed using a single mass-spring-dashpot system to calculate the seismic response of approach embankments in the far field. This model was validated for four types of embankments using Pro-Shake. Finally, a three-degree-of-freedom system (Figure 2-102) was proposed for calculating the seismic response of IABs using an equivalent linear analysis. This model was validated with time history analyses of continuum soil finite element models using ABAQUS.

2.6.7. Lu et al. (2011) and Lu et al. (2012)

Lu et al. (2012) presented a recent user interface within OpenSees developed by PEER for time-history analysis of bridge-abutment-ground systems implementing performance-based earthquake engineering (PBEE) framework. This interface is available for single column bents. Eight types of abutments are implemented in this interface as described by Lu et al. (2011) and summarized below.

Elastic abutment model includes 6 translational elastic springs as shown in Figure 2-103. Roller Model shown in Figure 2-104 consists of rollers in transverse and longitudinal directions. A single-point constraint against displacement in vertical direction exists that constrains deck rotation. This model provides a lower bound estimate of the longitudinal and transverse resistance of bridge

The simplified model (SDC 2004) as shown in Figure 2-105 consists of a rigid element with the length of superstructure width, a rigid point connecting the rigid element to the superstructure and 3 longitudinal, transverse and vertical springs at each corner of abutment. The longitudinal nonlinear springs represent the gap and embankment response in accordance with Caltrans SDC 2004 (Figure 2-106):

$$K_{abut} = 11500.0\, wH\left(\frac{H}{1.7\ m}\right) \tag{2-43}$$

$$P_{abut} = 239.0\, wH\left(\frac{H}{1.7\ m}\right) \tag{2-44}$$

The transverse nonlinear springs account for wingwall and pile resistance resulted from multiplying the longitudinal backbone by C_L=2/3 and C_W=4/3 with no gap. Since flexible wingwalls are not usually fully effective, the effective width is taken as the length of wingwalls multiplied by the factor of C_L=2/3. Furthermore, the soil between the wingwalls is more effective than the exterior soil by 33%, so that the factor of C_W=4/3 is applied. These assumptions were based on several experimental tests and field inspections. The vertical response is modeled by elastic springs representing the vertical stiffness of embankment soil.

The spring model proposed by Mackie & Stojadinovic (2006) as shown in Figure 2-107 consists of participating mass corresponding to the concrete abutment and mobilized embankment soil. The longitudinal nonlinear springs account for bearings, gap, abutment backwall, abutment piles and soil backfill material. The transverse nonlinear springs represent the bearings, shear keys, abutment piles, wingwalls and backfill materials. The vertical nonlinear springs account for vertical stiffness of bearing in series with vertical stiffness of trapezoidal embankment.

The SDC (2010) sand and clay models are the simplified SDC 2004 models with parameters of SDC 2010 for sand and clay backfills, respectively.

The EPP-gap model is the simplified SDC 2004 model with user-defined parameters of stiffness, maximum resistance and gap size

The HFD model utilizes the hyperbolic force-displacement relationship to represent the abutment resistance in the longitudinal direction (Shamsabadi et al. 2007)

Lu et al. (2012) modeled the abutment passive earth pressure resistance against bridge longitudinal displacement by the hyperbolic force-displacement relationship proposed by Shamsabadi et al. (2007, 2010). The system response was investigated for a two-span bridge with different gap sizes between the bridge and abutments. For the specific bridge that was studied, the wide gap reduced the potential cost and time of repair when the bridge experienced low to moderate levels of seismic excitation. For strong events, no significant difference was observed except for a slightly higher repair cost when the gap was wide.

2.7. Analytical studies of skewed abutments

2.7.1. Shamsabadi & Yan (2007)

Shamsabadi & Yan (2007) developed a 3D bridge model to investigate the response of two bridges with 0º and 45º skew angles under the ground motions with asymmetric high amplitude velocity pulse. Such motions could led to a biased, one-sided response of bridge structure. Asymmetrical impulsive loading generates large displacements in one direction leading to a significant residual displacement and rotation of bridge structures.

3D nonlinear bridge model was developed using SAP2000. For single-span bridges, the dynamic behavior is controlled by the boundary conditions at two ends of model including the nonlinear abutment-backfill in longitudinal direction and nonlinear abutment shear keys in the transverse direction. Therefore, the bridge abutments were modeled as a set of nonlinear springs in both longitudinal and transverse directions as shown in Figure 2-108. Three types of bridges were studied including a single-span bridge, a 2-span bridge with a single-column bent and a 3-span bridge with single-column bents.

For the case of single-span bridge under a seismic event, the deck imposes time varying pounding forces and displacement directly to the bridge abutments in both horizontal directions. The single-span bridge was modeled with skew angles of 0º and 45º. Interaction between abutments and backfill was modeled by two rows of four nonlinear springs at each abutment, oriented normal to the backwall (Figure 2-109). The two rows of springs were placed at the deck level and at the soffit level. This set of nonlinear springs was chosen to simulate the soil-abutment system behavior during a dynamic analysis.

Figure 2-110 shows the results for the non-skew case. Despite the presence of biased velocity pulse in the longitudinal direction, the normal passive forces were distributed uniformly along the width of abutment. The abutment backwall provided resistance during the entire shaking without any significant bridge rotation. The bridge deck continued pounding on spring D while it had stopped pounding on other springs, which caused a slight rotation of bridge deck. The residual displacement of abutment-backfill was about 2.5 in. (a net displacement of 1.5 in. considering the 1-in. expansion gap).

For the 45º skew angle, the impact between the abutment and bridge deck took place between 2 and 3 seconds from the beginning of excitation as shown in Figure 2-111. This showed that superstructure experienced significant in-plane rotations and was permanently displaced from its original position by 20 in. in the direction normal to the abutment. The normal passive forces were distributed non-uniformly along the width of the abutment due to the deck rotation resulting in a smaller amount of soil resisting force in the acute corners of the deck compared to the obtuse corners.

The single-span bridge with different skew angles was subjected to seven sets of ground motions. The results indicated that once a large rotation occurred, the deck did not return to its original position regardless of the skew angle. The decks experienced significant rotations during initial peak cycles shortly after the velocity pulses occurred as displayed in Figure 2-112. There was a clear trend between the magnitude of deck rotation and skew angle for all seven input ground motions. As the number of spans increased, the max deck rotation and the average residual deck rotation increased due to presence of columns as depicted in Figure 2-113.

2.7.2. Shamsabadi & Kapuskar (2008)

Shamsabadi & Kapuskar (2008) conducted finite element analyses to develop the nonlinear force-displacement capacity of abutment backfill with a particular focus on effect of skew angle. Investigation of skewed abutments after earthquakes showed that the passive wedge forming behind the skewed walls tend to be asymmetric along the abutment backwall due to the deck rotation. PLAXIS program was used to evaluate the development of passive resistance behind a 75 ft wide, 5.5 ft high backwall. The soil was first excavated and then the backwall was loaded monotonically using a displacement control approach in normal direction to simulate the non-skewed abutment failure mechanism as shown in Figure 2-114. The hardening soil (HS) model was used to simulate the abutment backfill material. This model is an extension of Duncan & Chang (1970) hyperbolic model combined with classical plasticity model.

The same displacement controlled FE model was used to investigate the failure mechanism of the skewed abutment with different skew angles. Figure 2-114 also shows the result for the 45º skew angle. The analysis showed that the asymmetric passive wedges behind the skewed walls could result in a reduced mobilized soil capacity as compared to the non-skewed abutments due to non-uniform loading of the backwall.

The abutment response resistance consisted of normal and tangential passive resistance due to the in-plane motions induced by pounding forces of bridge deck. These components are shown in Figure 2-115 for the 30º skew angle. In this case, the tangential component of passive resistance was about one third of the normal component.

The normal components of passive resistance are shown in Figure 2-116 for different skew angles. It shows that the mobilized passive capacity would decrease by the skew angle at large displacement levels. At higher skew angles, the capacity is significantly less than the non-skewed case capacity. This is caused by the small size of the mobilized soil in the acute corners and formation of significant heave near the obtuse corners of the deck.

2.7.3. Shamsabadi & Yan (2008)

Shamsabadi & Yan (2008) developed a 3D model for the seismically instrumented Painter Street Overpass with a skew angle of 39º based on the dynamic soil-abutment-foundation-structure interaction. It has been recognized that the seismic response of short-span highway bridges is highly influenced by the configuration and characteristics of abutments during strong excitations especially for skewed abutments.

A 3D model was developed using SAP2000 for the overpass, which is displayed in Figure 2-117. In traditional bridge design, the dynamic performance of skewed bridges is evaluated using lumped springs. When a bridge has skewed abutments, the longitudinal response is affected by transverse loading due to the coupling in horizontal directions. Dynamic interaction between the deck, abutment, and soil in the direction perpendicular to the abutment wall was modeled by a gap element and a nonlinear spring. The interaction along the skew angle in the transverse direction was modeled by a gap element, nonlinear shear key, and nonlinear soil springs. The soil-abutment-foundation-structure interaction was separately modeled by PLAXIS. The results of analyses showed that the 3D model could represent the seismic response reasonably well.

The results were substantially more sensitive to modeling of the abutments than the modeling of the pile foundations. Vertical pile-soil interaction at three supports did not significantly affect the results and may be represented by simple linear springs in similar bridge evaluations.

2.7.4. Dimitrakopoulos (2011)

Dimitrakopoulos (2011) showed that the transverse displacements and rotations after the deck-abutment collisions are not only a factor of skew angel, but also a factor of friction. They investigated the seismic response of short bridges with skew-abutment pounding joints. Studying the oblique impact of a planar skew rigid body resulted in two dimensionless skew ratios for frictionless and frictional impact:

$$\eta_0 = \frac{\sin 2\alpha}{2(W/L)} \tag{2-45}$$

$$\eta_1 = \eta_0\left(1 + \frac{\mu}{\tan\alpha}\right) \tag{2-46}$$

As shown in Figure 2-118, for η_0<1, the angular moments are in different directions with respect to center of mass and cancel out. When η_0>1, the angular moments are in the same direction and contact at the acute corner is lost. Rotation occurs due to friction when the angular moments of two impulses are in the same direction with respect to the center of mass.

The physical mechanism of the contact-induced coupling was used in a non-smooth rigid body approach capturing all states of single or multi-point frictional contact and impact with formulation of linear complementarity problem (LCP) (Figure 2-119).

Figure 2-120 presents the displacement (the first row), rotation (the second row) and the relative distance of the two potential contact points (the bottom row) response histories. The difference between the two columns in Figure 2-120 is in the geometry of contact. In the first case (η_0=0.87<1), no rotation was developed in the response history despite the numerous full-edge contacts shown in the bottom row. For the second case (η_0=1.07>1), the system vibrated in rotational degree of freedom after the first contact. The rotational response was found to be very sensitive to small changes of η_0 for values slightly more than 1. In other words, the rotation did not occur for the larger skew angle of 30º but for the smaller skew angle of 20º with larger dimensionless skew ratio (η_0>1).

A similar trend was observed for the frictional contact as shown in Figure 2-121, the history of displacement (the first row), rotation (the second row) and the relative distance of the two potential contact points (the bottom row). The two cases differ only in the coefficient of friction of μ=0.08 for left, and μ=0.10 for the right column, respectively. The close values of friction coefficient distinguish the responses around the critical value of the dimensionless skew ratio of η_1=1. For μ=0.08, frictional contact did not yield rotation, since the angular moments were in different directions with respect to the center of mass (η_1=0.99<1) and cancel out. On the contrary for μ=0.10, the angular moments were in the same direction (η_1=1.02>1) and rotation occurred after full-edge contact. Therefore, it was shown that the transverse displacements and rotations after the deck-abutment collisions are not only a factor of skew angel, but also a factor of friction as defined by Eq. (2-46).

2.7.5. Kavianijopari (2011)

Kavianijapori (2011) developed skew angled abutment models to identify the most appropriate ground motion intensity measures and propose a probabilistic method for seismic response assessment of bridges with a focus on skew angle. Three representative bridges in California were selected that are seismically vulnerable due to the skewed abutments. Variations of these bridges were developed by varying both geometrical and ground motion properties. The spine-line 3D nonlinear analytical modeling techniques were enhanced and skew angled abutment models were developed. They conducted response history analyses with three sets of 40 ground motion records and identified the most significant structural and ground motion parameters. 3D spine-line model was used with line elements located at the centroid of superstructure cross section following the alignment of bridge (Figure 2-122).

According to Figure 2-123, when the deck collides with the abutment, the rotational moment produced around the deck center of stiffness is

$$M_R = P_A e_A + P_B e_B \tag{2-47}$$

$$e_A = \frac{\left(L \times \sin\alpha - \frac{W}{\cos\alpha}\right)}{2}, e_B = \frac{\left(L \times \sin\alpha + \frac{W}{\cos\alpha}\right)}{2} \tag{2-48}$$

The eccentricity e_A has a negative value for low abutment skew angles (-0.5 for 0º skew angle). Figure 2-124 shows the effect of skew angle on eccentricity parameters. At a certain value of skew angle, the term $P_A e_A$ became positive and could increase the rotational moment expressed by:

$$\sin 2\alpha_{cr} = \frac{2W}{L} \tag{2-49}$$

Deck Rotation Index (DRI) represents the tendency of the bridge to rotate (considering equal forces at two ends) as depicted in Figure 2-125.

$$DRI = e_A + e_B \tag{2-50}$$

Three recently designed bridges in California were selected and matrices of bridges were developed to investigate the sensitivity of response to variations in bridge geometry and ground motion properties presented in Table 2-5.

Kavianijapori (2011) proposed two abutment models for skewed bridges, named "friction abutment" model and "skewed abutment" model. Friction abutment model shown in Figure 2-126 consists of a rigid element (B1) connected to the superstructure and an elastic beam element (B2) with backwall properties. TwoNodeLink element (L1) only transfers the forces perpendicular to the abutment. There are zero-length elements representing the shear key (Z1), the gap as well as the soil pressure (Z2), and shear stiffness of backfill soil (Z3). Two zero-length elements represent the stiffness of bearings in the vertical direction.

The skewed abutment model is a simple version of friction model where only three characteristics of friction model are considered including the longitudinal response of backfill (passive pressure) and gap, the transverse response of shear keys, and the vertical response of bearing pads and stemwall. Kavianijapori (2011) adopted the skewed abutment model consisting of five nonlinear springs in series with gap elements having different stiffnesses that linearly increased depending on relative location to the obtuse angle as shown in Figure 2-127. It was postulated that the maximum stiffness/strength variation occurs for the largest skew angle of 60º and it is equal to 30%. Therefore, a stiffness variation factor for a given skew angle α was computed by

$$\beta = 0.3 \times \frac{\tan\alpha}{\tan 60^{\circ}} \tag{2-51}$$

Multiple analyses indicated that the results were not highly sensitive to β. There was 2% difference on the median of deck rotation of Bridge A when β varied from 0% to 60%.

To study the trends in response parameters of skewed bridges, three parameters were considered: maximum in-plane deck rotation, maximum abutment unseating, maximum column-bent drift ratio. It was found that the resultant PGV was the effective ground motion intensity measure (IM) for skewed bridges. The shear key failure significantly affected the deck rotation. While it had less effect on other parameters. Column height may have a large effect on abutment unseating and column-bent drift ratio.

2.7.6. Shamsabadi & Rollins (2014)

Shamsabadi & Rollins (2014) performed three-dimensional finite element models using PLAXIS3D and simulated the large-scale abutment tests at BYU (Marsh, 2013). They modeled the wall and backfill using the plate elements and the Hardening Soil model in PLAXIS3D, respectively. The wall was pushed longitudinally while it was restrained in the vertical and transverse directions.

Figure 2-128 shows the displacement contours and three-dimensional passive failure wedges of the backfill obtained from the analytical models. It was noted that asymmetric soil passive wedges were developed as a result of the skew. An exponential capacity reduction factor to modify the abutment backbone curve due to the skew angle as in Figure 2-129 was introduced.

$$F_\theta = R_\theta \times F_0 \tag{2-52}$$

$$R_\theta = e^{-\theta/45} \tag{2-53}$$

where R_θ is the capacity reduction factor to modify the backbone curve for skew angle, θ, and F_θ and F_0 are the backbone curves for the skewed abutment and non-skewed abutment, respectively. This capacity reduction factor was based on the passive forces calculated from this analytical study and measured in the previous experimental studies.

2.7.7. Guo (2015)

The researcher developed three-dimensional finite element models in PLASXIS3D to simulate the test by Marsh (2013) that was discussed in Section 2.5.2. Figure 2-130 presents the analytical models developed in PLAXIS3D. The hardening soil model was used to represent the backfill.

The PLAXIS3D model was first calibrated with the experimental data for the non-skew case. Small changes were necessary in the soil friction angle and the friction between the wall and the soil. The soil stiffness was significantly adjusted to match the test data. The calibrated parameters were used to analyze the skewed models.

Figure 2-131 compares the force-displacement curves of the analytical models with those of the experiments. The correlation between the measured and calculated forces was within 10% up to the displacement of approximately 2 in. The force-displacement curve of the analytical model continued to increase after the 2-in. displacement. Therefore, the accuracy of the analytical results decreased. The calculated passive force was 10 to 20% higher than the measured data up to the displacement of approximately 1.5 in. The agreement between the analytical and experimental data improved after the 1.5-in. displacement. The calculated force in the 45° skew model peaked at a displacement of approximately 1 in. and then decreased substantially. This occurred since the analytical model was not restrained in the transverse direction and the shear forces on the abutment-soil interface exceeded the shear resistance. Therefore, the passive force was not mobilized due to the soil failure at the acute corner and the abutment sliding in the transverse direction as shown in Figure 2-132.

Figure 2-133 shows the heave contours in the analytical models. The calibrated models provided good correlation between the calculated heaves and the measured heaves shown in Figure 2-65 for all the cases except for the 45° skew due to the abutment sliding discussed in the previous paragraph.

2.8. Summary and concluding remarks

Regarding the large-scale experimental tests addressing the abutment-soil systems behavior, different test groups were briefly described. A summary of these tests is provided in Table 2-6 to Table 2-9, which present different features of the tests including different characteristics of abutment or pile cap, wingwalls, and backfill soil. For the case of abutments or pile caps, dimensions and skew angle information is provided. For the wingwalls, the dimensions and the configuration of wingwalls, along with the fact whether they were separated or integrally connected to the abutments, are presented. The properties of backfill soil and foundation include the type of backfill soil and the abutment foundation as well as the dimensions and configuration of backfill soil which demonstrate the excavation configuration. Finally, two of the most important observations of different tests are summarized in Table 2-10 and Table 2-11, the observed distance of failure surface from the abutment or pile cap face and the required displacement to fully mobilize the passive resistance of backfill soil. Both parameters were normalized relative to the backfilled height of the abutment or pile cap.

The analytical studies discussed in this chapter addressed different approaches toward simulating the interaction between the abutment and bridge superstructure through the analytical modeling of different elements for both skewed and non-skewed abutments. A summary of the analytical studies is provided in Table 2-12 and Table 2-13 including different features associated with modeling the soil-abutment interaction.

2.8.1. Important parameters of experimental tests

The soil-supported height (H) of abutment changed between 3.5-5.5 ft for the concrete block and pile caps. For the walls, the backfill height was mostly 5.5 ft consistent with the height of UCD tests upon which the current Caltrans design criteria is based. There were three cases of relatively high soil-supported abutments of 6.75, 7.5, and 8.5 ft that investigated the effect of higher backfills. For the skewed tests, the abutment height was 2 ft in the laboratory and 5.5 ft in the field testing.

For the abutments without wingwalls, the width of backfill was mostly selected slightly wider than the wall to allow the backwall to move into the backfill without any friction on the concrete sidewall. In most of the tests, the soil was extended below the base of wall to allow for a potential log-spiral failure surface.

The backfill soil length was between 1.8-5 and 4-6.5 times the backfill height for the non-skewed and skewed abutments, respectively. The results showed that the location of the observed failure surface was variable depending on different boundary conditions, excavation configuration, backfill soil properties, underlying natural soil, etc. Generally, the failure occurred at a distance of 1.7-2 times the backfill height for clayey silt, sandy silt, and sandy clay backfills. For clayey sand and silty sand materials, the failure occurred at a distance of 1.6-3.1 times the backfill height. For gravel backfills, the failure location varied at 2-3.2 times the soil-supported height. For sand backfills, the failure surface was observed at 2.8-3.9 times the backfill height. For the skewed abutment tests with sand backfill, the failure surface occurred at 2.5-4.3 times the backfilled height of abutment measured at the center line of the backfill.

For the sake of comparison, the displacement of the backwall to fully mobilize the passive soil resistance is normalized relative to the backfill height (H). This ratio was 9% for one case of clayey silt backfill. For gravel backfills, the wall displacement changed 3-6% of the height to reach the maximum passive force. For the case of sandy silt and sandy clay, the required displacement was 3.8% of backfilled height. For clayey sand and silty sand backfills, the required wall displacement was 1.9-5.5% of the backfilled height. For sand backfills supporting the non-skewed abutments, the required displacement was 2.5-4.2% of the backfilled height. For the sand backfills behind the skewed abutments, the required displacement to reach the peak resistance was 2.5-6% of the backfilled height for conventional sandy material and 0.75-2% of the height for CLSM backfill. The results for the conventional backfills is consistent with the reported range for sand backfills supporting the non-skewed abutments.

2.8.2. Issues and recommendations related to the experimental tests

Generally, most of the large-scale abutment-soil system tests were done under static loading and dynamic loading was not addressed. However, the abutment-soil systems would behave differently under earthquake shaking due to high damping of the soil. Another issue in all the previous tests is that it is assumed that there is full contact between the superstructure and the abutment under lateral loading resulting in a uniform load transfer. Actual bridge performance has shown that uneven contacts (only partial engagement) may occur between the abutment and superstructure, which could lead to significant in-plane rotations and unseating of the superstructure as in the case reported by Nelson et al. (2007). Therefore, more large-scale experimental and analytical studies are needed to address the effect of uneven contacts between the abutment and the simulated superstructure and the corresponding mobilized passive resistance of backfill soil.

Regarding the vertical movement of the abutment walls, the boundary conditions were free or restrained in all the tests. In order to fully capture the behavior of a seat type abutment, variable boundary conditions may be defined during a test. The vertically restrained condition could be changed to the vertically free condition following the failure of the base of the backwall.

The most important parameter that is yet to be studied in depth is the skew angle of the abutment. Skew angles would significantly affect the mobilized passive resistance of the backfill and the behavior of bridge-abutment-soil system due to the induced in-plane rotations of the superstructure. More tests and analytical studies are required to be performed to address skewed abutments behavior and to improve the corresponding design criteria. Another concern with the previous skewed abutment tests is that the applied loading was not a dynamic type to address the effect of dynamic soil properties such as damping.

Caltrans SDC 2010 assumes that the initial abutment stiffness and ultimate passive resistance are proportional to the height of abutment backwall. As stated in Caltrans SDC 2010, such proportionality may be revised depending on the new information that may emerge as more test data become available.

When non-skewed abutments are investigated, the role of wingwalls on the abutment-backfill interaction is routinely eliminated. However, in the case of skewed abutments, wingwalls are expected to play a significant role on the abutment-backfill interaction.

Literature review also revealed that the previous tests on the skewed abutments only simulated the wall and the backfill while the effect of impact between the superstructure and the abutment was not considered. Furthermore, all the skewed abutments were restrained against rotation which could significantly affect the abutment-soil response.

3. PRELIMINARY ANALYTICAL STUDIES

3.1. Introduction

The literature review on soil-abutment studies was presented in the previous chapter. To assess the ability of some of the available software to reproduce test data obtained in past studies and help select the software to be used for the analysis of the planned shake table test models of the current study, two programs, PLAXIS (Plaxis, B. V., 2002) and FLAC3D version 5.0 (Fast Lagrangian Analysis of Continua in Three Dimensions, Itasca, 2002) were investigated. This chapter presents the analytical modeling of the University of California Los Angeles (UCLA) test model (Stewart et al., 2007) using PLAXIS and FLAC3D programs. Different constitutive models were assigned to the backfill to identify the model providing the best correlation between the analytical and experimental results.

3.2. Simulation in PLAXIS

The UCLA test model by Stewart et al. (2007) was developed in two and three dimensional versions of PLAXIS with two soil material models of Mohr-Coulomb and hyperbolic hardening soil. These models are the basic and advanced conventional soil models, respectively, used to represent the stress-strain behavior of different types of soil. In contrast to the Mohr-Coulomb model, the hardening soil model accounts for plastic straining. The parameters for these models can be obtained from conventional tests on soil samples (PLAXIS manual).

The UCLA abutment wall was 15×8.5×3 ft with a height of 5.5 ft in contact with the soil. The force-displacement analyses were conducted and the results were compared with the experimental data. Four different options of mesh size including coarse, medium, fine, and very fine are available in PLAXIS. Figure 3-1 presents the UCLA test models with different mesh sizes in PLAXIS3D Foundation. A similar mesh size pattern was applied to the two dimensional version of the program, for which the results are shown in the next sections.

Shamsabadi (2007) performed 2D and 3D analytical modeling using PLAXIS to simulate the UCLA, UCD (University of California Davis), and BYU (Brigham Young University) tests and found good correlation between the experimental and analytical force-displacement curves using the soil hardening model. The UCLA test was re-simulated in the current study to compare the results with those from Shamsabadi (2007) and FLAC3D modeling.

3.2.1. Mohr-Coulomb model

Mohr-Coulomb model in PLAXIS, along with an elasto-plastic model with a fixed yield surface, was first used to simulate the UCLA test. The fixed yield surface is fully defined by the model parameters and not affected by plastic straining. The Mohr-Coulomb model includes a limited number of soil model features which can be obtained from basic tests on soil samples (PLAIXS manual).

The soil material parameters defined in the analyses are shown in Table 3-1. The properties of interface elements between the soil and the structure in PLAXIS are assigned based on the adjacent soil properties by using a strength reduction factor, R_{int}, according to the following equations:

$$c_{\text{int}} = R_{\text{int}}.c \tag{3-1}$$

$$\tan\phi_{\text{int}} = R_{\text{int}}.\tan\phi \tag{3-2}$$

where c and ϕ are the soil cohesion and friction, and c_{int} and ϕ_{int} are the interface cohesion and friction, respectively.

3.2.2. Hardening soil model

In contrast to an elasto-plastic model, the yield surface of a hardening plasticity model is not fixed in principal stress space and can expand due to plastic straining. The hardening soil model is an advanced model for simulating different types of soil and includes both shear hardening and compression hardening. Shear hardening and compression hardening are used to model irreversible plastic strains due to primary deviatoric loading and primary compression in odometer loading, respectively. The hardening soil model is an extension of the hyperbolic model by Duncan & Chang (1970), but uses the theory of plasticity rather than the theory of elasticity and includes the soil dilatancy (PLAXIS manual). In this model, the relationship between the vertical strain, ε_1, and the deviatoric stress, q, is defined by the following hyperbolic formulation:

$$-\varepsilon_1 = \frac{2-R_f}{2E_{50}}\left(\frac{q}{1-q/q_a}\right) \text{ for } q < q_f \tag{3-3}$$

where q_a is the asymptotic value of the shear strength, R_f is the failure ratio of $\frac{q_f}{q_a}$ and E_{50} is the secant modulus at 50% strength (Figure 3-2) defined as follows:

$$E_{50} = E_{50}^{ref}\left(\frac{c\cos\phi + \sigma'_3 \sin\phi}{c\cos\phi + p_{ref}\sin\phi}\right)^m \text{ for } q < q_f \tag{3-4}$$

where E_{50}^{ref} is a reference stiffness modulus corresponding to the reference confining pressure of p_{ref}, σ'_3 is the confining pressure in a triaxial test, and m is the power defining the extent of stress dependency. The ultimate deviatoric stress, q_f, based on the Mohr-Coulomb failure criterion is defined by:

$$q_f = \frac{(c\cot\phi + \sigma'_3)2\sin\phi}{1-\sin\phi} = \frac{2c\cos\phi + 2\sigma'_3\sin\phi}{1-\sin\phi} \tag{3-5}$$

Figure 3-3 compares the force-displacement relationships of UCLA test analyses for the two- and three- dimensional analysis versions of PLAXIS using the hardening soil model. The force-displacement result by Shamsabadi (2007) using PLAXIS3D is also plotted for comparison. The results showed good correlation between the 2D and 3D analyses and the test data. Additional sensitivity analyses were performed using the PLAXIS2D. Figure 3-4 presents the effect of mesh size on the force-displacement relationships of the UCLA test model using the soil hardening model. The results showed that the PLAXIS2D analyses were not significantly sensitive to the mesh size but the maximum capacity was slightly reduced when a finer mesh was used.

Figure 3-5 compares force-displacement results among the analytical models of the UCLA test in PLAXIS. The results are only shown for the coarse mesh size since the mesh size did not affect the results significantly. To investigate the effect of modeling the interface, the wall and the interface elements (slip elements) were not included in some of the studies. The comparison showed that the capacity was reduced when the slip elements were used to account for the friction between the soil and the wall. The hardening soil model was less sensitive to modeling the interface than the Mohr-Coulomb model. The hardening soil model led to the best correlation with the test data. The initial stiffness from the Mohr-Coulomb model was significantly larger than that from the experimental results. The PLAXIS2D model with the wall and interface material could be considered as an upper-bound level for the UCLA test data.

3.3. Simulation in FLAC3D

FLAC3D (Itasca Consulting Group Inc. 2012) is a numerical modeling code for advanced geotechnical analysis of soil, rock, and structural support in three dimensions. FLAC3D utilizes an explicit finite difference formulation that can model complex behaviors that are suited to finite element codes, such as problems that consist of several stages, large displacements and strains, non-linear material behavior and unstable systems. FLAC3D could be used for both two and three dimensional analyses. Soil-abutment systems were not previously modeled by other researchers using FLAC3D program. The objective of the analysis in this study was to evaluate the applicability of FLAC3D to these types of soil-structure interaction problems.

A force-displacement analysis of the UCLA test model was conducted using FLAC3D under the plane-strain condition. Three soil models were used in the analyses using the conventional Mohr-Coulomb model in which the tangent modulus was changed. The models were developed using the initial tangent modulus, the modified stress-dependent tangent modulus using Duncan hyperbolic model, and an average stress-dependent tangent modulus.

A direct displacement-control loading is not an option in FLAC3D. A prescribed loading rate referred to as "velocity" is applied to the prescribed nodes for a given number of steps. A small velocity multiplied by a large number of steps defines a given displacement. An initial velocity of 3.94×10^{-5} in./sec (10^{-6} m/s) with 10^5 load steps was applied to the wall. This combination simulated a wall displacement of 3.94 in. (0.1 m) into the backfill, which was measured in the test.

Three mesh sizes of coarse, fine, and very fine were used in modeling the UCLA test. The mesh sizes in the *x* and *z* (longitudinal and vertical) directions were 18.2 and 16.4 in. for the coarse, 9.0 and 9.7 in. for the fine, and 5.0 and 4.7 in. for the fine mesh, respectively. Figure 3-6 shows the UCLA test model in FLAC3D with a very fine mesh.

3.3.1. Mohr-Coulomb model

The elasto-plastic Mohr-Coulomb model with the initial tangent modulus was first used to model the backfill soil. Gravity loading was initially applied to the abutment wall-soil system. Then, the lateral displacement loading was applied in the longitudinal (x) direction. Displacement contours in *x* direction are shown in Figure 3-7 clearly indicating the soil passive failure wedges.

3.3.2. Duncan hyperbolic model

Soil stiffness gradually decreases when it is subjected to deviatoric loading. In special case of a drained triaxial test, the stress-strain relationship can be approximated by a hyperbola. Such a relationship was first formulated by Kondner (1963) and later used in the hyperbolic model by Duncan & Chang (1970).

The objective was to modify the Mohr-Coulomb model to simulate the stress-dependent properties. Therefore, the Duncan hyperbolic model in conjunction with Mohr-Coulomb failure criterion was used to model the backfill soil. The Duncan hyperbolic model was modified using the parameters of strain hardening model available in PLAXIS program. The basis of hardening soil model in PLAXIS program is the hyperbolic relationship between the vertical strain and the deviatoric stress in triaxial tests (Figure 3-2) according to the following formulation for the initial stiffness, E_i:

$$E_i = \frac{2E_{50}}{2 - R_f} \tag{3-6}$$

The soil tangent modulus was evaluated according to the above hyperbolic relationship for each element depending on the stress level in each load step based on the FISH function option available in the FLAC3D program. FISH is short for "FLAC-ISH" or the language of FLAC. The FISH function is a built-in scripting language that gives the user control over different program operations. It enables the user to modify or reset conditions (e.g. stresses, strains, and strength and modulus properties) during execution.

3.3.3. Mohr-Coulomb model with average tangent modulus

Another study on soil model was made using the Mohr-Coulomb model with a constant average tangent modulus based on the following relationship. This modification could significantly reduce the computational efforts and eliminate the necessity to use the FISH functions to modify the Mohr-Coulomb parameters.

$$E_{ave} = \frac{1}{2} E_i = \frac{E_{50}}{2 - R_f} \tag{3-7}$$

The constant average young modulus was calculated for a mid-height soil element using Eq. (3-4). The goal was to estimate a constant average value for E-modulus that was close to E_{50}.

Figure 3-8 compares the force-displacement relationships for the UCLA test model using different models in FLAC3D. In contrast to PLAXIS, FLAC3D results were sensitive to the mesh size. The force estimates decreased for the finer mesh. The initial stiffness did not match the experimental data when the initial tangent modulus was used but it was significantly improved when the average tangent modulus or the Duncan model was used. The Mohr-Coulomb model with the average tangent modulus overestimated the capacity while using Duncan model underestimated the capacity.

Figure 3-9 shows the comparison of force-displacement relationships for the UCLA test using an average tangent modulus for the backfill. The force-displacement result by Shamsabadi (2007) using PLAXIS3D is also plotted for comparison. As previously concluded, the PLAXIS2D results were not sensitive to the mesh size. The FLAC3D model with very fine mesh led to the best correlation with PLAXIS2D results. The results from PLAXIS2D and FLAC3D overestimated the capacity by 10% compared to the test data at 2-in. displacement. The overestimation was higher for larger displacements since the test data reached a plateau but the curve continued with upward slope.

3.3.4. Comparison of PLAXIS2D and FLAC3D results with earth pressure theories

A sensitivity study was conducted using the average tangent modulus with different properties of soil-wall interface to determine the effect of these properties on the results from PLAXIS2D, FLAC3D, and earth pressure theories of Rankine, Coulomb, and log-spiral. The objective was to evaluate the average tangent modulus method compared to the conventional earth pressure theories. The backfill geometry was the same as that in the UCLA test, but the interface properties were different.

Table 3-2 shows the soil and interface properties. The maximum passive capacity from the earth pressure theories is compared with that from the PLAXIS2D and FLAC3D models. The best correlation between the PLAXIS2D and FLAC3D models was for "Sand-Int2" when the friction angle of the vertical interface was non-zero. For the two other cases, the wall and the interface were not modeled in PLAXIS2D since the interface reduction factor could not be set to zero. The corresponding force-displacement relationships for "Sand-Int2" are presented in Figure 3-10. The passive resistances given by the Coulomb and log-spiral earth pressure theories are also included in the figure. The Coulomb method overestimated the passive capacity but the log-spiral method estimation was in good agreement with both PLAXIS2D and FLAC3D models.

3.4. Concluding remarks

PLAXIS and FLAC3D could reasonably estimate the passive capacity of abutment backfill for the UCLA test model with good correlation with the test data. The results were comparable to those from the log-spiral earth pressure theory when the wall and the interface elements were included in the models.

The strain hardening model in PLAXIS estimated the force-displacement relationship of the UCLA test model with good correlation with the test data. The Mohr-Coulomb model with a constant average stress-dependent modulus led to the best match between the results of PLAXIS, FLAC3D, and earth pressure theories. This model overestimated the capacity when compared with the test data but could be considered as an upper-bound estimate compared to the experimental results.

4. ANALYTICAL STUDIES FOR PRELIMINARY DESIGN OF SHAKE TABLE TESTS

4.1. Introduction

A conceptual design of the shake table models with 0º, 30º, and 45º skew was developed. The models were analyzed using Open System for Earthquake Engineering Simulation (OpenSees, McKenna, 2011). This chapter presents the pre-test analytical modeling of the test models to evaluate the feasibility of the models before the design was finalized. Final details of the test models are presented in Chapter 5.

4.2. Conceptual design

Figure 4-1 shows the schematic test set up for the three shake table test models with skew angles of 0º, 30º, and 45º. An approximately 86-kip block resting on six lead rubber bearing isolators simulated the bridge superstructure, referred to as the "bridge block". The bearings simulated the substructure flexibility. A 25 ft long by 19 ft wide engineered backfill soil including embankments represented the abutment soil. The backfill soil was placed in a stationary timber box adjacent to the shake table on steel frame modules. Three, 5.5-ft high reinforced concrete walls at three skew angles of 0º, 30º and 45º with a projected width of 10 ft in the direction of motion represented the abutment backwalls in the test models. One of the four shake tables at the University of Nevada, Reno (UNR) was used to simulate earthquake motions to the structure-abutment-soil system in the direction parallel to the sides of the soil box. The specifications of the UNR biaxial shake tables are summarized in Table 4-1.

4.3. Bearing system simulating substructure

A two-dimensional single degree of freedom model shown in Figure 4-2 was built in OpenSees to simulate the test model and develop shake-table input motion testing protocol. The bridge block and the isolators were modeled with a mass-spring system connected to a fixed boundary. An "Isolator2spring" section available in OpenSees represented the six isolators.

The Isolator2spring model shown in Figure 4-3 was used to capture the bilinear behavior of the isolators. Axial flexibility is modeled by an additional spring in the vertical direction (not shown in the figure). The behavior of the nonlinear shear spring is shown in Figure 4-4 and defined by the initial stiffness, k_1, yield strength, F_{yo}, and post-yield stiffness, k_{2o}. The rotational stiffness, K_r, is defined by:

$$K_r = P_E h_b \tag{4-1}$$

where P_E is the Euler buckling load based on the bending stiffness, EI, and the bearing height, h_b, as in the following equation:

$$P_E = \frac{\pi^2 EI}{h_b^2} \tag{4-2}$$

The nominal shear stiffness and vertical stiffness are respectively defined by:

$$K_d = \frac{GA_b}{T_r} \tag{4-3}$$

$$K_v = \frac{E_c A_b}{T_r} \tag{4-4}$$

where G is the shear modulus, E_c is the compressive modulus of elasticity depending on the shape factor, A_b is the bonded cross sectional area, and T_r is the total height of rubber. The shape factor is the ratio between the loaded area and the lateral area that is free to bulge.

4.4. Isolator properties

Lead rubber bearing isolators manufactured by Dynamic Isolation System (DIS) were used in the shake-table tests. The isolator properties are determined by rubber shear modulus, the thickness and number of layers, and the plan view dimensions of the rubber and the lead core. The number of isolators was such that they allow for sufficient lateral displacement so the soil will reach its maximum displacement capacity. The isolator details are shown in Figure 4-5. The rubber shear modulus was 60 psi as verified by isolator tests at DIS. The minimum rubber thickness of 0.25 in. was used in the isolators. The steel shims were 11-Guage A36 steel plates with equivalent thickness of 0.1196 in. The rubber bonded diameter was 11 in. excluding the ½ -in. cover. The diameter of lead core was 3.125 in. corresponding to Q_d of 8.8 kips. Each isolator incorporated 8 layers of rubber and 7 steel shims resulting in a height of 2.837 in. The cover and masonry plates were both ¾ in. thick, which resulted in a total height of 5.387 in. for the isolators. The hysteretic response of isolators tested at DIS is shown in Figure 4-6. The measured data was in agreement with the calculated values of $Q_d = 8.8$ kips and $k_d = 2.62$ kips/in.

4.4.1. Vertical capacity of isolators

The vertical stability of isolators was checked under the laterally deformed shape. The undeformed vertical capacity, $P_{cr(\Delta=0)}$, is found by the following equations (AASHTO, 2014):

$$P_{cr(\Delta=0)} = \frac{k_d H_{eff}}{2}\left[\sqrt{1+\frac{4\pi^2 K_\theta}{K_d H_{eff}^2}}-1\right] \tag{4-5}$$

$$K_d = \frac{GA_b}{T_r} \tag{4-6}$$

$$H_{eff} = T_r + T_s \tag{4-7}$$

$$K_\theta = \frac{E_c I}{T_r} \tag{4-8}$$

$$E_c = E\left(1+0.67S^2\right) \tag{4-9}$$

$$I = \frac{\pi B^4}{64} \tag{4-10}$$

$$A_b = \frac{\pi}{4}\left(B^2 - d_L^2\right) \tag{4-12}$$

$$S = \frac{A_b}{\pi B t_r} \tag{4-13}$$

where k_d is the post-yield stiffness, G is the shear modulus of rubber, A_b is the bonded area of rubber, T_r is the total rubber thickness, T_s is the total steel shims thickness, I is the moment of inertia, E is the elastic modulus of rubber, B is the bonded diameter, d_L is the lead core diameter, S is shape factor, and t_r is the thickness of single rubber layer. Typical isolators have high shape factors making the second term inside the square root of Eq. (4-5) significantly greater than 1.0. Therefore, Eq. (4-5) is simplified as:

$$P_{cr(\Delta=0)} = \pi\sqrt{k_d K_\theta} \tag{4-13}$$

This capacity is reduced with increase in the isolator horizontal displacement and can be estimated based on the overlap area method as in the following equation:

$$P_{cr(\Delta)} = \pi\sqrt{k_d K_\theta}\left(\frac{A_r}{A_g}\right) \tag{4-14}$$

where A_g is the gross bearing area, and A_r is the overlap area as shown in Figure 4-7. The variations of the vertical capacity versus the displacement for the isolators in this study is shown in Figure 4-8.

To check the vertical stability of the isolators, the vertical demand from response history analysis (Section 4.6) of the OpenSees model was compared with the vertical capacity. For the vertical demand, the acceleration response history of the bridge block was derived to estimate the mass inertial forces, which included the impact forces when the bridge block closed the gap and hit the abutment. By finding the resultant moment of inertial forces considering a lever arm equal to the distance of center of the mass to the top of the isolator, the reaction forces on the isolators were determined due to earthquake and impact forces. The lever arm of the center of the mass was approximately 2.3 ft, while the lever arm of the impact force was assumed to be 2.75 ft, which is one-half of the backwall height. Therefore, an average lever arm of 2.53 ft was used in the calculations. The reaction forces due to the dead loads were added to the forces from the earthquake and impact forces to determine the total vertical demand force. The history of vertical capacity of isolators was determined in terms of the isolator displacement from Figure 4-8. The total demand forces were divided by the capacity to determine the demand to capacity ratio (DCR).

Figure 4-9 shows the isolators force and DCR histories under Sylmar motion with an acceleration factor of 1.5. The input motion is discussed in Section 4.6. The left and right isolators corresponds to the one close to and far from the abutment, respectively. The positive and negative forces show the compressive and tensile forces, respectively. The tensile capacity of isolators was 34.9 kips based on the tensile strength of 400 psi.

4.5. Soil-abutment wall system

The backfill soil and the abutment were modeled in OpenSees using a uniaxial spring to which the "Hyperbolic Gap Material" was assigned. The Hyperbolic Gap Material is a compression-only gap element modeling the soil as a nonlinear hyperbolic force-displacement element. The hyperbolic force-displacement model was developed based on the work by Duncan & Mokwa (2001) and Shamsabadi et al. (2007) with calibrated parameters from large-scale abutment tests at the University of California San Diego (UCSD) (Wilson and Elgamal, 2008). The force-displacement relationship for the model is:

$$F(x) = \frac{x}{\dfrac{1}{K_{\max}} + R_f \dfrac{x}{F_{ult}}} \tag{4-15}$$

where K_{max} is the initial stiffness, F_{ult} is the ultimate passive capacity, and R_f is the failure ratio of the soil. The failure ratio of the soil is the ratio between the failure and the ultimate asymptotic deviatoric stress in a hyperbolic stress-strain relationship. The parameters recommended by OpenSees program are $K_{max} = 34.91\ kips/in/ft$, $F_{ult} = 22.34\ kips/ft$, and $R_f = 0.7$ for which the force-displacement relationship is plotted in Figure 4-10 for a 1-in. gap.

Figure 4-11 shows different force-displacement relationships for unit width of backfill soil. The hyperbolic force-displacement relationship (HFD) by Shamsabadi et al. (2010) for the granular soil type was selected in the current analytical study. The results from Shamsabadi et al. (2010) were presented in the LRFD reference manual by Kavazanjian et al. (2011):

$$F(y) = \frac{8y}{1+3y} H^{1.5}\,(kips, in.) \text{ for granular backfill} \tag{4-16}$$

$$F(y) = \frac{8y}{1+1.3y} H(kips, in.) \text{ for cohesive backfill} \tag{4-17}$$

where y and H are the abutment displacement and height, respectively. The OpenSees input parameters of Eq. (4-15) were determined from matching the passive capacities from Eq. (4-15) and Eq. (4-16) at the maximum displacement capacity of the soil. Table 4-2 shows the measured displacements at maximum capacities from the UCD, BYU, and UCSD abutment tests. The maximum soil displacement varied between 0.025H to 0.052H for sand and silty sand. The maximum displacement of 0.05H was selected in the current study. This criterion was also suggested by Shamsabadi et al. (2010) and the LRFD reference manual by Kavazanjian et al. (2011). The corresponding hyperbolic force-displacement parameters that were used in the OpenSees model were $K_{max} = 100\ kips/in/ft$, $F_{ult} = 25.9\ kips/ft$, and $R_f = 0.75$. The resultant force-displacement relationship is plotted in Figure 4-12 for an abutment width of 10 ft, which was used in the current study. A 2-in. gap was assigned to the Hyperbolic Gap Material to simulate the gap in full-scale bridges.

Shamsabadi & Rollins (2014) suggested the following equation for the reduction factor to be applied to the backbone curve to account for the skew angle, θ:

$$R_\theta = e^{-\theta/45} \tag{4-18}$$

Therefore, the skew reduction factors were 0.51 and 0.37 for the 30° and 45° skew models, respectively. These factors were applied to the hyperbolic force-displacement behavior of the soil spring for the skew cases of the OpenSees models.

4.6. Loading protocol

Analytical studies were conducted on the OpenSees models to design the shake table loading protocol. The motion selected for the dynamic analysis was the 142-degree record of Sylmar Converter station of 1994 Northridge earthquake, which is a near field motion with high peak ground velocity. The original acceleration, velocity, and displacement histories of the Sylmar record are shown in Figure 4-13. The intensity parameters of the original record are presented in Table 4-3.

The time axis of the original motion was compressed by a factor of 0.75 to keep the input displacement within the shake table limits. This factor was selected after several analyses with different factors in an attempt to maximize the soil displacement without exceeding the base shear transmitted to the shake table. The motion was then filtered by SeismoSignal software using Butterwort bandpass 4th order filter for the frequencies exceeding 25 Hz and those below 0.1 Hz. The acceleration and displacement histories of the filtered time-scaled motion are shown in Figure 4-14. The intensity parameters of filtered time-compressed motion with a factor of 0.75 and acceleration factor of 1.00 are presented in Table 4-4.

The loading protocol for the shake table test is shown in Table 4-5. The acceleration amplitude was gradually increased during six runs by the factors of 0.25, 0.50, 0.75, 1.25, 1.50 and 2.00 to capture the response under low to high amplitude motions. White noise tests indicated by WN in the table were conducted to determine the effective stiffness and identify any major stiffness loss of the bridge block between the tests. The estimated displacement and acceleration histories for the six runs are shown in Figure 4-15.

The "multi-support excitation" pattern was used in the OpenSees model to apply different ground motions to different supports. Therefore, the nodal responses were the absolute values. The displacement loading protocol was applied to the mass support, while there was no excitation at the fixed end of the soil spring. The positive sign of input motion was applied in the direction toward the soil.

The abutment response histories and force-displacement relationships of the isolators and abutments are presented in Figure 4-16 to Figure 4-18 for the 0°, 30°, and 45° skew models, respectively. The positive and negative displacements are away from the soil and towards the soil, respectively. The maximum isolator displacements away from the soil were 5.3, 5.1, and 5.9 in., for the 0°, 30°, and 45° skew models, respectively. The corresponding isolator displacements towards the soil were 2.6, 1.7, 3.9 in., respectively. The maximum expected displacements of the soil were 3.85, 6.37, and 8.3 in. for the 0°, 30°, and 45° skew models, respectively, with the corresponding abutment forces of 317, 178, and 126 kips.

4.7. Concluding remarks

An analytical model was developed in OpenSees to develop the shake table testing protocol. The Sylmar motion was modified using a time factor of 0.75 to ensure reaching the maximum soil displacement within the shake table limits. The expected displacements and forces of the abutment were estimated based on the loading protocol.

5. TEST MODEL DESIGN AND CONSTRUCTION

5.1. Introduction

Pre-test studies and shake table test model design were discussed in previous chapters. This chapter presents design, construction, installation, and instrumentation of the test model components including the bridge block, the abutment backwall, the soil box and the backfill soil.

5.2. Test layout

The test model consisted of four primary components: the bearings, the bridge block, the abutment backwall, and the soil box. An approximately 86-kip block resting on six lead rubber bearing (LRB) isolators simulated the bridge superstructure, referred to as the “bridge block”. The bearings simulated the substructure flexibility. A 25 ft long by 19 ft wide engineered backfill soil including embankments represented the abutment soil. The backfill soil was placed in a stationary timber box adjacent to the shake table on steel frame modules. Three, 5.5-ft high reinforced concrete walls at three skew angles of 0º, 30º and 45º with a projected width of 10 ft in the direction of motion represented the abutment backwalls in the test models. Figure 5-1 to Figure 5-3 present the plan view drawings of the test set up for the 0°, 30°, and 45° skew angles, respectively.

5.3. Bridge block system

The bridge block system consisted of the main bridge block, superimposed mass, isolators, and skew wedges for skewed cases. The “main bridge block” is referred to the concrete block that carried the additional concrete and steel mass, while its combination with the superimposed mass and the skew wedge is referred to as the “bridge block”. This section presents design and construction of the bridge block components. The installation procedure is discussed in Section 5.5.

5.3.1. Isolators

Six lead rubber bearing (LRB) isolators manufactured by Dynamic Isolation Systems (DIS) were used in this study. The isolator properties were presented in Chapter 4. The rubber bonded diameter and the total height of the isolators including the base plates was 11 and 5.387 in., respectively.

5.3.2. Main bridge block

The main bridge block was designed as an approximately 35-kip reinforced concrete block and consisted of two main parts, a wall and a slab with side walls to carry the superimposed mass components. The thickness of the wall was 18 in. and matched the thickness of the abutment backwalls. The 8-in. thick slab was designed to carry a weight of approximately 60 kips (three 20-kip concrete blocks) for the case of 0° skew. The main bridge block drawings and reinforcement are presented in Appendix A.

The target weight of the bridge block for the 0° skew test model was 95 kips close to the maximum allowable payload on the shake table. The goal was to keep the weight constant in the three skew test models. Concrete skew wedges (Section 5.3.3) were attached to the main bridge block by post-tensioned rods to simulate the skew configurations. Therefore, the superimposed mass in the skew test models were different from that in the non-skew case (Section 5.3.4). The measured weight of the main bridge block was 32.6 kips.

The maximum superimposed mass was for the case of the 0° skew angle in which three reinforced concrete blocks with the dimensions of 4×4×8 ft were attached to the main bridge block. The plan view dimensions of the main bridge block were 10 by 14.5 ft.

Two sets of four P52 swift lift anchors each with the capacity of 8 tons were installed during construction of the bridge block formwork. The anchors were used to lift the main bridge block either from the side walls or the slab. The anchors were placed so that their center coincided with the center of the mass of the main bridge block. Different holes were provided in the slab to attach different components of the LRBs the superimposed mass. Three vertical shear keys were provided on the outer surface of the main bridge block wall to prevent horizontal sliding between the main bridge block and the 30° skew wedge during post tensioning.

Figure 5-4 and Figure 5-5 show different stages of the main bridge block construction. The 7-day and 28-day cylindrical compressive strength of concrete components are presented in Table 5-1.

5.3.3. Skew wedges

Two reinforced concrete wedges were attached to the main bridge block to simulate the 30° and 45° skew effects. The skew wedge drawings are presented in Appendix A. The measured weight of the first and the second skew wedges were 25.7 and 20.2 kips, respectively. Figure 5-6 shows construction of the 30° skew wedge.

In each skew wedge, two 8-ton P52 swift lift anchors were placed on the top surface of the wedge, so that their center coincided with the center of the mass of the wedge. The skew wedges were constructed adjacent to the main bridge block using the match-cast method. Upon completion and curing, the wedges were attached to the main bridge block using post-tensioned Dywidag rods of 1-1/4 in. diameter. Therefore, six 2-1/2 in. PVC pipes were placed before pouring concrete so that they connected the main bridge block wall to the skew wedges. Six shear keys were provided between the two skew wedges to prevent horizontal slippage during post tensioning.

5.3.4. Superimposed mass

Three 20-kip, 4×4×8 ft reinforced concrete blocks were superimposed on the main bridge block in the 0° skew configuration. The measured weights of the concrete blocks were 17.6, 17.6, and 17.9 kips for the blocks from the back to front adjacent to the soil box. The combination of these components resulted in a total weight of 85.7 kips for the bridge block system while the target weight was 95 kips.

For the 30° skew case, the rear concrete block was kept in place, but the second block was replaced with steel plates. The concrete block adjacent to the soil box was removed. The required steel plates weight to reach a target weight of 85.7 kips was 9.8 kips. Nineteen 0.5-kip 3ft×4ft×1in. and two 1ft×4ft×1in. steel plates at the east side of the main bridge block were used in this case. This configuration led to the least eccentricity between the centers of the mass and stiffness of the bridge block in the direction perpendicular to the direction of motion.

For the 45° skew angle, the rear concrete block was removed from the bridge block system and replaced with steel plates. This configuration helped compensate for the overturning moment caused by the cantilevered 30° and 45° skew wedges attached to the main bridge block. The required weight of the steel plates was 7.2 kips. Fourteen 0.5-kip 3ft×4ft×1in. and one 1ft×4ft×1in. steel plates were used as the additional mass.

5.4. Abutment backwall system

The abutment backwall components include the backwall, the vertical support, the vertical restrainer system, and the lateral restrainer cables. Design and construction of these components is presented in this section. The installation procedure is explained in Section 5.5.

5.4.1. Backwalls

Three reinforced concrete walls with the height of 5.5 ft with three different skew angles of 0º, 30º, and 45º with a projected width of 10 ft in the direction of motion represented the backwalls in three skew test models. The backwall thickness was 18 in.. The width of the backwall was 10 ft, 11ft-6.5in., and 14ft-1.7in. for the 0°, 30°, and 45° skew cases, respectively. Figure 5-7 presents different stages of the backwall construction. Two 8-ton P52 swift lift anchors were installed on the top surface of each concrete wall so that their center coincided with the center of the mass of the concrete wall

5.4.2. Backwall support

A 7-1/2-in high, 10-ft long, and 18-in wide wooden platform was constructed in the 0° skew test model. The support was 11ft-6.5in. and 14ft-1.7in. long in the 30° and 45° skew cases with the same cross section as of the backwall. This platform was placed on the soil box floor to elevate the base of the backwall. This allowed for soil to extend below the base of the backwall. Figure 5-8 shows the backwall support on the soil box. Four 18×18×1/8 in. etched Teflon sheets were attached to the backwall base using a two-part BA-500 Teflon epoxy. A 1/16 in. thick Teflon sheet was nailed into the top surface of the backwall support. Figure 5-9 shows Teflon sheets at the backwall interface with the support. These Teflon sheets minimized friction at the base of the wall to allow for sliding into the backfill soil.

Figure 5-10 presents the backwall supports under the soil box. Eight 4×4 screw jacks each with 12 kips capacity were installed under the soil box since the steel frame modules could not be installed at this location close to the shake table.

5.4.3. Vertical restrainer system

The backwall was restrained in the vertical direction to simulate the actual behavior of an abutment. The restrainer system (10ft-3-3/4in. long) consisted of two in-line links (66.75 and 11 in. long), a load cell (10 in. long), and swivel connections at both sides to allow for horizontal movement of the backwall. Figure 5-11 shows the restrainer components.

The restrainer joints were attached to a steel beam (21ft-7-21/32in. long W21×55) at the top and to the backwall at the bottom. An adapter plate was used to connect the top swivel connection to the steel beam flange since the width of the swivel joint was larger than the width of the steel beam flange. A bottom adapter plate was also used to connect the swivel connection to the backwall. The swivel joint was connected to this adapter plate through four 1 in. rods in four threaded holes. The adapter plate was connected to the backwall by four 1 in. threaded rods anchored to the backwall. The steel beam was designed for a backwall vertical acceleration of 2g, and was connected to the large columns of the laboratory main safety frame (24ft-2in. long W14×159). Figure 5-12 illustrates the restrainer system drawing in the plan view for all models. The position of the columns and detailing of the beam connection to the columns were selected to yield the least possible longitudinal eccentricity between the top and the bottom swivel joints. The eccentricities were 39/64, 25/32, and 3/16 in. in the 0°, 30°, and 45° skew cases, respectively. The elevation view for of the 0° skew case is shown in Figure 5-13.

5.4.4. Lateral restrainer cables

3/8 in. diameter steel wire ropes with the capacity of 3,000 lbs. (with a safety factor of 5:1) were used as the lateral restrainer of the backwall so that the backwall could not move towards the bridge block beyond its initial position. Figure 5-14 shows the plan view of the restrainer cables in the 0° skew test.

5.5. Installation of bridge block-backwall system

This section describes the procedure of installing the bridge block and the backwall systems.

5.5.1. Bridge block system in non-skew case

The isolators and the load cells were first installed on the shake table (Figure 5-15). Six 18×30×1/2 in. base plates were placed below the isolators to engage strong bolts connected to the shake table to resist shear forces induced by the impact between the bridge block and the backwall.

Installation of the isolators and the loads cells on the shake table is illustrated in Figure 5-16. Hydrostone was applied on two of the load cells in the north side to compensate for their slightly short height. Then the main bridge block was placed on the load cells. Figure 5-17 shows the main bridge block installation. Bolts were tightened by applying 350 lb-ft torque. The next task was installing the concrete blocks as the superimposed mass inside the main bridge block, as shown in Figure 5-18. Each concrete block was attached to the main bridge block by two 1-1/4 in. Dywidag rods.

5.5.2. Backwall in non-skew case

The backwall was moved in place after installing its supports. The backwall support was installed at 2 in. from the main bridge block to provide a 2-in. gap between the bridge block and the backwall. Figure 5-19 presents the bridge block and the backwall in the 0° skew test model.

The backwall vertical restrainer link was installed next. Figure 5-20 shows the process of installing the restrainer in the 0° skew case. The links, the swivel joints, the adapter plates, and the supporting beam were assembled on the floor before installation.

During the low amplitude motions in the non-skew case, the backwall was pushed back beyond its initial position towards the bridge block. This movement occurred since the wall was supported on Teflon sheets with very low friction and led to the settlement of the soil adjacent to the backwall. The shake table had to be moved to provide a gap of 2 in. between the bridge block and the backwall to reinstate the initial test setup. This was not possible after a few runs due to the shake table displacement limit. Therefore, the test was stopped to provide a restrainer system for the backwall. The failed part of the soil adjacent to the backwall was removed using a shop vacuum and the backwall was moved to its initial position. A new backfill was placed and compacted. Figure 5-21 shows the removal and re-construction of the soil adjacent to the backwall in the 0° skew test.

Two trenches were made through the embankment slopes of the backfill at the east and west sides of the backwall using a shop vacuum. A restrainer cable was passed through the soil box walls and the trench at each side of the backwall. The cable was connected to the 1 in. threaded rod anchored to the backwall mid height in one side. The other side was connected to the soil box lateral supports (Section 5.6.3), the column of the steel frame at the east side and the concrete block at the west side. The cables were tightened after installation. Figure 5-22 and Figure 5-23 show the cable trenches and installation of the restrainer cable, respectively. The end connections of the restrainer cables are presented in Figure 5-24 and Figure 5-25. The trenches were then filled with soil and compacted. The restrainer system was effective in preventing the movement of the backwall beyond its initial position. These observations are discussed in Chapter 6 based on the measured longitudinal displacement of the backwall.

5.5.3. Bridge block and backwall in skew cases

Figure 5-26 shows installation of the superimposed mass in the 30° skew test model. The two concrete blocks close to the soil box were removed and replaced with steel plates. The 30° skew wedge was attached to the main bridge block by post tensioning six 1-1/4 in. Dywidag rods, as shown in Figure 5-27.

Figure 5-28 presents installation of the backwall on its support in the 30º skew test model. Installing the backwall vertical restrainer was similar to the non-skew case. The swivel joint was rotated to adjust for the skew angle. The locations where the swivel joint was attached to the beam and where the beam was attached to the column were also changed to minimize eccentricity between the centers of the top and the bottom swivel joints (Figure 5-29).

For the 45º skew case, the remaining concrete block in the bridge block system was removed and replaced with steel plates. Installation of the 45° skew wedge encountered some challenges. It was not feasible to move the combined skew wedges by the crane. Although four swift lift anchors on the two wedges could be used by the crane, only two of the crane chains could be engaged due to the geometry of the wedges. The combined weight of the two wedges (45.9 kips) exceeded the capacity of two chains. Modification of the crane chain system to engage all four chains was not feasible. The final solution was keeping the top Dywidag rod connecting the main bridge block and the 30° skew wedge. The rest of the post-tensioned rods were removed while the cantilevered 30° wedge was temporarily supported for safety considerations. Then the 45° skew wedge was moved in place by the crane. This required cutting the top middle shear key in the 45° wedge. Finally, the 45° wedge was connected to the bridge block by post-tensioning five Dywidag rods.

Installation of the support and the backwall in the 45° skew test model are shown in Figure 5-30 and Figure 5-31, respectively. Figure 5-32 presents the backwall vertical restrainer system after modifications similar to those in the 30° skew case.

The backwall restrainer cables in the skew cases were installed inside the soil box before placing the soil. Figure 5-33 shows the cable installation in the skew cases.

5.6. Backfill soil system

Components of the backfill soil system consisted of the soil, the soil box, the lateral supports, and the water mitigation system.

5.6.1. Soil material

A comprehensive soil test study was conducted to select the soil material. The results of the sieve analysis, Atterberg limit, Proctor compaction, direct shear and triaxial tests on five types of soil are presented in Appendix B. The Paiute Pit sand satisfied the requirements of the California Department of Transportation (Caltrans). The Paiute Pit sand is a clean sand with approximately 2% fines classified as SP (poorly graded sand) according to the Unified Soil Classification System. The maximum dry density of the sand was 107 pcf with an optimum water content of 10%. The measured shear strength parameters of friction and cohesion were 40° and 292 psf, respectively, based on the triaxial tests. 180 tons of Paiute Pit sandy soil were transferred to the laboratory site for this study.

5.6.2. Soil box

Soil box was placed on 15 steel frame modules (Figure 5-34) connected to the strong lab floor. Figure 5-35 and Figure 5-36 show the plan and the elevation views of the soil box, respectively. Plan view layout of the steel frame modules is presented in Figure 5-35 for all cases. Soil box length was 25 ft equal to 4.5 times the backwall height in the 0° skew case to prevent interference from boundary elements on the soil abutment interaction. The distance from the backwall mid width to the end of the soil box was 3.8 and 3.3 times the backwall height in the 30° and 45° skew cases, respectively. The shorter distance for the skew cases was believed to be sufficient because the zone of influence in skew cases is shorter than that for non-skew case.

The soil box consisted of 4ft×8ft×1-1/8in. Douglas-fir plywood sheets at the base and the sides. The box was connected to the steel frames using 20 shear studs (9-1/2 in. long HSS 2×1/4 in.) flushed with the soil box base. Steel tubes were designed to carry the shear at the base of the soil box and transfer the shear to the steel frame modules. The tubes were passed through the wooden base of the soil box and placed inside the 2 in. pipe sleeves (8-5/16 in. long). Configuration of the shear studs was the same in all the tests, as shown in Figure 5-35.

4×4 in. wooden studs at 2 ft spacing were designed based on the in situ soil lateral pressure and a dynamic factor of 1.75. Additional supports for the studs were also required for the lateral soil pressure demands (Section 5.6.3). 2×4 in. wooden wales were attached to the studs to confine the soil box and provide additional supports for the studs. The wales were connected at the corners using corner locks. Figure 5-37 shows construction of the soil box components. 3/8 in. threaded rod ties connected the bottom of the studs to other studs to brace them against lateral movement, as illustrated in Figure 5-38. Figure 5-39 shows the double 6 mil plastic sheeting along the sides of the soil box to minimize the friction between the soil and the box. Details of the soil box design is presented in Appendix C.

Re-configuration of the soil box was necessary for each skew case since the location of the backwall vertical restrainer system changed based on the new backwall position. Figure 5-40 shows the soil box modification from the 0° to the 30° skew test model. The north-west corner steel frame module was rotated to provide the space for the new location of the backwall vertical restrainer system.

5.6.3. Lateral supports

Additional lateral supports were necessary outside the soil box based on the soil pressure design loads. Concrete blocks were used as the lateral supports on the west and south sides of the soil box. Those blocks could not be installed at the east and north sides due to the space limitation. The north side was close to the shake table and the east side had to be left open to all for movement of the forklift for soil backfilling and removal. Therefore, external steel frames were used to support the soil box at the east and north sides. Figure 5-41 and Figure 5-42 show the drawings of the lateral supports of the soil box in the west and east sides of the 0° skew test model, respectively. The transverse section is shown in Figure 5-43.

Figure 5-44 presents the additional lateral supports installed outside the soil box. All the external supports were tied down to the strong floor of the laboratory. 4×4 in. horizontal wooden posts were installed along the height of the studs to transfer the loads to the concrete blocks or the steel frames. Additional wooden shims were used to fill any existing gaps.

A similar configuration of the external supports was used in the skew cases but the locations of the steel columns changed based on the new configuration of the soil box, the backwall, the vertical restrainer system, and the instrumentation reference frame. Figure 5-45 and Figure 5-46 show the external lateral supports for the 30° and 45° skew cases, respectively.

5.6.4. Water mitigation system

The soil in the non-skew test model was drained gradually after it was placed and compacted. This led to water leakage from the soil box, which could be problematic in the laboratory. Therefore, a water mitigation system was utilized in the skew test models.

After soil removal in the non-skew case, soil at the bottom of the box was placed and compacted so that it provided a 2.5% slope in the east-west direction. 3/8 in. plywood sheets were placed on the sloped soil for attaching water barrier sheets. A perforated pipe was installed along the east side of the soil box to direct the drained water outside the laboratory. Figure 5-47 presents the water mitigation system in the 30° skew test model. The system could direct the drained water to the east side of the soil box but the perforated pipe was not effective since the soil fines clogged the pipe.

For the 45° skew case, two types of drainage sheets (MiraDRAIN and American Wick Drain) with a compressive strength of 9000 psf were installed on top of the water barrier sheets at the bottom of the soil box. The drainage sheet is composed of a polystyrene core with a filter fabric bonded to one side. The filter fabric prevents soil intrusion into the core flow channel and allows for fast drainage. The 4-ft wide drainage sheets were placed in the north-south direction and overlapped in the east-west direction. The overlap was sealed using an adhesive sealant. Figure 5-48 shows the water mitigation system in the 45° skew test model. This system was successful in directing the water through the perforated pipe to the east-south corner of the soil box and then outside the laboratory through a drainage hose.

5.7. Structural instrumentation

Structural instrumentation included the isolator load cells, triaxial accelerometers, impact accelerometers, string potentiometers, and LVDTs. The total number of channels used in each case was 250-270 depending on the skew angle. Table 5-2 summarizes the instrumentation labeling and definitions of the structural instrumentation.

5.7.1. Triaxial accelerometers

Triaxial MEM-326 accelerometers with a capacity range of ±16g were used to measure the accelerations of the bridge block and the backwall. The layout of these accelerometers is presented in Figure 5-49 to Figure 5-51 for the 0°, 30°, and 45° skew tests, respectively.

Four accelerometers (BAC1-BAC4) were installed at the four corners on the top of the bridge block. BAC1 and BAC2 accelerometers were located near the abutment backwall at the corners of the bridge block southern edge (skewed edge of concrete wedges in the non-zero skew angles). BAC3 and BAC4 accelerometers were located at the corners of the bridge block northern edge on the top of the corresponding side wall at a height lower than that of the accelerometers near the backwall. Three accelerometers (WAC1-WAC3) were installed on the top of the backwall at the east and west edges and the center. Figure 5-52 shows the bridge block and the backwall accelerometers at the obtuse corner of the bridge block in the 30° skew test.

5.7.2. Impact accelerometers

Four PCB and four Kistler accelerometers were installed in the direction of motion at the mid-height eastern and western vertical edges of both the bridge block and the backwall to measure the longitudinal impact acceleration after the gap closure in the 0° skew test. The layout of these accelerometers (IAC1-IAC8) is presented in Figure 5-49 to Figure 5-51 for the 0°, 30°, and 45° skew tests, respectively. Since the Kistler accelerometers reached their limit of about 50g in the 0° skew test, only four PCB accelerometers (IAC1-IAC4) were used in the 30° and 45° skew models. Figure 5-53 and Figure 5-54 illustrate configuration of the impact accelerometers in the 0° and 45° skew tests, respectively.

5.7.3. String potentiometers

Four string potentiometers were attached to the top plates of north-west and south-west isolators to measure the longitudinal (BLSP1 and BLSP2) and transverse (BTSP1 and BTSP2) displacements of the bridge block. The layout of these string potentiometers are presented in Figure 5-49 to Figure 5-51 for the 0°, 30°, and 45° skew tests, respectively. Figure 5-55 shows the longitudinal and transverse string potentiometers of the backwall at the south-west corner.

Four string potentiometers (WLSP1-WLSP4) were installed longitudinally at the four corners of the backwall at the top and the bottom of the eastern and western sides to measure the backwall displacement in the direction of motion. Two string potentiometers (WTSP1 and WTSP4) were installed in the transverse direction at the top and the bottom western corners to measure the backwall transverse displacement. In addition, one string potentiometer (WDSP1) was installed on the west side of the backwall to measure the vertical displacement.

Figure 5-56 to Figure 5-58 show the backwall string potentiometers in the 0°, 30°, and 45° skew test models, respectively. WDSP1 in the 45° skew model was vertical but had to be diagonal in the other two cases due to geometric limitations. For the case of 0° skew, the diagonal string potentiometer was connected to the top west corner of the backwall at the same point that the longitudinal string potentiometer (WLSP1) was connected, so that they formed a vertical plane (Figure 5-56). In the 30° skew test model, a diagonal string potentiometer was connected to the bottom west corner of the backwall at the same point that the transverse string potentiometer (WTSP2) was connected. The diagonal and the transverse potentiometers were on a vertical plane (Figure 5-57). For the case of 45° skew model, a vertical string potentiometer was connected to the top west corner of the backwall to measure the vertical displacement directly.

5.7.4. LVDTs

Novotechnik TR100 with a 4-in. stroke was used as the position transducer to measure the vertical displacement of the bridge block (BLVDT1-BLVDT4). Figure 5-49 to Figure 5-51 present the layout of these LVDTs in the 0°, 30°, and 45° skew cases, respectively. The vertical LVDTs at the south-east and south-west isolators are shown in Figure 5-59.

Figure 5-60 shows two control LVDTs attached to the bottom plate of north-west and south-west isolators. These LVDTs were consistently checked during the tests to measure the possible slippage between the isolators and the base plates.

5.8. Soil instrumentation

Soil instrumentation included pressure cells, accelerometers, force sensors, string potentiometers, and LVDTs. Table 5-3 summarizes the instrumentation labeling and definitions of the soil instrumentation. Figure 5-61 to Figure 5-63 present the soil instrumentation plan for the 0°, 30°, and 45° skew tests, respectively. The corresponding elevation views are shown in Figure 5-64 to Figure 5-66, respectively.

5.8.1. Pressure cells

Six Geokon earth pressure cells (contact type) were installed on the surface of the backwall to measure the soil pressure. Pressure cell Model 3500 shown in Figure 5-67 is able to measure dynamic pressures using a semiconductor pressure transducer. The pressure cells had a diameter of 9 in. and a working stress range of 12.5 or 20.9 ksf (known as 600 kPa or 1 MPa) with a linear gage factor of 2.5 or 4.2 ksf/Volts, respectively. Figure 5-64 to Figure 5-66 illustrate layout of the pressure cells (PC1-PC6) in the 0°, 30°, and 45° skew tests, respectively.

The contact pressure cell type consists of a thick back plate and four lugs to connect the cell to the surface of the structure. Full contact between the cell and the structure surface was provided by applying a mortar pad. To accommodate the mortar pad, unthreaded spacers with the outside diameter of 3/8 in. and length of 9/16 in. were screwed to the backwall to make the gap between the cell and the concrete surface. Next, wooden forms were installed around the cells and later filled with grout. Installation of the pressure cells on the backwall in the 0°, 30°, and 45° skew tests is shown in Figure 5-68 to Figure 5-70, respectively.

5.8.2. Triaxial accelerometers

Triaxial MEM-326 accelerometers with a capacity range of ±16g were sealed each in a plastic box, as shown in Figure 5-71. The accelerometers were mounted inside the backfill soil at three levels along the height. The corresponding height from the backwall bottom was 0.75, 2.75, and 4.75 ft, respectively. Figure 5-74 to Figure 5-82 present layout of the accelerometers (labeled SAC) for the bottom, middle and top layers of the soil in the 0°, 30°, and 45° skew tests, respectively. Each accelerometer box could be individually nailed into the soil or attached to a cluster box when FlexiForce and/or string potentiometer were used at the same location. Figure 5-73 illustrates configuration of the soil sensor cluster.

5.8.3. Flexiforce sensors

Tekscan FlexiForce sensor, Model B201-M (Figure 5-72) with 0.375 in. diameter of the sensor and a medium force range of 0-25 lb. was used to measure the soil pressure inside the backfill. Each FlexiForce sensor was attached to a cluster box, as shown in the bottom row of

Figure 5-73. The cable connection was sealed using a liquid tape. The layout of FlexiForce sensors (labeled FL) is presented in Figure 5-74 to Figure 5-82.

5.8.4. String potentiometers

String potentiometers were hooked to the soil sensor clusters to measure the longitudinal displacement inside the backfill soil. Six string potentiometers (SSP1-SSP6) were installed at the middle layer of the soil at the backwall mid height. Layout of the string potentiometers is presented in Figure 5-74 to Figure 5-82. The strings were passed through stiff plastic tubes before placing inside the backfill soil. Approximately 6-8 in. of the strings connected to the sensor cluster was out of the plastic tube to allow the string movement during the test.

5.8.5. LVDTs

Novotechnik TR100 sensors with a 4-in. stroke were used to measure the vertical displacement of the soil surface. Figure 5-83 to Figure 5-85 present the layouts of LVDTs in the 0°, 30°, and 45° skew tests, respectively. LDVTs were attached to a fixed aluminum reference frame as shown in Figure 5-61 to Figure 5-63. The LVDT reference frame detail drawings are presented in Appendix D. The aluminum beams were connected to a steel reference frame. Figure 5-86 and Figure 5-87 show preparation, assembly and installation of the steel reference frame.

5.9. Backfilling

This section discusses soil backfilling process including soil compaction, measurement of density and moisture content, and installing the instruments, gypsum, and colored sand columns, and surface LVDTs. Table 5-4 presents key dates of soil backfilling, shake table tests, and soil removal.

5.9.1. Soil compaction

The soil compaction target was 95% of the Proctor maximum dry density (101.7 pcf) under an optimum moisture content of 10%. Figure 5-88 shows the soil piles preparation outside the laboratory. A sample layer of the soil was compacted and checked for the density and moisture content using a nuclear density gauge.

Soil was placed inside the soil box in 8-in. layers or less and compacted to reach the 95% relative compaction using a vibrating plate compactor. Figure 5-89 and Figure 5-90 present soil placement and compaction in the 0° skew model in the bottom half and top half of the soil box, respectively. Figure 5-91 and Figure 5-92 show soil backfilling process in the 30° and 45° skew cases, respectively.

5.9.2. Measured density and moisture content

A Troxler nuclear density gauge (Model 3440) shown in Figure 5-93 was used to measure the soil density and moisture content of each compacted layer. Figure 5-94 shows measurement of density and moisture content using the nuclear density gauge. The moisture content and density in different depths were measured at a minimum of three random locations after compacting each layer.

A total of 65, 76, and 51 readings were taken in a total of 10 lifts in the 0°, 30°, and 45° skew tests, respectively. Figure 5-95 to Figure 5-97 present the measured density, relative compaction, and moisture content in different lifts and different depths in the test models, respectively. Distribution of these measurements is shown in Figure 5-98 to Figure 5-100. The average measured density of the backfill was 104.2, 103.9, and 104.0 pcf in the 0°, 30°, and 45° skew cases, respectively, corresponding to the average relative compaction of 97.3%, 97.1%, and 97.2%. The average moisture contents were 7.2%, 7.2%, and 7.9%, respectively. The results showed that the soil compaction properties were consistent in all the cases. The best consistency of the results was achieved in the 30° skew test model.

A sand cone test was conducted in the third lift of the 0° skew backfill to compare with the density gauge results. The cone test yielded a maximum dry density of 109.6 pcf and a moisture content of 10.1%. The corresponding measurements based on the nuclear density gauge were 106.9 pcf and 8.1%, respectively. The nuclear density gauge errors were -2.5% and -25.7% for the maximum dry density and moisture content, respectively. Two samples from the third lift at the same locations of the density gauge measurement were dried in a microwave. The measured moisture contents were 11.0% and 14.0% from the oven-dry method versus 9.0% and 10.8% from the density gauge, respectively. The corresponding density gauge errors were -22.2% and -29.6%, respectively. The comparisons showed that the nuclear density gauge estimated the moisture content 20% to 30% less than the laboratory test. However, the density measured by the gauge was in an acceptable range.

5.9.3. Installation of internal instrumentation

Figure 5-101 to Figure 5-103 present installation of instruments in the bottom, middle, and top layers of the soil, respectively. Trenches 2 to 3 in. deep and 5 in. wide were made after the compaction. Since the backfill was not perfectly leveled, the height relative to the backwall top was checked by a rotary laser level at each instrument location. The instruments were carefully installed and anchored into the soil. The accelerometers were checked to be leveled at all locations. The instrument cables were passed towards the end of the soil box and trenches were filled with soil and compacted with hand tamper.

5.9.4. Placement of gypsum and colored sand columns

Small diameter gypsum and colored sand columns were embedded at different locations inside the backfill soil to identify the failure planes after the tests. Layouts of the gypsum and colored sand columns are presented in Figure 5-104 to Figure 5-106 for the 0°, 30°, and 45° skew tests, respectively.

Plaster of Paris was mixed with water with a water to powder ratio of 0.7 to make the gypsum columns. The 7-day compressive strength of the 3×6 in. gypsum cylinders with different water to powder ratios are shown in Table 5-5.

The smaller diameter gypsum columns (approximately 1-1/2 in.) in the non-skew test broke at several points along the column height. One 2 in. diameter column built at the west side of the backwall broke at fewer points. Therefore, it was decided to use the 2 in. diameter gypsum columns in the skew tests to better track the failure planes. The holes were made at most 5 ft deep to avoid damage to the water mitigation system at the bottom of the soil box. A 2 in. hand auger was used to make the holes for the colored sand columns. The soil was mixed with red chalk, placed and compacted in layers inside the holes.

Figure 5-107 to Figure 5-109 present making gypsum and colored sand columns in the 0°, 30°, and 45° skew case backfills, respectively. Finally, the soil surface was covered with plastic sheets to keep the soil moist until the testing day.

5.9.5. Installation of surface LVDTs

Soil surface LVDTs were installed in the testing day after watering the soil before the test. 12×12 in. 22-gauge sheet metal pieces of plain steel or 8×12 in. shingle flashing were nailed into the soil at the LVDT locations. The LVDTs were attached to the aluminum reference frames using hot glue. LVDTs on the slopes were installed perpendicular to the slope. Figure 5-110 to Figure 5-112 show the LVDTs installed in the 0°, 30°, and 45° skew cases, respectively. A steel beam hanging from the lab overhead crane was placed on the aluminum frames to minimize their vibrations during the test, as shown in Figure 5-110. Color grids were marked on the surface of the soil to easily track the surface crack locations during the tests.

5.10. Shake table test

Figure 5-113 to Figure 5-115 present the completed test model in the 0°, 30°, and 45° skew cases, respectively. The testing dates are shown in Table 5-4.

5.10.1. Cameras

Several cameras were installed to capture the shake table test model construction and test. A time-lapse video of the backfill soil construction was recorded in the 0° skew case. Two HD cameras recorded the entire east and west views of the test model. Two GoPro cameras were installed on the shake table to capture the south-west isolator and an entire view of all the isolators. Two GoPro cameras captured the gap between the bridge block and the backwall at the east and west sides. One GoPro camera on the crane and one HD camera on the beam supporting the backwall vertical restrainer captured the soil top view in the 0° skew test. One HD camera was connected to the crane in the skew test models to capture the top view of the backfill soil.

5.11. Test model disassembly

The dates of the test model disassembly including removal of the soil, the soil box and the complete set up are presented in Table 5-4.

5.11.1. Removal of instruments and gypsum columns

The LVDT's and the reference were removed after completing each test. Then the gypsum columns were carefully excavated using a shop vacuum, as shown in Figure 5-116. The next step was removing the top layer instruments by making trenches inside the backfill, as presented in Figure 5-117. The bottom layer instruments could not be reached at this stage and had to be removed later during the soil removal.

5.11.2. Removal of backfill soil

The east wall of the soil box was detached from the soil box before the soil removal. Figure 5-118 shows preparation of the soil box before removing the east wall. Plywood sheets were attached to the sides of the steel frame modules at the east side to cover them before the soil removal. Two of the east wall studs were attached to the lab overhead crane. Straps in the east-west direction were used to support the studs of the east side wall.

Removal of the east wall is presented in Figure 5-119. The crane pushed up the east wall and disconnected it from the soil box. Figure 5-120 shows the soil removal process after each test. Soil was stored and compacted in a container outside the laboratory after the final test, as shown in Figure 5-121.

5.11.3. Excavation of colored sand columns

Figure 5-122 shows excavation of the colored sand columns as the soil removal progressed from the east to the west side of the backfill.

5.11.4. Removal of test set up

Following the soil removal after completion of the 45° skew test, the soil box components and the lateral supports were disassembled. The bridge block, isolators, and the steel frame modules were removed last. Figure 5-123 and Figure 5-124 illustrate the removal of the soil box and the bridge block system, respectively.

6. SHAKE TABLE TESTING PROGRAM AND EXPERIMENTAL RESULTS

6.1. Introduction

The test model, instrumentation, and the loading were discussed in previous chapters. A large number of transducers of different types were used to collect the response of the abutment and the bridge block under different excitations. The measured results were grouped into the response of the bridge block, the lead rubber bearing supports of the bridge block, abutment wall, and the backfill. This chapter presents the measured results and a discussion of data from different sensors. Reference to the "acute corner" is made to the acute corner of the bridge block in all the discussions in this document. Similarly, the "obtuse corner" refers to the obtuse corner of the bridge block.

6.2. Data acquisition system

Two data acquisition (DAQ) systems of regular and high speed were used in this shake table study. The regular DAQ recorded the data with a common sampling frequency rate of 256 Hz, while the high speed DAQ could record the data with higher sampling frequency rates of up to 40,000 Hz. For the first sets of tests with abutments of 0° skew angle, the regular DAQ with a sampling frequency rate of 256 Hz was used to record all the data except for the impact accelerometers. The impact accelerometers were installed at the east and west vertical edges of the bridge block and the backwall to measure the acceleration due to the impact between these two elements. The impact accelerometers were connected to the high speed DAQ with a sampling frequency rate of 40,000 Hz up to the end of Run 4 and 8,000 Hz for Run 6 and 7 of the 0° skew test. However, further investigations of the recorded data of the 0° skew test (as described in Section 6.4.5) concluded that the triaxial accelerometers of the bridge block and the backwall that were connected to the low speed DAQ could not fully capture the impact response due to the insufficiency of sampling frequency rate. Therefore, it was decided that a higher sampling frequency rate should be used for the subsequent sets of tests. Accordingly, all the accelerometers installed on the bridge block and the backwall were connected to the high speed DAQ with a sampling rate frequency of 4,000 Hz for the 30° and 45° skew tests. Furthermore, the pressure cells installed on the backwall were also connected to the high speed DAQ for the 30° and 45° skew tests.

To determine the time lag between the regular and high speed DAQs, the data was carefully investigated, and time zero was defined as when significant data began to be recorded in each DAQ. The time lag between the regular and high speed DAQs for different runs of the 0°, 30°, and 45° skew tests are presented in Figure 6-1 to Figure 6-3, respectively. Therefore, adjustments were made to the starting point of data from each DAQ based on the time lag for each single run as presented in Table 6-1. All the presented data in this study are based on the corrected starting points. This correction improved the coincidence of impact time between different runs in each case. The improvement was most significant for larger time lags of 7.46 and 2.32 seconds for Run 6 and 7 of the 0° skew test with the amplitudes of 150% and 200% times the Sylmar motion, respectively.

6.3. Shake table response

Table 6-2 presents the amplitude scale factors of Sylmar motion that were applied to the shake table tests. The motions were simulated perpendicular to the projected width of abutment backwall in all the cases.

The achieved shake table motion including displacement, velocity, and acceleration histories are presented in this section. The displacement and acceleration histories of target motions are also compared with the corresponding achieved motions. Positive values indicate data towards the backfill soil throughout this section.

The comparison between the target motion and achieved motion histories are shown in Figure 6-4 to Figure 6-6 for different runs of the 0° skew test. The maximum values noted in the figures are related to the achieved motions. The displacement histories show perfect match between the target and achieved motions. However, there were some variations between the acceleration histories of the target and achieved motions since the shake table excitation was applied in a displacement control mode. These errors were more significant in Run 2 and 4. The shake table was stopped automatically in Run 6 with the amplitude of 150% times the Sylmar motion after reaching the maximum velocity pulse of motion in the direction away from the backfill soil (38.20 in./sec) that was followed by the first two high velocity pulses of motion in the direction towards the backfill soil. This automatic stop is implemented in the shake table run program after reaching the limit of actuator force with a 160-kip capacity. The next run was applied with the same amplitude of 150% times the Sylmar motion, but with the truncated motion excluding the maximum velocity pulse of target motion in the direction away from the backfill soil, as seen in Figure 6-6.

The combined shake table actuator force histories are shown in Figure 6-7 for all the runs of the 0° skew test. The maximum actuator force was 174 kips that resulted in an automatic stop of shake table.

The combined achieved motions histories are presented in Figure 6-8 for all the runs of the 0° skew test. The achieved maximum displacement and velocity towards the backfill soil occurred during the last truncated motion of Run 7 and were 6.59 in. and 34.30 in./sec, respectively. However, the achieved maximum acceleration towards the backfill soil occurred during the automatically stopped Run 6 and was 1.40g.

The comparison between the target and achieved motion are shown in Figure 6-9 to Figure 6-11 for different runs of the 30° skew test. The maximum values noted in the figures are related to the achieved motions. Similar to the 0° skew case, the displacement histories show perfect match between the target and achieved motions. However, there were some variations between the acceleration histories of the target and achieved motions since the shake table excitation was applied in a displacement control mode. These errors were less significant than the corresponding errors in the 0° skew test, except for Run 2. The shake table was stopped automatically in Run 3 with the amplitude of 125% times the Sylmar motion after reaching the maximum velocity pulse of motion in the direction away from the backfill soil (32.57 in./sec) that was followed by the first two high velocity pulses of motion towards the backfill soil. This automatic stop is implemented in the shake table run program after reaching the limit of actuator force with a 160-kips capacity. The subsequent runs were applied with the amplitudes of 150% and 200% times the Sylmar motion, respectively, but with the truncated motions excluding the maximum velocity pulse of target motion in the direction away from the backfill soil, as seen in Figure 6-10 and Figure 6-11.

The combined shake table actuator force histories are shown in Figure 6-12 for all the runs of the 30° skew test. The maximum actuator force was 167 kips away from the backfill soil in Run 3 that resulted in the automatic stop of shake table.

The combined achieved motions histories are presented in Figure 6-13 for all the runs of the 30° skew test. The achieved maximum displacement and velocity of shake table towards the backfill soil occurred during the last truncated motion of Run 5 and were 9.02 in. and 43.59 in./sec, respectively. However, the achieved maximum acceleration towards the backfill soil occurred during the automatically stopped Run 3 and was 1.32g.

The comparison between the target and achieved motion histories are shown in Figure 6-14 to Figure 6-16 for different runs of the 45° skew test. The maximum values noted in the figures are related to the achieved motions. Similar to the 0° and 30° skew cases, the displacement histories show perfect match between the target and achieved motions. However, there were some variations between the acceleration histories of the target and achieved motions since the shake table excitation was applied in a displacement control mode. These errors were less significant than the corresponding errors of the 0° skew test, except for Run 2. The higher amplitude runs were applied with the amplitudes of 125%, 150%, and 200% times the Sylmar motion, but with the truncated motions excluding the maximum velocity pulse of target motion in the direction away from the backfill soil, as seen in Figure 6-15 and Figure 6-16.

The combined shake table actuator force histories are shown in Figure 6-17 for all the runs of the 45° skew test. The maximum actuator force was 125 kips in the direction away from the backfill soil during the last truncated motion of Run 5.

The combined achieved motions histories are presented in Figure 6-18 for all the runs of the 45° skew test. The achieved maximum displacement, velocity and acceleration of shake table towards the backfill soil were all occurred during the last truncated motion of Run 7 and were 9.32 in., 42.00 in./sec, and 0.92g, respectively.

6.4. Bridge block response

The key measured response of the bridge block representing the superstructure mass is presented in this section. First, calculation of the fundamental period of the bridge block is discussed. Then the bridge block response is presented that include the longitudinal and transverse displacements, in-plane rotation, and longitudinal acceleration. Finally, response of the lead rubber bearing isolators representing the substructure stiffness is presented that include the longitudinal and transverse displacement, and longitudinal shear.

6.4.1. Fundamental period

Triaxial accelerometers were installed at the four corners on the top of the bridge block. The layout of these accelerometers (BAC1, BAC2, BAC3 and BAC4) was presented in Chapter 5. Response of these accelerometers under the white noise motions was used to determine the fundamental period of the bridge block.

Two methods were used to determine the fundamental frequency of the bridge block. The Fast Fourier Transform (FFT) spectra of longitudinal acceleration measured by the four corner accelerometers were calculated in the first method. The frequency corresponding to the maximum peak in each spectrum was selected as the fundamental frequency of the bridge block. A transfer function equal to the ratio of the response of the bridge block accelerometers to the base acceleration of shake table in the frequency domain was determined in the second method using "tfestimate" function in MATLAB program. The frequency corresponding to the maximum peak of the transfer function was selected as the fundamental frequency of the bridge block. The details of the calculated spectra to determine the natural frequency of the bridge block are presented in Appendix E.

The fundamental frequency of the bridge block was 5.1 Hz with a corresponding fundamental period of 0.20 seconds.

6.4.2. Longitudinal displacements of bridge block

Two string potentiometers were attached to the top plates of north-west and south-west isolators in the direction of motion to measure movement of the bridge block. Note that the top plates of the isolators were connected to the bottom slab of the bridge block. The layout of these string potentiometers (BLSP1 and BLSP2) was presented in Chapter 5.

The bridge block displacement histories measured in the direction of motion are presented in this section in two forms of incremental and combined displacement responses for different runs. The incremental displacement is shown to start from zero for each run, with the permanent displacement from the previous run removed. However, the combined displacement histories include the residual displacement from the previous runs. The direct displacement of the bridge block was measured relative to the shake table. Therefore, displacement of shake table was added to the measured relative displacement of the bridge block to obtain the absolute displacement of the bridge block because the soil-abutment system of the test model was stationary and off the shake table and was affected by the absolute displacement of the bridge block. A positive displacement indicates movement towards the backfill soil throughout this section.

The relative displacement histories measured at the north-west and south-west supports of the bridge block are shown in Figure 6-19 for different runs of the 0° skew test. The two string potentiometers recorded very similar data since there was no significant transverse movement. The maximum relative displacement increments of the bridge block away from the backfill soil were 0.03, 0.41, 0.95, 0.13, 2.23, and 1.61 in. for Run 1, 2, 3, 4, 6, and 7, respectively. The bridge block experienced some residual displacements with respect to the shake table in the direction away from the backfill soil in some cases and towards the backfill soil in other cases due to the residual displacement within the isolators.

The absolute displacement histories of the bridge block are shown in Figure 6-20 for different runs of the 0° skew test. The maximum absolute displacement increments of the bridge block towards the backfill soil were 1.29, 1.95, 2.51, 2.36, 4.01, and 5.04 in. for Run 1, 2, 3, 4, 6, and 7, respectively. The maximum absolute displacement increments of the bridge block away from the backfill soil were 1.32, 2.96, 4.60, 2.63, and 9.23 in. for Run 1, 2, 3, 4, and 6, respectively. These motions included the high velocity pulse of the target motion in the direction away from the backfill soil. However, for the truncated motion of Run 7, this maximum displacement was reduced to 2.84 in.. The latter motion excluded the high velocity pulse of the target motion in the direction away from the backfill soil. The bridge block experienced some residual displacement away from the backfill soil due to the residual displacement within the isolators.

Figure 6-21 shows the combined displacement histories of the bridge block and the shake table for all the runs of the 0° skew test. Starting from Run 2, when the first impact between the bridge block and the backwall occurred, the absolute displacement of the bridge block towards the backfill soil was smaller than the shake table displacement since the bridge block moved opposite to the shake table. However, the absolute displacement of the bridge block away from the backfill soil was larger than the corresponding shake table displacement. The maximum combined displacement of the bridge block towards the backfill soil was 1.29, 1.97, 2.33, 3.50, and 3.79 in. with respect to its initial position for Run 1, 2, 3, 6, and 7, respectively.

The relative displacement histories measured at the north-west and south-west supports of the bridge block are shown in Figure 6-22 for different runs of the 30° skew test. The relative displacement of the bridge block was primarily towards the backfill soil in Run 1. However, for the subsequent runs when there were impacts between the bridge block and the backwall, the relative displacement of the bridge block was primarily away from the soil. The maximum relative displacement of the bridge block towards the backfill soil was 0.09 in. (relative to the shake table) in Run 1. The maximum relative displacement increments of the bridge block away from the backfill soil were 0.21, 1.43, 1.21, and 1.61 in. (relative to the shake table) for Run 2, 3, 4, and 5, respectively. The bridge block experienced some residual displacements with respect to the shake table in the direction away from the backfill soil in some cases and towards the backfill soil in other cases due to the residual displacement within the isolators.

The absolute displacement histories of the bridge block are shown in Figure 6-23 for different runs of the 30° skew test. The maximum absolute displacement increments of the bridge block towards the backfill soil were 1.27, 2.18, 4.25, 5.69, and 7.59 in. for Run 1, 2, 3, 4, and 5, respectively. The maximum absolute displacement increments of the bridge block away from the backfill soil were 1.28, 2.71, and 7.50 in. for Run 1, 2, and 3, respectively. However, for the truncated motion of Run 4 and 5, the maximum absolute displacement increments of the bridge block away from the backfill soil reduced to 2.69 and 3.45 in., respectively. The latter motions excluded the high velocity pulse of the target motion in the direction away from the backfill soil. The bridge block experienced some residual displacement away from the backfill soil due to the residual displacement within the isolators.

Figure 6-24 shows the combined displacement histories of the bridge block and the shake table for all the runs of the 30° skew test. Starting from Run 2, when the first impact between the bridge block and the backwall occurred, the absolute displacement of the bridge block towards the backfill soil was smaller than the shake table displacement since the bridge block moved opposite to the shake table. However, the absolute displacement of the bridge block away from the backfill soil was larger than the shake table displacement. The maximum combined displacement of the bridge block towards the backfill soil was 1.27, 2.26, 4.36, 5.34, and 6.85 in. for Run 1, 2, 3, 4, and 5, respectively.

The relative displacement histories measured at the north-west and south-west supports of the bridge block are shown in Figure 6-25 for different runs of the 45° skew test. The maximum relative displacement increments of the bridge block towards the backfill soil were 0.08 and 0.15 in. (relative to the shake table) for Run 1 and 2, respectively. The maximum relative displacement increments of the bridge block away from the backfill soil were 0.18, 0.82, 0.76, and 1.08 in. (relative to the shake table) for Run 2, 3, 4, and 5, respectively. Similar to the 0º skew case, the bridge block exhibited some residual displacements with respect to the shake table in the direction away from the backfill soil in some cases and towards the backfill soil in other cases.

The absolute displacement histories of the bridge block are shown in Figure 6-26 for different runs of the 45° skew test. The maximum absolute displacement increments of the bridge block away from the backfill soil were 1.28 and 2.68 in. for Run 1 and 2, respectively. However, for the truncated motion of Run 3, 4, and 5, the maximum absolute displacement increments of the bridge block away from the backfill soil reduced to 2.32, 2.53, and 3.41 in., respectively. The latter motions excluded the high velocity pulse of the target motion in the direction away from the backfill soil. The maximum absolute displacement increments of the bridge block towards the backfill soil were 1.29, 2.39, 5.22, 6.42, and 8.41 in. for Run 1, 2, 3, 4, and 5, respectively. There were residual relative displacements in the bridge block in the direction away from the backfill soil in some cases and towards the backfill soil in other cases due to the residual displacements within the isolators.

Figure 6-27 shows the combined displacement of the bridge block and the shake table for all the runs of the 45° skew test. Starting from Run 3, the absolute displacement of the bridge block toward the backfill soil was smaller than the shake table displacement since the bridge block moved opposite to the shake table. However, the absolute displacement of the bridge block away from the backfill soil was larger than the shake table displacement. The maximum combined displacement of the bridge block towards the backfill soil was 1.30, 2.45, 5.37, 6.28, and 8.13 in. with respect to its initial position for Run 1, 2, 3, 4, and 5, respectively.

6.4.3. Transverse displacements of bridge block

Some out of plane rotation of the bridge block due to uneven impact with the abutment wall of the latter two tests (tests with skew) was expected. Two string potentiometers were attached to the top plates of north-west and south-west isolators in the transverse direction perpendicular to the direction of motion to measure the transverse movement of the bridge block. Note that the top plates of isolators were connected to the bottom slab of the bridge block. The layout of these string potentiometers (BTSP1 and BTSP2) was presented in Chapter 5.

The bridge block displacement histories measured in the transverse direction are presented in this section in two forms of incremental and combined displacements for different runs in all the cases. The incremental displacement is shown to start from zero for each run, with the permanent displacement from the previous run removed. However, the combined displacement histories include the residual displacement from the previous runs. The direct displacement of the bridge block was measured relative to the shake table. However, displacement of shake table was negligible in the transverse direction, and hence the relative transverse displacement of the bridge block was the same as the absolute displacement. A positive displacement indicates movement towards the west (acute corner in the skew cases) throughout this section.

The bridge block displacement histories measured at the north-west and south-west supports are shown in Figure 6-28 for different runs of the 0° skew test. The displacement of the bridge block measured by the two transverse string potentiometers were different and indicated in-plane rotation of the bridge block even for the non-skew case. The difference between the transverse displacement of the bridge block at the north-west and south-west supports was used to calculate the in-plane rotation of the bridge block that is discussed in Section 6.4.4. The transverse displacement of the bridge block measured by the two string potentiometers were in opposite directions for the entire duration of motion for all the runs except for Run 6. The displacement of the bridge block was towards the west for the southern string potentiometer and towards the east for the northern string potentiometer for Run 1, 2, 3, and 7. The difference between the maximum displacements measured by the two transverse string potentiometers was 0.16, 0.16, and 0.17 in. for Run 2, 3, and 7, respectively.

Figure 6-29 shows the combined displacement histories of the bridge block for all the runs of the 0° skew test. The maximum difference between the combined displacements between measurements of the two transverse string potentiometers was 0.27 in.

The bridge block displacement histories measured at the north-west and south-west supports are shown in Figure 6-30 for different runs of the 30° skew test. The difference between the bridge block displacements measured by the two transverse string potentiometers was more significant than the 0° skew case due to the skew angle. The difference between the transverse displacements of the bridge block at the north-west and south-west supports was used to calculate the in-plane rotation of the bridge block that is discussed in Section 6.4.4. The transverse displacement of the bridge block measured by the two string potentiometers were in opposite directions for the entire duration of motion for all the runs. Starting from Run 2, the bridge block displacement was towards the acute corner for the southern string potentiometer and towards the obtuse corner for the northern string potentiometer. The difference between the maximum displacements of the two transverse string potentiometers was 0.10, 1.38, 1.44, and 1.81 in. for Run 2, 3, 4, and 5, respectively. This trend showed that the maximum in-plane rotation of the bridge block increased during the higher amplitude runs.

Figure 6-31 shows the combined bridge block displacement histories for all the runs of the 30° skew test. The maximum difference between the combined transverse displacements between measurements of the two string potentiometers was 3.23 in.

The bridge block displacement histories of the bridge block measured at the north-west and south-west supports are shown in Figure 6-32 for different runs of the 45° skew test. The difference between the bridge block displacements measured by the two transverse string potentiometers was more significant than the 0° and 30° skew cases because of the skew angle. The in-plane rotation is further discussed in Section 6.4.4. Similar to the case with the 30° skew, the transverse displacement of the bridge block measured by the two string potentiometers were in opposite directions for the entire duration of motion for all the runs. Starting from Run 3, the displacement of the bridge block was towards the acute corner for the southern string potentiometer and towards the obtuse corner for the northern string potentiometer. The difference between the maximum displacements of the two transverse string potentiometers was 0.62, 1.63, 1.65, and 2.70 in. for Run 2, 3, 4, and 5, respectively. This trend shows that the maximum in-plane rotation of the bridge block increased at the higher amplitude runs similar to that observed in the case with the 30° skew. Furthermore, there was some increase in the in-plane rotation of the bridge block compared to the 30° skew case for the similar amplitude runs due to the increased skew angle.

Figure 6-33 shows the combined bridge block displacement histories for all the runs of the 45° skew test. The maximum difference between the combined transverse displacements between measurements of the two string potentiometers was 3.57 in.

6.4.4. In-plane rotations of bridge block

Two string potentiometers were attached to the top plates of north-west and south-west isolators in the transverse direction perpendicular to the direction of motion to measure the transverse movement of the bridge block. The layout of these string potentiometers (BTSP1 and BTSP2) was presented in Chapter 5. The difference between the transverse displacements of the bridge block at the north-west and south-west supports was used to calculate the in-plane rotation of the bridge block.

The in-plane rotation histories of the bridge block are presented in this section in two forms of incremental and combined rotation for different runs. The incremental rotation is shown to start from zero for each run, with the permanent rotation from the previous run removed. However, the combined rotation histories include the residual rotation from the previous runs. A "rotation increase" indicates counterclockwise rotation throughout this section.

The in-plane rotation histories of the bridge block are shown in Figure 6-34 for different runs of the 0° skew test. For the first run with no impact between the bridge block and the backwall, very small in-plane rotation of the bridge block was observed with the maximum transverse displacement of the north-west support towards the east direction. This negligible in-plane rotation was observed in spite of a symmetric configuration of mass and stiffness about the centerline of the bridge block parallel to the direction of motion. However, larger in-plane rotation was observed in the subsequent runs when there were impacts between the bridge block and the backwall. Starting from Run 2, the high pulses of the bridge block rotation corresponding to the maximum response of the abutment system were clockwise with the movement of the southern side towards the west direction for all the runs. Furthermore, the bridge block experienced some rotation pulses in the counterclockwise direction during Run 4 and 6. The maximum rotation increments of the bridge block in the clockwise direction were 0.08, 0.07, 0.01, 0.03, and 0.07 degree for Run 2, 3, 4, 6, and 7, respectively.

Figure 6-35 shows the combined in-plane rotation histories of the bridge block for all the runs of the 0° skew test. The maximum rotation of the bridge block in the clockwise direction was 0.08, 0.12, 0.11, and 0.12 degree for Run 2, 3, 6, and 7, respectively. The maximum rotation of 0.12 degree corresponded to the maximum difference between the transverse displacements of the north-west and south-west supports of the bridge block (0.27 in.).

The in-plane rotation histories of the bridge block for different runs of the 30° skew test are shown in Figure 6-36. For the first run with no impact between the bridge block and the backwall, very small in-plane rotation of the bridge block was observed with the maximum rotation in the counterclockwise direction. The direction of this rotation was consistent with the small eccentricity between the centers of mass and stiffness of the bridge block in the direction perpendicular to the direction of motion. However, the direction of rotation reversed in the subsequent runs when there were impacts between the bridge block and the backwall. Starting from Run 2, the high pulses of the in-plane rotation corresponding to the maximum response of the abutment system were clockwise. Furthermore, the in-plane rotation increased during the runs when there were impacts between the bridge block and the backwall. The bridge block rotated counterclockwise after returning from a relatively large clockwise rotation. This resulted in some counterclockwise residual in-plane rotation. Some small counterclockwise rotation occurred at the beginning of the impact that was more visible under the higher amplitude runs. This shows that the bridge block was initially rotating in the counterclockwise direction that was consistent with the eccentricity between the centers of mass and stiffness of the bridge block. However, after the impact between the bridge block and the backwall, the direction of the bridge block rotation reversed since the resistance of the backfill soil was higher at the acute corner and the backwall had the tendency to rotate towards that acute corner. This shows that the final rotation of the bridge block that resulted in the maximum response of the abutment system was independent of the bridge block eccentricity and was controlled by the skew angle. The maximum in-plane rotation increments of the bridge block in the clockwise direction were 0.05, 0.64, 0.67, and 0.83 degree for Run 2, 3, 4, and 5, respectively.

Figure 6-37 shows the combined in-plane rotation histories of the bridge block for all the runs of the 30° skew test. The maximum in-plane rotation of the bridge block occurring in the clockwise direction was 0.04, 0.66, 0.98, and 1.51 degrees for Run 2, 3, 4, and 5, respectively. The maximum in-plane rotation of 1.51 degrees corresponded to the maximum difference between the transverse displacements of the north-west and south-west supports of the bridge block (3.23 in.).

The in-plane rotation histories of the bridge block are shown in Figure 6-38 for different runs of the 45° skew test. For the first run with no impact between the bridge block and the backwall, the in-plane rotation was in the counterclockwise direction and exceeded the measured rotation of the 0° and 30° skew cases. This larger in-plane rotation during the first run was as a result of a larger eccentricity between the centers of mass and stiffness of the bridge block compared to the 0° and 30° skew cases. For the subsequent runs when there were impacts between the bridge block and the backwall, the in-plane rotation increased. Starting from Run 2, the high pulses of the bridge block in-plane rotation corresponding to the maximum response of the abutment system were clockwise. The bridge block rotated counterclockwise after returning from a relatively large clockwise rotation. This resulted in some counterclockwise residual in-plane rotation. Similar to the 30° skew case, some small counterclockwise rotation occurred at the beginning of the impact that was more visible during the higher amplitude runs. This shows that the bridge block was initially rotating in the counterclockwise direction that was consistent with the eccentricity between the centers of mass and stiffness of the bridge block. However, after the impact between the bridge block and the backwall, the direction of the bridge block rotation reversed since the resistance of the backfill soil was higher at the acute corner and the backwall had the tendency to rotate towards that acute corner. Similar to the 30° skew case, the final rotation of the bridge block that resulted in the maximum response of the abutment system was independent of the bridge block eccentricity and was controlled by the skew angle. The maximum in-plane rotation increments of the bridge block in the clockwise direction were 0.05, 0.77, 0.79, and 1.29 degrees for Run 2, 3, 4, and 5, respectively.

Figure 6-39 shows the combined in-plane rotation histories of the bridge block for all the runs of the 45° skew test. The maximum in-plane rotation of the bridge block occurring in the clockwise direction was 0.03, 0.74, 1.04, and 1.70 degrees for Run 2, 3, 4, and 5, respectively. The maximum in-plane rotation of 1.70 degrees corresponded to the maximum difference between the transverse displacements of the north-west and south-west supports of the bridge block (3.57 in.).

6.4.5. Longitudinal accelerations of bridge block

Triaxial accelerometers were installed at the four corners on the top of the bridge block. The layout of these accelerometers (BAC1, BAC2, BAC3 and BAC4) was presented in Chapter 5. BAC1 and BAC2 accelerometers were located near the abutment backwall at the corners of the bridge block southern edge (skewed edge of concrete wedges in the cases of non-zero skew angles). BAC3 and BAC4 accelerometers were located at the corners of the bridge block northern edge on the top of the corresponding side wall at a height lower than that of the accelerometers near the backwall. Positive acceleration indicates data towards the backfill soil throughout this section.

The measured acceleration histories of the bridge block in the direction of motion are shown in this section for different runs in all the cases. The average acceleration histories for the two cases of 1) for all the four accelerometers and 2) for the two accelerometers near the backwall are also presented.

The acceleration histories of the bridge block corners and the corresponding average acceleration histories are shown in Figure 6-40 to Figure 6-45 for different runs of the 0° skew test. All the corner accelerometers recorded similar data in Run 1 where there was no impact between the bridge block and the backwall. However, the response of accelerometers near the backwall was different from the response of accelerometers far from the backwall in the subsequent runs during which the bridge block came into contact with the backwall. The maximum accelerations near the backwall (BAC1 and BAC2) exceeded those at the far end of the bridge block (BAC3 and BAC4).

In BAC1 and BAC2, the maximum accelerations of the east corner were higher than those of the west corner during the first impact in Run 2, 3, and 4. However, the maximum accelerations in BAC1 and BAC2 during Run 6 and 7 were higher at the west corner than at the east corner of the bridge block.

The maximum average acceleration of BAC1 and BAC2 during the first impact was 0.65g, 3.03g, 1.95g, 1.81g, and 4.68g towards the backfill soil for Run 2, 3, 4, 6, and 7, respectively. The corresponding maximum average acceleration was 2.59g, 3.48g, 2.89g, 2.98g, and 6.59g away from the backfill soil.

Further investigation into the recorded accelerations after running the 0° skew test showed that the sampling rate of 256 Hz was not sufficient to capture the response in cases with impacts between the bridge block and the backwall. Therefore, a higher speed data acquisition system with a sample rate of 4,000 Hz was used in the 30° and 45° skew tests.

The acceleration histories of the bridge block corners and the corresponding average acceleration histories are shown in Figure 6-46 to Figure 6-50 for different runs of the 30° skew test. Similar to the 0° skew test, the maximum accelerations in BAC1 and BAC2 were higher than those in BAC3 and BAC4 in the runs when impacts between the bridge block and the backwall occurred. The bridge block acceleration exceeded the 16g capacity of the accelerometers near the backwall in Run 4 and 5. Therefore, the corresponding average acceleration histories are not shown for these runs.

In BAC1 and BAC2, the maximum accelerations at the obtuse corner were higher than those at the acute corner for all the runs. This is in agreement with the clockwise rotation of the bridge block during the maximum response of the abutment system.

The maximum average acceleration of BAC1 and BAC2 during the first impact was 0.35g and 8.11g towards the backfill soil for Run 2 and 3, respectively. The corresponding maximum average acceleration was 2.66g and 8.92g away from the backfill soil.

The acceleration histories of the bridge block corners and the corresponding average acceleration histories are shown in Figure 6-51 to Figure 6-55 for different runs of the 45° skew test. Similar to the 0° and 30° skew cases, the maximum accelerations in BAC1 and BAC2 exceeded than those in BAC3 and BAC4. The maximum bridge block accelerations were greater than the 16g capacity of the accelerometers near the backwall in Run 4 and 5. Therefore, the corresponding average acceleration histories are not shown for those runs.

Similar to the case with the 30º skew, the maximum accelerations in BAC1 and BAC2 at the obtuse corner exceeded those at the acute corner for all the runs. This is also in agreement with the clockwise rotation of the bridge block during the maximum response of the abutment system.

The maximum average acceleration of BAC1 and BAC2 was 0.45g and 8.25g towards the backfill soil for Run 2 and 3, respectively. The corresponding maximum average acceleration during the first impact was 2.84g and 8.16g away from the backfill soil.

6.4.6. Horizontal displacements of isolators

Four string potentiometers were attached to the top plates of north-west and south-west isolators to measure the longitudinal (BLSP1 and BLSP2) and transverse (BTSP1 and BTSP2) movement of the bridge block. The layout of the string potentiometers was presented in Chapter 5. The longitudinal and transverse displacements of the isolators are the same as the corresponding measurements of the bridge block that were presented in Section 6.4.2 and Section 6.4.3.

6.4.7. Longitudinal shear in isolators

Six load cells were installed on the top of the isolators to measure the induced forces and moments in different directions. The layout of these load cells (BLC1 to BLC6) was presented in Chapter 5.

The longitudinal shear histories measured by the six load cells are presented in this section. Furthermore, the longitudinal force-displacement behavior of the isolators is presented for the incremental and combined displacement of the isolators. Positive shear indicates force towards the backfill soil throughout this section.

The shear histories in the isolators and their force-displacement behavior are presented in Figure 6-56 to Figure 6-58 for different runs of the 0° skew test. The maximum shear towards the backfill soil was smaller than that away from the backfill for all the runs, except for Run 1 when there was no impact between the bridge block and the backwall. The maximum total shear towards the backfill soil was 22, 29, 35, 31, 51, and 37 kips for Run 1, 2, 3, 4, 6, and 7, respectively.

The combined shear histories in the isolators are presented in Figure 6-59 for all the runs of the 0° skew test. The variation in shear versus combined displacement in the direction of motion is shown in Figure 6-60 for all the runs of the 0° skew test. The maximum combined displacement of isolators was 2.73 and 2.86 in. with the corresponding shear of 129 and 115 kips away from the backfill soil for Run 6 and 7, respectively.

The shear histories in the isolators and their force-displacement behavior are presented in Figure 6-61 to Figure 6-63 for different runs of the 30° skew test. Similar to the non-skew case, the maximum shear towards the backfill soil was smaller than that away from the backfill soil for all the runs except for Run 1. The maximum total shear towards the backfill soil was 21, 27, 51, 356, and 44 kips for Run 1, 2, 3, 4, and 5, respectively.

The combined shear histories in the isolators are presented in Figure 6-64 for all the runs of the 30° skew test. The variation in shear versus combined displacement in the direction of motion is shown in Figure 6-65 for all the runs of the 30° skew test. The maximum combined displacement of isolators was 1.59 and 2.18 in. with the corresponding shear of 77 and 67 kips away from the backfill soil for Run 4 and 5, respectively.

The shear histories in the isolators and their incremental force-displacement behavior are presented in Figure 6-66 to Figure 6-68 for different runs of the 45° skew test. Similar to the 0º and 30º skew cases, the maximum shear towards the backfill soil was smaller than that away from the backfill soil for all the runs except for Run 1. The maximum measured total shear towards the backfill soil was 20, 35, 31, 37, and 45 kips for Run 1, 2, 3, 4, and 5, respectively.

The combined shear histories in the isolators are presented in Figure 6-69 for all the runs of the 45° skew test. The isolators shear variations versus combined displacement in the direction of motion are shown in Figure 6-70 for all the runs of the 45° skew test. The maximum combined displacement of isolators was 0.92 and 1.36 in. with the corresponding shear of 47 and 37 kips away from the backfill soil for Run 4 and 5, respectively.

6.4.8. Concluding remarks on bridge block response

The data presented on the bridge block response reveal important information about the in-plane rotations and accelerations of the block.

The bridge block in-plane rotations increased after the closure of the gap between the bridge block and the backwall in all cases. The rotations in the non-skew case were very small and oscillated in both clockwise and counterclockwise directions. These rotations are attributed to impact at random points between the bridge block and the backwall. The bridge block in the skewed cases initially rotated in the counterclockwise direction that was consistent with the eccentricity between the centers of mass and stiffness of the bridge block. However, after the bridge block came into contact with the backwall, the direction of the rotation reversed since the resistance of the backfill soil was relatively higher at the acute corner and the backwall had the tendency to rotate towards that acute corner. Therefore, the maximum rotation of the bridge block corresponding to the maximum response of the abutment system was found to be independent of the bridge block eccentricity and was controlled by the abutment skew angle.

The bridge block accelerations near the backwall were different from those far from the backwall during the runs when the bridge block impacted the backwall due to the in-plane rotation. The maximum accelerations near the gap exceeded those at the far end of the bridge block in all the cases. Those accelerations near the backwall did not follow a specific trend in the non-skew case. However, they were higher at the obtuse corner than at the acute corner for both skew cases. This was in agreement with the clockwise rotation of the bridge block during the maximum response of the abutment system.

6.5. Abutment backwall response

Key measured response histories of the abutment backwall are presented in this section including the longitudinal, transverse, and vertical displacements, rotation about the vertical axis, and triaxial accelerations.

6.5.1. Longitudinal displacements

Four string potentiometers were installed at the four corners of the backwall at the top and the bottom of eastern and western sides to measure the longitudinal backwall displacement in the direction of motion. The layout of these string potentiometers (WLSP1, WLSP2, WLSP3 and WLSP4) was presented in Chapter 5.

The measured longitudinal displacement histories of the backwall are presented in this section in two forms of incremental and combined displacements for different runs in all the cases. The incremental displacement histories exclude any residual displacement from the previous run, but the combined histories include these displacement. A positive displacement indicates movement towards the backfill soil throughout this section.

The displacement histories of the backwall measured at the four corners are shown in Figure 6-71 to Figure 6-73 for different runs of the 0° skew test. Starting from Run 2 with the amplitude of 50% times the Sylmar motion, the top of the backwall was pushed back beyond its initial position towards the bridge block which resulted in a negative residual displacement at the east side of the backwall, as seen in Figure 6-71. Following the second impact during Run 3, the backwall was pushed backwards by soil again for about 2 in. towards the bridge block (Figure 6-72). This backward movement occurred since the wall was supported on Teflon sheets with very low friction. The vertical restraining ram was connected to the wall with a swivel joint on the top of the backwall. Run 4 with the amplitude of 50% times the Sylmar motion was repeated to check the system response. Again, the wall moved 1.5 in. towards the bridge block (Figure 6-72). The shake table had to be moved backwards to provide the gap of 2 in. between the bridge block and the backwall and re-simulate the initial situation of the test. However, this was not possible due to the shake table displacement limit. Therefore, the test was stopped to provide a restrainer system for the backwall. The settled soil adjacent to the backwall was removed and a new backfilled was placed and compacted using a hand tamper for a width of approximately 1 ft along the backwall. Two trenches were made through the embankment slopes of backfill and two cable restrainers were attached to the backwall. The trenches were then filled and compacted. Subsequently the high-amplitude motions were simulated with the backwall placed in its initial position providing the initial gap between the backwall and the bridge block. Figure 6-73 shows the displacement at the four corners of the backwall that verified the effectiveness of the added the backwall restrainer system to prevent the backward movement of the backwall beyond its initial position.

Figure 6-74 shows the comparison of the backwall displacement at the east and west sides during the impact. The displacement was larger at the west side of the backwall than at the east side for all the runs except for Run 6. However, the difference between the displacements at the east and west sides was not significant for the higher amplitude runs. This trend shows an almost pure longitudinal movement of the backwall into to the backfill soil. The maximum average backwall displacement increments towards the backfill soil were 0.31, 0.68, 1.78, and 2.07 in. for Run 2, 3, 6, and 7, respectively (Figure 6-75).

The combined displacement histories of the backwall measured at the four corners are shown in Figure 6-76 and Figure 6-77 for different runs of the 0° skew test. The maximum combined displacement of the backwall towards the backfill soil was 0.31, 0.62, 1.78, and 2.31 in. for Run 2, 3, 4, and 5, respectively. The displacement of 2.31 in. in Run 7 included the residual displacement only from Run 6.

The displacement histories of the backwall measured at the four corners are shown in Figure 6-78 and Figure 6-79 for different runs of the 30° skew test. The movement of the top of the backwall towards the backfill soil was slightly larger than the movement of the bottom of the backwall for all the runs. This was also true for movements in the opposite direction. Some small negative residual displacement was recorded at the west side of the backwall (acute corner) indicating backward movement of the wall beyond its initial position. This is believed to be due to the larger volume of soil at the acute corner that pushed back the backwall. However, such movement reduced compared to the wall displacement towards the backfill due to the restraining action of the cables.

Figure 6-80 shows the comparison of the backwall displacement at the east and west sides during the impact for different runs of the 30° skew test. The displacement was always larger at the obtuse corner than that at the acute corner for all the runs, except for Run 4 and 5 before 10.67 and 10.68 seconds, respectively. This comparison was used to determine the direction of the backwall rotation about the vertical axis that is discussed in Section 6.5.5. The larger displacement of the backwall at the obtuse corner was due to the lower stiffness of backfill soil at the obtuse corner. The maximum average backwall displacement increments towards the backfill soil were 0.23, 1.01, 1.28, and 1.87 in. for Run 2, 3, 4, and 5, respectively (Figure 6-81).

The combined displacement histories of the backwall measured at the four corners are shown in Figure 6-82 and Figure 6-83 for all the runs of the 30° skew test. The maximum combined displacement of the backwall was 1.36 and 4.07 in. in Run 5 at the acute and obtuse corner, respectively. Therefore, the maximum average displacement of the backwall at the center reached 2.57 in. in the final run. The maximum combined displacement of the backwall towards the backfill soil was 0.23, 1.04, 1.64, and 2.57 in. for Run 2, 3, 4, and 5, respectively.

The displacement histories of the backwall measured at the four corners are shown in Figure 6-84 and Figure 6-85 for different runs of the 45° skew test. Similar to the 30° skew case, movement of the top of the backwall both towards and away from the soil was larger than that of the bottom of the backwall for all the runs. Some small negative residual displacement was recorded at the higher amplitude runs at the west side of the backwall (acute corner) showing a backward movement of the backwall beyond its initial position due to the larger volume of the soil at the acute corner that pushed back the backwall.

Figure 6-86 shows the comparison of the backwall displacement at the east and west sides during the impact for different runs of the 45° skew test. The maximum displacement was larger at the obtuse corner than that at the acute corner for all the runs except for Run 2 (Similar to the case with the 30° skew). Larger displacement of the backwall at the obtuse corner was due to the lower stiffness of backfill soil at that corner. Starting from Run 3, the displacement was larger at the acute corner than that at the obtuse corner, except for Run 4 and 5 before 10.7 seconds. This comparison was used to determine the direction of the backwall rotation about the vertical axis that is discussed in Section 6.5.5. The maximum average backwall displacement increments towards the backfill soil were 0.18, 0.82, 1.53, and 1.64 in. for Run 2, 3, 4, and 5, respectively (Figure 6-87).

The combined displacement histories of the backwall measured at the four corners are shown in Figure 6-88 and Figure 6-89 for all the runs of the 45° skew test. The maximum combined displacement of the backwall was 1.11 and 2.93 in. in Run 5 at the acute and obtuse corner, respectively. Therefore, the maximum average displacement of the backwall at the center reached 1.78 in. in the final run. The maximum combined displacement of the backwall towards the backfill soil was 0.18, 0.84, 1.47, and 1.78 in. for Run 2, 3, 4, and 5, respectively.

6.5.2. Transverse displacements

The shake table motion in all the cases was in the longitudinal direction of the bridge block, causing only longitudinal motion in an ideal zero-degree skew case but potentially both longitudinal and transverse motion in skewed cases. Two string potentiometers were installed in the transverse direction at the top and the bottom western corners to measure the backwall transverse displacement. The layout of these string potentiometers (WTSP1 and WTSP4) was presented in Chapter 5.

Similar to the longitudinal displacements, the measured transverse displacement histories of the backwall are presented in two forms of incremental and combined displacements for different runs in all the cases. The incremental displacement is shown to start from zero for each run, with the permanent displacement from the previous run removed. However, the combined displacement histories include the residual displacement from the previous runs. A positive displacement indicates movement towards the east (obtuse corner in skewed cases) throughout this section.

The displacement histories of the backwall measured at the top and the bottom western corners are shown in Figure 6-90 to Figure 6-92 for different runs of the 0° skew test. The displacements were very small as expected. The backwall displacement was primarily towards the west during Run 2, 3, and 4, except for the period that the backwall was pushed backed significantly towards the bridge block after about 12 seconds in Run 3 and 4. However, at the higher amplitude runs (Run 6 and 7), the backwall displacement was primarily towards the east. The maximum backwall displacement increments measured from averaging displacements at the two west corners were 0.03 and 0.05 in. towards the west for Run 2 and 3, respectively. The maximum average displacement of the backwall was 0.13 and 0.10 in. towards the east for Run 6 and 7, respectively. The combined displacement histories of the backwall at the top and the bottom western corners are shown in Figure 6-93 for all the runs of the 0° skew test.

The displacement histories of the backwall measured at the top and the bottom western corners are shown in Figure 6-94 and Figure 6-95 for different runs of the 30° skew test. It can be seen that even though the displacements are relatively small, they are substantially larger than the displacement of the 0° case because of significant in-plane rotation of the wall caused by the skew. The backwall displacement was primarily towards the acute corner during the low amplitude Run 2. However, at the higher amplitude runs (Run 3, 4, and 5), the backwall displacement was primarily towards the obtuse corner. The maximum average displacement of the backwall was 0.06 in. towards the acute corner in Run 2. The maximum average displacement increments of the backwall were 0.27, 0.29, and 0.47 in. towards the obtuse corner for Run 3, 4, and 5, respectively. These displacements were larger than those in the 0° skew case. The combined displacement histories of the backwall at the top and the bottom western corners are shown in Figure 6-96 for all the runs of the 30° skew test.

The displacement histories of the backwall measured at the top and the bottom western corners are shown in Figure 6-97 and Figure 6-98 for different runs of the 45° skew test. The general trend of the backwall displacement histories shows that the backwall movement was first towards the obtuse corner and then towards the acute corner. The maximum average displacement increments of the backwall were 0.05, 0.09, 0.25, and 0.44 in. towards the obtuse corner for Run 2, 3, 4, and 5, respectively. These displacements were larger than those in the 0° skew but close to those in the 30° skew case. The corresponding displacement increments were 0.12, 0.35, 0.73, and 0.72 in. towards the acute corner. The combined displacement histories of the backwall at the top and the bottom western corners are shown in Figure 6-99 for all the runs of the 45° skew test.

6.5.3. Vertical displacements

One string potentiometer was installed on the west side of the backwall to measure the vertical displacement. The potentiometer in the 45° skew model was vertical but had to be diagonal in the other two cases. The measurement in the former case provided the vertical displacement directly. For the other two case vertical displacements were found using triangulation. The different set ups used for different skew angles was due to geometric limitations. The layout of this string potentiometer (WDSP1) was presented in Chapter 5. For the case of 0° skew, a diagonal string potentiometer was connected to the top west corner of the backwall at the same point that the longitudinal string potentiometer (WLSP1) was connected, so that they formed a vertical plane. In the 30° skew test model, a diagonal string potentiometer was connected to the bottom west corner of the backwall at the same point that the transverse string potentiometer (WTSP2) was connected, so that they formed a vertical plane. The vertical displacement was determined in the 0º and 30º skew cases using geometric relationship between the two data sets. For the case of 45° skew model, a vertical string potentiometer was connected to the top west corner of the backwall to measure the vertical displacement directly.

The backwall vertical displacement histories are presented in this section in the form of incremental displacement for different runs. A positive displacement indicates the upward movement throughout this section.

The backwall displacement histories are shown in Figure 6-100 and Figure 6-101 for different runs of the 0° skew test. The top figure in each run shows the displacements measured by the intersecting longitudinal and diagonal string potentiometers and the bottom figure shows the vertical displacement. The data from the diagonal string potentiometer included some longitudinal displacement. The maximum upward displacement of the backwall was 0.03, 0.04, 0.07, and 0.10 in. for Run 2, 3, 6, and 7, respectively. These small upward movements of the backwall showed the effectiveness of the vertical restrainer link system on the top of the backwall. The maximum displacement in Run 3 (0.04 in.) occurred at 10.65 seconds, before the backwall was pushed back by the soil towards the bridge block. Afterwards, the displacement increased to 0.21 in. that was not considered as the maximum displacement.

The backwall displacement histories are shown in Figure 6-102 and Figure 6-103 for different runs of the 30° skew test. The top figure in each run shows the displacements measured by the intersecting transverse and diagonal string potentiometers and the bottom figure shows the vertical displacement. The data from the diagonal string potentiometer included some transverse displacement in this case. The maximum displacement of the backwall was 0.03, 0.19, 0.32, and 0.49 in. for Run 2, 3, 4, and 5, respectively. It is clear that the maximum displacements were significantly larger than those of the 0° skew case

The displacement histories of the backwall are shown in Figure 6-104 for different runs of the 45° skew test. The maximum displacement of the backwall was 0.07, 0.28, 0.40, and 0.53 in. for Run 2, 3, 4, and 5, respectively. These upward movements were close to those in the 30° skew case.

6.5.4. Axial forces in vertical restrainer link

A mass rig swivel link was installed vertically on the top of the backwall to restrain the vertical movement of the backwall. A load cell was attached to the swivel link to measure the vertical force.

The vertical force histories of the link are shown in Figure 6-105 for different runs of the 0° skew test. Positive force indicates the compression force. The maximum compression force in the link was 3.16, 4.20, 10.71, and 7.29 kips for Run 2, 3, 6, and 7, respectively.

The vertical force histories of the link are shown in Figure 6-106 for different runs of the 30° skew test. The maximum compression force in the link was 1.83, 8.15, 12.50, and 17.98 kips for Run 2, 3, 4, and 5, respectively. The link forces were larger than those in the non-skew case and were consistent with the upward movements of the backwall.

The vertical force histories of the link are shown in Figure 6-107 for different runs of the 45° skew test. The maximum compression force in the link was 1.95, 9.60, 11.22, and 13.06 kips for Run 2, 3, 4, and 5, respectively. The link forces were larger than those in the non-skew case. However, they did not follow a trend when compared with those from the 30° skew case, but were comparable.

6.5.5. Rotations about vertical axis

Four string potentiometers were installed at the four corners of the backwall at the top and the bottom of eastern and western sides to measure the backwall displacement in the direction of motion. The difference between the longitudinal displacement of the backwall at the eastern and western sides was used to calculate the backwall rotation about the vertical axis.

The calculated rotation histories of the backwall about the vertical axis are presented in this section in the form of combined rotation for different runs in all the cases. The combined rotation of the backwall includes the residual rotation from the previous runs. A positive displacement indicates movement towards the backfill soil and a rotation increase indicates counterclockwise rotation throughout this section.

The backwall rotation histories and the average longitudinal displacements of the backwall at the east and west sides are shown in Figure 6-108 and Figure 6-109 for different runs of the 0° skew test. The backwall primarily rotated counterclockwise followed by the clockwise rotation while returning to its initial position in Run 2 and 3. In Run 6 and 7, the backwall rotation was clockwise before 10.6 seconds and then became counterclockwise. Finally the backwall returned to its initial position in the clockwise direction while retaining some residual rotation.

Figure 6-110 shows the combined backwall rotation histories and the average longitudinal displacements of the backwall at the east and west sides for all the runs of the 0° skew test. The maximum rotation reached 0.15 and 0.19 degree in the counterclockwise direction in Run 2 and 3, respectively. In Run 6 after resetting the backwall to its initial position, the backwall rotated up to the maximum clockwise rotation of 0.19 degree. During Run 7, the backwall reached the maximum rotation of 0.03 degree in the counterclockwise direction and later rotated up to the maximum 0.23 degree in the clockwise direction.

The backwall rotation histories and the average longitudinal displacement of the backwall at the east and west sides are shown in Figure 6-111 and Figure 6-112 for different runs of the 30° skew test. The backwall rotation is shown to start from 30° that is the initial skew angle. The displacement of the backwall was always higher at the obtuse corner than that at the acute corner, except for Run 4 and 5 before 10.67 and 10.68 seconds, respectively, as previously discussed in Section 6.5.1. A very slight counterclockwise backwall rotation was observed up to 10.66, 10.59, 10.62, and 10.63 seconds for Run 2, 3, 4, and 5, respectively. Later while the backwall displacement was increasing, the backwall rotation reversed to the clockwise direction. Then the backwall returned towards its initial position in the counterclockwise direction while retaining some residual rotation. This trend was observed in all the runs. However, the first counterclockwise rotation and the following clockwise rotation increased in the higher amplitude runs.

Figure 6-113 shows the combined backwall rotation histories and the average longitudinal displacement of the backwall at the acute and obtuse corners of the bridge block for all the runs of the 30° skew test. The maximum backwall rotation was 29.96, 29.48, 29.25, and 28.89 degrees in the clockwise direction for Run 2, 3, 4, and 5, respectively.

The backwall rotation histories and the average longitudinal displacement of the backwall at the east and west sides are shown in Figure 6-114 and Figure 6-115 for different runs of the 45° skew test. The rotation of the backwall is shown to start from 45° that is the initial skew angle. For Run 2 when the first impact between the bridge block and the backwall occurred, the backwall rotated counterclockwise followed by the clockwise rotation while returning to its initial position. However, a similar trend to the 30° skew case was observed in the subsequent runs starting from Run 3. A very slight counterclockwise backwall rotation was observed up to 10.60, 10.63, and 10.62 seconds for Run 3, 4, and 5, respectively. Later while the backwall displacement was increasing, the backwall rotation reversed to the clockwise direction. Then the backwall returned towards its initial position in the counterclockwise direction while retaining some residual rotation. Similar to the 30° skew case, the first counterclockwise rotation and the following clockwise rotation increased in the higher amplitude runs.

Figure 6-116 shows the combined backwall rotation histories and the average longitudinal displacement of the backwall at the acute and obtuse corners of the bridge block for all the runs of the 45° skew test. The backwall reached the maximum counterclockwise rotation of 45.03 degrees in Run 2. The backwall rotated up to the maximum of 44.78, 44.65, and 44.34 degrees in the clockwise direction for Run 3, 4, and 5, respectively.

More discussion on the comparison of the bridge block and the backwall rotation is presented in Section 6.6.2.

6.5.6. Triaxial accelerations

Triaxial accelerometers were installed at three locations on the top of the backwall at the east and west edges and the center to measure the backwall acceleration due to the impact between the bridge block and the backwall. The layout of these accelerometers (WAC1, WAC2 and WAC3) was presented in Chapter 5. WAC1, WAC2 and WAC3 were placed at the west corner, center and east corner of the backwall, respectively.

6.5.6.1. Longitudinal accelerations

The measured acceleration histories of the backwall in the longitudinal direction are presented in this section for different runs in all the cases. The average the backwall acceleration histories are also presented. Positive acceleration indicates data towards the backfill soil throughout this section.

The backwall acceleration histories for different runs of the 0° skew test are shown in Figure 6-117 and Figure 6-118. The maximum backwall acceleration towards the soil was higher at the west corner than that at the east corner for all the runs. The maximum average acceleration of the backwall towards the soil was 2.39g, 4.56g, 5.87g, and 5.57g for Run 2, 3, 6, and 7, respectively.

The backwall acceleration histories for different runs of the 30° skew test are shown in Figure 6-119 and Figure 6-120. The maximum backwall acceleration towards the soil was higher at the acute corner than that at the obtuse corner for all the runs except for Run 4. The maximum acceleration exceeded the sensor capacity of 16g from Run 3 with the amplitude of 125% times the Sylmar motion. Therefore, the corresponding average acceleration histories are not shown for those runs. The maximum average acceleration towards the backfill soil was 7.24g in Run 2 but unknown in the subsequent runs.

The backwall acceleration histories for different runs of the 45° skew test are shown in Figure 6-121 and Figure 6-122. The maximum backwall acceleration towards the soil was higher at the obtuse corner than that at the acute corner for Run 2 and 5. However, the maximum acceleration towards the soil was higher at the acute corner than that at the obtuse corner for Run 3 and 4. The maximum acceleration exceeded the sensor capacity of 16g from Run 3 with the amplitude of 125% times the Sylmar motion. The maximum average acceleration towards the soil was 4.71g in Run 2 but unknown in the subsequent runs.

6.5.6.2. Transverse accelerations

The transverse acceleration histories of the backwall are presented in this section for different runs. The average acceleration histories of the backwall are also presented. Positive acceleration indicates data towards the west (acute corner in skewed cases) throughout this section.

The acceleration histories measured on the top of the backwall are shown in Figure 6-123 and Figure 6-124 for different runs of the 0° skew test. The maximum average acceleration of the backwall towards the west was 0.32g, 0.63g, 0.76g, and 1.82g for Run 2, 3, 6, and 7, respectively. The corresponding acceleration towards the east was 0.26g, 0.58g, 1.40g, and 1.76g. These accelerations were significantly smaller than the corresponding longitudinal accelerations.

The backwall acceleration histories are shown in Figure 6-125 and Figure 6-126 for different runs of the 30° skew test. The maximum acceleration exceeded the sensor capacity of 16g from Run 3 with the amplitude of 125% times the Sylmar motion. Therefore, the corresponding average acceleration histories are not shown for those runs. The maximum average acceleration was 2.05g towards the acute corner and 2.39g towards the obtuse corner in Run 2 but unknown in the subsequent runs. Again, these peak accelerations were significantly smaller that the corresponding maximum longitudinal acceleration of 7.24g.

The backwall acceleration histories are shown in Figure 6-127 and Figure 6-128 for different runs of the 45° skew test. The maximum acceleration exceeded the sensor capacity of 16g from Run 3. Therefore, the corresponding average acceleration histories are not shown for those runs. The maximum average acceleration of the backwall was 7.41g towards the acute corner and 4.78g towards the obtuse corner in Run 2 and greater than the corresponding maximum longitudinal acceleration of 4.71g. It can be seen that the maximum transverse accelerations increased as the skew angle increased due to the induced shear forces.

6.5.6.3. Vertical accelerations

The vertical acceleration histories measured on the top of the backwall are shown in this section for different runs. The average acceleration histories of the backwall are also presented. Positive acceleration indicates data in the upward direction throughout this section.

The backwall acceleration histories are shown in Figure 6-129 and Figure 6-130 for different runs of the 0° skew test. The maximum average upward acceleration of the backwall was 0.23g, 0.62g, 1.30g, and 0.49g for Run 2, 3, 6, and 7, respectively. The maximum average downward acceleration exceeded the corresponding upward acceleration and was 0.31g, 1.04g, 1.21g, and 2.01g.

The backwall acceleration histories are shown in Figure 6-131 and Figure 6-132 for different runs of the 30° skew test. The maximum upward acceleration of the backwall was higher at the acute corner than that at the obtuse corner for all the runs except for Run 4 (similar to the case of longitudinal acceleration). The maximum acceleration exceeded the sensor capacity of 16g from Run 3. The maximum average acceleration was 2.36g upwards and 2.11g downwards in Run 2 and was greater than the corresponding maximum acceleration of 0.23g and 0.31g in the non-skew case.

The backwall acceleration histories are shown in Figure 6-133 and Figure 6-134 for different runs of the 45° skew test. The maximum upward acceleration of the backwall was higher at the acute corner than that at the obtuse corner for all the runs except for Run 2. The maximum downward acceleration of the backwall was higher at the acute corner than that at the obtuse corner for all the runs except for Run 3. The maximum acceleration exceeded the sensor capacity of 16g from Run 3. The maximum average acceleration was 4.54g upwards and 4.66g downwards in Run 2 which was greater than the corresponding maximum accelerations in the 0° and 30° skew cases.

6.5.7. Concluding remarks on backwall response

Key findings from the backwall rotation response are discussed in this section. In contrast to the non-skew case, the backwall rotation followed a trend in the skewed cases. A very slight counterclockwise rotation was observed at first consistent with the initial in-plane rotation of the bridge block. Then the backwall rotation reversed to the clockwise direction while the backwall displacement increased since the resistance of the backfill soil was higher at the acute corner and the backwall had the tendency to rotate towards the acute corner. This movement of the backwall affected the bridge block rotation after the closure of the gap between the bridge block and the backwall regardless of the eccentricity between the centers of mass and stiffness of the bridge block.

6.6. Comparison of bridge block and backwall response

To capture the effect of interaction between the bridge block and the abutment backwall, key measured response parameters in Section 6.4 and 6.5 are compared in this section. The response parameters are the longitudinal displacement (direction of the shake table motions), rotation about the vertical axis, and the longitudinal impact acceleration.

6.6.1. Longitudinal displacements

The average relative displacements between the bridge block and the backwall are compared here. The bridge block displacement was taken as the average of data obtained from the two longitudinal string potentiometers at the north-west and south-west supports of the bridge block. The backwall displacement was the average of data obtained from the four longitudinal string potentiometers at the four corners of the backwall. Note that the bridge block had to close the 2-in. gap between the bridge block and the backwall before engaging the abutment. A positive displacement indicates movement towards the backfill soil throughout this section.

Figure 6-135 presents the comparison of average displacement of the bridge block (referred to as “Mass Block” in the figures) and the backwall for the 0° skew test. The maximum displacement of the bridge block and the backwall towards the soil occurred at almost the same time. The maximum average displacement increments of the bridge block towards the backfill soil were 1.95, 2.51, 4.01, and 5.07 in. for Run 2, 3, 6, and 7, respectively. The corresponding backwall displacement increments after the gap closure were 0.31, 0.68, 1.78, and 2.07 in., respectively. The bridge block displacements were larger than the backwall displacement since the backwall started to move after the bridge block displacement exceeded the 2-in. gap. The corresponding differences between the bridge block and the backwall maximum displacements were 1.64, 1.83, 2.23, and 3.00 in., respectively.

Figure 6-136 presents the comparison of average displacement of the bridge block and the backwall for the 30° skew test. Similar to the 0° skew case, the maximum displacement of the bridge block and the backwall towards the soil occurred at almost the same time. The maximum average displacement increments of the bridge block towards the backfill soil were 2.18, 4.25, 5.69, and 7.59 in. for Run 2, 3, 4, and 5, respectively. The corresponding backwall displacement increments after the gap closure were 0.23, 1.01, 1.28, and 1.87 in., respectively. The differences between the bridge block and the backwall maximum displacements were 1.95, 3.24, 4.41, and 5.72 in., respectively. The relative displacement between the bridge block and the backwall increased compared to the non-skew case, mostly in the high amplitude runs.

Figure 6-137 presents the comparison of average displacement of the bridge block and the backwall for the 45° skew test. Similar to the 0° and 30 ° skew cases, the maximum displacement of the bridge block and the backwall towards the soil occurred at almost the same time. The maximum average displacement increments of the bridge block towards the backfill soil were 2.39, 5.22, 6.42, and 8.41 in. for Run 2, 3, 4, and 5, respectively. The corresponding backwall displacement increments after the gap closure were 0.18, 0.81, 1.54, and 1.64 in., respectively. The differences between the bridge block and the backwall maximum displacements were 2.21, 4.41, 4.88, and 6.77 in., respectively. The relative displacement between the bridge block and the backwall increased compared to the 0° and 30° skew cases, mostly in the high amplitude runs.

6.6.2. Rotations about vertical axis

The in-plane rotation of the bridge block is compared with the backwall rotation about the vertical axis. The bridge block in-plane rotation was calculated based on the difference between data obtained from the two transverse string potentiometers at the north-west and south-west supports of the bridge block. The backwall rotation about the vertical axis was calculated based on the difference between data obtained from the longitudinal string potentiometers at the east and west corners of the backwall. A "rotation increase" indicates counterclockwise rotation throughout this section.

Figure 6-138 presents the comparison of the bridge block and the backwall rotation about the vertical axis for the 0° skew test. The peak rotations were relatively small in all cases because of the symmetry of loading and the test model components. The backwall and the bridge block rotated in opposite directions in all the runs except for Run 6, indicating no consistent trend when the skew angle was 0°.

Figure 6-139 presents the comparison of the bridge block and the backwall rotation about the vertical axis for the 30° skew test. The rotations were very close in Run 2 when the first impact between the bridge block and the backwall occurred. For the subsequent runs, the backwall rotation was generally less than the bridge block rotation, but in the same direction as of the bridge block for all the runs. Both the bridge block and the backwall rotated in the clockwise direction when the backwall reached its maximum longitudinal displacement. As previously discussed in Section 6.4.4, the bridge block initially rotated in the counterclockwise direction that was consistent with the existing eccentricity between the centers of mass and stiffness of the bridge block. However, after the impact between the bridge block and the backwall, the direction of the bridge block rotation reversed since the resistance of the backfill soil was higher at the acute corner and the backwall had the tendency to rotate towards the acute corner. This showed that the maximum rotation of the bridge block that resulted in the maximum response of the abutment system was independent of the bridge block eccentricity and was controlled by the skew angle. The bridge block rotation followed the same direction as the backwall rotation due to the impact between the bridge block and the backwall.

Figure 6-140 presents the comparison of the bridge block and the backwall rotation about the vertical axis for the 45° skew test. The backwall rotation was primarily in the same direction as the bridge block rotation for all the runs except for Run 2 with small rotation values. Starting from Run 3, both the bridge block and the backwall rotated in the clockwise direction when the backwall reached its maximum longitudinal displacement. Similar to the case with the 30° skew, the maximum rotation of the bridge block that resulted in the maximum response of the abutment system was independent of the bridge block eccentricity and was controlled by the skew angle. The bridge block rotation followed the same direction as the backwall rotation due to the impact between the bridge block and the backwall.

6.6.3. Longitudinal impact accelerations

Four PCB and four Kistler accelerometers were installed in the direction of motion at the miF-height eastern and western vertical edges of both the bridge block and the backwall to measure the longitudinal acceleration due to the impact after the gap closure in the 0° skew case. However, since the Kistler accelerometers reached their limit of about 50g in the 0° skew test, only four PCB accelerometers were used in the 30° and 45° skew tests.

The acceleration histories measured by the impact accelerometers on the bridge block and the backwall are presented in this section for different runs. Positive acceleration indicates data towards the backfill soil throughout this section.

Comparison of impact acceleration measured by PCB and Kistler accelerometers is shown in Figure 6-141 and Figure 6-142 for different runs of the 0° skew test. The peak values shown in the figures are for the PCB accelerometers. The measured data from the two accelerometer types were comparable. The maximum average acceleration of the bridge block corners towards the soil was 7.59g, 7.25g, 25.04g, and 42.39g for Run 2, 3, 6, and 7, respectively. The corresponding maximum average acceleration of the backwall corners towards the soil was 6.99g, 32g, 28.65g, and 31.45g, respectively.

Comparison of impact acceleration measured by PCB impact accelerometers is shown in Figure 6-143 and Figure 6-144 for different runs of the 30° skew test. The maximum acceleration of the backwall at each corner was higher than that of the bridge block. The maximum acceleration of both the bridge block and the backwall towards the soil was higher at the obtuse corner than that at the acute corner for all the runs. The maximum average acceleration of the bridge block corners towards the soil was 2.02g, 8.95g, 22.52g, and 17.99g for Run 2, 3, 4, and 5, respectively. The corresponding maximum average acceleration of the backwall corners towards the soil was 3.95g, 19.91g, 46.61g, and 65.13g, respectively. Similar to the 0° skew case, the maximum average acceleration of the backwall corners was higher than that of the bridge block corners for all the runs.

Comparison of impact acceleration measured by PCB impact accelerometers is shown in Figure 6-145 and Figure 6-146 for different runs of the 45° skew test. The maximum acceleration of both the bridge block and the backwall towards the soil was higher at the obtuse corner than that at the acute corner for all the runs. The maximum average acceleration of the bridge block corners towards the soil was 4.52g, 21.50g, 28.25g, and 12.99g for Run 2, 3, 4, and 5, respectively. The average maximum acceleration of the two corners of the backwall towards the soil was 5.04g, 15.57g, 20.54g, and 12.08g for Run 2, 3, 4, and 5, respectively.

6.6.4. Concluding remarks on bridge block and backwall response

Important findings from comparing the bridge block and the backwall response are presented in this section to explain the interaction between the bridge block and the abutment.

The comparison of the bridge block and the backwall rotations did not follow a consistent trend as the motion amplitude increased in the non-skew case. Also, the rotations were very small and attributed to impact at random points between the bridge block and the backwall. However, in the skew cases, the bridge block initially rotated in the counterclockwise direction that was consistent with the eccentricity between the centers of mass and stiffness of the bridge block. After the impact between the bridge block and the backwall, the direction of the bridge block rotation reversed since the resistance of the backfill soil was higher at the acute corner and the backwall had the tendency to rotate towards the acute corner. Therefore, the maximum rotation of the bridge block corresponding to the maximum response of the abutment system was independent of the bridge block eccentricity and followed the abutment backwall rotation due to the skew angle configuration.

6.7. Backfill soil response

Observations and measured data were used to investigate the backfill soil response. These consisted of soil pressure, soil surface cracks, soil surface heaves, triaxial accelerations, longitudinal displacements, and failure planes.

6.7.1. Soil pressure measured by pressure cells

Six earth pressure cells were installed on the surface of the backwall to measure the soil pressure. The layout of pressure cells (PC1, PC2, PC3, PC4, PC5 and PC6) was presented in Chapter 5.

The measured soil pressure histories are presented in this section for different runs. Positive pressure indicates data towards the bridge block throughout this section. The distribution of maximum measured pressure along the backwall height is also presented for each run.

During a uniform push of abutment backwall into the backfill, it is expected that the pressure at the acute corner of the bridge be higher than the pressure at the obtuse corner due to the larger volume of soil resisting at the acute corner of the bridge. This was observed in the previous static testing of abutments in which a concrete wedge was pushed into the soil with almost no rotations (Rollins et al., 2010; Marsh et al., 2012; Marsh et al., 2013; Rollins & Jessee, 2012). However, this trend was not always seen in the current tests in which dynamic earthquake loading was simulated. The variation of pressure at the acute and obtuse corners in the shake table tests depended mostly on the direction of the backwall rotation. Effect of backwall rotation on the soil pressure distribution is analyzed in detail in the next section. Non-uniform contacts between the bridge deck and abutment backwall might occur after the gap closure in case of a seat-type abutment due to the in-plane rotation of the bridge. Therefore, the soil pressure could vary along the width even when the skew angle is zero.

The soil pressure histories measured on the backwall and the maximum pressure distribution along the backwall height are shown in Figure 6-147 to Figure 6-151 for different runs of the 0° skew test. As a general trend, the maximum mid height pressure at the west corner of the backwall was higher than that at the east corner of the backwall in Run 2 and 3. In contrast, the maximum mid height pressure at the east corner of the backwall was higher than that at the west corner of the backwall for Run 4, 6, and 7 of the 0° skew test. The ratio of the maximum mid height pressure at the west to the east corner was 4.47 and 2.10 for Run 2 and 3, respectively. However, this ratio was less than 1 equal to 0.85, 0.63 and 0.95 in Run 4, 6 and 7, respectively.

The soil pressure histories measured on the backwall and the maximum pressure distribution along the backwall height are shown in Figure 6-152 to Figure 6-155 for different runs of the 30° skew test. As a general trend, the maximum mid height pressures at the obtuse corner were higher than those at the acute corner in all the runs except for Run 4. The ratio of the maximum mid height pressure at the acute corner to the obtuse corner was 0.58 and 0.87 for Run 2 and 3, respectively. However, this ratio was greater than 1 equal to 1.23 in Run 4 and was less than 1 equal to 0.87 in Run 5.

The soil pressure histories measured on the backwall and the maximum pressure distribution along the backwall height are shown in Figure 6-156 to Figure 6-159 for different runs of the 45° skew test. In contract to the 30° skew case, the maximum mid height pressure at the acute corner was higher than that at the obtuse corner for all the runs of the 45° skew test. The ratio of the maximum mid height pressure at the acute corner to the obtuse corner was 7.58, 1.85, 1.21, and 1.25 for Run 2, 3, 4, and 5, respectively.

6.7.2. Effect of backwall rotation on soil pressure

Pressure cell data could be affected by the backwall rotation about the vertical axis because rotation could increase pressure in some area while reducing it in others. A "rotation increase" indicates counterclockwise rotation throughout this section and "positive pressure difference" means higher pressure at the west corner (acute corner in the skew cases) than the east corner (obtuse corner in the skew cases) pressure.

The influence of backwall rotation on the soil pressures at the backwall corners is presented in Figure 6-160 and Figure 6-161 for different runs of the 0° skew test. The top figure of each run shows the backwall rotation history and the bottom figure shows the pressure difference history (the difference between the west and the east corner pressures). As previously discussed in Section 6.5.5, the abutment maximum response in Run 2 and 3 occurred when the backwall rotation was counterclockwise (Figure 6-108). In contrast, the maximum response in Run 6 and 7 occurred when the backwall rotation was clockwise (Figure 6-109). Figure 6-160 and Figure 6-161 clearly show that rotation of the backwall affected the difference in the soil pressures. The pressure difference increased as the backwall rotation increased, and vice versa. The pressure at the west corner was higher than that at the east corner (positive pressure difference) when the backwall rotation was counterclockwise, as seen in Run 2 and 3. However, the pressure at the west corner was lower than the east corner pressure (negative pressure difference) when the backwall rotation was clockwise, as seen in Run 6 and 7.

The effect of backwall rotation on the soil pressures at the backwall corners is presented in Figure 6-162 and Figure 6-163 for different runs of the 30° skew test. As previously discussed, the abutment maximum response in all the runs occurred when the backwall rotation was clockwise (Figure 6-111 and Figure 6-112). Similar to the 0° skew case, the change in the backwall rotation was consistent with the difference between the corner pressures. The pressure difference increased as the backwall rotation increased, and vice versa. The pressure at the acute corner was lower than that at the obtuse corner (negative pressure difference) since the backwall rotation was clockwise.

The trend that was seen for the 0° and 30° skew cases is also evident in Figure 6-164 and Figure 6-165 for different runs of the 45° skew test. Recall that the abutment maximum response in all the runs in the 45° skew case occurred when the backwall rotation was clockwise (Figure 6-114 and Figure 6-115). The pressure at the acute corner was lower than the pressure at the obtuse corner (negative pressure difference), similar to the 30° skew test, since the backwall rotation was clockwise.

6.7.3. Soil pressure measured by FlexiForce sensors

FlexiForce sensors were attached to the box of soil sensors clusters to measure the longitudinal pressure inside the backfill soil. FlexiForce sensors were installed at three different layers of the top, middle and the bottom of the soil, at the same heights where the pressure cells had been installed on the backwall. The layout of FlexiForce sensors was presented in Chapter 5. In addition, one FlexiForce sensor (FLPC) was installed on the central pressure cell (PC3) in the 0° and 45° skew tests to compare the data from the two devices. The total number of FlexiForce sensors was 17, 15, and 13 for the 0°, 30°, and 45° skew tests, respectively.

Experimental data measured by each FlexiForce sensor at different locations inside the backfill soil are presented in this section for different runs. The pressure histories measured by the earth pressure cells along the same longitudinal line (north-south direction) of FlexiForce sensors in the corresponding layer are also shown for comparison. Positive pressure indicates data towards the backfill soil throughout this section except for the FlexiForce sensor installed directly on the pressure cell (FLPC) for which the positive direction is towards the bridge block.

The soil pressure histories in the direction of motion are shown in Figure 6-166 to Figure 6-175 for different runs of the 0° skew test. Six out of the 17 FlexiForce sensors (FL25, FL34, FL38, FL39, FL40, and FL45) did not record reasonable data probably due to damage to the sensor during soil compaction. The data recorded by the FlexiForce sensor installed on the central pressure cell (FLPC) was not reliable in Run 4. After the impact in Run 3, the wall was pushed back towards the bridge block more that it was expected, as discussed in Section 6.5.1. Therefore, FLPC was disconnected from the pressure cell since its cable ran towards the end of the soil box. FLPC could not be re-installed during the re-construction of backfill soil adjacent to the backwall after Run 4. Therefore, there is no data measured by FLPC for Run 6 and 7. The maximum mid height pressure measured by FlexiForce sensors cannot be compared between the east and west corners of the backwall for the row of sensors installed at 6.5-ft distance from the backwall (FL23, FL24, and FL25) since FL25 data was not reliable. The data obtained from

FL25 was not comparable to the adjacent sensors since Run 2. It was concluded that the sensor was damaged.

The soil pressure histories in the direction of motion are shown in Figure 6-176 to Figure 6-183 for different runs of the 30° skew test. Three out of the 15 FlexiForce sensors (FL9, FL28, and FL36) did not record reasonable data probably due to damage to the sensor during soil compaction. The data from the row of the FlexiForce sensors at 6.5-ft distance from the backwall at the middle layer of soil (FL22, FL23, and FL24) showed that the maximum mid height pressure at the obtuse corner was higher than that at the acute corner for all the runs. This trend is in agreement with the pressure cells data except for Run 4.

The soil pressure histories in the direction of motion are shown in Figure 6-184 to Figure 6-191 for different runs of the 45° skew test. Four out of the13 FlexiForce sensors (FL27, FL35, FL36, and FL37) did not record reasonable data probably due to damage to the sensor during soil compaction. The data obtained from FLPC was not also reliable to compare with the data obtained from the pressure cells.

6.7.4. Surface cracks

The observed crack patterns of backfill soil surface were marked after each run to track the progression of surface cracks.

Figure 6-192 to Figure 6-195 show the crack patterns of backfill soil surface from different views for different runs of the 0° skew test. After Run 2 when the first impact between the bridge block and the backwall occurred, the surface cracks were observed at a distance of about 1 ft from the east corner of the backwall and about 1 to 2 ft from the west corner. After Run 3, the surface cracks extended to a distance of more than 3 ft from the center of the backwall and up to about 1.5 ft from the east corner. During Run 3, the backwall was pushed back towards the shake table after it was hit by the backfill soil. This occurred because the backwall was nearly free to move with little friction at the base. The movement led to the settlement of the soil adjacent to the backwall approximately 6 to 8 in., as seen in Figure 6-193. As mentioned in Section 6.5.1, the next run was repeated with the amplitude of 50% times the Sylmar motion and the same system response was observed. Due to the limits of the shake table, the test was stopped to provide a lateral restrainer system for the backwall. The failed part of the soil adjacent to the backwall was removed using a shop vacuum and the backwall was placed in its initial position. The soil was then placed in layers and compacted using a hand tamper (Figure 6-196). After re-construction of soil, Run 6 with the amplitude of 150% times the Sylmar motion was applied. In addition to the surface cracks from the previous runs, new cracks were observed at a distance of about 4 ft from the center of the backwall (Figure 6-194). After Run 7, the surface cracks remained at about 4 ft from the center of the backwall with no new cracks observed (Figure 6-195). Figure 6-197 presents the progression of surface crack during the 0° skew test.

Figure 6-198 to Figure 6-201 show the crack patterns of backfill soil surface at different views of the backwall for different runs of the 30° skew test. After Run 2 when the first impact between the bridge block and the backwall occurred, a major surface crack at a distance of about 2 ft from the center of the backwall to the acute corner was observed. However, the crack did not extend to the obtuse corner (Figure 6-198). After Run 3, new surface cracks (marked with blue color) extended to both corners of the backwall and embankment slopes at both sides. Cracks perpendicular to the direction of motion were extended towards the acute corner and at a distance of about 1.5 ft from the corner of the backwall at the obtuse corner (Figure 6-199). After Run 4, some new surface cracks (marked with white color) were observed at a distance of about 1 ft from the backwall at the acute corner. Furthermore, cracks propagated to about 4 ft and 6 ft from the center of the backwall in the directions perpendicular and parallel to the direction of motion, respectively (Figure 6-200). After Run 5, new surface cracks (marked with red color) were extended up to a distance of about 5 ft from the center of the backwall and about 8 ft from the obtuse corner (Figure 6-201). Surface cracks perpendicular to the direction of motion were generally formed parallel to the skew angle. The backwall corner cracks were formed at both sides, mostly concentrated at the acute corner but were scattered at the obtuse corner. Figure 6-202 presents the progression of surface crack during the during the 30° skew test.

Figure 6-203 to Figure 6-206 show the crack patterns of backfill soil surface at different views of the backwall for different runs of the 45° skew test. After Run 2 when the first impact between the bridge block and the backwall occurred, a major surface crack propagated from the center of the backwall towards the obtuse corner at a distance of about 2 ft from the backwall. This crack extended to the backwall corner at the acute side of the bridge block (Figure 6-203). After Run 3, new surface cracks (marked with blue color) extended at a distance of about 3 ft from the center of the backwall and about 3.5 ft from the backwall at the obtuse corner (Figure 6-204). After Run 4, some new surface cracks (marked with yellow color) propagated at a distance of about 6 ft from the backwall center and from the backwall corner at the obtuse side of the bridge block. New cracks were extended to a distance of about 3 ft from the backwall comer at the acute side of the bridge block (Figure 6-205). After Run 5, more surface cracks (marked with red color) were observed at a distance of about 5 ft from the center of the backwall (Figure 6-206). Similar to the 30° skew case, surface cracks perpendicular to the direction of motion were primarily formed parallel to the skew angle. The crack patterns show the engaged part of the soil, mostly concentrated at the acute corner but were scattered at the obtuse corner. Figure 6-207 the global views of crack patterns of backfill soil surface for different runs of the 45° skew test.

6.7.5. Surface heaves

LVDTs were installed on the surface of the backfill soil to measure the vertical displacement (heaving) of soil surface. The total number of LVDTs was 20, 17, and 17 for the 0°, 30°, and 45° skew tests, respectively. The LDVTs locations were presented in Chapter 5. LVDTs were installed on the soil surface within the backwall width as well as on the embankment slopes. The LVDTs on the embankment slopes were installed perpendicular to the slope. Therefore, the measured heaving of embankment slopes was converted to vertical displacement based on the angle of the LVDTs.

The measured heaving of the soil surface is presented in this section in two forms of incremental and combined displacements for different runs. The incremental displacement is shown to start from zero for each run, with the permanent displacement from the previous run removed. However, the combined displacement histories include the residual displacement from the previous runs. Finally, contour plots of the maximum combined heaves of the soil surface are presented for clear qualitative observation of the performance of the abutment soil. A positive displacement indicates the upward movement throughout this section.

Groundwater Modeling System (GMS 10.1.3) was used to plot the heave contours. A grid of cells was created in GMS so that the location of each sensor corresponded to the center of each cell. The maximum response of each sensor (maximum vertical displacement of soil surface) was assigned to the property of each cell. GMS interpolates data from the center of the cells to the corners of the cells and mid sides of the cells in order to triangulate and contour the grids. Five cells were created in the north-south direction with the total length of 22 ft for the 0° and 45° skew cases with the sizes of 4 ft and 5 ft to match with the distance of the first sensor from the backwall and the spacing between the sensors in the direction of motion. However, due to the different configuration of sensors for the 30° skew case and limitation of grid making in GMS, ten cells in the north-south direction were created with the size of 2.25 ft equal to half of the spacing between the sensors in the direction of motion. Since the data for some of the cells were not recorded according to this configuration, the Inverse Distance Weighting (IDW) method was first used to estimate the displacement for those cells based on the displacement of the adjacent cells.

The heave histories measured on the soil surface are shown in Figure 6-208 to Figure 6-212 for different runs of the 0° skew test. The heave was slightly larger at the center and west corner of the backwall than the east corner heave in all the runs except for Run 6, but the difference was not significant.

The combined heave histories are shown in Figure 6-213 for all the runs of the 0° skew test. Residual heaves increased as the amplitude of the earthquake increased. Similar to the heave increments, the combined heaves at the center of the backwall were slightly larger than those at the corners. The soil heaves on the embankment slopes were about one-half of those on the adjacent flat surface.

The contours of the maximum combined heaving of the soil surface are shown in Figure 6-214 for different runs of the 0° skew test. The general trend was a symmetric distribution of the maximum heave about the centerline of the bridge block because of the zero skew case. The maximum combined heave was 1.52 in. The area with the maximum heave greater than 0.1 in. extended to about 3.1 times the backwall height from the center of the backwall in Run 7. The 3D effect was also seen beyond the backwall width on the embankment slopes under the higher amplitude runs.

The heave histories measured on the soil surface are shown in Figure 6-215 to Figure 6-218 for different runs of the 30° skew test. Two LVDTs close to the backwall at the obtuse corner (SLVDT4 and SLVDT5) could not be installed due to an issue with the reference frame installation. The heave increments were larger at the center and the obtuse corner than those at the acute corner for all the runs due to the direction of backwall rotation.

The combined heave histories are shown in Figure 6-219 for all the runs of the 30° skew test. Residual heaves increased as the amplitude of the motion increased. Similar to the heave increments, the combined heave at the obtuse corner was larger than that at the acute corner. The soil heave on the embankment slope near the backwall at the acute corner was about quarter of that on the adjacent flat surface. In contrast, a reverse trend was observed at the obtuse corner. The heaves of the embankment slope and the flat surface were very close at the obtuse corner.

The contours of the maximum combined heaving of the soil surface are shown in Figure 6-220 for different runs of the 30° skew test. The general trend was an un-symmetric distribution of the maximum heave about the centerline of the bridge block due to the skew. The maximum combined heave was 1.37 in. The area with the maximum heave greater than 0.1 in. extended to about 2.4 times and 3 times the backwall height from the center of the backwall for Run 4 and 5, respectively. The area affected by the surface heaves propagated towards the obtuse corner.

The heave histories measured on the soil surface for different runs of the 45° skew test are shown in Figure 6-221 to Figure 6-224. One of the LVDTs close to the backwall at the obtuse corner (SLVDT5) could not be installed due to an issue with the reference frame installation. Another LVDT close to the backwall at the obtuse corner (SLVDT10) could not be retrieved. Similar to the 30° skew case, the heave increments were larger at the center and the obtuse corner than that at the acute corner for all the runs due to the smaller volume of soil providing the passive resistance at the obtuse corner.

The combined heave histories are shown in Figure 6-225 for all the runs of the 45° skew test. Residual heaves increased as the amplitude of the motion increased except for the LVDT adjacent to the backwall center (SLVDT3). The soil settled down at this location due to the movement of the backwall away from the soil. Similar to the heave increments, the combined heave at the obtuse corner was larger than those at the acute corner. The soil heave on the embankment slope near the acute corner was much lower than that on the adjacent flat surface. Therefore, the embankment slope at the acute corner of the 45° skew case was engaged less than the 30° skew case.

The contours of the maximum combined heaves of the soil surface are shown in Figure 6-226 for different runs of the 45° skew test. Similar to the 30° skew case, the general trend was an un-symmetric distribution of the maximum heave about the centerline of the bridge block due to the skew. The maximum combined heave was 1.04 in. The area with the maximum heave greater than 0.1 in. extended to about 1.9 times and 2.1 times the backwall height from the center of the backwall for Run 4 and 5, respectively. Similar to the 30° skew case, the area affected by the surface heaves propagated towards the obtuse corner.

The comparison of maximum combined heave contours for the three skew angles is presented in Figure 6-227. The maximum heaving decreased when the skew angle increased. The area affected by the maximum heaves reduced by increasing the skew angle in a similar amplitude run.

6.7.6. Triaxial accelerations

Triaxial accelerometers were installed inside the backfill soil at three different layers of top, middle, and bottom of the soil, at the same height where the pressure cells had been installed. The total number of accelerometers was 47, 43, and 42 for the 0°, 30°, and 45° skew tests, respectively. The layout of accelerometers was presented in Chapter 5.

Experimental data measured by each accelerometer in the longitudinal, transverse, and vertical directions at different locations inside the backfill soil are presented in this section for different runs. The measured triaxial acceleration histories are presented in Appendix F. Each figure in the appendix shows the measured acceleration in one specific direction at the three different layers. Furthermore, contour plots of the maximum measured acceleration in different directions are presented for a clear qualitative observation of the experimental results. Groundwater Modeling System (GMS 10.1.3) was used to plot the maximum acceleration contours, as described in Section 6.7.5.

6.7.6.1. Longitudinal accelerations

The backfill acceleration histories are shown in Figure F-1 to Figure F-5 for different runs of the 0° skew test. Positive acceleration indicates data towards the backfill soil throughout this section. The data from Run 6 and 7 in one of the accelerometers in the middle layer (SAC19) was erratic perhaps due to damage to the sensor.

The contours of the maximum accelerations are shown in Figure 6-228 for different runs of the 0° skew test. The plots showed a nearly symmetric distribution of accelerations in the non-skew case, which was expected. The maximum acceleration was slightly higher at the west corner of the backwall than that at the east corner in Run 2 and 3. In contrast, the maximum acceleration was slightly lower at the west corner of the backwall than that at the east corner in Run 6 and 7. This trend was very similar to the variation of the maximum pressure measured by the pressure cells at the two corners of the backwall, as discussed in Section 6.7.1. The trend is attributed to the backwall rotation about the vertical axis. The calculated rotations (Section 6.5.5) showed that the maximum response in Run 2 and 3 occurred when the backwall rotation was counterclockwise (Figure 6-108). In contrast, the maximum response in Run 6 and 7 occurred when the backwall rotation was clockwise (Figure 6-109). The acceleration peaked in the middle and the bottom layers of the soil rather than in the top layer for all the runs except for Run 7. The maximum acceleration was 7.75g in the bottom layer of the soil at the center of the backwall in Run 6.

The backfill acceleration histories are shown in Figure F-6 to Figure F-9 for different runs of the 30° skew test. The data from five of the 43 accelerometers (SAC7, SAC11, SAC18, SAC24, and SAC41) could not be retrieved.

The contours of maximum accelerations are shown in Figure 6-229 for different runs of the 30° skew test. The plots showed an un-symmetric distribution of accelerations due to the skew. The maximum acceleration was generally higher at the obtuse corner than that at the acute corner. The trend was attributed to the backwall rotation about the vertical axis. The calculated rotations (Section 6.5.5) showed that the maximum response of all the runs occurred when the backwall rotation was clockwise (Figure 6-111 and Figure 6-112). The maximum acceleration occurred in the middle and the bottom layers of the soil rather than in the top layer. The maximum acceleration was 11.34g in the middle layer of the soil at the obtuse corner in Run 5.

The backfill acceleration histories are shown in Figure F-10 to Figure F-13 for different runs of the 45° skew test. The data from three out of the 42 accelerometers (SAC8, SAC20, and SAC23) was unreliable starting from the first run perhaps due to damage to the sensor.

The contours of the maximum accelerations are shown in Figure 6-230 for different runs of the 45° skew test. The plots showed an un-symmetric distribution of accelerations due to the skew. The maximum acceleration was higher at the acute corner than that at the obtuse corner for all the runs except for the top and middle layers of the soil in Run. This trend was attributed to the backwall rotation about the vertical axis. Similar to the 30° skew case, the calculated rotations (Section 6.5.5) showed that the maximum response of all the runs occurred when the backwall rotation was clockwise (Figure 6-114 and Figure 6-115). Therefore, it was expected that the maximum acceleration of the backfill soil occur at the obtuse corner. This was the case only for the top and middle layers of the soil in Run 5. The backfill soil at the bottom obtuse corner was not engaged until Run 4. This is attributed to the fact that the gap between the backwall and the bridge block on the east side was significantly larger than that on the west side. The variation in the gap was due to slight irregularity of the bridge block surface and the residual displacement in the isolators. Table 6-3 presents the measured gaps between the backwall and the bridge block before starting each run. The average gap was larger at the acute corner than that at the obtuse corner for the 45° skew case. The difference between the average gap of the two corners was 1.5, 1.25, 2.25, and 2.91 in. before starting Run 2, 3, 4, and 5, respectively. The maximum acceleration occurred in the middle and the top layers of the soil rather than in the bottom layer for all the runs except for Run 3. The maximum acceleration was 5.90g in the bottom layer at the acute corner in Run 3. The maximum acceleration was relatively low because of the large gap at the obtuse corner.

6.7.6.2. Transverse accelerations

The transverse acceleration histories of the backfill soil are shown in Figure F-14 to Figure F-18 for different runs of the 0° skew test. Positive acceleration indicates data towards the west (acute corner in skew cases) throughout this section. One of the accelerometers in the middle layer (SAC19) was damaged and did not record any data in Run 6 and 7.

The contours of maximum transverse accelerations towards the east and the west are shown in Figure 6-231 and Figure 6-232, respectively, for different runs of the 0° skew test. The contours show that the maximum acceleration towards the east increased from the top layer to the bottom layer of the soil. The maximum acceleration towards the east and the west occurred at the east corner and west corner of the backwall, respectively. The maximum acceleration towards the east was 2.73g in the bottom layer at the east corner of the backwall in Run 7. The maximum acceleration towards the west was 3.22g in the middle layer at the west corner of the backwall in Run 6.

The backfill acceleration histories are shown in Figure F-19 to Figure F-22 for different runs of the 30° skew test. Data from five out of the 43 accelerometers (SAC7, SAC11, SAC18, SAC24, and SAC 41) could not be retrieved.

The contours of maximum accelerations towards the obtuse corner and the acute corner are shown in Figure 6-233 and Figure 6-234, respectively, for different runs of the 30° skew test. The maximum acceleration towards the obtuse and the acute corner occurred at the obtuse corner. This was similar to what was seen in the maximum longitudinal acceleration. The maximum acceleration towards the obtuse corner was 4.18g in the top layer at the center of the backwall in Run 4. The maximum acceleration towards the acute corner was 3.92g in the middle layer at the obtuse corner in Run 5.

The backfill acceleration histories are shown in Figure F-23 to Figure F-26 for different runs of the 45° skew test. Data from three out of the 42 accelerometers (SAC8, SAC20, and SAC23) were unreliable starting from the first run probably because of damage to the sensor or to the connection cables during the previous tests.

The contours of maximum accelerations towards the obtuse corner and the acute corner are shown in Figure 6-235 and Figure 6-236, respectively, for different runs of the 45° skew test. The maximum acceleration towards the obtuse corner was 4.01g in the top layer of the soil at the obtuse corner in Run 5. The maximum acceleration towards the acute corner was 1.97g in the middle layer at the center of the backwall in Run 4.

6.7.6.3. Vertical accelerations

The vertical acceleration histories of backfill soil are shown in Figure F-27 to Figure F-31 for different runs of the 0° skew test. Positive acceleration indicates data the upward acceleration throughout this section. One of the accelerometers in the middle layer of the soil (SAC19) was damaged and did not record any data in Run 6 and 7.

The contours of the maximum upward accelerations are shown for different runs of the 0° skew test in Figure 6-237. Although the maximum acceleration pattern in the middle layer was symmetrical, distribution of acceleration in the top and the bottom layers was unsymmetrical. Similar to the case of longitudinal acceleration, the maximum response in Run 2 and 3 occurred when the backwall rotation was counterclockwise. In contrast, the maximum response of Run 6 and 7 occurred when the rotation of the backwall was clockwise. The maximum upward acceleration was 6.85g in the top layer of the soil at the east corner of the backwall in Run 6.

The vertical acceleration histories of backfill soil are shown in Figure F-32 to Figure F-35 for different runs of the 30° skew test. Data from five out of the 43 accelerometers (SAC7, SAC11, SAC18, SAC24, and SAC41) could not be retrieved.

The contours of the maximum upward accelerations are shown in Figure 6-238 for different runs of the 30° skew test. The maximum upward acceleration occurred at the obtuse corner. This was similar to the case of maximum longitudinal acceleration and maximum transverse acceleration in which the maximum response of all the runs occurred when the backwall rotation was clockwise. The maximum upward acceleration was 4.89g in the top layer of soil at the acute corner in Run 5.

The vertical acceleration histories of backfill soil are shown in Figure F-36 to Figure F-39 for different runs of the 45° skew test. Data from three out of the 42 accelerometers (SAC8, SAC20, and SAC23) were unreliable starting from the first run probably because of damage to the sensor or to the connection cables during the previous tests.

The contours of the maximum upward accelerations are shown in Figure 6-239 for different runs of the 45° skew test. The maximum upward acceleration was 2.56g in the middle layer of soil at the obtuse corner in Run 5.

6.7.7. Longitudinal displacements

String potentiometers were attached to the soil sensor clusters to measure the longitudinal displacement inside the backfill soil. Six string potentiometers were installed at the middle layer of the soil matching the mid height of the backwall. The layout of string potentiometers was presented in Chapter 5. In addition, two string potentiometers were installed on the concrete blocks restraining the south end wall of the soil box to measure any movement of the end wall. Three string potentiometers were also attached to the south end wall of the soil box in the 45° skew case to compare the displacements relative to those measured by the string potentiometers inside the backfill soil.

Experimental data measured by the string potentiometers at different locations inside the backfill soil are presented in this section in two forms of incremental and combined displacements for different runs. The incremental displacement is shown to start from zero for each run, with the permanent displacement from the previous run removed. However, the combined displacement histories include the residual displacement from the previous runs. The displacement histories at the corners and the center of the backwall are also shown for comparison. A positive displacement indicates movement towards the backfill soil throughout this section.

The backfill displacement histories are shown in Figure 6-240 to Figure 6-244 for different runs of the 0° skew test. Soil displacement at a distance of 6.5 ft from the backwall center was 0.04, 0.13, 0.56, and 0.34 in. for Run 2, 3, 6, and 7, respectively. The combined displacement histories of backfill soil are shown in Figure 6-245 for all the runs of the 0° skew test. The maximum combined displacement of soil at a distance of 6.5 ft from the backwall was 0.73, 1.00, and 0.83 in. at the western corner, center, and the eastern corner of the backwall, respectively.

The backfill displacement histories are shown in Figure 6-246 to Figure 6-249 for different runs of the 30° skew test. The variation of displacements of the backfill soil at the acute and obtuse corners of the bridge block followed the same trend as of the displacement of the backwall. The maximum backfill displacement at a distance of 6.5 ft from the backwall center was 0.04, 0.34, 0.35, and 0.54 in. for Run 2, 3, 4, and 5, respectively. The combined displacement histories of backfill soil are shown in Figure 6-250 for all the runs of the 30° skew test. The maximum combined displacement of soil at a distance of 6.5 ft from the backwall was 0.37, 1.13, and 1.43 in. at the acute corner, center, and the obtuse corner, respectively.

The backfill displacement histories are shown in Figure 6-251 to Figure 6-254 for different runs of the 45° skew test. One of the string potentiometers (SSP27) could not be installed during the backfilling process due to the lack of the connection cable. The variation of displacements of the backfill soil at the acute and obtuse corners of the bridge block followed the same trend as of the displacement of the backwall. The maximum displacement of soil at a distance of 6.5 ft from the backwall center was 0.02, 0.15, 0.11, and 0.12 in. for Run 2, 3, 4, and 5, respectively. The combined longitudinal displacement histories of the backfill soil are shown in Figure 6-255 for all the runs of the 45° skew test. The maximum combined displacement of soil at a distance of 6.5 ft from the backwall was 0.11, 0.30, and 0.54 in. at the acute corner, center, and the obtuse corner, respectively.

6.7.8. Failure planes

Small diameter gypsum and colored sand columns were embedded at different locations inside the backfill soil to identify the failure planes after the tests. The layout of gypsum and colored sand columns was presented in Chapter 5. The right column is the nearest to the backwall in all the figures throughout this section.

The gypsum columns excavated from the backfill soil after the 0° skew test are shown in Figure 6-256. The figures show the gypsum columns of both east and west sides of the backwall placed in one single row based on their distance from the backwall. The marked columns in the top figure and the bottom figure show the gypsum columns from the line close to the west corner and east corner of the backwall, respectively. The smaller diameter gypsum columns (about 1-1/2 in.) broke at several points along the column height. The west gypsum columns were built at a distance of 2 and 5 ft from the backwall, respectively. The east gypsum columns were built at a distance of 1, 3, 7.5, and 13 ft from the backwall, respectively. One larger diameter column (about 2-3/4 in.) was built at the west side of the backwall and broke at fewer points. Therefore, it was decided to use the larger diameter gypsum columns in the skew tests to better track the failure planes. The asymptotic failure planes could not be identified in this case since the gypsum columns were not stiff enough and broke at several close points. This problem was not encountered in the skewed cases.

The gypsum columns excavated from the backfill soil after the 30° skew test are shown in Figure 6-257. The top and middle figures show the gypsum columns within the backwall width along the line close to the acute corner and obtuse corner, respectively. The bottom figure shows the gypsum columns within the embankment slope along the line close to the obtuse corner. The west gypsum columns were built at a distance of 2, 6, and 10 ft from the backwall, respectively. The east gypsum columns were built at a distance of 1, 4, 8, and 12 ft from the backwall, respectively. The columns close to the obtuse corner broke at fewer points than the columns close to the acute corner due to the lower resistance of soil at the obtuse corner. The gypsum columns from the embankment slope showed the engagement of the embankment slope at the obtuse corner. Figure 6-258 shows the asymptotic progression of the failure planes for the 30° skew test based on the breakage points along the height of excavated columns.

The colored sand columns excavated during the soil removal process after the 30° skew test are shown in Figure 6-259 and Figure 6-260. The bottom figures show a close up view of the colored sand columns in the order presented in the top figures. Figure 6-259 shows the colored sand columns within the backwall width along the line close to the acute corner. The west colored sand columns were built at a distance of 1, 4, 8, and 12 ft from the backwall, respectively. Some breakage points were observed along the columns height in which the colored sand was faded away due to the movement of the soil. However, no shifted column was observed as was seen in the previous abutment test with static push (Rollins et al., 2010; Marsh et al., 2012; Marsh et al., 2013; Rollins & Jessee, 2012). Unlike those tests, the soil was allowed to move back towards the bridge block after failure in the current test. Figure 6-260 shows the colored sand columns within the backwall width along the lines close to the obtuse corner. The east colored sand columns were built at a distance of 2, 6, 10, and 14 ft from the backwall, respectively.

The gypsum columns excavated from the backfill soil after the 45° skew test are shown in Figure 6-261. The top figure and middle figure show the gypsum columns within the backwall width along the lines close to the acute corner and obtuse corner, respectively. The bottom figure shows the gypsum columns within the embankment slope along the line close to the obtuse corner. The observed breakage points showed the progressive failure planes during the test. The west gypsum columns were built at a distance of 2, 6.5, and 11 ft from the backwall, respectively. The east gypsum columns were built at a similar distance of 2, 6.5, and 11 ft from the backwall, respectively. Figure 6-262 shows the asymptotic progression of failure planes for the 45° skew test based on the breakage points along the height of excavated columns.

The colored sand columns excavated during the soil removal process after the 30° skew test are shown in Figure 6-263 to Figure 6-265. The bottom figures show a close up view of the colored sand columns in the order presented in the top figures. Figure 6-263 shows the colored sand columns within the backwall width along the line close to the acute corner. The west colored sand columns were built at a distance of 1, 4, 8.5, and 13 ft from the backwall, respectively. Similar to the 30° skew case, some breakage points were observed along the height of columns in which the colored sand was damaged due to the movement of the soil. Figure 6-264 shows the colored sand columns within the backwall width along the line close to the obtuse corner. The east colored sand columns were built at a distance of 1, 4, 8.5, and 13 ft from the backwall, respectively. Figure 6-265 shows the colored sand columns within the embankment slope along the line close to the obtuse corner. Similar to the case of gypsum columns, the engagement of embankment slope was observed from the excavated colored sand columns.

6.7.9. Concluding remarks on backfill soil response

Important information on the soil behavior was found from the backfill response that was presented.

The soil pressure at the acute corner was not always higher that than at the obtuse corner in the tests in which dynamic earthquake loading was simulated. The variation of pressure at the acute and obtuse corners depended mostly on the direction of backwall rotation about the vertical axis. The change in the soil corner pressures was consistent with the backwall rotation. The pressure difference at the backwall corners increased as the backwall rotation increased, and vice versa. The pressure at the acute corner was lower than that at the obtuse corner since the backwall rotation was clockwise.

The tests indicated that soil surface cracks were primarily formed parallel to the skew angle. The backwall corner cracks were mostly concentrated at the acute corner but were scattered at the obtuse corner.

The general pattern of the maximum soil heave distribution was symmetric about the centerline of the bridge block for the non-skew case. In contrast, the distribution was un-symmetric for the skew cases. Furthermore, the heave increments were larger at the obtuse corner than those at the acute corner due to the smaller volume of the soil providing the passive resistance at the obtuse corner.

The general trend of the maximum heave pattern was symmetric about the centerline of the bridge block for the non-skew case. The maximum combined heave was 1.52 in. and the area with the maximum heaves greater than 0.1 in. extended to about 3.1 times the backwall height from the center of backwall in the last run of the non-skew case with the amplitudes of 150% times the Sylmar motion. The maximum heave distribution was un-symmetric about the centerline of the bridge block for both skew cases, as expected. The heave increments were larger at the obtuse corner than those at the acute corner due to the smaller volume of soil providing the passive resistance at the obtuse corner. The maximum combined heave was 1.37 in. in the 30° skew test and the area with the maximum heaves greater than 0.1 in. propagated to about 2.4 times and about 3 times the backwall height from the center of backwall for the last runs with the amplitudes of 150% and 200% times the Sylmar motion, respectively. The maximum combined heave was 1.04 in. in the 45° skew test and the area with the maximum heaves greater than 0.1 in. extended to about 1.9 times and about 2.1 times the backwall height from the center of backwall for the last runs with the amplitudes of 150% and 200% times the Sylmar motion. The area affected by the maximum soil surface heaves extended towards the obtuse corner for both skew cases. It was also concluded that the maximum heaving of soil surface decreased and the area of the maximum heave was reduced when the skew angle increased.

The maximum longitudinal acceleration in the backfill soil decreased when the skew angle increased from 30° to 45° (11.34g to 5.33g). This agrees with the expectation of lower passive capacity when the skew angle is increased. With this trend, the maximum acceleration in the non-skew case would be expected to exceed 11.34g. However, the maximum accelerations for this case were 7.75g and 6.66g in the last two runs that occurred in the bottom and top layer of the soil, respectively. The maximum acceleration could be higher in the middle layer at the center of the backwall but those data are not known due to damage to the sensor in that location in the last two runs. This is discussed in detail in Chapter 7.

7. INTERPRETATION OF EXPERIMENTAL RESULTS

7.1. Introduction

The test model, instrumentation and the experimental results were discussed in previous chapters. The measured response was presented for the bridge block, the abutment wall, and the backfill and was discussed. This chapter presents interpretation of the experimental data with the focus on studying the skew angle effect on the key soil-abutment response. Also included is a comparison of the measured passive force-displacement response of the soil-abutment system with results from previous experimental studies of skewed abutment tests (Jessee, 2012; Marsh et al., 2012; Rollins & Jessee, 2013; Marsh, 2013; Marsh et al., 2013; Palmer, 2013).

7.2. Effect of skew angle on abutment-soil response

The abutment response histories and the maximum backfill response contours were presented and discussed in Chapter 6. Effect of skew angle and progression of the fundamental abutment response are discussed in this section. The response parameters include the backwall displacement and rotation, backwall accelerations, soil pressure, soil surface heaves, and soil accelerations. The part of the measured data that was deemed unreliable is excluded in the discussions.

7.2.1. Backwall movements

Effect of skew angle on the accumulated (combined) rotation and rotation in each run (rotation increment) of the backwall is presented in Figure 7-1 and Figure 7-2, respectively. The plots show the variations of the maximum rotations versus the maximum longitudinal displacements in consecutive runs. Recall that longitudinal displacements decreased when the skew angle increased. Figure 7-2 does not include data for the 0º skew case because of the inconsistency in the direction of backwall rotation in different runs due to the random contact points. The top and the bottom figures show counterclockwise (CCW) and clockwise (CW) rotations, respectively. The backwall rotation plots in Chapter 6 were shown to start from the initial skew angle to better understand the rotation direction. Contrary to Chapter 6, the net values of rotations are discussed in this chapter.

As stated in Chapter 6, the backwall initially rotated CCW that was consistent with the eccentricity between the centers of mass and stiffness of the bridge block. Subsequently, the rotations became CW because the resistance of the backfill soil was higher at the acute corner, and hence a point near the acute corner acted as a pivot about which the wall rotated. Therefore, the backwall experienced both CWW and CW rotations, although the peak CW rotations were substantially higher than CWW rotations in most cases. The data in the CCW plot in Figure 7-2 is the difference between the first peak rotation in each run and the rotation prior to that run. The CW rotation increments in the figure are the difference between the first CCW peak to the second CW peak rotation for each run.

Note that a rotation increase indicates CCW rotation. It can be seen in the top plot of Figure 7-1 that the combined CCW rotation signs became negative in high amplitude runs. This occurred in the last run of the non-skew case (-.0345º) due to the residual rotation from the previous run (-0.14º in Figure 6-110). The residual rotations in Run 3 of the skewed cases (29.65º in Figure 6-113 and 44.83º in Figure 6-115) was the reason for the negative CCW peak rotations in the subsequent runs.

The maximum CCW rotation increments increased as the skew angle increased (Figure 7-2). The maximum combined CCW rotations in Run 2 and 3 of the 45° skew were larger than the 30° skew case rotations, as expected. However, these rotations decreased in the subsequent runs as the skew angle increased. This was due to the larger maximum CW rotation during Run 3 in the 30° skew case (-0.515°) compared to that in the 45° skew case (-0.22°).

Unlike the CCW direction, the maximum CW rotation increments decreased when the skew angle increased (Figure 7-2). The maximum combined CW rotations in the 30° skew model were larger than those in the 45° skew model (Figure 7-1). The results clearly showed that an increase in the skew angle resulted in a lower rotation of the backwall relative to its original position. This is illustrated in Figure 7-3 presenting the backwall positions associated with the maximum rotation of the backwall in different runs. The initial positions are shown by dotted lines. The other two lines depict the backwall position for the maximum CW rotations and the residual positions. Note that the backwall displacements and the gap between the bridge block and the backwall are exaggerated for clarity. The cable restrainer of the acute corner engaged in both cases at the end of Run 3 but there was some slack in the obtuse corner.

7.2.2. Backwall accelerations

Effect of skew angle on the maximum average accelerations of the backwall is presented in Figure 7-4. The data for the skewed cases were only available for the run with the amplitude factor of 50%. The data in the subsequent runs was unreliable since the sensors exceeded their capacity.

The trend in the maximum accelerations in the non-skew case was not always consistent with the input motion amplitude, although a general upward trend could be observed. The maximum accelerations increased when the skew angle increased, but the trend could not be confirmed because the data was saturated.

The skew angle effect on the maximum average impact accelerations on the backwall is presented in Figure 7-5. The impact accelerations generally decreased when the skew angle increased from 30° to 40°. This trend is in agreement with the soil pressure response that is discussed in the next section.

7.2.3. Soil pressure

Progression of the maximum soil pressure distribution along the backwall height is presented in Figure 7-6. Most pressure cells recorded the maximum pressure in the last run. However, the progression was not always consistent with the motion amplitude increase most likely because of local soil failures near the pressure cells.

Progression of the maximum soil pressure distribution across the backwall width is presented in Figure 7-7. The lowest pressure occurred during the low amplitude motion of Run 2. However, the pressures did not always increase with the amplitude of the motion in subsequent runs. An exception to this is the pressures measured in Run 3 versus those in Run 2, which increased for all three skew angles. The variations of the pressures across the backwall also changed in different runs, although the data for Run 3 showed a somewhat of a consistent trend with that from Run 2, regardless of the skew angle. At higher runs, for example in the case with 0° skew, the distance of the maximum pressure that was at 7 ft. in Run 2 and 3 changed to 9 ft. in Run 6 and 7. The somewhat of a consistent trend in Run 2 and 3, but erratic trend in higher-amplitude runs is attributed to local soil failures during the low-amplitude runs and the backwall rotation about the vertical axis that changed the pressures.

The effect of skew angle on the maximum soil pressures recorded by the pressure cells is presented in Figure 7-8. The maximum pressures generally decreased as the skew angle increased from 30 to 45 degrees, except for PC1 and PC2 in Run 2 and 3 (50% and 125% Sylmar). The reduction in the average maximum pressure was 14.3%, 27.7%, 52.3%, and 69.5% for Run 2, 3, 4, and 5, respectively.

Figure 7-9 shows the skew angle influence on the maximum soil pressure at mid height of the backwall regardless of the distance from the edge. The mid-height pressures substantially decreased in the high amplitude runs when the skew angle increased from 30 to 45 degrees. The maximum pressures in the non-skew case was expected to exceed those in the skew cases. However, this trend was not observed for possibly two reasons. First, the unexpected trend could be because the sampling rate of the pressure cell data was too low in the non-skew case (256 Hz) to capture the peak pressures. An investigation was carried out to determine the effect of sampling rate on the maximum pressures by using the data for the skew cases and changing the sampling rate from the actual rate of 4,000 Hz to 256 Hz. The results showed that although there were some differences but the reduction in the measured peak pressure was not significant. Second and the more likely reason was the reconstruction of the backfill adjacent to the backwall before Run 6. The results indicate that the backfill continuity was not restored after the reconstruction in the non-skew case. This was also observed in the backwall response and the surface cracks that did not extend as far as those of the skew cases.

7.2.4. Soil surface heaves

The maximum surface heave distributions across the 19-ft wide backfill are presented in this section for points A to E from the west corner to the east corner (Fig. 7-10). A and E are on the slopes, while others are on the flat surface of the backfill. Therefore, the heaves at A and E indicate movement at the edges of the backfill, which are lower than the top of the soil. A to E are at 1.5, 5.5, 9.5, 13.5, and 17.5 ft from the east edge (top edge in Figure 7-10) of the backfill, respectively. Row 1, 2, and 3 are at 2, 6.5, and 11 ft from the backwall, respectively.

The maximum heave distributions for the points across the backfill are shown in Figure 7-11. As expected, the heaves increased as the motion amplitude increased. The maximum heave distribution was symmetric in the non-skew case. The data for row 1 was not obtained at D and E (skew cases) because sensors were not installed at these locations. A part of the reference frame could not be installed in these locations since the frame conflicted with the skew wedge of the bridge block. However, the data for row 2 and 3 indicated larger heaves at D and E, which were close to the obtuse corner. This is attributed to backwall rotation in the clockwise direction.

Effect of skew angle on the maximum heaves for the points across the backfill is presented in Figure 7-12. The maximum heaves decreased as the skew angle increased from 0 to 45 degrees, except for points D and E in row 2 and 3 in which the non-skew case heaves were smaller than those in the 30º skew case. Those points were close to the obtuse corner and were more sensitive to heaving in the skew cases than in the non-skew case because of the backwall rotation.

Figure 7-13 shows the skew angle effect on the maximum heaves regardless of the location on the soil surface. The maximum heaves were 0.20, 0.09, and 0.10 in. for the 0º, 30º, and 45º skew tests, respectively, during the first run (50% Sylmar) in which the bridge block impacted the backwall. A decreasing trend was seen in the subsequent runs for the skewed cases in which the maximum heave decreased from 0.57 to 0.48 in. when the skew angle increased from 30 to 45 degrees. The maximum heave could have exceeded 0.49 in. if the 125% Sylmar motion was simulated in the non-skew case. A consistent trend was not seen in the next run with the motion amplitude factor of 150%. The maximum heaves during this run were within 15% of each other for different skew angles. However, the decreasing trend was observed during the last run in which the maximum heaves decreased from 1.52 to 1.37 and 1.04 in. in the non-skew case to the 30 and 45 degrees skew cases, respectively. The maximum heave could have exceeded 1.52 in. if the motion with an amplitude factor of 200% had been applied in the non-skew case.

7.2.5. Soil longitudinal accelerations

The maximum soil acceleration distributions across the backfill are presented for points A to E from the west corner to the east corner. The location of these points was described in the previous section.

Progression of the maximum accelerations across the backfill for the 0°, 30°, and 45° skew tests is shown in Figure 7-14 to Figure 7-16, respectively. Unlike the surface heaves, the peak accelerations did not always increase with the motion amplitude. The highest accelerations in the non-skew case were for Run 6 due to the increase of motion amplitude factor from 75% to 150%. The highest accelerations in the skew cases were for Run 3 in some cases and for Run 5 in the other cases. The significant acceleration increases in Run 3 were due to the increase of motion amplitude factor from 50% to 125%. The distribution in the non-skew case was nearly symmetric in all the runs except for Run 2 and 7 in some rows. The distribution along the skewed interface in the 30° skew case was almost symmetric in some cases and towards the obtuse corner in the other cases. The high accelerations at the obtuse corner were attributed to the backwall rotation about the vertical axis (affected by the backfill stiffness), as discussed in Section 6.7.6. The distribution in the 45° skew case was symmetric in some cases, towards the obtuse corner in some cases, and towards the acute corner in the other cases. The high accelerations at the obtuse and acute corners were attributed to the backwall rotation and the gap between the backwall and the bridge block, as discussed in Section 6.7.6.

An expected general trend was the reduction of peak accelerations as the distance to the backwall increased. For example, the peak acceleration in the middle layer in Run 2 of the non-skewed wall was 4.65g in Row 1 dropping to 1.84g and 0.83g in Rows 2 and 3, respectively. The same trend was observed in the skewed cases. The reductions indicate dissipation of energy through the soil as the distance to the wall increases. Another general observation is in the distribution of peak accelerations across the backfill soil as the distance to the backwall increases. For example in the top layer of the non-skew case, the ratio of the highest to lowest peak acceleration in Run 3 in Row 1 was 2.12 dropping to 1.44 in Row 2 and 1.02 in Row 3. The decreasing trend is attributed to the spread of movement over a wider zone as the distance to the backwall increased. This trend was the opposite in the skewed cases. For example, for the top layer of the 30° skew case, the ratios were 1.32, 1.57, and 1.73, for Rows 1 to 3. When the skew angle was changed to 45 degrees, the ratios were 1.16, 1.45, and 2.17, indicating increasing trends. The increasing trends showed that the variation of stiffness across the soil was more pronounced away from the backwall than that close to the backwall. This is in agreement with the spread of soil movement toward the obtuse corner.

Effect of skew angle on the maximum accelerations the backfill at the top, middle, and bottom layers is presented in Figure 7-17 to Figure 7-19, respectively. The maximum accelerations of the 30° skew case were generally higher than those in the 45° skew case in most locations. Accelerations of point C at the center of the backwall were also affected by the skew angle. The accelerations of points A and B (close to the acute corner) were less sensitive to the skew angle than those of points D and E (close to the obtuse corner) and C. This is attributed to the backwall rotation in the clockwise direction.

Figure 7-20 shows the skew angle effect on the maximum accelerations regardless of the location inside the backfill. The maximum accelerations did not follow a consistent trend in the first two runs. The maximum acceleration was reduced from 7.75g to 6.73g and 5.25g in the run with the motion amplitude factor of 150% in the 0° to the 30° and 45° skew cases. The maximum acceleration for the motion with amplitude factor of 200% was reduced from 11.34g to 5.33g when the skew angle increased from 30 to 45 degrees. The maximum acceleration under the motion amplitude of 150% Sylmar in the non-skew case (7.75g and 6.66g) occurred in the bottom and top layer of the soil, respectively, but could be higher as mentioned in the figure. The maximum accelerations in these runs could occur in the middle layer of the soil in the sensor at the center of the backwall but data could not be obtained due to damage to the sensor in the last two runs. Therefore, the maximum accelerations for the motion amplitude factor of 150% was expected to be higher than that in the 30° skew case

7.2.6. Soil transverse accelerations

The peak transverse accelerations were lower than the peak longitudinal accelerations because the primary direction of the motion was in the longitudinal direction. Skew angle effect on the maximum accelerations towards the west (acute corner in the skew cases) at the top, middle, and bottom layers is presented in Figure 7-21 to Figure 7-23, respectively. The trend was similar to the longitudinal acceleration trend. The accelerations at A and B (close to the acute corner) were less sensitive to the skew angle than those at D and E (close to the obtuse corner) and C.

Figure 7-24 shows the skew angle effect on the maximum accelerations towards the west regardless of the location inside the backfill. A decreasing trend was observed in the last three runs when the skew angle increased from 30 to 45 degrees. The maximum accelerations for the motion amplitude factor of 150% in the non-skew case (3.22g and 2.56g) could be higher than shown, but the data at the backwall center in the middle layer was lost due to malfunction of the sensor.

Effect of skew angle on the maximum accelerations towards the east (obtuse corner in the skew cases) at the top, middle, and bottom layers is presented in Figure 7-25 to Figure 7-27, respectively. Again, the accelerations close to the acute corner were less sensitive to the skew angle than those close to the center and the obtuse corner.

Figure 7-28 shows the skew angle effect on the maximum accelerations towards the east regardless of the location inside the backfill. The maximum accelerations increased when the skew angle increased from 0 to 45 degrees except for the runs with the motion amplitude factors of 50% and 150%. The maximum accelerations towards the east (obtuse corner in the skew cases) followed a more consistent trend than the accelerations towards the west since the movement of the soil body was mostly towards the obtuse corner. The same explanation holds true about the observation that the maximum eastward accelerations were generally higher than the maximum westward accelerations. The ratio of the peak eastward and westward accelerations did not always follow a consistent trend with the motion amplitude increase but a consistent trend was observed when the skew angle increased except for the run with the motion amplitude factor of 50%. The ratio of the peak eastward to westward acceleration for 125% Sylmar motion was 1.23 and 2.02 for 30° and 45° skew angle. The corresponding ratio was 0.59, 1.62, and 1.79 for 0°, 30°, and 45° skew angle for the motion amplitude factor of 150%. The ratio increased from 1.01 to 3.01 in 200% Sylmar motion when the skew angle increased from 30 to 45 degrees.

7.2.7. Soil vertical accelerations

Effect of skew angle on the maximum vertical accelerations for different points along the backfill width at the top, middle, and bottom layers is presented in Figure 7-29 to Figure 7-31, respectively. Observations were similar to the other directions. The accelerations of the points close to the acute corner were less sensitive to the skew angle than those of the points close to the center and the obtuse corner because of backwall rotation in the clockwise direction.

Figure 7-32 shows the skew angle effect on the maximum accelerations regardless of the occurrence location inside the backfill. The maximum acceleration decreased when the skew angle increased in all the runs. The maximum upward acceleration decreased by 63.5% and 32.0% for the motion amplitude factor of 50% and 150%, respectively, when the skew angle increased from 0 to 30 degrees. The reduction was 1.5%, 25.9%, 48.5%, and 47.9% for the runs with 50%, 125%, 150%, and 200% Sylmar motion, respectively, when the skew angle increased from 30 to 45 degrees. The decreasing trend is in agreement with the maximum surface heaves.

7.2.8. Concluding remarks on skew angle effect

The trends in the data presented on the abutment wall and backfill response revealed important information about the skew angle effect.

The maximum longitudinal displacement of the backwall decreased when the skew angle increased. The skew angle increase led to larger initial CCW rotations of the backwall. However, the subsequent maximum CW rotations decreased by increasing the skew angle.

The soil pressure variation was not always consistent with the motion amplitude increase due to the uneven and local soil failure. The maximum soil pressures substantially decreased when the skew angle increased from 30 to 45 degrees. It was expected that the maximum pressures in the non-skew case be larger than those in the skew cases. However, this trend was not observed due to the backfill reconstruction in the non-skew case. The maximum average impact accelerations on the backwall in the non-skew case were also lower than those of skewed cases for the same reason.

The increase in the surface heave distributions across the backfill was consistent with the motion amplitude increase. Unlike the symmetric distribution of the heaves in the non-skew case, the distributions in the skew cases were mostly towards the obtuse corner due to the lower stiffness of the backfill in that zone. The maximum heaves decreased as the skew angle increased.

In contrast to the surface heaves, the acceleration progression was not always consistent with the motion amplitude increases. The accelerations increased substantially when the motion amplitude factor increased. The maximum accelerations primarily decreased as the skew angle increased. The effect of skew angle was more pronounced in the accelerations near the center and the obtuse corner than that at the acute corner. The peak transverse accelerations towards the obtuse corner were higher than those towards the acute corner since the soil body movement was mostly towards the obtuse corner. The ratio of the peak transverse accelerations generally increased when the skew angle increased.

7.3. Estimation of passive capacity of abutment-soil system

Five approaches were used to estimate the mobilized passive capacity of the backfill soil based on the measured earth pressure cell data. In the first three approaches, the maximum soil pressure data were used in each run regardless of time of occurrence, whereas synchronous data were used in the latter two approaches.

The main goal of each approach was to estimate the soil pressure distribution along the backwall height in five vertical planes passing the pressure cells at a projected distance of 1, 3, 5, 7, and 9 ft from the backwall corner. The central vertical plane (with at least two pressure cells along the backwall height) was used as the baseline to estimate the pressure distribution at other locations. In the first three approaches, only the maximum mobilized passive capacity of the backfill soil was estimated, while the total passive capacity histories were determined in the last two methods.

7.3.1. Estimation of maximum passive forces

The maximum passive forces are estimated in this section based on the maximum soil pressures disregarding the fact that they were not necessarily synchronous (Approaches I to III). The time lag between the soil pressure peaks could be as a result of the in-plane rotation of the backwall that affected the impact points between the bridge block and the backwall.

As stated in previous chapters, four (in the non-skew case) or five (in the skew cases) of the six pressure cells were installed across the backwall mid-height.

7.3.1.1. Approach I

The variation of the maximum soil pressure along the backwall height was assumed to be linear in this approach. This assumption was made although a nonlinear distribution was observed in some cases. The pressure at the bottom of the backwall was estimated based on the linear pressure diagram passing through the maximum pressure at mid height. The total force perpendicular to the backwall was calculated based on the tributary area for each pressure cell. The results are presented in Section 7.2.1.4 along with those from the other approaches.

7.3.1.2. Approach II

The variation of the maximum soil pressure along the backwall height was assumed to be bi-linear in this approach. This assumption was made based on the data obtained along the height of the center of the backwall. The resultant forces for the upper half and lower half were calculated for the central part of the wall based on the tributary width of the pressure cells. The ratio of the upper and lower forces was assumed to be constant across the backwall in each run. The upper forces at other locations of the wall were determined based on the measured pressures at those locations and their tributary width. Subsequently, the lower forces at these locations were calculated using the ratio at the center of the wall. Finally, the total force perpendicular to the backwall was calculated by summing all the forces. The results are discussed in Section 7.2.1.4 along with the other approaches results.

7.3.1.3. Approach III

A regression analysis method was used in this approach to fit a polynomial to the maximum soil pressure distribution as a function of *x* and *z*, the coordinates of each pressure cell across the width and the height of the backwall, respectively. The maximum soil pressures matrix, *P*, consists of the known maximum soil pressures at 10 points in the 0° skew case and 11 points in the 30° and 45° skew cases, assuming zero pressures at the surface of the backfill. The fitted polynomial function was formulated as below for the *k* known maximum soil pressures:

$$P_{\max,\,1}(x_1, z_1) = A_0 + A_1 x_1 + A_2 x_1^{\,2} + \ldots + A_m x_1^{\,m} + B_1 z_1 + B_2 z_1^{\,2} + \ldots + B_n z_1^{\,n}$$

$$\vdots$$

$$P_{\max,\,k}(x_k, z_k) = A_0 + A_1 x_k + A_2 x_k^{\,2} + \ldots + A_m x_k^{\,m} + B_1 z_k + B_2 z_k^{\,2} + \ldots + B_n z_k^{\,n}$$

where $P_{max,k}$ is the k^{th} soil pressure, x_k and z_k are the k^{th} point coordinates along the width and the height of the backwall, respectively, and A_0, A_1, ..., A_m, B_1, ..., B_n are the regression coefficients that build matrix *A*. The top formulation is written in a matrix form of

$$P_{k\times 1} = X_{k\times(1+m+n)} A_{(1+m+n)\times 1}$$

Matrix *X* consists of the *x* and *z* coordinates of the known pressures. Matrix *A* was found using the 'pinv' function in MATLAB program that returned the pseudoinverse of matrix X. The pressure distribution along the backwall height for each vertical plane was calculated using matrix *A* and the desired coordinates. The total force perpendicular to the backwall was calculated as the volume of the 3D surface formed by the maximum pressures behind the backwall. Four combinations of *m* and *n* were chosen for the orders of the polynomials in *x* and *z* directions, respectively: a) *m*=1, *n*=1, b) *m*=1, *n*=2, c) *m*=2, *n*=2, and d) *m*=1, *n*=3. These were selected to capture the maximum soil pressure variations along the backwall height and width. The results are discussed in the next section.

7.3.1.4. Maximum soil pressure distributions (approaches I-III)

This section discusses the soil pressure distributions estimated based on approaches I-III. The final purpose of pressure estimation is calculating the resultant forces on the backwalls (Section 7.2.3). Therefore, the pressure distribution plots are presented separately in Appendix G.

Figure G-1 to Figure G-4 present the maximum soil pressure distributions along the backwall height for approach I, II, and III in different runs of the 0° skew test. The estimated pressure at the backwall bottom was generally higher in Approach II than that in Approach I since the measured pressure in the bottom half of the central vertical plane was relatively large. The estimated pressure at the bottom of the backwall peaked in some cases in Approach II and in others in Approach III (combination d). Pressure estimates at the backwall bottom from combination a and b in Approach III were close in most cases. The maximum mid-height pressure in the last run was 3.07 ksf at the east corner. The corresponding estimated bottom pressures were 6.14, 8.41, 6.31, 7.87, and 12.26 ksf for Approach I, II, III (a), III (b), and III (d), respectively.

The maximum soil pressure distributions along the backwall height in different runs of the 30° skew test are shown in Figure G-5 to Figure G-8. Unlike the 0° skew case, the bottom estimated pressure was generally lower in Approach II than that in Approach I since the measured pressure in the bottom half of the central vertical plane was relatively small. The ratio of the maximum bottom pressure to the mid height pressure decreased with the increase in the motion amplitude. Furthermore, the maximum measured pressure in the central vertical plane decreased from the mid-height to the lower half of the backwall in Run 5 (Figure G-8). This was probably due to the backwall tilting about the horizontal axis, which led to the lower pressures at the lower part of backwall. This trend was also seen in previous studies on retaining wall and abutments (Mock & Cheng, 2011; Palmer, 2013; Smith, 2014). The estimated pressure at the backwall bottom peaked in some cases in Approach I and in others in Approach III (combination a). The maximum mid-height pressure in the last run was 8.31 ksf at the obtuse corner. The corresponding estimated bottom pressures were 16.62, 4.43, 11.97, 3.49, and -0.11 ksf for Approach I, II, III (a), III (b), and III (d), respectively.

Figure G-9 to Figure G-12 present the maximum soil pressure distributions along the backwall height in different runs of the 45° skew test. The estimated pressure at the backwall bottom was higher in Approach I than that in Approach II for all the runs except for Run 5 since the pressure in the bottom half of the central vertical plane was relatively small. The estimated pressure at the backwall bottom peaked in some cases in combination a of Approach III and in others in combination c. The maximum mid-height pressure in the last run was 3.52 ksf at the acute corner. The corresponding estimated bottom pressures were 7.04, 10.90, 4.78, 3.90, and 2.26 ksf for Approach I, II, III (a), III (b), and III (d), respectively. Clearly, larger values of m and n in the regression analysis method (approach III) led to higher accuracy in estimating the measured soil pressures. However, increasing m and n did not always result in a better approximation of the pressure distribution that affected the total force. For example, the results from n=3 (order 3 in z direction) was not reasonable since the fitted polynomial led to tensile pressures at the bottom of the backwall in all the runs except for Run 5 (bottom rows in Figure G-9 to Figure G-11).

7.3.2. Estimation of passive force histories

In the three approaches in Section 7.2.1, only the maximum mobilized passive capacity of the backfill soil was estimated disregarding the fact that the peak pressures were not always synchronous. The total passive capacity histories are determined in the section based on the soil pressure histories multiplied by the tributary areas of the pressure cells. The force history plots are presented in Appendix G.

7.3.2.1. Approach IV

The passive force history was calculated for each vertical plane using the same method as in approach I but based on the estimated pressure distribution using synchronous pressures at different time steps. The total force history was calculated based on the tributary area across the backwall.

Figure G-13 to Figure G-18 present the force histories perpendicular to the backwall for each vertical plane and the corresponding backwall displacement histories for different runs of the 0°, 30°, and 45° skew tests. The maximum estimated force in Approach V was larger than that in Approach IV for the 0° and 45° skew cases in all the runs except for Run 2. In contrast, the maximum force estimated in Approach V was smaller than that in Approach IV for the 30° skew case. These histories are used in Section 7.3.1 to determine the force-displacement relationship of the abutment.

7.3.2.2. Approach V

The force history was calculated using the same method as that in approach II but based on the estimated pressure distribution for each vertical plane using synchronous pressures at different time steps. The total force history was calculated based on the tributary area of each vertical plane along the backwall width.

Figure G-19 to Figure G-24 present the force histories perpendicular to the backwall for each vertical plane and the corresponding backwall displacement histories for different runs of the 0°, 30º, and 45° skew tests. The measured pressures were negative in some instances and were discarded. Some of the calculated force histories in the 45º skew case were erroneous leading to unreasonably large forces. This was believed to be due to sudden changes in the pressure distribution caused by impact between the bridge block and the backwall. Therefore, engineering judgment was used to estimate forces in determining the force-displacement relationship of the abutments in Section 7.3.1.

7.3.3. Concluding remarks on passive capacity estimation

Comparison of the maximum backfill capacity estimated from different approaches is presented for different runs in Figure 7-33.

Different combinations of the parameters in approach III led to approximately the same maximum forces for the 0° skew test except for the last combination with m=1 and n=3 at the high amplitude motions of Run 6 and 7 that resulted in larger forces compared to the other combinations. This was as a result of overestimation of the pressure distribution, as it was shown in Figure G-3 and Figure G-4. It was concluded that n=2 (polynomial order in the z direction) yielded more reasonable results than n=3 because the MSE errors were very close in both cases. Comparison between the orders of the polynomials in x direction (m=1 and m=2) for the same order in z direction (n=2) showed that the estimated forces were very close for all the runs of the 0° and 30° skew cases. However, m=2 for the 45° skew case resulted in approximately 10% larger forces than m=1 as a result of smaller error in estimating the maximum pressures along the backwall width. This is explained by the pressure distribution across the backwall for the 45° skew test (bottom row in Figure 7-7) in which the measured pressure distribution was close to a parabolic shape. In contrast, for the 0° and 30° skew tests, using m=1 and m=2 resulted in relatively similar errors. Although m=2 led to a more accurate estimation of pressure than m=1 in the case of 45° skew angle, a linear distribution of the maximum pressures along the backwall width (m=1) is preferable because it leads to consistent results for all skew cases. Therefore, combination b (m=1, n=2) is considered as the optimum combination of parameters in approach III.

Between the two force history prediction methods, Approach IV underestimated the forces in the 0° skew case and Run 5 of the 45° skew case and approach V underestimated the forces in Run 4 and 5 of the 30° skew case.

In general, all the methods led to reasonably close estimates of the passive forces. The forces in the 0° skew case were in the range of those in the 45° skew case, even though they were expected to be higher. The lower than expected forces in the 0° skew case are attributed to sliding of the backwall and reconstruction of the backfill, as discussed in Section 7.1.3.

7.4. Passive force-displacement relationship of abutment-soil system

One of the main goals of this study was to determine the effect of skew angle on the passive force-displacement relationship of the abutment. The backfill force-displacement curves obtained in the present study are presented in this section and compared with previous test data obtained in Jessee (2012), Marsh et al. (2012), Rollins & Jessee (2013), Marsh (2013), Marsh et al. (2013), and Palmer (2013).

7.4.1. Results from current study

The backfill force-displacement relationships were obtained based on forces that were determined using approach IV and V described in Section 7.2.2.17.2.2.2. Note that approaches I to III could not estimate the total force history but only the peak forces. The displacement is the average longitudinal displacement of the backwall and the force is the passive capacity of the backfill perpendicular to the abutment backwall throughout this section.

Backfill force-displacement curves based on forces obtained using approach IV for the 0°, 30°, and 45° skew tests are presented in Figure 7-34 to Figure 7-36, respectively, for different earthquake runs. The displacements include residual displacement from previous runs. The initial stiffness was very large in Run 2 and 3 since the backfill soil was nearly undisturbed. Comparing the initial stiffness in the skew cases with that of the non-skew case, it is noted that the former is higher perhaps because of higher sampling frequency rate in the skewed case data. The initial stiffness was reduced in the subsequent runs in all cases because of damage in the backfill soil. Both softening and hardening phenomena were observed as the backfill displacement increased.

Figure 7-37 to Figure 7-39 present the force-displacement envelopes for all the runs based on forces obtained using approach IV for the 0°, 30°, and 45° skew tests, respectively. Residual displacements are included in these figures but the negative residual displacements are ignored for determining the force-displacement envelopes. Approach IV in Run 5 of the 30º skew case resulted in a peak at the displacement of approximately 0.83 in. Force-displacement curves for Run 2 and 3 were ignored in determining the envelopes in the skew cases because of the large initial stiffness and small residual displacement in those runs. The maximum passive capacity was 104.8 kips at 1.14 in., 295.9 kips at 0.95 in., and 167.2 kips at 0.32 in. in the 0º, 30º, and 45º skew cases, respectively. The maximum capacity of the non-skew case was smaller than both skew cases, contrary to the expectation. As mentioned in Section 7.1.3, the non-skew case data underestimated the backfill capacity mainly due to the reconstruction of the backfill in the course of testing.

Backfill force-displacement curves based on forces obtained using approach V for the 0°, 30°, and 45° skew tests are presented in Figure 7-40 to Figure 7-42, respectively. Similar to the curves with forces based on approach IV, the initial stiffness was very large in Run 2 and 3 since the backfill soil was nearly undisturbed. However, the initial stiffness was reduced in the subsequent runs due to failure of some of soil. Figure 7-42 indicates large spikes in forces obtained using approach V in the force in the 45° skew case. This is attributed to sudden changes in the pressure distribution along the backwall height due to impact.

Figure 7-43 to Figure 7-45 present the combined force-displacement envelopes of all the runs based on approach V for the 0°, 30°, and 45° skew tests, respectively. Similar to the envelopes shown in Figure 7-37 to Figure 7-39, Run 2 and 3 were ignored in determining the envelopes in the skew cases. The maximum passive capacity was 194.7 kips at 2.23 in. and 259.9 kips at 1.04 in. in the 0º and 30º skew case, respectively. The maximum capacity of the non-skew case was smaller than the 30º skew case due to reasons explained before. Two envelopes were determined for the 45° skew case. The higher amplitude motions of Run 4 and 5 were used in the first envelope, similar to the previous cases. The second envelope disregarded Run 4 and was based on only the data for Run 5. This was done because including Run 4 resulted in a relatively high initial stiffness. The high stiffness was caused by a lack of residual displacement after Run 3, unlike the previous cases. The lack of residual displacement was due to the backward movement of the backwall towards the bridge block at the end of Run 3. Recall that friction at the base of the backwall was nearly zero. Both envelopes resulted in the same maximum passive capacity of 155.9 kips at the displacement of 1.69 in. but different initial stiffnesses because the peak force was controlled by the results from Run 5.

Figure 7-46 presents the comparison between the passive force-displacement envelopes of the skew cases with forces based on approach V. The envelope for the non-skew case is not shown in this comparison because the forces were unreasonably small due to backwall movement and reconstruction of the soil. The two envelopes for the 45º skew case are considered as the upper-bound and lower-bound response of the abutment. It can be seen that the passive capacity was reduced by increasing the skew angle from 30 to 45 degrees. The peak force was reduced by approximately 50% at displacement of 1 in.

7.4.2. Comparison between test results from the current and previous studies

Backfill passive force-displacement curves of the skewed abutment tests at the Brigham Young University (BYU) (Jessee, 2012; Marsh et al., 2012; Rollins & Jessee, 2013; Marsh, 2013; Marsh et al., 2013; Palmer, 2013) are compared in this section with those at the current study.

Figure 7-47 and Figure 7-48 show the passive force-displacement curves of the abutments tested at BYU for the small-scale (lab) and large-scale (field) tests, respectively. The backwall height and width were 2 and 4 ft in the lab tests and 5.5 and 11 ft in the field tests, respectively, maintaining the same width to height ratio of 2. The BYU lab and field test results are compared in Figure 7-49. The displacement was normalized relative to the backwall height and the force was normalized relative to the backwall height squared multiplied by the projected width of the backwall. The ratio of the peak normalized force between the lab and field test results was 1.94, 1.69, and 2.05 for 0°, 30°, and 45° skew cases, respectively. The ratio of the peak force reduction in the lab test was 49.2% and 62.2% when the skew angle increased from zero to 30 and 45 degrees, respectively. The corresponding ratios in the field test were 41.7% and 64.3%, respectively. Marsh et al. (2013) attributed the larger passive force in the lab tests to simulating the plane strain condition (mobilizing a higher friction angle) while the field test used an unconfined geometry. Moreover, the soil was compacted to a relative density higher in the lab test than that in the field test. .

Figure 7-50 presents the force-displacement curves of large-scale tests at BYU with a larger width to height ratio of 3.7 (Palmer, 2013). The backwall height and width were 3 and 11 ft, respectively.

Lateral force-displacement curve of the current study at the UNR for the 30º skew angle is compared with those from BYU in Figure 7-51. The forces were normalized using the same method as that described for Figure 7-49. The initial stiffness in the UNR curve was close to the BYU lab result but higher than that in the BYU field tests. The normalized passive capacity of the UNR test was larger than the BYU field tests and smaller than the BYU lab test.

Figure 7-52 presents the comparison between the force-displacement relationship of the UNR current study with that from BYU for the 45º skew angle. The initial stiffness in the UNR upper-bound curve was comparable to that in the BYU lab test. The same consistency was observed between the initial stiffness in the UNR lower-bound curve and the BYU field tests. However, the normalized passive capacity of the UNR test was close to BYU field tests and much smaller than the BYU lab test.

7.4.3. Concluding remarks on passive force-displacement relationship

In general, the initial stiffness of the force-displacement relationship of the current test was comparable to that in the BYU lab tests but the normalized capacity was comparable to that in the BYU field tests.

8. ANALYTICAL STUDIES AND DESIGN RECOMMENDATIONS

8.1. Introduction

The test model, experimental results, and the interpretation of the results were discussed in previous chapters. This chapter presents the analytical studies of the soil-abutment models using FLAC3D and modeling of the three-dimensional soil-abutment response. The FLAC3D analyses were static and were conducted simulating both uniform and non-uniform wall displacements, with the latter to account for the rotation of the wall that was observed in the tests. Finally, design recommendations are made to account for the effect of skew angle on the force-displacement relationship of the abutments.

8.2. Analysis with FLAC3D

A lateral force-displacement analysis of the soil-abutment test models using FLAC3D is presented in this section. The analyses were done initially under uniform displacement loading on the backwall. However, additional analysis was conducted under non-uniform displacement loading to account for rotation of the wall that was observed in the shake table tests. The calculated results are compared with the experimental data.

8.2.1. Geometry

The concrete backwall and the soil embankment with three skew angles of 0°, 30°, and 45° were modeled in FLAC3D as shown in Figure 8-1. The maximum mesh size in the model was approximately 6 in.

8.2.2. Boundary conditions

The translational degrees-of-freedom at backfill soil base nodes were fixed. The nodes on the backfill sides were fixed in the x and y directions shown in Figure 8-1. These excluded the backfill nodes on the interface with the wall so that all the interface nodes on the wall were free to move. All the wall nodes were fixed in the vertical direction to prevent tilting. The exterior nodes on the wall face were first fixed longitudinally under the gravity loading and then were internally released when the longitudinal displacement was initiated on the wall face.

8.2.3. Constitutive model

The constitutive models were the elastic model for the wall and the elasto-plastic Mohr-Coulomb model for the soil. Table 8-1 lists the soil material properties defined in this study. Since the Young modulus is a stress dependent property, a constant average value of $(E_{50})_{ave}$ was used for the entire backfill. This selection was based on the analytical studies in Chapter 3 that resulted in a good match between the PLAXIS2D, FLAC3D, and experimental results. The constant average young modulus was calculated for a mid-height soil element using Duncan model (Eq. (8-3)).

8.2.3.1. Duncan model parameters

Duncan model parameters were determined based on the triaxial test results on the Paiute Pit sand (Appendix B). The hyperbolic stress-strain relationship is determined from the following equations:

$$\sigma_d = \frac{\varepsilon_1}{\dfrac{1}{E_i} + R_f \dfrac{\varepsilon_1}{\sigma_{df}}} \tag{8-1}$$

$$\frac{\varepsilon_1}{\sigma_d} = \left(\frac{R_f}{\sigma_{df}}\right)\varepsilon_1 + \frac{1}{E_i} \tag{8-2}$$

Figure 8-2 presents $\frac{\varepsilon_1}{\sigma_d}$ versus ε_1 relationship for each triaxial test and the corresponding values of E_i and R_f. The slope and intercept of the linear regression curve were used to determine $\frac{R_f}{\sigma_{df}}$ and $\frac{1}{E_i}$, respectively.

Table 8-2 shows the calculation details that led to an average R_f of 0.75. The relationship between E_{50} and E_{50}^{ref} based on Duncan's model is:

$$E_{50} = E_{50}^{ref}\left(\frac{\sigma'_{3c}}{P_a}\right)^n \tag{8-3}$$

$$\log E_{50} = \log E_{50}^{ref} + n.\log\frac{\sigma'_{3c}}{P_a} \tag{8-4}$$

$\log E_{50}$ versus $\log\frac{\sigma'_{3c}}{P_a}$ relationship for each triaxial test is plotted in Figure 8-3. The slope and intercept of the linear regression determine n and $\log E_{50}^{ref}$, respectively. Table 8-3 presents the corresponding calculation details that resulted in $n = 0.33$ and $E_{50}^{ref} = 9{,}123$ psi.

8.2.4. Interface elements

Interface elements in FLAC3D are characterized by Coulomb sliding and tensile and shear bonding. The properties of the interface between the soil and the wall in the test model were determined based on the procedure in PLAXIS manual using an "interface reduction factor", R_{int}, according to the following equations:

$$c_{\text{int}} = R_{\text{int}}.c \tag{8-5}$$

$$\tan\phi_{\text{int}} = R_{\text{int}}.\tan\phi \tag{8-6}$$

where c and ϕ are the soil cohesion and friction, and c_{int} and ϕ_{int} are the interface cohesion and friction, respectively. A reduction factor of 0.8-1.0 is suggested for sand-concrete interface. An average value of 0.9 was assumed in the current study. It is recommended in the FLAC3D manual that the normal and shear stiffness be approximated by the following formula:

$$k_n = k_s = 10 \times \max\left[\frac{(K + \frac{4}{3}G)}{\Delta z_{\min}}\right] \tag{8-7}$$

where $\Delta z_{\min}$ is the smallest dimension in the normal direction, K is the bulk modulus and G is the shear modulus of the zone adjacent to the interface. K and G in this study were calculated based on $\left(E_{50}\right)_{ave}$. According to FLAC3D manual, Eq. (8-7) is reasonable if the materials on the two sides of the interface are similar. However, if the material on one side is much stiffer than that on the other side, Eq. (8-7) should be applied for the softer side. Therefore, the deformability of the entire system is dominated by the soft side. This recommendation was used to determine the interface stiffness based on the soil properties. A sensitivity analysis on the interface stiffness properties by Xie et al. (2013) showed that the FLAC3D results are very sensitive to the interface properties.

8.2.5. Gravity loading

Gravity loading was first applied to the FLAC3D models to induce the initial stresses in the elements. Figure 8-4 and Figure 8-5 present displacement and stress contours of FLAC3D models under the gravity loading, respectively. The displacements were symmetric in the non-skew case but were parallel to the wall in the skew cases. The maximum vertical displacement under the gravity loading was 0.028 in. in all cases. The maximum transverse displacement occurred on the slopes in opposite directions in the non-skew case and across the backwall in the skew cases. The maximum stress in the vertical direction was approximately 4.63 psi. The stress contours in the soil followed the same patterns as the displacement contours.

8.2.6. Uniform displacement loading

As discussed in Chapter 3, a direct displacement-control loading is not an option in FLAC3D. A prescribed loading rate referred to as "velocity" is applied at prescribed nodes for a given number of steps. The velocity multiplied by number of steps defines a given displacement. The velocity should be small enough to minimize shocks in the model. The optimal velocity should be found for each model by trial and error such that the results are not significantly sensitive to the applied velocity.

Figure 8-6 presents the effect of loading velocity on the force-displacement relationship in the 30° skew model with an assumed interface reduction factor of 0.7. The analysis for the velocity of 1e-7 in./sec was stopped at the displacement of approximately 1 in. since it was unreasonably time-consuming, and the result initially matched that of the 1e-6.5 in./sec velocity. In general, a velocity of 1e-6 in./sec seemed to be sufficiently small leading to converging results.

Figure 8-7 presents displacement contours of the FLAC3D models under uniform displacement loading of 3 in. into the backfill soil. The displacements were symmetric in the non-skew case but were parallel to the wall in the skew cases. This pattern was also observed in the test data and surface cracks. The maximum transverse displacements (0.8 in. in the non-skew model) occurred on the slopes in opposite directions. The maximum transverse displacements in the 30° skew model were 0.6 and 1.0 in. on the obtuse and acute side slopes, respectively. The backfill transverse displacements were not directly measured in the shake table test. However, the maximum transverse accelerations were 3.92g and 4.18g towards the acute and obtuse corners, respectively. The maximum transverse movement occurred at the acute corner in the analytical model, but at the obtuse corner in the shake table test due to the clockwise rotation of the wall. The maximum heaves were 1.90 and 1.88 in. in the 0° and 30° skew models, respectively. The vertical displacements in the 30° skew model peaked at the acute corner. This was consistent with the observation in previous tests (Kyle et al., 2006; Shamsabadi & Rollins, 2014) under uniform lateral loading but was in contrast to the observation in the current test study in which the maximum heaves occurred at the obtuse corner. This difference is also attributed to the rotation of the wall in the shake table tests.

8.2.7. Passive soil capacity under uniform displacement

Figure 8-8 presents the force-displacement relationships under the uniform displacement loading in the 0° skew model. The curves are shown for the applied velocity of 1e-5 in./sec below which the results were relatively insensitive to any further reduction in velocity. Furthermore, the results were also insensitive to the interface reduction factor. The force-displacement curves did not change as the interface reduction factor changed from 0.7 to 1.0. The force corresponding to the wall displacement of 3.0 in. decreased by 7.6% when the interface reduction factor was reduced from 0.7 to 0.5. The experimental results for the 0° skew angle are not shown in Figure 8-8 since they were affected by unrestrained wall movement toward the bridge block, as discussed in Chapter 6 and 7.

Figure 8-9 illustrates the force-displacement curves for the 30° skew models compared with the test data. The results are shown for the applied velocity of 1e-6 in./sec based on the sensitivity analyses presented in Figure 8-6. The curves from top to the bottom correspond to the interface reduction factors of 1.0, 0.9, 0.8, 0.7, and 0.65, respectively. The test data were close to the curves with the interface reduction factor of 0.7 to 1. The measured force at the displacement of 1.04 in. was 260 kips versus the calculated forces of 249, 275, 281, and 284 kips for the interface reduction factor of 0.7, 0.8, 0.9, and 1.0, respectively.

Figure 8-10 shows the force-displacement relationships in the 45° skew models compared with the test data. The results are shown for the applied velocity of 1e-5 and 1e-6 in./sec to assess the velocity sensitivity in the analyses. Using the smaller velocity led to less shock in the model. Furthermore, the sensitivity to the interface reduction factor was higher than that in the 0° and 30° skew models. The passive capacity from the analytical models was smaller than that from the experimental data. The measured force at the displacement of 1.69 in. was 156 kips while the calculated forces were 87, 79, and 52 kips for the interface reduction factor of 1.0, 0.9, and 0.8, respectively.

Displacement contours for the 45° skew model are presented in Figure 8-11 for interface reduction factors of 0.9 and 1.0. The total displacement vectors are also shown on the contour plots. The vectors showed that although the wall was pushed longitudinally, its total movement was parallel to the interface with the soil towards the acute corner and that the backfill movement was minimal. The maximum heave occurred at the acute corner for the interface reduction factor of 1.0, which was consistent with the heave pattern in the 30° skew model (Figure 8-7). In contrast, the maximum heave for $R_{\text{int}} = 0.9$ occurred at the obtuse corner. In both cases, the maximum heaves were not in the range of those in the 0° and 30° skew models. The right column shows the normal separation contours in the interface elements indicating that the interface was not in contact at the acute corner and the bottom of the wall for the reduction factor of 1.0. Such response led to the fact that the passive capacity of the backfill was not fully mobilized in the 45° skew model. Overall, the calculated results for the 45° skew model appeared to be highly sensitive to the input parameters with poor correlation with the test results. One possible reason is that under high skew angles the shear component and its modeling in FLAC3D on the backfill wall interface would require additional modeling considerations. Exploring this option was beyond the scope of the current study.

Figure 8-12 presents the force-displacement relationships for all the above cases with the interface reduction factor of 0.8 to 1.0. It can be seen while the correlation between the calculated and measured results was reasonable for the 30º skew model, simulation of the response for the 45º skew model led to substantial underestimation of the capacity.

8.2.8. Non-uniform displacement loading

As discussed in Chapter 6, the maximum wall displacement in the test occurred when the wall rotated clockwise about the vertical axis. To account for the rotation of the wall another analytical study was conducted using FLAC3D, applying a non-uniform displacement loading so that the maximum displacement at each corner reached the maximum measured displacements obtained in the tests. The analysis was conducted for both skew angles. However, the results are presented only for the 30º skew model because the analytical results for the 45º skew model showed a great deal of scatter with poor correlation with the test data.

The maximum backwall displacement was 4.08 and 1.36 in. in the 30º skew model at the obtuse corner and the acute corner of the bridge block, respectively. A non-uniform linear velocity (1e-6 in./sec at the obtuse corner) was applied across the wall to simulate these displacements that were caused by the wall rotation. Figure 8-13 presents the displacement contours of the 30º skew model under the non-uniform displacement loading. The corresponding uniform displacement contours from Figure 8-7 are also shown for comparison. The total displacement contours are also shown on the heave contours. The maximum heave was 1.88 in. at the obtuse corner. The heave was close to that in the uniform loading but occurred on the opposite side. The obtuse corner heaving was consistent with the test observations. The longitudinal displacement contours shifted towards the obtuse corner when the loading was changed to non-uniform. This was also seen from the displacement vectors shown in the heave contours. In contrast to the uniform loading, the transverse displacements under the non-uniform case were larger on the embankment slope at the obtuse corner than that at the acute corner. Overall, the non-uniform displacement loading improved the correlation between the measured and calculated displacement contours.

8.2.9. Passive soil capacity under non-uniform displacement

Figure 8-14 shows the comparison of the force-displacement curves between the uniform and non-uniform displacement loading for the interface reduction factor of 0.8 to 1.0 in the 30º skew model. Clearly, the calculated force-displacement curve was lowered when the non-uniform displacement loading was applied. Under uniform displacement, both corners were pushed with the same rate while the backfill stiffness was higher at the acute corner of the bridge block. Therefore, the capacity was higher under the uniform displacement than that under the non-uniform displacement loading. The best match between the estimated force-displacement curves and the measured data was for the interface reduction factor of 0.9 and 1.0 in the non-uniform loading. It is clear that the correlation between the measured and calculated lateral load capacity was improved when the wall rotation was simulated.

8.3. Three-dimensional factor due to skew

Previous tests on pile caps and abutment walls suggested that stresses spread beyond the abutment wall width. This effect results in contribution of a larger width of soil in the response. The surface crack patterns in Kyle et al. (2006) showed this 3D effect. Brinch Hansen (1966) suggested an empirical equation for the 3D correction factor based on small-scale lateral pressure tests on anchor slabs:

$$R_{3D} = 1 + \left(k_p - k_a\right)^{0.67}\left(1.1A^4 + \frac{1.6B_b}{1+5\left(B/h\right)} + \frac{0.4R_0A^3B_b^2}{1+0.05\left(B/h\right)}\right) \tag{8-8}$$

where A and B_b are dimensionless parameters related to the anchor slab. B and h are the anchor slab width and height, and H is the embedment depth according to Figure 8-15. R_0 is $\left(k_p - k_a\right)$ and A and B_b are determined from the following equations:

$$A = 1 - \frac{h}{H} \tag{8-9}$$

$$B_b = 1 - \left(\frac{B}{S'}\right)^2 \tag{8-10}$$

where S' is the spacing between a row of anchor slabs. The 3D correction factor for an abutment ($\frac{h}{H} = 0$ and $\frac{B}{S'} = 0$) is determined from the following equation:

$$R_{3D} = 1 + \left(k_p - k_a\right)^{0.67} \left(\frac{1.6}{1 + 5\left(B/h\right)} \right) \tag{8-11}$$

Rollins et al. (2010) reported 3D correction factors for the tests on non-skewed abutments with four different backfill materials. Table 8-4 presents the 3D factor estimation for those abutment tests at BYU and the current study at UNR based on the above formulation. The first and the second row for each test estimated the 3D factor based on the coulomb and log-spiral passive pressure coefficients, respectively. The reported 3D factors for BYU tests (Rollins et al., 2010) are shown in the last column. The coulomb passive pressure coefficient underestimated the 3D factor. The 3D factor based on the log-spiral passive pressure coefficients were close to that reported by the researchers. Similarly, the non-skewed 3D factor for the current study at the UNR was estimated 1.92 for a non-sloped embankment.

This section proposes a procedure for determining the skewed 3D factor as a function of the non-skewed 3D factor. The formulation was developed based on the embankment geometrical properties.

The "3D factor" is the ratio of the maximum effective width of failure wedge to the backwall width, and the "skewed 3D factor" is the maximum effective width in the skewed 3D wedge to the width of skewed backwall. Previous tests by Kyle et al. (2006) and Shamsabadi & Rollins (2014) showed that the skewed 3D factors were less than the corresponding 3D factors in the non-skew cases.

8.3.1. Procedure

The non-skewed 3D factor, R_{3D}, is defined with the following equation:

$$R_{3D} = \frac{W + 2L\tan\alpha}{W} = 1 + \frac{2L.\tan\alpha}{W} \tag{8-12}$$

where W is the non-skew abutment width, L is the length to the maximum effective width in the 3D failure wedge, and α is the stress spread angle, as shown in Figure 8-16.

The skewed 3D factor, $\left(R_{3D}\right)_{skew}$, is defined by the following formula:

$$R_{3D}^{Skew} = \frac{W_\theta + L_\theta.\tan\alpha + L_\theta.\tan\alpha_\theta}{W_\theta} = 1 + \frac{L_\theta.\cos\theta}{W}\left(\tan\alpha + \tan\alpha_\theta\right) \tag{8-13}$$

where α and α_θ are the stress spread angles at the acute and the obtuse corners of the bridge, respectively, L_θ is the distance to the maximum effective width as a result of the skew angle θ. L and L_θ are referred to as "non-skewed wedge length" and "skewed wedge length", respectively, and are both limited by the point of intersection of the spreading line and the edge of the backfill.

The spread angle is expected to be smaller at the obtuse corner than that at the acute corner, unless the soil extension beyond the wall edge is large enough to allow for pressure distribution. The backfill extension beyond the wall edge is referred to as "extension", denoted by e. The reduced spread angle at the obtuse corner is found based on the trigonometric relationships. Parameter x in Figure 8-16 is related to the skew angle, extension, spread angle, and the length to the maximum effective width using the two following equations:

$$x = \frac{e}{\sin(\alpha_\theta + \theta)} \tag{8-14}$$

$$x = \frac{L_\theta}{\cos \alpha_\theta} \tag{8-15}$$

By equating the right hand sides of these equations, the spread angle at the obtuse corner is determined:

$$\tan \alpha_\theta = \frac{e}{L_\theta . \cos \theta} - \tan \theta \tag{8-16}$$

The angle at the obtuse corner is a function of L_θ. Substituting α_θ in Eq. (8-13) results in:

$$R_{3D}^{Skew} = 1 + \frac{e}{W} + \frac{L_\theta}{W}(\cos \theta . \tan \alpha - \sin \theta) \tag{8-17}$$

For a relatively small extension, the stress spread angle differs between the acute and obtuse corners. In such case, the skewed wedge length can be found from the assumption that the skewed 3D factor equals to the non-skewed 3D factor when the skew angle is zero (equating Eq. (8-12) and Eq. (8-17)). This assumption leads to the skewed wedge length based on the non-skewed wedge parameters according to the following equation. This relationship is valid up to a certain extension labeled as "balanced extension" that is defined in the next section.

$$\theta = 0 \rightarrow 1 + \frac{e}{W} + \frac{L_\theta}{W}(\cos \theta . \tan \alpha - \sin \theta) = 1 + \frac{2L . \tan \alpha}{W} \tag{8-18}$$

Substituting $\theta = 0$ and simplifying the above equation:

$$e \le e_{bal} \rightarrow L_\theta = 2L - \frac{e}{\tan \alpha} \tag{8-19}$$

8.3.1.1. Balanced extension

The balanced extension, e_{bal}, is defined as the extension which is large enough so that the spread angle at the obtuse corner is the same as that in the acute corner.

Replacing *e* with e_{bal} in Eq. (8-16) and Eq. (8-19) yields the following relationship:

$$e_{bal} = L_\theta(\tan \alpha \cos \theta + \sin \theta) = \left(2L - \frac{e_{bal}}{\tan \alpha}\right)(\tan \alpha \cos \theta + \sin \theta) \tag{8-20}$$

$$e_{bal} = \frac{2L \tan \alpha \left(\cos \theta + \dfrac{\sin \theta}{\tan \alpha}\right)}{1 + \cos \theta + \dfrac{\sin \theta}{\tan \alpha}} \tag{8-21}$$

Substituting Eq. (8-12) in the above equation results in:

$$e_{bal} = \frac{W(R_{3D} - 1)\left(\cos \theta + \dfrac{\sin \theta}{\tan \alpha}\right)}{1 + \cos \theta + \dfrac{\sin \theta}{\tan \alpha}} \tag{8-22}$$

Defining $\mu = \cos \theta + \dfrac{\sin \theta}{\tan \alpha}$ results in:

$$e_{bal} = \frac{\mu W(R_{3D} - 1)}{1 + \mu} \tag{8-23}$$

For extensions that are equal or exceed the balanced extension, the spread angles are equal at the obtuse and acute corners. However, the skewed 3D factor is still smaller than the corresponding non-skewed 3D factor up to the "maximum extension" that is defined in next section. The following procedure is used to obtain the skewed 3D factor.

Substituting $\tan\alpha_\theta = \tan\alpha$ in Eq. (8-16)

$$\tan\alpha = \frac{e}{L_\theta.\cos\theta} - \tan\theta \tag{8-24}$$

The skewed wedge length is determined by:

$$L_\theta = \frac{e}{\tan\alpha\left(\cos\theta + \dfrac{\sin\theta}{\tan\alpha}\right)} \tag{8-25}$$

Substituting $\mu = \cos\theta + \dfrac{\sin\theta}{\tan\alpha}$ results in:

$$L_\theta = \frac{e}{\tan\alpha.\mu} \tag{8-26}$$

Substituting the above relationship in Eq. (8-13) yields:

$$R_{3D}^{Skew} = 1 + \frac{2e\cos\theta}{\mu W} \le R_{3D} \tag{8-27}$$

8.3.1.2. Maximum extension

The maximum extension is defined as the extension beyond which the skewed 3D factor is equal to the non-skew 3D factor since the extension is sufficiently large to allow for stress distribution. Equating (8-12) and Eq. (8-27) results in:

$$1 + \frac{2e_{\max}\cos\theta}{\mu W} = 1 + \frac{2L\tan\alpha}{W} \tag{8-28}$$

Therefore, the maximum extension is determined according to the following equation:

$$e_{\max} = \frac{\mu W(R_{3D} - 1)}{2\cos\theta} \tag{8-29}$$

8.3.1.3. Critical skew angle

The general relationship for the spread angle at the obtuse corner in Eq. (8-16) is valid up to a "critical skew angle" at which the spread angle is equal or greater than zero. When the skew angle is equal or exceeds the critical skew angle, the spread angle at the obtuse corner is set equal to zero to avoid negative angle entering the formulation and resulting in erroneous results. The critical skew angle is determined by substituting $\tan\alpha_\theta = 0$ in Eq. (8-16).

$$\tan\alpha_\theta = \frac{e}{L_\theta.\cos\theta} - \tan\theta = 0 \tag{8-30}$$

Simplifying the above equation results in:

$$\frac{e}{L_\theta} = \sin\theta \tag{8-31}$$

Substituting Eq. (8-19) in the above relationship yields:

$$\frac{e}{2L - \dfrac{e}{\tan\alpha}} = \sin\theta \tag{8-32}$$

Simplifying the above relationship and using Eq. (8-12) results in the following equations for the critical skew angle.

$$\theta_{cr} = \sin^{-1}\left(\frac{e.\tan\alpha}{2L\tan\alpha - e}\right) = \sin^{-1}\left(\frac{e.\tan\alpha}{W(R_{3D} - 1) - e}\right) \tag{8-33}$$

8.3.1.4. Summary

A procedure was presented to determine the skewed passive wedge geometry (skewed wedge length, spread angle at the obtuse corner, and skewed 3D factor) based on the non-skewed passive wedge properties. This required defining some boundary parameters including the balanced extension, maximum extension, and critical skew angle to determine the corresponding skewed failure wedge properties. A summary of the entire formulation is presented in Table 8-5.

8.3.2. Effect of embankment slope

The soil wedge volume contributing to the passive capacity is reduced when the embankment is sloped. The 3D factor is also reduced accordingly. Figure 8-17 presents a schematic cross section of the skewed 3D wedge. The skewed wedge volume is proportional to its cross sectional area.

The reduced cross section area is $\frac{1}{2}L_\theta^2 \tan\beta\left[(\tan\alpha)^2 + (\tan\alpha_\theta)^2\right]$, where β is the angle of the slope with a horizontal line, L_θ is the skewed wedge length, and α and α_θ are the spread angles at the acute and obtuse corners, respectively. The total cross section area ignoring the embankment slope is $H.W\cos\theta.R_{3D}^{Skew}$. Therefore, the reduction factor considering the embankment slope is determined by the following equation:

$$R_{Embank} = 1 - \frac{L_\theta^2 \tan\beta.\cos\theta.\left[(\tan\alpha)^2 + (\tan\alpha_\theta)^2\right]}{2H.W.R_{3D}^{Skew}} \tag{8-34}$$

where H is the backwall height. The final skewed 3D factor of embankment, $\left(R_{3D}^{Skew}\right)_{Embank}$, is:

$$\left(R_{3D}^{Skew}\right)_{Embank} = R_{3D}^{Skew}.R_{Embank} \tag{8-35}$$

$$\left(R_{3D}^{Skew}\right)_{Embank} = R_{3D}^{Skew}\left[1 - \frac{L_\theta^2 \tan\beta.\cos\theta.\left[(\tan\alpha)^2 + (\tan\alpha_\theta)^2\right]}{2H.W.R_{3D}^{Skew}}\right] \tag{8-36}$$

8.3.3. Skewed 3D factor for BYU test model (Marsh et al., 2013)

Figure 8-18 shows the heave contours obtained in the BYU tests (Marsh et al., 2013). The passive wedge had an effective width of approximately 20 ft in the non-skew case corresponding to a 3D factor of 1.82. The same width was observed in the 30° skew passive wedge but led to a reduced 3D factor of 1.57 due to the larger width of abutment compared to that in the non-skew case.

The formulation proposed in Section 8.2.1 was used to calculate the skewed 3D factor from the non-skewed 3D factor. There was no additional reduction per as in Section 8.2.2 because the embankment was not sloped. Figure 8-19 presents the skewed 3D factor variations for different skew angles in this test. The 3D factor started from the calculated value for the non-skew case and was reduced to 1.0 for the 90° skew angle. The 3D factor for a 30° skew case was calculated 1.49 while the measured 3D factor was 1.57, indicating good correlation. The details of the 3D factor calculation are presented in Table 8-6. Since the backfill extension was larger than $e_{\max}$ for the 5° skew angle, the skewed 3D factor was the same as that for the non-skew case. The critical skew angle was 61.5° beyond which the spread angle at the obtuse corner was zero.

Figure 8-20 compares the measured and the calculated 3D wedge geometries for the BYU test (Marsh et al., 2013). It is evident that the proposed formulation leads to close correlation with the measured results. As previously discussed, the spread angle at the obtuse corner and the length to the effective width decreased as the skew angle increased.

The influence of extension length on the skewed 3D factor formulation proposed in this chapter was studied for the BYU test model. Figure 8-21 shows the effect of backfill extension on the calculated 3D factor. The actual extension was 5.5 ft. The other extensions assumed in the sensitivity study were 4, 6, and 7 ft. Clearly, the skewed 3D factor increased as the backfill extension increased. The 3D factor remained constant for relatively small skew angles. However, this small skew angle changed for different extensions. For example, the skewed 3D factor remained unchanged up to a skew angle of 20° for the 7-ft extension, which allowed for full pressure spread, but the 3D factor decreased at the skew angle of 10° or more for the actual extension of 5.5 ft.

Figure 8-22 presents the effect of the ratio of the extension to the wall projected width on the 3D factor. As the extension ratio increased, the skew factor also increased and then remained constant at some point. This constant 3D factor point (corresponding to $e_{\max}$) was increased as the skew angle increased. In other words, the extension length affected the 3D factor more significantly for larger skew angles.

Figure 8-23 shows the effect of extension ratio on the spread angle at the obtuse corner. As the extension decreased, the obtuse corner spread angle remained constant up to a certain point (corresponding to e_{bal}) and then decreased as expected.

8.3.4. Skewed 3D factor for current test study

Figure 8-24 presents the 3D factor variations by the change in the skew angle calculated for the models tested in the current test study. The top curve shows only the effect of skew angle while the bottom curve combines the effects of skew angle and sloped embankment. The combined estimated 3D factors were 1.67, 1.28, and 1.18 for the 0°, 30°, and 45° skew cases, respectively. The variations showed that the effect of skew angle on the 3D factor reduction was more significant for the small skew angles. Furthermore, the effect of embankment slope was more noticeable when the skew angle was relatively small. The details of 3D factor calculation due to the skew angle and the embankment slope are presented in Table 8-7 and Table 8-8, respectively. The critical skew angle was 28.3° beyond which the spread angle at the obtuse corner was zero. The critical skew angle decreased substantially for the UNR test model compared to that of the BYU test model mostly because of a smaller backfill extension in the UNR case.

8.4. Design recommendations

Hyperbolic force-displacement relationships are compared with the measured results from the test results from the current study.

8.4.1. Comparison of test results with HFD relationship

The hyperbolic force-displacement relationship (HFD) was calculated using a method developed by Shamsabadi et al. (2010) and compared with the test data:

$$F(y) = \frac{8y}{1+3y} H^{1.5} (kips, in.) \text{ for granular backfill} \tag{8-37}$$

$$F(y) = \frac{8y}{1+1.3y} H (kips, in.) \text{ for cohesive backfill} \tag{8-38}$$

where y and $F(y)$ are the abutment displacement and force per unit width, respectively, and H is the abutment backwall height.

The HFD relationship is found for a unit width of the abutment and excludes the 3D factor. Therefore, the results from the method need to be modified to account for the abutment wall width and the 3D factor. Shamsabadi & Rollins (2014) suggested the following equation for the reduction factor to be applied to the backbone curve (Figure 8-25) to account for the skew angle, θ:

$$R_\theta = e^{-\theta/45} \tag{8-39}$$

There are three factors incorporated in the HFD relationship. The normalized width factor is the ratio of the abutment width to the projected width ($\frac{1}{\cos\theta}$). The skewed 3D factor was previously calculated in Section 8.2.4 and shown in Figure 8-24, and the skew reduction factor was plotted based on Eq. (8-39). Figure 8-26 shows the variation of the three factors used in the HFD relationship for the test model in the current study. Figure (a) presents the variation for each factor. The effect of normalized width factor and the skewed 3D factor partially cancelled each other but the skew reduction factor played a significant role. The combined effect of the factors referred to as the "combined skew factor" is shown in Figure (b). The combined skew factor (normalized relative to the abutment projected width) were 1.67, 0.76, and 0.62 for the 0°, 30°, and 45° skew cases of the current study, respectively.

Figure 8-27 presents the HFD curves for the UNR test models with 0°, 30°, and 45° skew based on the combined skew factors. The hyperbolic relationship was multiplied by the skew 3D factor (Section 8.2.4) and the skew reduction factor, R_θ, by Shamsabadi & Rollins (2014). The multipliers of Eq. (8-37) were 1.67, 0.76, and 0.62 multiplied by the 10-ft projected width for the 0°, 30°, and 45° skew cases, respectively. The passive force for the non-skew case was reduced by 54% and 63% for the 30° and 45° skew cases, respectively. The reduction was 18% when the skew angle changed from 30° to 45°.

Figure 8-28 and Figure 8-29 show the HFD force-displacement relationships compared with the test data for the 30° and 45° skew abutments, respectively. The HFD method underestimated the passive capacity by 25% and 23% at the displacements of 0.5 and 1.0 in., respectively, in the 30° skew abutment. The HFD estimation was closer to the test data in the 45° skew than that in the 30° skew case. The calculated initial stiffness was close to the lower-bound measured stiffness. The HFD relationship overestimated the capacity by 16% and 23% compared the lower-bound measured data at displacements of 0.5 and 1.0 in., respectively. The upper-bound data was underestimated by the HFD method by 8% and overestimated by 10% at the displacements of 0.5 and 1.0 in., respectively. The combined curves of the HFD relationships compared with the test data are presented in Figure 8-30.

Figure 8-31 presents the measured force ratios between the 30° and 45° skew tests for different approaches discussed in Section 7.2.2. The average measured force reduction was 0.81, 0.83, 0.68, and 0.58 for Run 2, Run 3, Run 4, and Run 5, respectively. The passive force reduction based on the abutment width, skew reduction, and 3D factors was 0.81 shown as the dashed line. This factor led to a close estimation of the average measured force in Run 2 and Run 3 but was higher than that in Run 4 and Run 5. The passive force-displacement relationships in Figure 8-30 also showed larger force reduction for larger displacement compared to that for the smaller displacement when the skew angle changed from 30° to 45°.

8.4.2. Comparison of test results with S-LSH force-displacement relationship

Another analytical study that was conducted in the current investigation was to analyze the test models using the skewed log-spiral hyperbolic (S-LSH) method developed and implemented in a computer program by Shamsabadi (2017). This program is designated to estimate the passive force-displacement relationship of abutments with different skew angles based on different methods from the classic Rankine and Coulomb methods to the force and moment approaches of the log-spiral method.

8.4.2.1. Procedure

The program performs two types of two and three-dimensional analyses. The two-dimensional analysis provides the overall stiffness of the abutment. In case the distribution of stiffness across the abutment is also required, a three-dimensional analysis is necessary, but the two-dimensional analysis has to be first conducted. The skew effect is directly defined by the "skew angle" in the 2D analysis, but is simulated by the "eccentricity" parameter in the 3D analysis.

The abutment input parameters are shown in Table 8-9. Note that the actual width (not the projected width) of the abutment should be specified. The skew reduction factor is internally calculated based on Eq. (8-39) by Shamsabadi & Rollins (2014) but the 3D factor should be specified by the user. The program limits the soil strength reduction factor to 0.9-1.0. This limit was incorporate in the S-LSH program by Shamsabadi (2017) based on the calibration of the test data in previous abutment tests.

8.4.2.2. Two-dimensional analysis

A two-dimensional analysis was performed to determine the total force-displacement curve considering the effect of skew angle. Figure 8-32 to Figure 8-34 show the force displacement curves from the S-LSH program (log spiral methods) for the 0°, 30°, and 45° skew UNR test models, respectively. The measured results for the 30° and 45° skew tests are also shown in the graphs. The skewed 3D factors were assigned 1.67, 1.28, and 1.18, respectively, based on Section 8.2.2.

Figure 8-35 presents the results of the force method with curved failure planes for the three UNR abutments. The force was reduced by 52.0% and 62.3% when the skew angle changed from 0° to 30° and 45° skew, respectively. The force reduction was 21.6% when the skew angle was increased from 30° to 45°.

8.4.2.3. Three-dimensional analysis

The three-dimensional analysis of the test models was performed to determine force-displacement relationships across the wall subsequent to the two-dimensional analysis. According to the S-LSH program by Shamsabadi (2017), the eccentricity parameter is varied in 3D analysis until the overall force-displacement curve from the 3D and 2D analysis match.

Figure 8-36 shows the total force-displacement curve from the two-dimensional analysis for the 30° skew abutment versus the three-dimensional analysis with eccentricities of 0.5, 0.55, 0.6 ft. These were the eccentricities that led to close match between the 2D and 3D analysis results. Figure 8-37 presents a similar comparison for the 45° skew abutment and eccentricities of 1.5, 1.6, and 1.7 ft. The eccentricity of 0.5 and 1.6 ft led to a close match between the 2D and 3D results for the 30° and 45° skew abutments, respectively.

The 3D analysis of S-LSH led to the distribution of force-displacement relationships per unit width of the abutment, which can be used to assign to a series of springs modeling the backfill. Figure 8-38 and Figure 8-39 present the corresponding force-displacement curves for the 30° and 45° skew UNR abutments, respectively. The abutments were 11.55 and 14.14 ft wide and the number of output curves were 11 and 14, respectively. The top curve utilized the full strength parameters of the soil whereas the lower curves simulated the mobilized strength parameters. These were calculated based on a trapezoidal pressure distribution behind the abutment under a back-calculated eccentricity of the applied force. These curves can be added together to determine the force-displacement relationships for any arbitrary number of springs across the abutment for design purposes.

8.5. Concluding remarks

The FLAC3D models were developed to simulate the backfill response under the static uniform and non-uniform displacement loading on the wall. The displacement contours from the analytical models under the non-uniform displacement were similar to those obtained in the shake table tests. The passive force-displacement relationship from the 30° skew abutment was in good agreement with that from the experimental results. However, the force-displacement response of the 45° skew model underestimated the soil capacity significantly. More investigations and sensitivity analyses are required to better simulate the interface elements for relatively large skew angles. Future research includes dynamic analysis of similar models in FLAC3D to investigate the effects of material properties, damping, and dynamic loading.

HFD formulation and S-LSH program were utilized to estimate the force-displacement relationship of the test models. Both methods led to the results that matched the test data reasonably well. The HFD relationship underestimated the passive force in the 30° skew abutment but overestimated the capacity in the 45° skew case. The S-LSH force-displacement curves led to results in close agreement with the test data in the 30° skew case. In contrast, they overestimated the passive capacity in the 45° skew abutment.

The S-LSH program was used to find the soil pressure distribution behind the test model abutment walls. First, a two-dimensional analysis was conducted to determine the total force-displacement curve considering the effect of skew angle. Then, a three-dimensional analysis was performed by determining the eccentricity that resulted in the same total force-displacement curve as of that from the two-dimensional analysis. The linear variation of the force-displacement curves could be used to model springs across the abutment. The eccentricity was dependent on both the skew angle and the backwall width and should be individually determined for each specific abutment through trial and error.

The HFD formulation by Shamsabadi et al. (2010) is generally used to determine the passive force per unit width of non-skew abutments. A skew factor was specified in this study that combined the effects of the skewed 3D factor, normalized width factor, and the skew reduction factor. It is suggested to estimate the skewed 3D factor from the formulation proposed in this study. For the skew reduction factor, it is recommended to use the method proposed by Shamsabadi & Rollins (2014) to account for the capacity reduction due to the skew angle. In general, it is concluded that both HFD formulation and S-LSH program are reliable tools to determine the passive force-displacement relationship of skewed abutments.

9. SUMMARY AND CONCLUSIONS

9.1. Summary

Skewed abutments are vulnerable to high velocity pulse motions due to the induced large residual displacements. Skew angle significantly affects the distribution of soil pressure behind the abutment and therefore, influences the mobilized passive resistance of the backfill soil and the behavior of soil-abutment system caused by large in-plane rotations and translation of the superstructure.

Shake-table test models on large-scale 5.5-ft high abutments with the projected widths of 10 ft at three skew angles of 0°, 30°, and 45° were designed and tested under simulated earthquake motions at the University of Nevada, Reno (UNR). The bridge block on the shake table was placed adjacent to the abutment wall with a 2-in. gap and was excited by the motions in the longitudinal direction of the bridge. The abutment wall represented a backwall in a seat-type abutment with sliding base that simulated a failed backwall-footing connection consistent with the assumption made in seismic design of bridges. The backfill was extended 4.5 ft beyond the abutment width on each side and consisted of sand with 95% relative compaction.

The primary objectives of the experiments were to study the bridge block and abutment movements and the soil pressure, heaves, and accelerations and investigate the skew effect on the seismic response. The displacements and accelerations of the bridge block and the abutment were measured using displacement and acceleration transducers. Soil pressure was determined from readings of pressure cells on the abutment wall face in contact with the backfill. Contours of maximum soil heaves and three-dimensional accelerations were investigated to determine the backfill response caused by closure of the gap between the bridge block and the abutment wall. Gypsum and colored sand columns were embedded inside the backfill to investigate the soil passive failure mechanism.

The experimental studies also included developing the envelopes of the measured force-displacement relationships of the abutments based on progressive mobilization of soil passive capacity during gradually intensified earthquake motions. The force-displacement curves of the abutments in the current study at the UNR were compared with those from the previous experiments.

The preliminary analytical modeling using PLAXIS and FLAC3D were performed with the objective to assess the applicability of FLAC3D software to reproduce the test data obtained from the previous experiments on the abutments. The hardening soil model in PLAXIS has been demonstrated by other researchers to result in good correlation between the measured and the calculated force-displacement relationships of the abutments. This model was incorporated along with available Mohr-Coulomb model in FLAC3D. The Mohr-Coulomb model modified based on the stress-dependent modulus was evaluated through comparison of results between PLAXIS2D, FLAC3D, and the earth pressure theories.

The analytical studies were followed by static analysis of the soil-abutment part of the shake table test models in FLAC3D. The static analyses were performed on the soil-abutment system by simulating uniform and non-uniform displacement loading on the abutment wall, with the latter simulating the wall rotations observed in the tests. The non-uniform displacement loading was based on the maximum displacements of the abutment wall corners measured during the shake table tests to account for the wall rotation. The stress-dependent modified Mohr-Coulomb model based on the preliminary analytical studies was used to represent the backfill material. The displacement contours and the passive force-displacement curves obtained from the analytical models were compared with those from the shake table experiments.

The analytical studies also included evaluating the most recent available models estimating the passive force-displacement relationships of the abutments accounting for the skew effect. The hyperbolic force displacement (HFD) formulation by Shamsabadi et al. (2010) and the skewed log-spiral hyperbolic (S-LSH) program by Shamsabadi (2017) were used for estimating force-displacement relationships. The applicability of the capacity reduction factor due to the skew effect using the method proposed by Shamsabadi & Rollins (2014) was evaluated for the shake table test models of the current study. The capacity reduction factor was applied in the S-LSH program by defining the skew parameter, but was multiplied by the HFD formulation in skewed cases.

A 2D analysis in S-LSH was performed to determine the overall force-displacement relationship of the abutments. A 3D analysis in S-LSH was used to determine the passive soil pressure distribution behind the skewed abutments based on the eccentricity parameter as the input to the program. The eccentricity was determined by the trial and error method for each abutment so that the 3D analysis yielded the same overall force-displacement curve as that obtained from the 2D analysis.

The 3D passive failure wedge from the previous experiments on the unconfined abutment backfills showed that the effective width of soil contributing to the backfill capacity could be determined by a 3D factor applied to the abutment width. The 3D factor to account for the three-dimensional shear effect was calculated by the Brinch Hansen (1996) method for non-skewed abutments based on the active and passive pressure coefficients of the soil. A formulation was proposed in this study to calculate the skewed 3D factor based on the non-skewed 3D factor and the backfill geometry. The proposed formulation calculated dimensions of the skewed 3D passive wedge of the backfill based on the probable reduced spread angle at the obtuse corner of the bridge.

9.2. Key observations from experimental studies

The main observations in the experimental studies were:

1. The peak bridge block accelerations near the abutment exceeded those at the far end of the bridge block upon impact with the backwall. The accelerations near the backwall did not follow a specific trend in the non-skew case. The accelerations in the skew cases were higher at the obtuse corner than those at the acute corner. This was in agreement with the maximum clockwise rotation of the bridge block.
2. The backwall rotations about the vertical axis were very small in the non-skew, as expected, because of the nearly uniform contact between the bridge block and the backwall. The bridge block and the abutment wall in the skew cases, however, rotated about the vertical axis under impact. The backwall initially rotated in the counterclockwise direction that was consistent with the eccentricity between the centers of mass and stiffness of the bridge block. Then the direction of rotation reversed since the resistance of the backfill soil was higher at the acute corner and the bridge block and the abutment wall had the tendency to rotate in the direction of reducing the skew angle. The maximum rotation of the bridge block corresponding to the maximum displacement of the abutment was independent of the bridge block eccentricity and followed the abutment wall rotation due to the skew configuration.
3. The maximum longitudinal displacement of the backwall decreased when the skew angle increased. The skew angle increase led to larger initial counterclockwise rotations of the backwall. However, the subsequent maximum clockwise rotations decreased by increasing the skew angle.
4. The variation of pressure at the acute and obtuse corners depended mostly on the direction of backwall rotation about the vertical axis. The soil pressure at the acute corner was initially higher than that at the obtuse corner when the abutment wall displacements were relatively small. In contrast, the soil pressure at the obtuse corner was higher than that at the acute corner when the backwall displacement peaked since the backwall rotation was clockwise in the direction of reducing the skew angle.

5. The measured soil pressure variation was not always consistent with the motion amplitude increase due to the uneven and local soil failure. The maximum soil pressures substantially decreased when the skew angle increased from 30 to 45 degrees.
6. The soil surface cracks were primarily parallel to the skew angle. The backwall corner cracks were mostly concentrated at the acute corner but were scattered at the obtuse corner.
7. The general pattern of the maximum soil heave distribution was symmetric about the centerline of the bridge block for the non-skew case with the maximum heave at the center of the abutment wall. Distribution of the maximum soil heaves was un-symmetric in the skew cases. The heaves were larger at the obtuse corner than those at the acute corner due to the backwall rotation.
8. The maximum heaves decreased when the skew angle increased. The decrease was more significant for the locations close to the abutment wall than for those far from the wall.
9. The maximum heaves became insignificant (less than 0.1 in.) at approximately 3.1, 3, and 2.1 times the backwall height from the center of backwall for the last runs in the 0°, 30°, and 45º skew tests, respectively.
10. The area affected by the soil maximum heaves extended towards the obtuse corner for both skew cases. The maximum heaves and the area of the maximum heaves was reduced when the skew angle increased.
11. The failures observed in the gypsum and colored sand columns showed a progressive failure mechanism of the backfill passive capacity.
12. The capacity in the passive force-displacement relationship of the abutment was significantly reduced (by approximately 50% at displacement of 1 in.) when the skew angle increased from 30° to 45°
13. The initial stiffness of abutment force-displacement relationship in the current study was comparable to that in the BYU lab tests but the normalized capacity was comparable to that in the BYU field tests.

9.3. Key observations from analytical studies

The key observations from the analytical studies were:

1. The preliminary analytical studies showed that the Mohr-Coulomb model with an average stress-dependent Young modulus using Duncan model for a mid-height soil element led to good correlation between the measured force-displacement results and those from PLAXIS2D and FLAC3D.
2. The displacement contours obtained from the FLAC3D models using the non-uniform displacement loading on the abutment wall were similar to those measured in the shake table tests.
3. The passive force-displacement relationships obtained from the 30° skew analytical models in FLAC3D were in good agreement with those from the experimental results. The correlation was improved when the non-uniform displacement loading was applied to the abutment wall to account for the rotation of the backwall.
4. The passive force-displacement relationships of the 45° skew model obtained from FLAC3D significantly underestimated the soil capacity. This is believed to be because the interface shear strength was underestimated and not properly modeled in the analysis. The underestimation of the interface shear strength led to premature slippage along the interface and significantly reduced the mobilized soil and its contribution to the passive capacity.

5. The capacity reduction factor proposed by Shamsabadi & Rollins (2014) proved valid for the measured response of the abutments under the simulated dynamic loadings in the current study.
6. The 3D factor calculated by the Brinch Hansen (1966) method was in good agreement with the measured 3D passive failure wedges obtained from the previous tests on the non-skewed abutments.
7. The passive pressure coefficient by the Coulomb method significantly underestimated the 3D factor. It was found that good correlation can be obtained if the active pressure coefficient from the Coulomb method and the passive pressure coefficient from the log-spiral method are used.
8. The 3D factor should be adjusted to account for three-dimensional shear effects in any embankment.
9. The skewed 3D factor formulation proposed in this study resulted in good agreement with the previous test data for the 3D passive failure wedge of backfill.
10. The HFD formulation by Shamsabadi et al. (2010) in combination with the capacity reduction factor proposed by Shamsabadi & Rollins (2014) and the skewed 3D factor suggested in this study led to good correlation between the measured and the estimated force-displacement curves.
11. The estimated force-displacement relationship of the test model using the S-LSH program in combination with the skewed 3D factor proposed in this study resulted in close agreement with the measured response of the 30° skew test model but overestimated the response of the 45° skew test.

9.4. Conclusions

The main findings from the experimental and analytical studies presented in this document led to the following conclusions:

1. Abutment wall rotation is very likely upon impact of superstructure on the abutment in skewed bridges. This could affect distribution of backfill soil pressure across the abutment wall.
2. Even though a sliding abutment wall represents a failed wall-footing connection reasonably well, sliding towards the superstructure should be controlled during shake table tests to maintain the initial abutment gap to avoid underestimating the effect of impact between the superstructure and the abutment.
3. The shake table experiments verified that skewed bridges tend to rotate in the direction of reducing the skew angle. This corresponds to impacting abutment at the obtuse corner and unseating of superstructure at the acute corner.
4. The backfill response including soil pressure, displacement, and acceleration is controlled by abutment wall rotation.
5. The peak soil heaves and accelerations decrease as the skew angle increases with larger values at the obtuse corner than those at the acute corner.
6. The peak soil heaves and accelerations decrease as distance to the abutment wall increases indicating dissipation of energy through the soil.
7. Variation of peak accelerations across the backfill soil in skewed abutments is more pronounced away from the backwall than that close to the backwall due to the spreading of soil movement toward the obtuse corner.
8. Variation of soil stiffness across skewed abutments may be assumed to be linear with higher stiffness at the obtuse corner and lower stiffness at the acute corner. This would be simple and sufficiently accurate for design purposes.
9. To model the entire backfill in FLAC3D or similar software, it is sufficiently accurate to use the Mohr-Coulomb model with an average stress-dependent Young

modulus that is based on the Duncan model using the vertical stress at mid-height of the soil backfill.

10. The backfill passive capacity is reduced when abutment rotation is accounted for.
11. The capacity reduction factor proposed by Shamsabadi & Rollins (2014) may be successfully used to account for the reduction of passive capacity due to the skew.
12. The Brinch Hansen (1966) method may be effectively utilized to estimate the 3D factor for a non-skew abutment. It would be accurate for the 3D factor estimation to calculate the active pressure coefficient from the Coulomb method and the passive pressure coefficient from the log-spiral method.
13. The skewed 3D factor formulation proposed in this study successfully accounts for the skew angle effect on the 3D passive failure wedge of the backfill. This factor could be used in combination with other available models and tools such as the HFD formulation and the S-LSH program.
14. To represent the force-displacement behavior of skewed abutments in bridge design, the HFD formulation by Shamsabadi et al. (2010) could be used in combination with the capacity reduction factor proposed by Shamsabadi & Rollins (2014) and the skewed 3D factor developed in this study.
15. To estimate the distribution of force-displacement relationships across the skewed abutments, the 3D analysis in the S-LSH program in combination with the skewed 3D factor proposed in this study is sufficiently accurate for design purposes.

REFERENCES

AASHTO. (2012). *AASHTO LRFD bridge design specifications*. Washington, DC: American Association of State Highway and Transportation Officials.

AASHTO. (2012). *Guide specifications for seismic isolation design*. Washington, DC: American Association of State Highway and Transportation Officials.

Abdollahi, B., Saiidi, M., Siddharthan, R., Elfass, S., and Shamsabadi, A. (2016). Pre-test studies on seismic soil-abutment interaction in skewed bridges. *IABMAS2016, 8th International Conference on Bridge Maintenance, Safety and Management*. Brazil. June 26-30, 2016. Pages 2075-2082.

ACI. (2011). *Building code requirements for structural concrete* (*ACI 318-11*). Detroit, MI: American Concrete Institute.

AISC. (2011). *Steel construction manual* (13th ed.). Chicago, IL: American Institute of Steel Construction, Inc.

Anderson, D. G., Martin, G. R., Lam, I (P.), Wang, J. N. (J.). (2008). *Seismic analysis and design of retaining walls, buried structures, slopes, and embankments* (Vol. 611). Transportation Research Board.

ASTM. D1557 (2012). *Standard test methods for laboratory compaction characteristics of soil using modified effort (56,000 ft-lbf/ft3 (2,700 kN-m/m3))*. PA: American Society for Testing and Materials.

ASTM. D2487 (2011). *Standard practice for classification of soils for engineering purposes (unified soil classification system)*. PA: American Society for Testing and Materials.

ASTM. D3080 (2011). *Standard test method for direct shear test of soils under consolidated drained conditions*. PA: American Society for Testing and Materials.

ASTM. D698 (2012). *Standard test methods for laboratory compaction characteristics of soil using standard effort (12,400 ft-lbf/ft3 (600 kN-m/m3))*. PA: American Society for Testing and Materials.

ASTM. D7181 (2011). *Standard test method for consolidated drained triaxial compression test for soils*. PA: American Society for Testing and Materials.

Bozorgzadeh, A. (2007). *Effect of structure backfill on stiffness and capacity of bridge abutments*. (Doctoral dissertation, University of California, San Diego)

Bozorgzadeh, A., Ashford, S. A., & Restrepo, J. I. (2006). *Effect of backfill soil type on stiffness and ultimate capacity of bridge abutments: large-scale tests.* Fifth National Seismic Conference on Bridges & Highways. Multidisciplinary Center for Earthquake Engineering Research. California Department of Transportation. Federal Highway Administration. Transportation Research Board (No. B01).

Bozorgzadeh, A., Ashford, S. A., & Restrepo, J. I. (2008). Effect of backfill soil type on stiffness and ultimate capacity of bridge abutments. *Geotechnical Earthquake Engineering and Soil Dynamics IV* (pp. 1-10).

Bozorgzadeh, A., Ashford, S. A., Restrepo, J. I., & Nimityongskul, N. (2008). *Experimental and analytical investigation on stiffness and ultimate capacity of bridge abutments* (No. SSRP-07/12).

Brinch Hansen, J. (1966). Resistance of a rectangular anchor slab. *Bull*, *21*, 12-13.

Caltrans, S. D. C. (2013). Caltrans seismic design criteria, v. 1.7.

Carvajal Uribe, J. C. (2011). *Seismic embankment-abutment-structure interaction of integral abutment bridges* (Doctoral dissertation, University of British Columbia).

Dimitrakopoulos, E. G. (2011). Seismic response analysis of skew bridges with pounding deck–abutment joints. *Engineering Structures*, *33*(3), 813-826.

Duncan, J. M., & Chang, C. Y. (1970). Nonlinear analysis of stress and strain in soils. *Journal of Soil Mechanics & Foundations Div*.

Duncan, J. M., & Mokwa, R. L. (2001). Passive earth pressures: theories and tests. *Journal of Geotechnical and Geoenvironmental Engineering*, *127*(3), 248-257.

Earth Mechanics, I. N. C. (2005). *Field investigation report for abutment backfill characterization*. Report No. SSRP-05/02, University of California, San Diego, CA.

Elgamal, A., Yan, L., Yang, Z., & Conte, J. P. (2008). Three-dimensional seismic response of Humboldt Bay bridge-foundation-ground system. *Journal of structural engineering*, *134*(7), 1165-1176.

Franke, B. W. (2013). *Passive force on skewed abutments with mechanically stabilized earth (MSE) wingwalls based on large-scale tests*. (Master's thesis, Brigham Young University).

Guo, Z. (2015). *Numerical analysis of passive force on skewed bridge abutments*. (Master's thesis, Brigham Young University).

Heiner, L., Rollins, K. M., & Gerber, T. M. (2008). Passive force-deflection curves for abutments with MSE confined approach fills. *Sixth National Seismic Conference on Bridges and Highways*.

Itasca, H. C. (2002). Flac3D, fast lagrangian analysis of continua in 3 dimensions. *Computer Program*.

Jessee, S. J. (2012). *Skew effects on passive earth pressures based on large-scale tests*. (Master's thesis, Brigham Young University).

Jessee, S., & Rollins, K. (2013). Passive pressure on skewed bridge abutments. *Proceedings of the 18th International Conference on Soil Mechanics and Geotechnical Engineering*, *Paris.*

Kalasin, T., & Wood Muir, D. Seismic analysis of retaining walls within plasticity framework. The 14th WCEE, Beijing, China, 12-17.

Kavazanjian, E., Wang, J. N. J., Martin, G. R., Shamsabadi, A., Lam, I., Dickenson, S. E., & Hung, C. J. (2011). LRFD seismic analysis and design of transportation geotechnical features and structural foundations reference manual. *Publication No. FHWA-NHI-11-032, FHWA, US Department of Transportation, Federal Highway Administration, Washington DC*.

Kavianijopari, P. (2011). *Performance-based seismic assessment of skewed bridges*. (Doctoral dissertation, University of California, Irvine).

Kawashima, K., Unjoh, S., Hoshikuma, J., & Kosa, K. (2010). Damage of transportation facility due to 2010 Chile Earthquake. *Bridge Team Dispatched by Japan Society of Civil Engineers*.

Kondner, R. L. (1963). Hyperbolic stress-strain response: cohesive soils. *J. Geotech. Engrg. Div.*, *89*(1), 115-143.

Kramer, S. L. (1996). *Geotechnical Earthquake Engineering.* Prentice Hall. New York.

Lemnitzer, A., Ahlberg, E. R., Nigbor, R. L., Shamsabadi, A., Wallace, J. W., & Stewart, J. P. (2009). Lateral performance of full-scale bridge abutment wall with granular backfill. *Journal of Geotechnical and Geoenvironmental Engineering*, *135*(4), 506-514.

Lu, J., Elgamal, A., Mackie, K., & Shamsabadi, A. (2012). A framework for performance-based earthquake engineering of bridge-abutment systems. *GeoCongress 2012: State of the Art and Practice in Geotechnical Engineering* (pp. 1680-1689).

Lu, J., Mackie, K. R., & Elgamal, A. (2011). BridgePBEE: OpenSees 3D pushover and earthquake analysis of single-column 2-span bridges, User manual, beta 1.0.

Mackie, K. R., & Stojadinović, B. (2006). Post-earthquake functionality of highway overpass bridges. *Earthquake engineering & structural dynamics*, *35*(1), 77-93.

Maroney, B. H. (1995). *Large scale bridge abutment tests to determine stiffness and ultimate strength under seismic loading* (Doctoral dissertation, University of California, Davis).

Maroney, B., Kutter, B., Romstad, K., Chai, Y. H., & Vanderbilt, E. (1994, June). Interpretation of large scale bridge abutment test results. In *Proc., 3rd Annual Seismic Research Workshop*. Sacramento, Calif.: California Dept. of Transportation.

Marsh, A. K. (2013). *Evaluation of passive force on skewed bridge abutments with large-scale tests*. (Master's thesis, Brigham Young University).

Marsh, A., Rollins, K., Franke, B., Smith, J., & Palmer, K. (2013). Passive force-deflection behavior for 0 and 30 skewed abutments. *Transportation Research Record: Journal of the Transportation Research Board*, (2363), 12-20.

McKenna, F. (2011). OpenSees: a framework for earthquake engineering simulation. *Computing in Science & Engineering*, *13*(4), 58-66.

Mock, E., & Cheng, L. (2011). *Full-scale shake table test of retaining walls with and without sound wall*. Report No. CA10-2039. University of California, Davis.

Nelson, R. B. (2007). *Experimental evaluation of performance of conventional bridge systems*. (Doctoral dissertation, University of Nevada, Reno).

Ovesen, N. K. (1964). *Anchor slabs: Calculation methods and model tests*.

Ovesen, N. K., & Stromann, H. (1972, June). Design method for vertical anchor slabs in sand. *Performance of Earth and Earth-Supported Structures* (p. 1481). ASCE.

Palmer, K. N. (2013). *Large-scale testing of passive force behavior for skewed abutments with high width-height ratios.* (Master's thesis, Brigham Young University).

Plaxis, B. V. (2002). User's manual of PLAXIS.

Rankine, W. M. (1857). On the stability of loose earth. *Philosophical transactions of the Royal Society of London*, *147*, 9-27.

Rollins, K. M., & Cole, R. T. (2006). Cyclic lateral load behavior of a pile cap and backfill. *Journal of Geotechnical and Geoenvironmental Engineering*, *132*(9), 1143-1153.

Rollins, K. M., Gerber, T. M., & Heiner, L. (2010). *Passive force-deflection behavior for abutments with mse confined approach fills* (No. UT-10.15).

Rollins, K. M., & Jessee, S. J. (2012). Passive force-deflection curves for skewed abutments. *Journal of Bridge Engineering*, *18*(10), 1086-1094.

Rollins, K. M., Palmer, K., & Fredrickson, A. (2015). Performance of skewed abutments from large-scale testing. *IFCEE 2015* (pp. 1267-1277).

Rollins, K. M., & Sparks, A. (2002). Lateral resistance of full-scale pile cap with gravel backfill. *Journal of Geotechnical and Geoenvironmental Engineering*, *128*(9), 711-723.

Romstad, K., Kutter, B., Maroney, B., Vanderbilt, E., Griggs, M., & Chai, Y. H. (1995). Experimental measurements of bridge abutment behavior. *Rep. No. UCD-STR-95*, *1*.

Romstad, K., Kutter, B., Maroney, B., Vanderbilt, E., Griggs, M., & Chai, Y. H. (1996). *Longitudinal strength and stiffness behavior of bridge abutments* (No. UCD-STR-96-1).

Sadrossadat-Zadeh, M., & Saiidi, M. (2007). Analytical study of NEESR-SG 4-span bridge model using OpenSees. *Center for Civil Engineering Earthquake Research, Dept. of Civil Engineering, University of Nevada, Reno, Nevada, Report No. CCEER-07-03, January*.

Saiidi, M. S., Vosooghi, A., & Nelson, R. B. (2012). Shake-table studies of a four-span reinforced concrete bridge. *Journal of Structural Engineering*, *139*(8), 1352-1361.

Sandford, T. C., & Elgaaly, M. (1993). Skew effects on backfill pressures at frame bridge abutments. *Transportation research record*, (1415).

Shamsabadi, A. (2007). *Three-dimensional nonlinear seismic soil-abutment-foundation-structure interaction analysis of skewed bridges*. (Doctoral dissertation, University of Southern California).

Shamsabadi A. (2017). S-LSH. *Computer program*.

Shamsabadi, A., & Kapuskar, M. (2010). Nonlinear soil-abutment-foundation-structure interaction analysis of skewed bridges subjected to near-field ground motions. *Transportation Research Record: Journal of the Transportation Research Board*, (2202), 192-205.

Shamsabadi, A., Kapuskar, M., & Martin, G. R. (2006). Three-dimensional nonlinear finite-element soil-abutment structure interaction model for skewed bridges. *Fifth National Seismic Conference on Bridges & Highways* (No. B15).

Shamsabadi, A., Khalili-Tehrani, P., Stewart, J. P., & Taciroglu, E. (2009). Validated simulation models for lateral response of bridge abutments with typical backfills. *Journal of Bridge Engineering*, *15*(3), 302-311.

Shamsabadi, A., Rollins, K. M. (2014). Three-dimensional nonlinear continuum seismic soil-structure interaction analysis of skewed bridge abutments. *8th European Conference on Numerical Methods in Geotechnical Engineering.*

Shamsabadi, A., Rollins, K. M., & Kapuskar, M. (2007). Nonlinear soil–abutment–bridge structure interaction for seismic performance-based design. *Journal of Geotechnical and Geoenvironmental Engineering*, *133*(6), 707-720.

Shamsabadi, A., & Yan, L. (2008). Dynamic-soil abutment-foundation-structure interaction of an instrumented skewed bridge. *12th International Conference of International Association for Computer Methods and Advances in Geomechanics.*

Smith, J. C. (2014). *Evaluation of passive force behavior for bridge abutments using large-scale tests with various backfill geometries*. (Master's thesis, Brigham Young University).

Smith, K. M. (2014). *Passive force on skewed bridge abutments with reinforced concrete wingwalls based on large-scale tests*. (Master's thesis, Brigham Young University).

Stewart, J. P., Taciroglu, E., Wallace, J. W., Ahlberg, E. R., Lemnitzer, A., Rha, C., ... & Salamanca, A. (2007). Full scale cyclic testing of foundation support systems for highway bridges. Part II: Abutment backwalls. *UCLA Structural and Geotechnical Engineering Laboratory*, (UCLA-SGEL 2007/02).

Terzaghi, K. (1943). *Theoretical soil mechanics* (Vol. 18). New York: Wiley.

Trenching and shoring manual (2011). Revision No. 01. California Dept. of Transportation. Sacramento. California.

Wagstaff, K. B. (2016). *Evaluation of passive force on skewed bridge abutments with controlled low-strength material backfill*. (Master's thesis, Brigham Young University).

Wilson, P. R. (2009). *Large scale passive force-displacement and dynamic earth pressure experiments and simulations*. (Doctoral dissertation, University of California, San Diego)

Wilson, P., & Elgamal, A. (2008, October). Full scale bridge abutment passive earth pressure tests and calibrated models. *Proceedings of the 14th world conference on earthquake engineering, Beijing, China*.

Wilson, P., & Elgamal, A. (2010). Large-scale passive earth pressure load-displacement tests and numerical simulation. *Journal of Geotechnical and Geoenvironmental Engineering*, 136(12), 1634-1643.

Xie, Q., Da Gamma, C. D., Yu, Xianbin, Chen, Yuxin. (2013). A parametric study of interface characteristics in a buttress retaining wall. *Electronic Journal of Geotechnical Engineering*, *18*, 1477-1492.

Yen, W. H. P., Chen, G., Buckle, I., Allen, T., Alzamora, D., Ger, J., & Arias, J. G. (2011). Post-earthquake reconnaissance report on transportation infrastructure: impact of the February 27, 2010, Offshore Maule earthquake in Chile (No. FHWA-HRT-11-030).

TABLES

Table 2-1 Passive earth pressure coefficients for zero slope backfill (Trenching and Shoring Manual, 2011).

ϕ	δ/ϕ	K_{ph}						
		Straight Line		Log Spiral				
		Rankine	Coulomb/ Trial Wedge	Forces			Moment	
				Trial	Curve	Composite	Curve	Composite
30°	0	3.00	3.00	3.00	3.00	3.00	3.00	3.00
	1/3	3.00	4.14	4.13	4.14	4.11	3.98	3.96
	2/3	3.00	6.11	5.01	5.01	4.85	5.05	4.94
	1	3.00	10.10	5.68	6.56	5.45	6.03	5.78
35°	0	3.69	3.69	3.69	3.69	3.69	3.69	3.69
	1/3	3.69	5.68	5.57	5.58	5.53	5.36	5.31
	2/3	3.69	9.96	7.13	7.14	6.84	7.35	7.15
	1	3.69	22.97	8.39	9.79	8.02	9.26	8.82
40°	0	4.60	4.60	4.60	4.60	4.60	4.60	4.60
	1/3	4.60	8.15	7.75	7.76	7.66	7.46	7.37
	2/3	4.60	18.72	10.60	10.62	10.07	11.33	10.94
	1	4.60	92.59	13.09	15.40	12.47	15.33	14.45

Table 2-2 Conditions under which seismic analysis are not required for a free standing earth retaining wall (Anderson et al. (2008)).

Slope Angle Above Wall	$F_{PGA}PGA$
Flat	0.3 g
3H:1V	0.2 g
2H:1V	0.1 g

Table 2-3 Bridge-abutment program test matrix, Phase I (Bozorgzadeh et al., 2008).

Variables	Phase I				Phase II
	Test 1	Test 2	Test 3	Test 4	System Test
Soil Type	clayey sand	silty sand	silty sand	silty sand	silty sand
Structure Backfill Height	5.5 ft	5.5 ft	7.5 ft	5.5 ft	5.0 ft
Structure Backfill Area	small	small	Large	large	large
Vertical Movement of Wall	restrained	allowed	allowed	allowed	allowed

Table 2-4 Comparison of measured and computed peak passive force (Rollins et al., 2008).

Peak horizontal passive force (kips)					
		Computed			
Backfill Type	Measured	Rankine	Coulomb	Log spiral	Caltrans
MSE wall confined fill	305	81	375	213	298
Fill without MSE walls	398	144	668	380	298

Table 2-5 Geometric and ground motion characteristics used in the sensitivity study (Kavianijapori, 2011).

Sensitivity Parameters		Variation Range
Geometric characteristics	Abutment skew angle (deg.)	0, 15, 30, 45, 60
	Span arrangement	Symmetrical (span ratio = 1.0)
		Asymmetrical (span ratio = 1.2)
	Column height	Col_{orig} = Original column size
		$Col_{ext} = 1.5\ Col_{orig}$
Ground motion characteristics	Ground motion type	Soil-site
		Rock-site
		Pulse-like
	Angle of incidence (deg.)	0, 30, 60, 90, 120, 150

Table 2-6 Summary of abutments features of experimental studies.

Reference		Concrete Wall (Abutment or Pile cap)						Wingwall			
		Type	Dimensions				Skew angle	Config.	Dimensions		
			Height		Width	Thickness			Height	Length	Thickness
			Total	Soil-Supported (H)							
			(ft)			in	(deg.)		ft		in
UCD (Caltrans)	Maroney et al. (1994)	Abutment	6.75	6.75	15.5	18	0	Integral	1.5-6.75	7.25	10
	Maroney et al. (1994) Romstad et al. (1995)	Abutment	5.5	5.5	10	18	0	Integral	1.5-5.5	7.25	9
VPI (VTRC & VDOT)	Duncan & Mokwa (2001)	Anchor block	3.5	3.5	6.3	36	0	None	-	-	-
BYU (UDOT & FWHA)	Rollins & Sparks (2002)	Pile cap	4	4.0	9	108	0	None	-	-	-
	Rollins & Cole (2006)	Pile cap	3.7	3.7	17	120	0	None	-	-	-
									-	-	-
									-	-	-
									-	-	-
UCLA (CA DOT)	Stewart et al. (2007) Lemnitzer et al. (2009)	Abutment	8.5	5.5	15	36	0	Separated	7.5	22	Not reported
UCSD (CA DOT)	Bozorgzadeh (2007)	Abutment	7.5	5.5	15.5	18	0	Integral	4-7.5	7	10
				5.5			0				
				7.5			0				
				5.5			0				
	Bozorgzadeh et al. (2008)		5.0	5	20	36	0	Separated	4-9	11.5	12

Table 2-7 Summary of abutments features of experimental studies (continued).

Reference		Concrete Wall (Abutment or Pile cap)						Wingwall			
		Type	Dimensions				Skew angle	Config.	Dimensions		
			Height		Width	Thickness			Height	Length	Thickness
			Total	Soil-Supported (H)							
			(ft)			in	(deg.)		ft		in
BYU (DOTs of CA, MT, NY, OR, UT & FWHA)	Rollins et al. (2008) Rollins et al. (2010)	Pile cap	5.58	5.5	11	180	0	None	-	-	-
							0	MSE walls	5.5	24	6
UCSD (NSF)	Wilson & Elgamal (2008) Wilson (2009) Wilson & Elgamal (2010)	Abutment	7.0	5.5	9	8	0	Separated	7.0	18.4	Not reported
BYU (DOTs of CA, MT, NY, OR, UT & FWHA)	Jessee (2012) Rollins & Jessee (2013)	Abutment	2.0	2.0	4.125	variable	0	Separated	3.0	10-13	Not reported
							15				
							30				
							45				
	Marsh (2013) Marsh et al. (2013)	Pile cap	5.5	5.5	11	variable	0	None	-	-	-
							15				
							30				
	Frank (2013)	Pile cap	5.5	5.5	11	variable	0	MSE walls	5.5	24	6
							15, 30				
	Smith (2014)	Pile cap		5.5	11	variable	0, 45	RC walls			
	Wagstaff (2016)	Abutment	2.0	2.0	4.125	variable	0	Separated			
							30				

Table 2-8 Summary of backfill soil and foundation features of experimental studies.

Reference		Backfill Soil and Foundation							
		Backfill Soil Type	Backfill Configuration (Excavation)	Backfill Dimensions					Abutment Foundation
				Height		Width	Length		
				Total	Wall-contacted (H)		Abs.	Rel.	
				ft					
UCD (Caltrans)	Maroney et al. (1994)	Sand	3.75 ft below the wall	10.5	6.75	19-36	Not reported		9" dia. conc. piles
	Maroney et al. (1994) Romstad et al. (1995)	Clayey silt (Yolo Loam)	5.0 ft below the wall	10.5	5.5	14-36	Not reported		9" dia. conc. piles
VPI (VTRC & VDOT)	Duncan & Mokwa (2001)	Sandy silt & Sandy clay (natural soil)	up to the base of block	-	3.5	- (No excavation)			None
		Gravel		3.5		9.3	7.5	2H	
BYU (UDOT & FWHA)	Rollins & Sparks (2002)	Sandy Gravel	up to the base of pile cap	4	4	9	Not reported		12.75" dia. steel piles
	Rollins & Cole (2006)	Sand	1.0 ft below the pile cap	4.7	3.7	27	Not reported		12.75" dia. steel piles
		Silty sand							
		Fine gravel							
		Coarse gravel							
UCLA (CA DOT)	Stewart et al. (2007) Lemnitzer et al. (2009)	Silty sand	2.0 ft below the wall	7.5	5.5	16	22	4H	None
UCSD (CA DOT)	Bozorgzadeh (2007)	Clayey sand	up to the base of wall	5.5	5.5	13.8	10	1.8H	None
		Silty sand		5.5	5.5	13.8	13	2.4H	
				7.5	7.5	13.8-21.5	29.5	3.9H	
				5.5	5.5	13.8-21.5	27.5	5H	
	Bozorgzadeh et al. (2008)	Silty sand	4.0 ft below the wall	9	5	18-24	16	3.2H	

Table 2-9 Summary of backfill soil and foundation features of experimental studies (continued).

Reference		Backfill Soil and Foundation							
		Backfill Soil Type	Backfill Configuration (Excavation)	Backfill Dimensions					Abutment Foundation
				Height		Width	Length		
				Total	Wall-contacted (H)		Abs.	Rel.	
				ft					
BYU (DOTs of CA, MT, NY, OR, UT & FWHA)	Heiner et al. (2008) Rollins et al. (2010)	Sand	1.5 ft below the wall	7.0	5.5	21 11	27.3	5H	12.75" dia. steel piles
UCSD (NSF)	Wilson & Elgamal (2008) Wilson (2009)	Silty sand	1.5 ft below the wall	7.0	5.5	9.4	18.4	3.3H	None
	Wilson & Elgamal (2010)	Silty sand (dry condition)							
BYU (DOTs of CA, MT, NY, OR, UT & FWHA)	Jessee (2012) Rollins & Jessee (2013)	Sand	1.0 ft below the wall	3.0	2.0	4.215	10-13	5-6.5 H	None
	Marsh (2013) Marsh et al. (2013)	Sand	1.0 ft below the wall	5.5	5.5	21	30.35 28.76 27.175	5.5H 5.2H 4.9H	12.75" dia. steel piles
	Frank (2013)	Sand	1.0 ft below the wall	5.5	5.5	11.5	27.175 -30.35	4.9H-5.5H	12.75" dia. steel piles
	Smith (2014)	Sand	1.0 ft below the wall	5.5	5.5				12.75" dia. steel piles
	Wagstaff (2016)	CLSM	1.0 ft below the wall	3.0	2.0	4.25	8	4H	None

Table 2-10 Summary of measurements of experimental studies.

<table>
<tr><th rowspan="4">Reference</th><th rowspan="4"></th><th rowspan="4">Backfill Soil Type</th><th colspan="3">Test Measurements</th></tr>
<tr><th colspan="2">Failure Surface Location</th><th rowspan="3">Displacement at Peak Resistance</th></tr>
<tr><th>Absolute</th><th rowspan="2">Relative</th></tr>
<tr><th>ft</th></tr>
<tr><td rowspan="3">UCD (Caltrans)</td><td>Maroney et al. (1994)</td><td>Sand</td><td>Not reported</td><td>Not reported</td><td>Not reported</td></tr>
<tr><td>Maroney et al. (1994)</td><td rowspan="2">Clayey silt (Yolo Loam)</td><td rowspan="2">11.25</td><td rowspan="2">2H</td><td rowspan="2">9.0% H</td></tr>
<tr><td>Romstad et al. (1995)</td></tr>
<tr><td rowspan="2">VPI (VTRC & VDOT)</td><td rowspan="2">Duncan & Mokwa (2001)</td><td>Sandy silt & Sandy clay (natural soil)</td><td>6</td><td>1.7H</td><td>3.8% H</td></tr>
<tr><td>Gravel</td><td>7</td><td>2H</td><td>3.6% H</td></tr>
<tr><td rowspan="5">BYU (UDOT & FWHA)</td><td>Rollins & Sparks (2002)</td><td>Sandy Gravel</td><td>Not reported</td><td>Not reported</td><td>6.0% H</td></tr>
<tr><td rowspan="4">Rollins & Cole (2006)</td><td>Sand</td><td>10.5</td><td>2.8H</td><td>3.4% H</td></tr>
<tr><td>Silty sand</td><td>9.2</td><td>2.5H</td><td>5.2% H</td></tr>
<tr><td>Fine gravel</td><td>8.7</td><td>2.4H</td><td>3.0% H</td></tr>
<tr><td>Coarse gravel</td><td>11.8</td><td>3.2H</td><td>3.5% H</td></tr>
<tr><td rowspan="2">UCLA (CA DOT)</td><td>Stewart et al. (2007)</td><td rowspan="2">Silty sand</td><td rowspan="2">17</td><td rowspan="2">3.1H</td><td rowspan="2">3.0% H</td></tr>
<tr><td>Lemnitzer et al. (2009)</td></tr>
<tr><td rowspan="5">UCSD (CA DOT)</td><td rowspan="3">Bozorgzadeh (2007)</td><td>Clayey sand</td><td>11</td><td>2H</td><td>5.5% H</td></tr>
<tr><td rowspan="3">Silty sand</td><td>13.5</td><td>2.5H</td><td>2.1% H</td></tr>
<tr><td>15</td><td>2H</td><td>1.9% H</td></tr>
<tr><td rowspan="2">Bozorgzadeh et al. (2008)</td><td>9</td><td>1.6H</td><td>1.4% H</td></tr>
<tr><td>Silty sand</td><td>9</td><td>1.8H</td><td>3.7% H</td></tr>
</table>

Table 2-11 Summary of measurements of experimental studies (continued).

Reference		Backfill Soil Type	Test Measurements		
			Failure Surface Location		Displacement at Peak Resistance
			Absolute	Relative	
			ft		
BYU (DOTs of CA, MT, NY, OR, UT & FWHA)	Heiner et al. (2008) Rollins et al. (2010)	Sand	21.6	3.9H	3.8% H
			19.6	3.6H	4.2% H
UCSD (NSF)	Wilson & Elgamal (2008) Wilson (2009) Wilson & Elgamal (2010)	Silty sand (with placement water content)	15.4-16.1	2.8-2.9 H	2.7% H
		Silty sand (dry condition)	13.1-13.6	2.4-2.5 H	3.0% H
BYU (DOTs of CA, MT, NY, OR, UT & FWHA)	Jessee (2012) Rollins & Jessee (2012)	Sand	5.9, 6.2	3.0H, 3.1H	2.5-3.5% H
			6.6, 8.6	3.3H, 4.3H	
			6.7, 8.2	3.4H, 4.1H	
			7.0, 8.0	3.5H, 4.0H	
BYU (DOTs of CA, MT, NY, OR, UT & FWHA)	Marsh (2013) Marsh et al. (2013)	Sand			
	Frank (2013)	Sand	Not reported		
	Smith (2014)	Sand	14.0	2.5H	6% H
	Wagstaff (2016)	CLSM	6.0	3H	2% H
					0.75 H

Table 2-12 Summary of analytical studies (non-skewed abutments).

<table>
<tr><th colspan="2" rowspan="2">Reference</th><th>Skew angle</th><th rowspan="2">Purpose of study</th><th rowspan="2">Model description</th><th rowspan="2">Program used</th><th colspan="2">Soil-abutment Interaction model</th></tr>
<tr><th>(deg)</th><th>Direction</th><th>Elements at each end</th></tr>
<tr><td>Zadeh & Saiidi</td><td>2007</td><td>-</td><td>Pre-test analytical studies</td><td>4-span bridge</td><td>OpenSees</td><td>Long.</td><td>nonlinear spring
(Shamsabadi et al., 2005)
and gap element</td></tr>
<tr><td>Shamsabadi et al.</td><td>2007</td><td>-</td><td>Overall response of
bridge to motions with
different dynamic characteristic
and high velocity pulses</td><td>2-span bridge
with a
single-column
bent</td><td>SAP 2000</td><td>Long.</td><td>nonlinear spring
(modified hyperbolic
stress-strain relationship)
in series with gap element</td></tr>
<tr><td>Elgamal et al.</td><td>2008</td><td>-</td><td>Overall response of
Humboldt Bay Bridge</td><td>9-span bridge</td><td>OpenSees</td><td colspan="2">linear ZeroLength elements
with Hexahedra Solid elements</td></tr>
<tr><td rowspan="2">Shamsabadi et al.</td><td rowspan="2">2010</td><td rowspan="2">-</td><td rowspan="2">Evaluation of
numerical model
using UCLA and UCD
test data</td><td>Abutment:
5.5 ft high and
10 ft wide</td><td rowspan="2">Plaxis</td><td colspan="2" rowspan="2">Zero-thickness elements
with hardening soil model</td></tr>
<tr><td>Abutment:
5.5 ft high and
15 ft wide</td></tr>
<tr><td rowspan="2">Ebrahimpour et al.</td><td rowspan="2">2011</td><td rowspan="2">-</td><td rowspan="2">Simulation of
bridge-abutment interaction</td><td rowspan="2">4-span bridge</td><td rowspan="2">OpenSees</td><td>Long.</td><td>1 ZerolengthContact 3D element</td></tr>
<tr><td>Long.</td><td>2 Contact elements
at each corner</td></tr>
<tr><td rowspan="2">Carvajal Uribe</td><td rowspan="2">2011</td><td rowspan="2">-</td><td rowspan="2">Developing dynamic system
considering
near-field and far-field
embankment response</td><td rowspan="2">Integral
abutment
bridge</td><td>Pro-Shake</td><td colspan="2">1DOF mass-spring-dashpot system</td></tr>
<tr><td>Abaqus</td><td colspan="2">3DOF mass-spring-dashpot system</td></tr>
<tr><td>Lu et al.</td><td>2012</td><td>-</td><td>Performance-based
earthquake
engineering design</td><td>2-span bridge</td><td>PBEEBridge</td><td>Long.</td><td>Hyperbolic force-displacement
model
(Shamsabadi et al., 2007)</td></tr>
</table>

Table 2-13 Summary of analytical studies (skewed abutments).

Reference		Skew angle (deg)	Purpose of study	Model description	Program used	Soil-abutment Interaction model: Dir.	Soil-abutment Interaction model: Elements at each end
Shamsabadi & Yan	2007	0, 45	Evaluating bridge response to asymmetric high velocity pulses	Single-span bridge	SAP 2000	Long.	2 rows of 4 distributed nonlinear springs
				2-span bridge with a single-column bent			
				3-span bridge with single-column bents		Trans.	nonlinear spring (shear key)
Shamsabadi & Kapuskar	2008	0, 30, 45, 60	Force-displacement capacity of abutment	Abutment: 5.5 ft high and 75 ft wide	Plaxis	Hardening soil	
Shamsabadi & Yan	2008	39	Evaluating seismic response of Painter Street Overpass	2-span bridge with a two-column bent	SAP 2000 & Plaxis	Long.	Distributed nonlinear springs in 3 levels
							Gap element
						Trans.	nonlinear soil spring
							nonlinear shear key
							Gap element
Kavianijopari	2011	33	Proposing probabilistic method for seismic response assessment	2-span bridge with a single-column bent (Jack Tone Road Overcrossing)	SAP 2000 & OpenSees	Long.	Zerolength elements (linearly increased stiffness toward the acute corner)
		0		2-span bridge with a 2-column bent (La Veta Avenue Overcrossing)		Trans.	Zerolength elements (shear key)
		36		3-span bridge with a 2-column bent (Jack Tone Road Overhead)		Ver.	Elastic springs (bearings and stemwall)

Table 3-1 Mohr-Coulomb soil parameters of UCLA test.

Unit weight	Failure ratio	Poisson's ratio	cohesion	friction angle
γ	R_f	ν	c	ϕ
(pcf)	-	-	(psi)	(deg.)
127	0.97	0.3	3.48	39

Table 3-2 Maximum passive capacity of UCLA test in PLAXIS2D compared to the earth pressure theories.

Domain and Soil Properties				Theory			Classical Solution			
ID	Soil properties	Vertical interface	Horizontal interface	Method	K_p -	P_p kips/ft (kN/m)	Method	P_p kips/ft (kN/m)	Method	P_p kips/ft (kN/m)
Sand-Int1	$c=0$, $\phi=39^\circ$, $E=E_{ave}$	$c_1=0$, $\phi_1=0$	$c_2=0$, $\phi_2=0$	Rankine Coulomb	4.395	8.36 (122)	PLAXIS2D	~ 20.56 (300)	FLAC3D	~ 10.96 (160)
				Log-Spiral	3.948	7.47 (109)				
Clay-Int1	$c=3.48$ psi, $\phi=39^\circ$, $E=E_{ave}$	$c_1=0$, $\phi_1=0$	$c_2=0$, $\phi_2=0$	Rankine	4.395	19.87 (290)		~ 44.54 (650)		~ 23.98 (350)
Sand-Int2	$c=0$, $\phi=39^\circ$, $E=E_{ave}$	$c_1=0$, $\phi_1=22^\circ$	$c_2=0$, $\phi_2=0$	Coulomb	12.365	21.79 (318)		~ 20.56 (300)		18.09 (264)
				Log-Spiral	8.89	15.69 (229)		~ 15.76 (230)		

Table 4-1 UNR biaxial shake table specifications.

Table size		14 feet x 14.6 feet
Allowable specimen payload		50 ton
Allowable pitch moment		1000 kip-feet
Allowable yaw moment		400 kip-feet
Allowable roll moment		400 kip-feet
Force capacity of actuators	X axis	165 kip
	Y axis	165 kip
Dynamic displacement	X axis	±12 in
	Y axis	±12 in
Static displacement	X axis	±14 in
	Y axis	±14 in
Peak velocity with bare table	X axis	±50 in/sec
	Y axis	±50 in/sec
Peak acceleration @ 50 ton payload	X axis	±1 g
	Y axis	±1 g
Operating frequencies		0-50 Hz

Table 4-2 Measured soil displacement at maximum capacity.

Reference		Soil Type	Displacement at maximum capacity	Abutment height	Displacement to height ratio
			$y_{\max}$	H	$y_{\max} / H$
			(in.)	(ft)	-
Maroney et al. (1994)	UCD	Clay	7.00	5.5	0.10
Rollins & Cole (2006)	BYU	Clean Sand	1.50	3.67	0.034
		Silty Sand	2.28		0.052
		Fine Gravel	1.34		0.030
		Coarse Gravel	1.54		0.035
Wilson & Elgamal (2010)	UCSD	Silty Sand	1.97	5.5	0.030
Rollins & Jesse (2012)	BYU	Silty Sand	0.6 - 0.9	2.0	0.025 - 0.037
Marsh et al. (2013)	BYU	Silty Sand	2.0 - 3.0	5.5	0.030 - 0.045

Table 4-3 Intensity parameters of original Sylmar motion.

Intensity Parameter	Value	Time
Maximum acceleration	0.923g	6.995 sec
Maximum velocity	34.854 in/sec	6.145 sec
Maximum displacement	8.739 in	6.405 sec

Table 4-4 Intensity parameters of filtered time-scaled Sylmar motion.

Intensity Parameter	Value	Time
Maximum acceleration	0.977g	5.261 sec
Maximum velocity	24.773 in/sec	4.590 sec
Maximum displacement	4.849 in	4.755 sec

Table 4-5 Loading protocol.

Test No.	Test type	Acc. factor	PGA
WN1	White Noise - Longitudinal	-	-
Run 1	25% of Sylmar motion - Longitudinal	0.25	0.244g
WN2	White Noise - Longitudinal	-	-
Run 2	50% of Sylmar motion - Longitudinal	0.50	0.488g
WN3	White Noise - Longitudinal	-	-
Run 3	75% of Sylmar motion - Longitudinal	0.75	0.733g
WN4	White Noise - Longitudinal	-	-
Run 4	125% of Sylmar motion - Longitudinal	1.25	1.221g
WN5	White Noise - Longitudinal	-	-
Run 5	150% of Sylmar motion - Longitudinal	1.50	1.466g
WN6	White Noise - Longitudinal	-	-
Run 6	200% of Sylmar motion - Longitudinal	2.00	1.955g

Table 5-1 Concrete compressive strength of test components.

Series No.	Concrete pouring date	Components	f'c (psi)	
			7-day	28-day
1	May 14, 2014	0° Backwall 0°	3,432	4,489
		30° Backwall		
		Main bridge block slab		
2	May 23, 2014	0° Backwall	4,156	5,380
		Main bridge block walls		
3	June 9, 2014	30° Skew wedge	3,354	4,059
4	June 19, 2014	45° Skew wedge	3,821	4,805

Table 5-2 Structural instrumentation labels.

Label range		Definition	Measurement
LLC1	-	**L**ink **L**oad **C**ell	Axial force on the backwall
BLC1	BLC6	**B**ridge block **L**oad **C**ell	Bridge block axial load, shear and moment loads
BLVDT1	BLVDT4	**B**ridge block **LVDT**	Vertical displacement of bridge block
BLSP1	BLSP2	**B**ridge block **L**ongitudinal **S**tring **P**otentiometer	Longitudinal displacement of bridge block
BTSP1	BTSP2	**B**ridge block **T**ransverse **S**tring **P**otentiometer	Transverse displacement of bridge block
BAC1	BAC5	**B**ridge block Accelerometer	Triaxial acceleration of bridge block
WLSP1	WLSP4	Abutment **W**all **L**ongitudinal **S**tring **P**otentiometer	Longitudinal displacement of abutment backwall
WTSP1	WTSP2	Abutment **W**all **T**ransverse **S**tring **P**otentiometer	Transverse displacement of abutment backwall
WDSP1	-	Abutment **W**all **D**iagonal **S**tring **P**otentiometer	Vertical displacement of abutment backwall
WAC1	WAC3	Abutment **W**all **Ac**celerometer	Triaxial acceleration of abutment backwall
IAC1	IAC4	**I**mpact **Ac**celerometer	Longitudinal impact acceleration between the bridge block and abutment backwall

Table 5-3 Soil instrumentation labels.

Label range		Definition	Measurement
PC1	PC6	**P**ressure **C**ell	Soil pressure on the abutment backwall
SAC1	SAC42	**S**oil **Ac**celerometer	Triaxial soil acceleration
FL3	FL37	**FL**exiForce	Force inside the soil
SSP22	SSP29	**S**oil **S**tring **P**otentiometer	Displacement inside the soil
FLPC1	-	**FL**exiForce on **P**ressure **C**ell	Force on the pressure cell
SLVDT1	SLVDT18	**S**oil **LVDT**	Vertical displacement of soil surface

Table 5-4 Important dates of construction and tests.

	0° skew	30° skew	45° skew
Soil backfilling	August 17-20, 2015	October 27-29, 2015	December 28-29, 2015
Shake table test	September 15-16*, 2015 September 25**, 2015	November 17, 2015	January 7, 2016
Soil removal	October 15-16, 2015	December 7-8, 2015	February 3-4, 2016
Soil box removal	-	-	February 12-16, 2016
Complete set up removal	-	-	February 24, 2016

* before installing the backwall restrainer cable.
** after installing the backwall restrainer cable.

Table 5-5 Gypsum compressive strength.

Series No.	Water to powder ratio	Wet density of the mix (pcf)	7-day f'_c (psi)
1	0.7	83.32	467
2	0.6	101.86	679
3	0.5	108.58	1,103

Table 6-1 Time lags between the regular and high speed DAQs in seconds.

	Skew angle (deg.)		
Run No.	0	30	45
Run 1	0.38083	0.54328	0.44563
Run 2	0.63641	0.06675	0.05353
Run 3	0.34146	0.25353	0.03803
Run 4	0.04269	0.47581	0.98253
Run 5	-	0.29466	0.00675
Run 6	7.45794	-	-
Run 7	2.31606	-	-

Table 6-2 Sylmar motion amplitude factors.

	Skew angle (deg.)		
Run No.	0	30	45
Run 1	25%	25%	25%
Run 2	50%	50%	50%
Run 3	75%	125%	125%
Run 4	50%	150%	150%
Run 5	-	200%	200%
Run 6	150%	-	-
Run 7	150%	-	-

Table 6-3 Longitudinal gap between the bridge block and the backwall in in.

		West side (acute corner of bridge)	East side (obtuse corner of bridge)	West side (acute corner of bridge)	East side (obtuse corner of bridge)	West side (acute corner of bridge)	East side (obtuse corner of bridge)	West side (acute corner of bridge)	East side (obtuse corner of bridge)
		Run2 – 50%		Run3 – 75%		Run6 – 150%		Run7 – 150%	
0° skew	The top	$1\frac{7}{8}$	$1\frac{5}{16}$	$\frac{3}{4}$	$\frac{1}{4}$	~2	~2	$3\frac{1}{8}$	$3\frac{3}{16}$
	The bottom	$1\frac{3}{4}$	$2\frac{1}{16}$	$\frac{5}{8}$	$\frac{3}{8}$	~2	~2	$3\frac{1}{4}$	$3\frac{1}{4}$
		Run2 – 50%		Run3 – 125%		Run4 – 150%		Run5 – 200%	
30° skew	The top	~2	~2	$2\frac{3}{8}$	$2\frac{3}{8}$	$2\frac{3}{4}$	3	$2\frac{3}{4}$	$3\frac{3}{8}$
	The bottom	~2	~2	$2\frac{3}{8}$	$2\frac{1}{4}$	$2\frac{1}{2}$	$3\frac{1}{4}$	$2\frac{3}{4}$	$3\frac{3}{4}$
		Run2 – 50%		Run3 – 125%		Run4 – 150%		Run5 – 200%	
45° skew	The top	$2\frac{1}{8}$	3	$1\frac{3}{4}$	$2\frac{1}{2}$	$1\frac{3}{8}$	$3\frac{1}{4}$	$1\frac{5}{16}$	$3\frac{5}{8}$
	The bottom	$2\frac{1}{8}$	$4\frac{1}{4}$	$2\frac{1}{8}$	$3\frac{7}{8}$	$2\frac{1}{4}$	5	$2\frac{1}{2}$	6

Table 8-1 Soil Mohr-Coulomb parameters.

Density		Young modulus	Poisson's ratio	cohesion	friction angle	dilation angle
γ	$(E_{50})_{ref}$	$(E_{50})_{ave}$		c	ϕ	ψ
(pcf)	(psi)	(psi)	-	(psi)	(deg.)	(deg.)
107	9,123	5,053	0.3	2.0	40	10

Table 8-2 Duncan model parameters (E_i and R_f).

σ_{3c}	σ_{df}	slope	intercept	R_f	E_i
(psi)	(psi)	-	(psi)	-	(psi)
10	48.91	0.01498	0.0000655	0.73	15,260
20	87.88	0.00856	0.0000643	0.75	15,549
25	109.89	0.00684	0.0000563	0.75	17,768
30	137.09	0.00503	0.0000605	0.69	16,525
				0.75	

Table 8-3 Duncan model parameters (E_{50}^{ref} and n).

σ_{3c}	σ_{max}	σ_{50}	ε_{50}	P_a	E_{50}	$\log\left(\frac{\sigma_{3c}}{P_a}\right)$	$\log E_{50}$	slope	intercept	n	E_{50}^{ref}
(psi)	(psi)	(psi)	(%)	(psi)	(psi)	-	(psi)	-	(psi)	-	(psi)
10	48.91	24.46	0.310	14.5	7,889	-0.161	3.897	0.326	3.960	0.33	9,123
20	87.88	43.94	0.405		10,843	0.140	4.035				
25	109.89	54.95	0.507		10,844	0.237	4.035				
30	137.09	68.55	0.617		11,118	0.316	4.046				

Table 8-4 Non-skewed 3D factors for abutment tests.

Abutment Test		Φ	δ	δ/Φ	Passive pressure coefficient				Active pressure coefficient	B	H	R_{3D}	Reported R_{3D}
					Log-spiral (Caquot & Kerisel, 1948)			Coulomb	Coulomb				
		(deg.)	(deg.)		K_p (initial)	Reduction factor	K_p	K_p	K_a	(ft)	(ft)		
Rollins et al. (2010)	BYU	27.7	20.8	0.75	-			2.737	0.365	17	3.67	1.118	1.179
					5.5	0.864	4.752	-				1.178	
	BYU	37	25.9	0.70	-			4.023	0.249	11	5.5	1.354	1.646
					13	0.815	10.595	-				1.696	
	BYU	42	33	0.79	-			5.045	0.198	17	3.67	1.191	1.44
					23	0.757	17.411	-				1.446	
	BYU	44.3	27	0.61	-			5.632	0.178	11	5.5	1.453	1.982
					29	0.616	17.864	-				1.997	
UNR		40	34	0.85	-			4.599	0.217	10	5.5	1.427	
					18	0.783	14.094	-				1.924	

Table 8-5 Skewed 3D factor formulation.

Skew angle	Backfill extension beyond backwall edges	Spread angle at the obtuse corner	Skew wedge length	Skewed 3D factor
$\theta < \theta_{cr}$ *	$e \le e_{bal}$**	$\tan\alpha_\theta = \dfrac{e}{L_\theta.\cos\theta} - \tan\theta$	$L_\theta = 2L - \dfrac{e}{\tan\alpha}$	$R_{3D}^{Skew} = \gamma R_{3D} + \left(1 + \dfrac{e}{W}\right)(1-\gamma) < R_{3D}$
	$e_{bal} < e < e_{\max}$ ***	$\tan\alpha_\theta = \tan\alpha$	$L_\theta = \dfrac{e}{\mu\tan\alpha}$	$R_{3D}^{Skew} = 1 + \dfrac{2e\cos\theta}{\mu W} < R_{3D}$
	$e \ge e_{\max}$	$\tan\alpha_\theta = \tan\alpha$	$L_\theta = L$	$R_{3D}^{Skew} = R_{3D}$
$\theta \ge \theta_{cr}$	-	$\tan\alpha_\theta = 0$	$L_\theta = \dfrac{e}{\sin\theta}$	$R_{3D}^{Skew} = 1 + \dfrac{e}{W}\dfrac{\tan\alpha}{\tan\theta}$

$$\mu = \cos\theta + \frac{\sin\theta}{\tan\alpha}$$

$$\gamma = \cos\theta - \frac{\sin\theta}{\tan\alpha}$$

$$*\,\theta_{cr} = \sin^{-1}\left(\frac{e.\tan\alpha}{W(R_{3D}-1)-e}\right)$$

$$**\,e_{bal} = \frac{\mu W(R_{3D}-1)}{1+\mu},\ ***\,e_{\max} = \frac{\mu W(R_{3D}-1)}{2\cos\theta}$$

Table 8-6 Skewed 3D factors for BYU test model (Marsh et al., 2013).

θ	W	tan α	R_{3D}	e/w	θ_{cr}	μ	e_{bal}	e_{max}	L	criteria	L_θ	tan α_θ	α_θ	γ	R_{3D}^{Skew}
(deg.)	(ft)	-	-	-	(deg.)	-	(ft)	(ft)	(ft)		(ft)	-		-	-
0	11	0.5625	1.82	0.5	61.51	1.000	4.510	4.510	8.02	e≥emax	8.02	0.563	29.36	1.00	1.820
5	11	0.5625	1.82	0.5	61.51	1.151	4.827	5.211	8.02	e≥emax	8.02	0.563	29.36	0.84	1.820
10	11	0.5625	1.82	0.5	61.51	1.294	5.087	5.924	8.02	ebal<e<emax	7.56	0.563	29.36	0.68	1.761
15	11	0.5625	1.82	0.5	61.51	1.426	5.302	6.658	8.02	ebal<e<emax	6.86	0.563	29.36	0.51	1.677
20	11	0.5625	1.82	0.5	61.51	1.548	5.480	7.428	8.02	ebal<e<emax	6.32	0.563	29.36	0.33	1.607
25	11	0.5625	1.82	0.5	61.51	1.658	5.626	8.249	8.02	e≤ebal	6.26	0.503	26.72	0.15	1.550
30	11	0.5625	1.82	0.5	61.51	1.755	5.746	9.139	8.02	e≤ebal	6.26	0.438	23.63	-0.02	1.493
35	11	0.5625	1.82	0.5	61.51	1.839	5.843	10.124	8.02	e≤ebal	6.26	0.373	20.44	-0.20	1.436
40	11	0.5625	1.82	0.5	61.51	1.909	5.919	11.238	8.02	e≤ebal	6.26	0.308	17.13	-0.38	1.379
45	11	0.5625	1.82	0.5	61.51	1.964	5.977	12.528	8.02	e≤ebal	6.26	0.243	13.66	-0.55	1.324
50	11	0.5625	1.82	0.5	61.51	2.005	6.018	14.065	8.02	e≤ebal	6.26	0.176	9.96	-0.72	1.270
55	11	0.5625	1.82	0.5	61.51	2.030	6.043	15.961	8.02	e≤ebal	6.26	0.104	5.95	-0.88	1.218
60	11	0.5625	1.82	0.5	61.51	2.040	6.053	18.397	8.02	e≤ebal	6.26	0.026	1.48	-1.04	1.167
65	11	0.5625	1.82	0.5	61.51	2.034	6.047	21.704	8.02	θ≥θcr	6.07	0.000	0.00	-1.19	1.131
70	11	0.5625	1.82	0.5	61.51	2.013	6.026	26.539	8.02	θ≥θcr	5.85	0.000	0.00	-1.33	1.102

Table 8-7 Skewed 3D factors for UNR test model (excluding effect of embankment slope).

θ	W	tan α	R_{3D}	e/w	θ_{cr}	μ	e_{bal}	e_{max}	L	criteria	L_θ	tan α_θ	α_θ	γ	R_{3D}^{Skew}
(deg.)	(ft)	-	-	-	(deg.)	-	(ft)	(ft)	(ft)		(ft)	-		-	-
0	10	0.5	1.924	0.45	28.34	1.000	4.620	4.62	9.24	e≤ebal	9.48	0.475	25.4	1.00	1.924
5	10	0.5	1.924	0.45	28.34	1.171	4.983	5.43	9.24	e≤ebal	9.48	0.389	21.3	0.82	1.840
10	10	0.5	1.924	0.45	28.34	1.332	5.278	6.25	9.24	e≤ebal	9.48	0.306	17.0	0.64	1.752
15	10	0.5	1.924	0.45	28.34	1.484	5.520	7.10	9.24	e≤ebal	9.48	0.223	12.6	0.45	1.662
20	10	0.5	1.924	0.45	28.34	1.624	5.718	7.98	9.24	e≤ebal	9.48	0.141	8.0	0.26	1.571
25	10	0.5	1.924	0.45	28.34	1.752	5.882	8.93	9.24	e≤ebal	9.48	0.057	3.3	0.06	1.479
30	10	0.5	1.924	0.45	28.34	1.866	6.016	9.95	9.24	θ≥θcr	9.00	0.000	0.0	-0.13	1.390
35	10	0.5	1.924	0.45	28.34	1.966	6.125	11.09	9.24	θ≥θcr	7.85	0.000	0.0	-0.33	1.321
40	10	0.5	1.924	0.45	28.34	2.052	6.212	12.37	9.24	θ≥θcr	7.00	0.000	0.0	-0.52	1.268
45	10	0.5	1.924	0.45	28.34	2.121	6.280	13.86	9.24	θ≥θcr	6.36	0.000	0.0	-0.71	1.225
50	10	0.5	1.924	0.45	28.34	2.175	6.330	15.63	9.24	θ≥θcr	5.87	0.000	0.0	-0.89	1.189
55	10	0.5	1.924	0.45	28.34	2.212	6.363	17.82	9.24	θ≥θcr	5.49	0.000	0.0	-1.06	1.158
60	10	0.5	1.924	0.45	28.34	2.232	6.381	20.62	9.24	θ≥θcr	5.20	0.000	0.0	-1.23	1.130

Table 8-8 Skewed 3D factors for UNR abutment (including effect of embankment slope).

θ	W	H	$\tan\beta$	R_{3D}^{Skew}	$\tan\alpha$	$\tan\alpha_\theta$	L_θ	R_{Embank}	$\left(R_{3D}^{Skew}\right)_{Embank}$
(deg.)	(ft)	(ft)	-	-	-	-	(ft)	-	-
0	10	5.5	0.667	1.924	0.5	0.475	9.48	0.87	1.665
5	10	5.5	0.667	1.840	0.5	0.389	9.48	0.88	1.622
10	10	5.5	0.667	1.752	0.5	0.306	9.48	0.89	1.568
15	10	5.5	0.667	1.662	0.5	0.223	9.48	0.91	1.505
20	10	5.5	0.667	1.571	0.5	0.141	9.48	0.91	1.433
25	10	5.5	0.667	1.479	0.5	0.057	9.48	0.92	1.354
30	10	5.5	0.667	1.390	0.5	0.000	9.00	0.92	1.283
35	10	5.5	0.667	1.321	0.5	0.000	7.85	0.94	1.245
40	10	5.5	0.667	1.268	0.5	0.000	7.00	0.96	1.211
45	10	5.5	0.667	1.225	0.5	0.000	6.36	0.96	1.182
50	10	5.5	0.667	1.189	0.5	0.000	5.87	0.97	1.155
55	10	5.5	0.667	1.158	0.5	0.000	5.49	0.98	1.131
60	10	5.5	0.667	1.130	0.5	0.000	5.20	0.98	1.109

Table 8-9 Input parameter of S-LSH program.

Geometry	Strength	Stiffness
Backwall height	Soil friction	ε_{50}
Backwall width	Wall friction	Poisson's ratio
3D factor	Soil Cohesion	Failure ratio
Beta (Slope angle relative to the top of the wall)	Abutment adhesion	-
Skew angle / Eccentricity	Soil density	-

FIGURES

Figure 1-1 Las Mercedes overpass (Yen et al., 2011).

Figure 1-2 Miraflores bridge (Yen et al., 2011).

Figure 1-3 Lo Echevers bridge (Yen et al., 2011).

Figure 1-4 Quilicura railway overcrossing (Yen et al., 2011).

Figure 1-5 No-damage straight bridge (Kawashima, 2010).

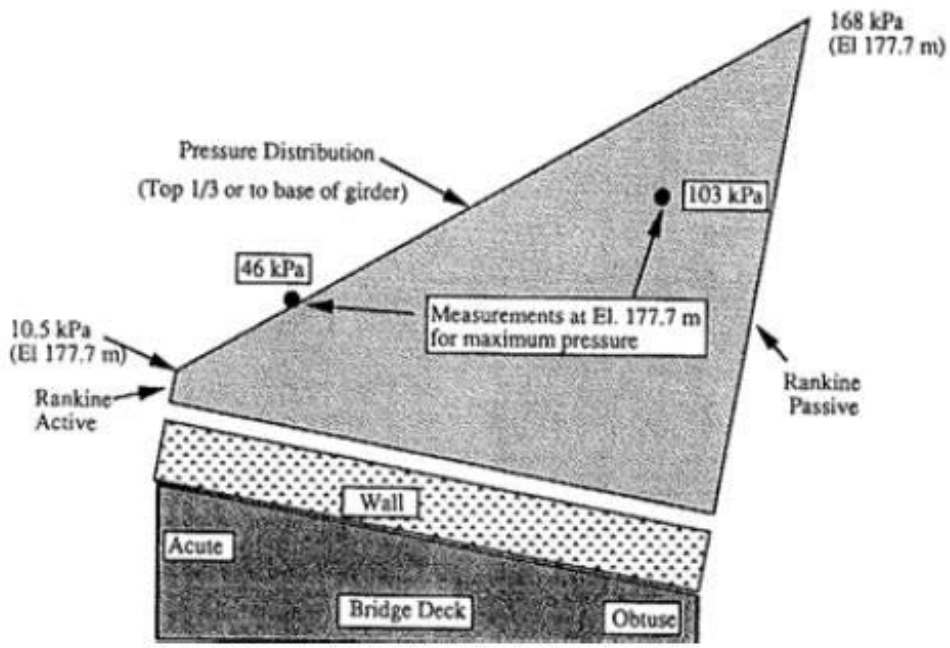

Figure 1-6 Soil pressure distribution due to temperature effect (Sanford and Elgaaly, 1993).

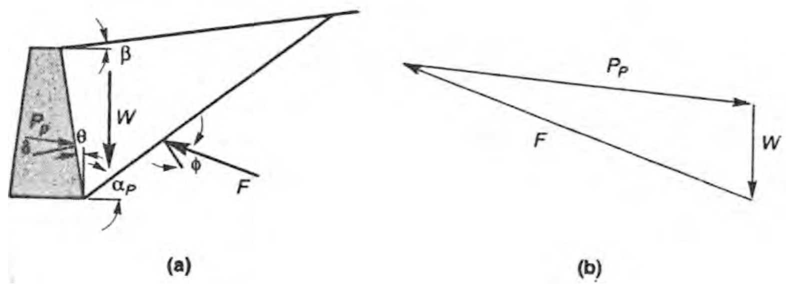

Figure 2-1 Coulomb theory of earth pressure; (a) Triangular passive wedge; (b) force polygon for passive wedge (Kramer, 1996).

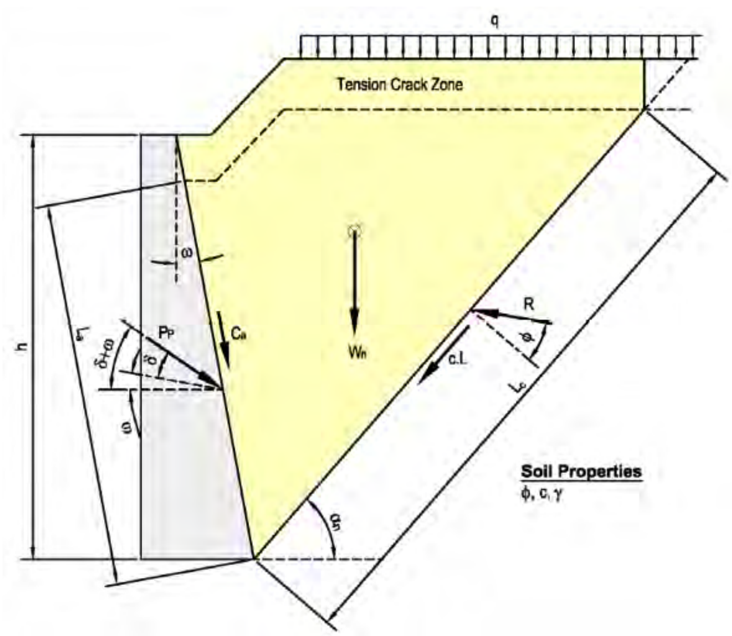

Figure 2-2 Passive trial wedge (Trenching and Shoring Manual, 2011).

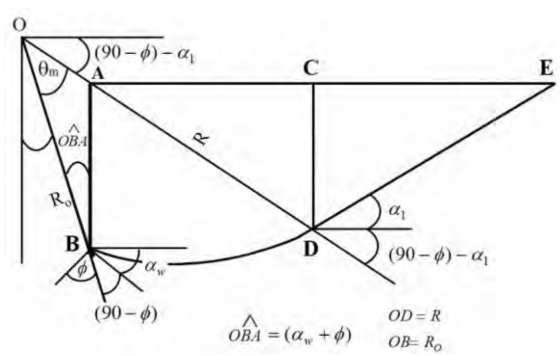

Figure 2-3 Geometry of log-spiral failure plane (Shamsabadi et al., 2005).

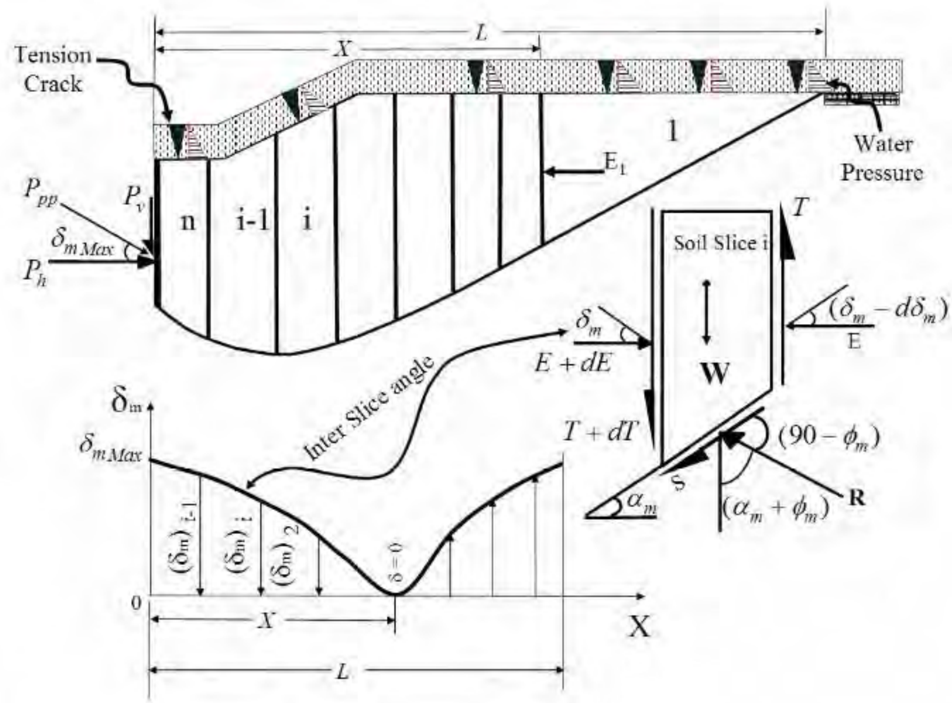

Figure 2-4 Geometry of failure surface and associated interslice forces (Trenching and Shoring Manual, 2011).

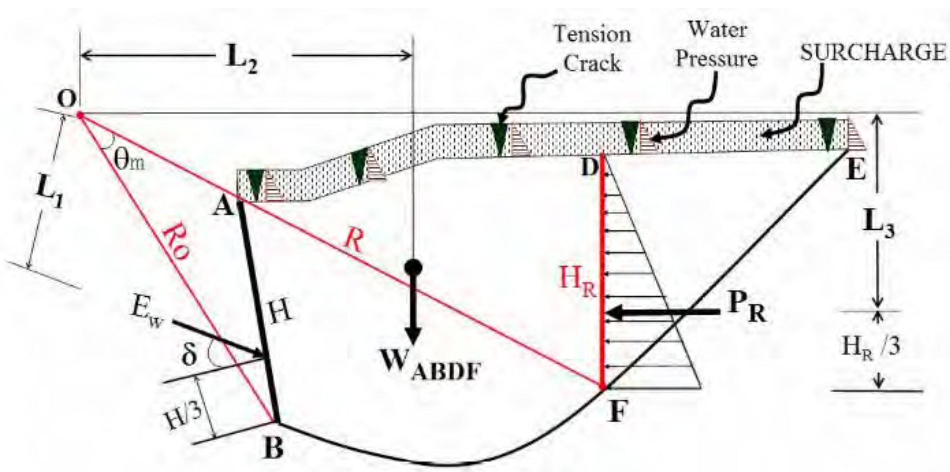

Figure 2-5 Geometry of failure surface due to weight (Trenching and Shoring Manual, 2011).

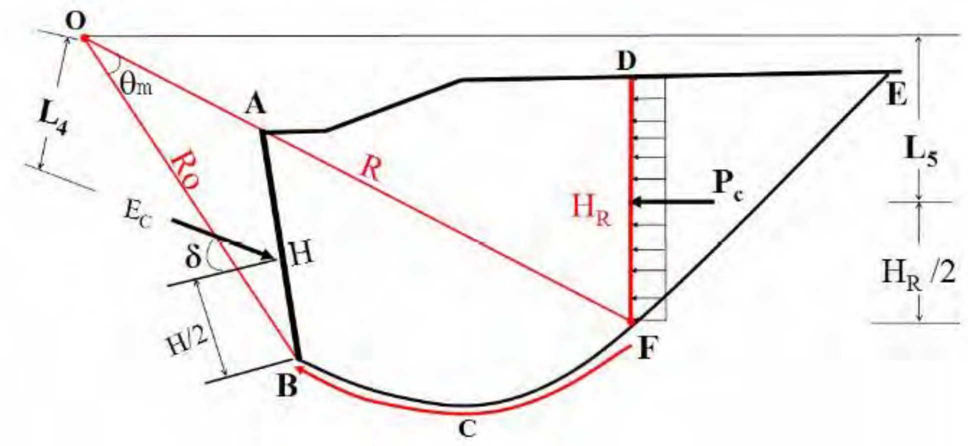

Figure 2-6 Geometry of failure surface due to cohesion (Trenching and Shoring Manual, 2011).

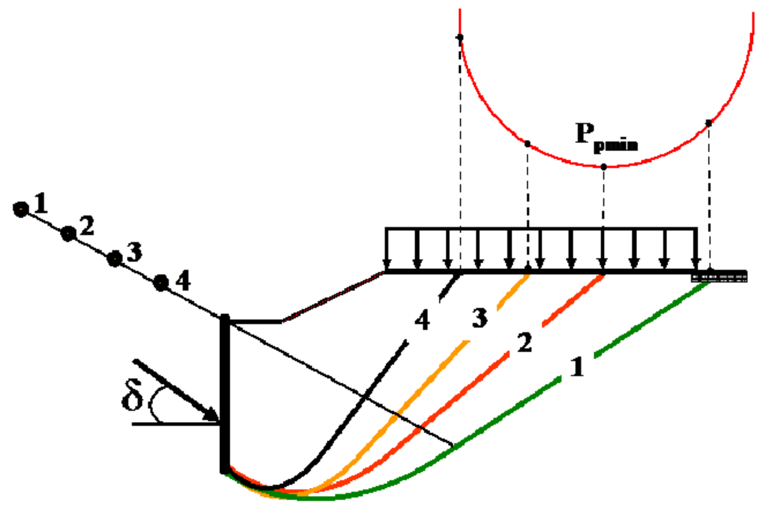

Figure 2-7 Moment method (Trenching and Shoring Manual, 2011).

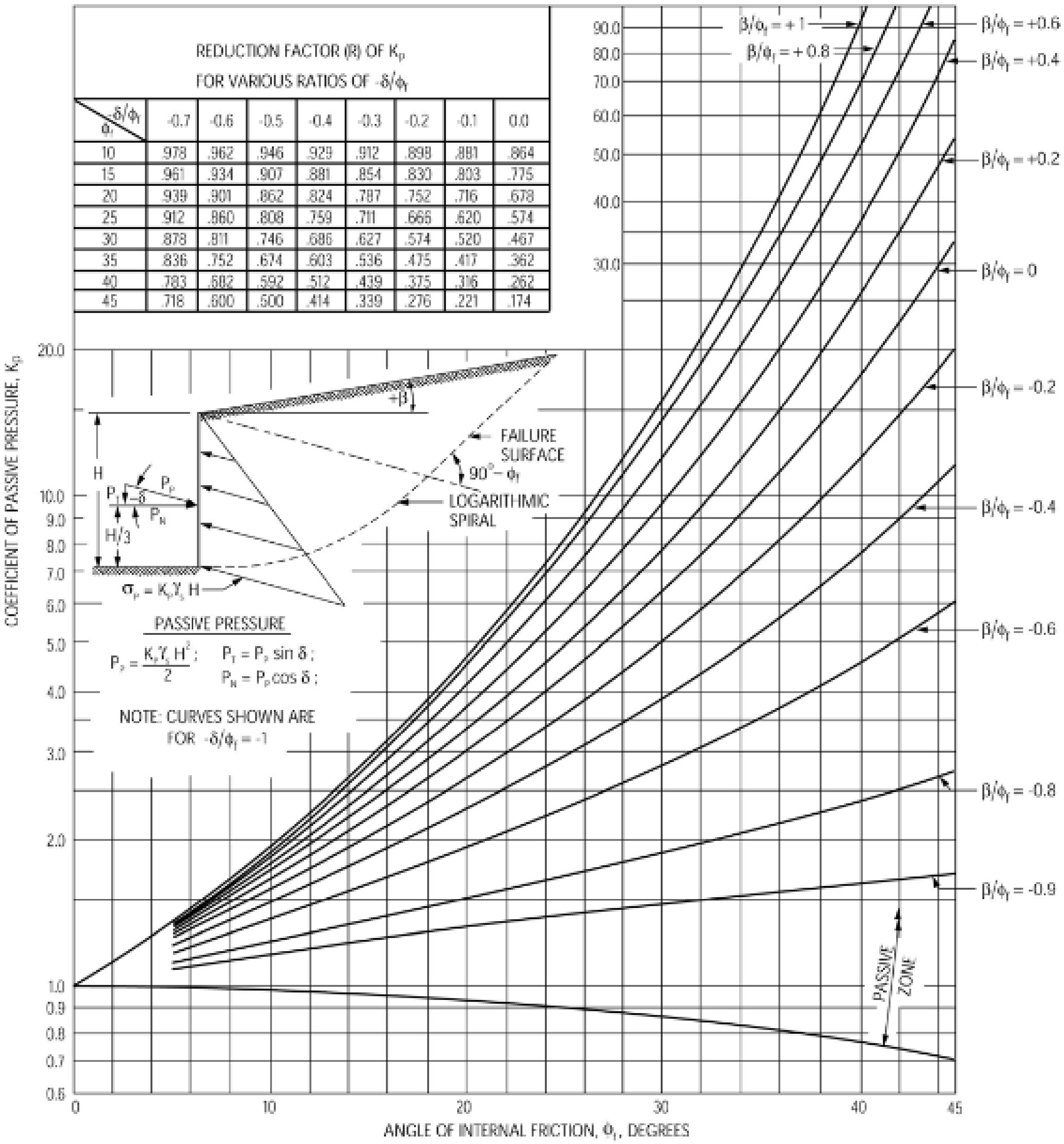

ϕ_f \ $-\delta/\phi_f$	-0.7	-0.6	-0.5	-0.4	-0.3	-0.2	-0.1	0.0
10	.978	.962	.946	.929	.912	.898	.881	.864
15	.961	.934	.907	.881	.854	.830	.803	.775
20	.939	.901	.862	.824	.787	.752	.716	.678
25	.912	.860	.808	.759	.711	.666	.620	.574
30	.878	.811	.746	.686	.627	.574	.520	.467
35	.836	.752	.674	.603	.536	.475	.417	.362
40	.783	.682	.592	.512	.439	.375	.316	.262
45	.718	.600	.500	.414	.339	.276	.221	.174

Figure 2-8 Passive earth pressure coefficient (Caquot & Kerisel, 1948).

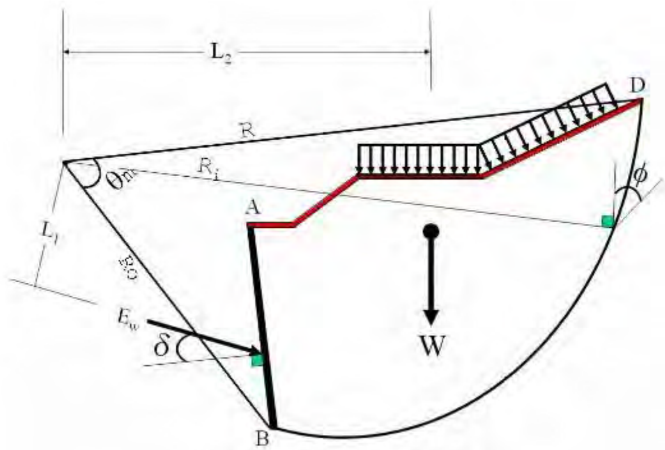

Figure 2-9 Mobilized full log-spiral failure surface (due to weight) (Trenching and Shoring Manual, 2011).

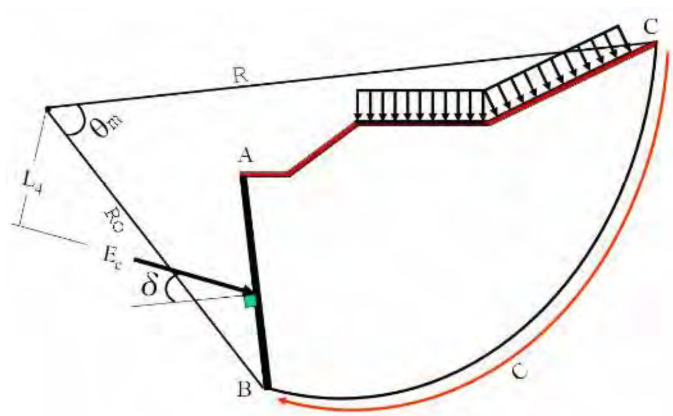

Figure 2-10 Mobilized full log-spiral failure surface (due to cohesion) (Trenching and Shoring Manual, 2011).

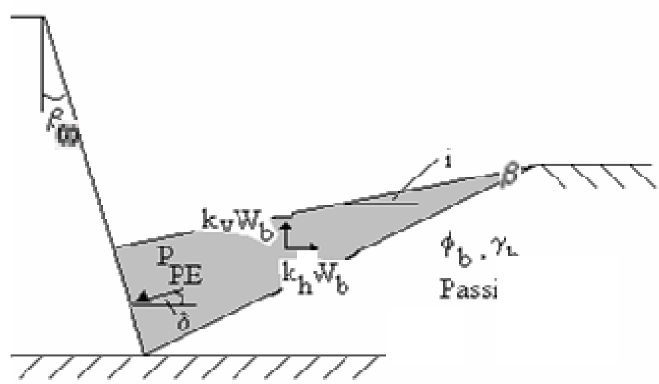

Figure 2-11 Mononobe-Okabe passive earth pressure theory (Kalasin & Wood, 2008).

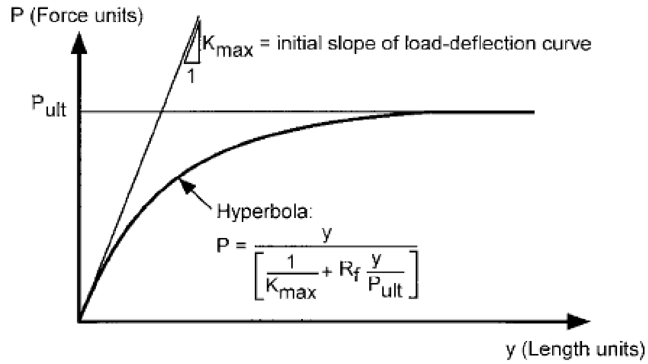

Figure 2-12 Hyperbolic force-displacement relationship (Duncan & Mokwa, 2001).

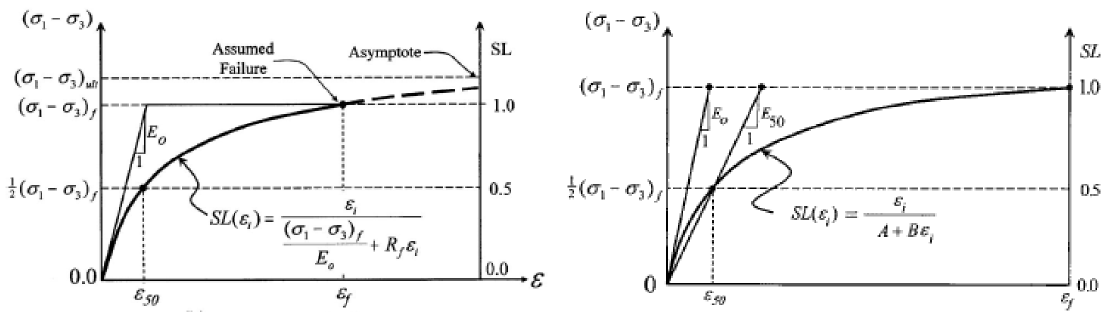

Figure 2-13 Hyperbolic model; left: original, right: modified (Shamsabadi et al. 2007).

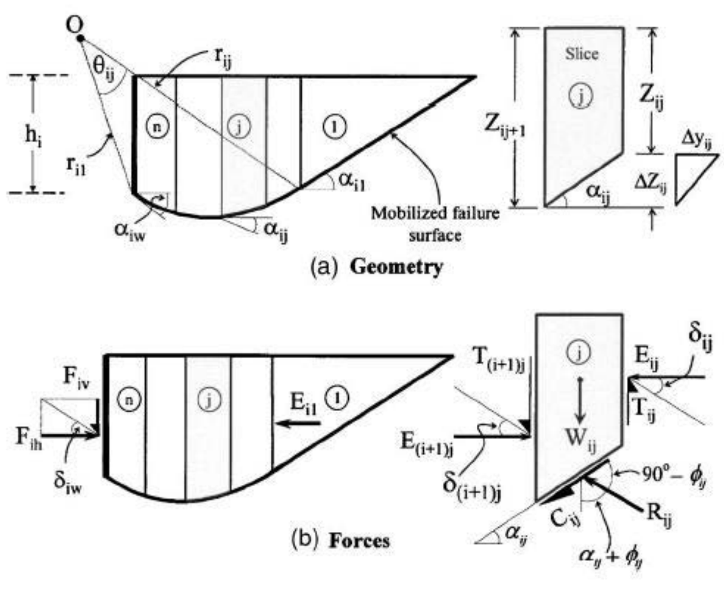

Figure 2-14 Mobilized logarithmic-spiral passive wedge (Shamsabadi et al., 2007).

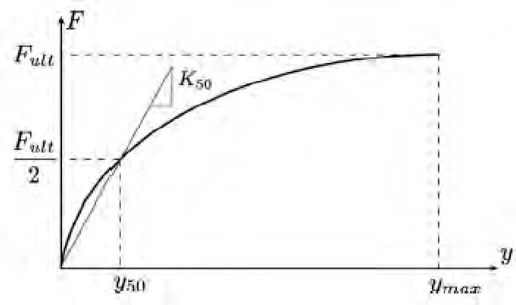

Figure 2-15 Hyperbolic force-displacement relationship (Shamsabadi et al., 2007).

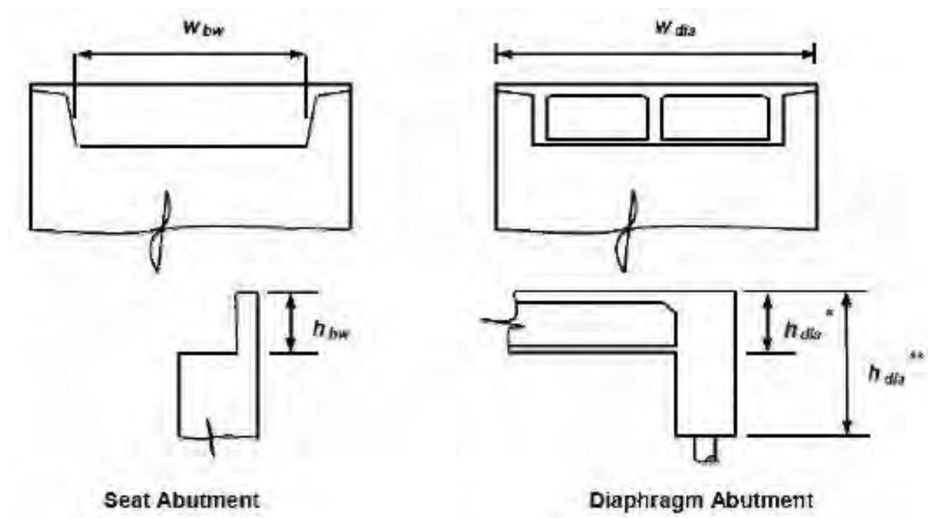

Figure 2-16 Effective abutment area (Caltrans SDC, 2010).

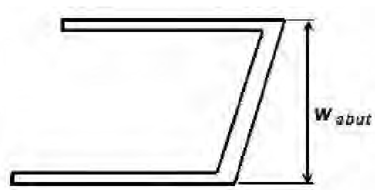

Figure 2-17 Effective abutment width for skewed abutments (Caltrans SDC, 2010).

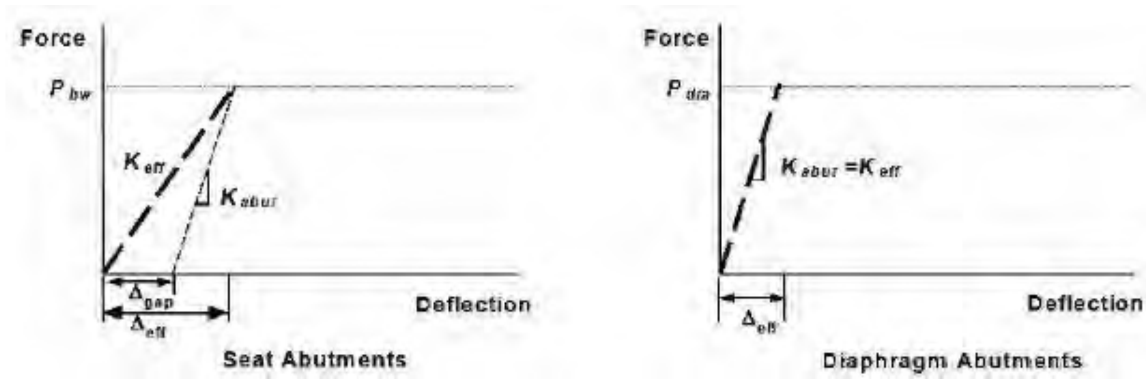

Figure 2-18 Effective abutment stiffness and force-displacement relationship (Caltrans SDC, 2010).

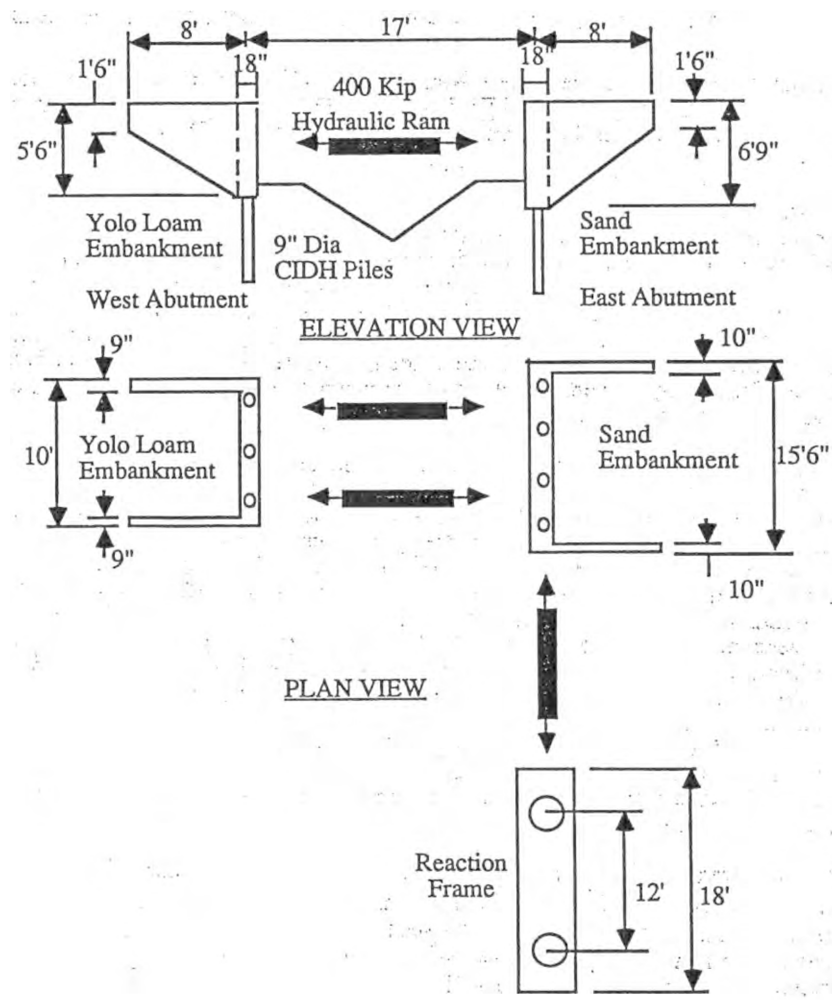

Figure 2-19 Plan and elevation view of the experimental test (Maroney et al., 1994).

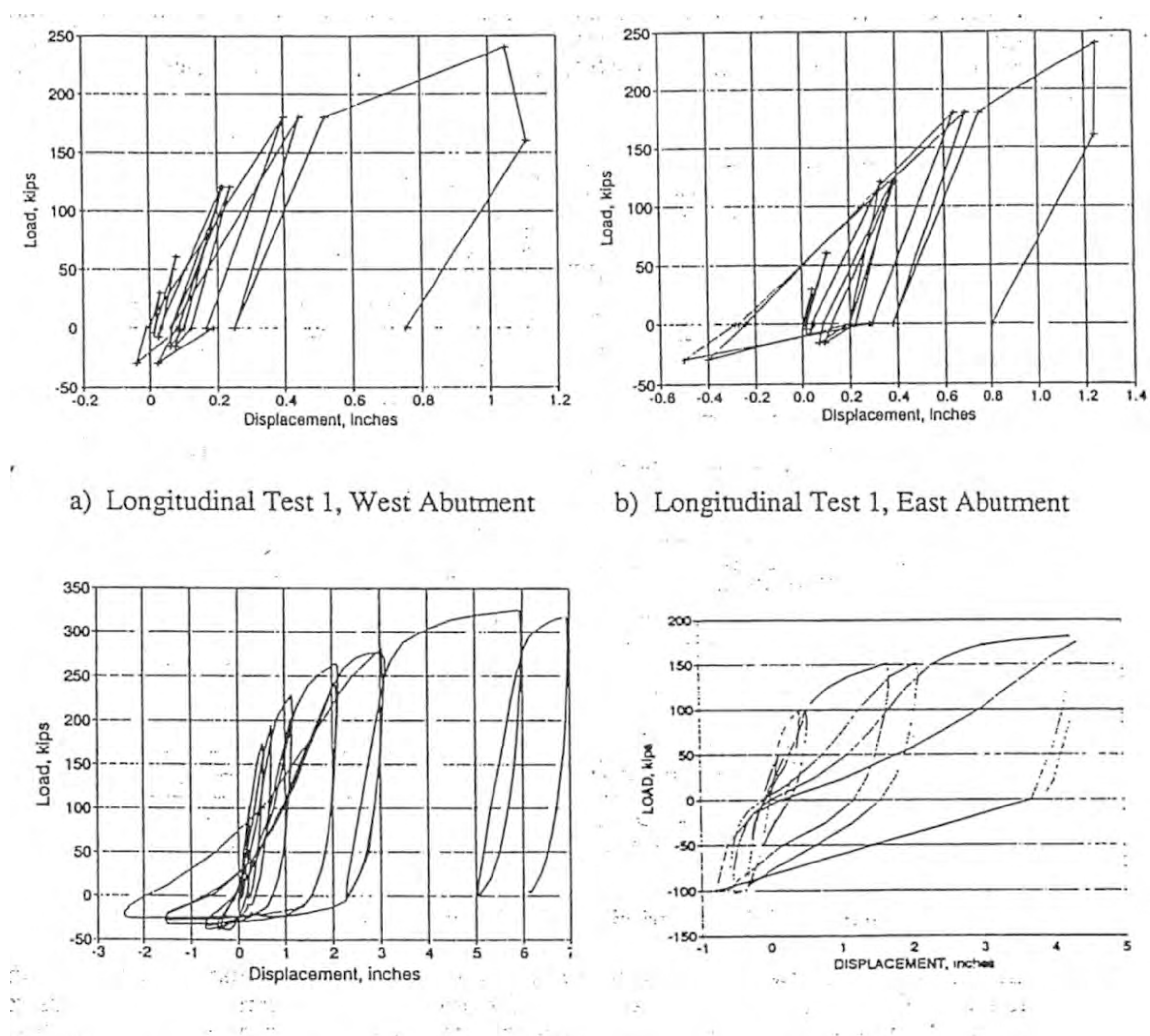

a) Longitudinal Test 1, West Abutment

b) Longitudinal Test 1, East Abutment

c) Longitudinal Test 2, West Abutment

d) Transverse Test

Figure 2-20 Load-displacement curves at superstructure level (Maroney et al., 1994).

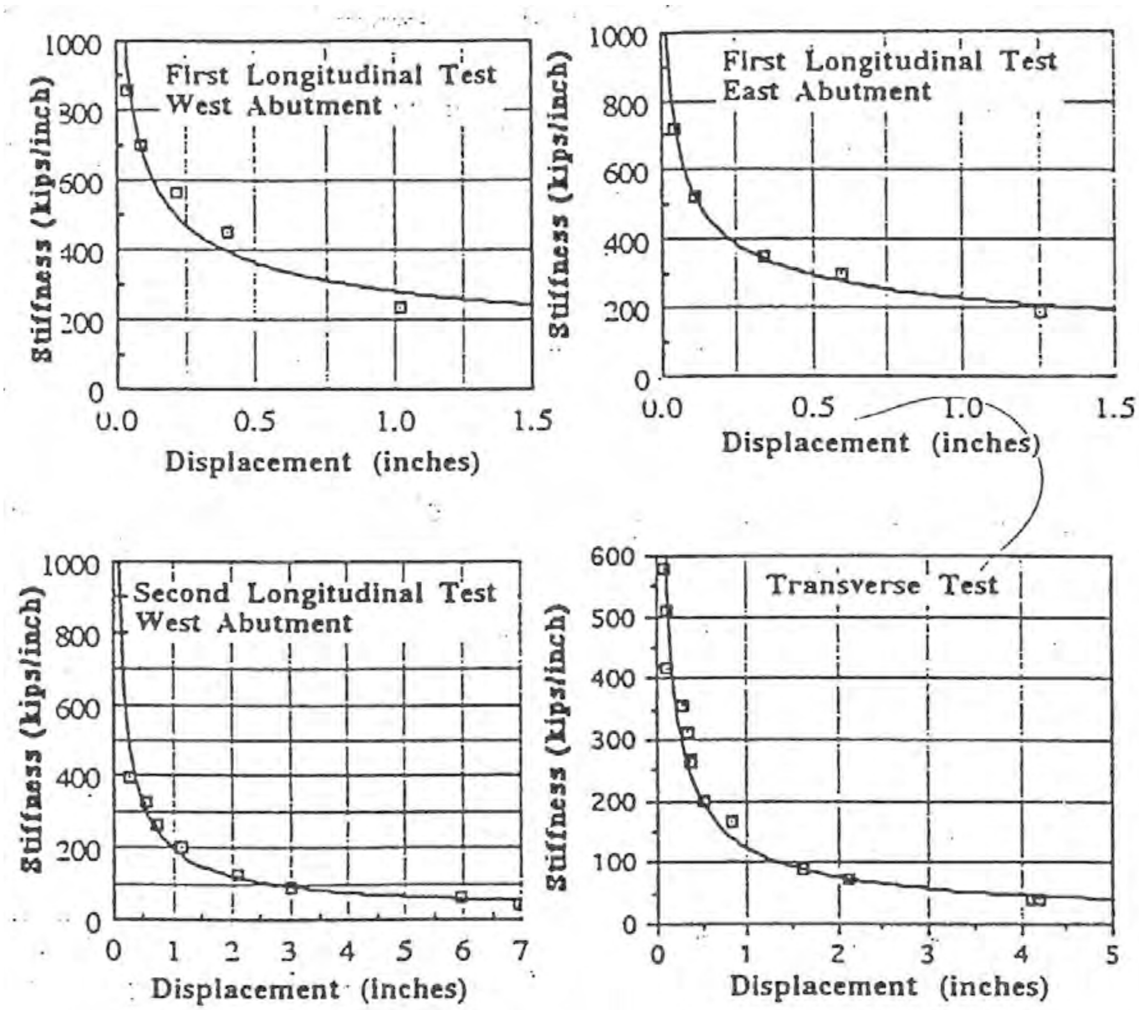

Figure 2-21 Secant stiffness variation with displacement level (Maroney et al., 1994).

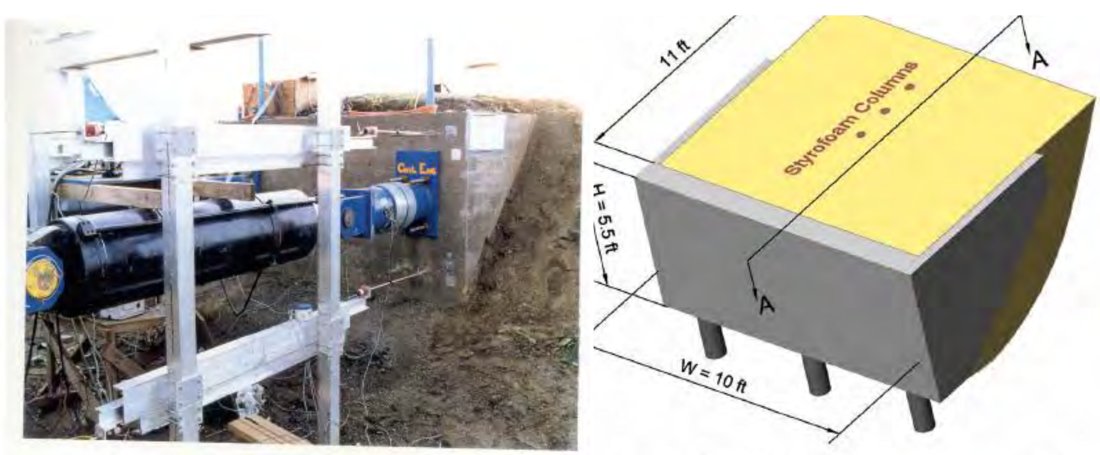

Figure 2-22 Test set up (Shamsabadi, 2007).

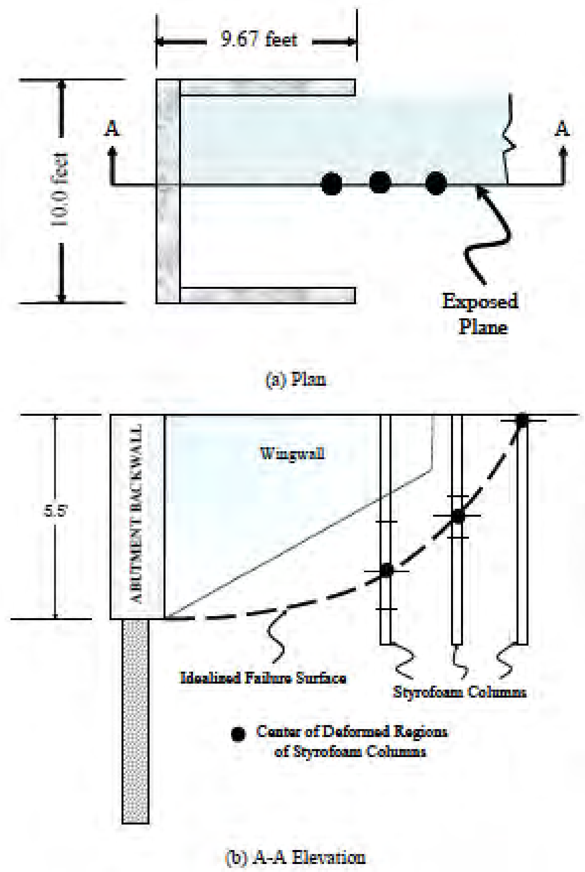

Figure 2-23 Failure surface; plan and elevation view (Shamsabadi, 2007).

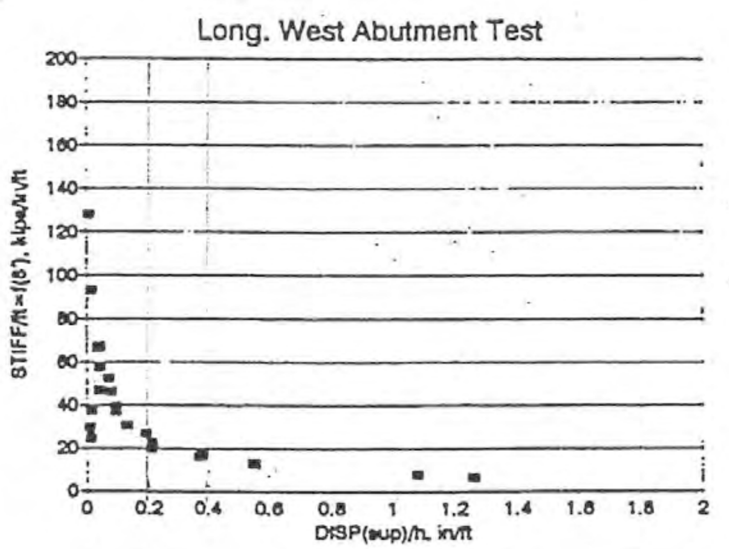

Figure 2-24 Stiffness adjusted to 8-ft wall height versus displacement (Maroney et al., 1994).

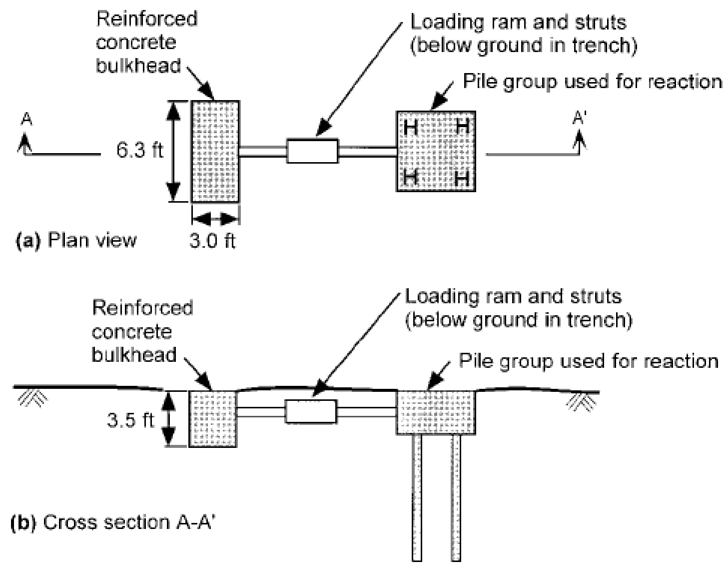

Figure 2-25 Plan and elevation view of test setup (Duncan & Mokwa, 2001).

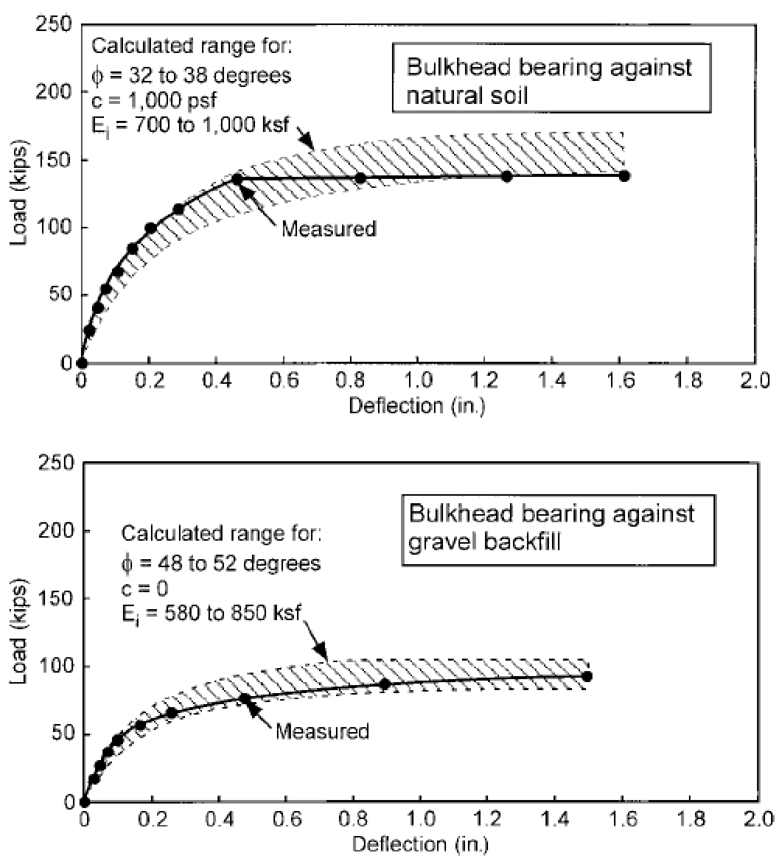

Figure 2-26 Computed and measured load-deflection curves (Duncan & Mokwa, 2001).

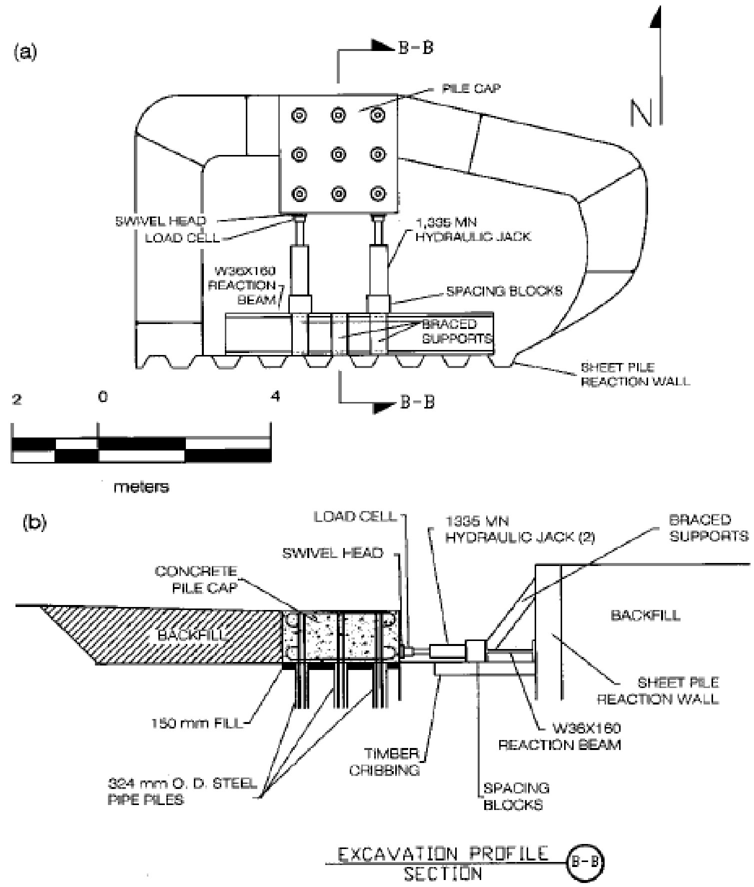

Figure 2-27 Plan and elevation view of test setup (Rollins & Sparks, 2002).

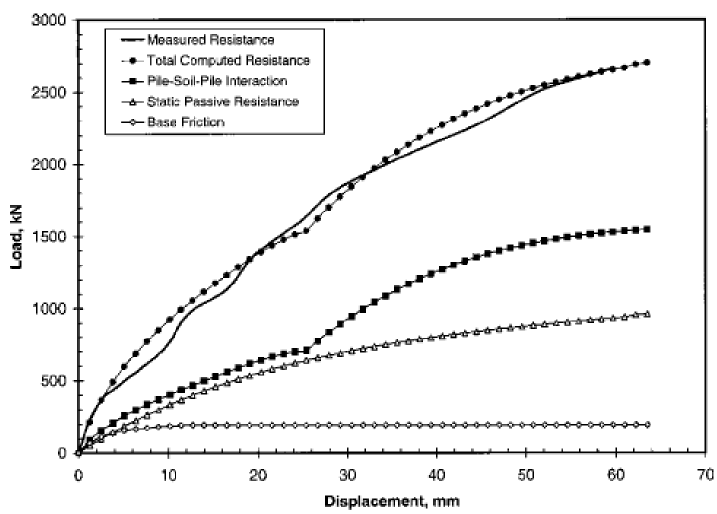

Figure 2-28 Computed load-deflection curves for base friction, pile-soil-pile interaction, passive and total resistance (Rollins & Sparks, 2002).

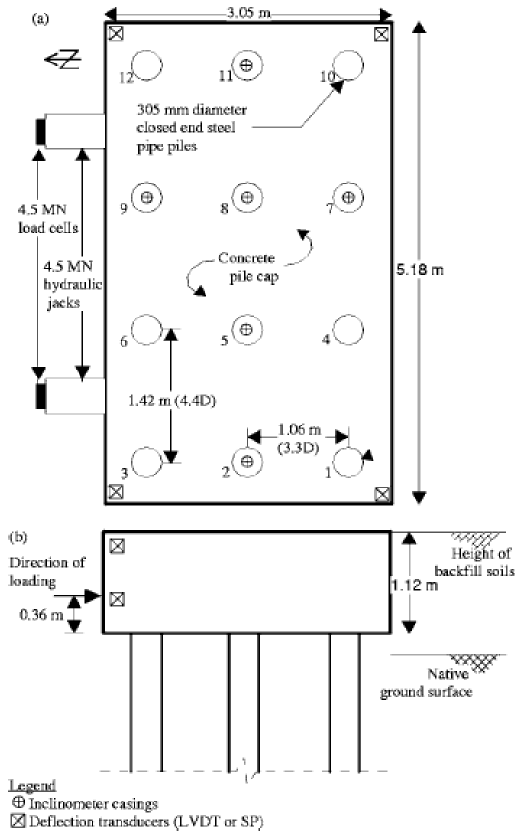

Figure 2-29 Pile cap plan and elevation view (Rollins & Sparks, 2006).

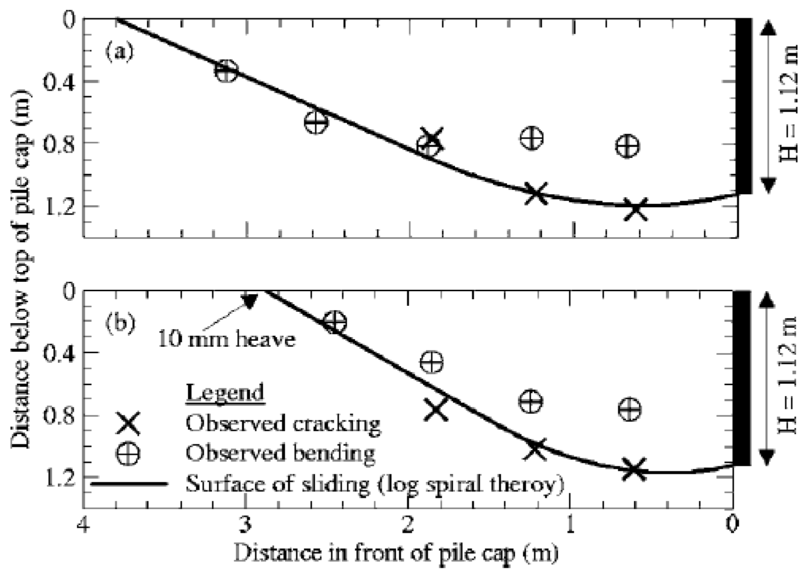

Figure 2-30 Observed cracking and bending of polystyrene columns, a) coarse gravel, b) silty sand (Rollins & Sparks, 2006).

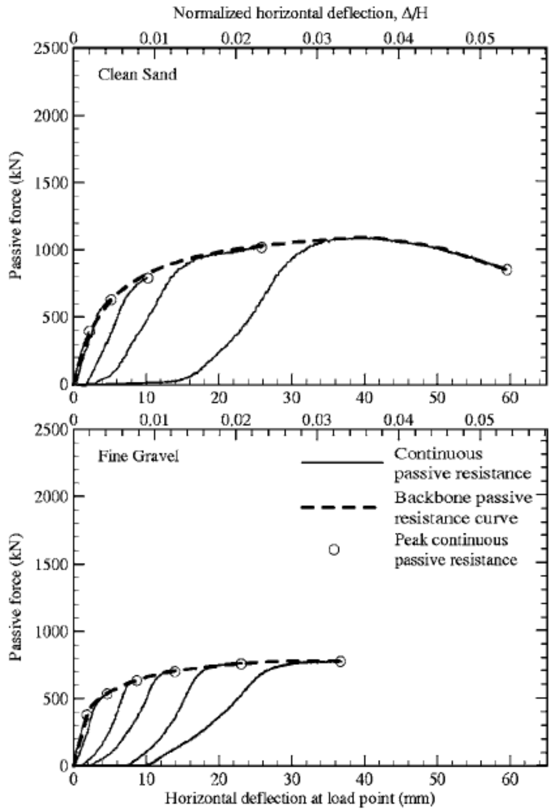

Figure 2-31 Measured first cycle and passive force-deflection curves (Rollins & Sparks, 2006).

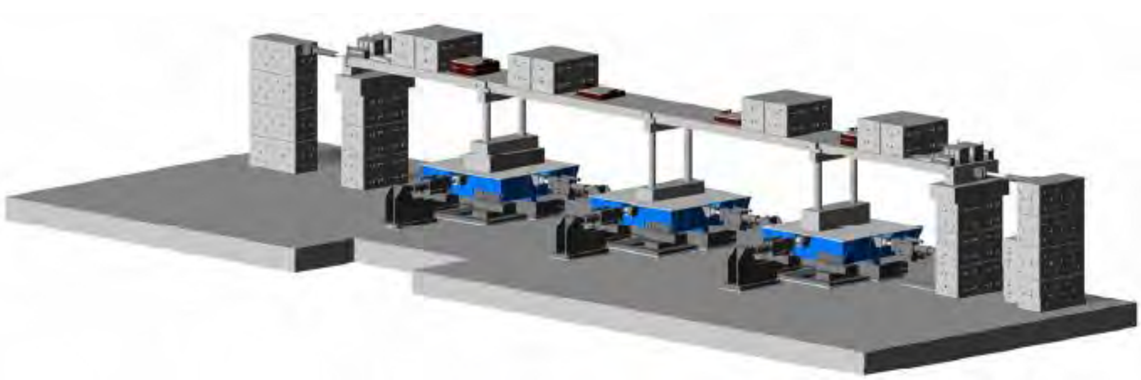

Figure 2-32 Overview of 4-span bridge model (Nelson et al., 2007).

Figure 2-33 Abutment system of test model (Nelson et al., 2007).

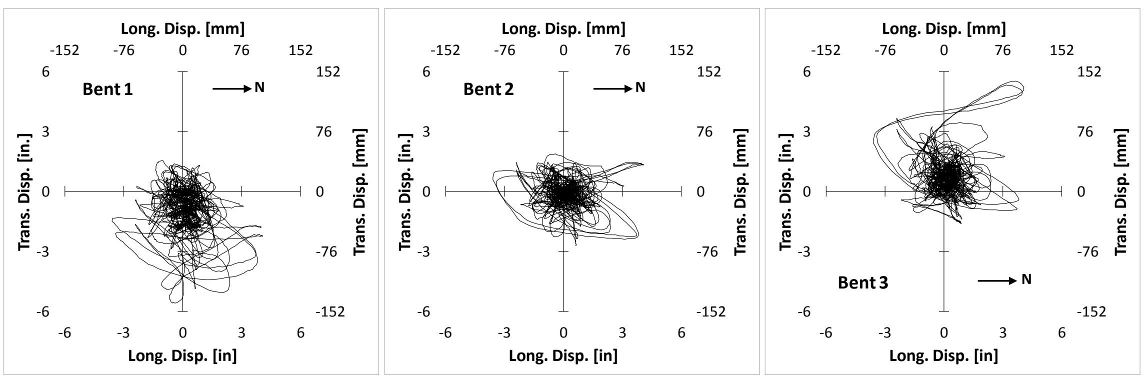

Figure 2-34 Measured particle movements (Saiidi et al., 2012).

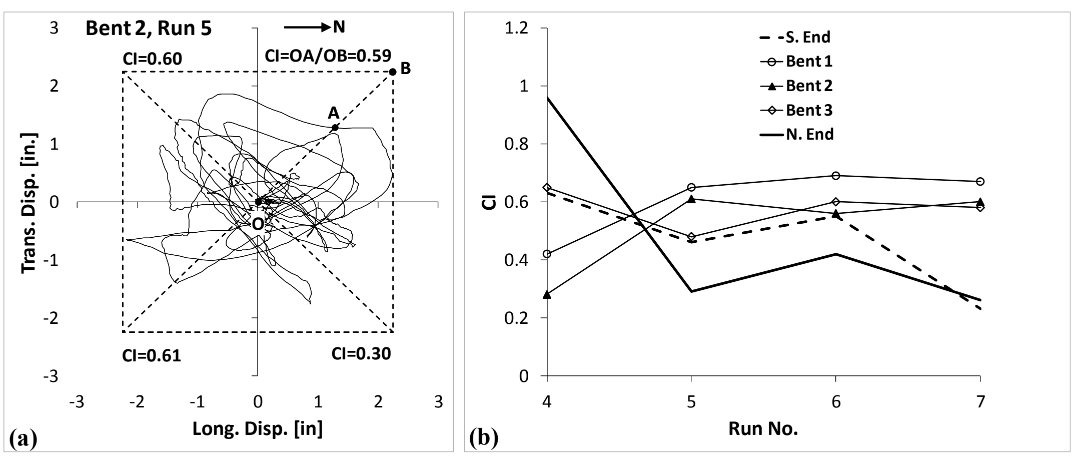

Figure 2-35 Coupling index; a) definition, b) results (Saiidi et al., 2012).

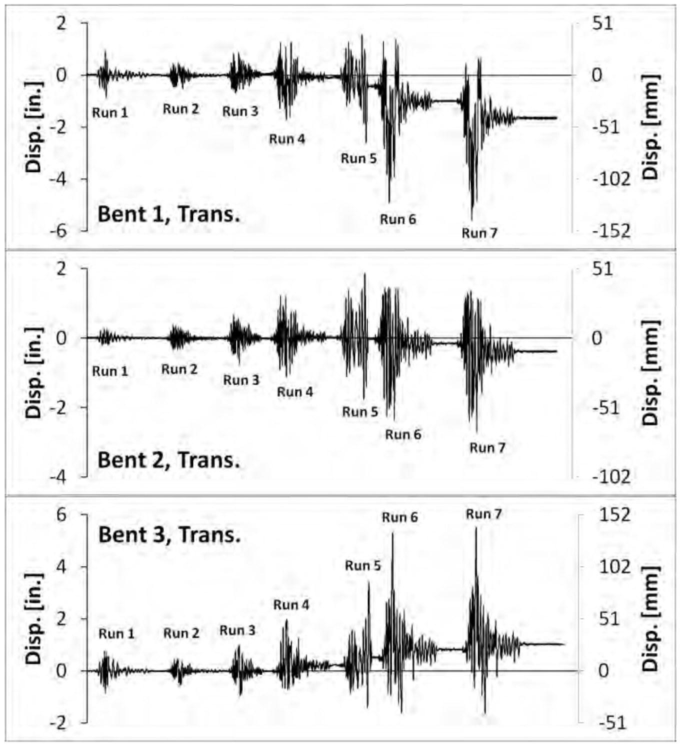

Figure 2-36 Combined relative displacement histories (Saiidi et al., 2012).

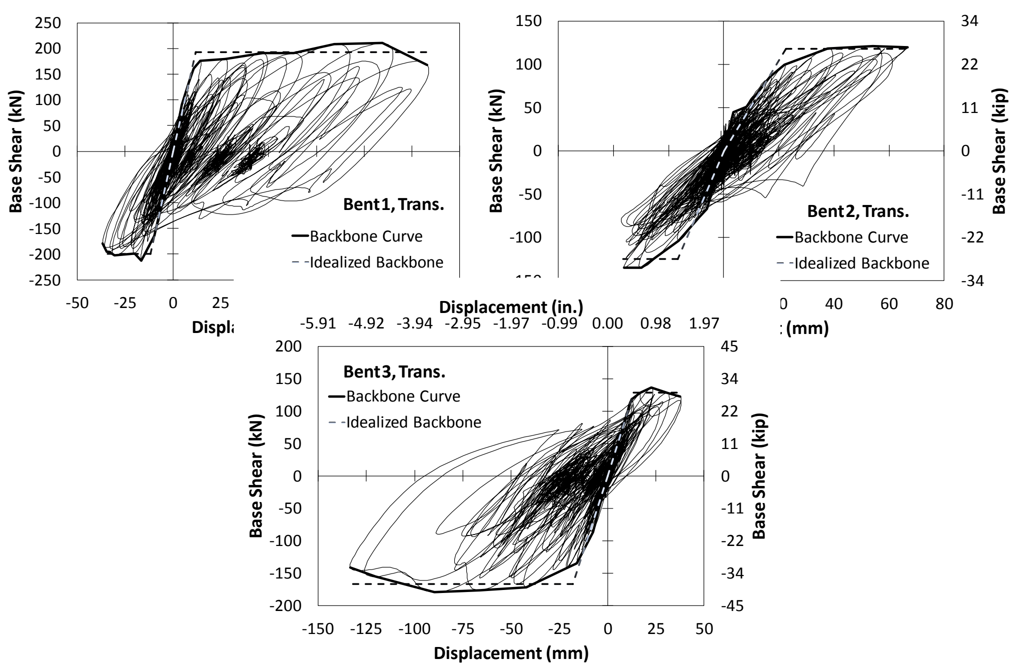

Figure 2-37 Cumulative measured force-displacement hysteresis, envelope, and idealized curves in transverse direction (Saiidi et al., 2012).

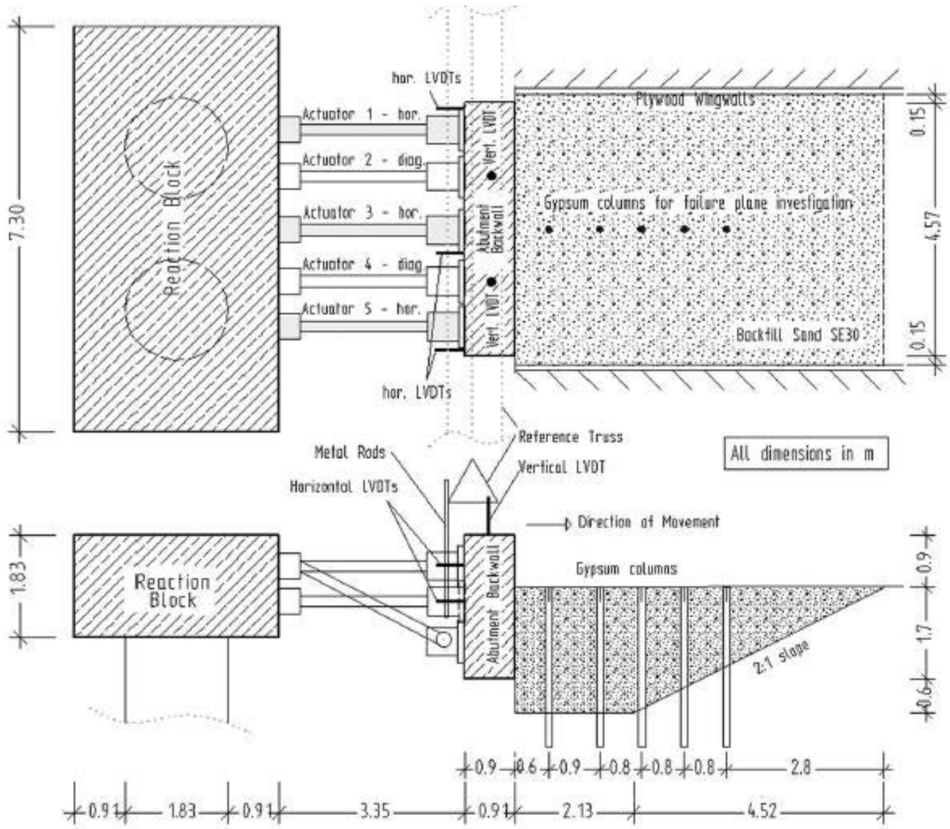

Figure 2-38 Plan and elevation view (Lemnitzer et al., 2009).

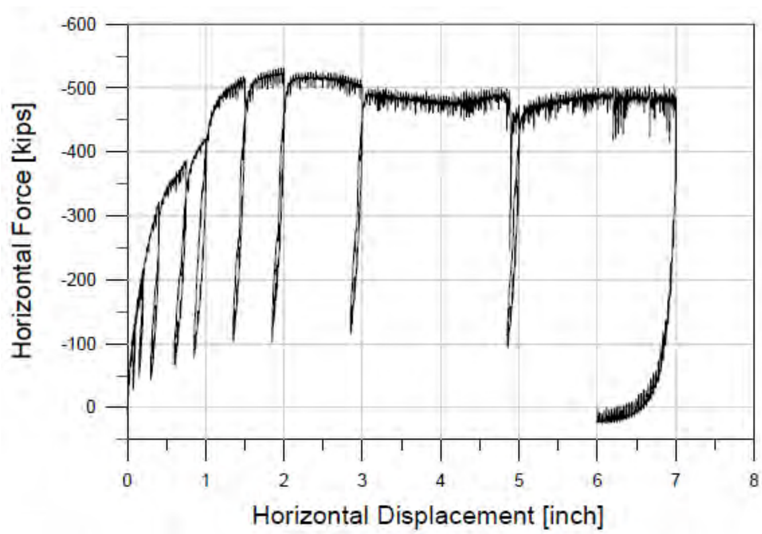

Figure 2-39 Load-displacement curve with backfill soil (Stewart et al., 2007).

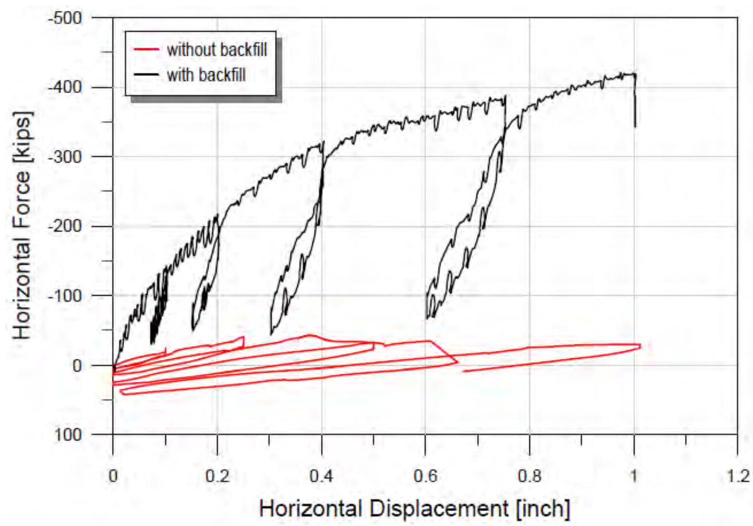

Figure 2-40 Load-displacement curve up to max displacement of 1 in with and without backfill soil (Stewart et al., 2007).

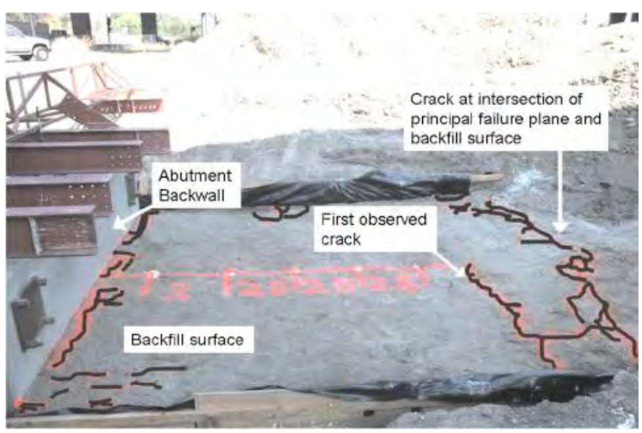

Figure 2-41 Observed test results; left: gypsum columns, right: crack patterns (Stewart et al., 2007).

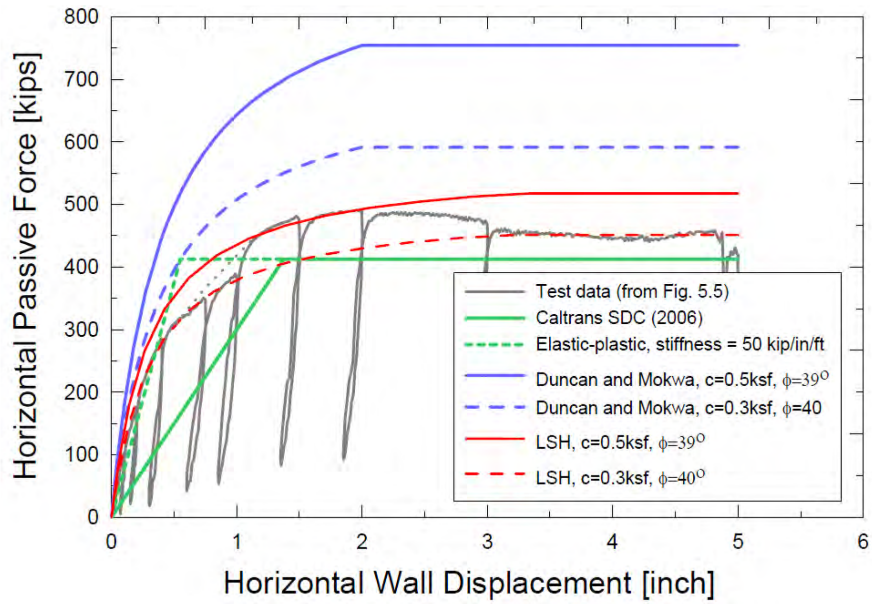

Figure 2-42 Predicted load-deflection relationships (Stewart et al., 2007).

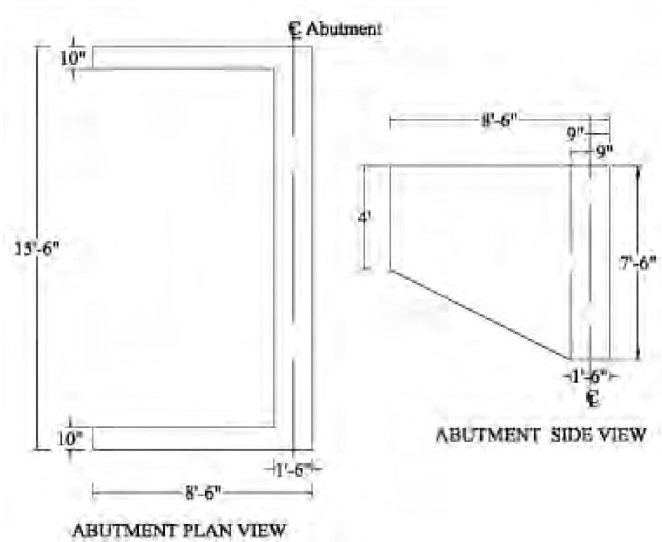

Figure 2-43 Plan and elevation view of abutment wall (Bozorgzadeh, 2007).

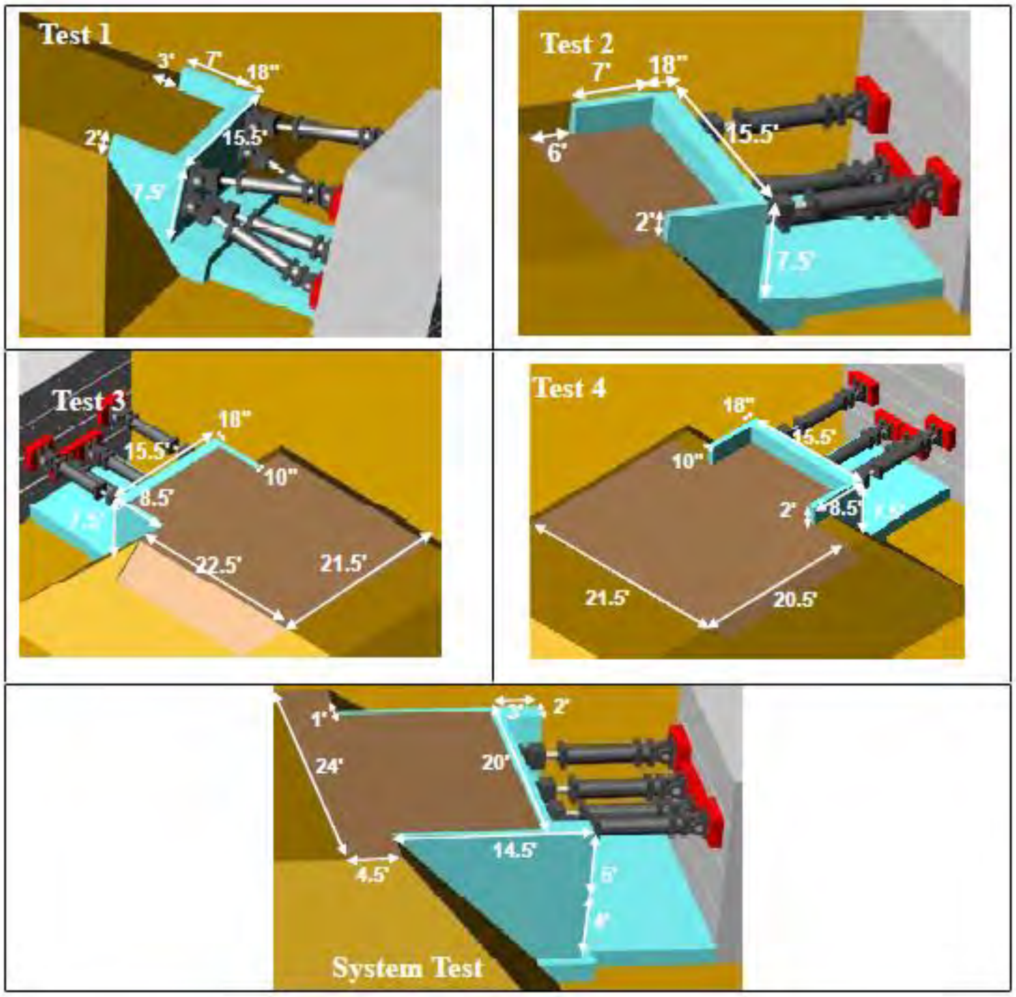

Figure 2-44 Overall test setup (Bozorgzadeh et al., 2008).

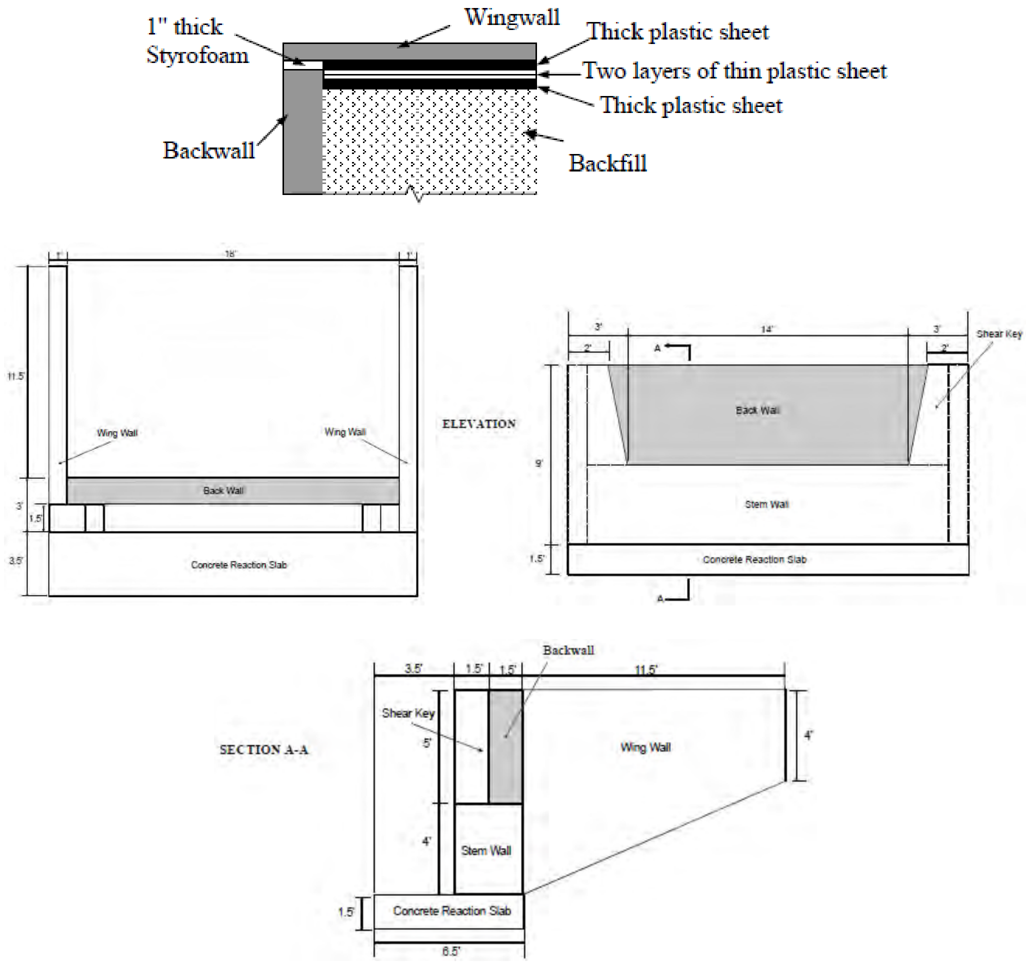

Figure 2-45 System test set up configuration (Bozorgzadeh, 2007).

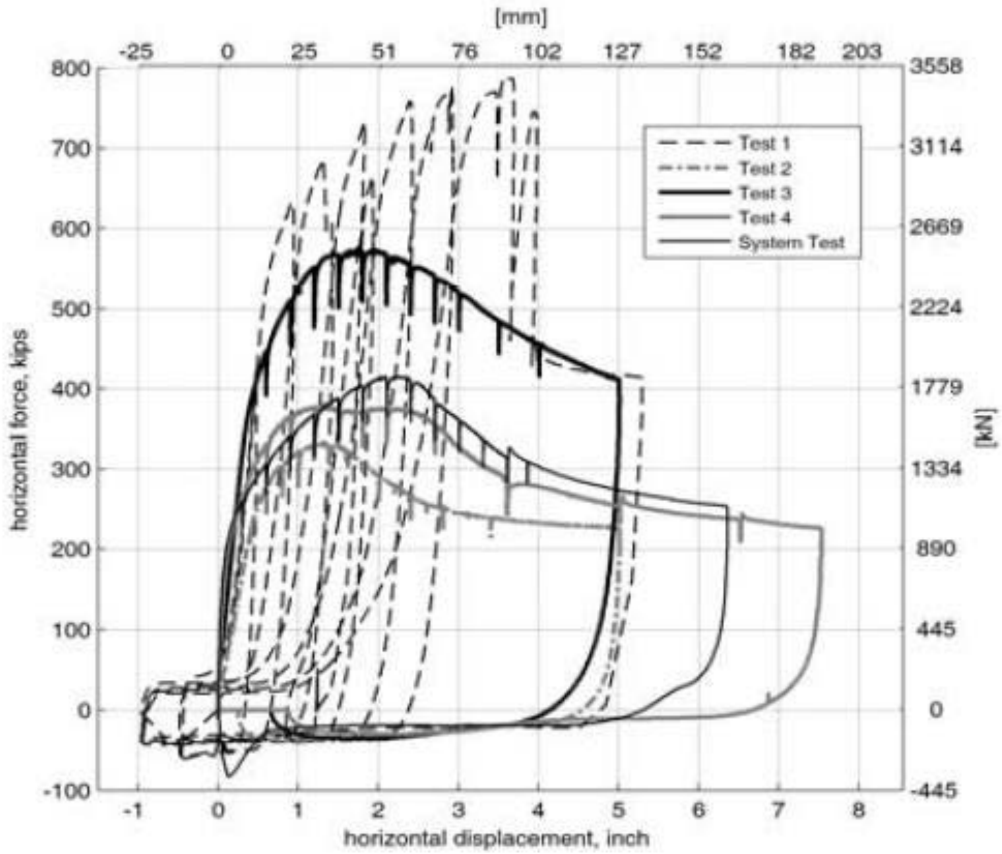

Figure 2-46 Horizontal force-displacement response (Bozorgzadeh, 2007).

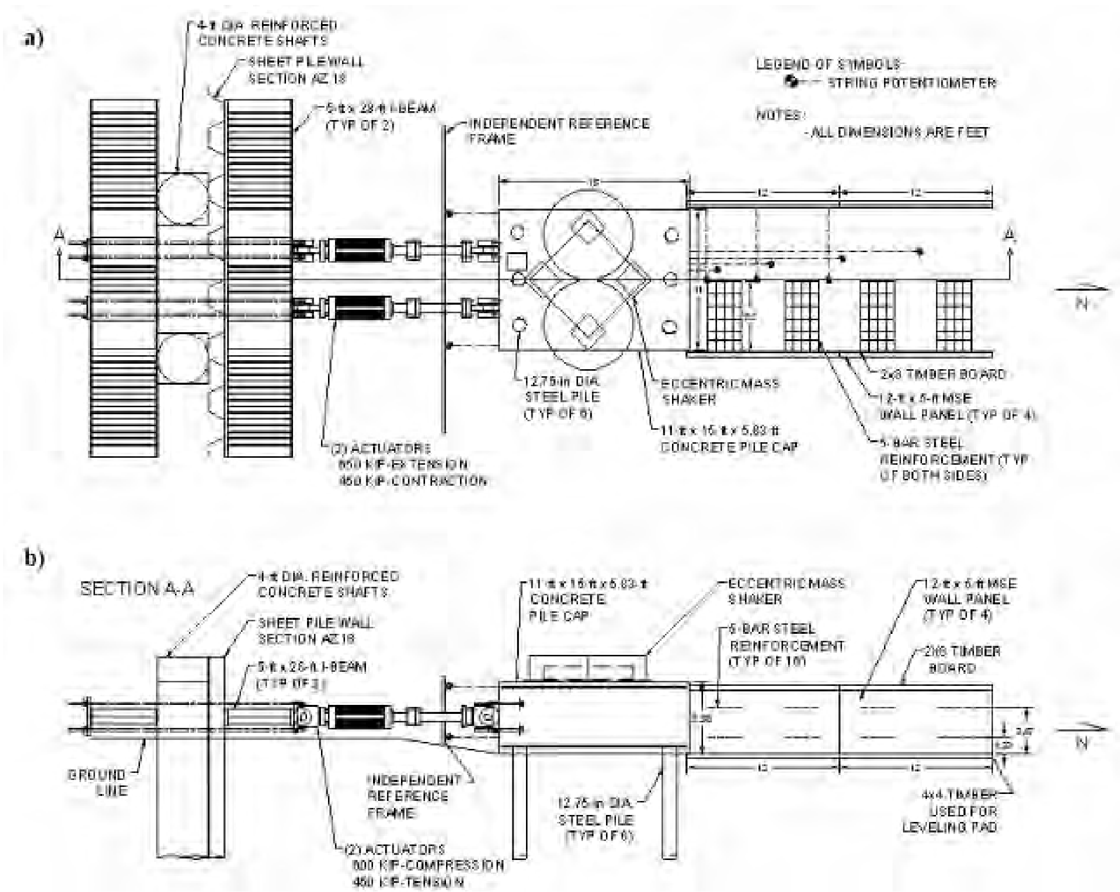

Figure 2-47 a) Plan view and b) elevation view of MSE wall confined backfill test (Heiner et al., 2008).

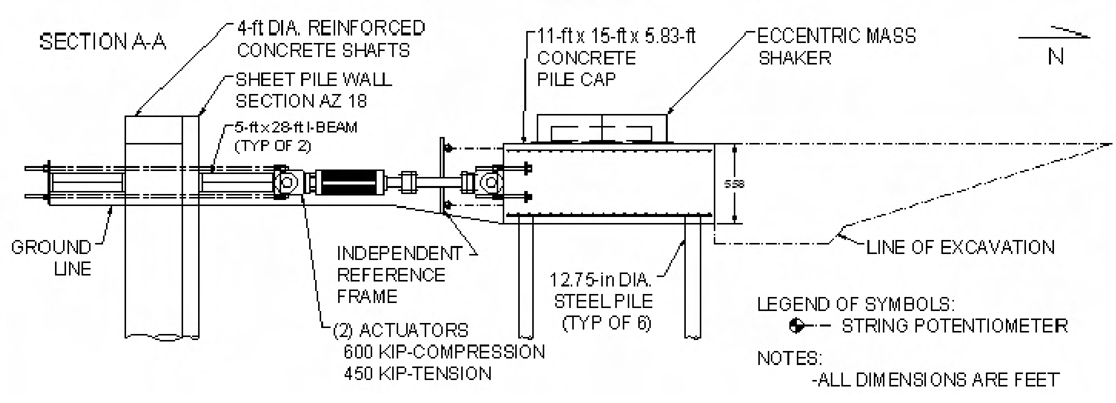

Figure 2-48 Elevation view of unconfined soil backfill test (Heiner et al., 2008).

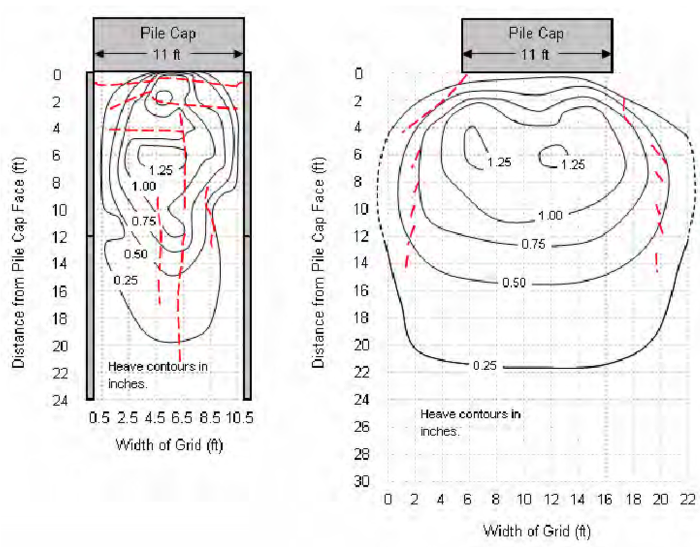

Figure 2-49 Observed cracking (dashed line) and vertical heave patterns (solid lines) at maximum displacement (Heiner et al., 2008).

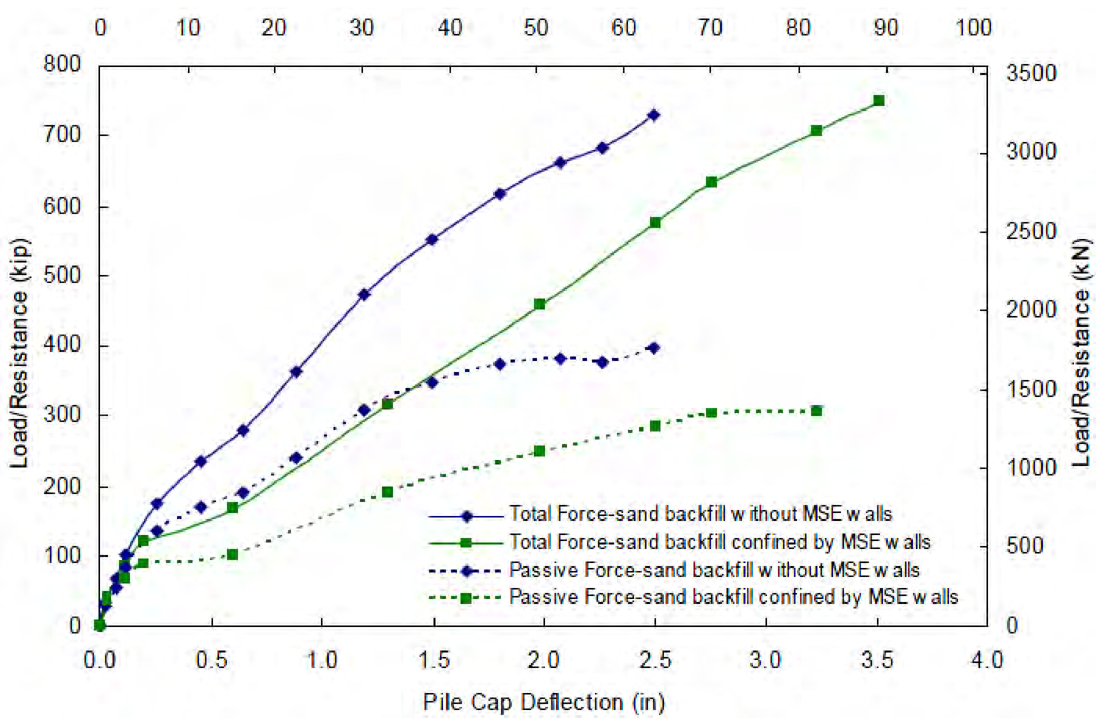

Figure 2-50 Total and passive force-displacement relationship (Heiner et al., 2008)

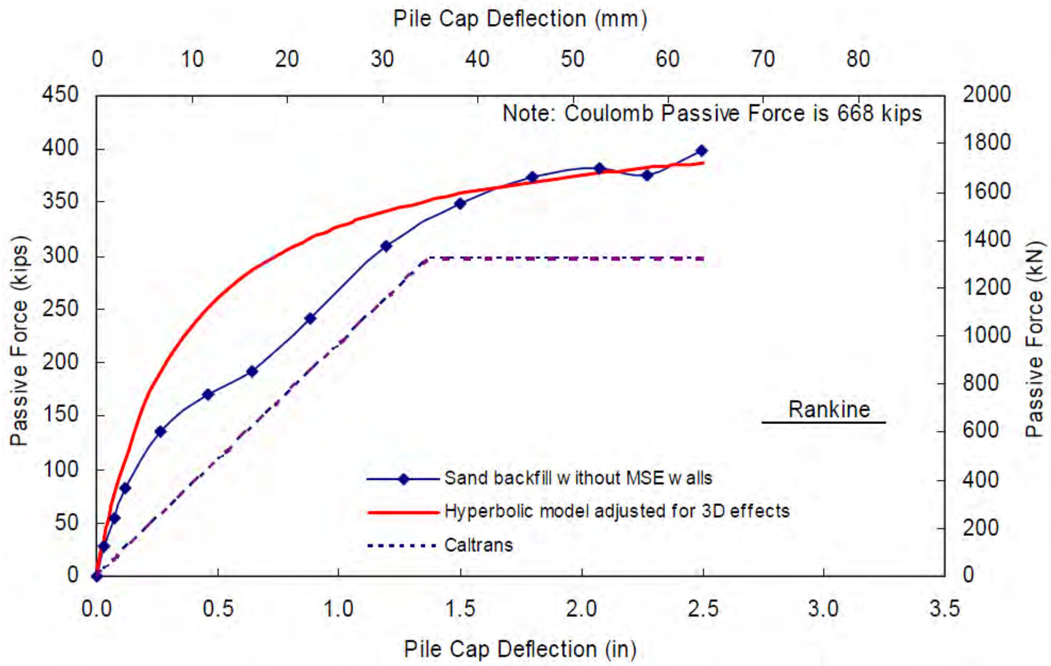

Figure 2-51 Comparison of measured and computed passive force-deflection for the backfill without MSE wingwalls (Heiner et al., 2008).

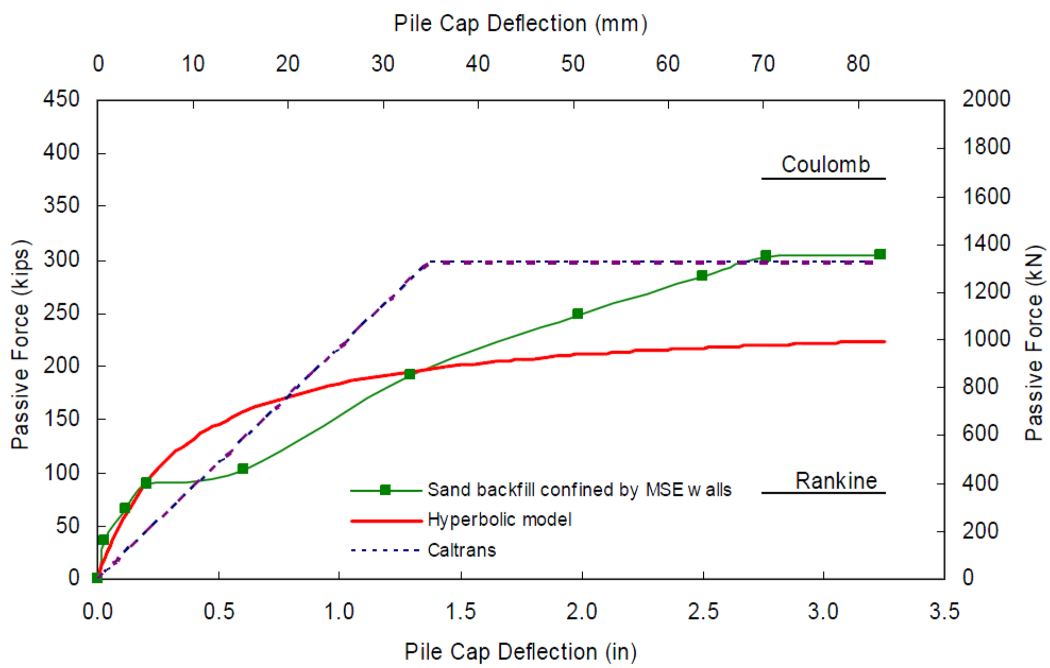

Figure 2-52 Comparison of measured and computed passive force-deflection for the backfill with MSE wingwalls (Heiner et al., 2008).

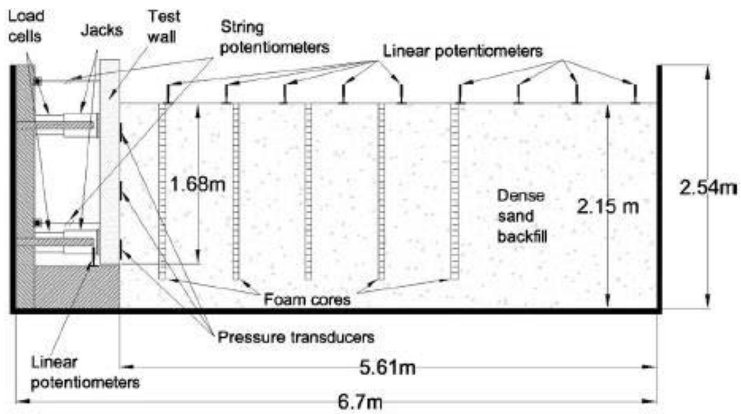

Figure 2-53 Test elevation view (1 m=3.28 ft) (Wilson & Elgamal, 2010).

Figure 2-54 Test setup; left: soil container, right: suspended wall system (Wilson & Elgamal, 2010).

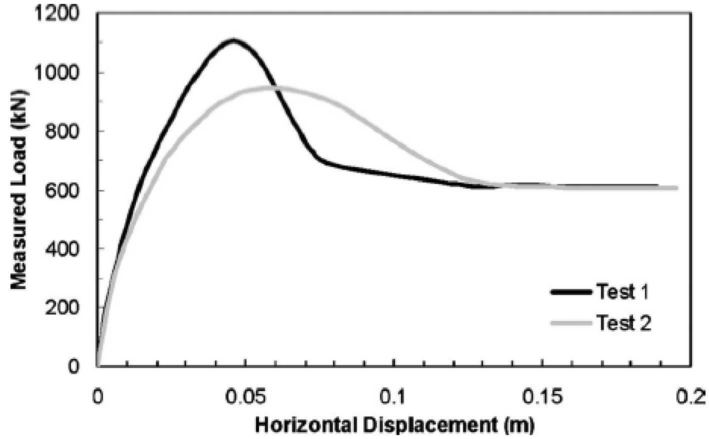

Figure 2-55 Total measured load displacement relationship (1 m=3.28 ft, 1 kN=0.2248 kips) (Wilson & Elgamal, 2010).

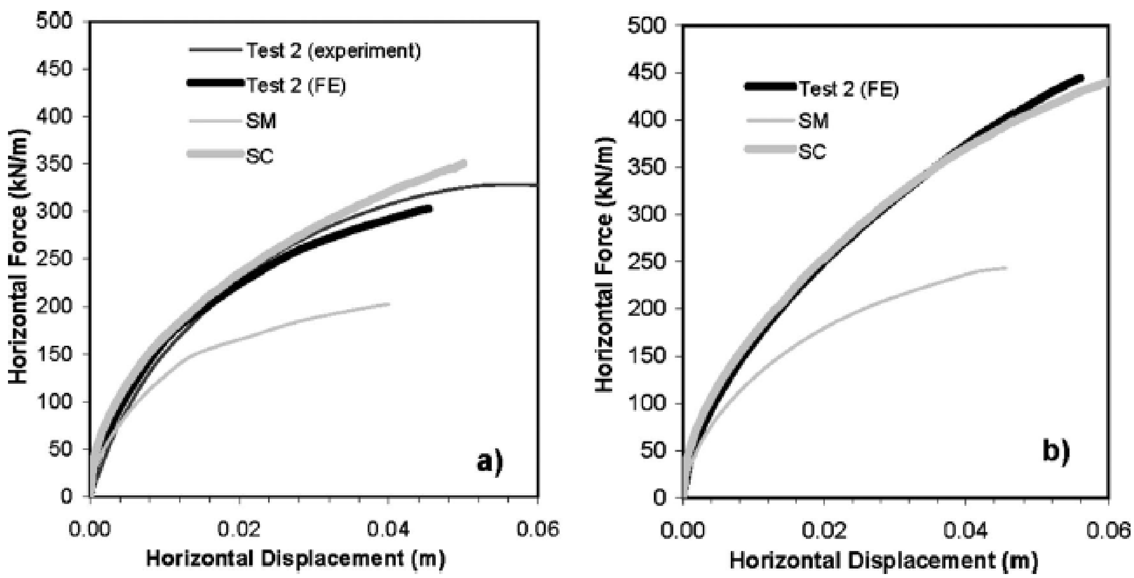

Figure 2-56 Load-displacement results from FE passive pressure simulations, a) δ governed by vertical equilibrium requirements (vertical uplift condition), b) δ=0.35ϕ (without vertical uplift) (1 m=3.28 ft, 1 kN=0.2248 kips) (Wilson & Elgamal, 2010).

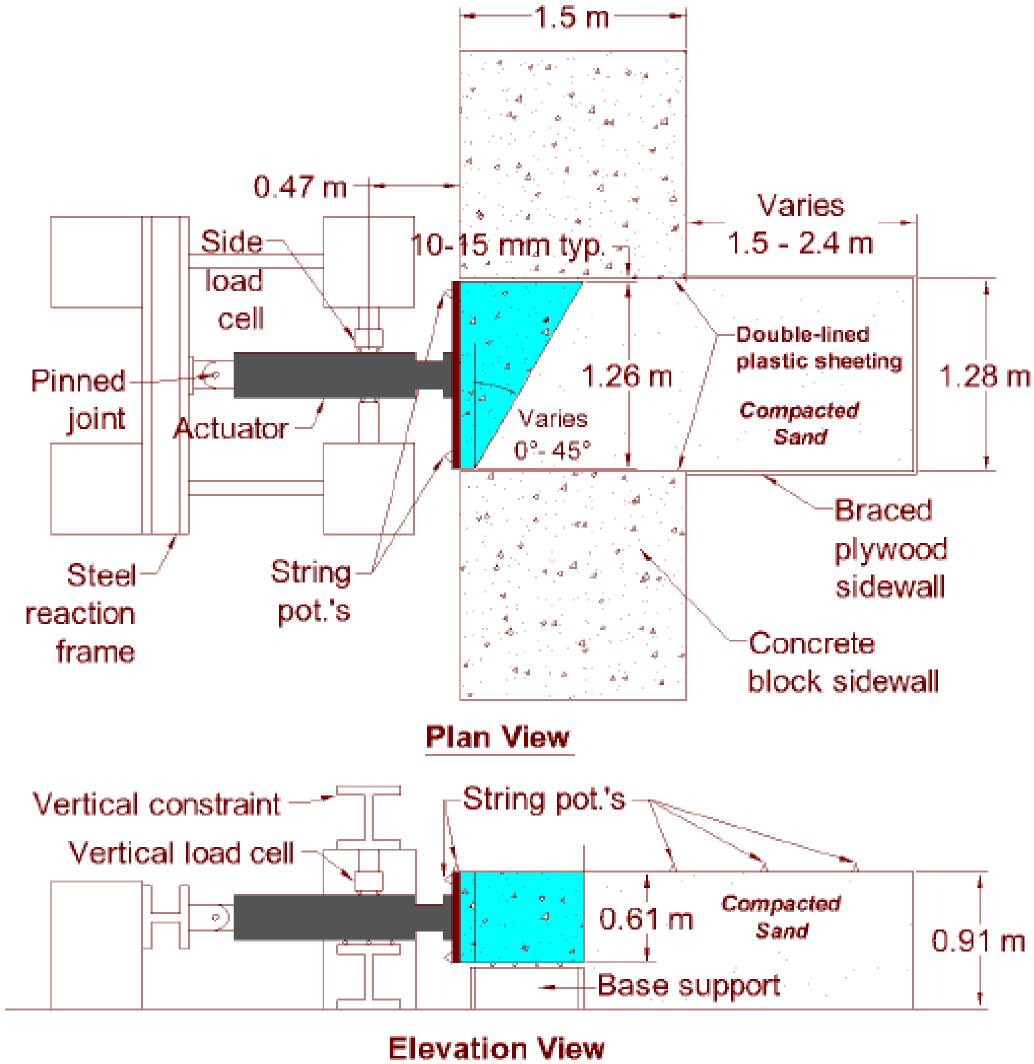

Figure 2-57 Plan and elevation view of test setup (1 m=3.28 ft) (Rollins & Jessee, 2013)

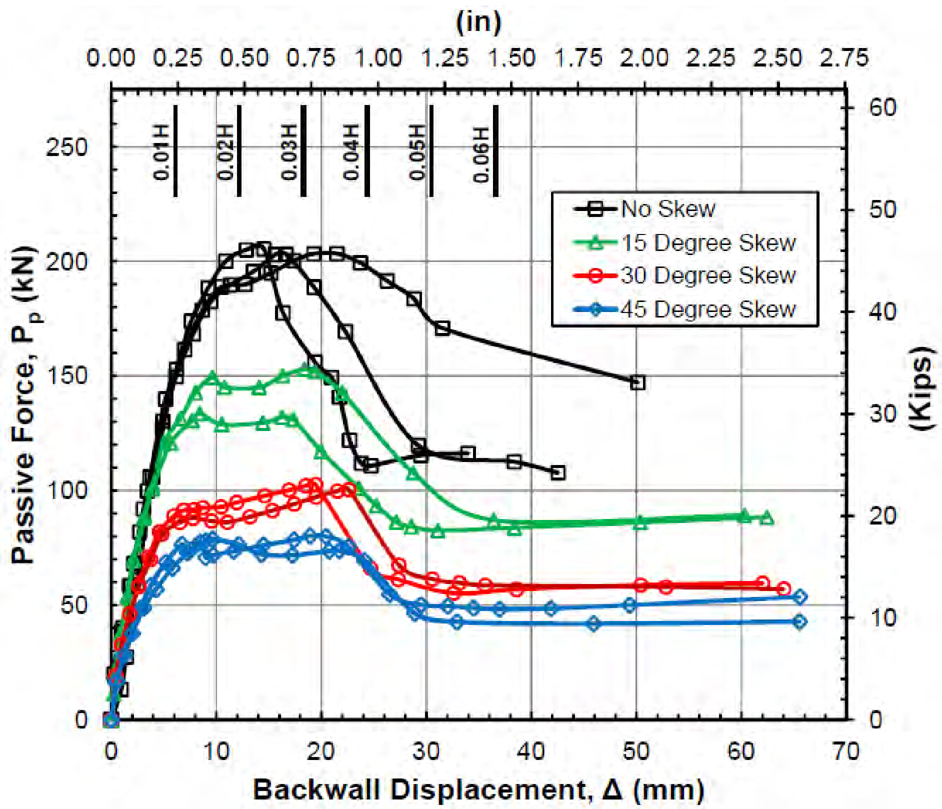

Figure 2-58 Passive force-deflection relationship (Rollins & Jessee, 2013).

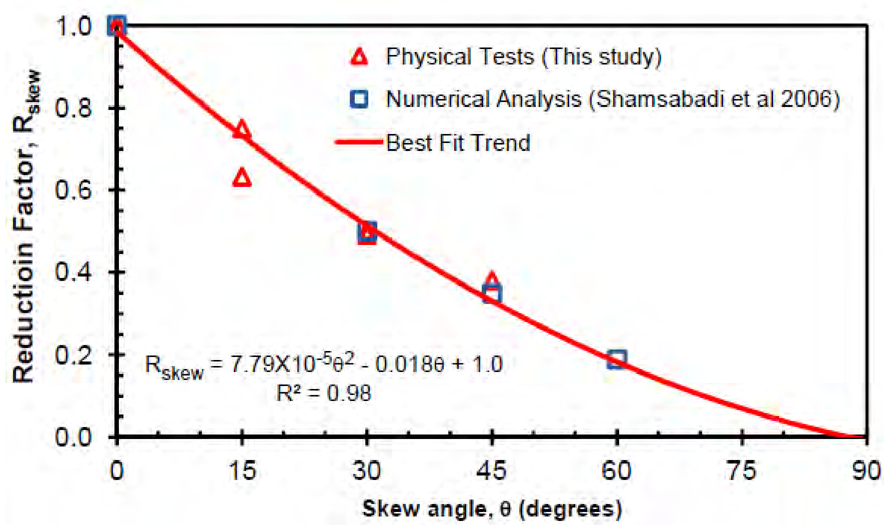

Figure 2-59 Reduction factor versus skew angle (Rollins & Jessee, 2013).

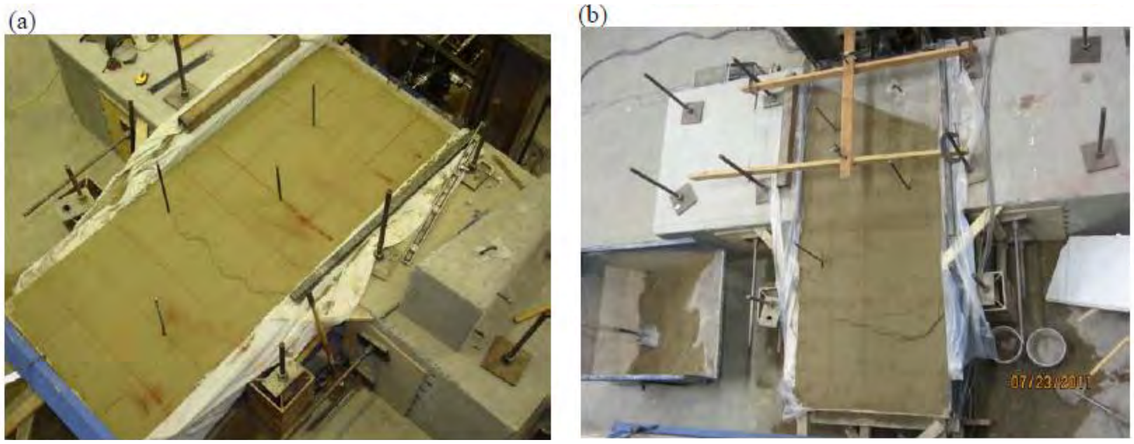

Figure 2-60 Observed failure surface: a) non-skewed, b) skewed (Rollins & Jessee, 2013).

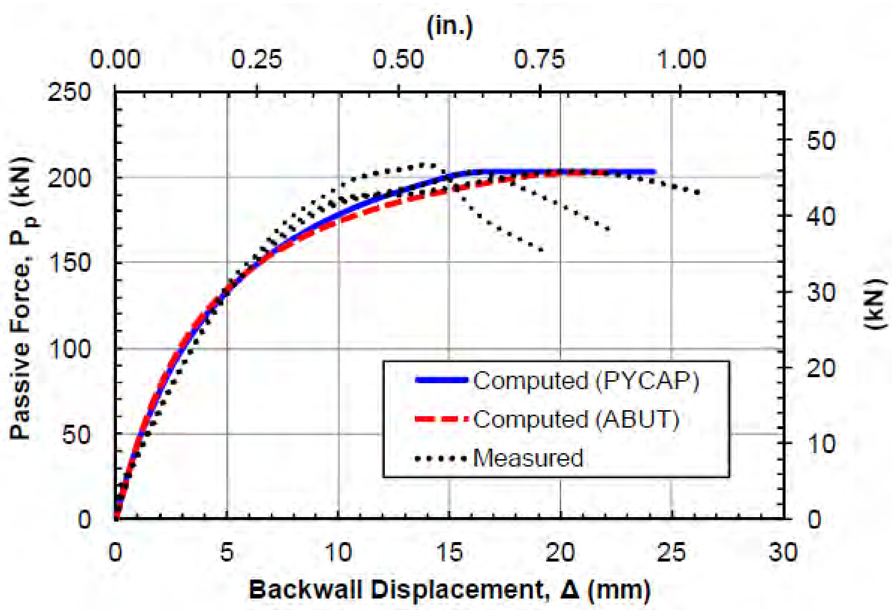

Figure 2-61 Comparison of measured and computed force-displacement relationship (Rollins & Jessee, 2013).

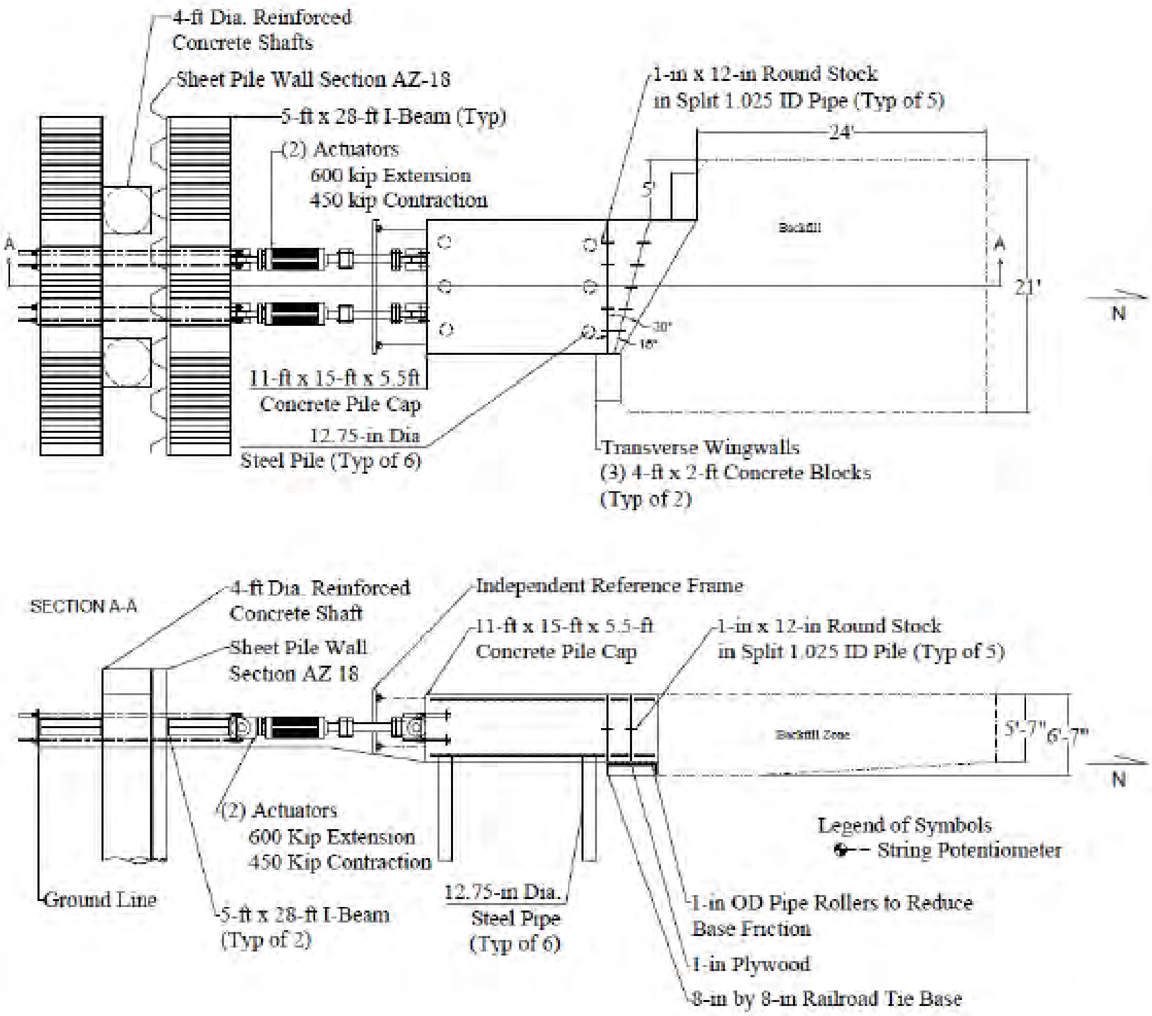

Figure 2-62 Plan and elevation view of test setup (Marsh, 2013; Marsh et al., 2013).

(a)

(b)

(c)

Figure 2-63 Field test setup: (a) 0° skew, (b) 15° skew, and (c) 30° skew (Marsh, 2013; Marsh et al., 2013).

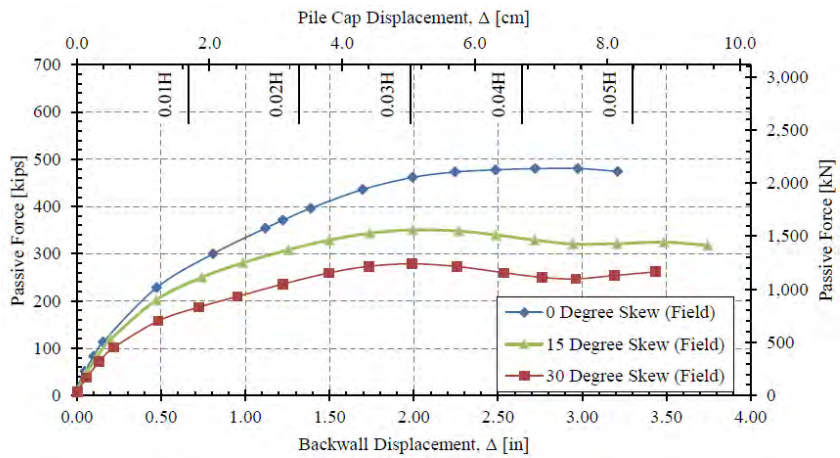

Figure 2-64 Passive force-displacement curves (Marsh, 2013; Marsh et al., 2013).

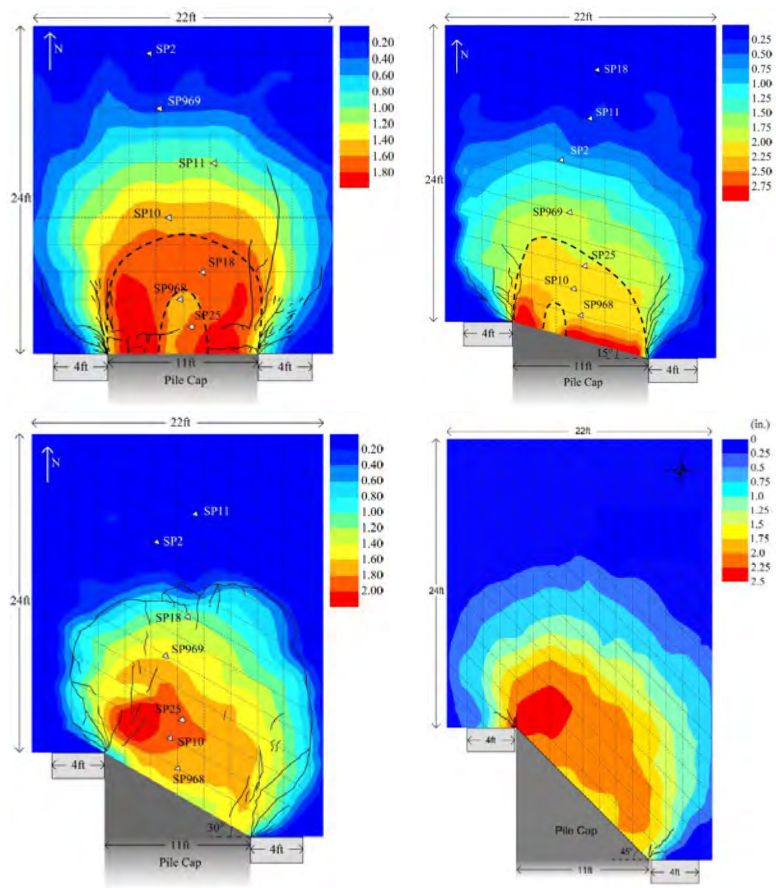

Figure 2-65 Backfill heave contours (Marsh, 2013; Marsh et al., 2013; Rollins & Smith, 2014).

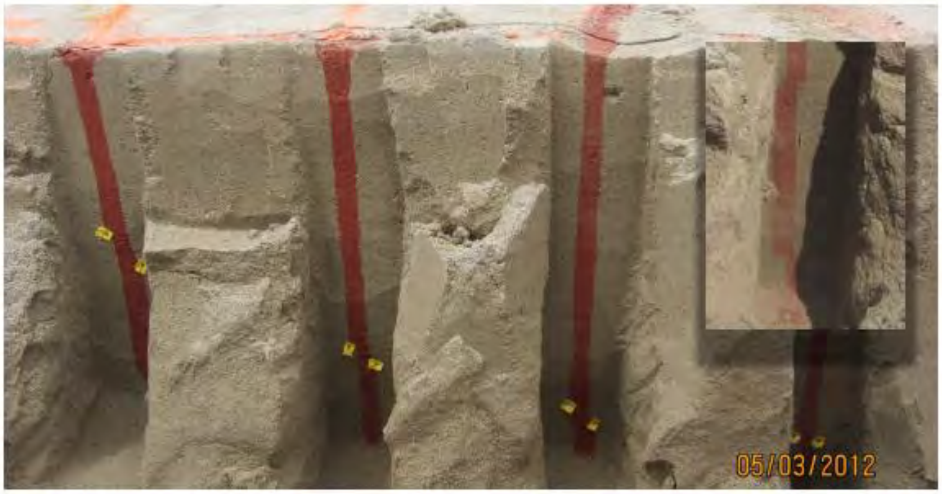

Figure 2-66 Colored sand columns in the non-skew test (Marsh, 2013; Marsh et al., 2013).

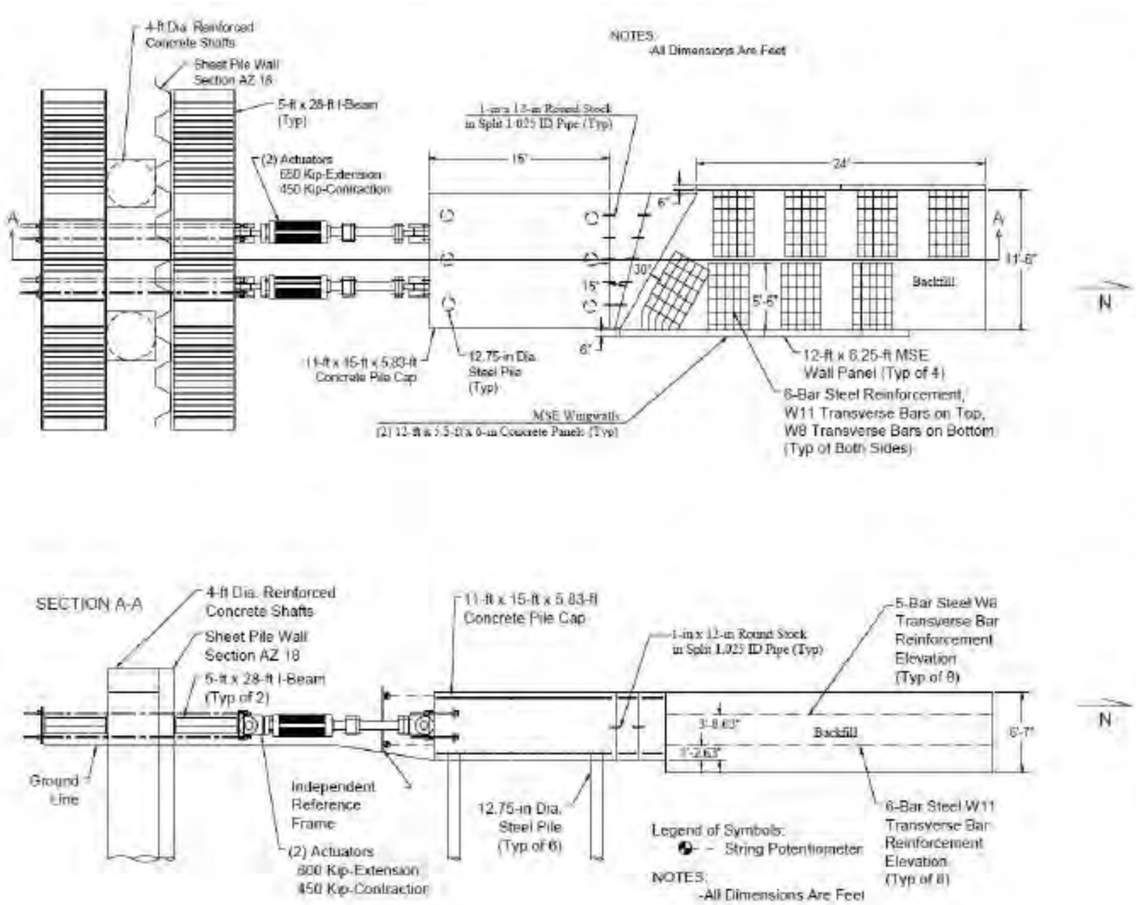

Figure 2-67 Plan view of test set up (Franke, 2013).

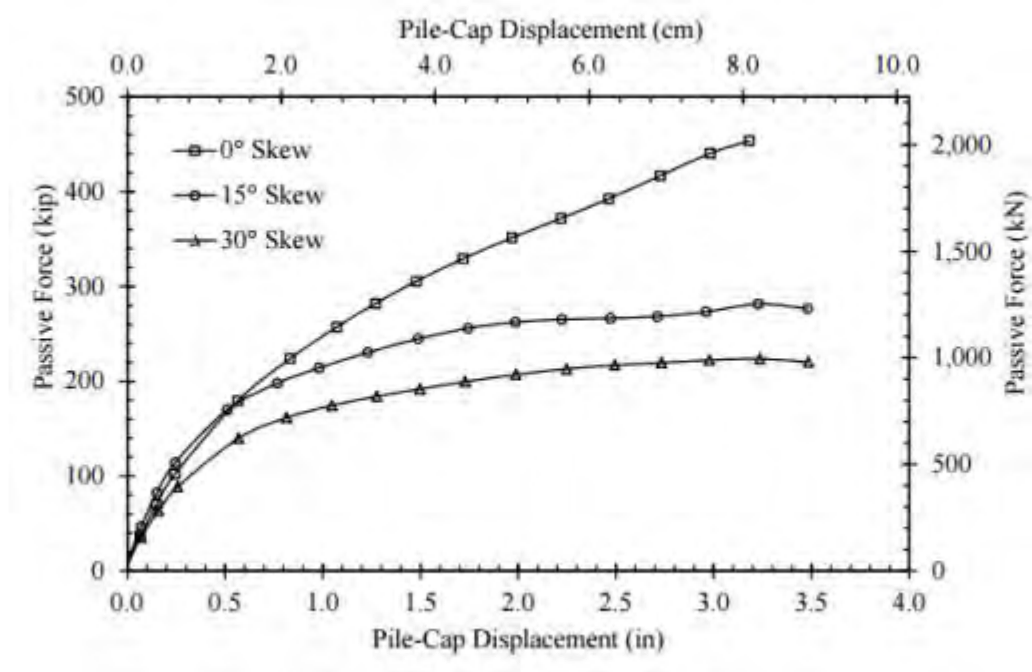

Figure 2-68 Passive force-displacement curves (Franke, 2013).

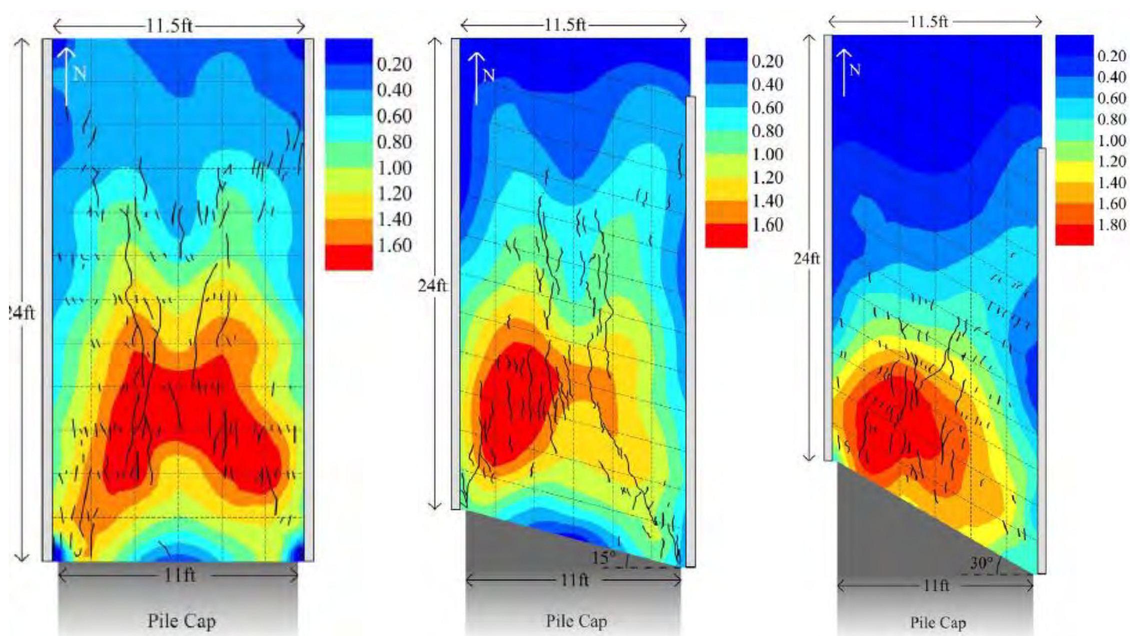

(a) (b) (c)

Figure 2-69 Heave contours: (a) 0° skew, (b) 15° skew, and (c) 30° skew (Franke, 2013).

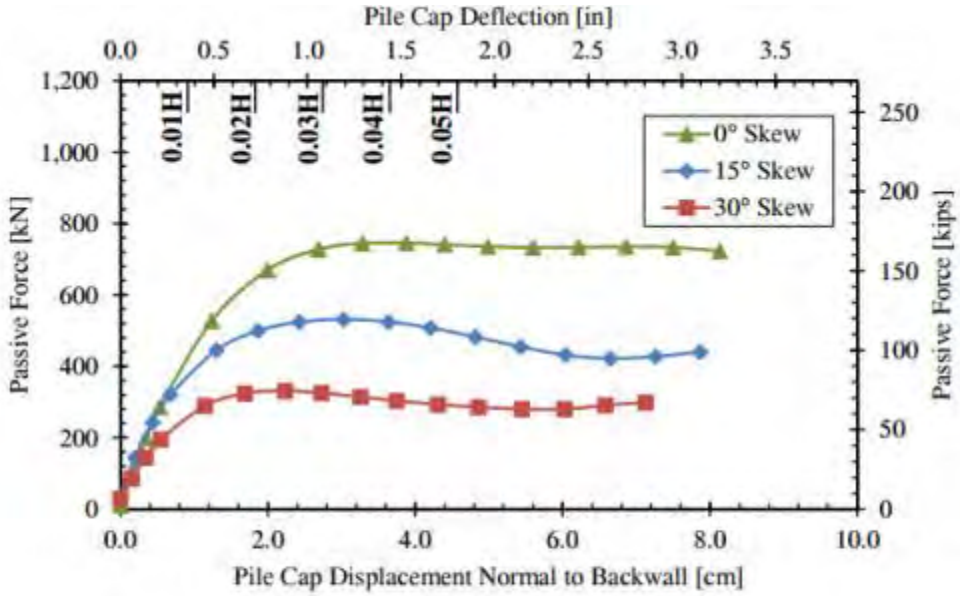

Figure 2-70 Passive force-displacement curves (Palmer, 2013; Rollins et al., 2015).

Figure 2-71 Test set up in the 45° skew abutment (Smith, 2014).

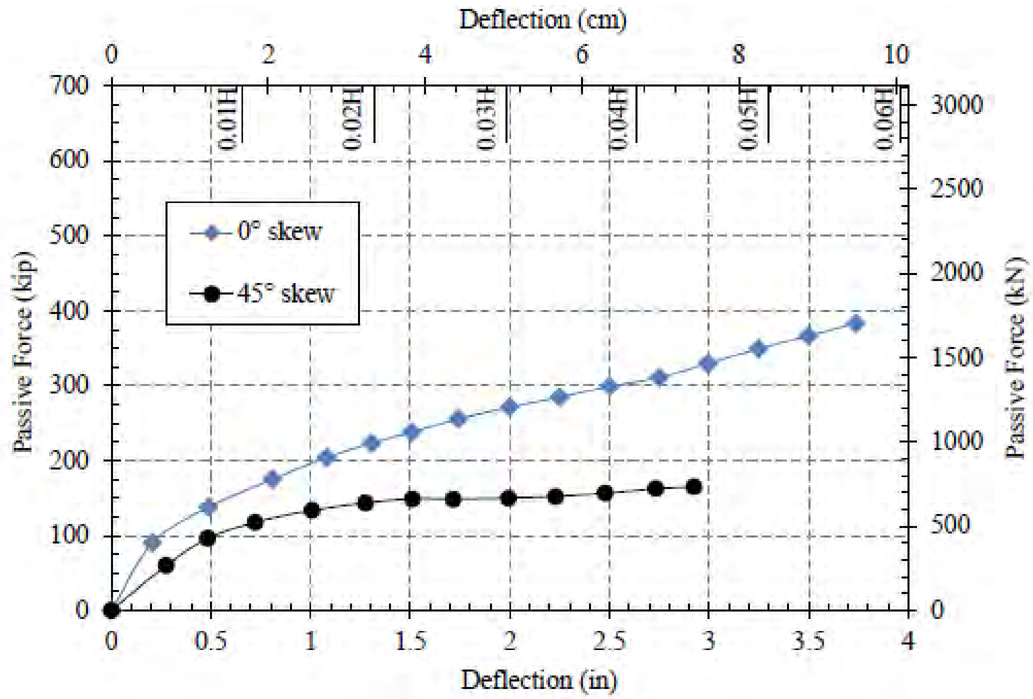

Figure 2-72 Force-displacement relationships (Smith, 2014).

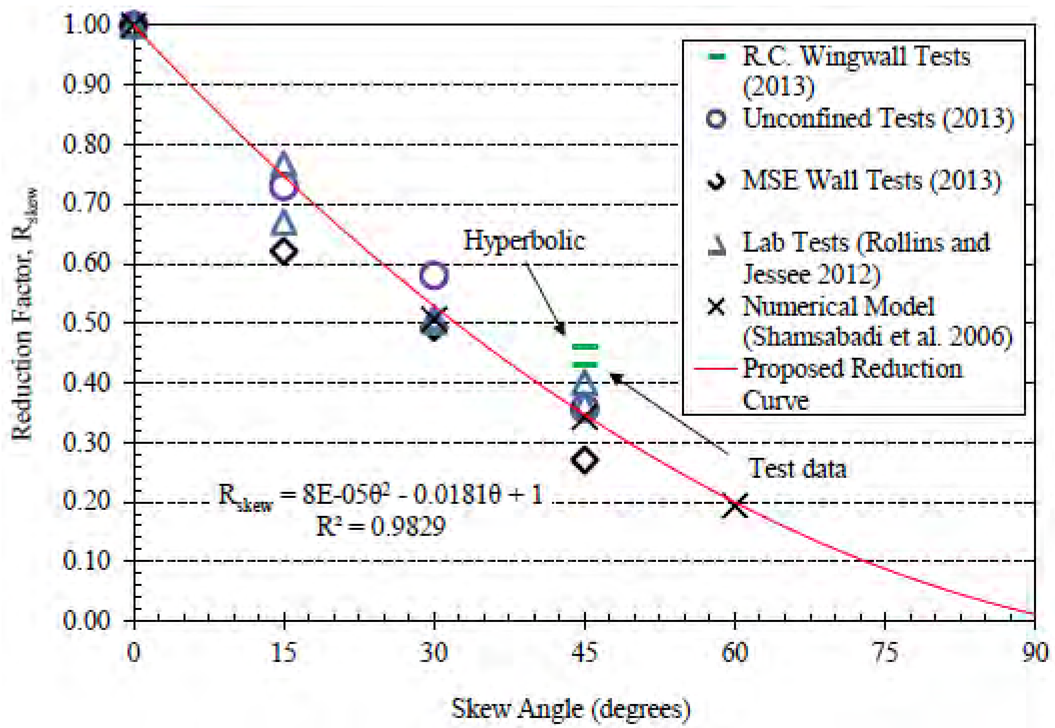

Figure 2-73 Capacity reduction factors (Smith, 2014).

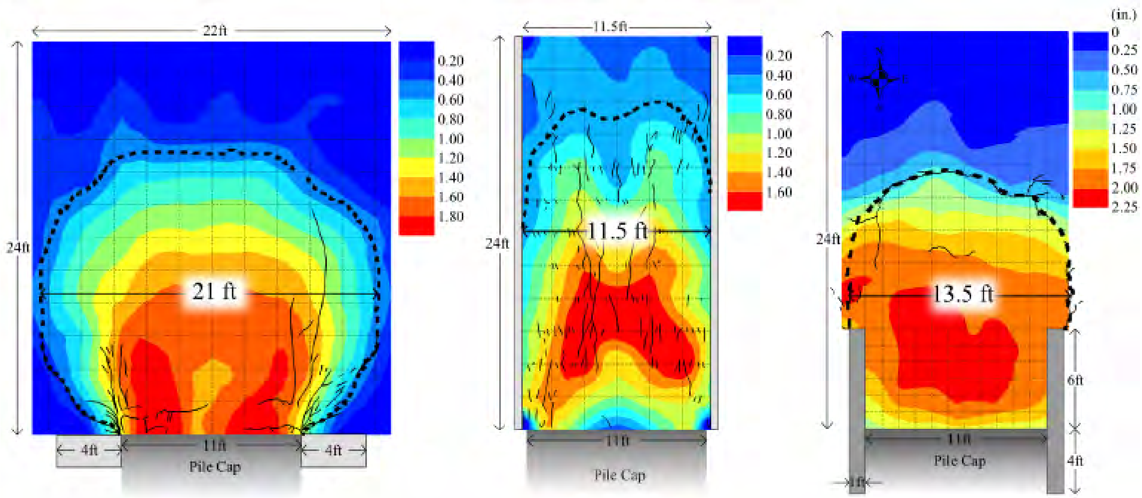

(a)

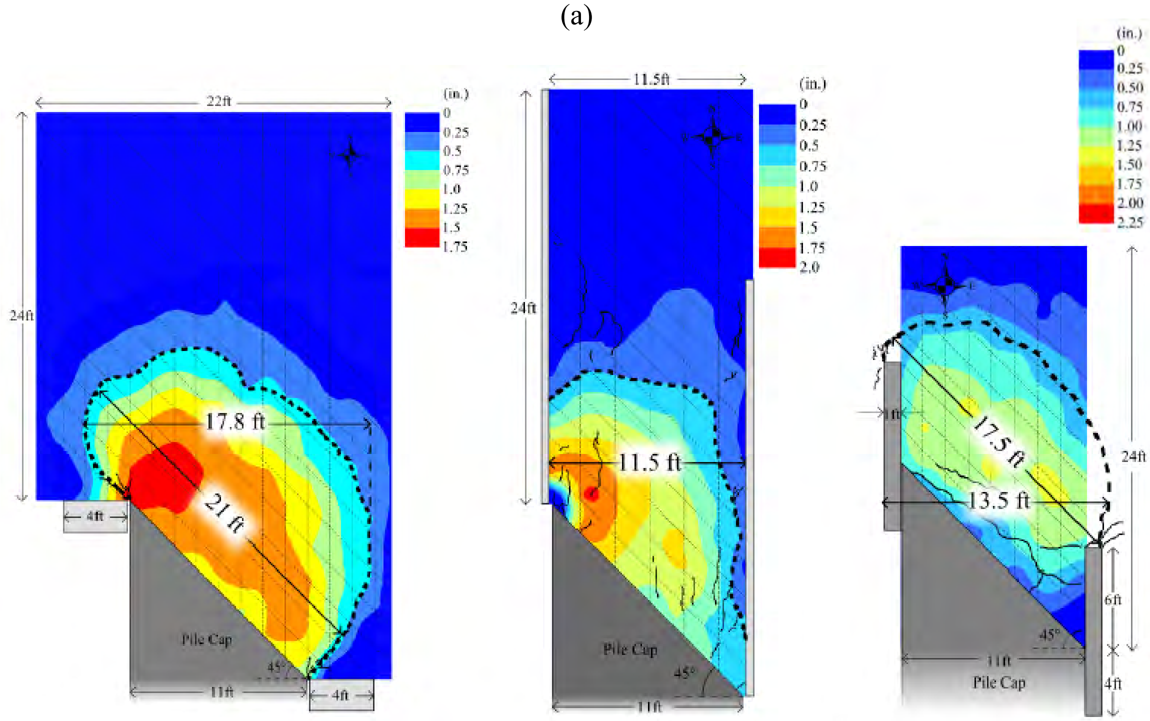

(b)

Figure 2-74 Heave contours: (a) 0° skew, and (b) 45° skew (Smith, 2014).

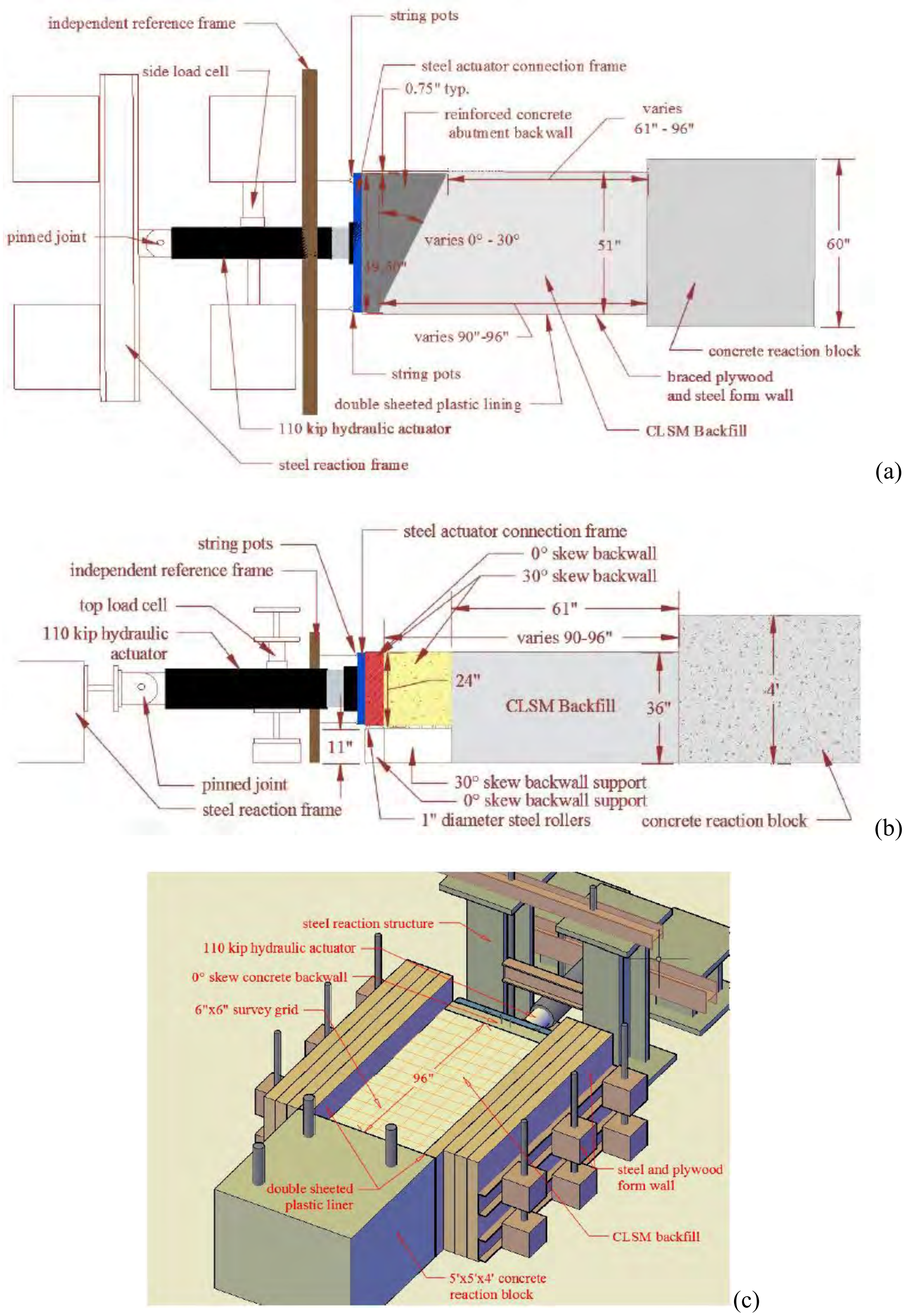

Figure 2-75 Test set up: (a) plan view, (b) elevation view, and (c) 3D view (Wagstaff, 2016).

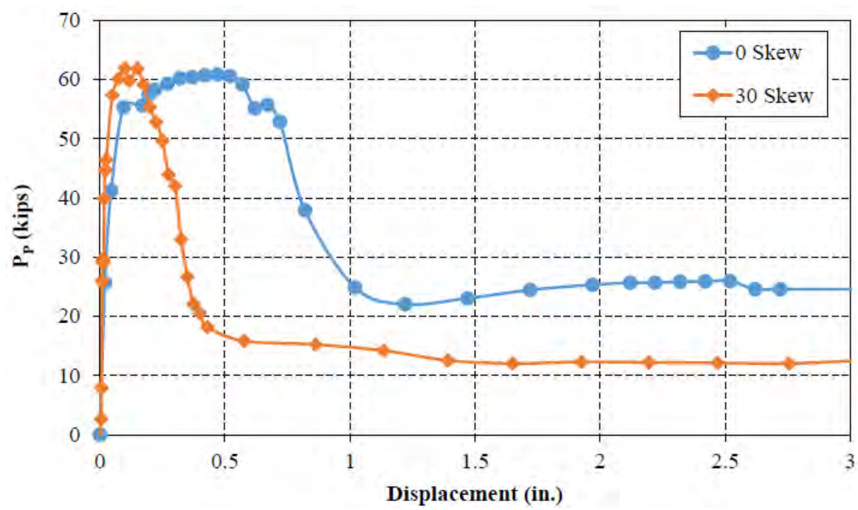

Figure 2-76 Force-displacement relationships (Wagstaff, 2016).

Figure 2-77 Soil failure planes in the 30° skew abutment (Wagstaff, 2016).

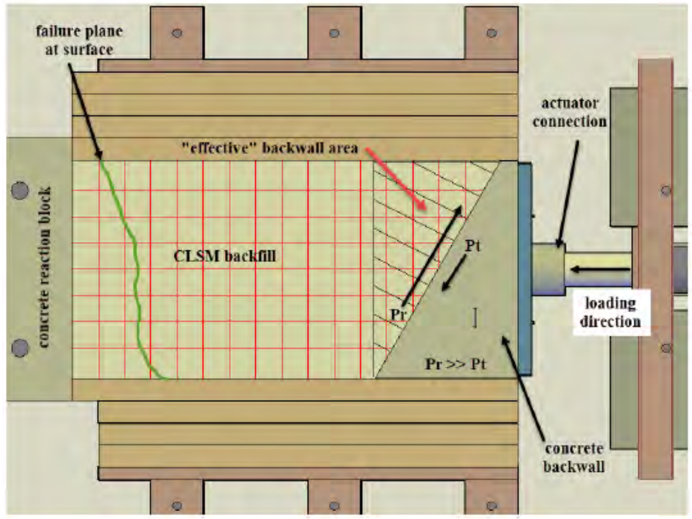

Figure 2-78 CLSM block at the obtuse corner (Wagstaff, 2016).

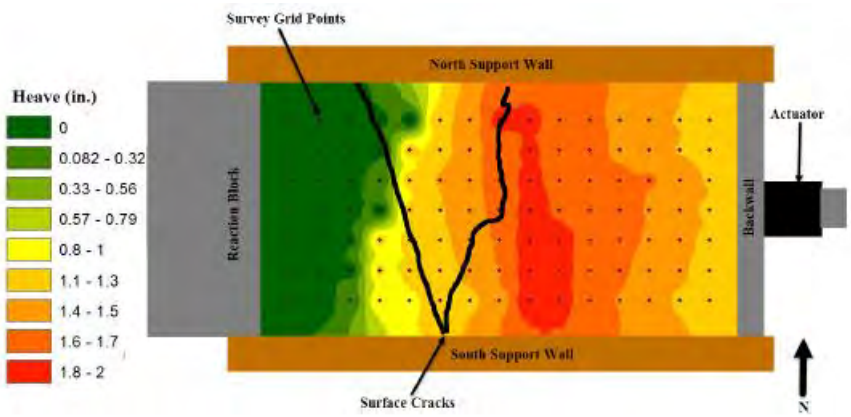

(a)

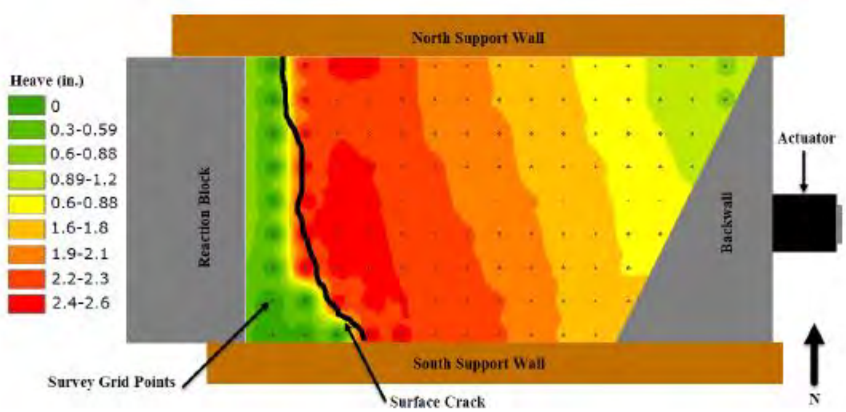

(b)

Figure 2-79 Heave contours of backfill (Wagstaff, 2016).

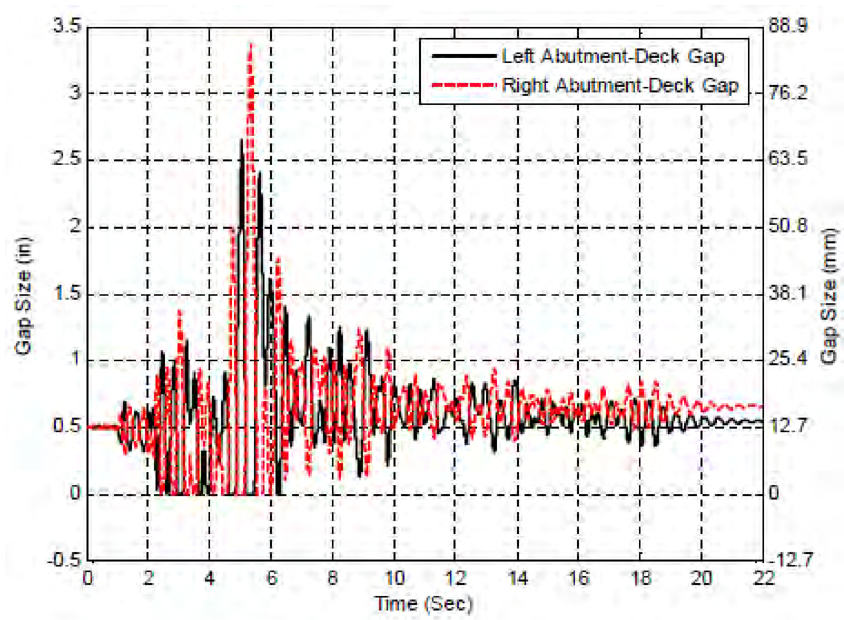

Figure 2-80 Abutment-deck gap size history (Zadeh & Saiidi, 2007).

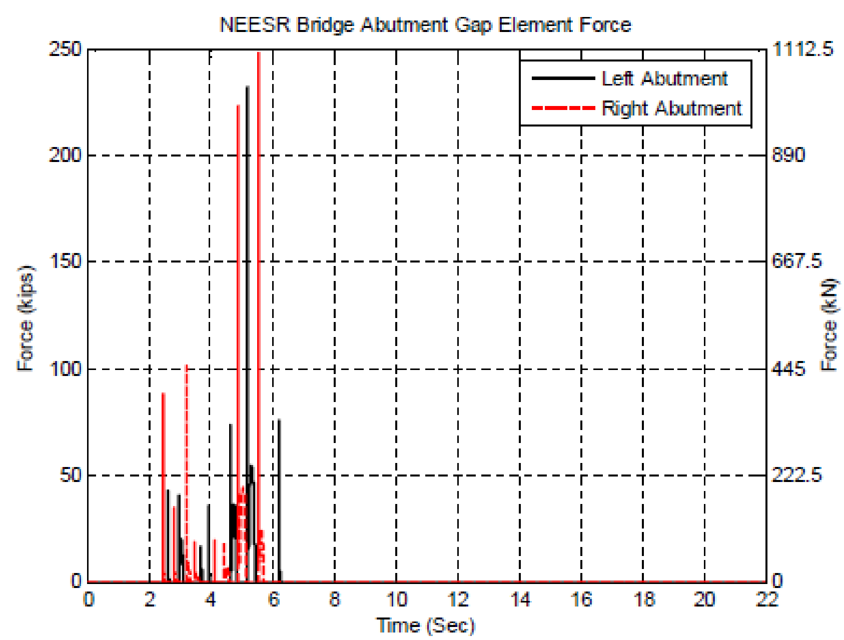

Figure 2-81 Abutment gap element (actuator) force (Zadeh & Saiidi, 2007).

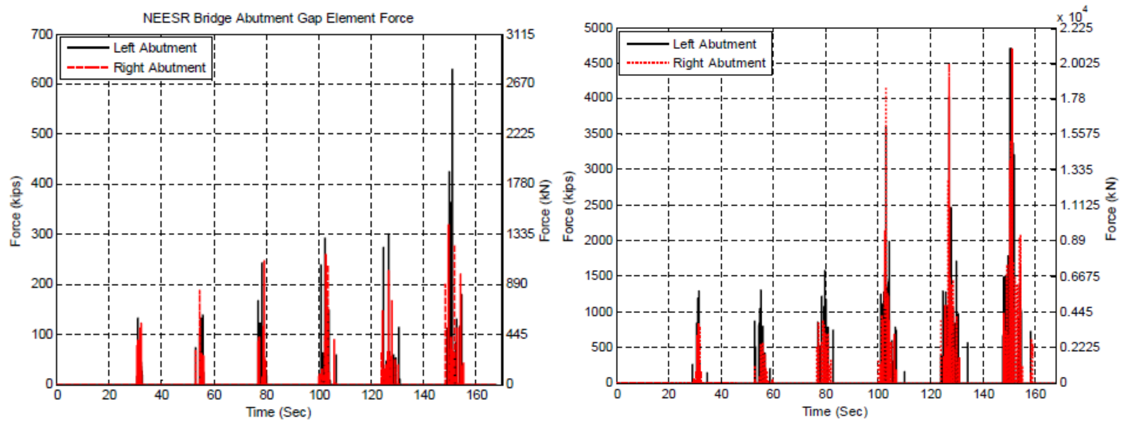

Figure 2-82 Abutment gap element force; left: Model 2, right: Model 3 (Zadeh & Saiidi, 2007).

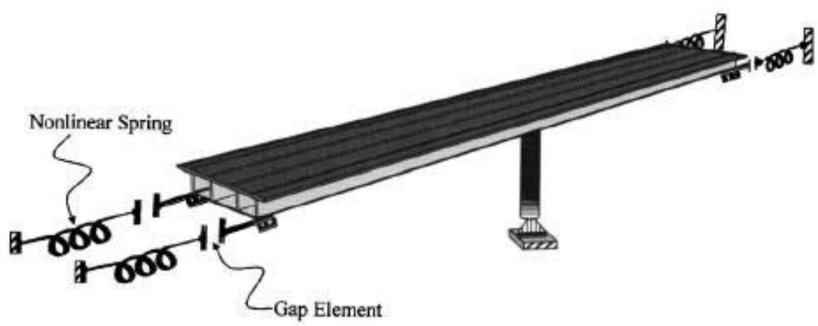

Figure 2-83 2-span bridge model (Shamsabadi et al., 2007).

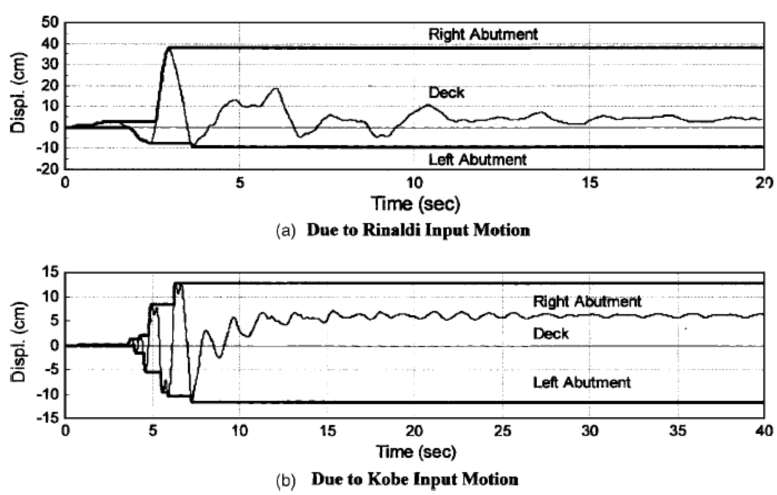

Figure 2-84 Displacement response of bridge deck and abutments (1 cm=2.54 in) (Shamsabadi et al., 2007).

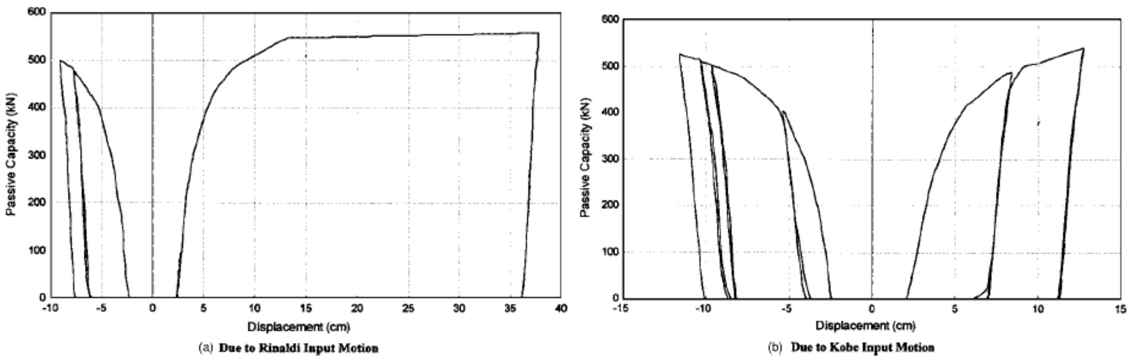

Figure 2-85 Hysteretic force-displacement response of abutments (1 cm=2.54 in, 1 kN=0.2248 kips) (Shamsabadi et al., 2007).

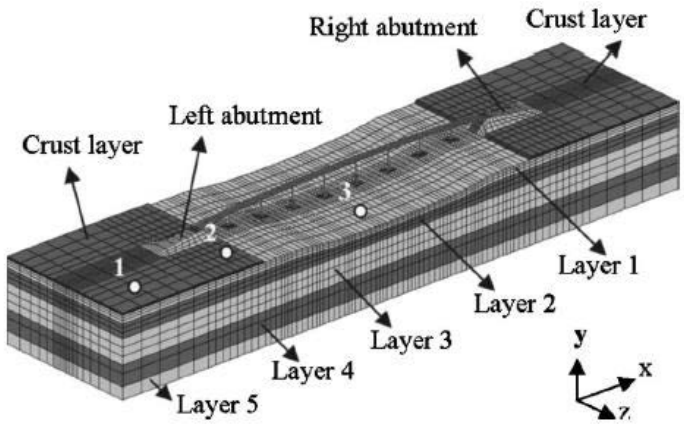

Figure 2-86 3D finite element model and idealized soil profile (Elgamal et al., 2008).

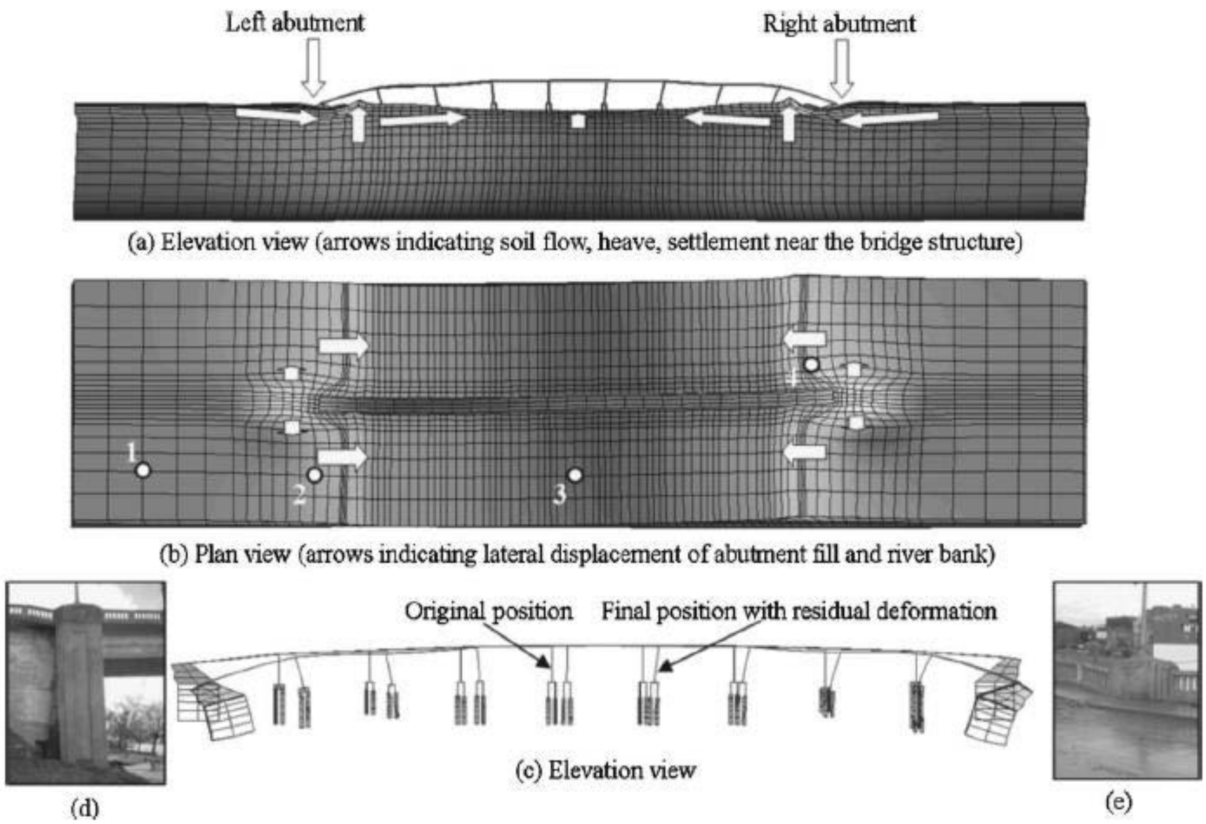

Figure 2-87 Residual deformation of bridge-foundation-ground system (Elgamal et al., 2008).

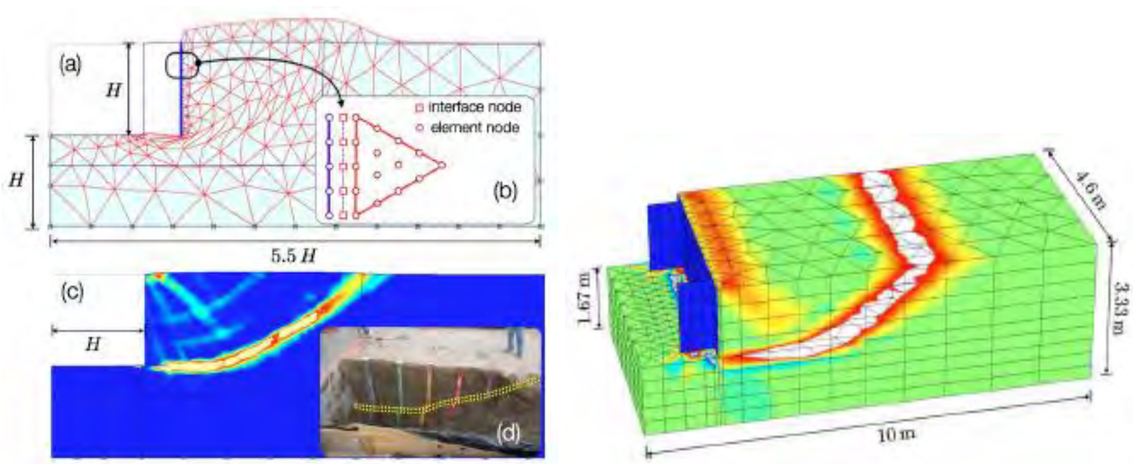

Figure 2-88 UCLA test modeling; left: a) deformed mesh of 2D model, b) interface elements, c) deviatoric shear strain distribution, d) observed failure surface; right: 3D model and) deviatoric shear strain distribution (1 m=3.28 ft) (Shamsabadi et al., 2010).

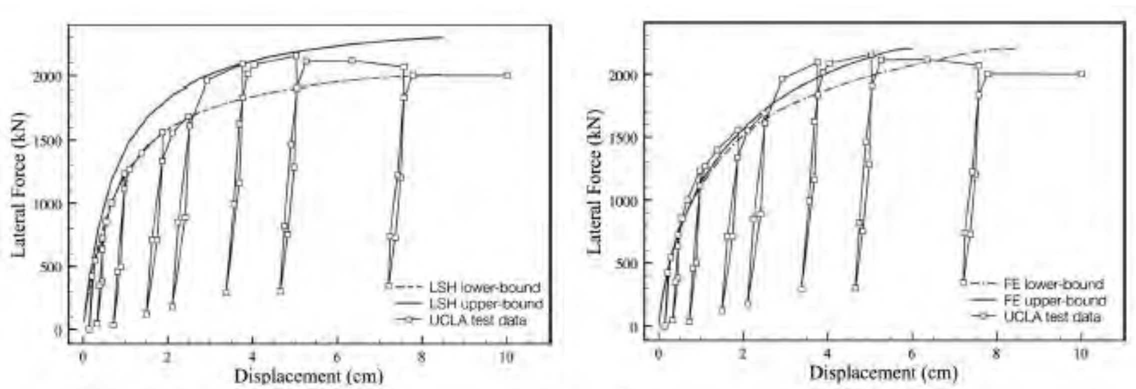

Figure 2-89 Force-displacement backbone curves of UCLA test; left: LSH model, right: 3D finite element model (1 cm=2.54 in, 1 kN=0.2248 kips) (Shamsabadi et al., 2010).

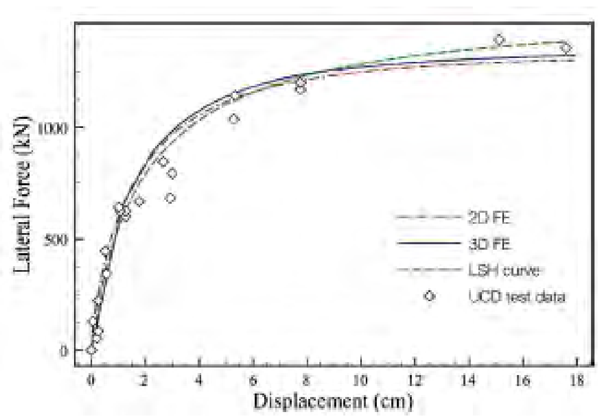

Figure 2-90 Force-displacement backbone curves of UCD test compared with LSH and finite element models (1 cm=2.54 in, 1 kN=0.2248 kips) (Shamsabadi et al., 2010).

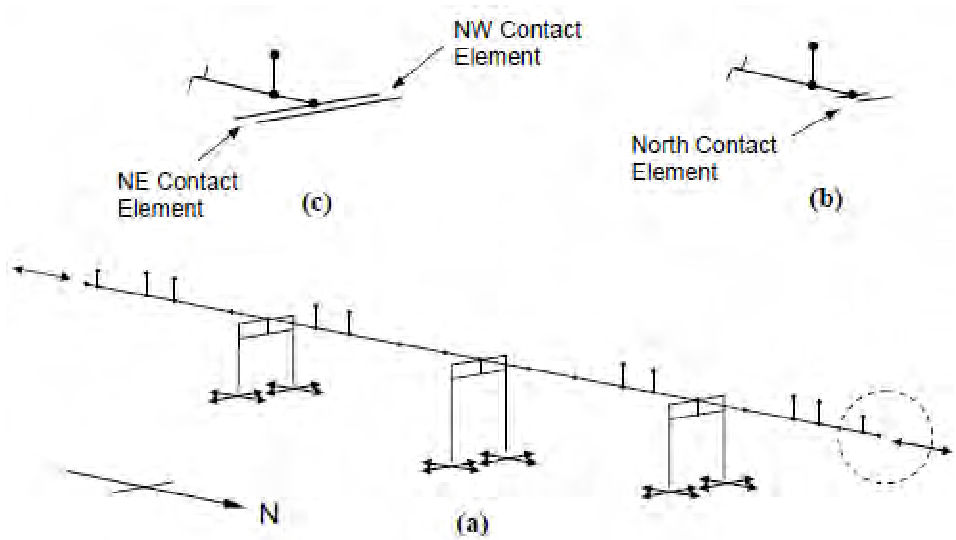

Figure 2-91 OpenSees model of the four-span bridge; a) overall model, b) North abutment with one contact element, c) North abutment with two contact elements (Ebrahimpour et al., 2011).

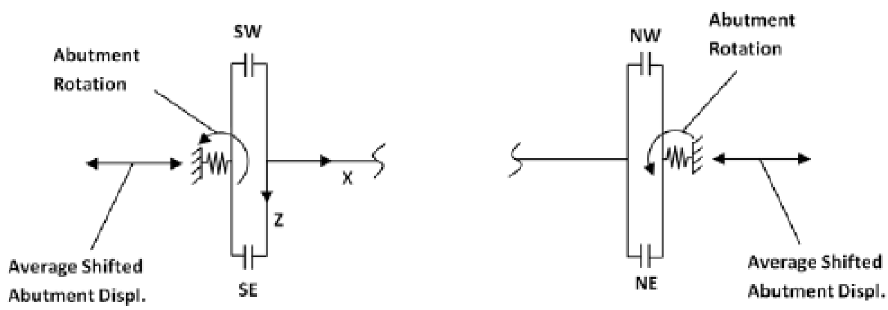

Figure 2-92 Abutment model with two contact elements (Ebrahimpour et al., 2011).

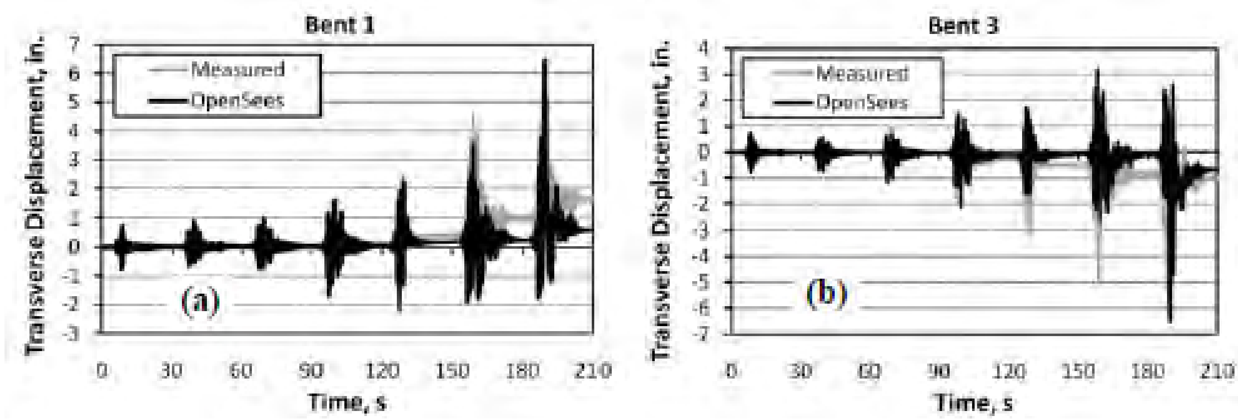

Figure 2-93 a) Bent 1 and b) Bent 3 transverse displacements with all contact elements having zero friction (Ebrahimpour et al., 2011).

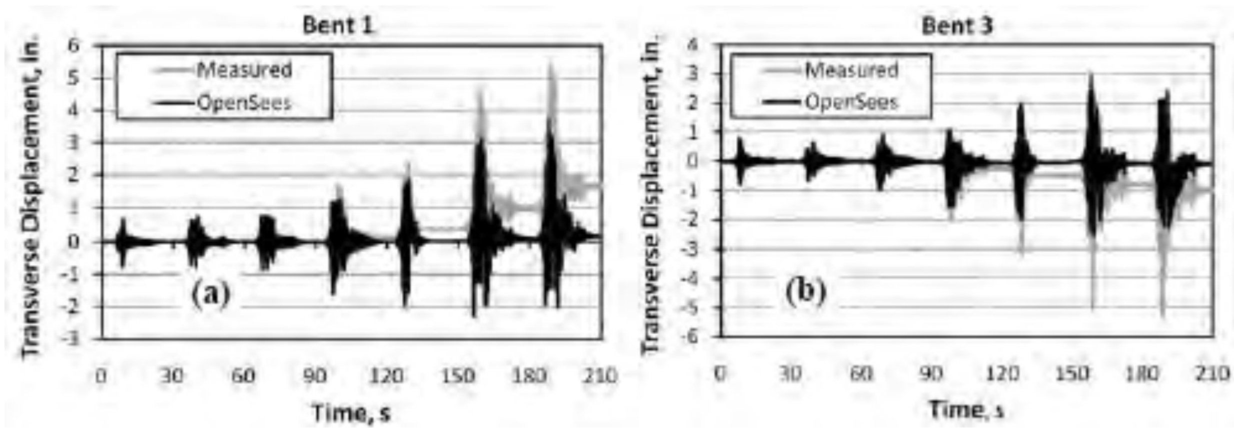

Figure 2-94 a) Bent 1 and b) Bent 3 transverse displacements with all contact elements having coefficient of friction of 0.1 (Ebrahimpour et al., 2011).

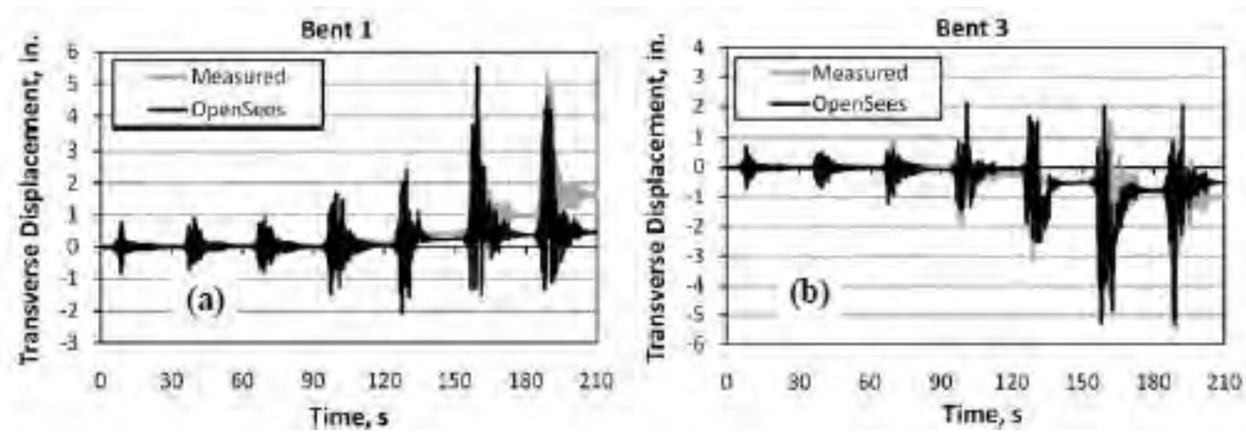

Figure 2-95 a) Bent 1 and b) Bent 3 transverse displacements for the case with friction at NE and SW contact elements with friction coefficient of 0.9 (Ebrahimpour et al., 2011).

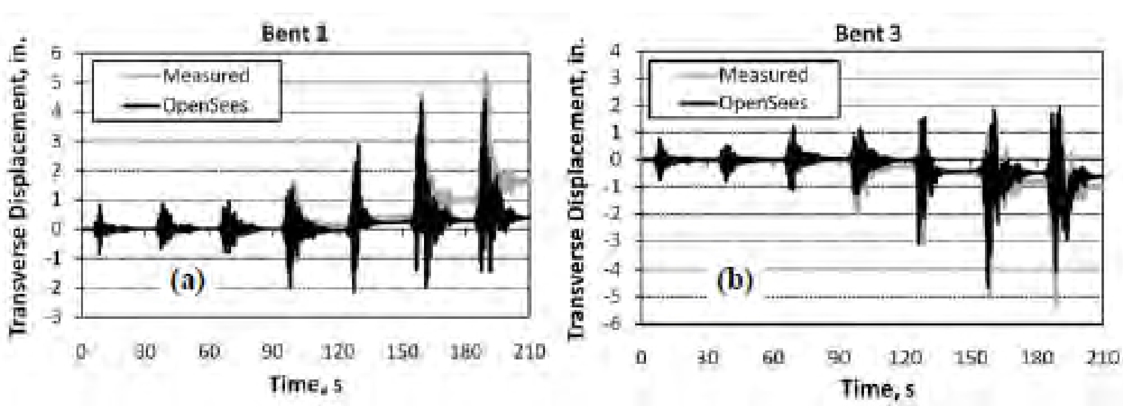

Figure 2-96 a) Bent 1 and b) Bent 3 transverse displacements for the model with localized damping, friction at NE and SW contact elements with friction coefficient of 0.7 (Ebrahimpour et al., 2011).

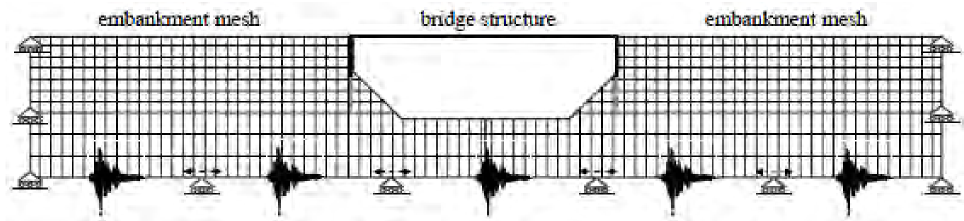

Figure 2-97 2D continuum finite element model of an IAB for time history analysis (Carvajal Uribe, 2011).

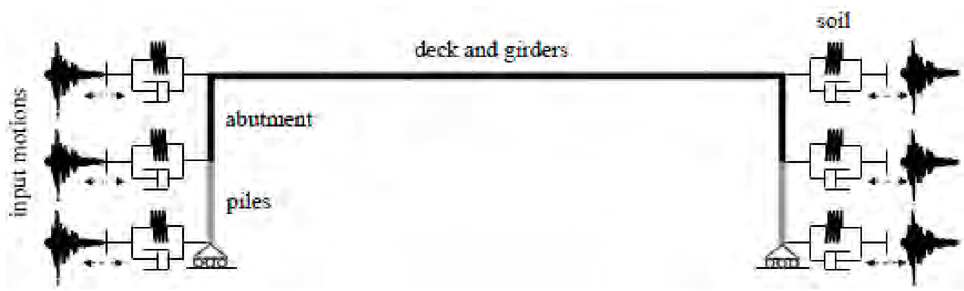

Figure 2-98 Frame-spring-dashpot model of an IAB for time history analysis (Carvajal Uribe, 2011).

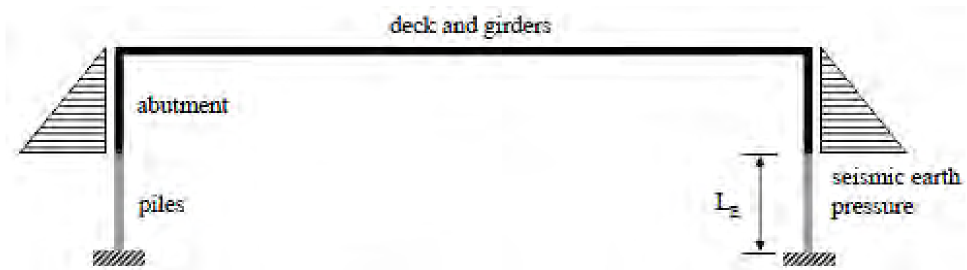

Figure 2-99 Frame model of an IAB for pseudo-static analysis (Carvajal Uribe, 2011).

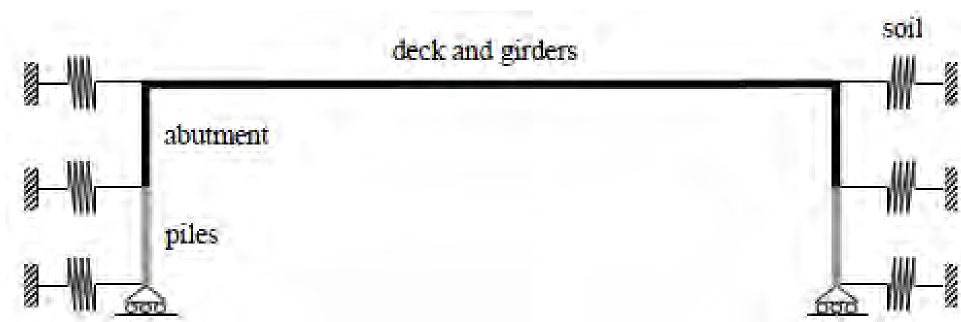

Figure 2-100 Frame-spring model of an IAB for pseudo-static analysis (Carvajal Uribe, 2011).

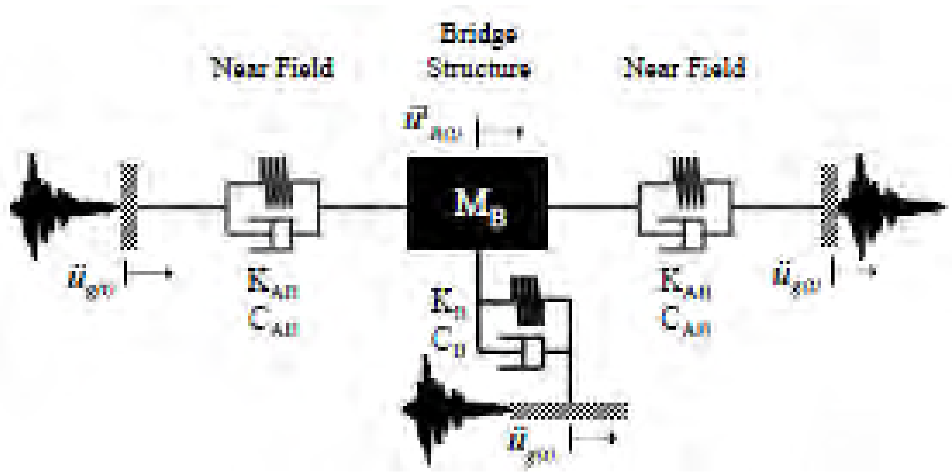

Figure 2-101 Proposed single mass-spring-dashpot system (Carvajal Uribe, 2011).

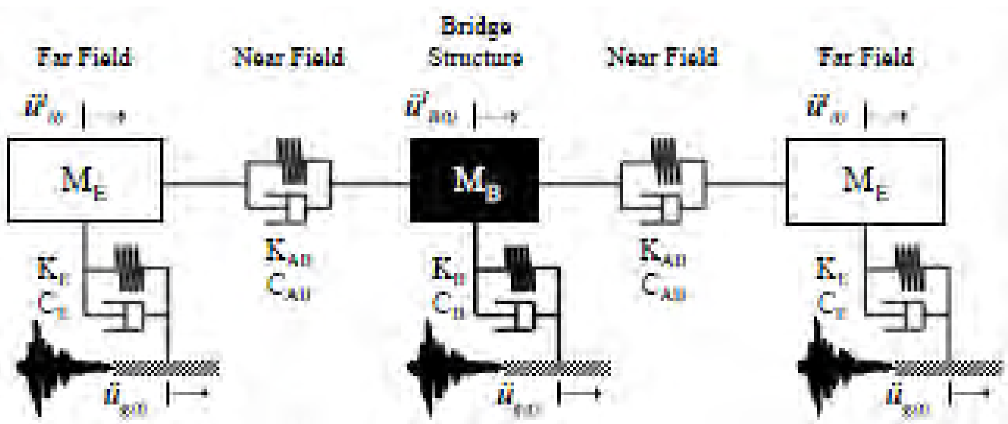

Figure 2-102 Proposed three-degree of freedom mass-spring-dashpot system (Carvajal Uribe, 2011).

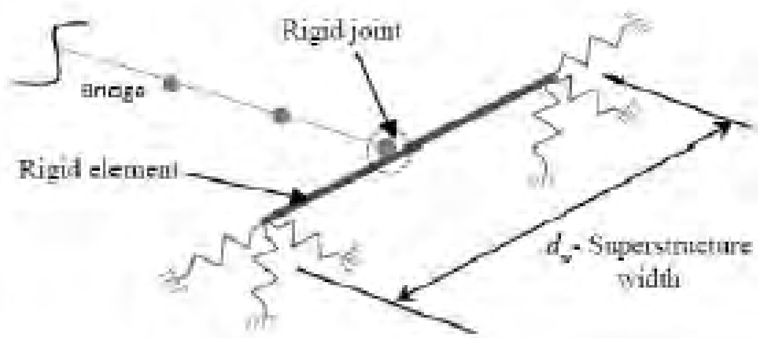

Figure 2-103 Elastic abutment model (Lu et al., 2012).

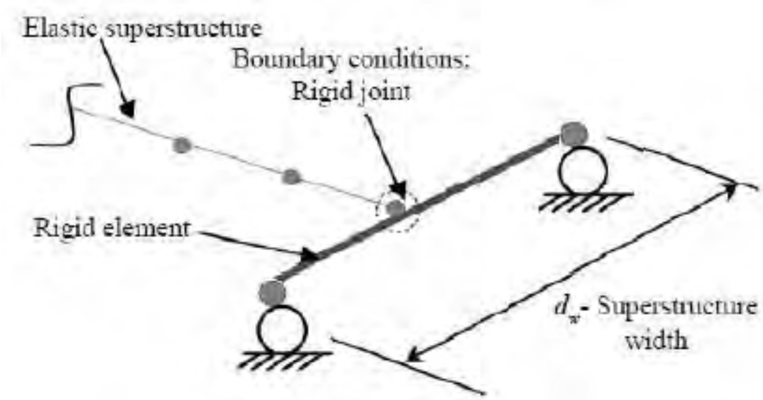

Figure 2-104 Roller abutment model (Lu et al., 2012).

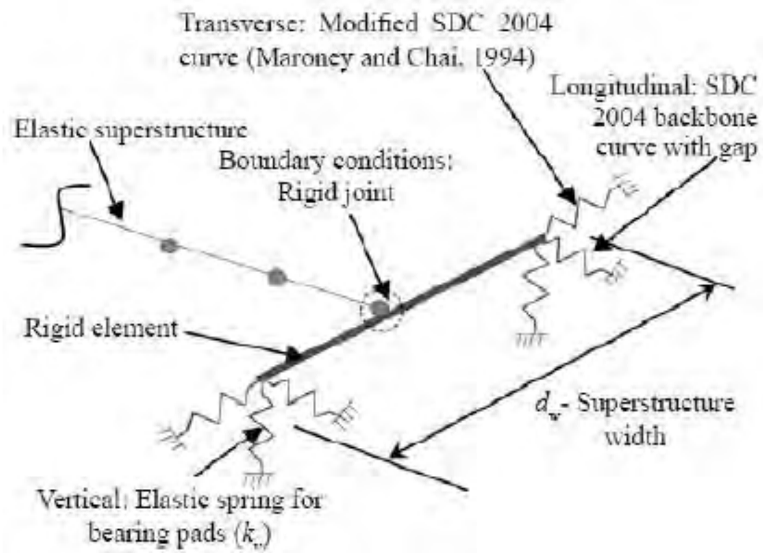

Figure 2-105 Simplified abutment model (Lu et al., 2012).

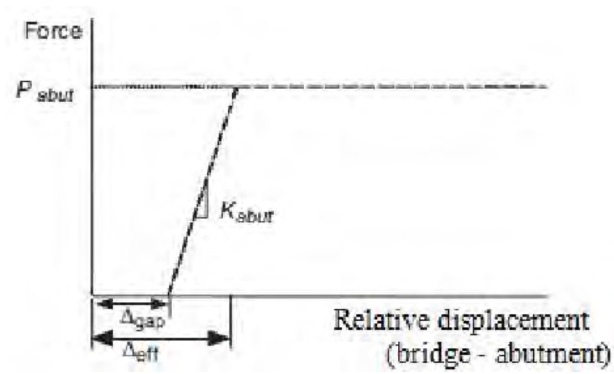

Figure 2-106 Longitudinal backbone curve of force-displacement relationship (Lu et al., 2012).

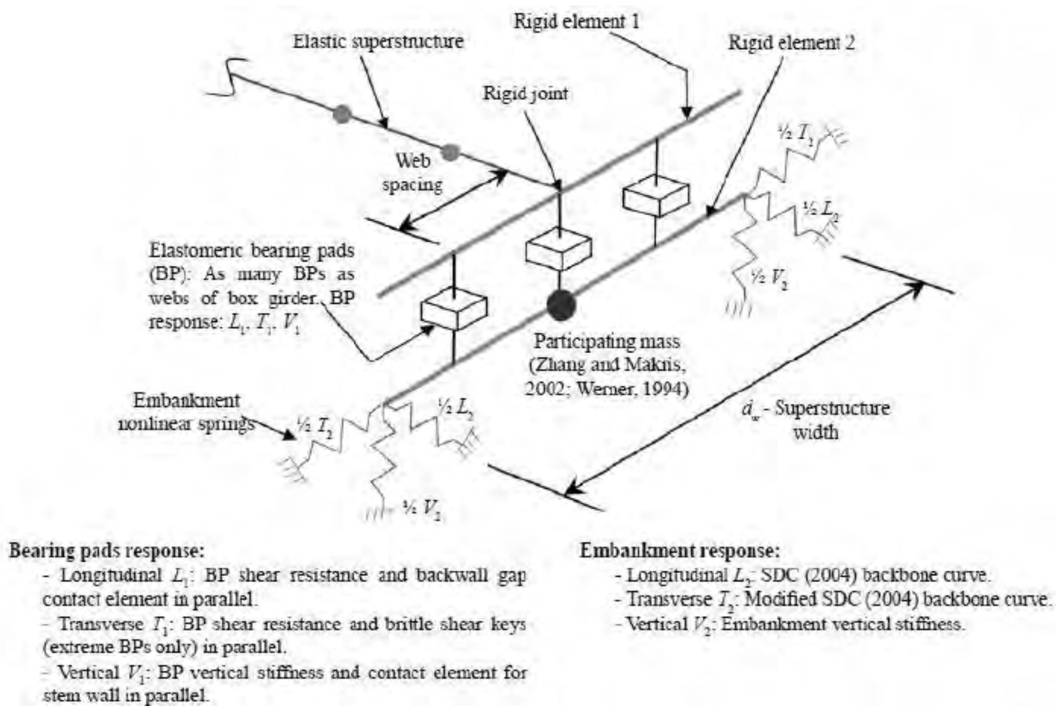

Figure 2-107 Spring abutment model (Lu et al., 2012).

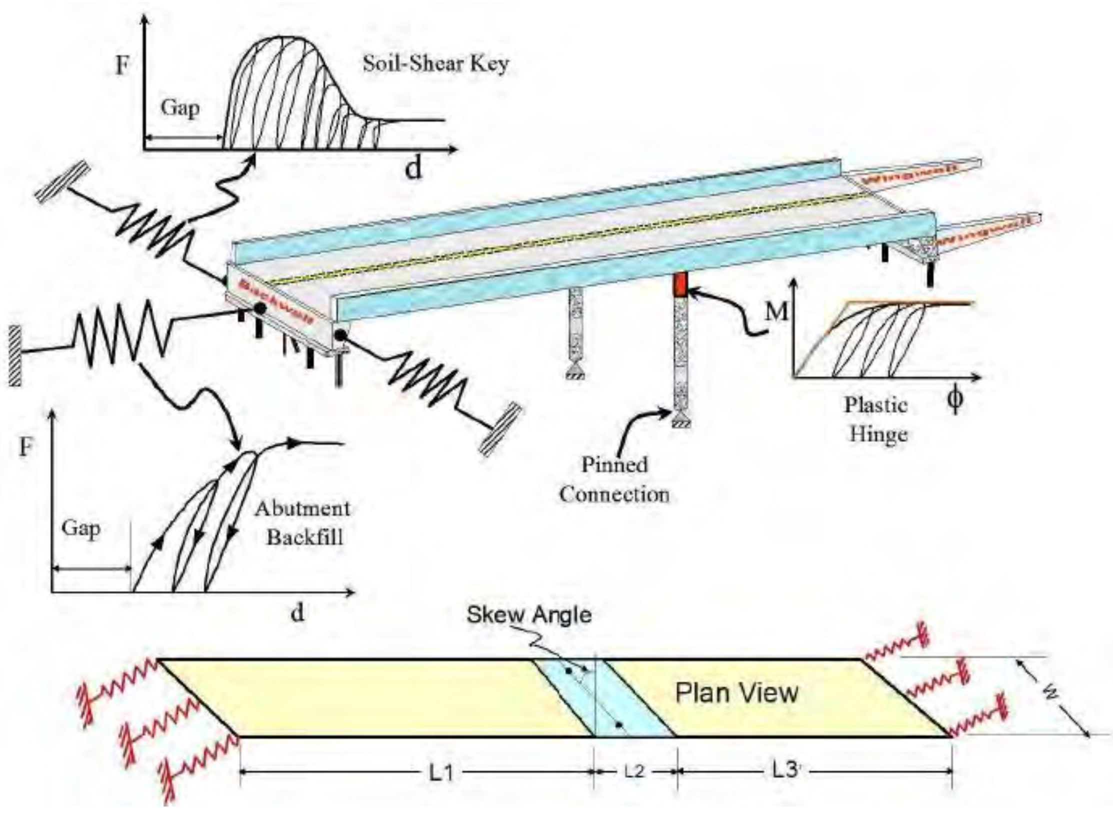

Figure 2-108 Schematic components of bridge system (Shamsabadi & Yan, 2007).

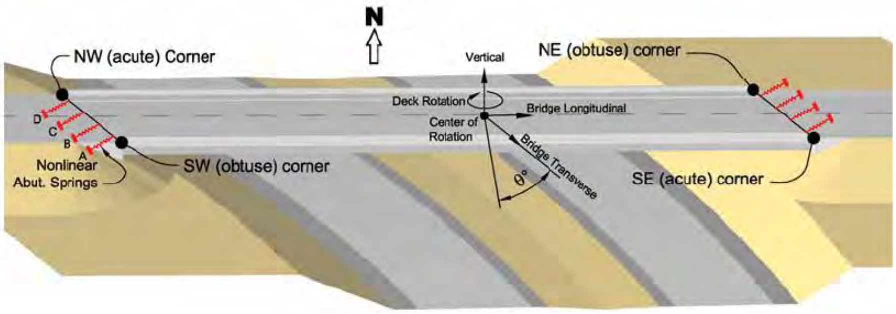

(a) 3-D Geometry

(b) Analytical Model

Figure 2-109 Single-span bridge with 45º skew angle (Shamsabadi & Yan, 2007).

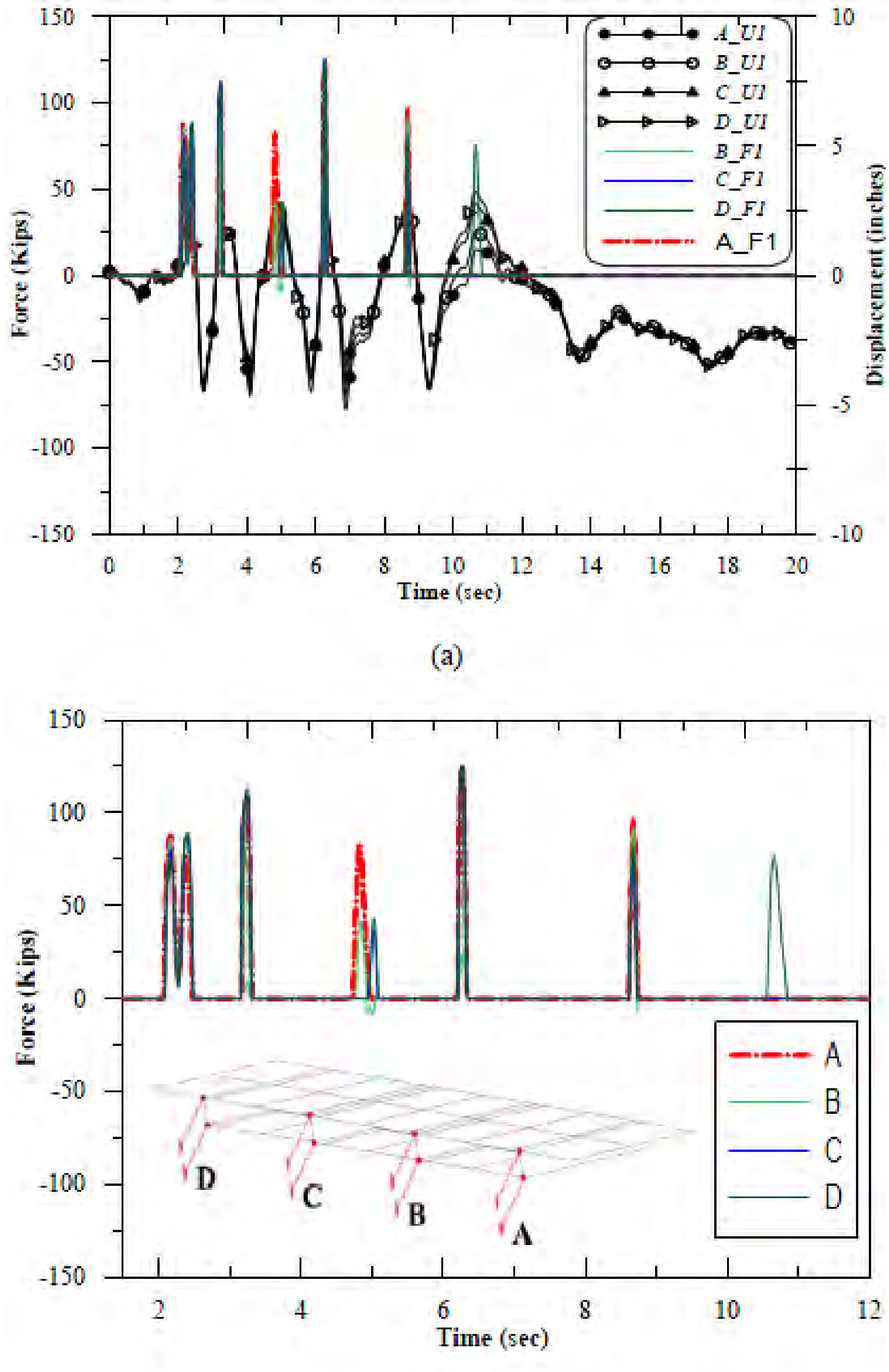

(a)

(b)

Figure 2-110 Variations of normal abutment forces for a single-span bridge with 0º skew angle (Shamsabadi & Yan, 2007).

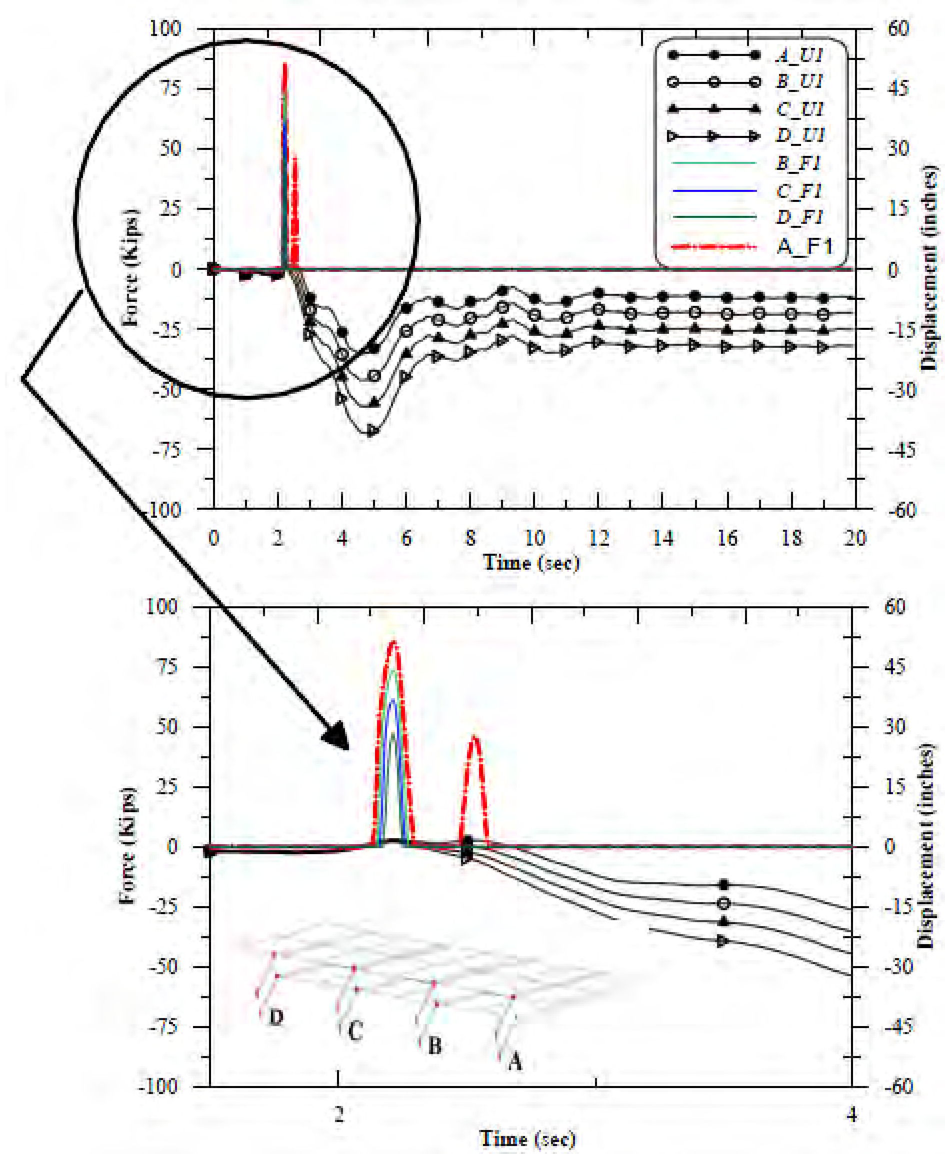

Figure 2-111 Variations of normal abutment impact forces for a single-span bridge with 45º skew angle during the first 4 seconds of shaking (Shamsabadi & Yan, 2007).

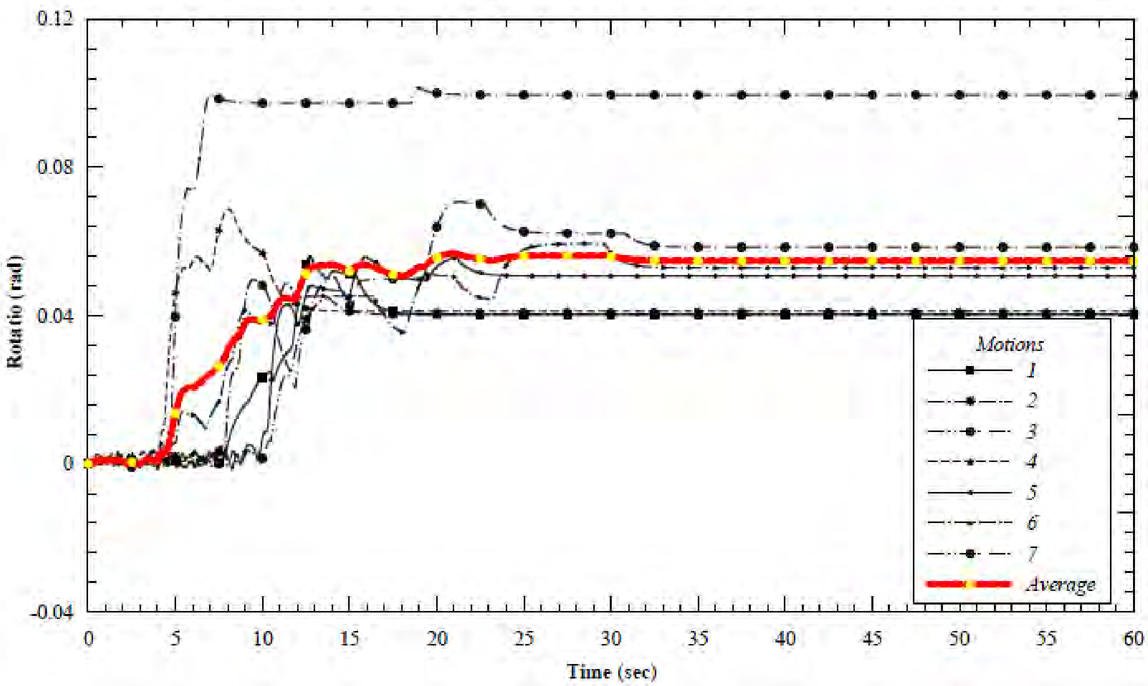

Figure 2-112 Rotation time history of single-span bridge with 45º skew angle (Shamsabadi & Yan, 2007).

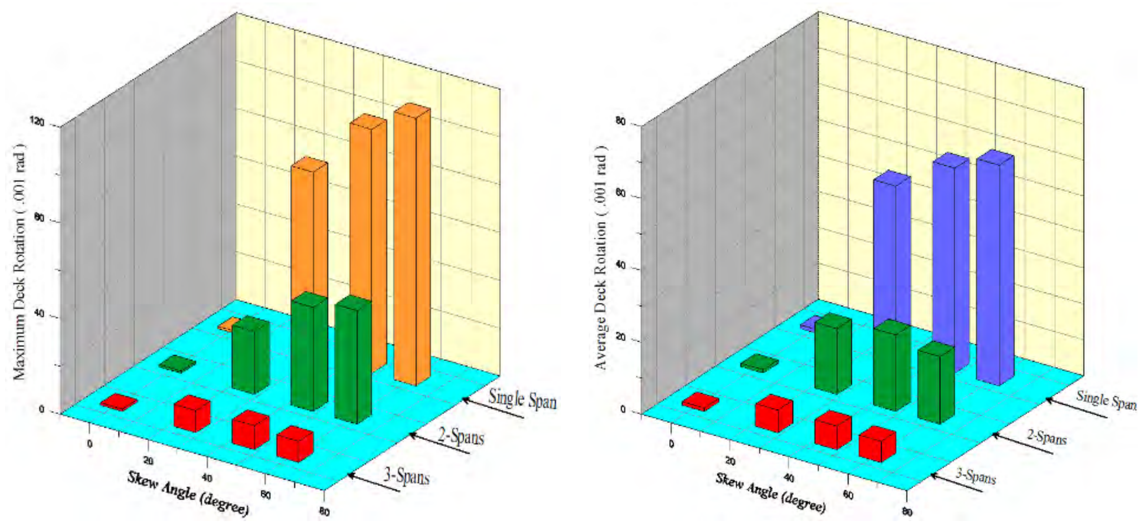

Figure 2-113 Comparison of maximum and average residual deck rotation for different types of studied bridges (Shamsabadi & Yan, 2007).

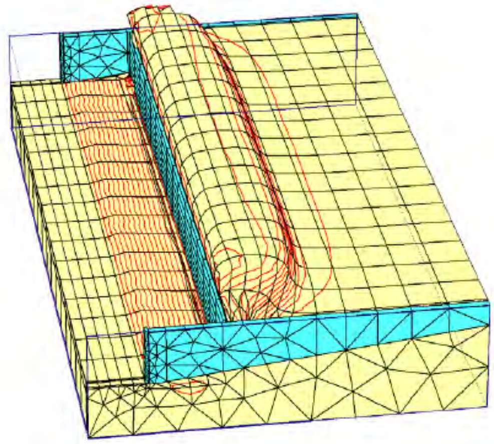

(a)

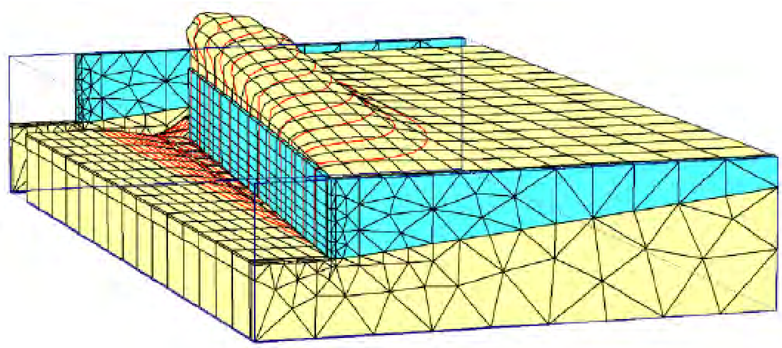

(b)

Figure 2-114 Deformed mesh and displacement contours: (a) non-skewed, and (b) skewed (Shamsabadi & Kapuskar, 2008).

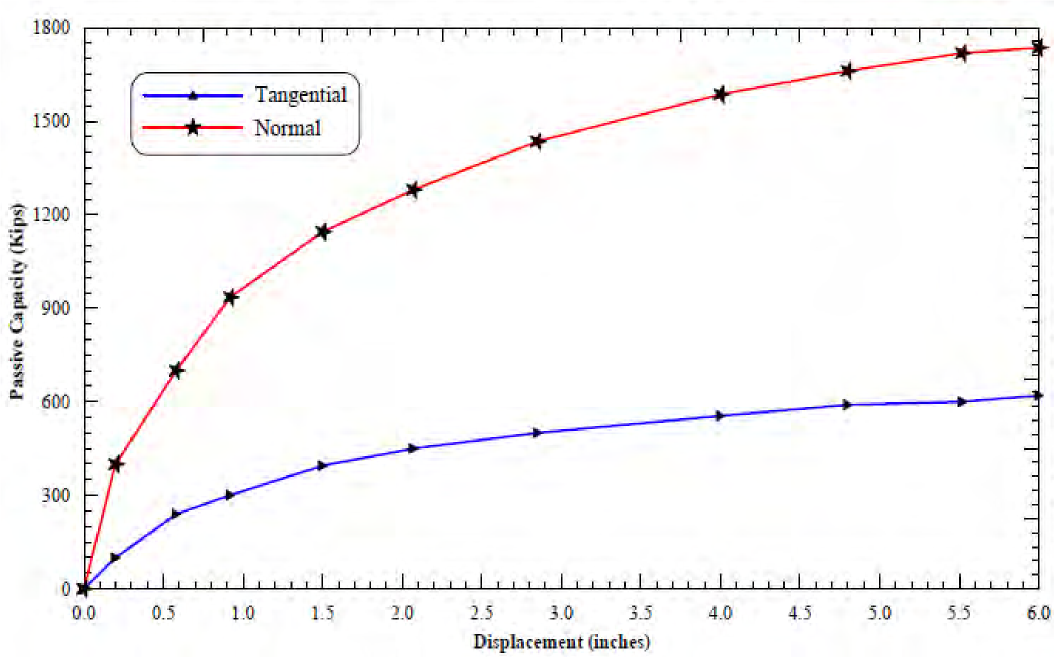

Figure 2-115 Normal and tangential components of passive resistance for a 30º skew angle (Shamsabadi & Kapuskar, 2008).

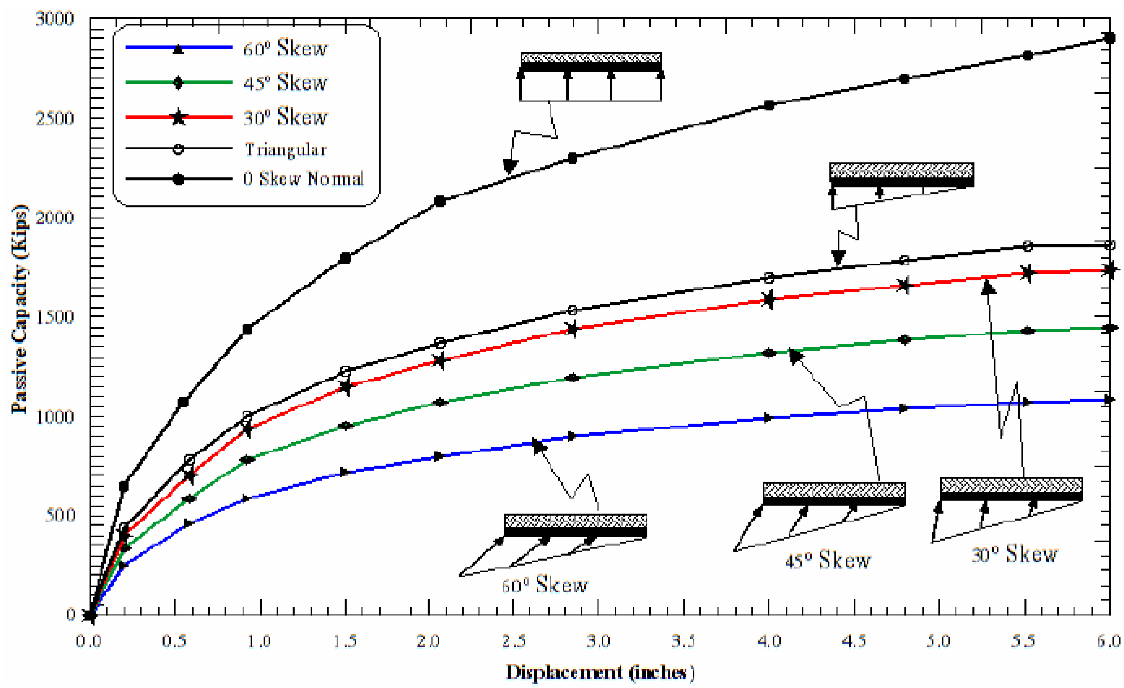

Figure 2-116 Impact of skew angle on the normal component of passive resistance (Shamsabadi & Kapuskar, 2008).

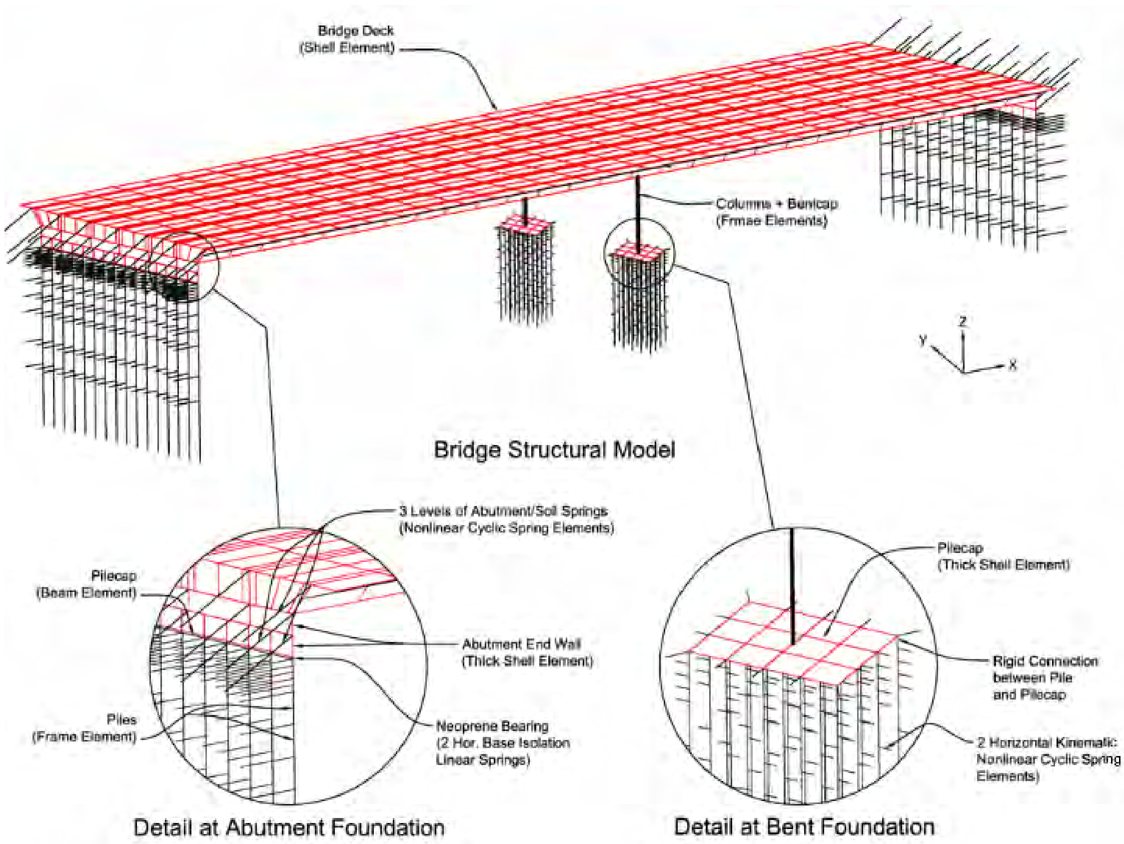

Figure 2-117 Painter street bridge model (Shamsabadi & Yan, 2008).

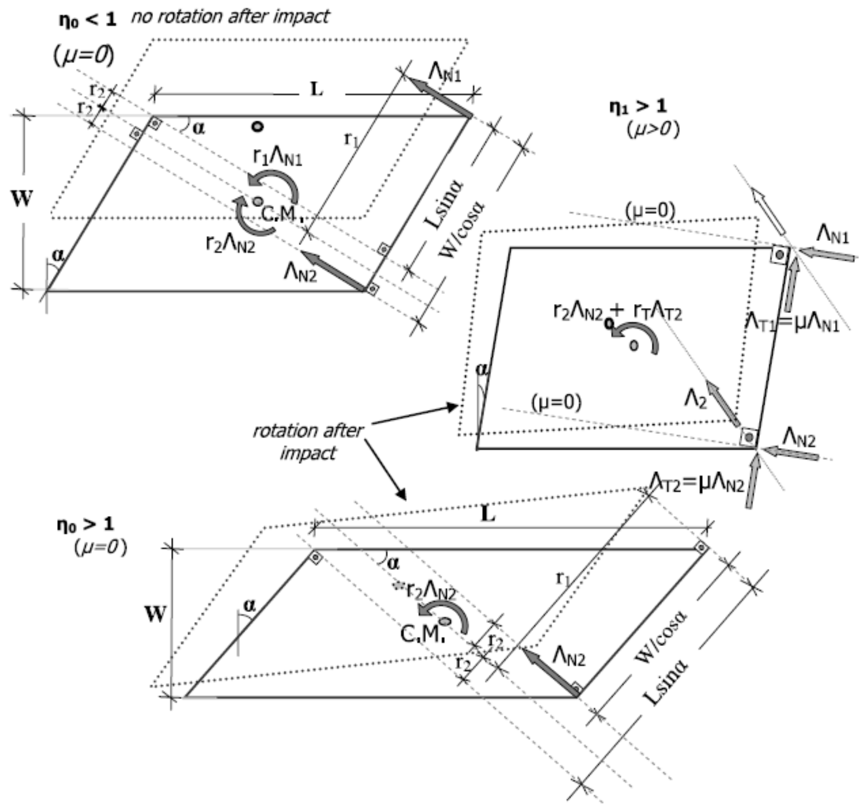

Figure 2-118 Geometrical interpretation of rotational mechanism by deck-abutment impact in skew bridges (Dimitrakopoulos, 2011).

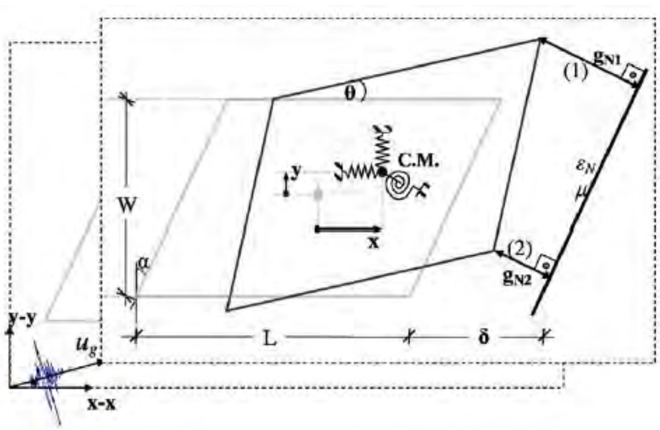

Figure 2-119 Relative distance of the two potential contacts for planar motion of a skewed bridge deck (Dimitrakopoulos, 2011).

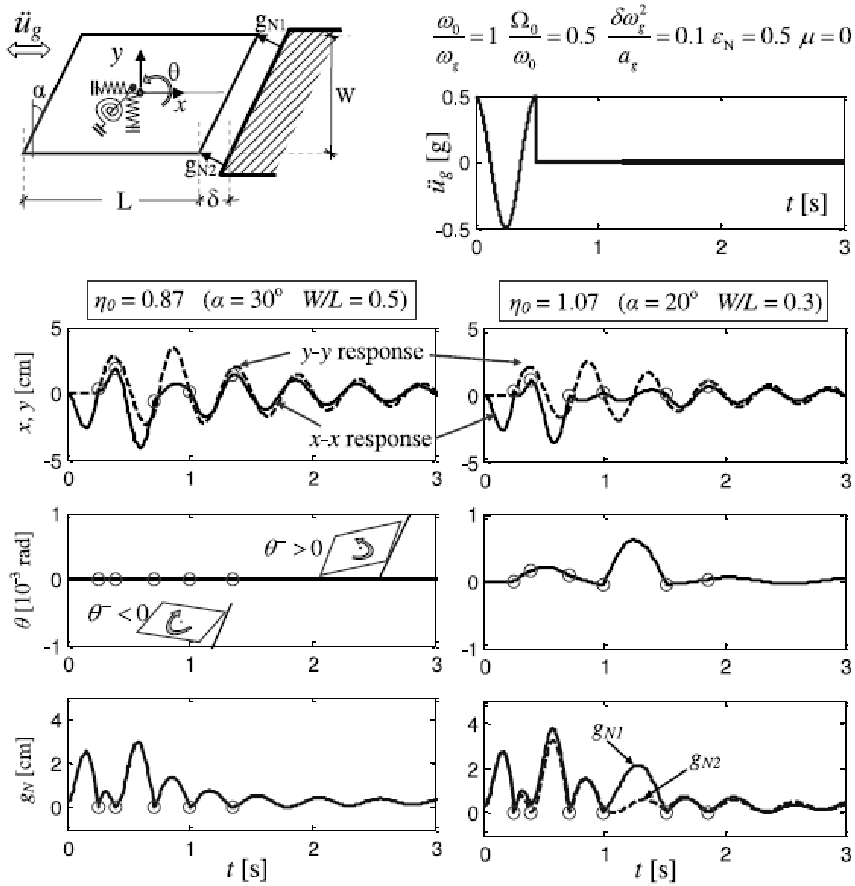

Figure 2-120 Seismic response of skewed bridge for frictionless contact (1 cm=2.54 in) (Dimitrakopoulos, 2011).

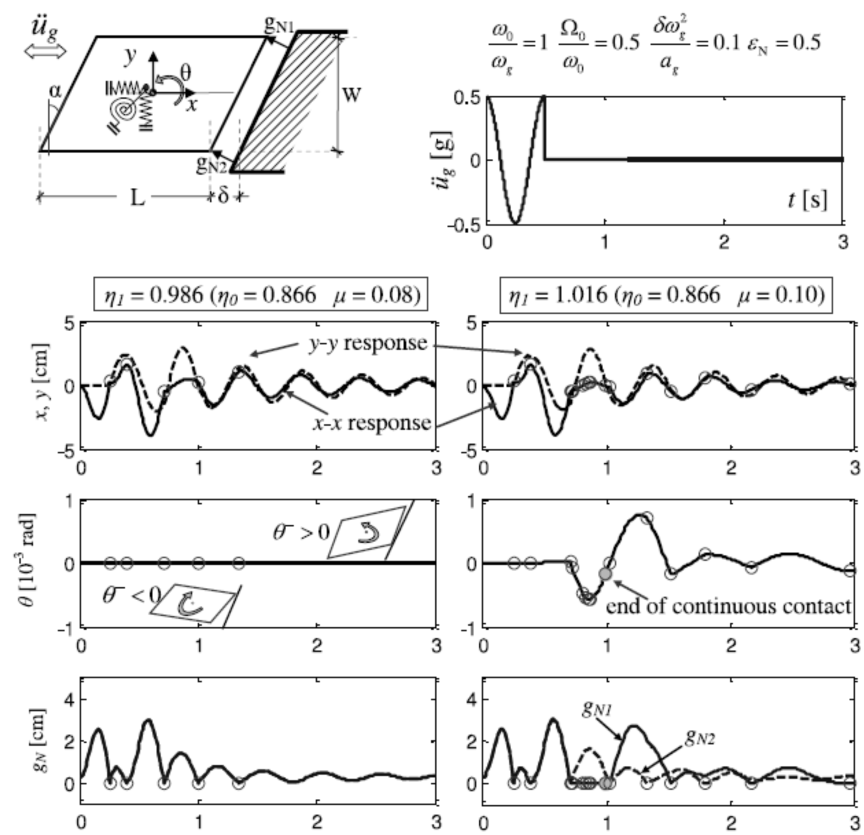

Figure 2-121 Seismic response of skewed bridge for frictional contact (1 cm=2.54 in) (Dimitrakopoulos, 2011).

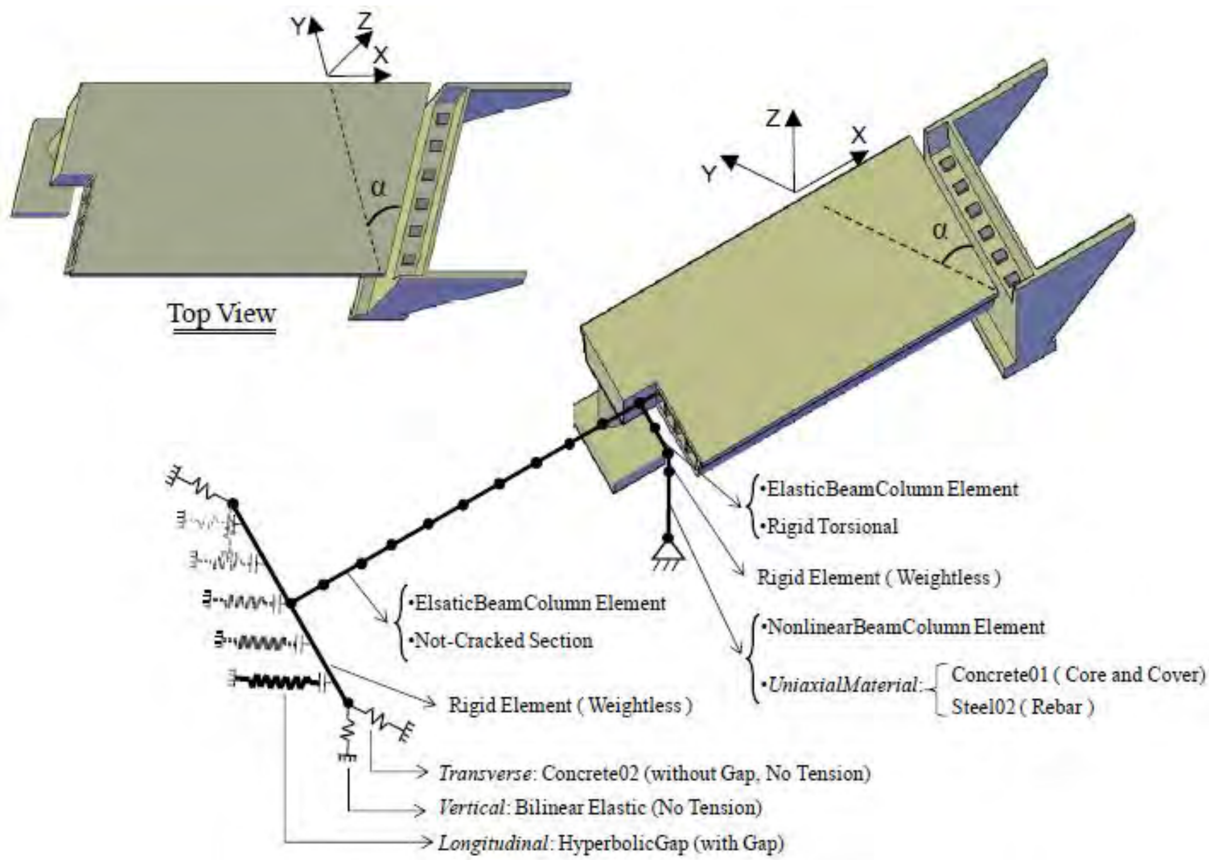

Figure 2-122 Schematic model of skewed bridge (Kavianijapori, 2011).

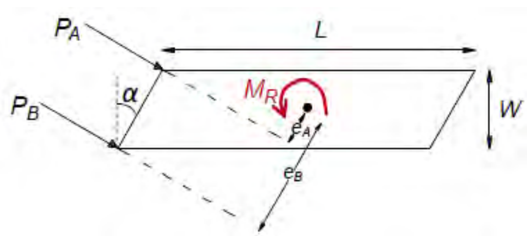

Figure 2-123 Rotational moment due to abutment impact forces (Kavianijapori, 2011).

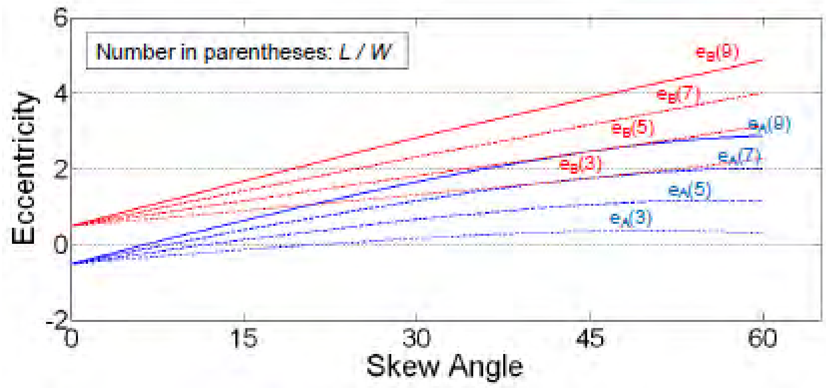

Figure 2-124 Effect of skew angle on eccentricity parameters (Kavianijapori, 2011).

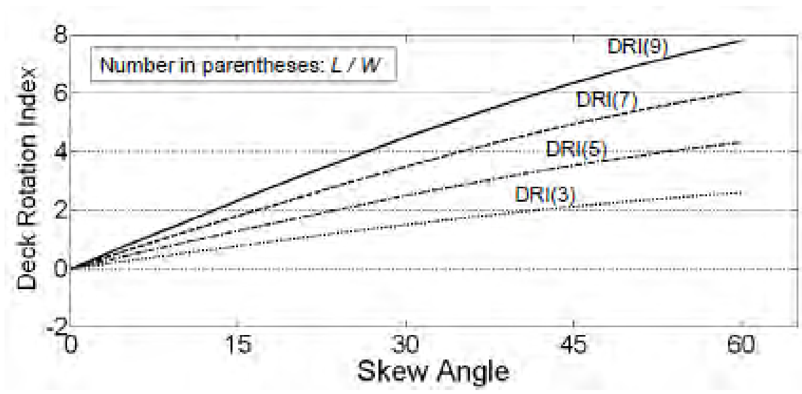

Figure 2-125 Effect of skew angel on deck rotation index (Kavianijapori, 2011).

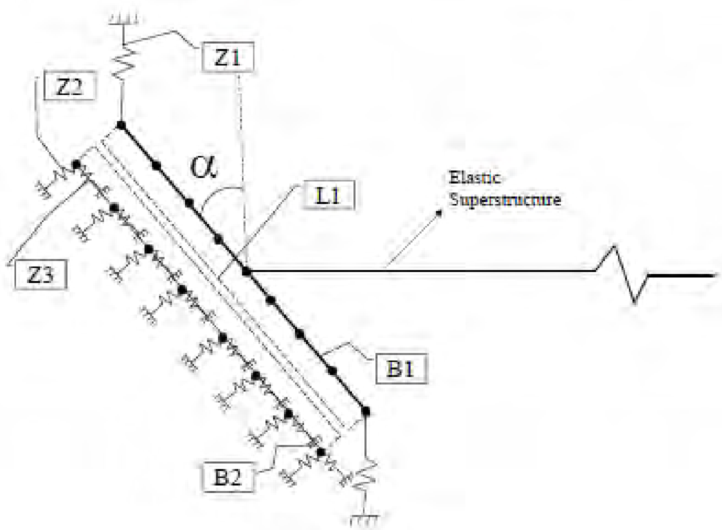

Figure 2-126 Friction abutment model (Kavianijapori, 2011).

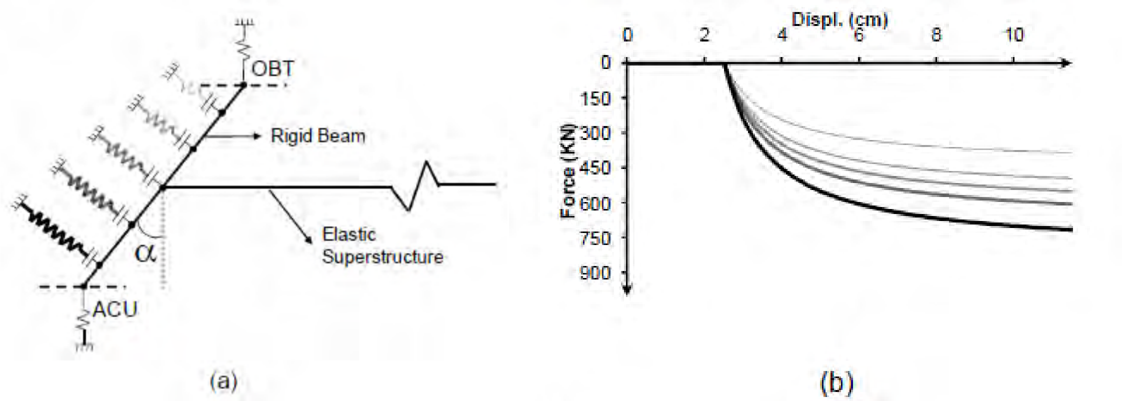

Figure 2-127 a) Skewed abutment model; b) Variable force-displacement relationships of springs (Kavianijapori, 2011).

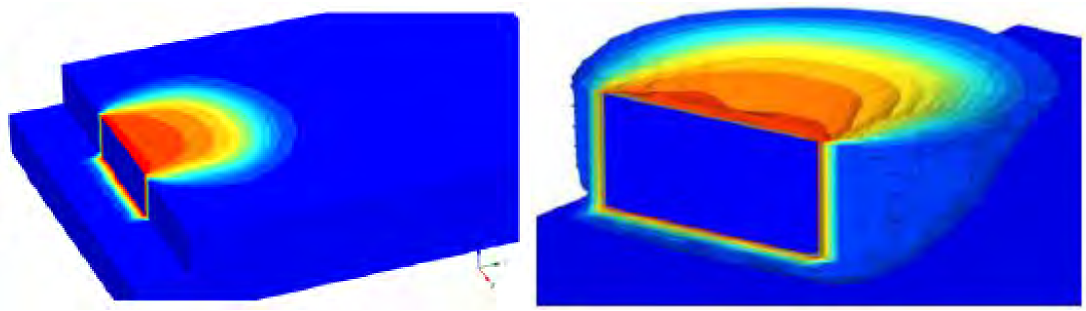

(a)

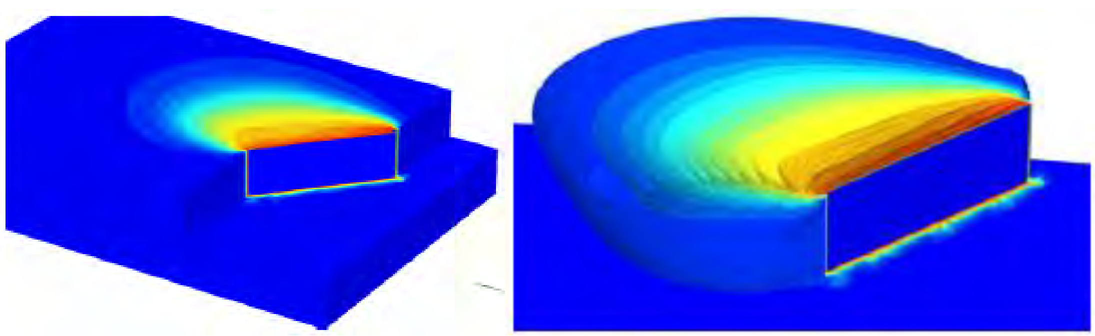

(b)

Figure 2-128 Displacemnt contours and 3D passive wedges: (a) 0° skew, and (b) 45° skew (Shamsabadi & Rolllins, 2014).

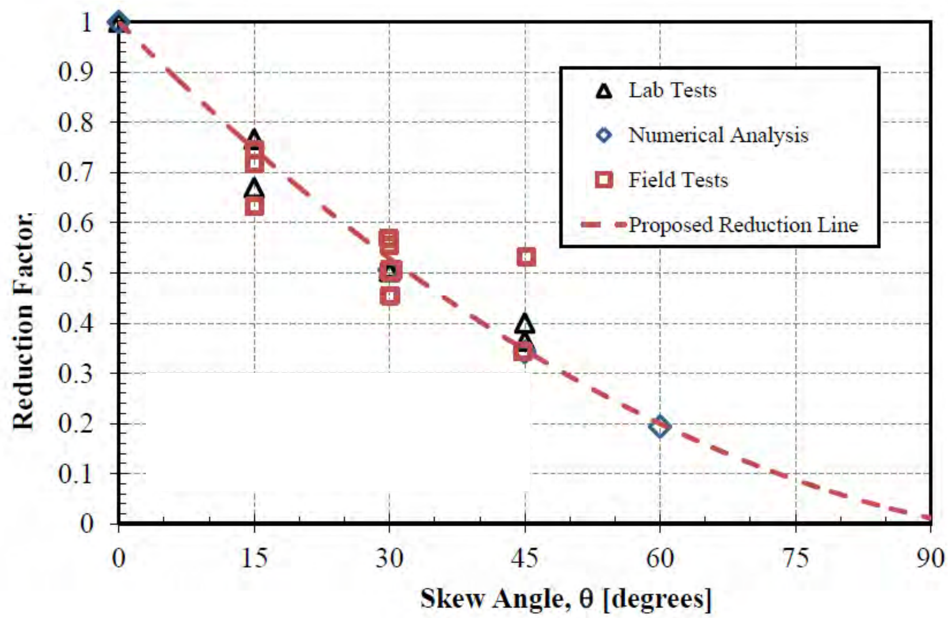

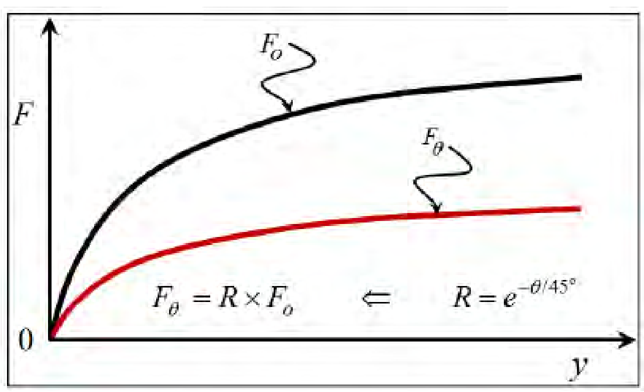

Figure 2-129 Capacity reduction factor of backbone curve due to the skew (Shamsabadi & Rollins, 2014).

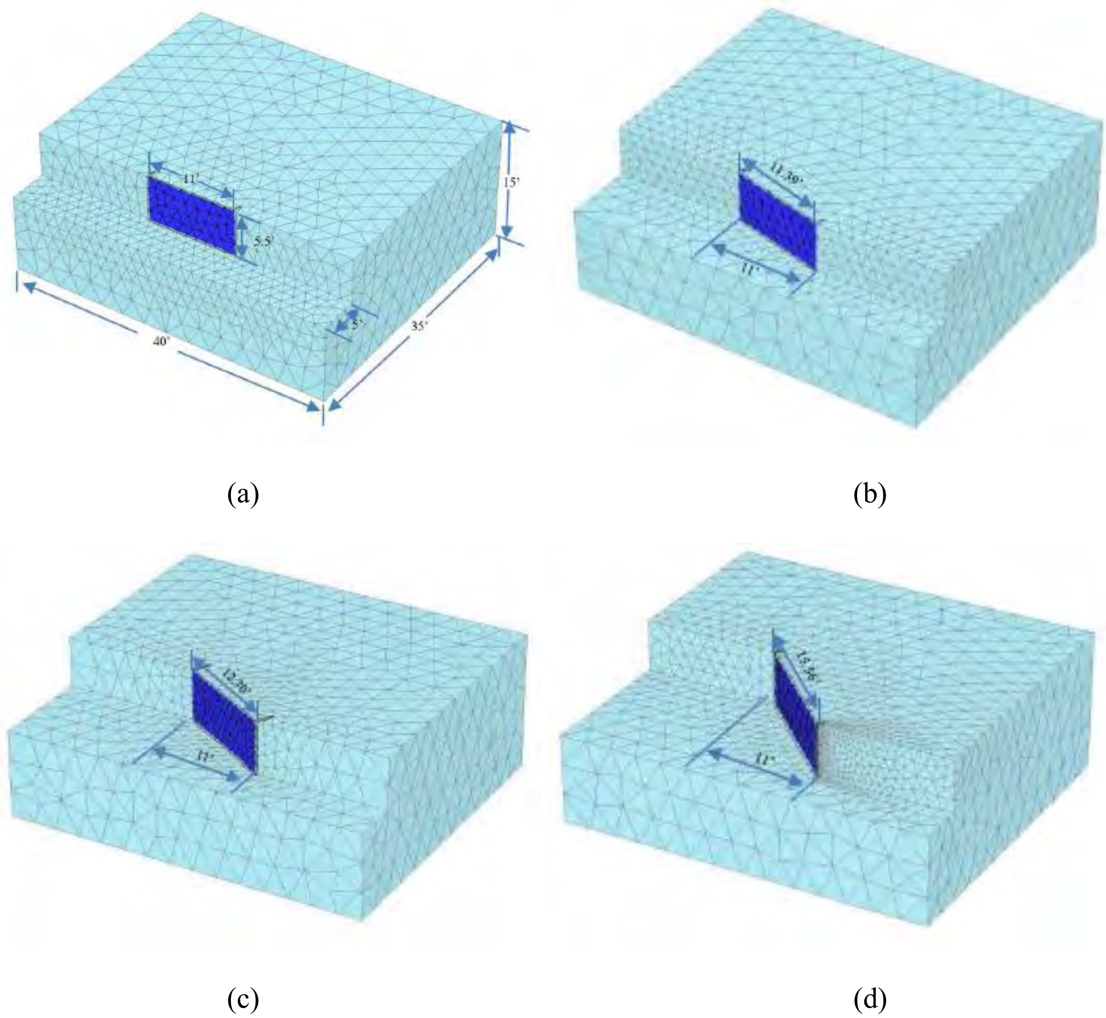

Figure 2-130 Analytical models in PLAXIS3D: (a) 0° skew, (b) 15° skew, (c) 30° skew, and (d) 45° skew (Guo, 2015).

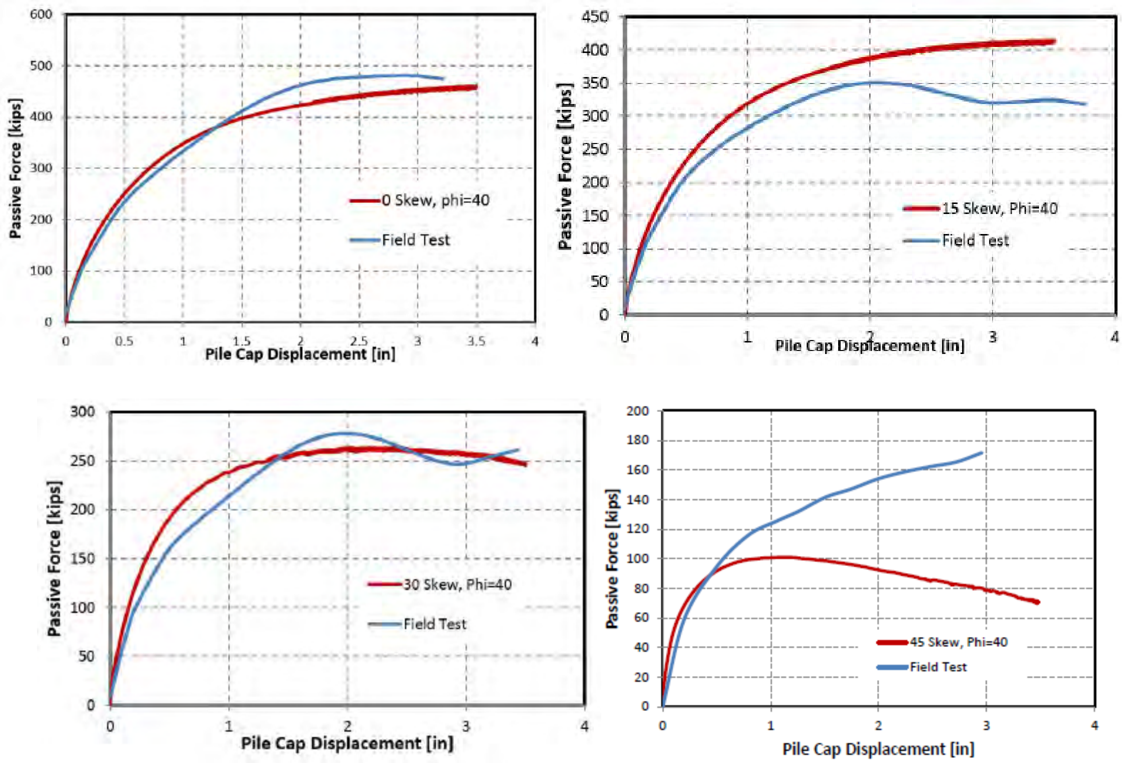

Figure 2-131 Analytical force-displacement curves compared to the test data (Guo, 2015).

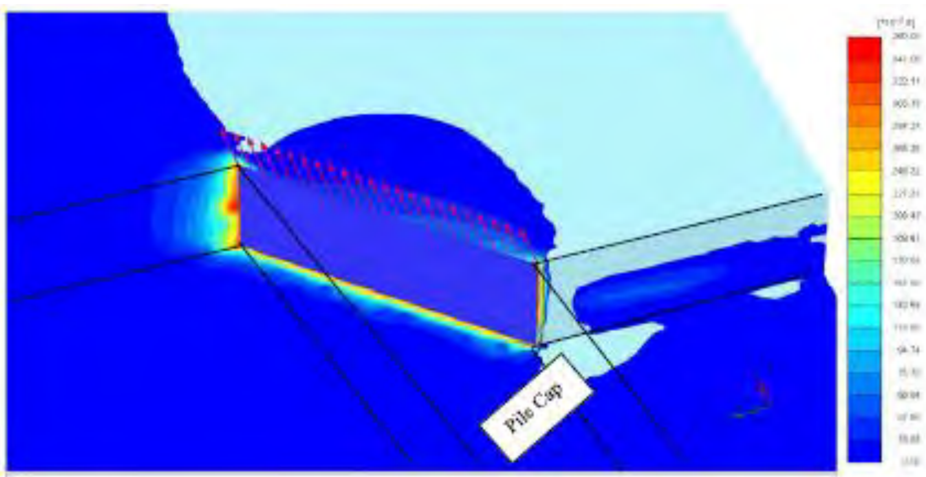

Figure 2-132 Abutment sliding in the 45° skew model (Guo, 2015).

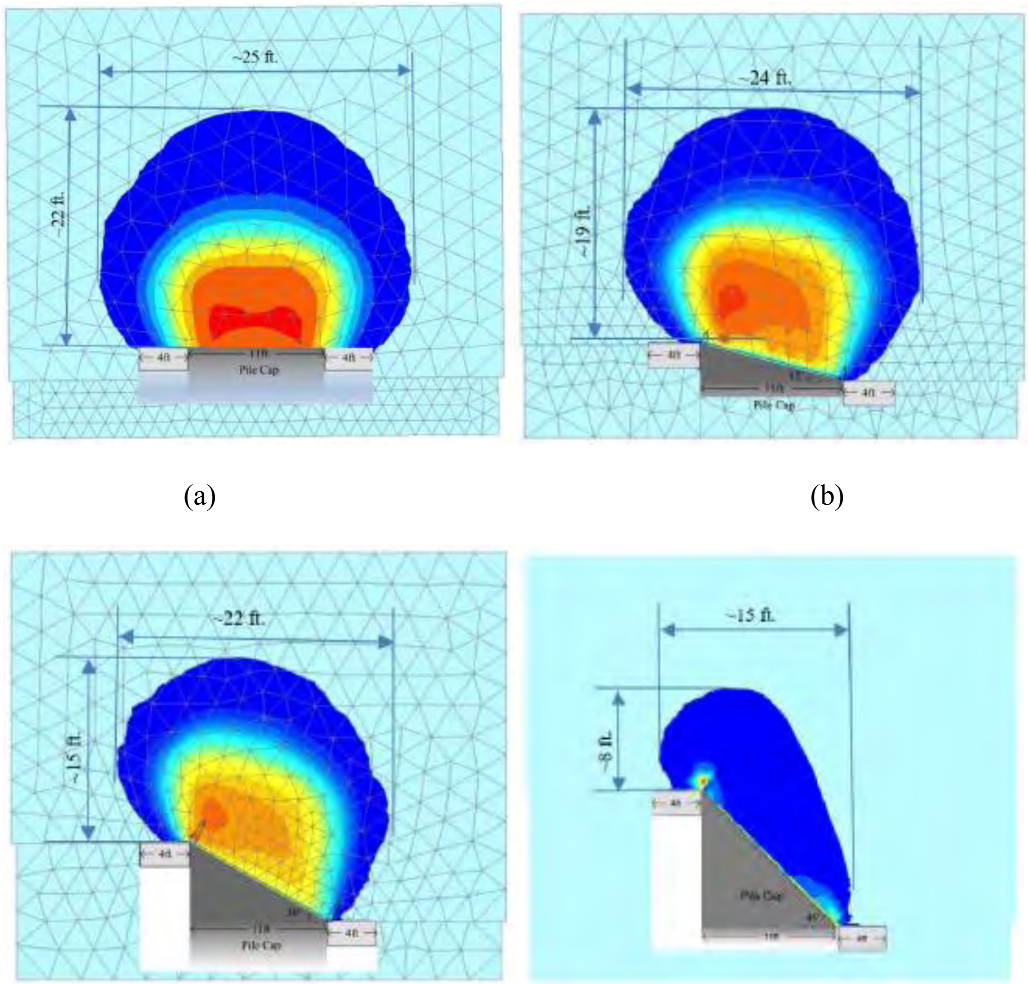

(a) (b)

(c) (d)

Figure 2-133 Heave contours of analytical models in PLAXIS3D: (a) 0°, (b) 15°, (c) 30°, and (d) 45° skew (Guo, 2015).

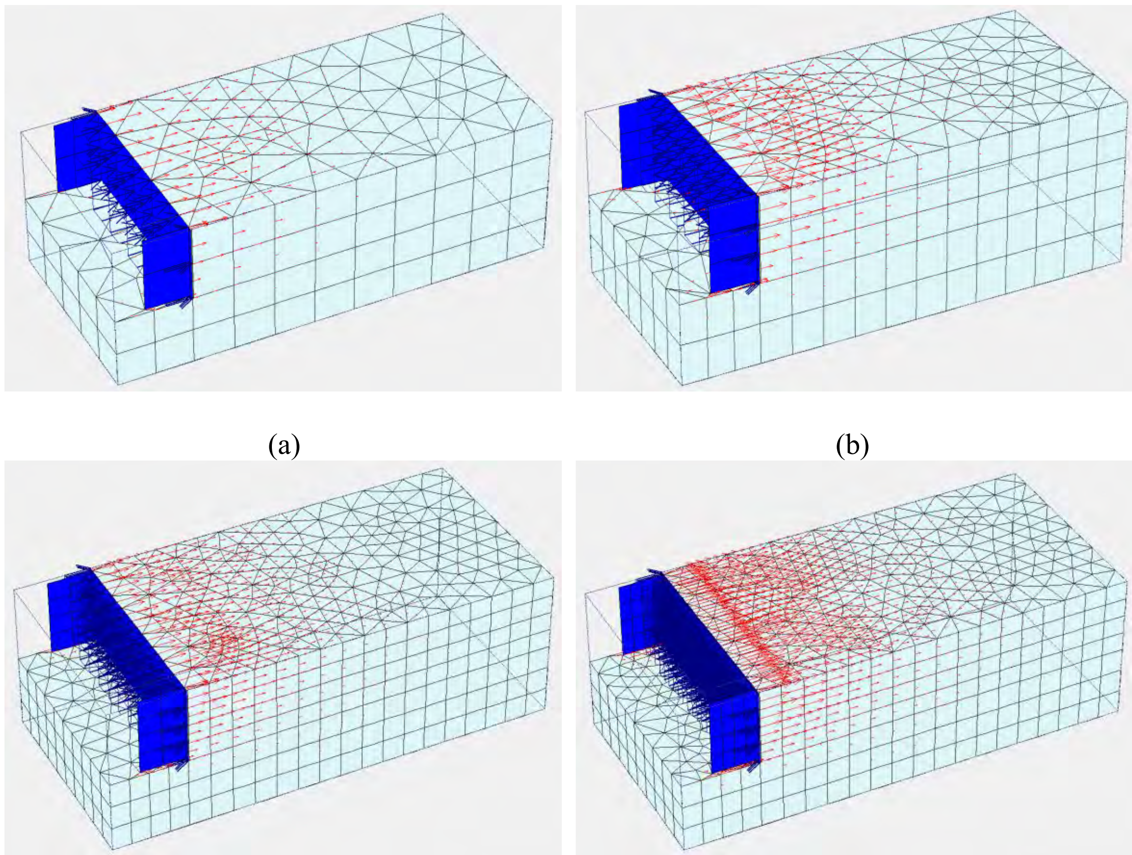

(a) (b)

(c) (d)

Figure 3-1 UCLA test model in PLAXIS3D Foundation: (a) coarse mesh, (b) medium mesh, (c) fine mesh, and (d) very fine mesh.

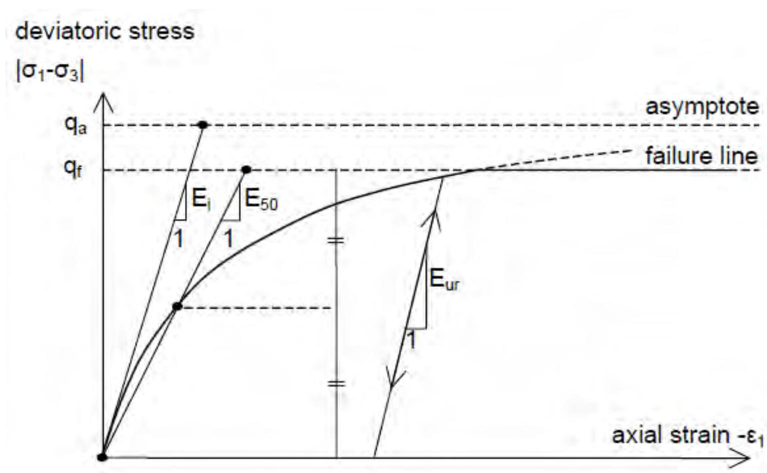

Figure 3-2 Hyperbolic stress-strain relationship.

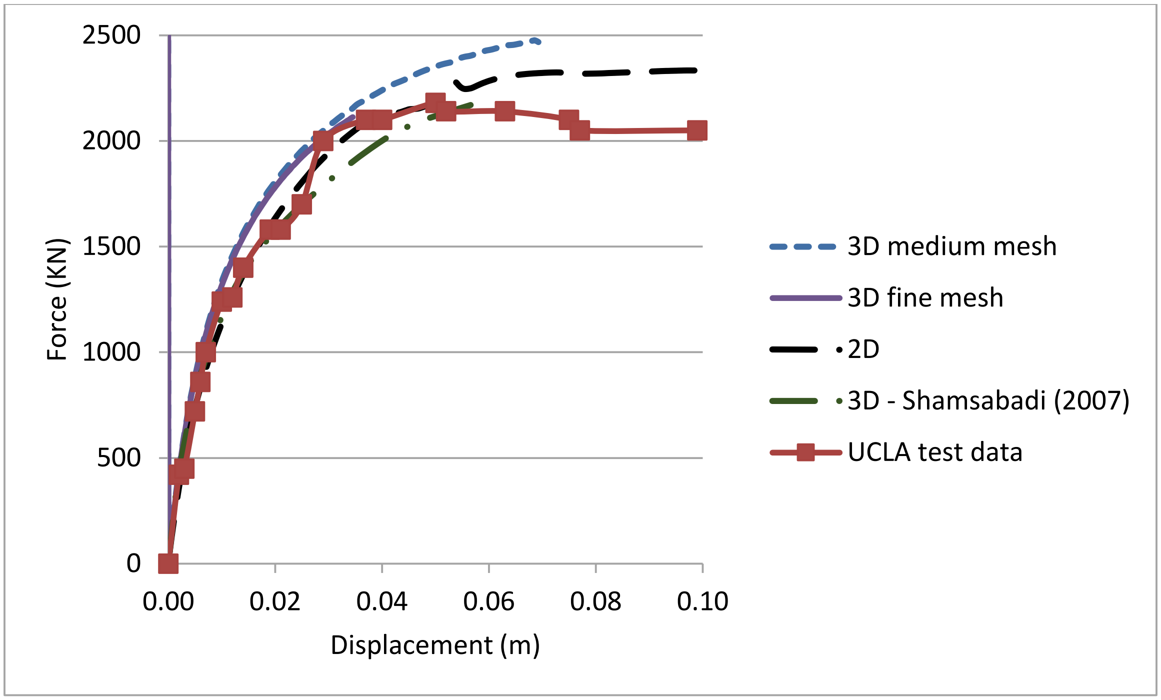

Figure 3-3 Force-displacement relationships of UCLA test using two and three dimensional versions of PLAXIS (1 m=3.28 ft, 1 kN=0.2248 kips).

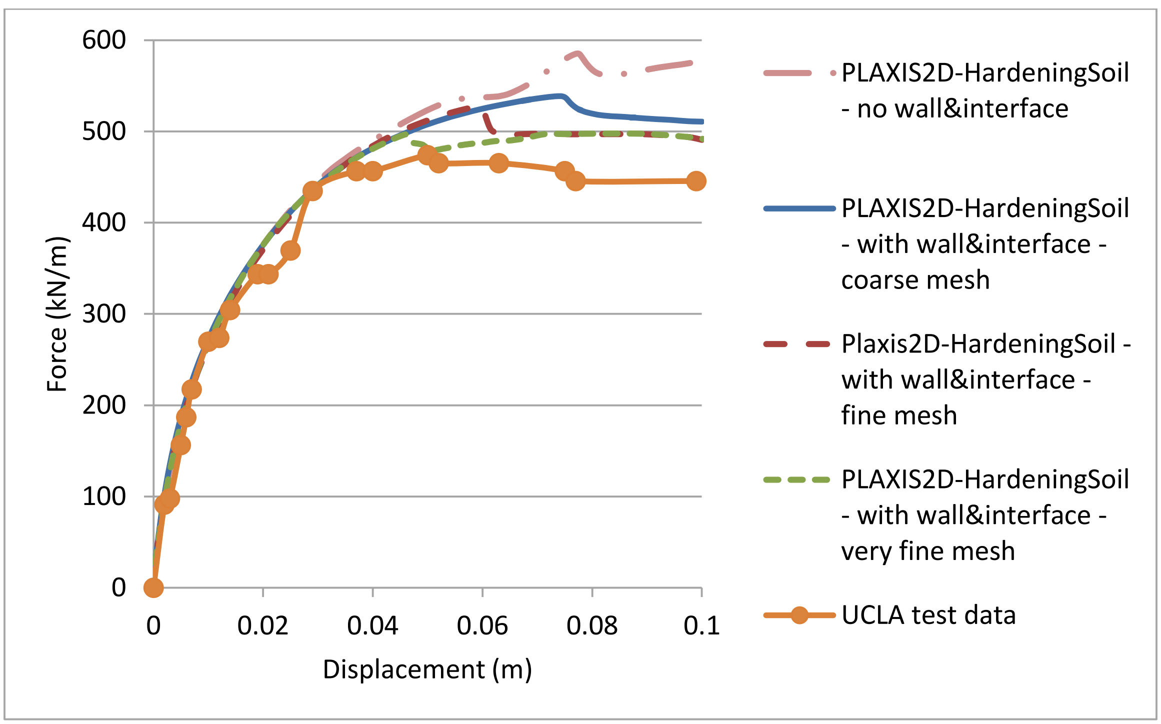

Figure 3-4 Force-displacement relationships of UCLA test using different mesh sizes in PLAXIS2D (1 m=3.28 ft, 1 kN=0.2248 kips).

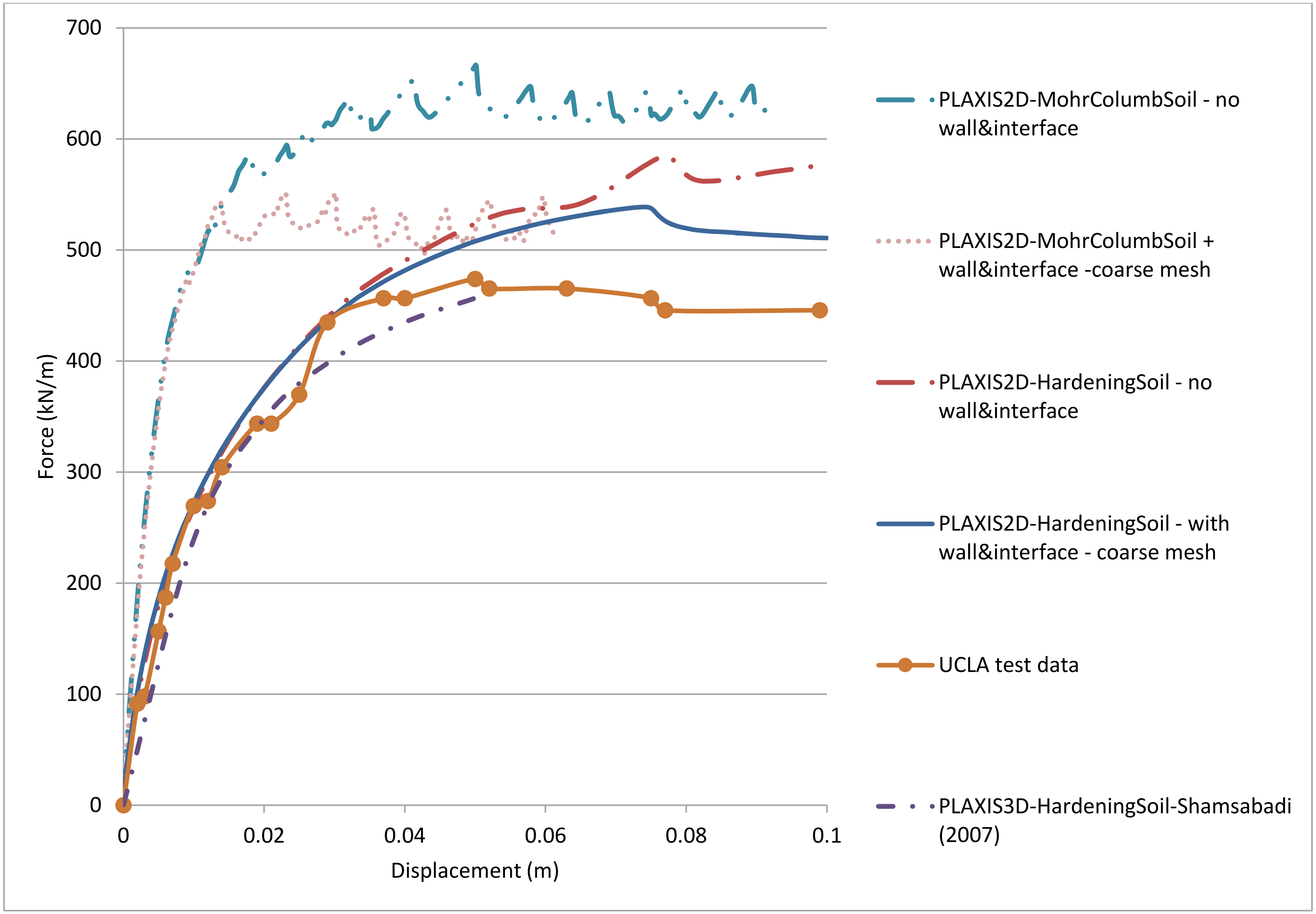

Figure 3-5 Force-displacement relationship of UCLA test model in PLAXIS (1 m=3.28 ft, 1 kN=0.2248 kips).

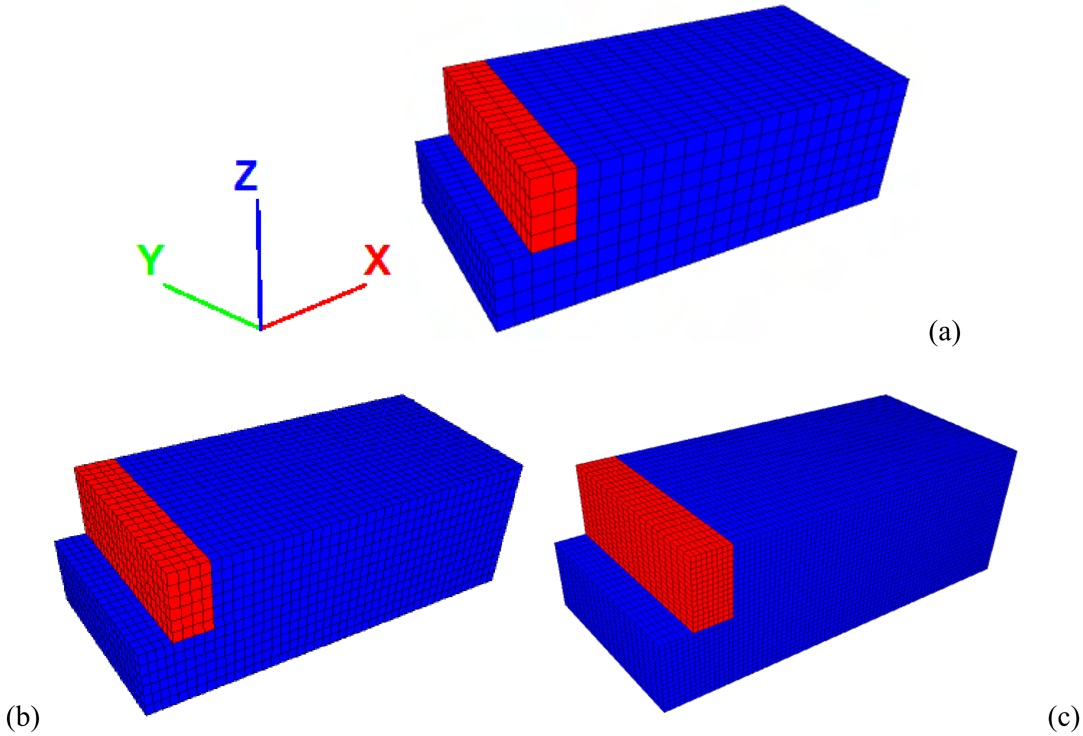

Figure 3-6 FLAC3D models of UCLA test: (a) coarse, (b) fine, and (c) very fine mesh.

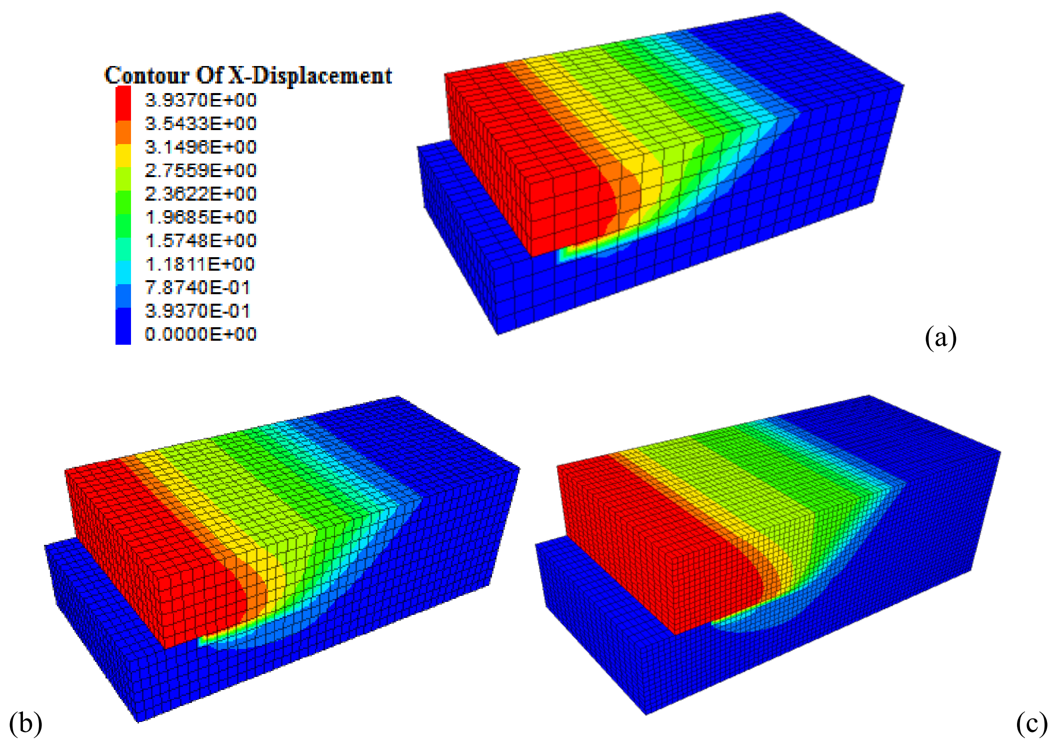

Figure 3-7 Displacement contours in x direction: a) coarse, (b) fine, and (c) very fine mesh.

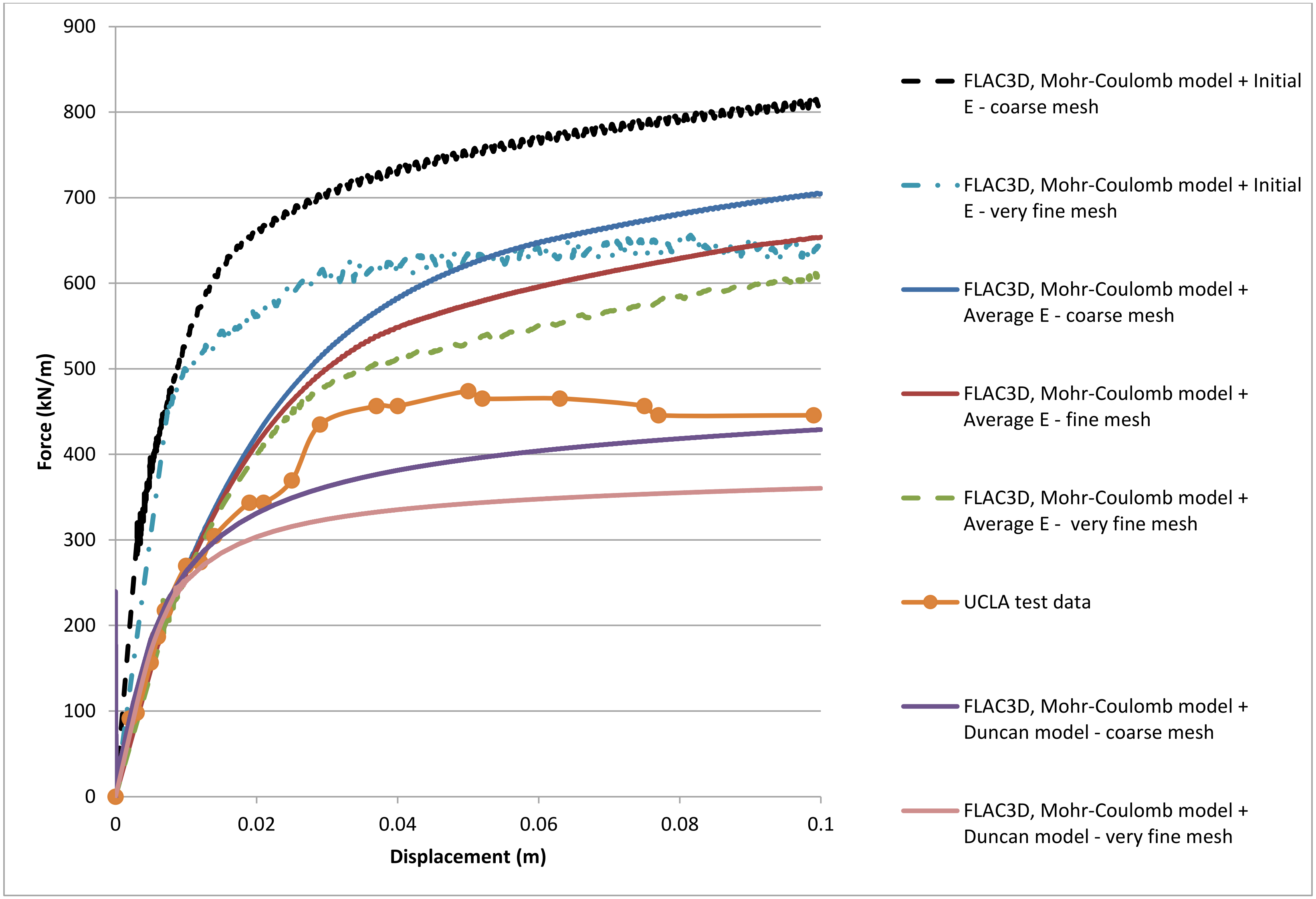

Figure 3-8 Force-displacement relationships of UCLA test model using FLAC3D (1 m=3.28 ft, 1 kN=0.2248 kips).

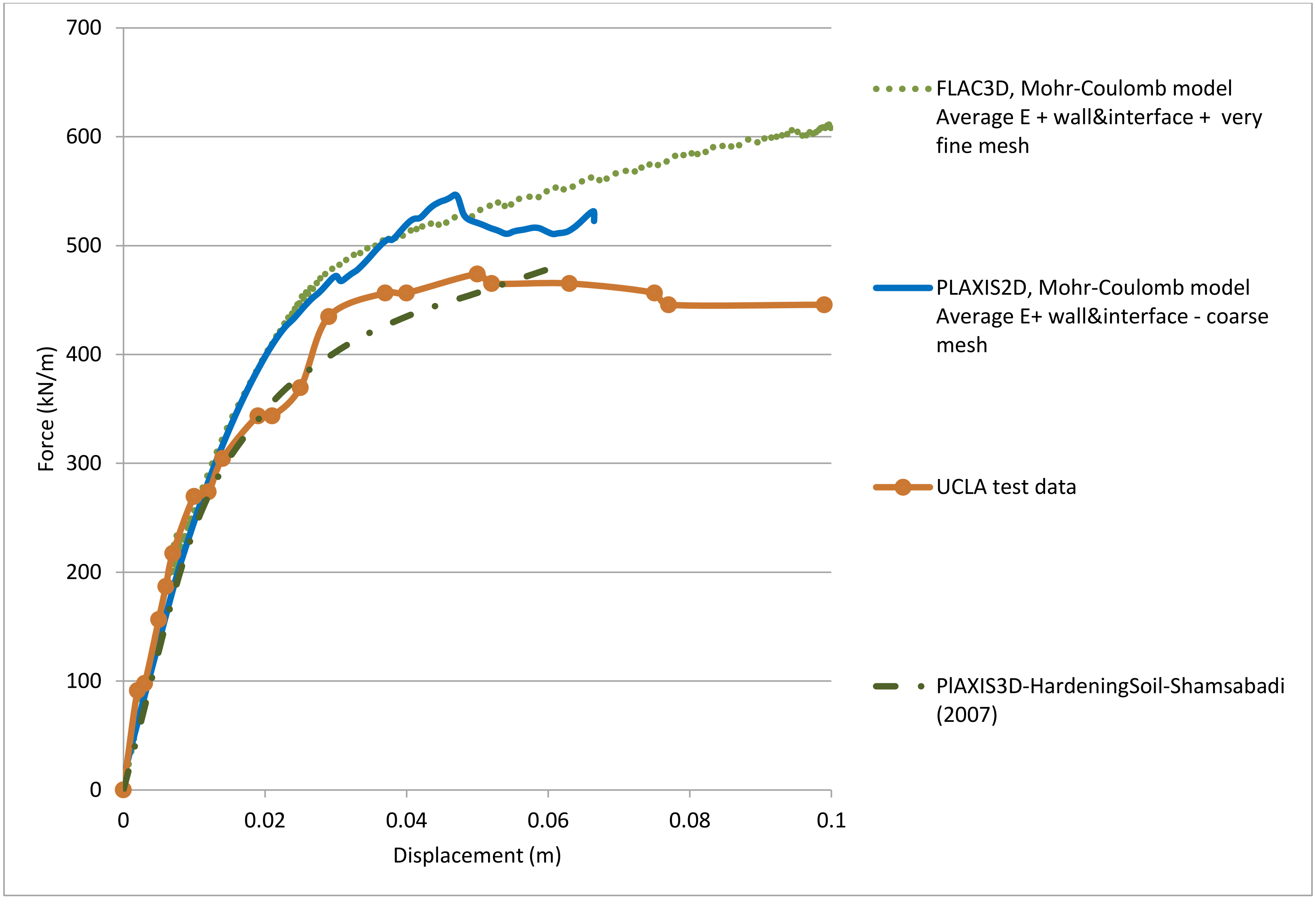

Figure 3-9 Force-displacement relationships of UCLA test model using an average E-modulus (1 m=3.28 ft, 1 kN=0.2248 kips).

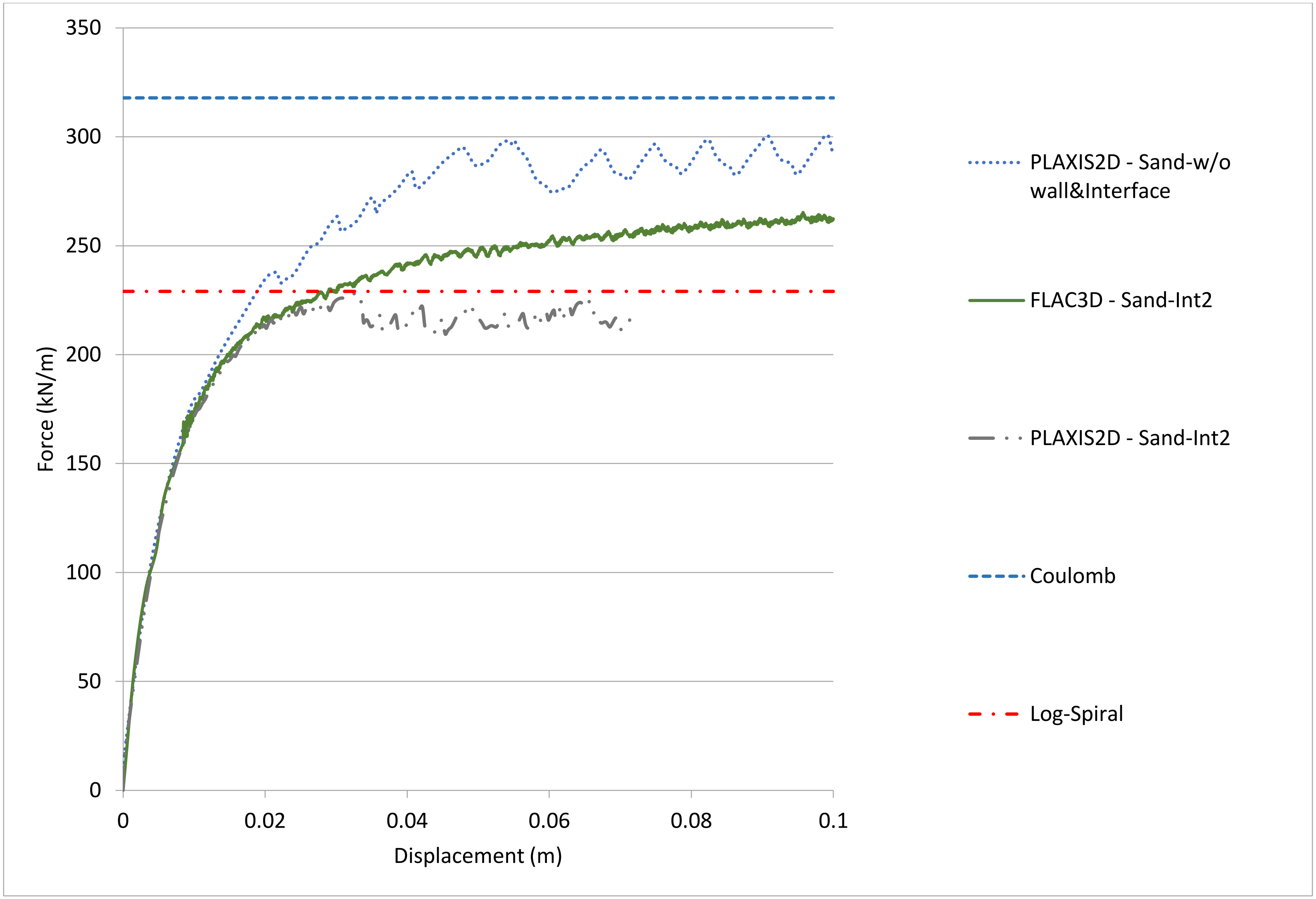

Figure 3-10 Force-displacement relationships of UCLA test model for interface sensitivity analysis (1 m=3.28 ft, 1 kN=0.2248 kips).

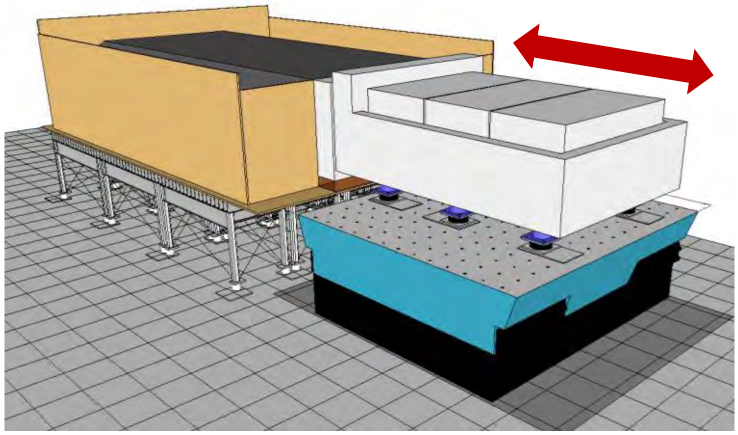

(a)

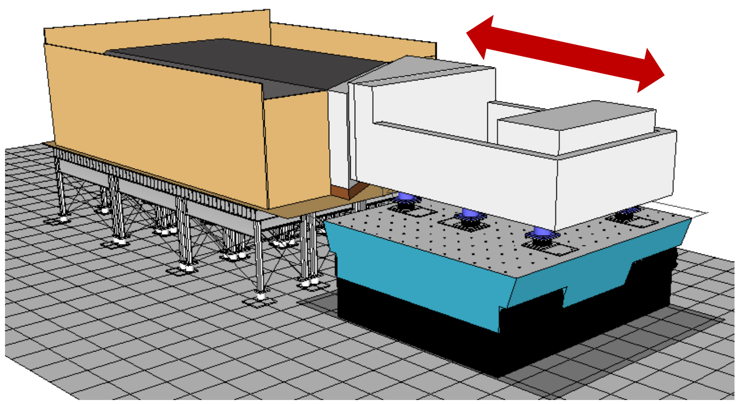

(b)

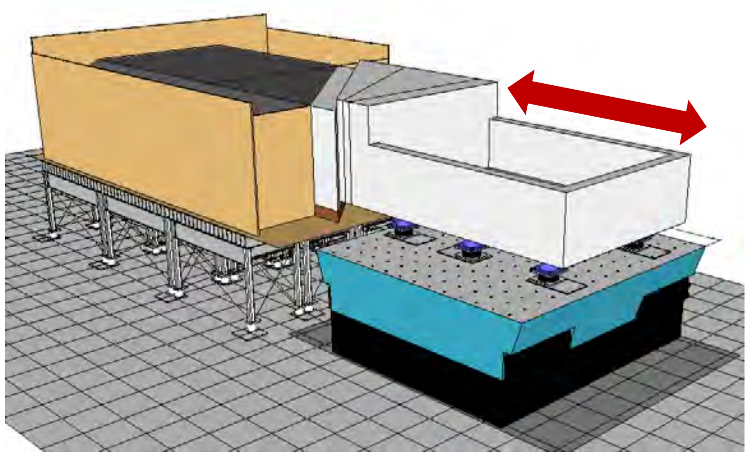

(c)
Figure 4-1 3D views of test models: (a) 0° skew, (b) 30° skew, and (c) 45° skew

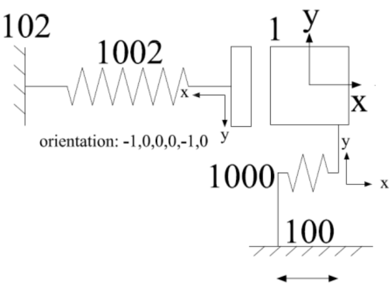

Figure 4-2 Analytical model in OpenSees.

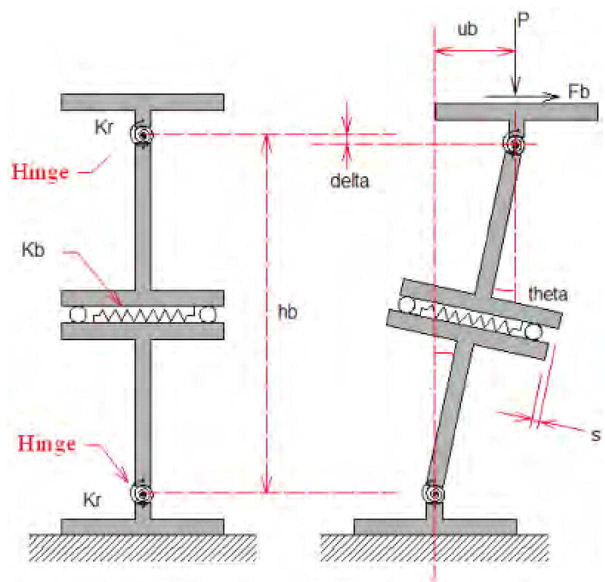

Figure 4-3 Two-spring model (Isolator2spring) of a bearing in undeformed and deformed conditions (OpenSees manual).

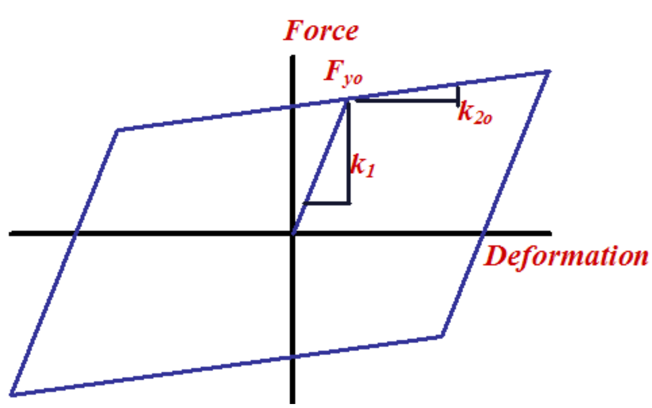

Figure 4-4 Bilinear force-deformation behavior of shear spring (OpenSees manual).

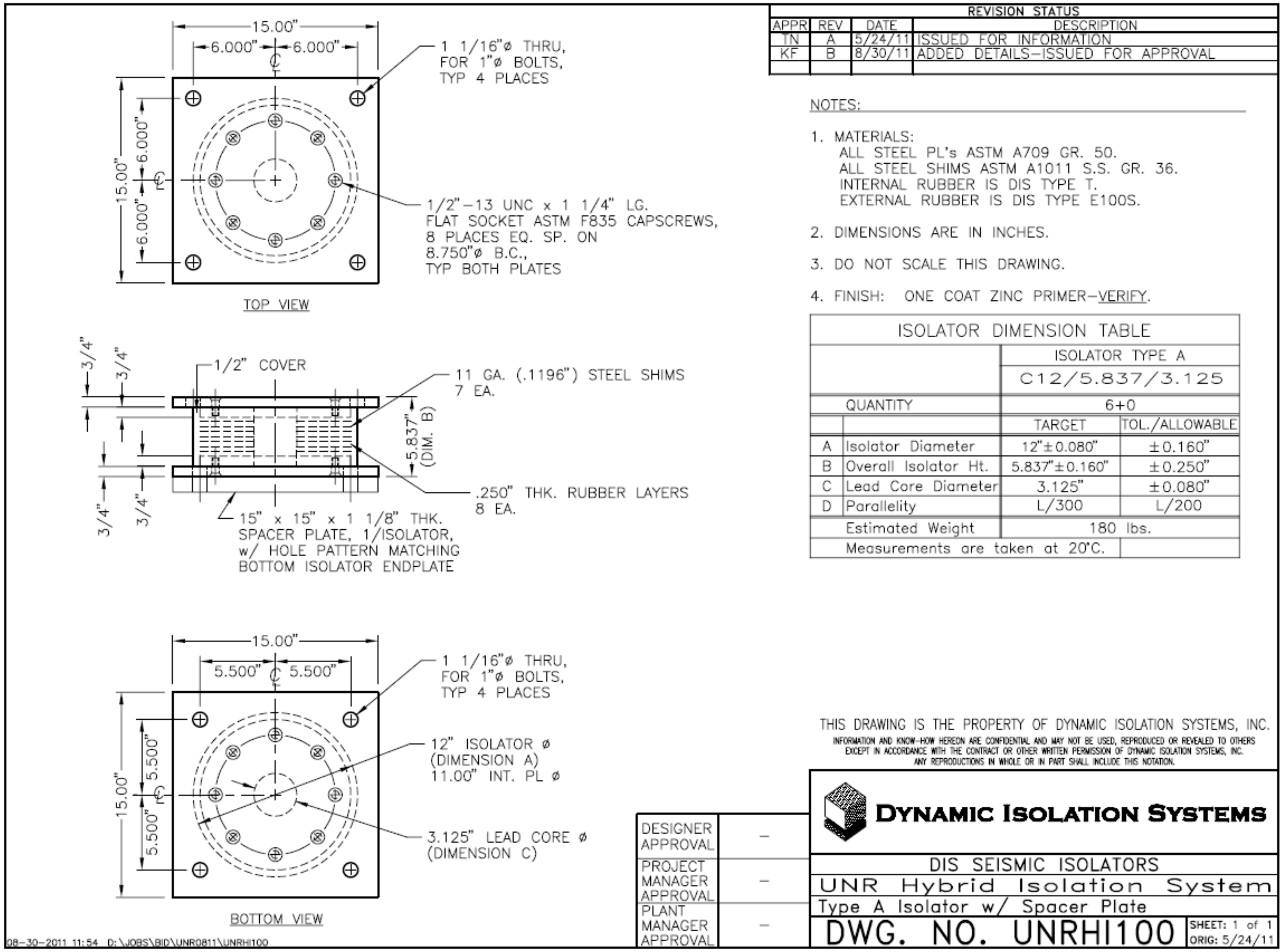

Figure 4-5 Selected force-displacement relationship of soil for this study.

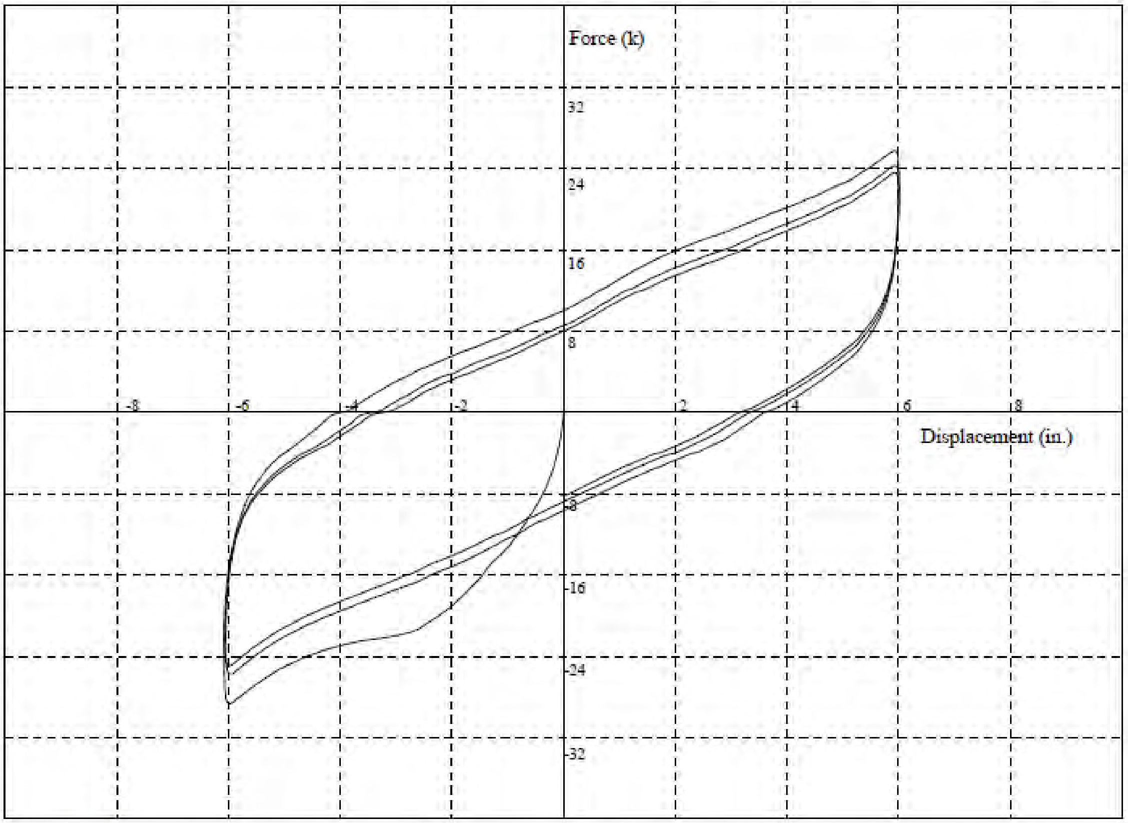

Job: 154 (UNR Hybrid Isolation) Test Name : 26763-001.dat

Class: Prototype Type: A Isolators 16547 & 16548 Tested: 5/24/2012 10:06:15 AM

Test Type: Prototype Test Matrix ID: I (Load: 0kips. Displacement: 6.0")

Cycle	Dmax(in)	Fmax(k)	Keff(k/in)	Qd(k)	EDC(k.in)	K2fit(k/in)	V(in/min)
1	6.04	27.20	4.50	9.84	245.1	2.73	58.63
2	6.03	25.00	4.15	8.67	206.8	2.66	67.80
3	6.04	24.27	4.02	8.10	191.0	2.65	69.18
AVERAGE	**6.04**	**25.49**	**4.22**	**8.9**	**214.3**	**2.68**	**65.2**

Figure 4-6 Force-deformation relationship of isolators based on the test results.

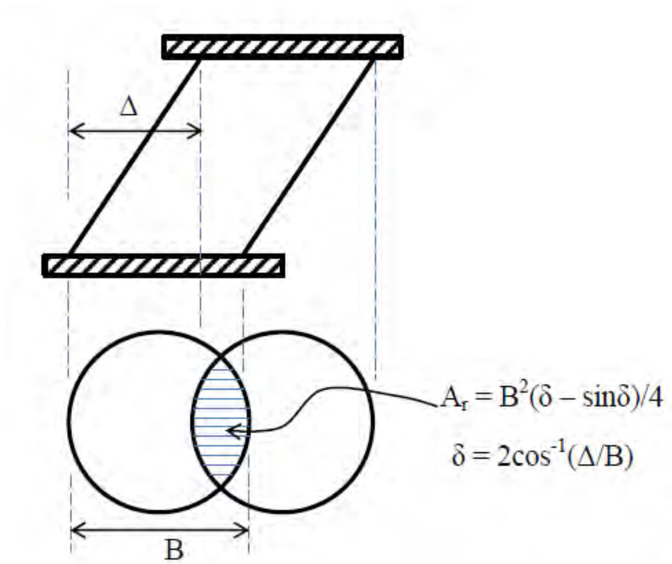

Figure 4-7 Bearing deformed shape.

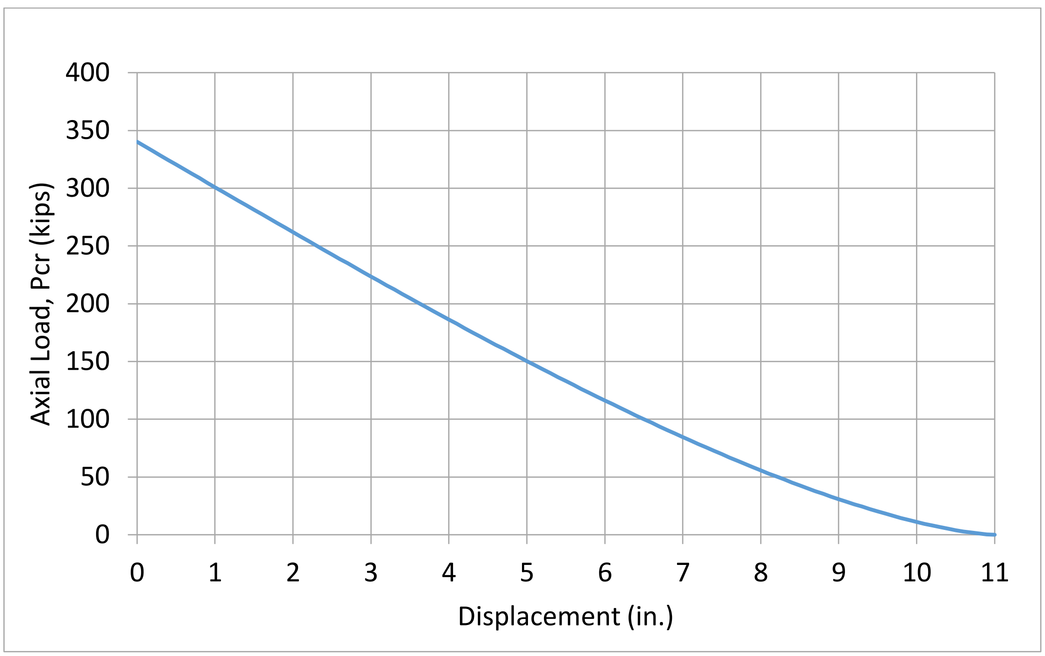

Figure 4-8 Variation of axial load capacity with the isolator displacement.

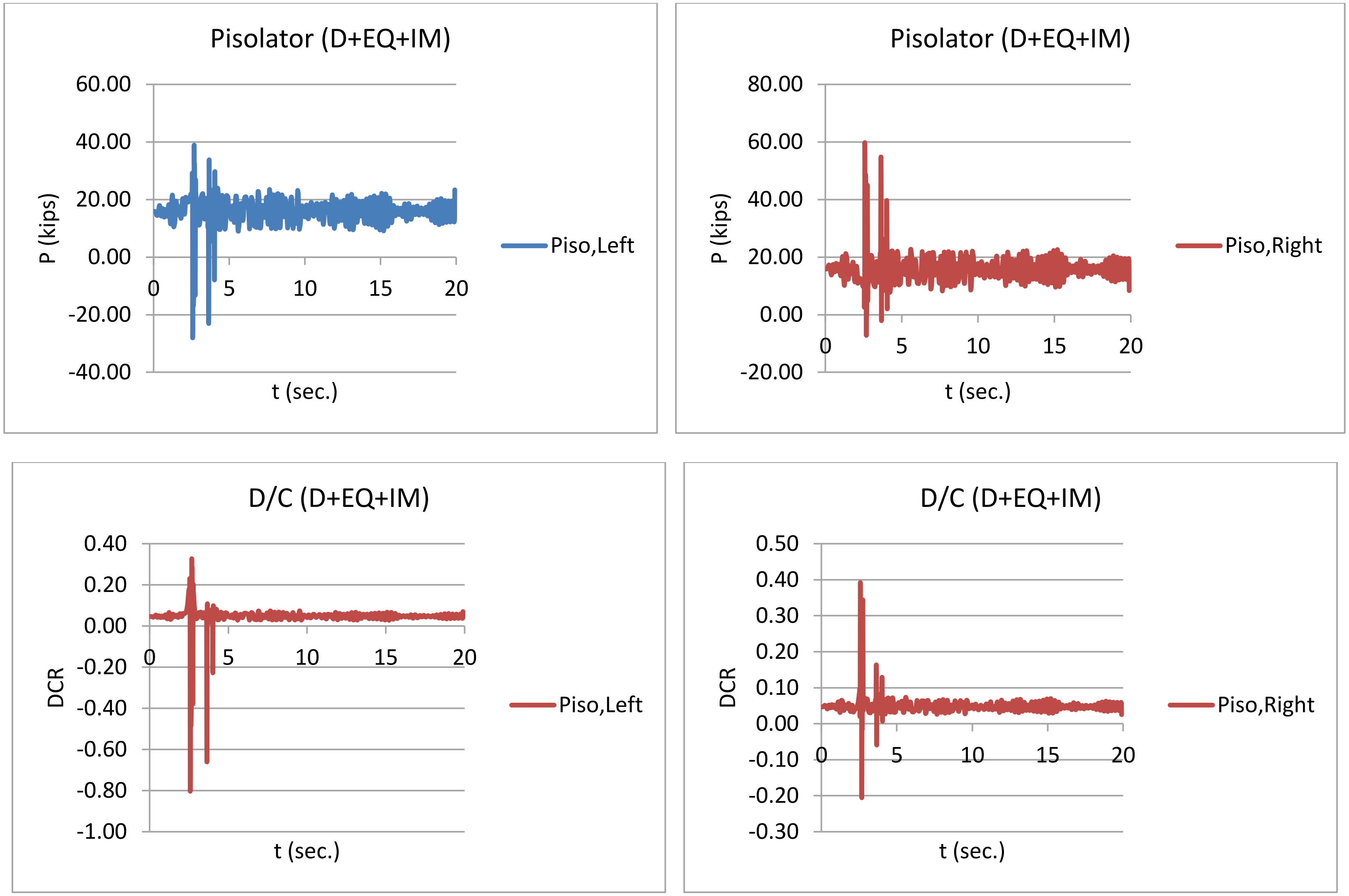

Figure 4-9 Isolators axial forces.

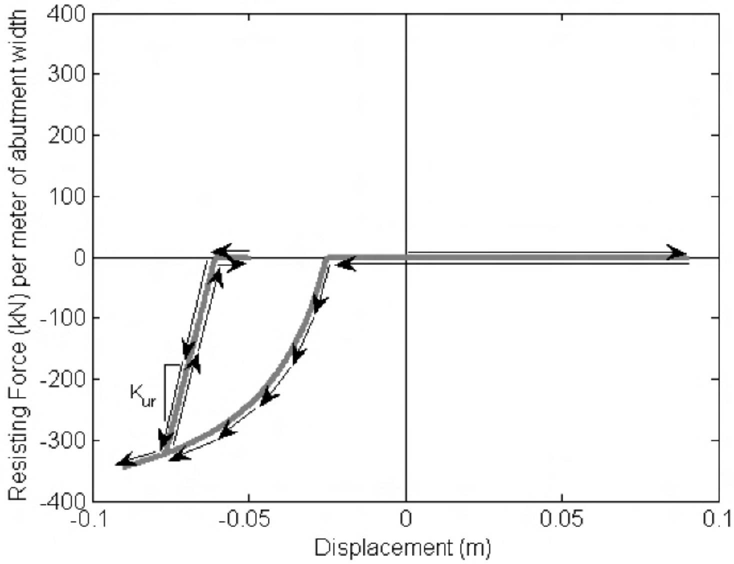

Figure 4-10 Force-displacement behavior of Hyperbolic Gap Material recommended by OpenSees (OpenSees manual).

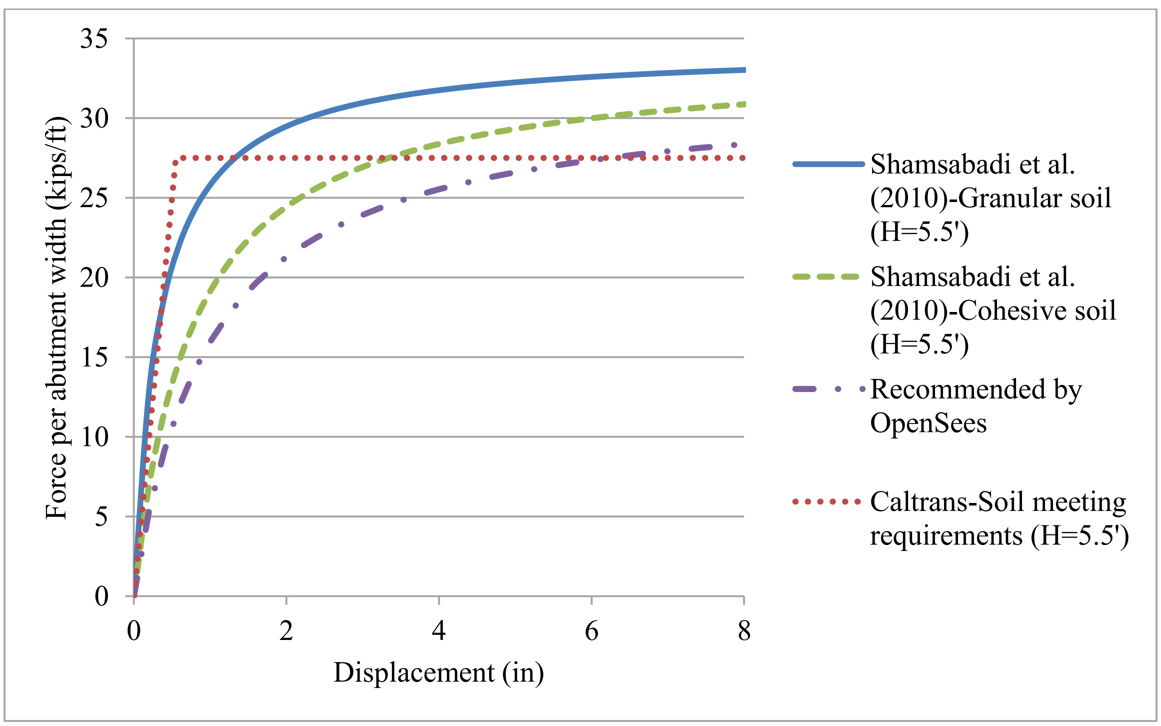

Figure 4-11 Force-displacement relationships of backfill soil.

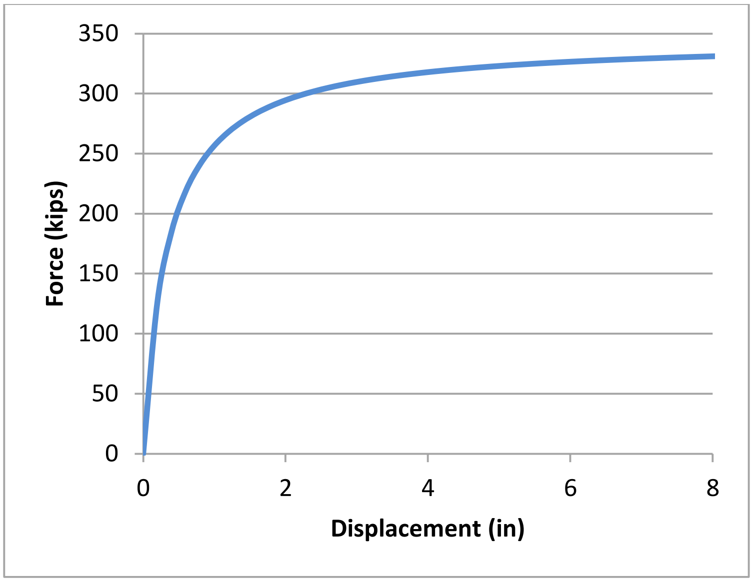

Figure 4-12 Force-displacement relationship of soil selected for this study.

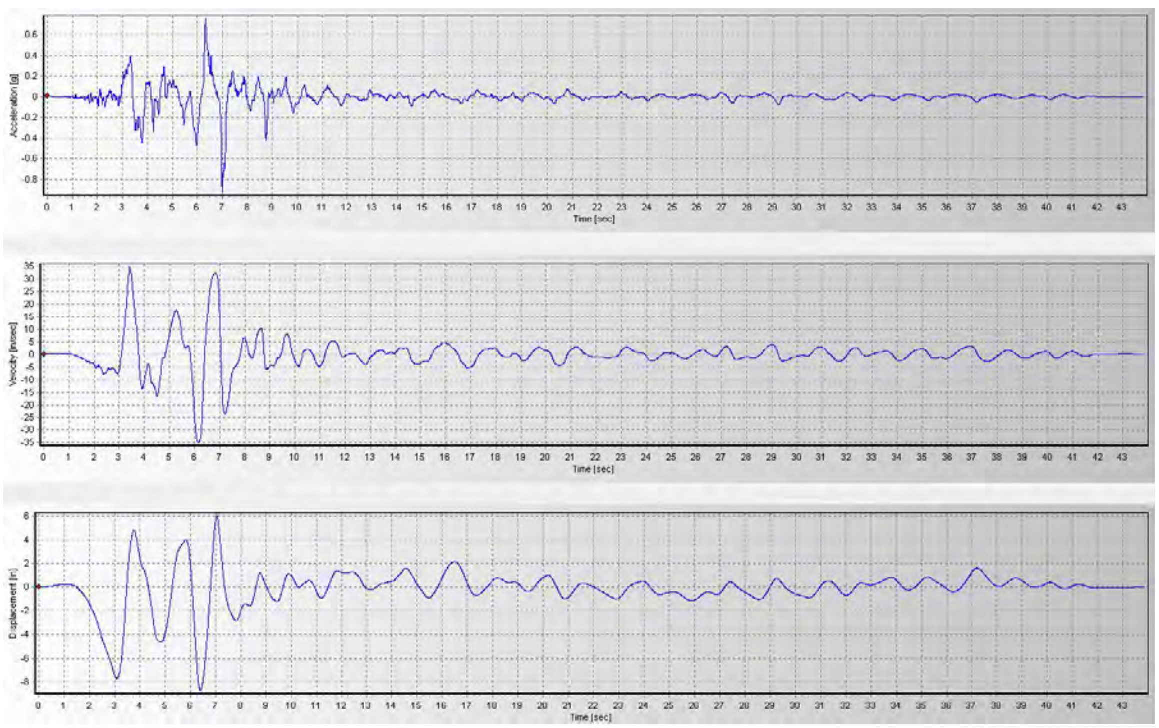

Figure 4-13 Original Sylmar motion histories.

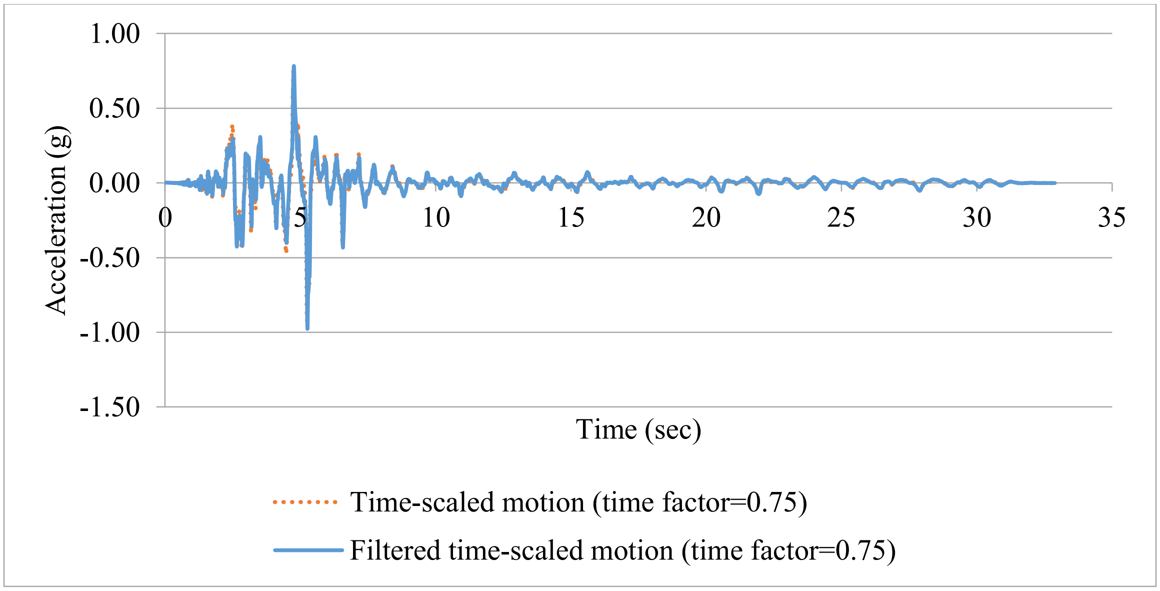

(a)

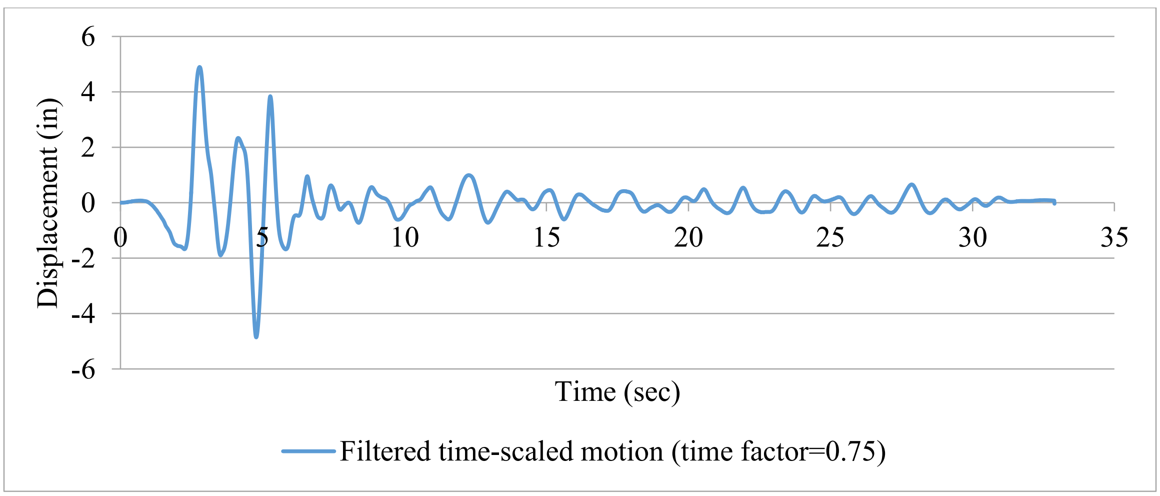

(b)

Figure 4-14 Time-scaled Sylmar motion histories: (a) acceleration, and (b) displacement.

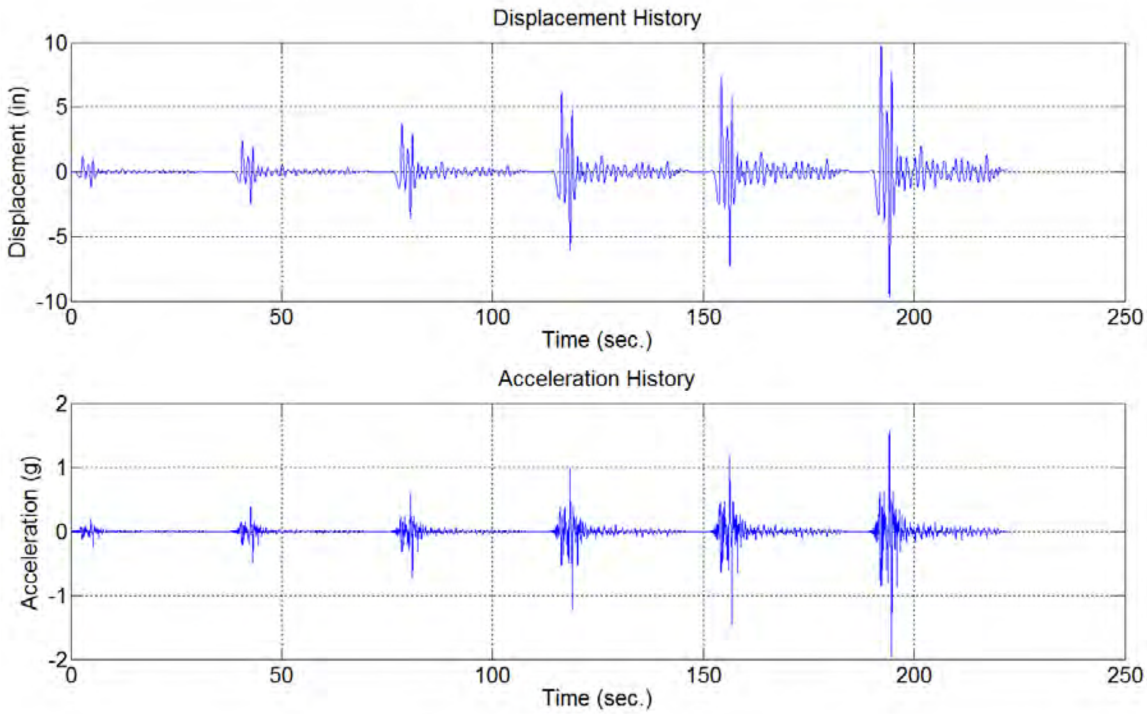

Figure 4-15 Input motion histories of loading protocol.

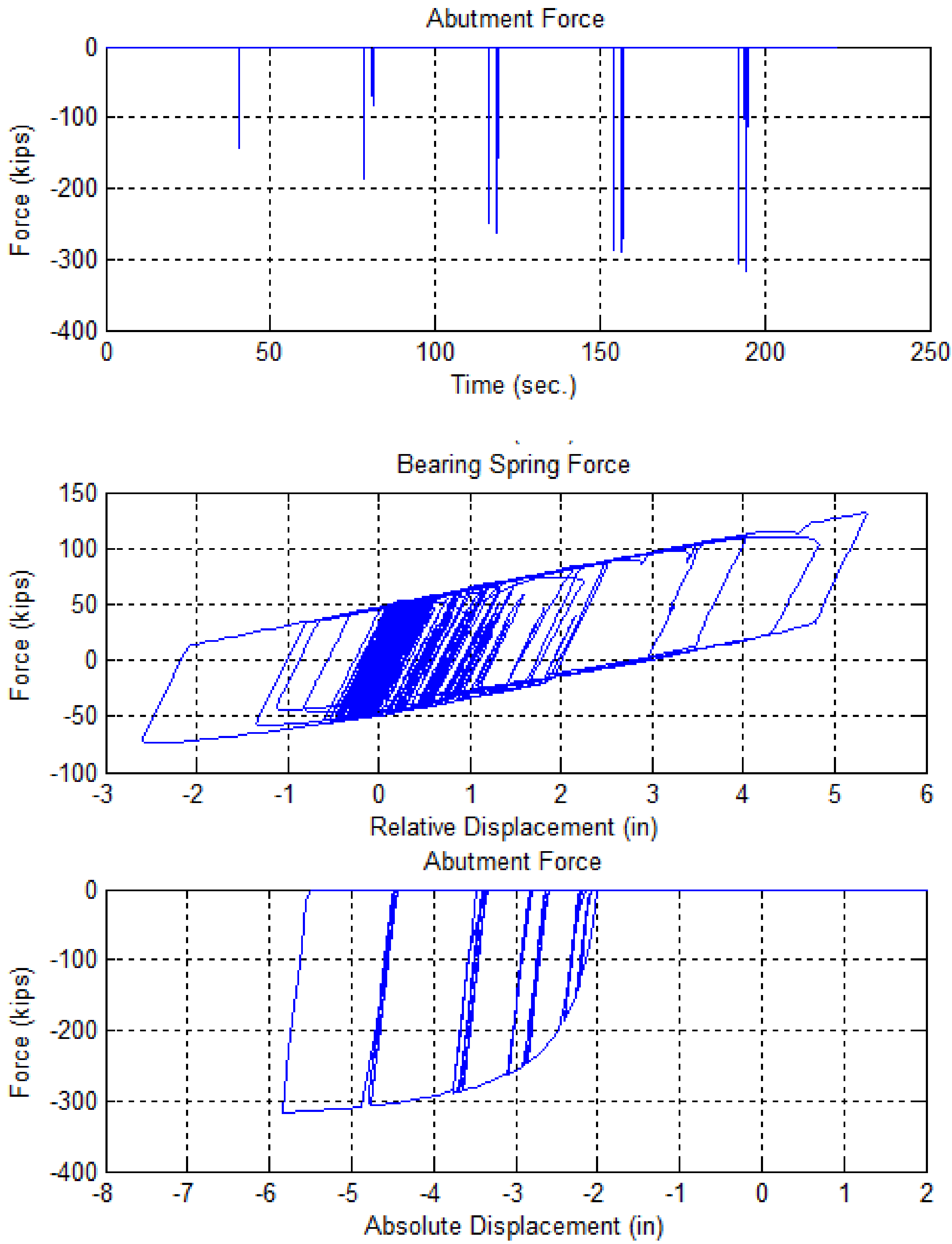

Figure 4-16 Abutment response history and force-displacement relatioships of analytical model (0° skew).

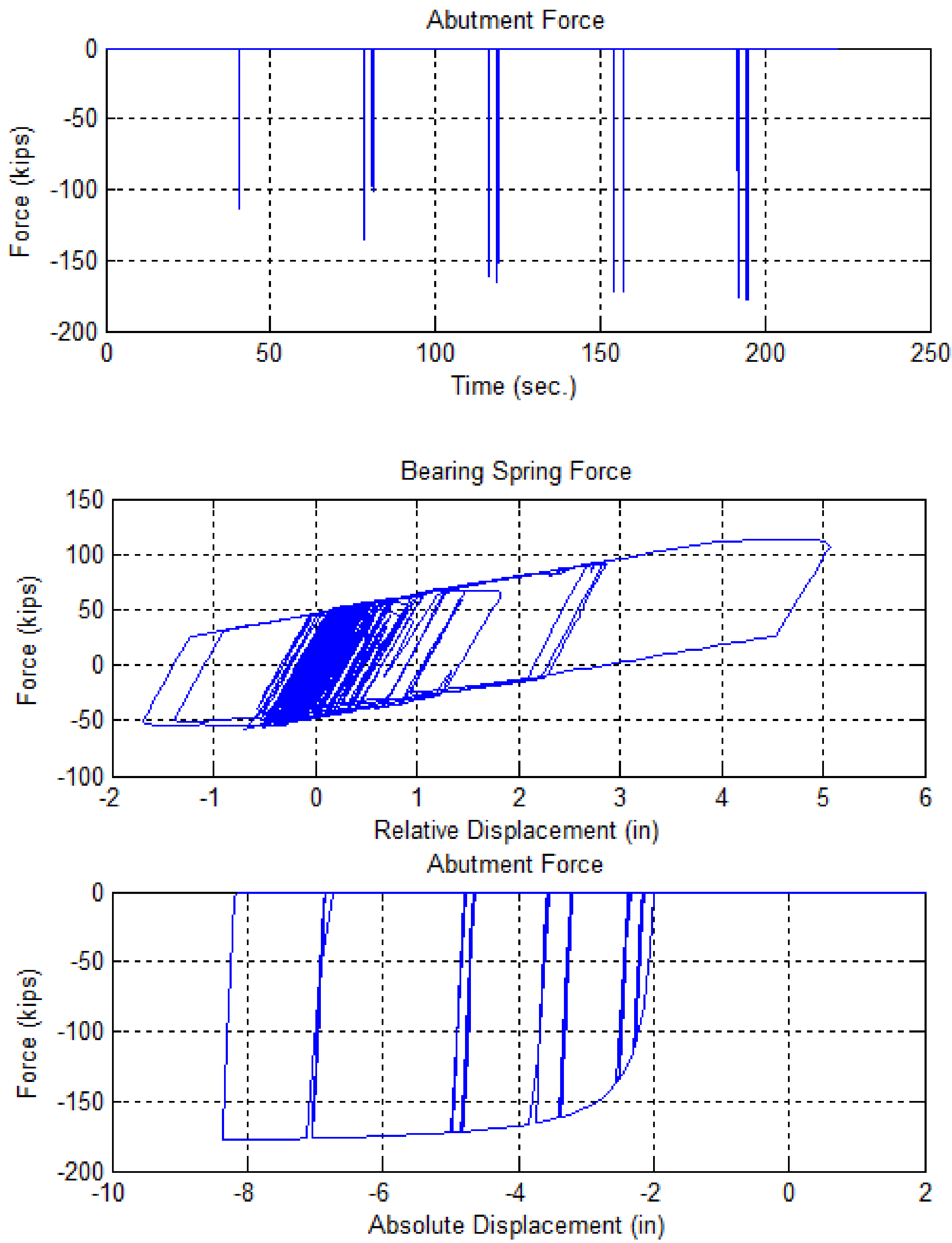

Figure 4-17 Abutment response history and force-displacement relatioships of analytical model (30° skew).

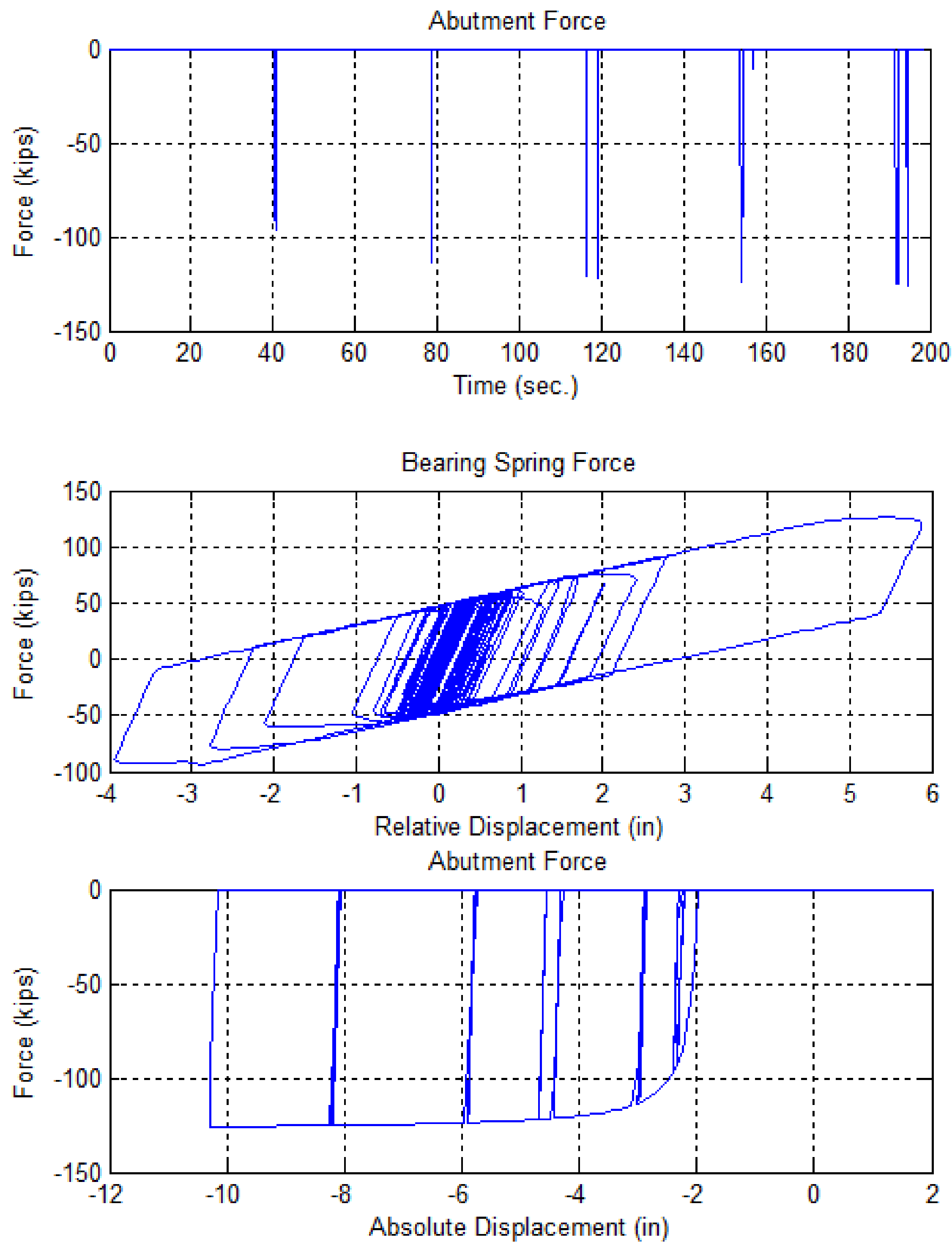

Figure 4-18 Abutment response history and force-displacement relatioships of analytical model (45° skew).

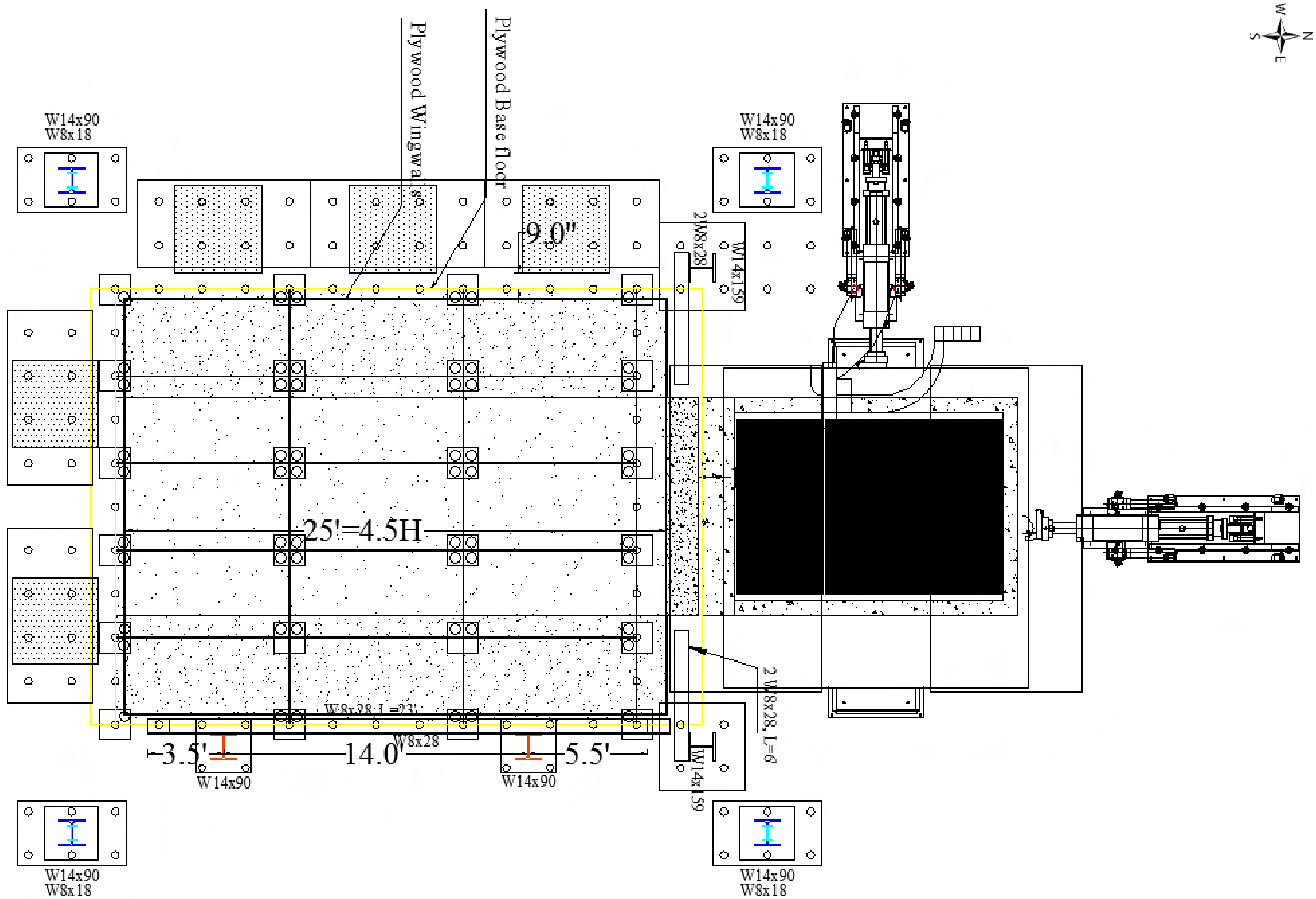

Figure 5-1 Plan view of the 0° skew test model.

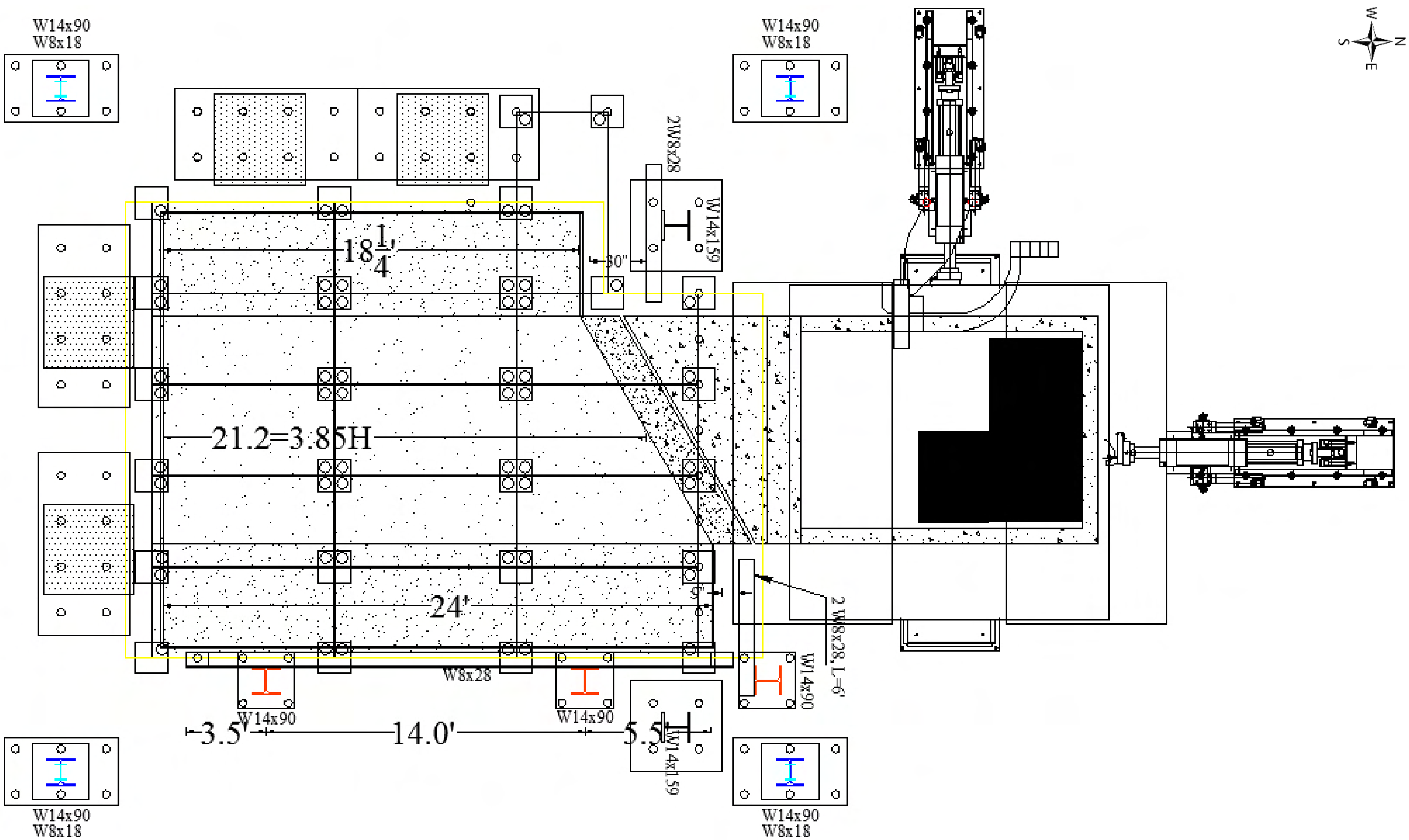

Figure 5-2 Plan view of the 30° skew test model.

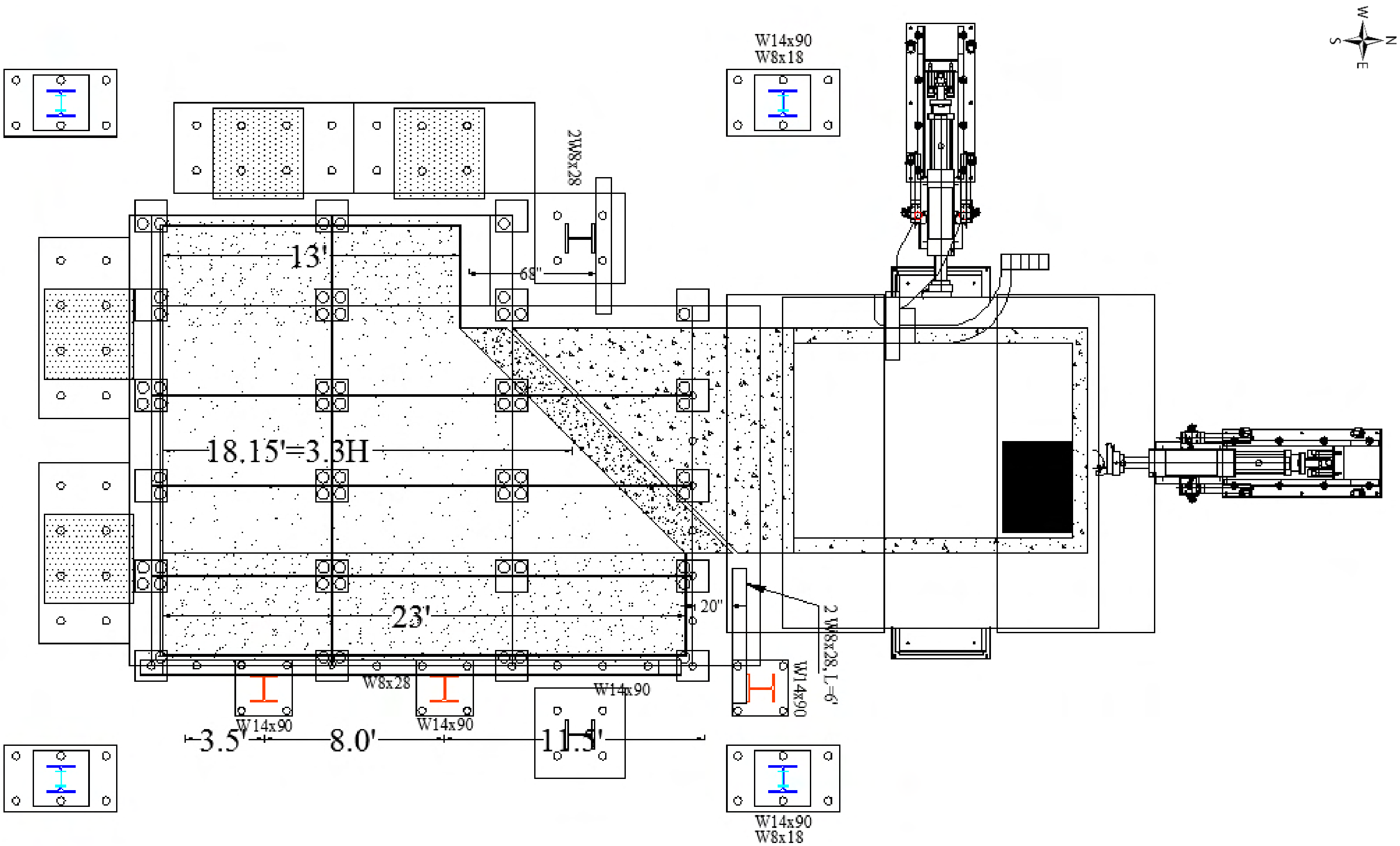

Figure 5-3 Plan view of the 45° skew test model.

Figure 5-4 Construction of the main bridge block slab.

Figure 5-5 Construction of the main bridge block side walls.

Figure 5-6 Construction of the 30° skew wedge.

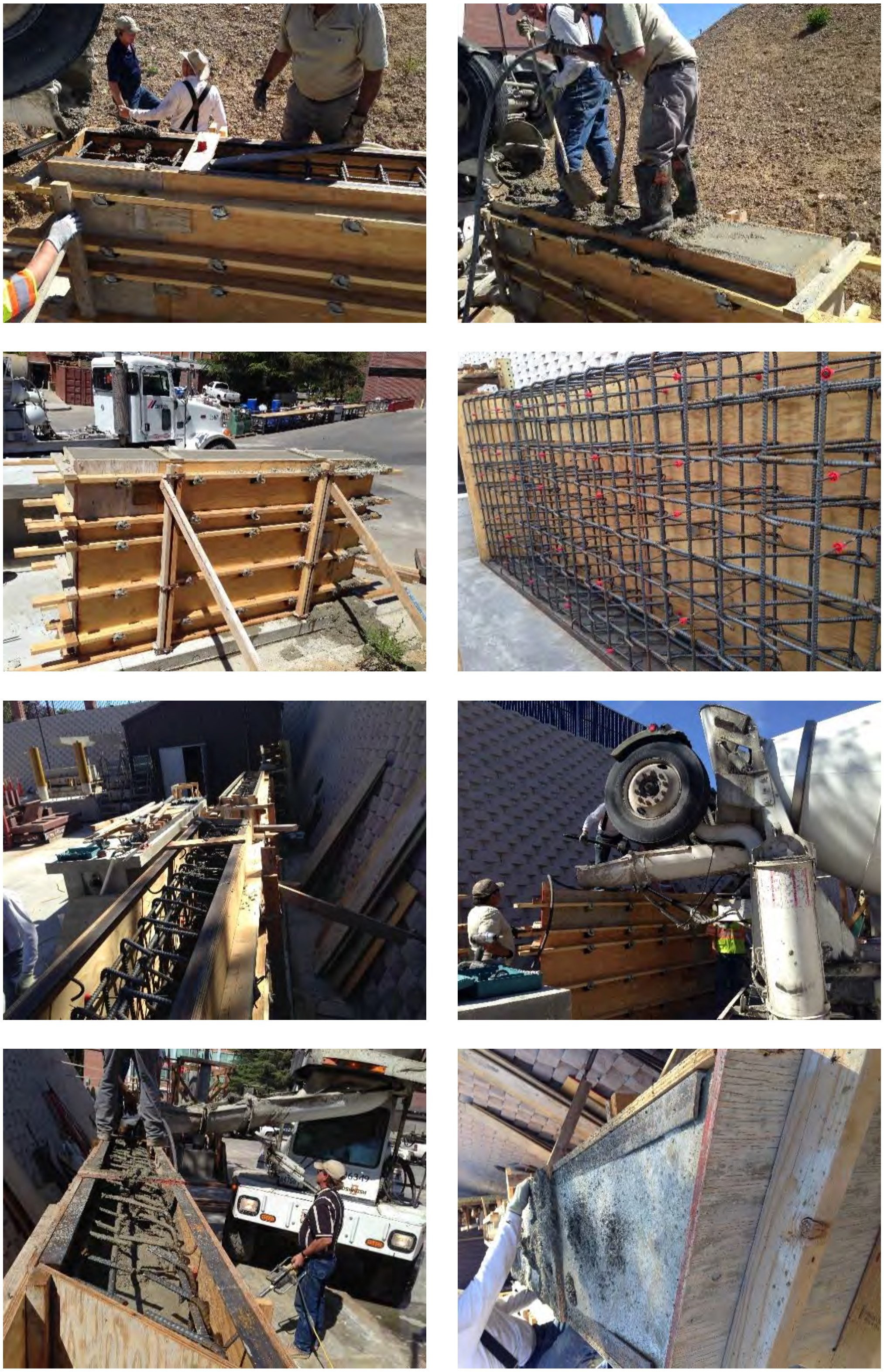

Figure 5-7 Construction of the abutment backwalls.

Figure 5-8 Backwall support on top of the soil box.

Figure 5-9 Teflon at the backwall base.

Figure 5-10 Backwall support under the soil box.

Figure 5-11 Components of backwall vertical restrainer system.

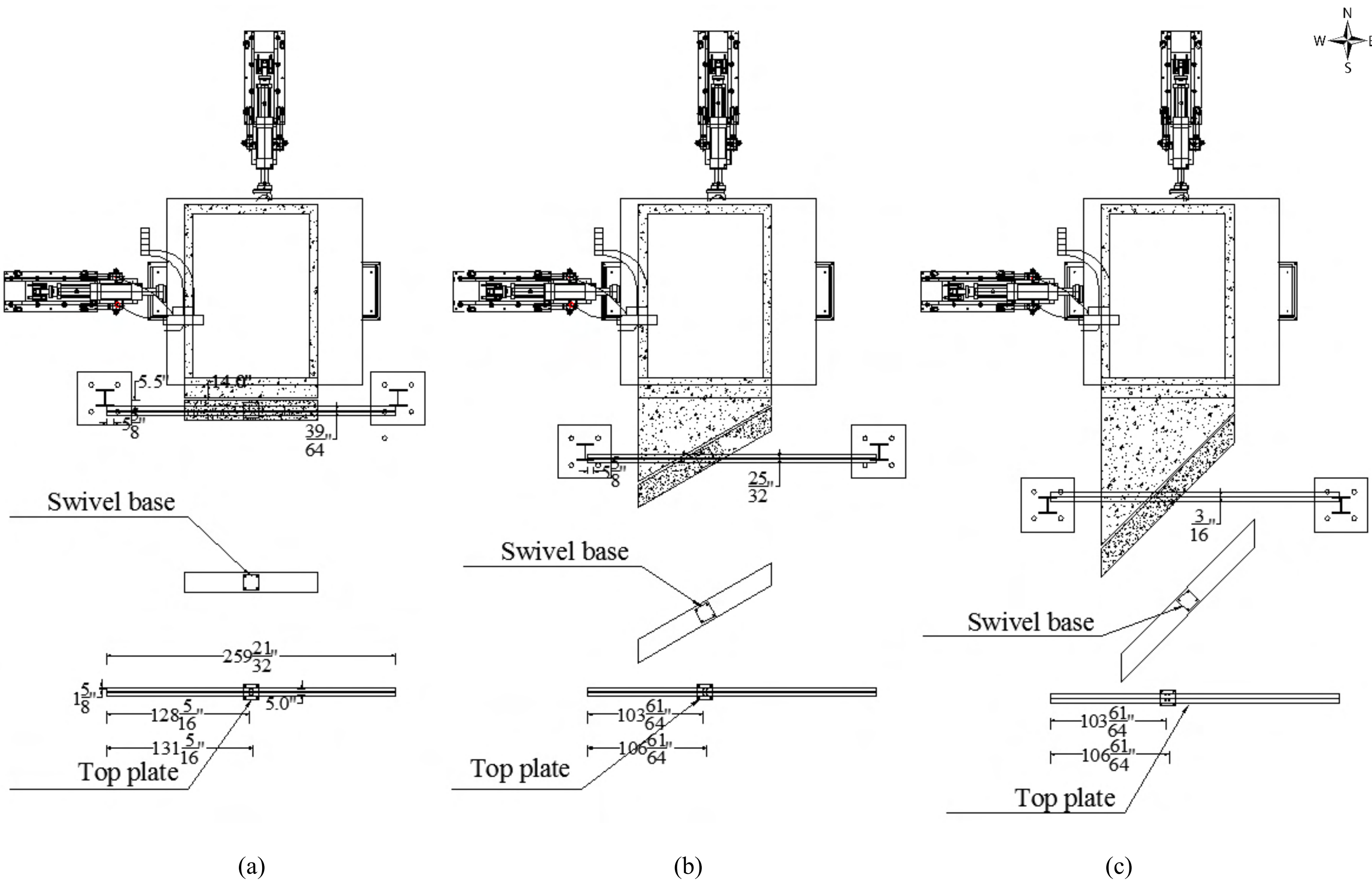

Figure 5-12 Backwall vertical restrainer system in the plan view: (a) 0° skew, (b) 30° skew, and (c) 45° skew.

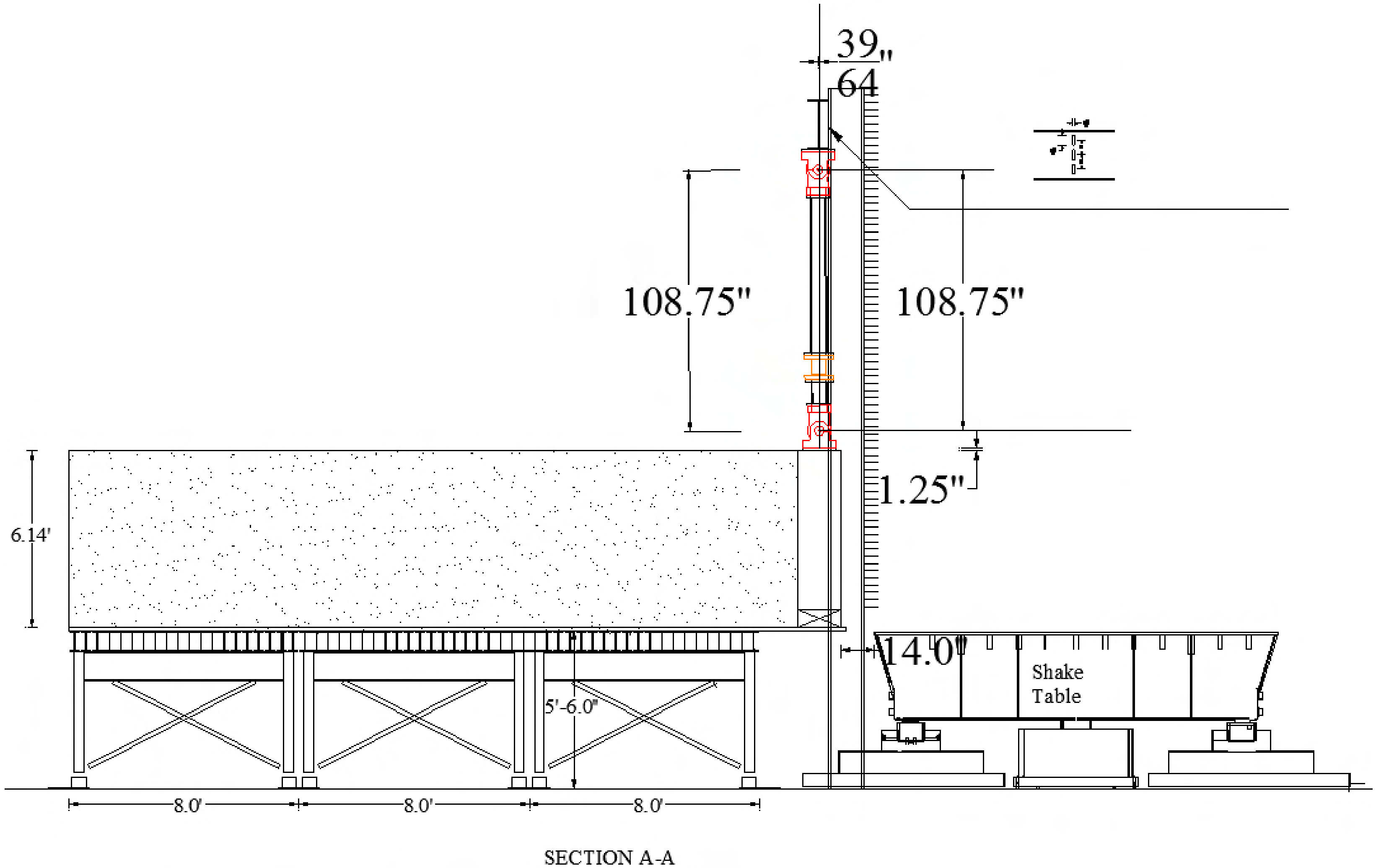

Figure 5-13 Backwall vertical restrainer system in the elevation view in the 0° skew test.

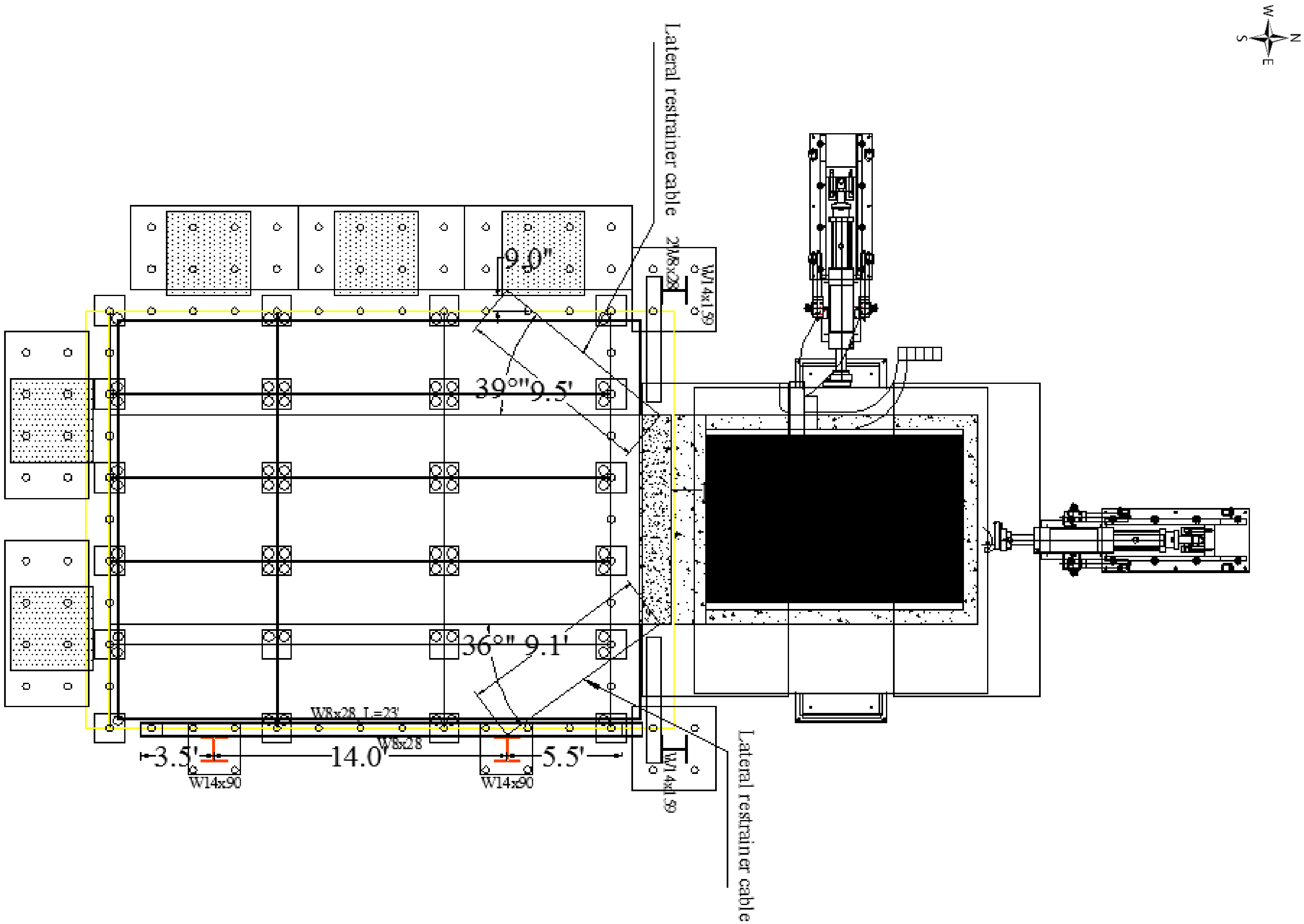

Figure 5-14 Lateral restrainer cables of the backwall in the 0° skew test.

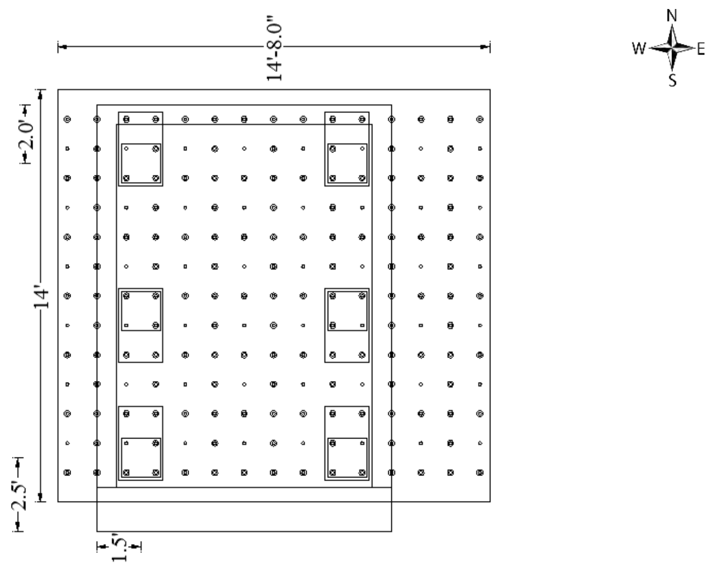

Figure 5-15 Main bridge block position on the shake table.

Figure 5-16 Installation of isolators and load cells.

Figure 5-17 Installation of the main bridge block.

Figure 5-18 Installation of superimposed mass in the 0° skew test.

Figure 5-19 Bridge block and backwall in the 0° skew test.

Figure 5-20 Installation of backwall vertical restrainer system in the 0° skew test.

Figure 5-21 Removal and re-construction of soil adjacent to the backwall in the 0° skew test.

Figure 5-22 Trenches inside the backfill soil in the 0° skew test (left: east side, and right: west side).

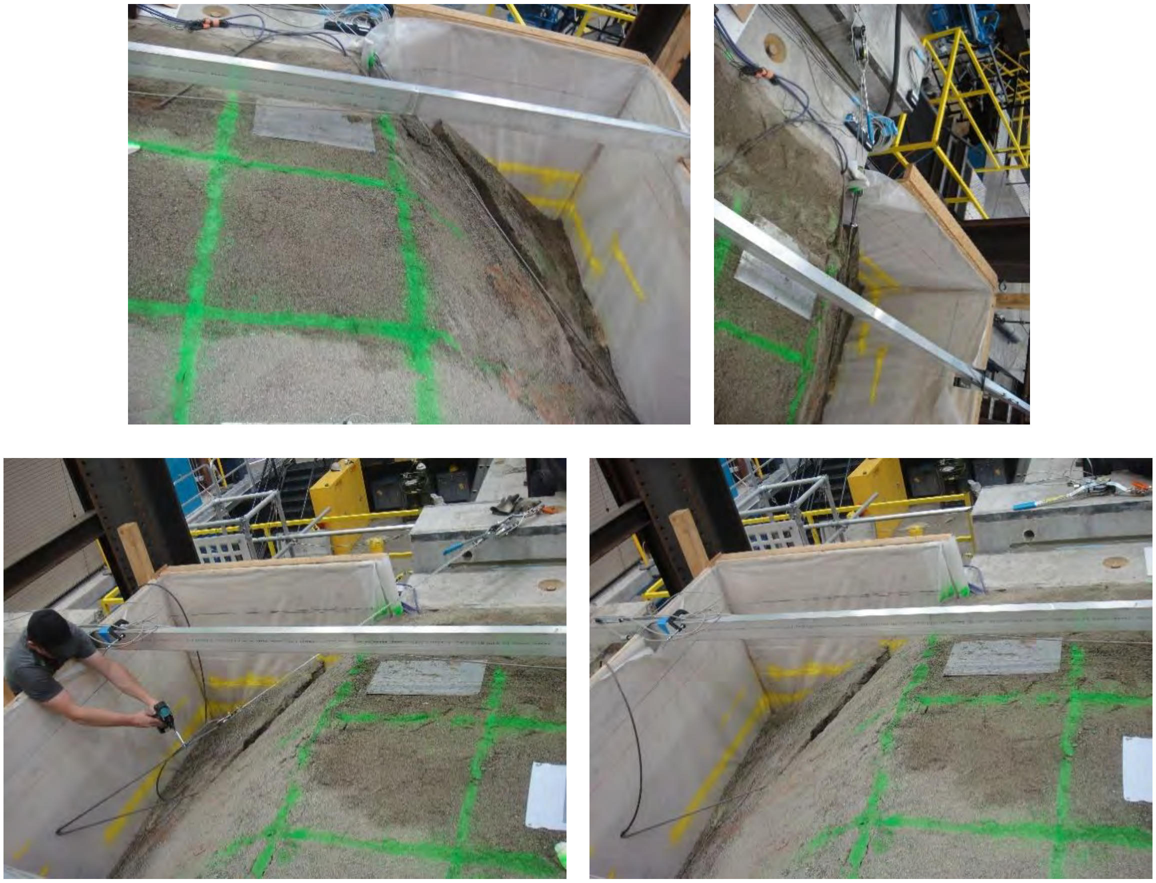

Figure 5-23 Installation of backwall restrainer cable in the 0° skew test (top: east side, and bottom: west side).

Figure 5-24 Connection of restrainer cable to the backwall (left: east side, and right: west side).

Figure 5-25 Connection of restrainer cable to the concrete block at the west side of the soil box.

Figure 5-26 Installation of superimposed mass in the 30° skew case.

Figure 5-27 Installation of skew wedge in the 30° skew case.

Figure 5-28 Installation of backwall in the 30° skew case.

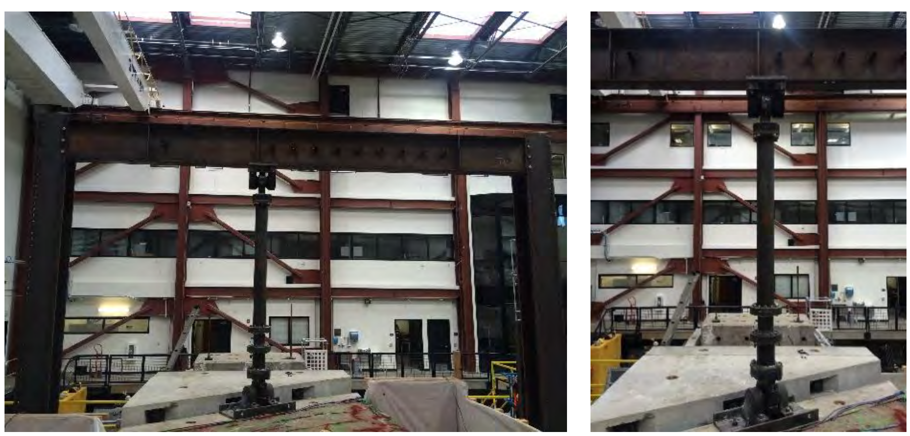

Figure 5-29 Backwall vertical restrainer system in the 30° skew case.

Figure 5-30 Installation of backwall support in the 45° skew test.

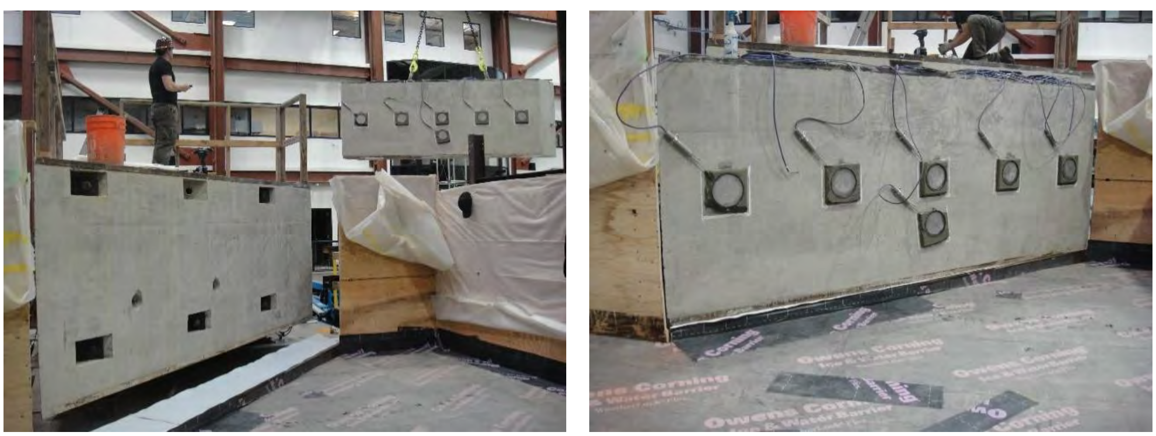

Figure 5-31 Installation of backwall in the 45° skew test.

Figure 5-32 Backwall vertical restrainer system in the 45° skew test.

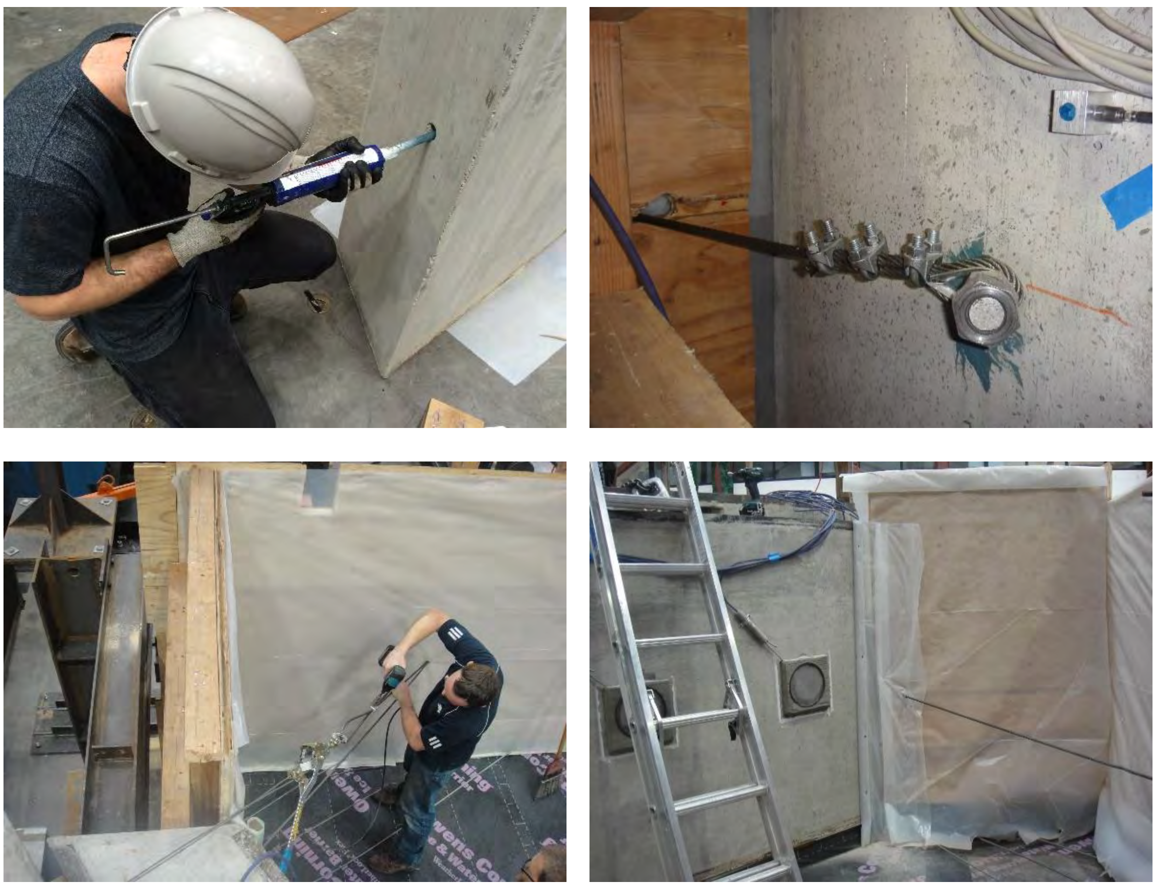

Figure 5-33 Installation of backwall restrainer cables in the 30° and 45° skew tests (top: connection to the backwall, and bottom: cable inside the soil box).

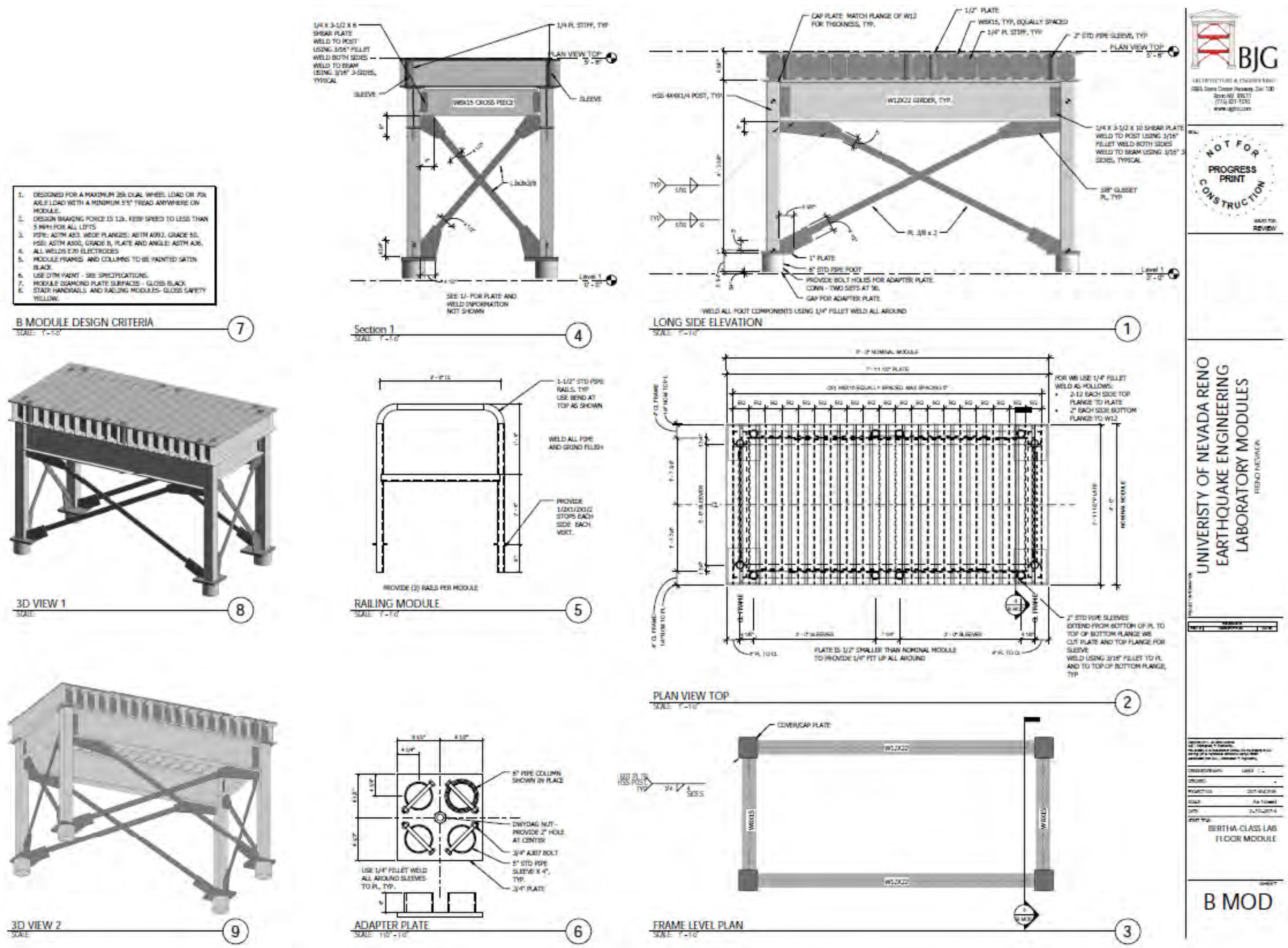

Figure 5-34 Soil box steel frame modules.

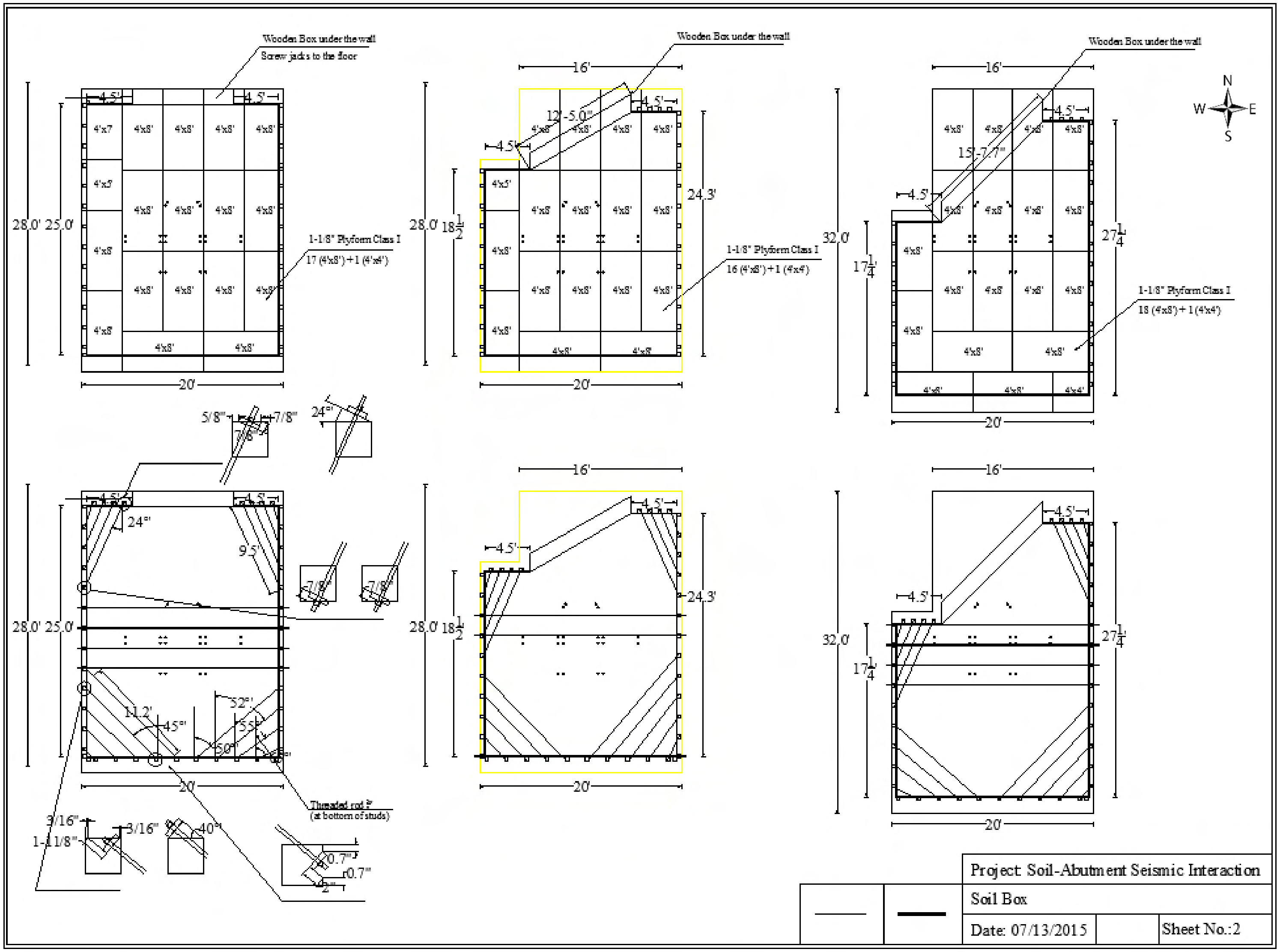

Figure 5-35 Soil box plan view.

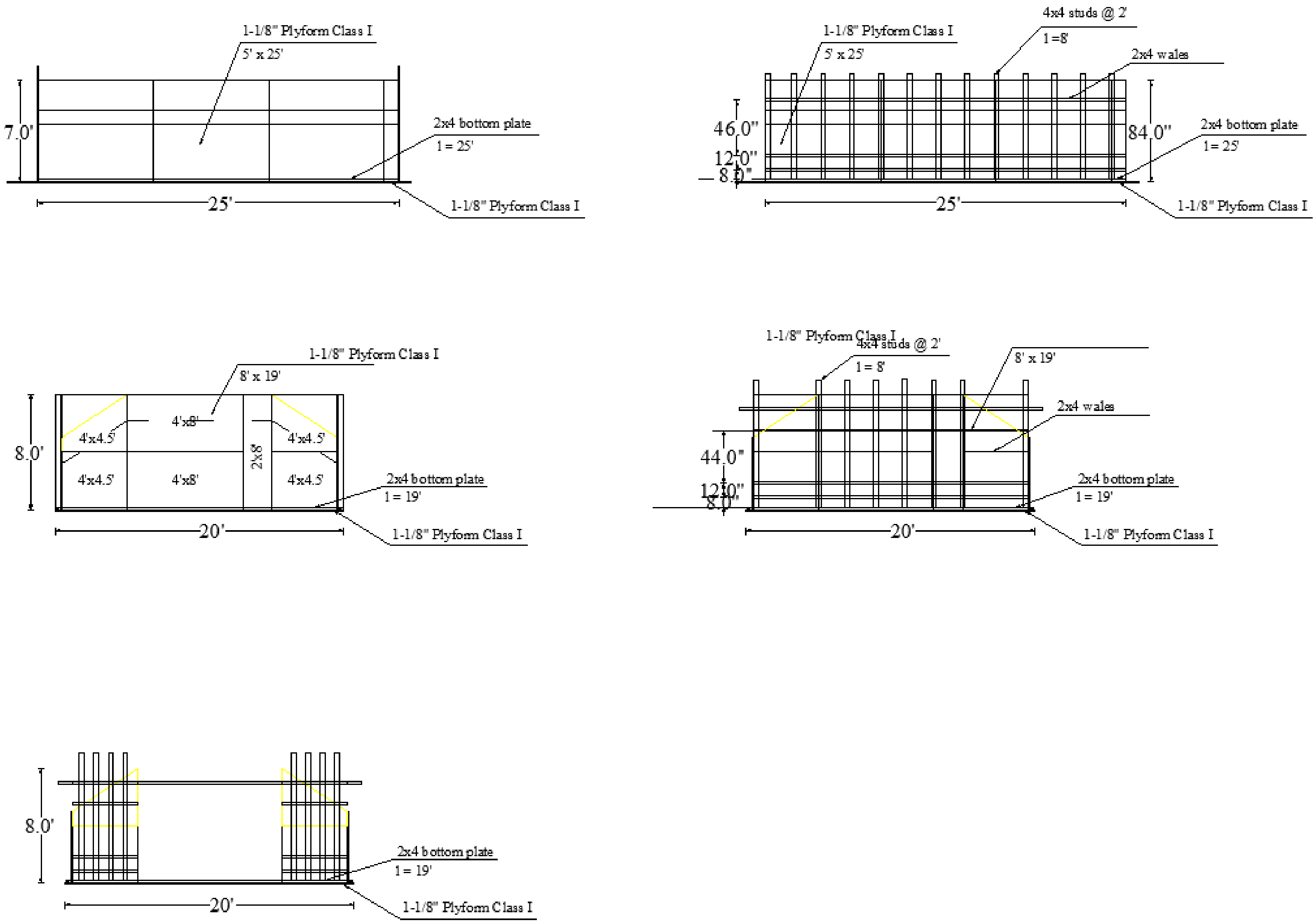

Figure 5-36 Soil box elevation view.

Figure 5-37 Construction of soil box in the 0° skew test.

Figure 5-38 Bottom ties of the soil box in the 0° skew test (top: inside the soil box, and bottom: outside the soil box).

Figure 5-39 Plastic sheeting inside the soil box in the 0° skew test.

Figure 5-40 Soil box modification from the 0° to 30° skew test.

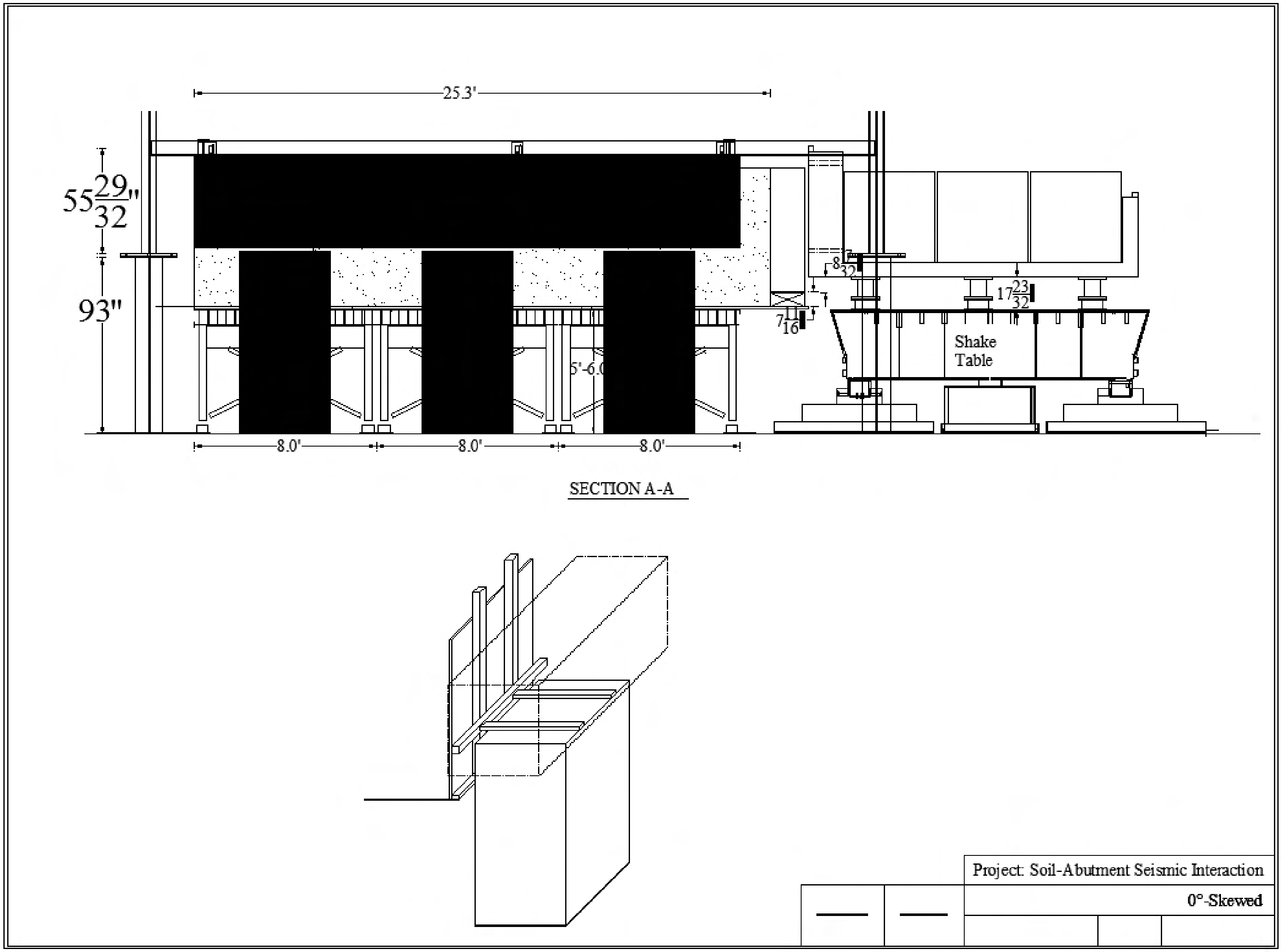

Figure 5-41 Lateral support of the soil box (west side) in the 0° skew test.

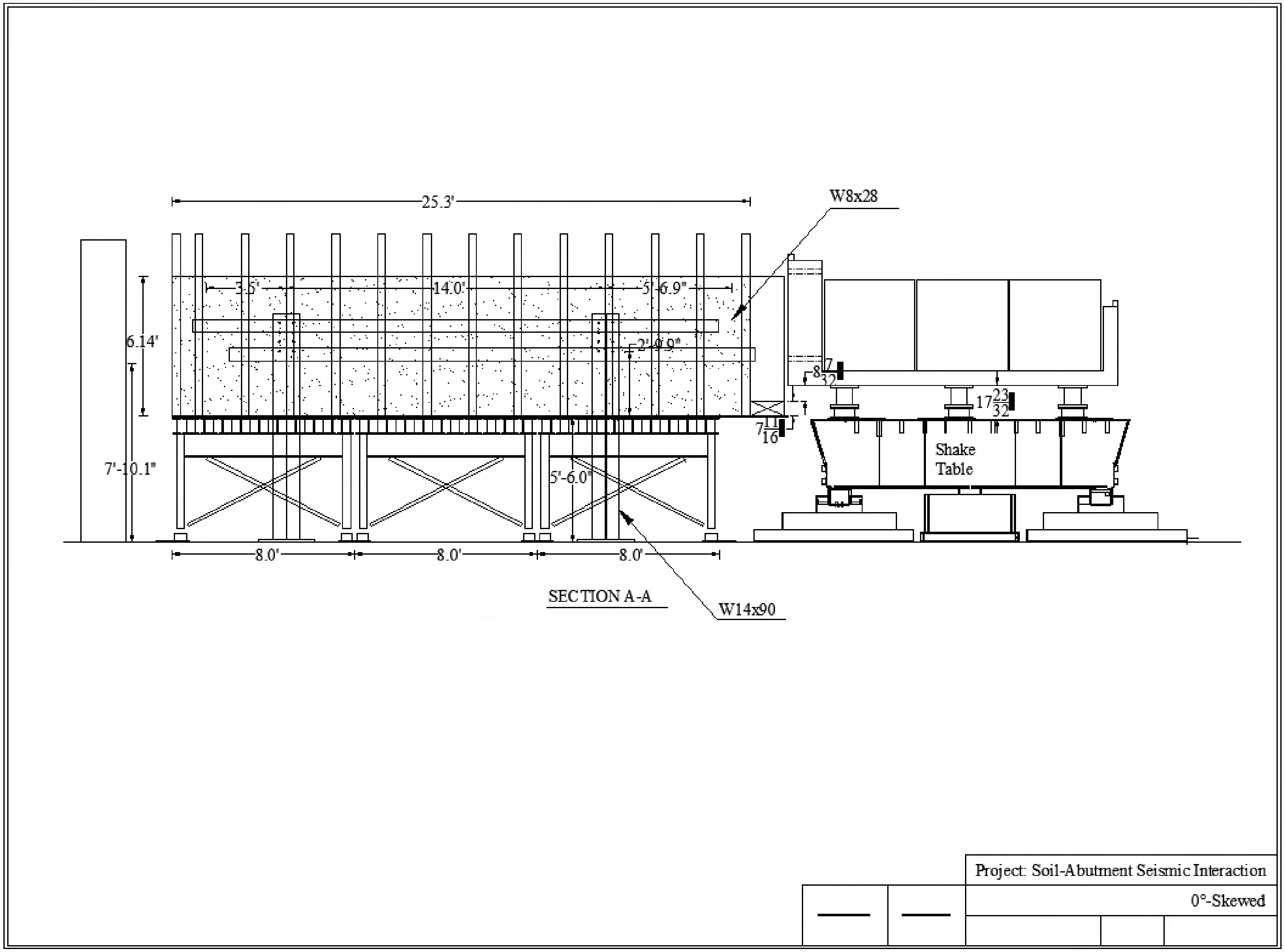

Figure 5-42 Lateral support of the soil box (east side) in the 0° skew test.

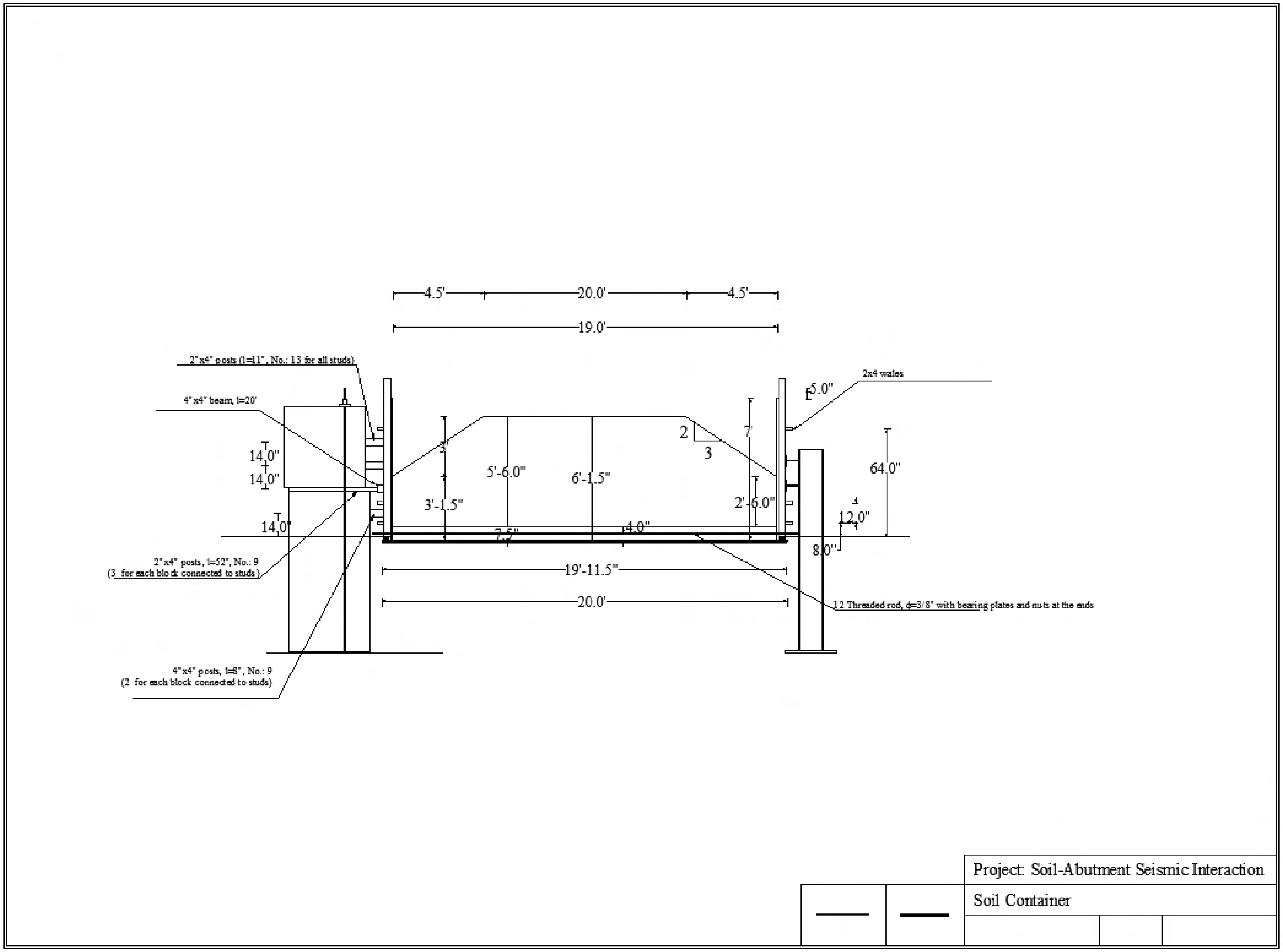

Figure 5-43 Lateral supports of the soil box in the transverse section.

Figure 5-44 Soil box lateral support in the 0° skew case (top: west side, middle: east and south sides, and bottom: north side)

Figure 5-45 Soil box lateral support in the 30° skew case (top: east side, and bottom: north-west side)

Figure 5-46 Soil box lateral support in the 45° skew case (top left: west side, top right: east side, middle: north-west side, and bottom: north-east side)

Figure 5-47 Water mitigation system in the 30° skew test.

Figure 5-48 Water mitigation system in the 45° skew test.

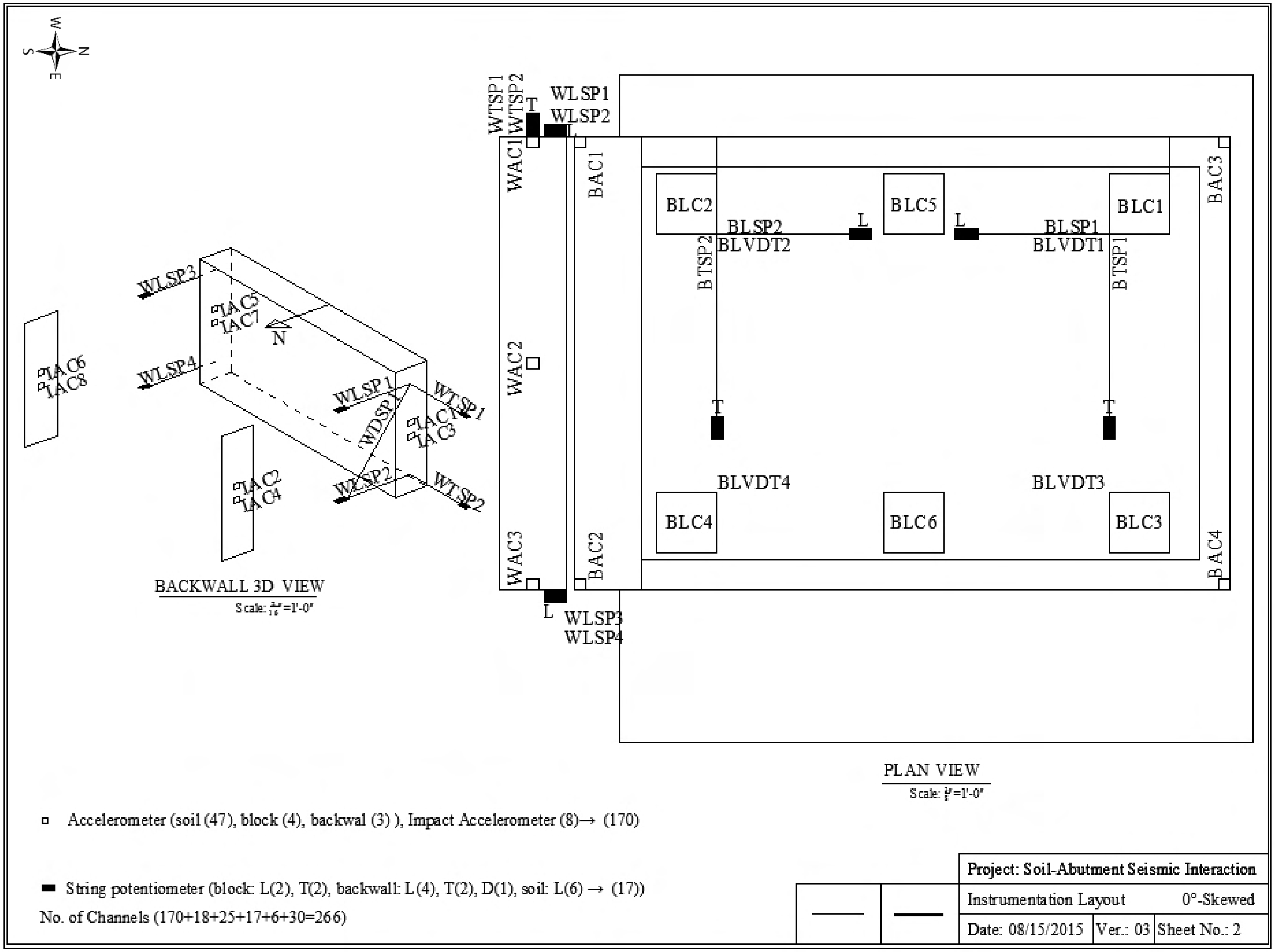

Figure 5-49 Structural instrumentation plan in the 0° skew test.

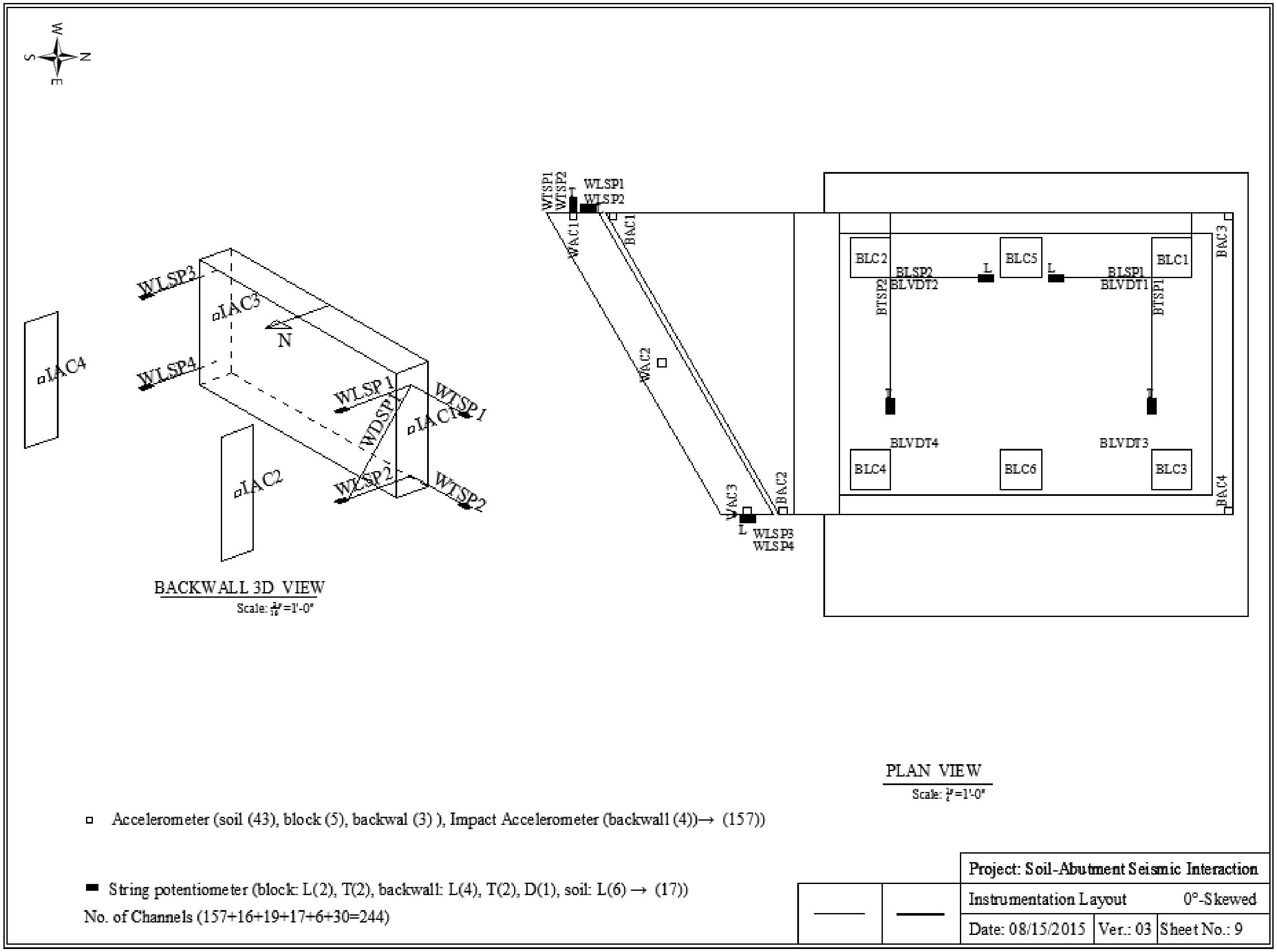

Figure 5-50 Structural instrumentation plan in the 30° skew test.

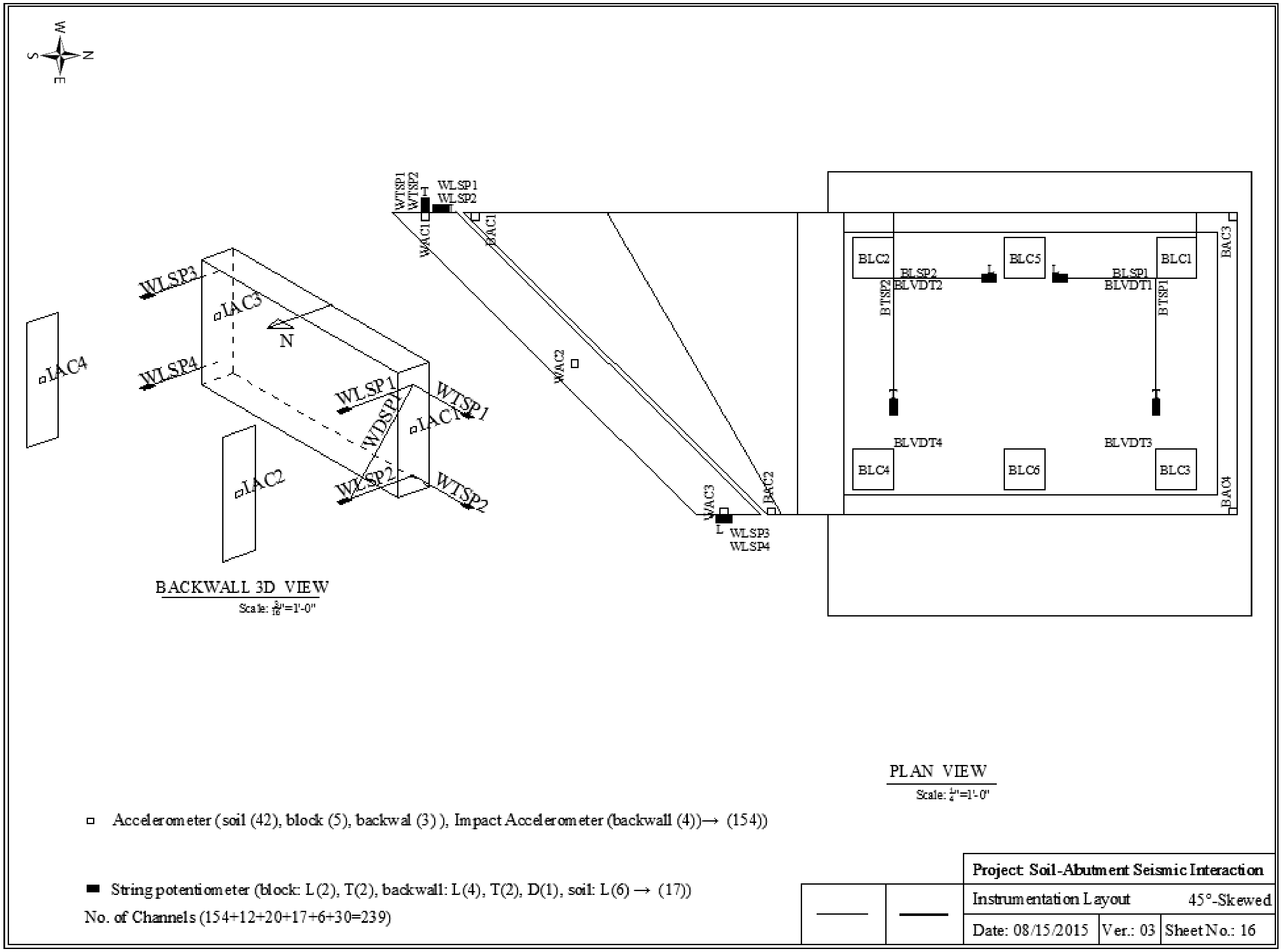

Figure 5-51 Structural instrumentation plan in the 45° skew test.

Figure 5-52 Triaxial accelerometers in the 30° skew test (left: backwall west side, and right: bridge block west side).

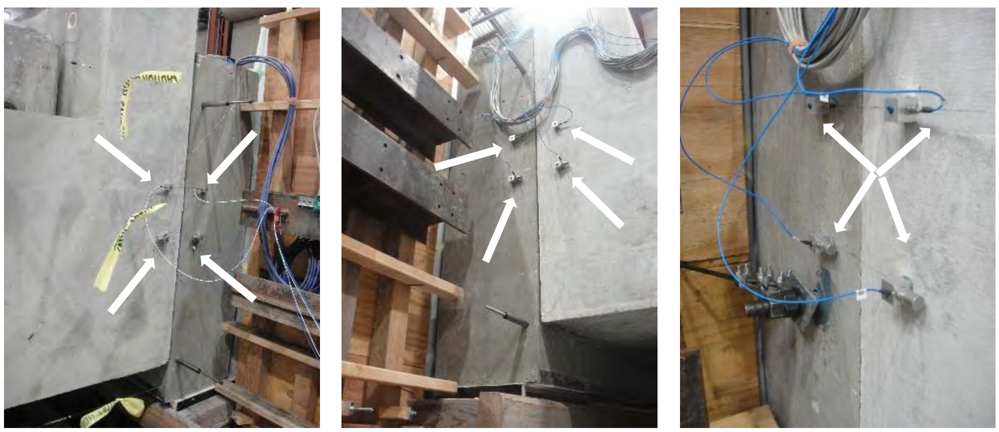

Figure 5-53 Impact accelerometers in the 0° skew test (left: west side, and right: east side).

Figure 5-54 Impact accelerometers in the 45° skew test (top: east side, and right: west side).

Figure 5-55 String potentiometers of the bridge block (left: longitudinal, and right: transverses south-west).

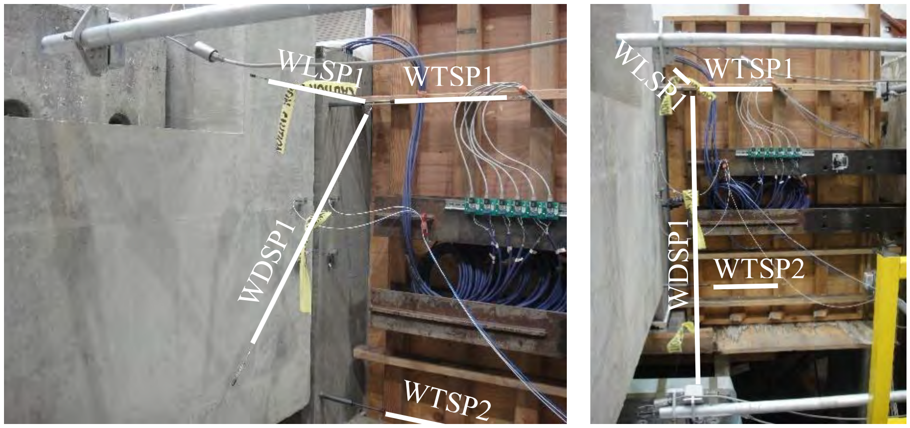

Figure 5-56 String potentiometers of the backwall in the 0° skew test (west side).

Figure 5-57 String potentiometers of the backwall in the 30° skew test (left: bottom west, and right: top west).

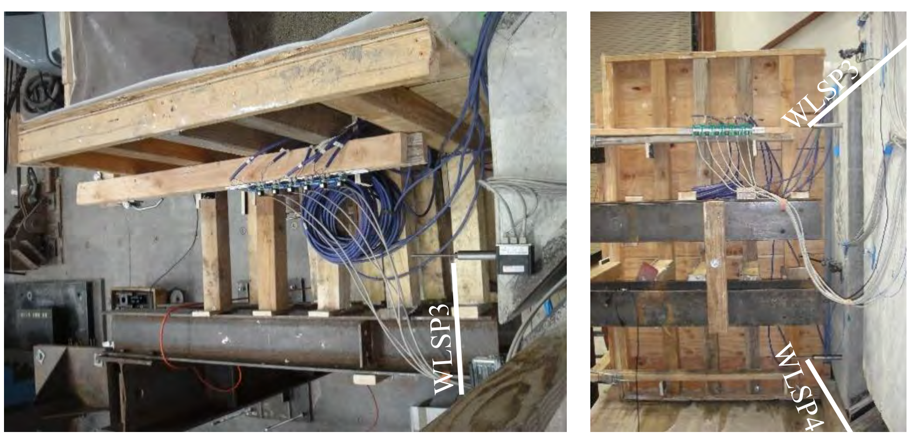

Figure 5-58 Longitudinal string potentiometers of the backwall in the 45° skew test (left: top east, and right: top and bottom east).

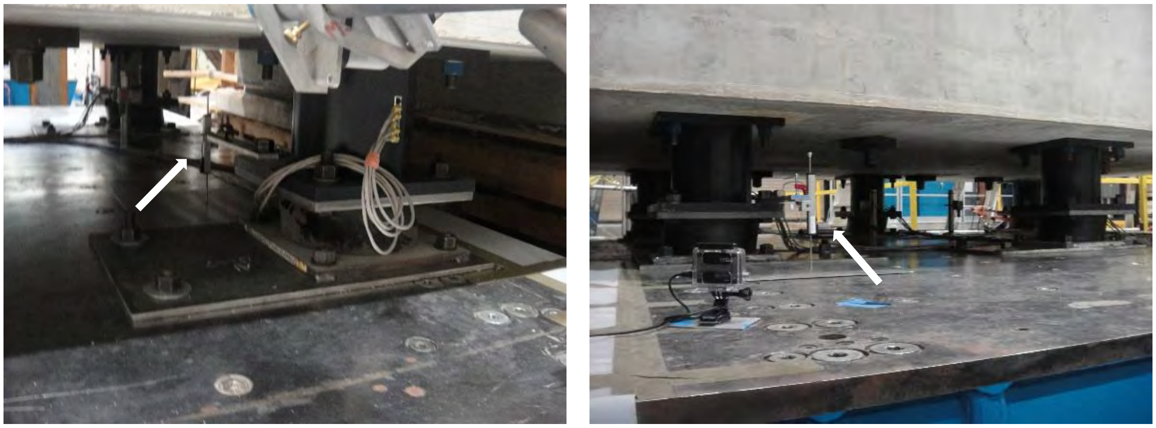

Figure 5-59 Vertical LVDTs of the bridge block (left: south-west, and right: south-east).

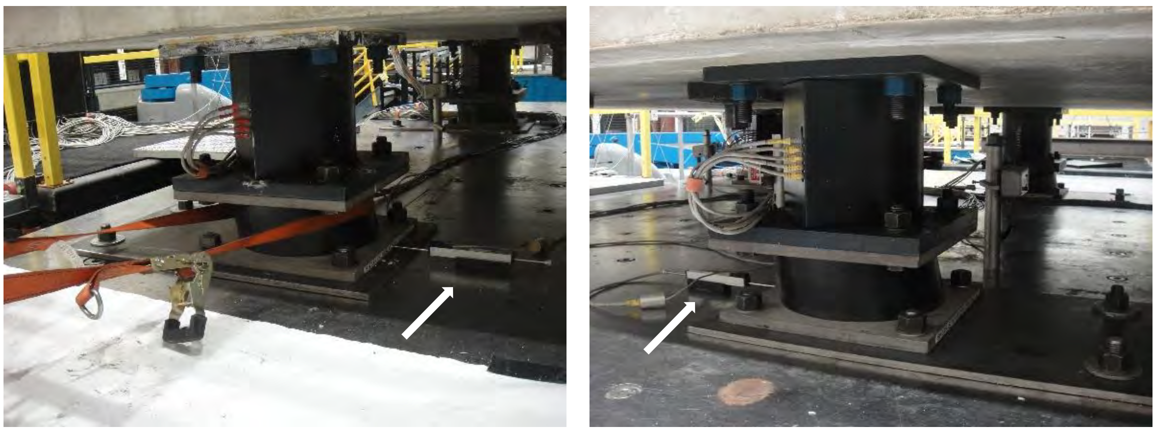

Figure 5-60 Isolator slippage LVDTs (left: north-west, and right: south-west).

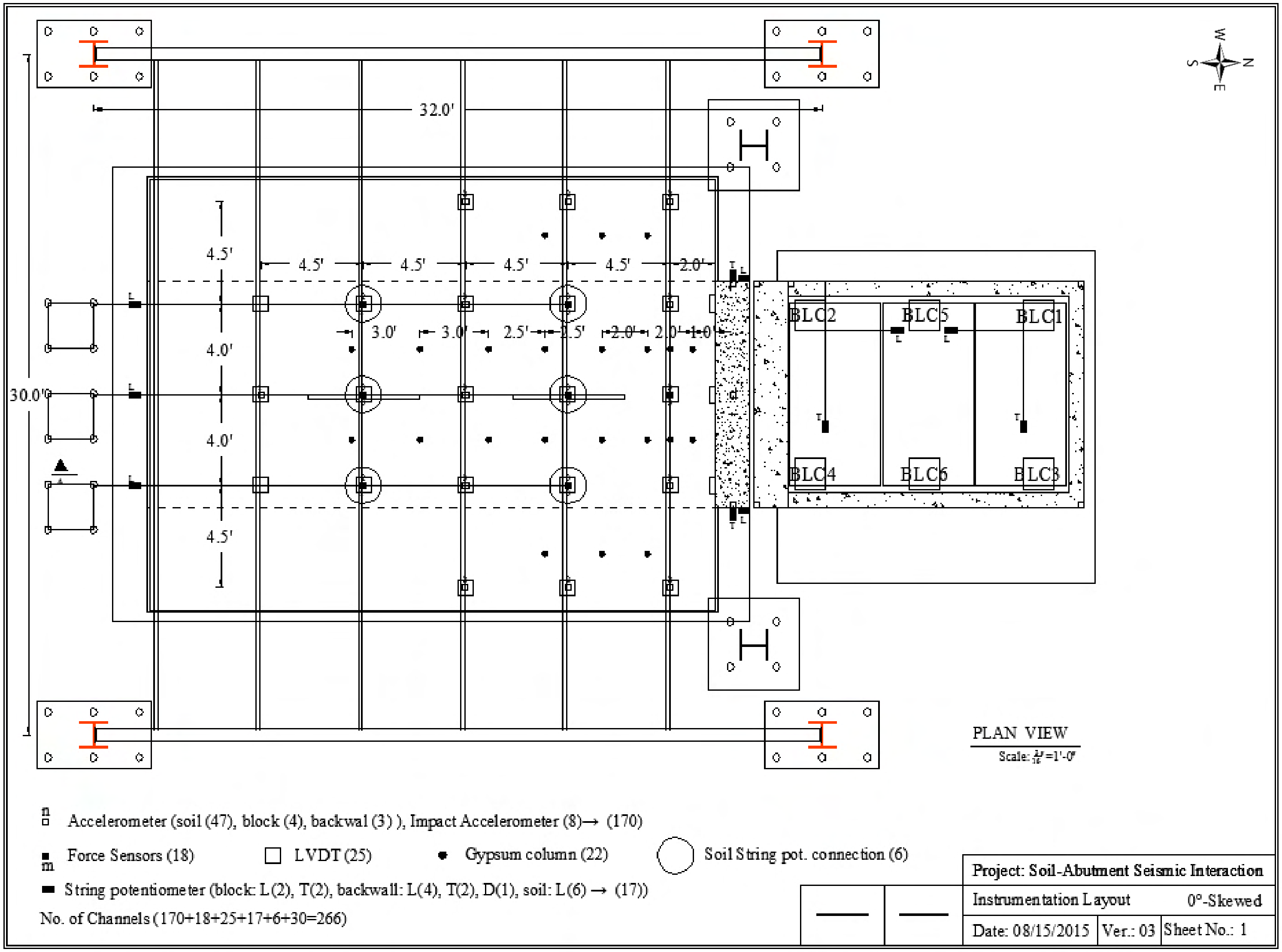

Figure 5-61 Soil instrumentation plan in the 0° skew test.

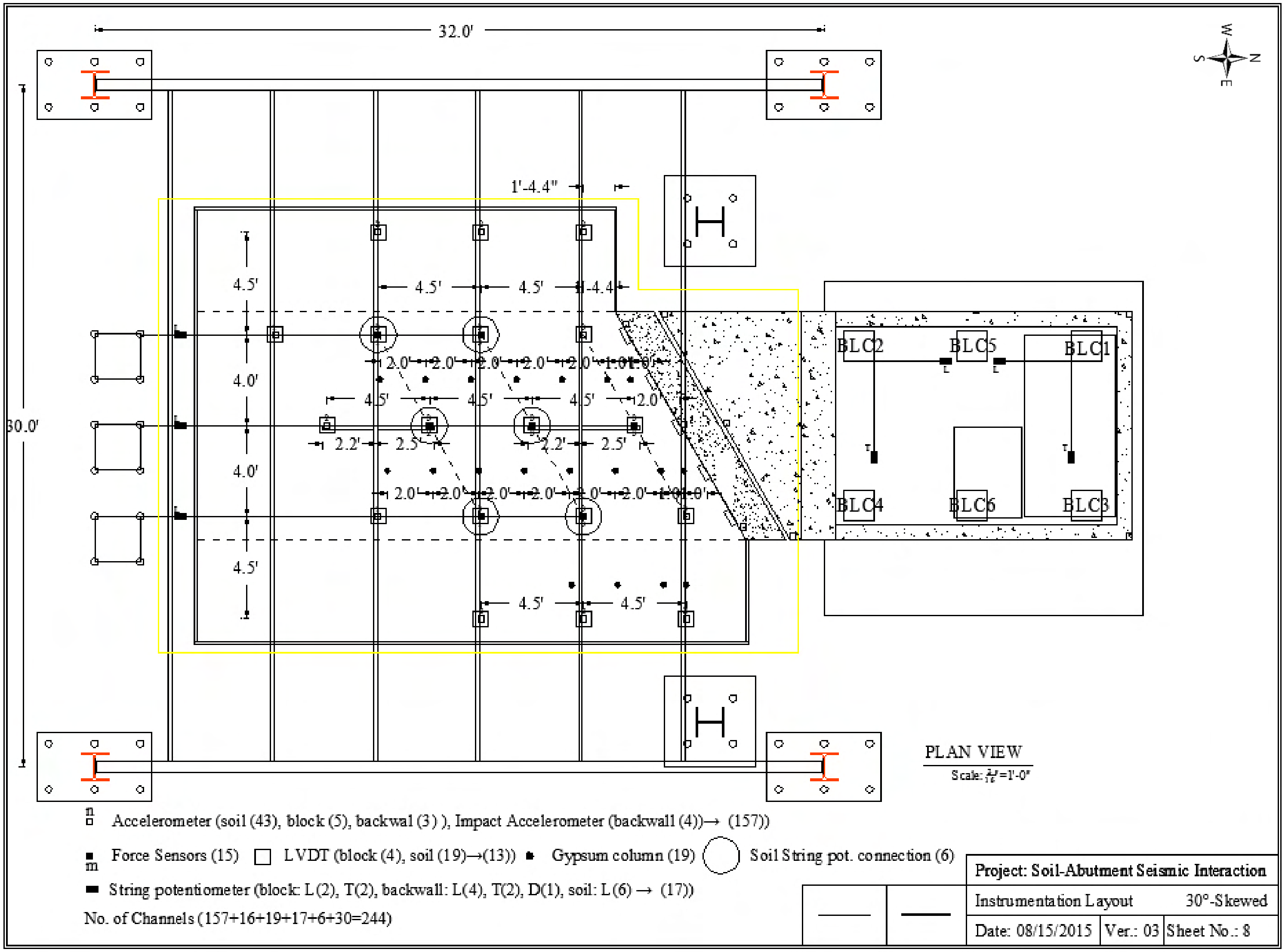

Figure 5-62 Soil instrumentation plan in the 30° skew test.

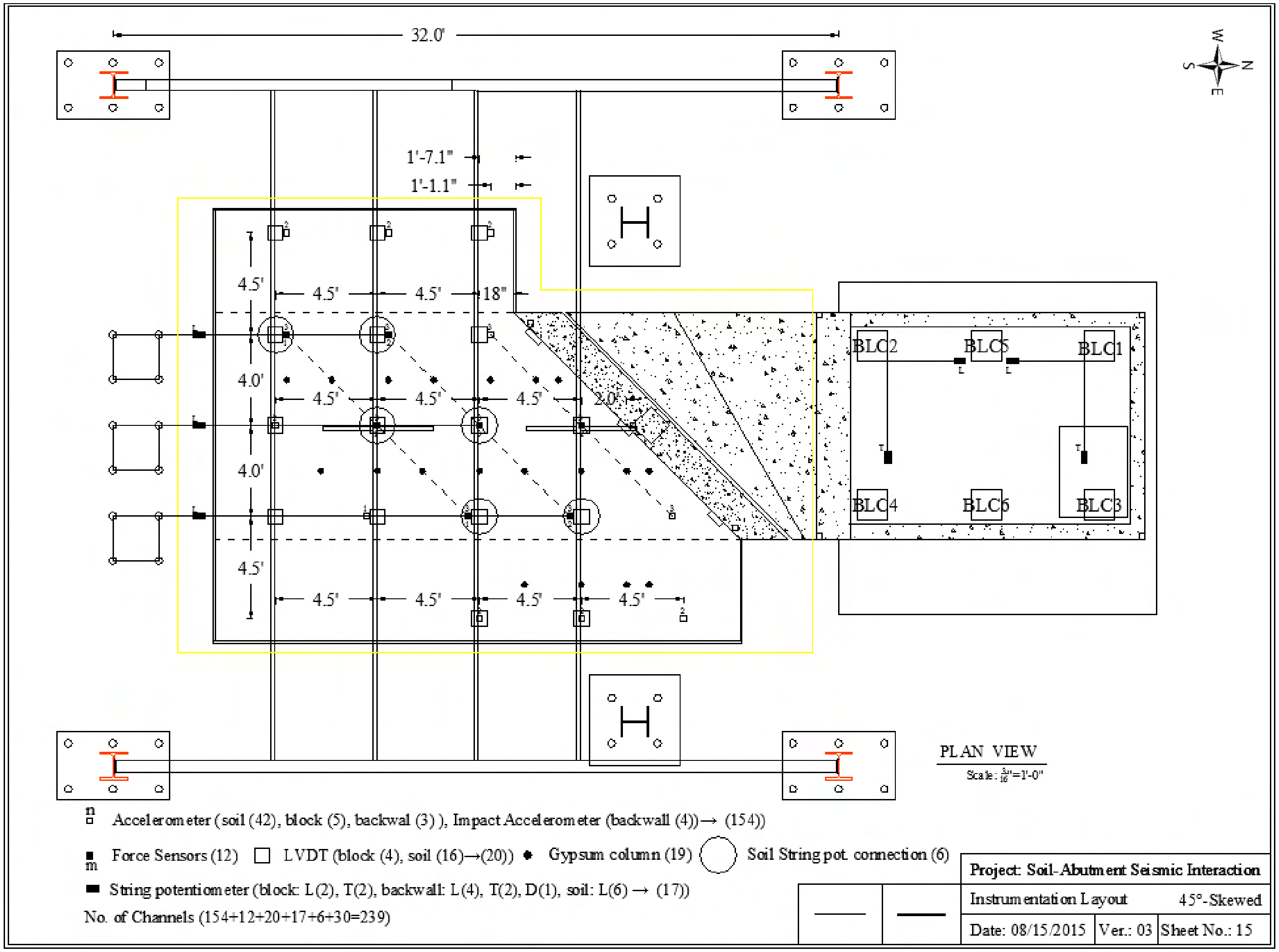

Figure 5-63 Soil instrumentation plan in the 45° skew test.

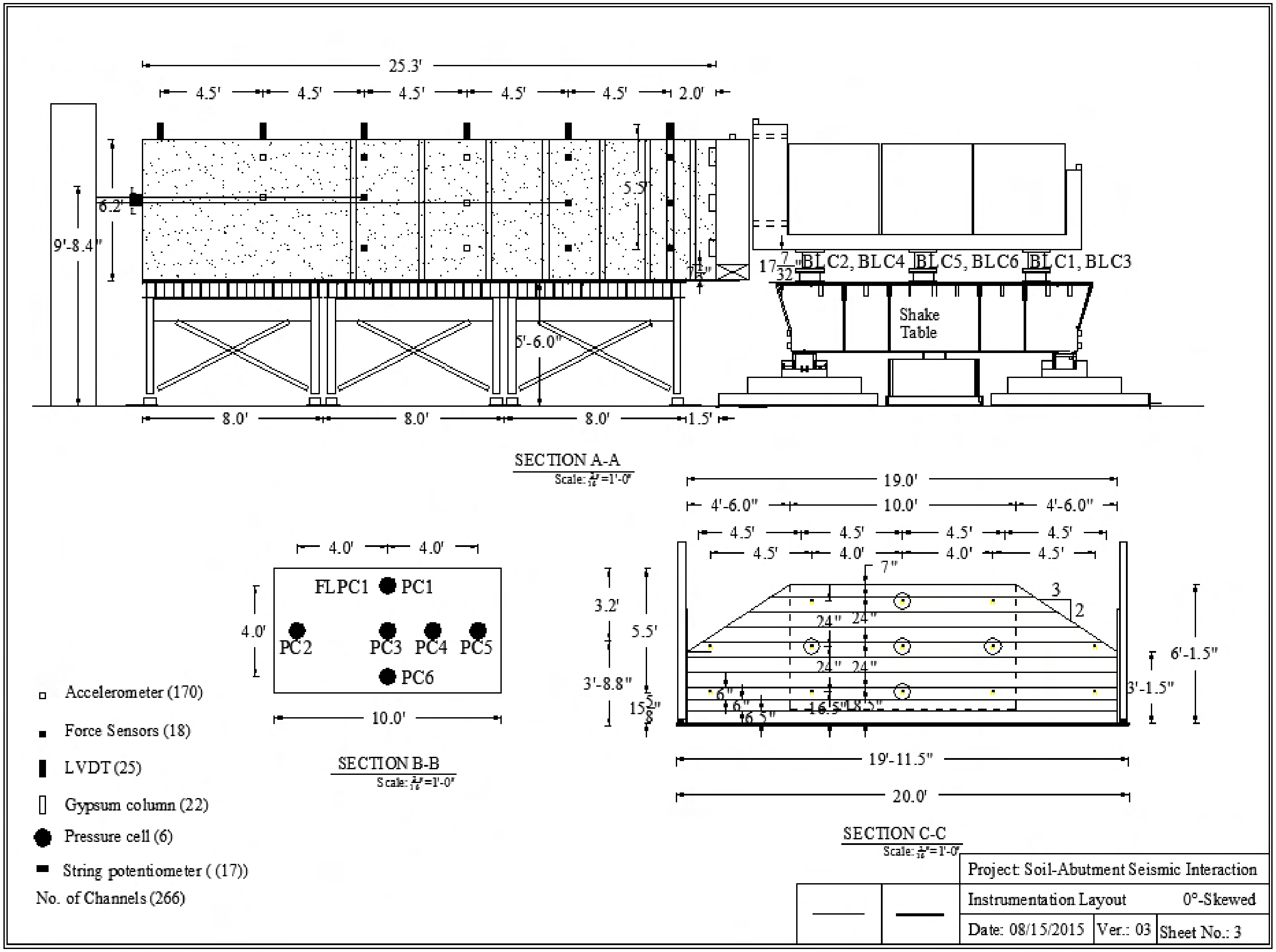

Figure 5-64 Soil instrumentation elevation in the 0° skew test.

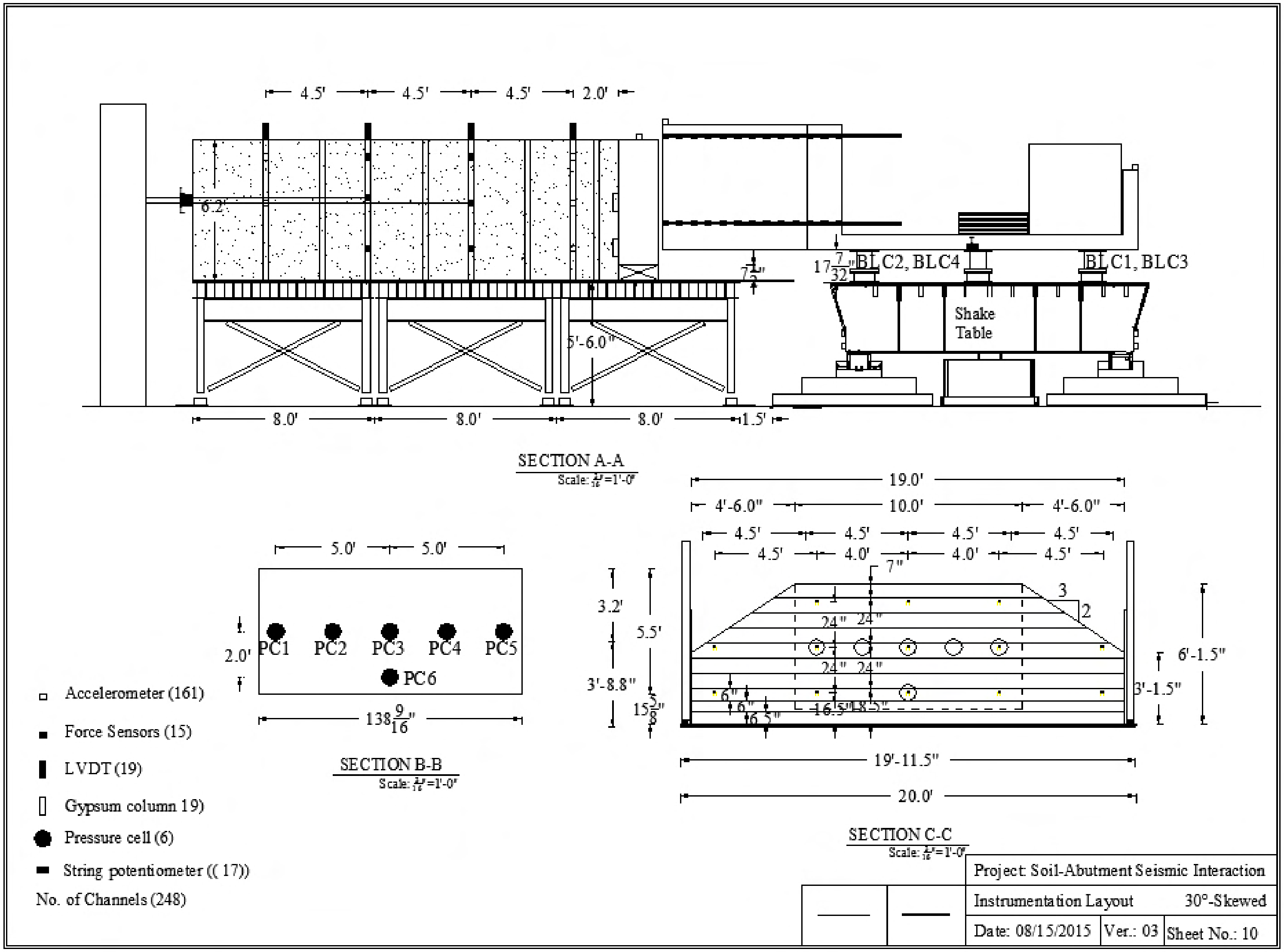

Figure 5-65 Soil instrumentation elevation in the 30° skew test.

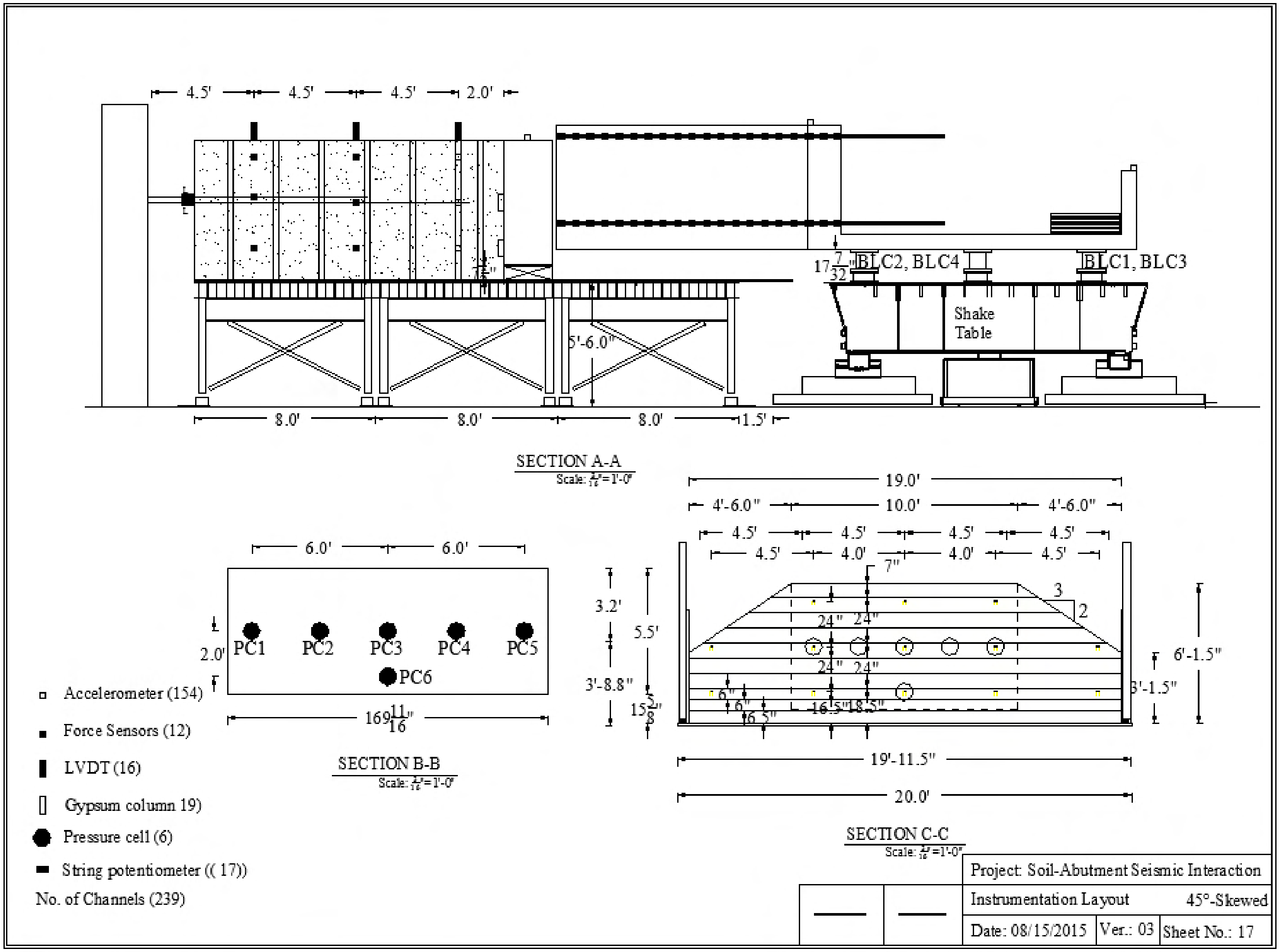

Figure 5-66 Soil instrumentation elevation in the 45° skew test.

Figure 5-67 Earth pressure cells.

Figure 5-68 Pressure cells in the 0° skew test.

Figure 5-69 Pressure cells in the 30° skew test.

Figure 5-70 Pressure cells in the 45° skew test.

Figure 5-71 Soil triaxial accelerometers.

Figure 5-72 FlexiForce sensor.

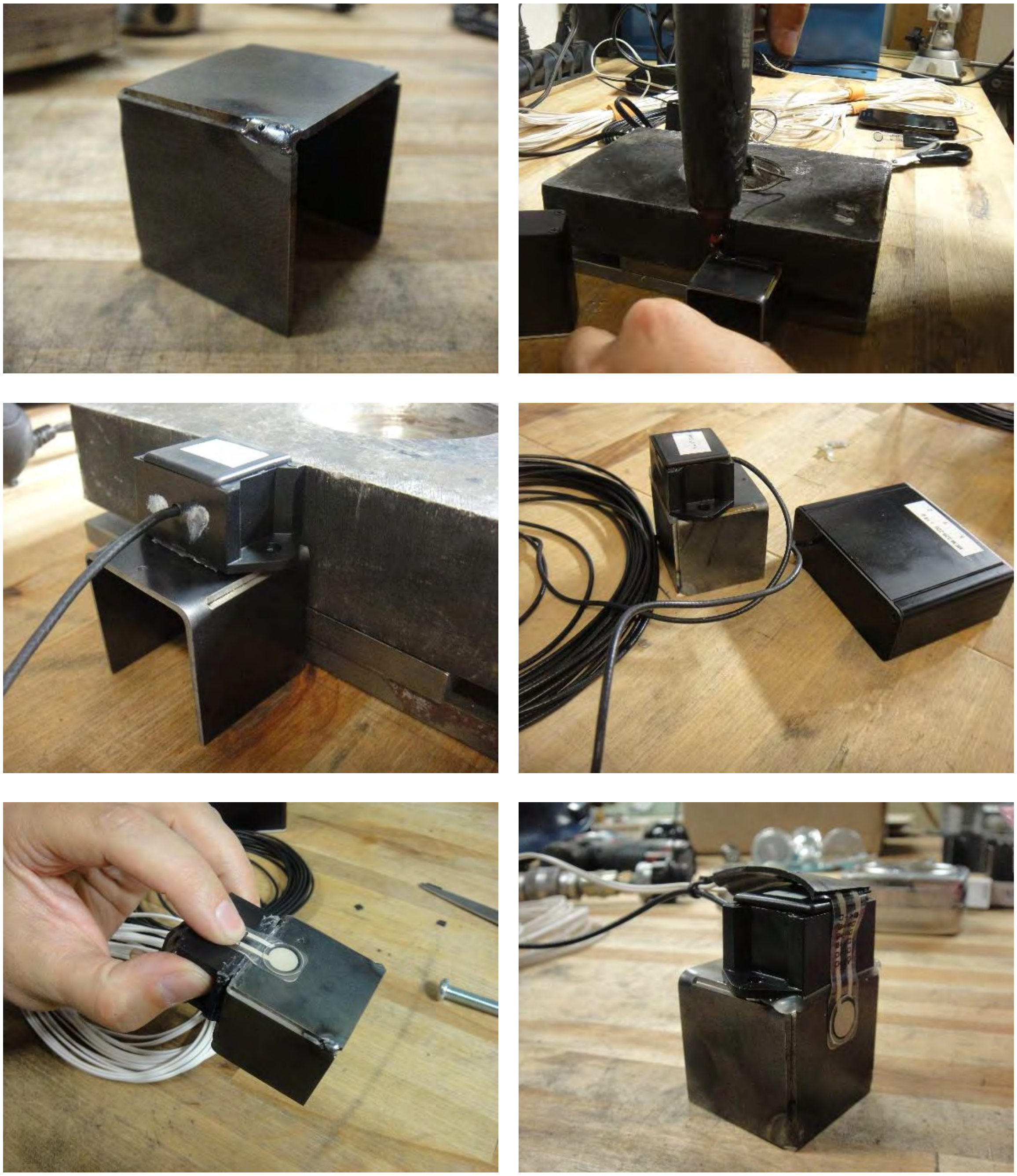

Figure 5-73 Soil sensor cluster (top: cluster box, middle: accelerometer on cluster box, and bottom: FlexiForce sensor on cluster box).

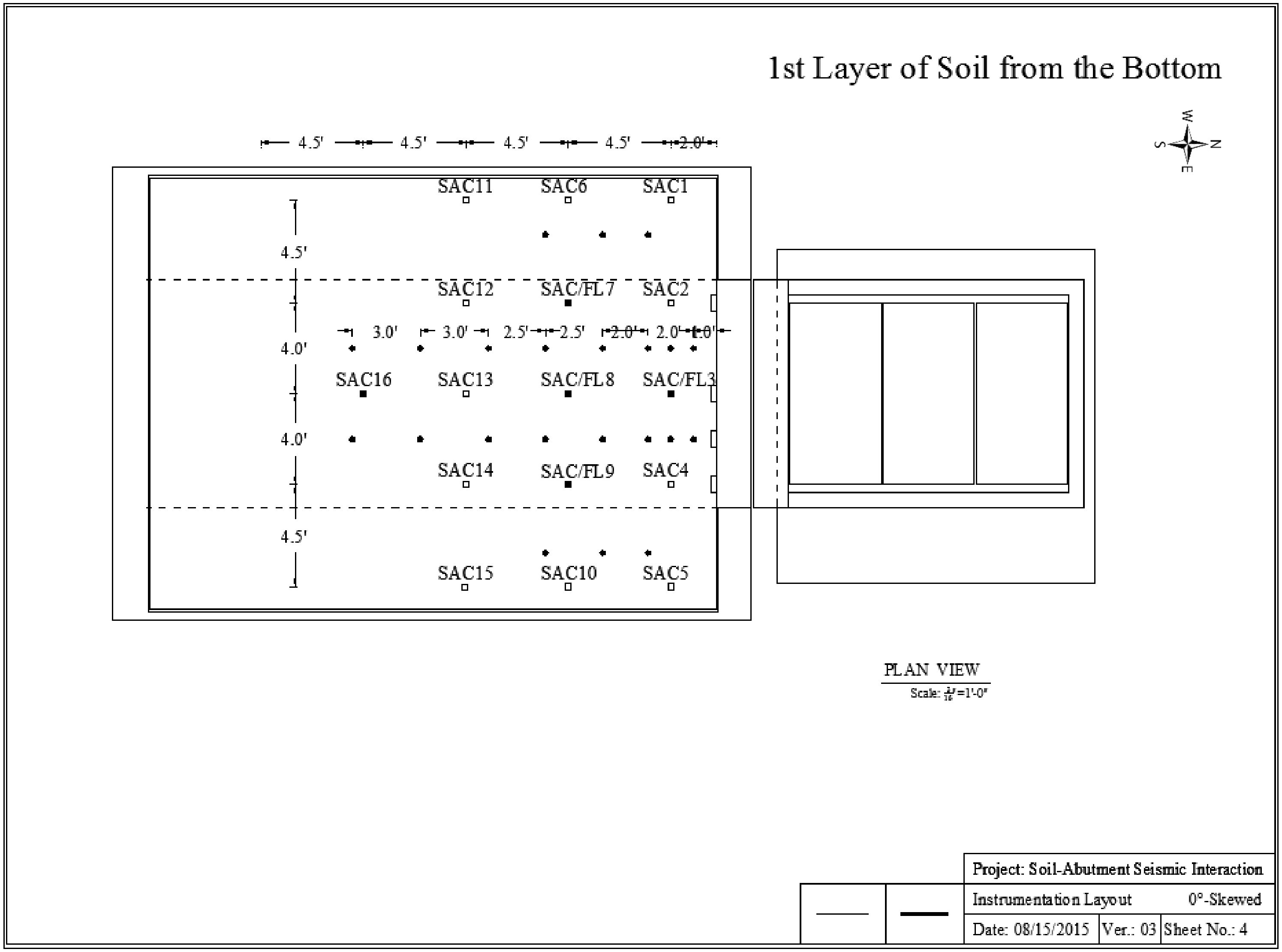

Figure 5-74 Soil internal instrumentation plan in the 0° skew test (bottom layer).

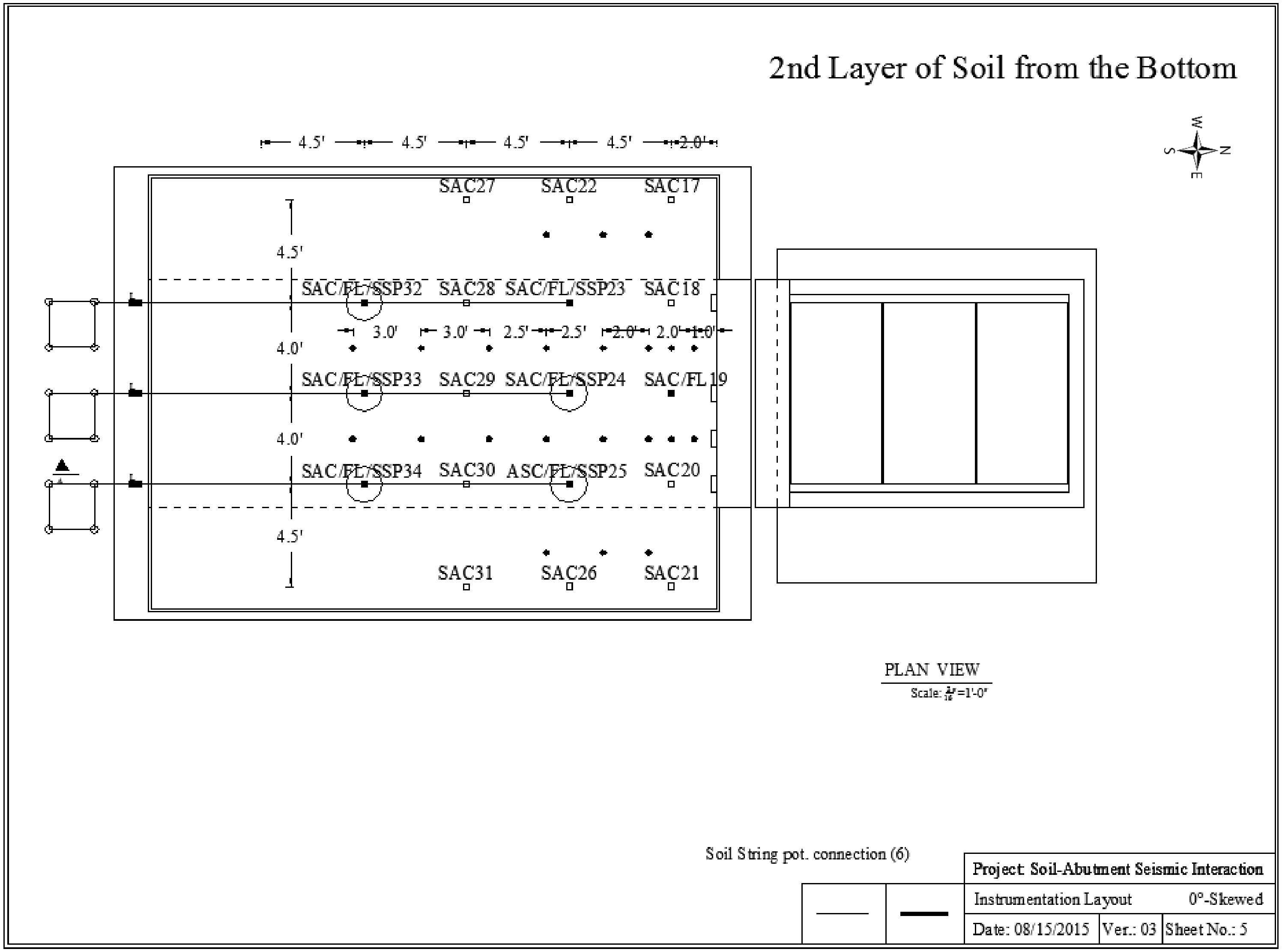

Figure 5-75 Soil internal instrumentation plan in the 0° skew test (middle layer).

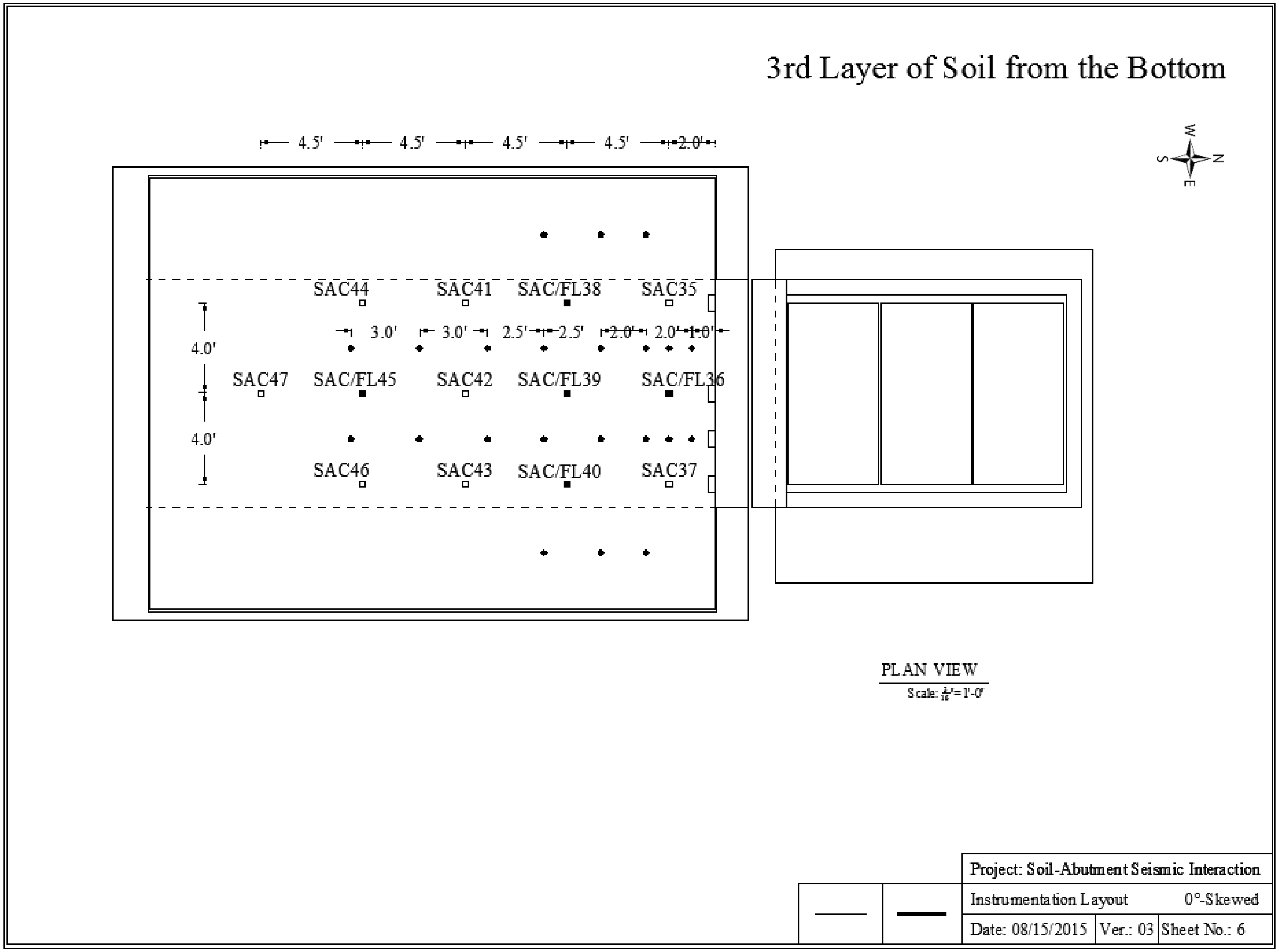

Figure 5-76 Soil internal instrumentation plan in the 0° skew test (top layer).

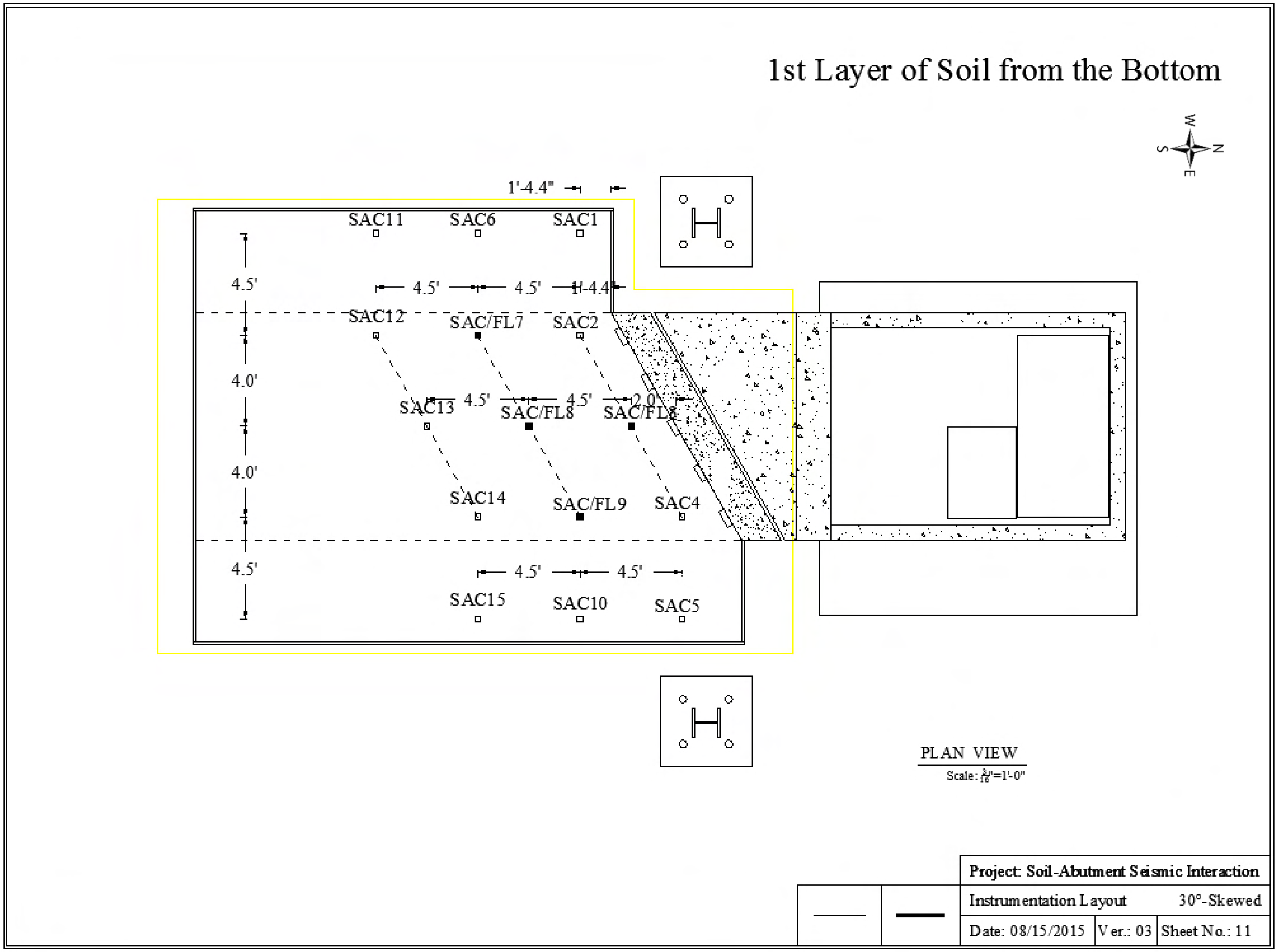

Figure 5-77 Soil internal instrumentation plan in the 30° skew test (bottom layer).

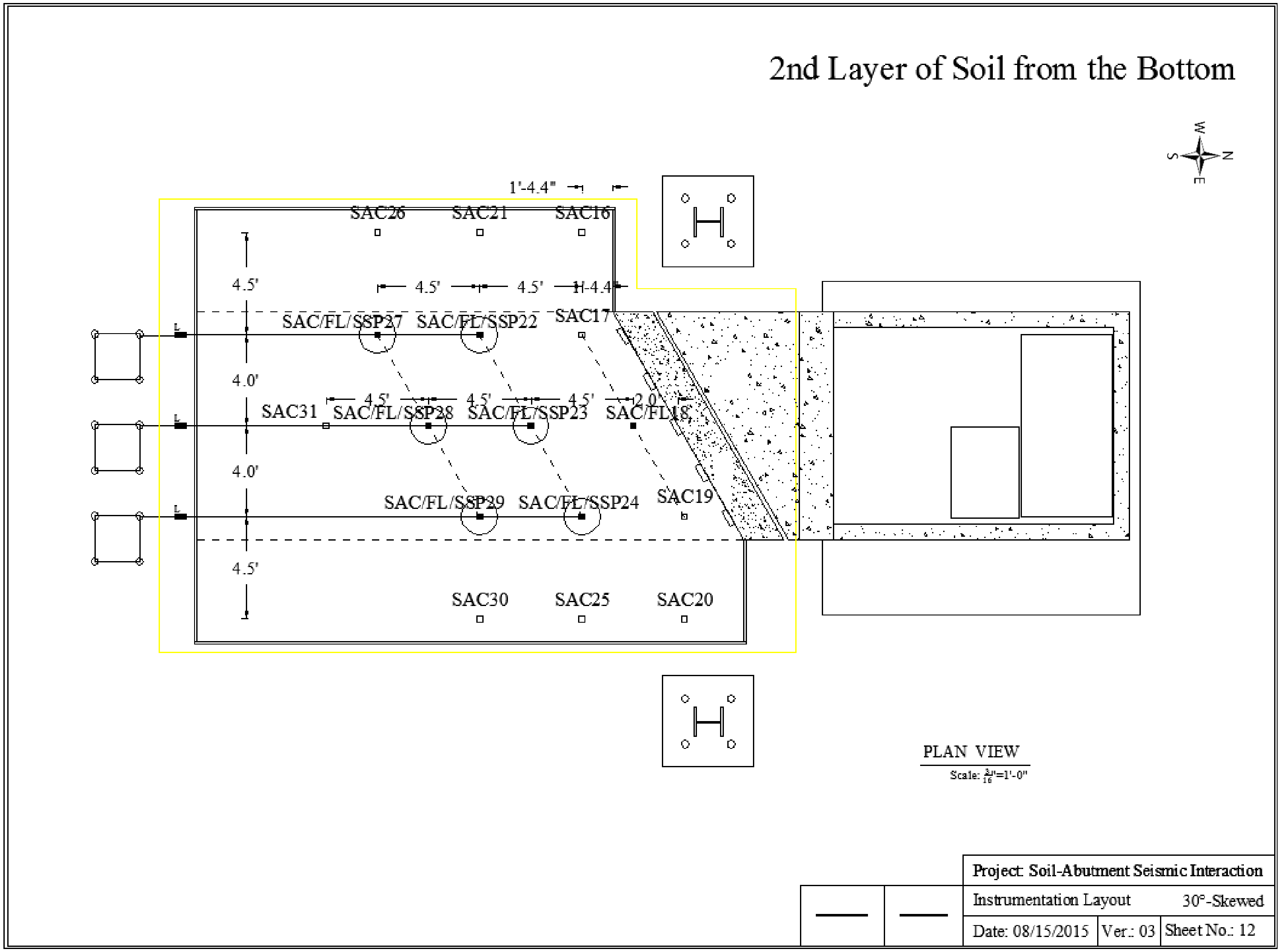

Figure 5-78 Soil internal instrumentation plan in the 30° skew test (middle layer).

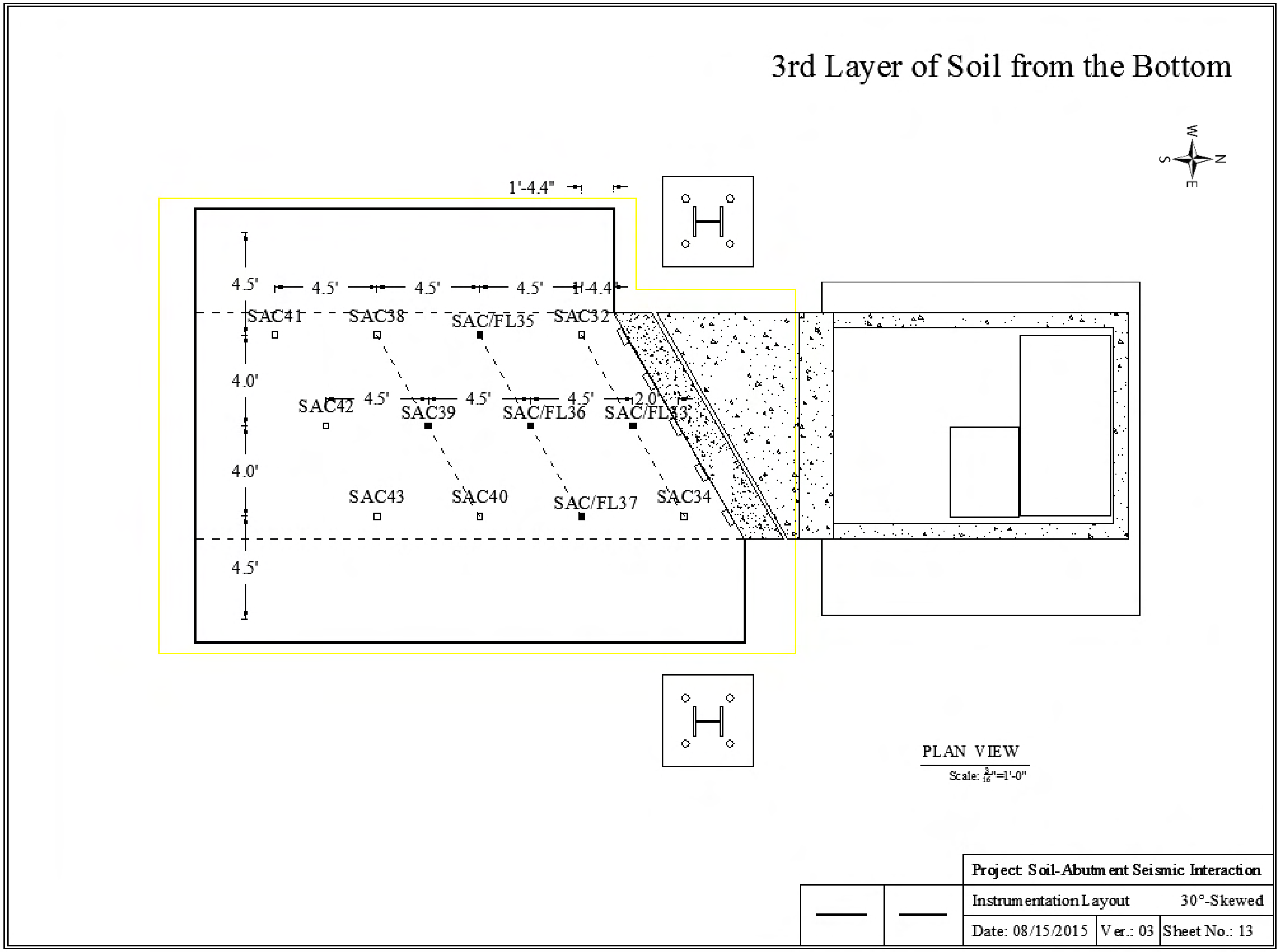

Figure 5-79 Soil internal instrumentation plan in the 30° skew test (top layer).

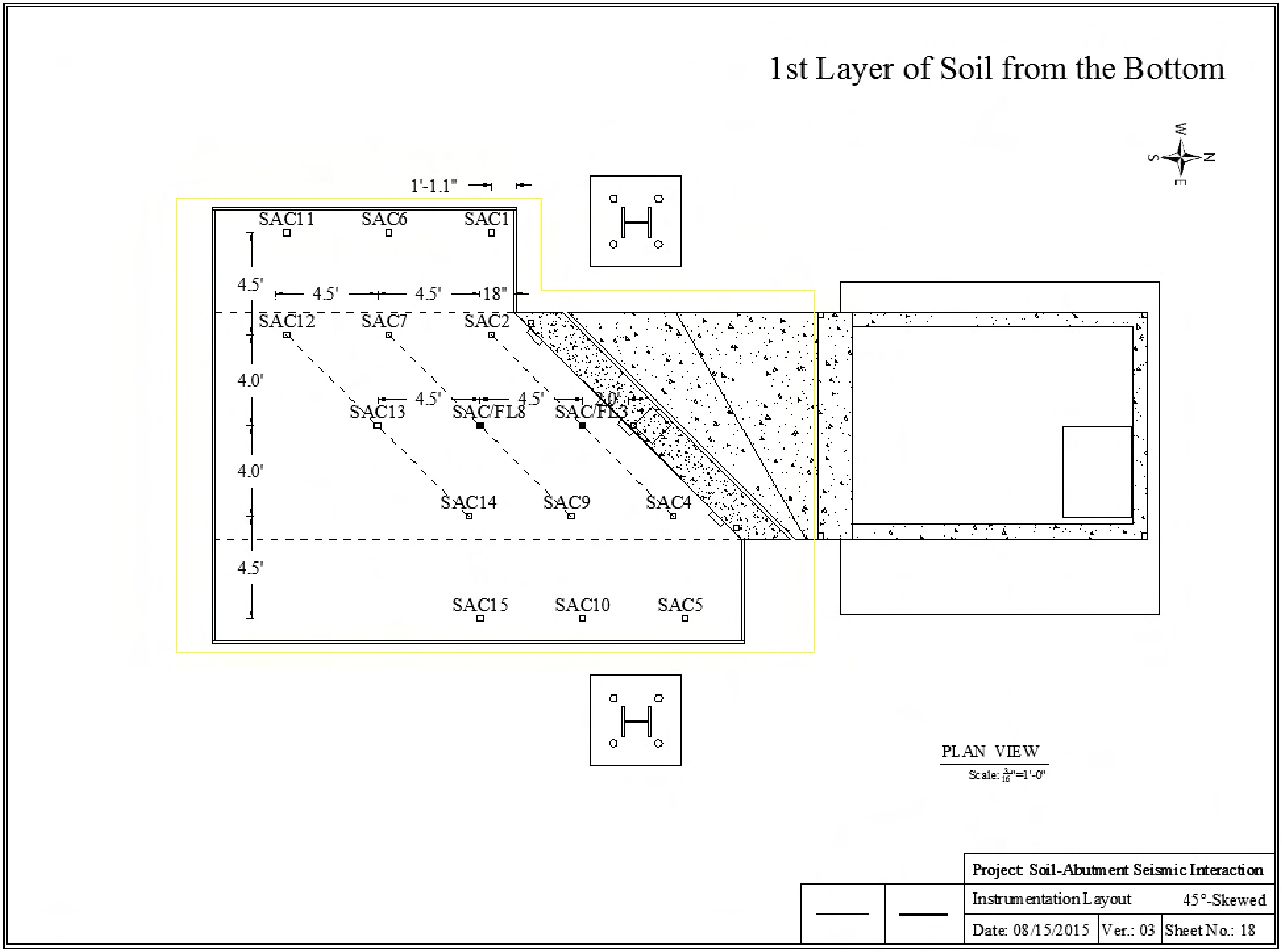

Figure 5-80 Soil internal instrumentation plan in the 45° skew test (bottom layer).

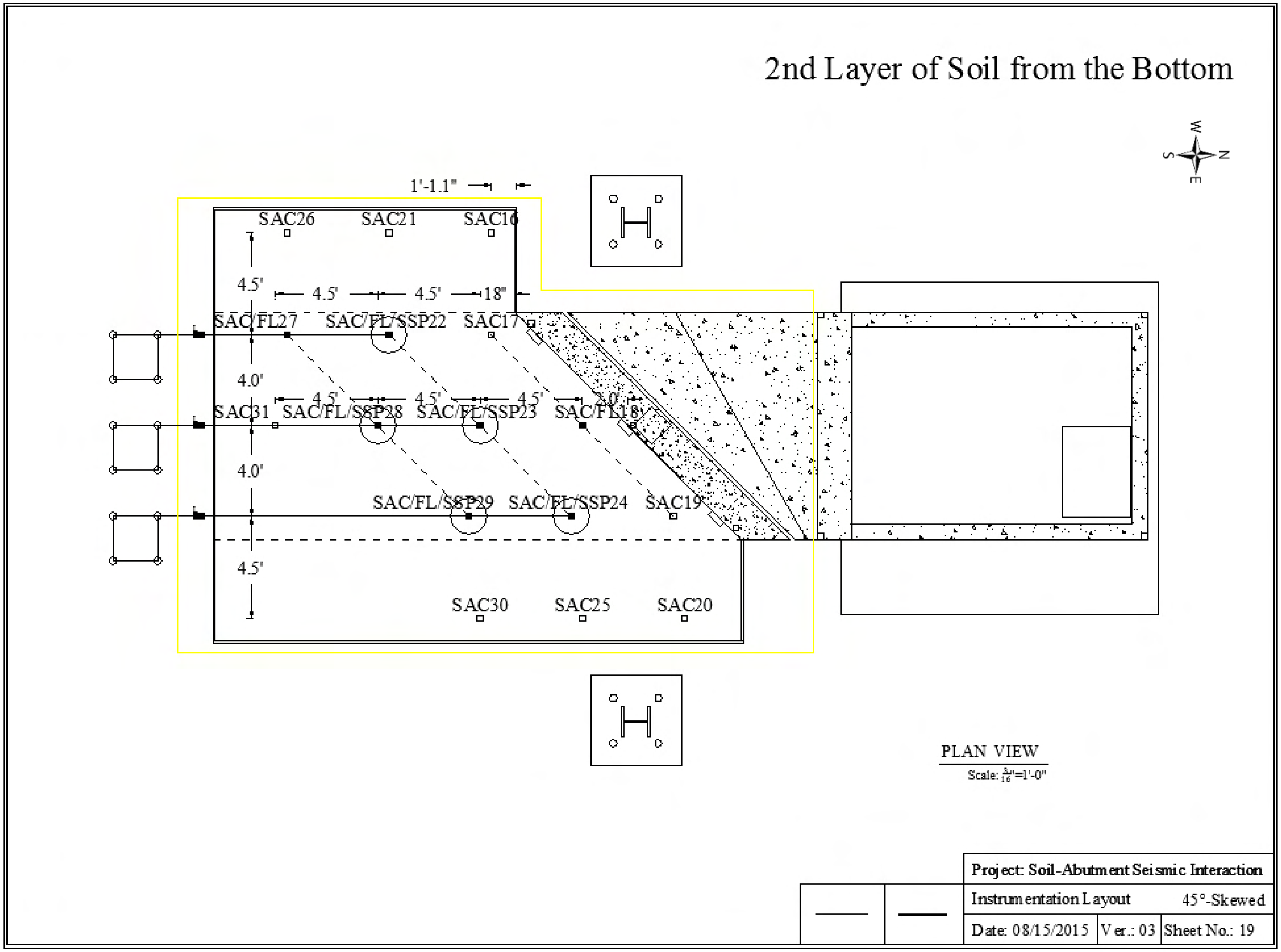

Figure 5-81 Soil internal instrumentation plan in the 45° skew test (middle layer).

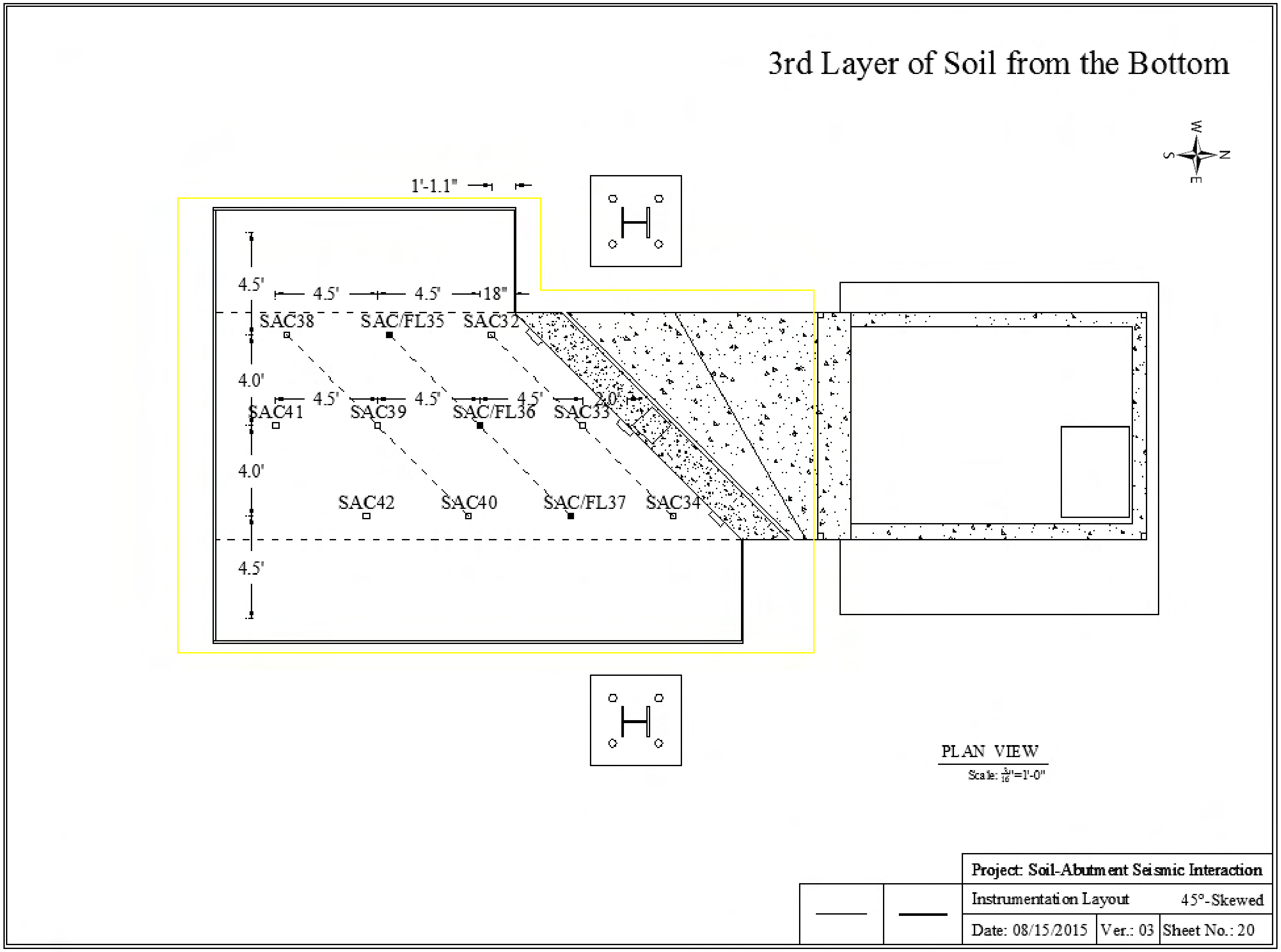

Figure 5-82 Soil internal instrumentation plan in the 45° skew test (top layer).

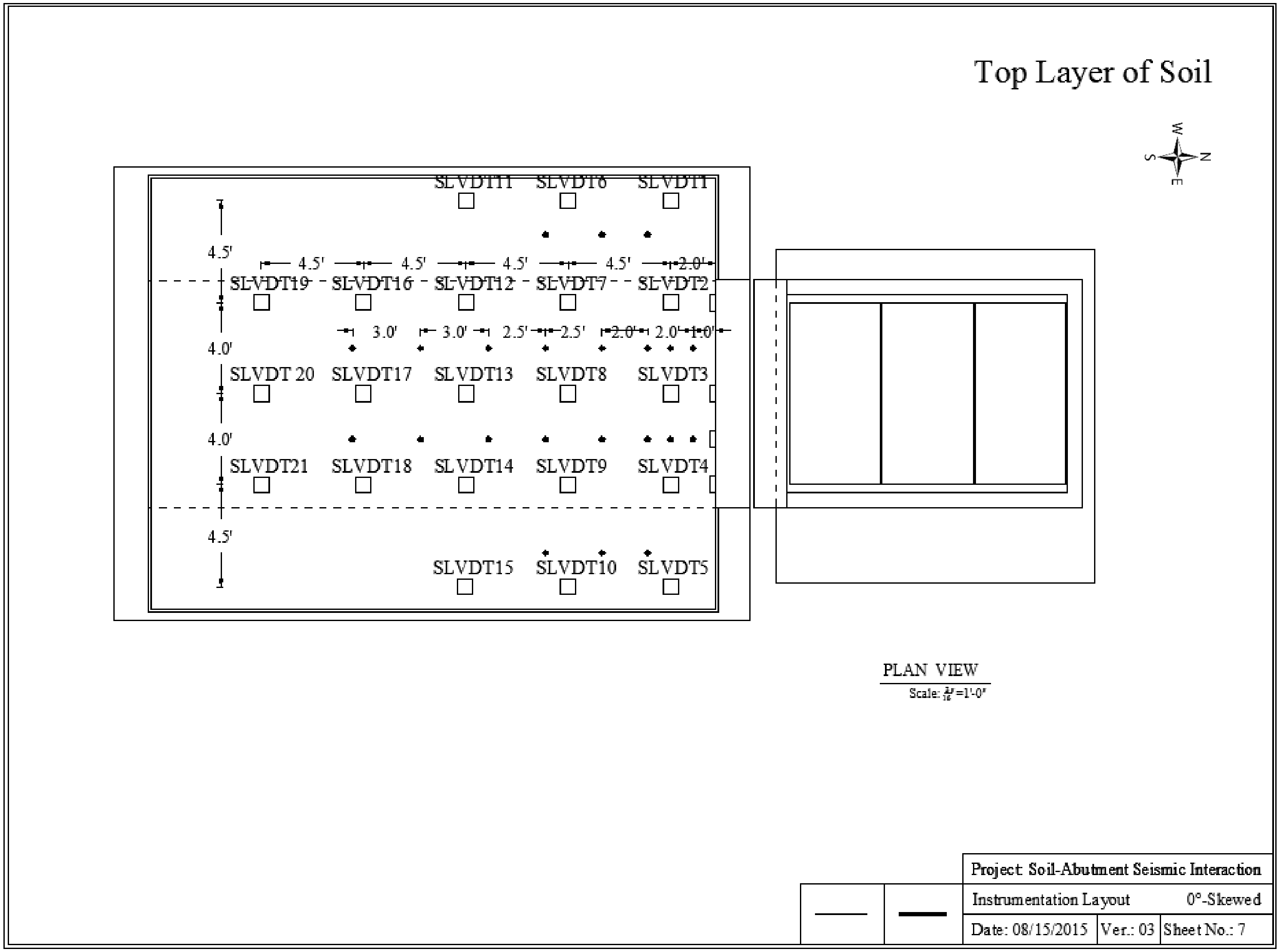

Figure 5-83 Soil surface LVDT instrumentation plan in the 0° skew test.

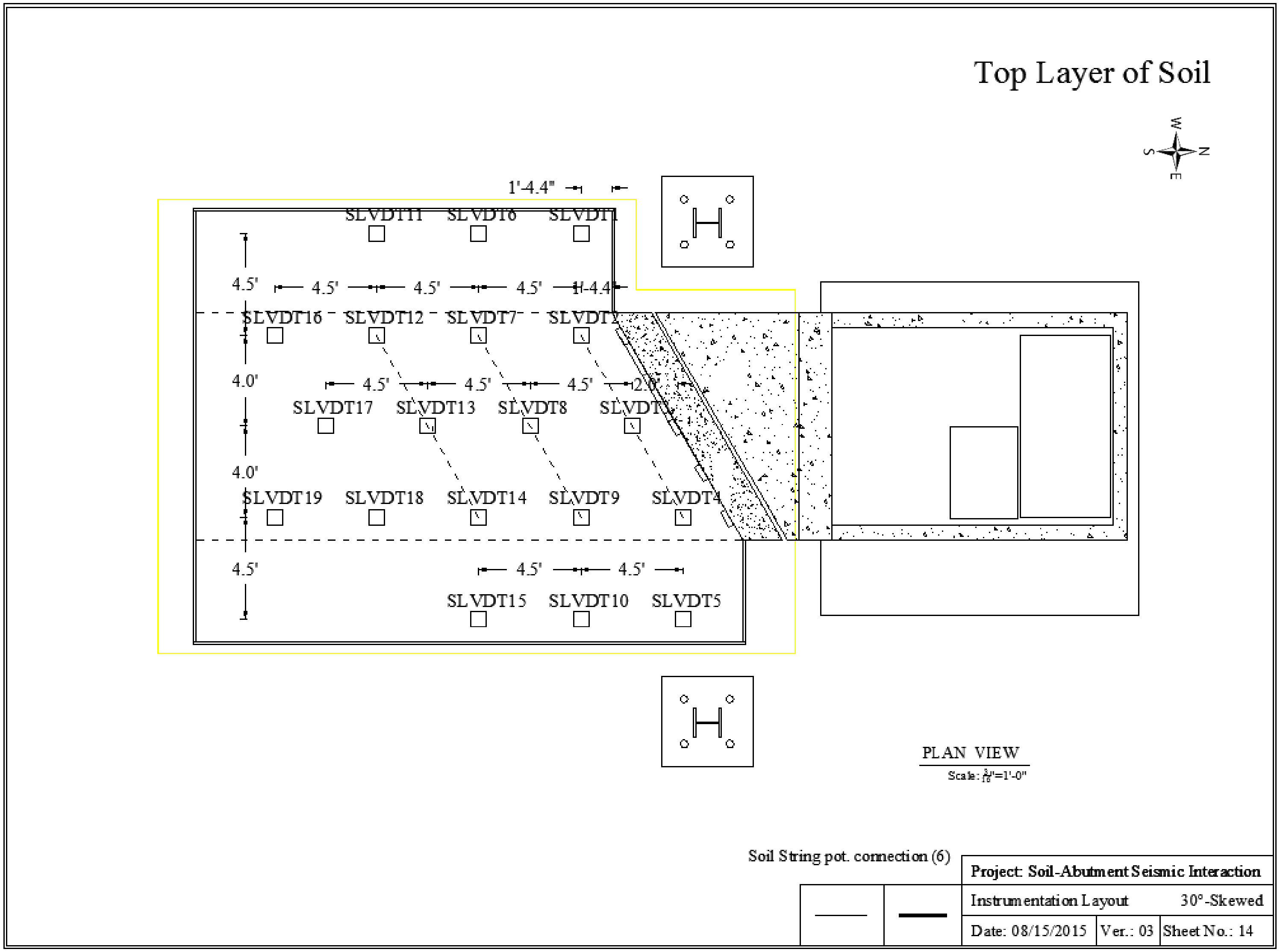

Figure 5-84 Soil surface LVDT instrumentation plan in the 30° skew test.

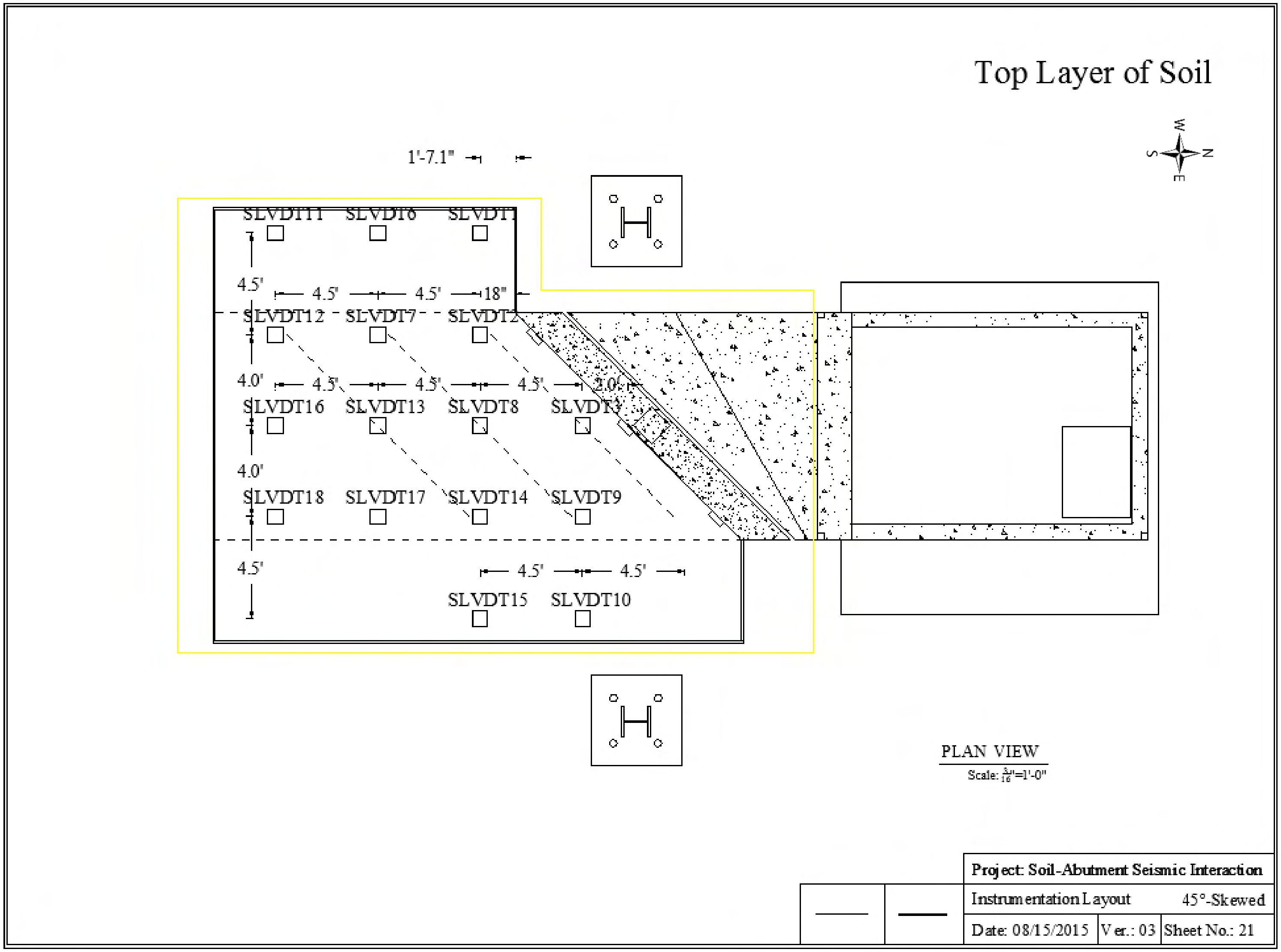

Figure 5-85 Soil surface LVDT instrumentation plan in the 45° skew test.

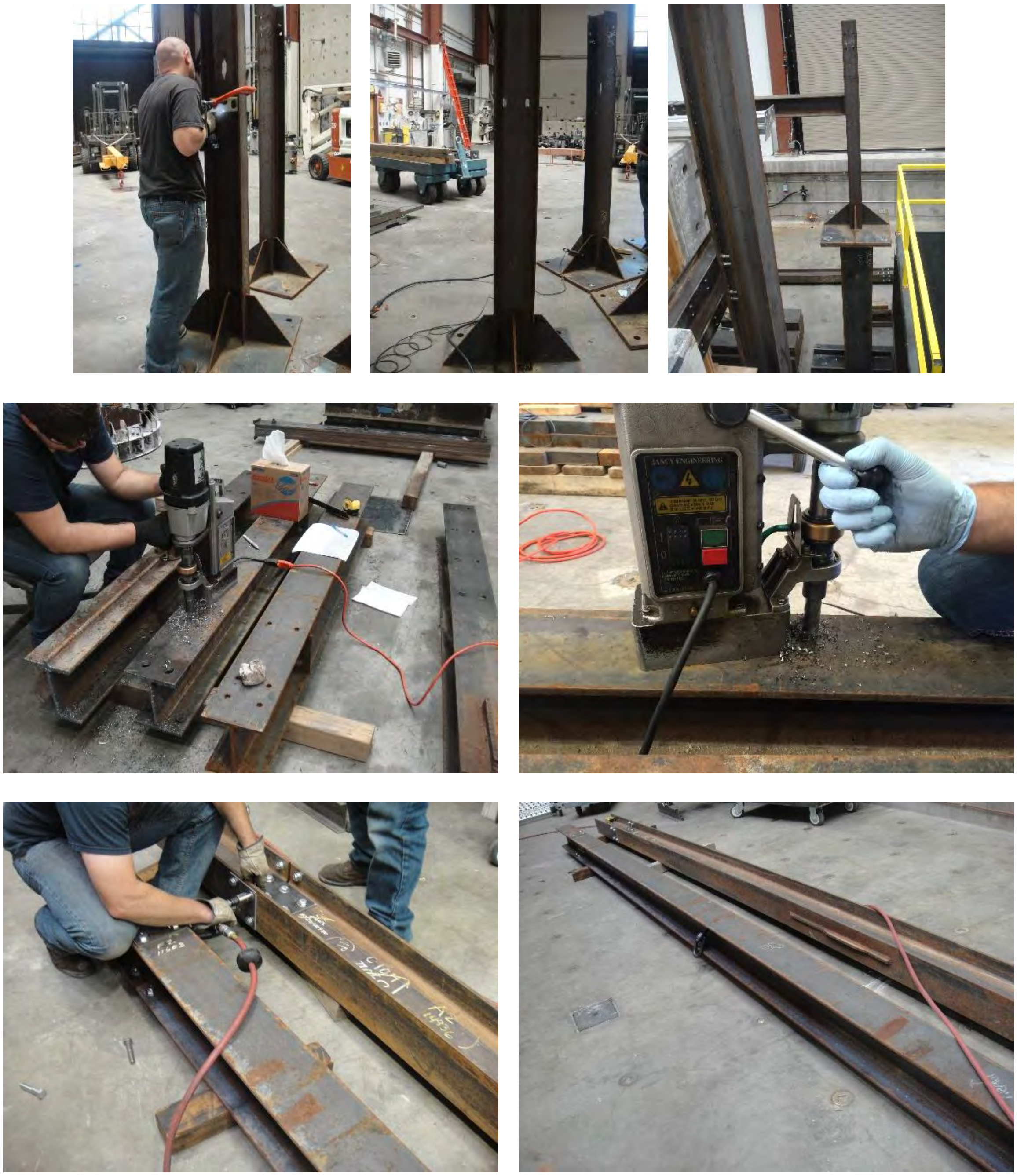

Figure 5-86 Construction of reference frame of soil surface LVDTs.

Figure 5-87 Installation of reference frame of soil surface LVDTs (top: west side, and right: east side).

Figure 5-88 Soil prepration.

Figure 5-89 Soil placement and compaction in 0° skew test (bottom half).

Figure 5-90 Soil placement and compaction in 0° skew test (top half).

Figure 5-91 Soil placement and compaction in the 30° skew test.

Figure 5-92 Soil placement and compaction in the 45° skew test.

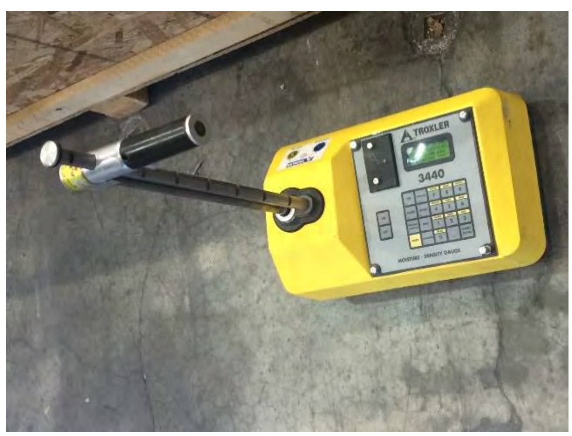

Figure 5-93 Nuclear density gauge.

Figure 5-94 Measurement of soil density and moisture content.

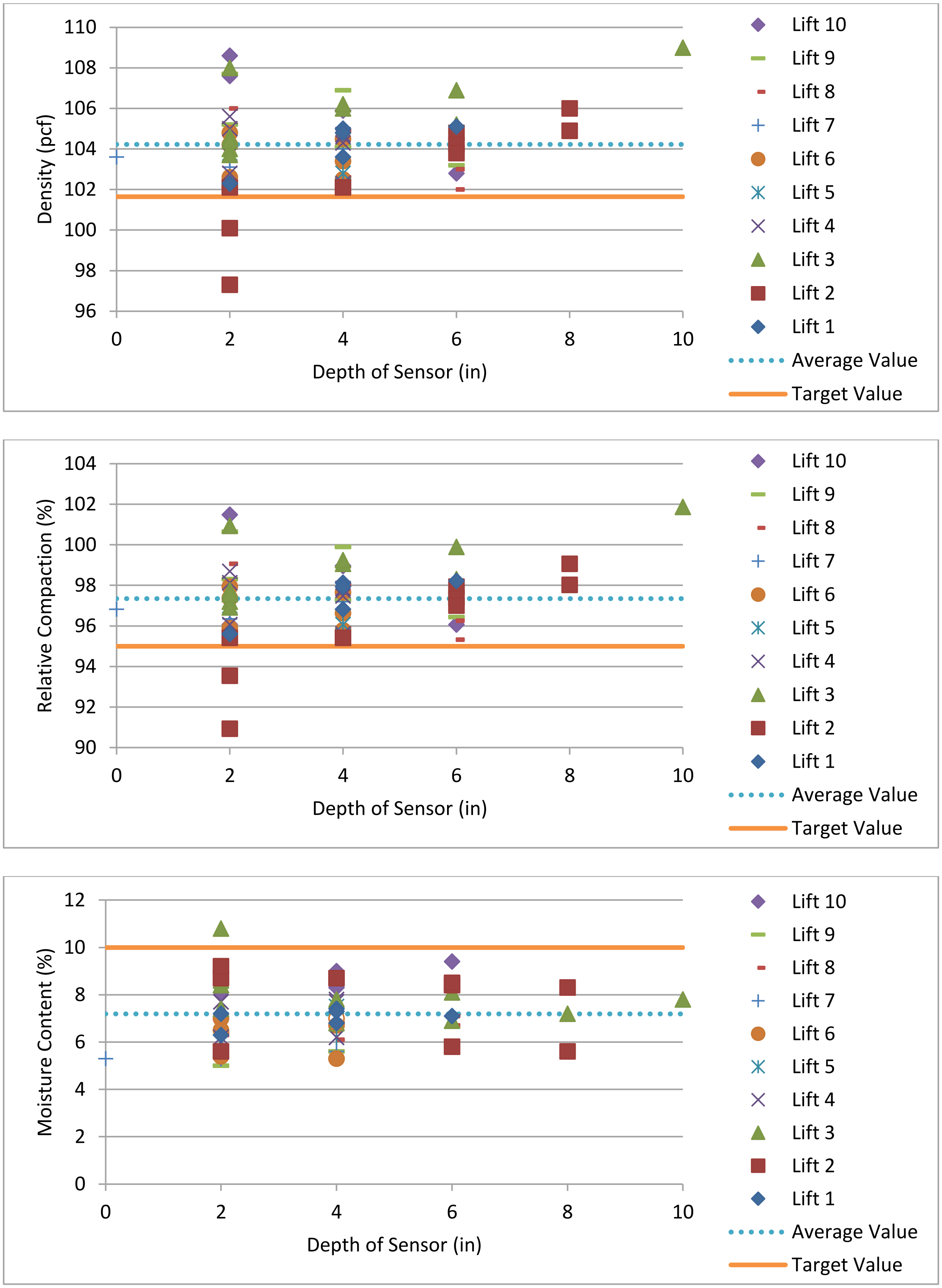

Figure 5-95 Measured density and moisture of the backfill in the 0° skew test.

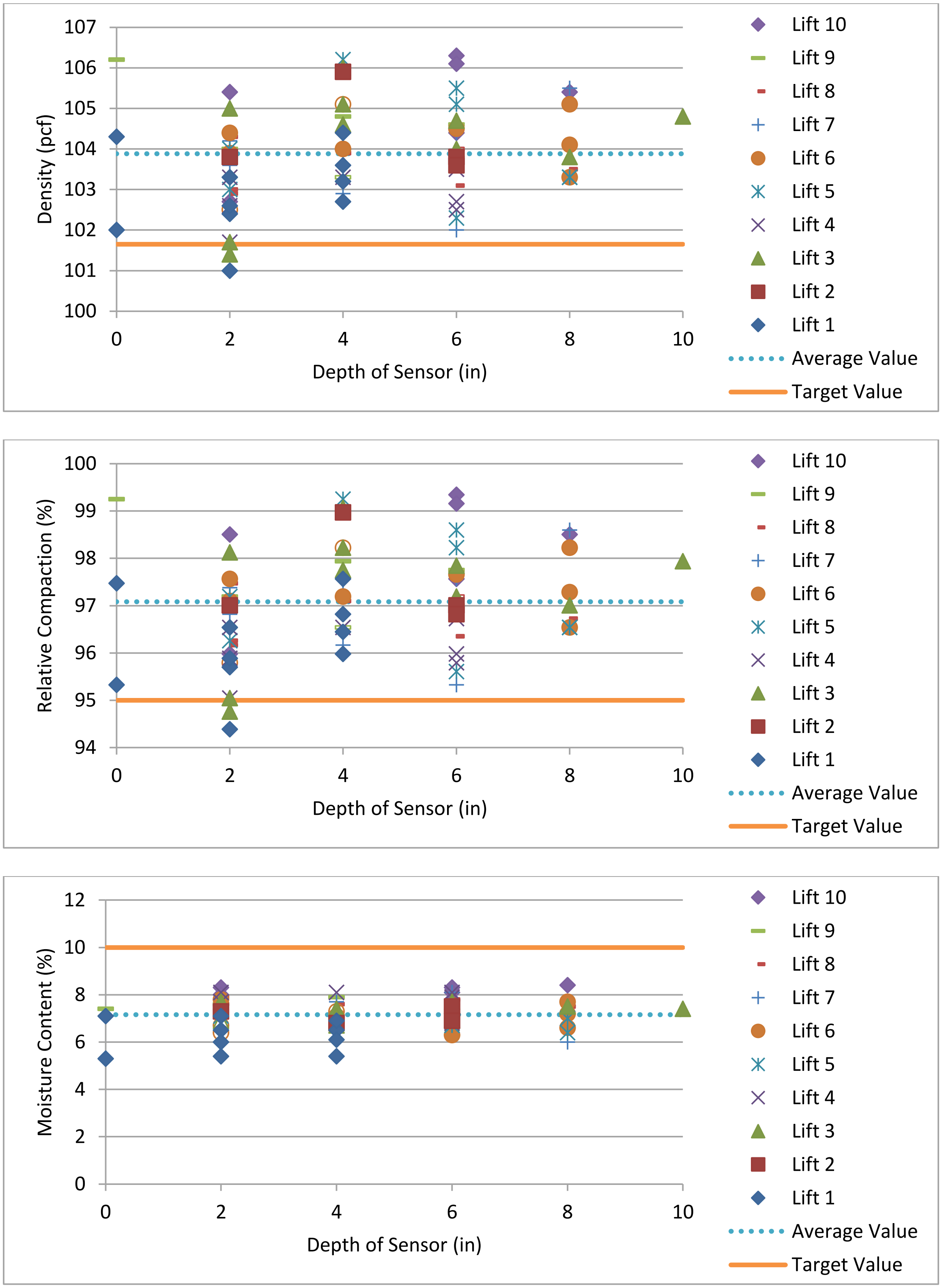

Figure 5-96 Measured density and moisture of the backfill in the 30° skew test.

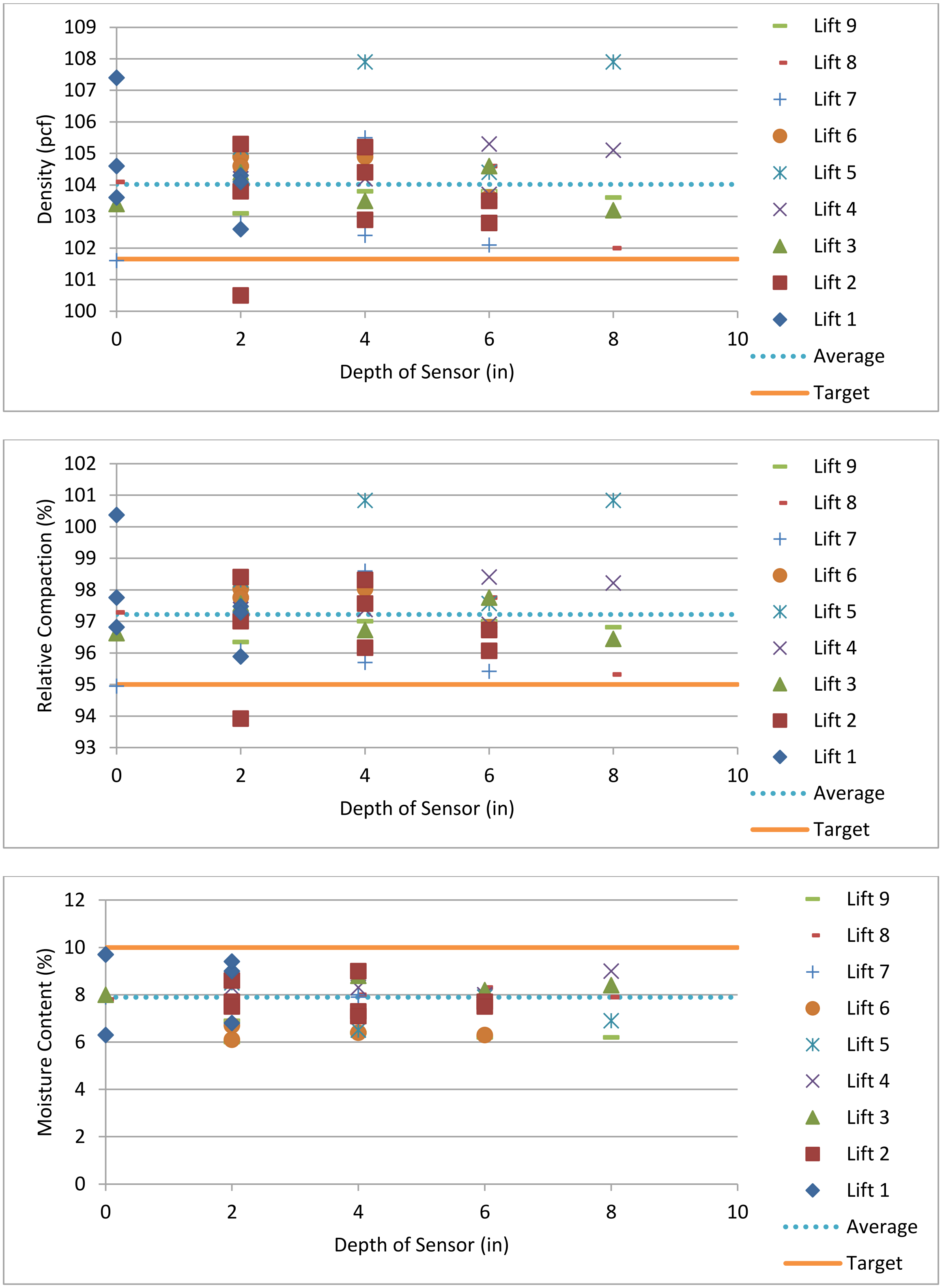

Figure 5-97 Measured density and moisture of the backfill in the 45° skew test.

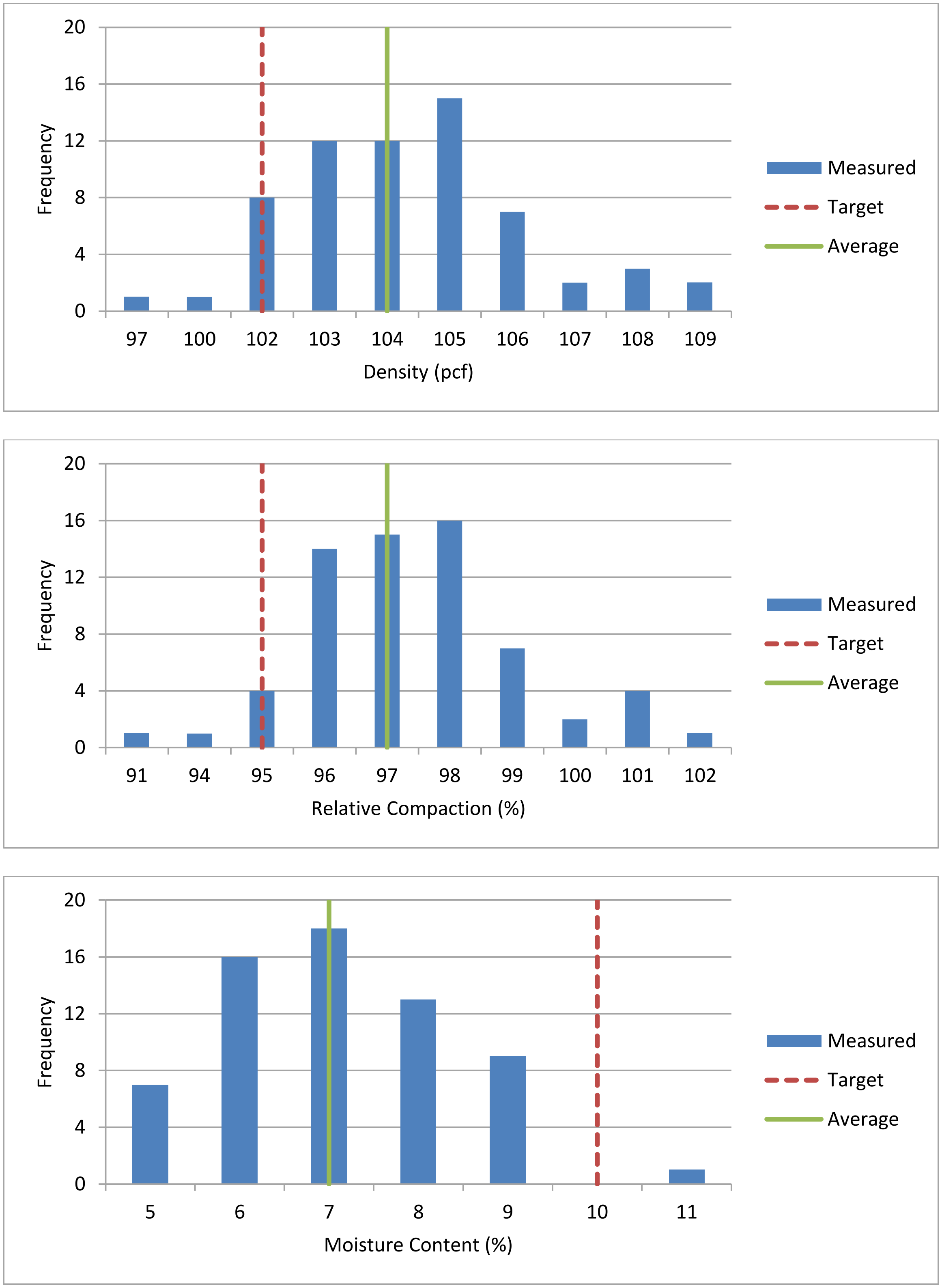

Figure 5-98 Distribution of density and moisture of the backfill in the 0° skew test.

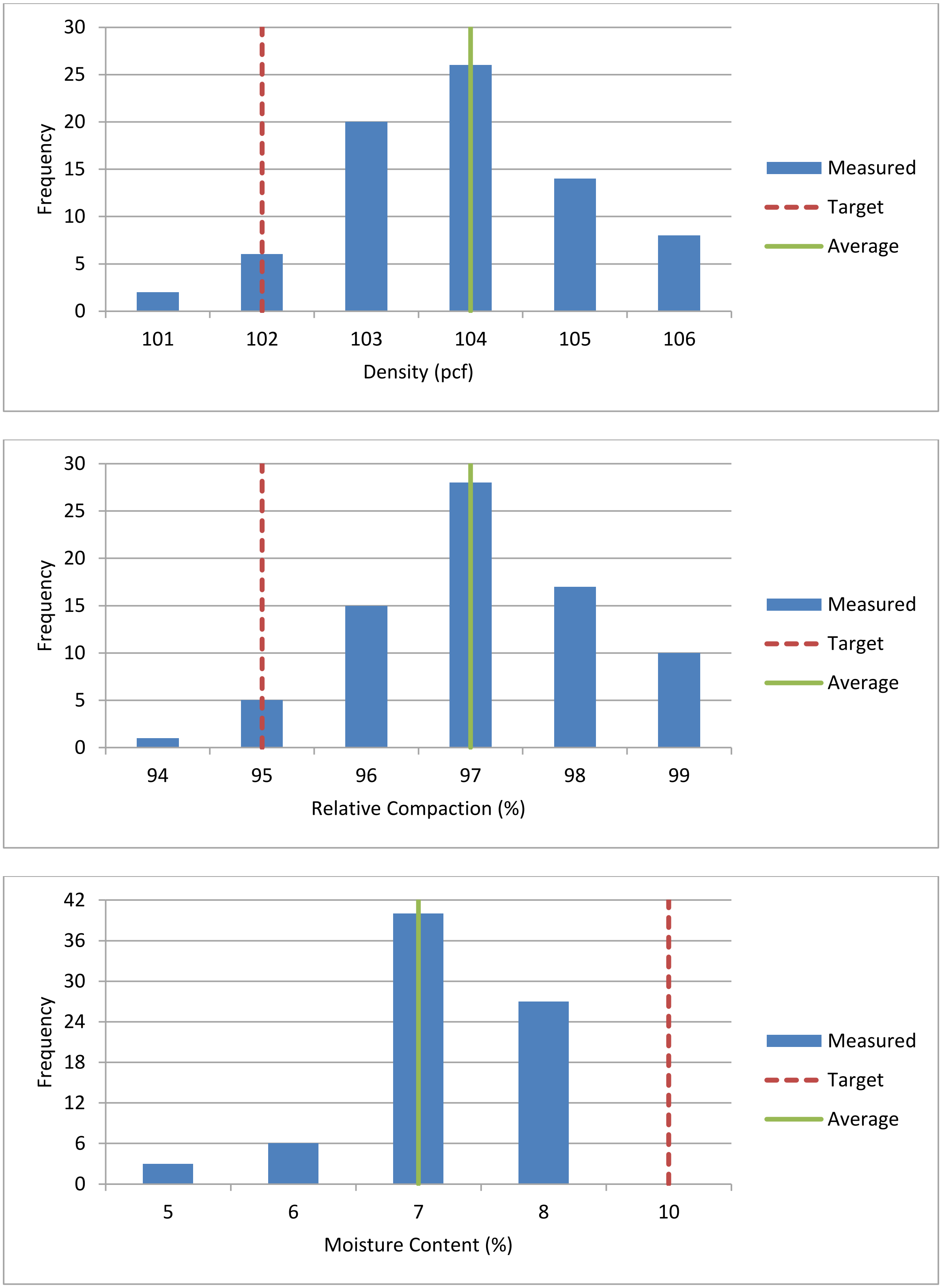

Figure 5-99 Distribution of density and moisture of the backfill in the 30° skew test.

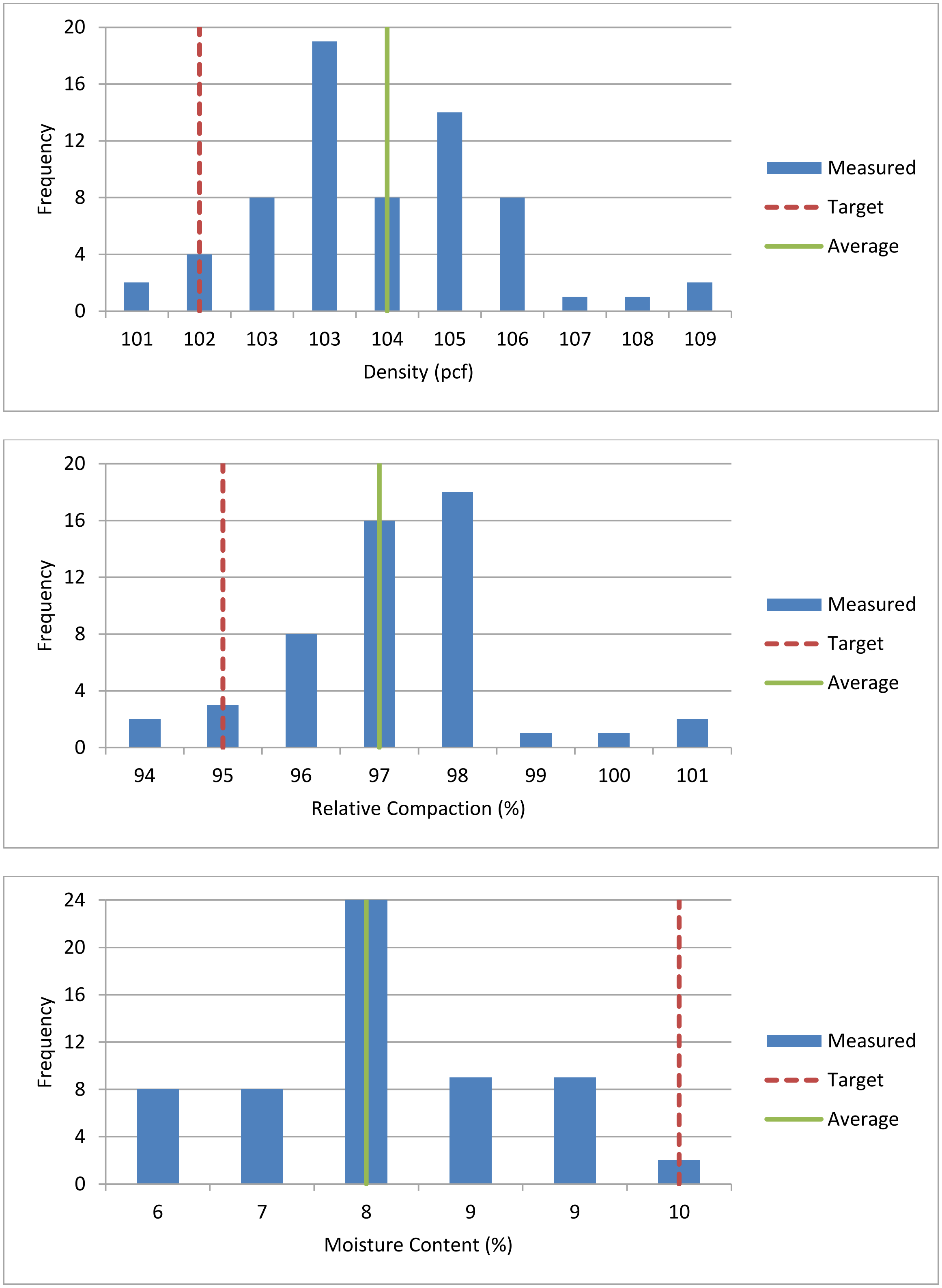

Figure 5-100 Distribution of density and moisture of the backfill in the 45° skew test.

Figure 5-101 Trenches for the bottom layer of soil instruments.

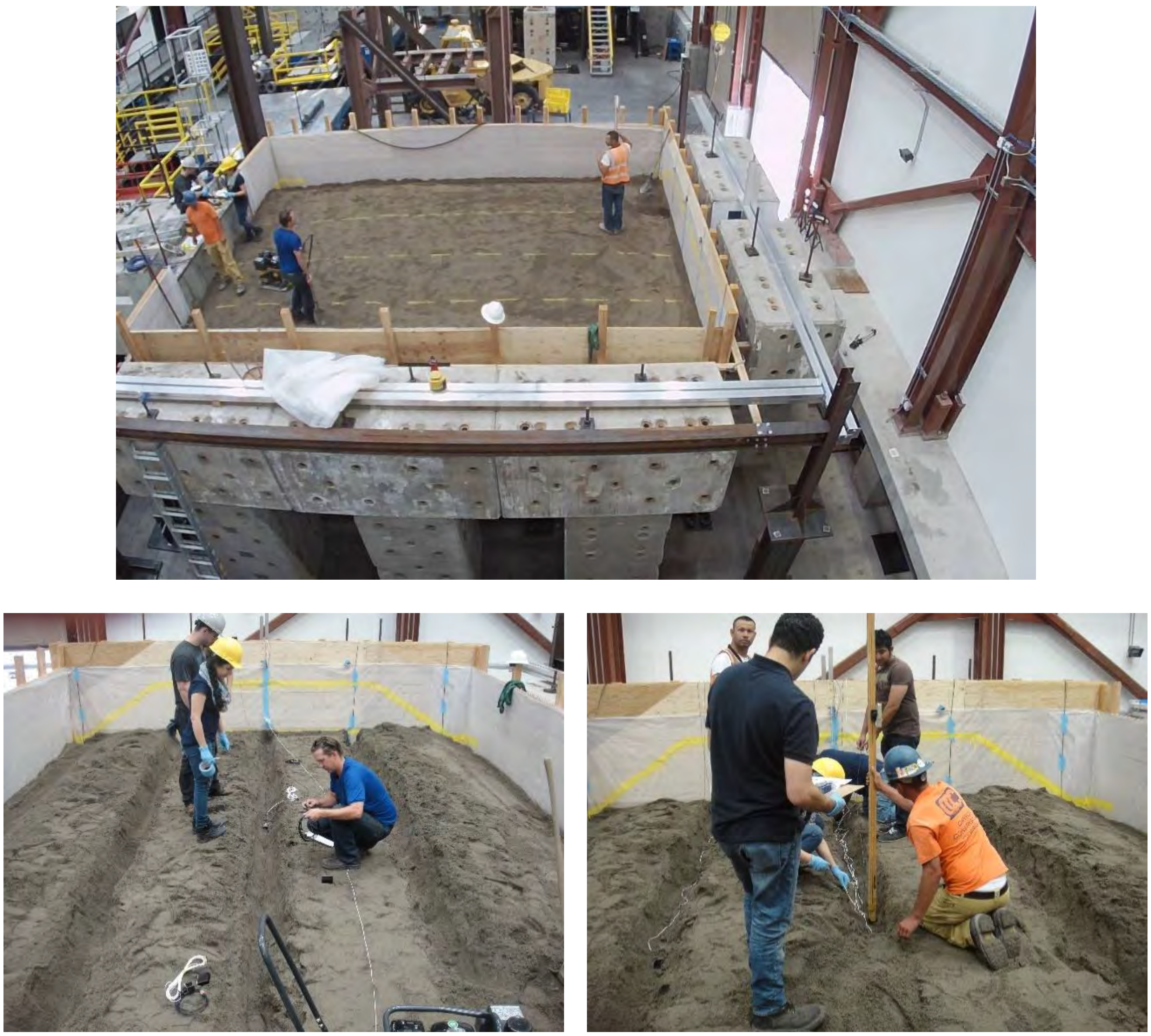

Figure 5-102 Installation of middle layer soil instruments.

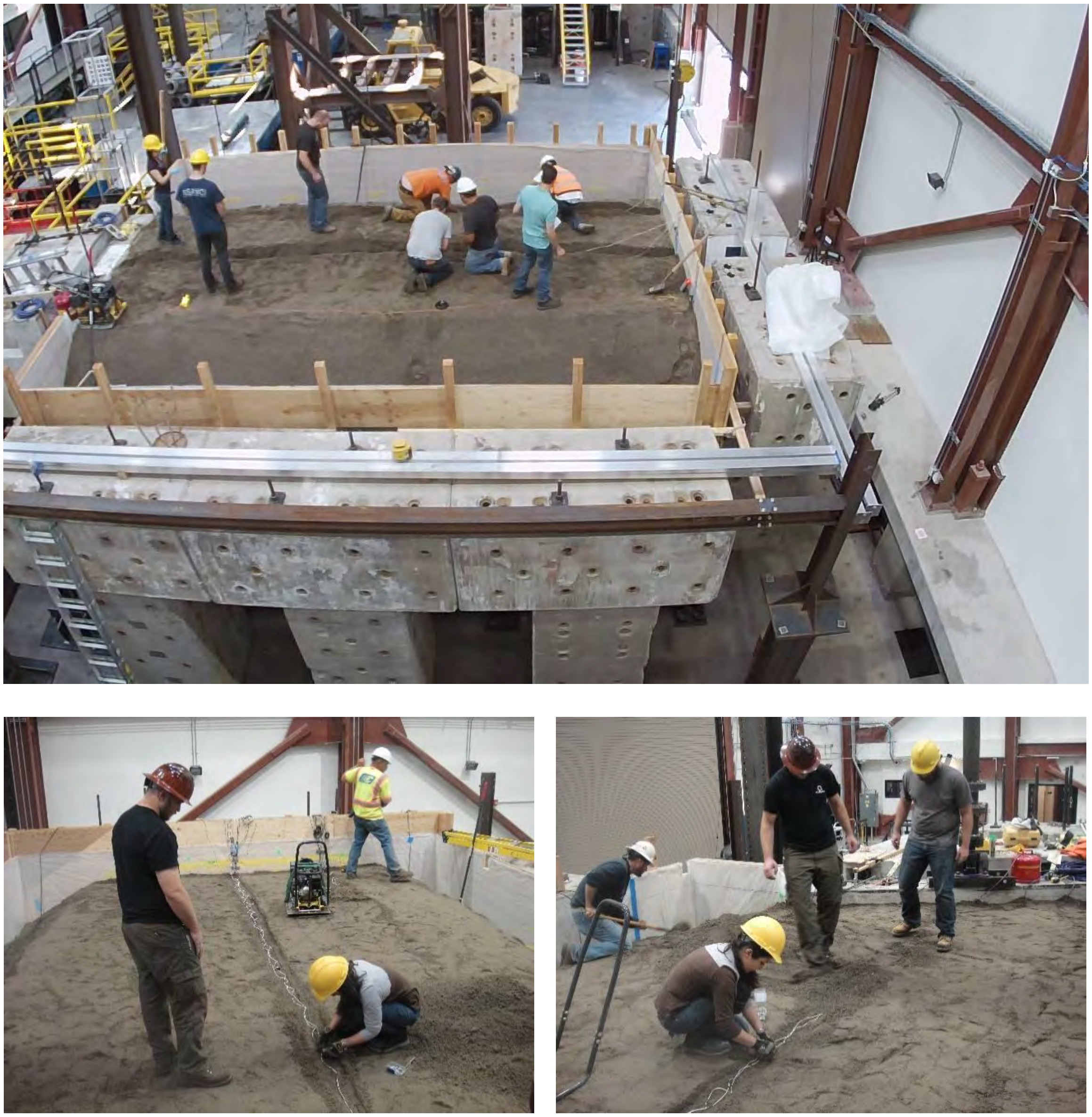

Figure 5-103 Installation of top layer soil instruments.

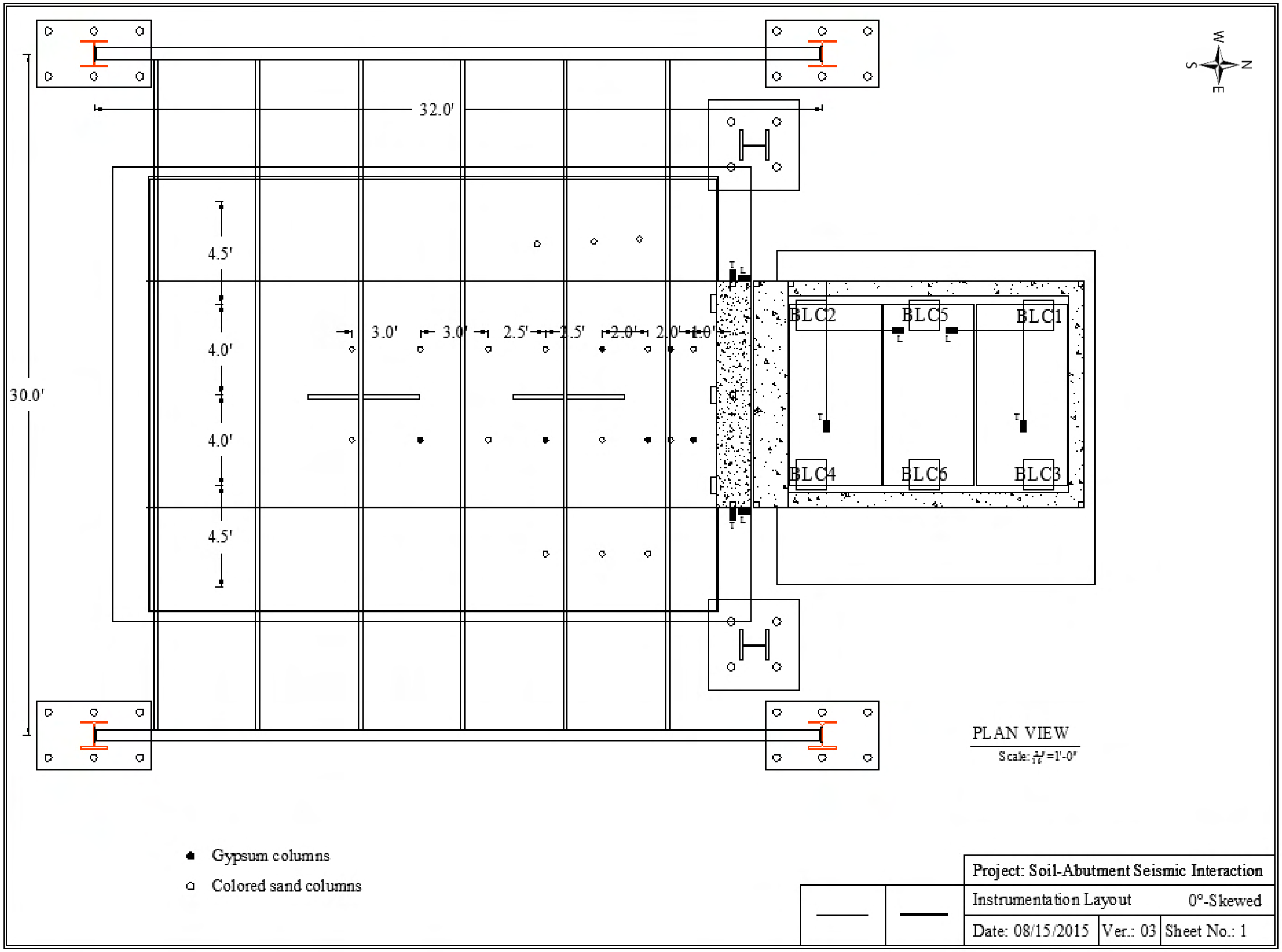

Figure 5-104 Gypum and colored sand column layout in the 0° skew test.

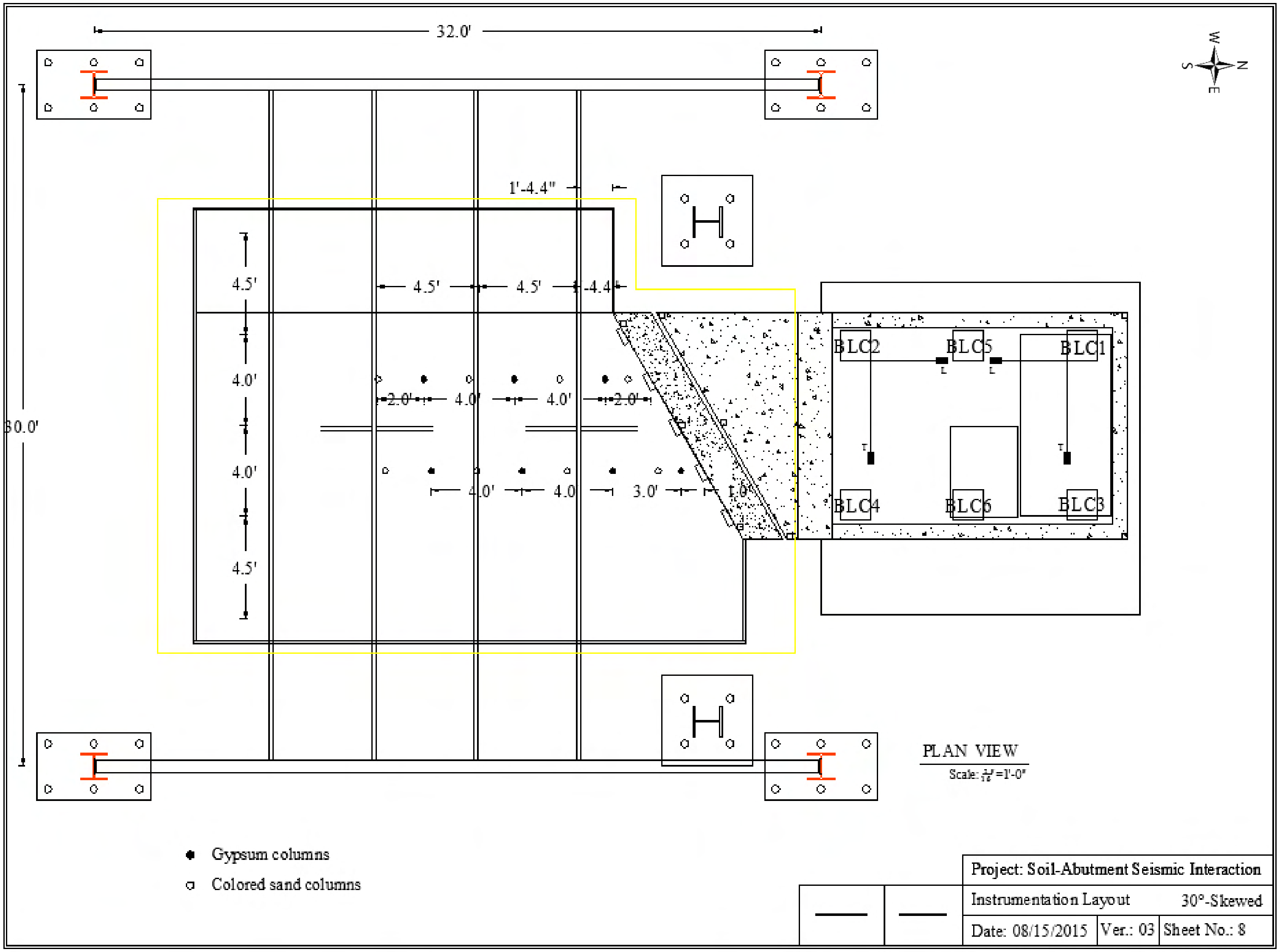

Figure 5-105 Gypum and colored sand column layout in the 30° skew test.

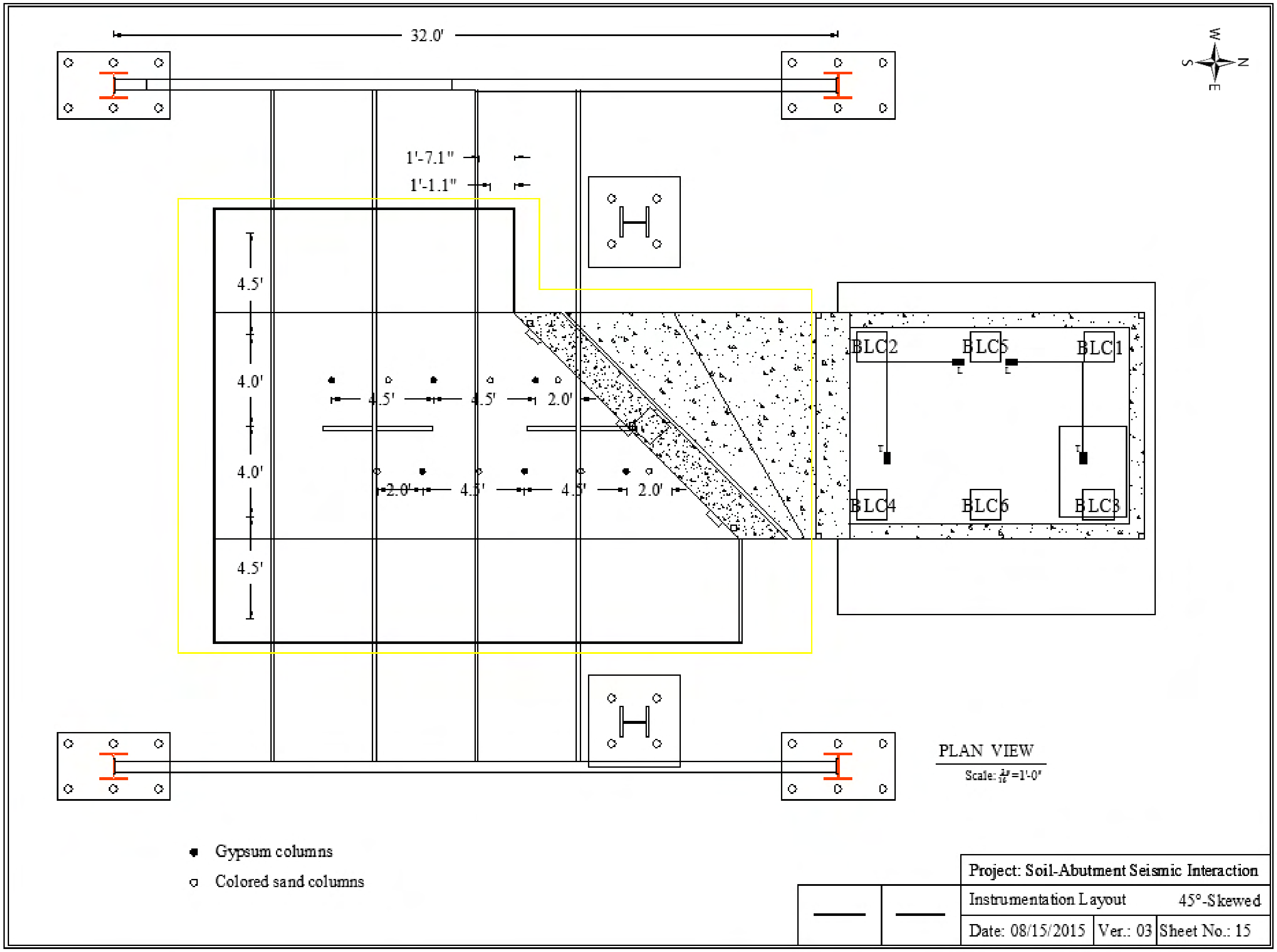

Figure 5-106 Gypum and colored sand column layout in the 45° skew test.

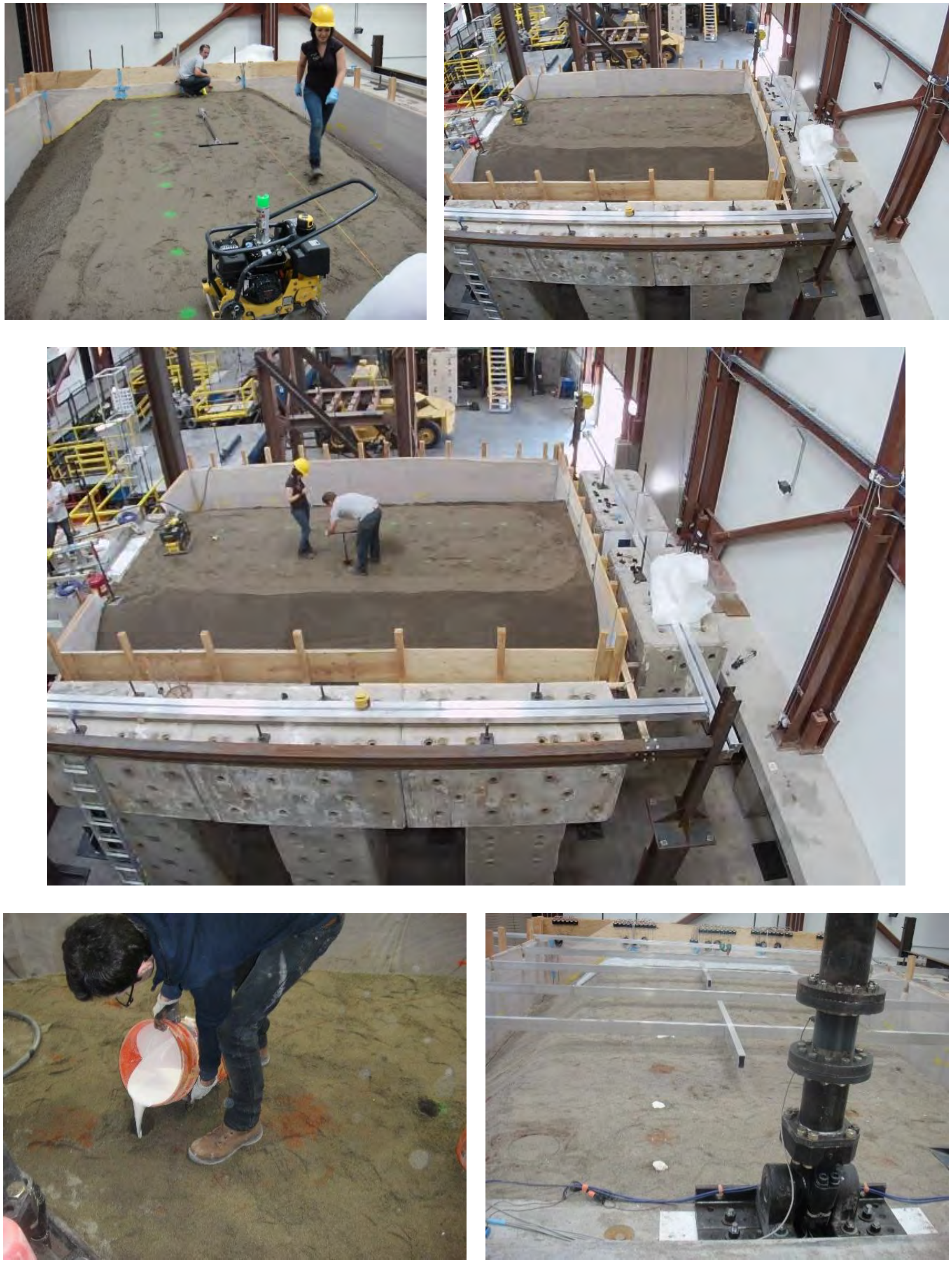

Figure 5-107 Gypsum and colored sand columns in the 0° skew test.

Figure 5-108 Gypsum and colored sand columns in the 30° skew test.

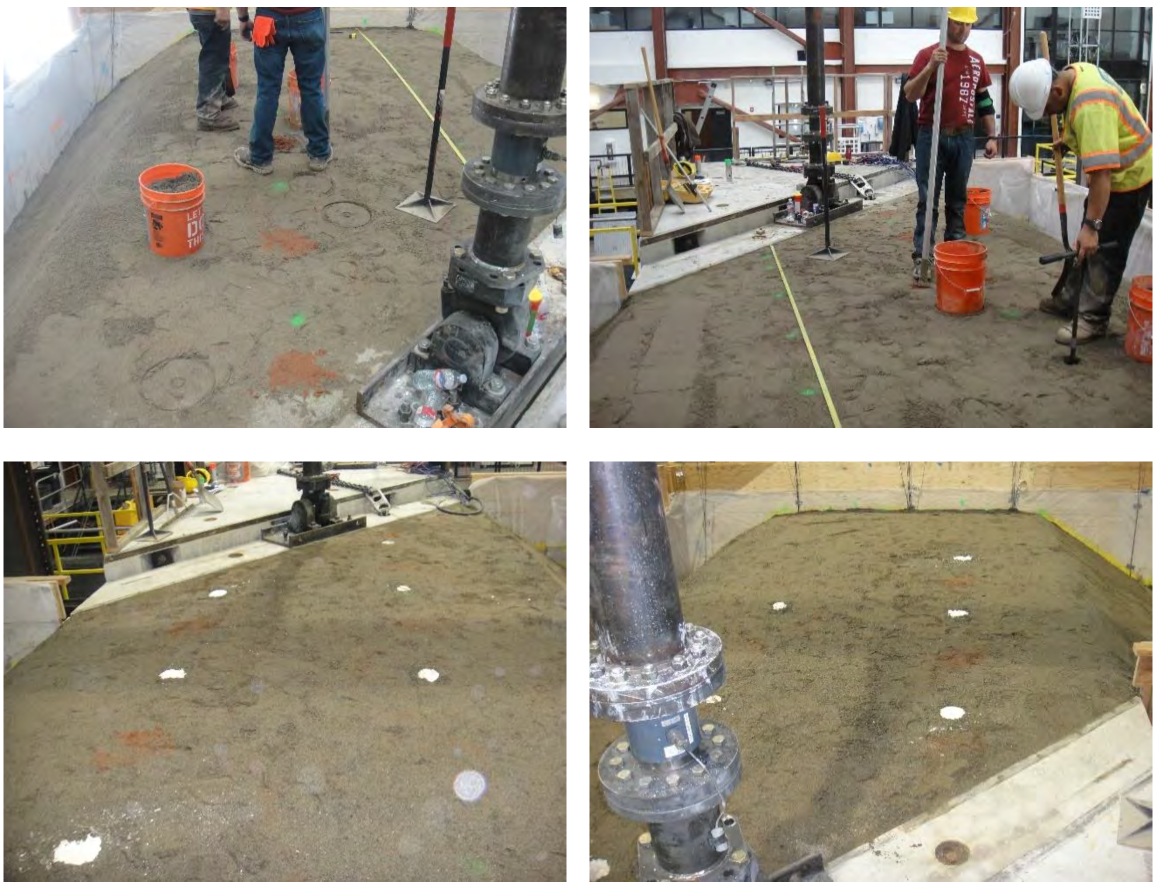

Figure 5-109 Gypsum and colored sand columns in the 45° skew test.

Figure 5-110 Soil surface LVDTs in the 0° skew test (left: flat surface, and right: slope surface).

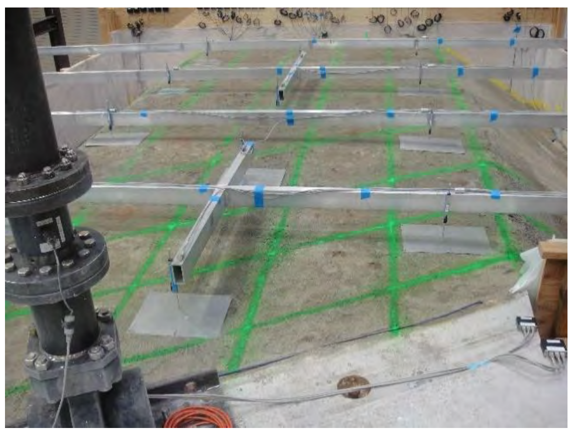

Figure 5-111 Soil surface LVDTs in the 30° skew test.

Figure 5-112 Soil surface LVDTs in the 45° skew test.

Figure 5-113 Test model in the 0° skew case.

Figure 5-114 Test model in the 30° skew case.

Figure 5-115 Test model in the 45° skew case.

Figure 5-116 Excavation of gypsum columns.

Figure 5-117 Removal of soil instruments in top layers.

Figure 5-118 Preparation for removing the east wall of soil box (top: top of soil box, and bottom: outside the soil box.

Figure 5-119 Removal of soil box east wall.

Figure 5-120 Removal of backfill soil.

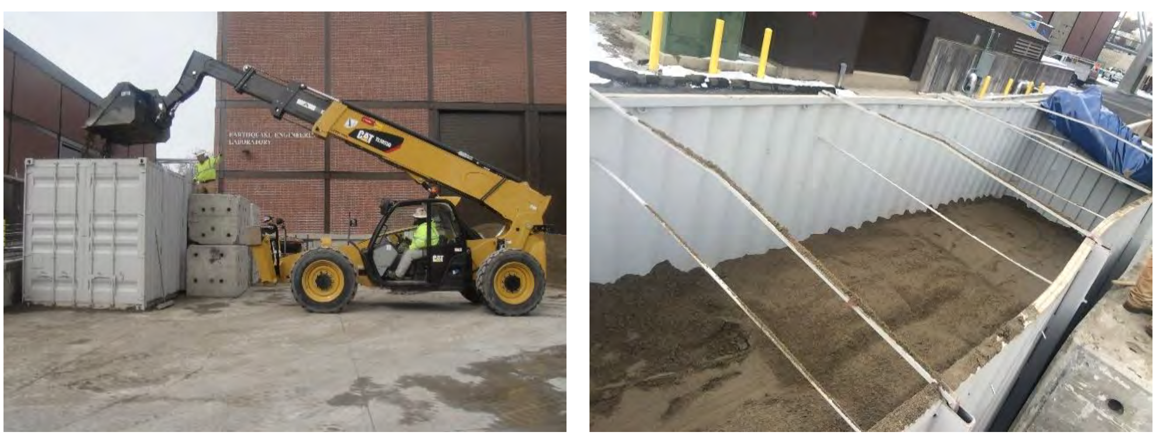

Figure 5-121 Soil storage.

Figure 5-122 Excavation of colored sand columns.

Figure 5-123 Removal of soil box.

Figure 5-124 Removal of bridge block system.

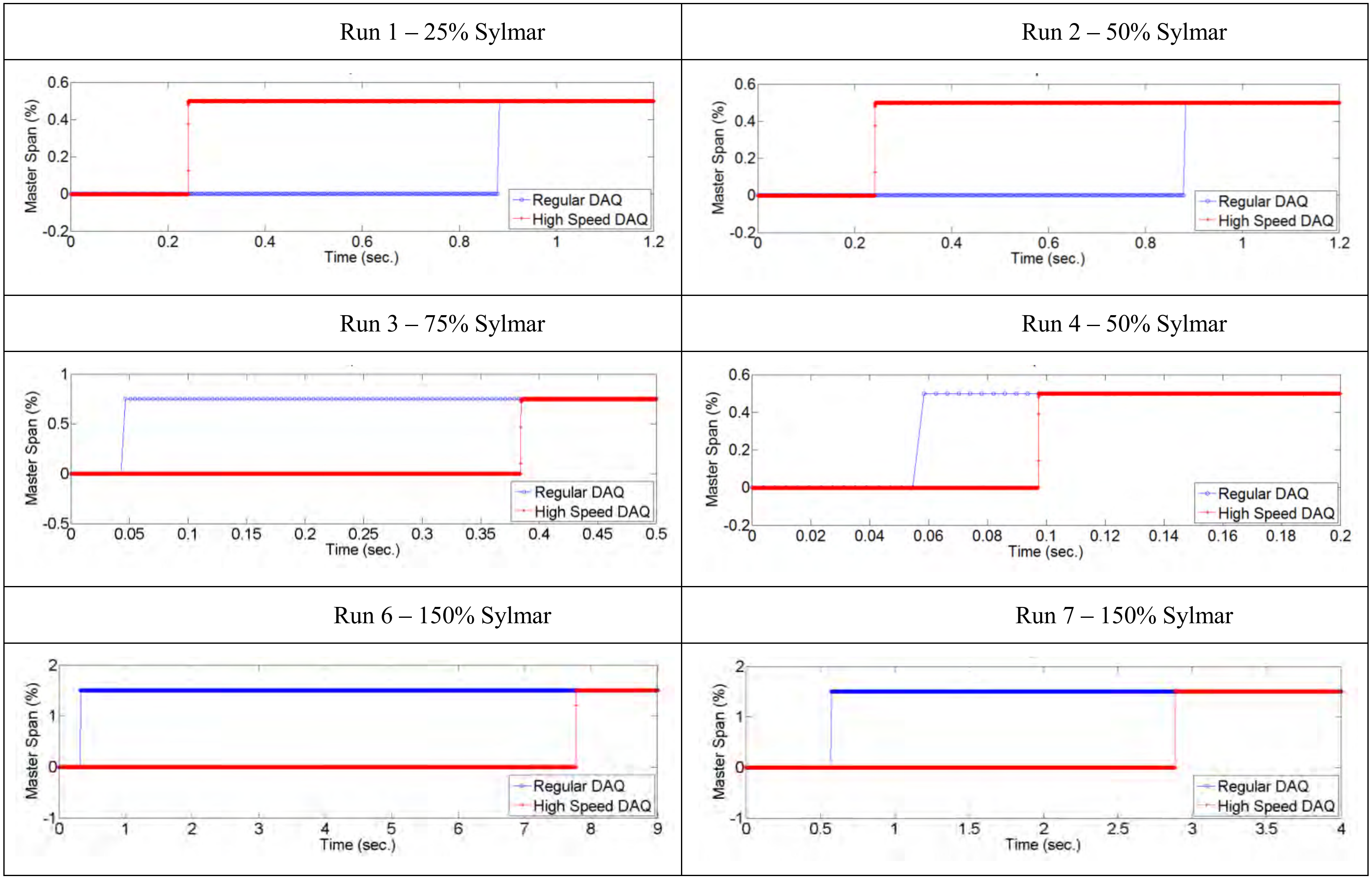

Figure 6-1 Time lag between the regular and high speed DAQs for the 0° skew test.

Run 1 – 25% Sylmar

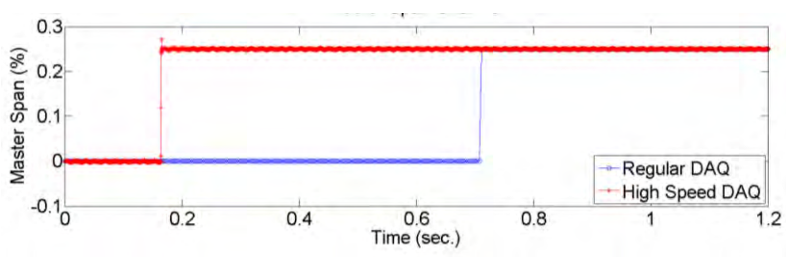

Run 2 – 50% Sylmar

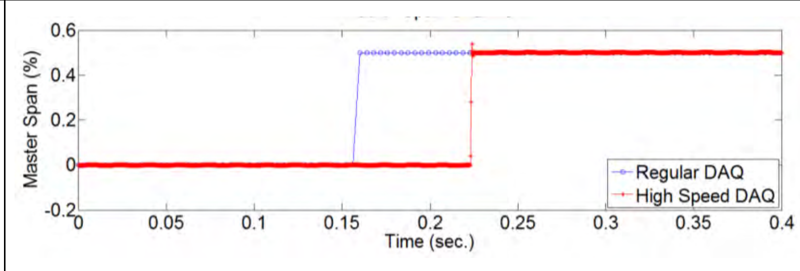

Run 3 – 125% Sylmar

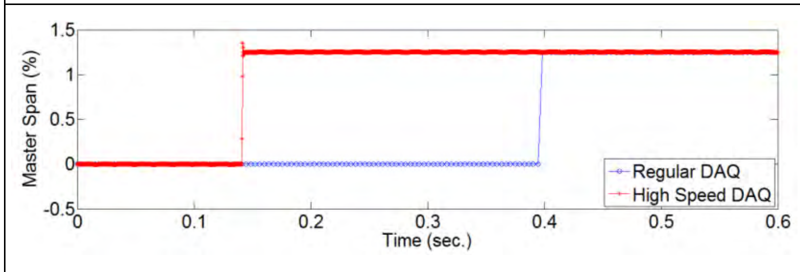

Run 4 – 150% Sylmar

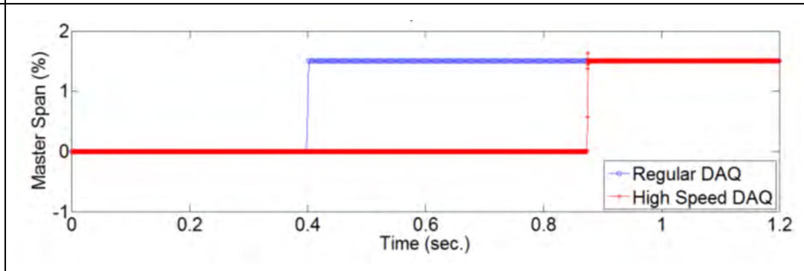

Run 5 – 200% Sylmar

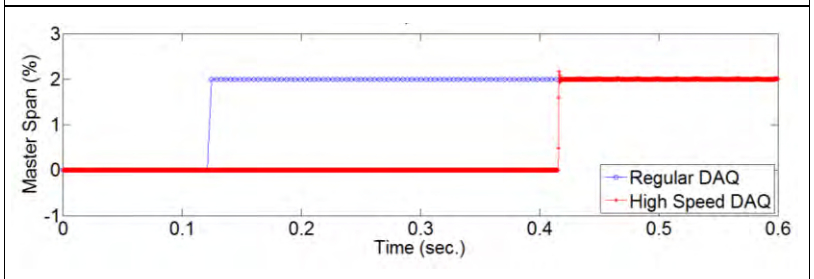

Figure 6-2 Time lag between the regular and high speed DAQs for the 30° skew test.

Run 1 – 25% Sylmar	Run 2 – 50% Sylmar
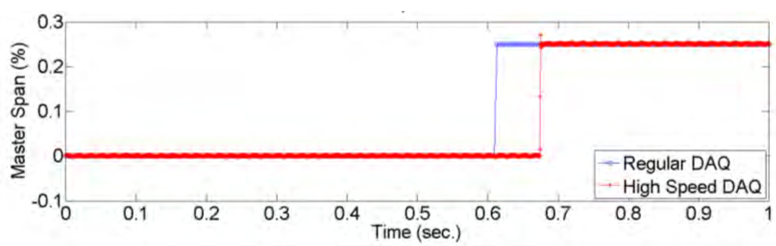	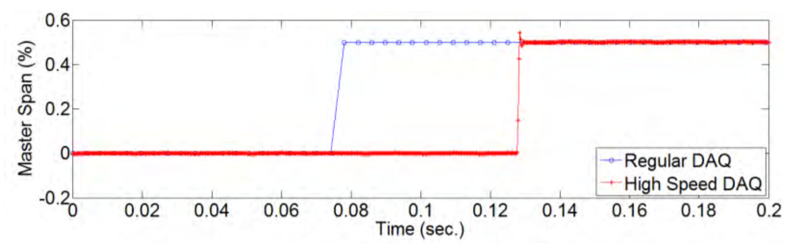
Run 3 – 125% Sylmar	**Run 4 – 150% Sylmar**
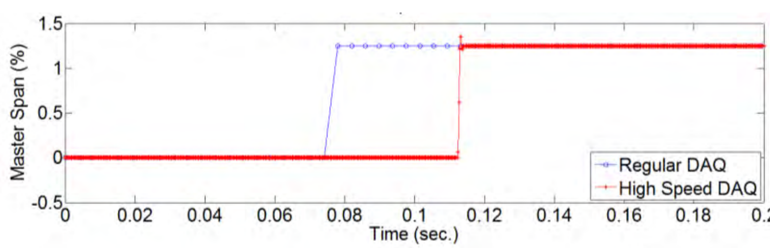	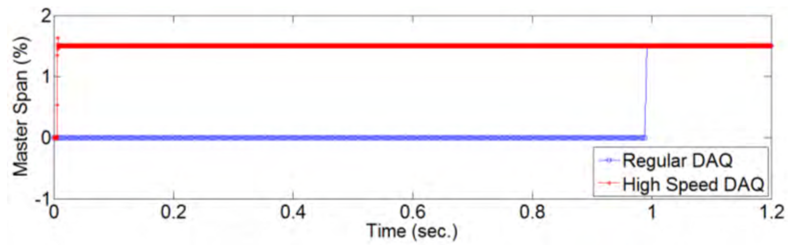
Run 5 – 200% Sylmar	
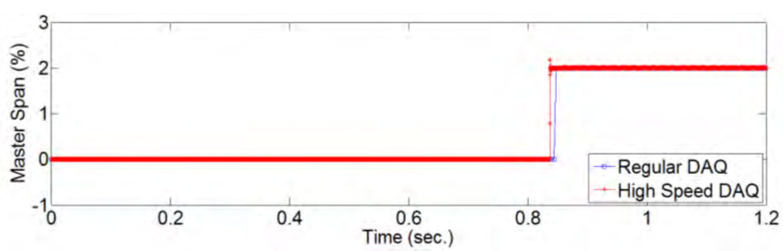	

Figure 6-3 Time lag between the regular and high speed DAQs for the 45° skew test.

Run 1 – 25% Sylmar

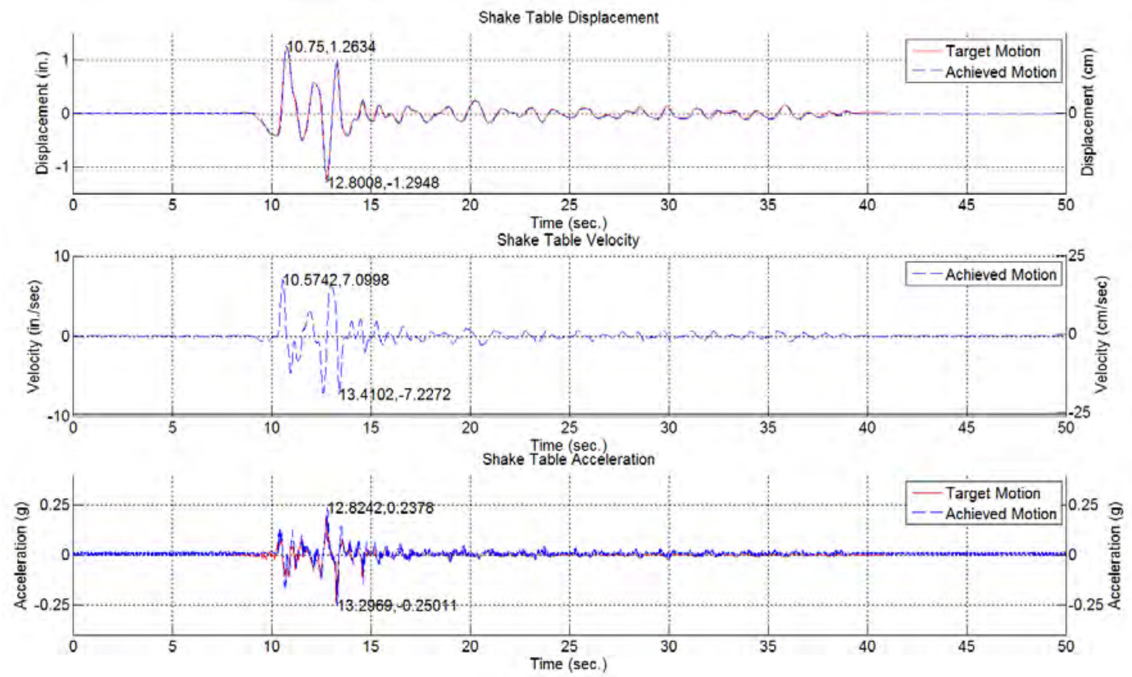

Run 2 – 50% Sylmar

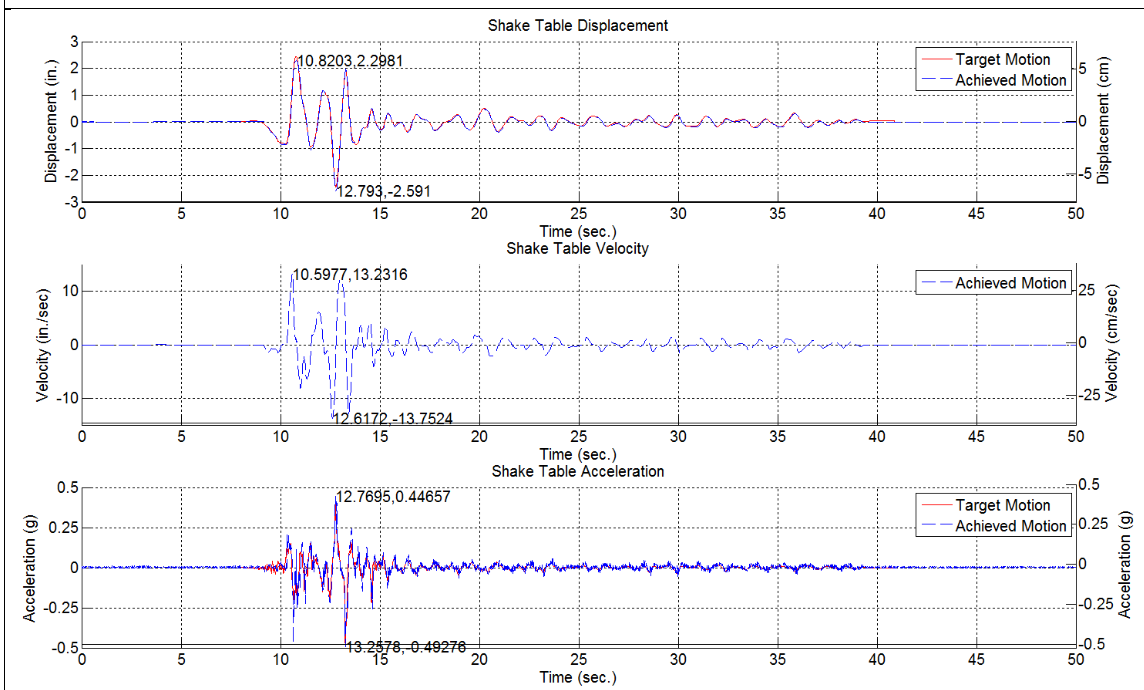

Figure 6-4 Comparison of target and achieved motions for the 0° skew test in Run 2 and 3.

Run 3 – 75% Sylmar

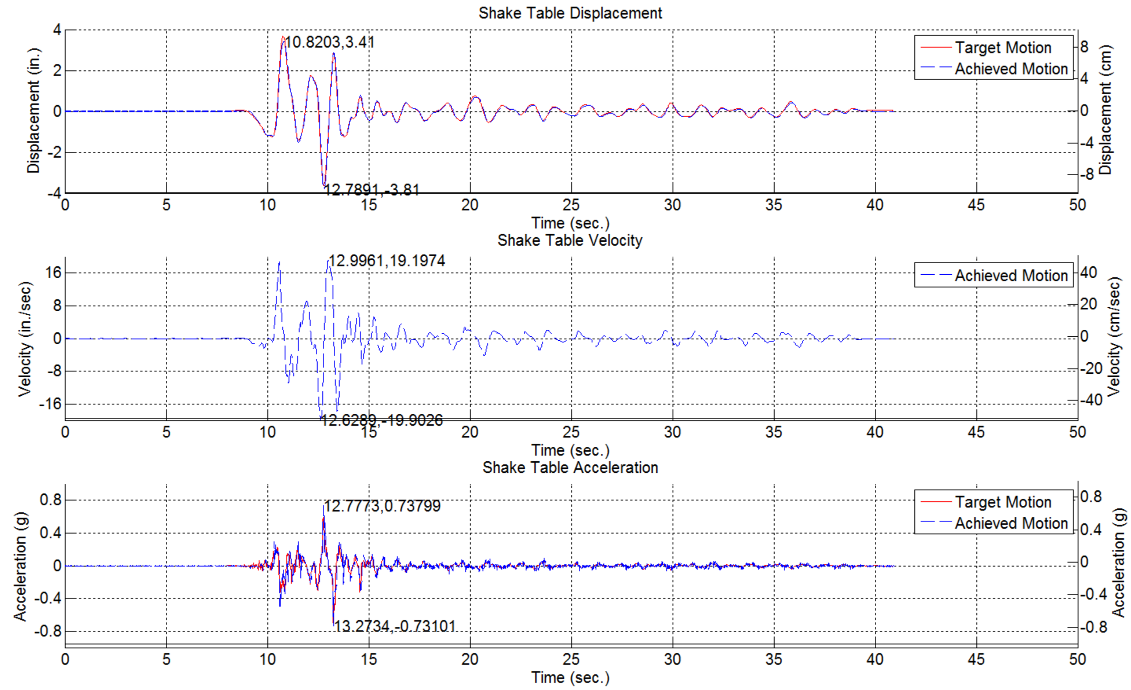

Run 4 – 50% Sylmar

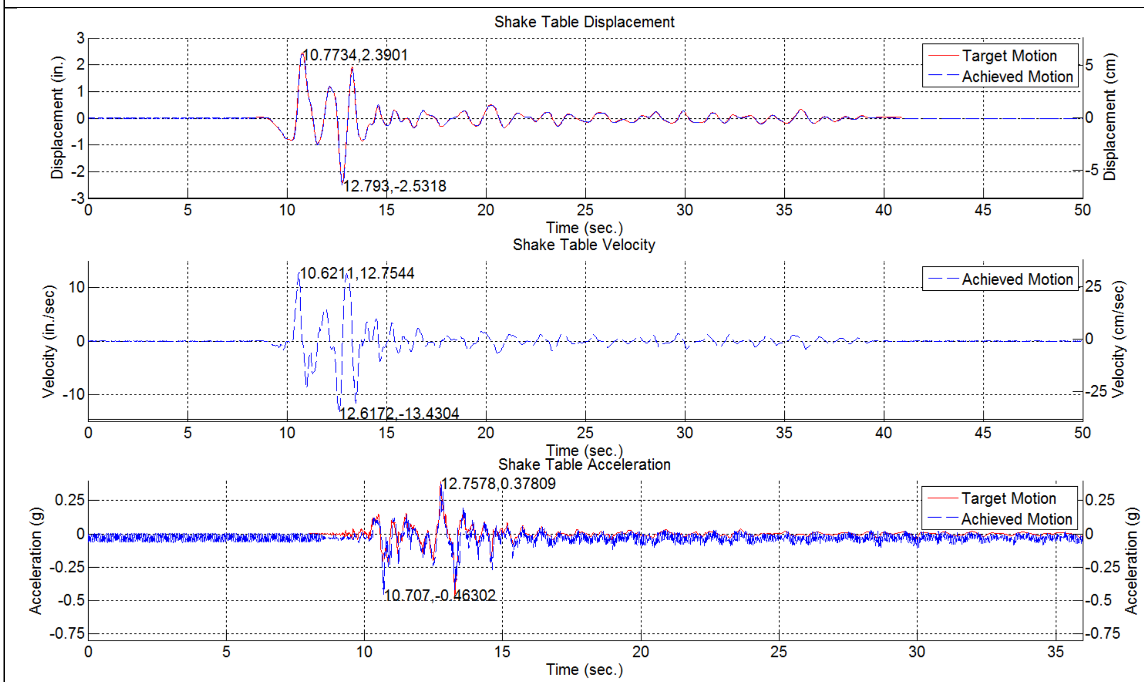

Figure 6-5 Comparison of target and achieved motions for the 0° skew test in Run 4 and 5.

Run 6 – 150% Sylmar

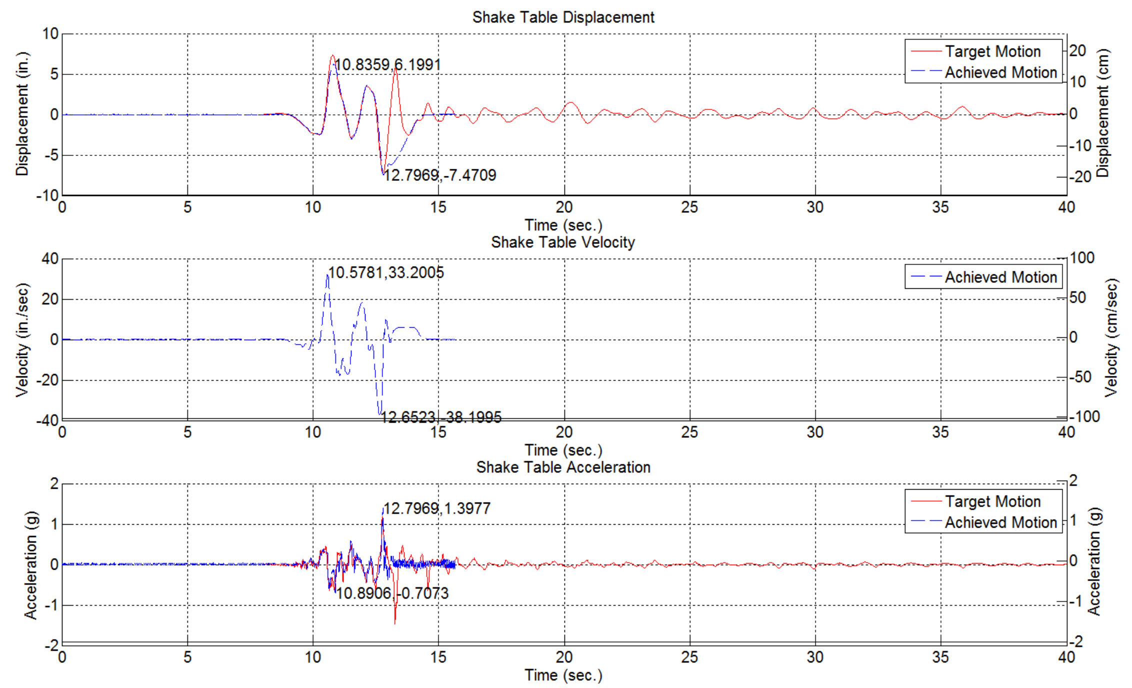

Run 7 – 150% Sylmar

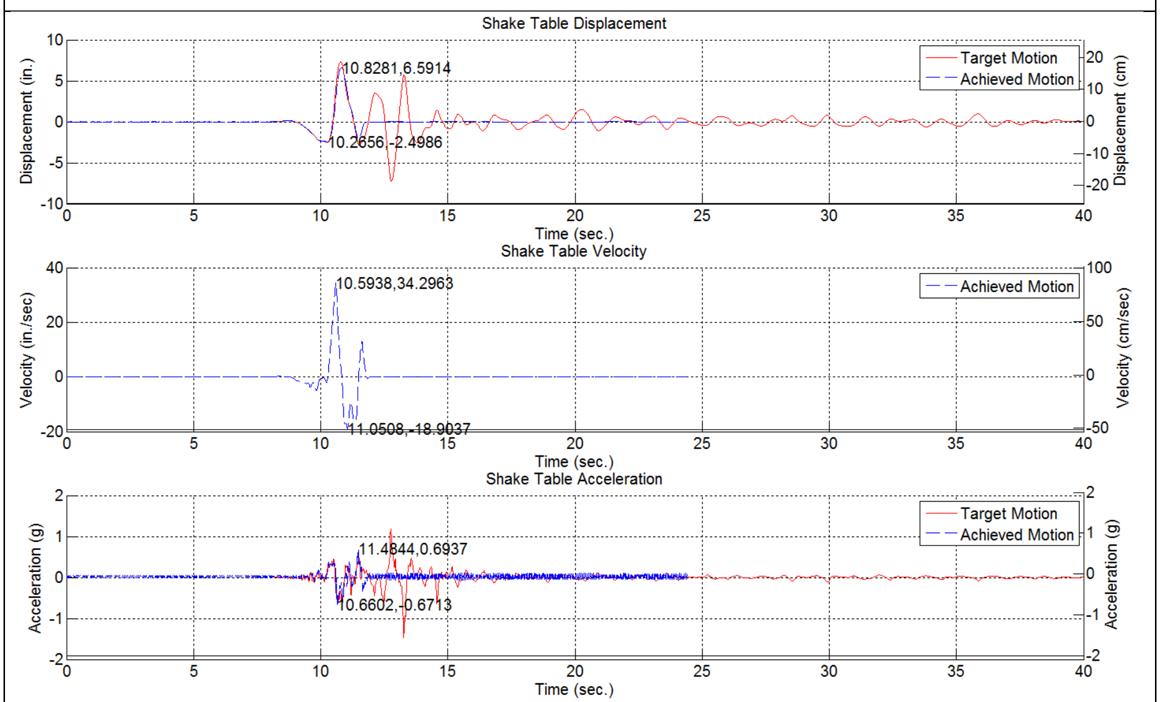

Figure 6-6 Comparison of target and achieved motions for the 0° skew test in Run 6 and 7.

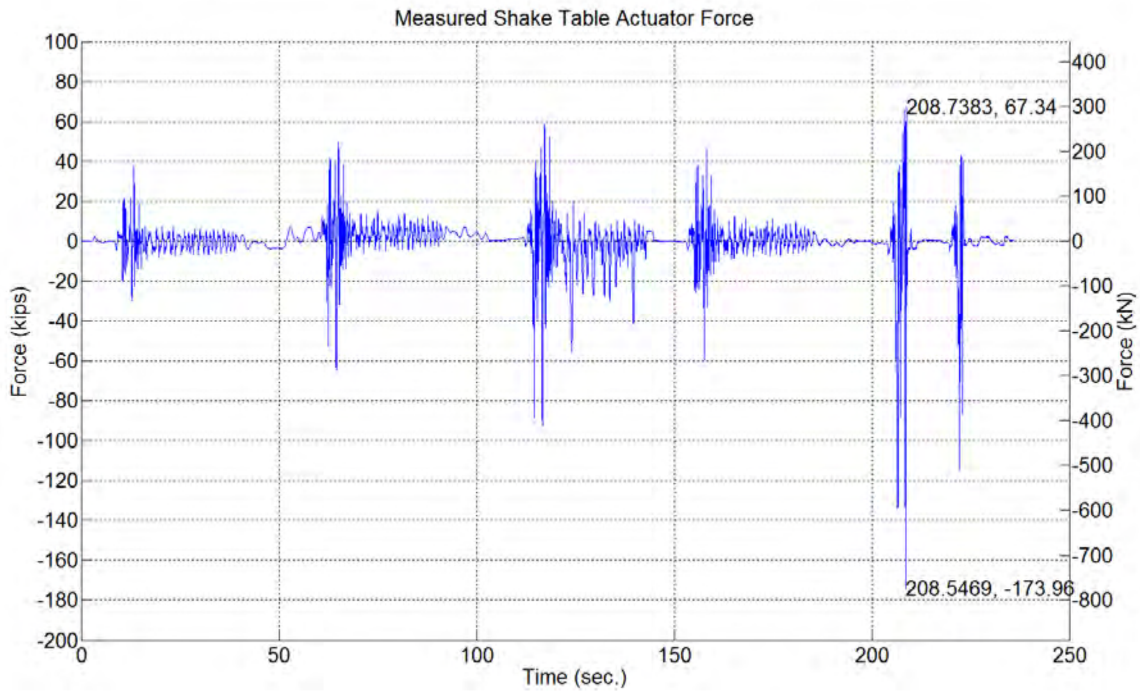

Figure 6-7 Combined shake table actuator force history for the 0° skew test.

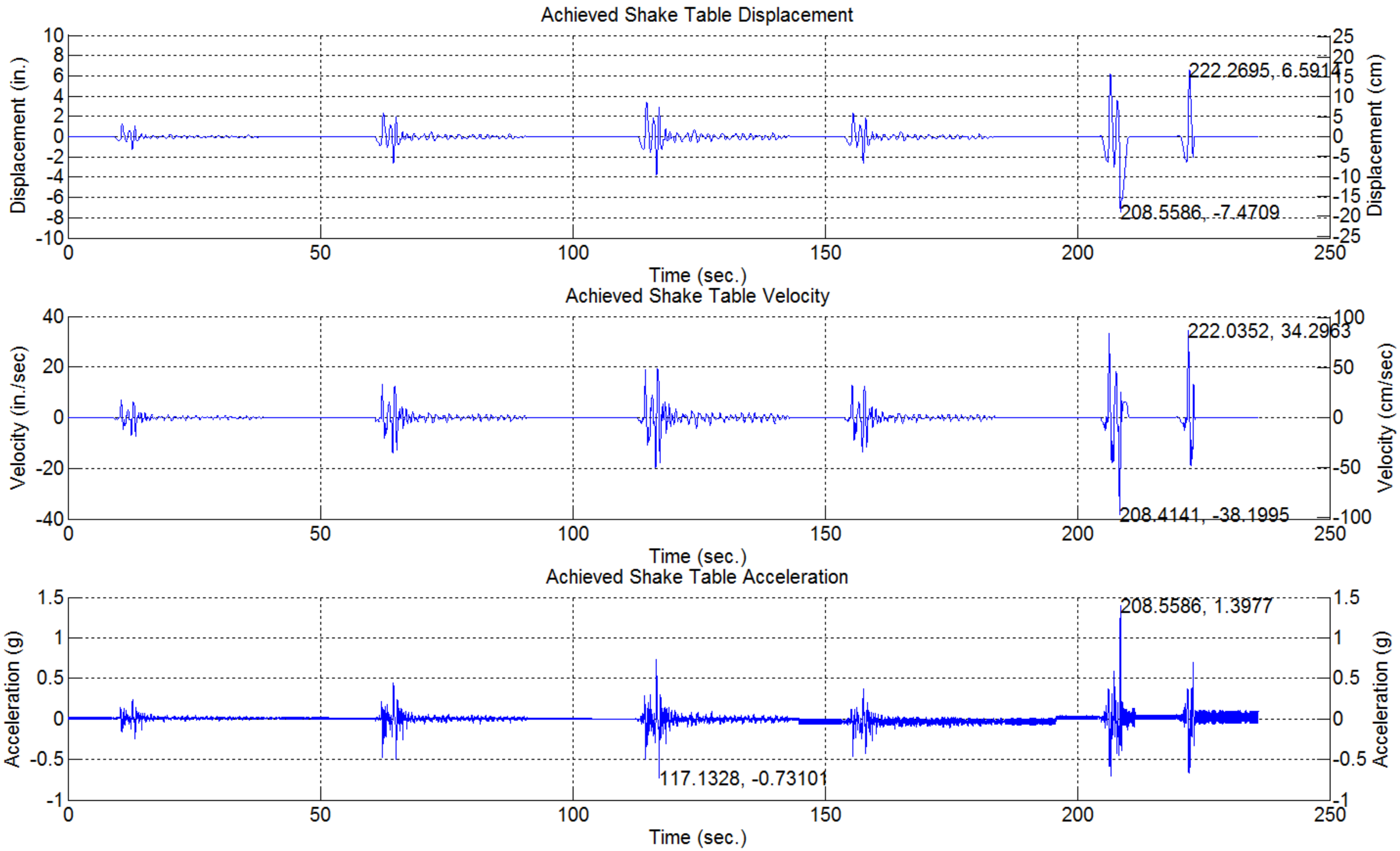

Figure 6-8 Combined achieved motions for the 0° skew test.

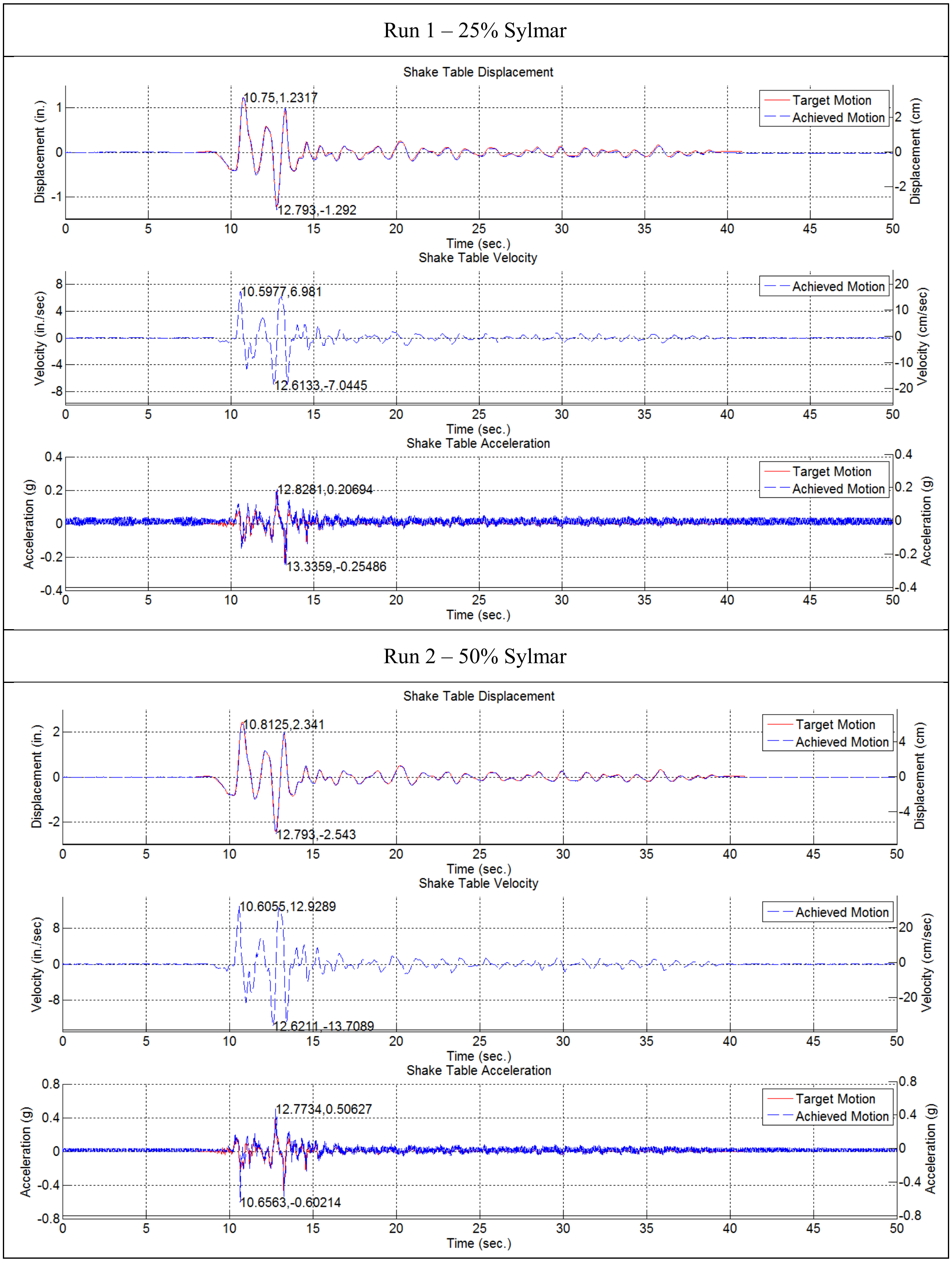

Figure 6-9 Comparison of target and achieved motions for the 30° skew test in Run 1 and 2.

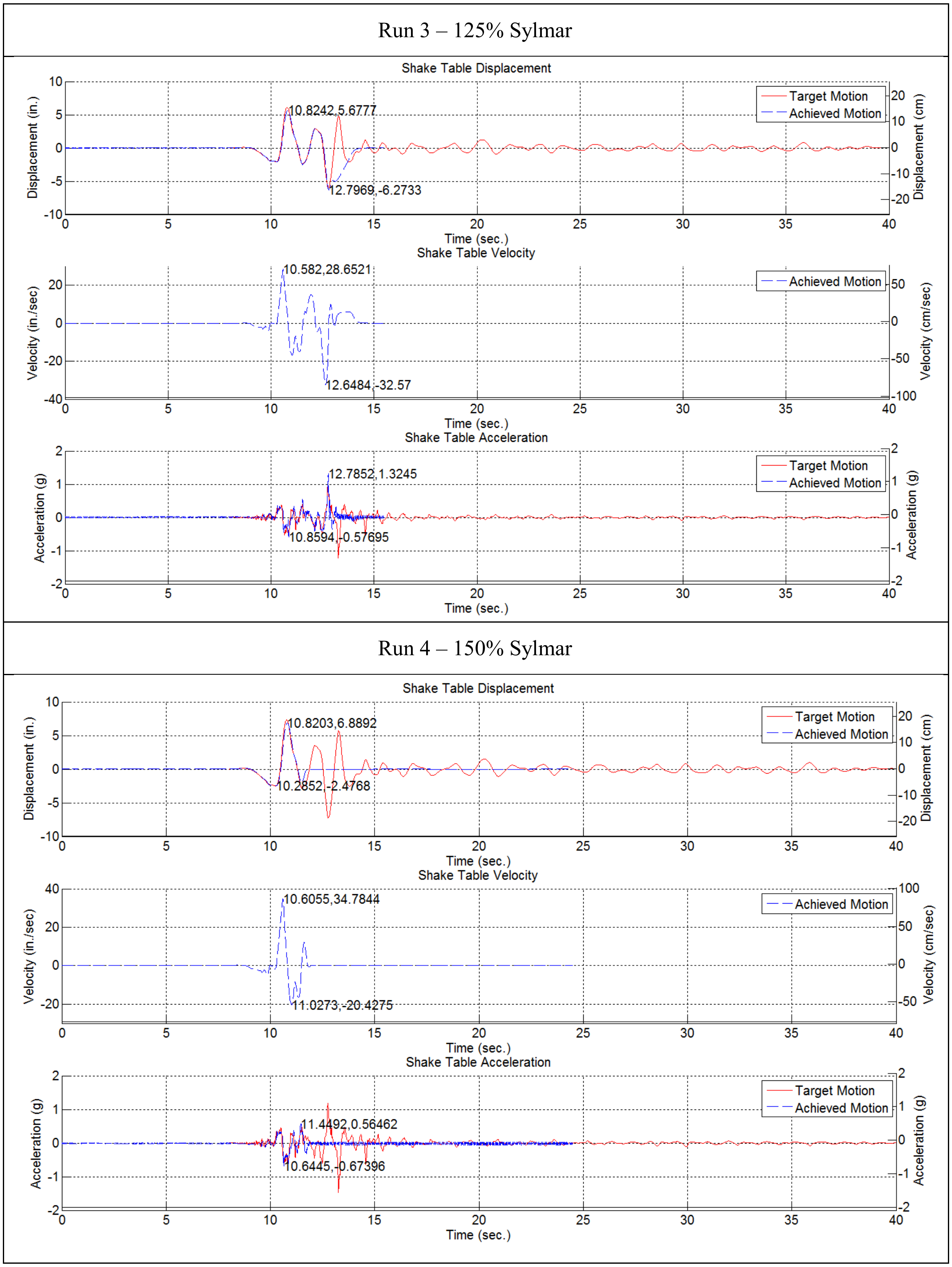

Figure 6-10 Comparison of target and achieved motions for the 30° skew test in Run 3 and 4.

Run 5 – 200% Sylmar

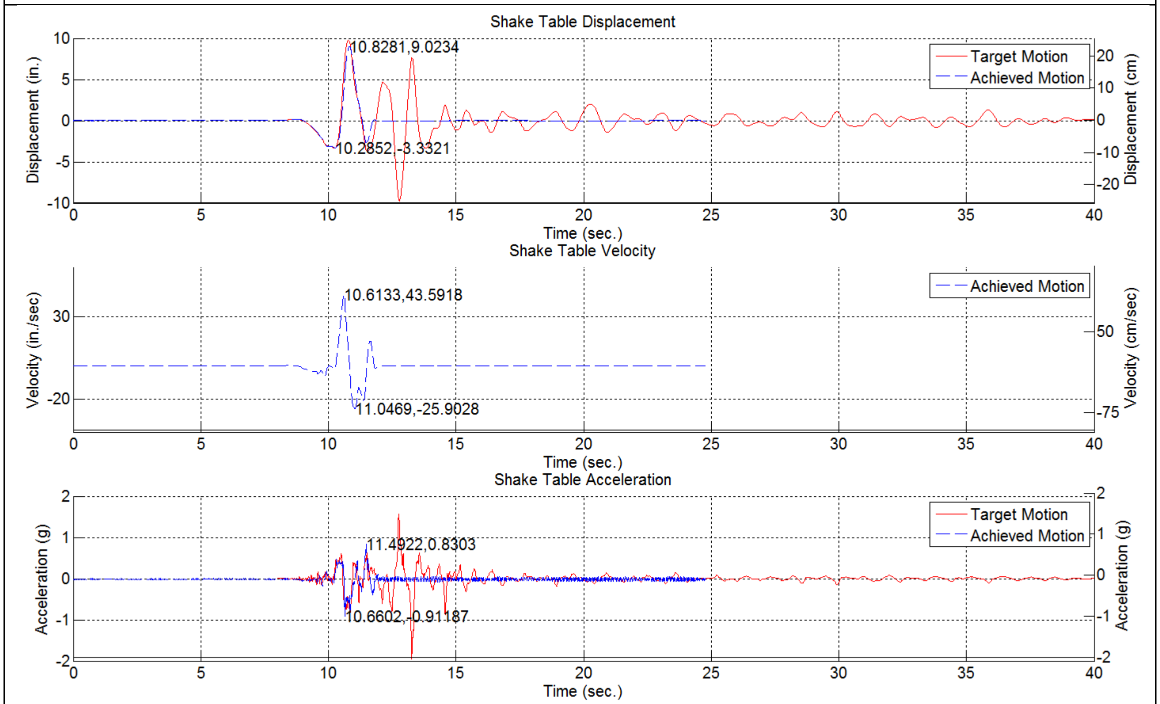

Figure 6-11 Comparison of target and achieved motions for the 30° skew test in Run 5.

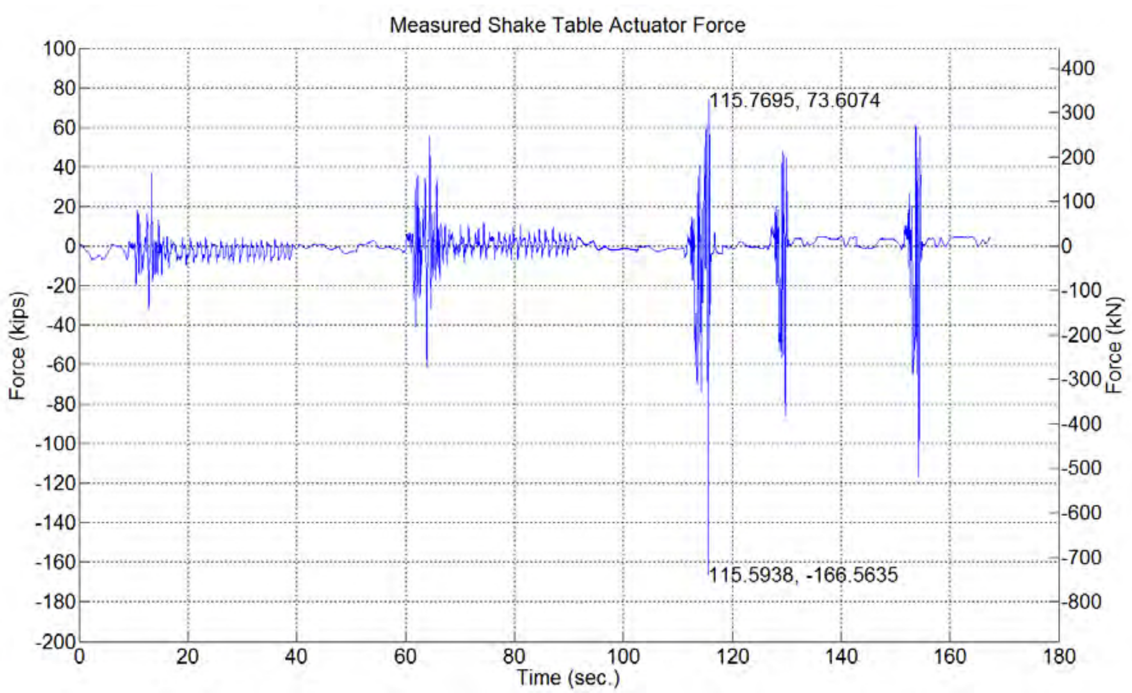

Figure 6-12 Combined shake table actuator force history for the 30° skew test.

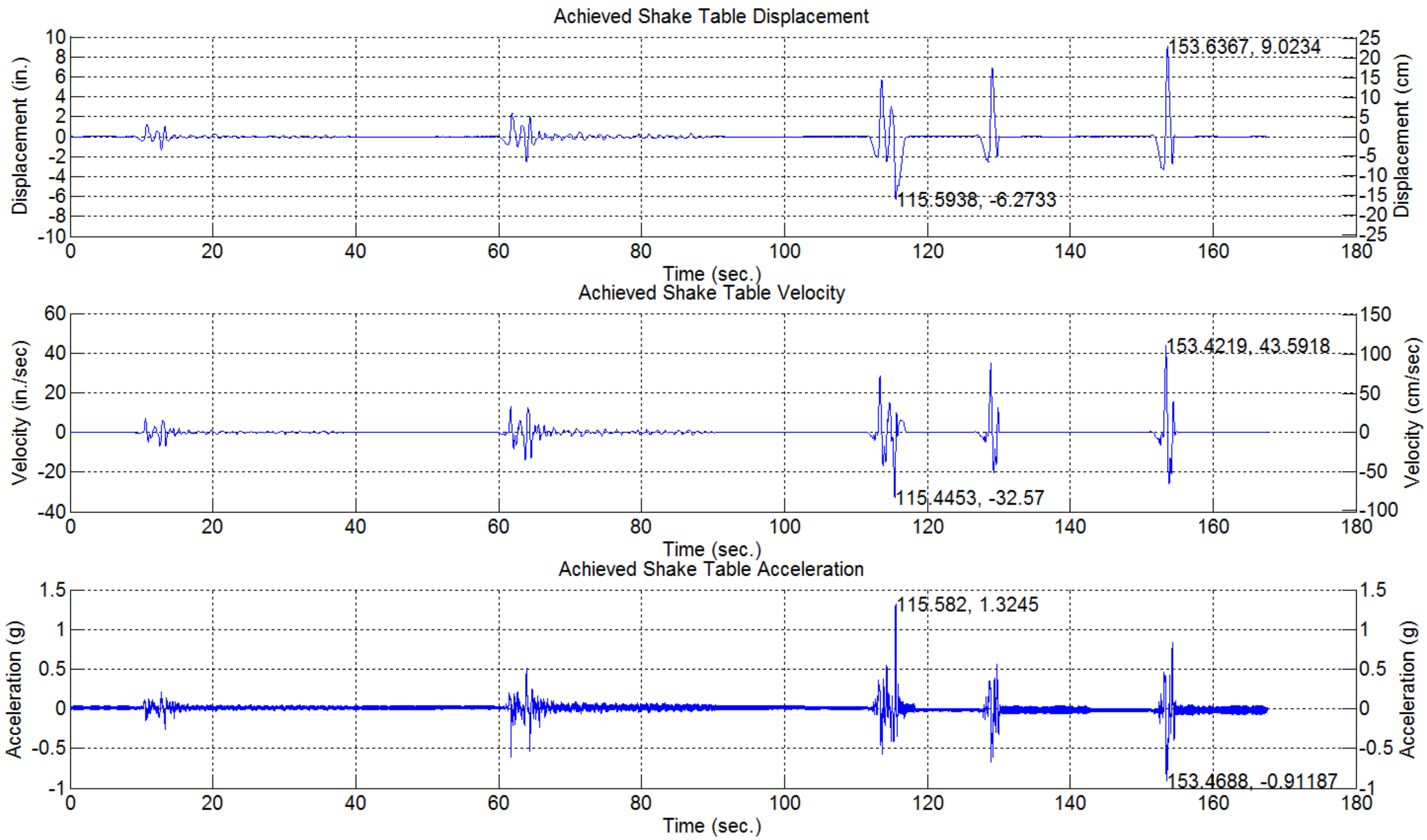

Figure 6-13 Combined achieved motions for the 30° skew test.

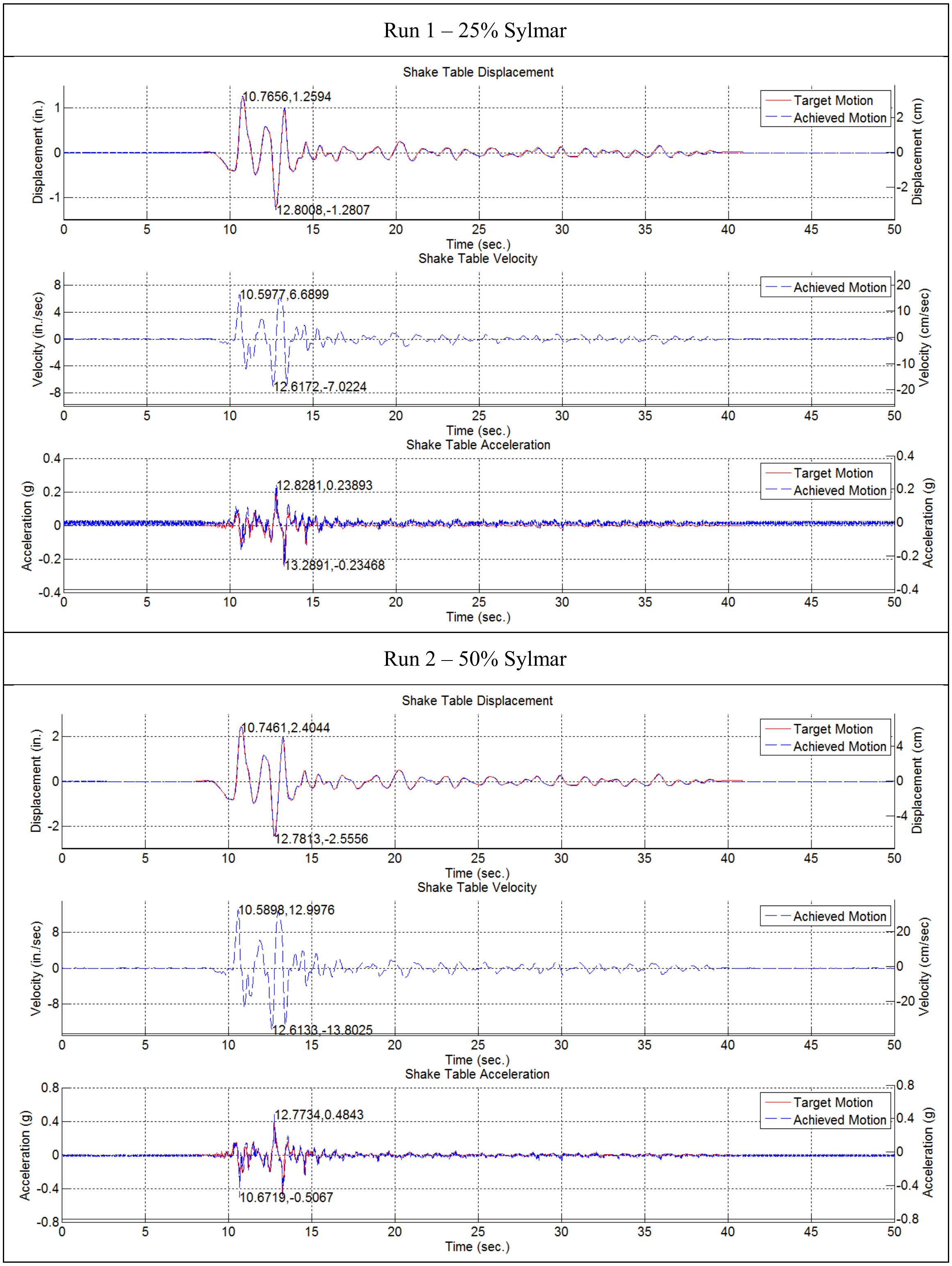

Figure 6-14 Comparison of target and achieved motions for the 45° skew test in Run 1 and 2.

Run 3 – 125% Sylmar

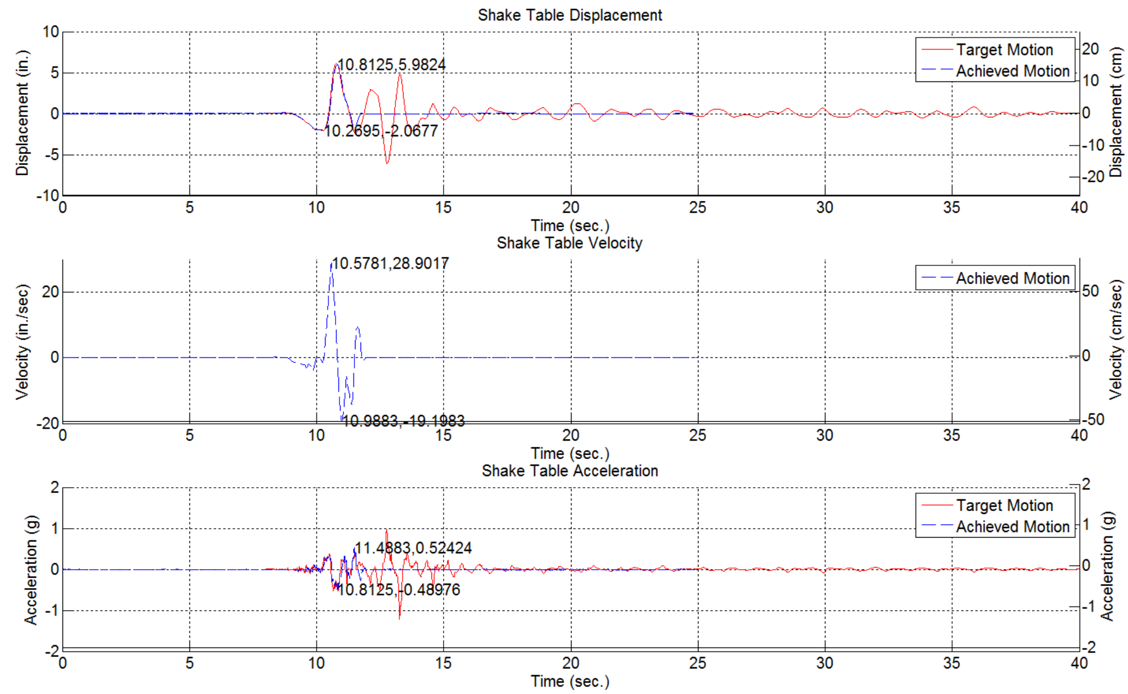

Run 4 – 150% Sylmar

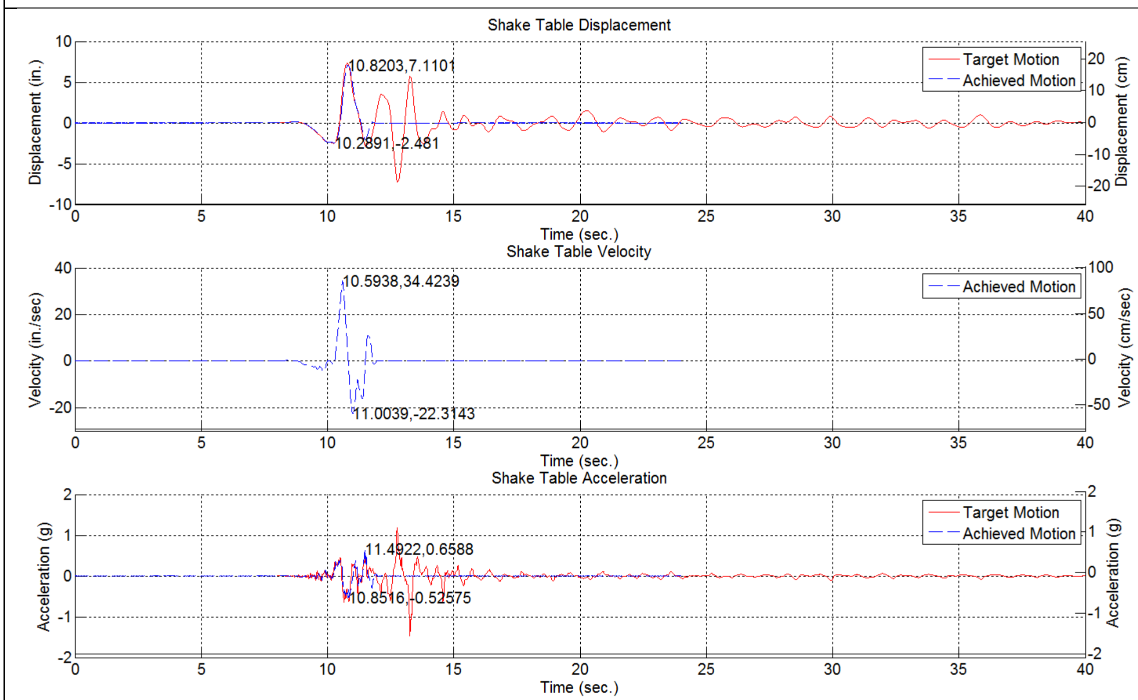

Figure 6-15 Comparison of target and achieved motions for the 45° skew test in Run 3 and 4.

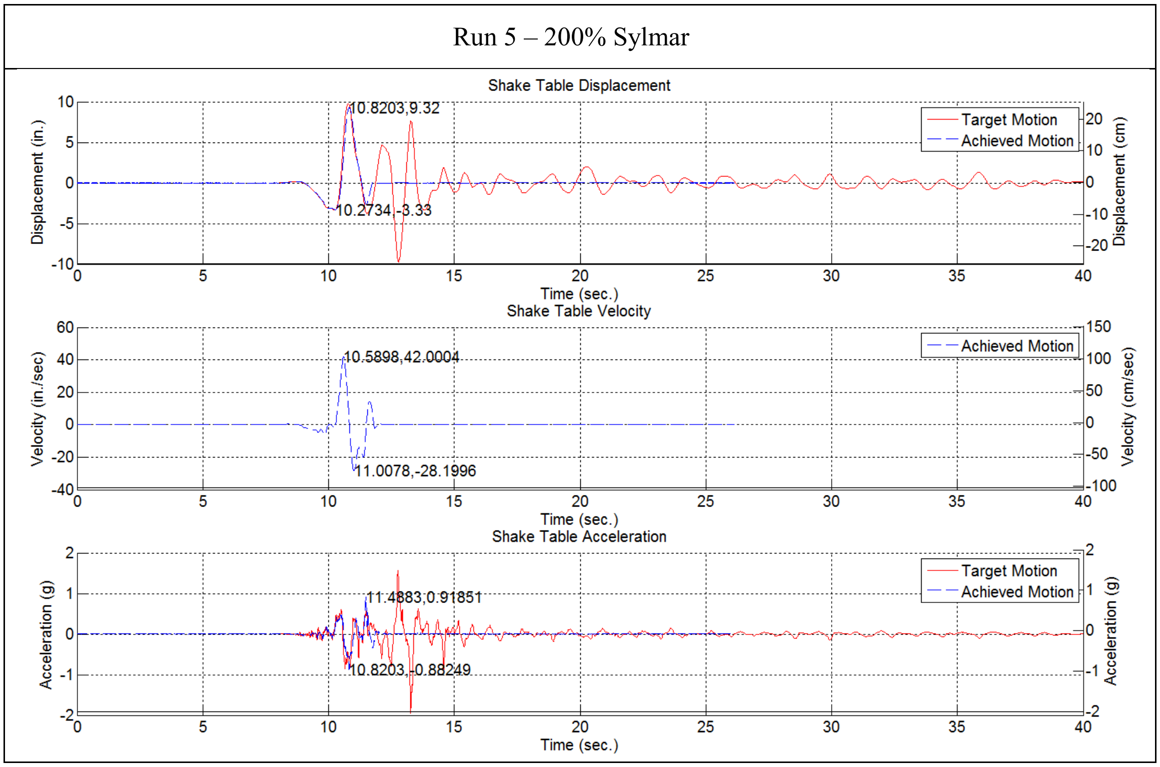

Figure 6-16 Comparison of target and achieved motions for the 45° skew test in Run 5.

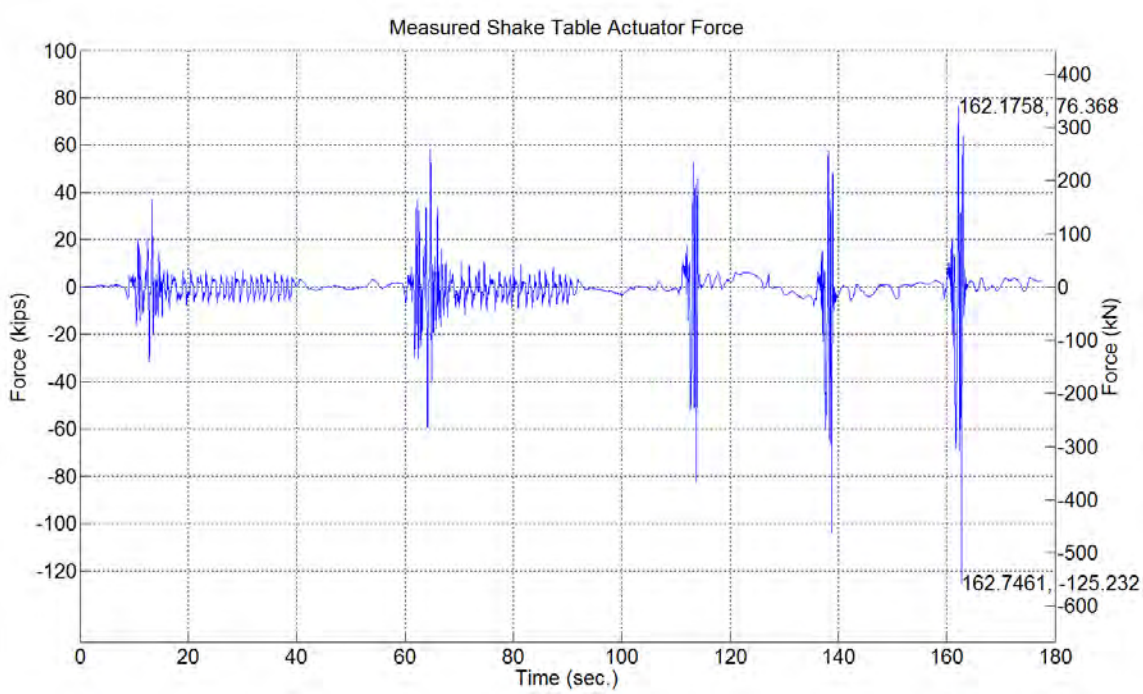

Figure 6-17 Combined shake table actuator force history for the 45° skew test.

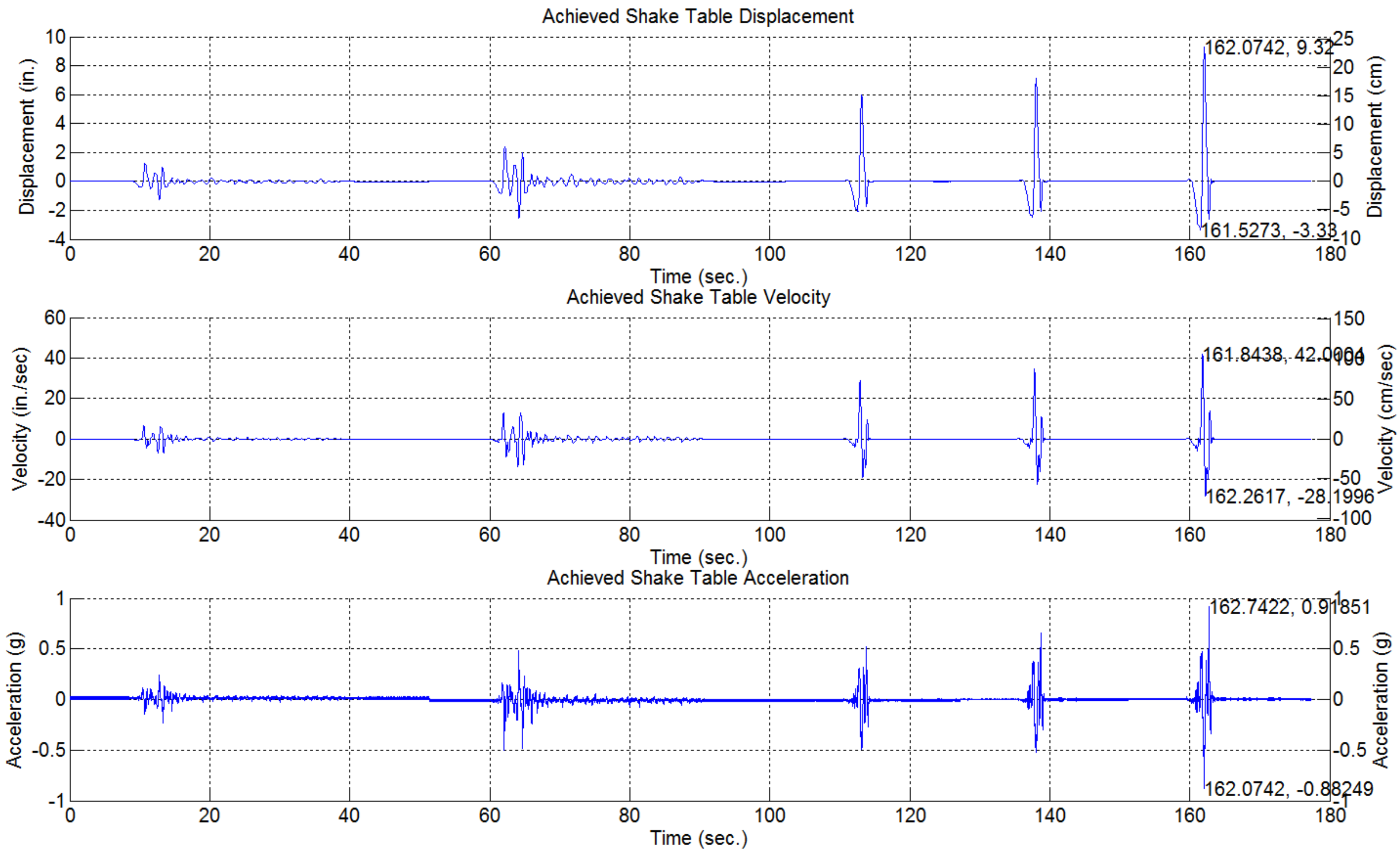

Figure 6-18 Combined achieved motions for the 45° skew test.

Run 1 – 25% Sylmar

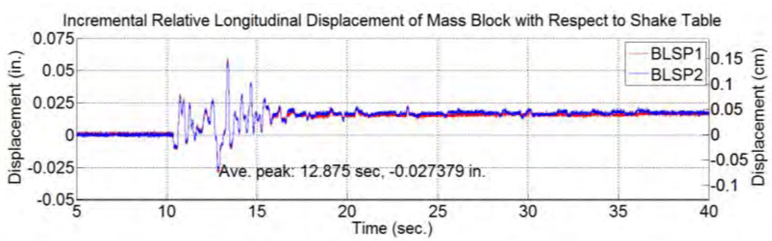

Run 2 – 50% Sylmar

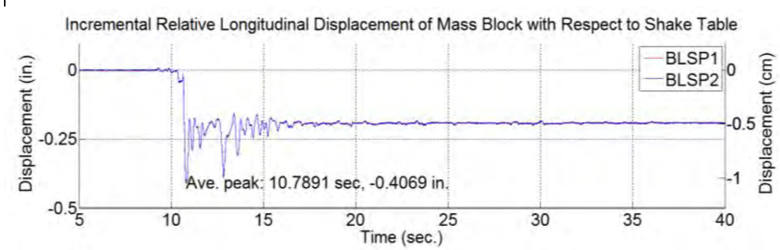

Run 3 – 75% Sylmar

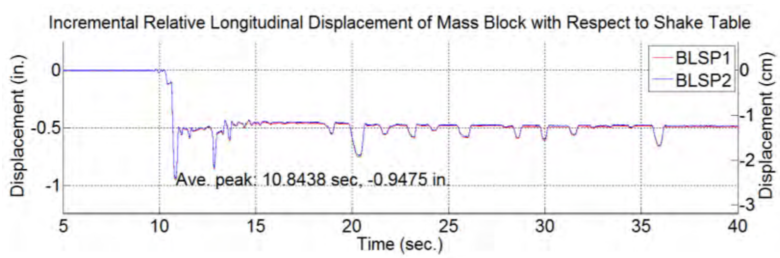

Run 4 – 50% Sylmar

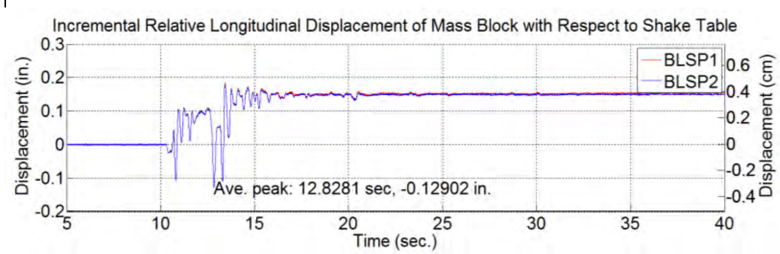

Run 6 – 150% Sylmar

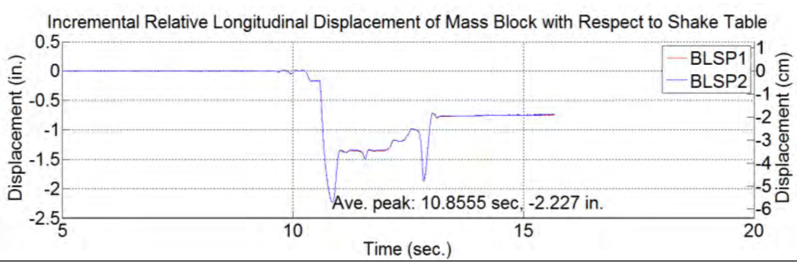

Run 7 – 150% Sylmar

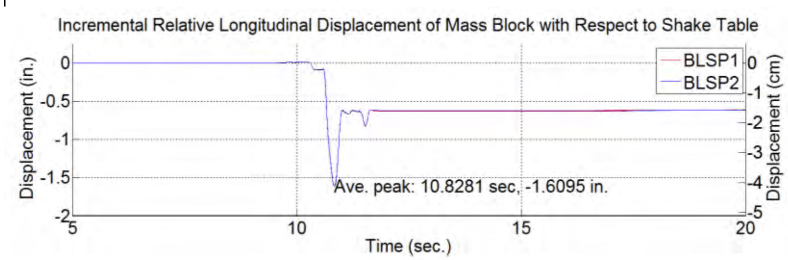

Figure 6-19 Longitudinal displacement of the bridge block relative to the shake table for the 0° skew test.

Run 1 – 25% Sylmar	Run 2 – 50% Sylmar
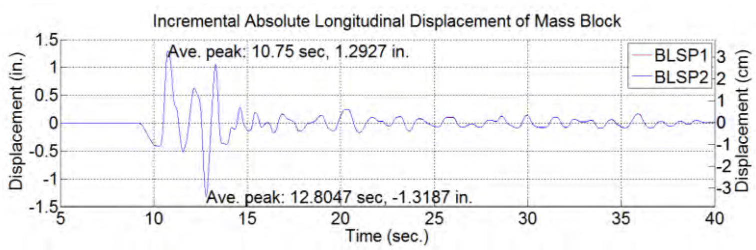	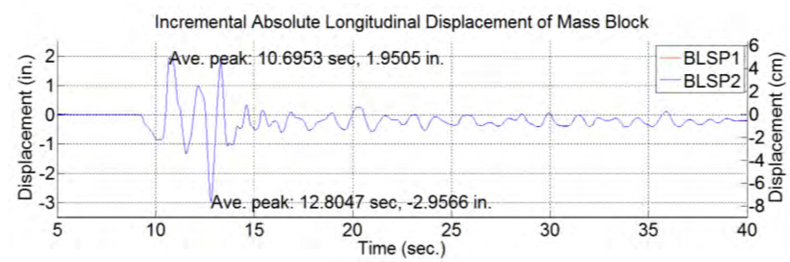
Run 3 – 75% Sylmar	Run 4 – 50% Sylmar
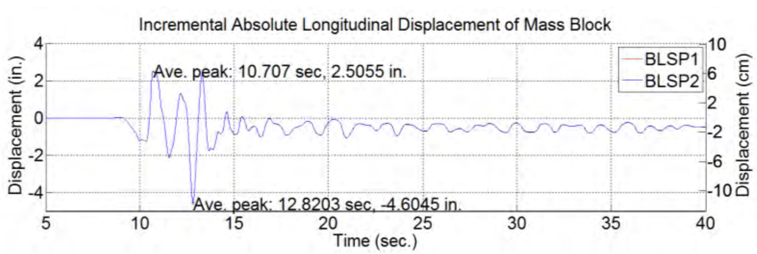	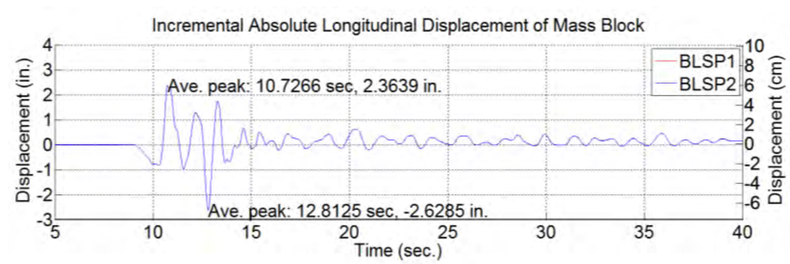
Run 6 – 150% Sylmar	Run 7 – 150% Sylmar
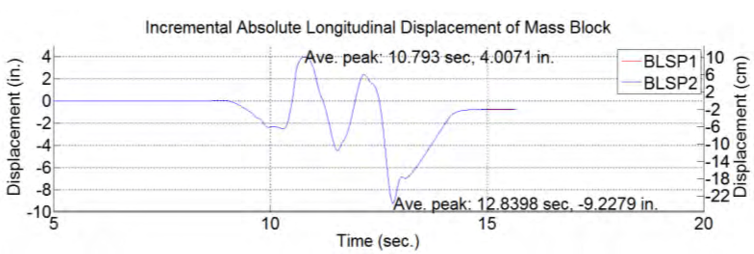	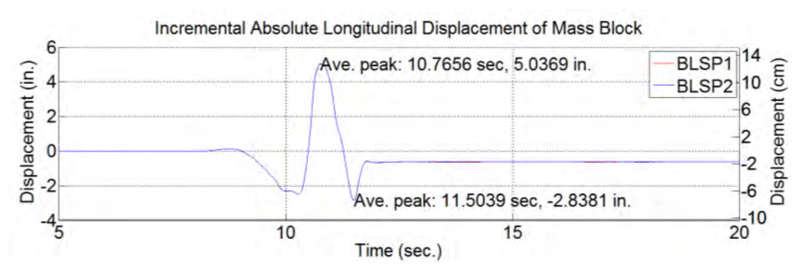

Figure 6-20 Absolute longitudinal displacement of the bridge block for the 0° skew test.

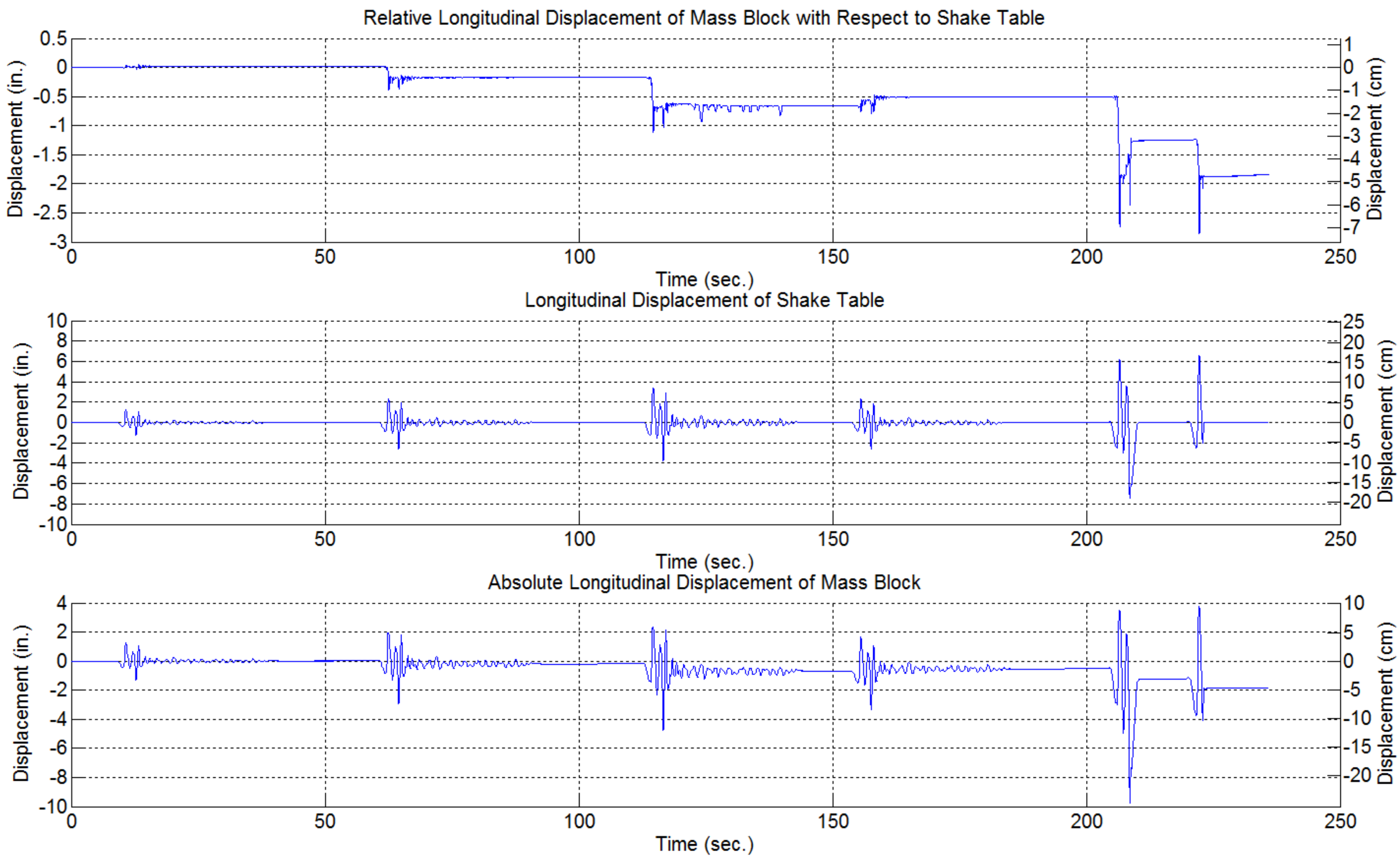

Figure 6-21 Combined longitudinal displacement of the bridge block for the 0° skew test.

Run 1 – 25% Sylmar

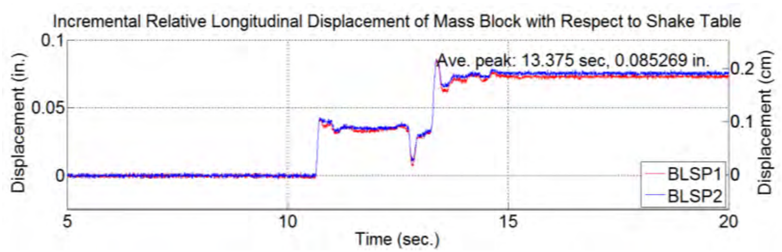

Run 2 – 50% Sylmar

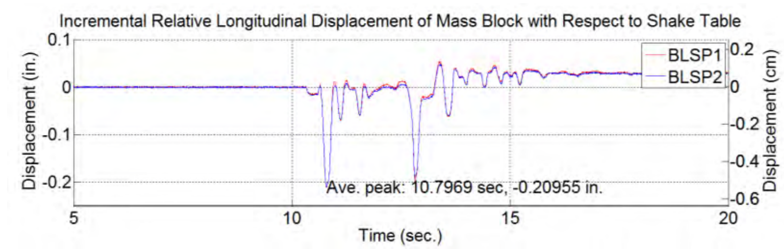

Run 3 – 125% Sylmar

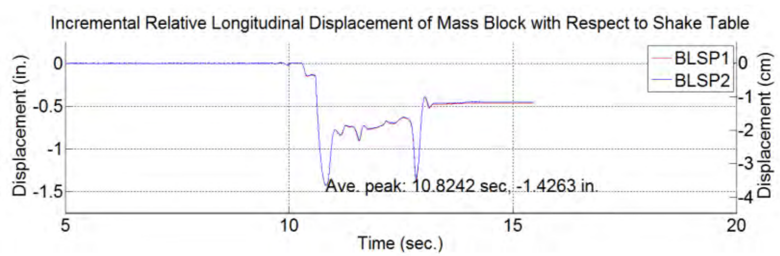

Run 4 – 150% Sylmar

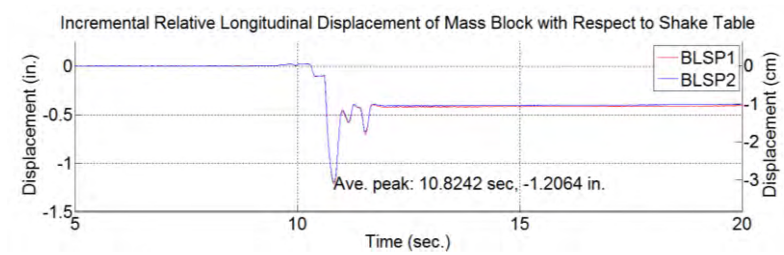

Run 5 – 200% Sylmar

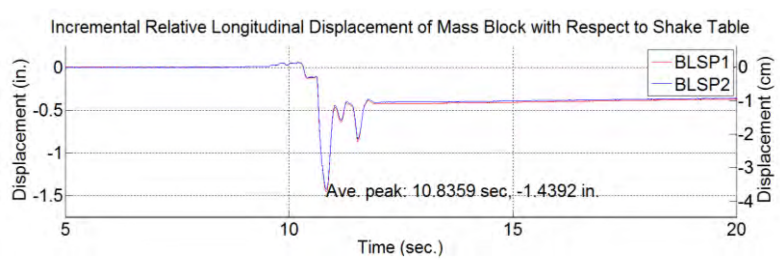

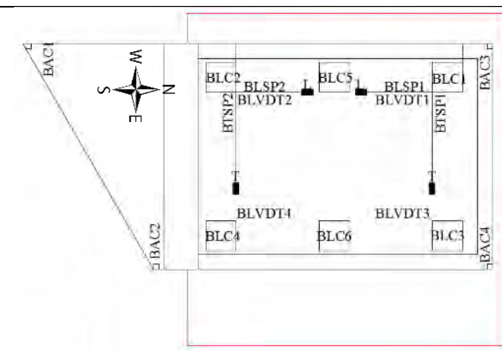

Figure 6-22 Longitudinal displacement of the bridge block relative to the shake table for the 30° skew test.

Run 1 – 25% Sylmar

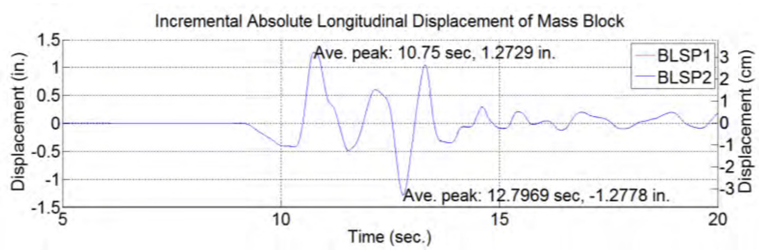

Run 2 – 50% Sylmar

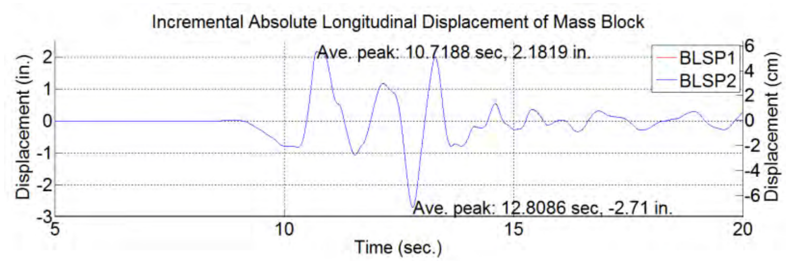

Run 3 – 125% Sylmar

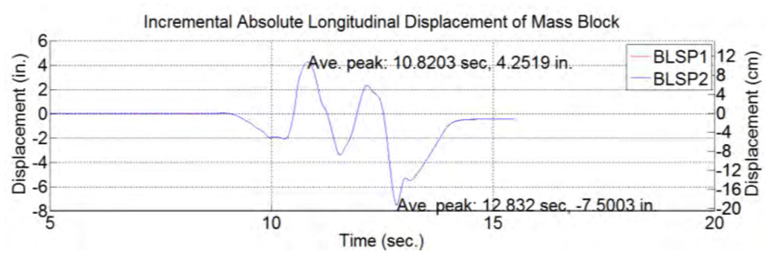

Run 4 – 150% Sylmar

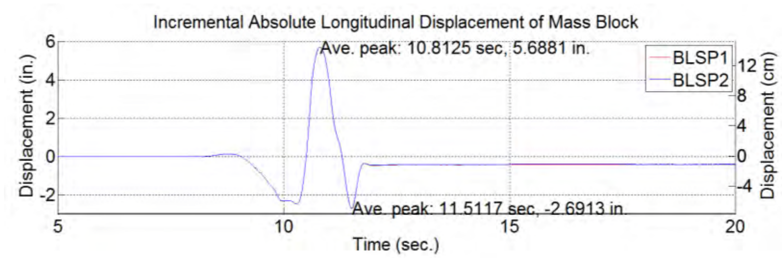

Run 5 – 200% Sylmar

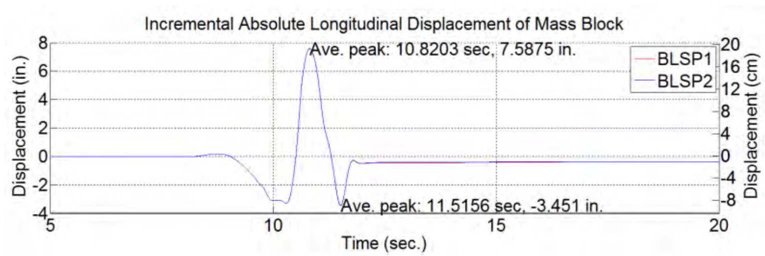

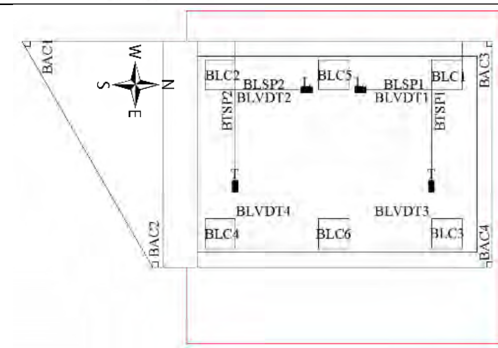

Figure 6-23 Absolute longitudinal displacement of the bridge block for the 30° skew test.

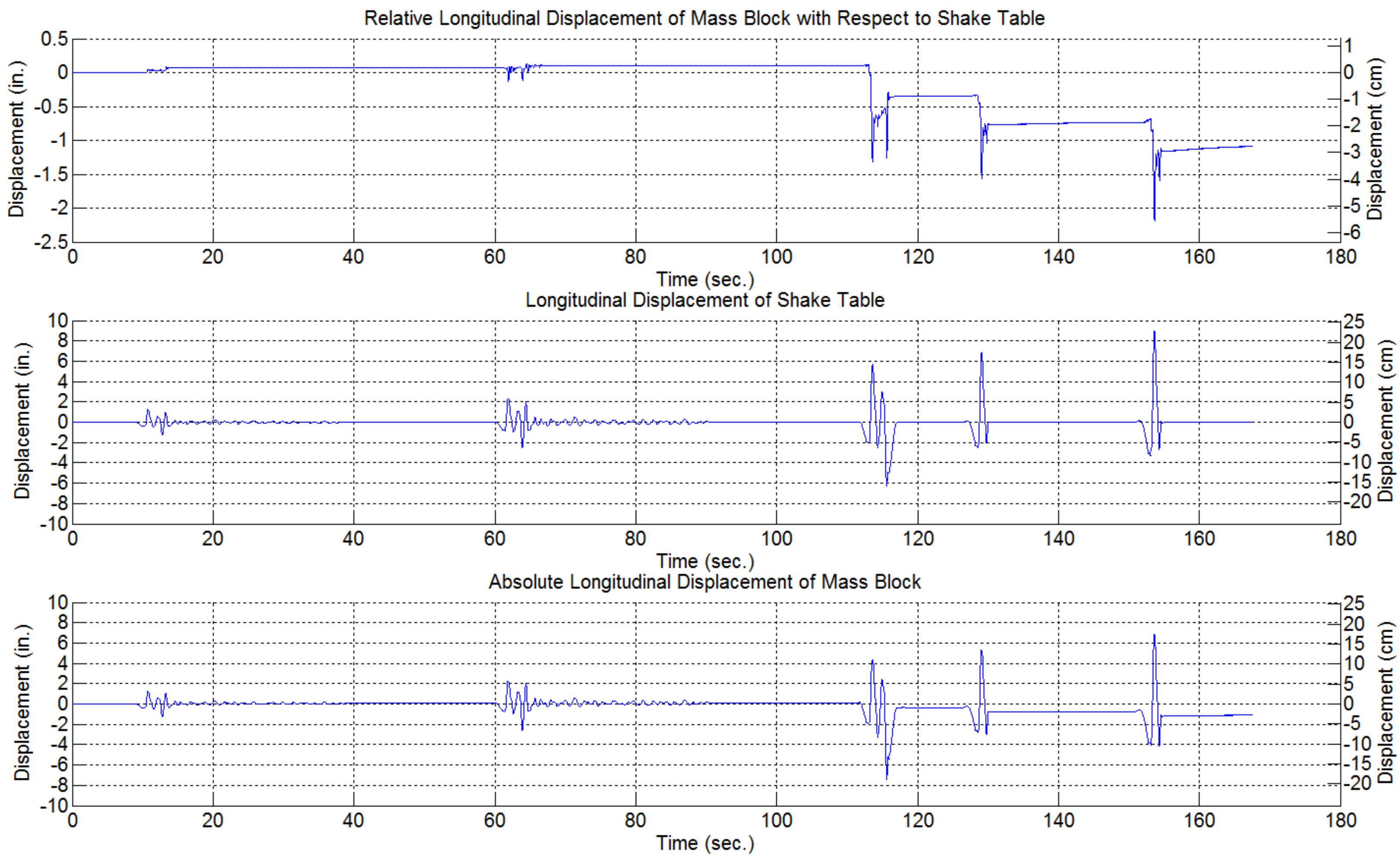

Figure 6-24 Combined longitudinal displacement of the bridge block for the 30° skew test.

Run 1 – 25% Sylmar

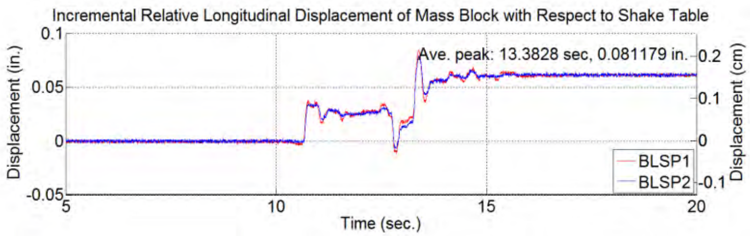

Run 2 – 50% Sylmar

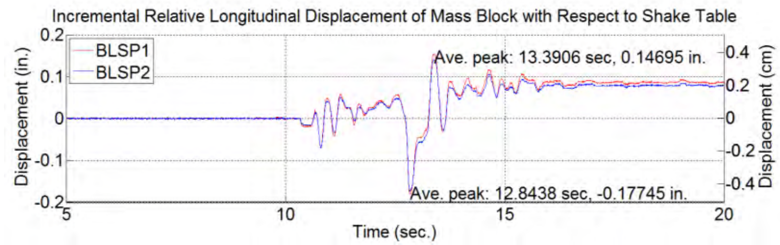

Run 3 – 125% Sylmar

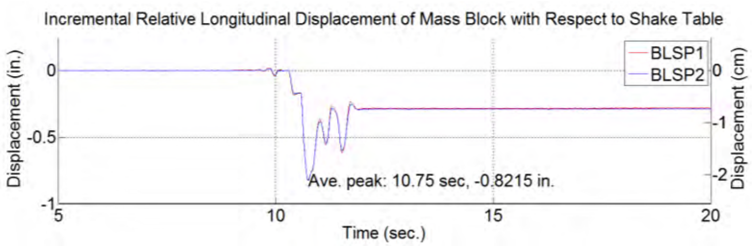

Run 4 – 150% Sylmar

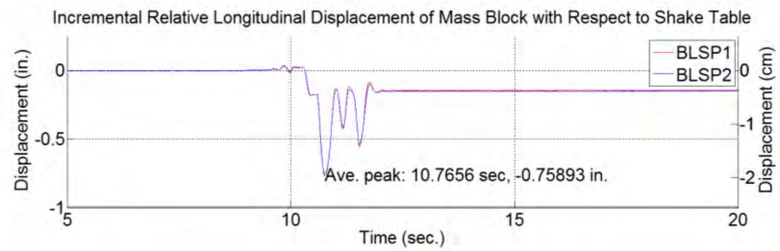

Run 5 – 200% Sylmar

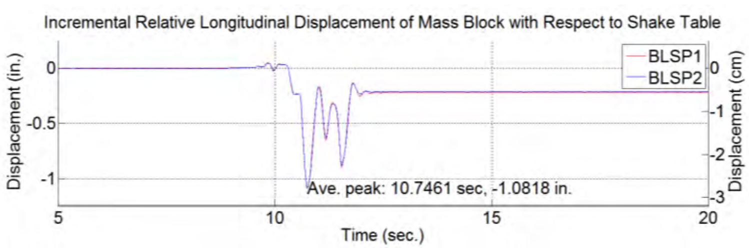

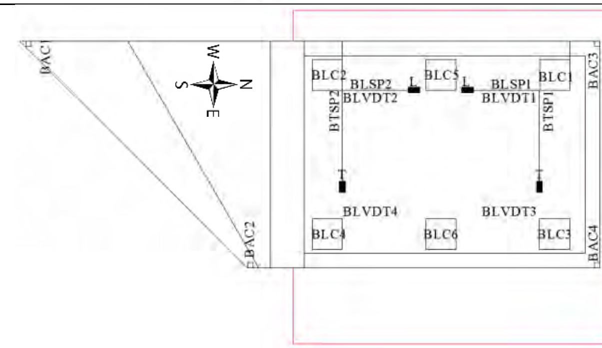

Figure 6-25 Longitudinal displacement of the bridge block relative to the shake table for the 45° skew test.

Run 1 – 25% Sylmar	Run 2 – 50% Sylmar
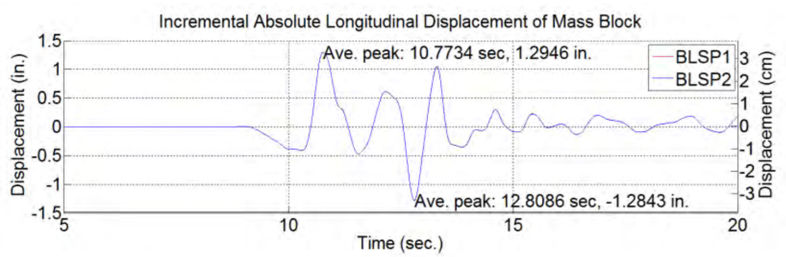	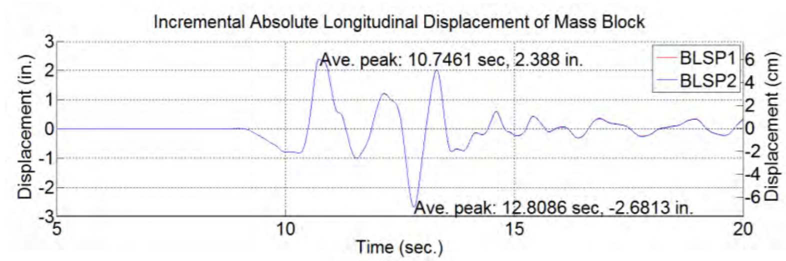
Run 3 – 125% Sylmar	Run 4 – 150% Sylmar
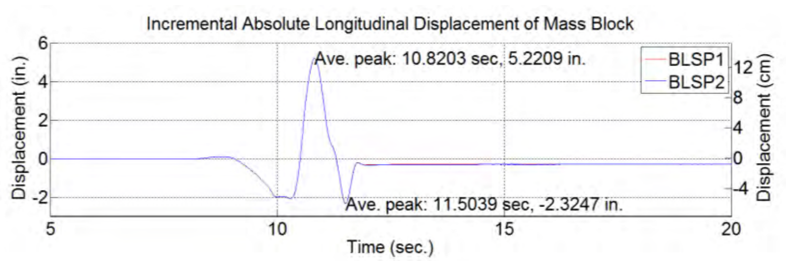	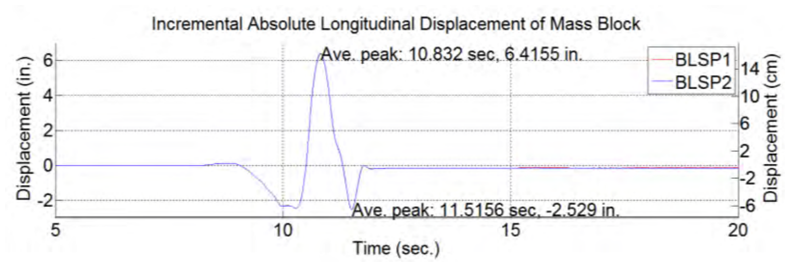
Run 5 – 200% Sylmar	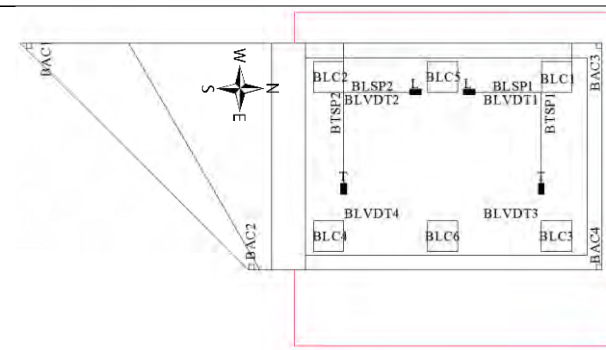
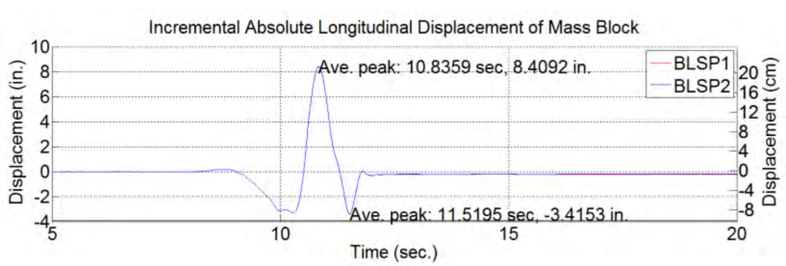	

Figure 6-26 Absolute longitudinal displacement of the bridge block for the 45° skew test.

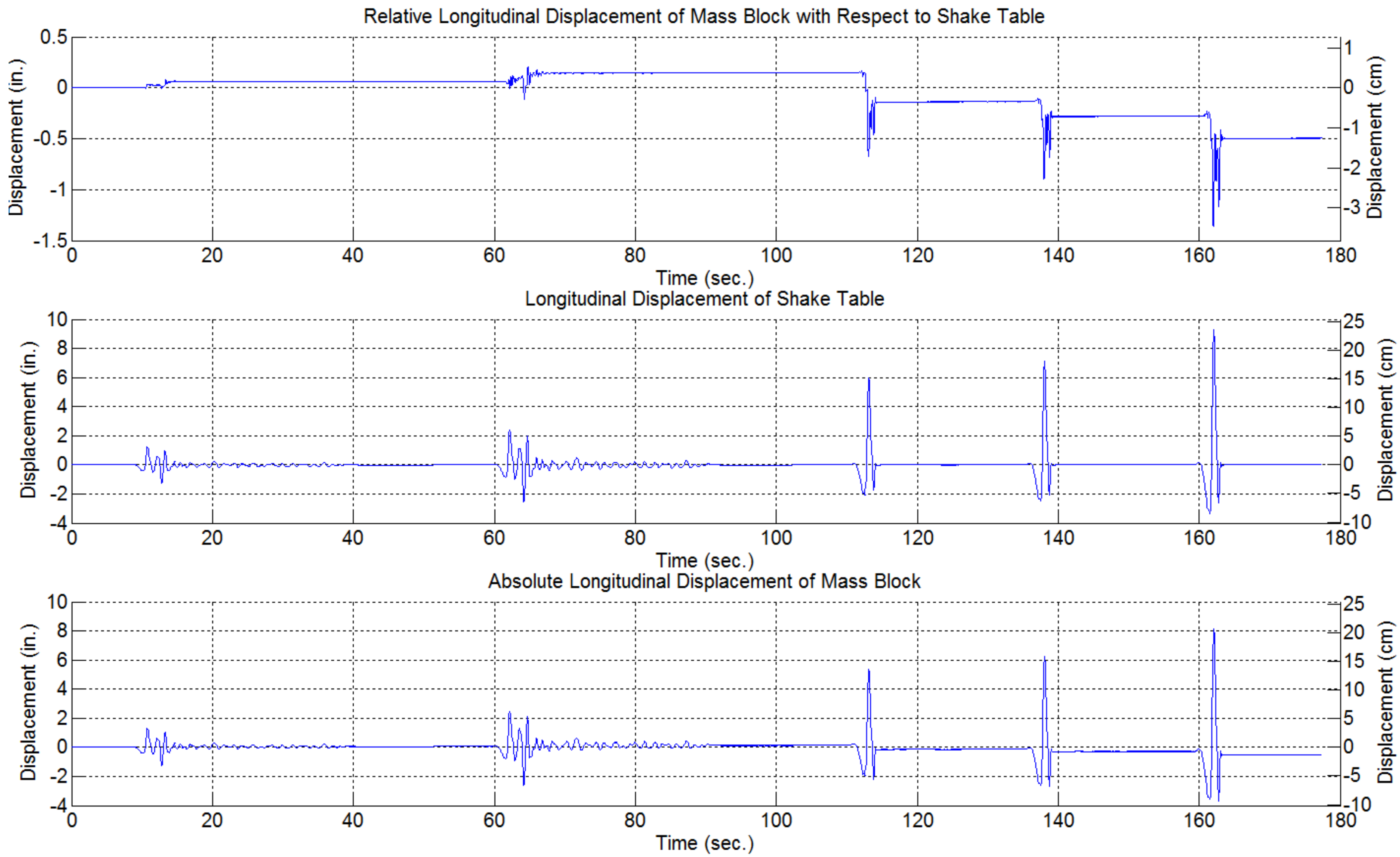

Figure 6-27 Combined longitudinal displacement of the bridge block for the 45° skew test.

Run 1 – 25% Sylmar

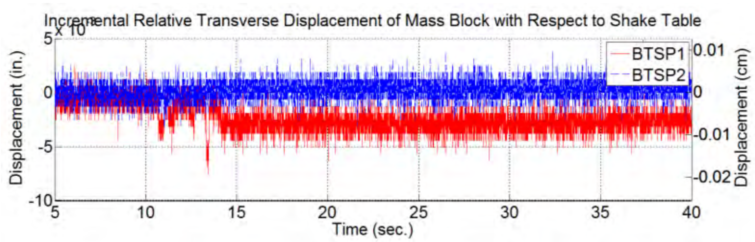

Run 2 – 50% Sylmar

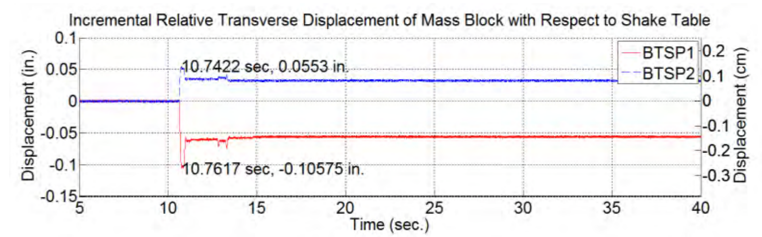

Run 3 – 75% Sylmar

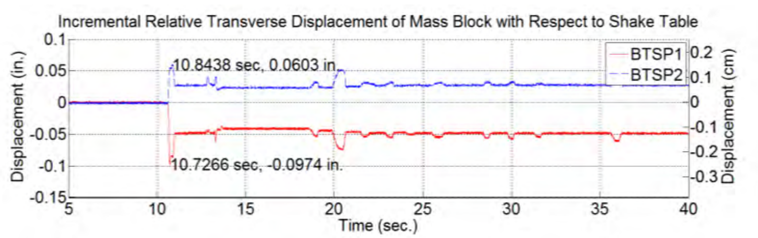

Run 4 – 50% Sylmar

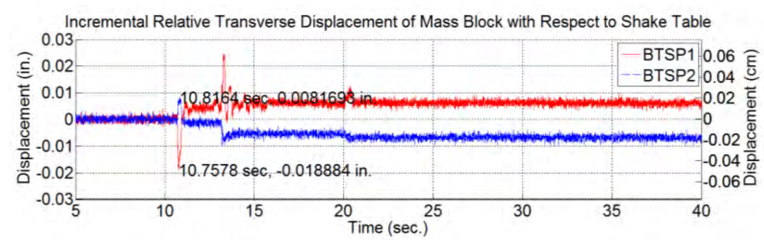

Run 6 – 150% Sylmar

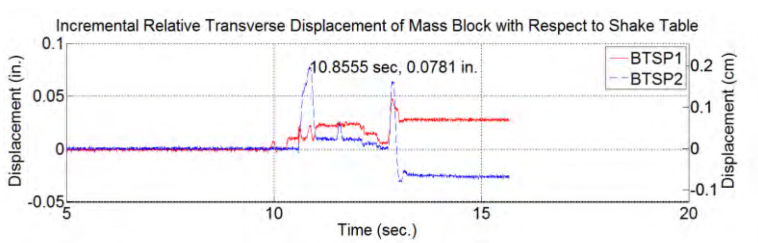

Run 7 – 150% Sylmar

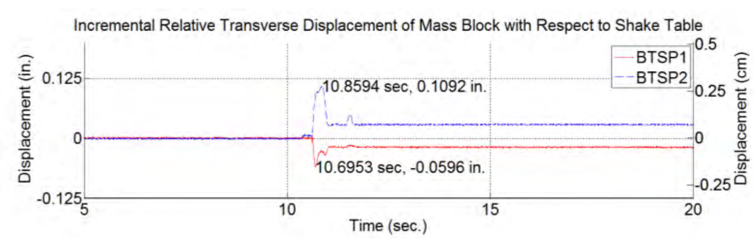

Figure 6-28 Transverse displacement of the bridge block for the 0° skew test.

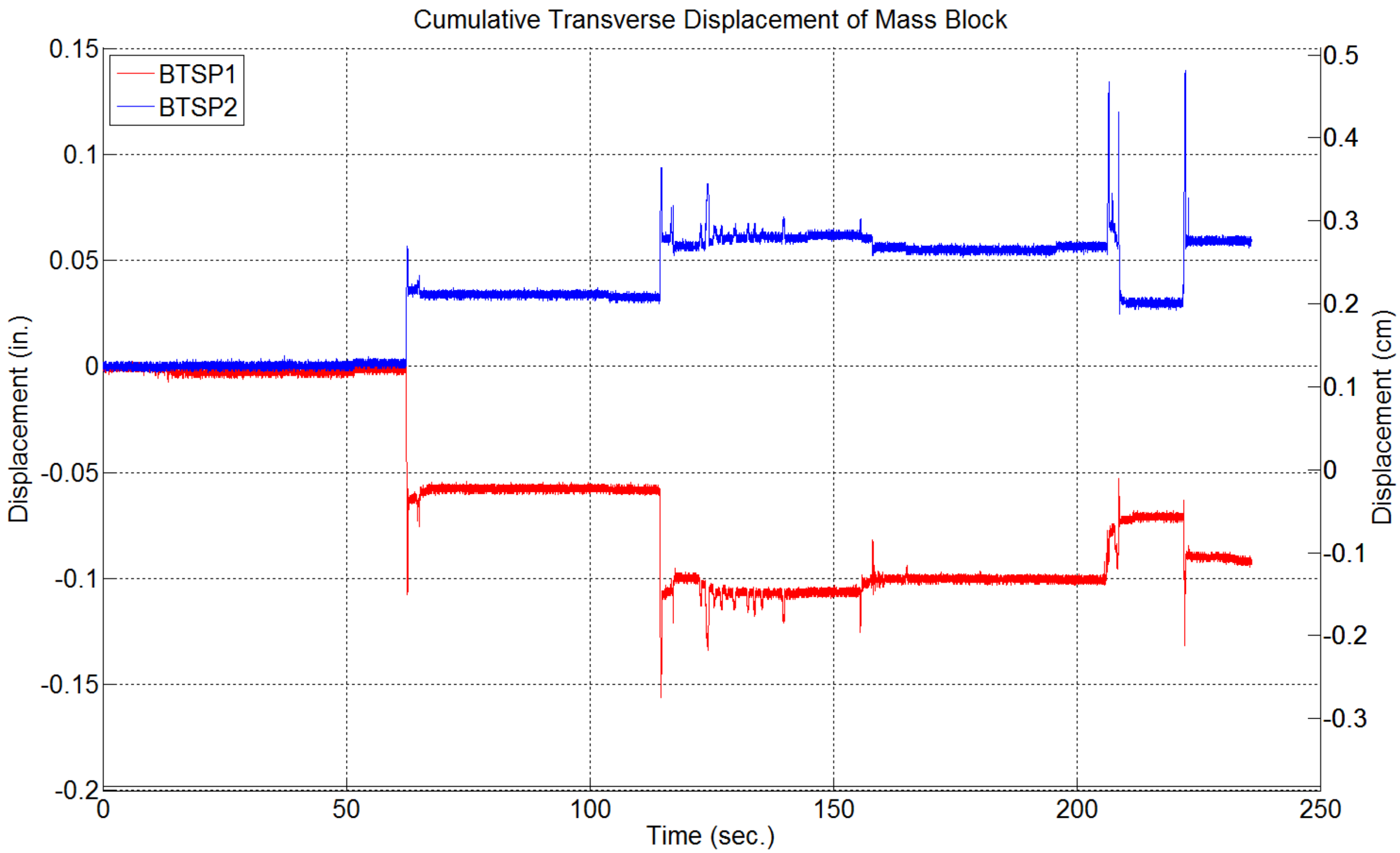

Figure 6-29 Combined transverse displacement of the bridge block for the 0° skew test.

Run 1 – 25% Sylmar	Run 2 – 50% Sylmar
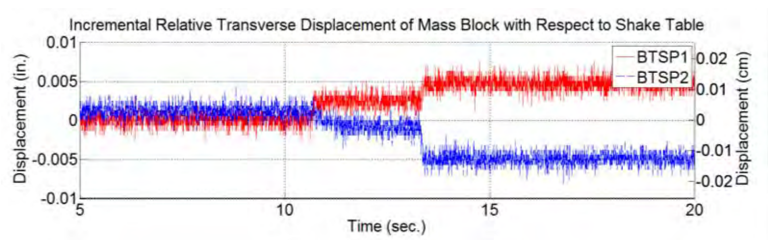	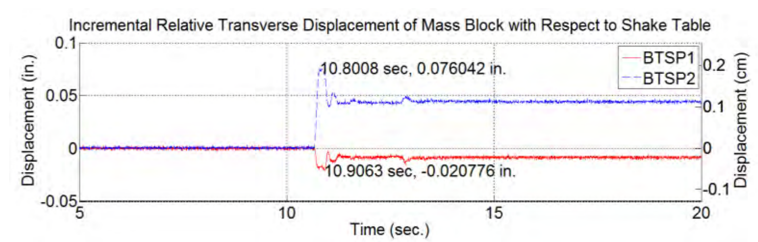
Run 3 – 125% Sylmar	Run 4 – 150% Sylmar
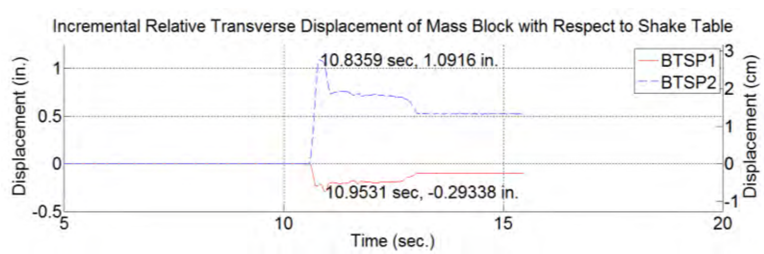	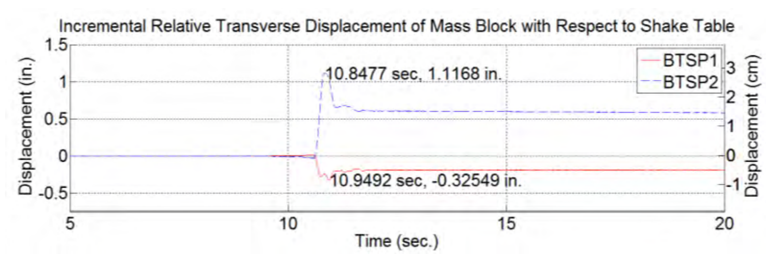
Run 5 – 200% Sylmar	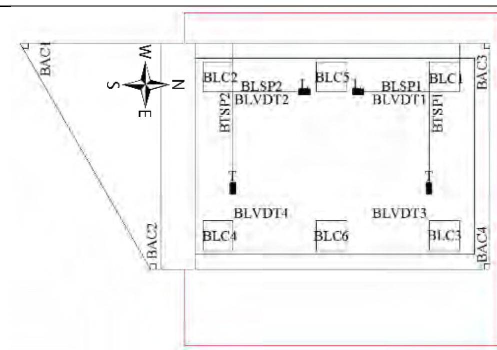
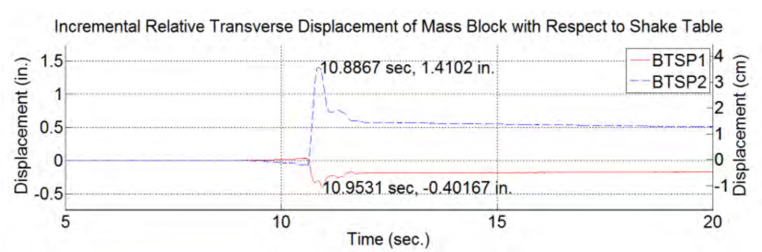	

Figure 6-30 Transverse displacement of the bridge block for the 30° skew test.

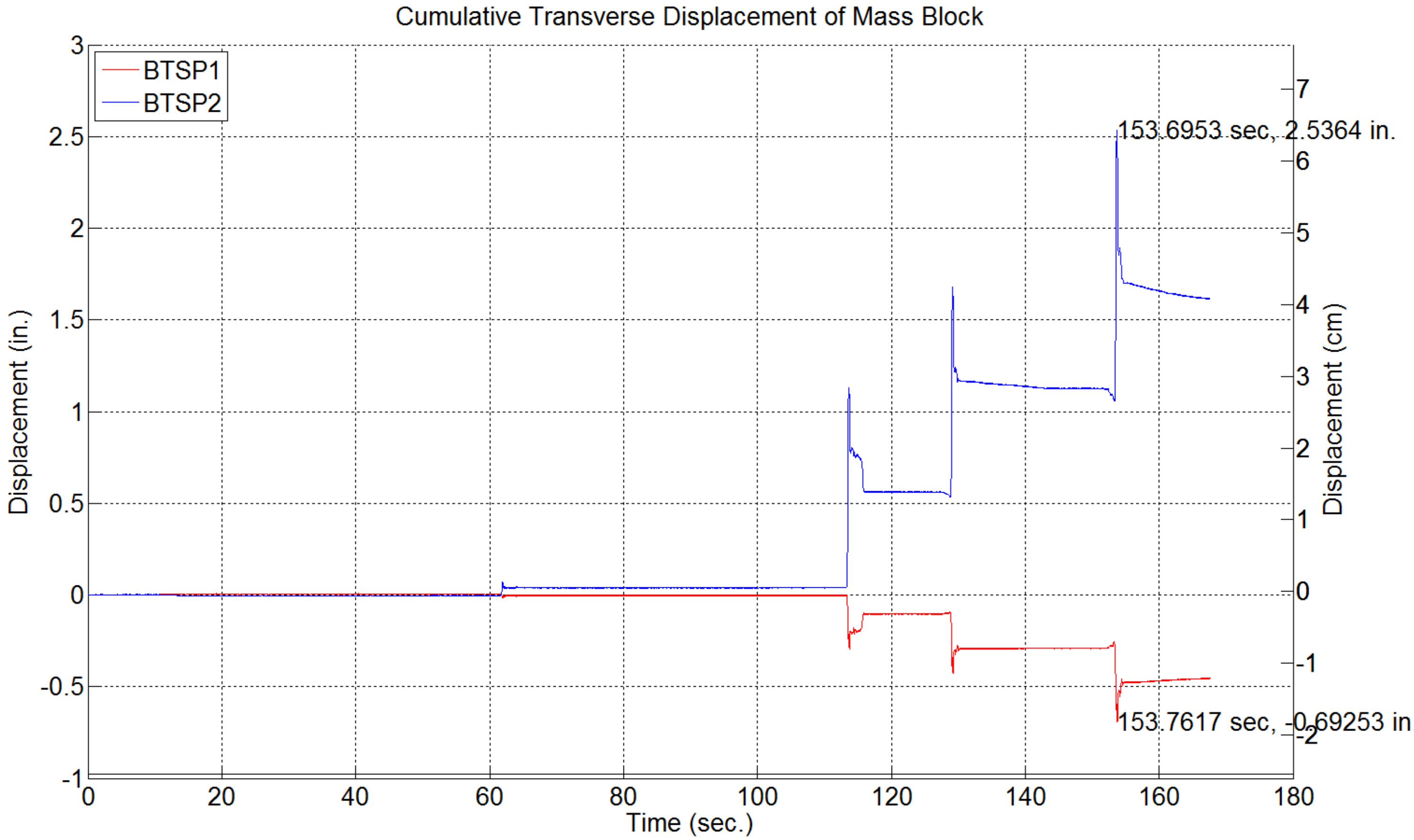

Figure 6-31 Combined transverse displacement of the bridge block for the 30° skew test.

Run 1 – 25% Sylmar

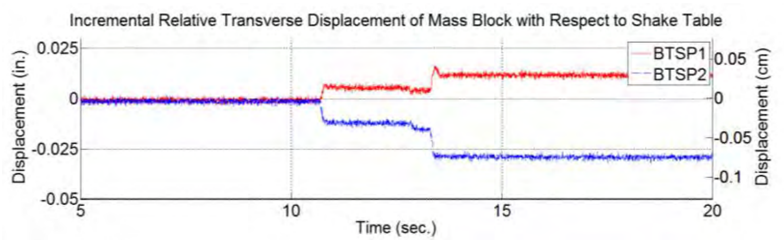

Run 2 – 50% Sylmar

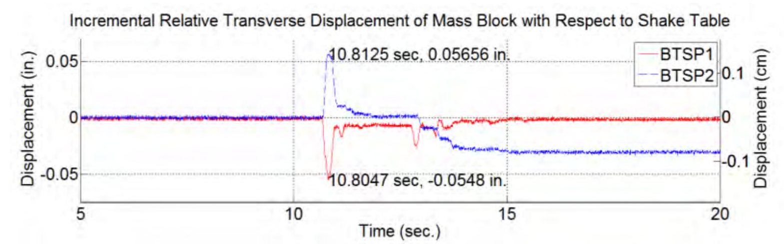

Run 3 – 125% Sylmar

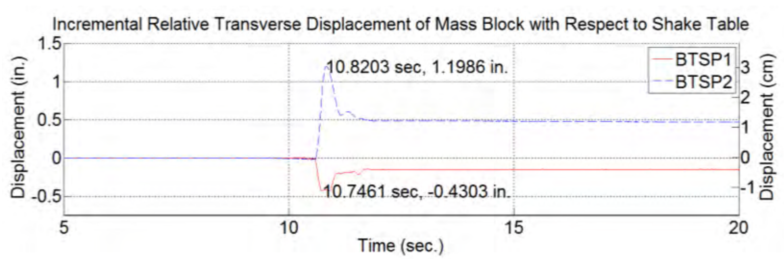

Run 4 – 150% Sylmar

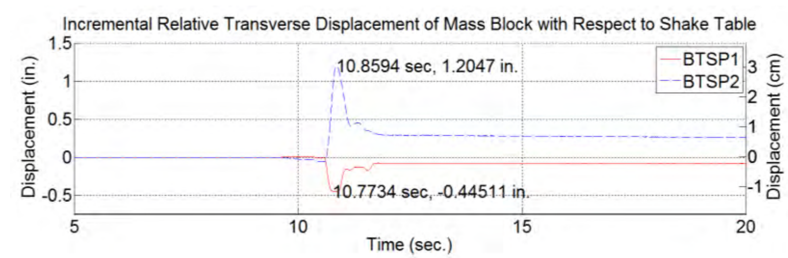

Run 5 – 200% Sylmar

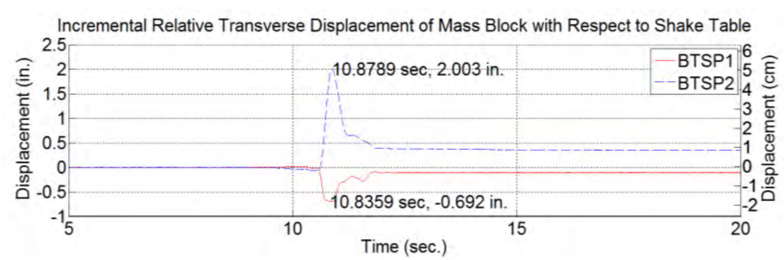

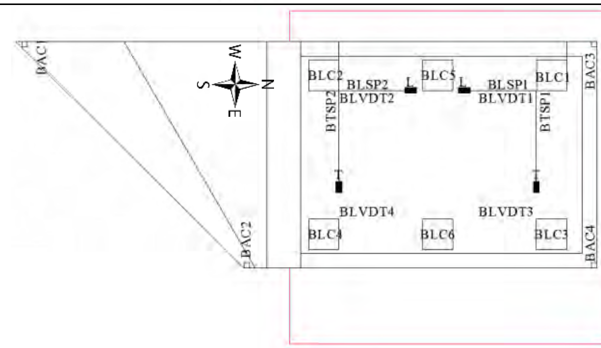

Figure 6-32 Transverse displacement of the bridge block for the 45° skew test.

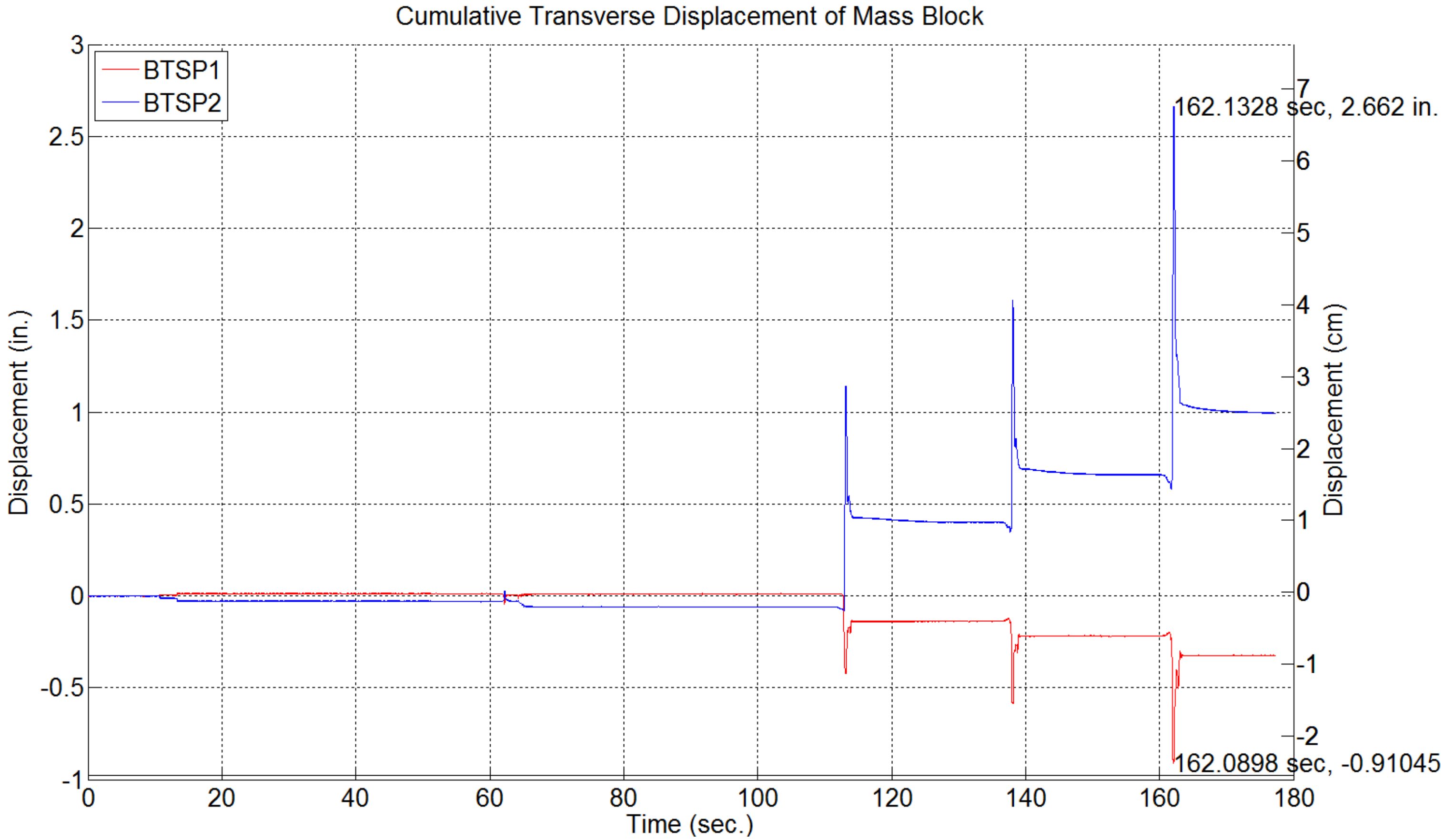

Figure 6-33 Combined transverse displacement of the bridge block for the 45° skew test.

Run 1 – 25% Sylmar

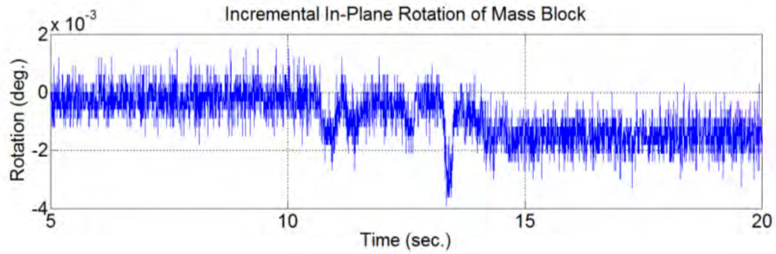

Run 2 – 50% Sylmar

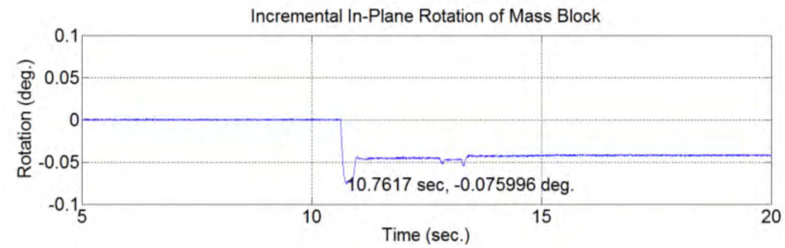

Run 3 – 75% Sylmar

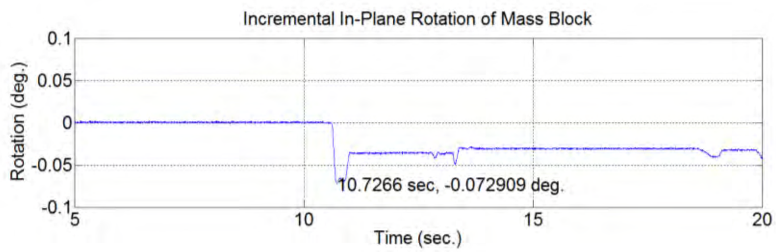

Run 4 – 50% Sylmar

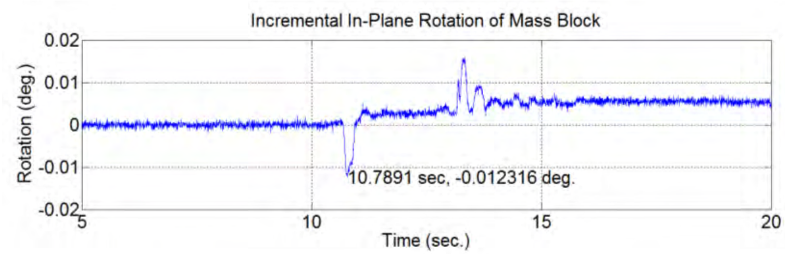

Run 6 – 150% Sylmar

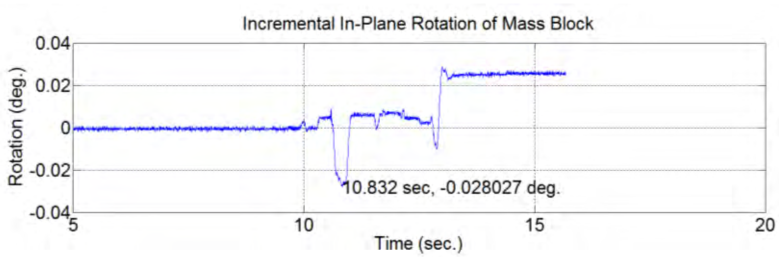

Run 7 – 150% Sylmar

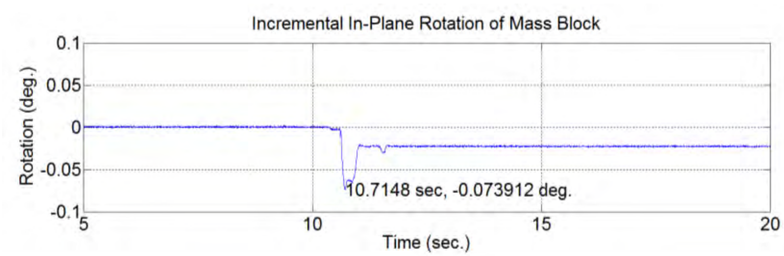

Figure 6-34 In-plane rotation of the bridge block for the 0° skew test.

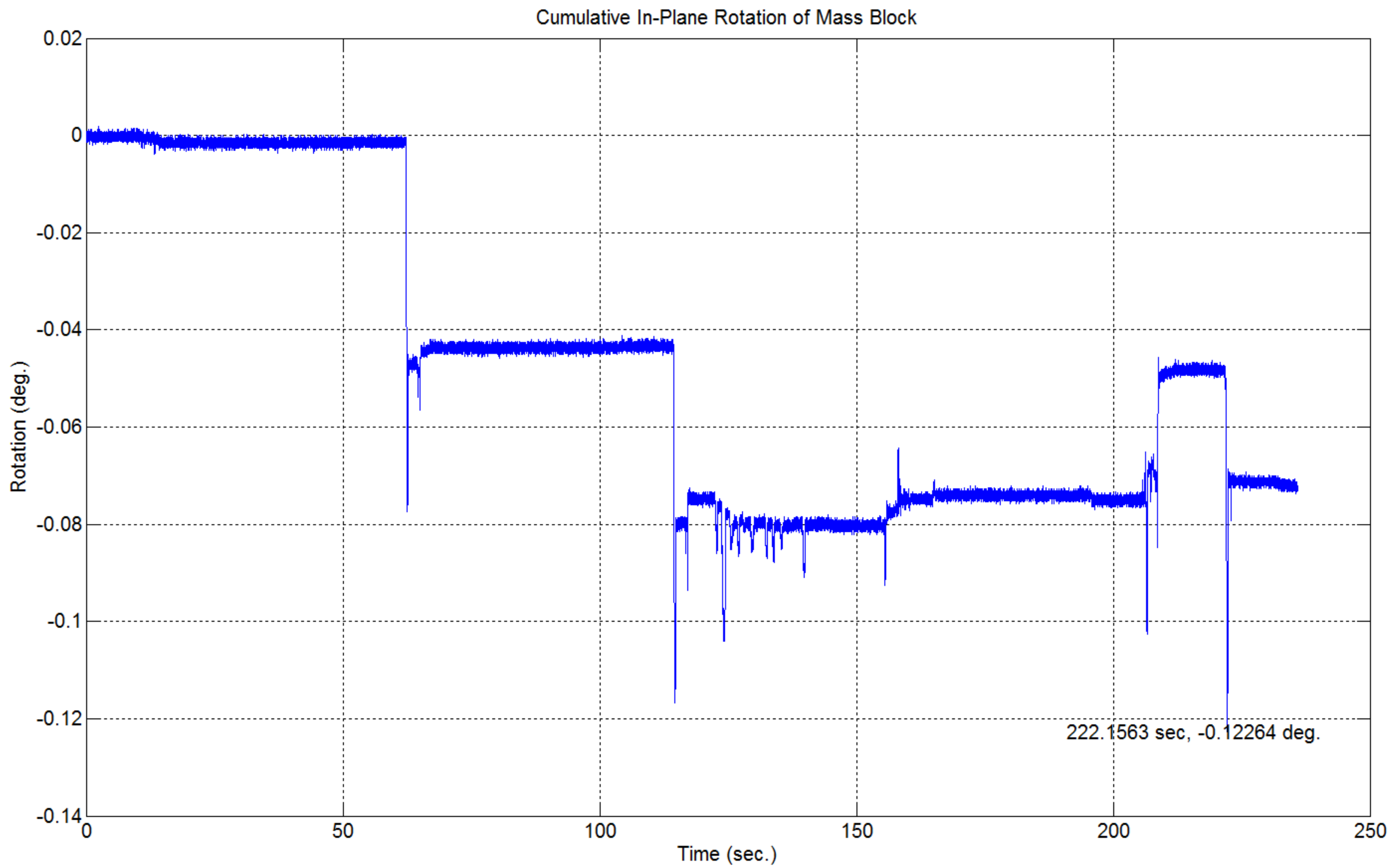

Figure 6-35 Combined in-plane rotation of the bridge block for the 0° skew test.

Run 1 – 25% Sylmar	Run 2 – 50% Sylmar
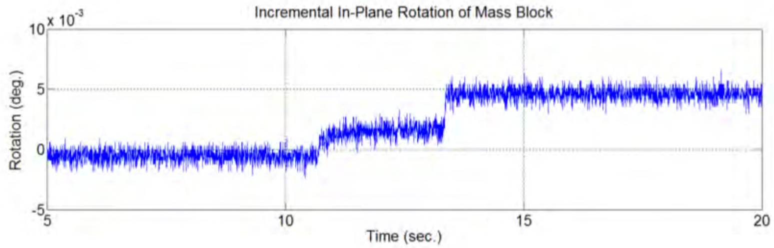	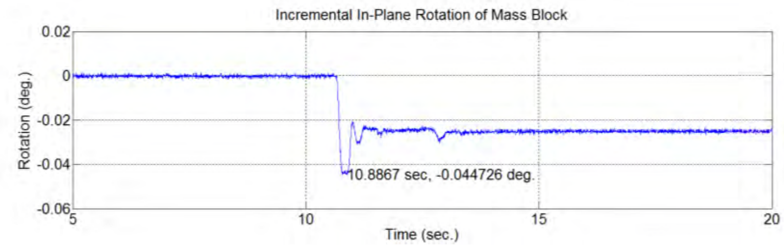
Run 3 – 125% Sylmar	Run 4 – 150% Sylmar
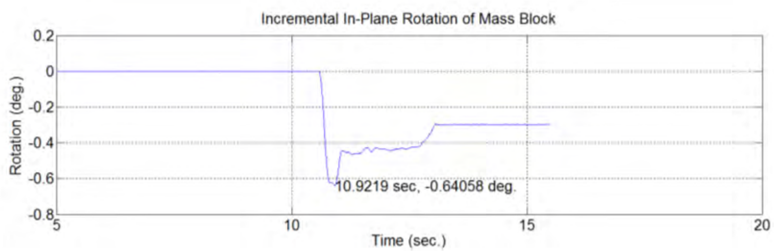	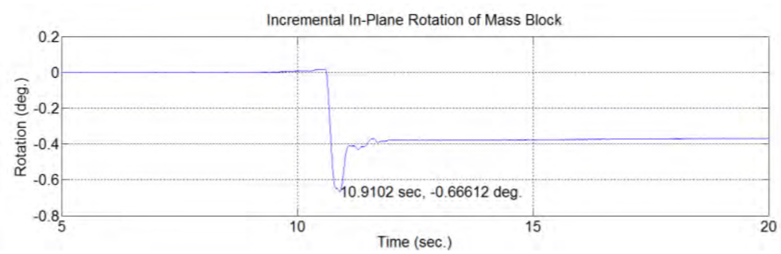
Run 5 – 200% Sylmar	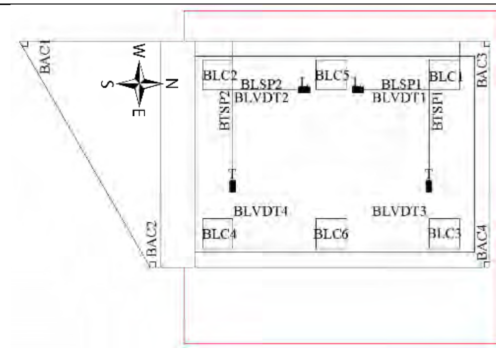
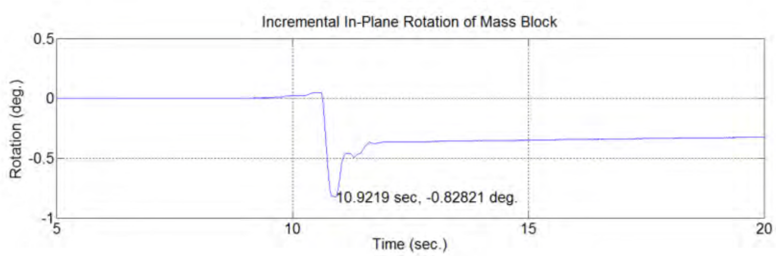	

Figure 6-36 In-plane rotation of the bridge block for the 30° skew test.

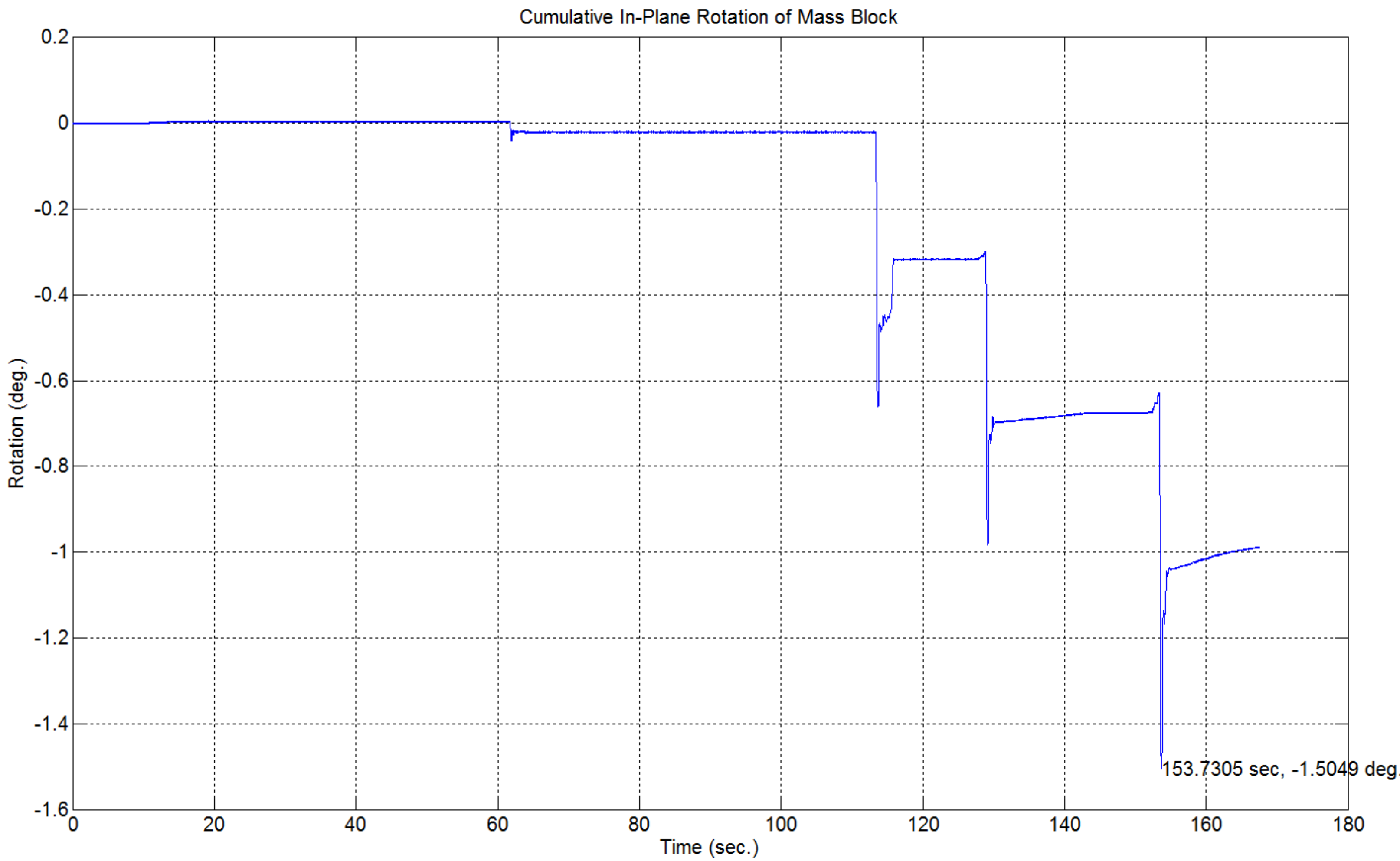

Figure 6-37 Combined in-plane rotation of the bridge block for the 30° skew test.

Run 1 – 25% Sylmar

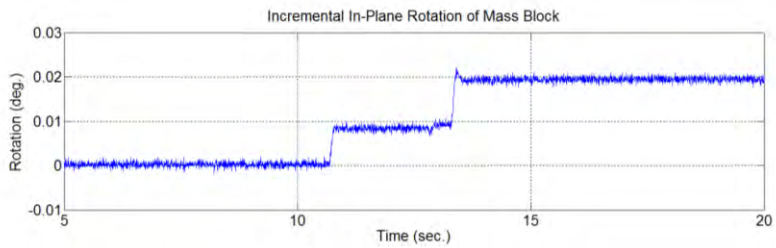

Run 2 – 50% Sylmar

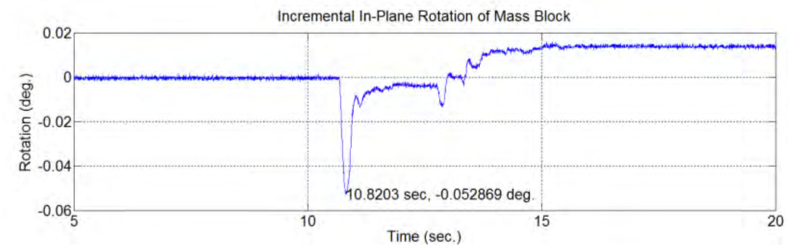

Run 3 – 125% Sylmar

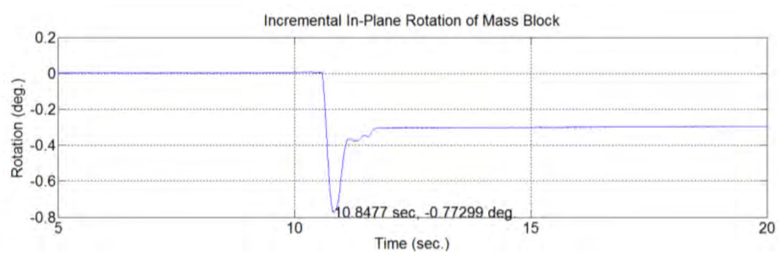

Run 4 – 150% Sylmar

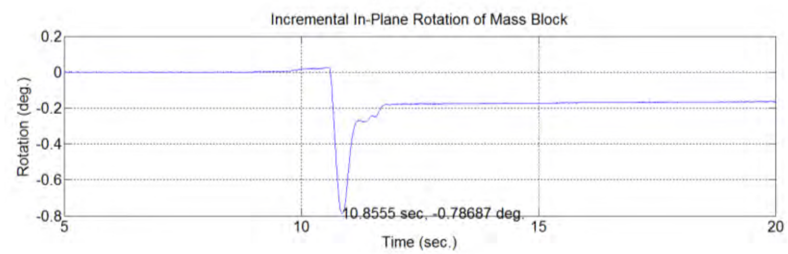

Run 5 – 200% Sylmar

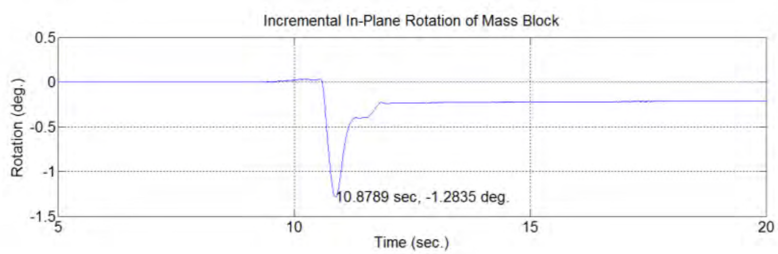

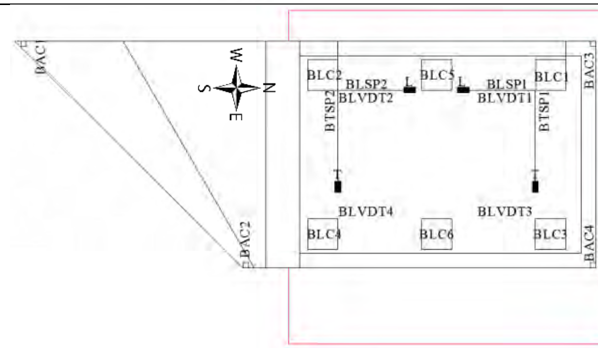

Figure 6-38 In-plane rotation of the bridge block for the 45° skew test.

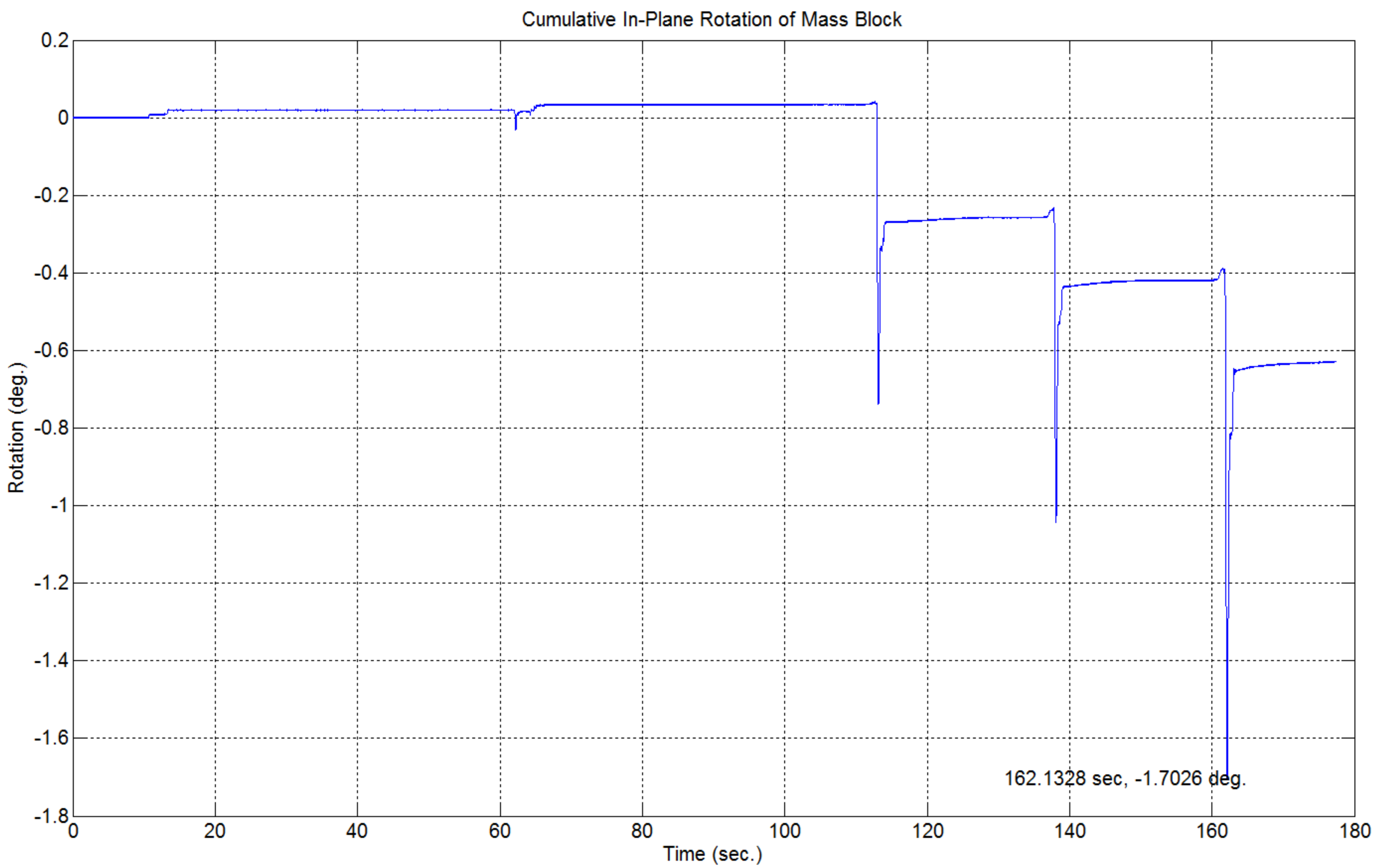

Figure 6-39 Combined in-plane rotation of the bridge block for the 45° skew test.

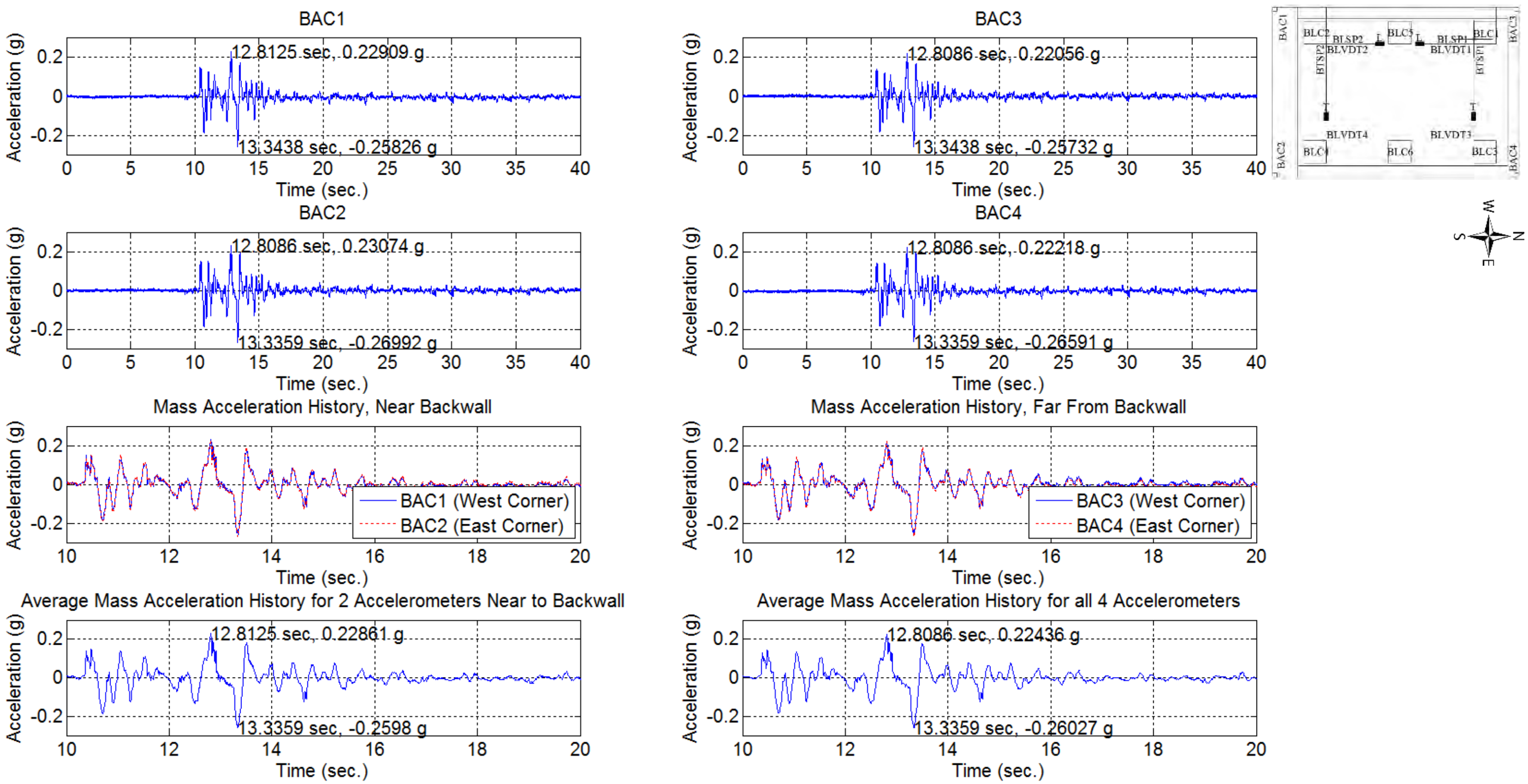

Figure 6-40 Longitudinal acceleration of the bridge block corners for the 0° skew test in Run 1.

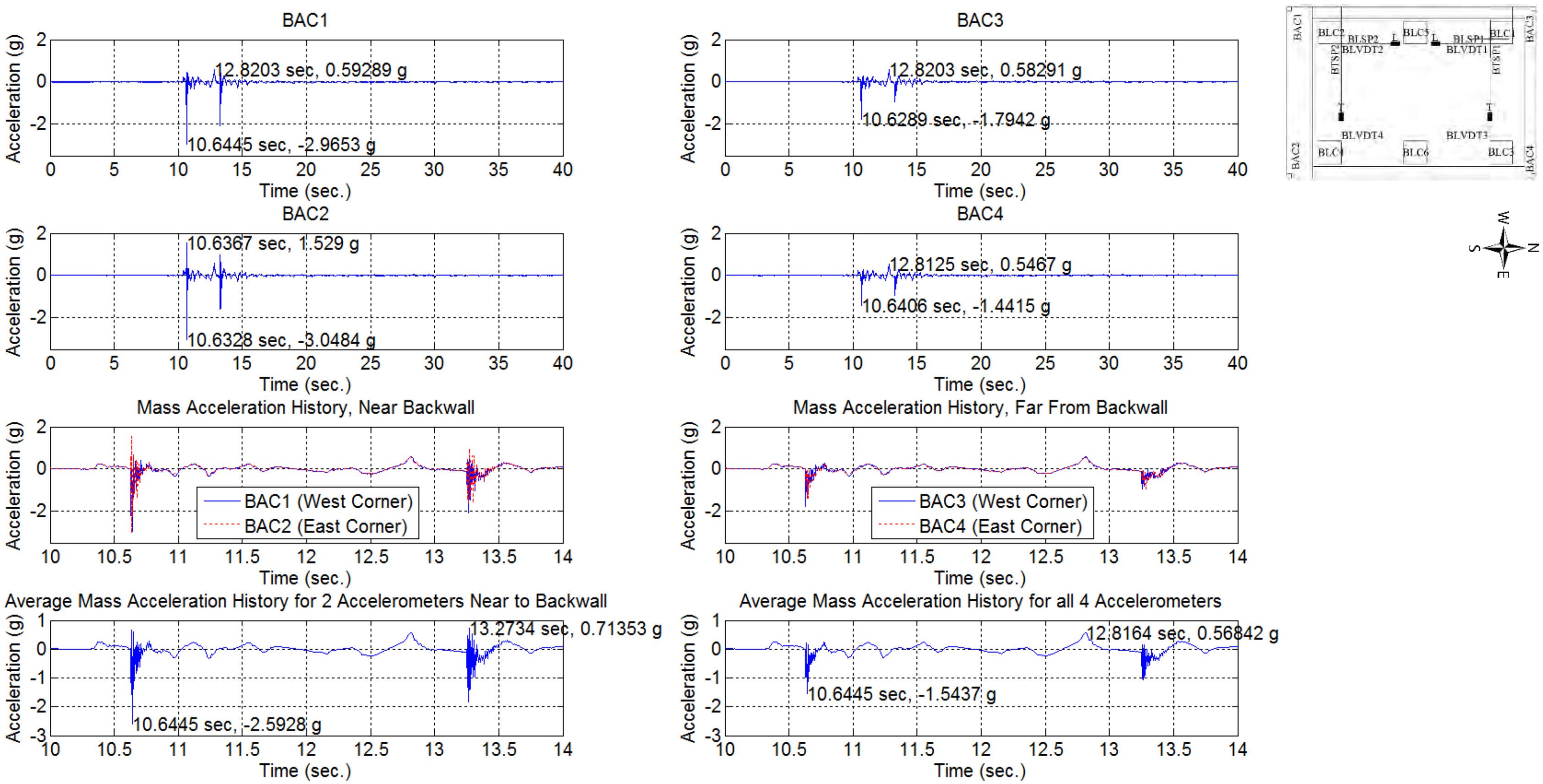

Figure 6-41 Longitudinal acceleration of the bridge block corners for the 0° skew test in Run 2.

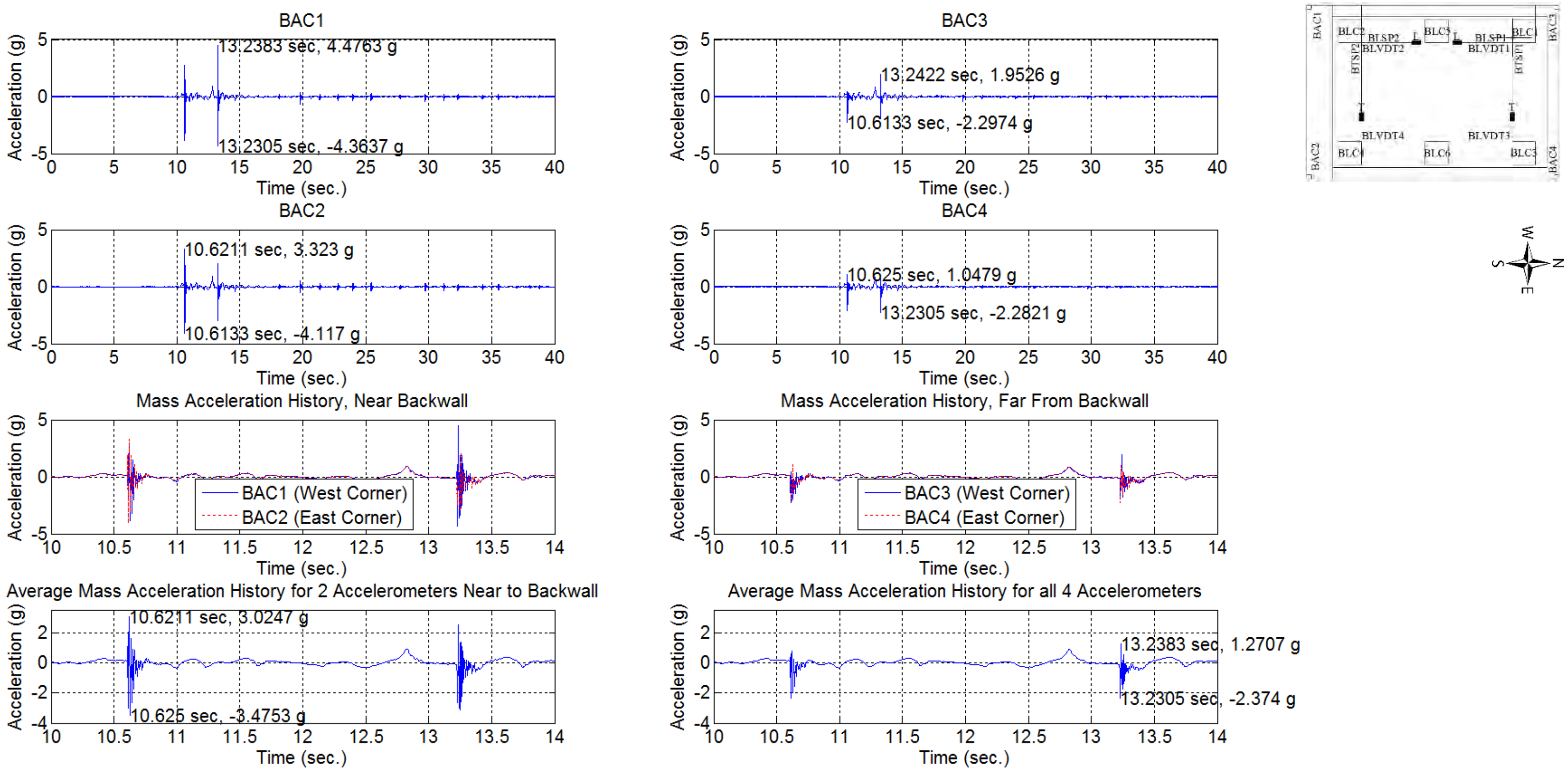

Figure 6-42 Longitudinal acceleration of the bridge block corners for the 0° skew test in Run 3.

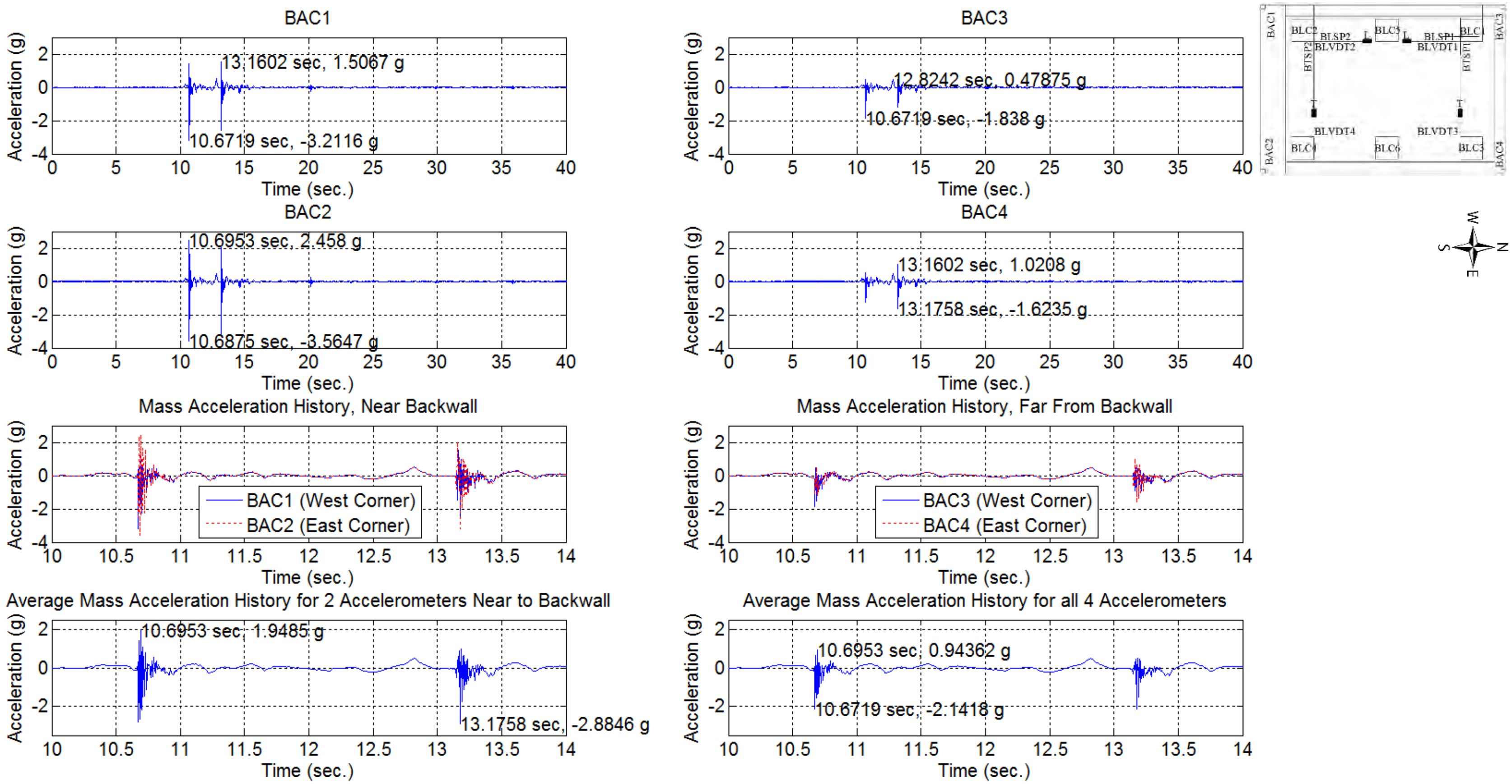

Figure 6-43 Longitudinal acceleration of the bridge block corners for the 0° skew test in Run 4.

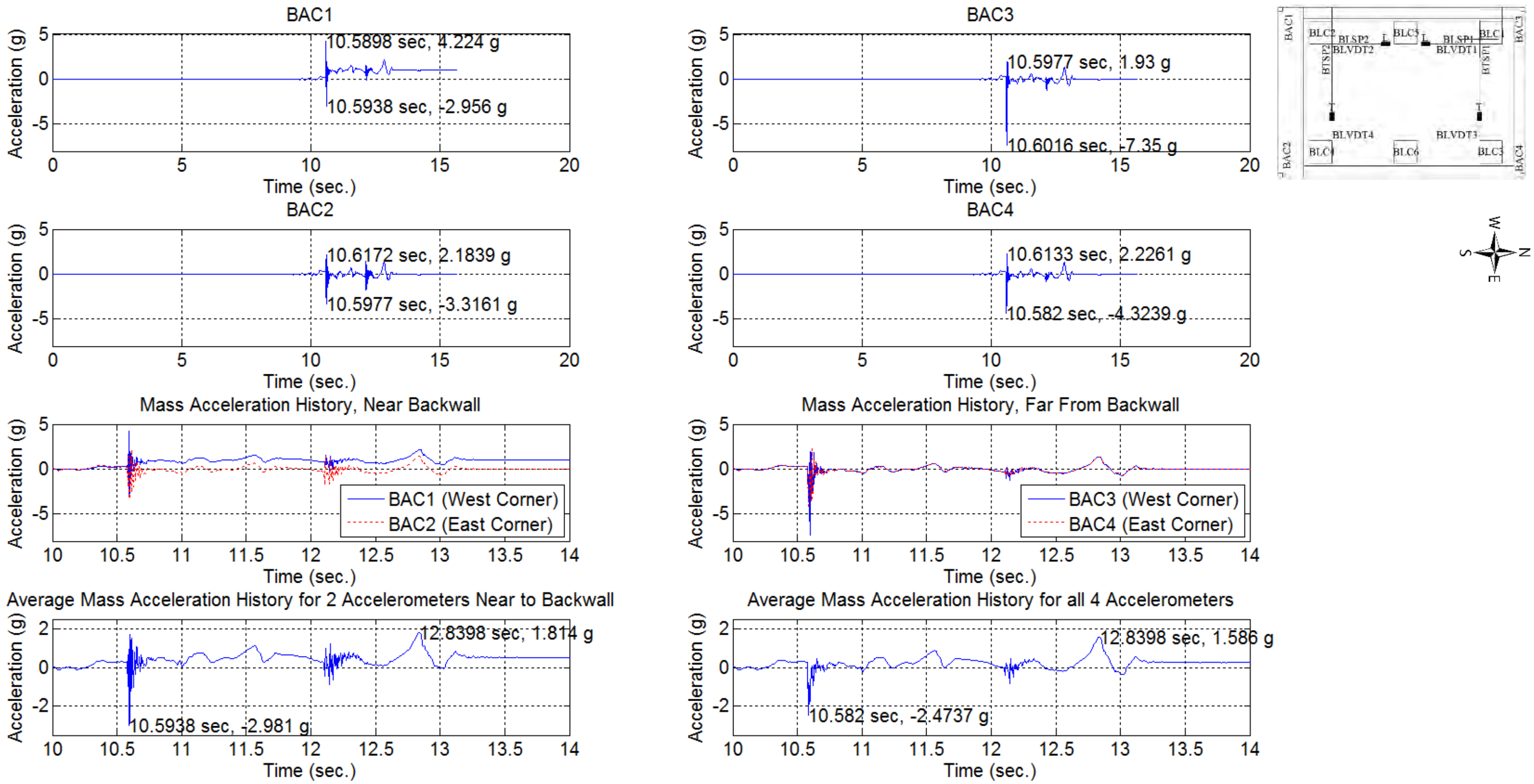

Figure 6-44 Longitudinal acceleration of the bridge block corners for the 0° skew test in Run 6.

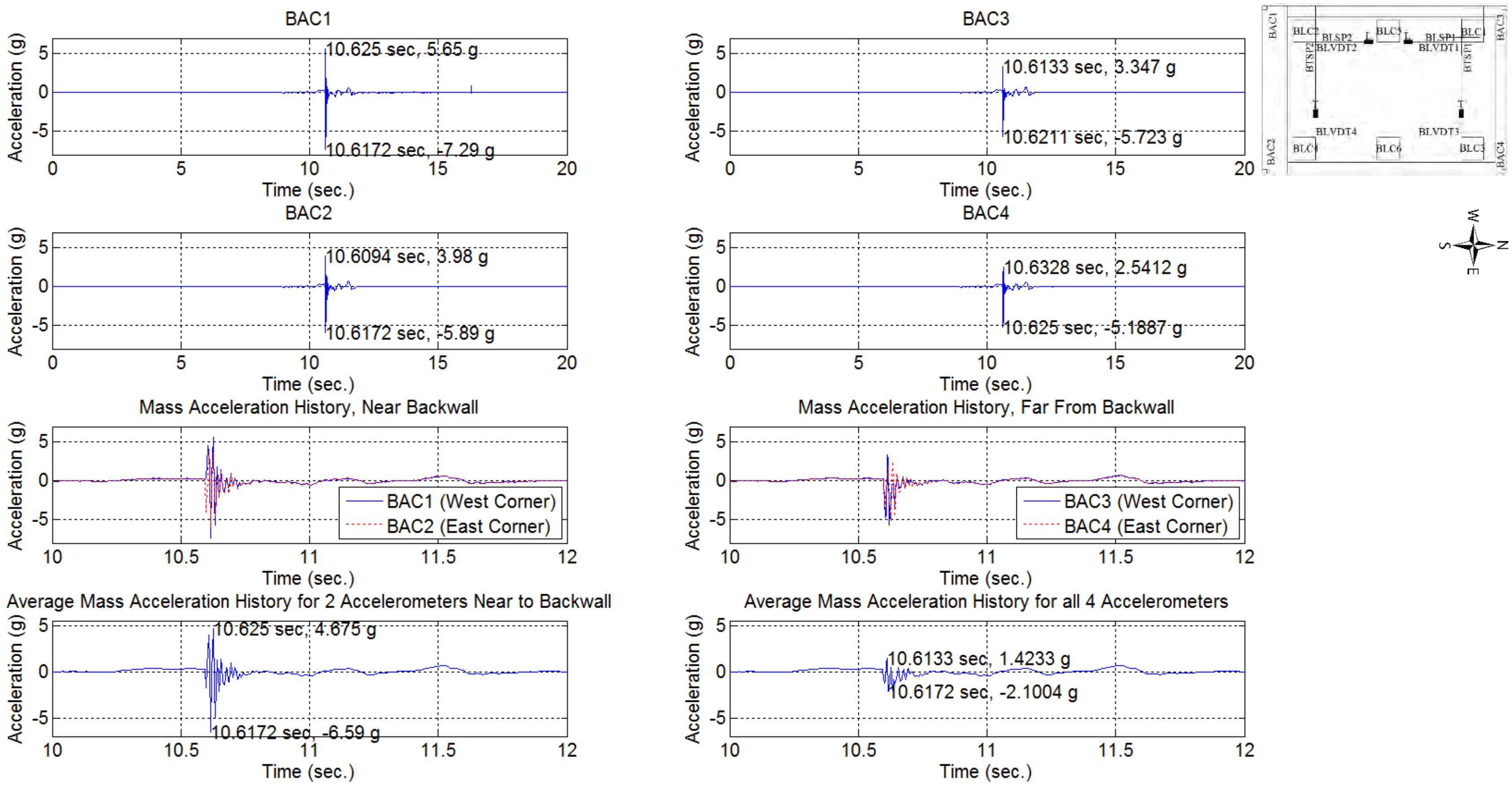

Figure 6-45 Longitudinal acceleration of the bridge block corners for the 0° skew test in Run 7.

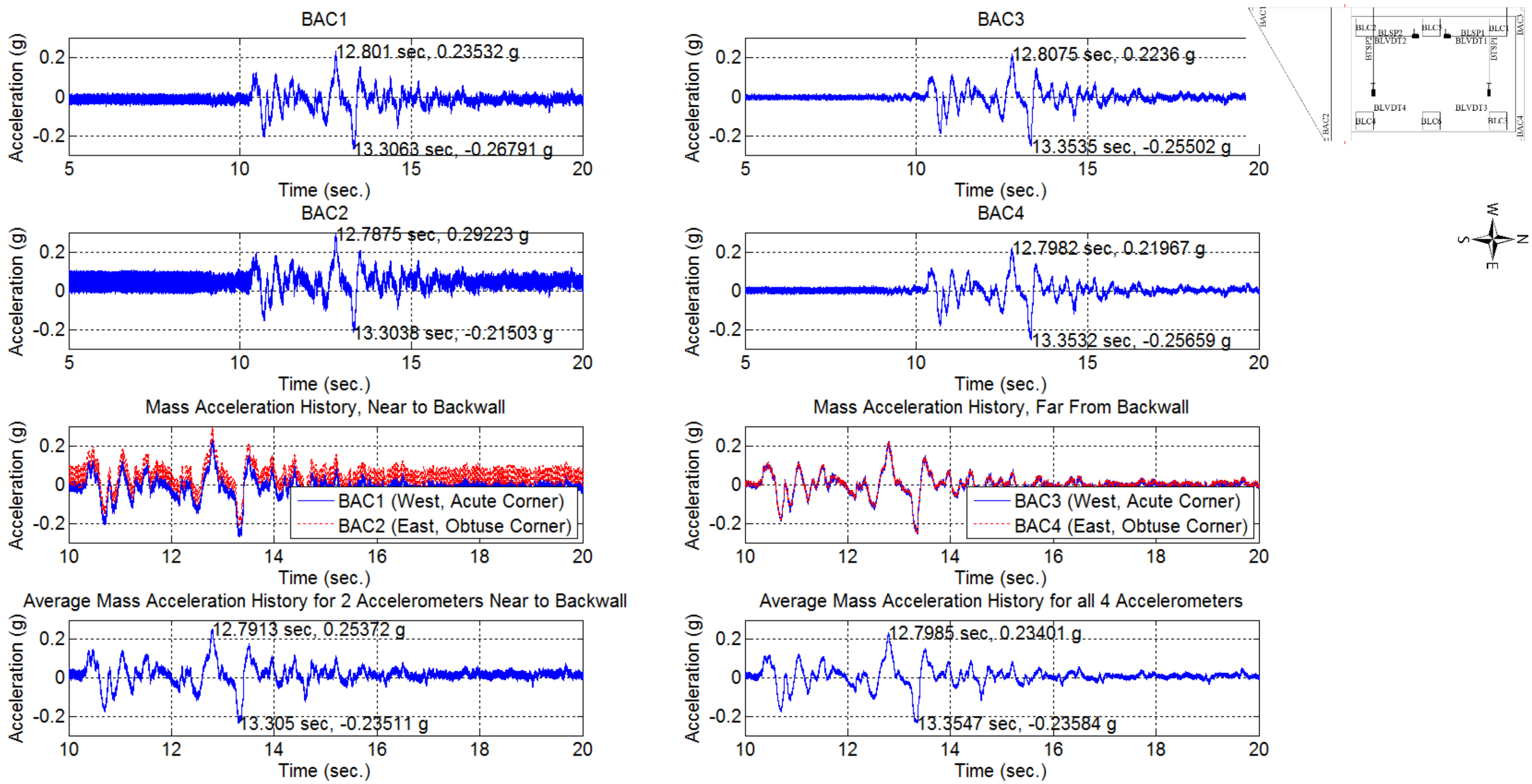

Figure 6-46 Longitudinal acceleration of the bridge block corners for the 30° skew test in Run 1.

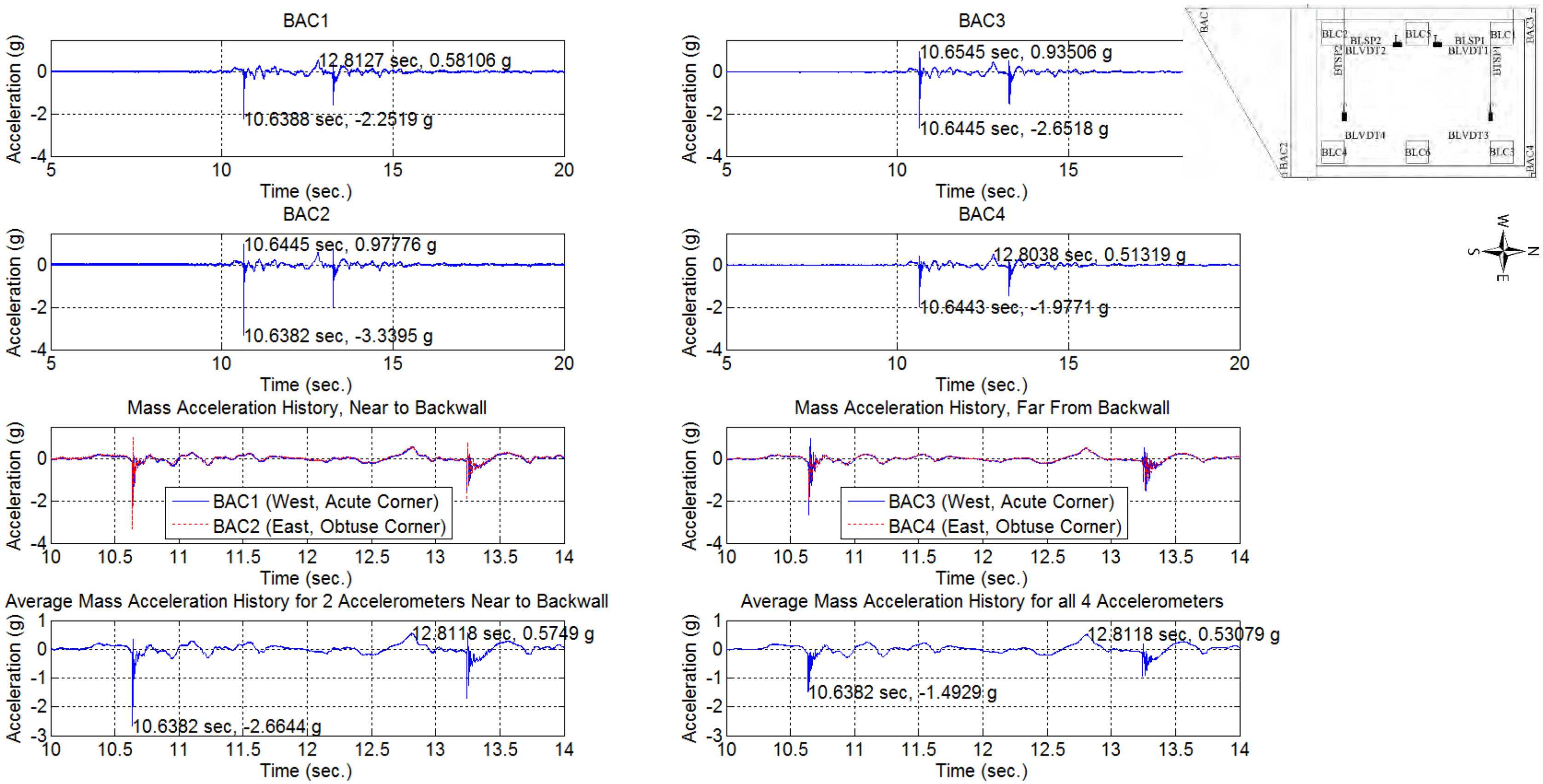

Figure 6-47 Longitudinal acceleration of the bridge block corners for the 30° skew test in Run 2.

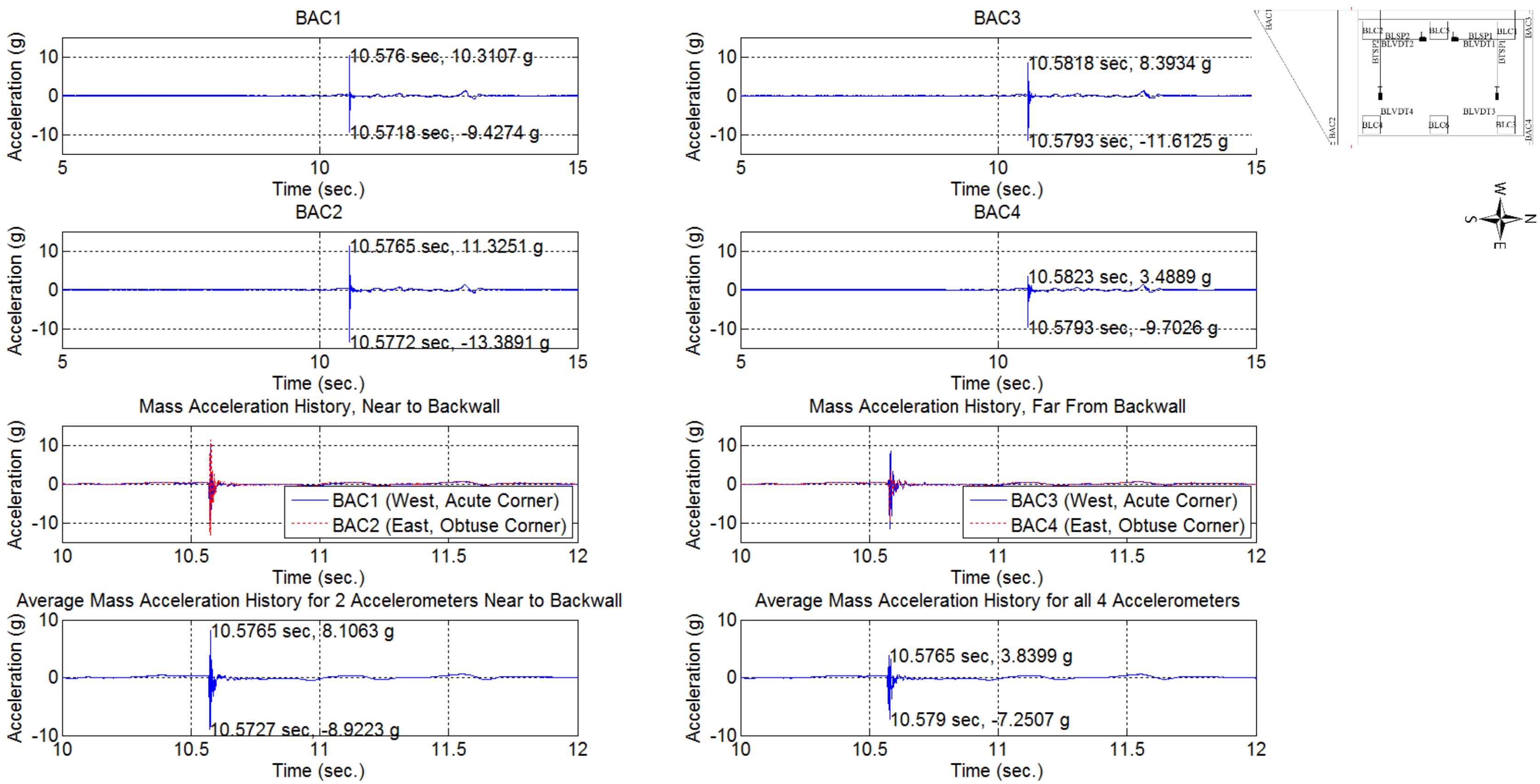

Figure 6-48 Longitudinal acceleration of the bridge block corners for the 30° skew test in Run 3.

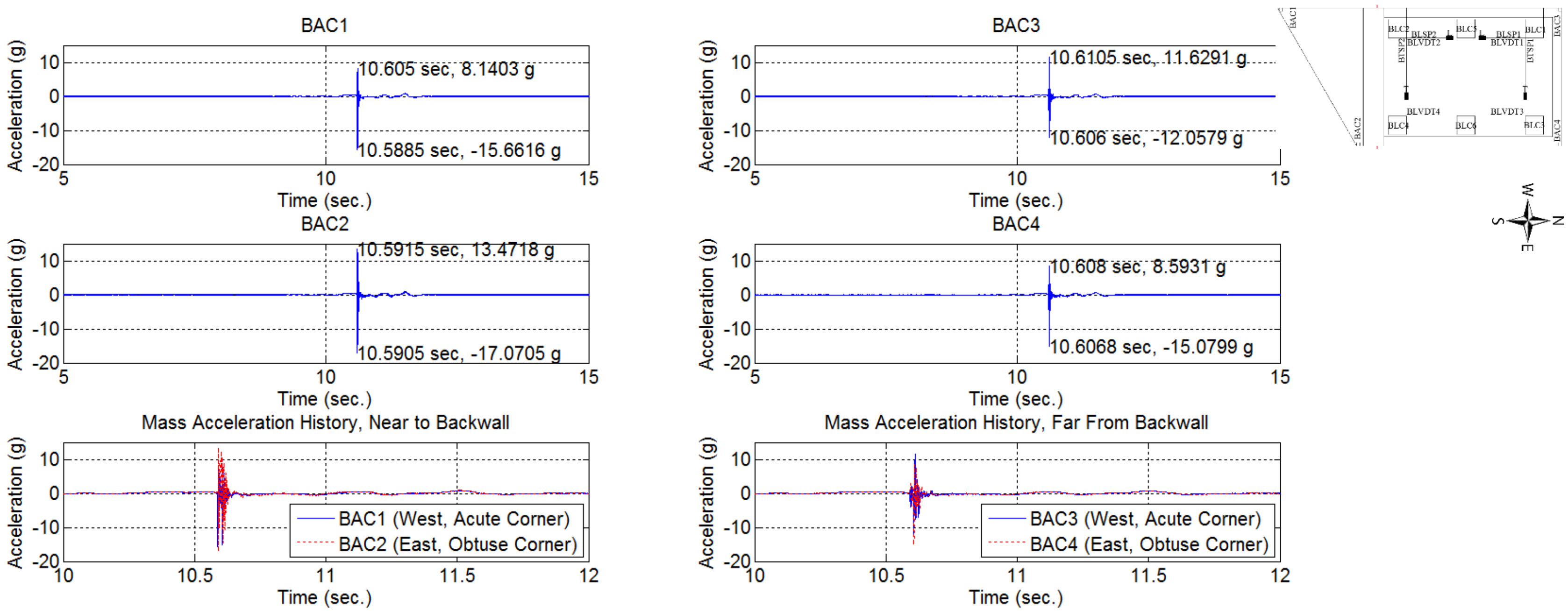

Figure 6-49 Longitudinal acceleration of the bridge block corners for the 30° skew test in Run 4.

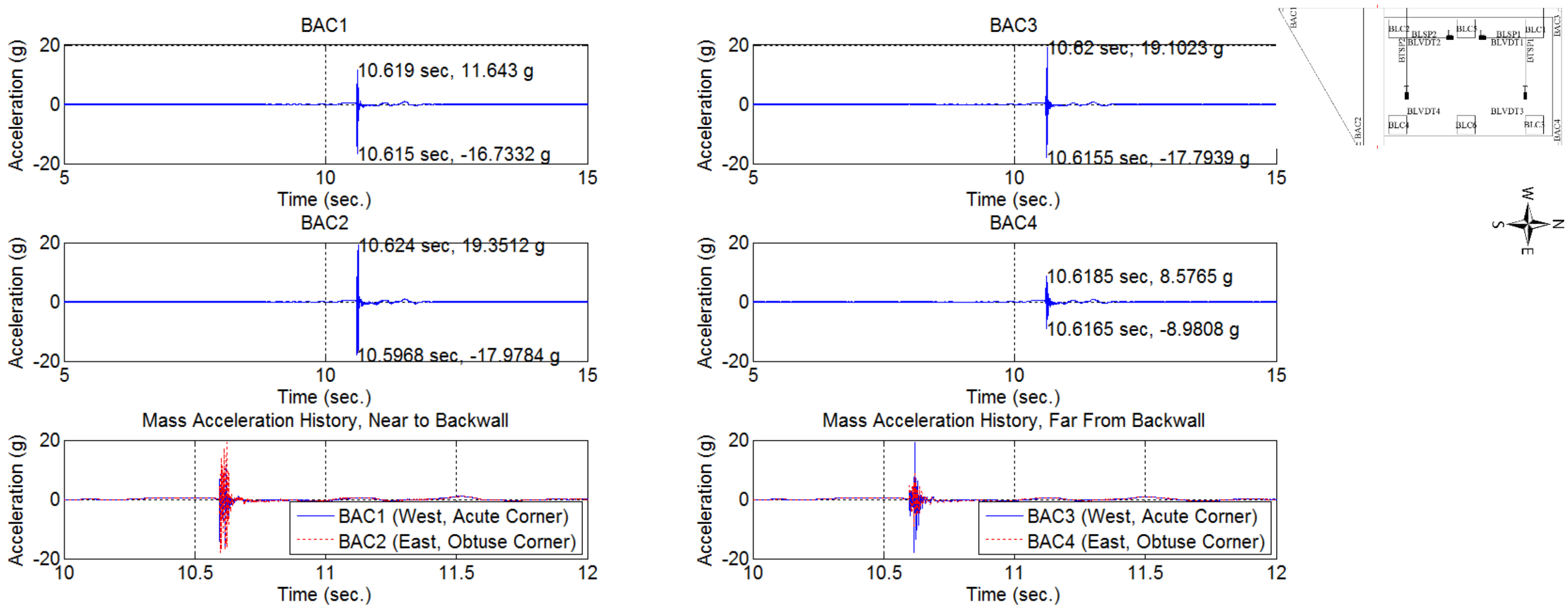

Figure 6-50 Longitudinal acceleration of the bridge block corners for the 30° skew test in Run 5.

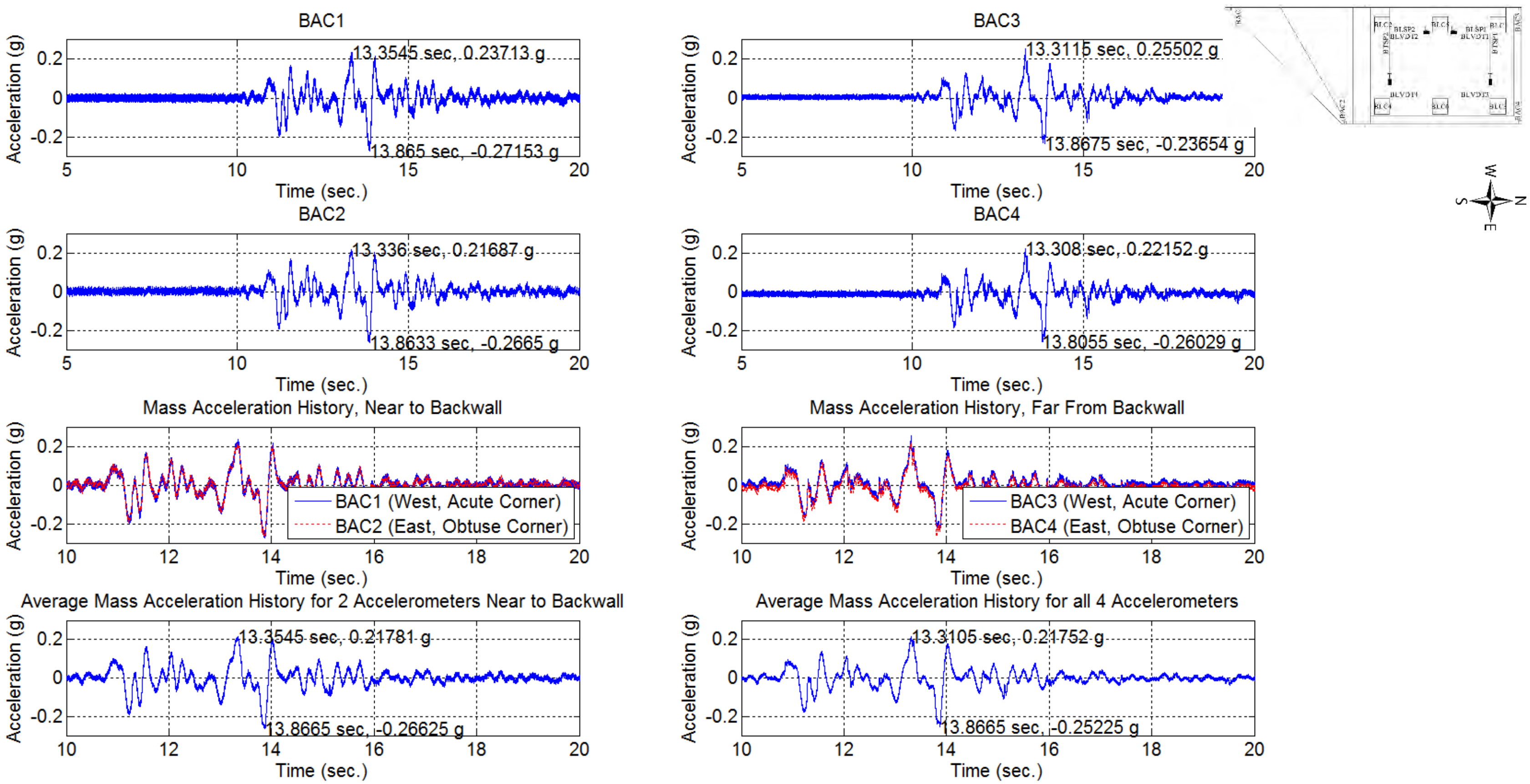

Figure 6-51 Longitudinal acceleration of the bridge block corners for the 45° skew test in Run 1.

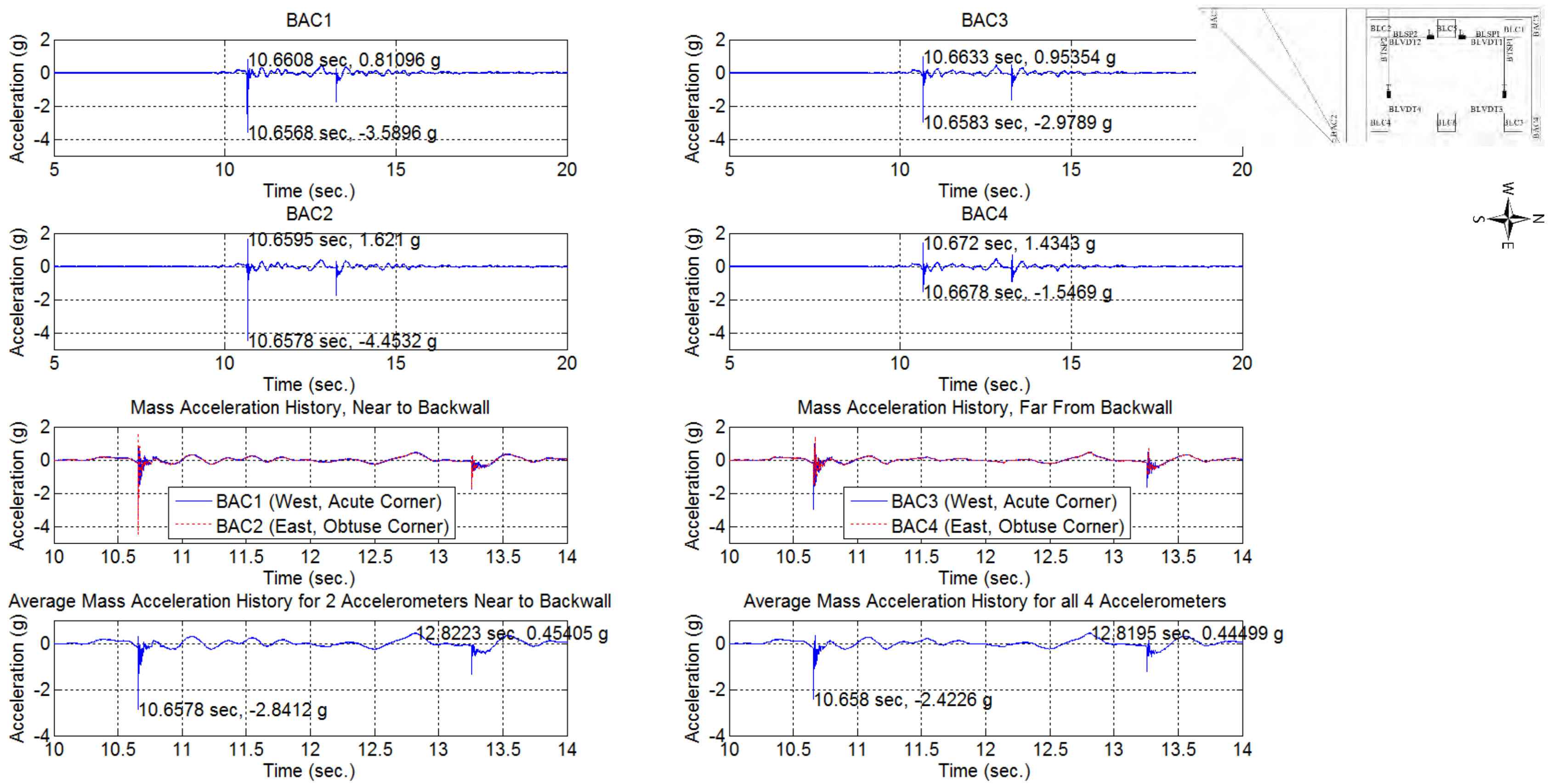

Figure 6-52 Longitudinal acceleration of the bridge block corners for the 45° skew test in Run 2.

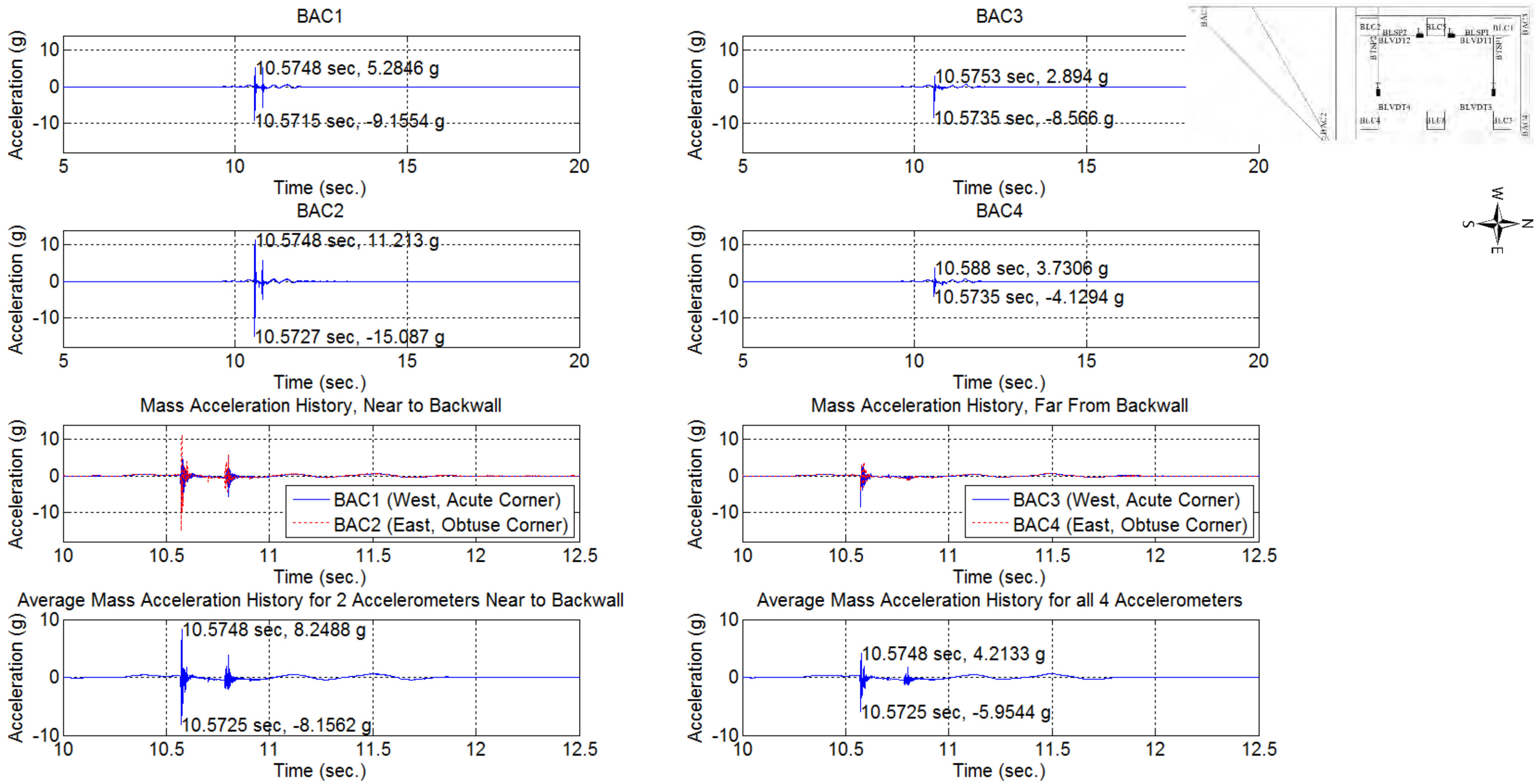

Figure 6-53 Longitudinal acceleration of the bridge block corners for the 45° skew test in Run 3.

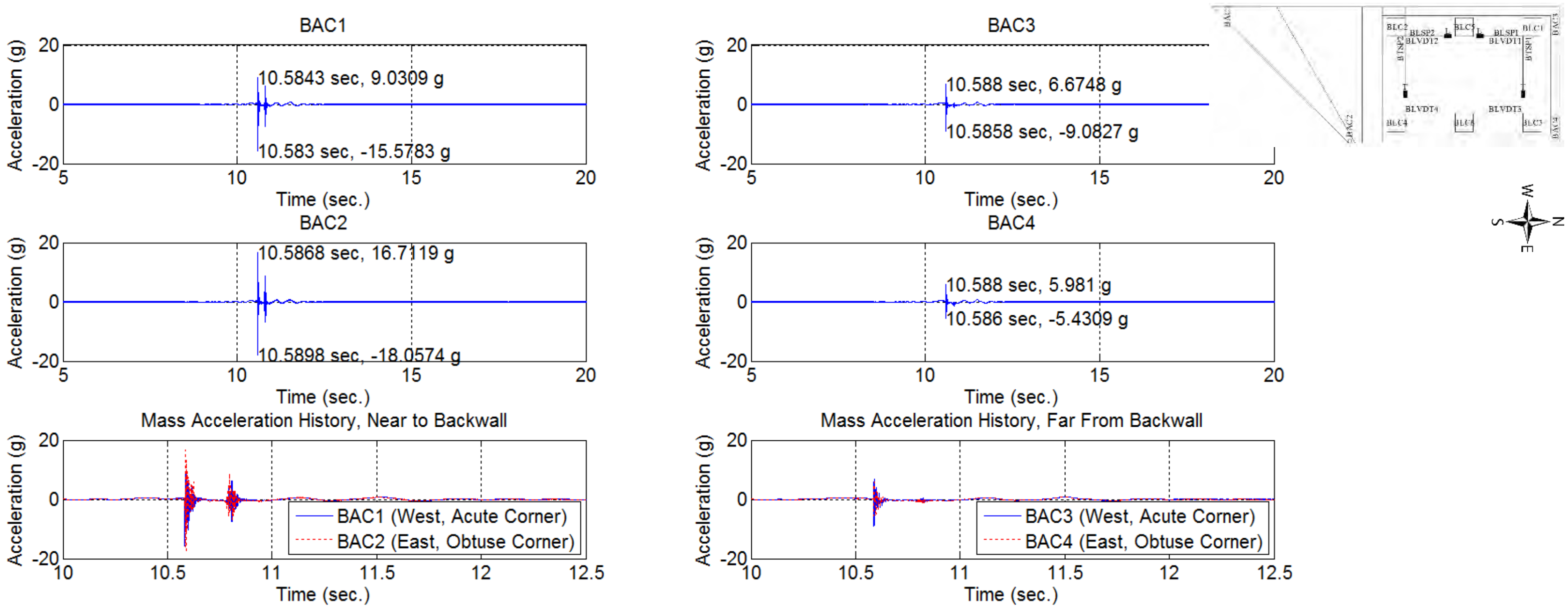

Figure 6-54 Longitudinal acceleration of the bridge block corners for the 45° skew test in Run 4.

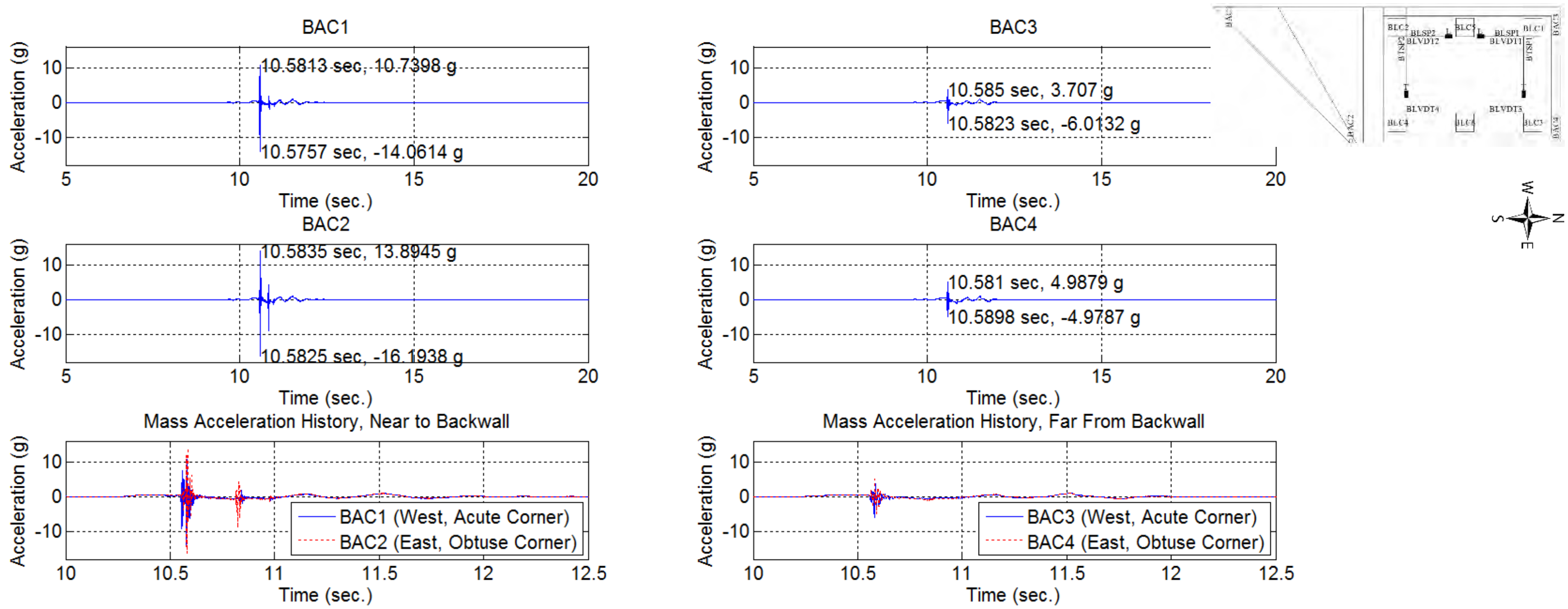

Figure 6-55 Longitudinal acceleration of the bridge block corners for the 45° skew test in Run 5.

Run 1 – 25% Sylmar

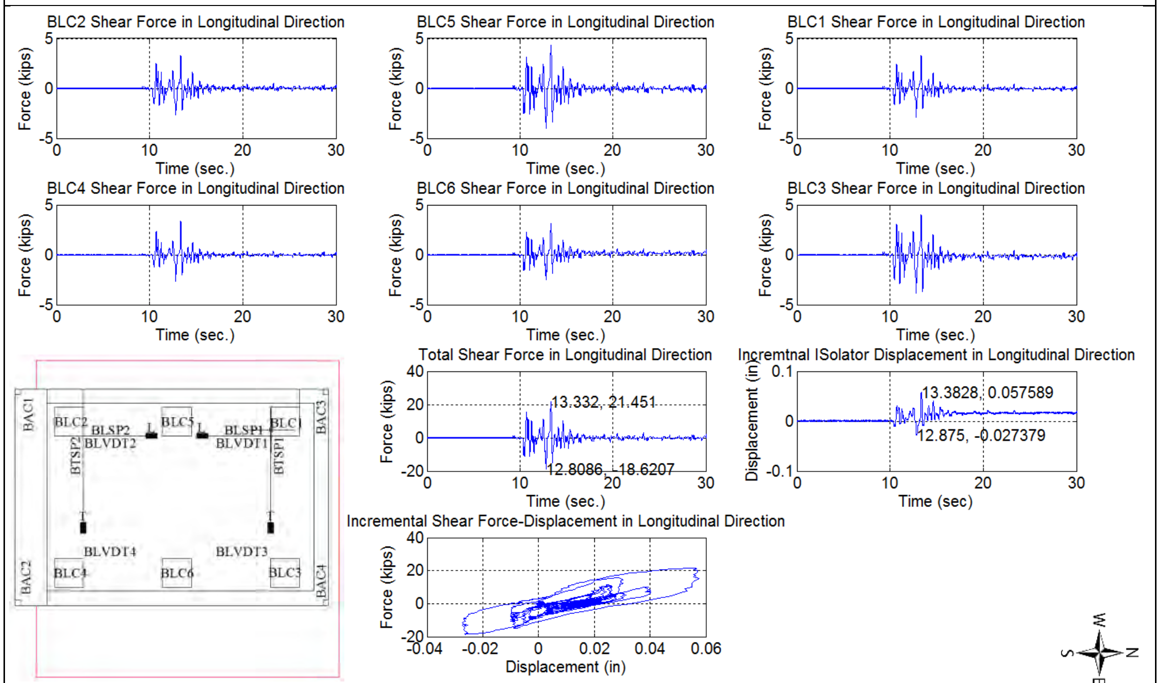

Run 2 – 50% Sylmar

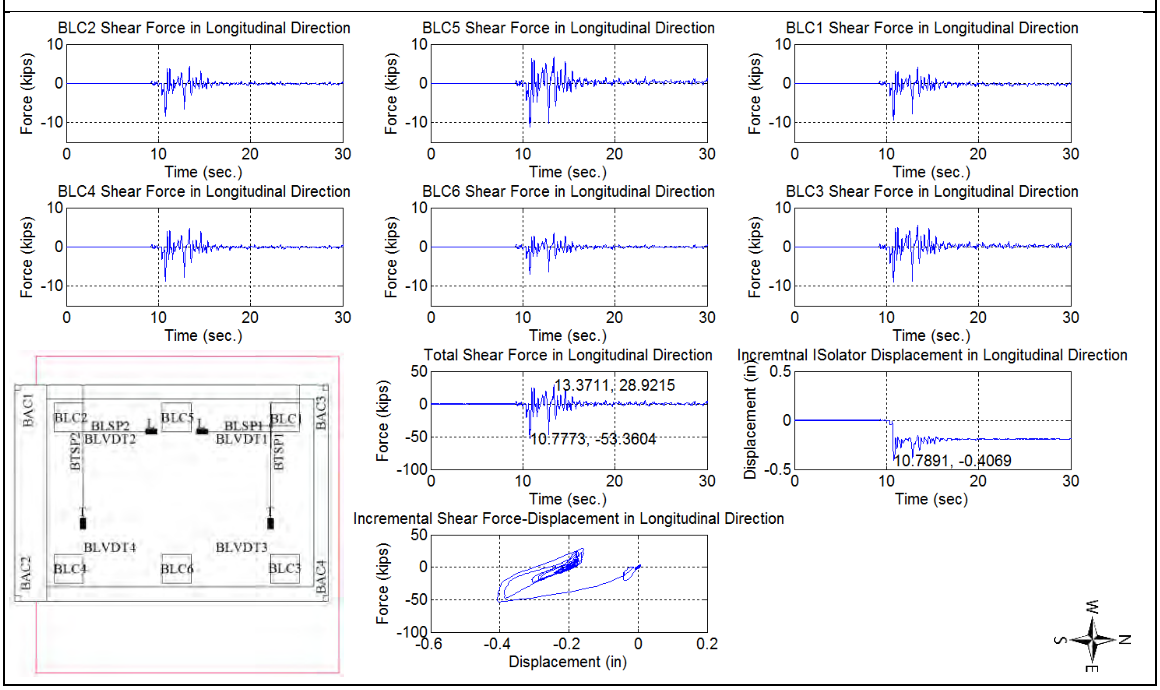

Figure 6-56 Longitudinal shear in the isolators for the 0° skew test in Run 1 and 2.

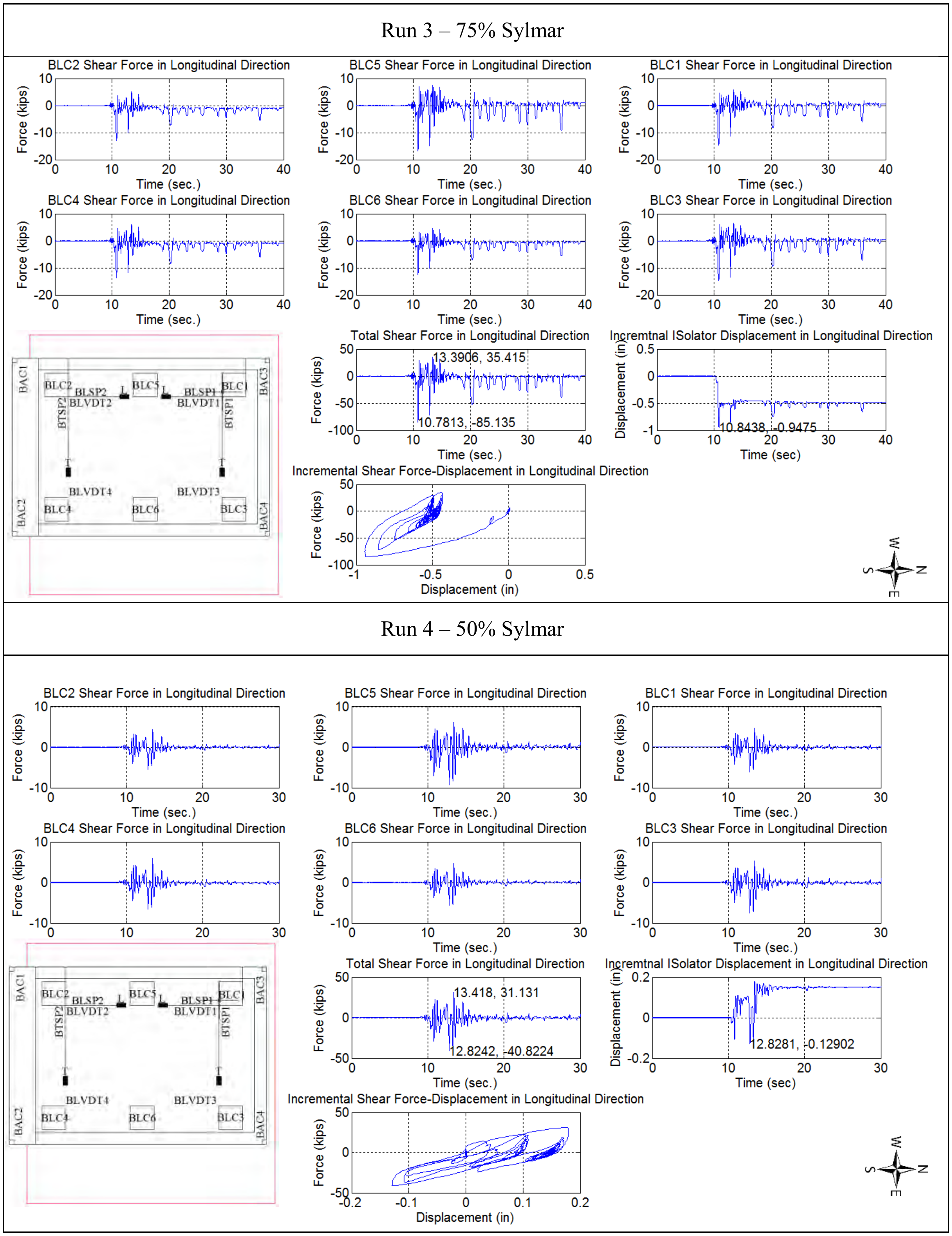

Figure 6-57 Longitudinal shear in the isolators for the 0° skew test in Run 3 and 4.

Run 6 – 150% Sylmar

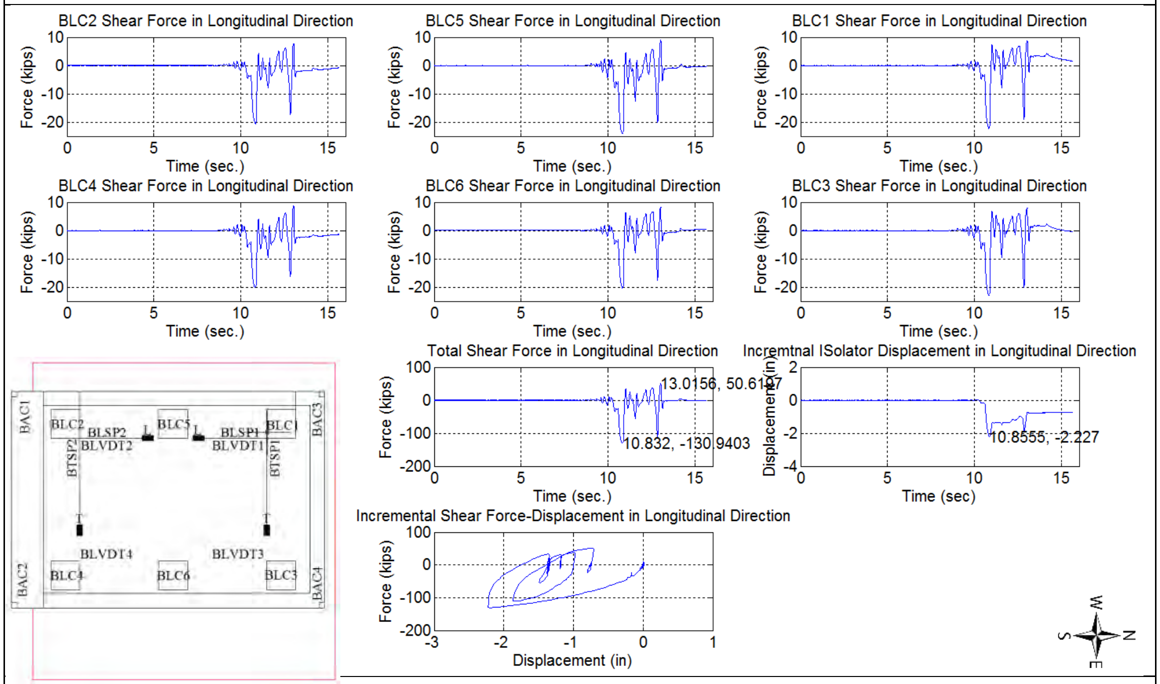

Run 7 – 150% Sylmar

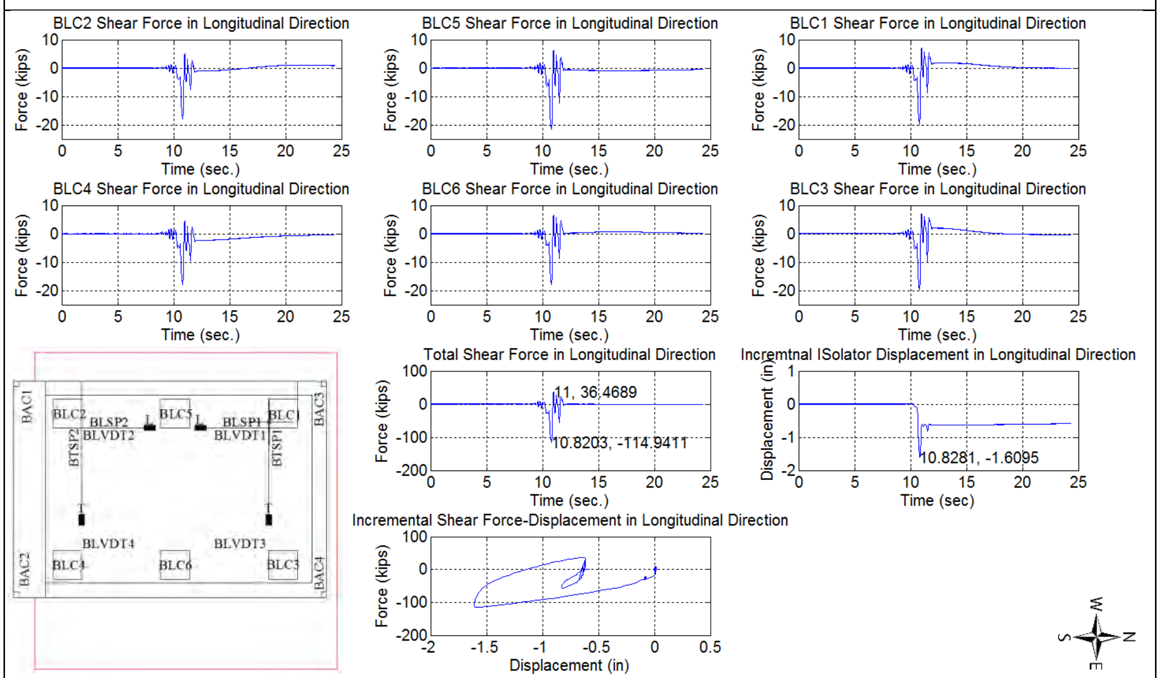

Figure 6-58 Longitudinal shear in the isolators for the 0° skew test in Run 6 and 7.

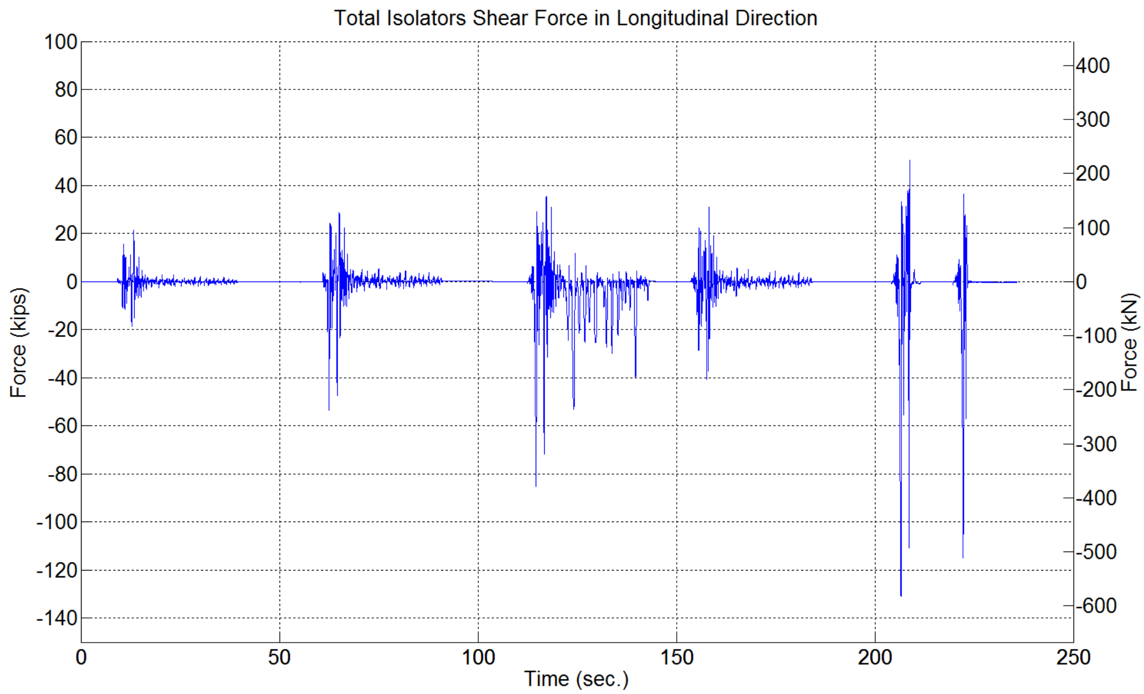

Figure 6-59 Combined longitudinal shear in the isolators for the 0° skew test.

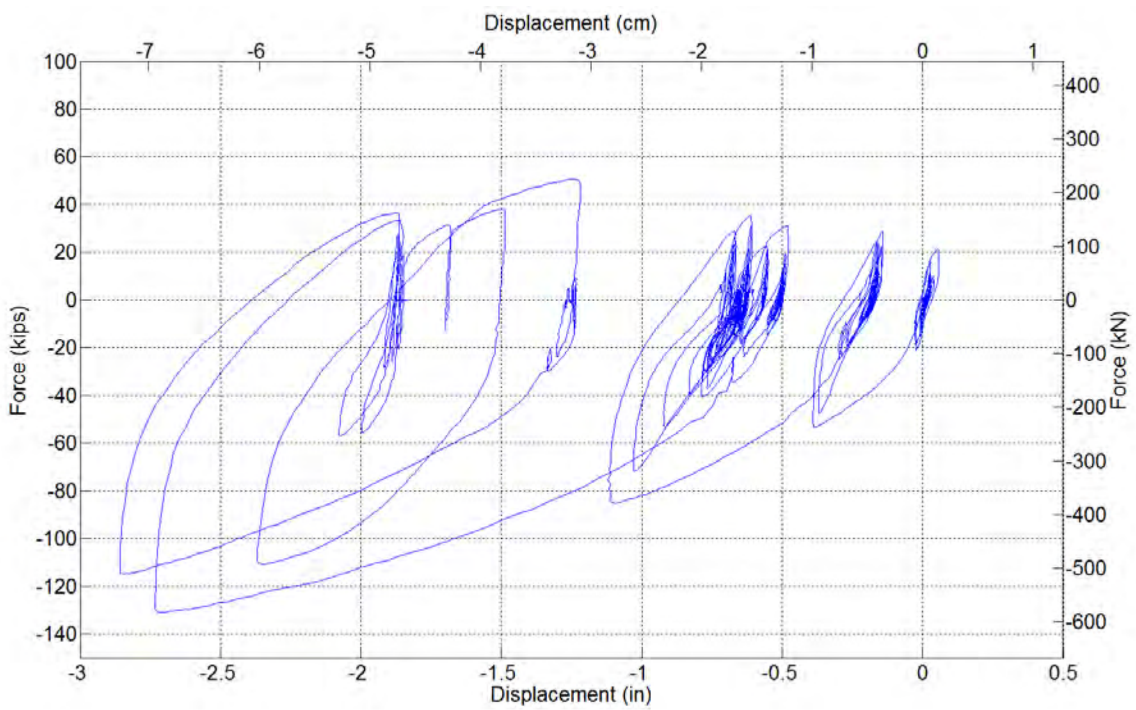

Figure 6-60 Combined longitudinal shear in the isolators versus longitudinal displacement for the 0° skew test.

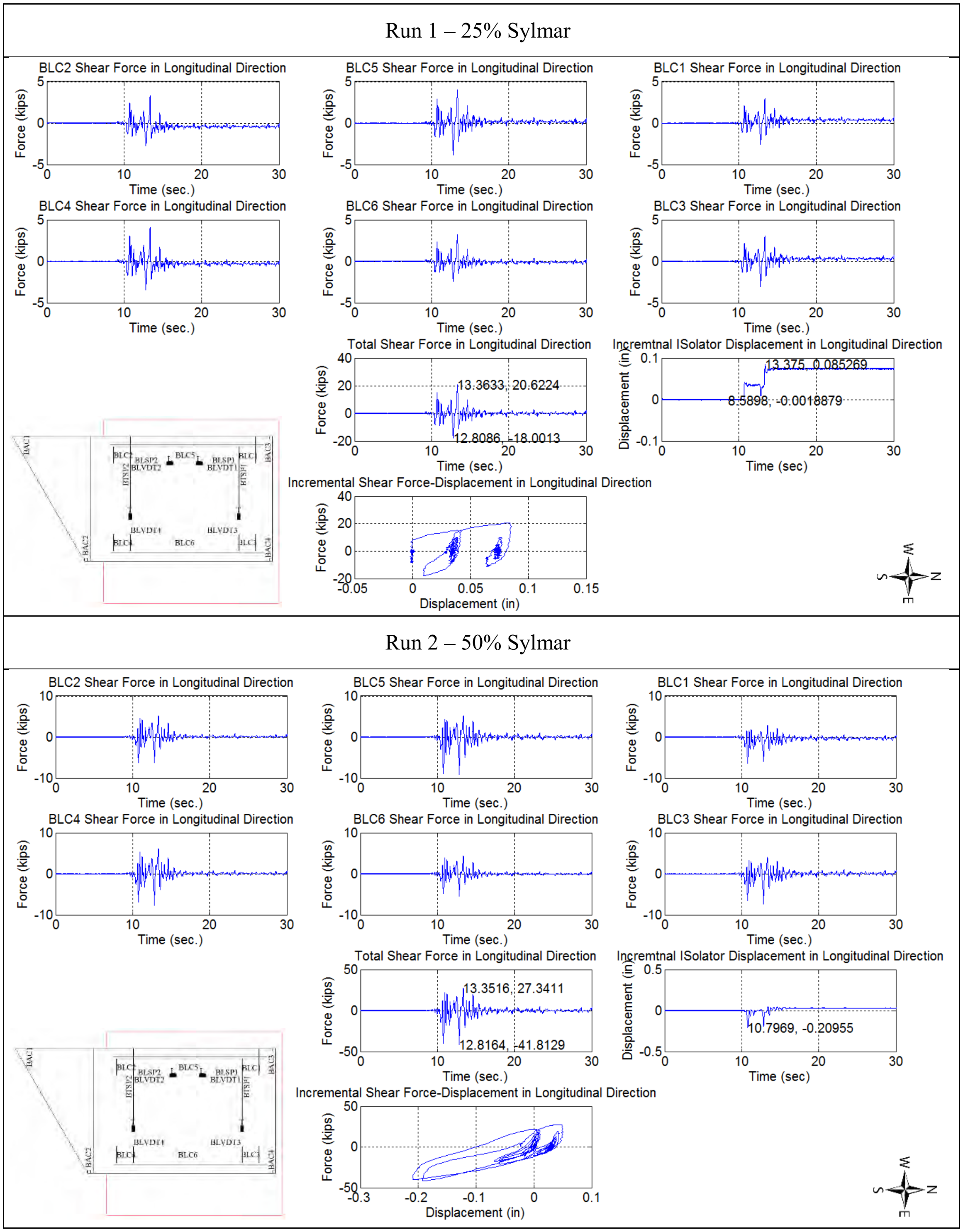

Figure 6-61 Longitudinal shear in the isolators for the 30° skew test in Run 1 and 2.

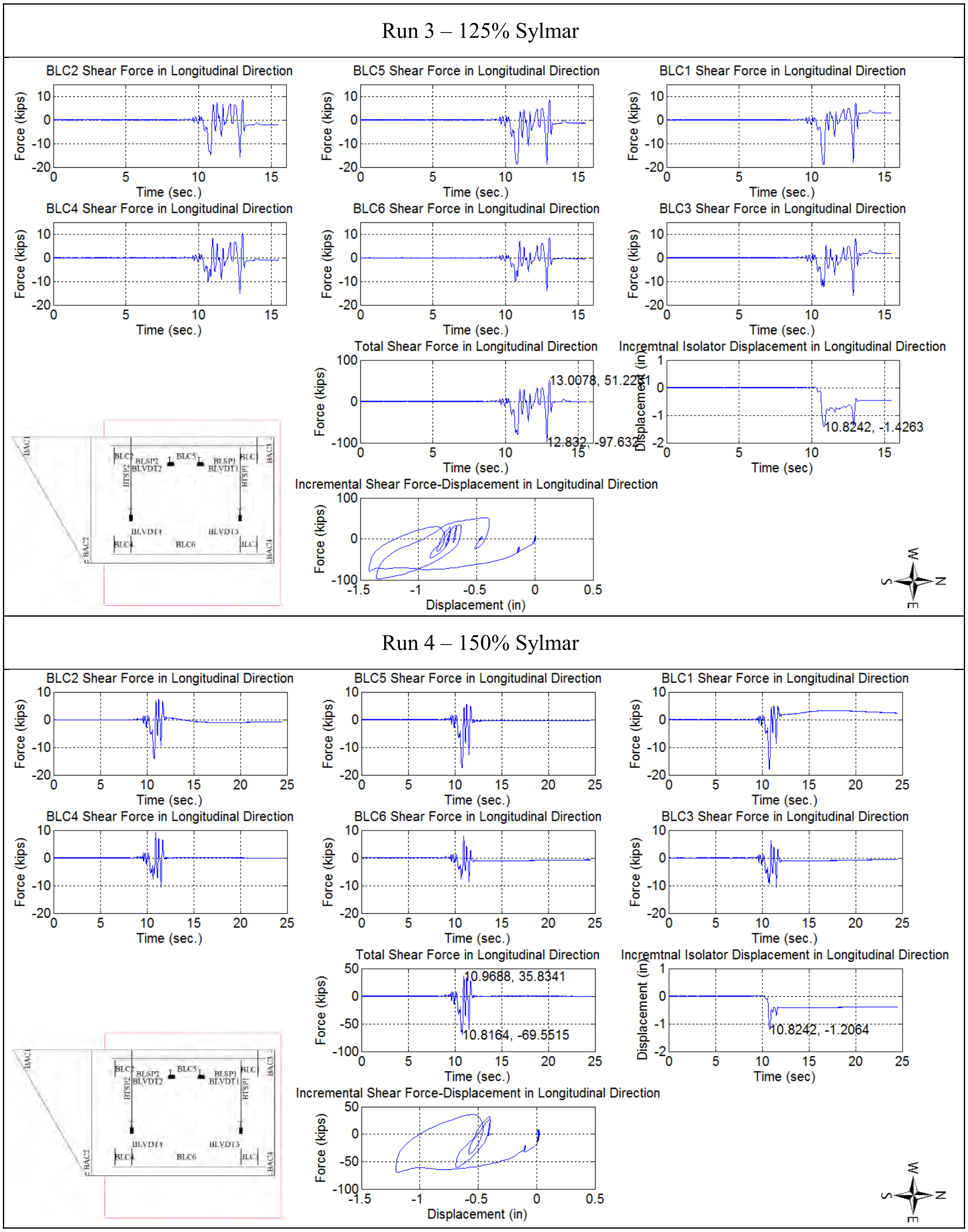

Figure 6-62 Longitudinal shear in the isolators for the 30° skew test in Run 3 and 4.

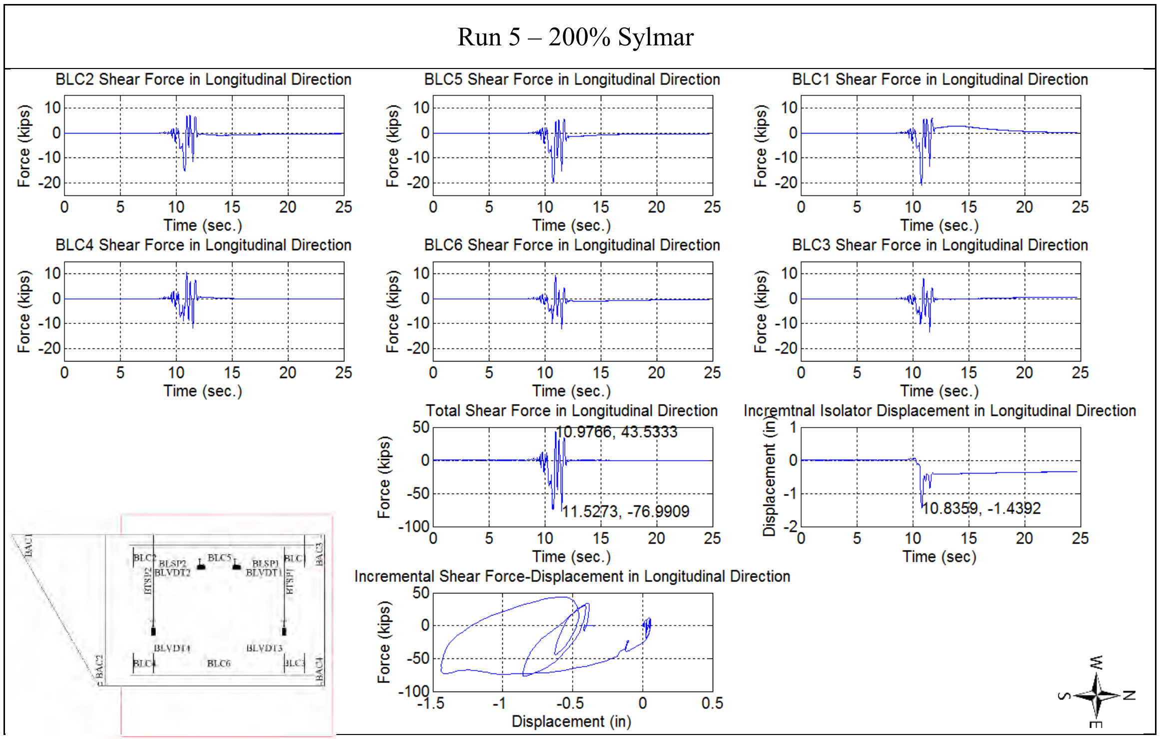

Figure 6-63 Longitudinal shear in the isolators for the 30° skew test in Run 5.

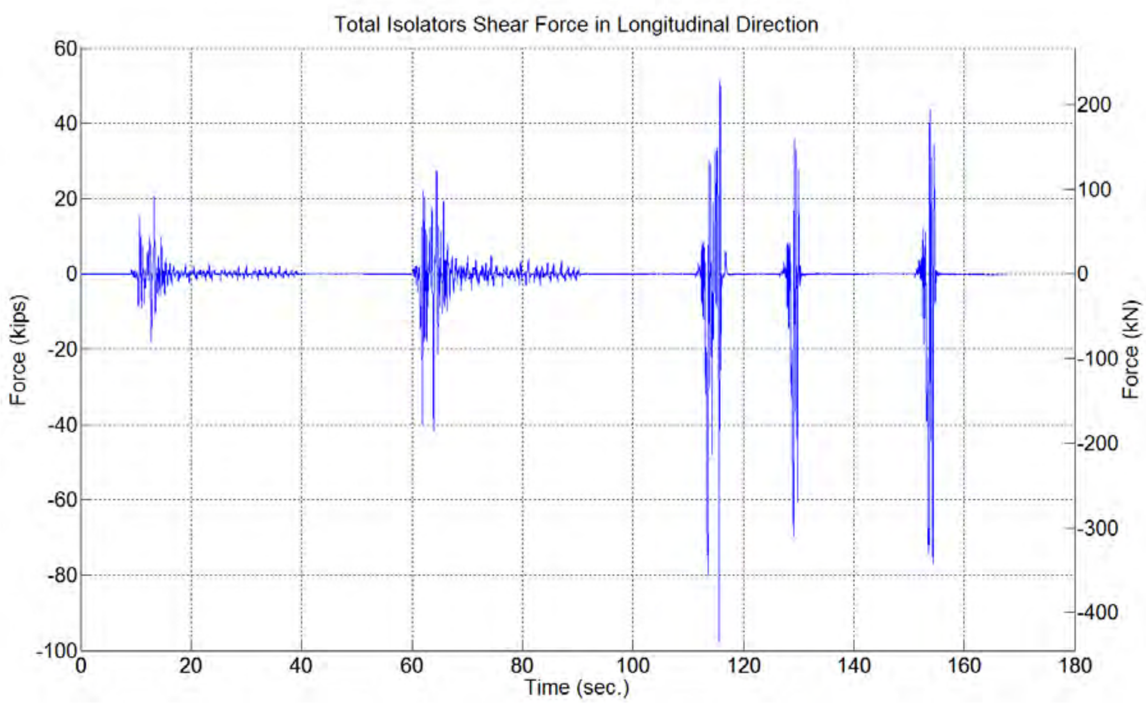

Figure 6-64 Combined longitudinal shear in the isolators for the 30° skew test.

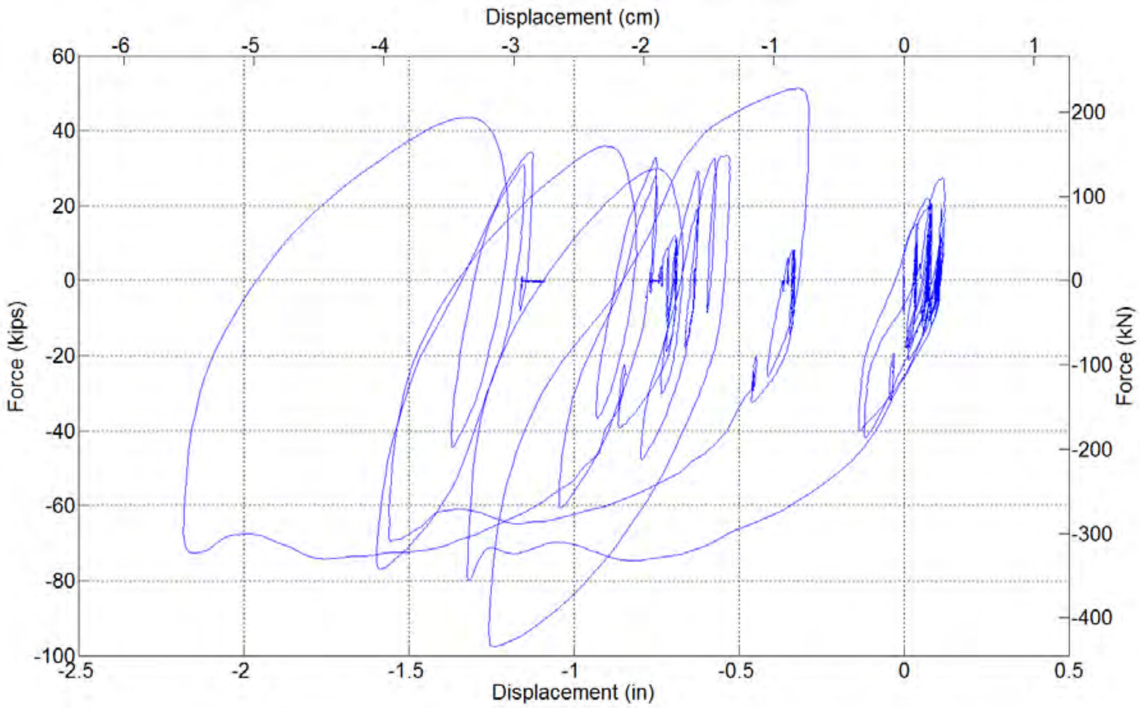

Figure 6-65 Combined longitudinal shear in the isolators versus longitudinal displacement for the 30° skew test.

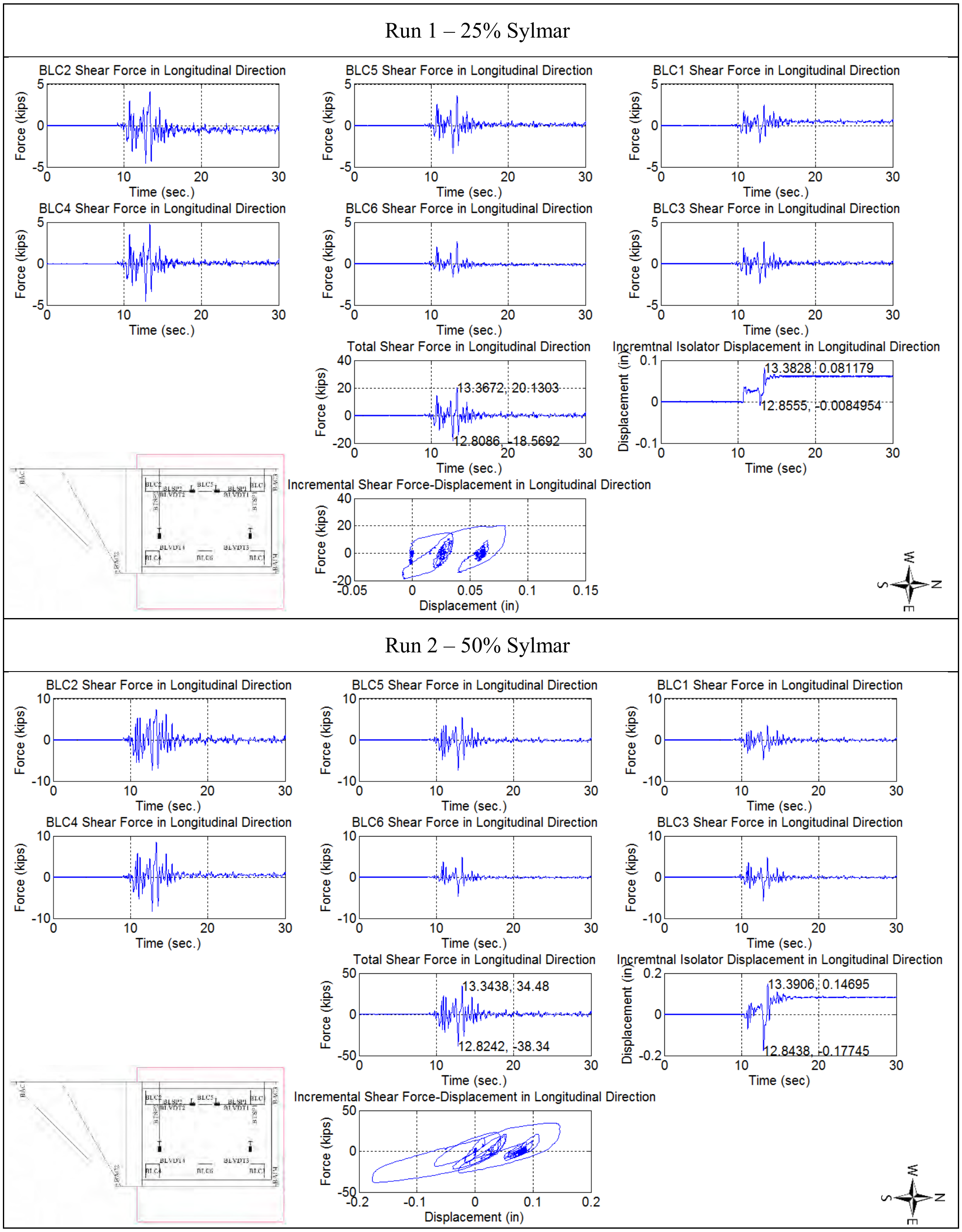

Figure 6-66 Longitudinal shear in the isolators for the 45° skew test in Run 1 and 2.

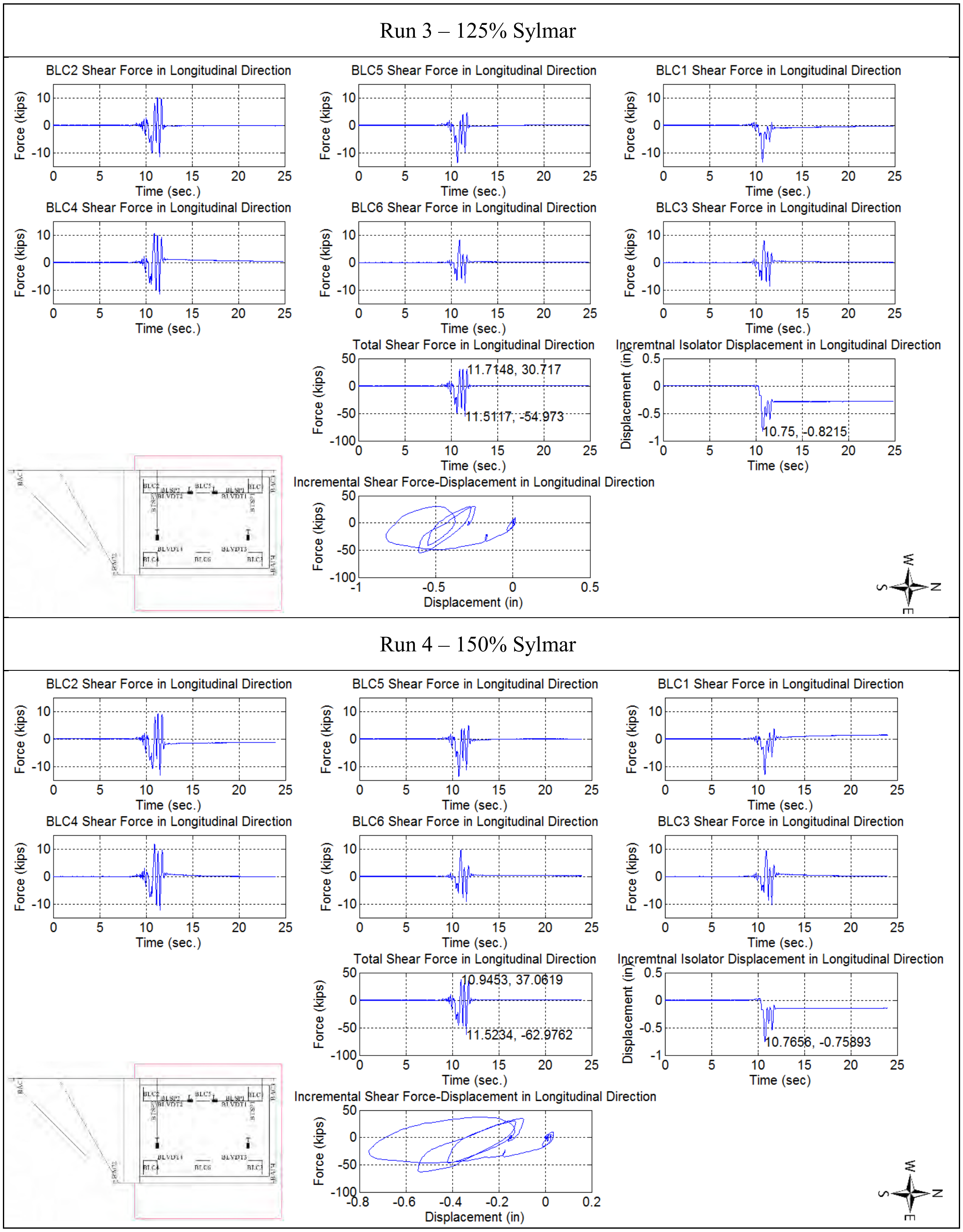

Figure 6-67 Longitudinal shear in the isolators for the 45° skew test in Run 3 and 4.

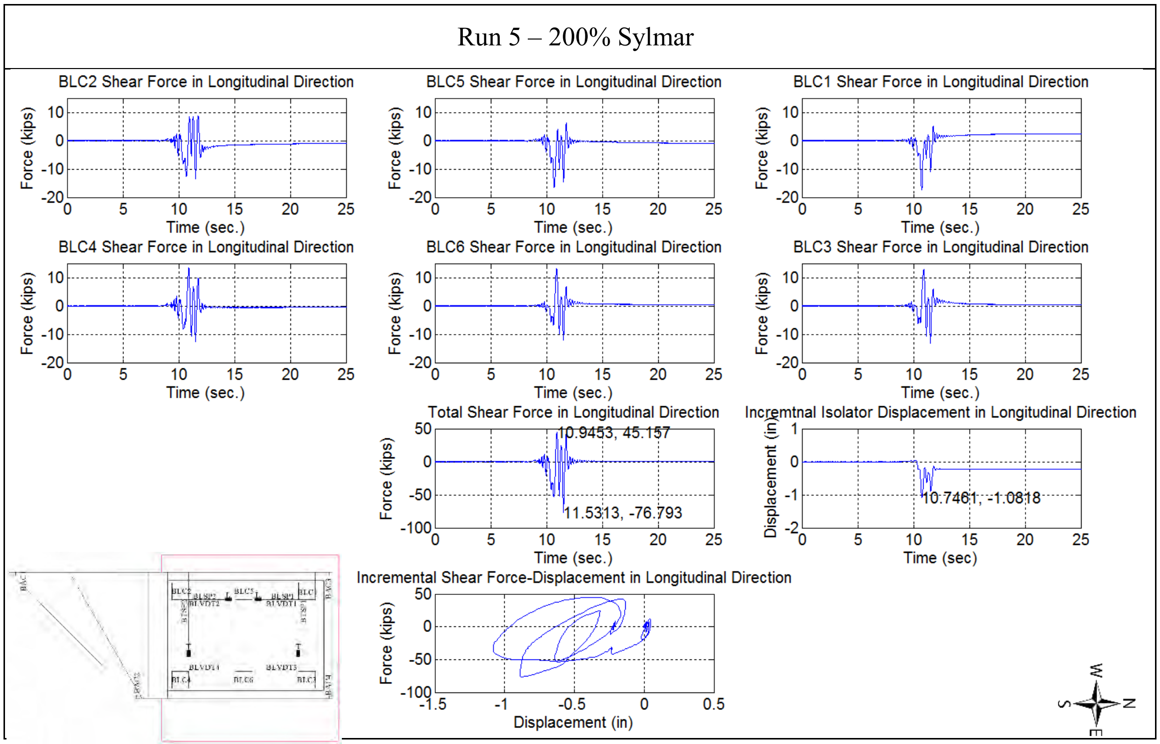

Figure 6-68 Longitudinal shear in the isolators for the 45° skew test in Run 5.

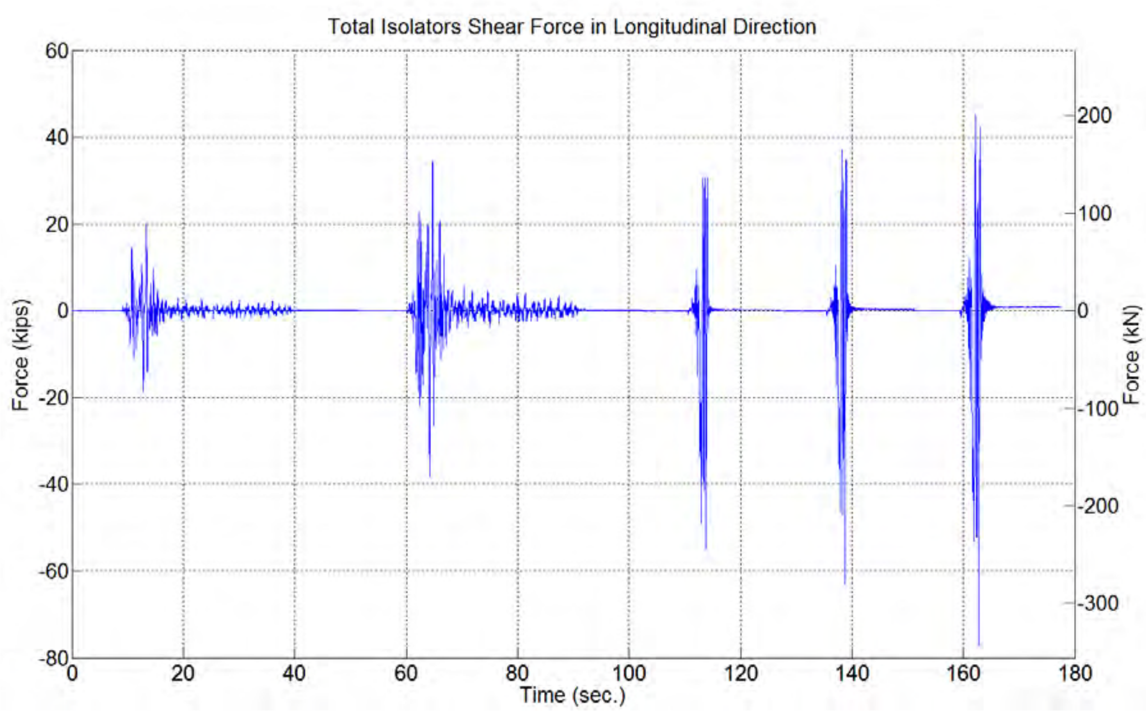

Figure 6-69 Combined longitudinal shear in the isolators for the 45° skew test.

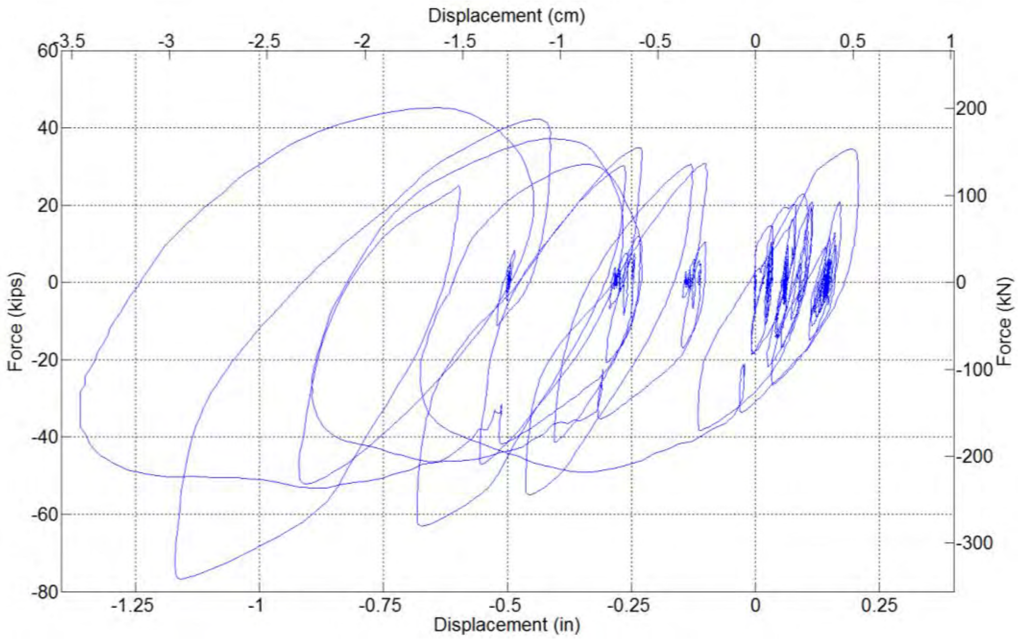

Figure 6-70 Combined longitudinal shear in the isolators versus longitudinal displacement for the 45° skew test.

Run 2 – 50% Sylmar

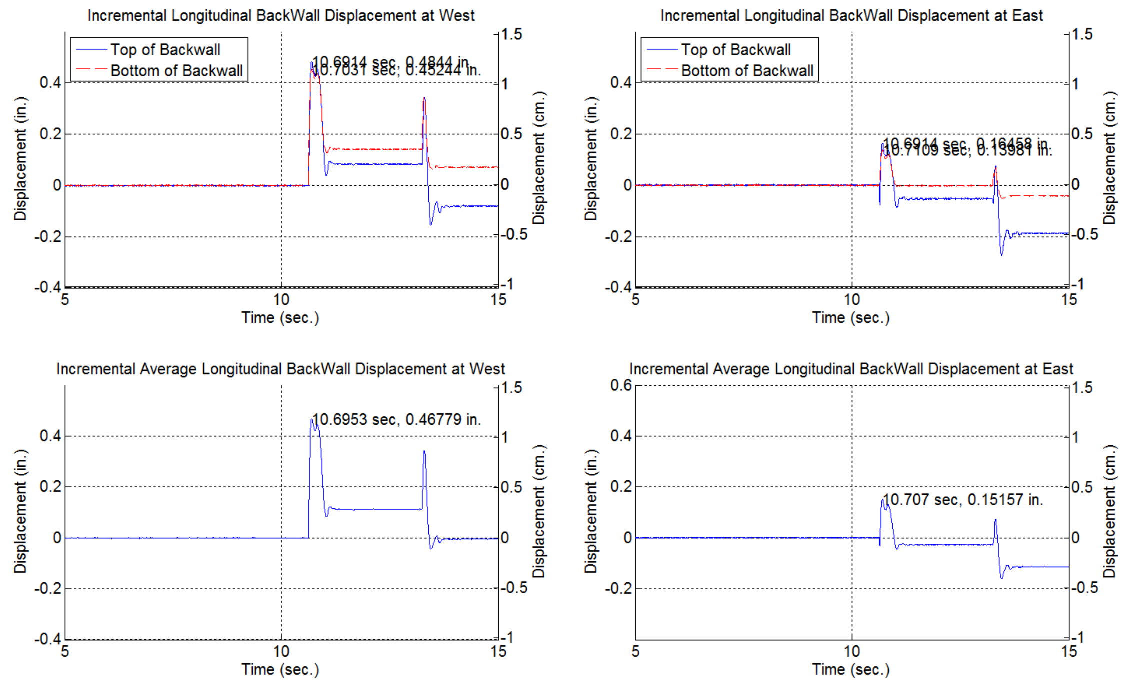

Figure 6-71 Longitudinal displacement of the backwall corners for the 0° skew test in Run 2.

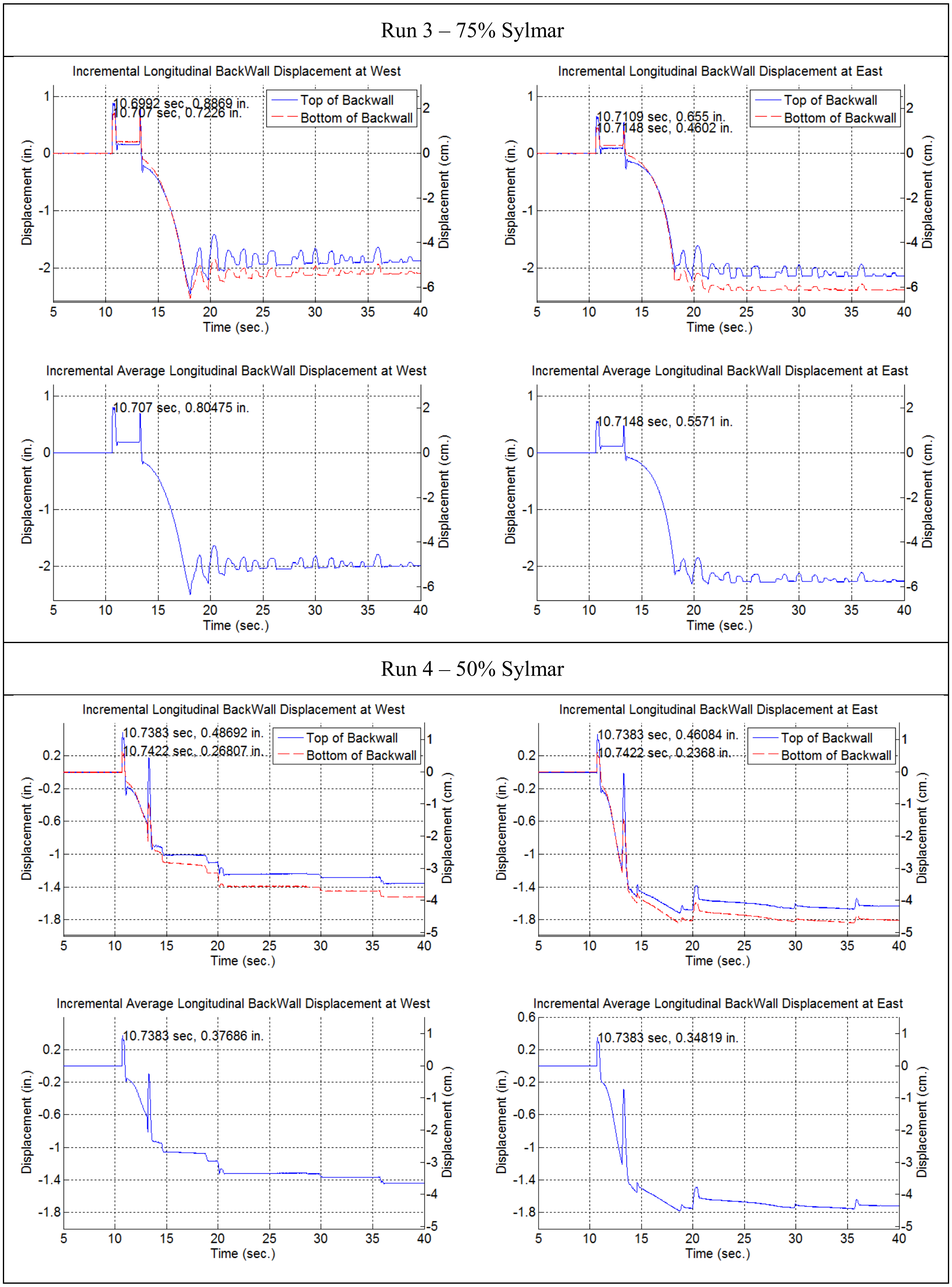

Figure 6-72 Longitudinal displacement of the backwall corners for the 0° skew test in Run 3 and 4.

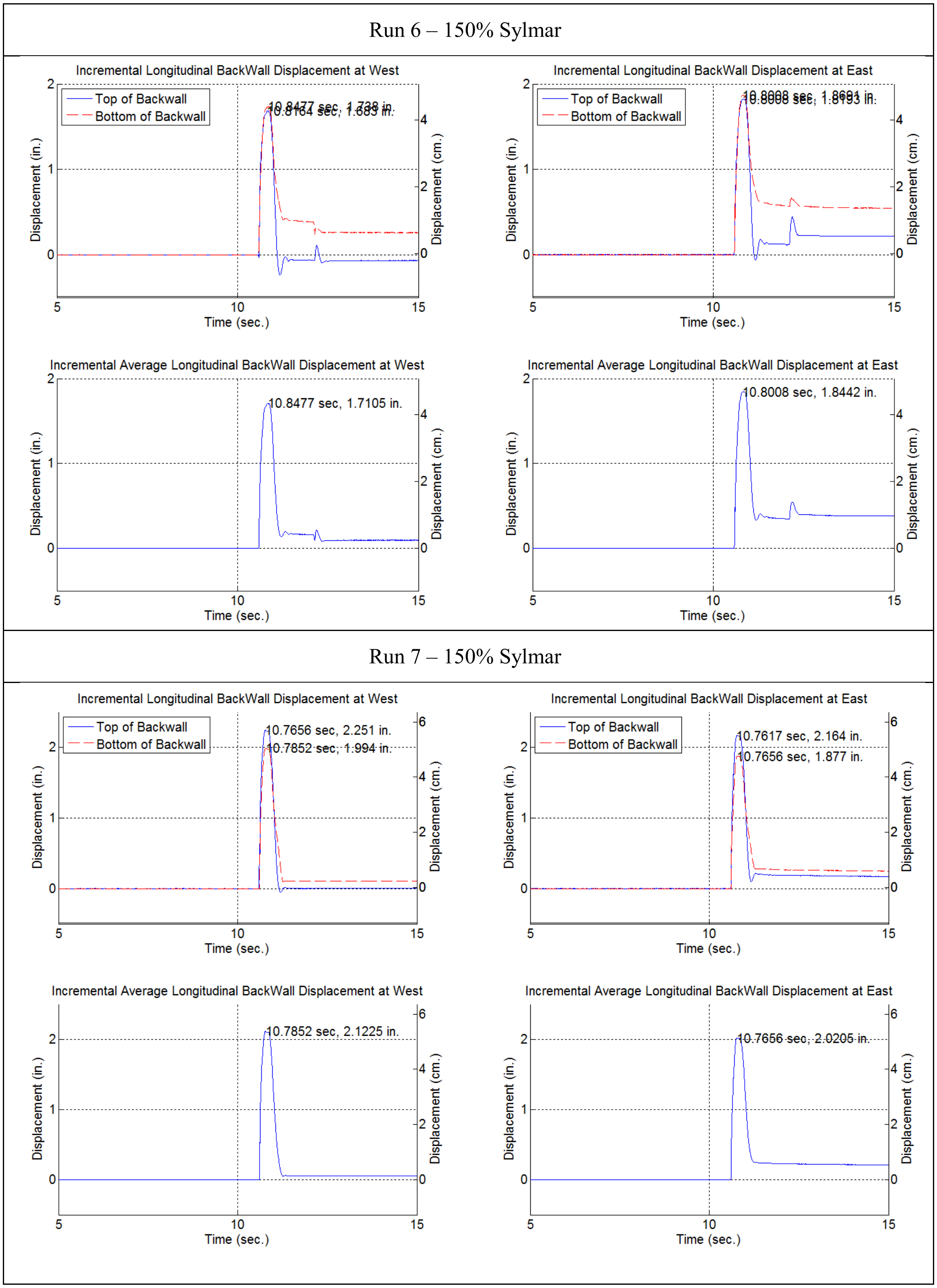

Figure 6-73 Longitudinal displacement of the backwall corners for the 0° skew test in Run 6 and 7.

Run 2 –50% Sylmar

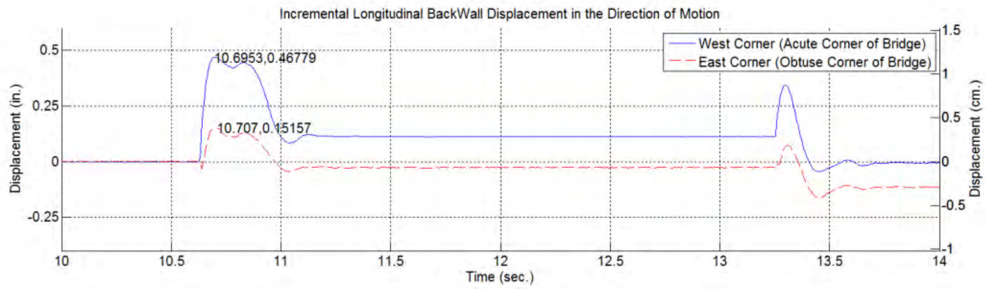

Run 3 – 75% Sylmar

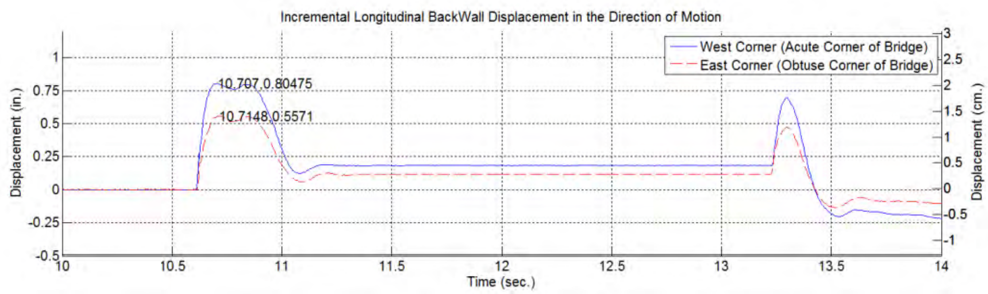

Run 6 – 150% Sylmar

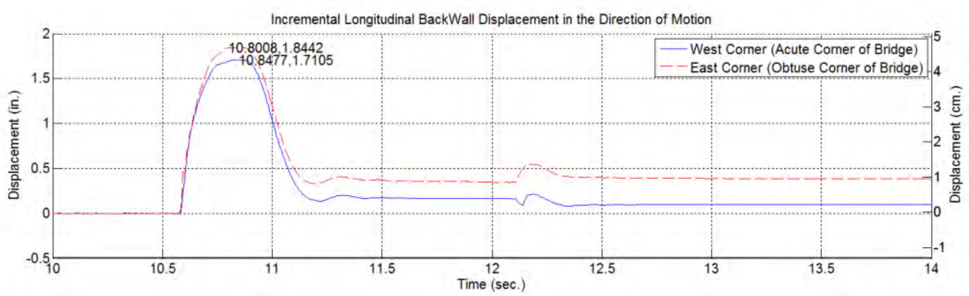

Run 7 – 150% Sylmar

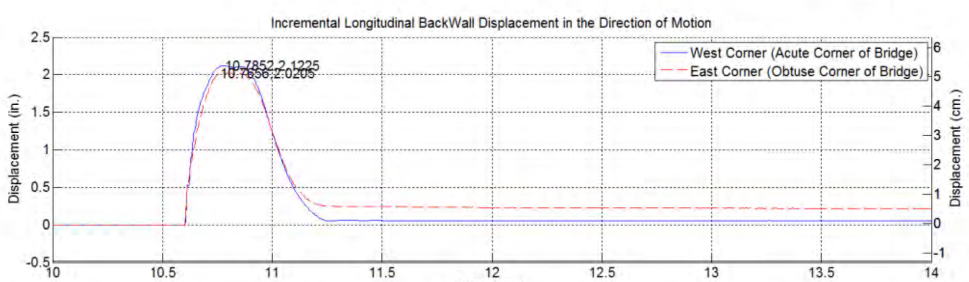

Figure 6-74 Longitudinal displacement of the backwall corners for the 0° skew test.

Run 2 – 50% Sylmar

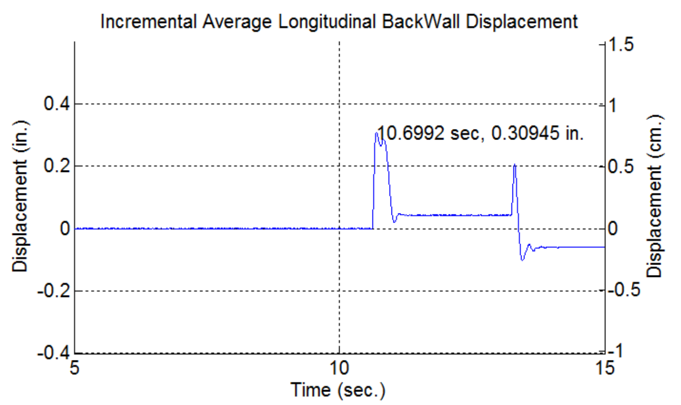

Run 3 – 75% Sylmar

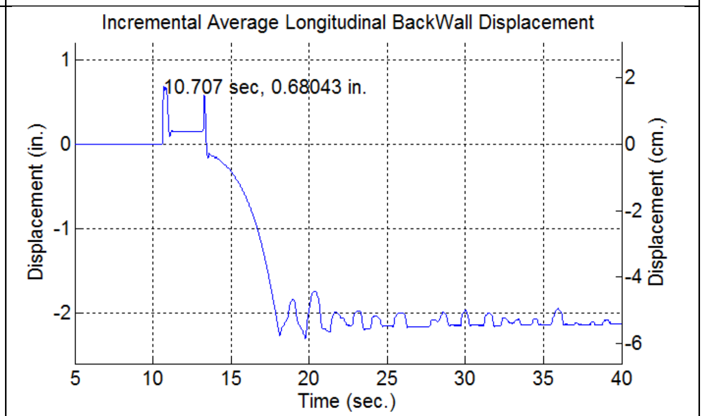

Run 6 – 150% Sylmar

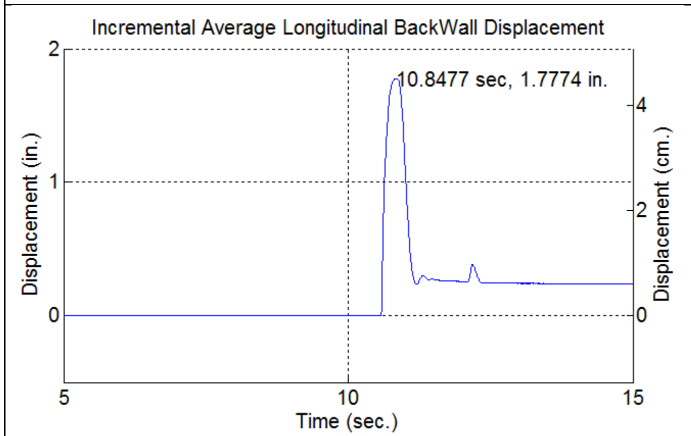

Run 7 – 150% Sylmar

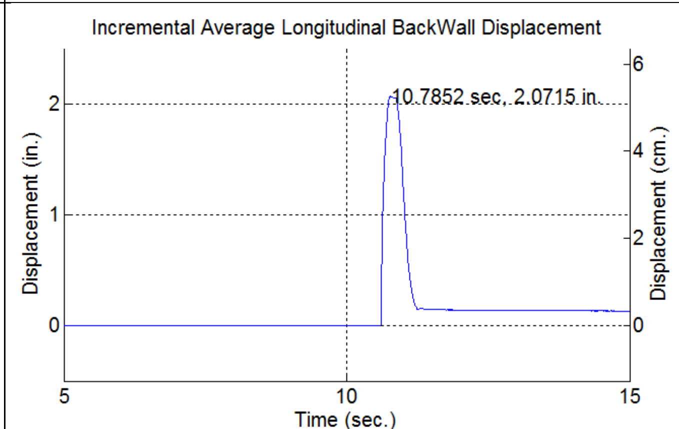

Figure 6-75 Average longitudinal displacement of the backwall for the 0° skew test.

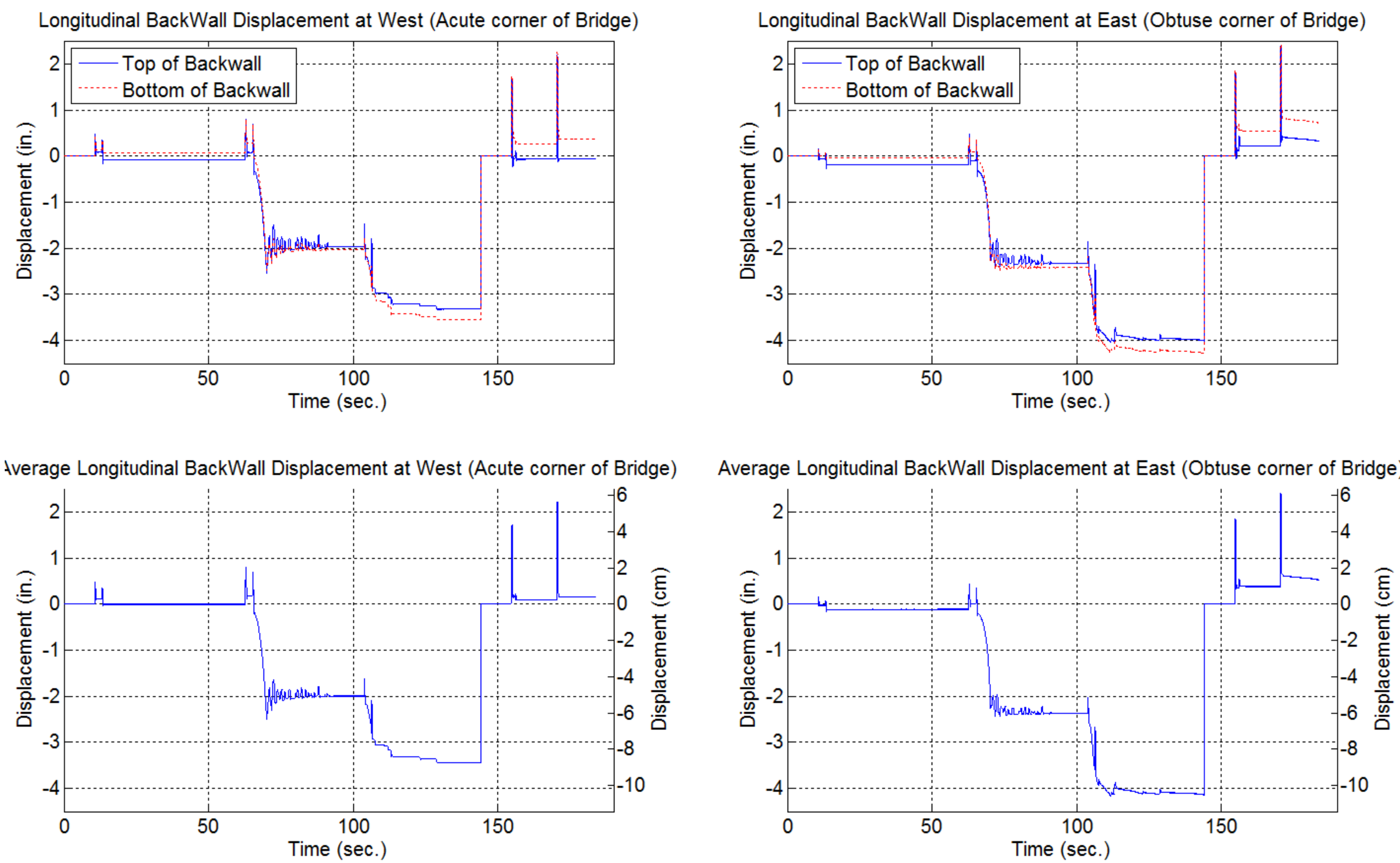

Figure 6-76 Combined displacement of the backwall corners for the 0° skew test.

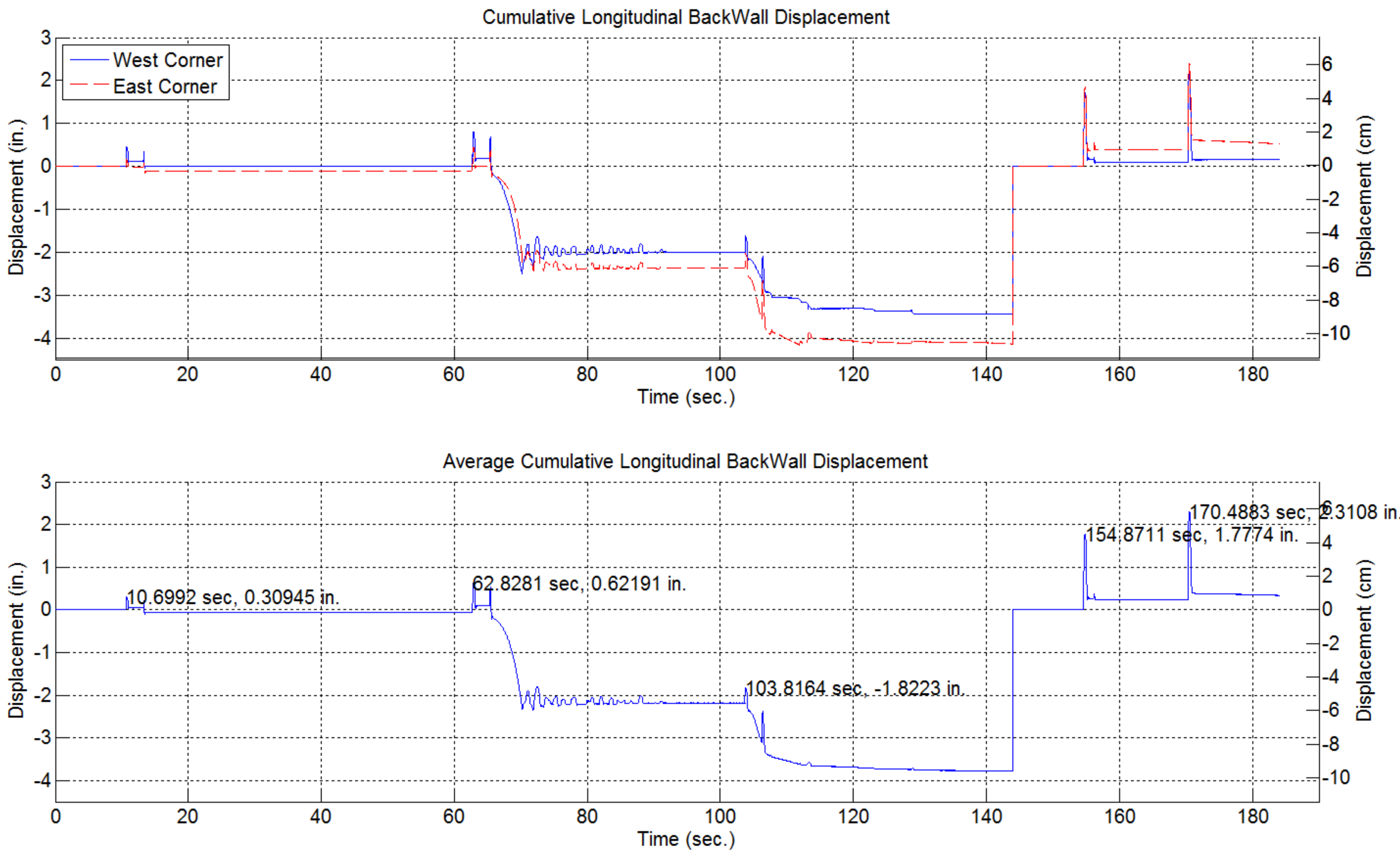

Figure 6-77 Average combined displacement of the backwall for the 0° skew test.

Run 2 – 50% Sylmar

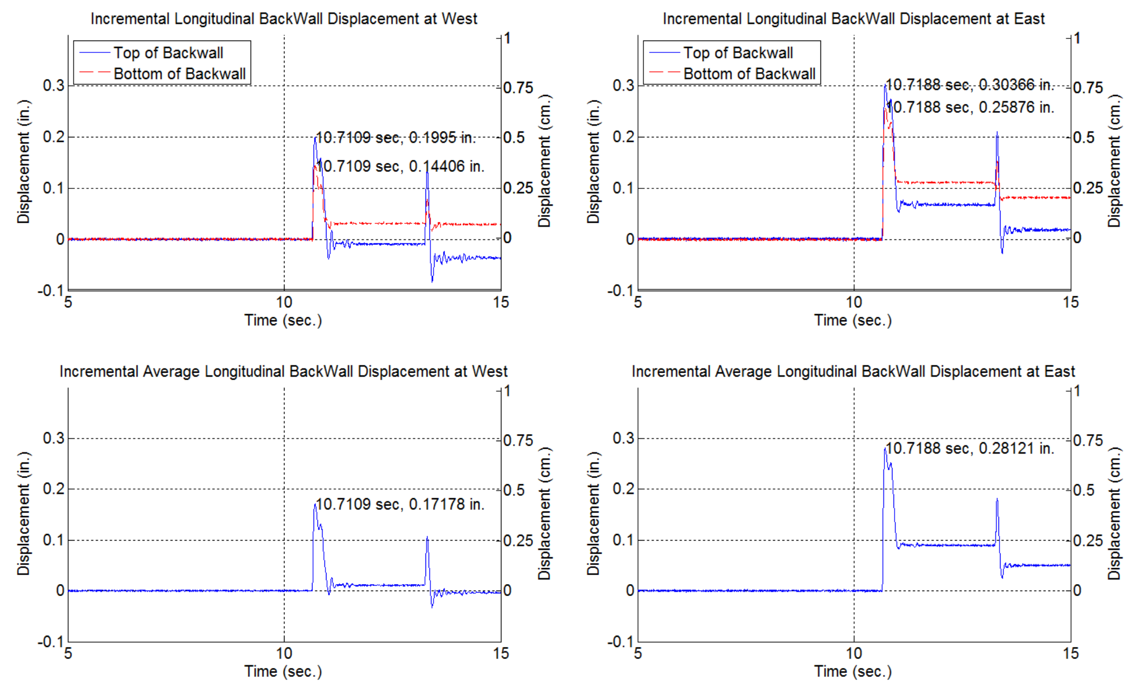

Run 3 – 125% Sylmar

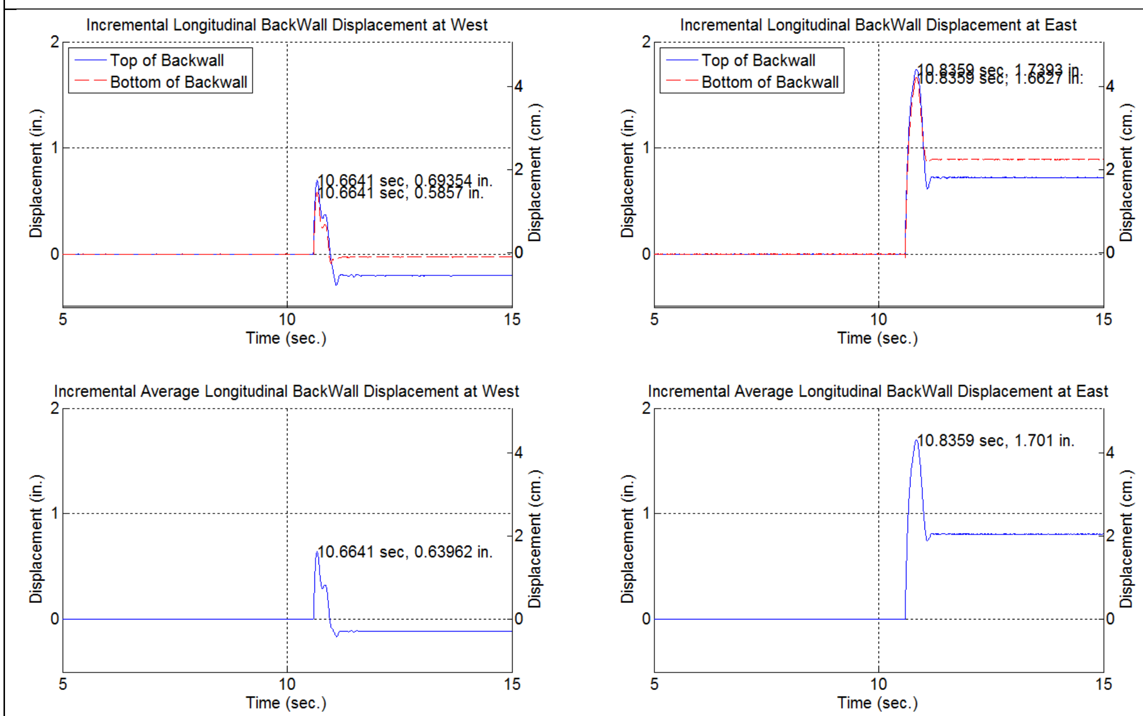

Figure 6-78 Longitudinal displacement of the backwall corners for the 30° skew test in Run 2 and 3.

Run 4 – 150% Sylmar

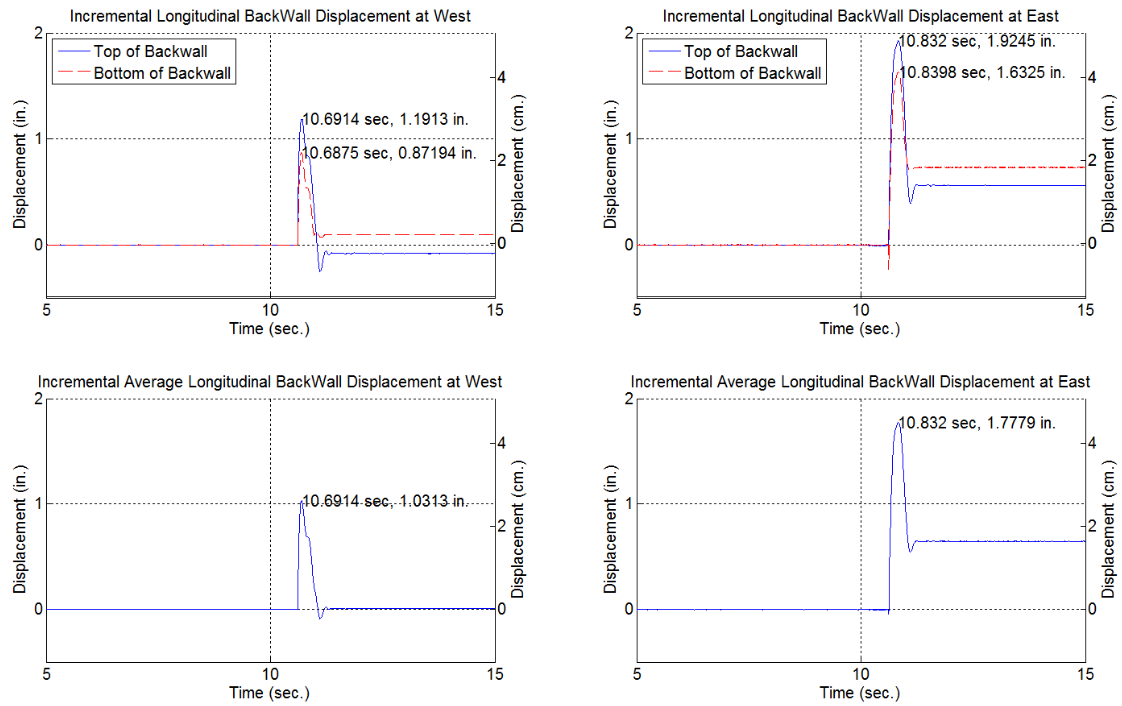

Run 5 – 200% Sylmar

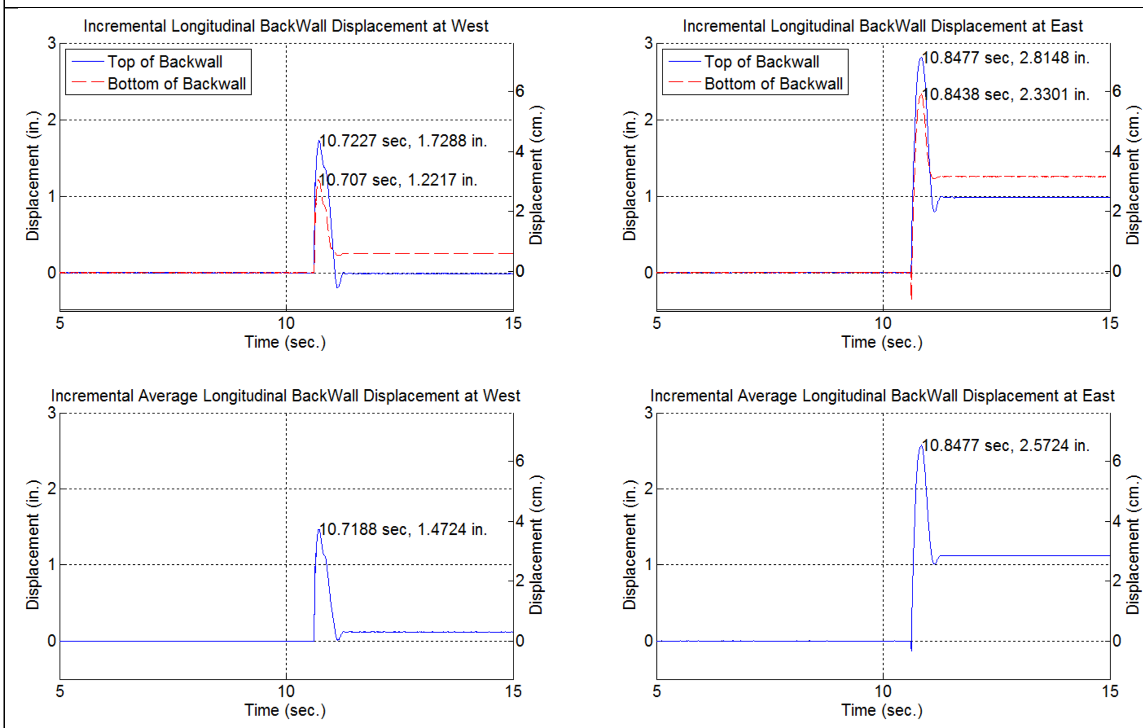

Figure 6-79 Longitudinal displacement of the backwall corners for the 30° skew test in Run 4 and 5.

Run 2 –50% Sylmar

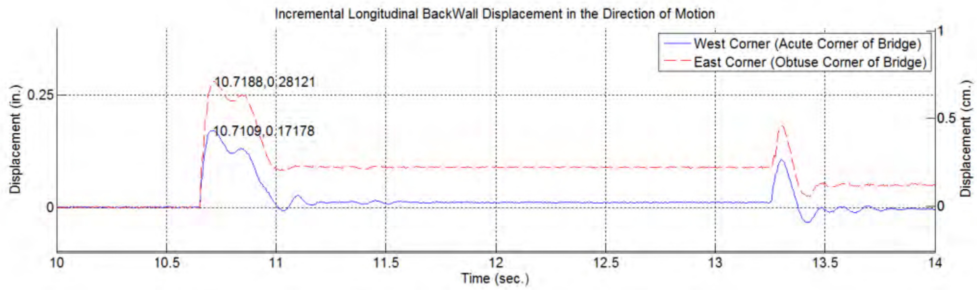

Run 3 – 125% Sylmar

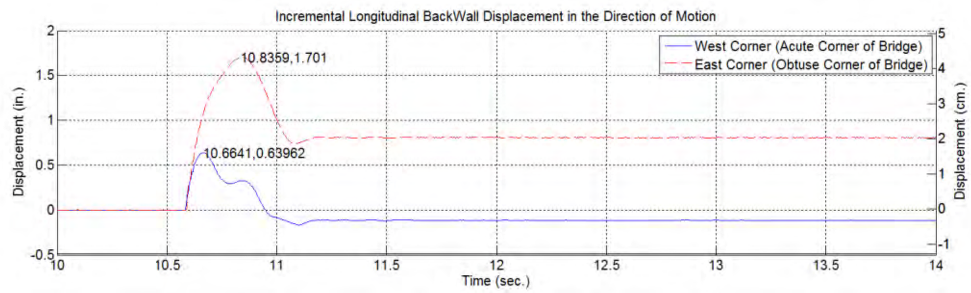

Run 4 – 150% Sylmar

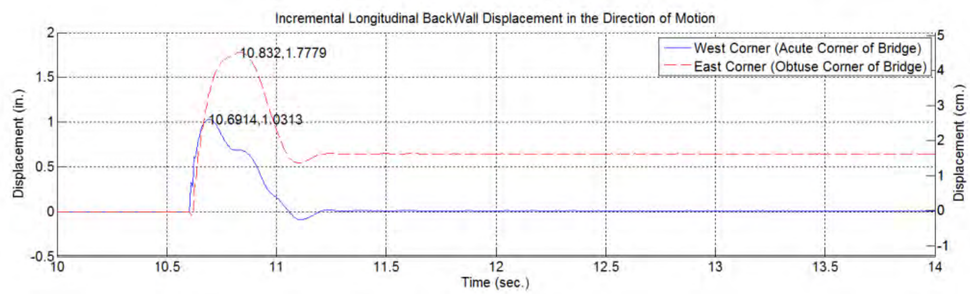

Run 5 – 200% Sylmar

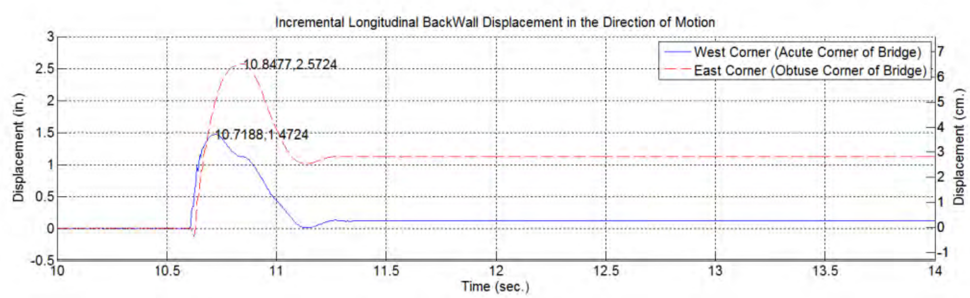

Figure 6-80 Longitudinal displacement of the backwall corners for the 30° skew test.

Run 2 –50% Sylmar

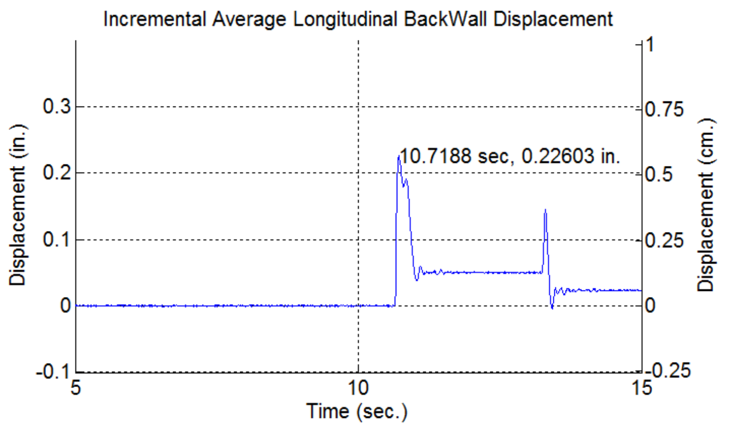

Run 3 – 125% Sylmar

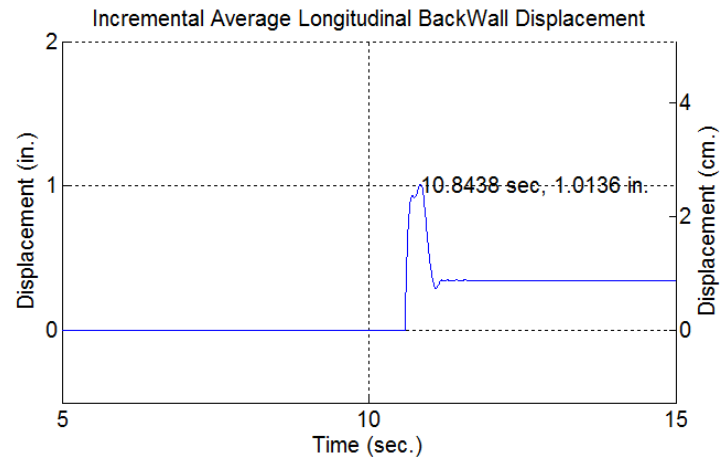

Run 4 – 150% Sylmar

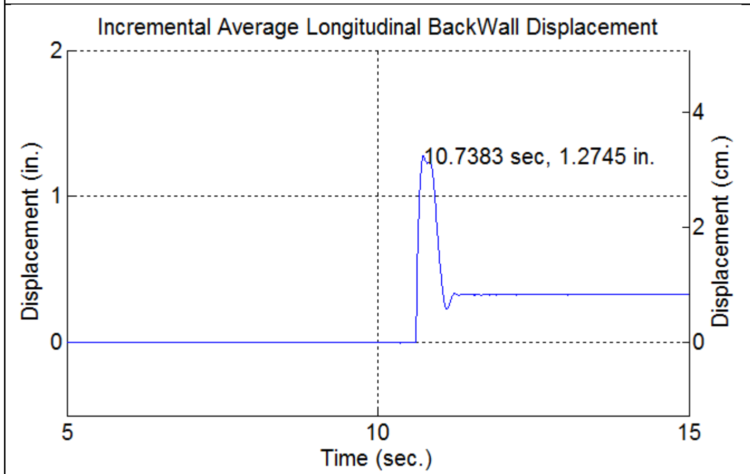

Run 5 – 200% Sylmar

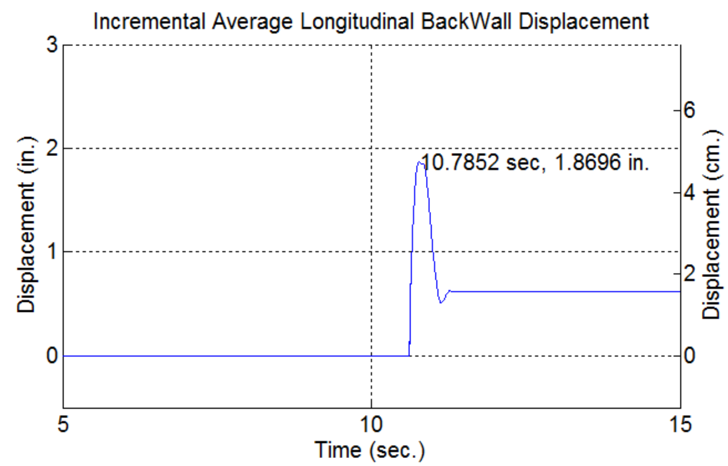

Figure 6-81 Average longitudinal displacement of the backwall for the 30° skew test.

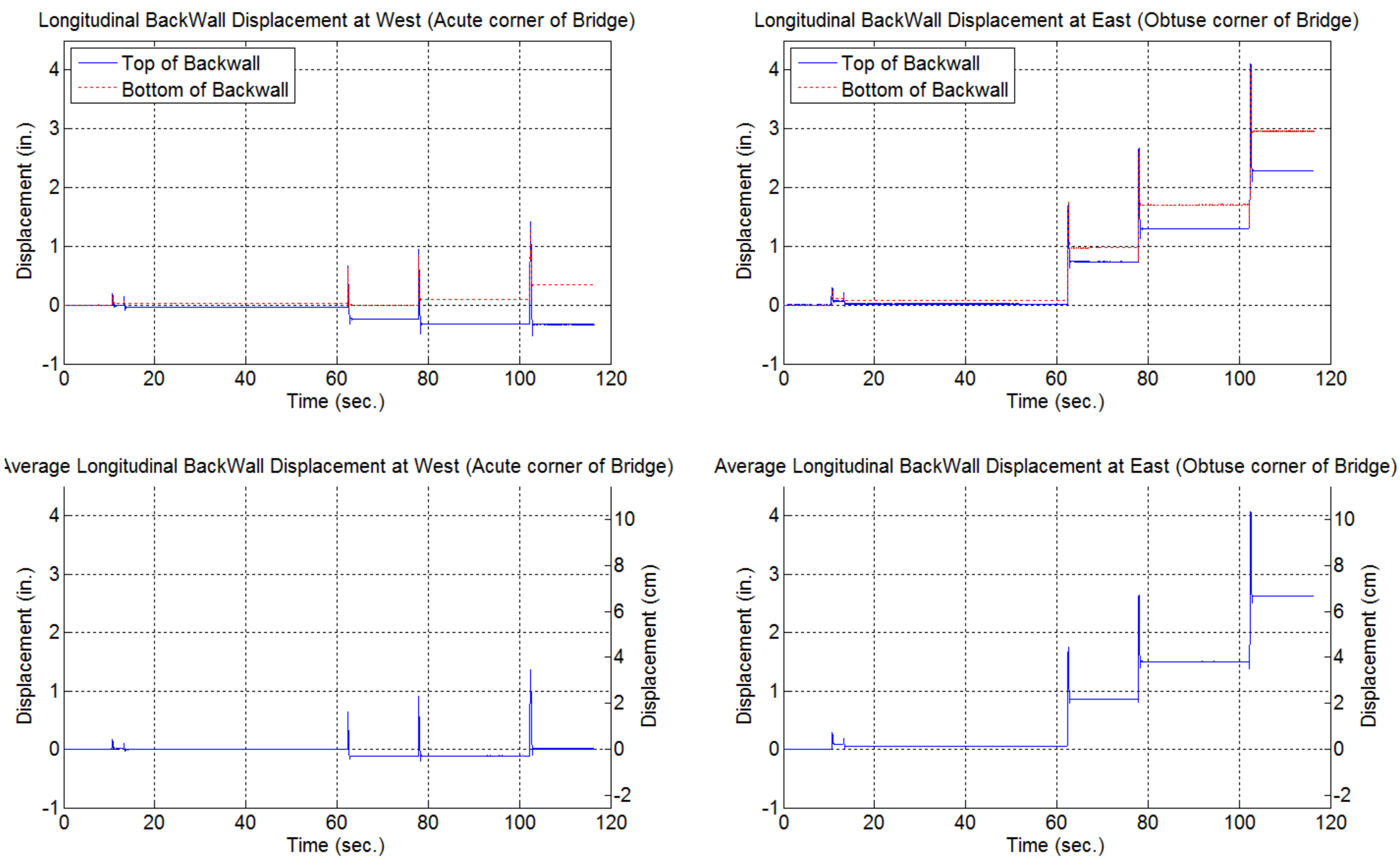

Figure 6-82 Combined displacement of the backwall corners for the 30° skew test.

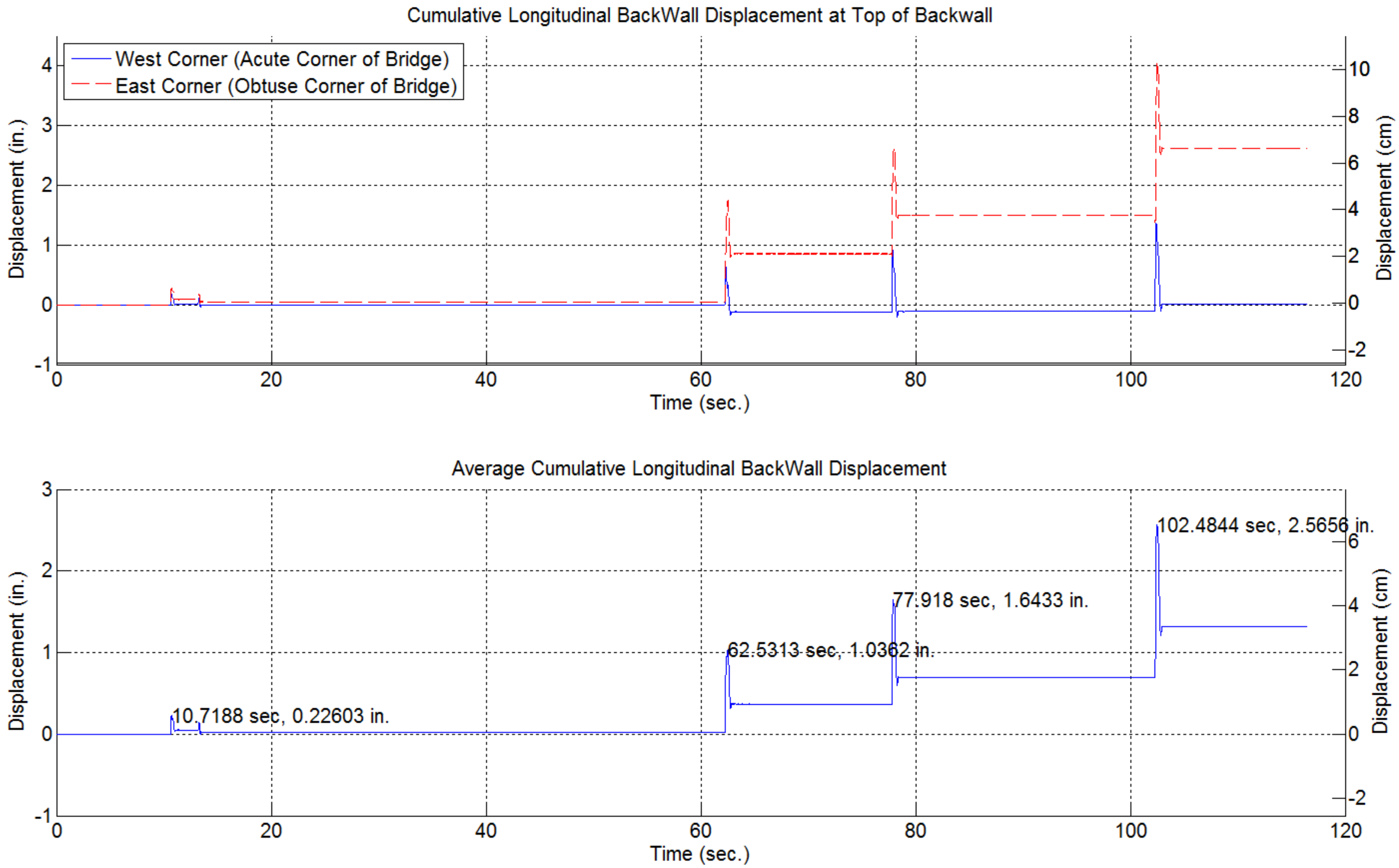

Figure 6-83 Average combined displacement of the backwall for the 30° skew test.

Run 2 – 50% Sylmar

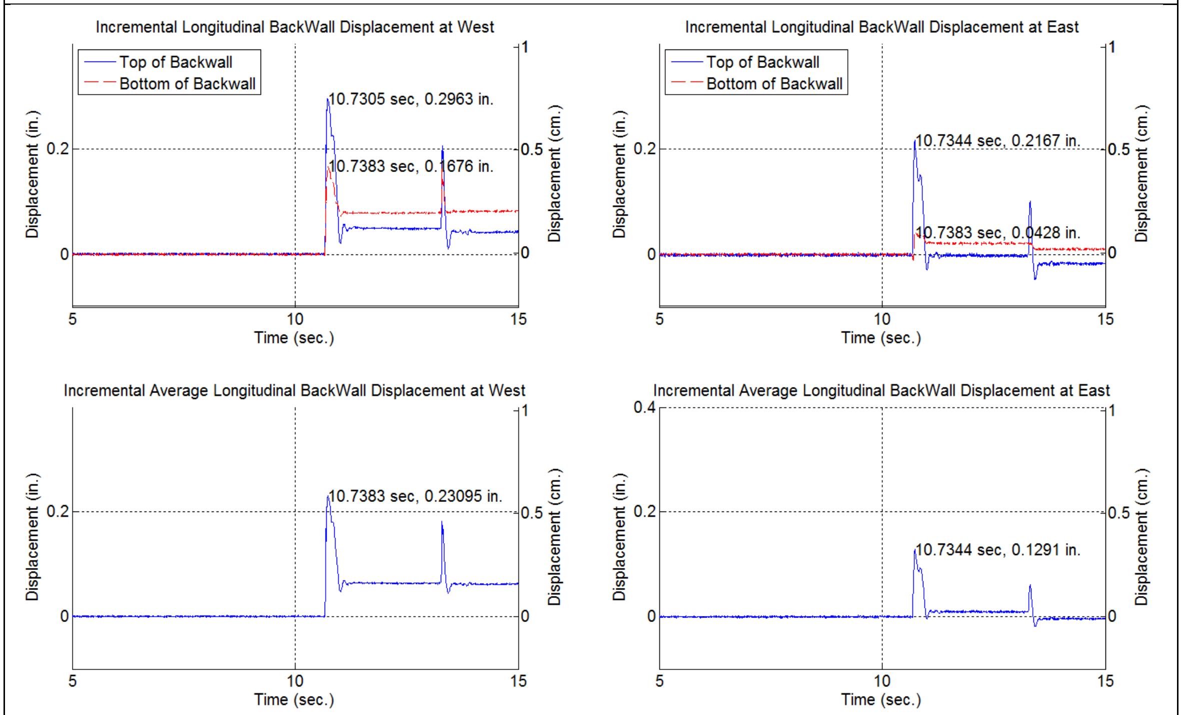

Run 3 – 125% Sylmar

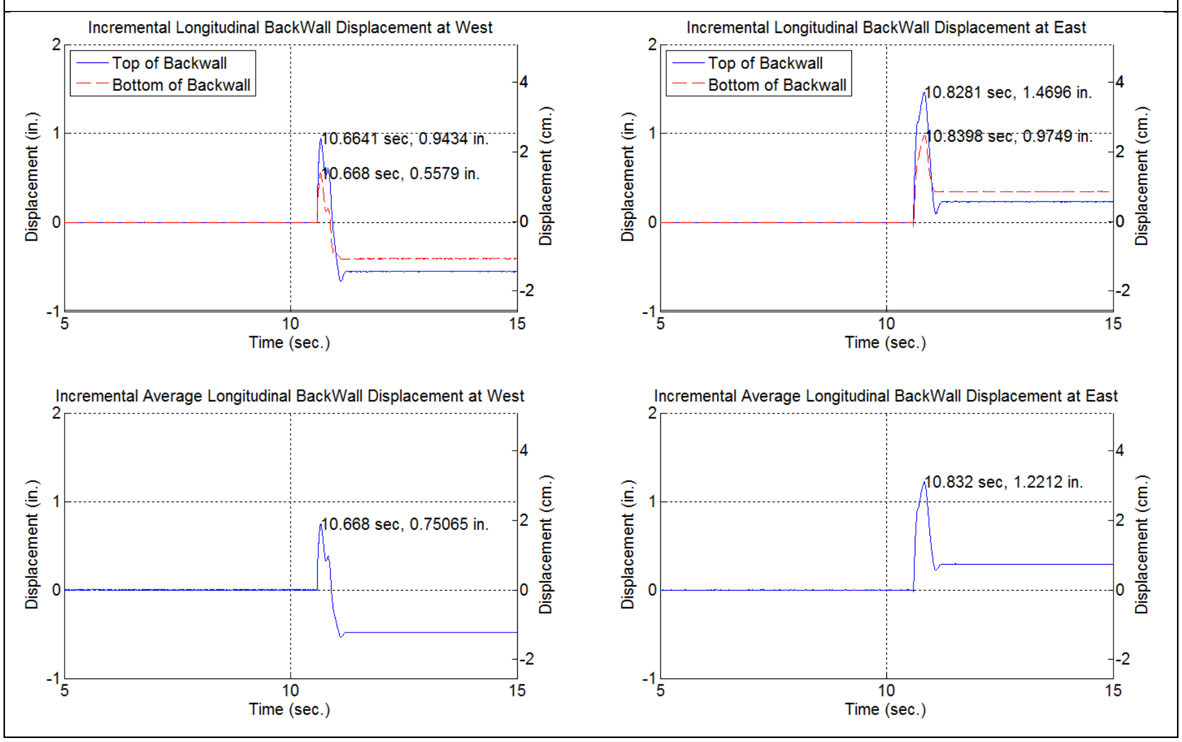

Figure 6-84 Longitudinal displacement of the backwall corners for the 45° skew test in Run 2 and 3.

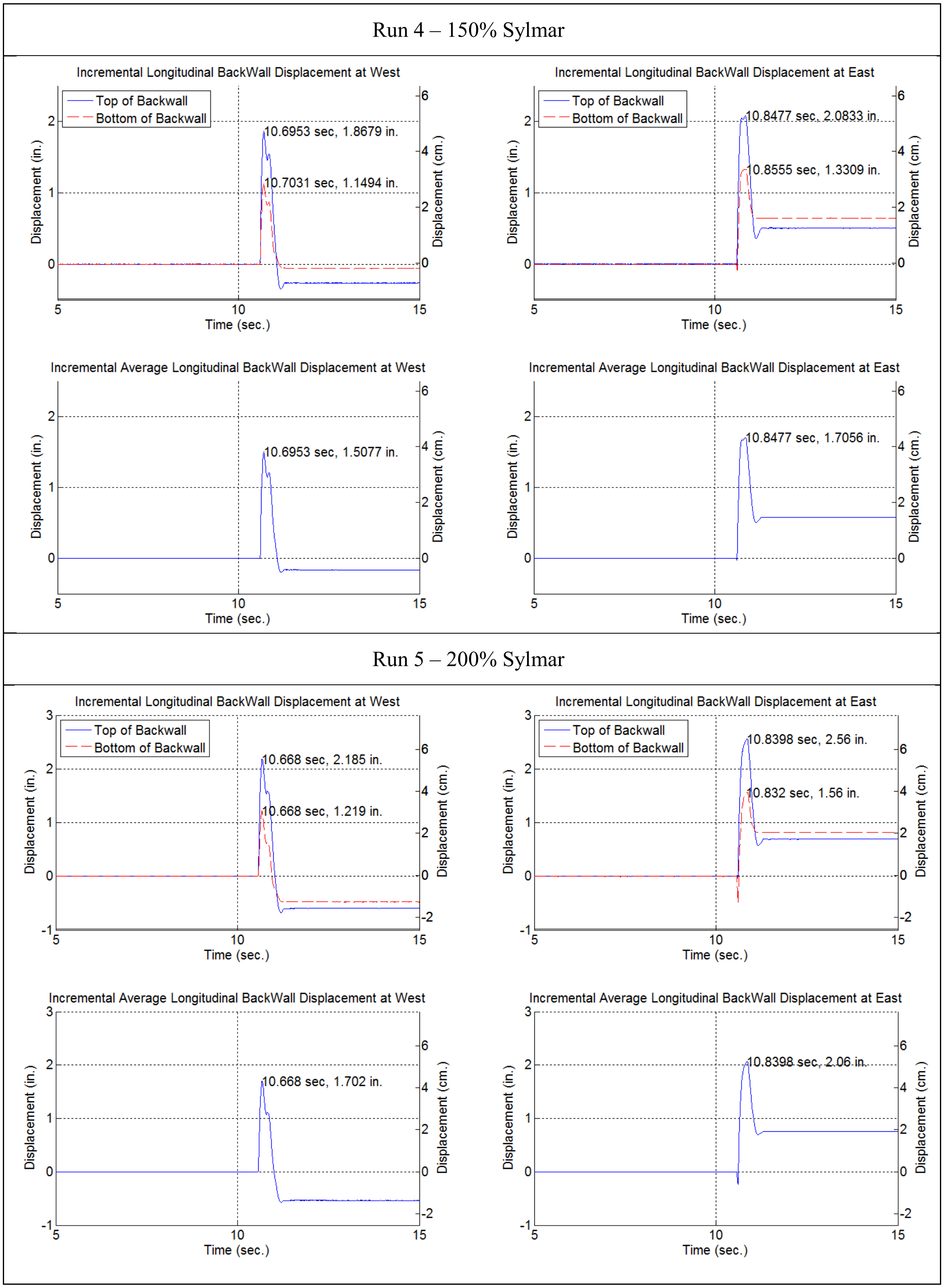

Figure 6-85 Longitudinal displacement of the backwall corners for the 45° skew test in Run 4 and 5.

Run 2 –50% Sylmar

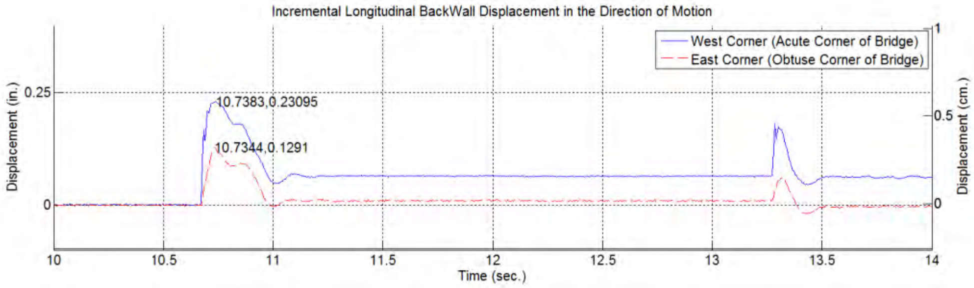

Run 3 – 125% Sylmar

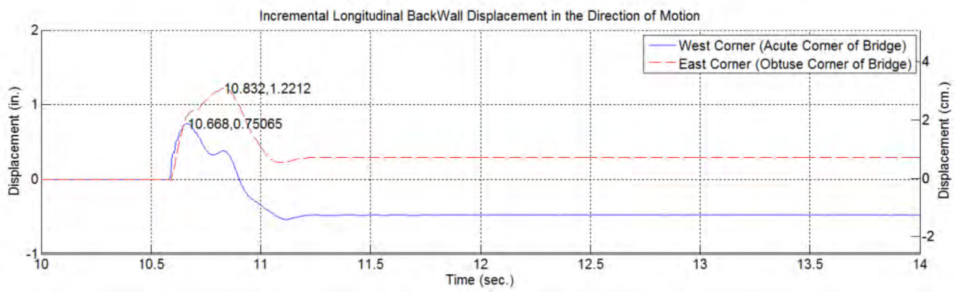

Run 4 – 150% Sylmar

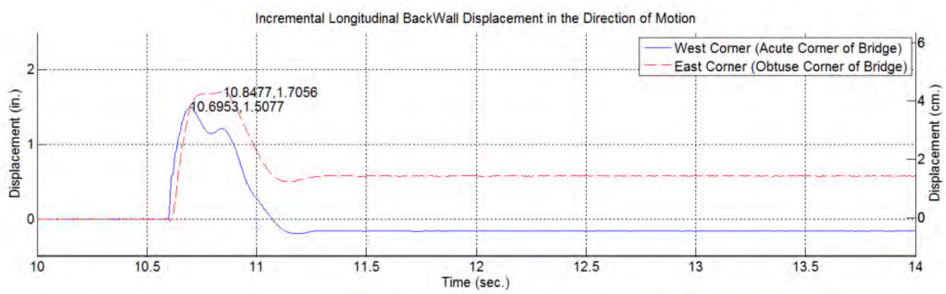

Run 5 – 200% Sylmar

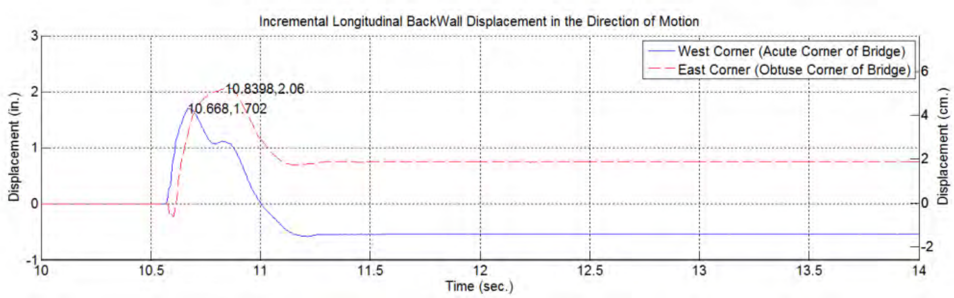

Figure 6-86 Longitudinal displacement of the backwall corners for the 45° skew test.

Run 2 –50% Sylmar

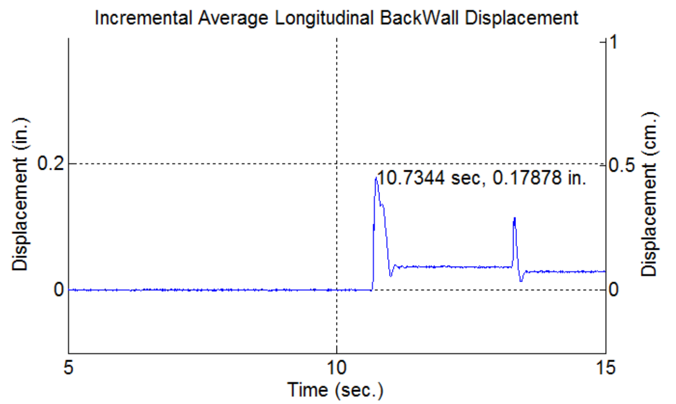

Run 3 – 125% Sylmar

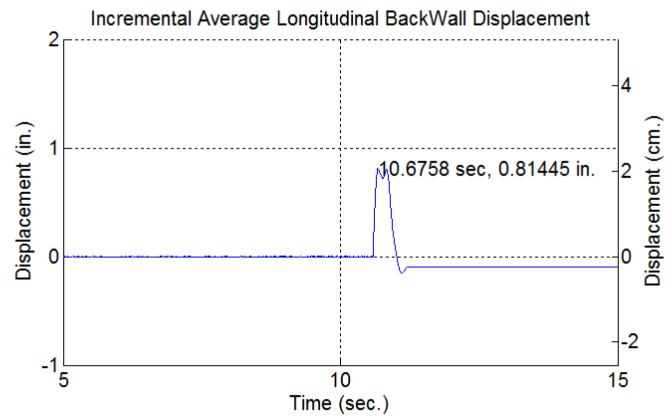

Run 4 – 150% Sylmar

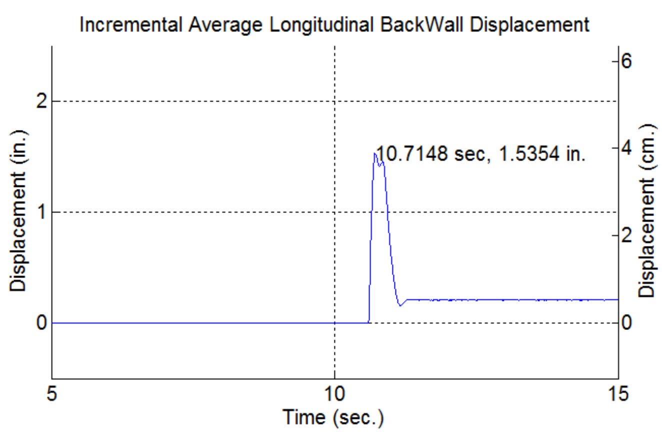

Run 5 – 200% Sylmar

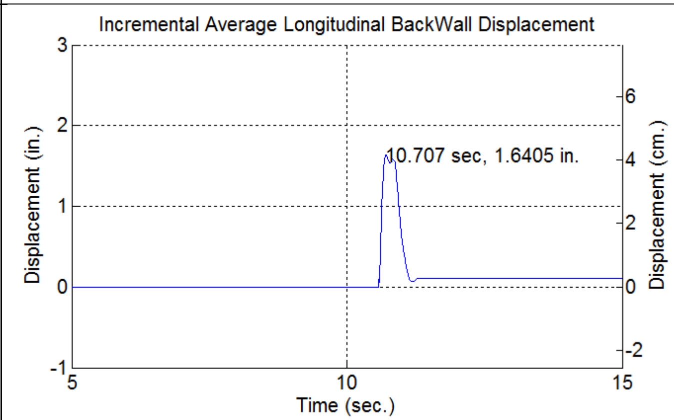

Figure 6-87 Average longitudinal displacement of the backwall for the 45° skew test.

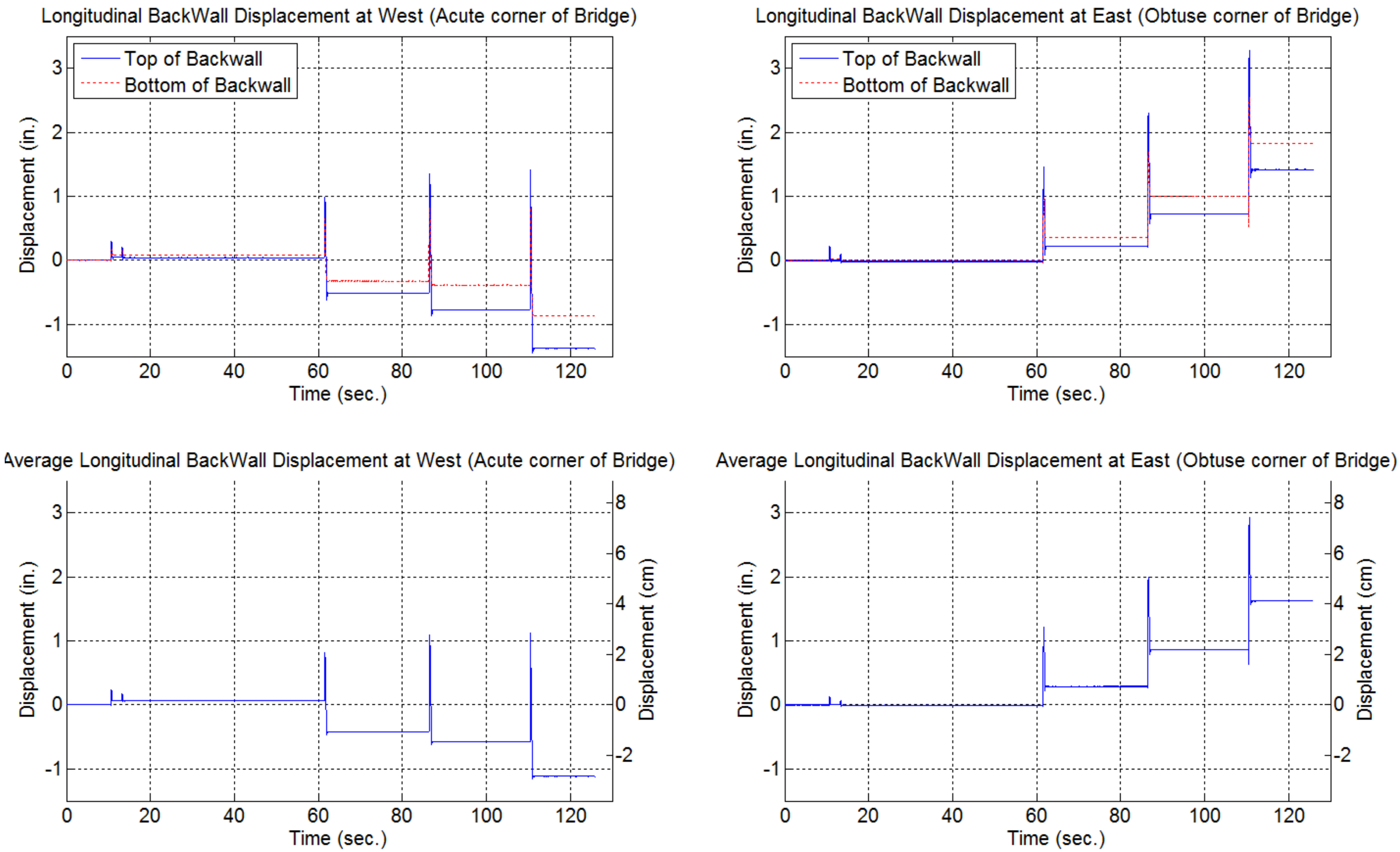

Figure 6-88 Combined longitudinal displacement of the backwall corners for the 45° skew test.

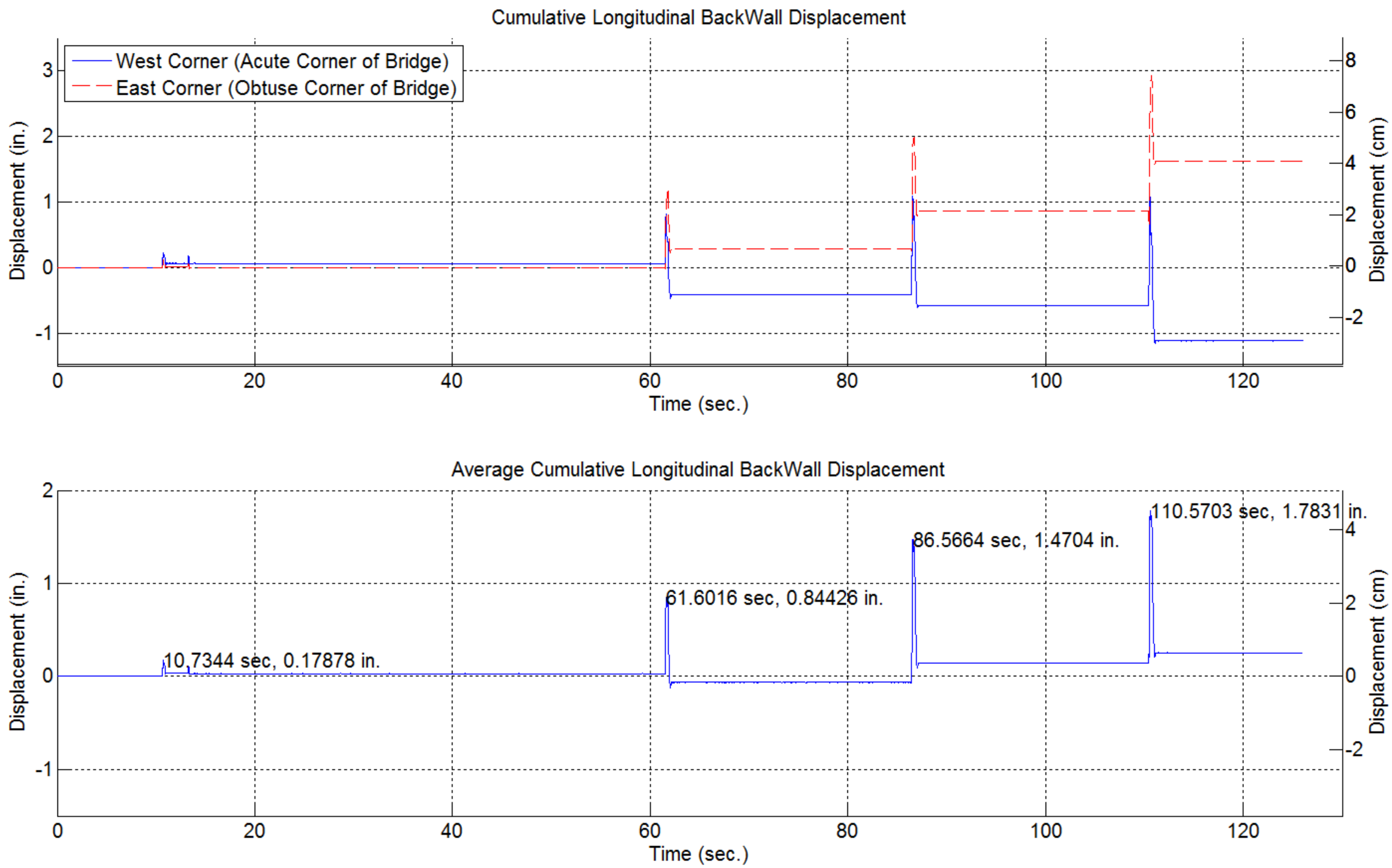

Figure 6-89 Average combined longitudinal displacement of the backwall for the 45° skew test.

Run 2 –50% Sylmar

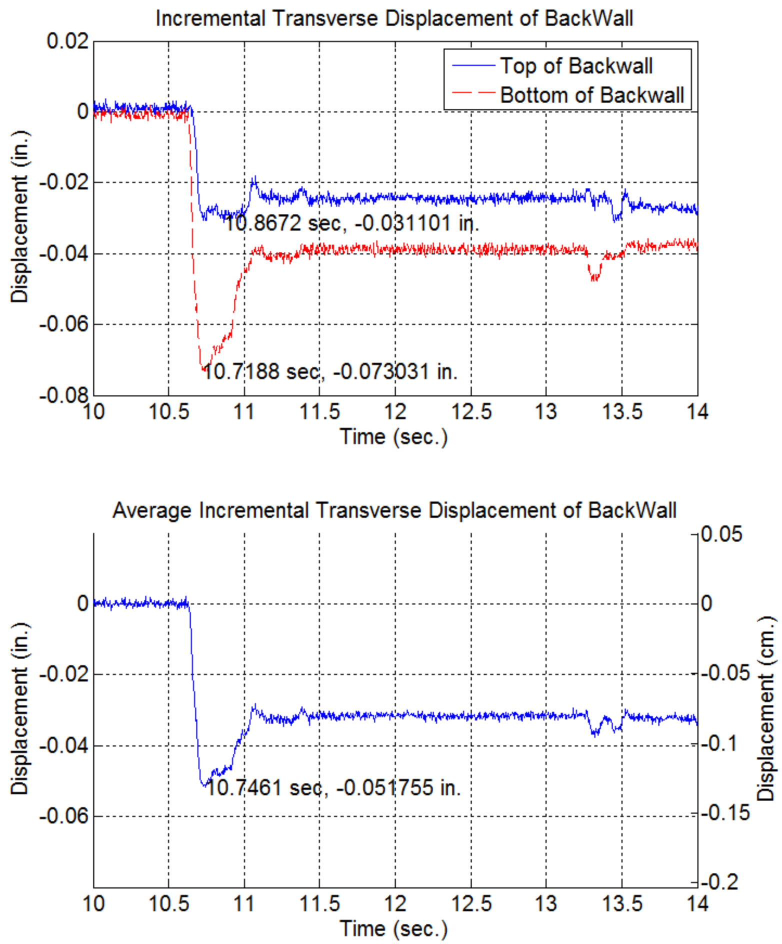

Figure 6-90 Transverse displacement of the backwall western corners for the 0° skew test (Run 2).

Run 3 – 75% Sylmar	Run 4 –50% Sylmar

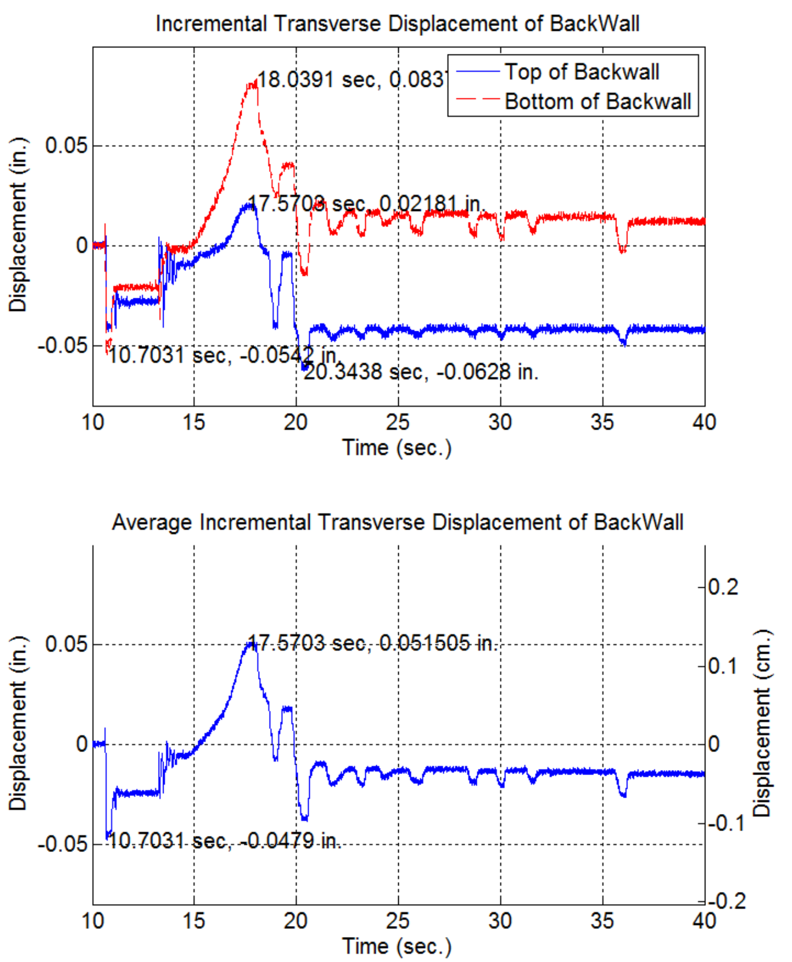

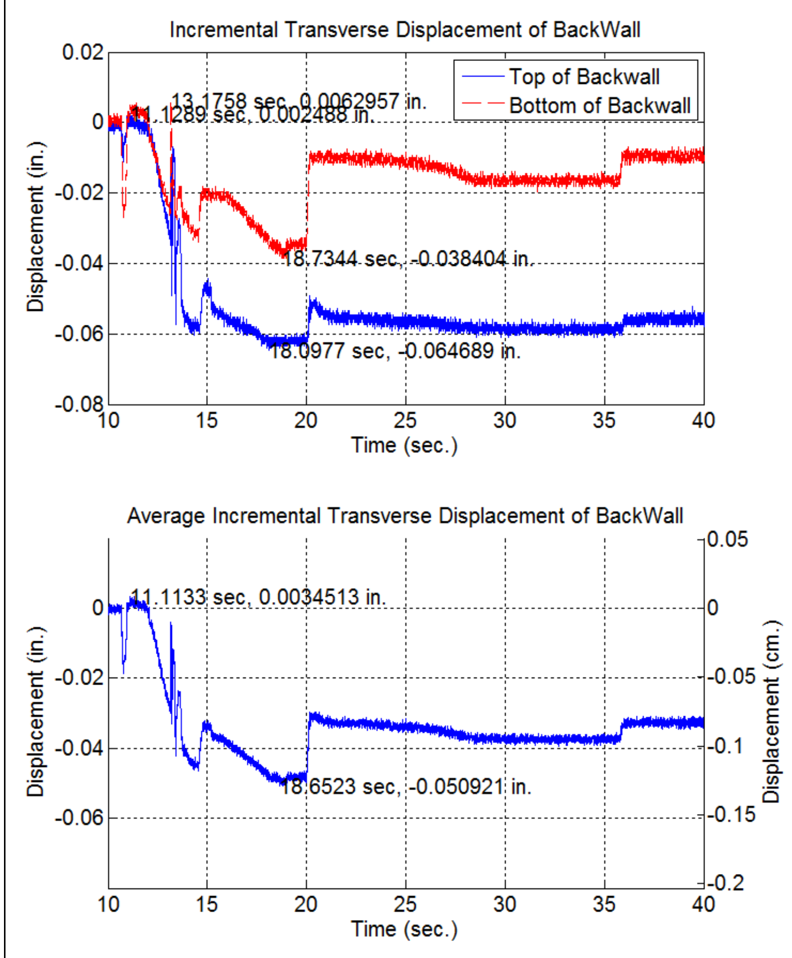

Figure 6-91 Transverse displacement of the backwall western corners for the 0° skew test in Run 3 and 4.

Run 6 –150% Sylmar	Run 7 –150% Sylmar
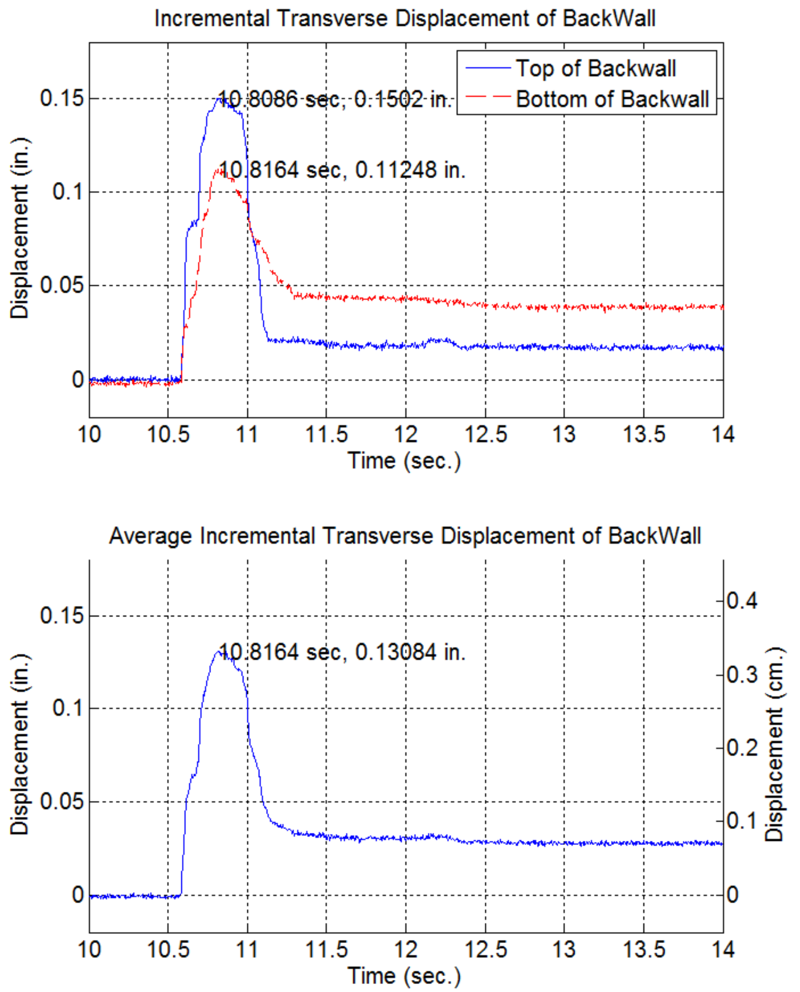	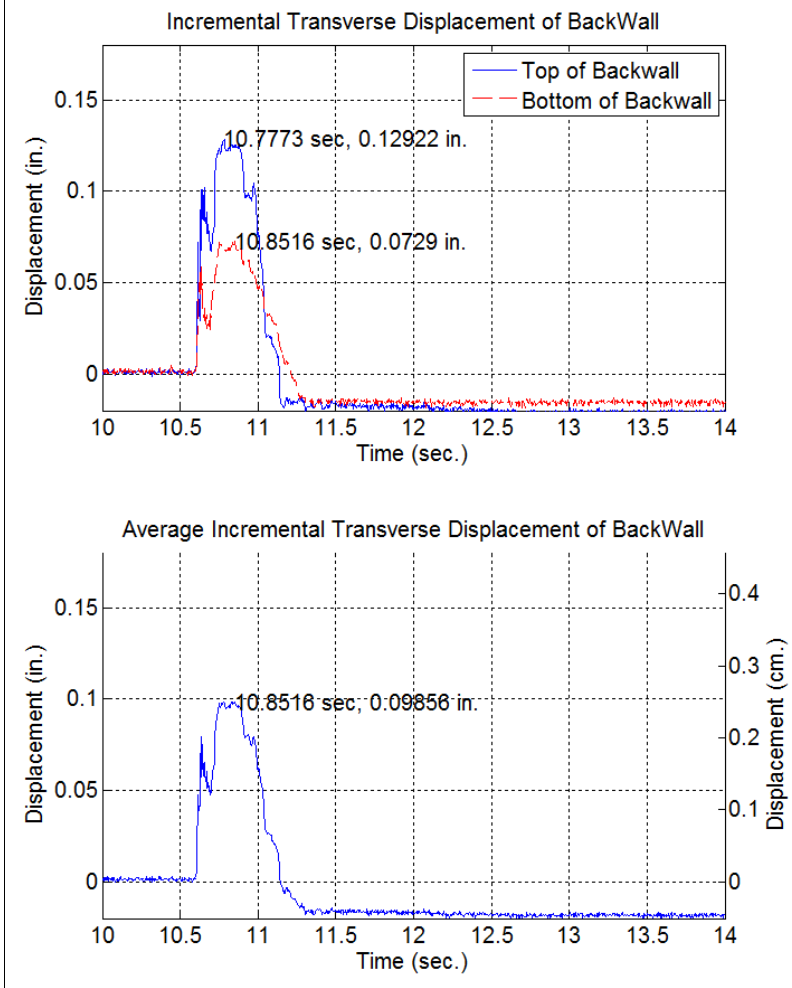

Figure 6-92 Transverse displacement of the backwall western corners for the 0° skew test in Run 6 and 7.

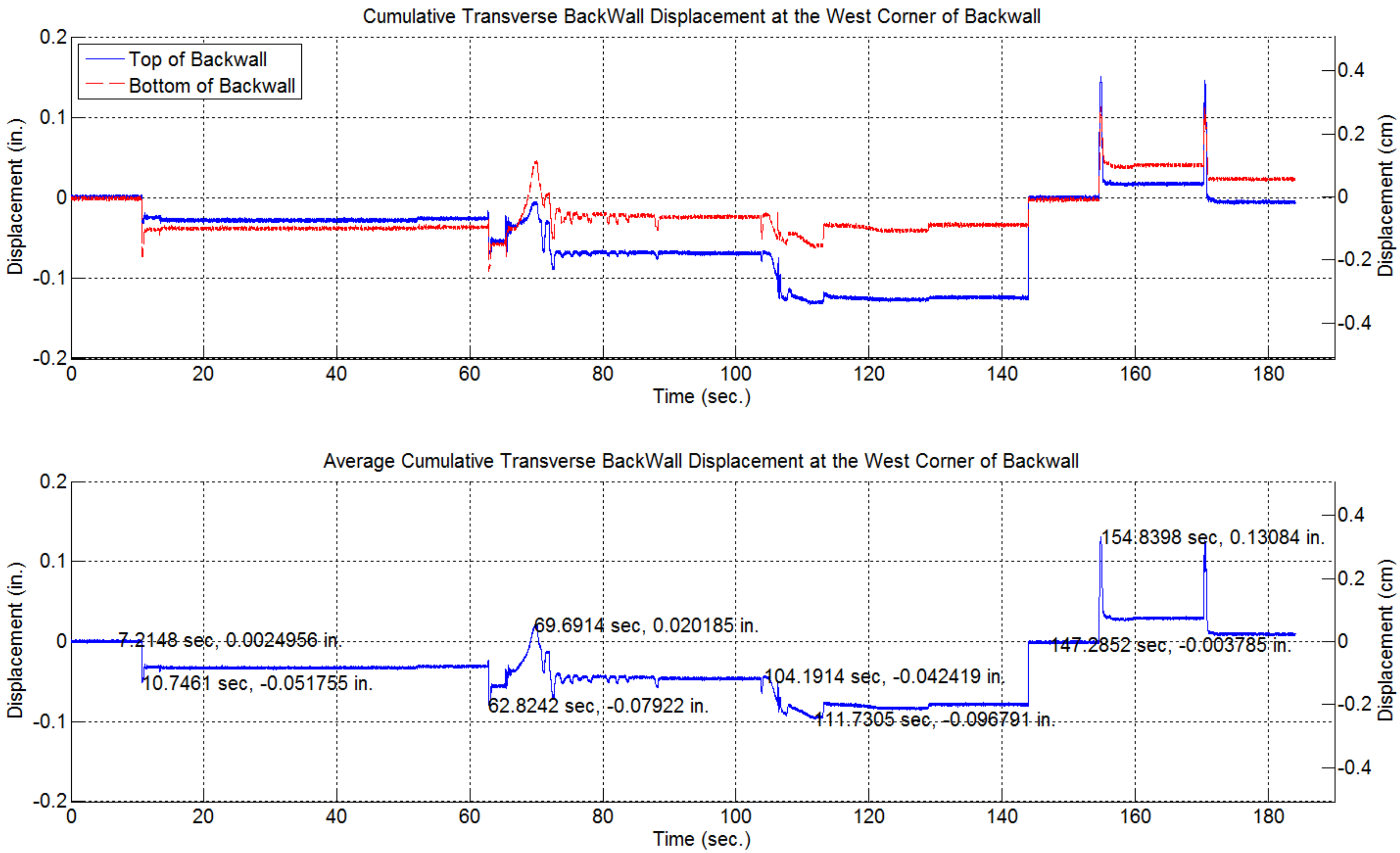

Figure 6-93 Combined transverse displacement of the backwall western corners for the 0° skew test.

Run 2 –50% Sylmar	Run 3 – 125% Sylmar

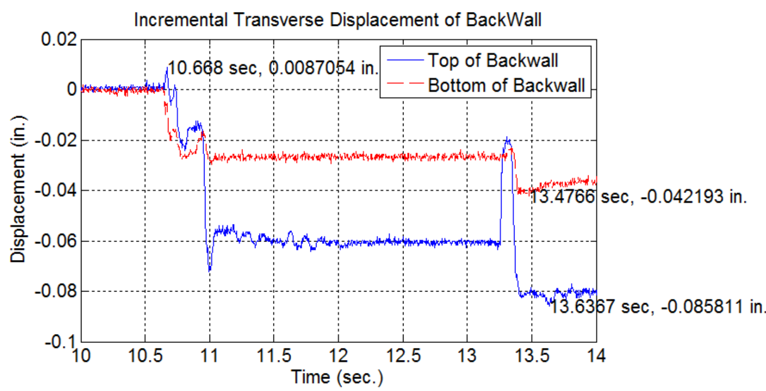

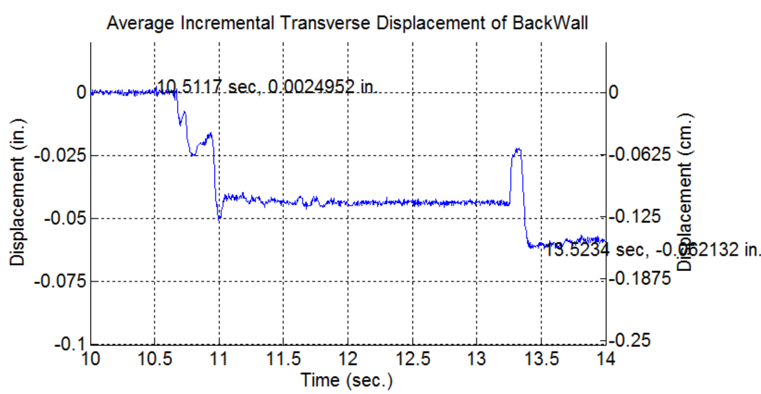

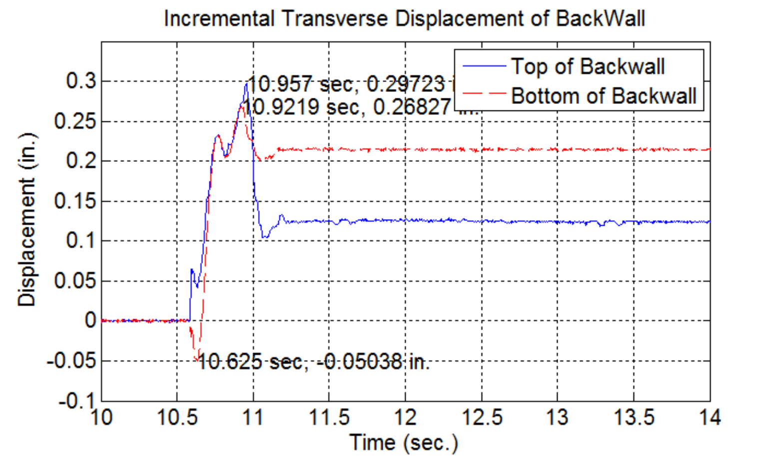

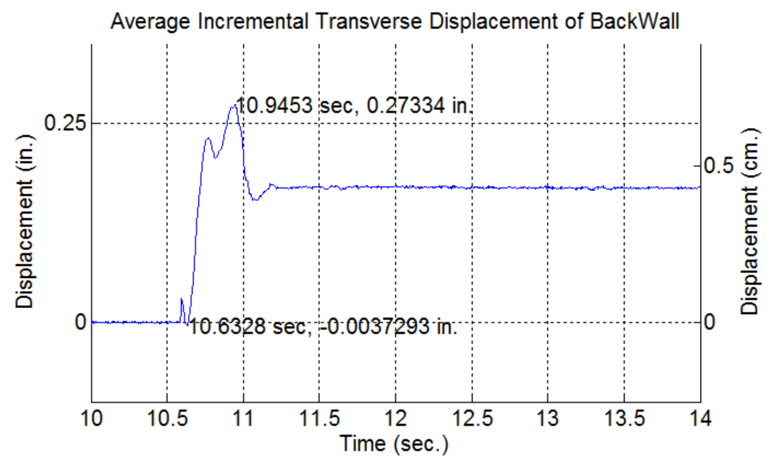

Figure 6-94 Transverse displacement of the backwall western corners for the 30° skew test in Run 2 and 3.

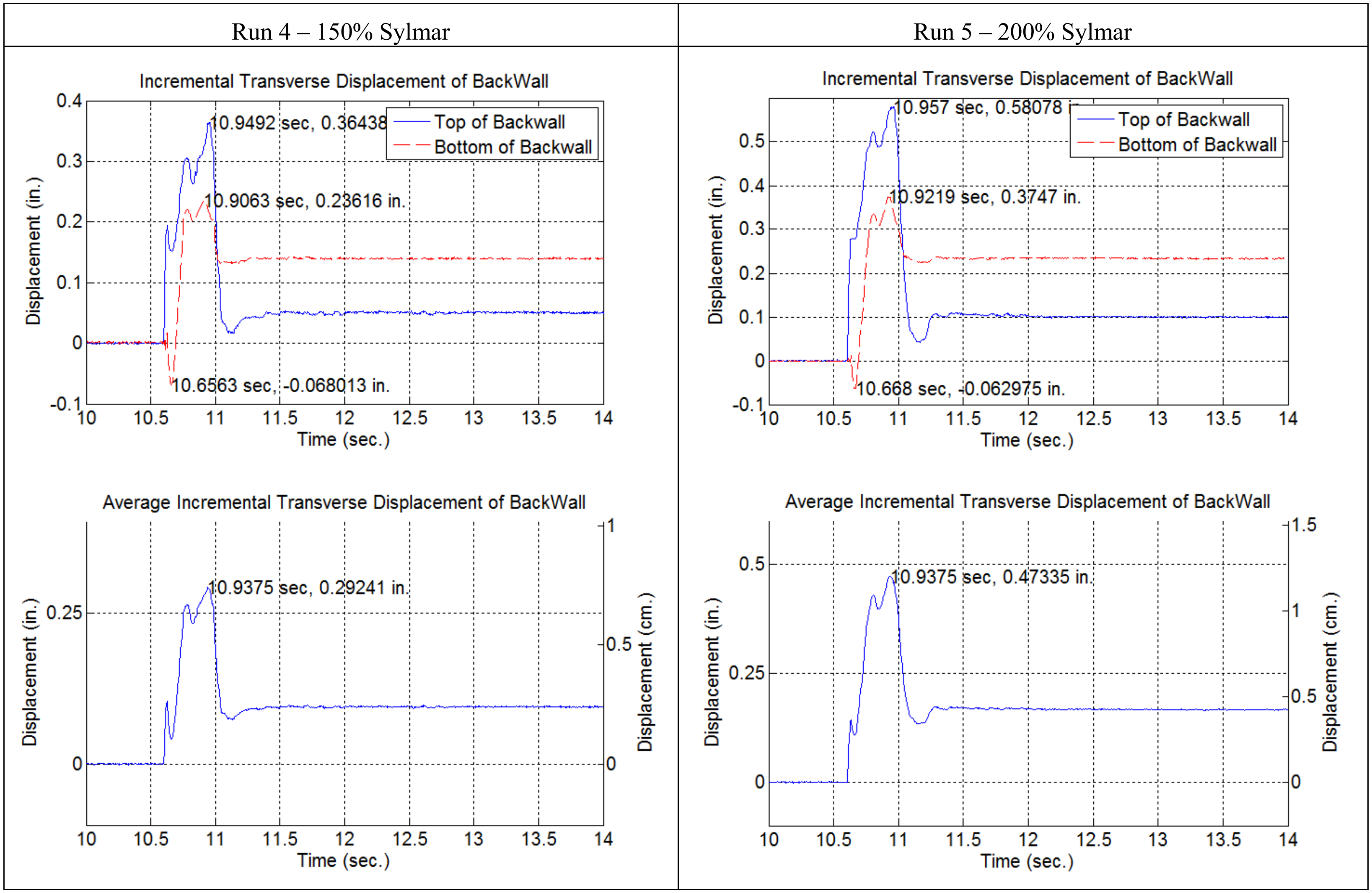

Figure 6-95 Transverse displacement of the backwall western corners for the 30° skew test in Run 4 and 5.

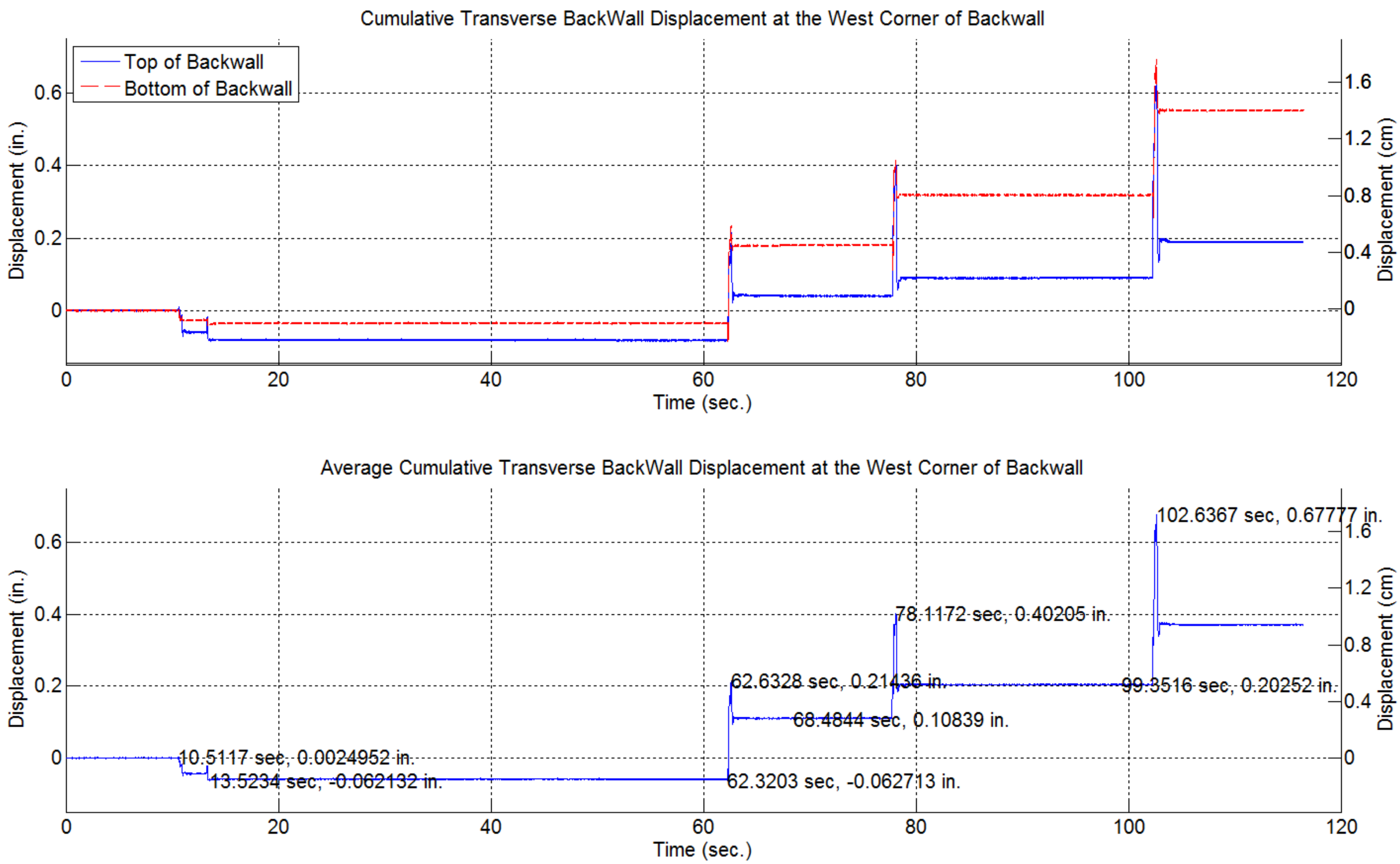

Figure 6-96 Combined transverse displacement of the backwall western corners for the 30° skew test.

Run 2 –50% Sylmar	Run 3 – 125% Sylmar
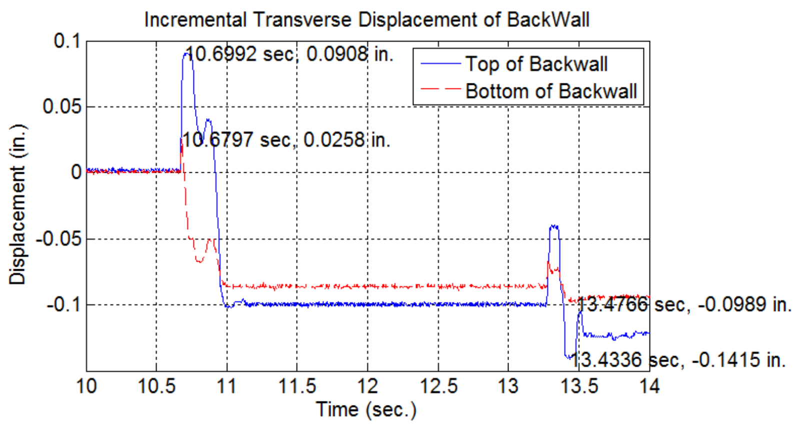	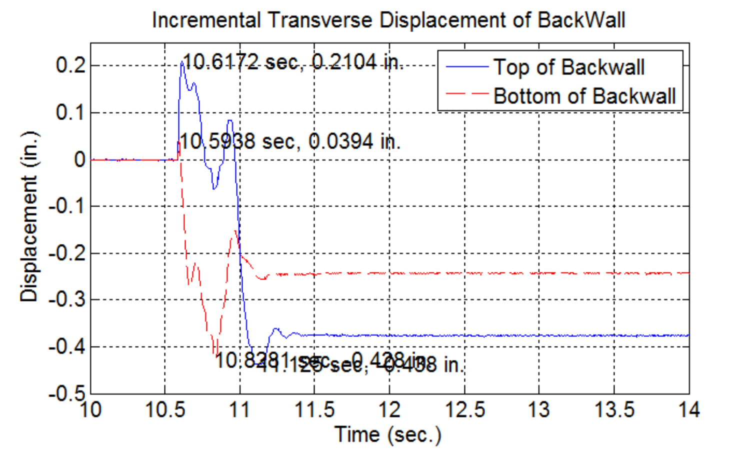
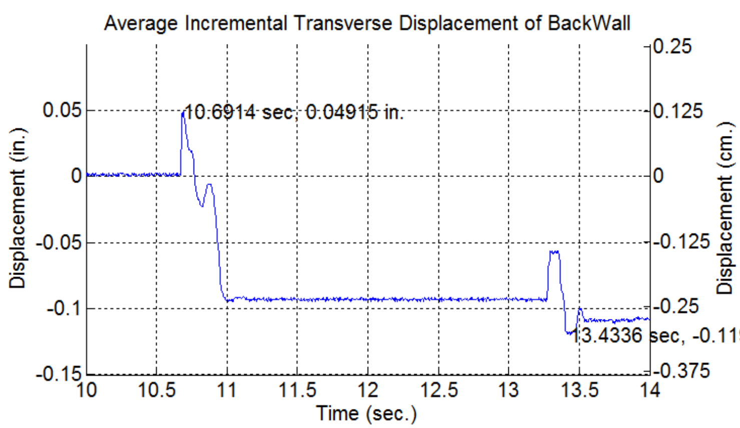	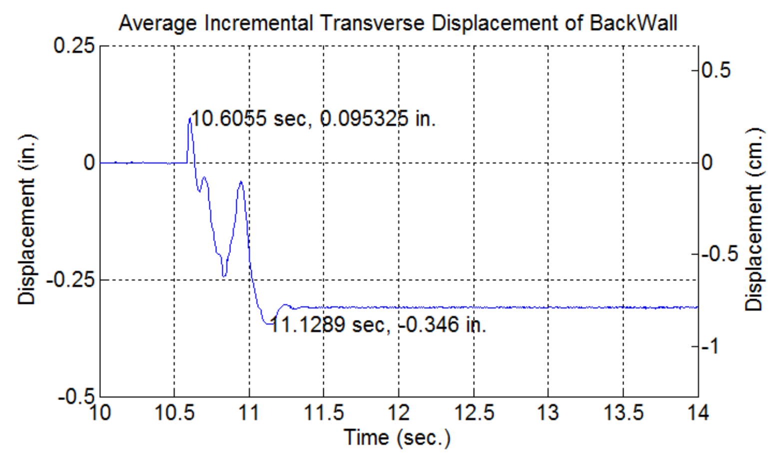

Figure 6-97 Transverse displacement of the backwall western corners for the 45° skew test in Run 2 and 3.

Run 4 – 150% Sylmar	Run 5 – 200% Sylmar

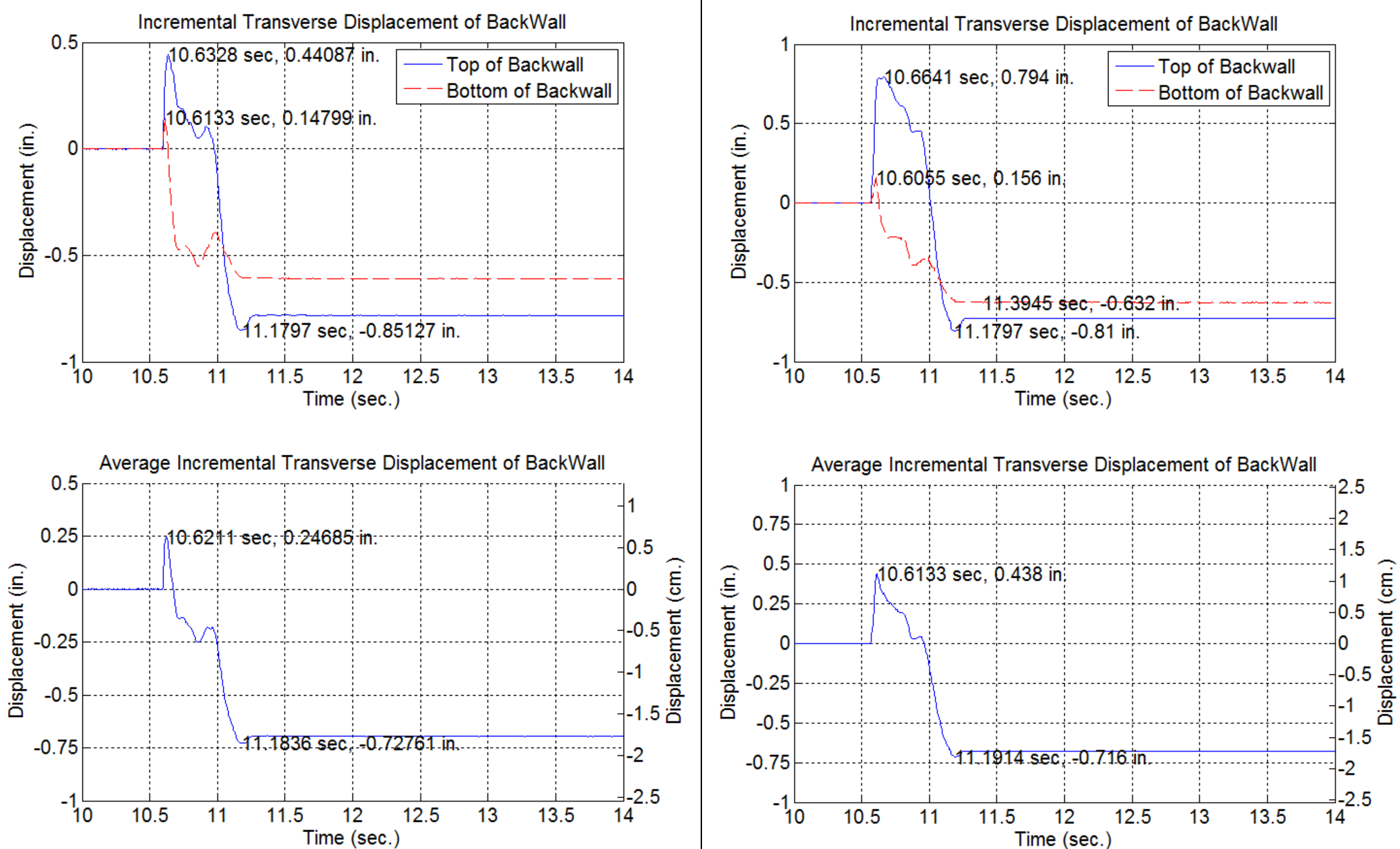

Figure 6-98 Transverse displacement of the backwall western corners for the 45° skew test in Run 4 and 5.

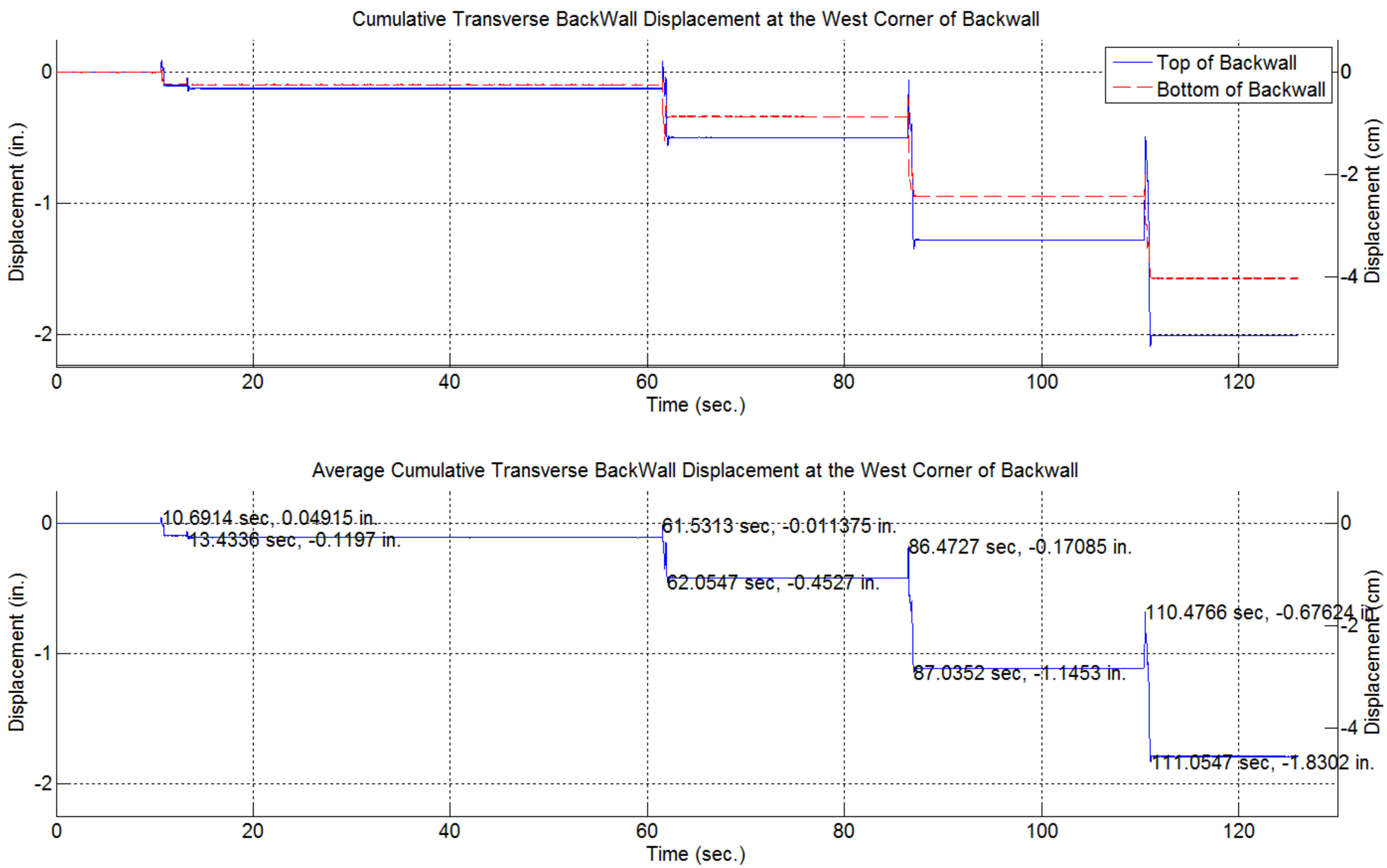

Figure 6-99 Combined transverse displacement of the backwall western corners for the 45° skew test.

Run 2 – 50% Sylmar

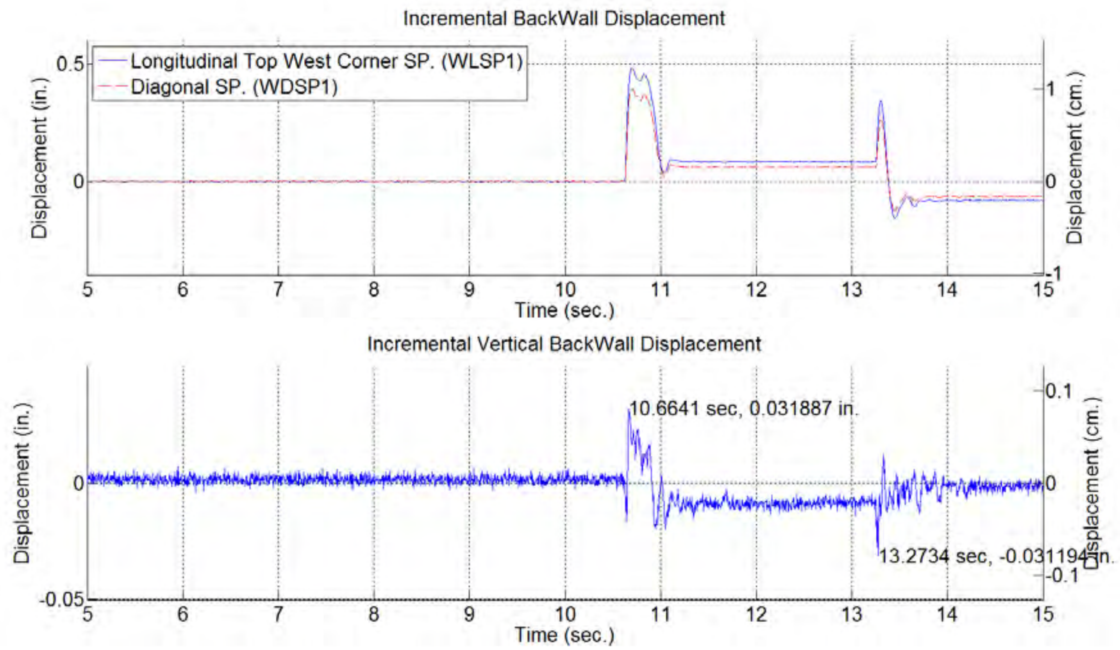

Run 3 – 75% Sylmar

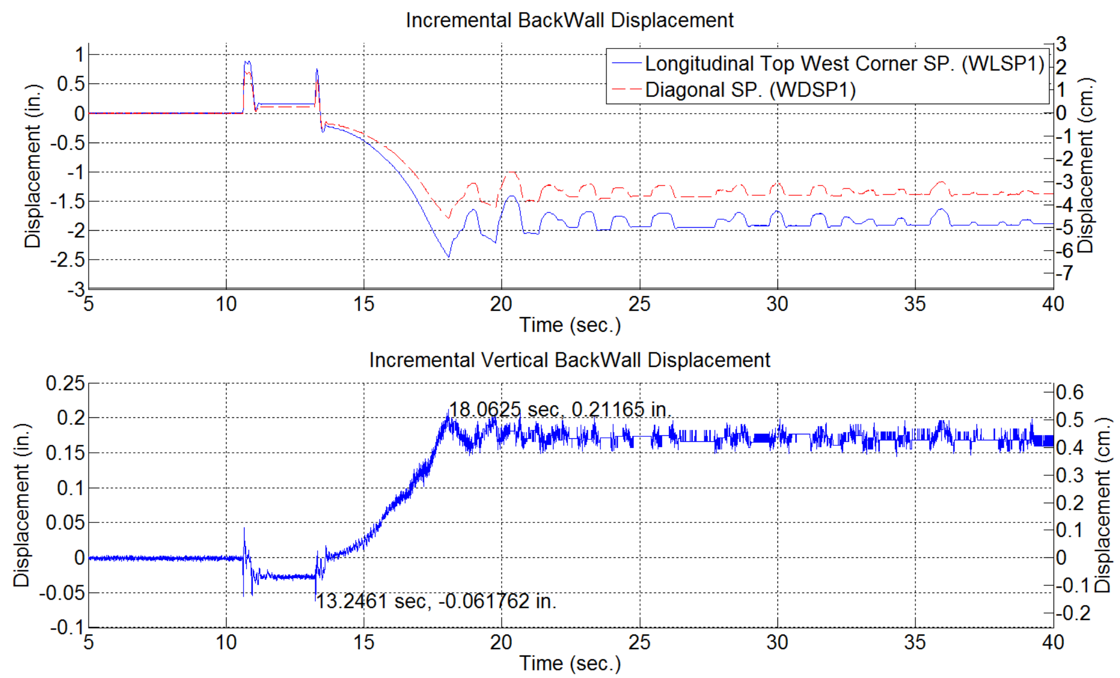

Figure 6-100 Vertical displacement of the backwall for the 0° skew test in Run 2 and 3.

Run 6 – 150% Sylmar

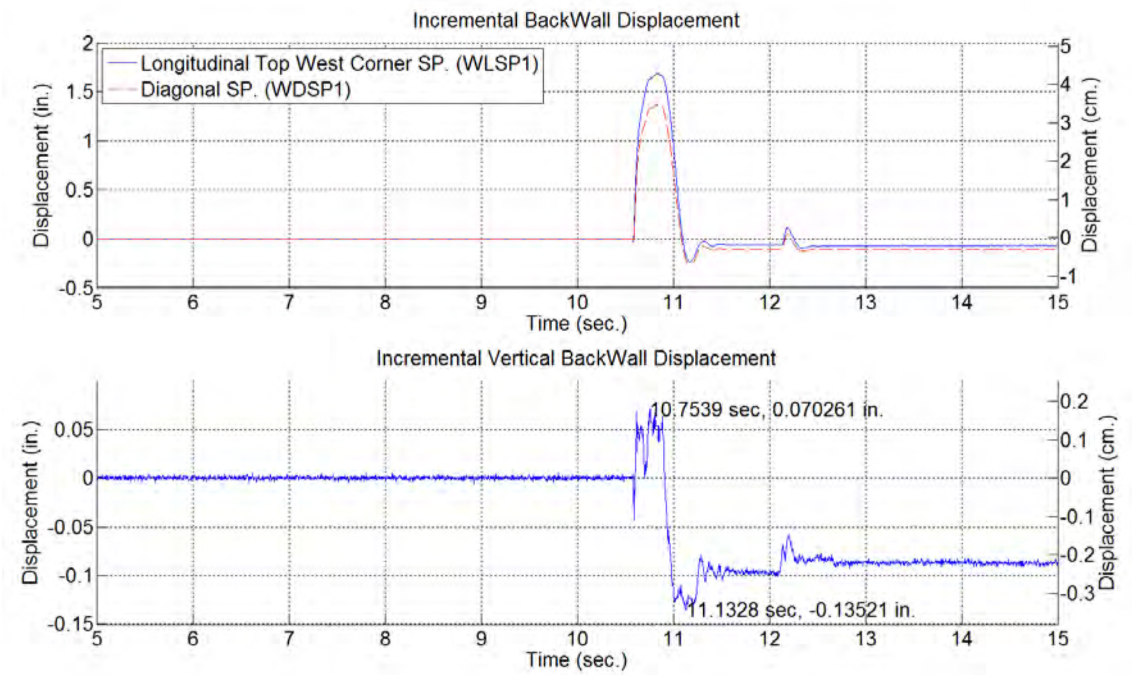

Run 7 – 150% Sylmar

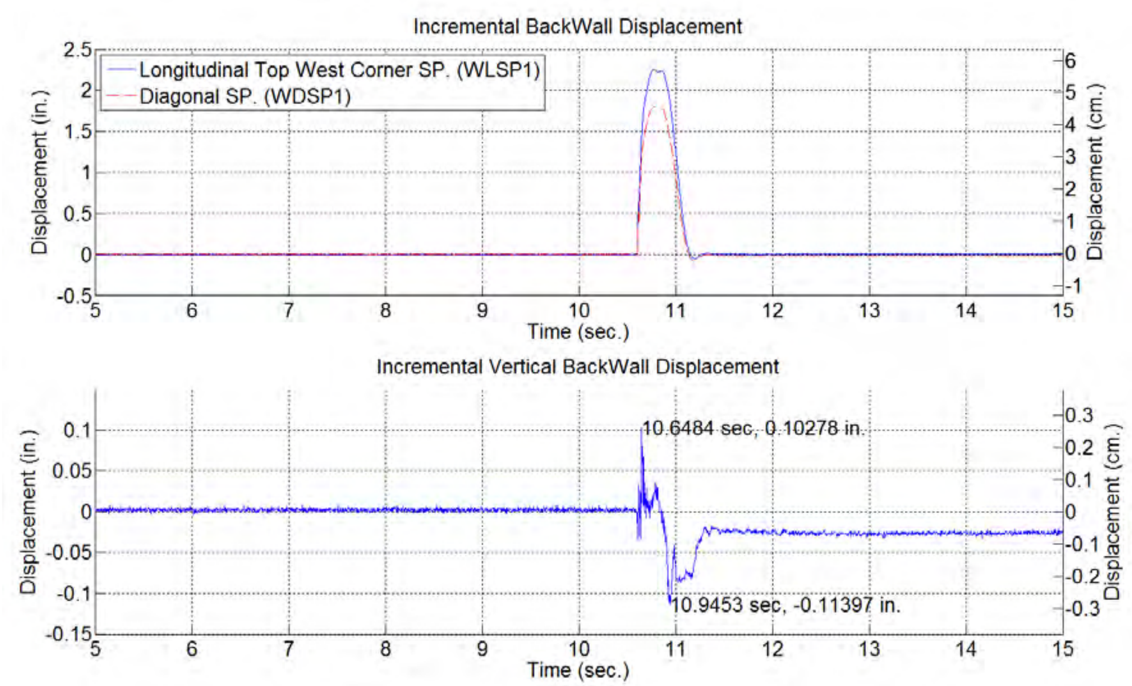

Figure 6-101 Vertical displacement of the backwall for the 0° skew test in Run 6 and 7.

Run 2 – 50% Sylmar

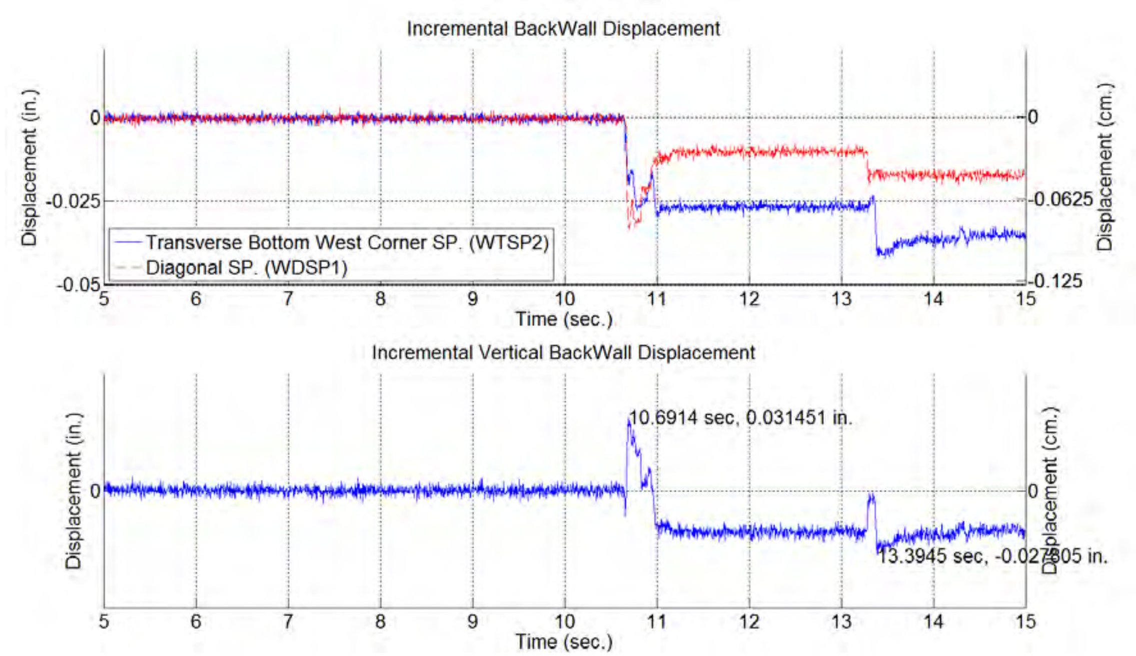

Run 3 – 125% Sylmar

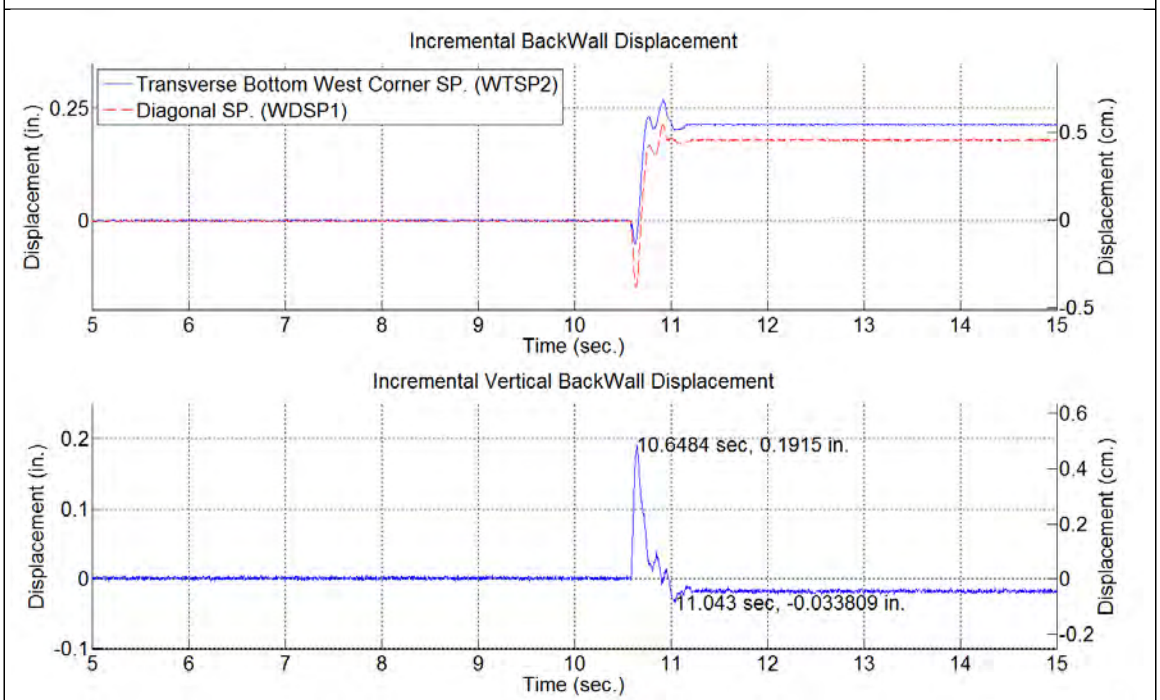

Figure 6-102 Vertical displacement of the backwall for the 30° skew test in Run 2 and 3.

Run 4 – 150% Sylmar

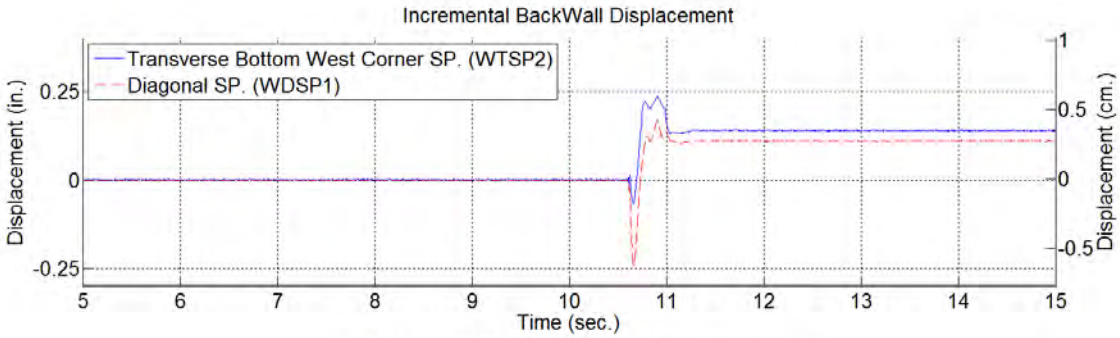

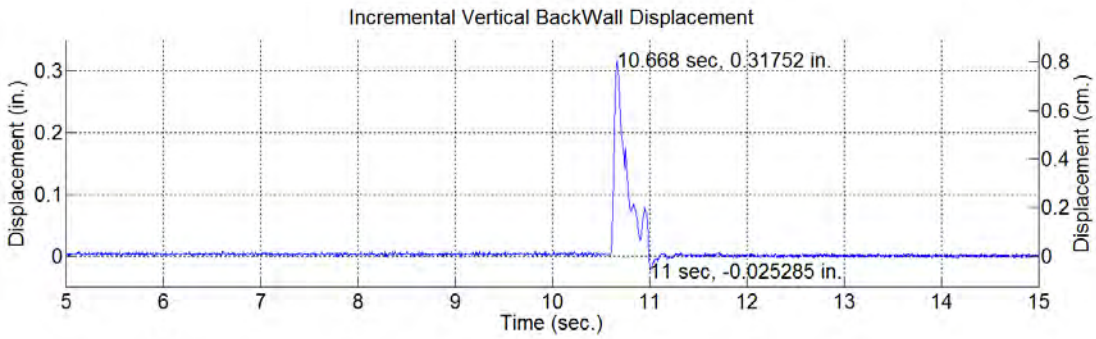

Run 5 – 200% Sylmar

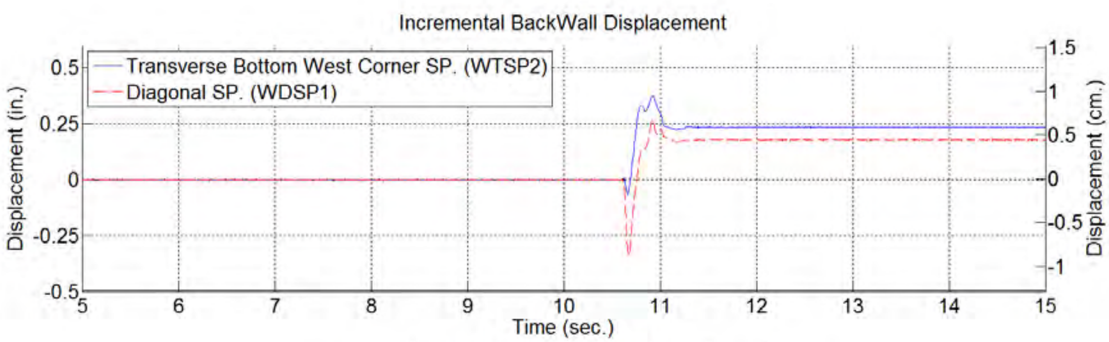

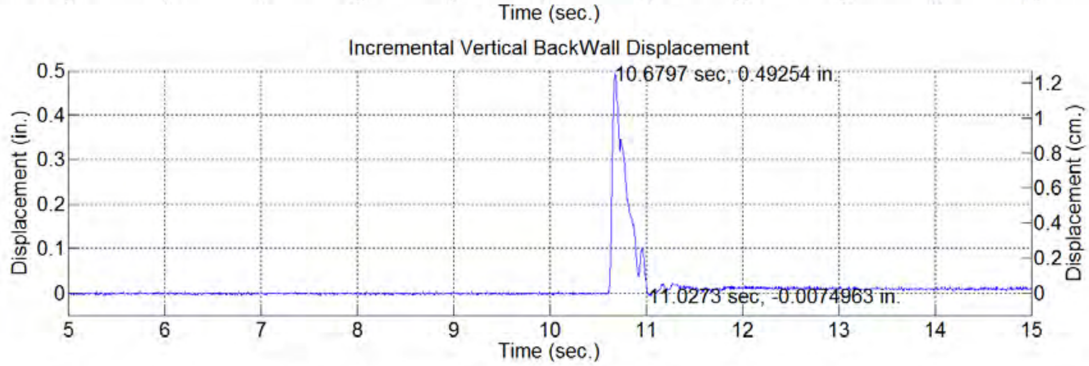

Figure 6-103 Vertical displacement of the backwall for the 30° skew test in Run 4 and 5.

Run 2 – 50% Sylmar

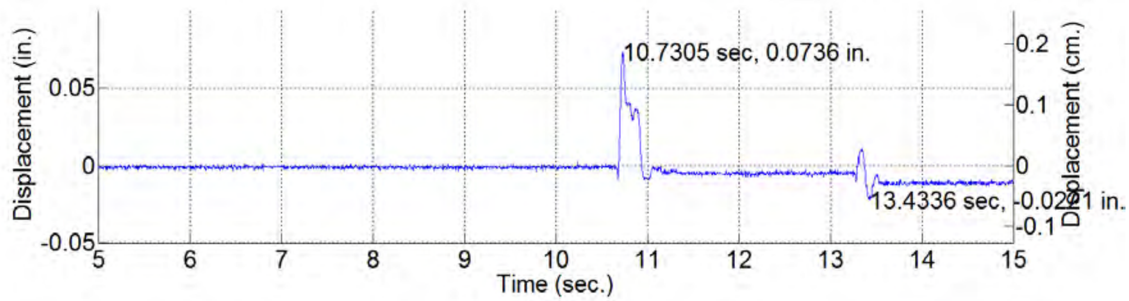

Run 3 – 125% Sylmar

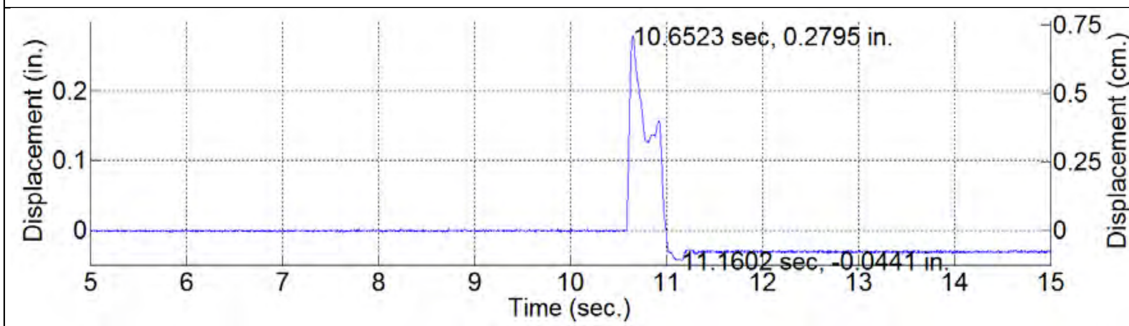

Run 4 – 150% Sylmar

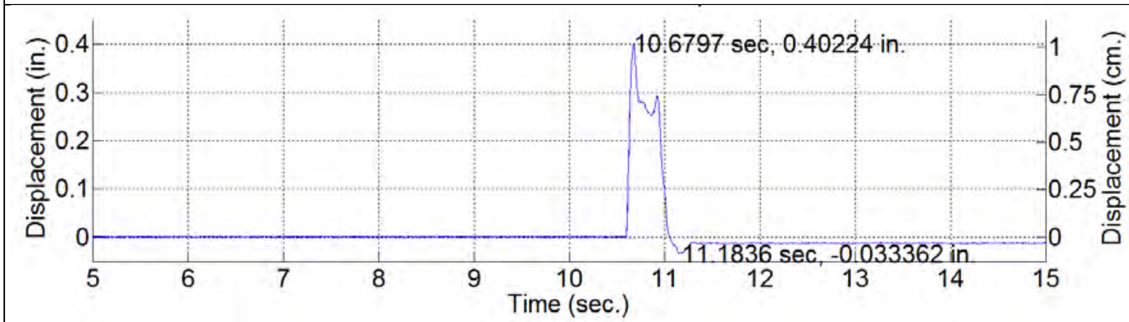

Run 5 – 200% Sylmar

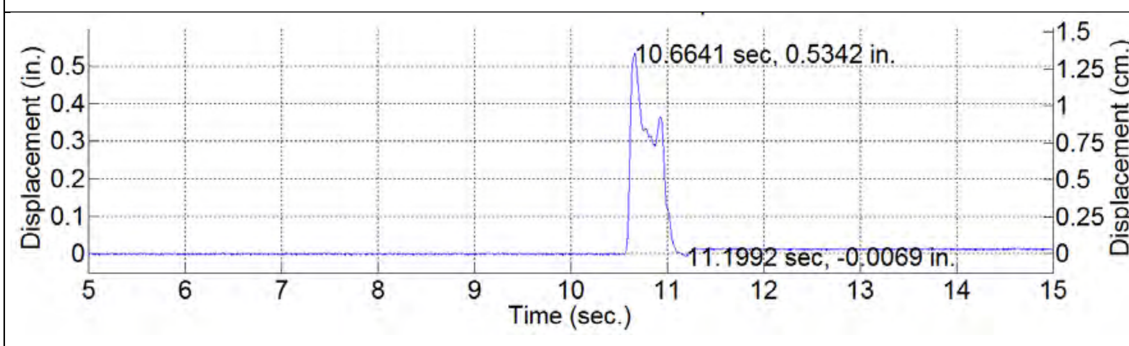

Figure 6-104 Vertical displacement of the backwall for the 45° skew test.

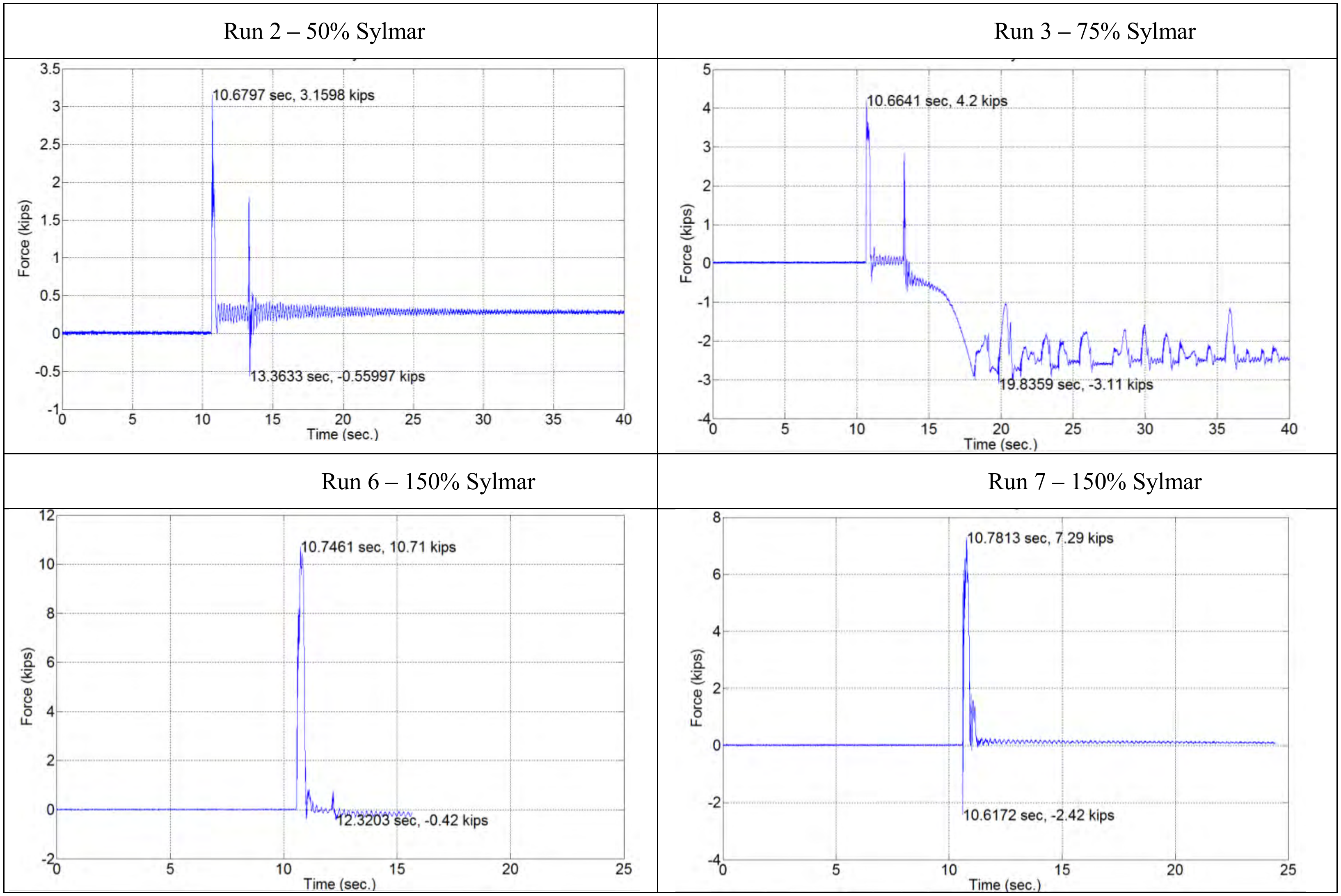

Figure 6-105 Axial force in the backwall restrainer link for the 0° skew test.

Run 2 – 50% Sylmar

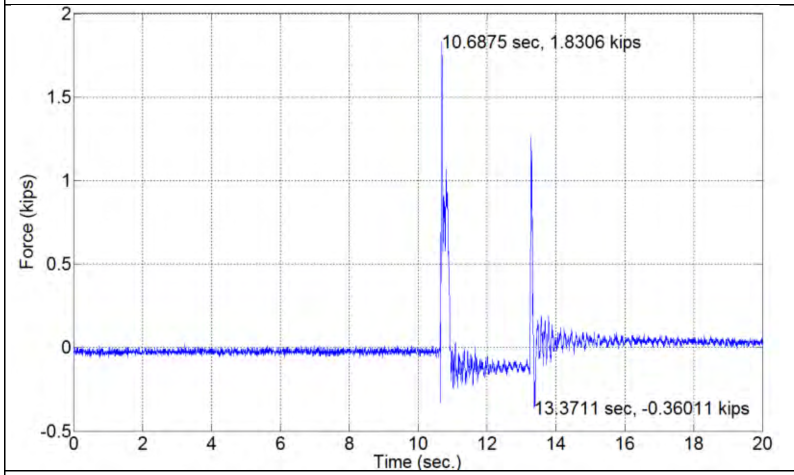

Run 3 – 125% Sylmar

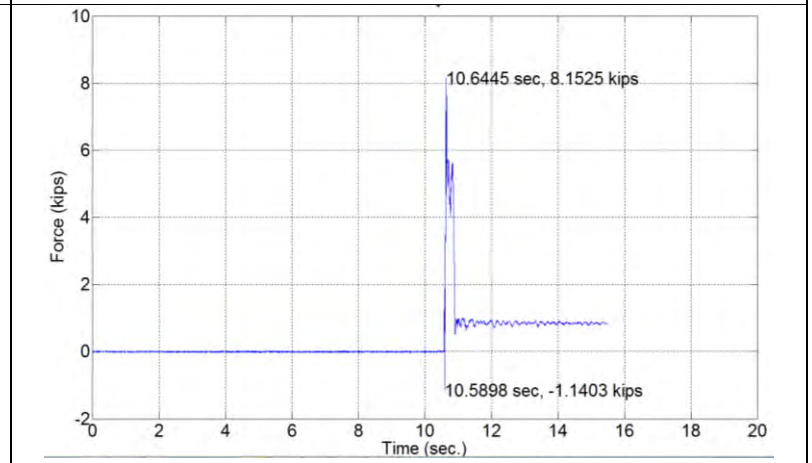

Run 4 – 150% Sylmar

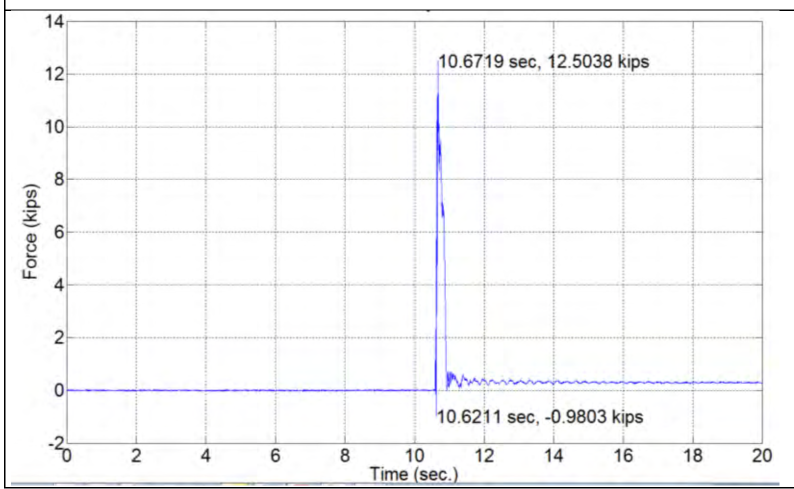

Run 5 – 200% Sylmar

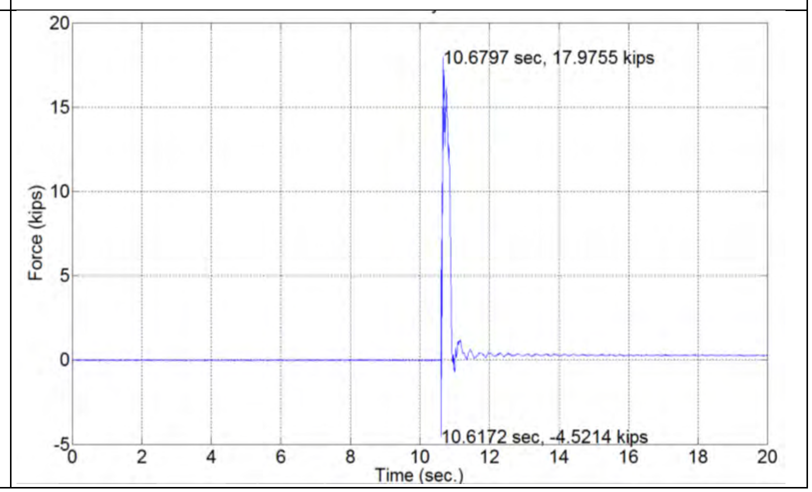

Figure 6-106 Axial force in the backwall restrainer link for the 30° skew test.

Run 2 – 50% Sylmar	Run 3 – 125% Sylmar
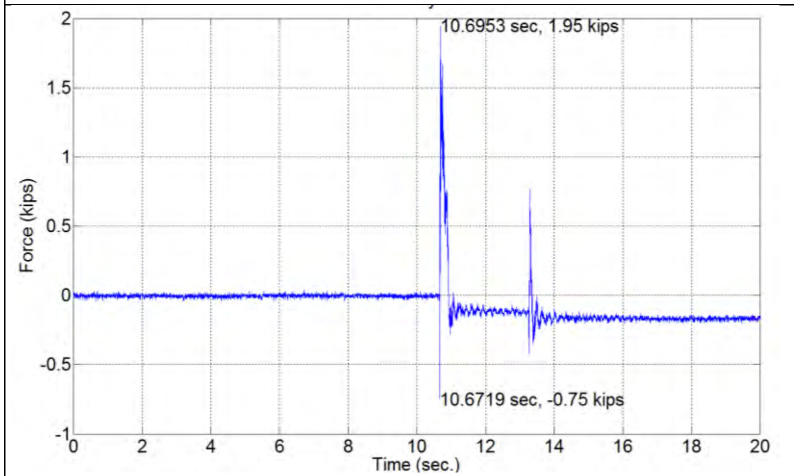	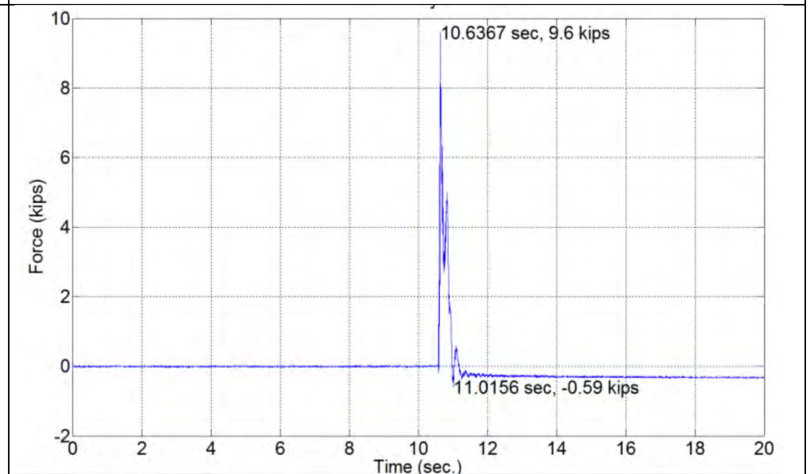
Run 4 – 150% Sylmar	**Run 5 – 200% Sylmar**
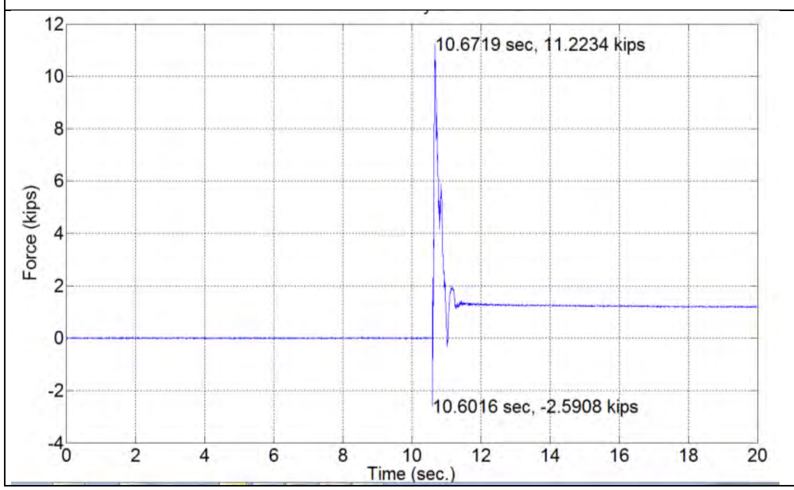	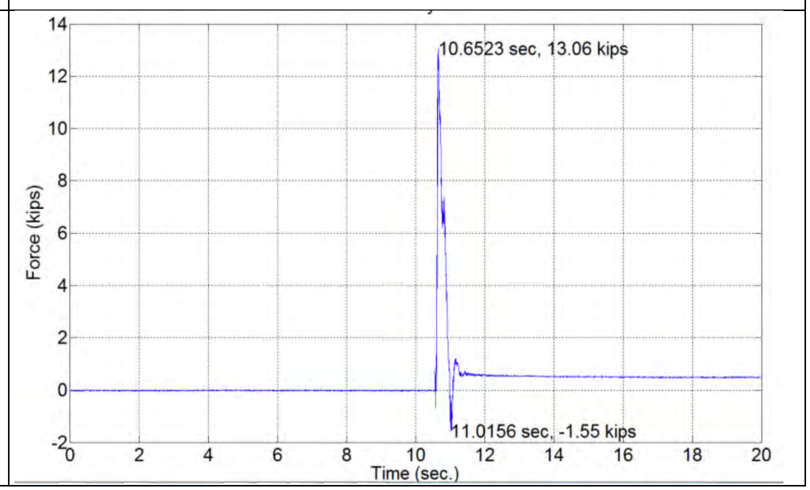

Figure 6-107 Axial force in the backwall restrainer link for the 45° skew test.

Run 2 –50% Sylmar

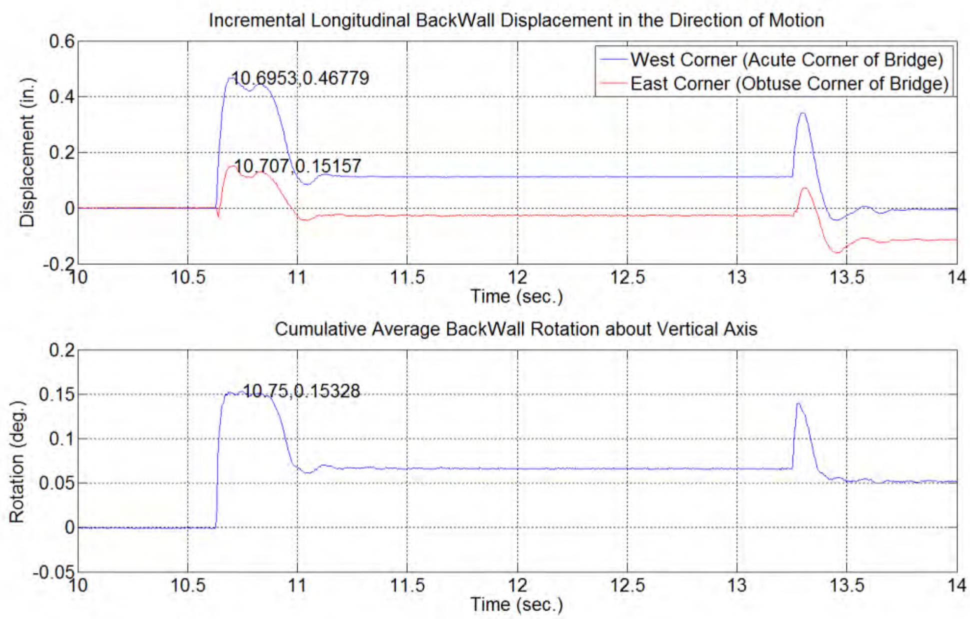

Run 3 – 75% Sylmar

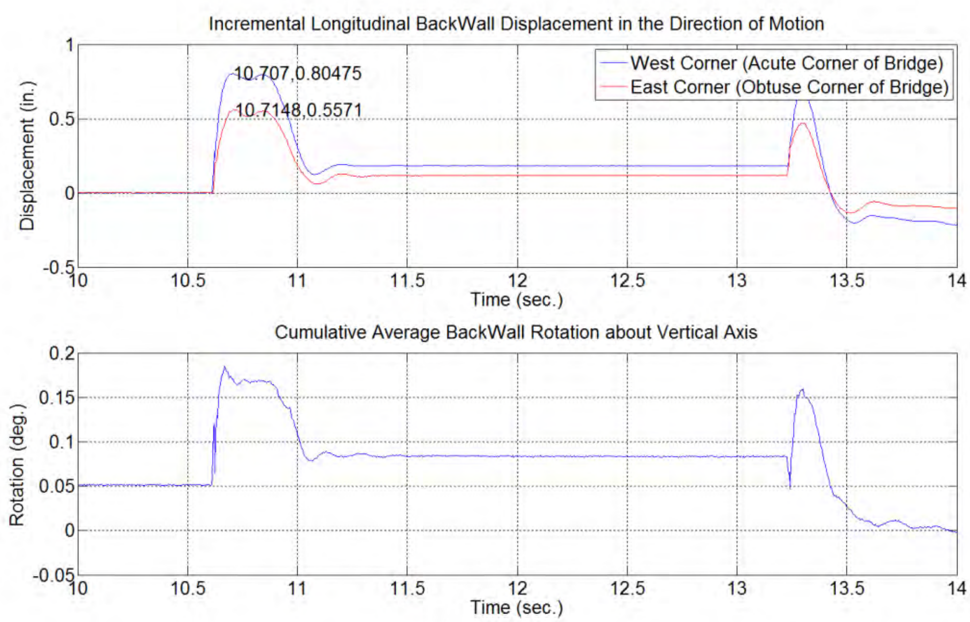

Figure 6-108 Backwall rotation about the vertical axis for the 0° skew test in Run 2 and 3.

Run 6 – 150% Sylmar

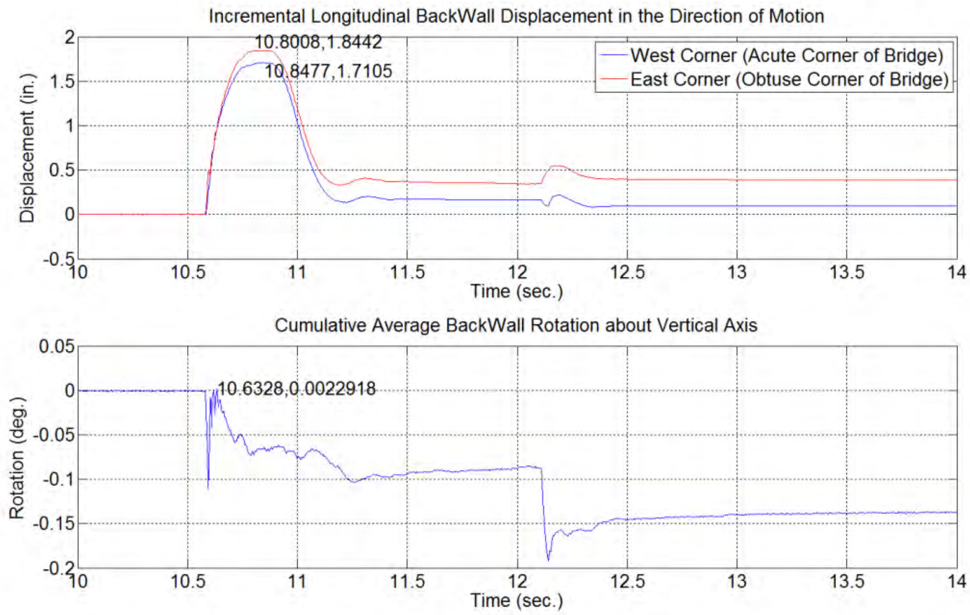

Run 7 – 150% Sylmar

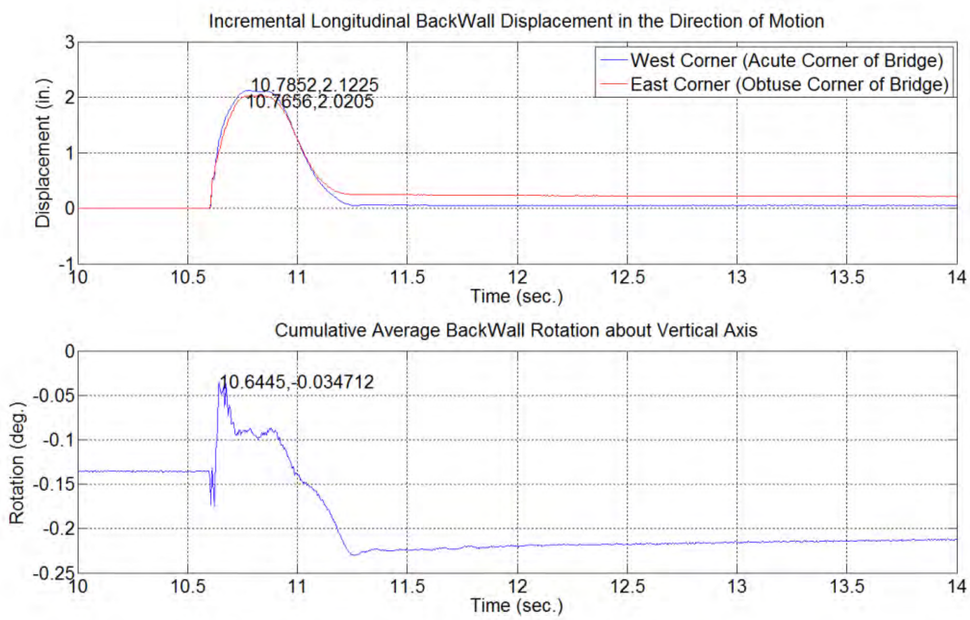

Figure 6-109 Backwall rotation about the vertical axis for the 0° skew test in Run 6 and 7.

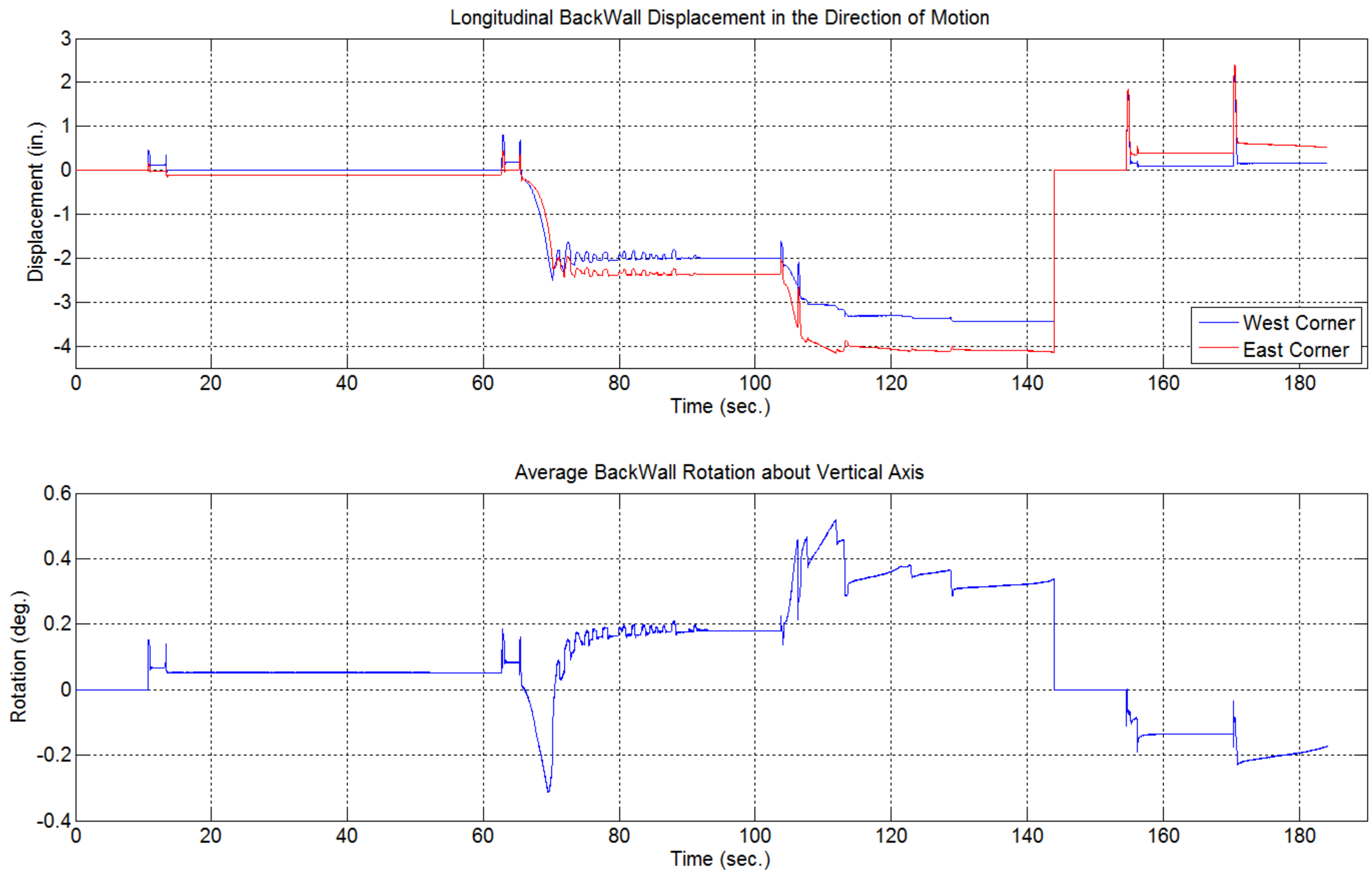

Figure 6-110 Combined backwall rotation about the vertical axis for the 0° skew test.

Run 2 –50% Sylmar

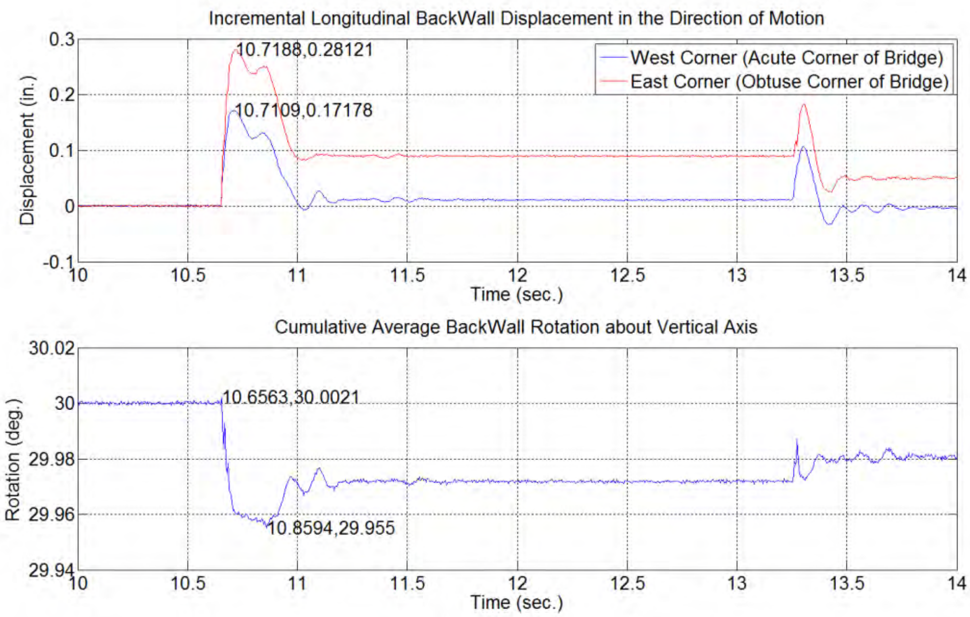

Run 3 – 125% Sylmar

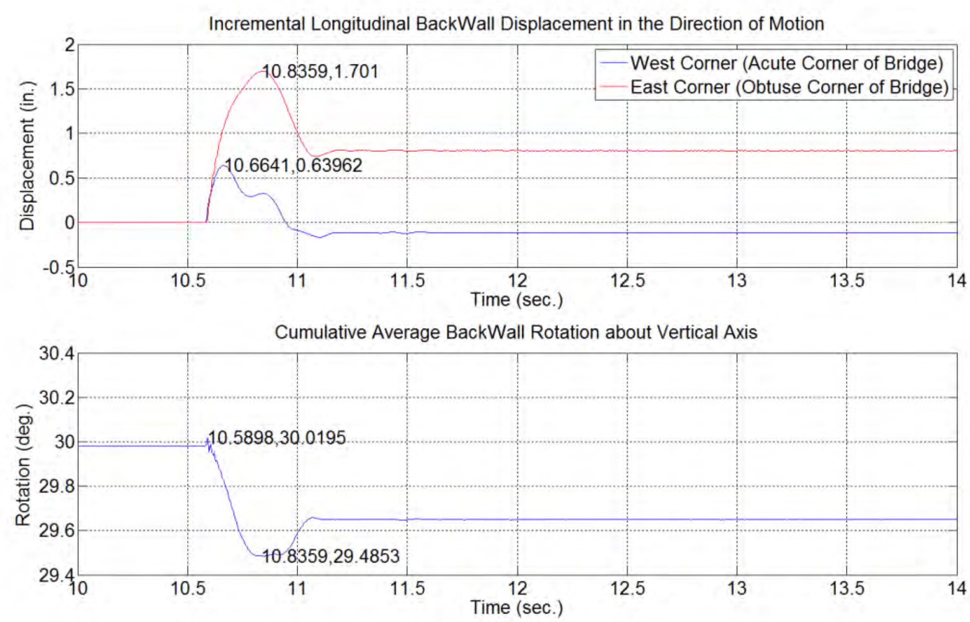

Figure 6-111 Backwall rotation about the vertical axis for the 30° skew test in Run 2 and 3.

Run 4 – 150% Sylmar

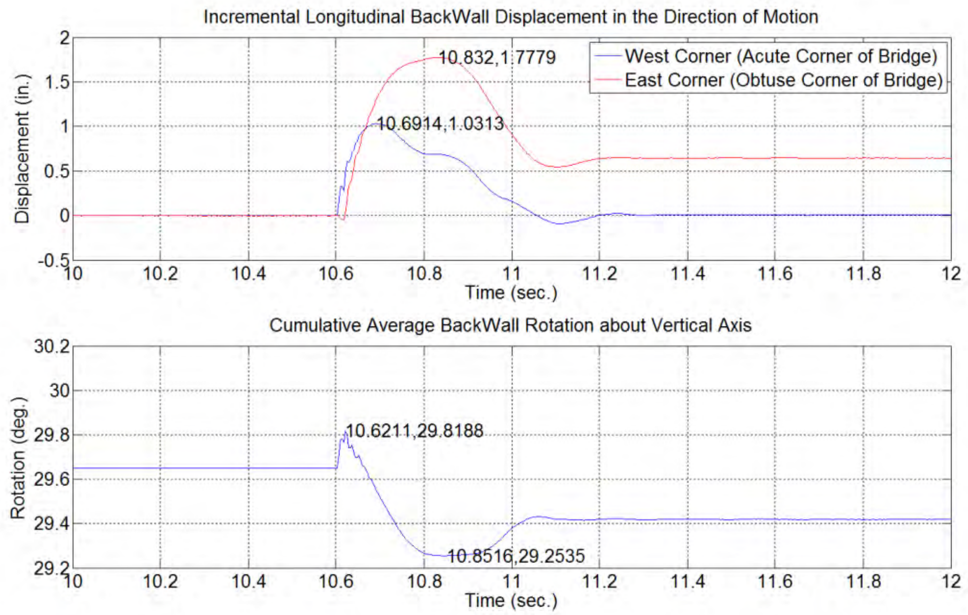

Run 5 – 200% Sylmar

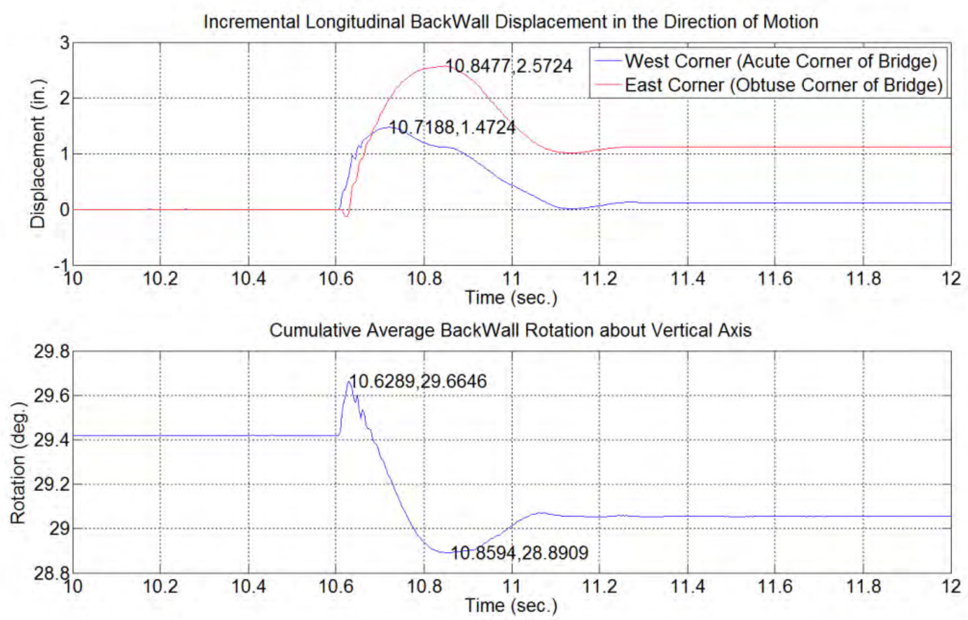

Figure 6-112 Backwall rotation about the vertical axis for the 30° skew test in Run 4 and 5.

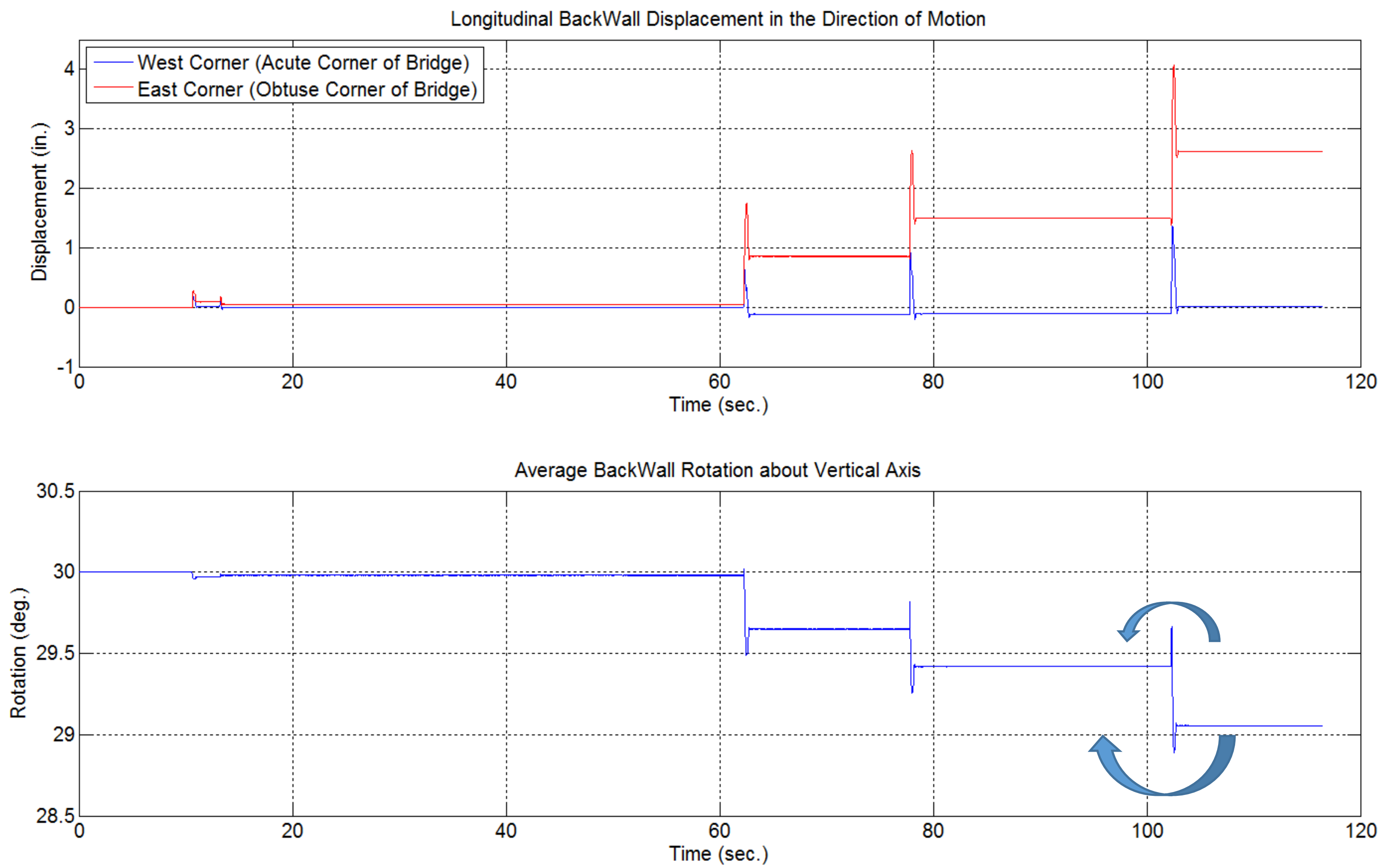

Figure 6-113 Combined backwall rotation about the vertical axis for the 30° skew test.

Run 2 –50% Sylmar

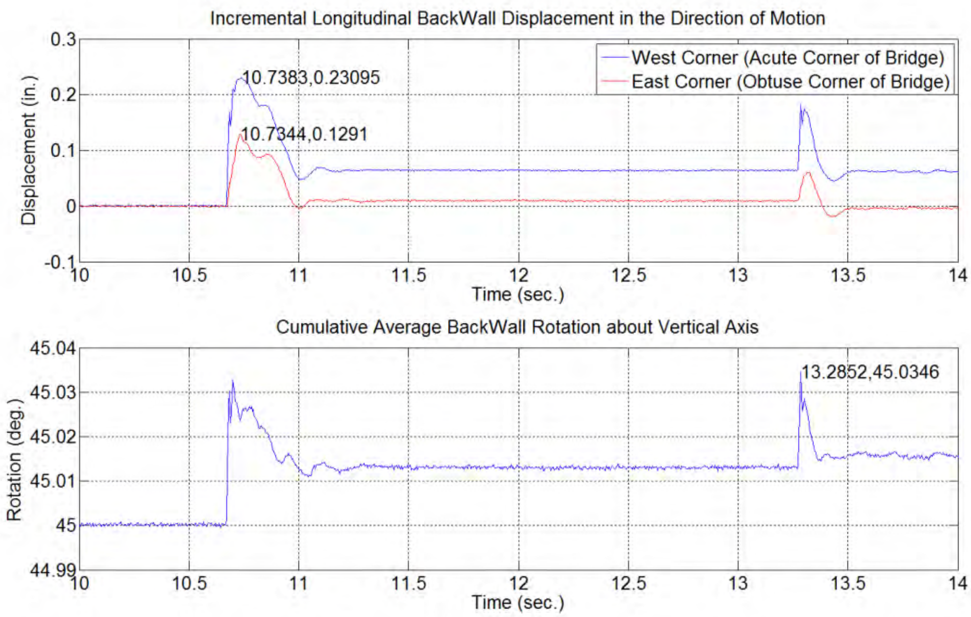

Run 3 – 125% Sylmar

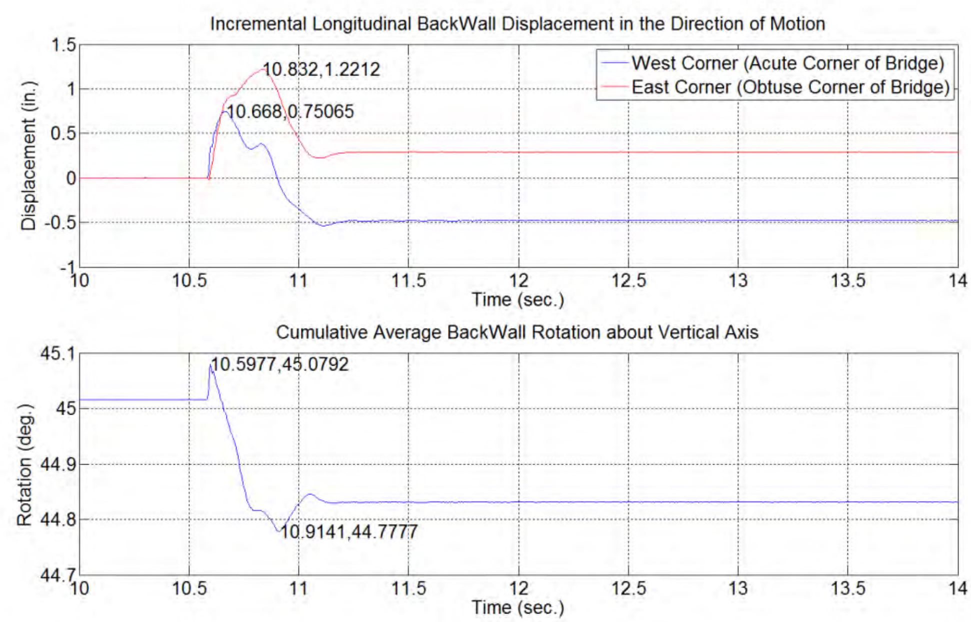

Figure 6-114 Backwall rotation about the vertical axis for the 45° skew test in Run 2 and 3.

Run 4 – 150% Sylmar

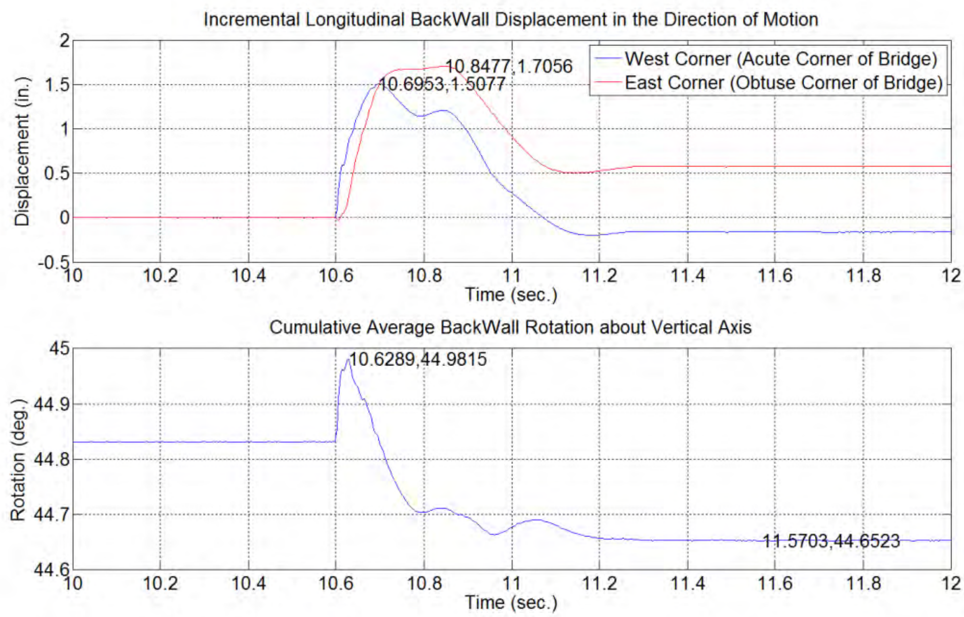

Run 5 – 200% Sylmar

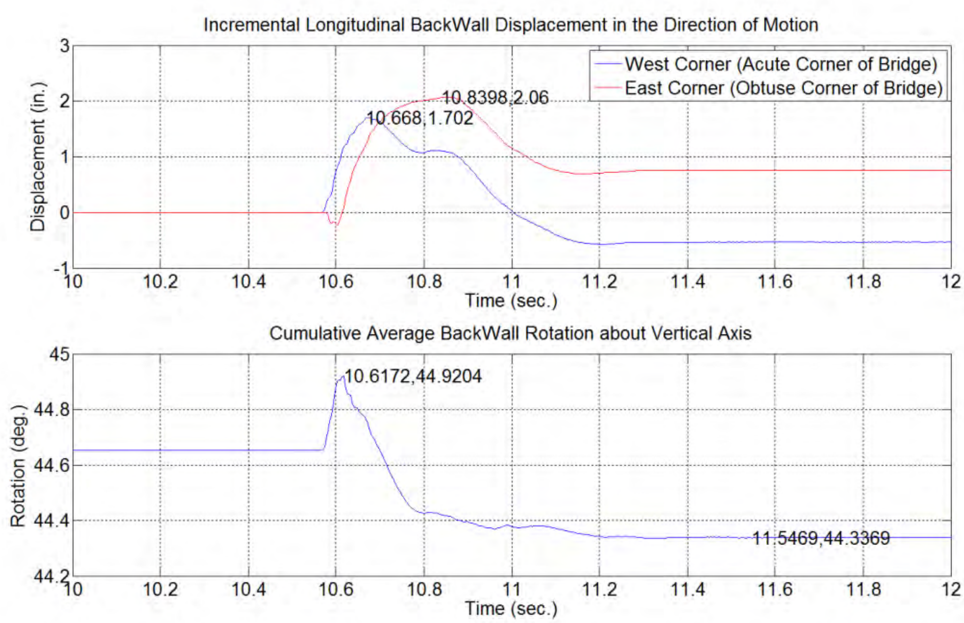

Figure 6-115 Backwall rotation about the vertical axis for the 45° skew test in Run 4 and 5.

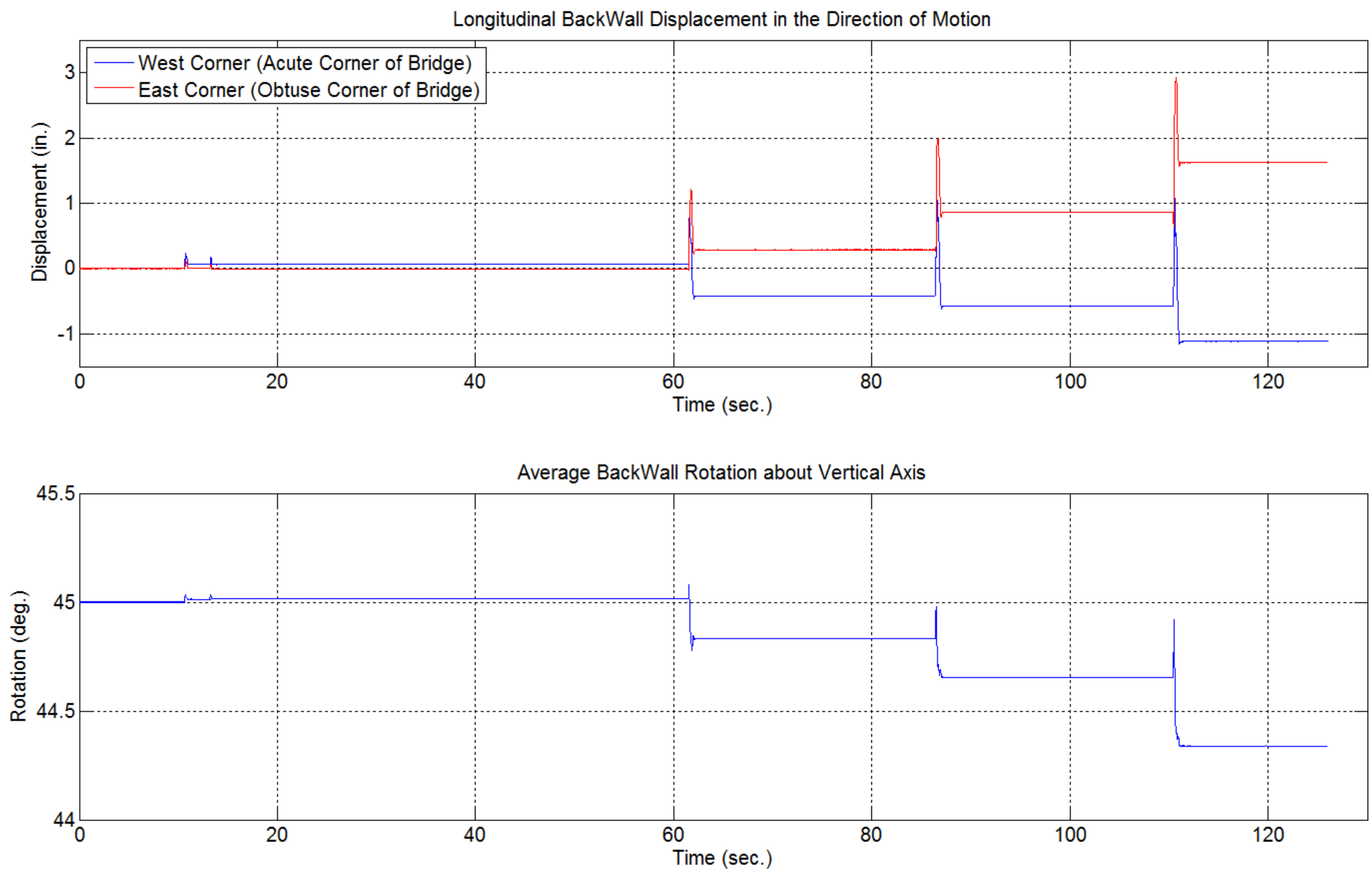

Figure 6-116 Combined backwall rotation about the vertical axis for the 45° skew test.

Run 2 –50% Sylmar

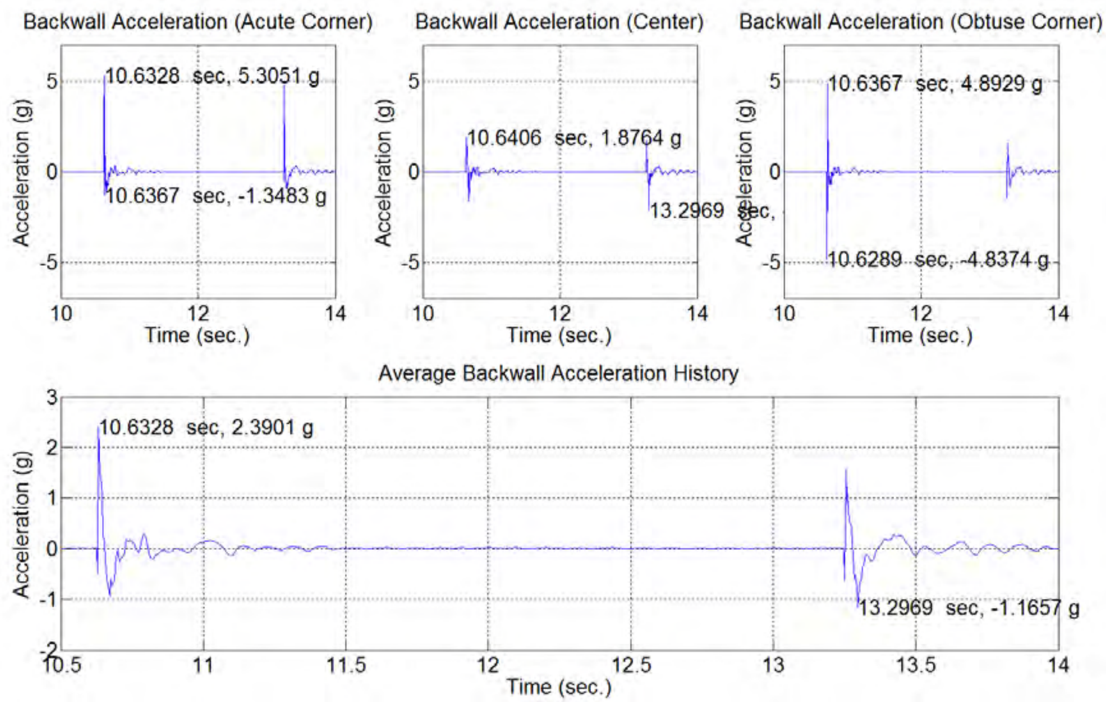

Run 3 – 75% Sylmar

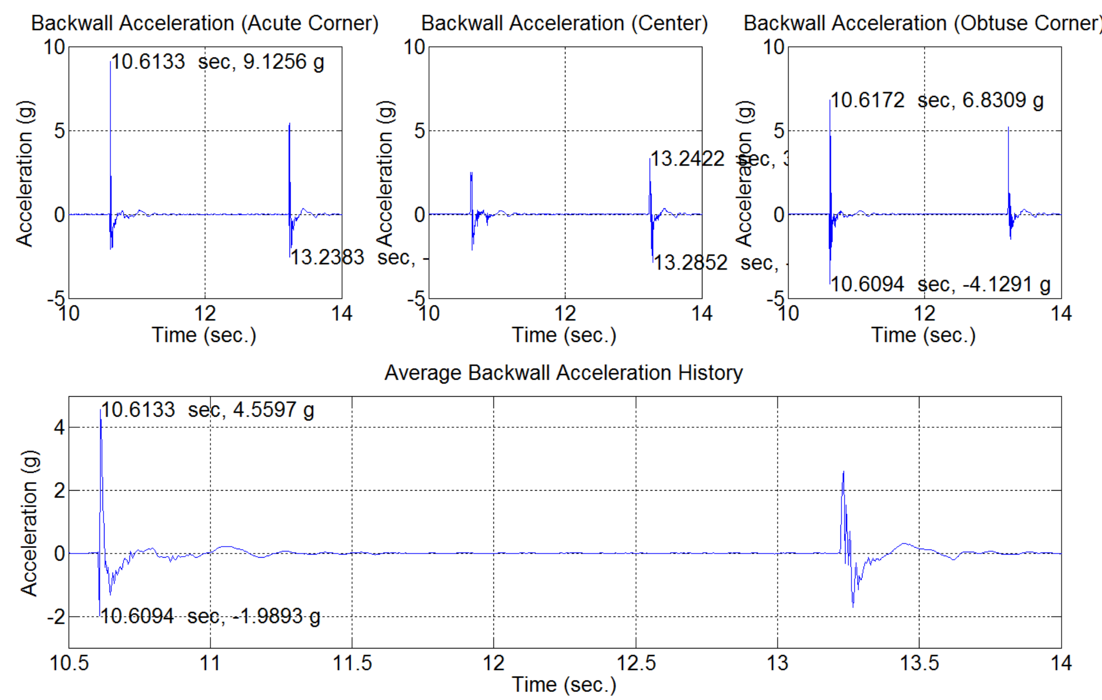

Figure 6-117 Longitudinal acceleration of the backwall for the 0° skew test in Run 2 and 3.

Run 6 – 150% Sylmar

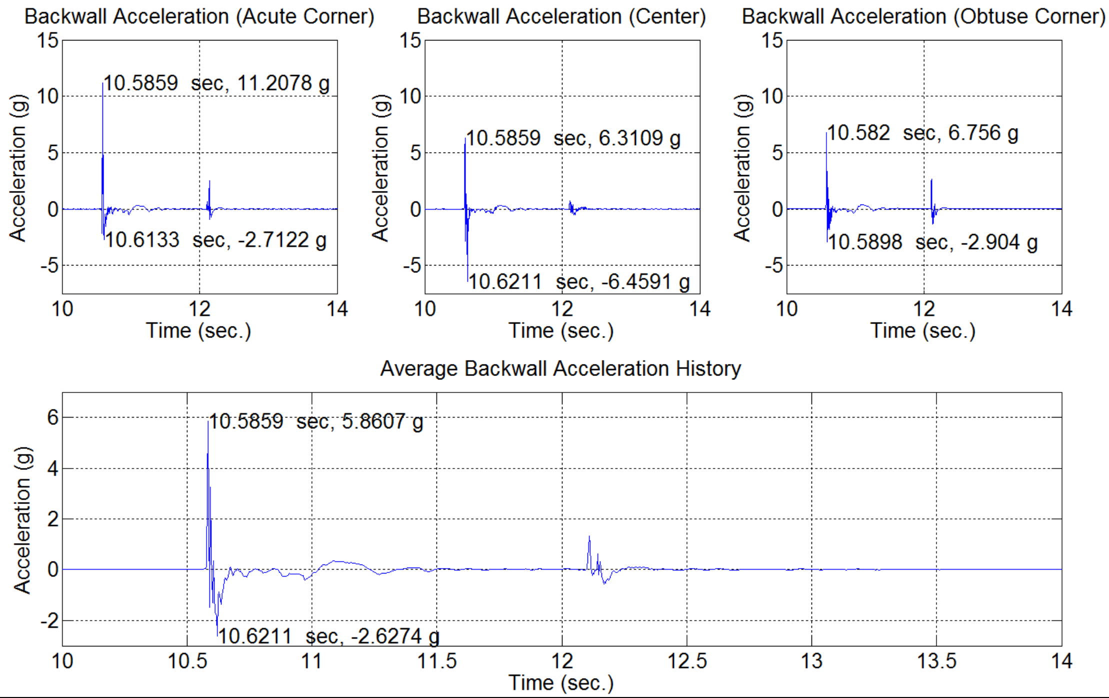

Run 7 – 150% Sylmar

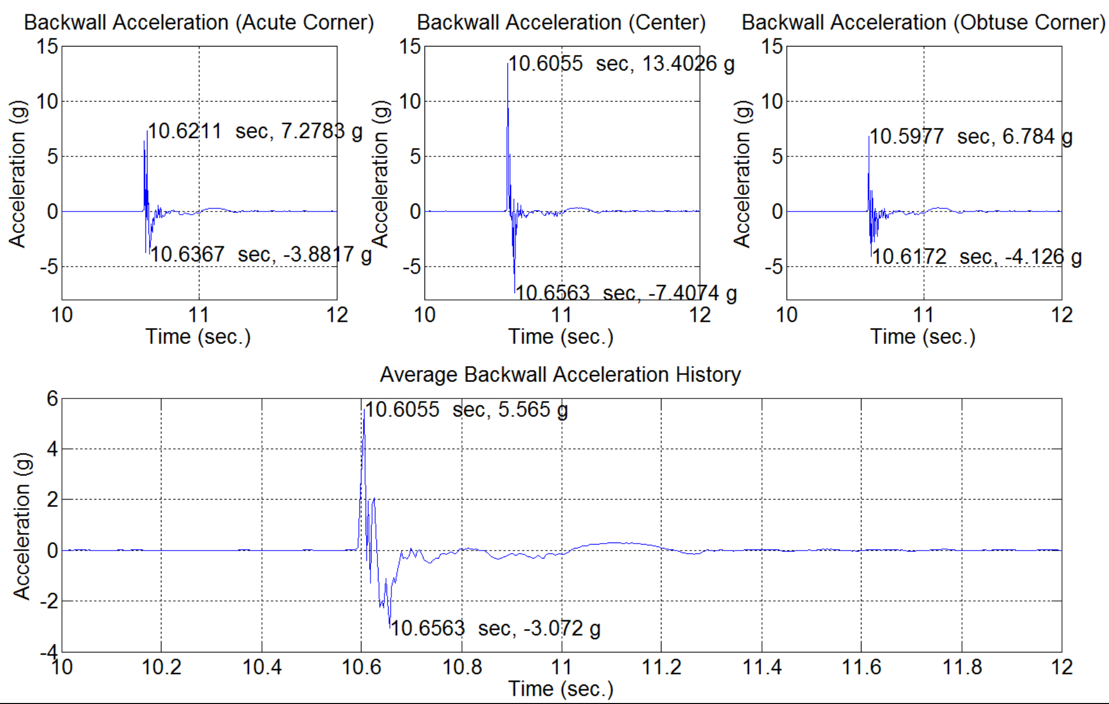

Figure 6-118 Longitudinal acceleration of the backwall for the 0° skew test in Run 6 and 7.

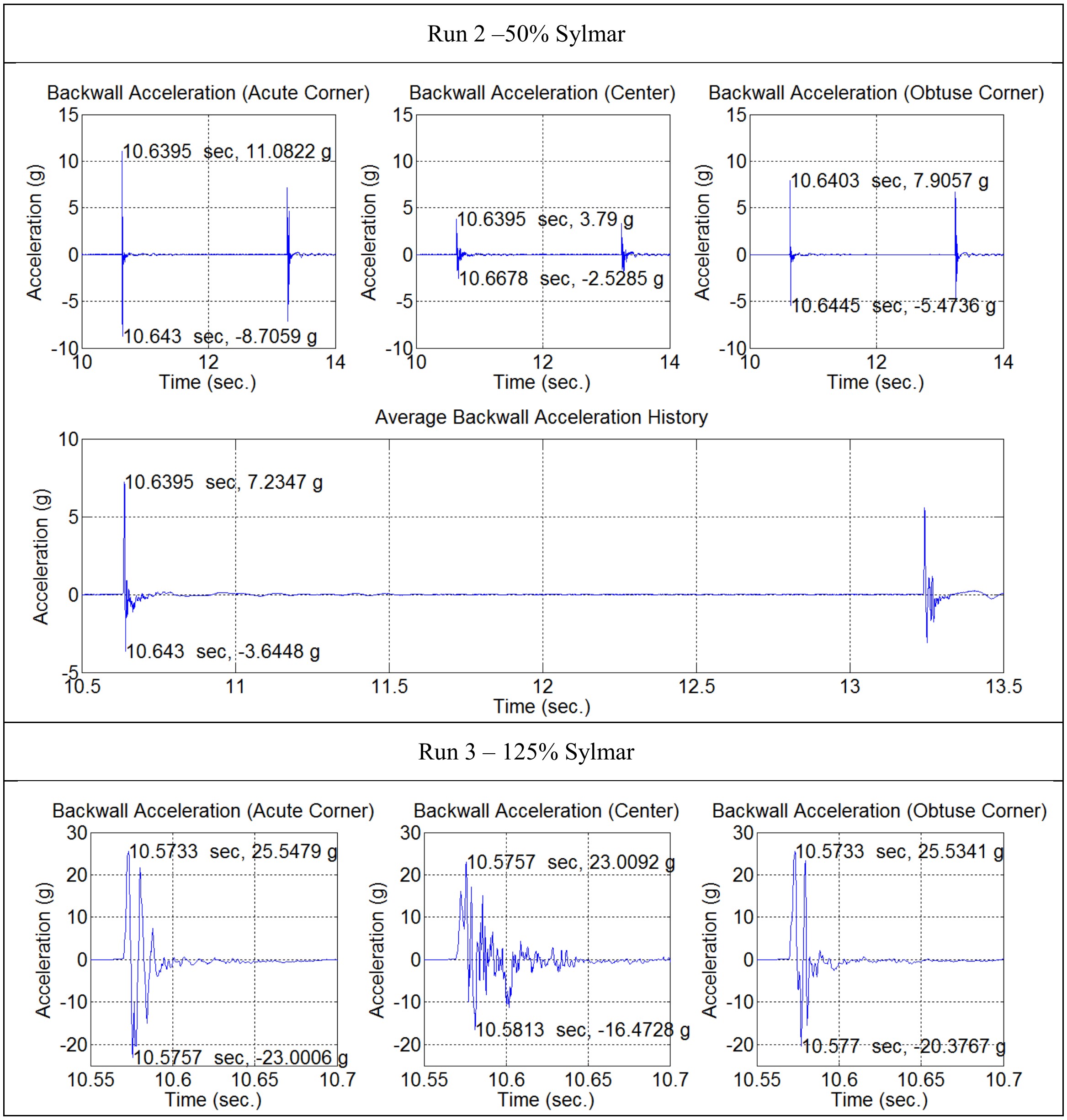

Figure 6-119 Longitudinal acceleration of the backwall for the 30° skew test in Run 2 and 3.

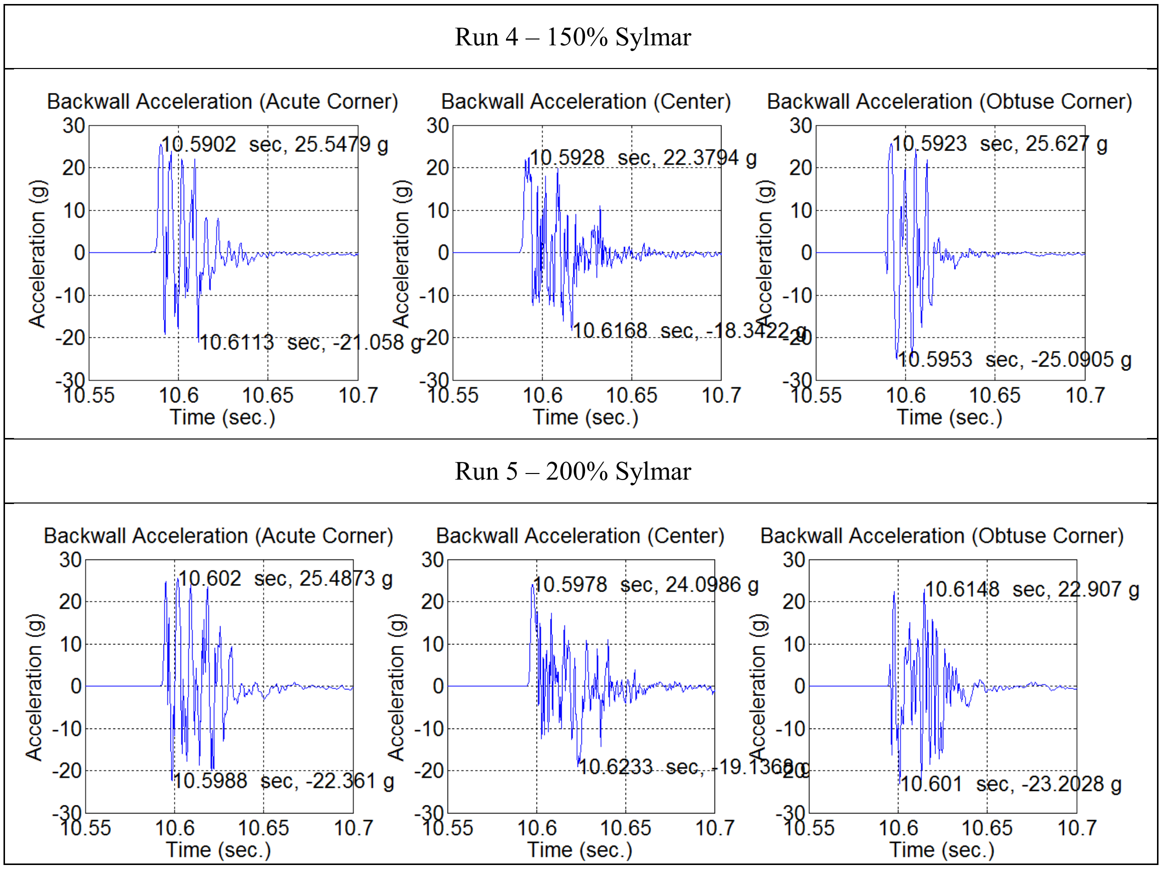

Figure 6-120 Longitudinal acceleration of the backwall for the 30° skew test in Run 4 and 5.

Run 2 –50% Sylmar

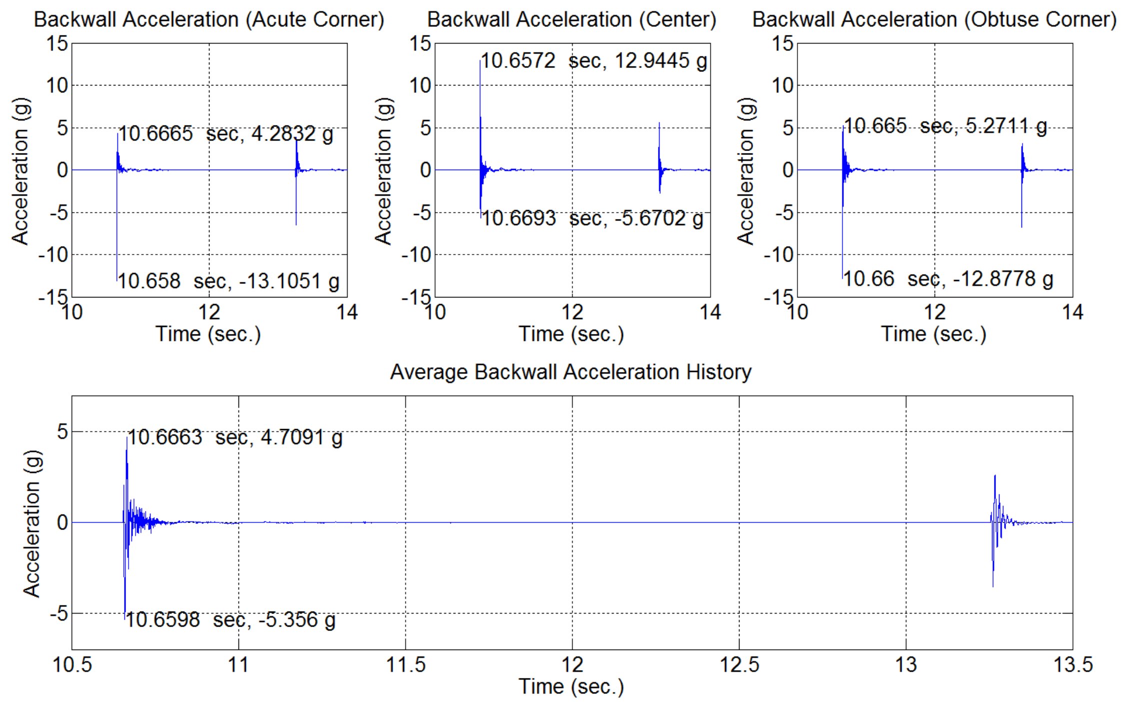

Run 3 – 125% Sylmar

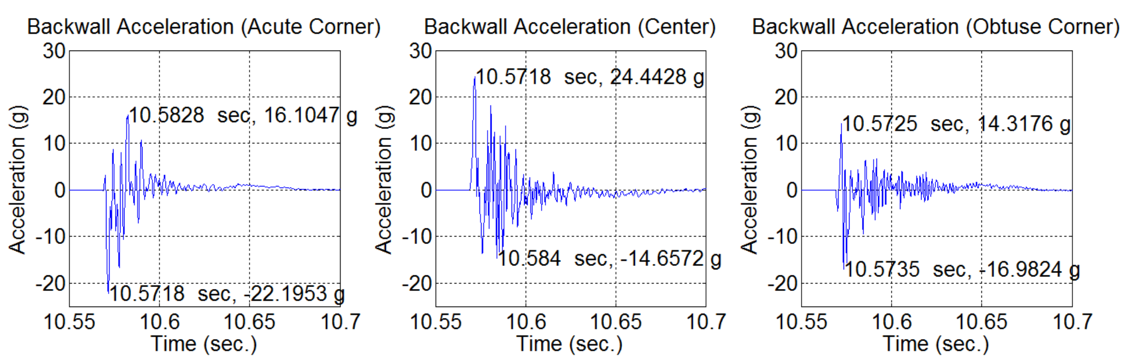

Figure 6-121 Longitudinal acceleration of the backwall for the 45° skew test in Run 2 and 3.

Run 4 – 150% Sylmar

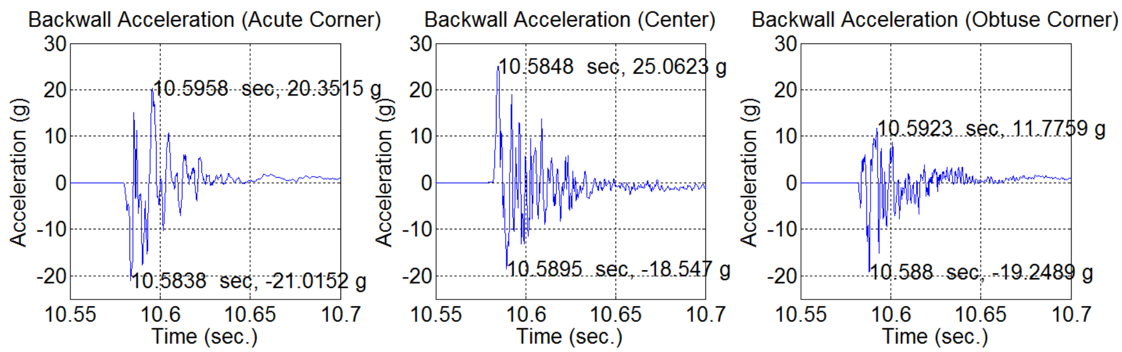

Run 5 – 200% Sylmar

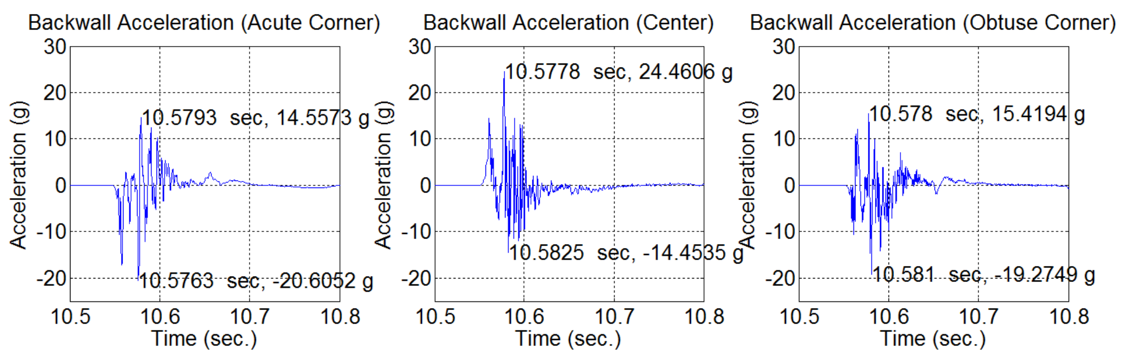

Figure 6-122 Longitudinal acceleration of the backwall for the 45° skew test in Run 4 and 5.

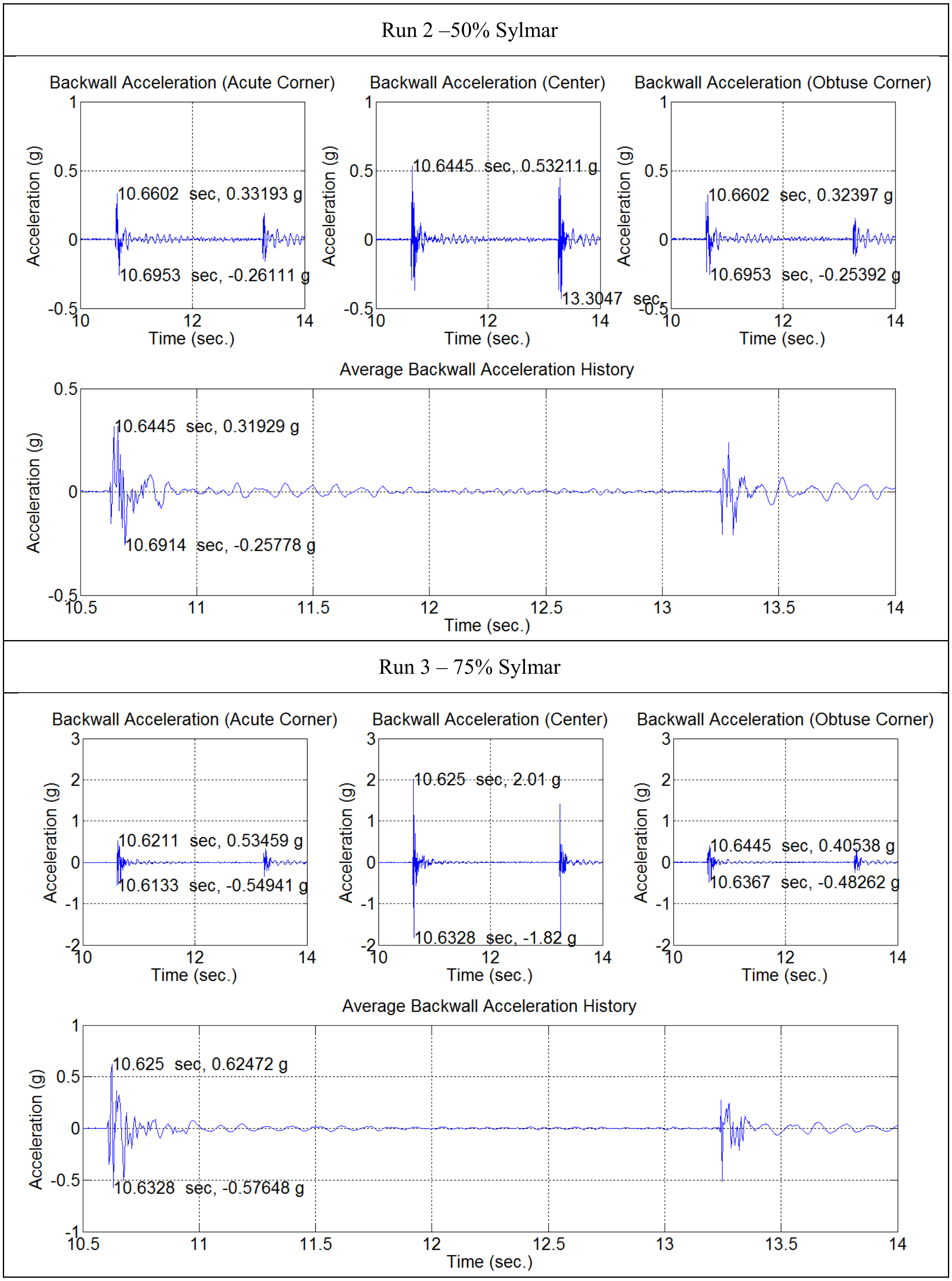

Figure 6-123 Transverse acceleration of the backwall for the 0° skew test in Run 2 and 3.

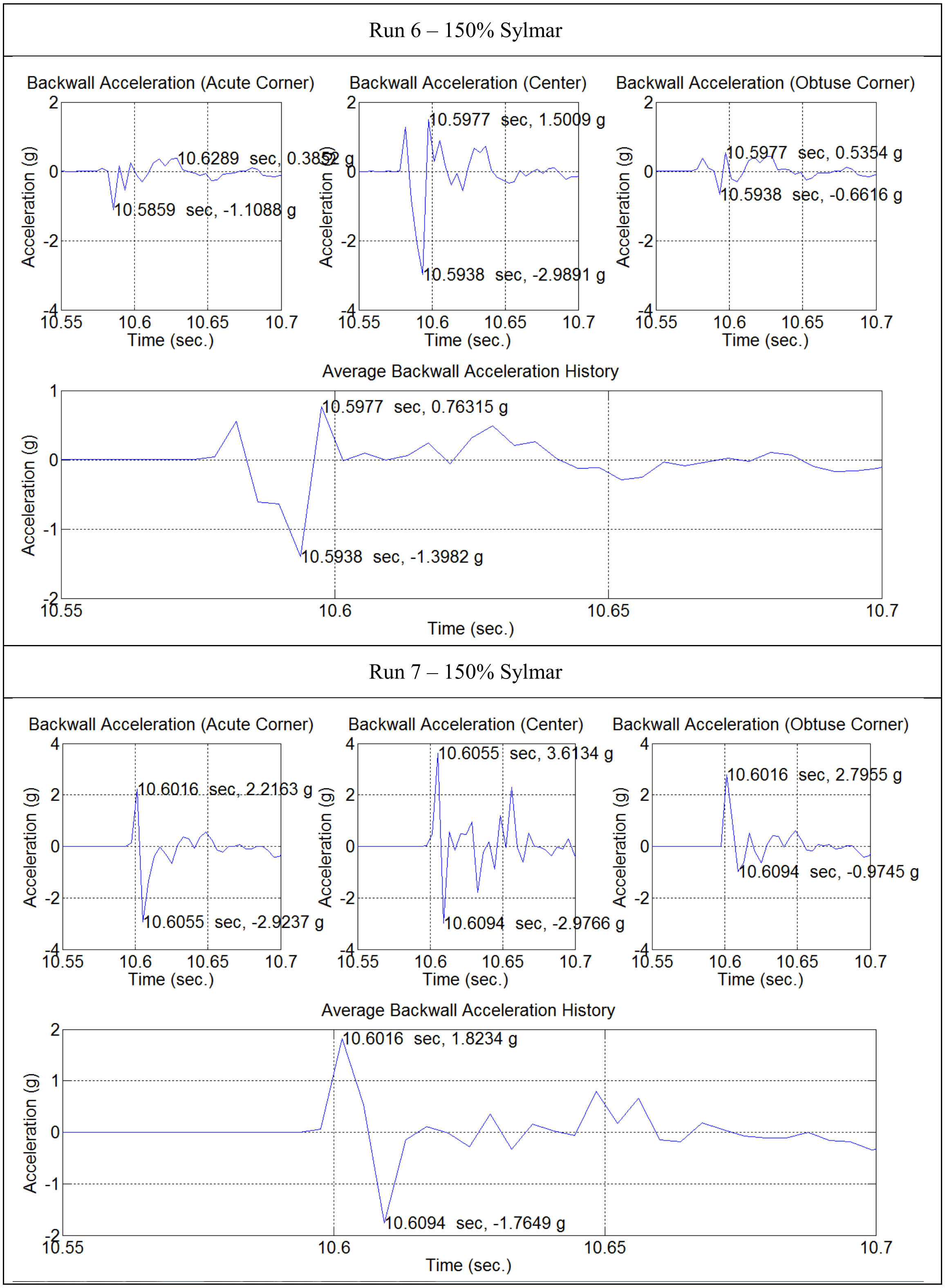

Figure 6-124 Transverse acceleration of the backwall for the 0° skew test in Run 6 and 7.

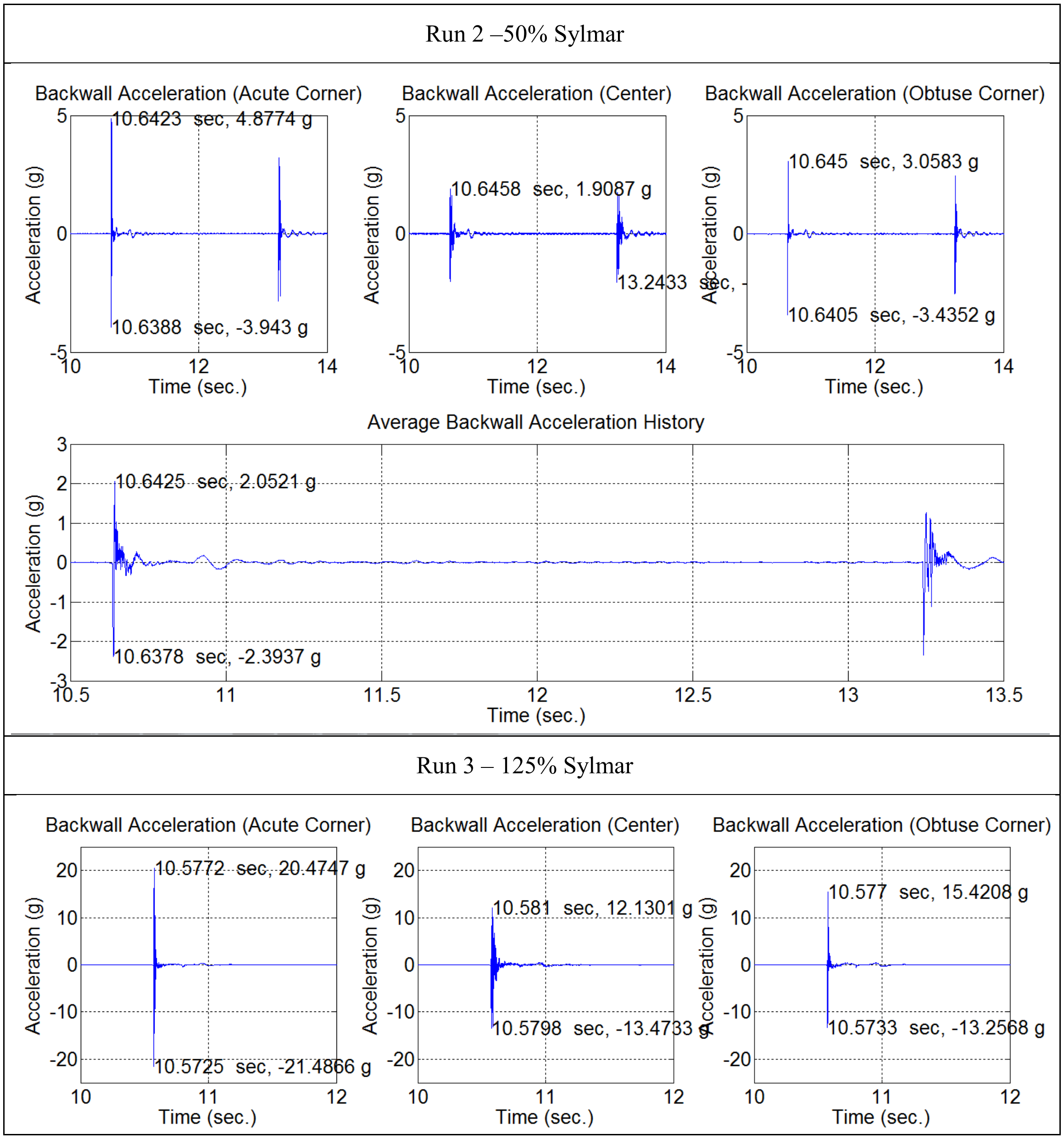

Figure 6-125 Transverse acceleration of the backwall for the 30° skew test in Run 2 and 3.

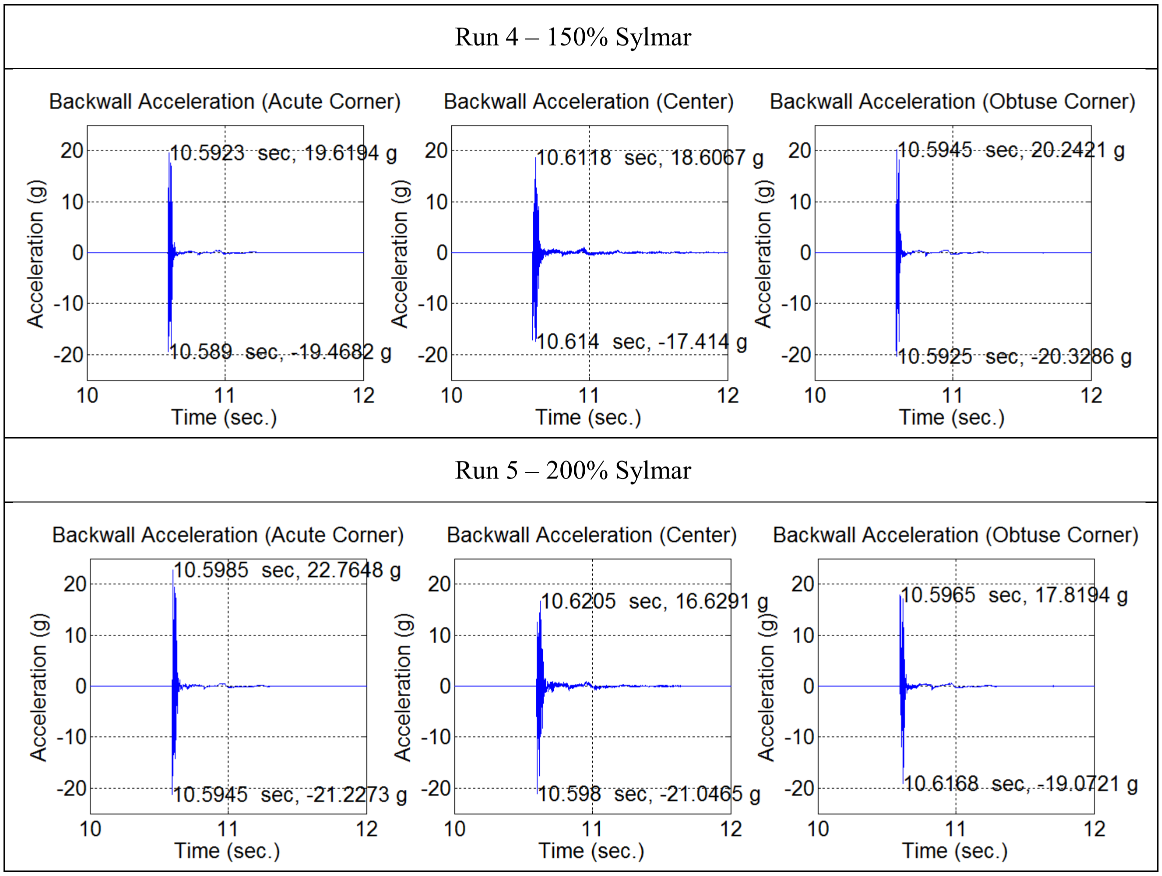

Figure 6-126 Transverse acceleration of the backwall for the 30° skew test in Run 4 and 5.

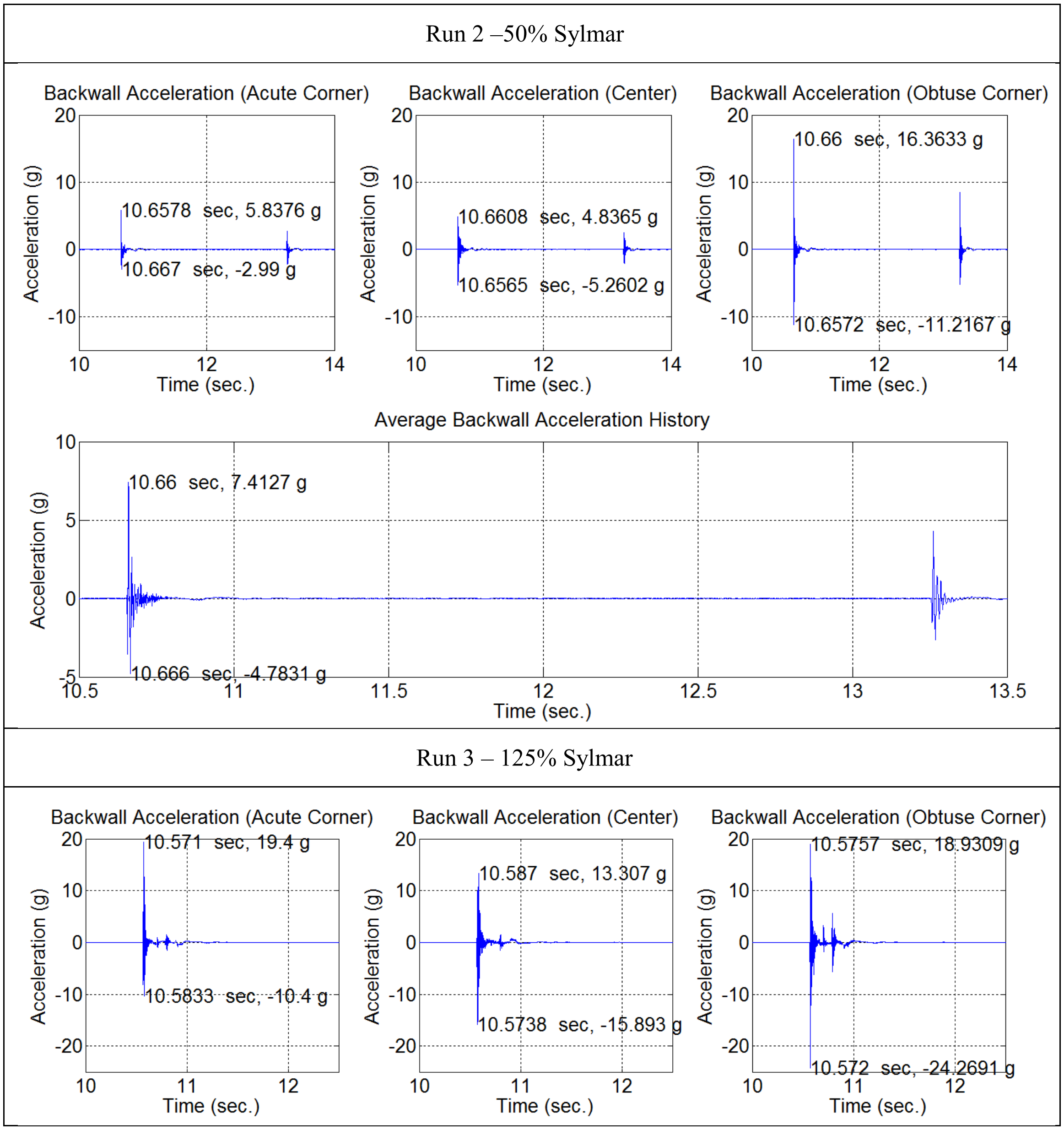

Figure 6-127 Transverse acceleration of the backwall for the 45° skew test in Run 2 and 3.

Run 4 – 150% Sylmar

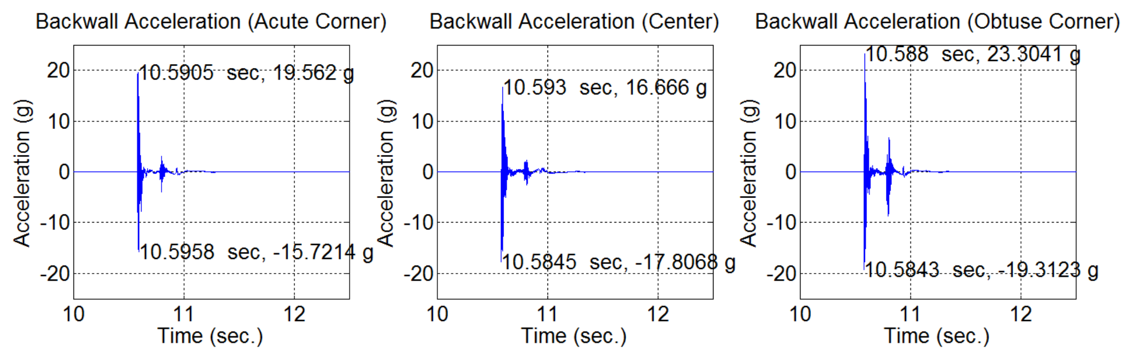

Run 5 – 200% Sylmar

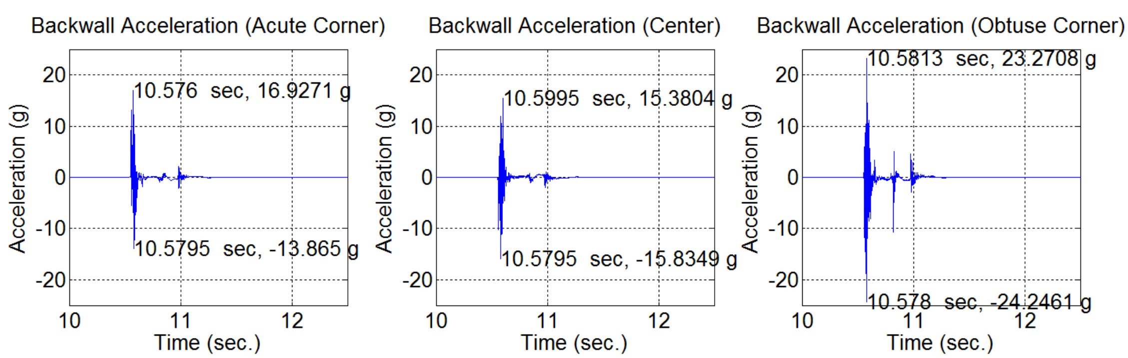

Figure 6-128 Transverse acceleration of the backwall for the 45° skew test in Run 4 and 5.

Run 2 –50% Sylmar

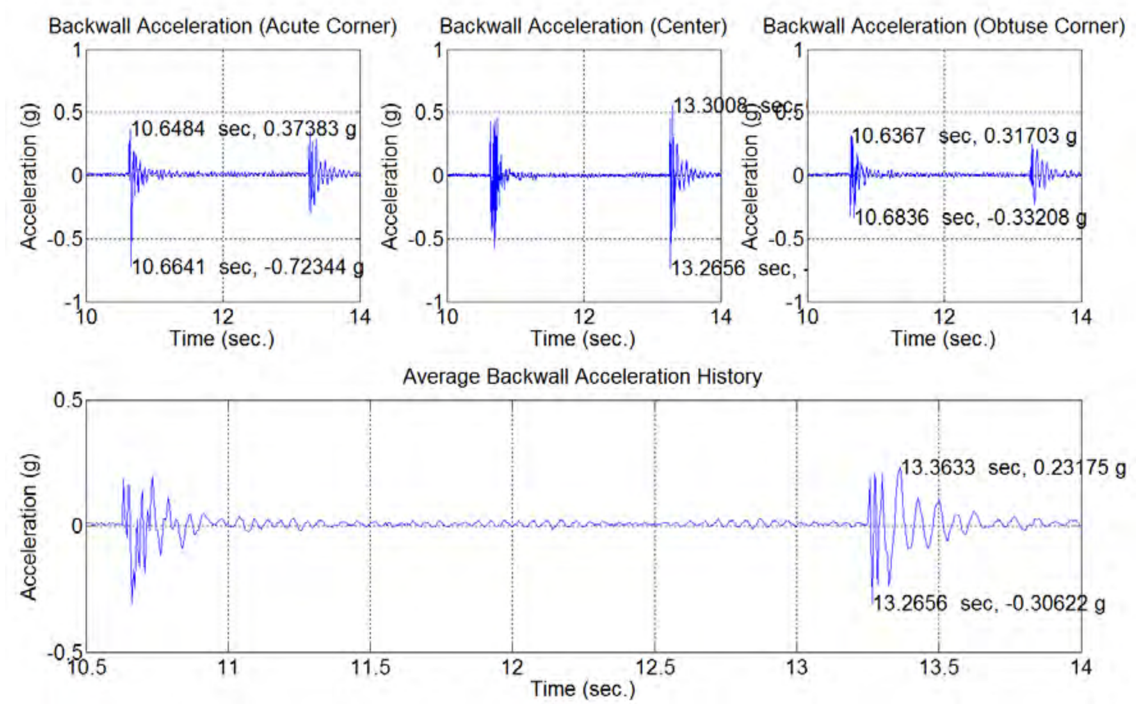

Run 3 – 75% Sylmar

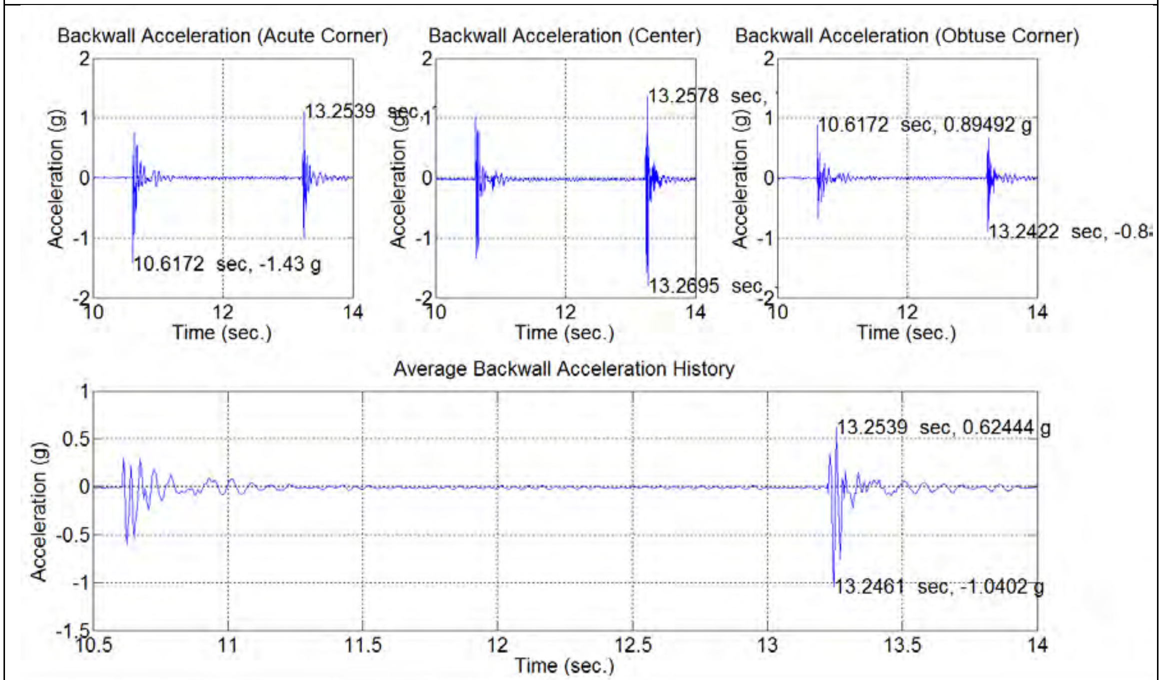

Figure 6-129 Vertical acceleration of the backwall for the 0° skew test in Run 2 and 3.

Run 6 – 150% Sylmar

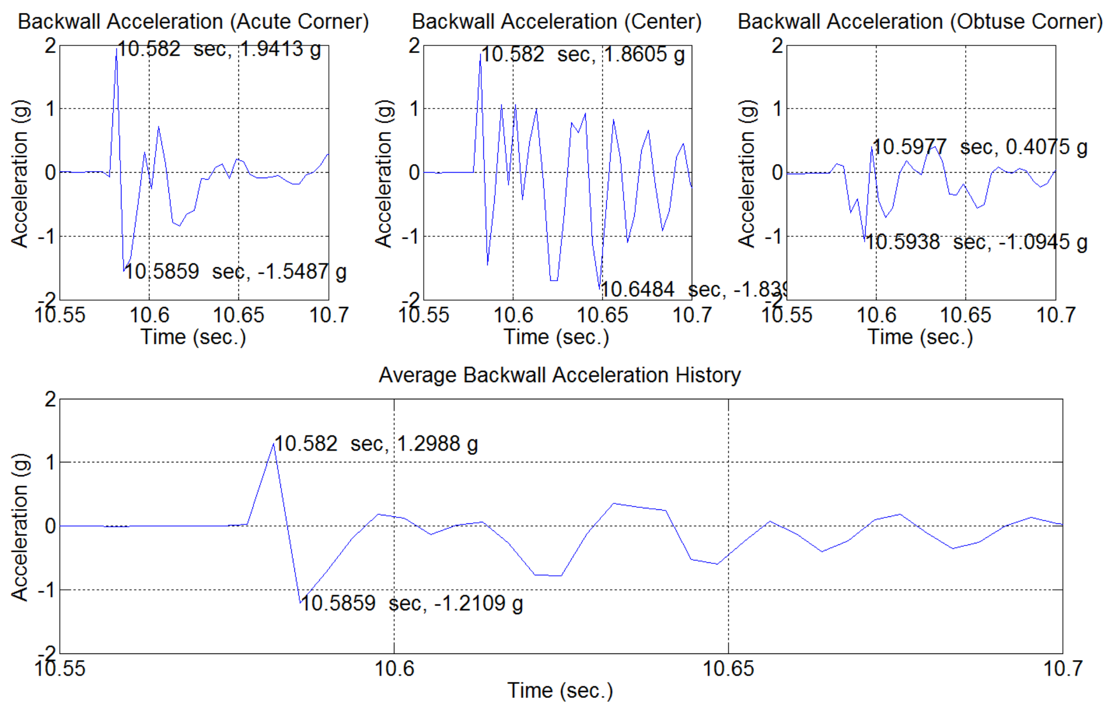

Run 7 – 150% Sylmar

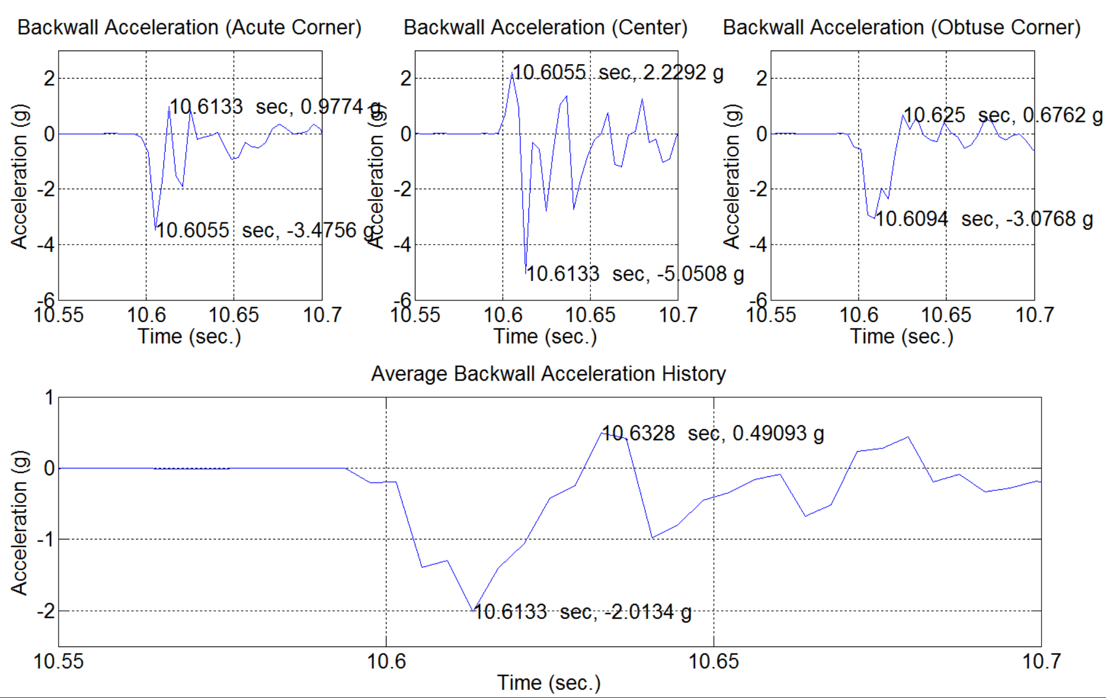

Figure 6-130 Vertical acceleration of the backwall for the 0° skew test in Run 6 and 7.

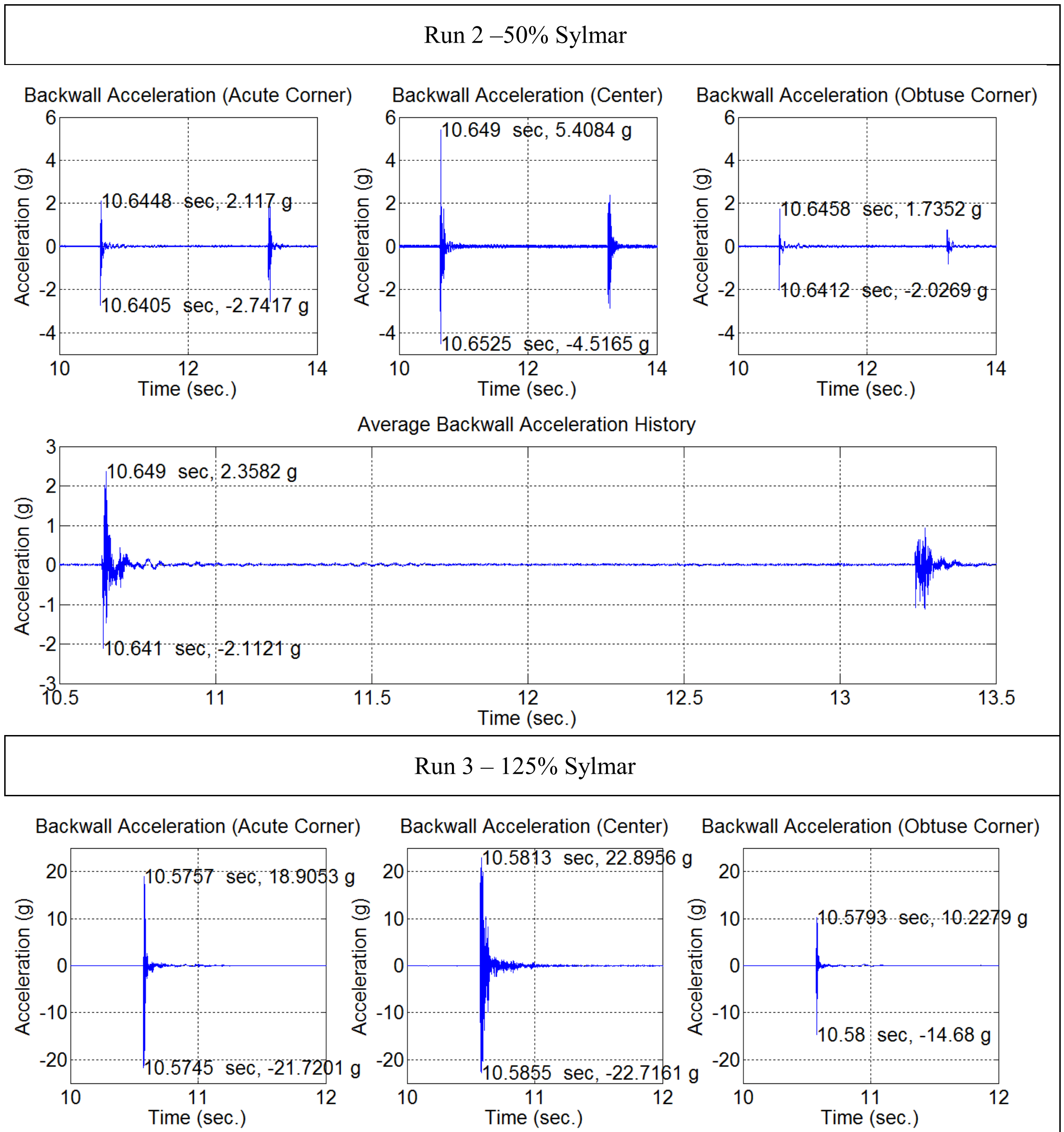

Figure 6-131 Vertical acceleration of the backwall for the 30° skew test in Run 2 and 3.

Run 4 – 150% Sylmar

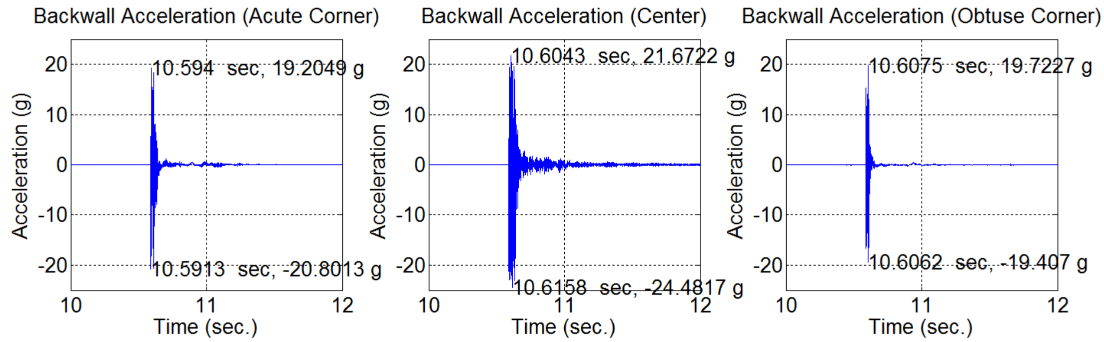

Run 5 – 200% Sylmar

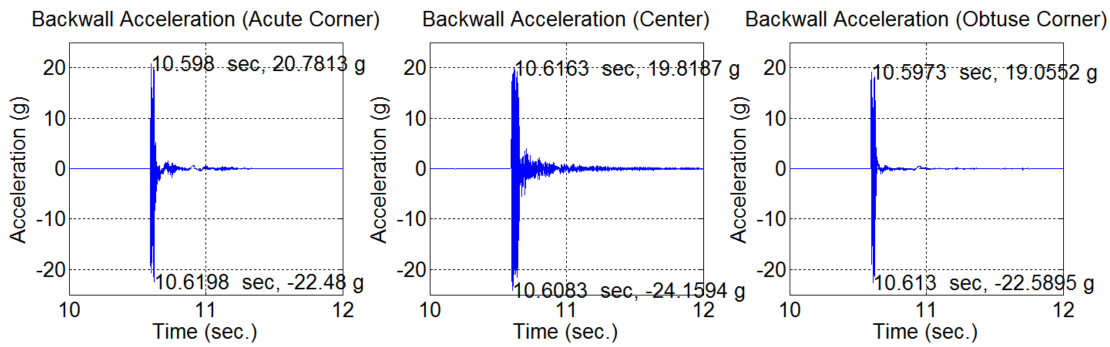

Figure 6-132 Vertical acceleration of the backwall for the 30° skew test in Run 4 and 5.

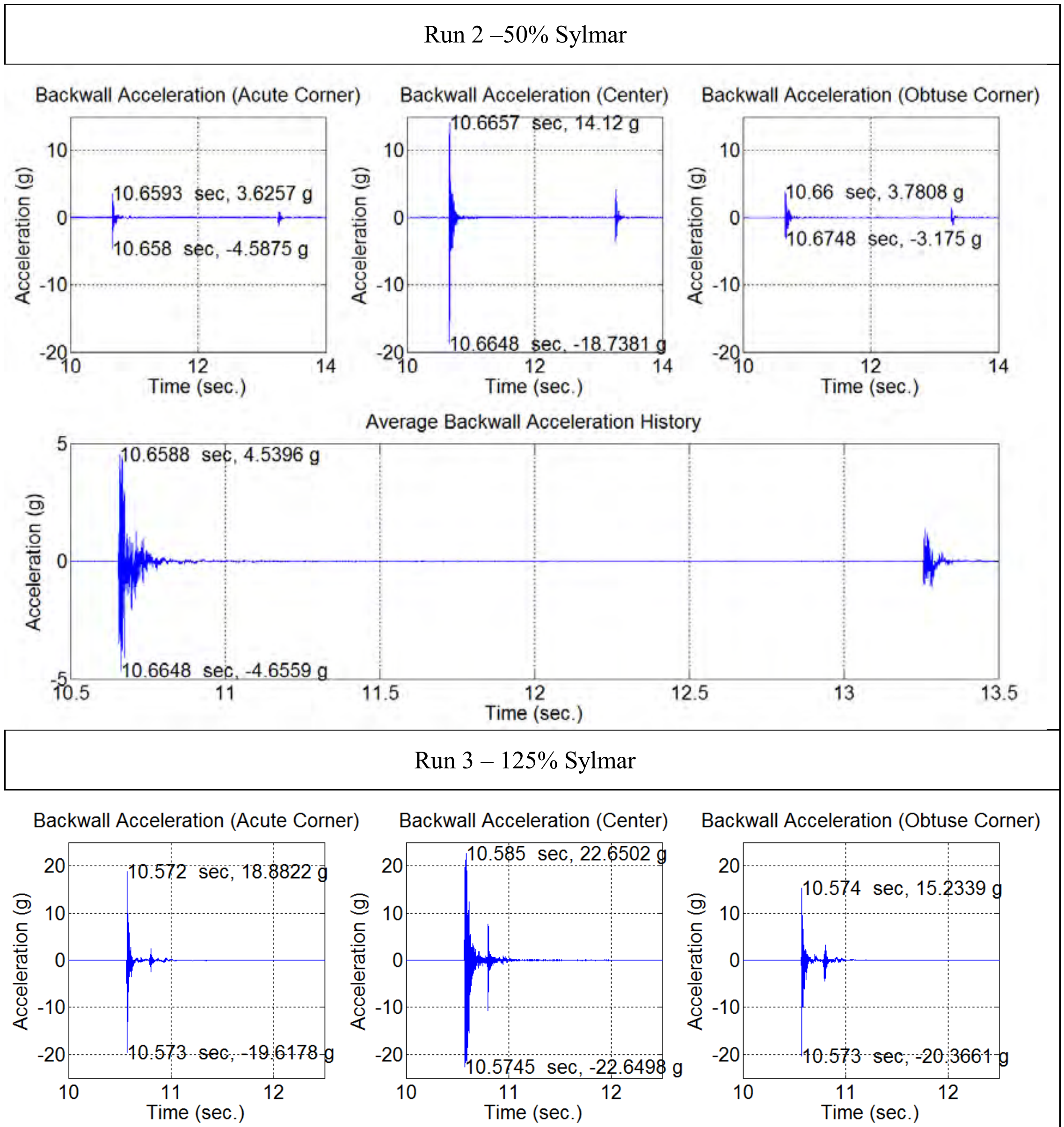

Figure 6-133 Vertical acceleration of the backwall for the 45° skew test in Run 2 and 3.

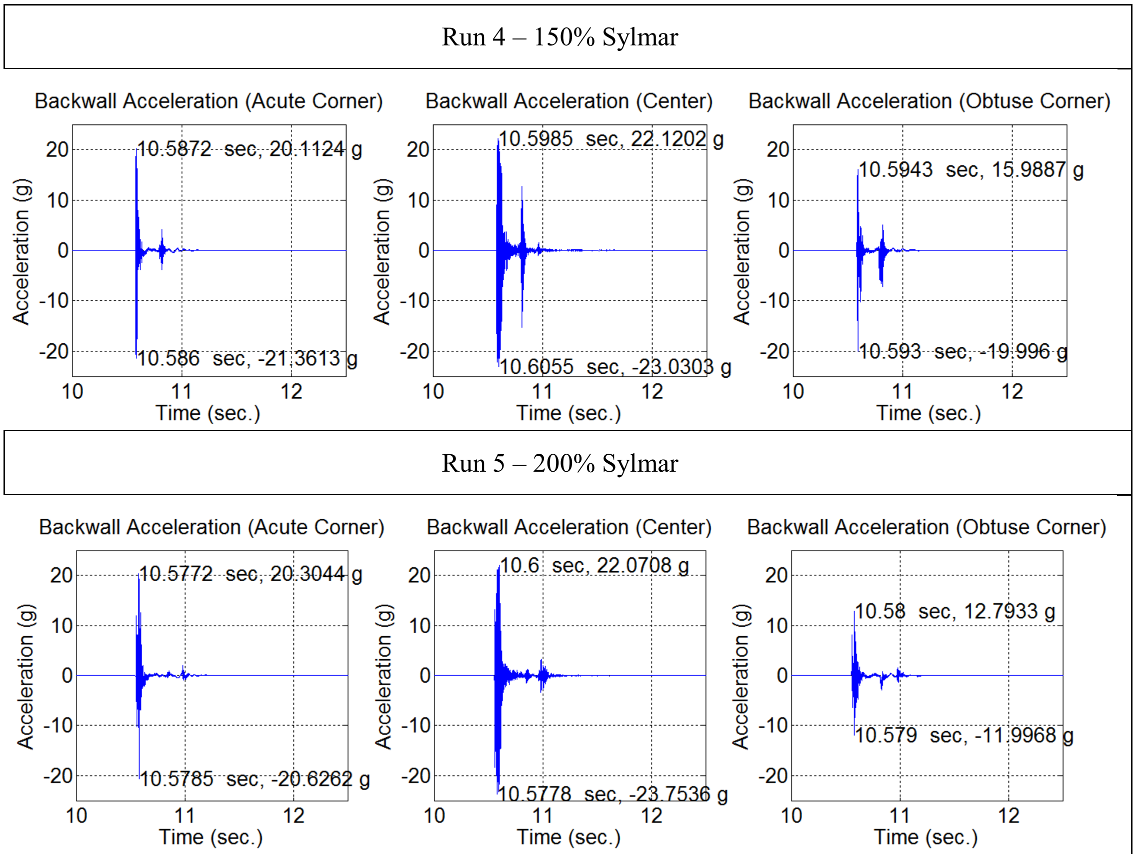

Figure 6-134 Vertical acceleration of the backwall for the 45° skew test in Run 4 and 5.

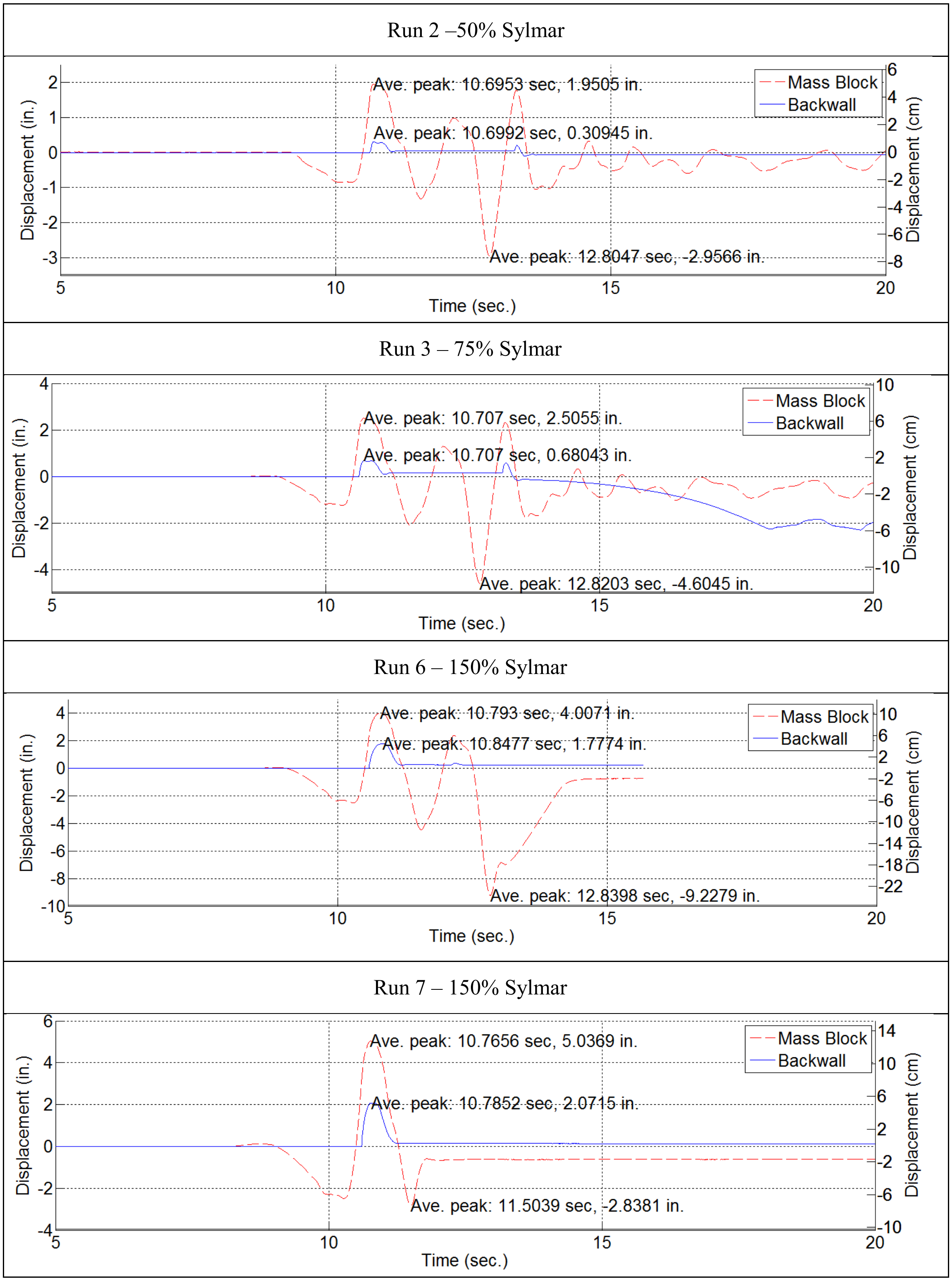

Figure 6-135 Comparison of longitudinal displacement of the bridge block and the backwall for the 0° skew test.

Run 2 –50% Sylmar

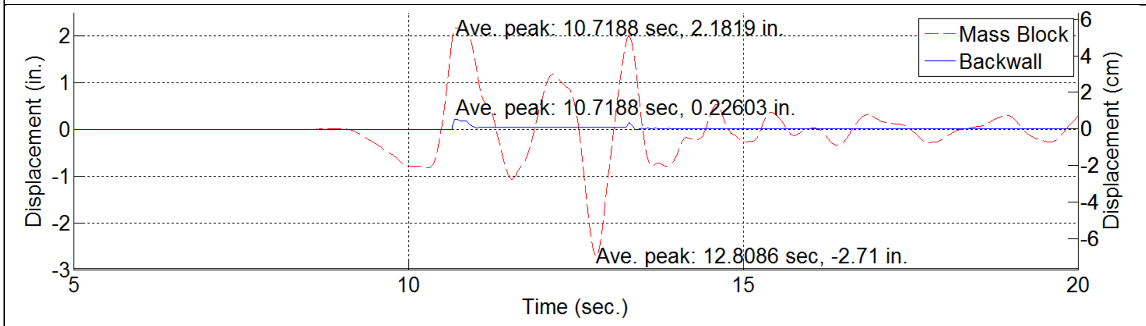

Run 3 – 125% Sylmar

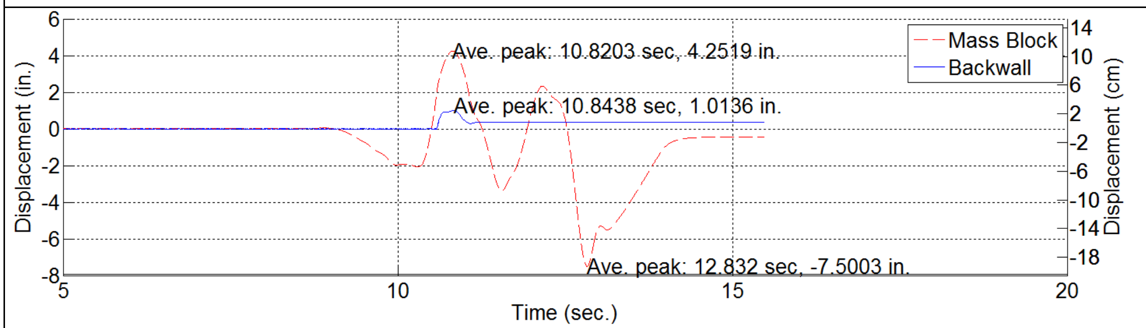

Run 4 – 150% Sylmar

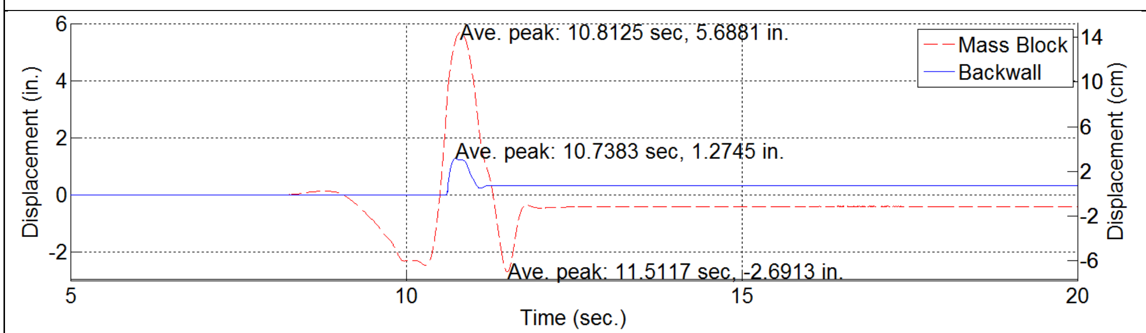

Run 5 – 200% Sylmar

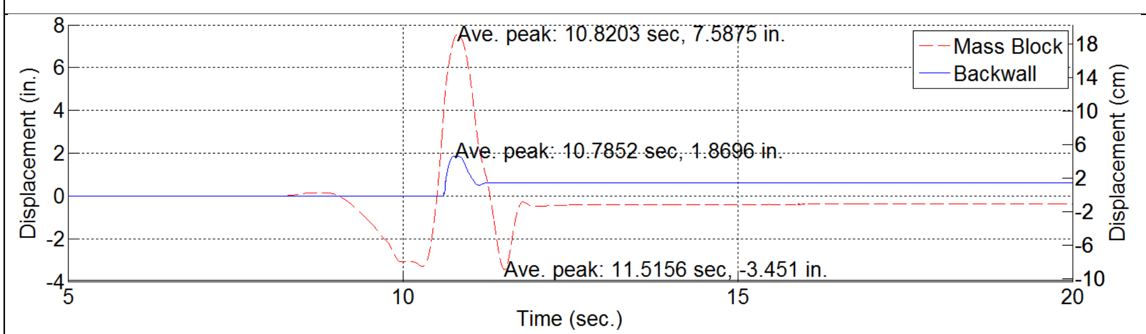

Figure 6-136 Comparison of longitudinal displacement of the bridge block and the backwall for the 30° skew test.

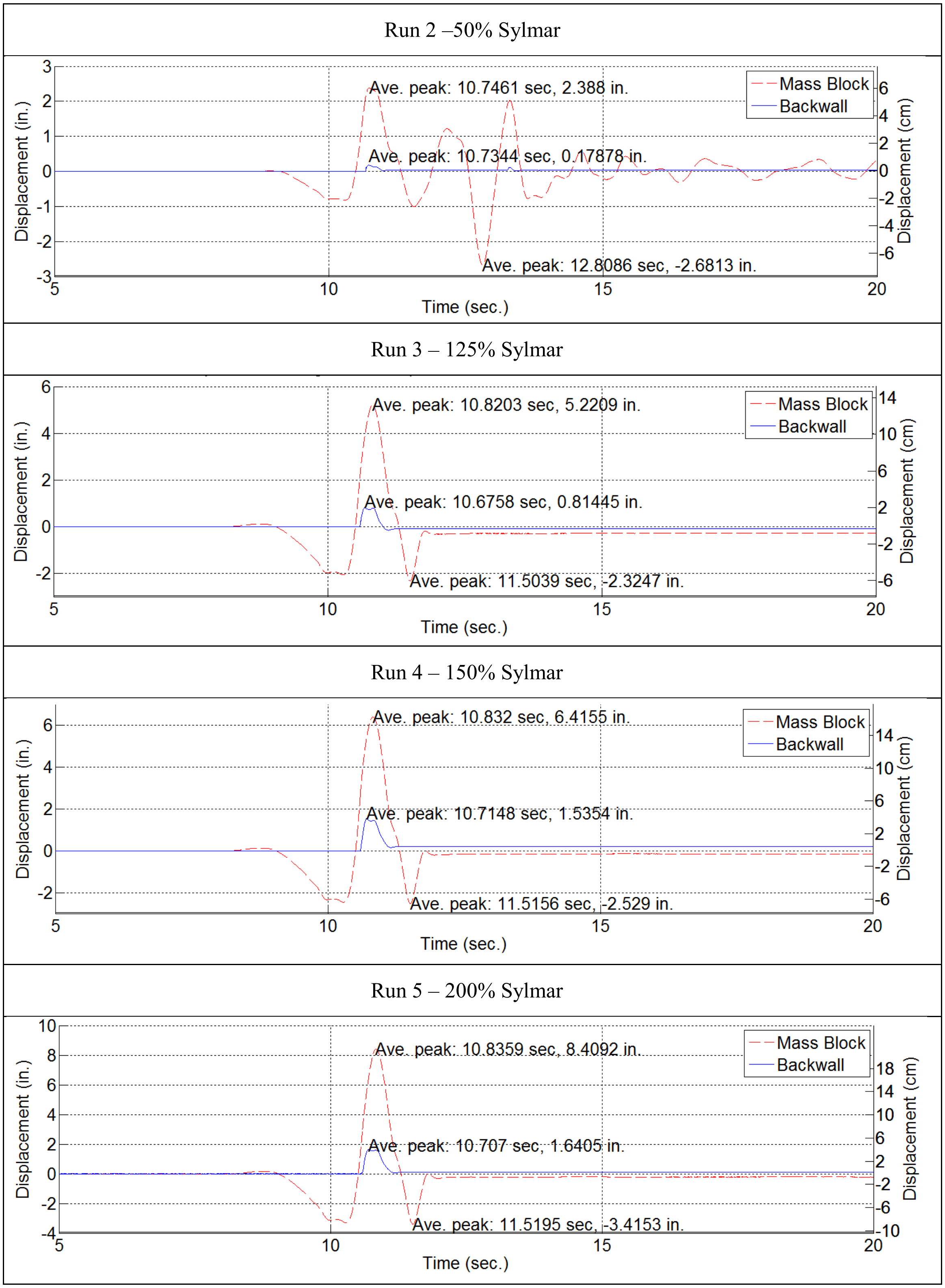

Figure 6-137 Comparison of longitudinal displacement of the bridge block and the backwall for the 45° skew test.

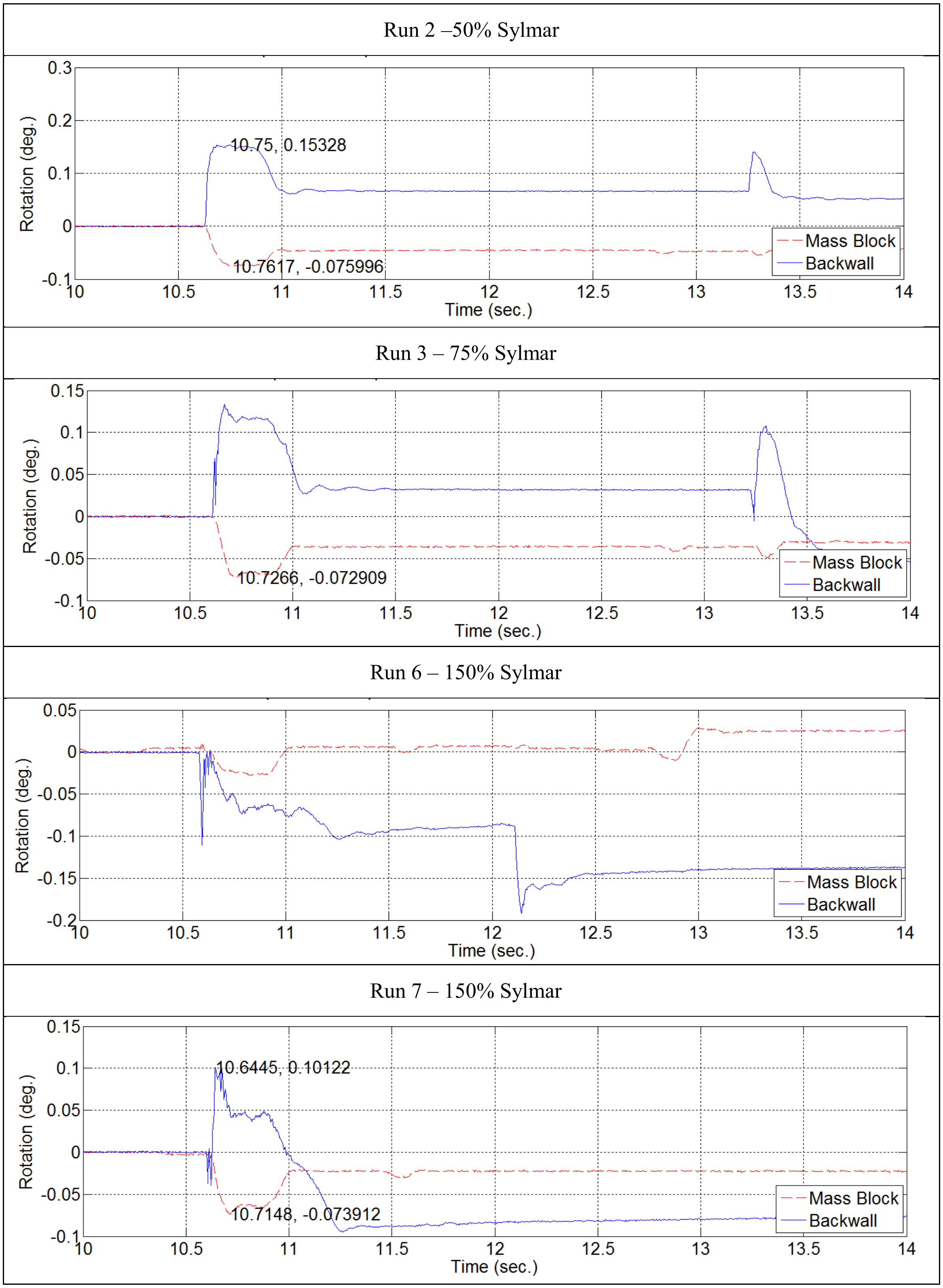

Figure 6-138 Comparison of in-plane rotation of the bridge block and the backwall rotation about the vertical axis for the 0° skew test.

Run 2 –50% Sylmar

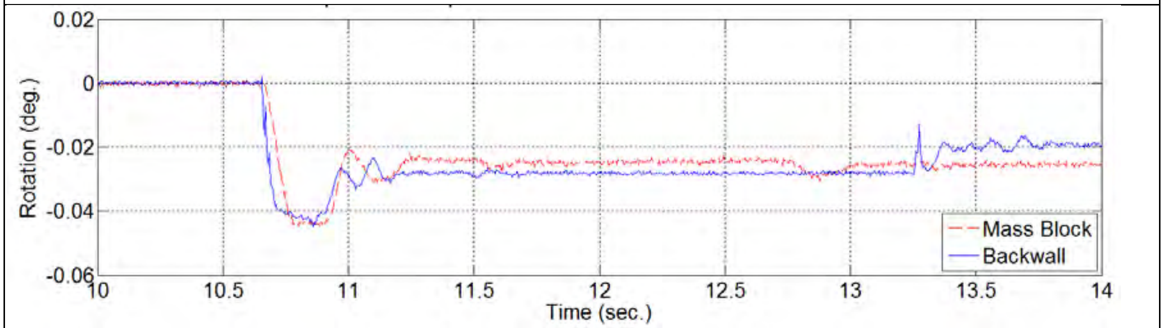

Run 3 – 125% Sylmar

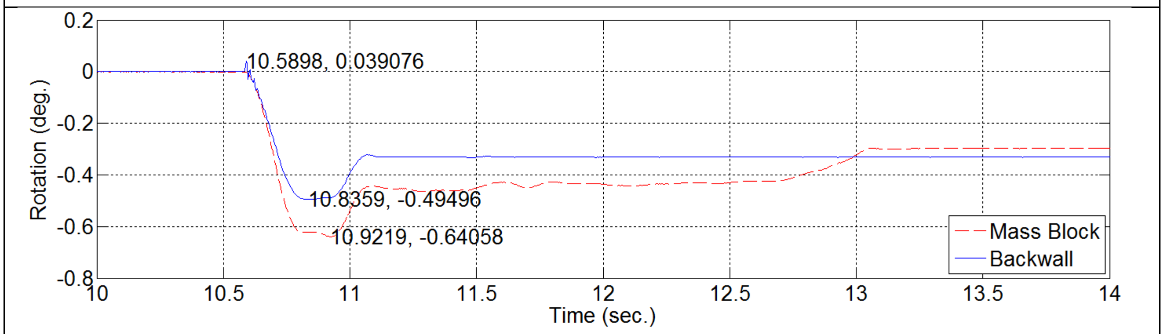

Run 4 – 150% Sylmar

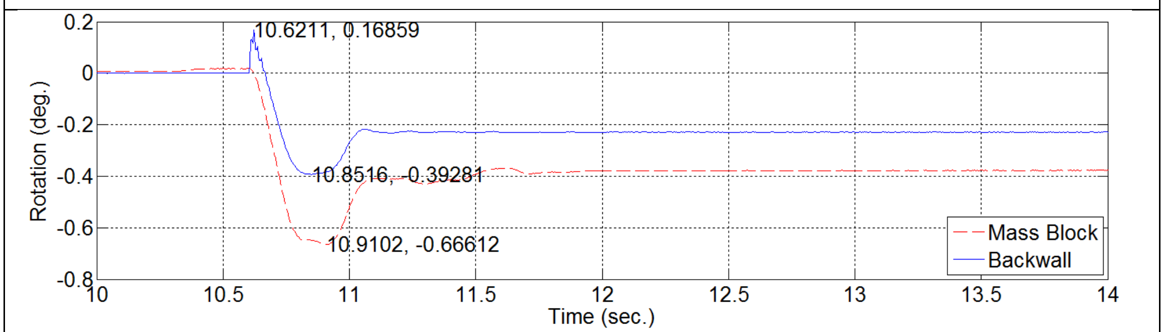

Run 5 – 200% Sylmar

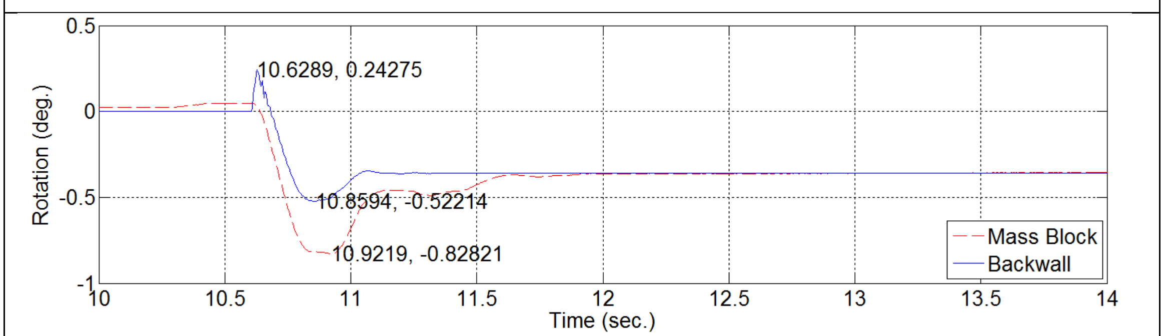

Figure 6-139 Comparison of the bridge block and the backwall rotation for the 30° skew test.

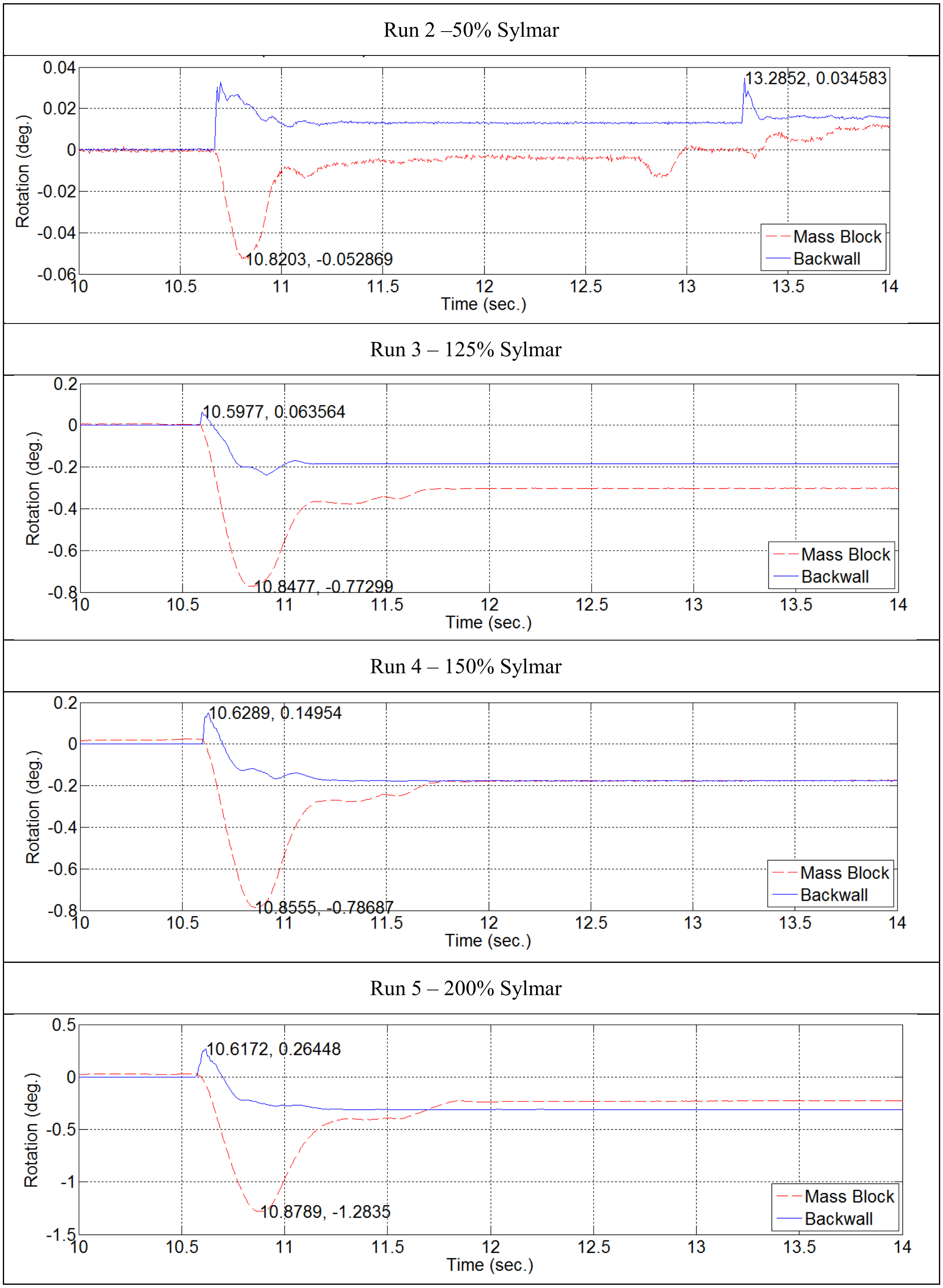

Figure 6-140 Comparison of the bridge block and the backwall rotation for the 45° skew test.

Run 2 – 50% Sylmar

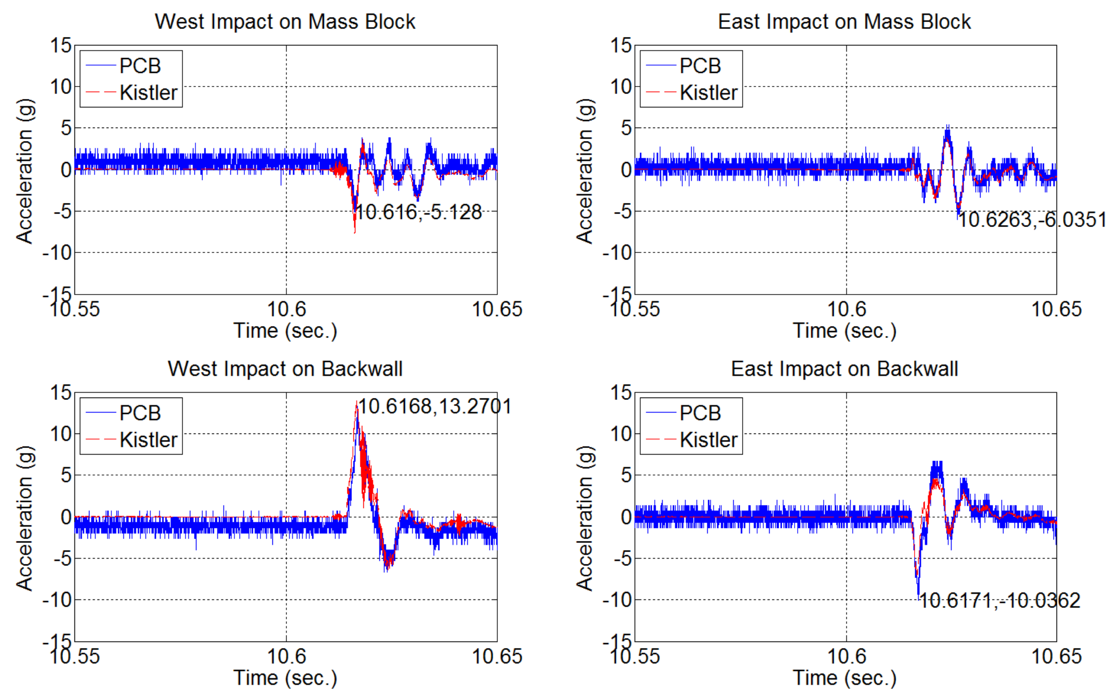

Run 3 – 75% Sylmar

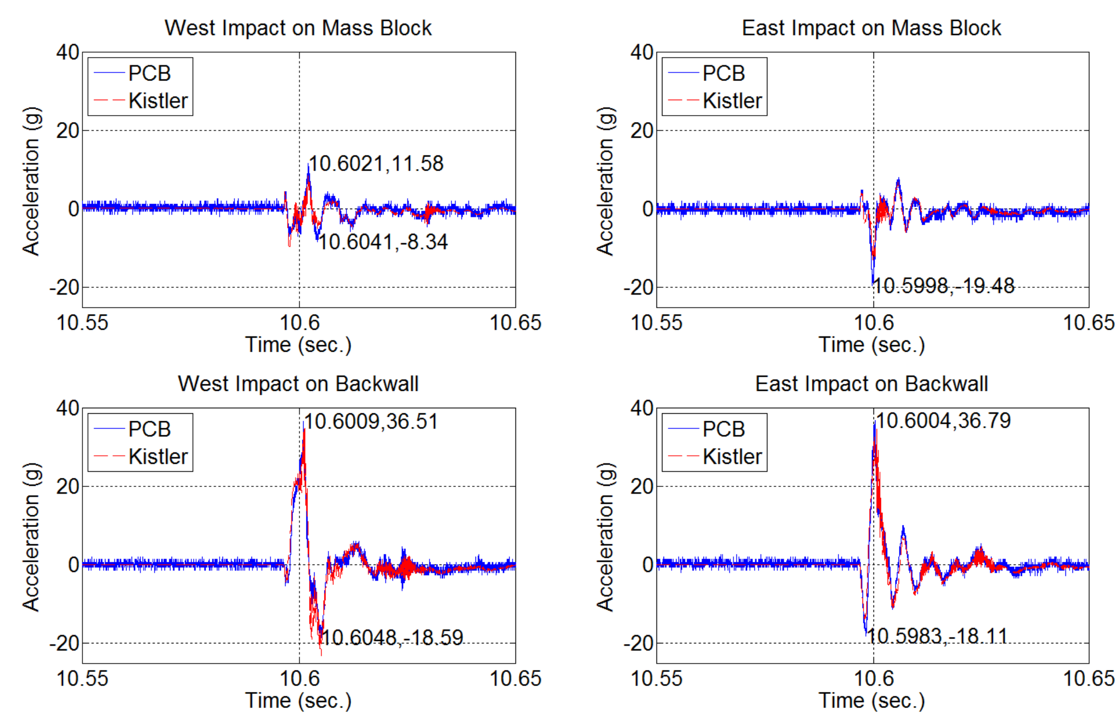

Figure 6-141 Comparison of longitudinal impact acceleration for the 0° skew test in Run 2 and 3.

Run 6 – 150% Sylmar

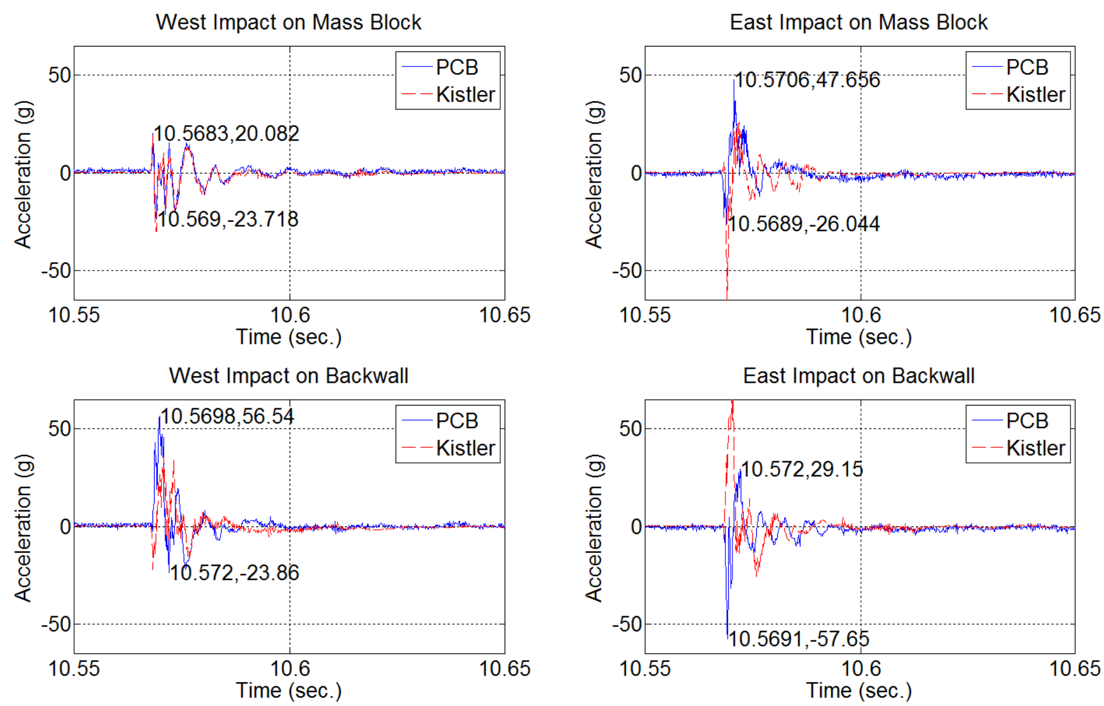

Run 7 – 150% Sylmar

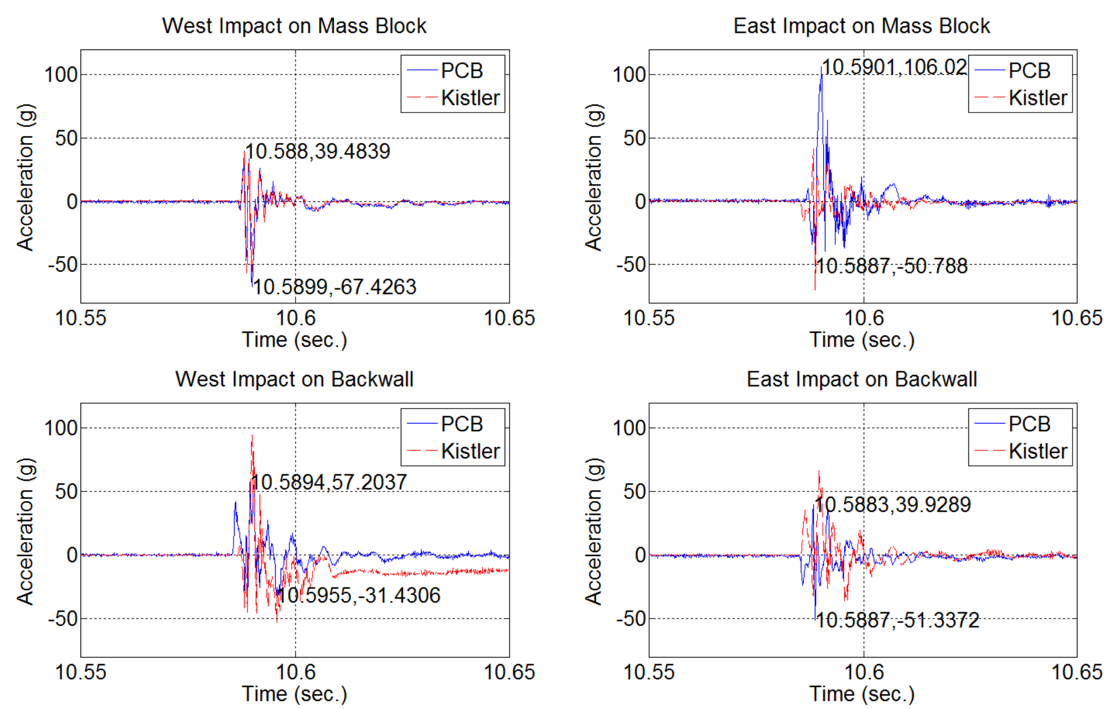

Figure 6-142 Comparison of longitudinal impact for the 0° skew test in Run 6 and 7.

Run 2 –50% Sylmar

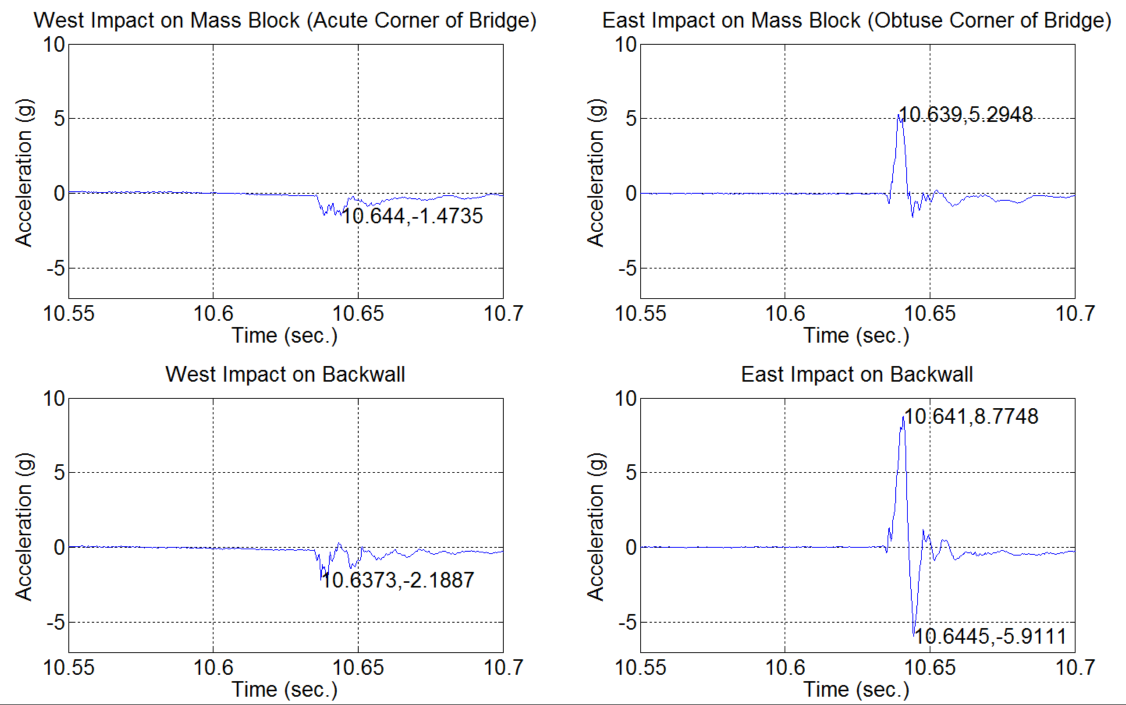

Run 3 – 125% Sylmar

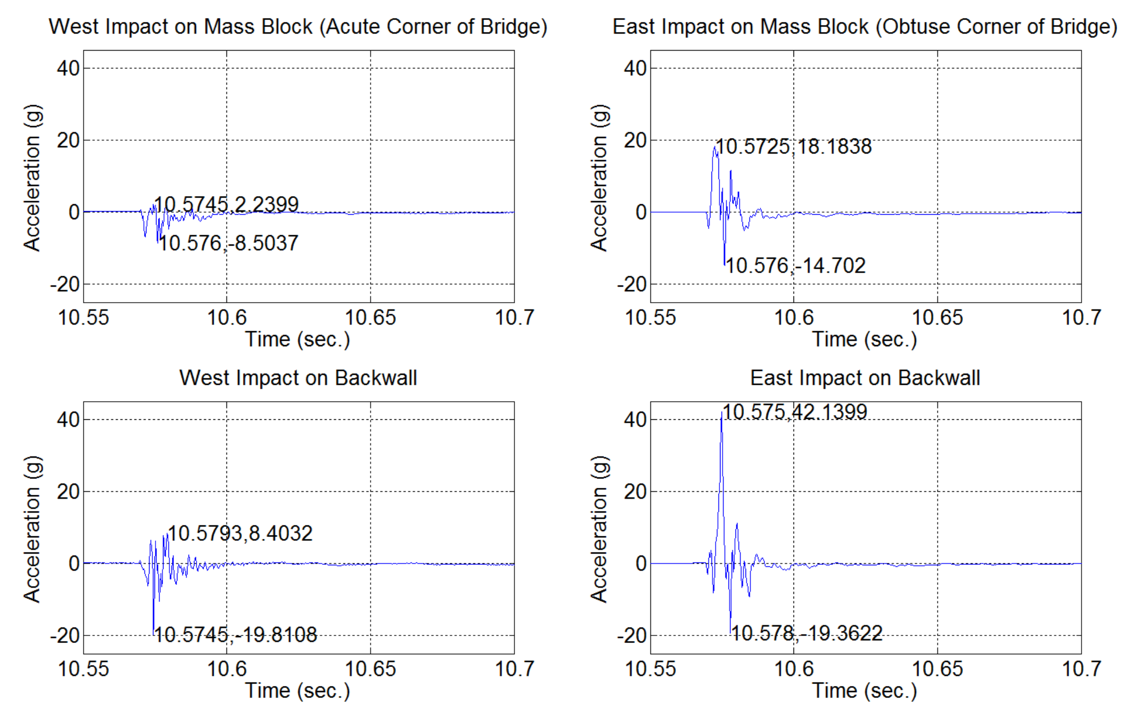

Figure 6-143 Comparison of longitudinal impact acceleration for the 30° skew test in Run 2 and 3.

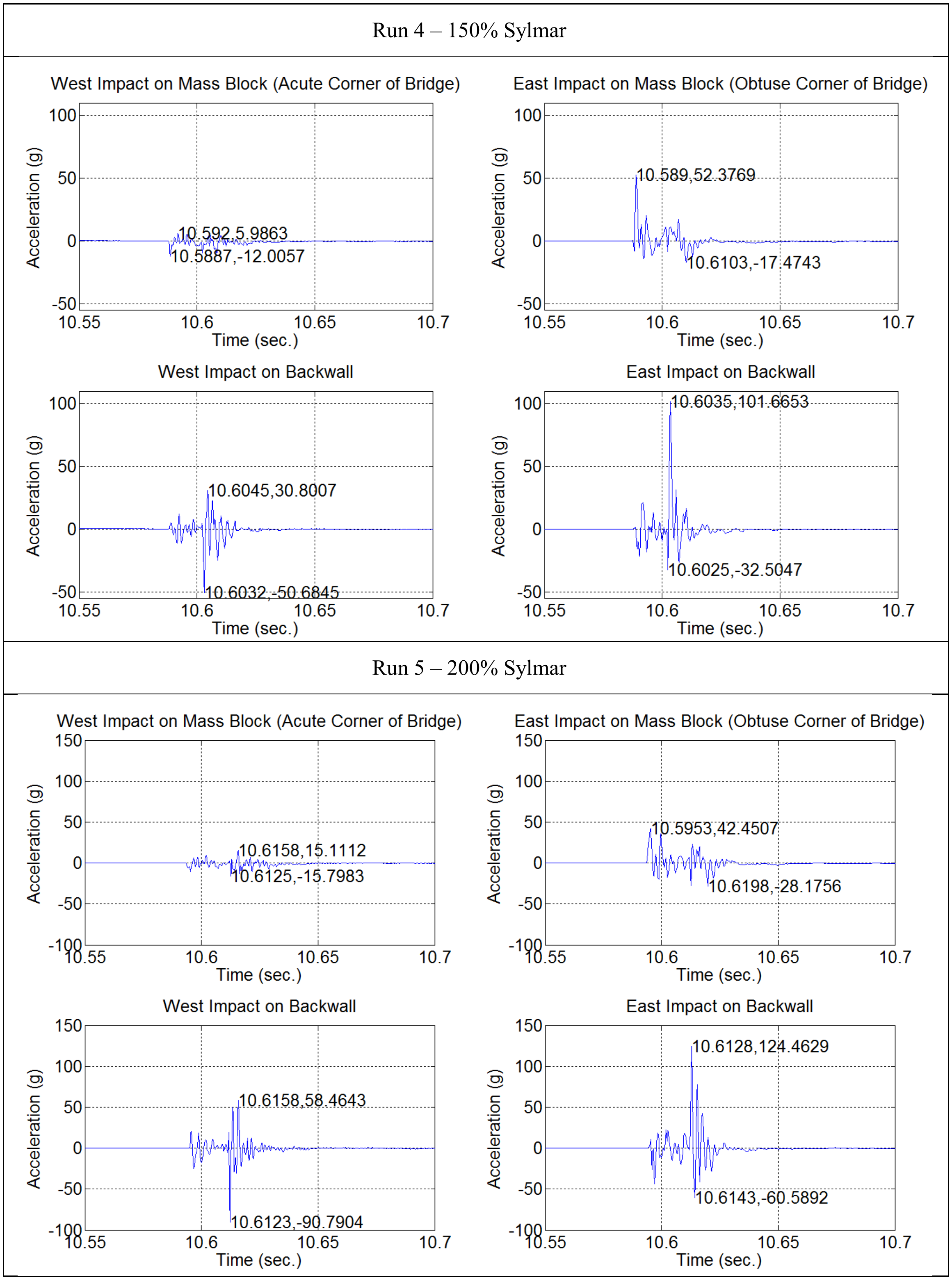

Figure 6-144 Comparison of longitudinal impact for the 30° skew test in Run 4 and 5.

Run 2 –50% Sylmar

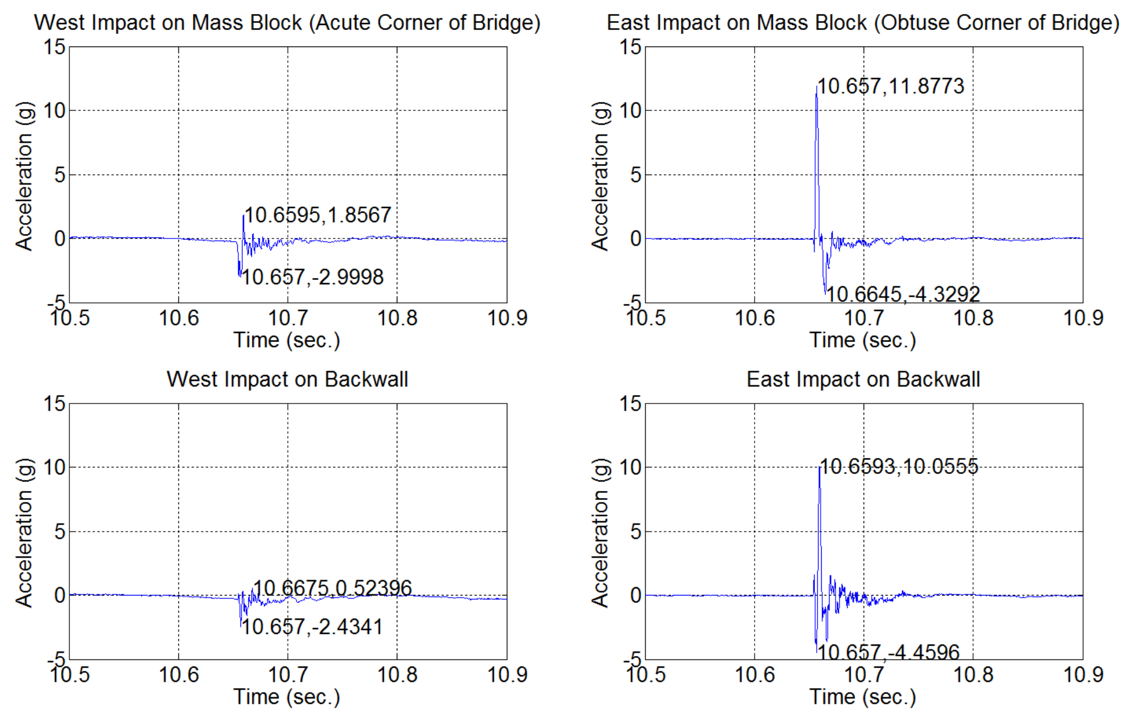

Run 3 – 125% Sylmar

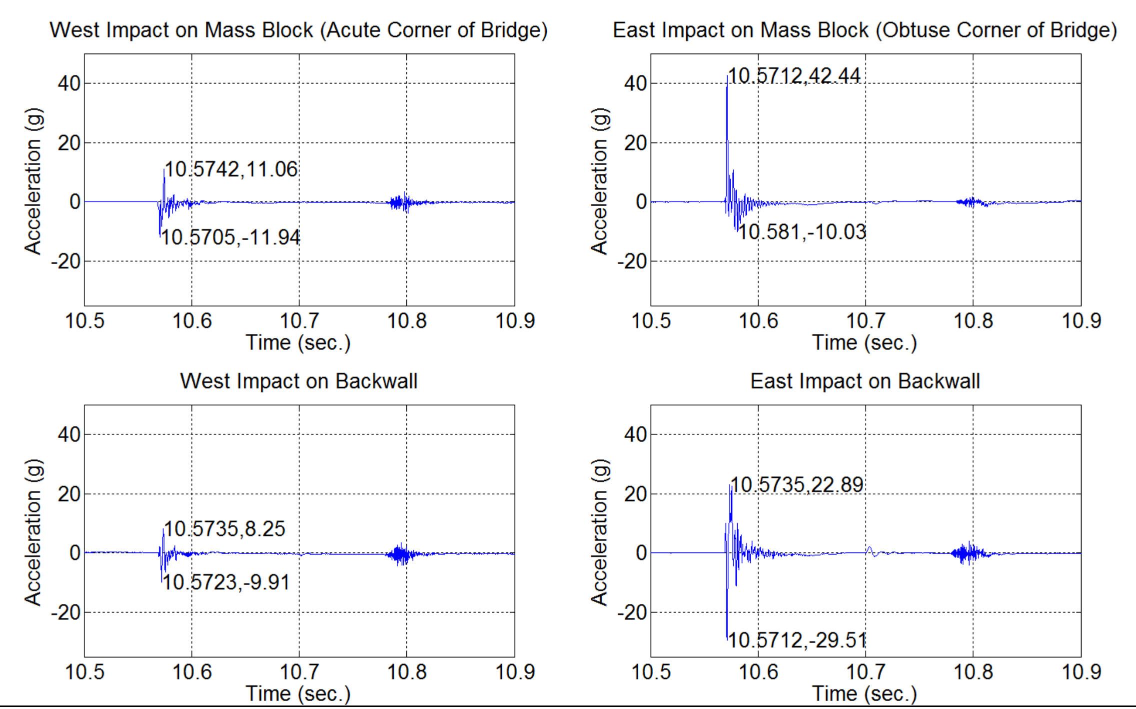

Figure 6-145 Comparison of longitudinal impact acceleration for the 45° skew test in Run 2 and 3.

Run 4 – 150% Sylmar

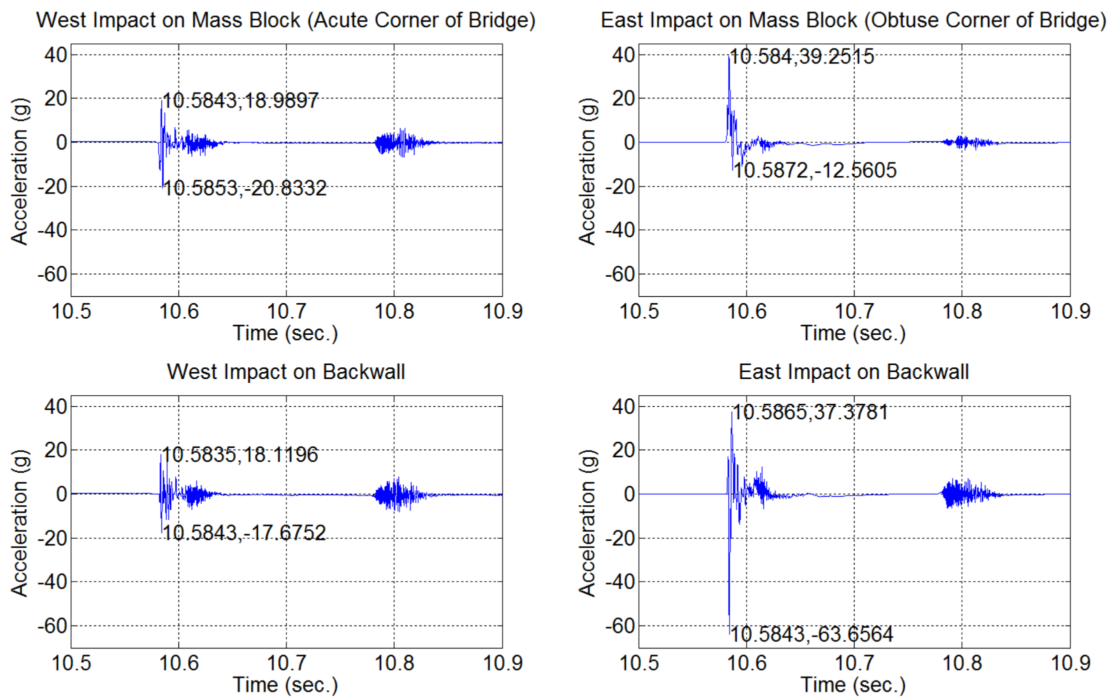

Run 5 – 200% Sylmar

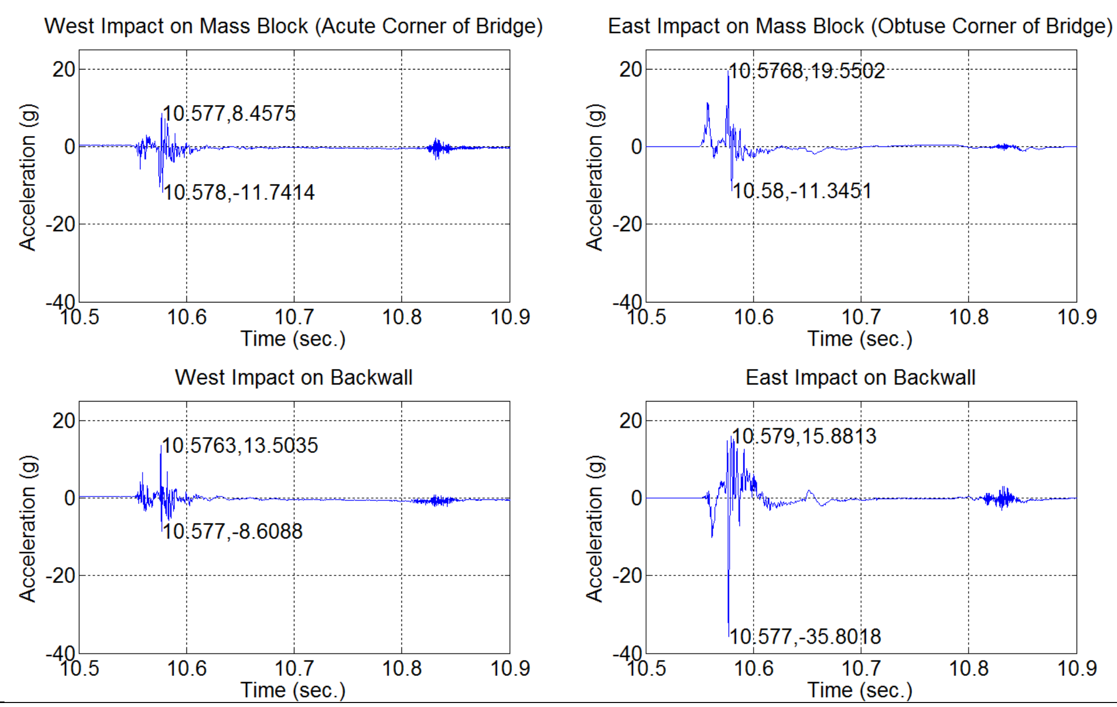

Figure 6-146 Comparison of longitudinal impact acceleration for the 45° skew test in Run 4 and 5.

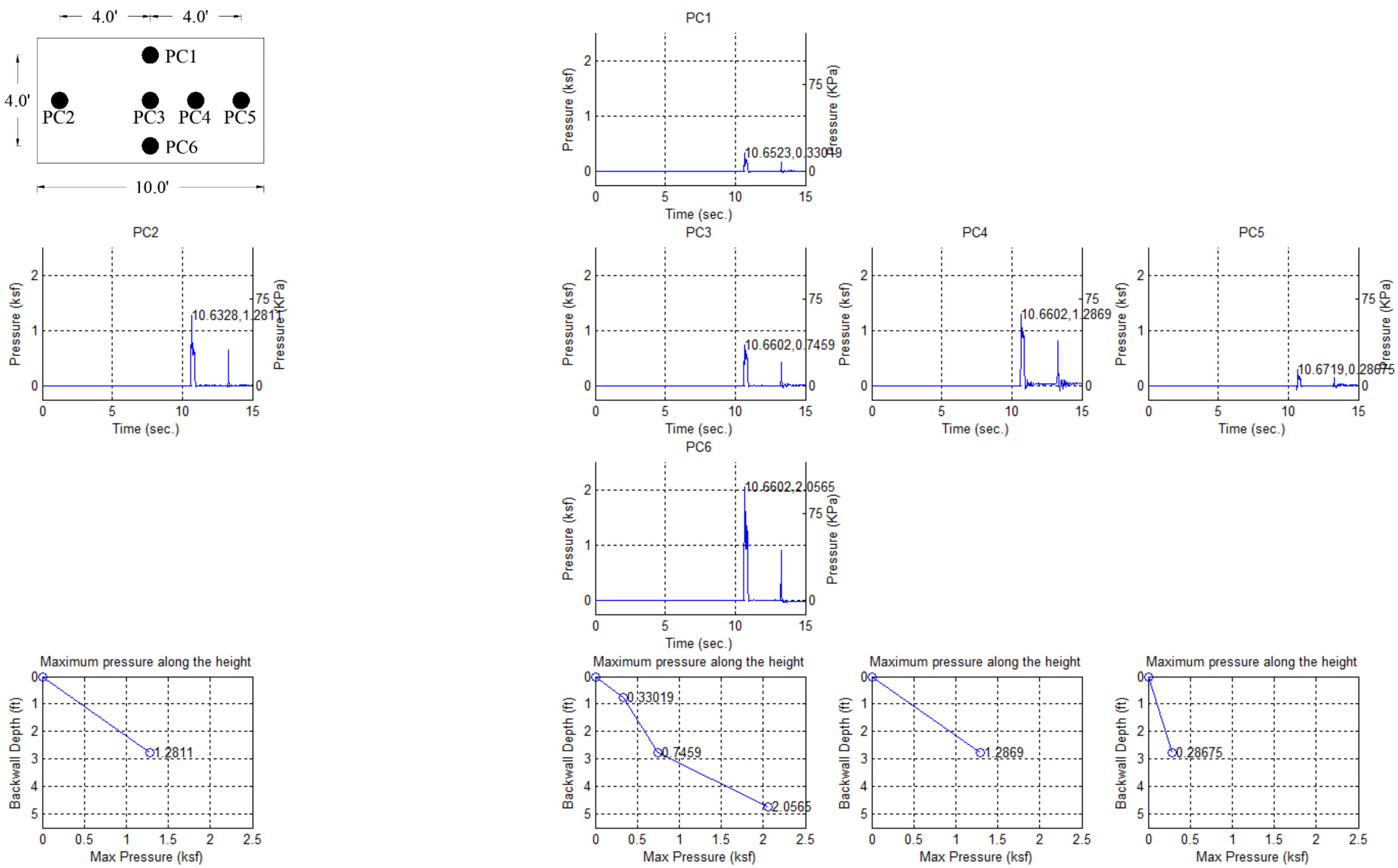

Figure 6-147 Soil pressure histories and maximum pressures for the 0° skew test in Run 2.

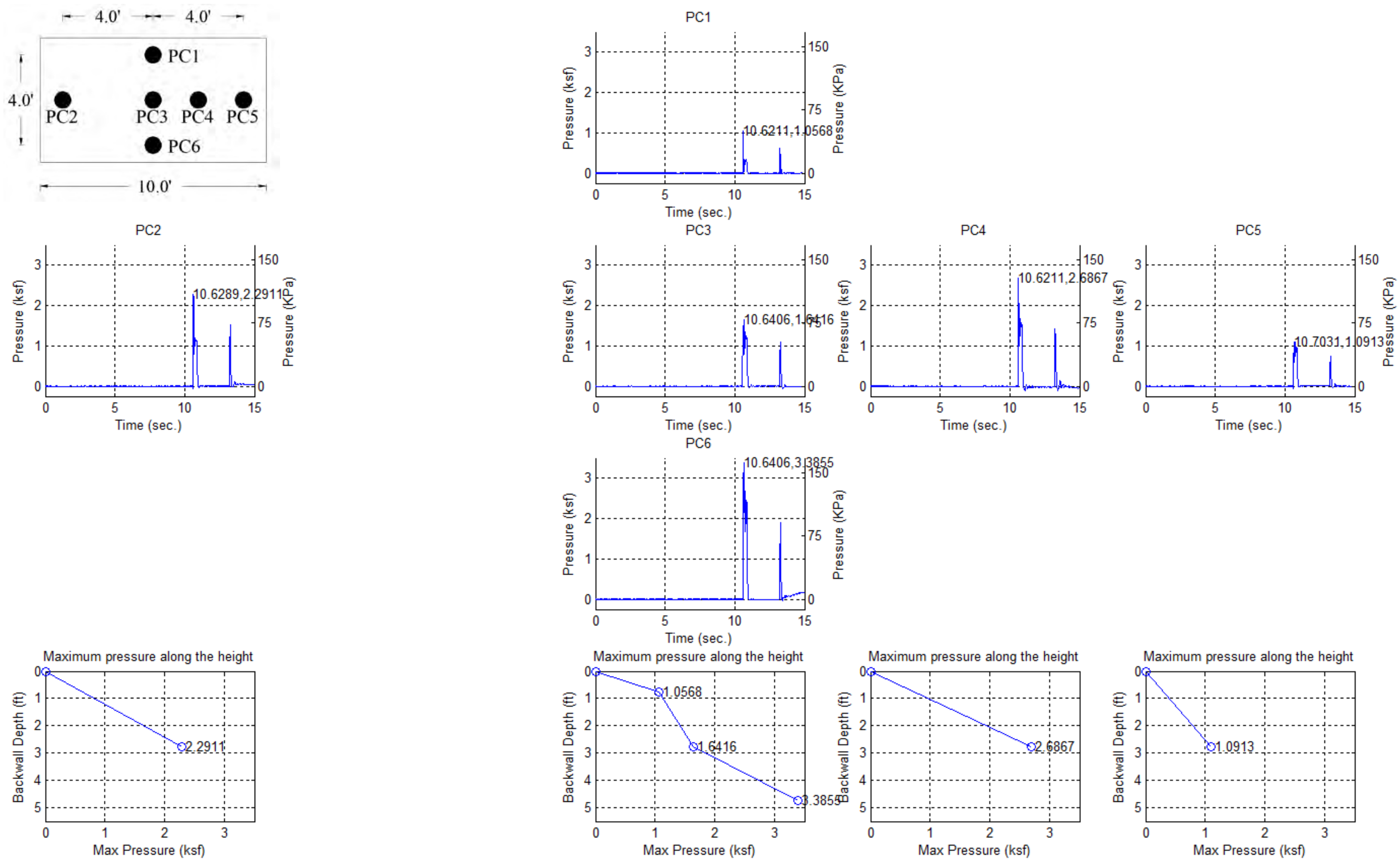

Figure 6-148 Soil pressure histories and maximum pressures for the 0° skew test in Run 3.

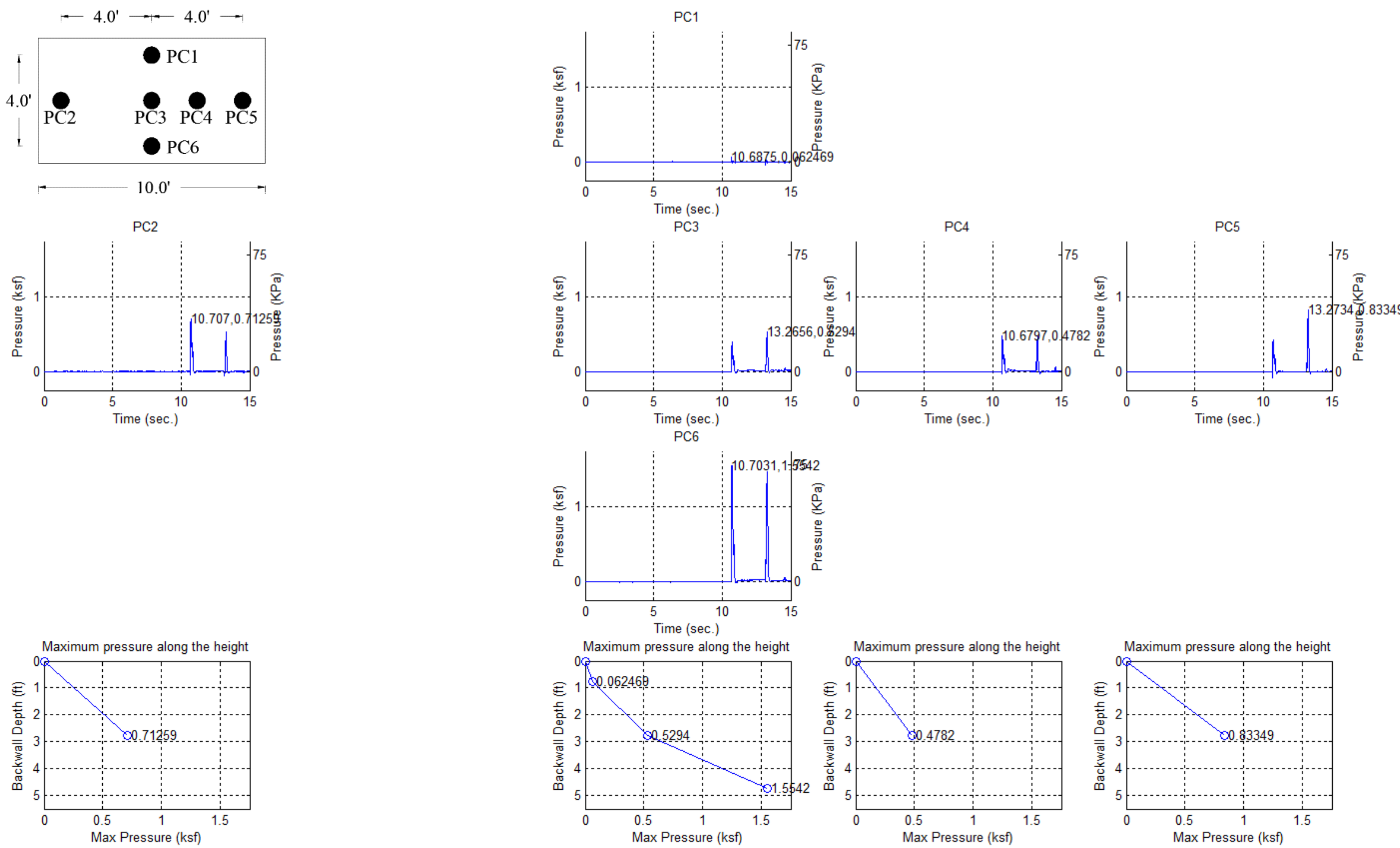

Figure 6-149 Soil pressure histories and maximum pressures for the 0° skew test in Run 4.

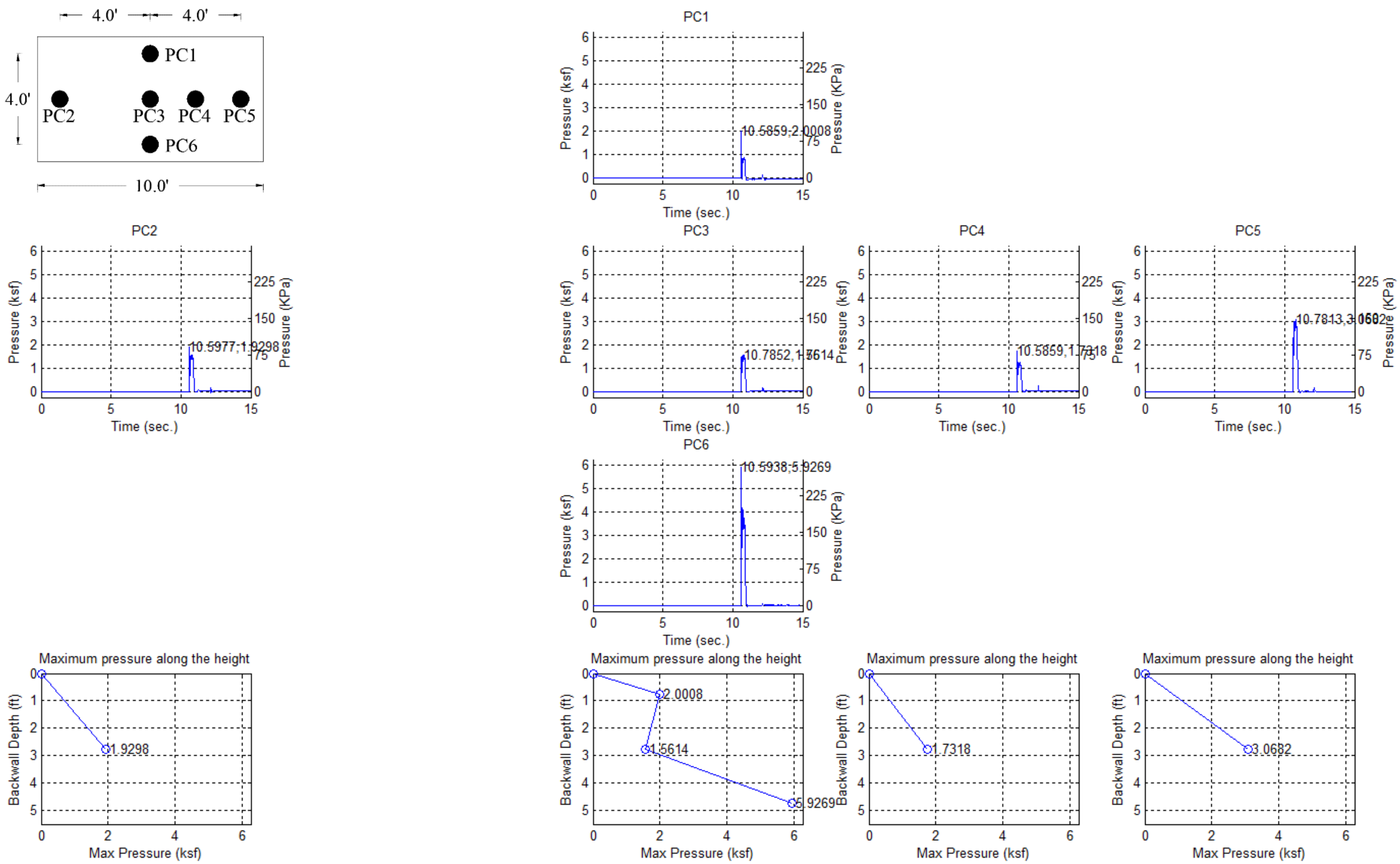

Figure 6-150 Soil pressure histories and maximum pressures for the 0° skew test in Run 6.

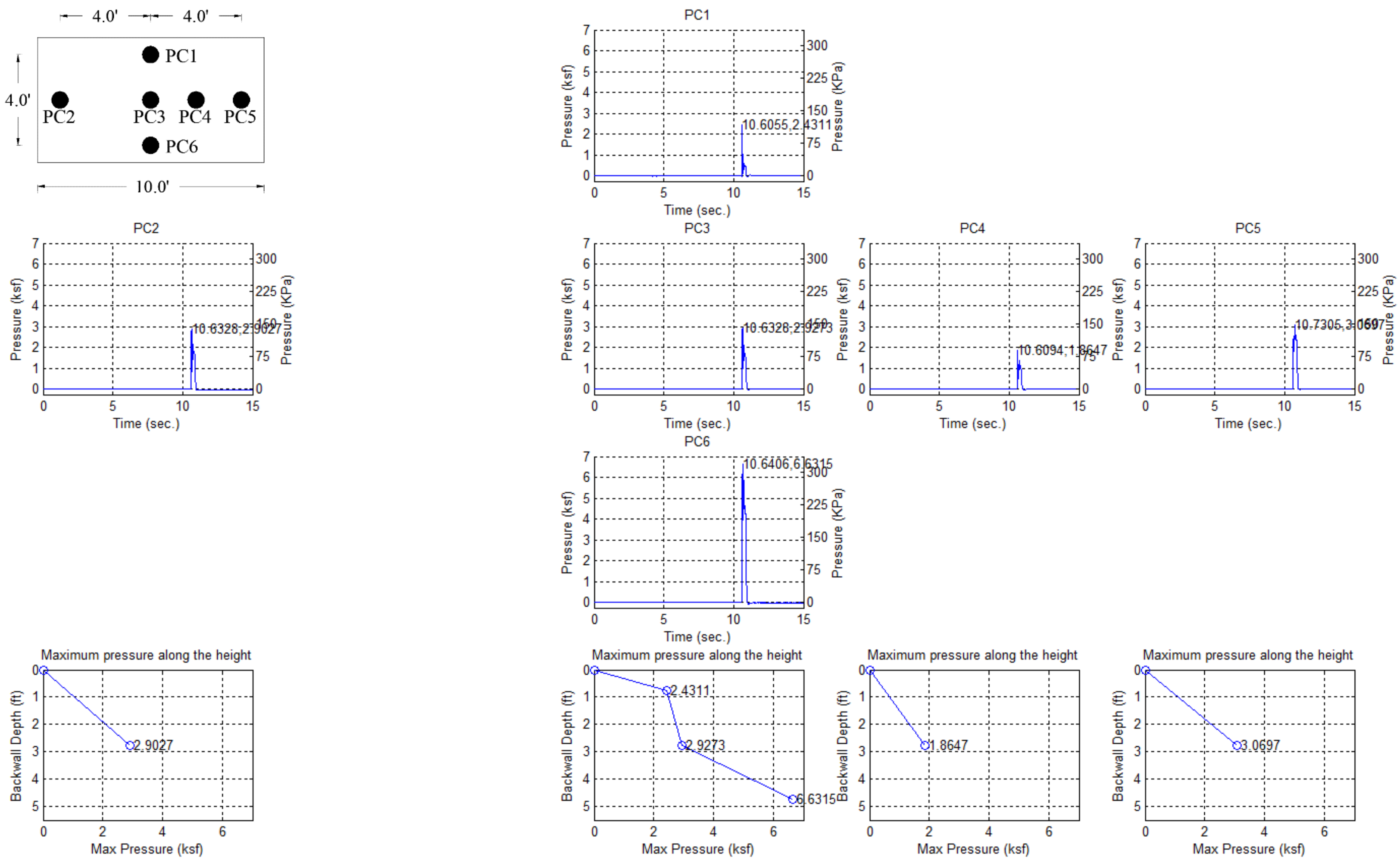

Figure 6-151 Soil pressure histories and maximum pressures for the 0° skew test in Run 7.

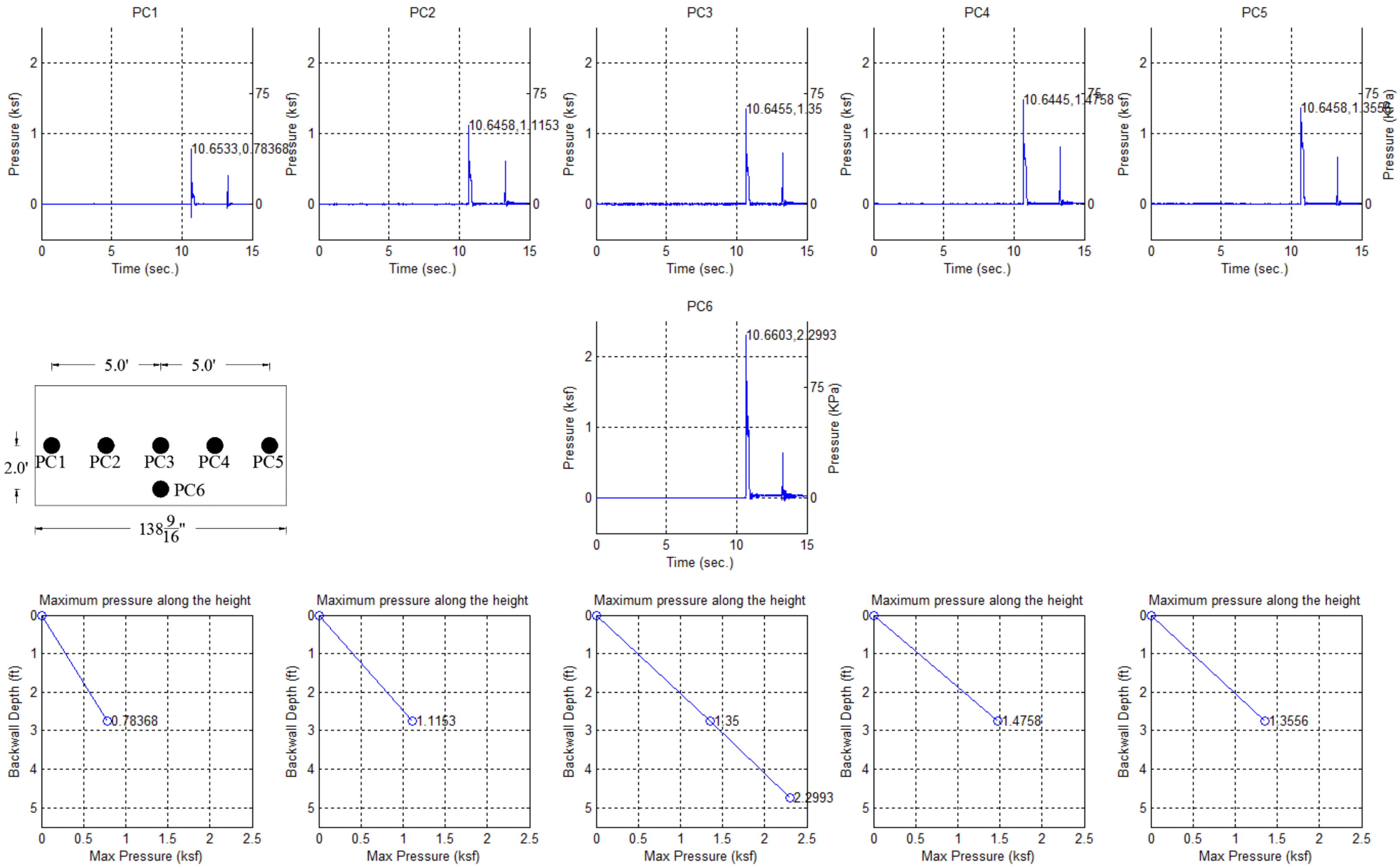

Figure 6-152 Soil pressure histories and maximum pressures for the 30° skew test in Run 2.

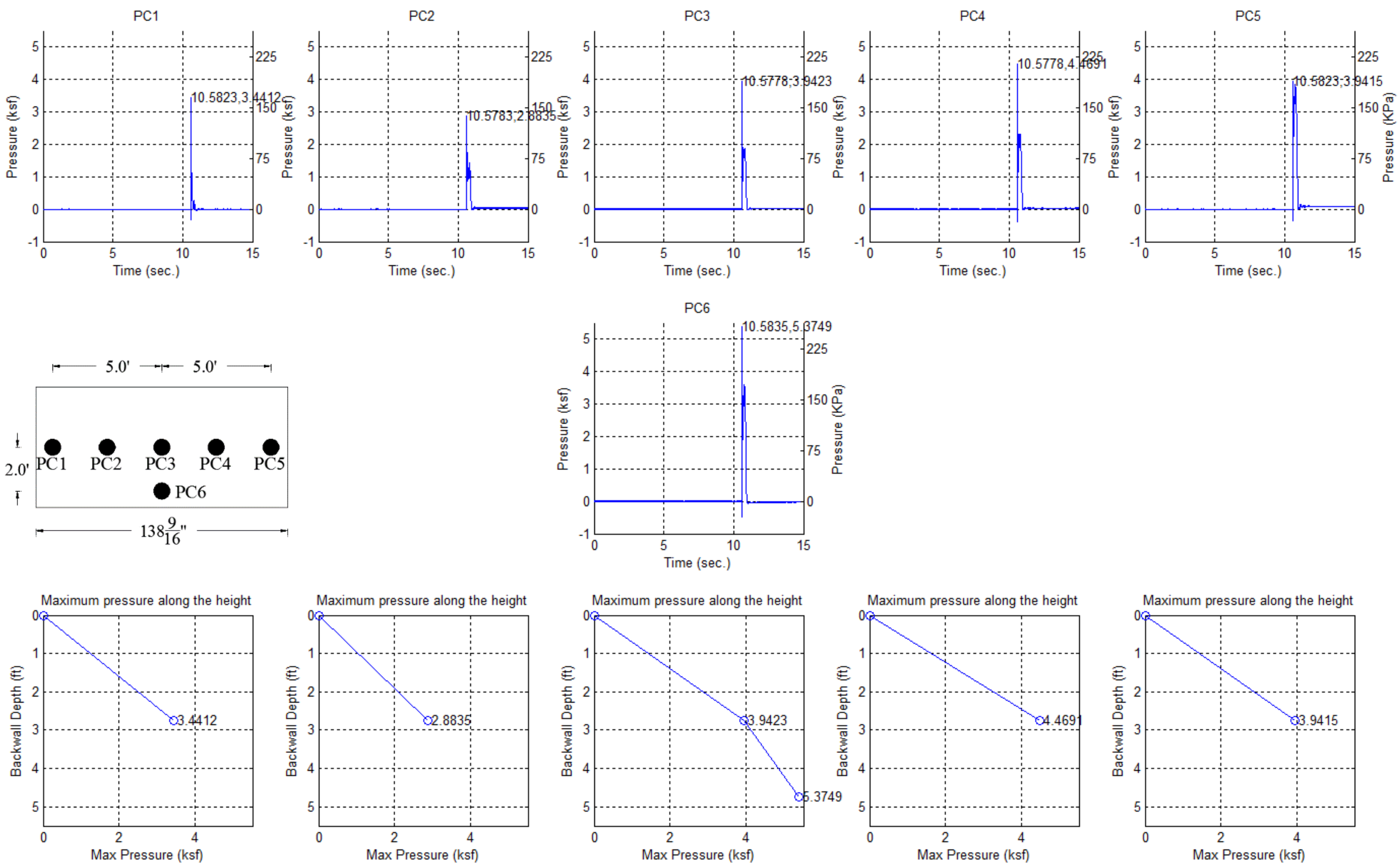

Figure 6-153 Soil pressure histories and maximum pressures for the 30° skew test in Run 3.

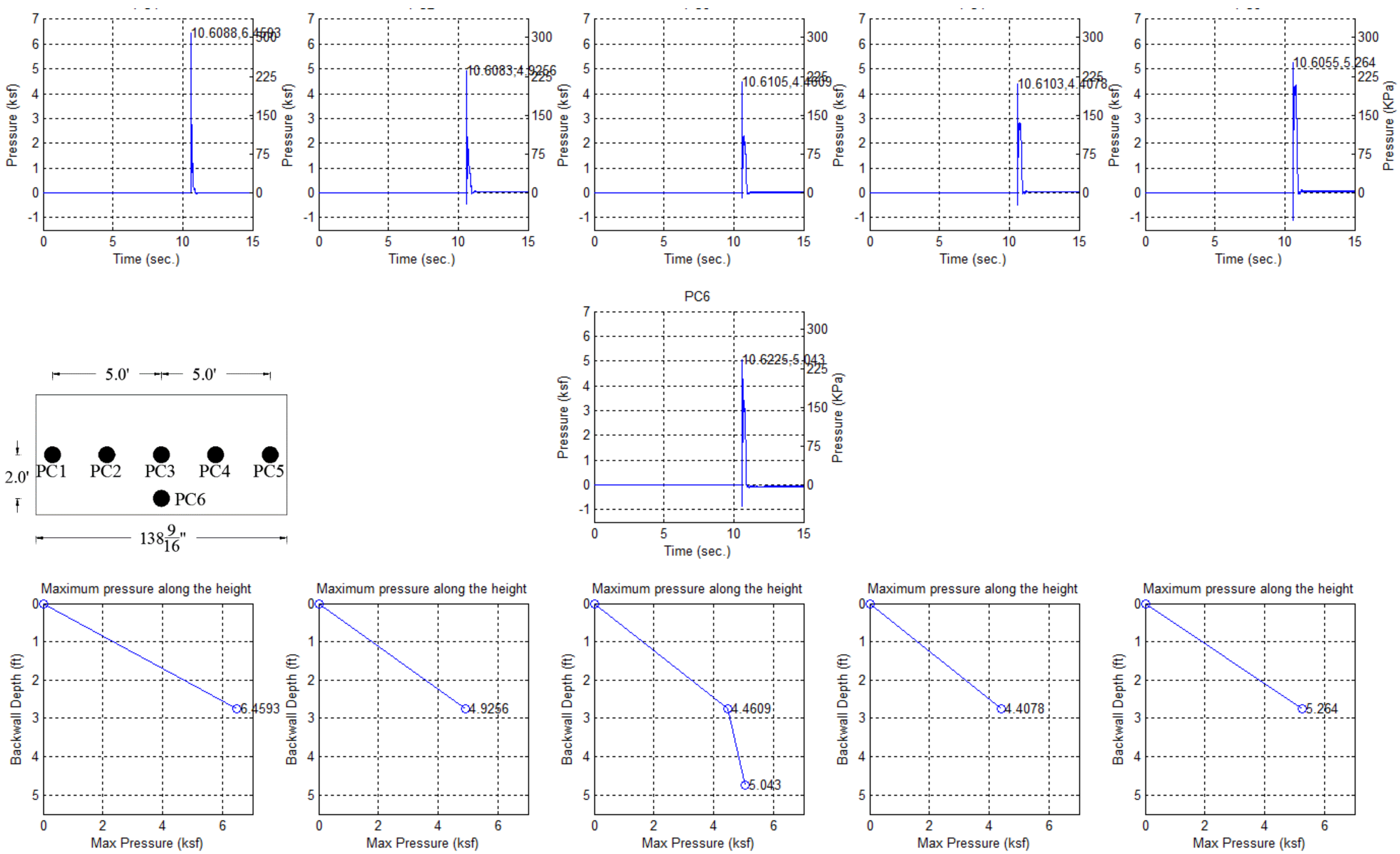

Figure 6-154 Soil pressure histories and maximum pressures for the 30° skew test in Run 4.

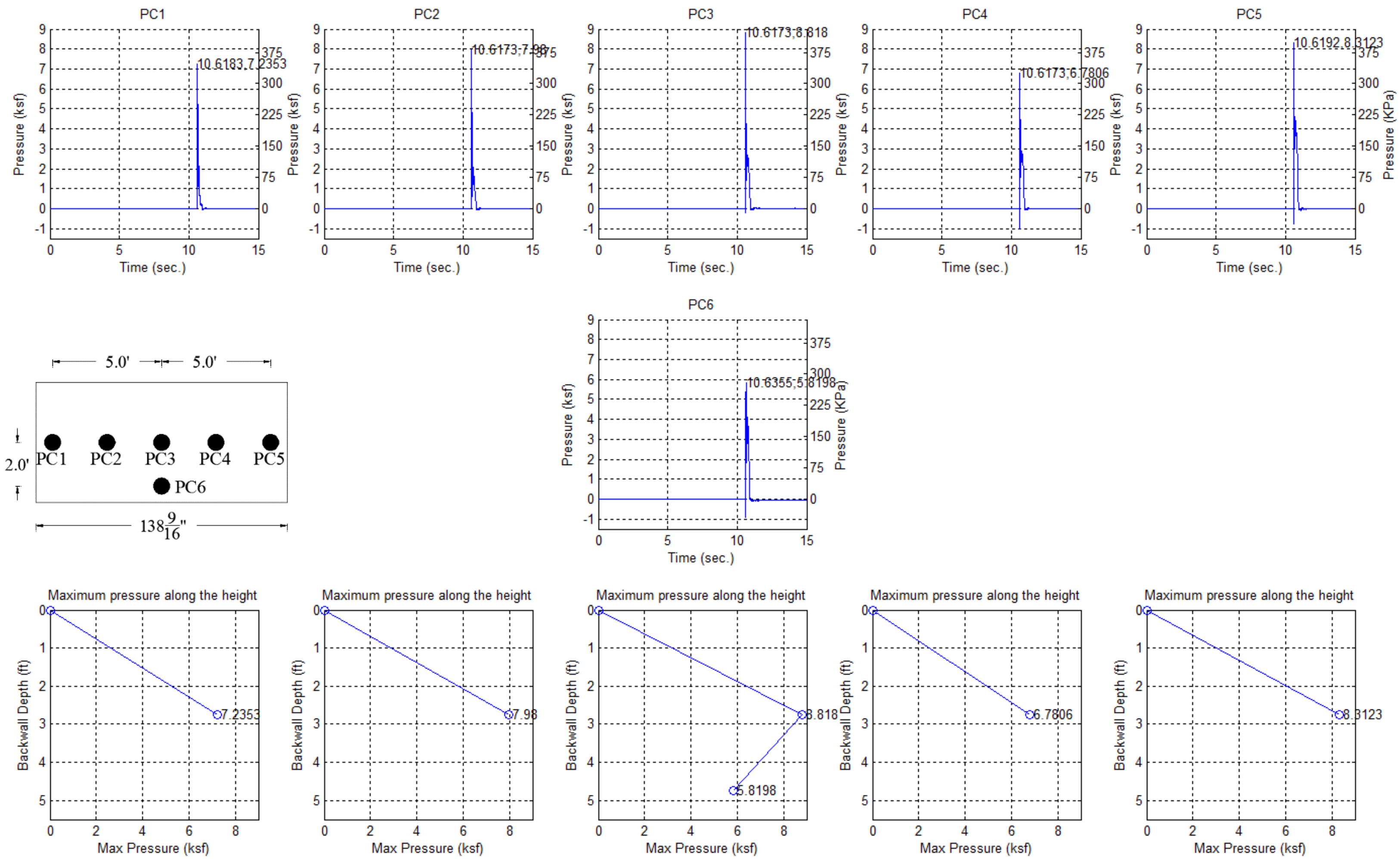

Figure 6-155 Soil pressure histories and maximum pressures for the 30° skew test in Run 5.

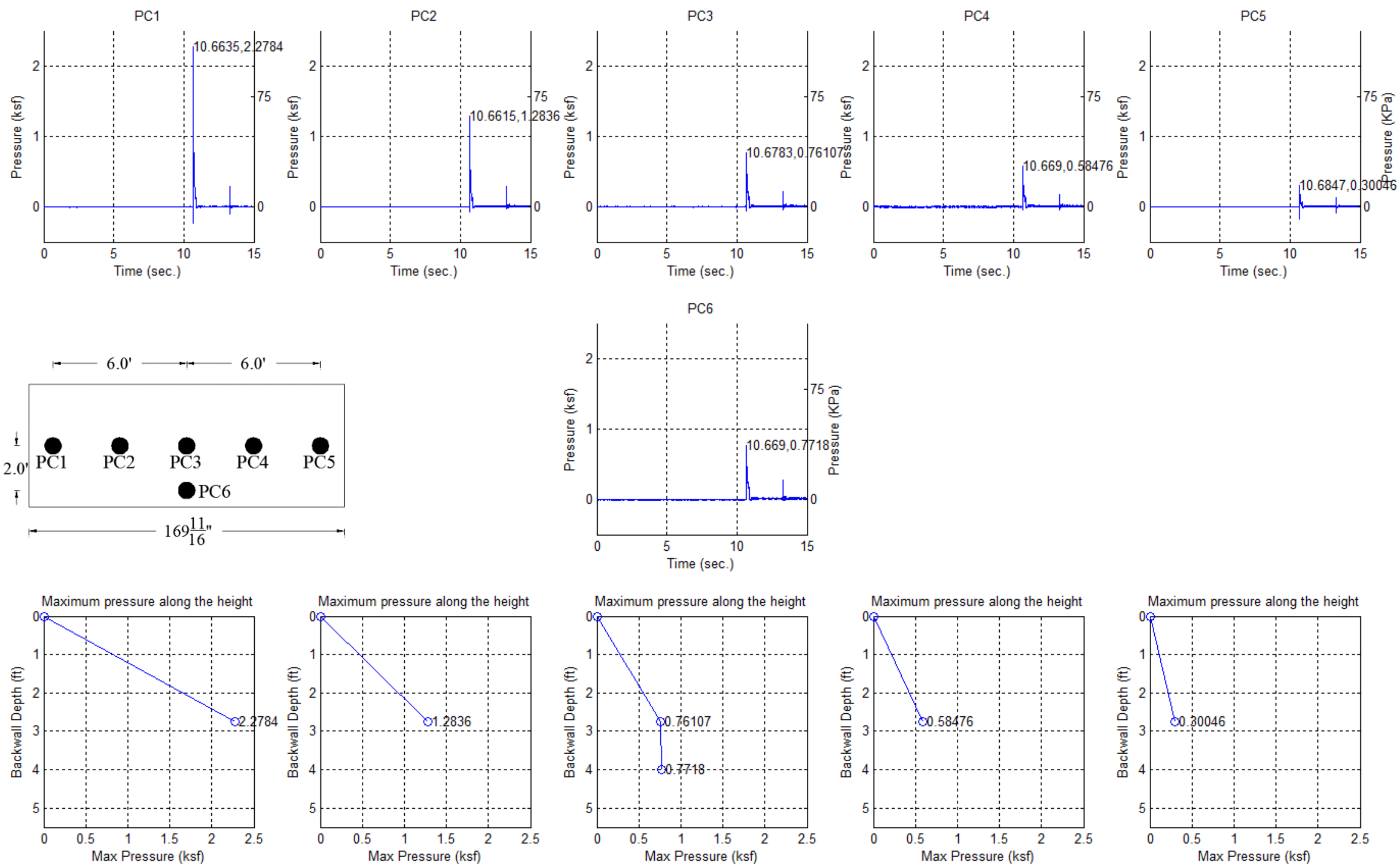

Figure 6-156 Soil pressure histories and maximum pressures for the 45° skew test in Run 2.

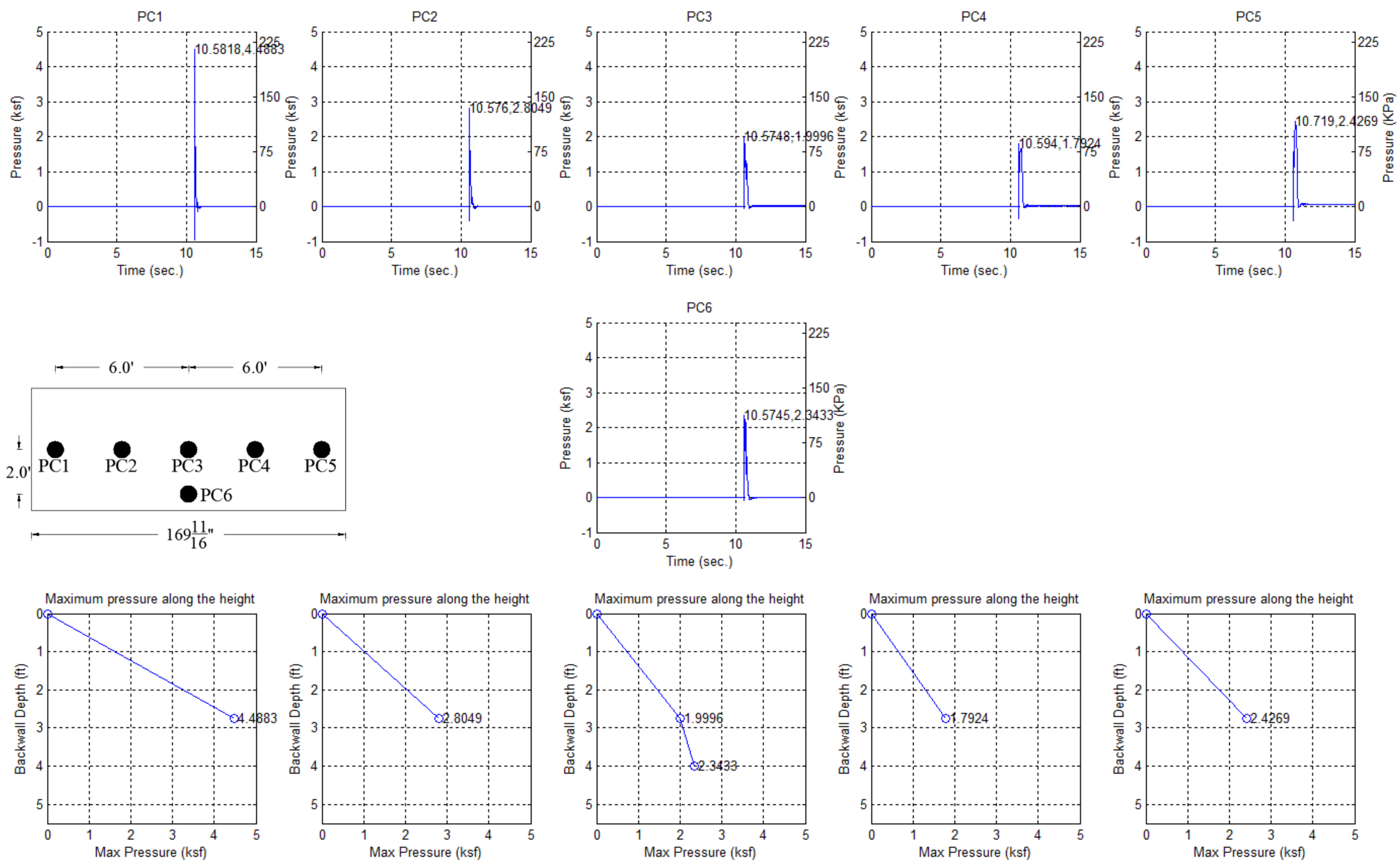

Figure 6-157 Soil pressure histories and maximum pressures for the 45° skew test in Run 3.

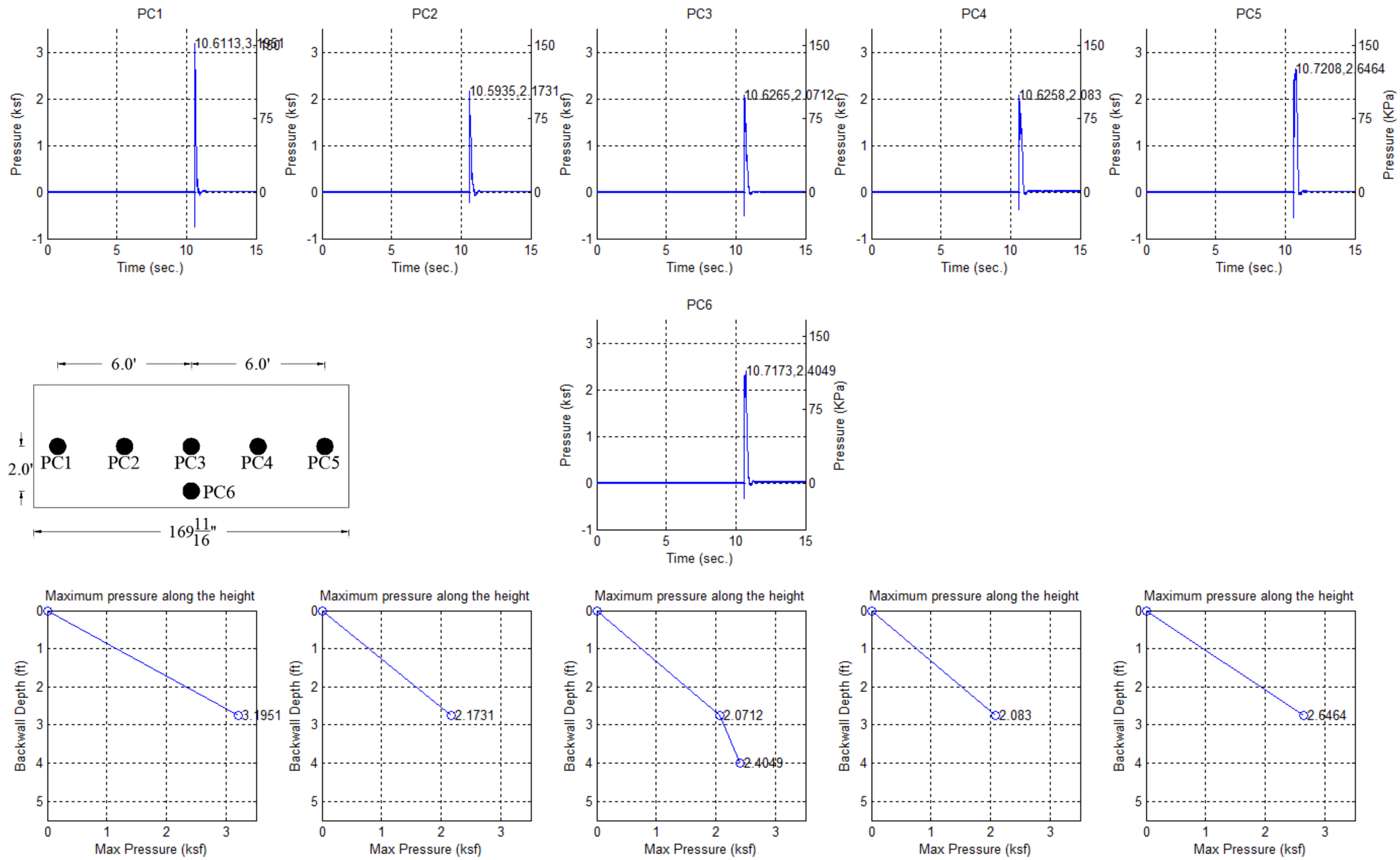

Figure 6-158 Soil pressure histories and maximum pressures for the 45° skew test in Run 4.

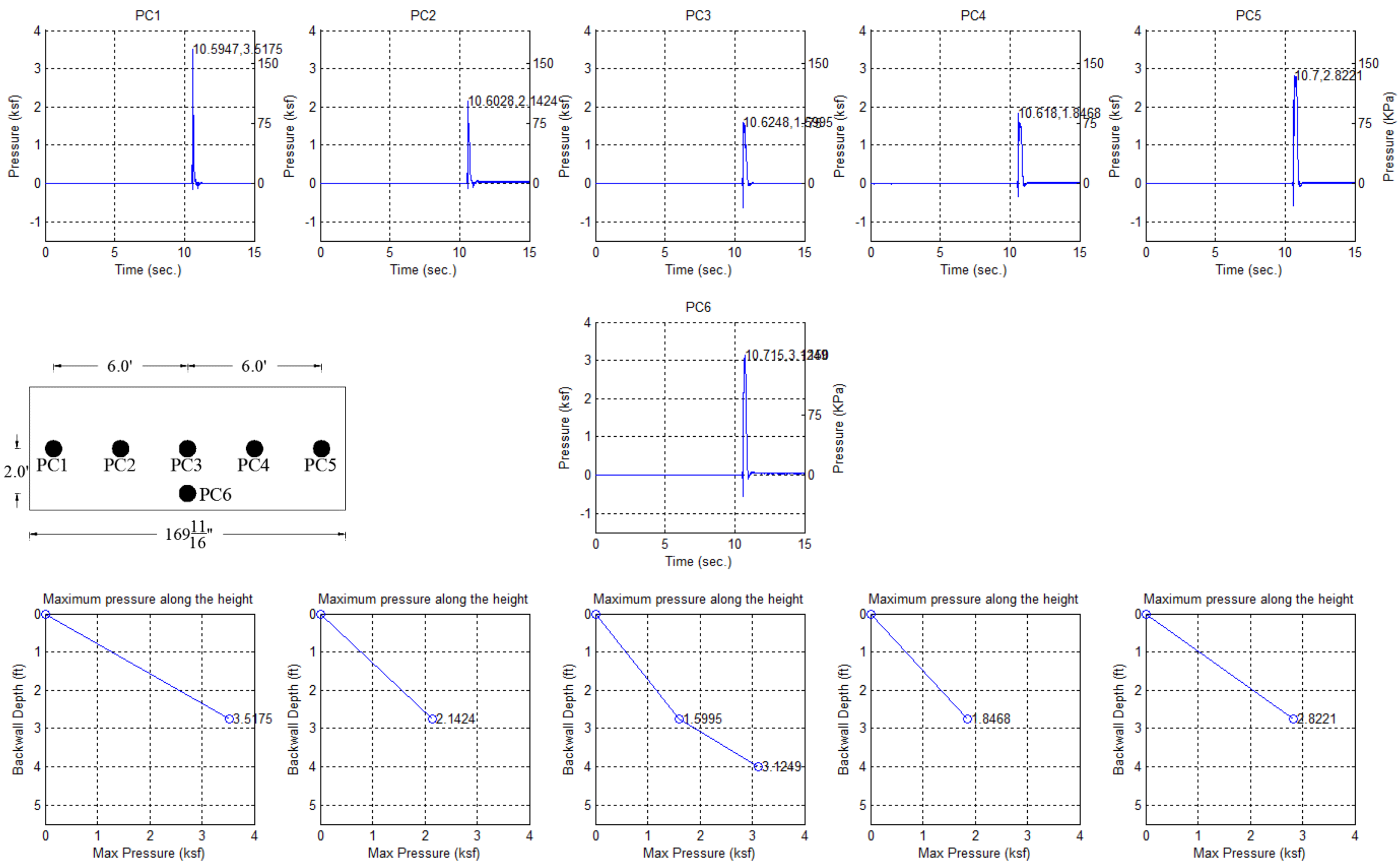

Figure 6-159 Soil pressure histories and maximum pressures for the 45° skew test in Run 5.

Run 2 – 50% Sylmar

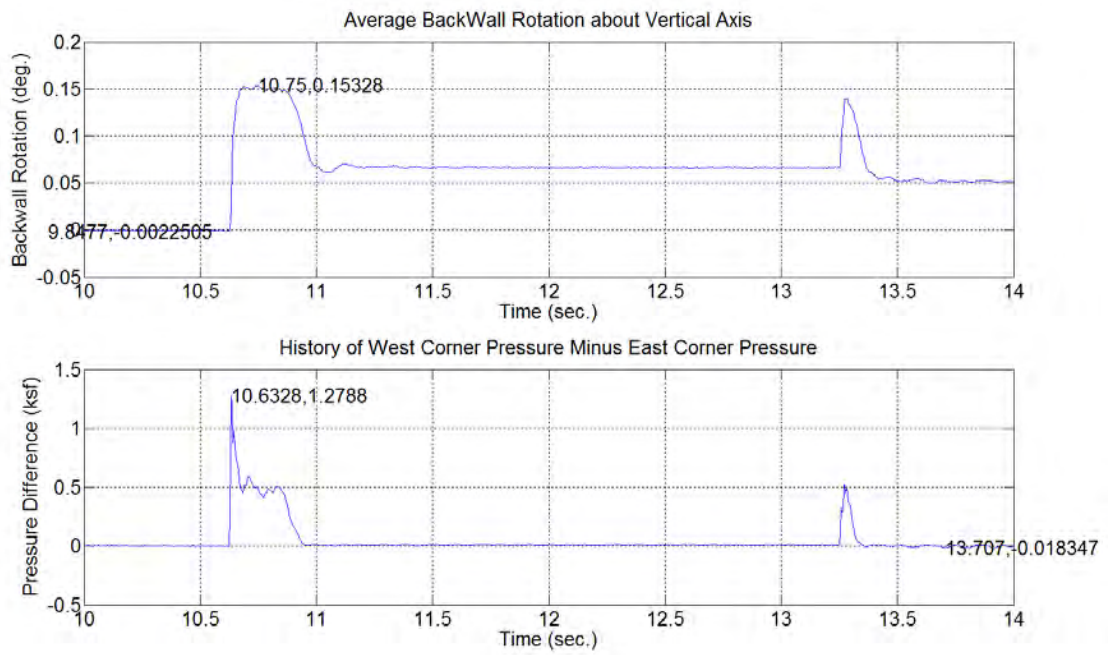

Run 3 – 75% Sylmar

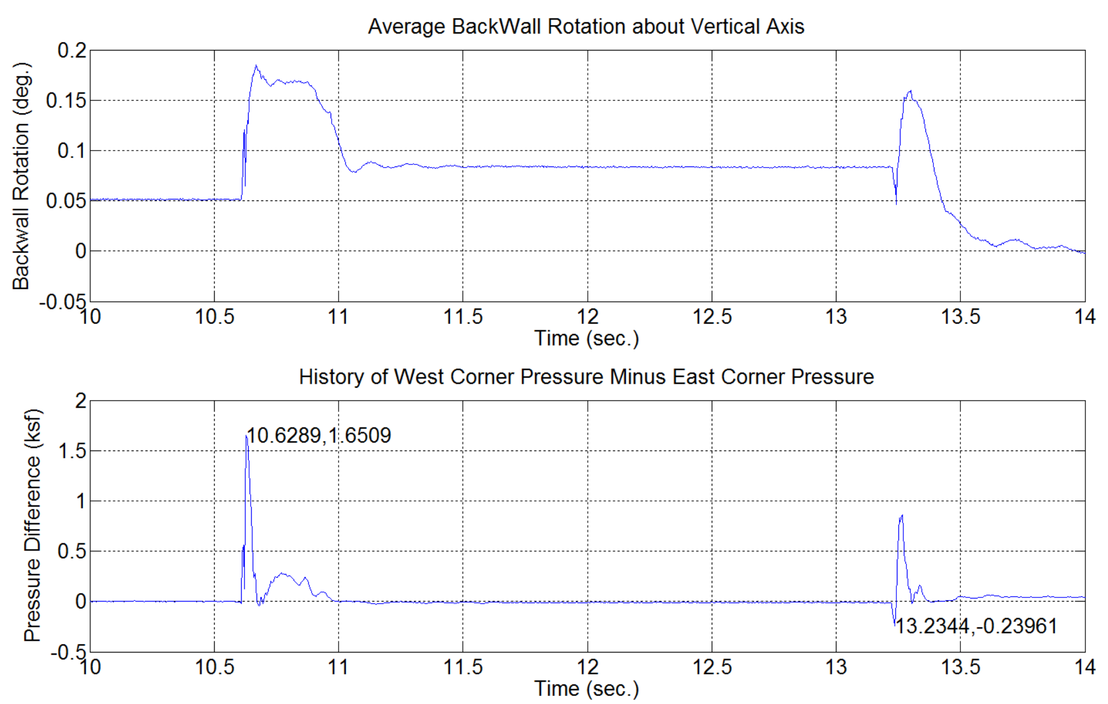

Figure 6-160 Effect of backwall rotation on the soil pressure for the 0° skew test in Run 2 and 3.

Run 6 – 150% Sylmar

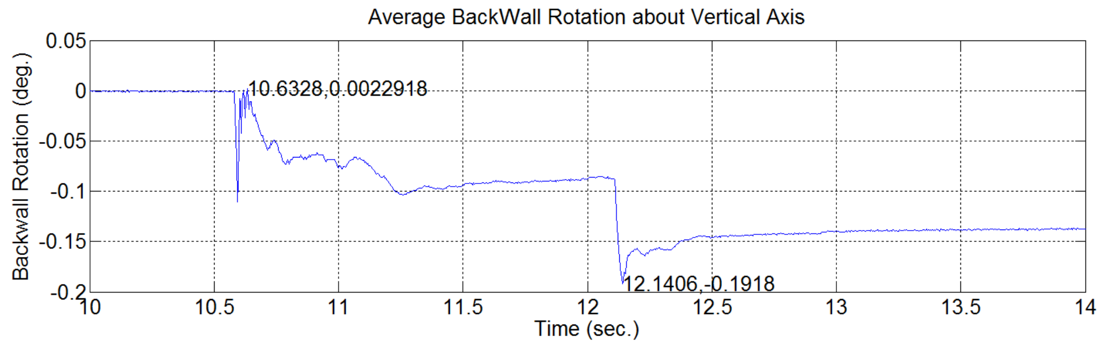

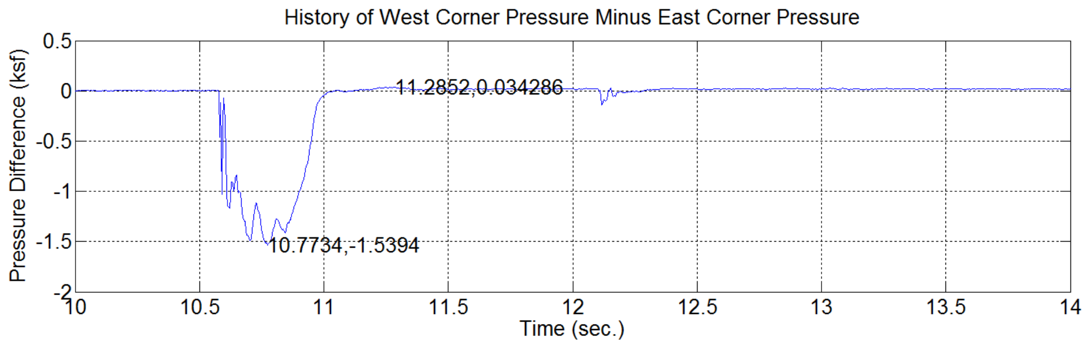

Run 7 – 150% Sylmar

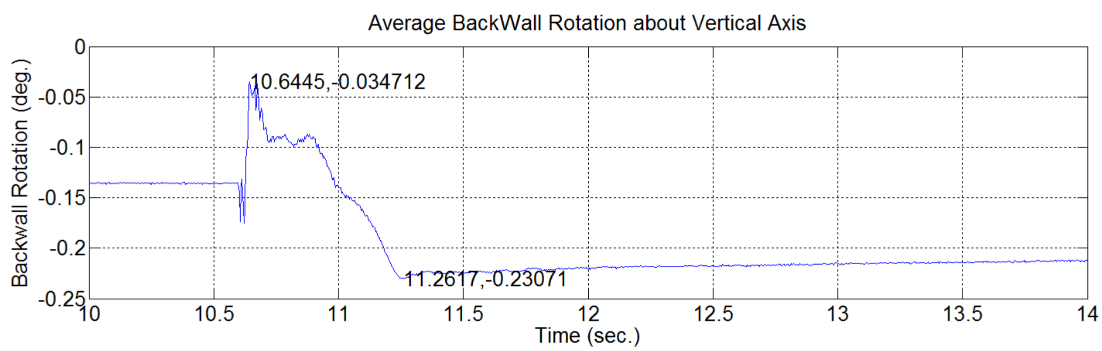

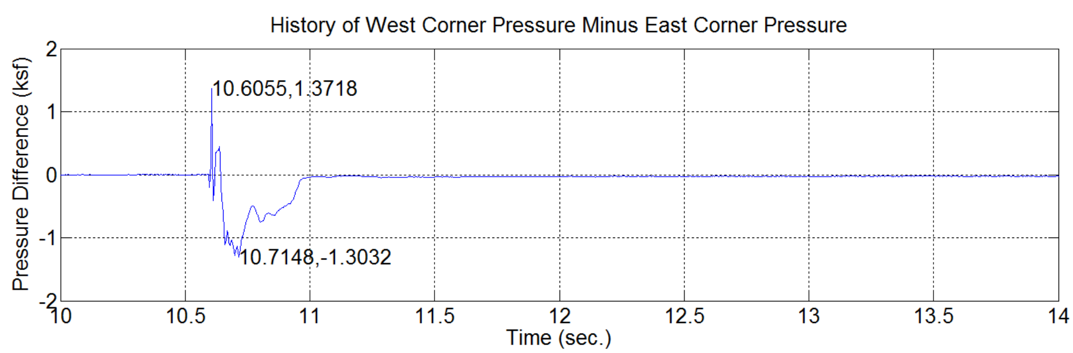

Figure 6-161 Effect of backwall rotation on the soil pressure for the 0° skew test in Run 6 and 7.

Run 2 – 50% Sylmar

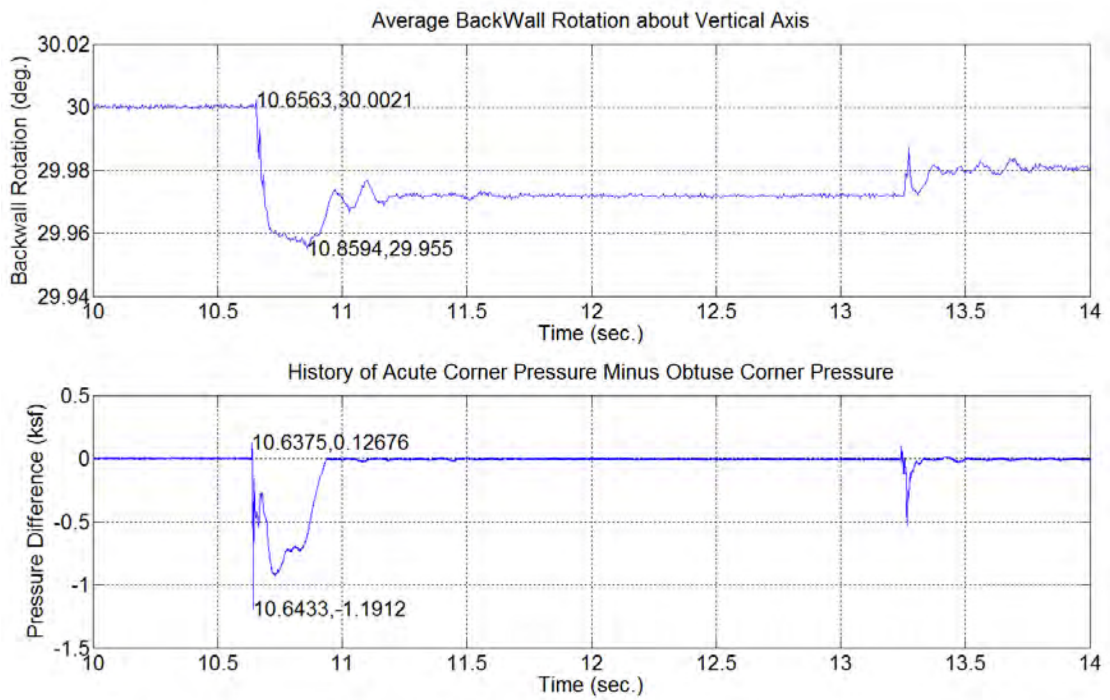

Run 3 – 125% Sylmar

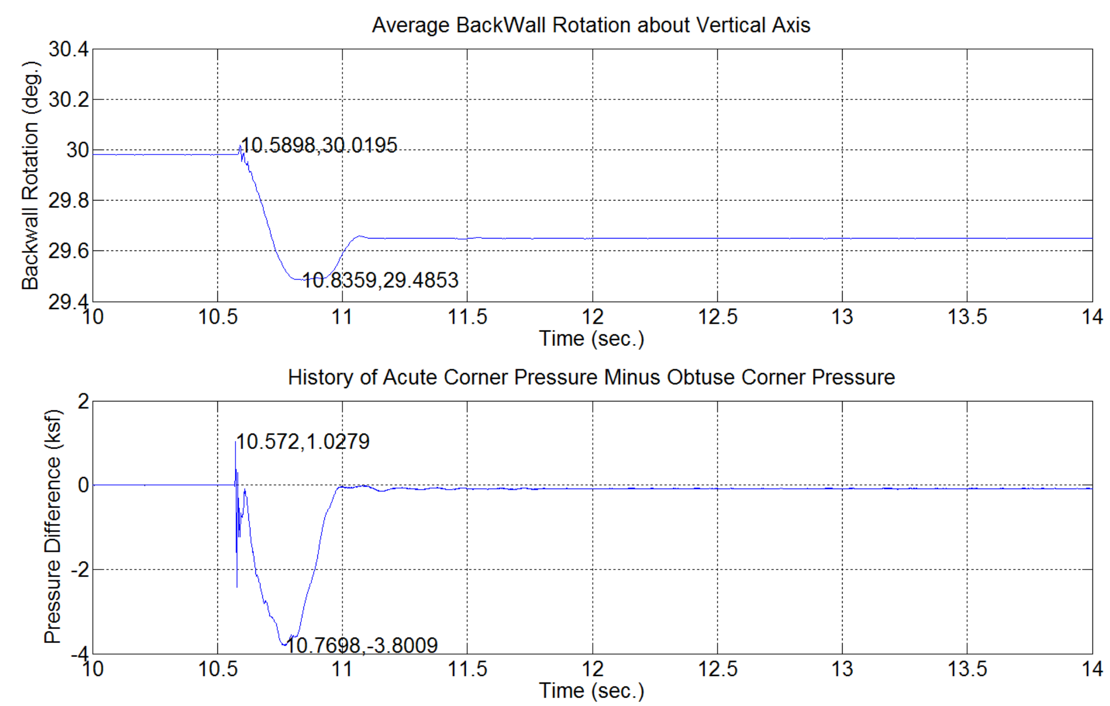

Figure 6-162 Effect of backwall rotation on the soil pressure for the 30° skew test in Run 2 and 3.

Run 4 – 150% Sylmar

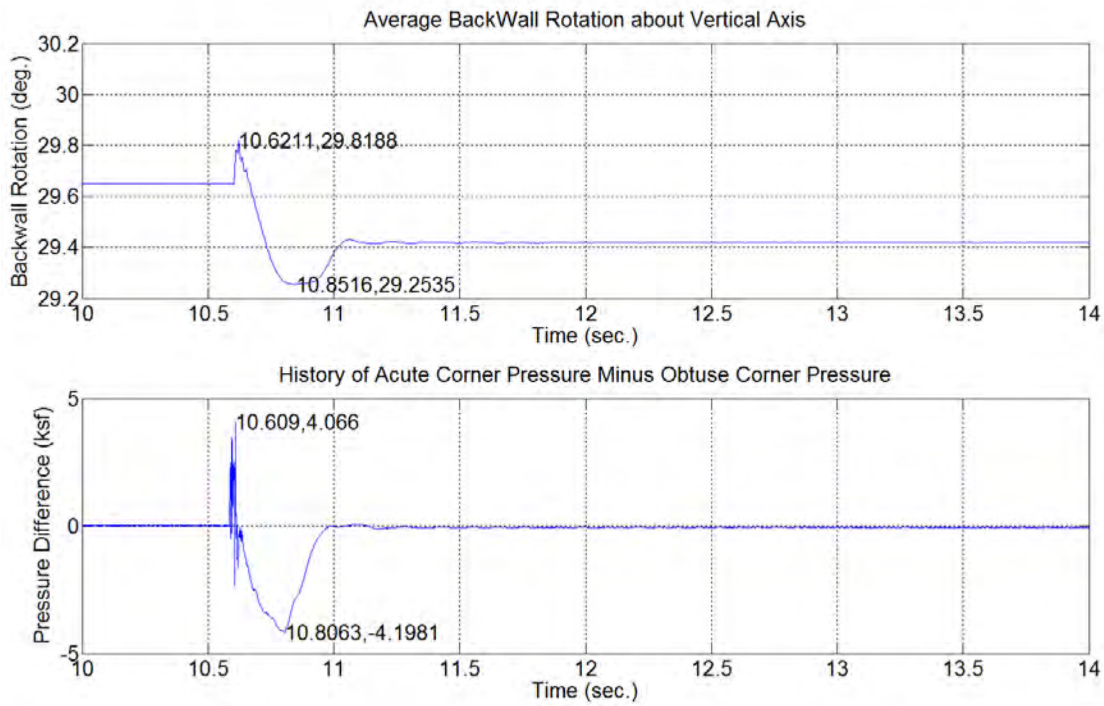

Run 5 – 200% Sylmar

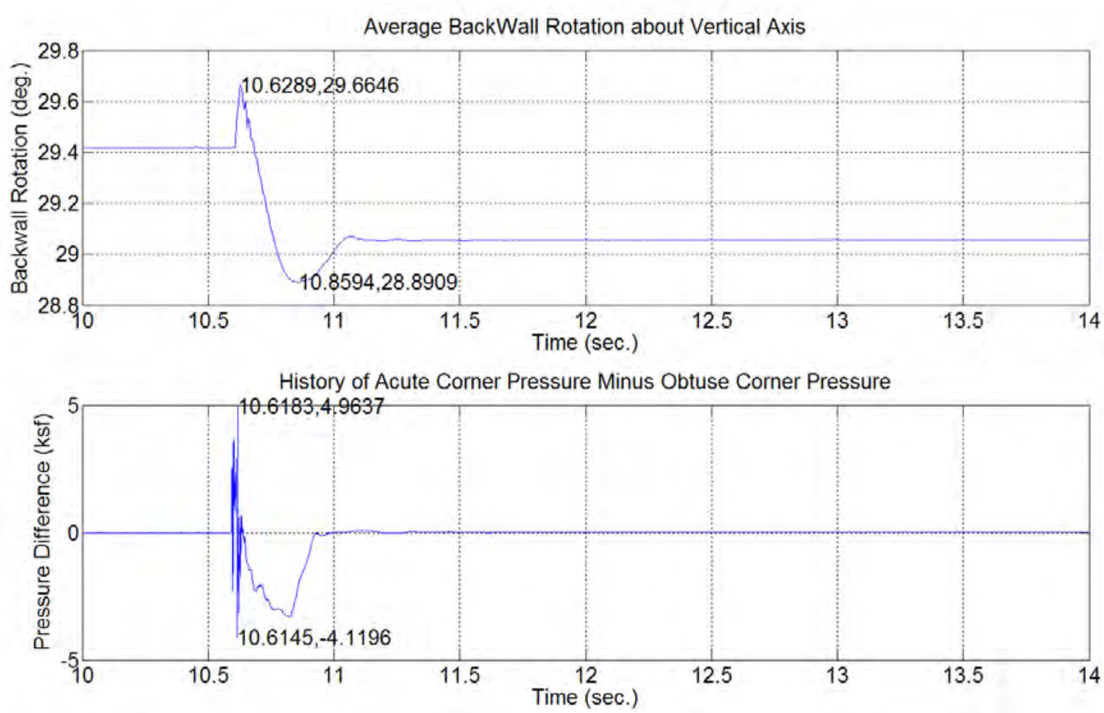

Figure 6-163 Effect of backwall rotation on the soil pressure for the 30° skew test in Run 4 and 5.

Run 2 – 50% Sylmar

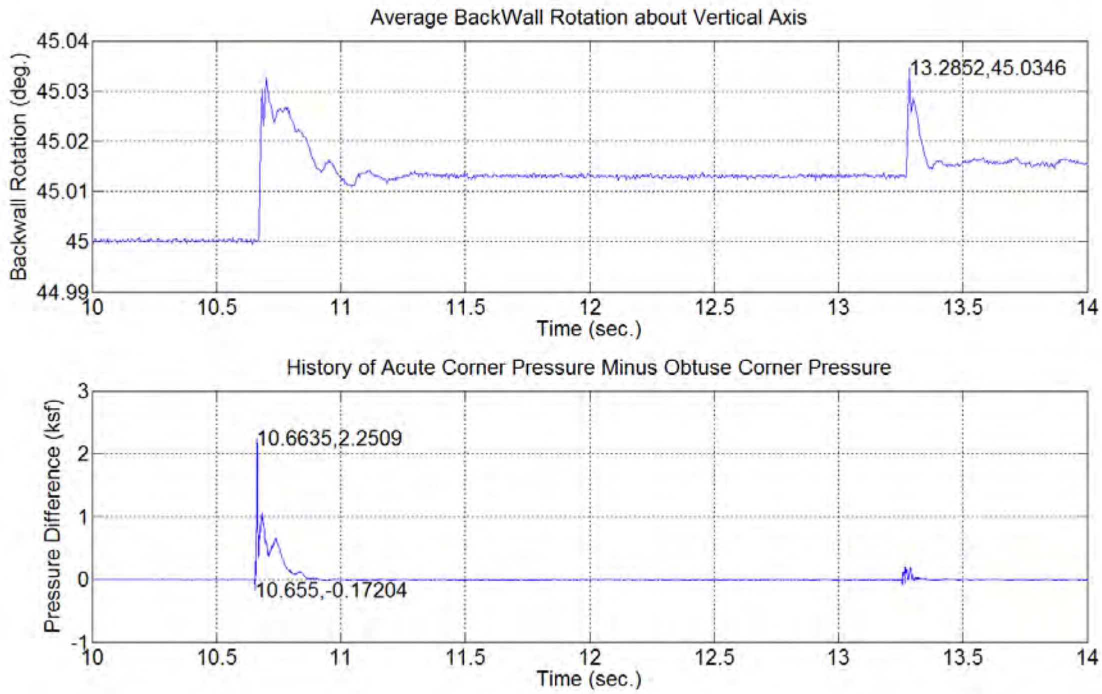

Run 3 – 125% Sylmar

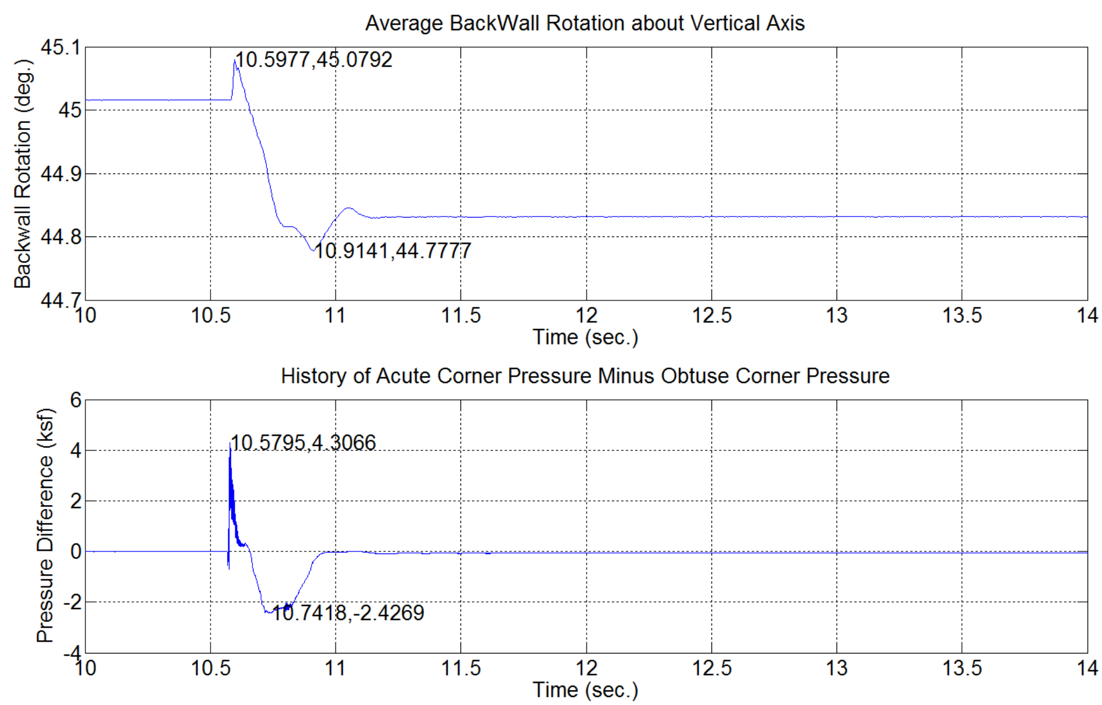

Figure 6-164 Effect of backwall rotation on the soil pressure for the 45° skew test in Run 2 and 3.

Run 4 – 150% Sylmar

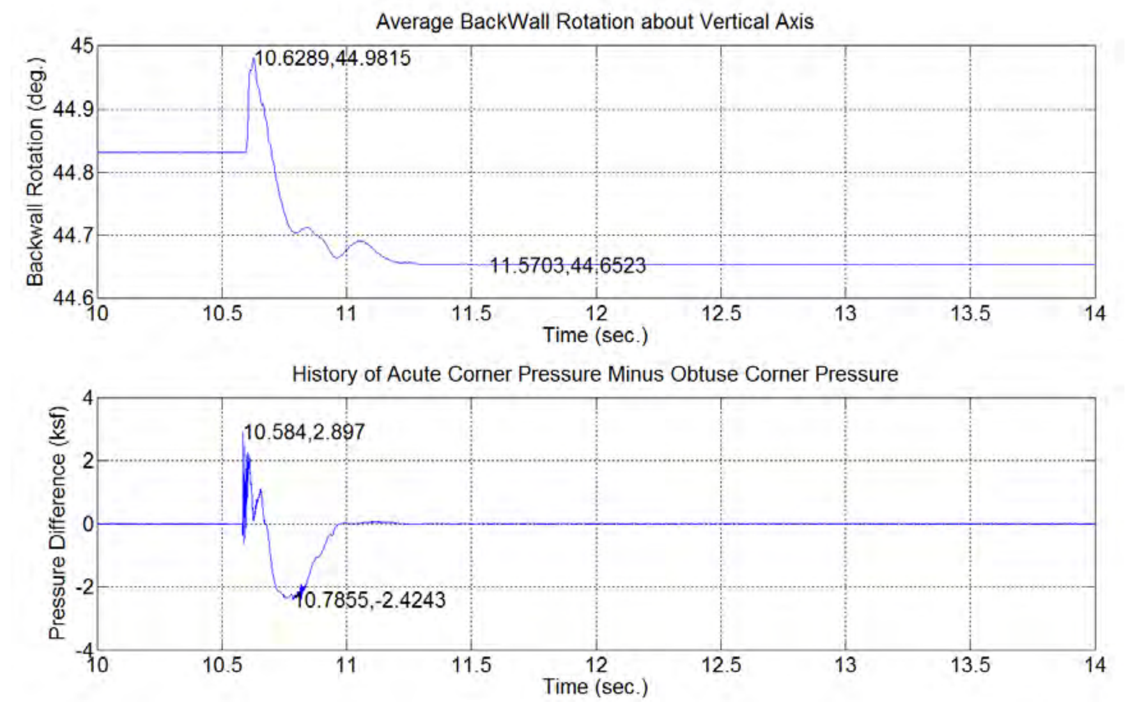

Run 5 – 200% Sylmar

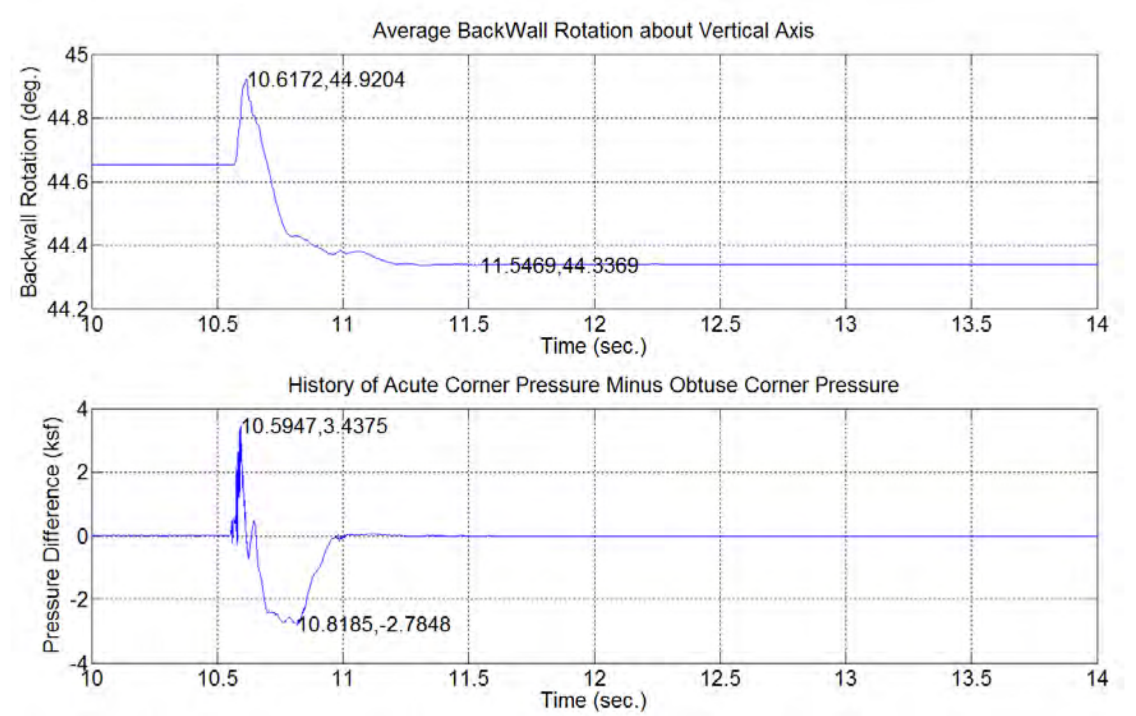

Figure 6-165 Effect of backwall rotation on the soil pressure for the 45° skew test in Run 4 and 5.

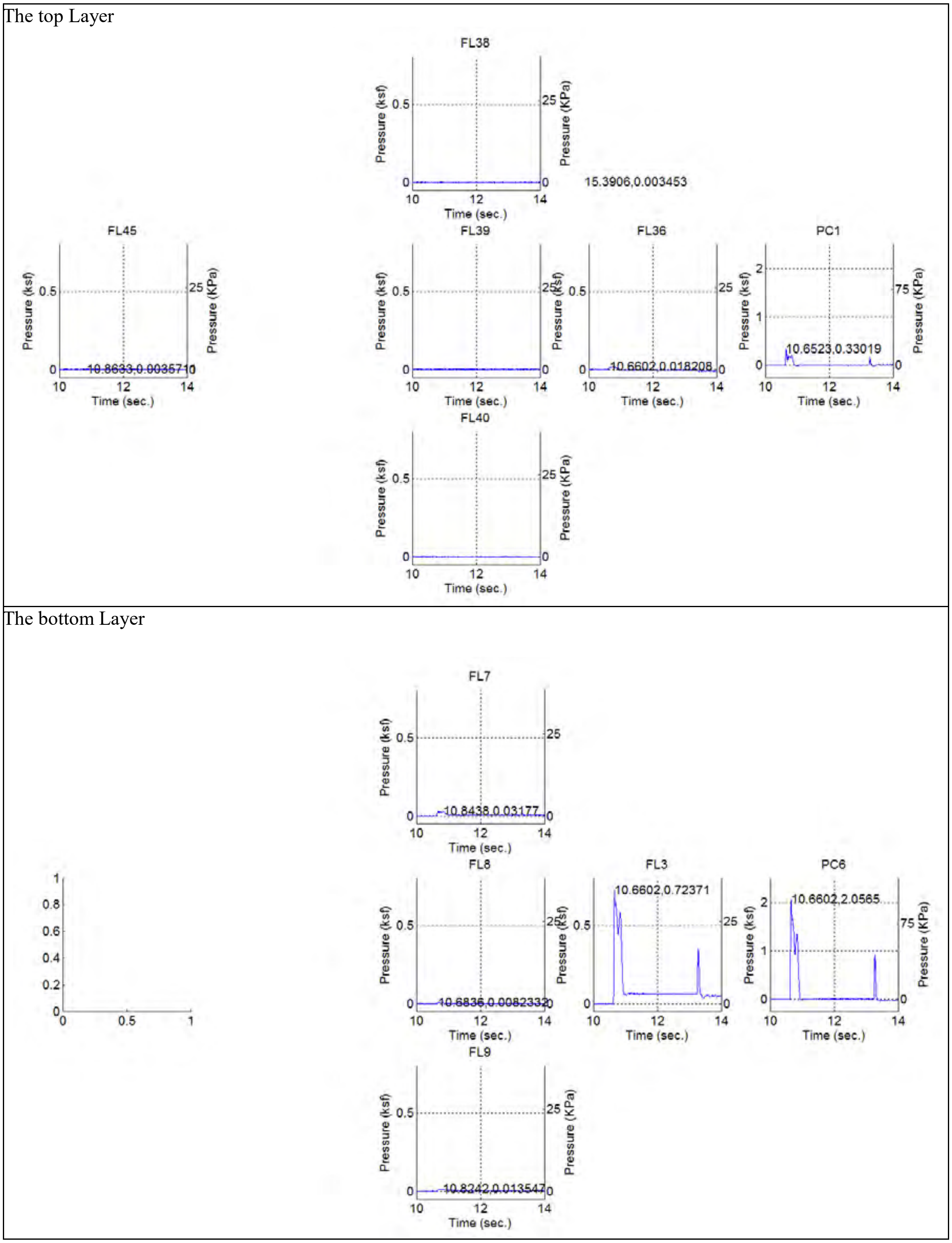

Figure 6-166 Soil pressure measured at the top and the bottom layers for the 0° skew test in Run 2.

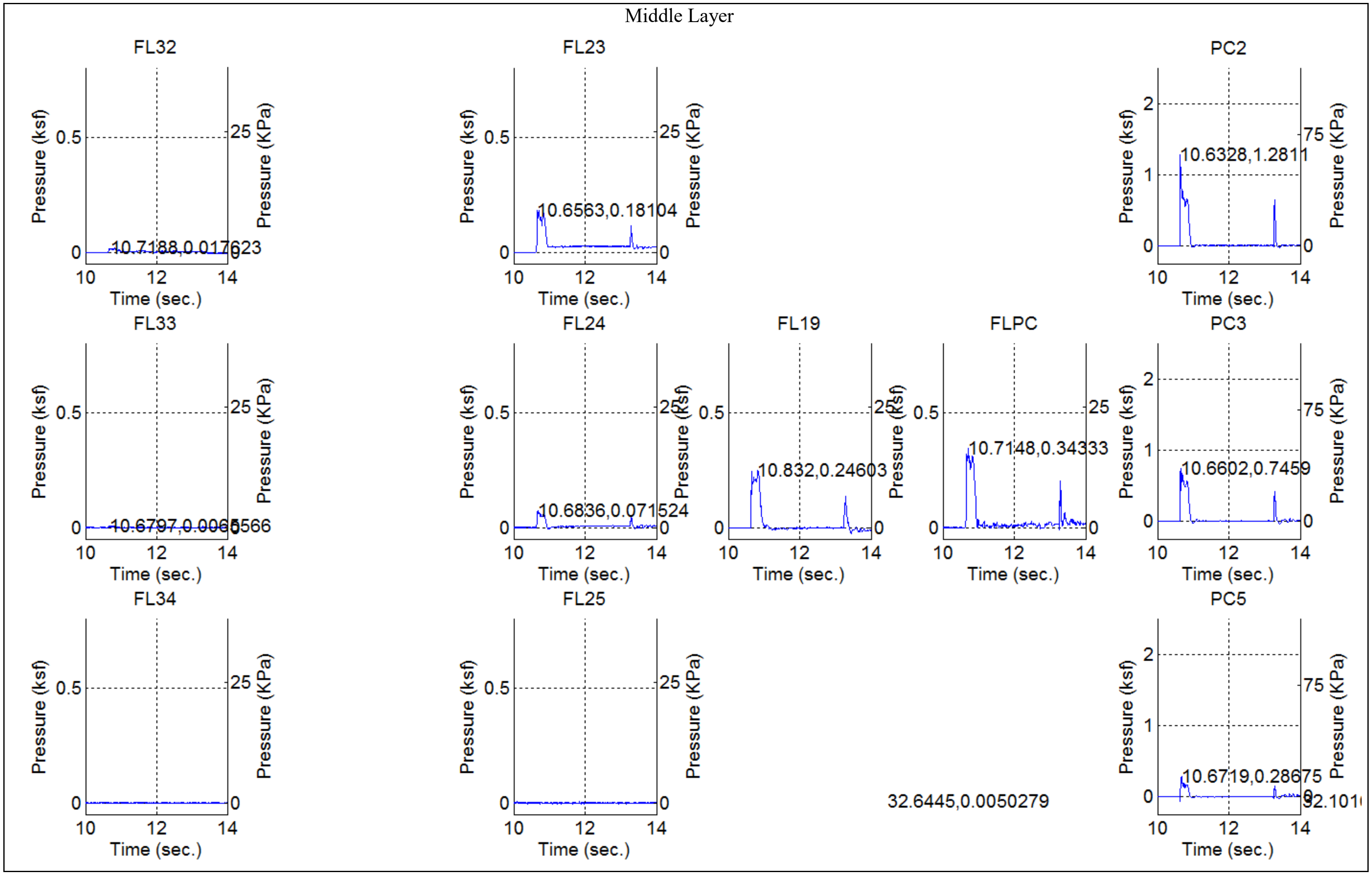

Figure 6-167 Soil pressure histories at the middle layer for the 0° skew test in Run 2.

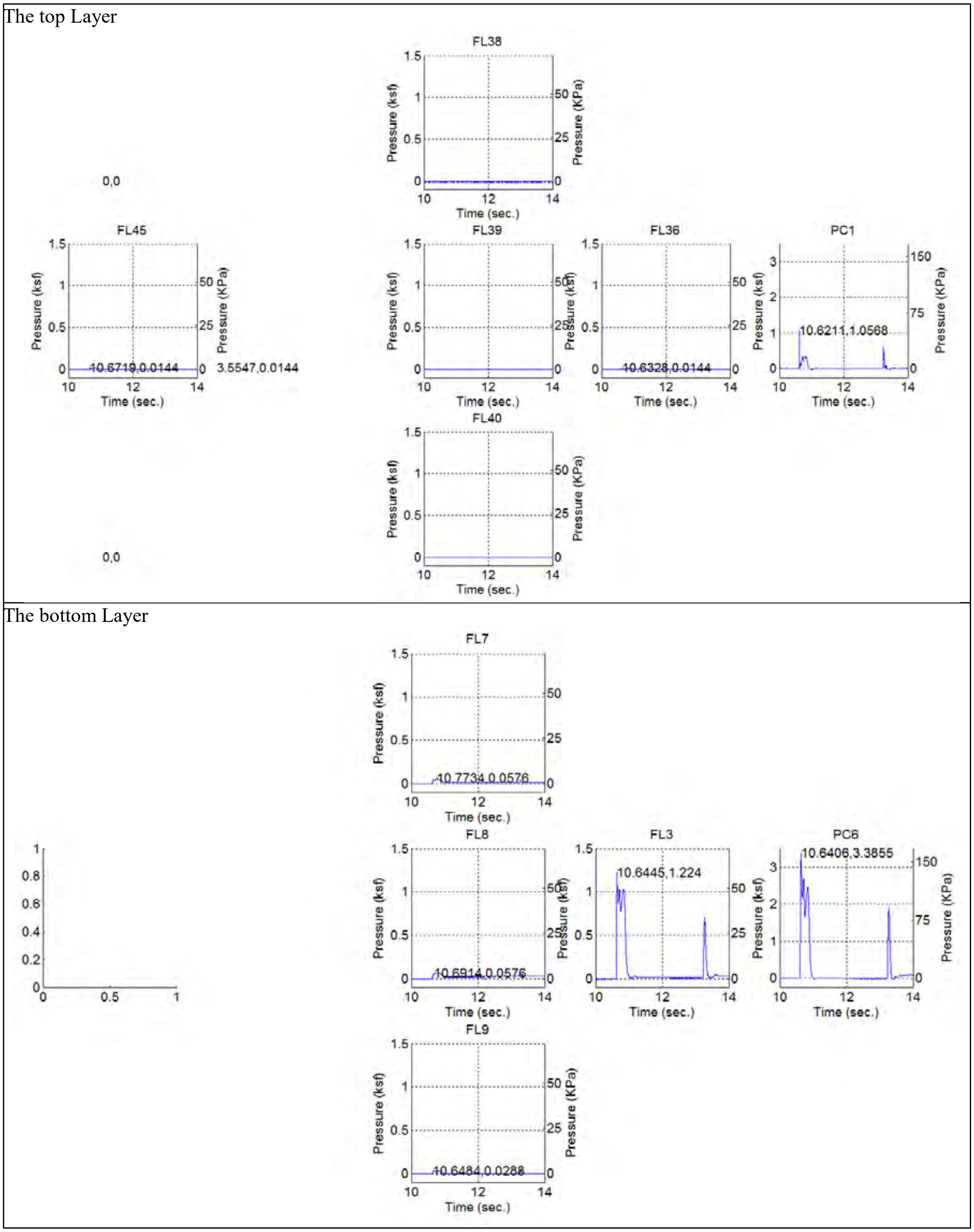

Figure 6-168 Soil pressure histories at the top and the bottom layers for the 0° skew test in Run 3.

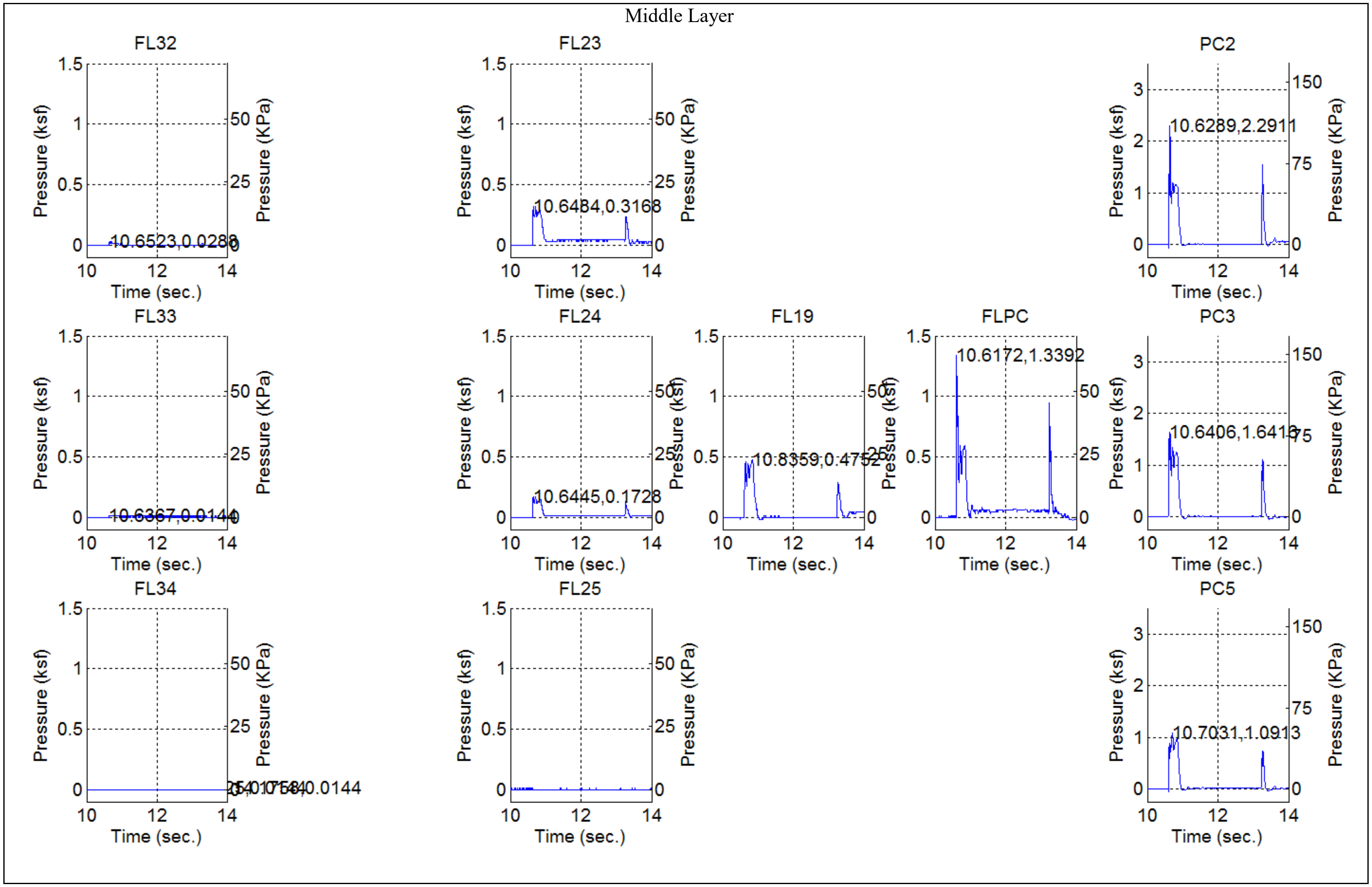

Figure 6-169 Soil pressure histories at the middle layer for the 0° skew test in Run 3.

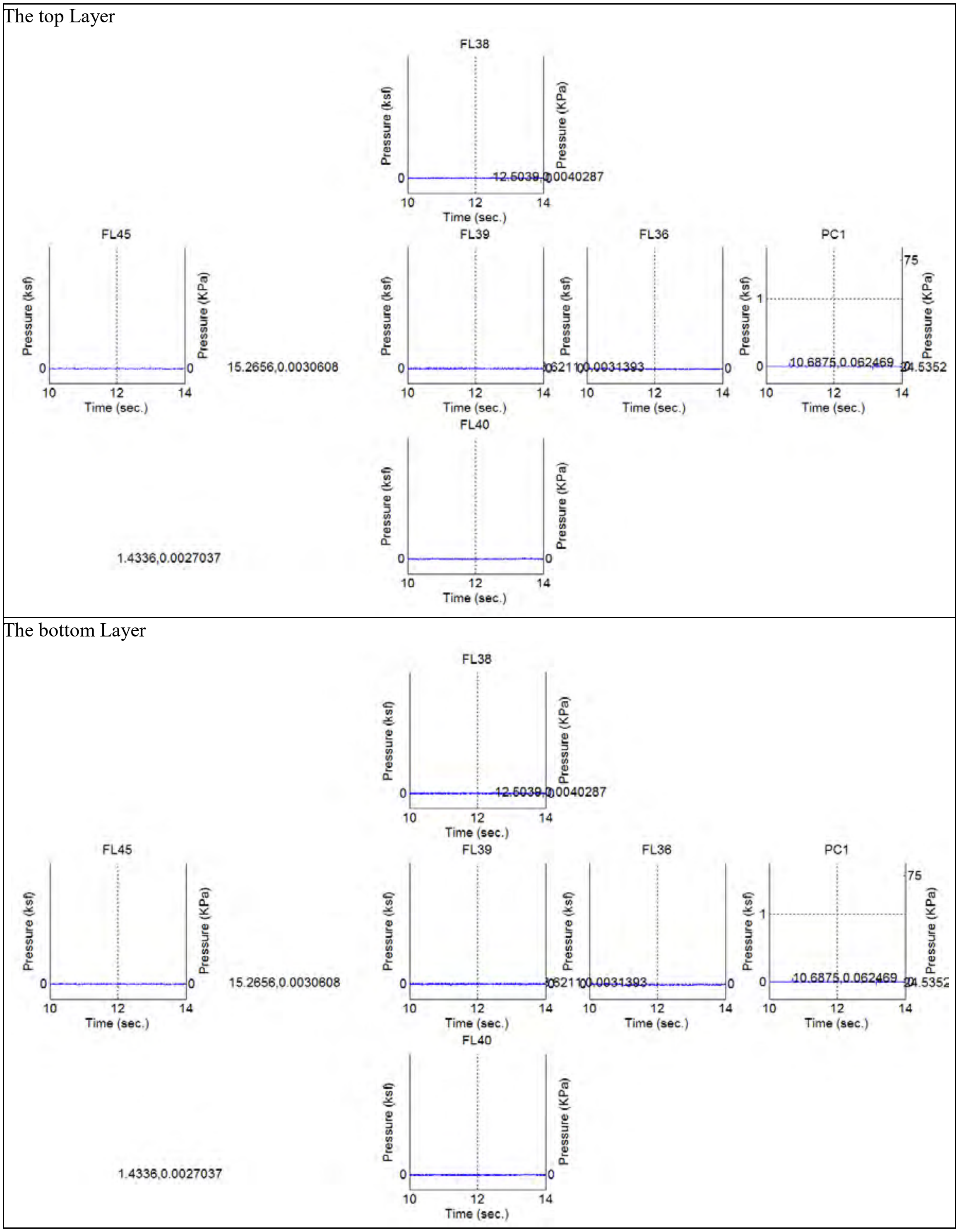

Figure 6-170 Soil pressure histories at the top and the bottom layers for the 0° skew test in Run 4.

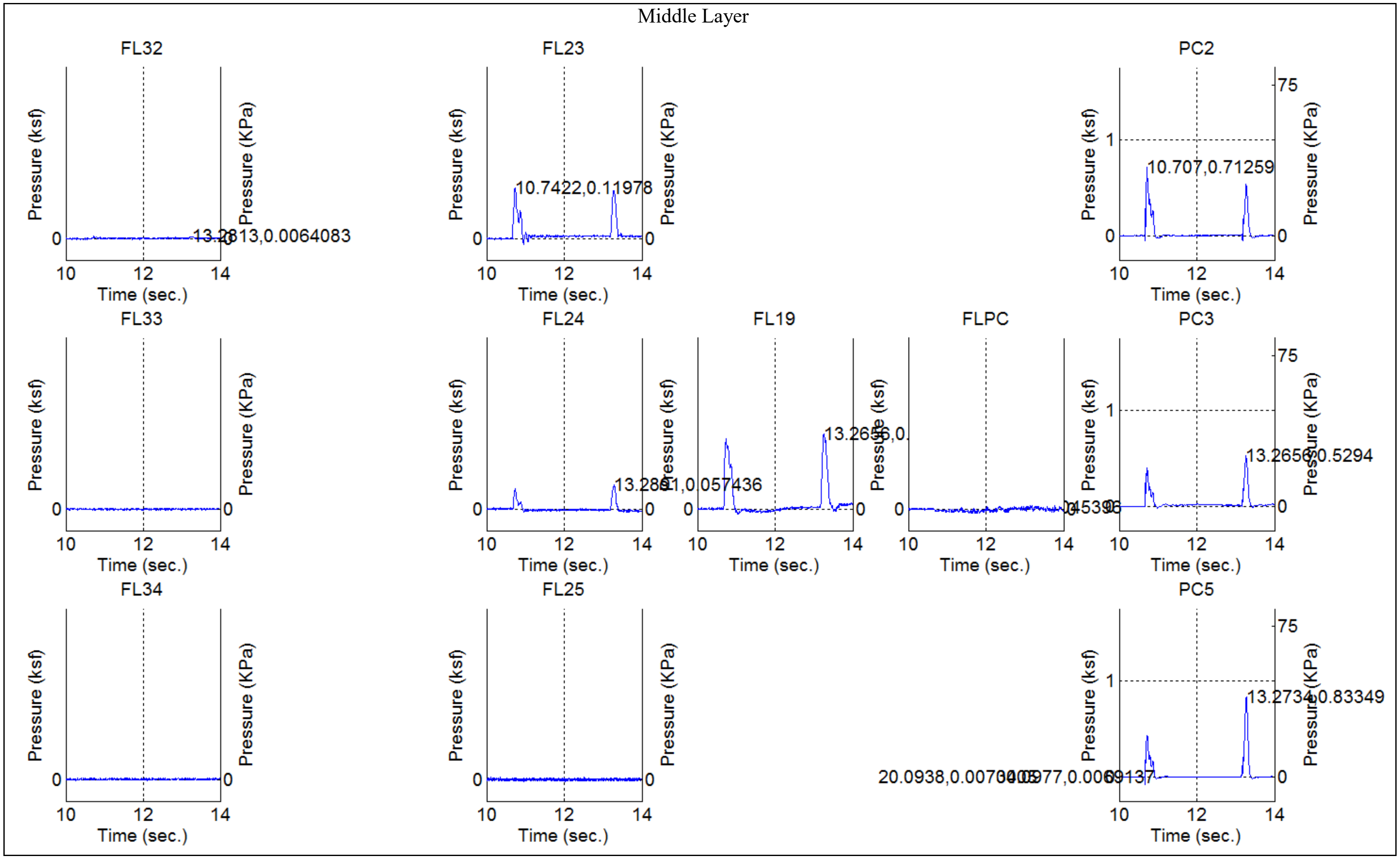

Figure 6-171 Soil pressure histories at the middle layer for the 0° skew test in Run 4.

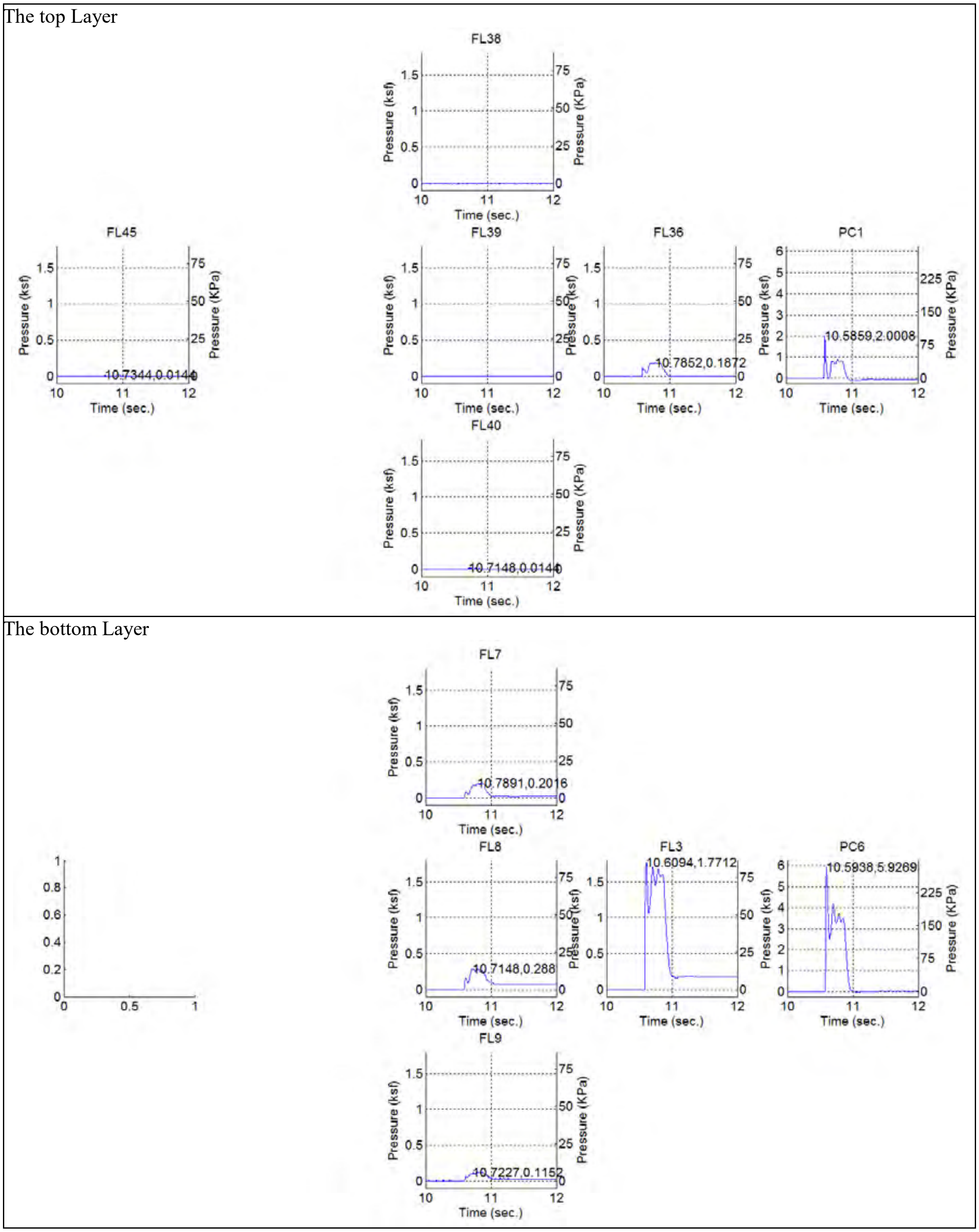

Figure 6-172 Soil pressure histories at the top and the bottom layers for the 0° skew test in Run 6.

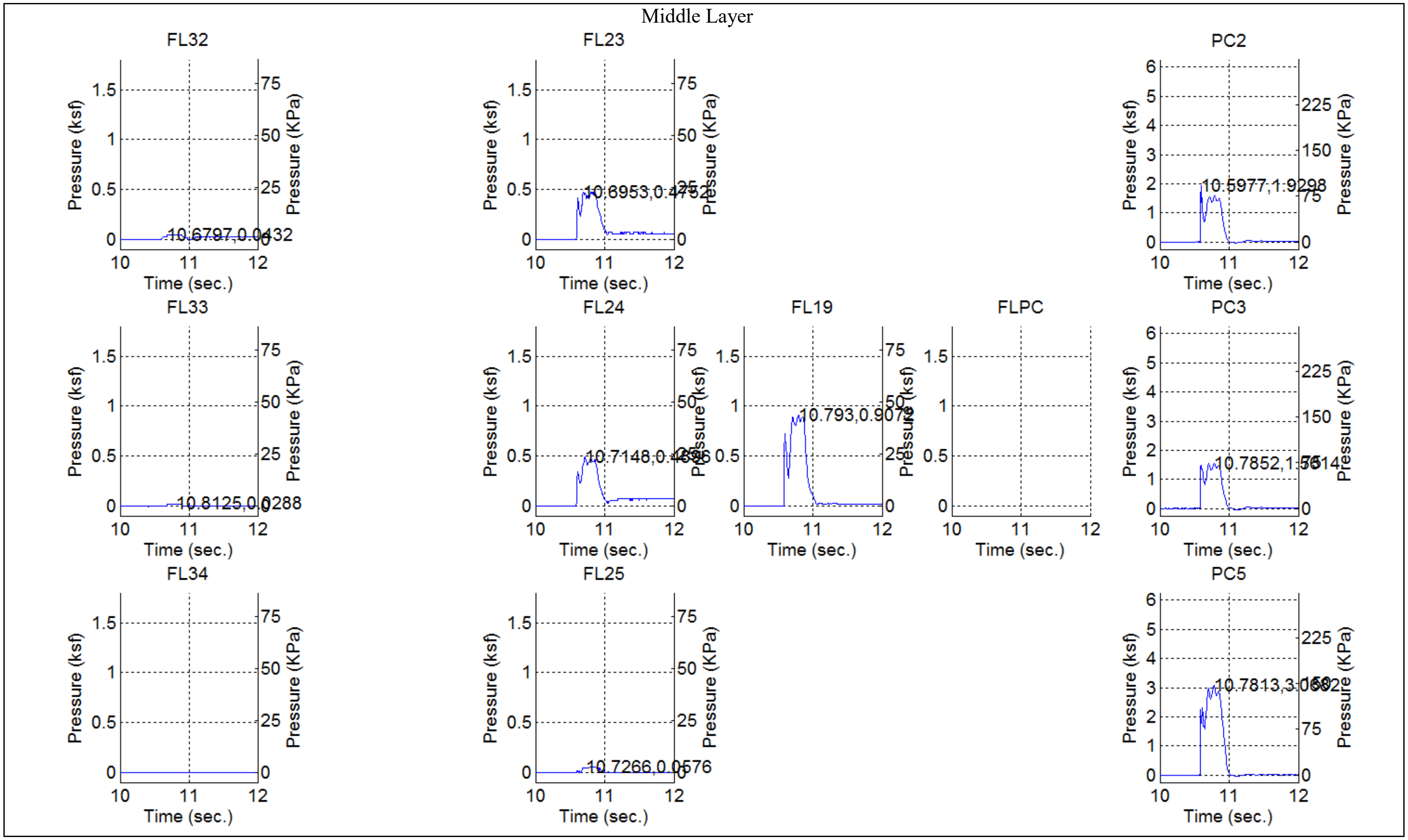

Figure 6-173 Soil pressure histories at the middle layer for the 0° skew test in Run 6.

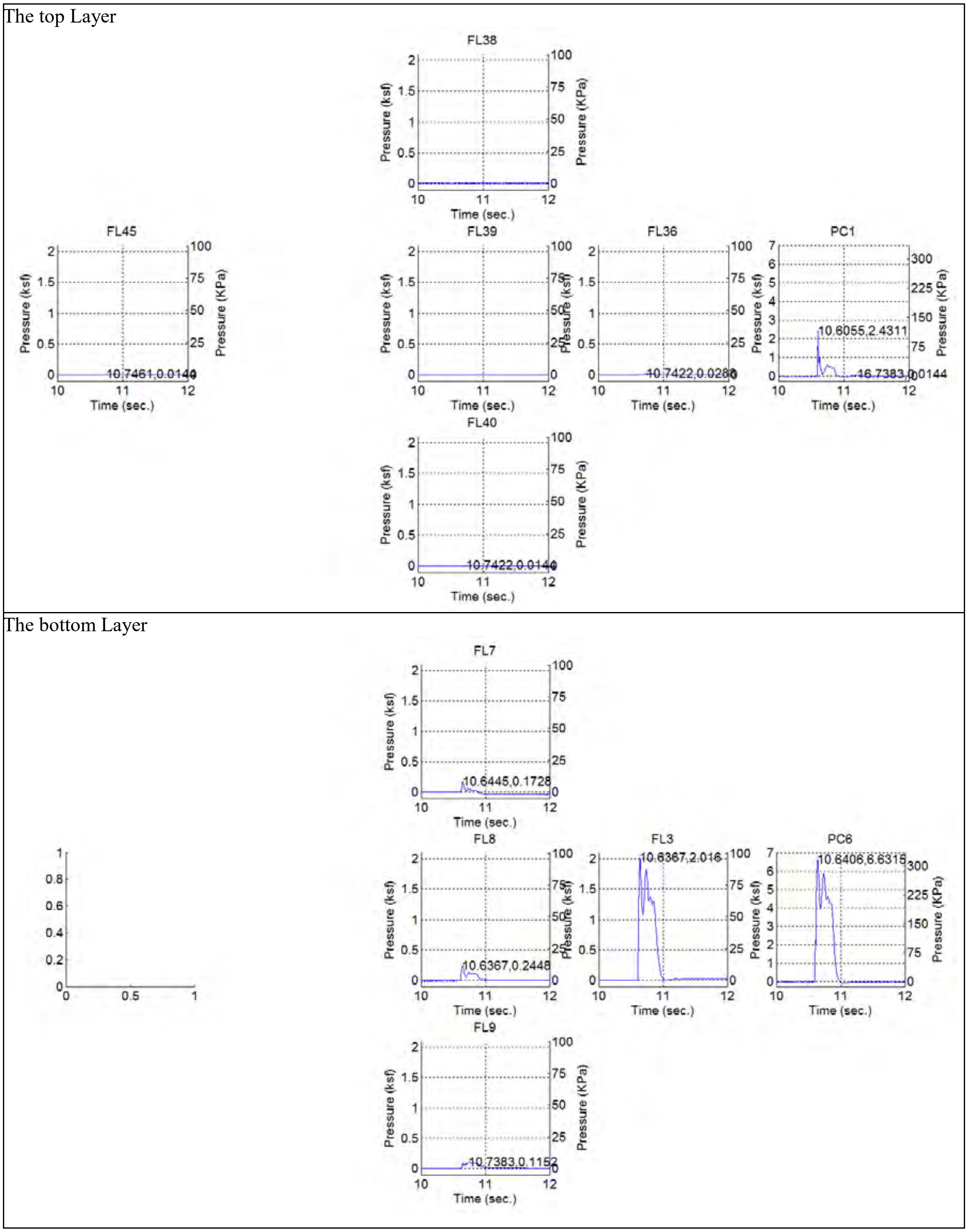

Figure 6-174 Soil pressure histories at the top and the bottom layers for the 0° skew test in Run 7.

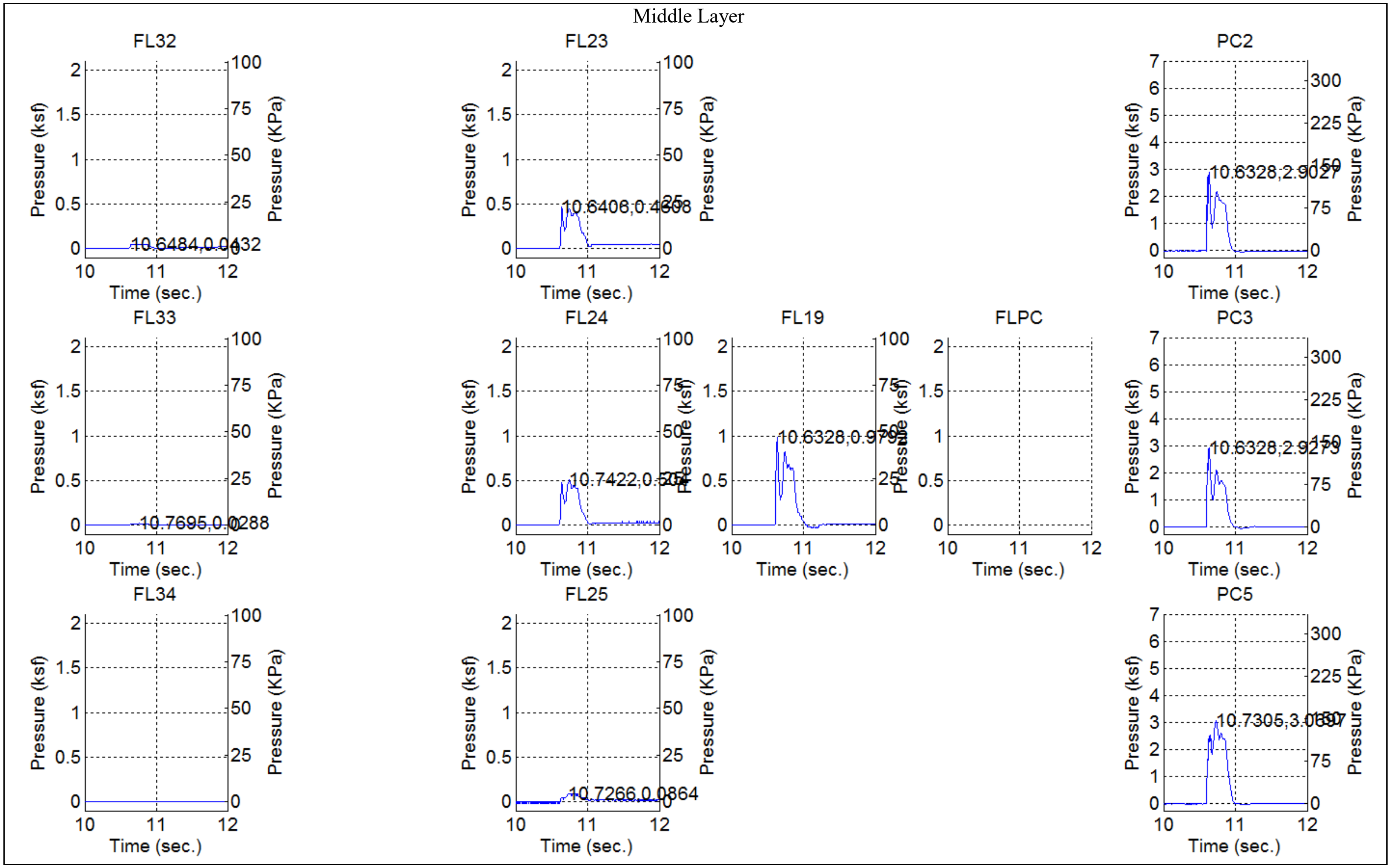

Figure 6-175 Soil pressure histories at the middle layer for the 0° skew test in Run 7.

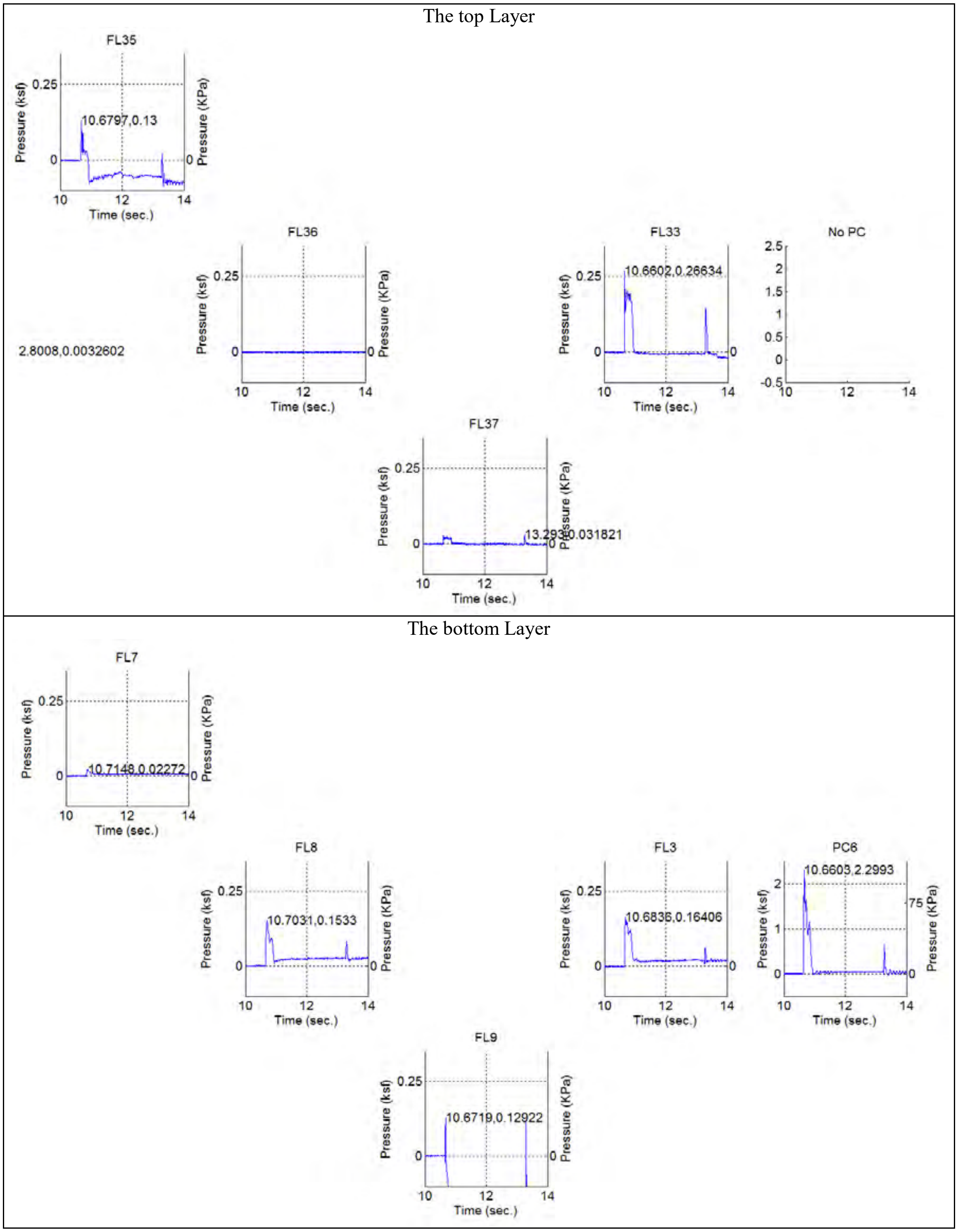

Figure 6-176 Soil pressure histories at the top and the bottom layers for the 30° skew test in Run 2.

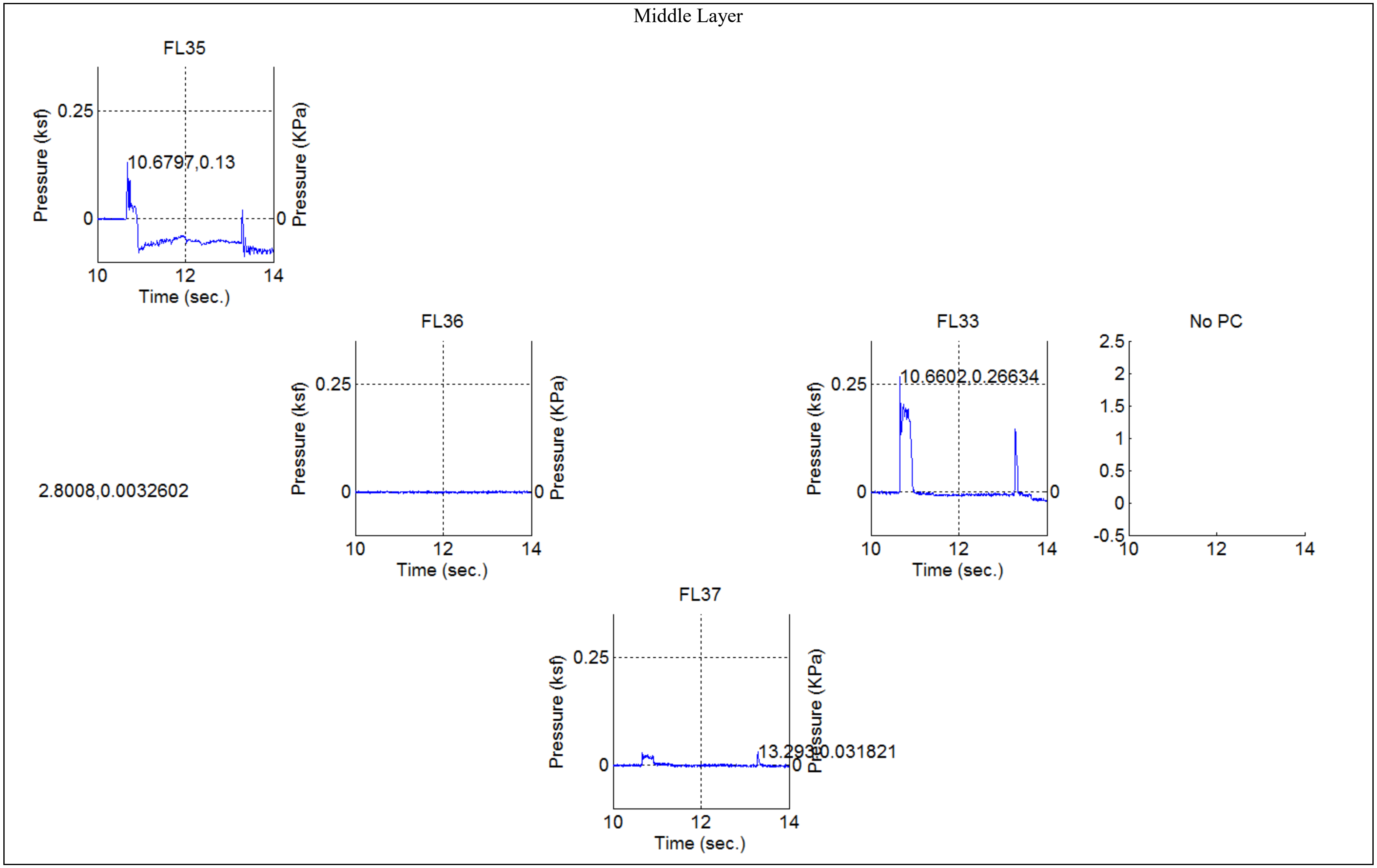

Figure 6-177 Soil pressure histories at the middle layer for the 30° skew test in Run 2.

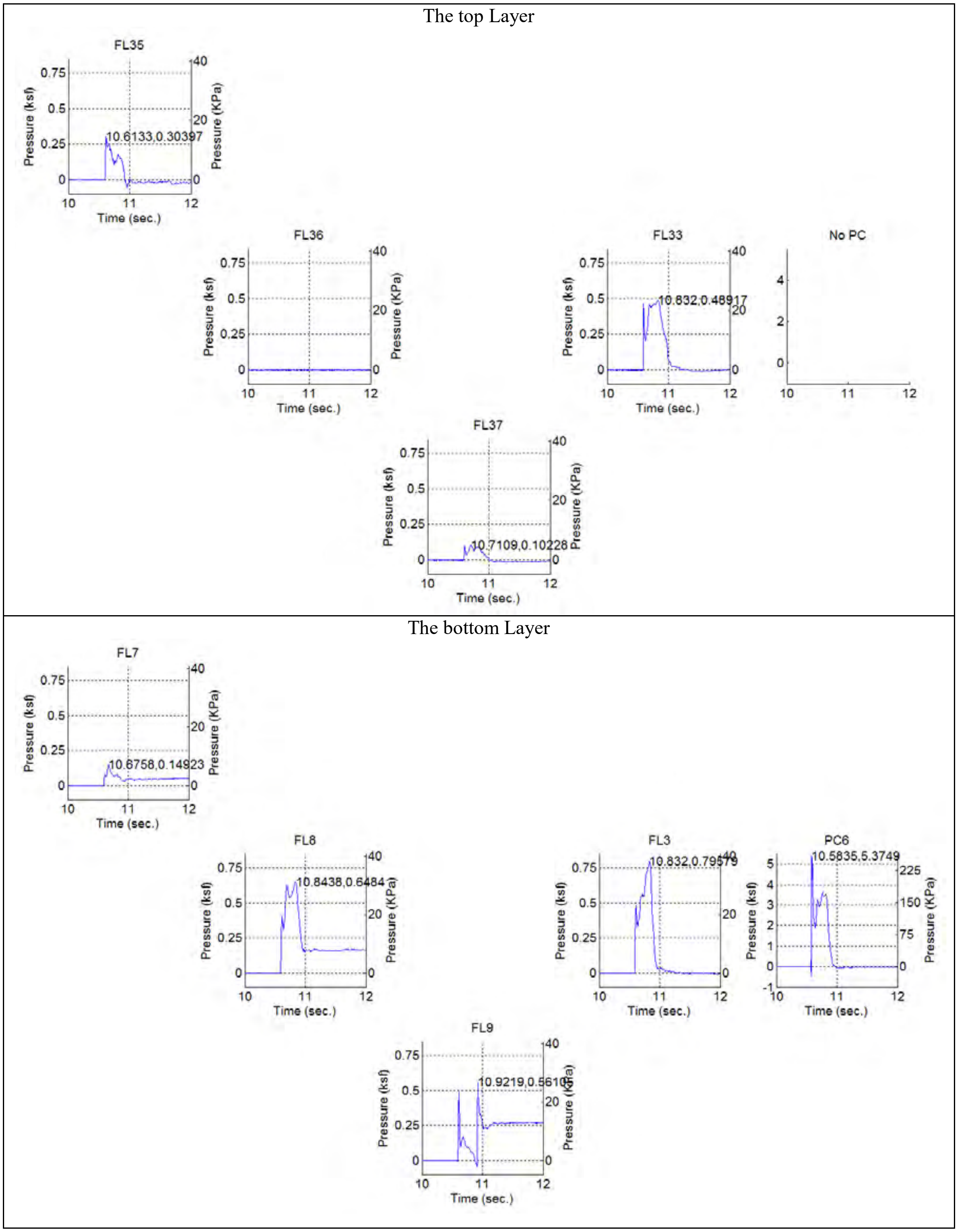

Figure 6-178 Soil pressure histories at the top and the bottom layers for the 30° skew test in Run 3.

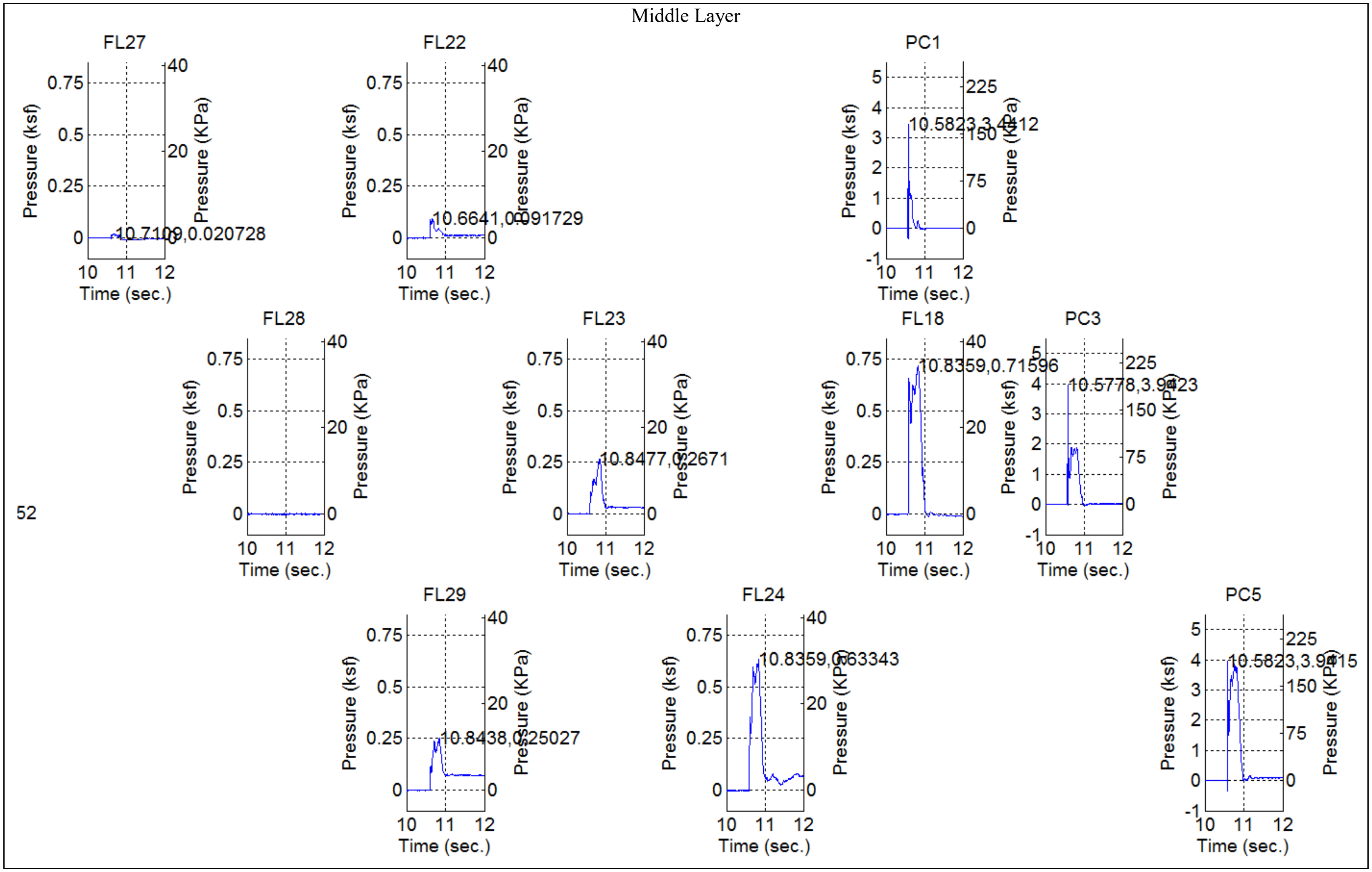

Figure 6-179 Soil pressure histories at the middle layer for the 30° skew test in Run 3.

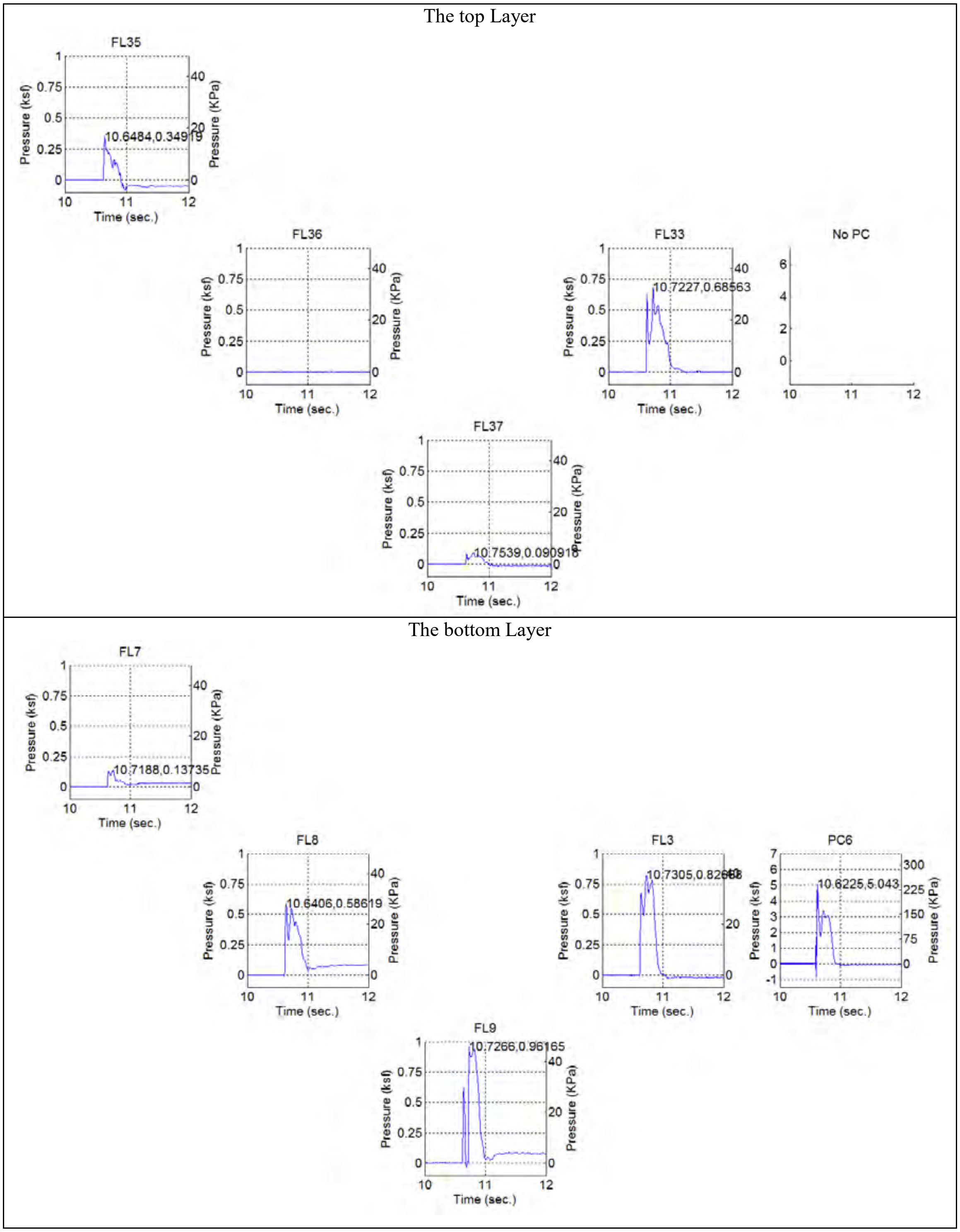

Figure 6-180 Soil pressure histories at the top and the bottom layers for the 30° skew test in Run 4.

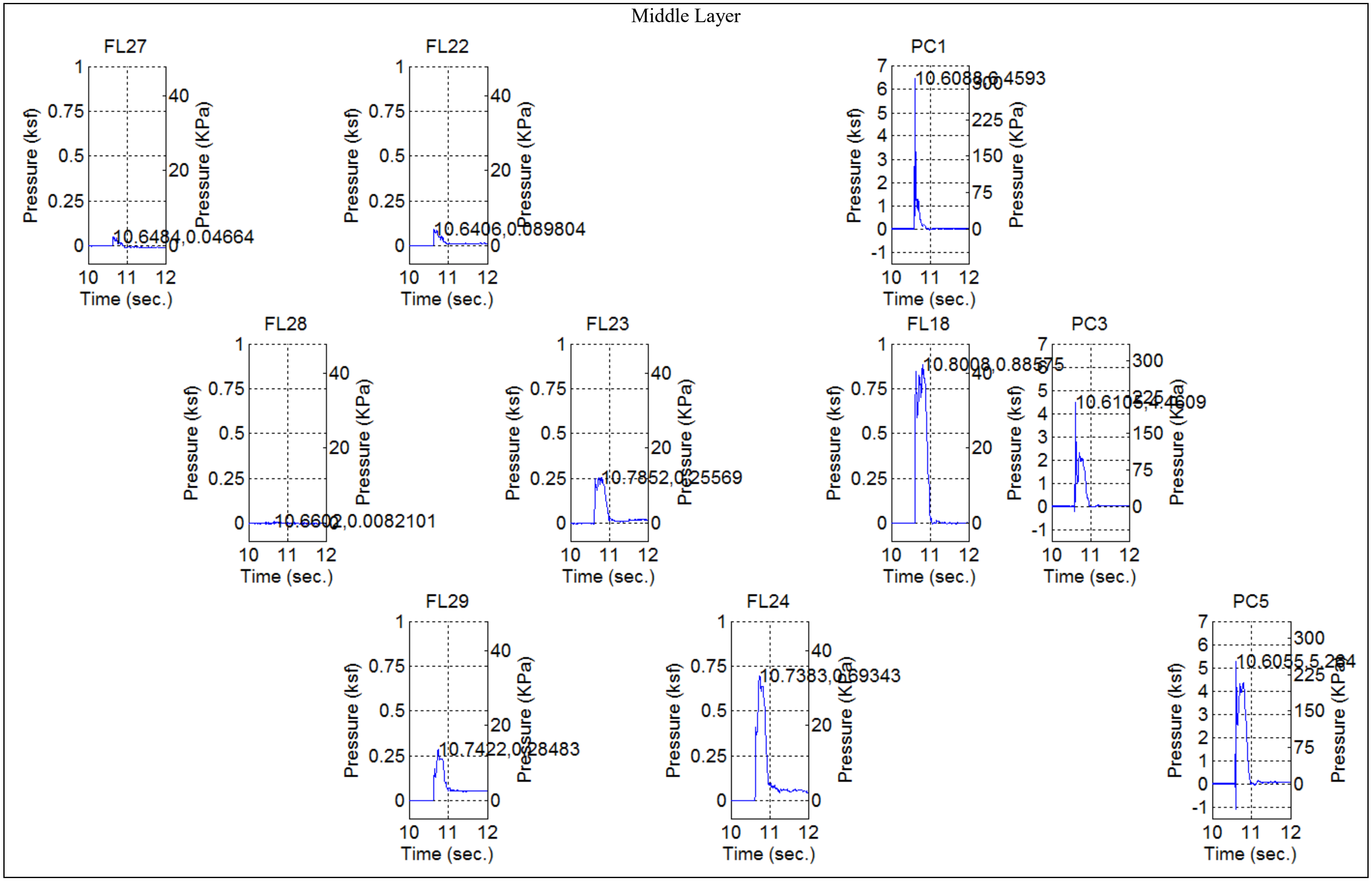

Figure 6-181 Soil pressure histories at the middle layer for the 30° skew test in Run 4.

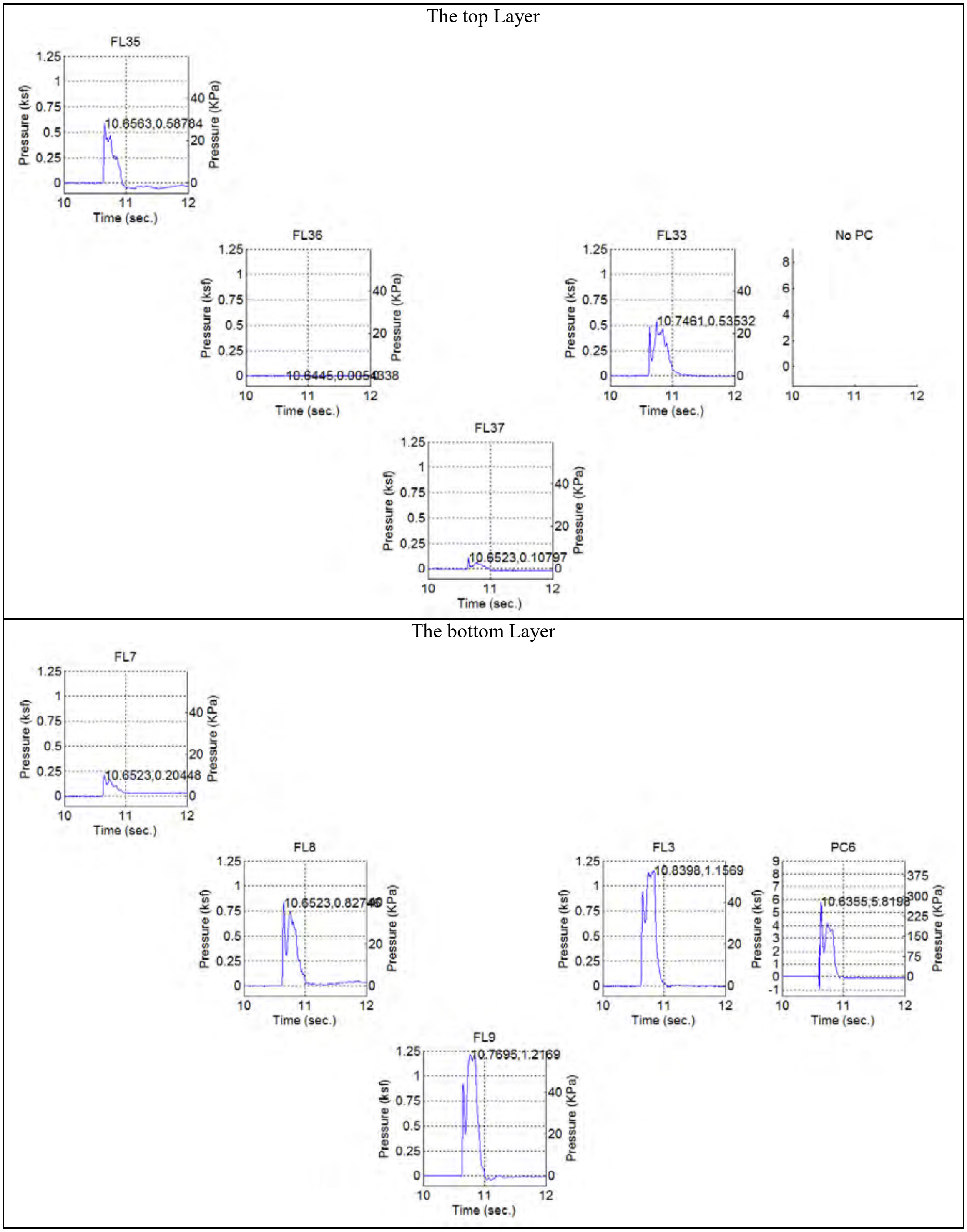

Figure 6-182 Soil pressure histories at the top and the bottom layers for the 30° skew test in Run 5.

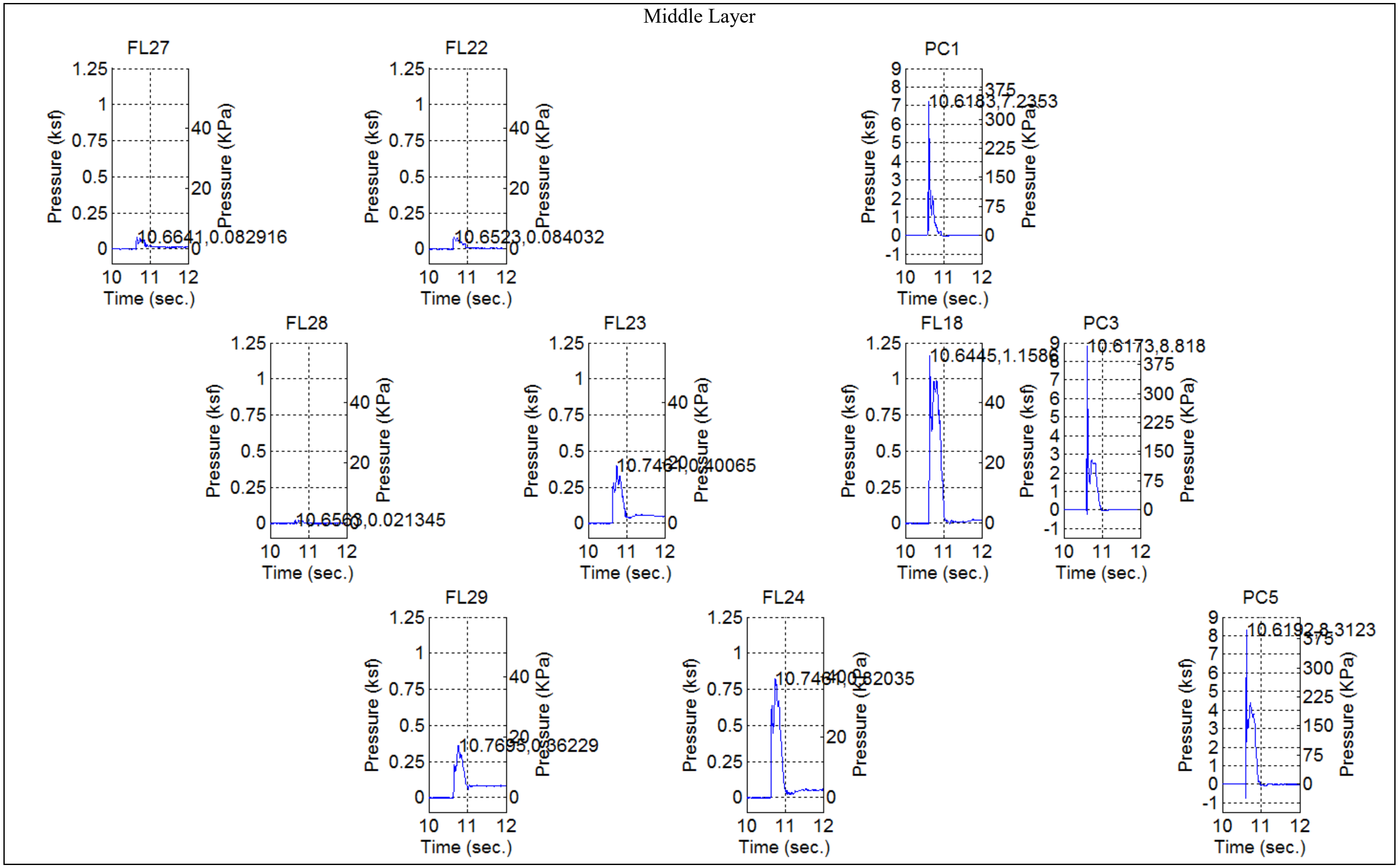

Figure 6-183 Soil pressure histories at the middle layer for the 30° skew test in Run 5.

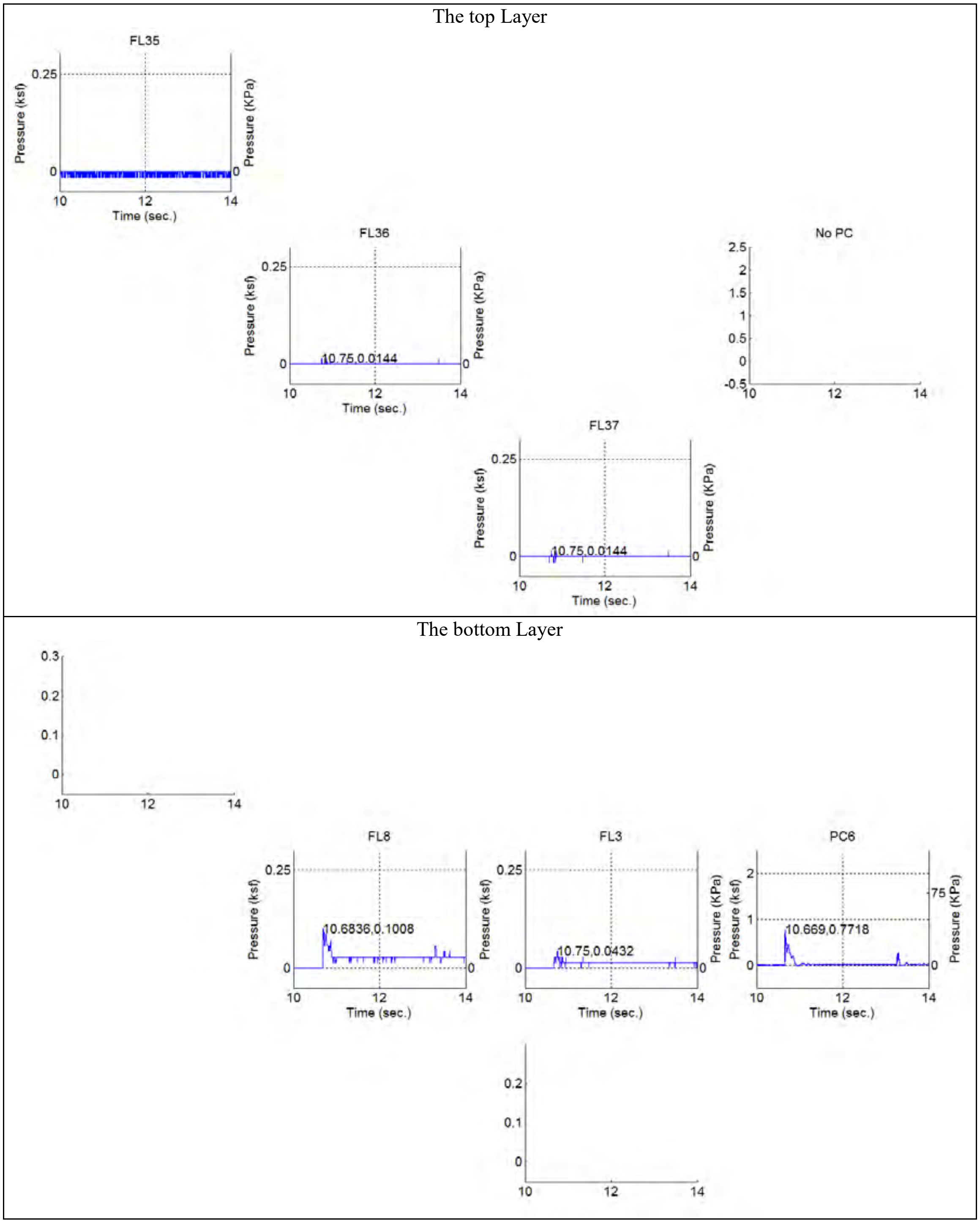

Figure 6-184 Soil pressure histories at the top and the bottom layers for the 45° skew test in Run 2.

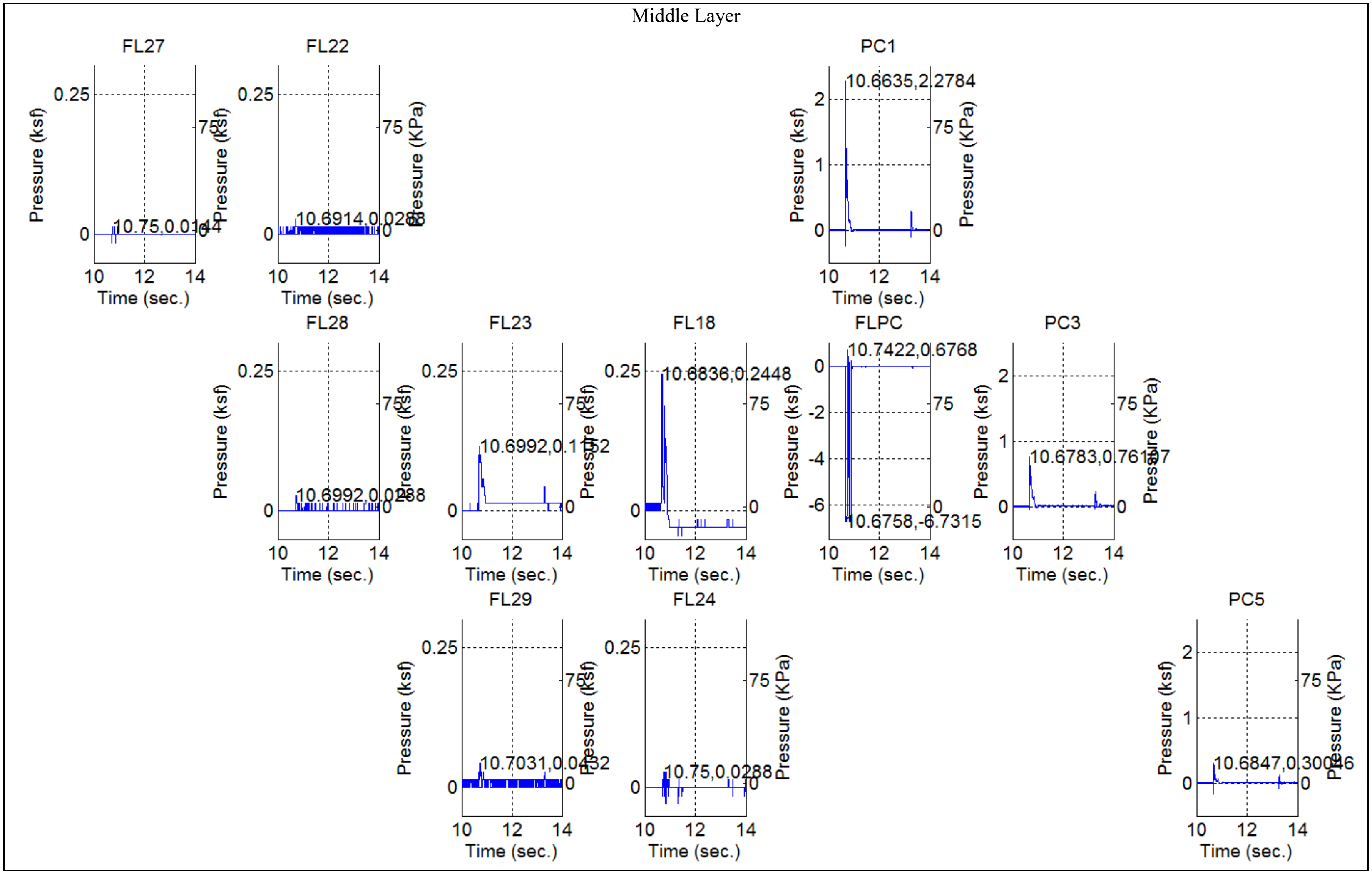

Figure 6-185 Soil pressure histories at the middle layer for the 45° skew test in Run 2.

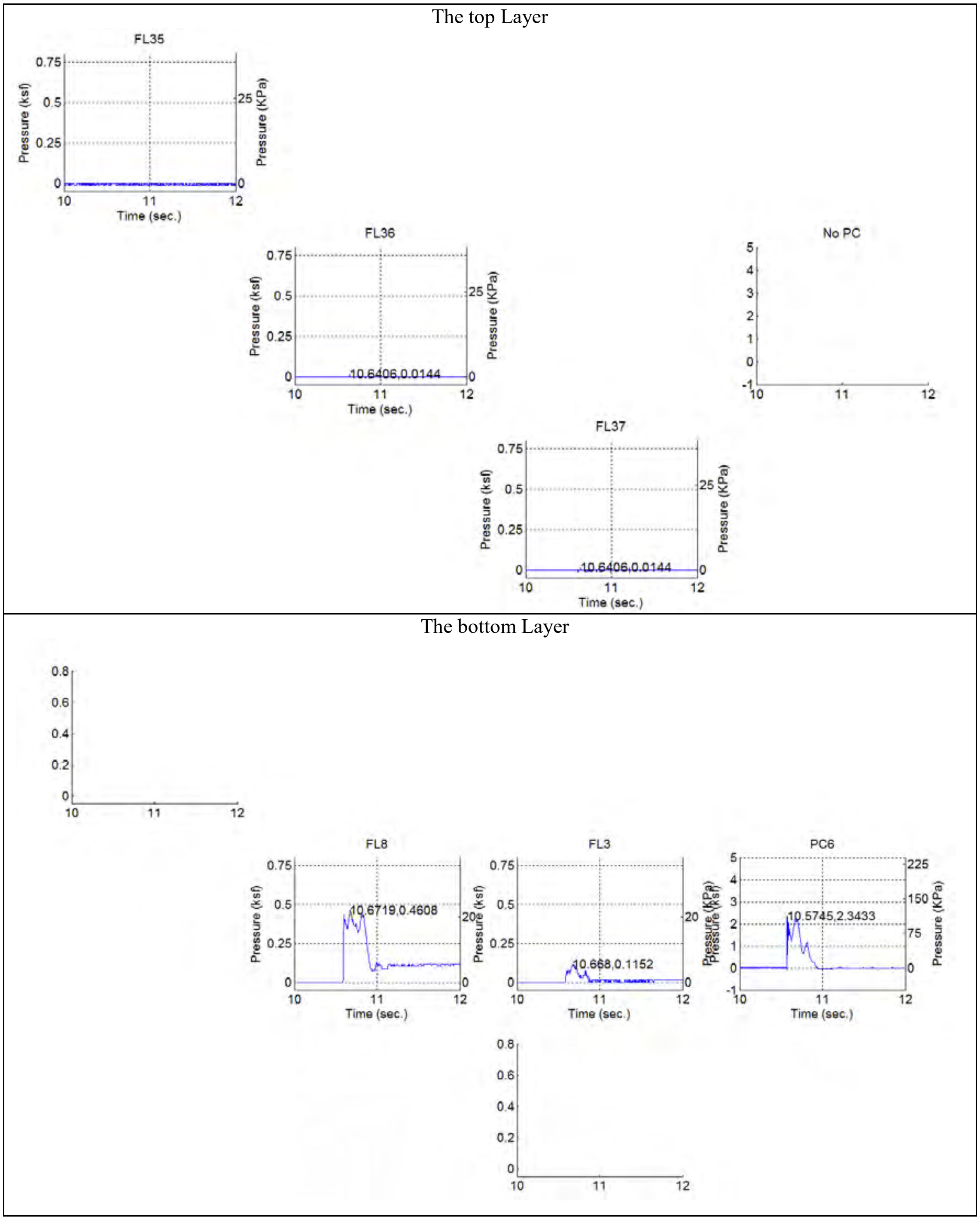

Figure 6-186 Soil pressure histories at the top and the bottom layers for the 45° skew test in Run 3.

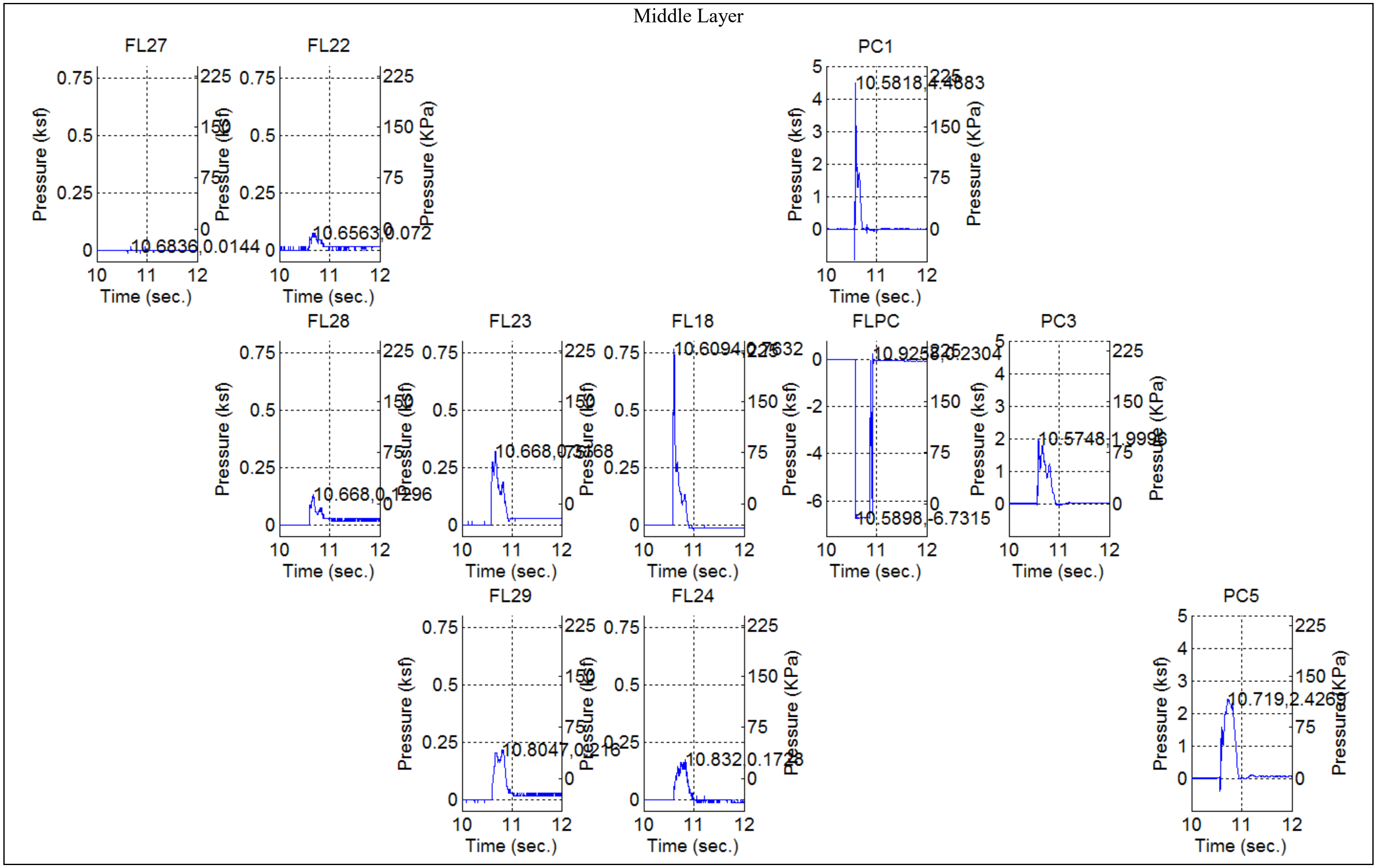

Figure 6-187 Soil pressure histories at the middle layer for the 45° skew test in Run 3.

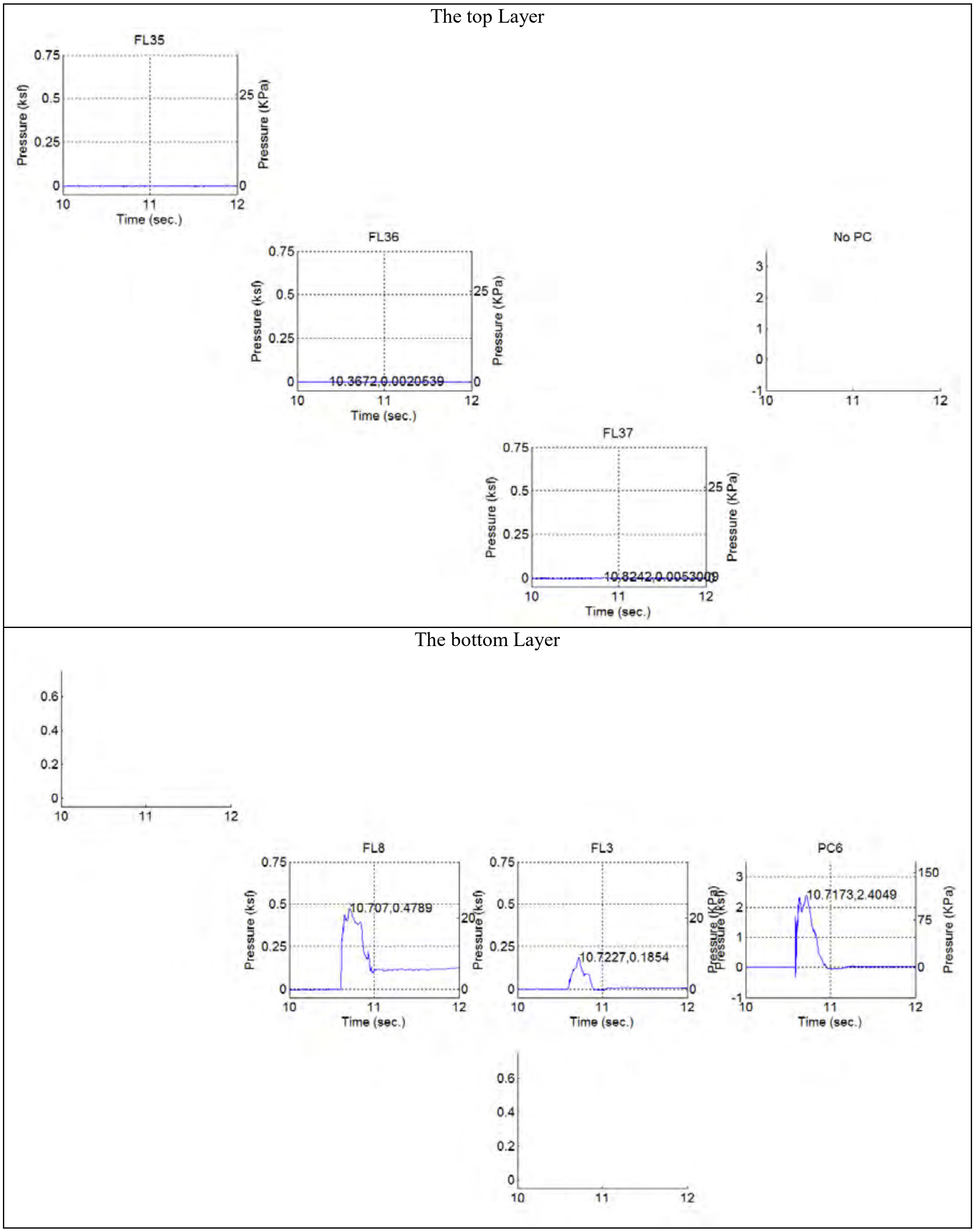

Figure 6-188 Soil pressure histories at the top and the bottom layers for the 45° skew test in Run 4.

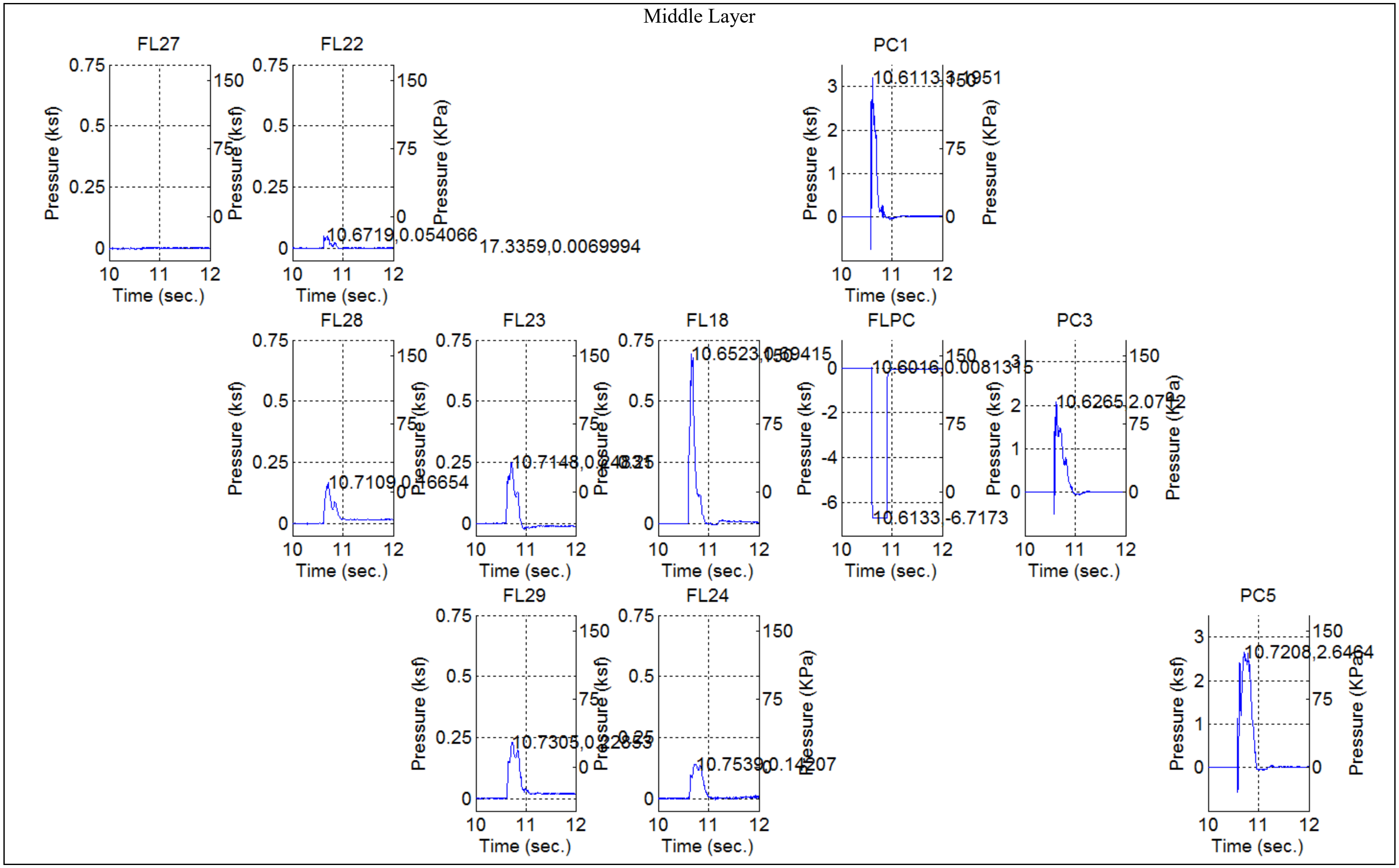

Figure 6-189 Soil pressure histories at the middle layer for the 45° skew test in Run 4.

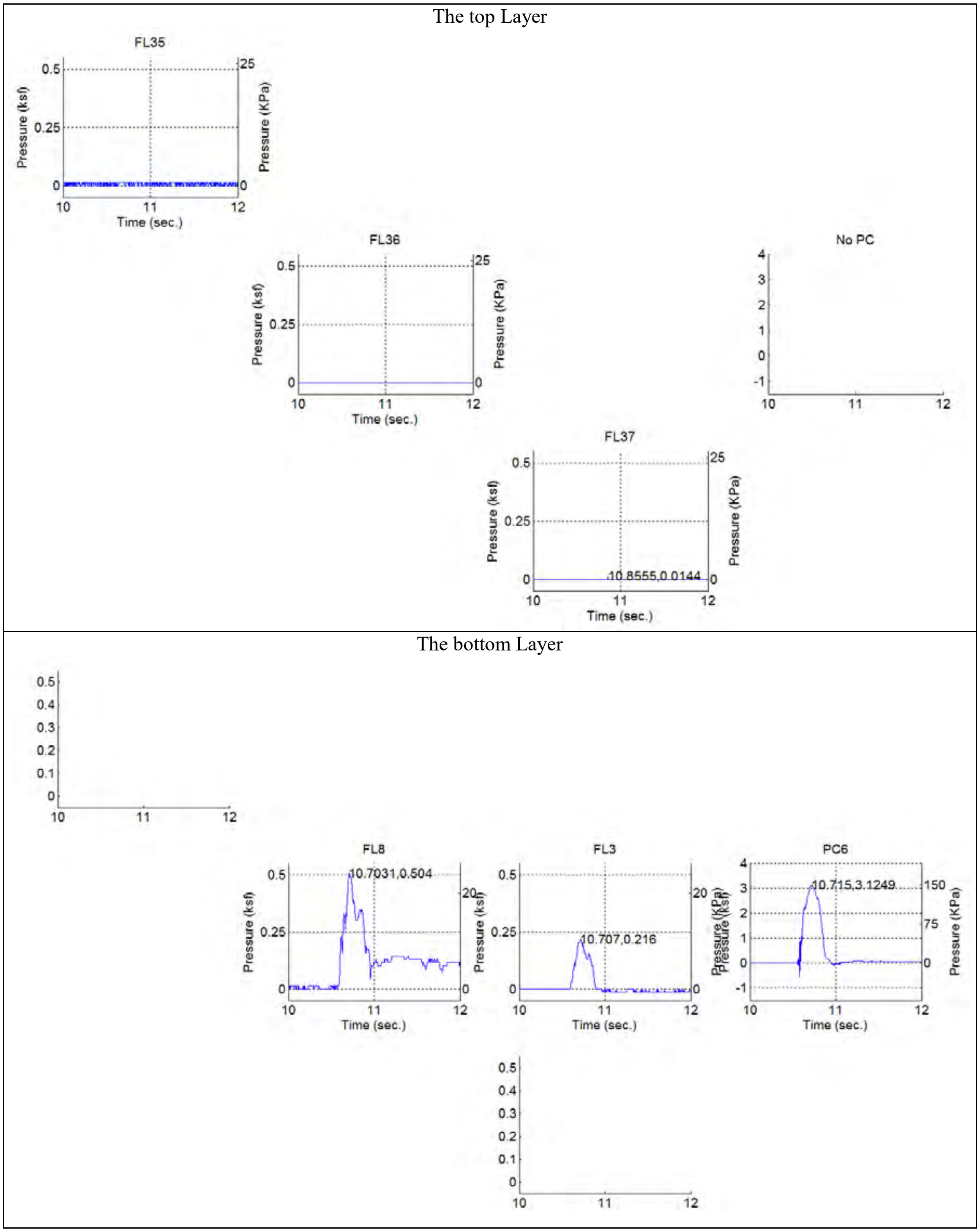

Figure 6-190 Soil pressure histories at the top and the bottom layers for the 45° skew test in Run 5.

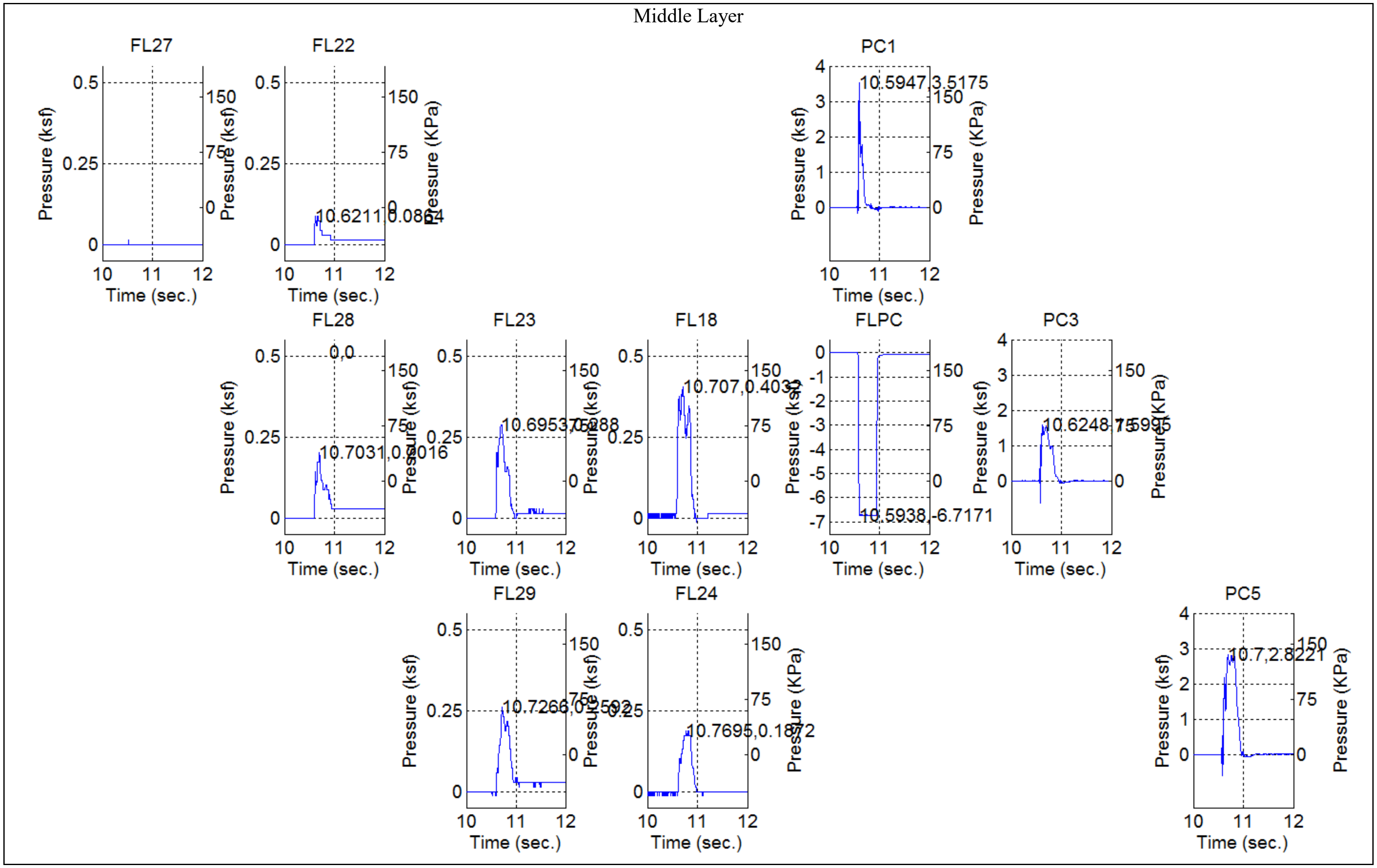

Figure 6-191 Soil pressure histories at the middle layer for the 45° skew test in Run 5.

East corner view (Obtuse corner)	Center view	West corner view (Acute corner)
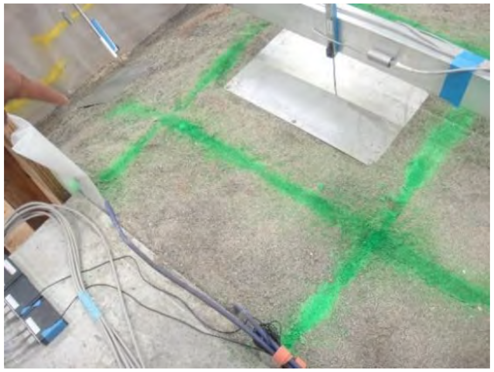	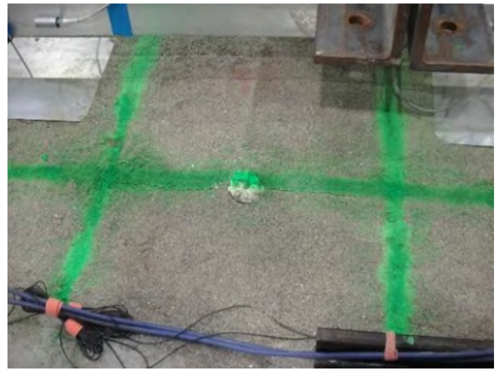	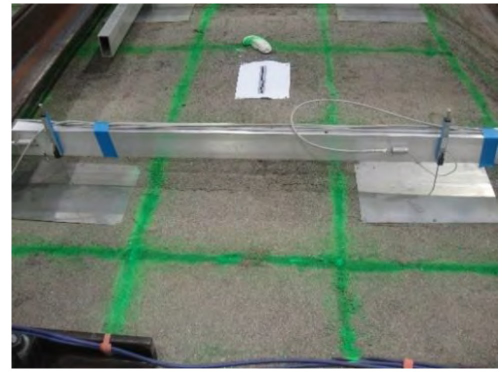

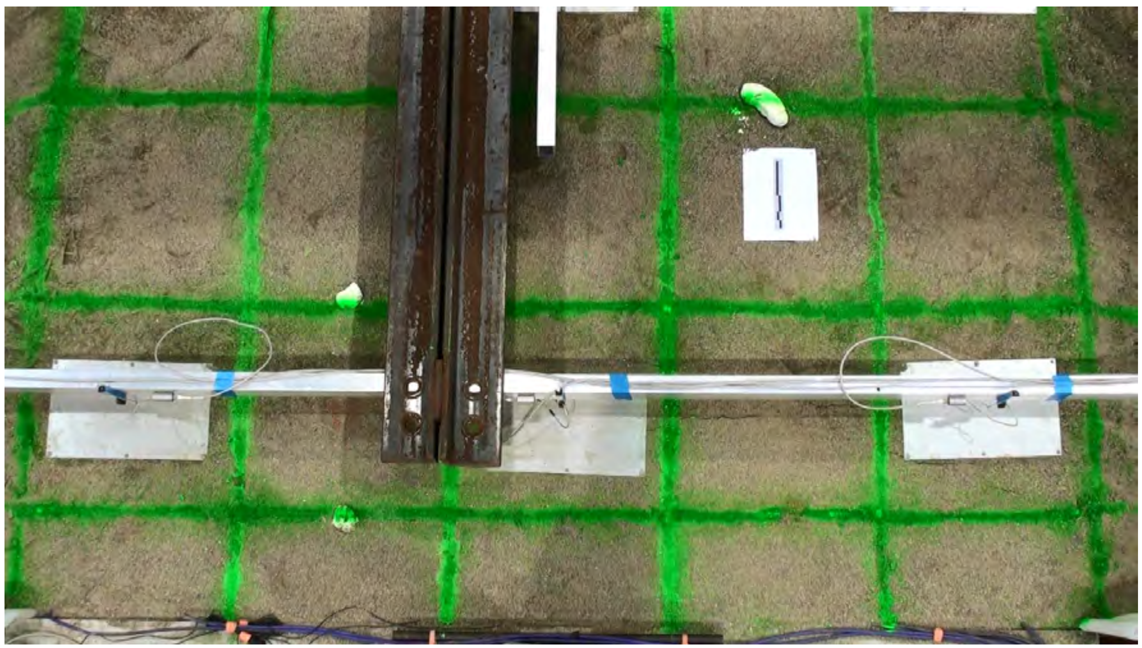

Figure 6-192 Cracks patterns of backfill soil surface for the 0° skew test in Run 2.

<table>
<tr><th>East corner view
(Obtuse corner)</th><th>Center view</th><th>West corner view
(Acute corner)</th></tr>
<tr><td></td><td></td><td>
</td></tr>
<tr><td colspan="3">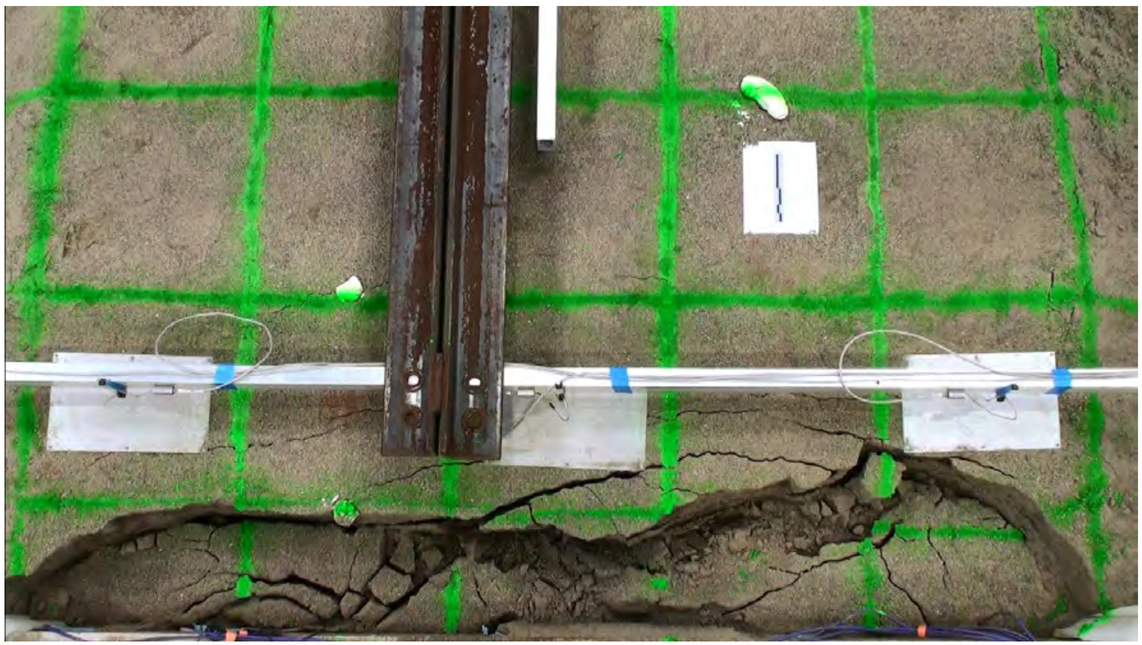</td></tr>
</table>

Figure 6-193 Cracks patterns of backfill soil surface for the 0° skew test in Run 3.

<table>
<tr><th>East corner view
(Obtuse corner)</th><th>Center view</th><th>West corner view
(Acute corner)</th></tr>
<tr><td>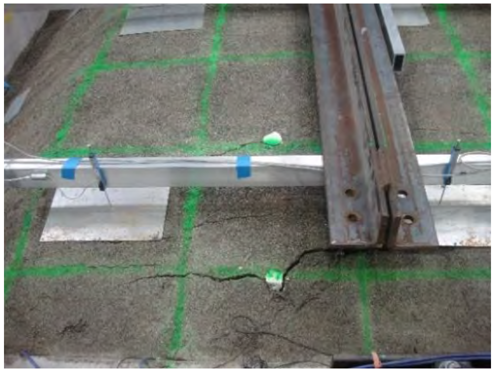</td><td>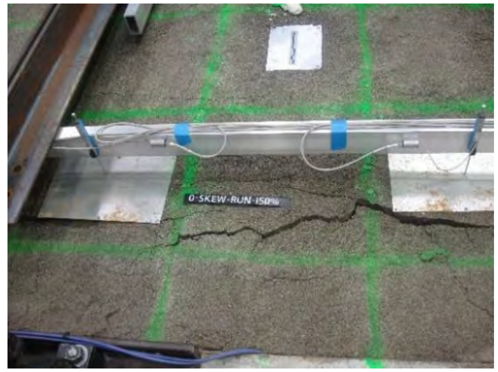
</td><td>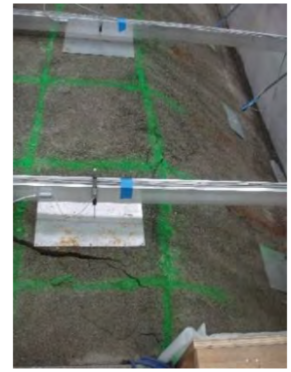</td></tr>
<tr><td colspan="3"></td></tr>
</table>

Figure 6-194 Cracks patterns of backfill soil surface for the 0° skew test in Run 6.

<table>
<tr><th>East corner view
(Obtuse corner)</th><th>Center view</th><th>West corner view
(Acute corner)</th></tr>
<tr><td>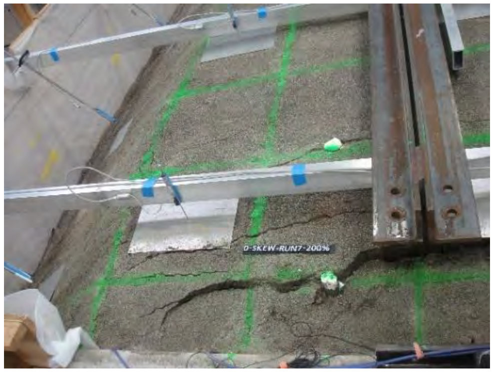
</td><td>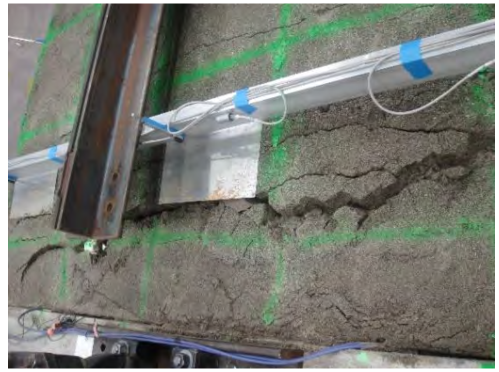</td><td>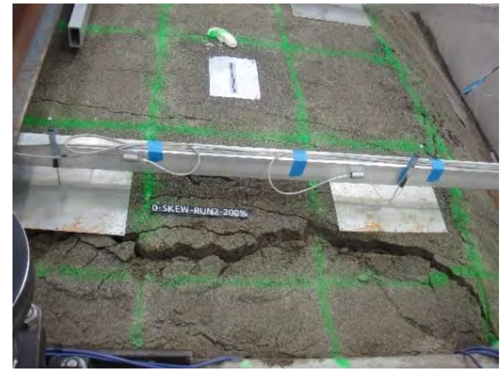</td></tr>
<tr><td colspan="3">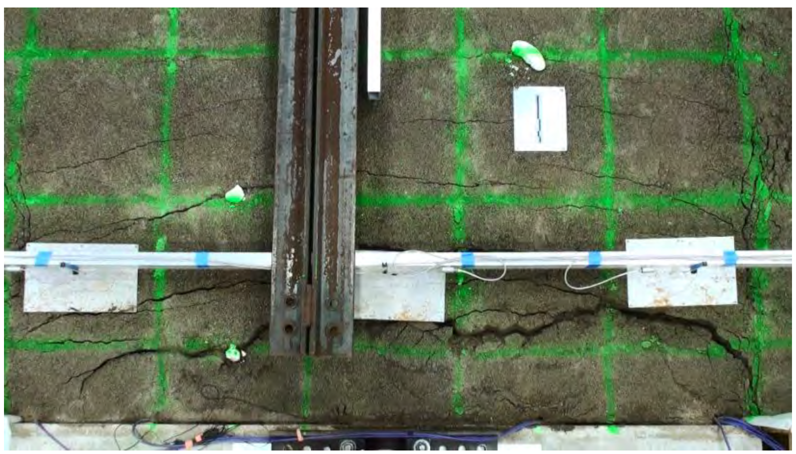 </td></tr>
</table>

Figure 6-195 Cracks patterns of backfill soil surface for the 0° skew test in Run 7.

Figure 6-196 Removal and re-construction of soil adjacent to the backwall after Run 4 of the 0° skew test.

Run 2 – 50% Sylmar	Run 3 – 75% Sylmar
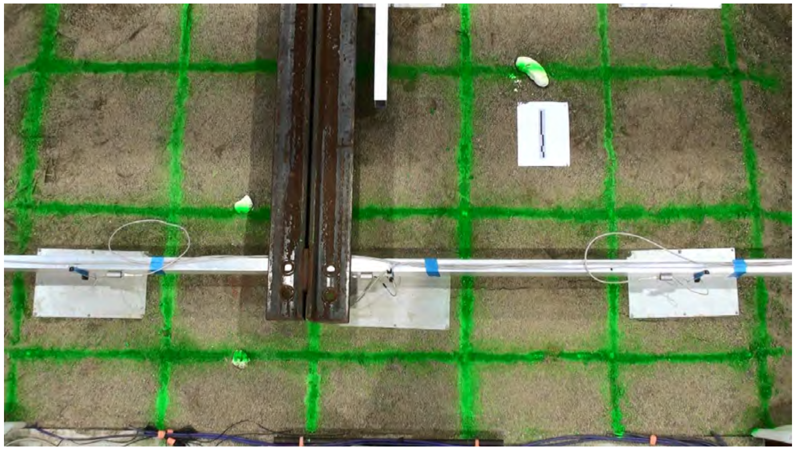	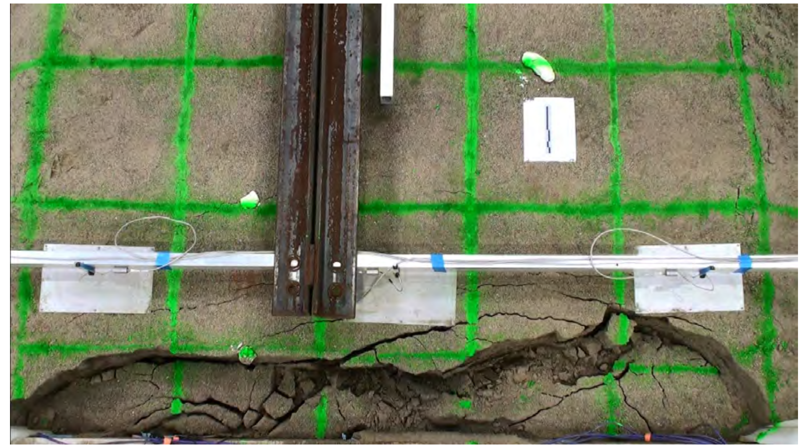
Run 6 – 150% Sylmar	Run 7 – 150% Sylmar
	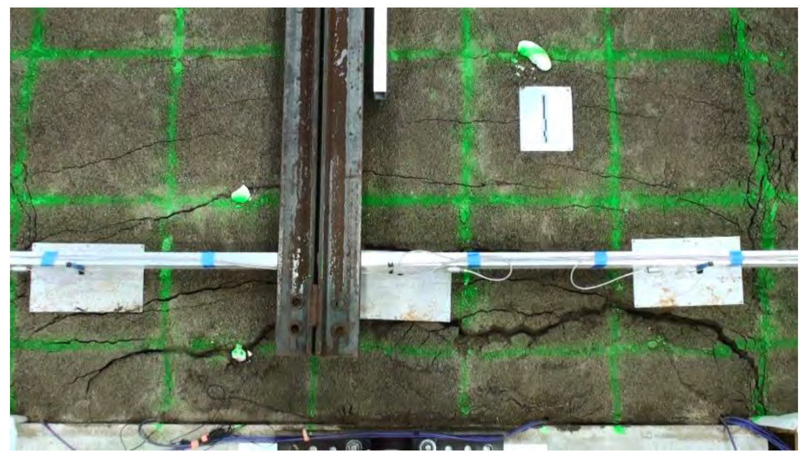

Figure 6-197 Cracks patterns of backfill soil surface for the 0° skew test.

East corner view (Obtuse corner)	Center view	West corner view (Acute corner)
	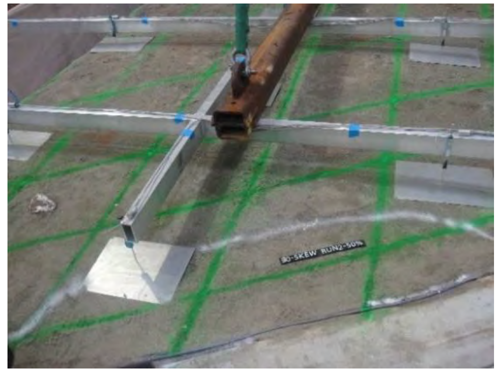	

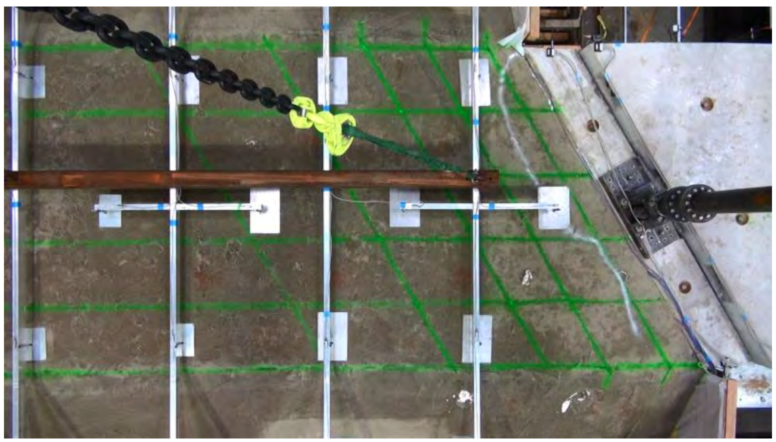

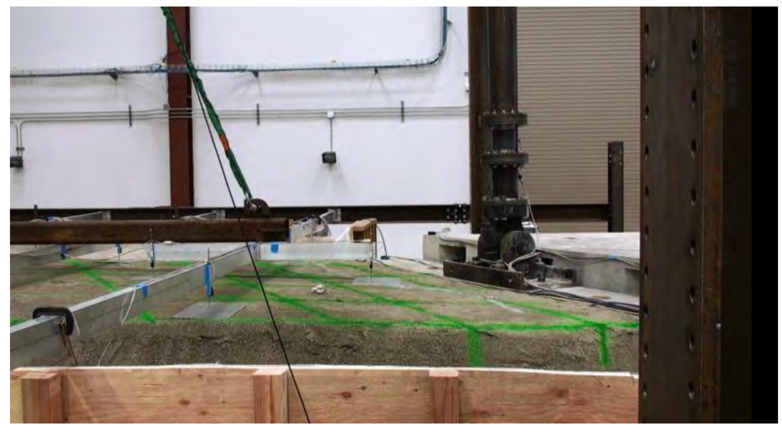

Figure 6-198 Cracks patterns of backfill soil surface for the 30° skew test in Run 2.

East corner view (Obtuse corner)	Center view	West corner view (Acute corner)
	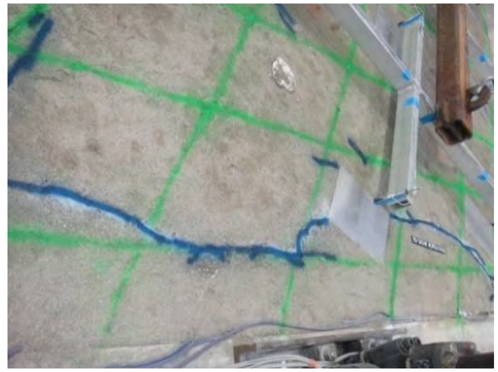	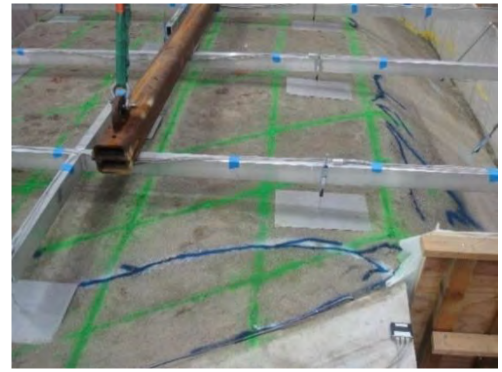
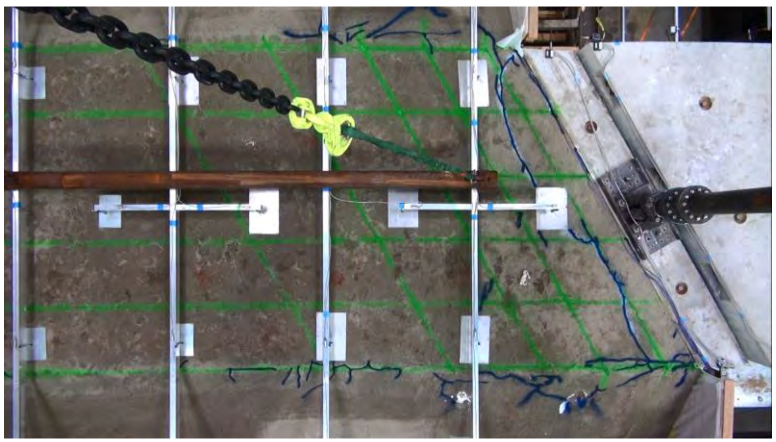		

Figure 6-199 Cracks patterns of backfill soil surface for the 30° skew test in Run 3.

East corner view (Obtuse corner)	Center view of the backwall	West corner view (Acute corner)
	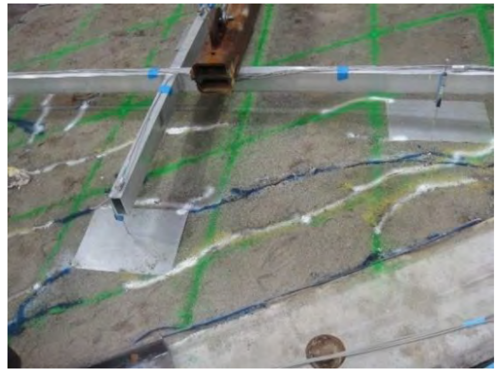	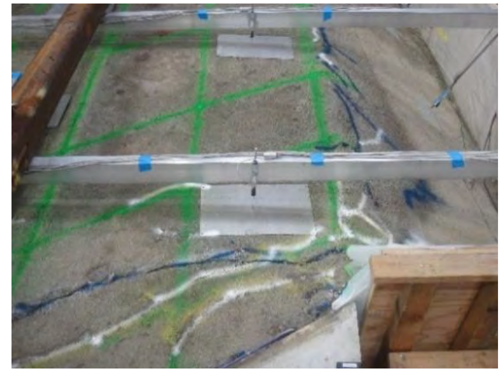

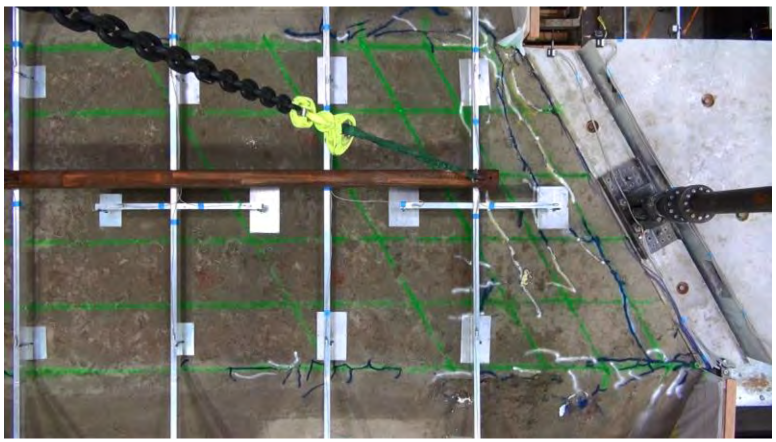

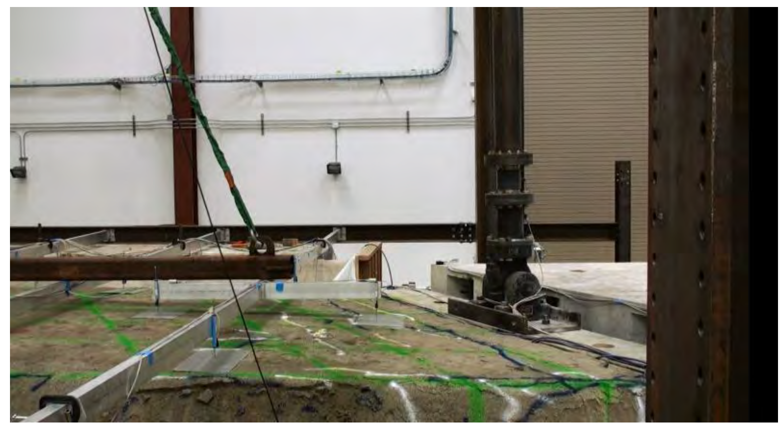

Figure 6-200 Cracks patterns of backfill soil surface for the 30° skew test in Run 4.

East corner view (Obtuse corner)	Center view of the backwall	West corner view (Acute corner)
		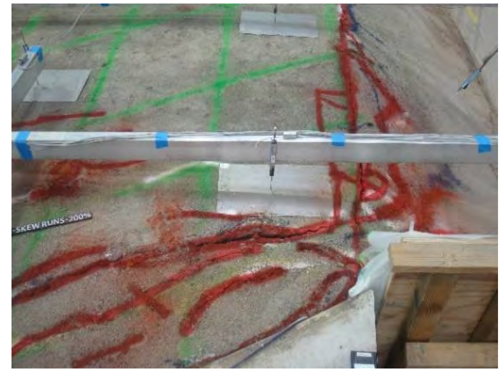
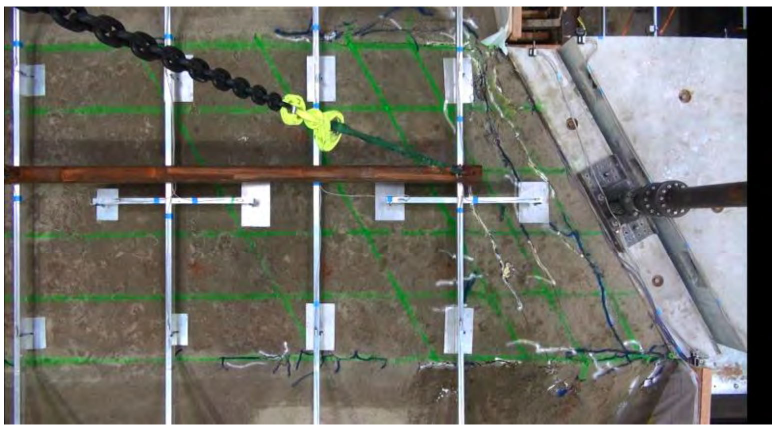	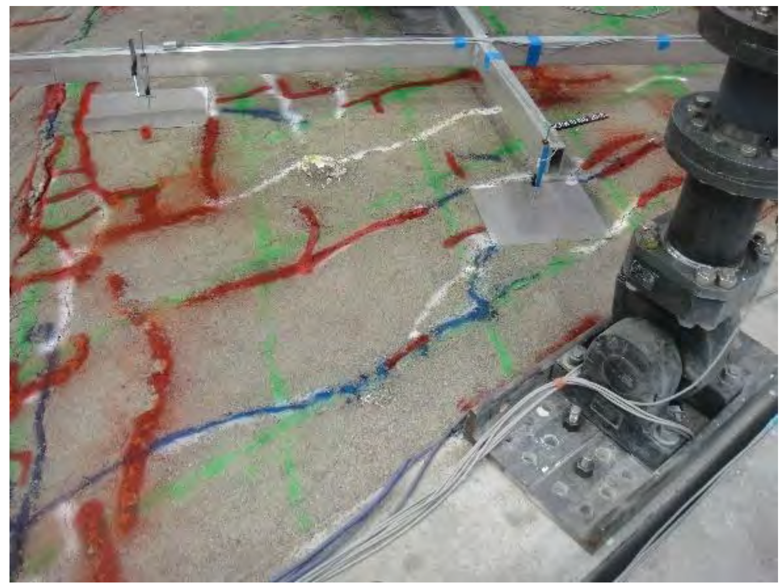	

Figure 6-201 Cracks patterns of backfill soil surface for the 30° skew test in Run 5.

Run 2 – 50% Sylmar	Run 3 – 125% Sylmar
	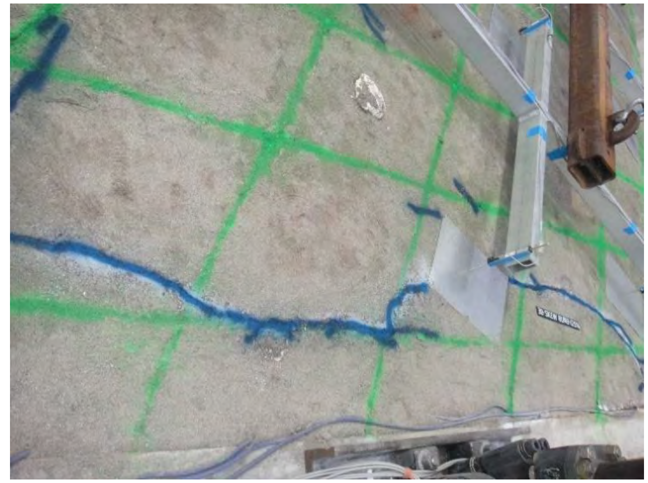
Run 4 – 150% Sylmar	**Run 5 – 200% Sylmar**
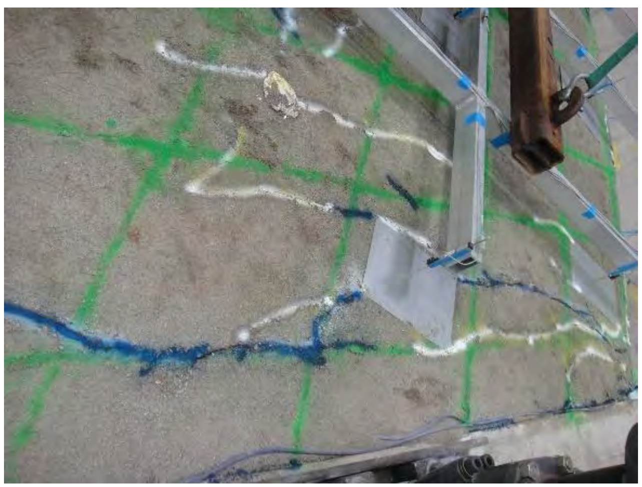	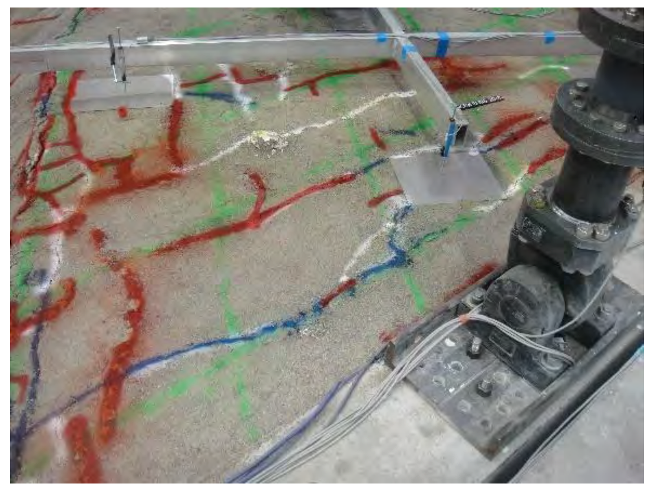

Figure 6-202 Cracks patterns of backfill soil surface for the 30° skew test.

East corner view (Obtuse corner)	Center view	West corner view (Acute corner)
	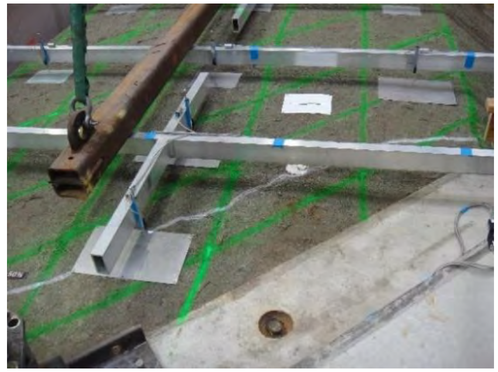	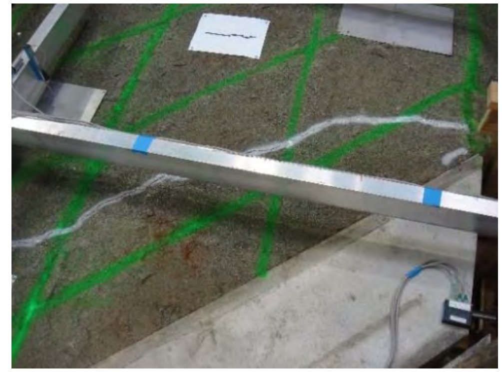
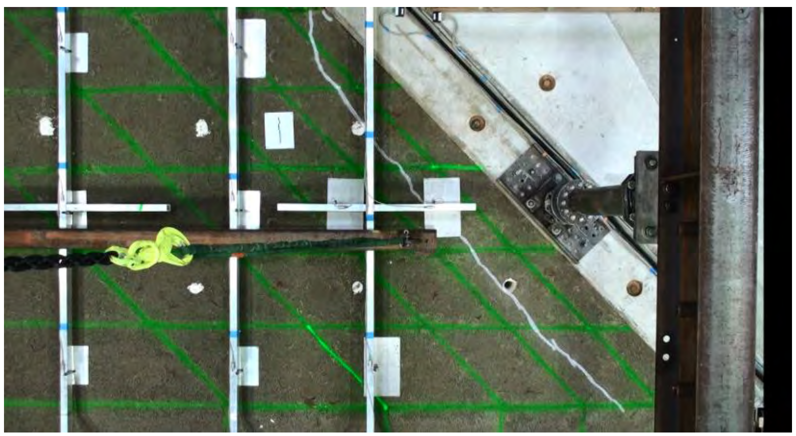		

Figure 6-203 Cracks patterns of backfill soil surface for the 45° skew test in Run 2.

East corner view of the backwall (Obtuse corner)	Center view of the backwall	West corner view of the backwall (Acute corner)
	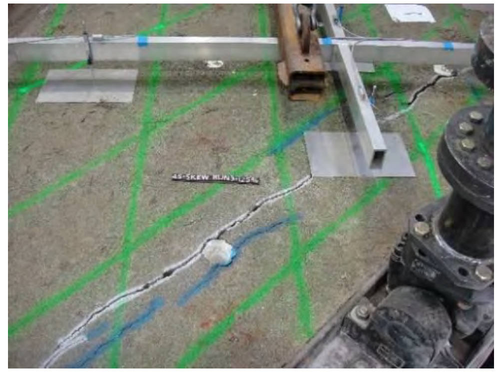	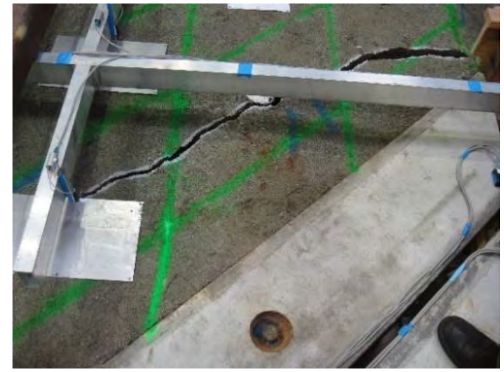

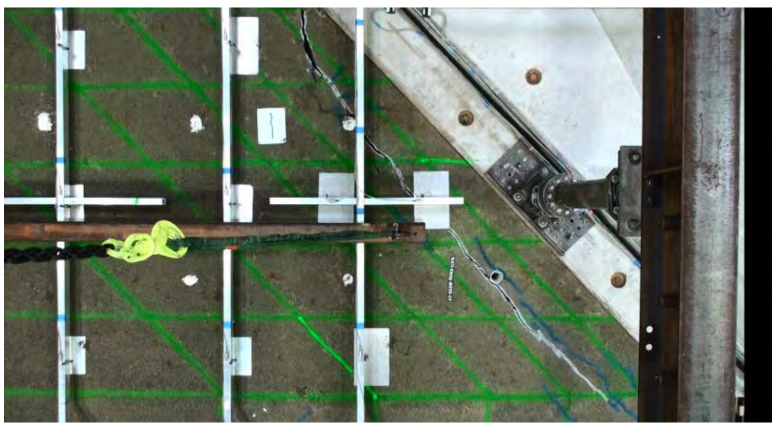

Figure 6-204 Cracks patterns of backfill soil surface for the 45° skew test in Run 3.

East corner view of the backwall (Obtuse corner)	Center view of the backwall	West corner view of the backwall (Acute corner)
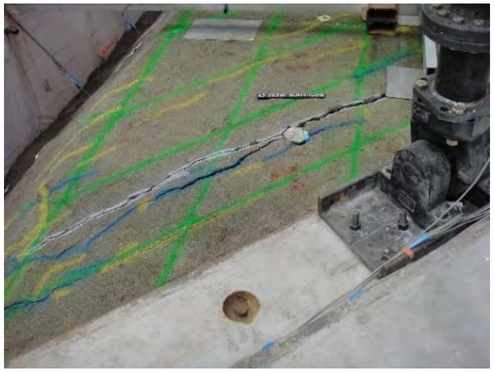		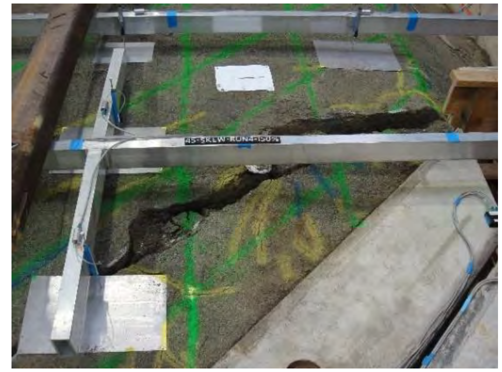
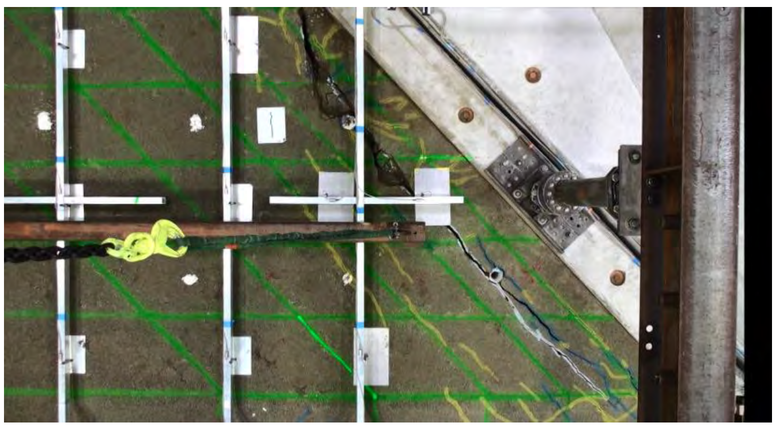		

Figure 6-205 Cracks patterns of backfill soil surface for the 45° skew test in Run 4.

East corner view of the backwall (Obtuse corner)	Center view of the backwall	West corner view of the backwall (Acute corner)
		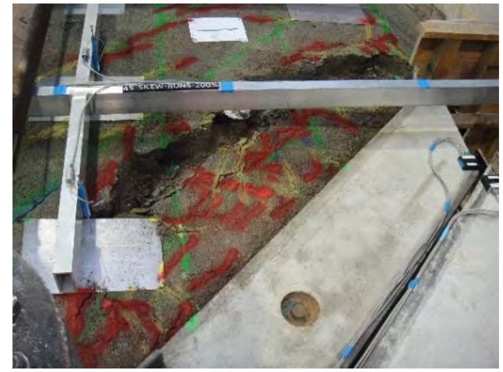
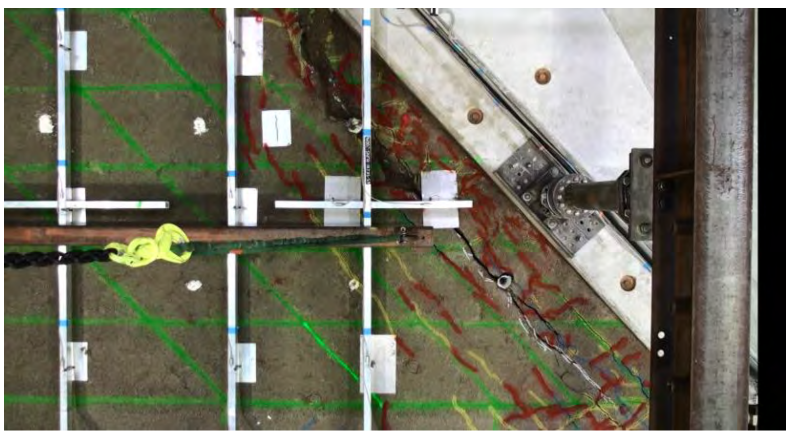		

Figure 6-206 Cracks patterns of backfill soil surface for the 45° skew test in Run 5.

Run 2 – 50% Sylmar	Run 3 – 125% Sylmar
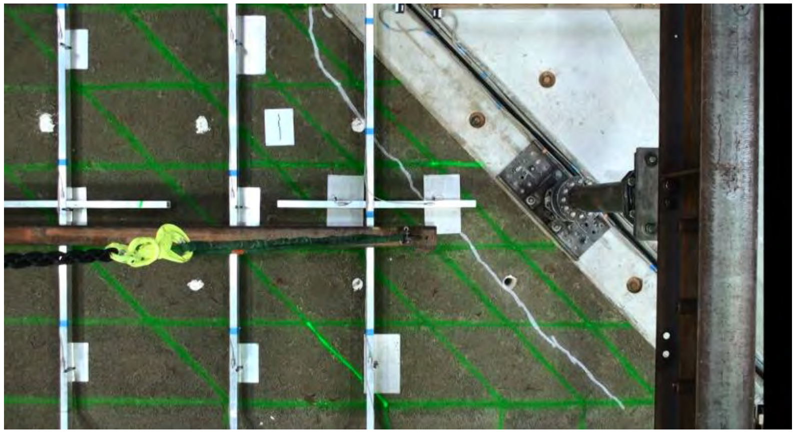	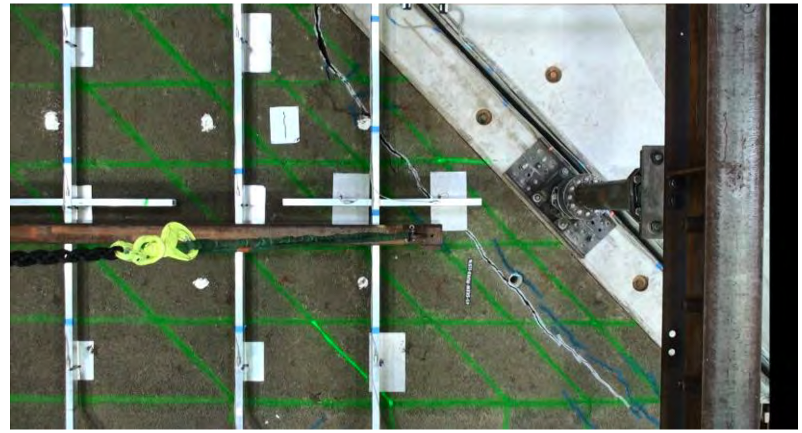
Run 4 – 150% Sylmar	Run 5 – 200% Sylmar
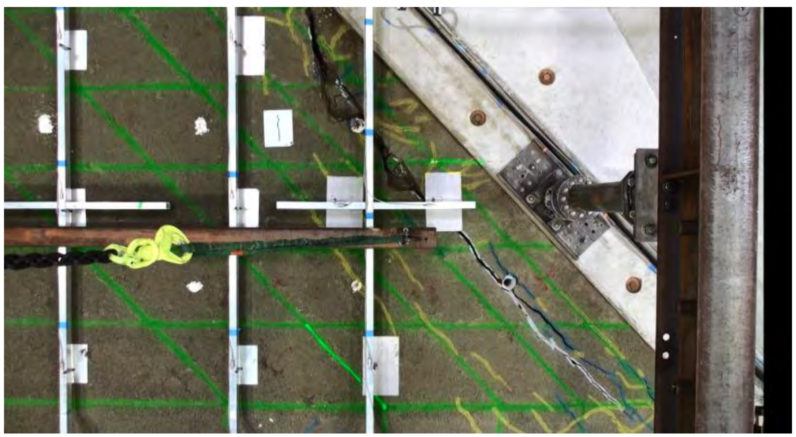	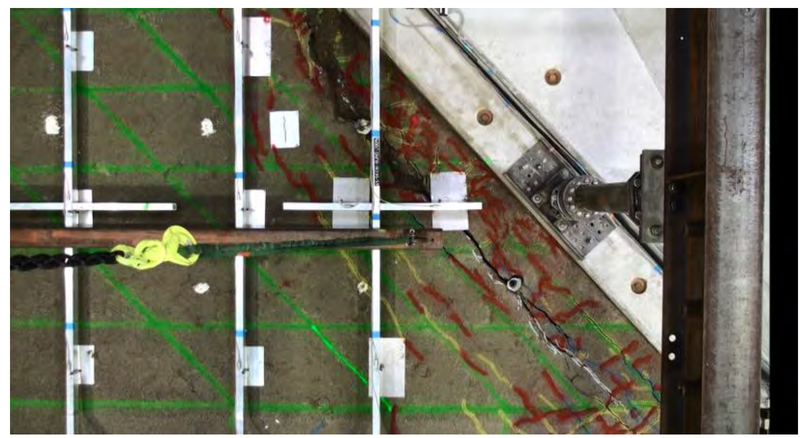

Figure 6-207 Cracks patterns of backfill soil surface for the 45° skew test.

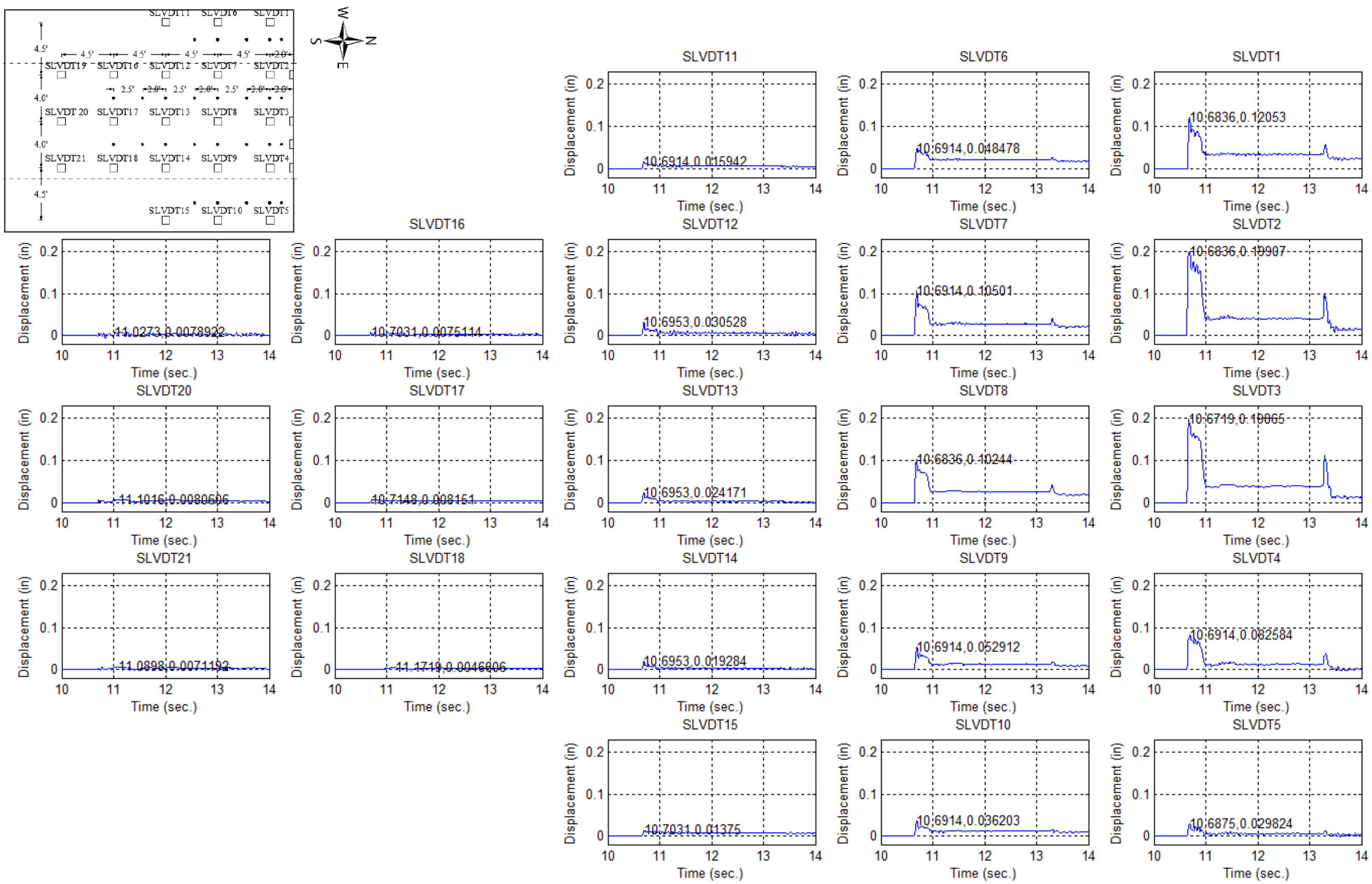

Figure 6-208 Vertical displacement histories on the soil surface for the 0° skew test in Run 2.

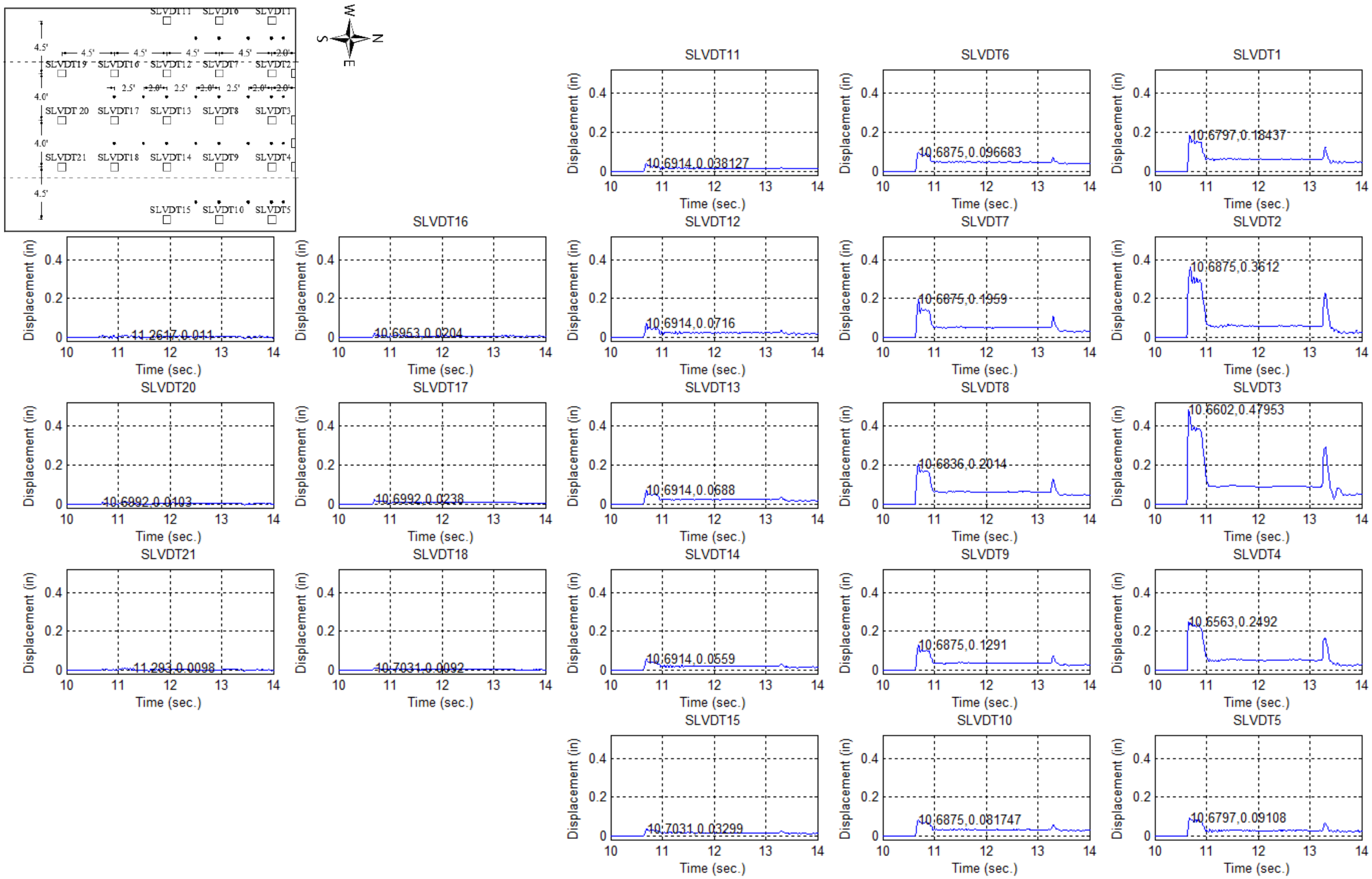

Figure 6-209 Vertical displacement histories on the soil surface for the 0° skew test in Run 3.

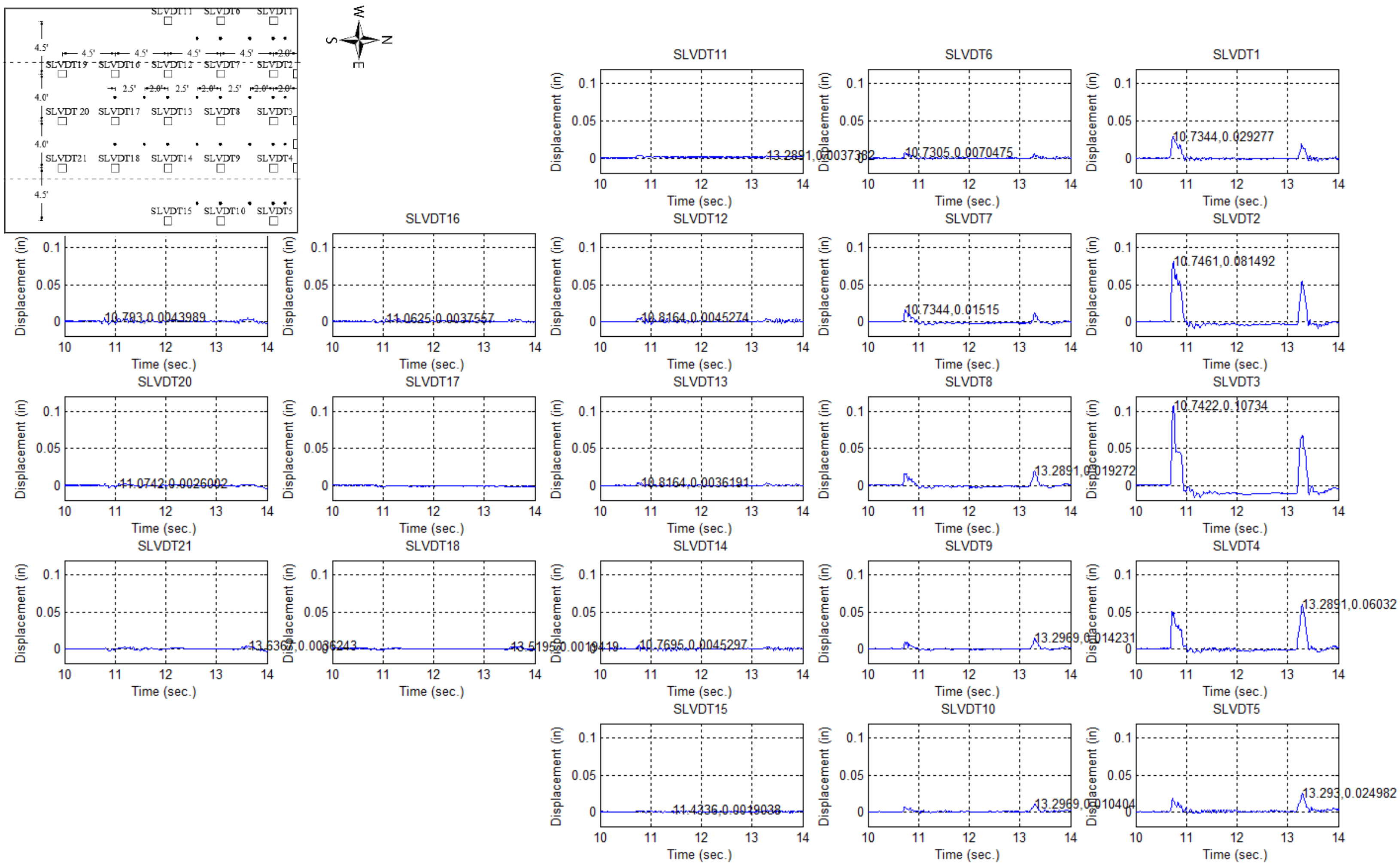

Figure 6-210 Vertical displacement histories on the soil surface for the 0° skew test in Run 4.

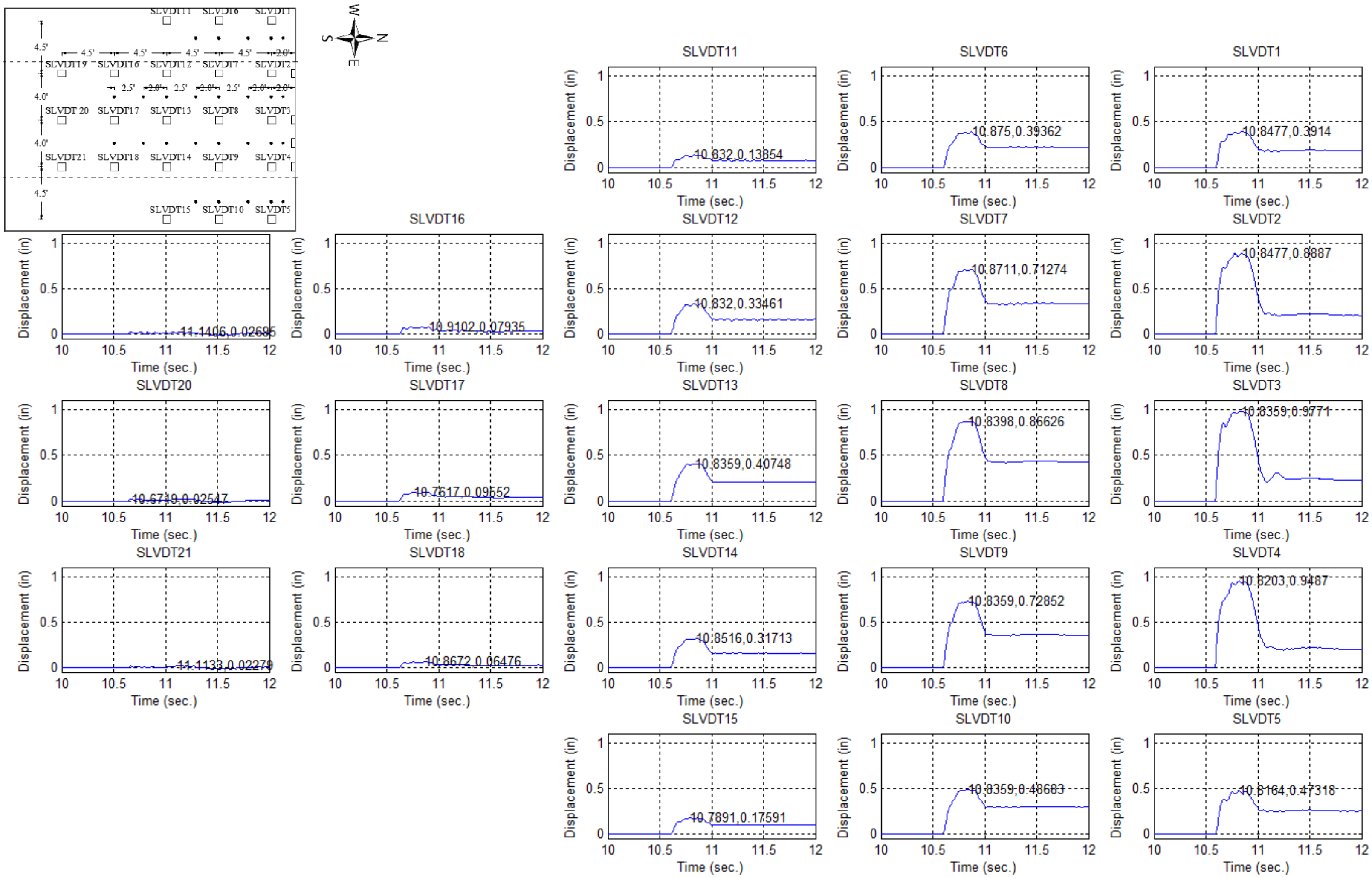

Figure 6-211 Vertical displacement histories on the soil surface for the 0° skew test in Run 6.

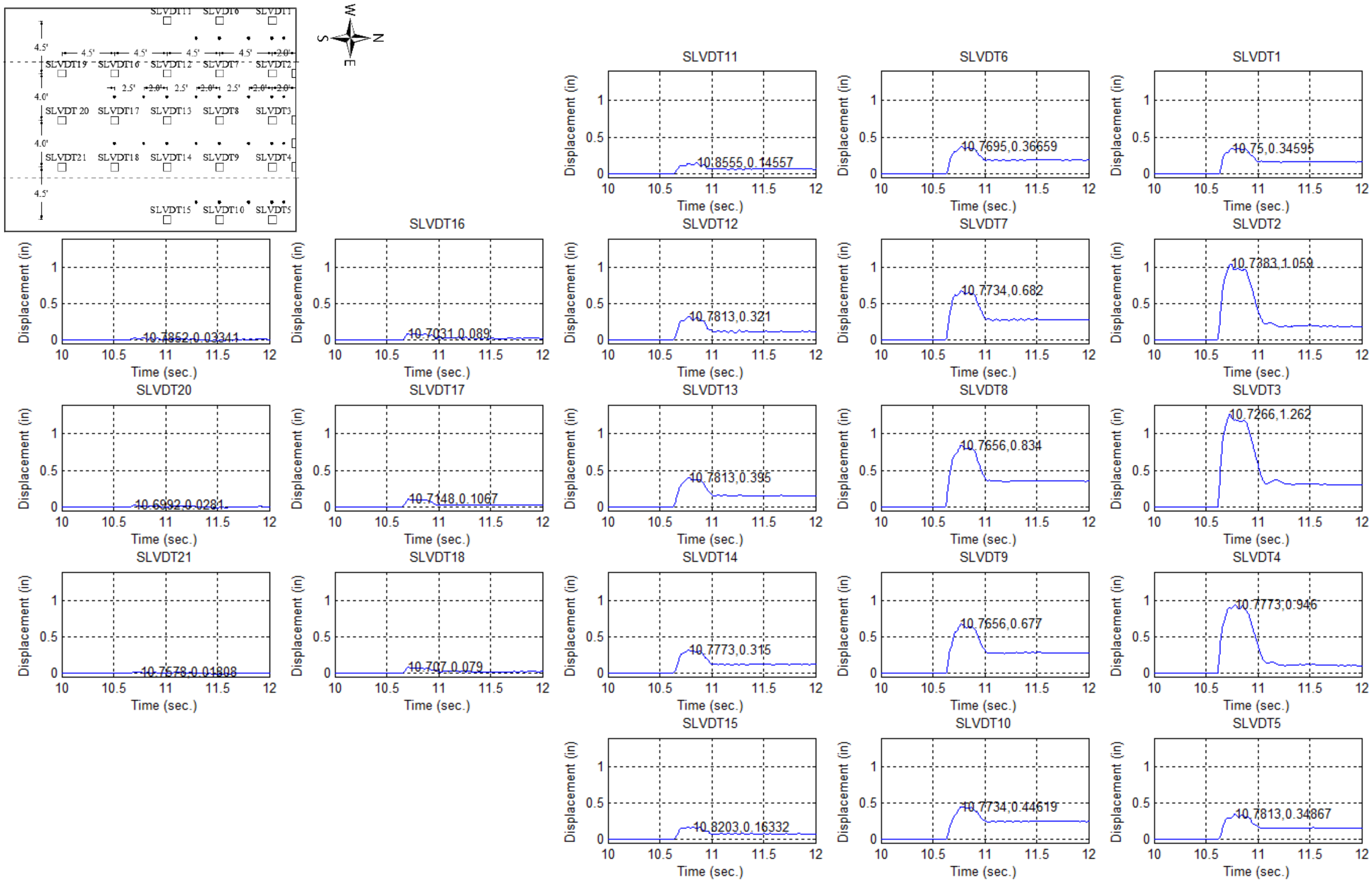

Figure 6-212 Vertical displacement histories on the soil surface for the 0° skew test in Run 7.

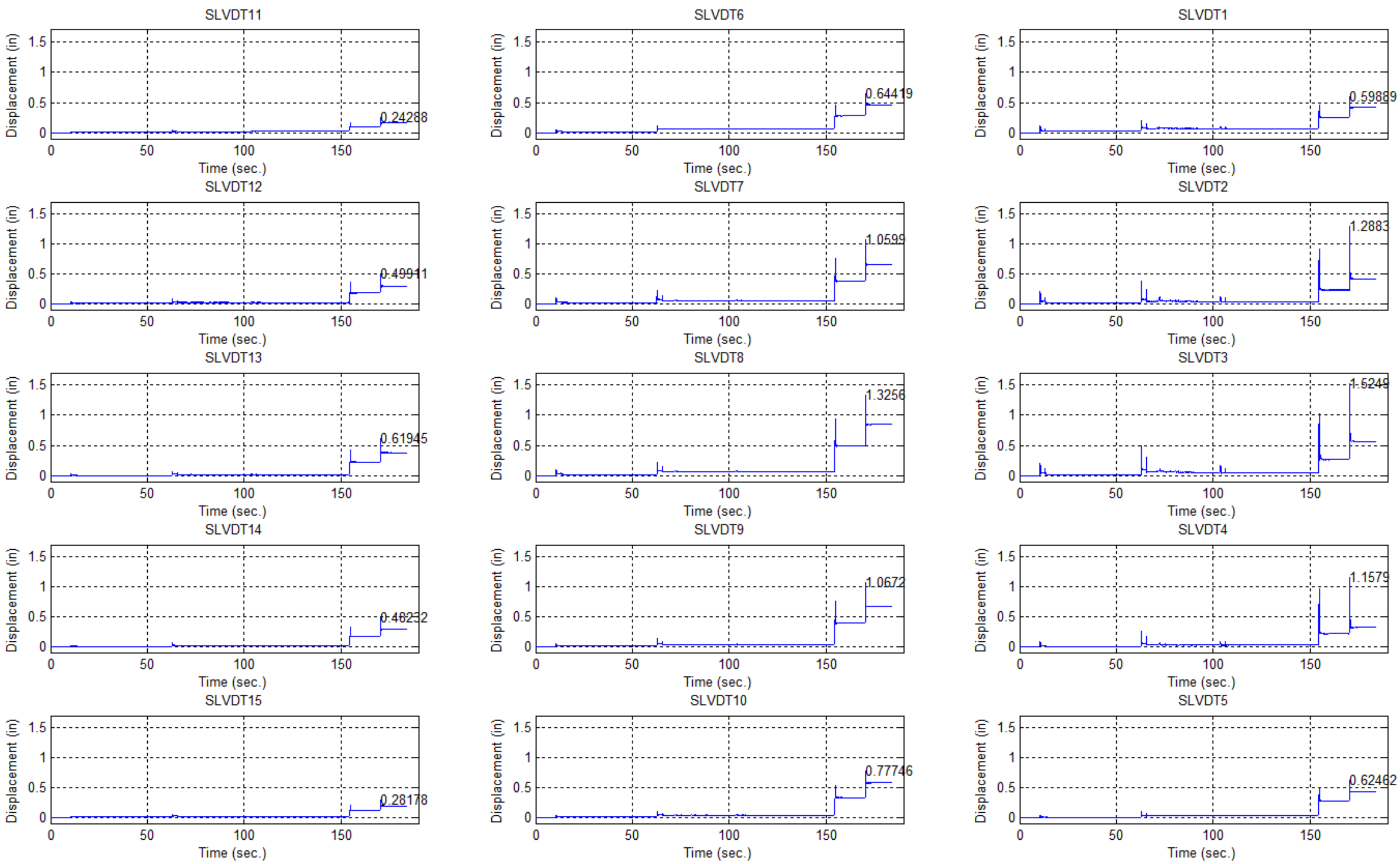

Figure 6-213 Combined vertical displacement histories on the soil surface for all the runs of the 0° skew test.

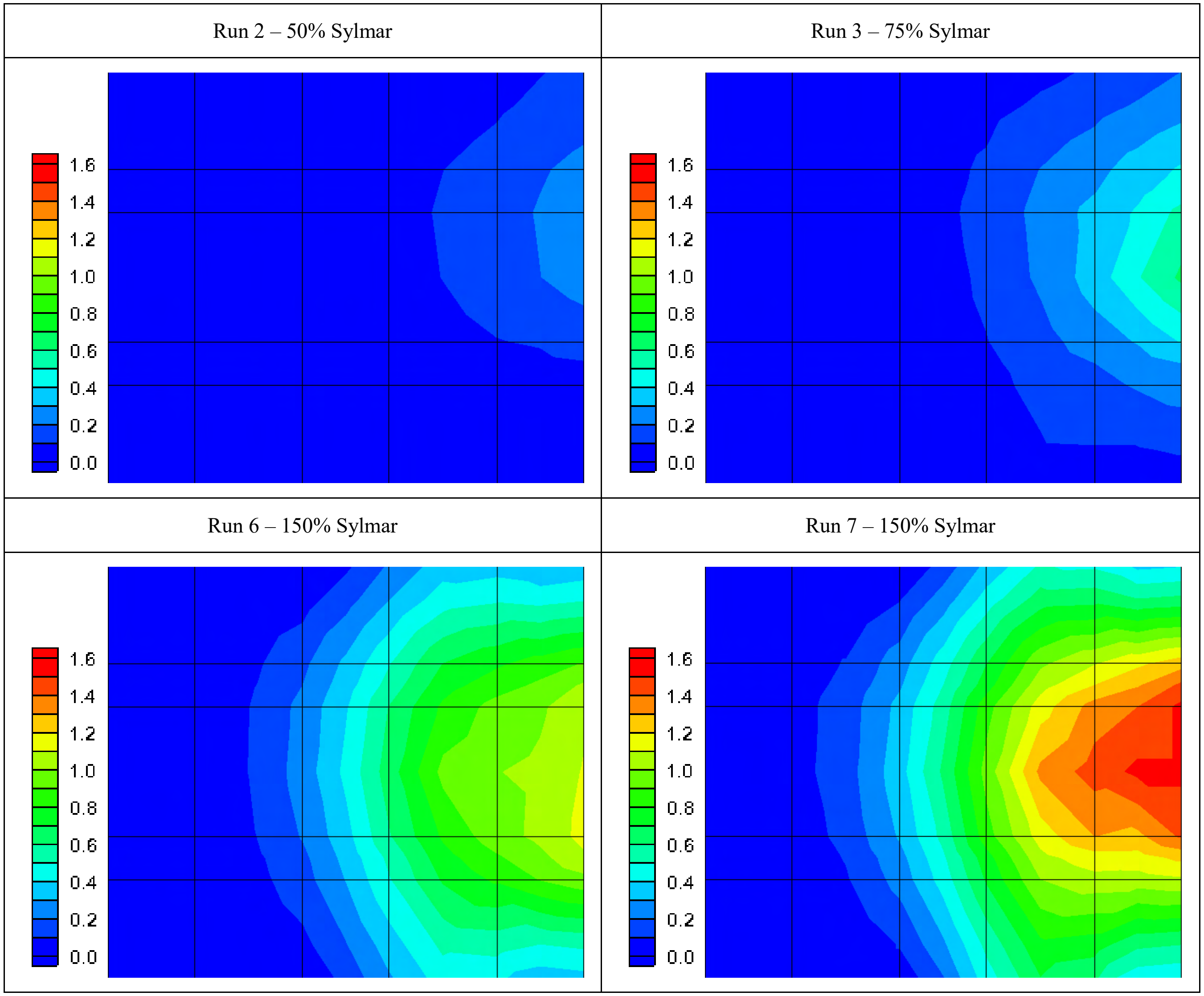

Figure 6-214 Contours of maximum heaves of soil surface for the 0° skew test in in.

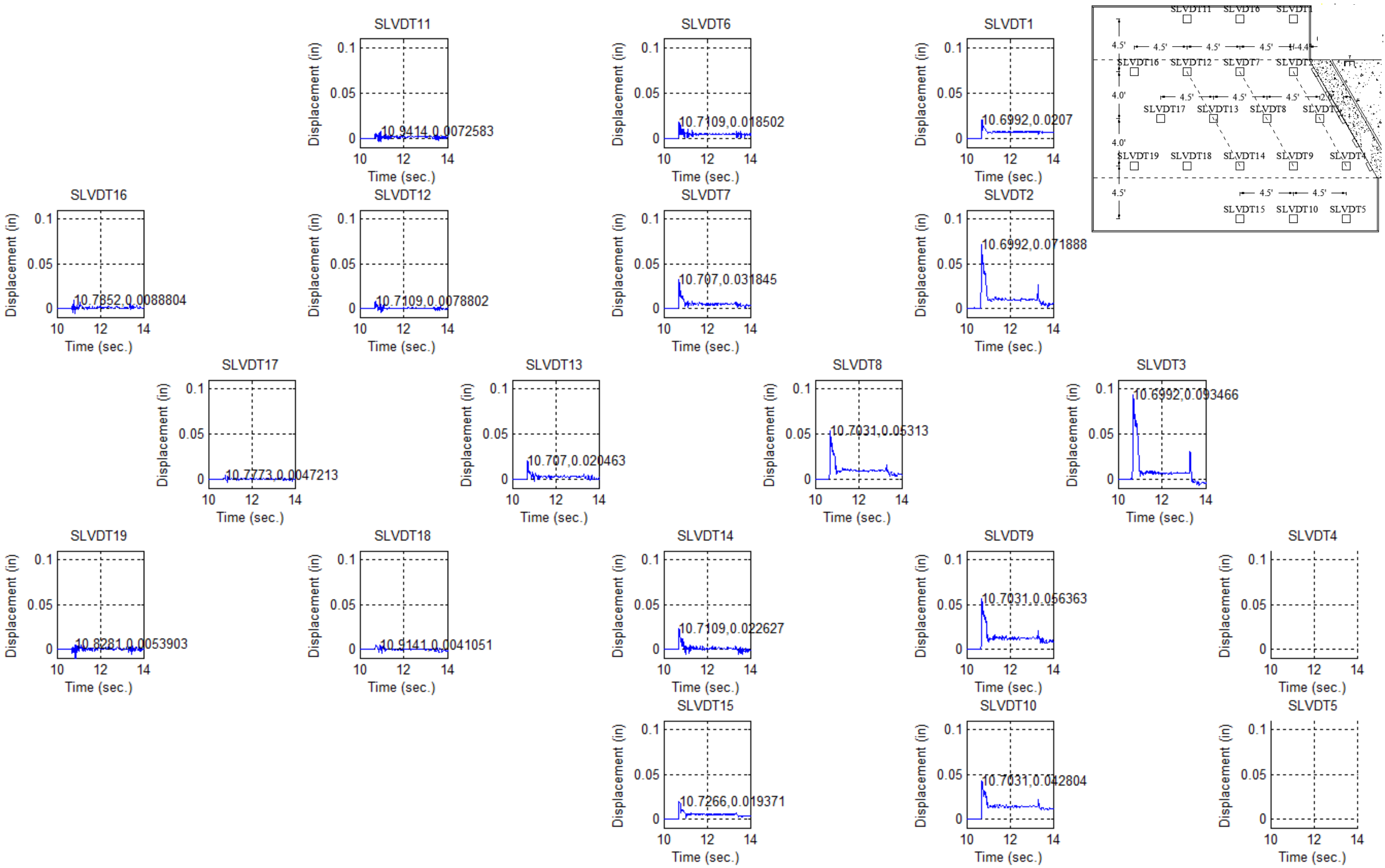

Figure 6-215 Vertical displacement histories on the soil surface for the 30° skew test in Run 2.

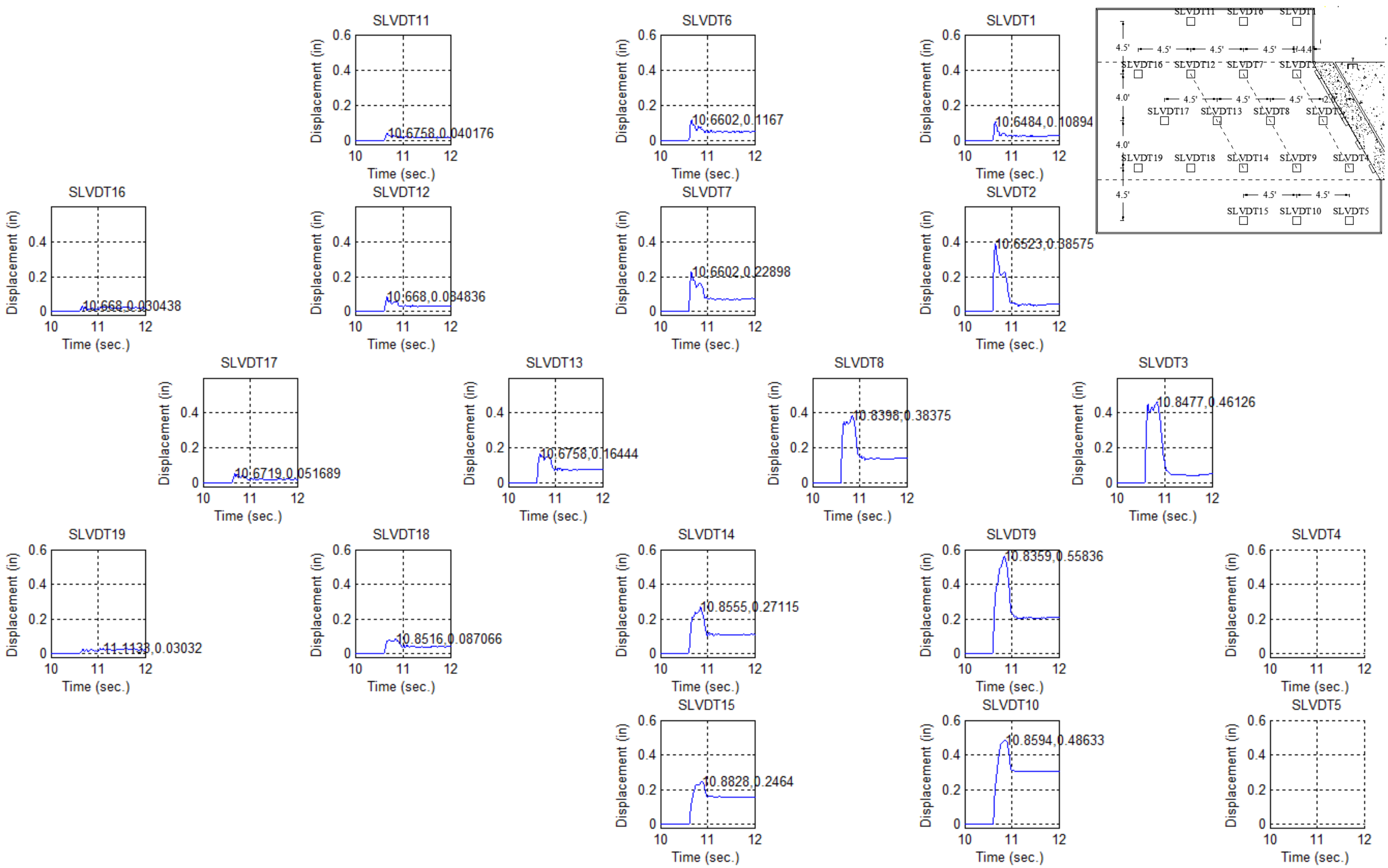

Figure 6-216 Vertical displacement histories on the soil surface for the 30° skew test in Run 3.

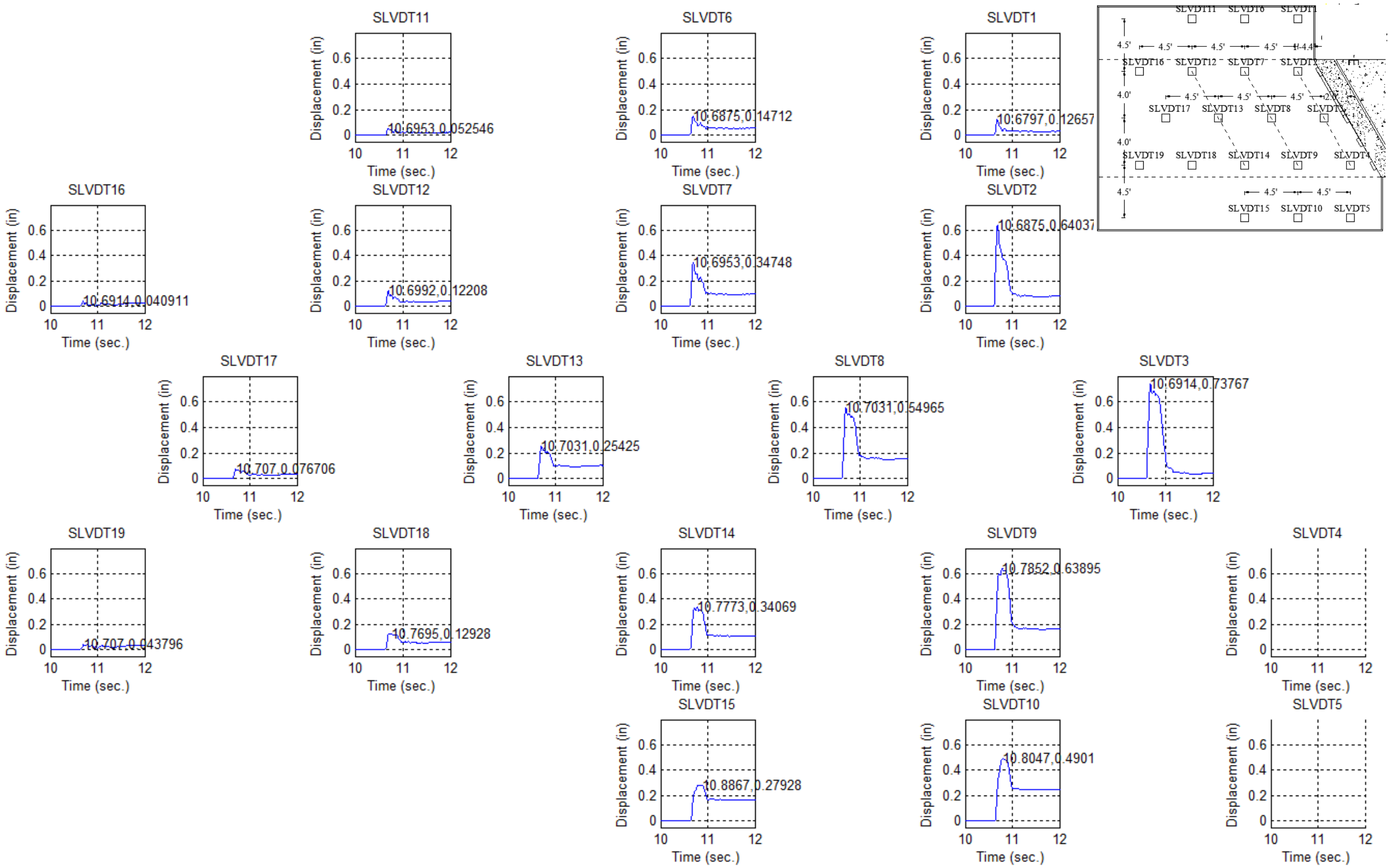

Figure 6-217 Vertical displacement histories on the soil surface for the 30° skew test in Run 4.

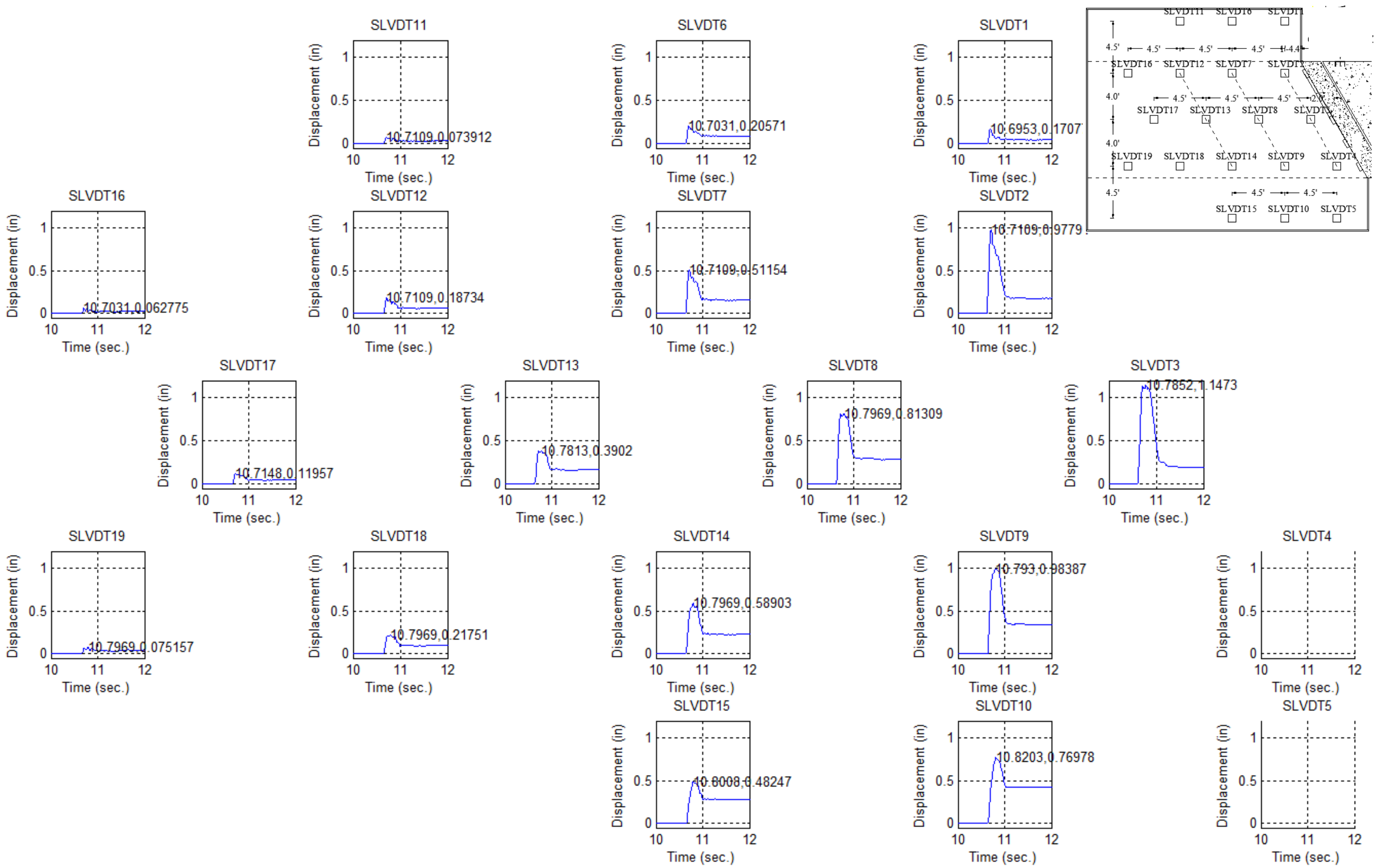

Figure 6-218 Vertical displacement histories on the soil surface for the 30° skew test in Run 5.

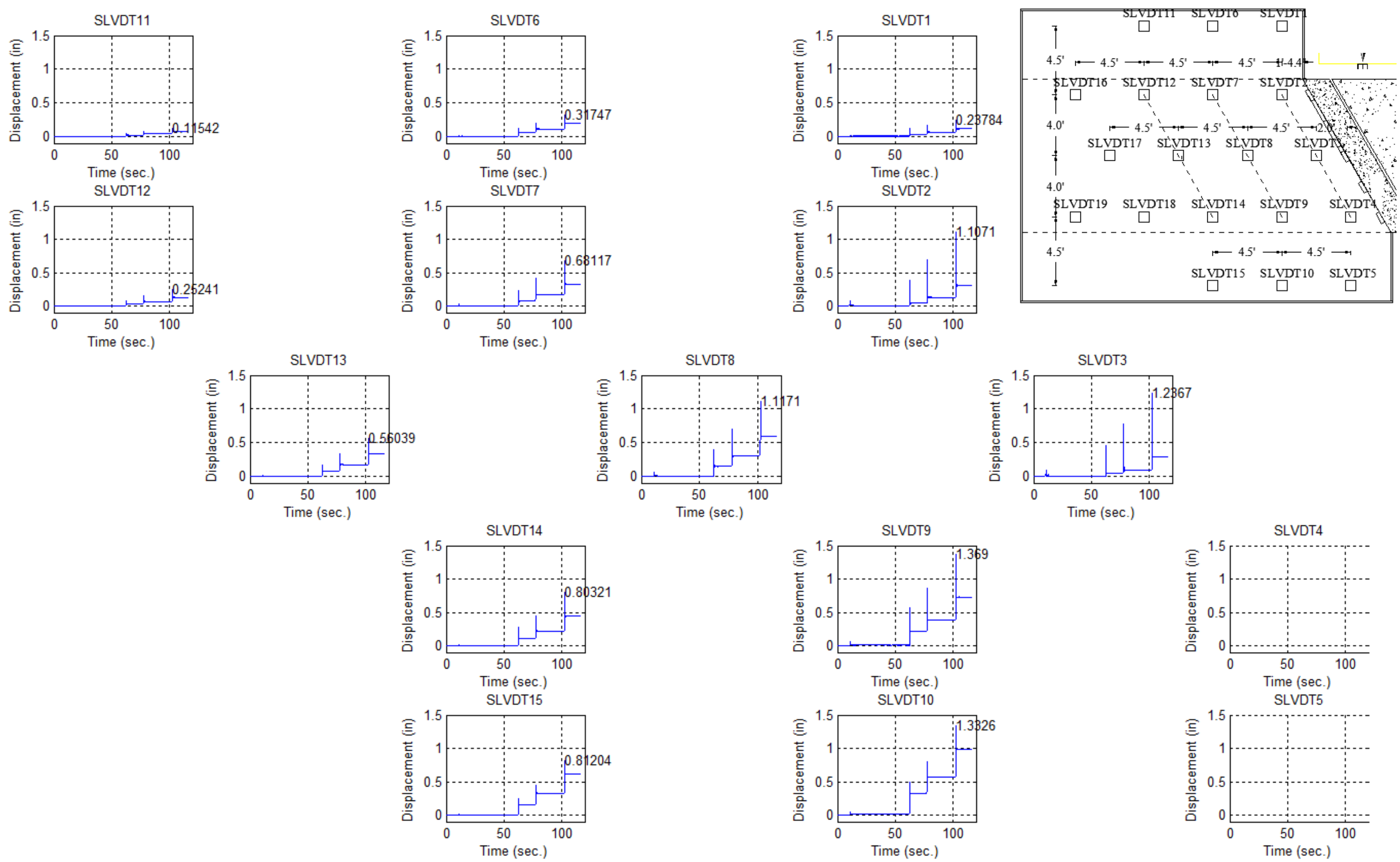

Figure 6-219 Combined vertical displacement histories on the soil surface for all the runs of the 30° skew test.

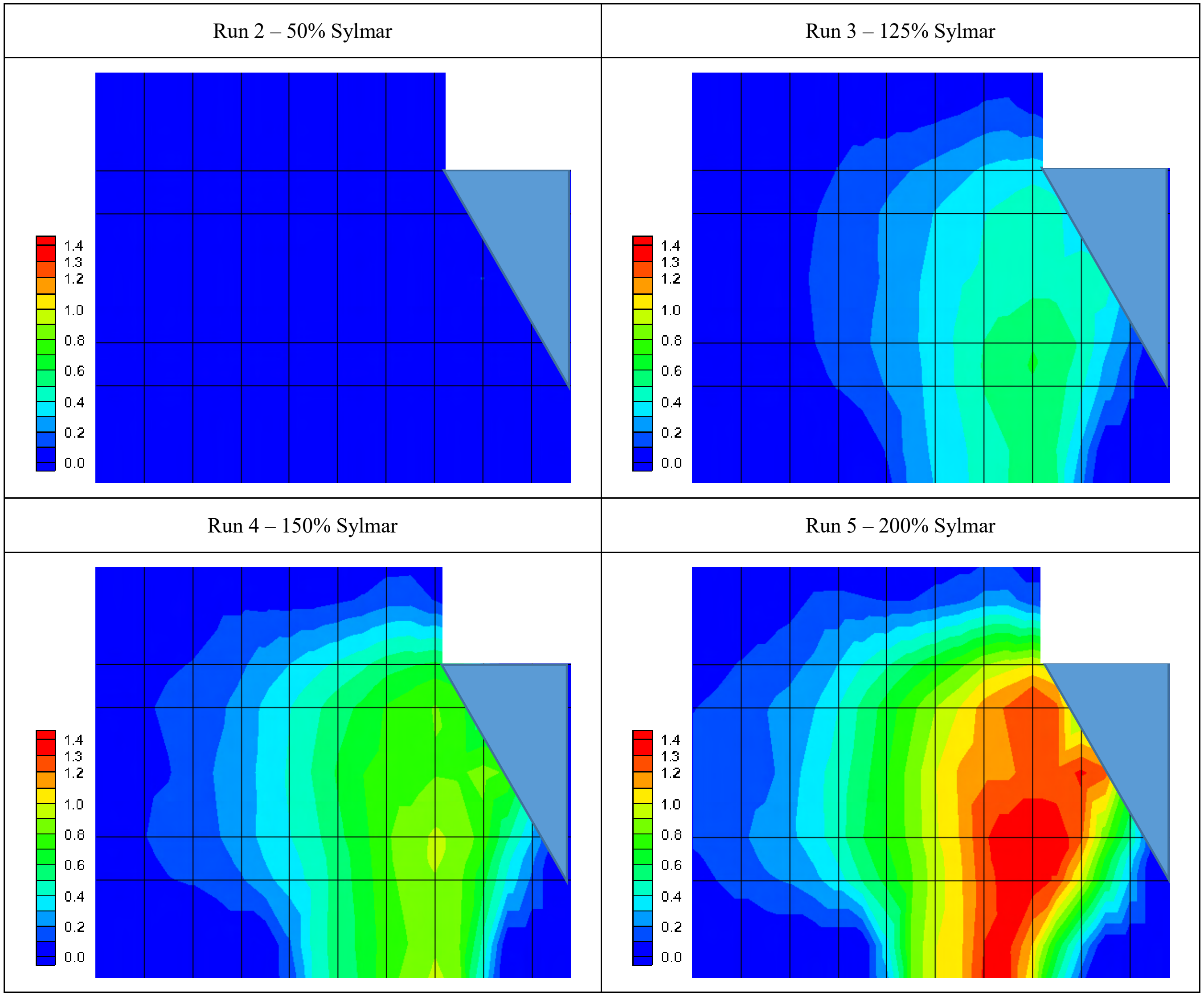

Figure 6-220 Contours of maximum heaves of soil surface for the 30° skew test in in.

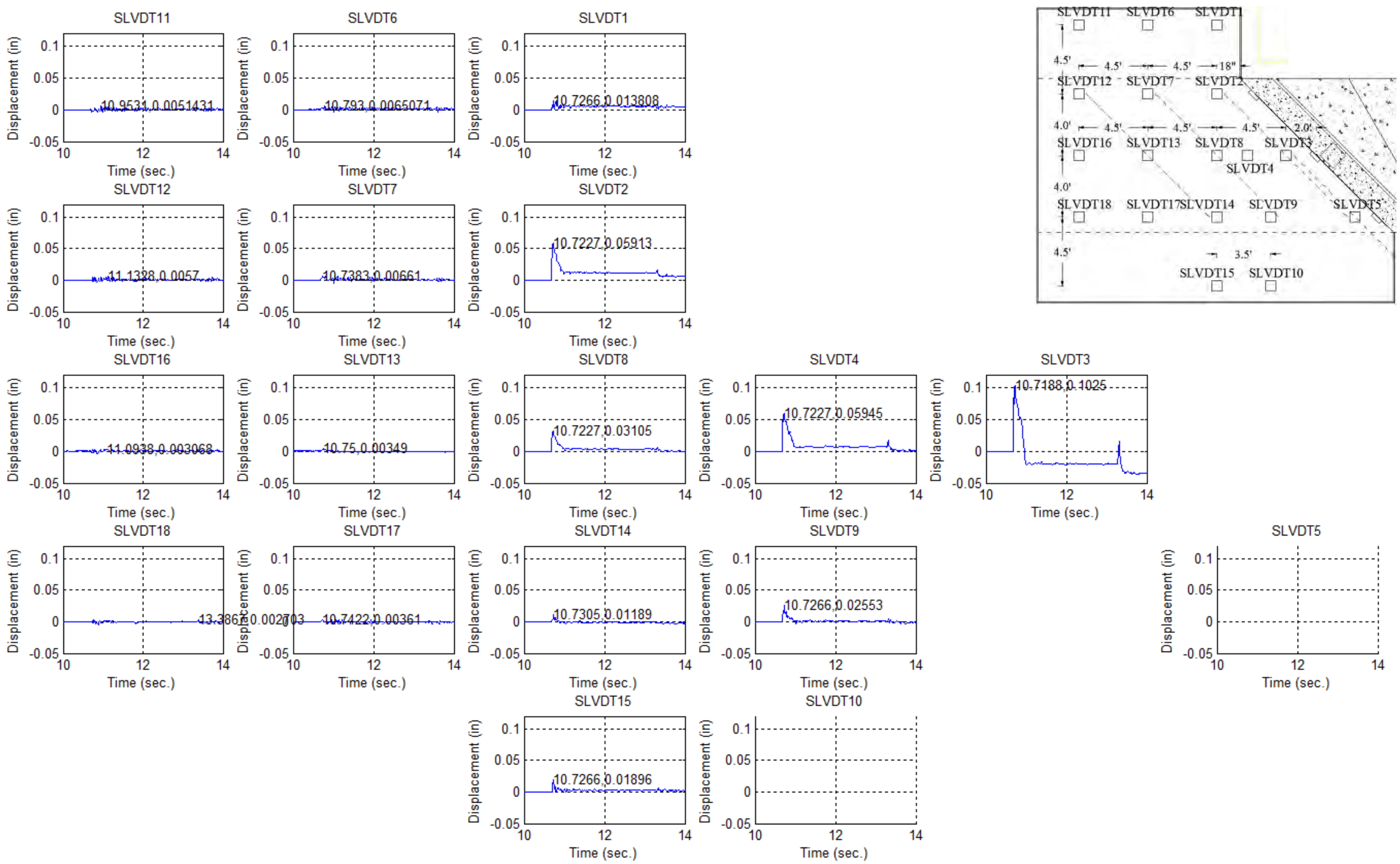

Figure 6-221 Vertical displacement histories on the soil surface for the 45° skew test in Run 2.

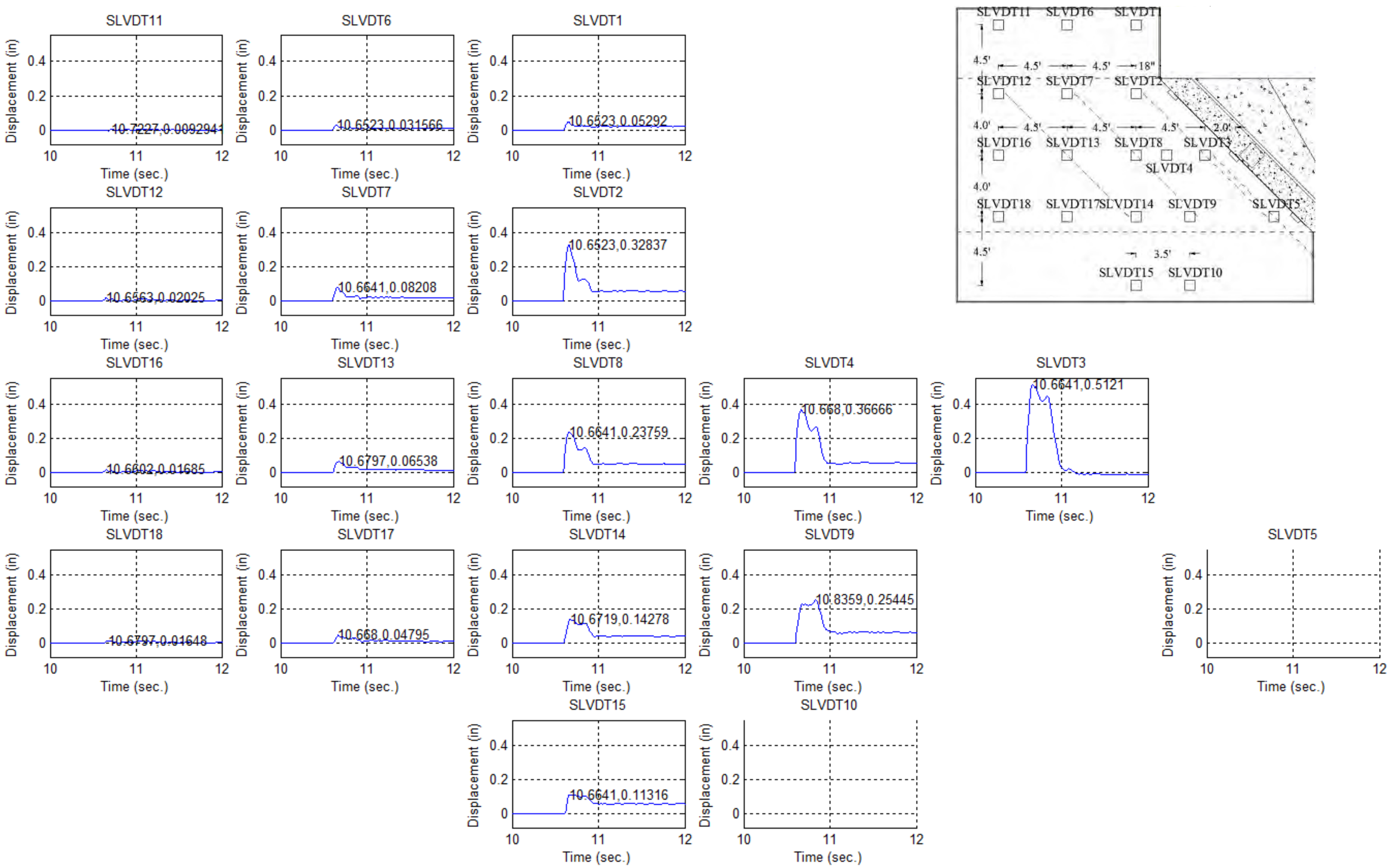

Figure 6-222 Vertical displacement histories on the soil surface for the 45° skew test in Run 3.

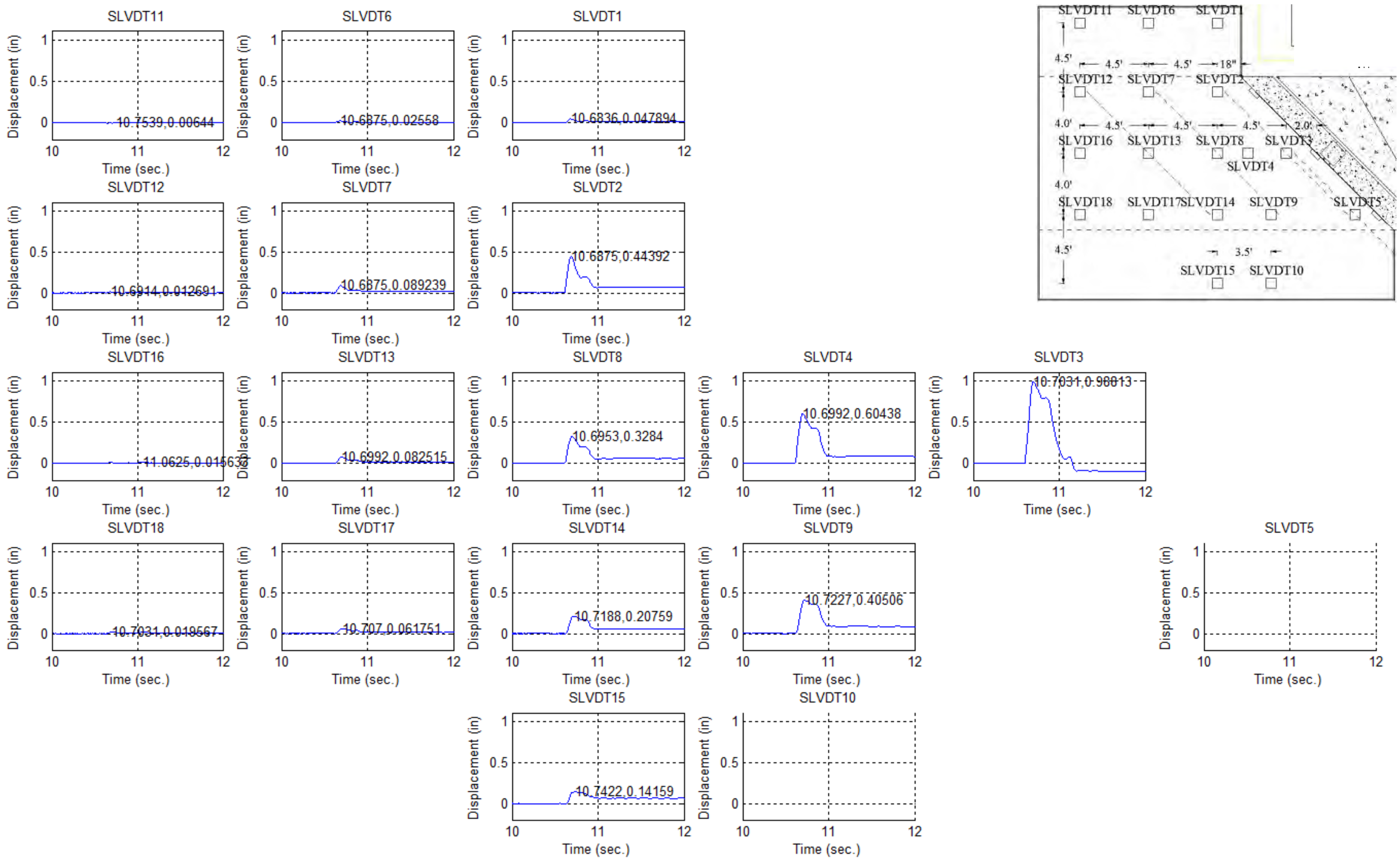

Figure 6-223 Vertical displacement histories on the soil surface for the 45° skew test in Run 4.

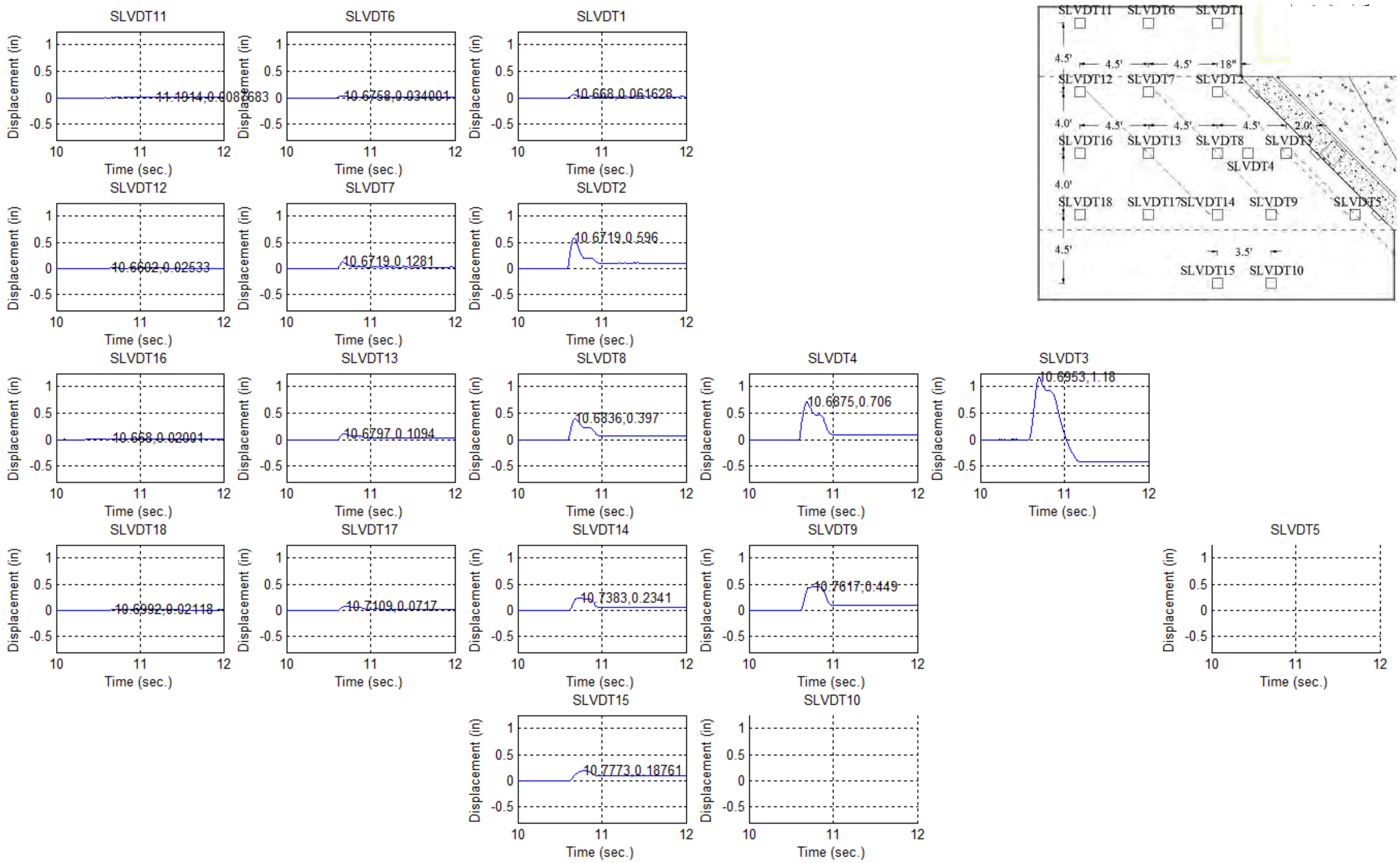

Figure 6-224 Vertical displacement histories on the soil surface for the 45° skew test in Run 5.

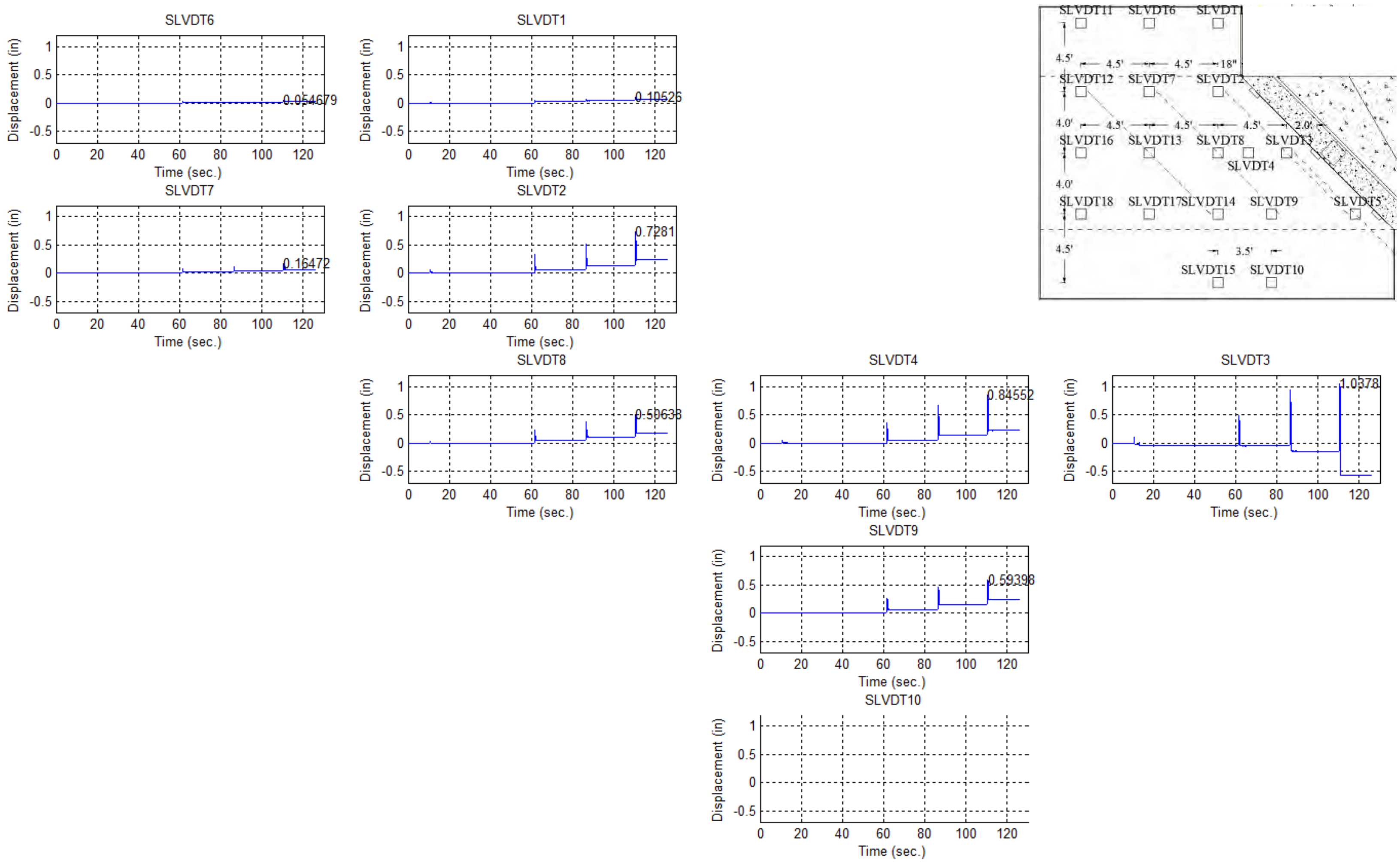

Figure 6-225 Combined vertical displacement histories on the soil surface for all the runs of the 45° skew test.

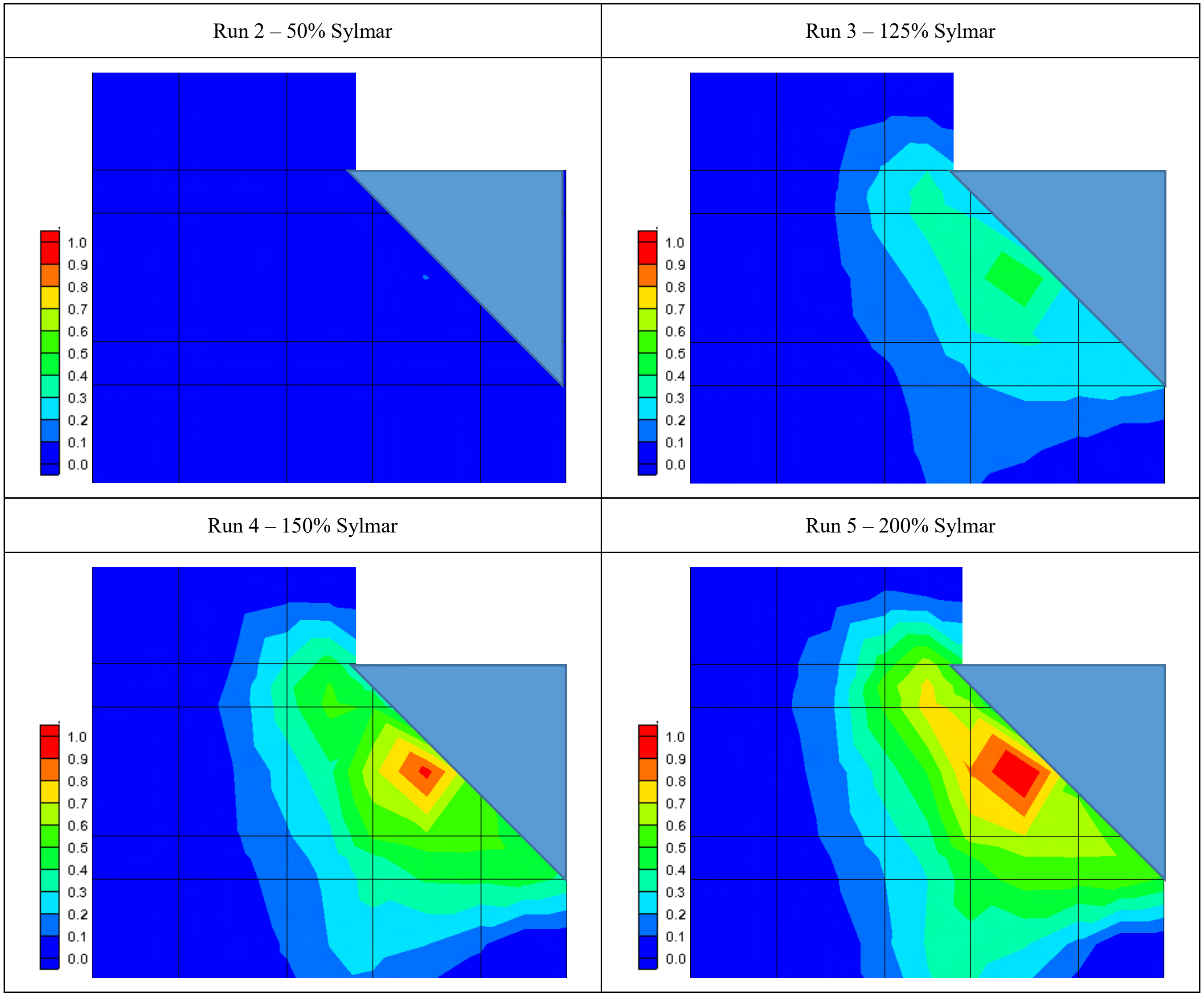

Figure 6-226 Contours of maximum heaves of soil surface for the 45° skew test in in.

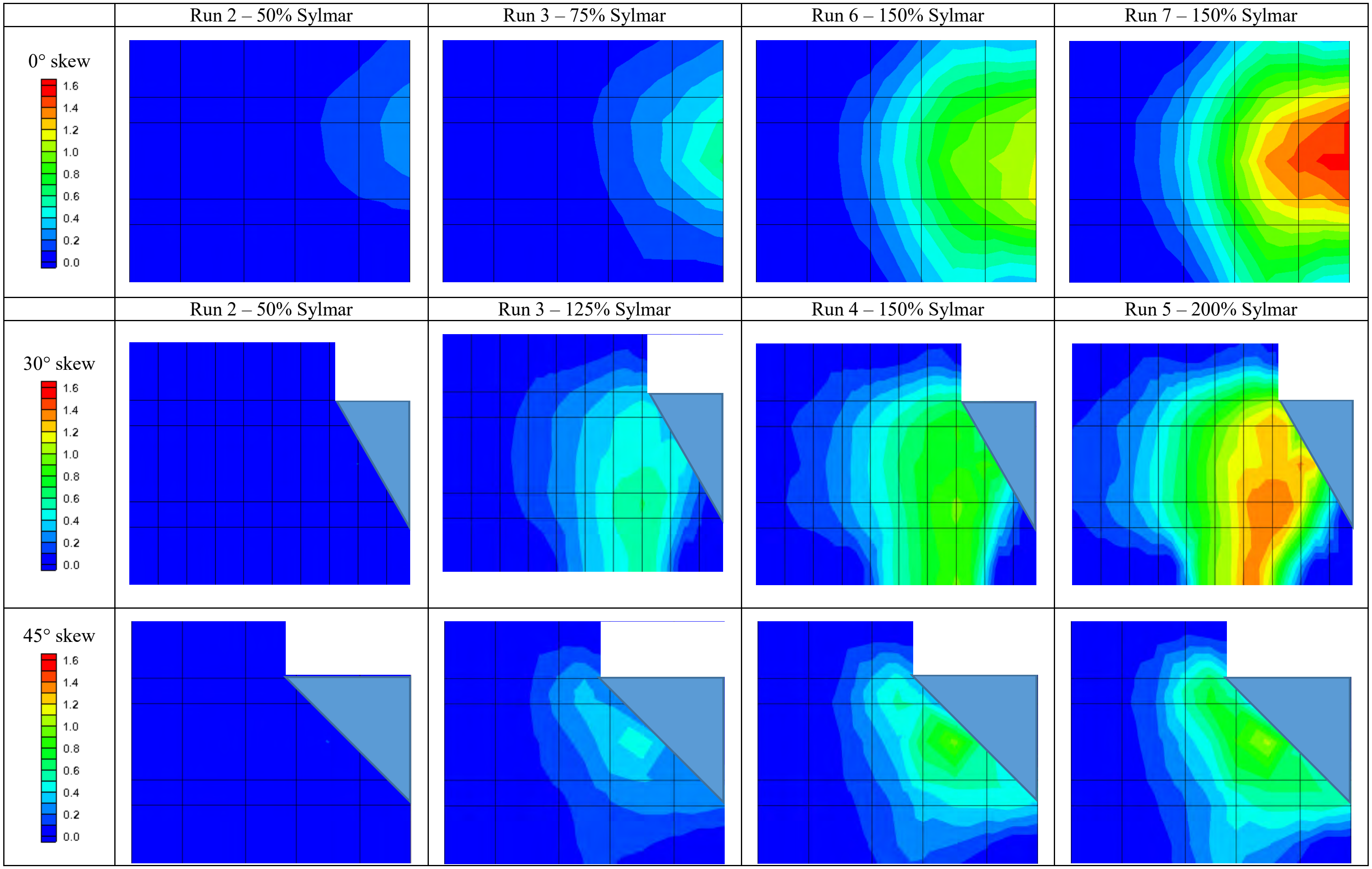

Figure 6-227 Comparison of contours of maximum heaves of soil surface in in.

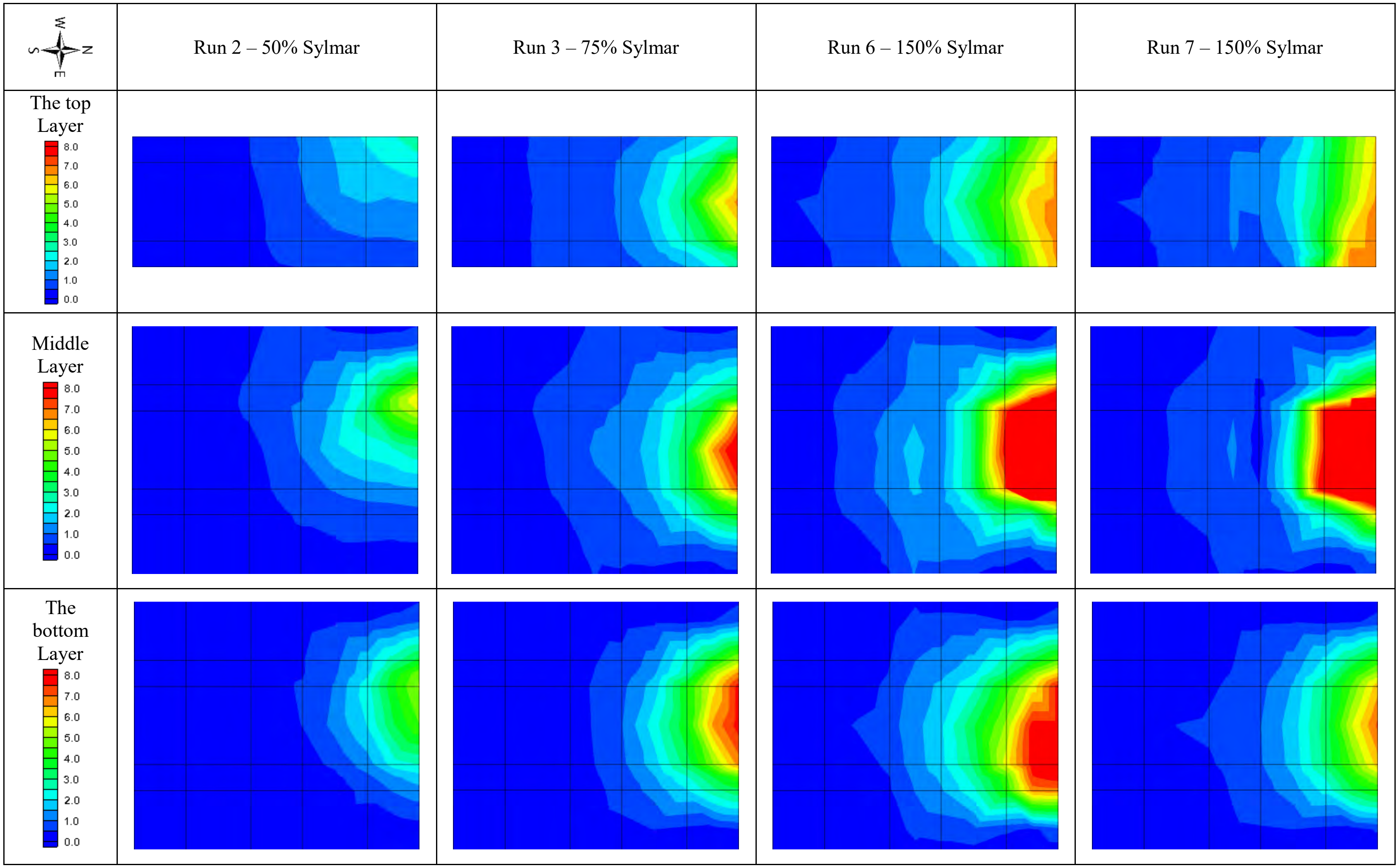

Figure 6-228 Contours of soil maximum longitudinal accelerations for the 0° skew test in terms of g.

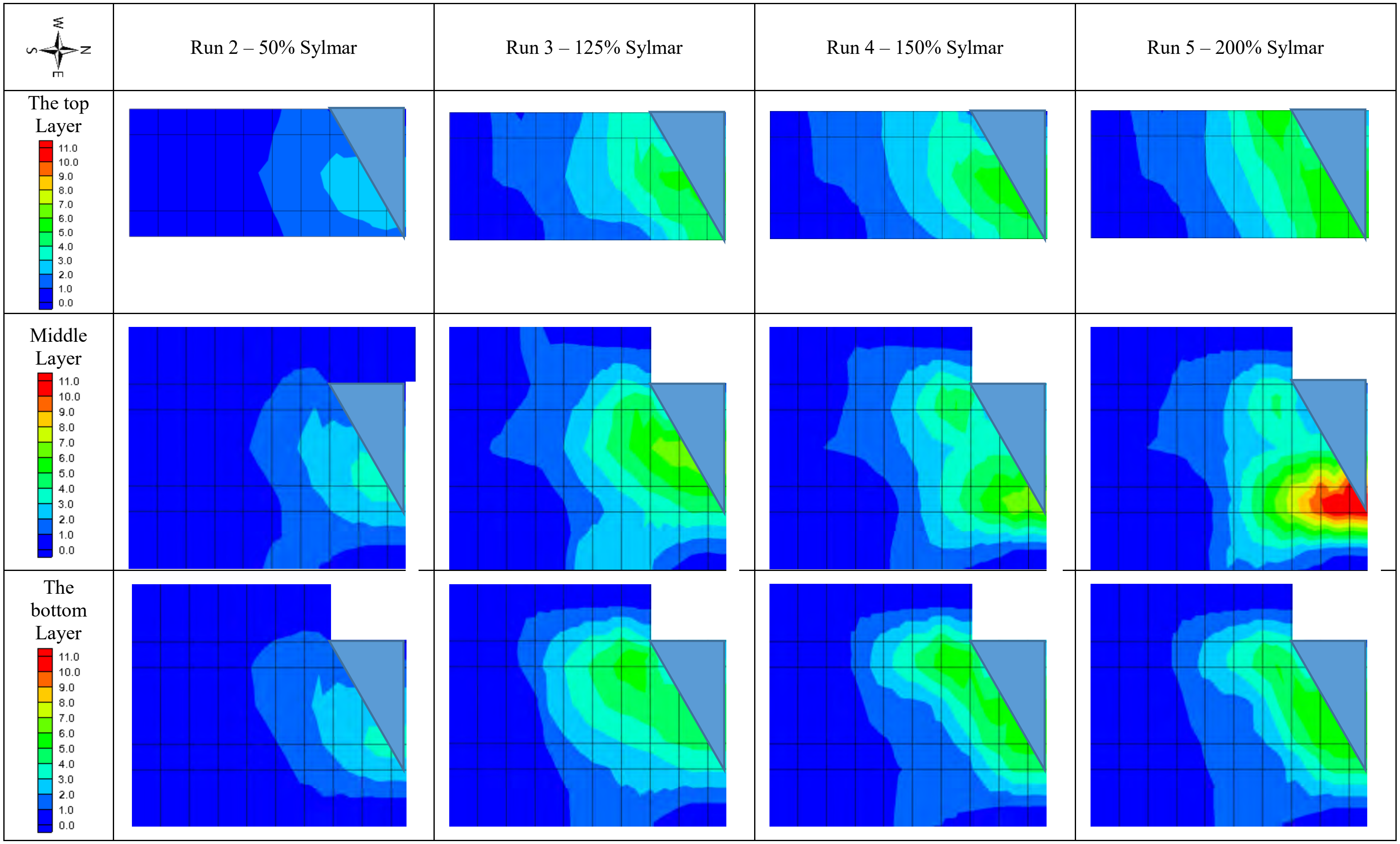

Figure 6-229 Contours of soil maximum longitudinal accelerations for the 30° skew test in terms of g.

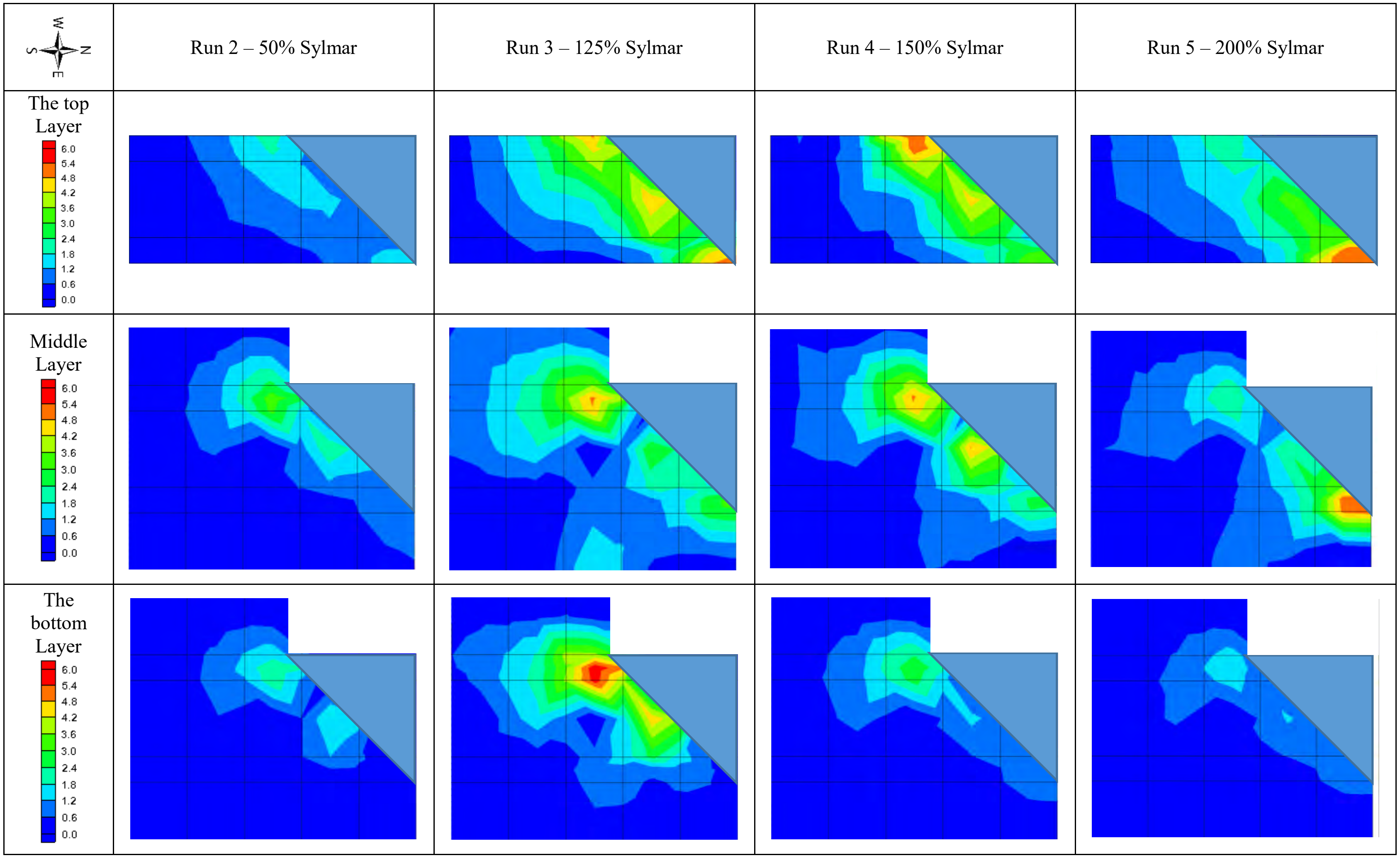

Figure 6-230 Contours of soil maximum longitudinal accelerations for the 45° skew test in terms of g.

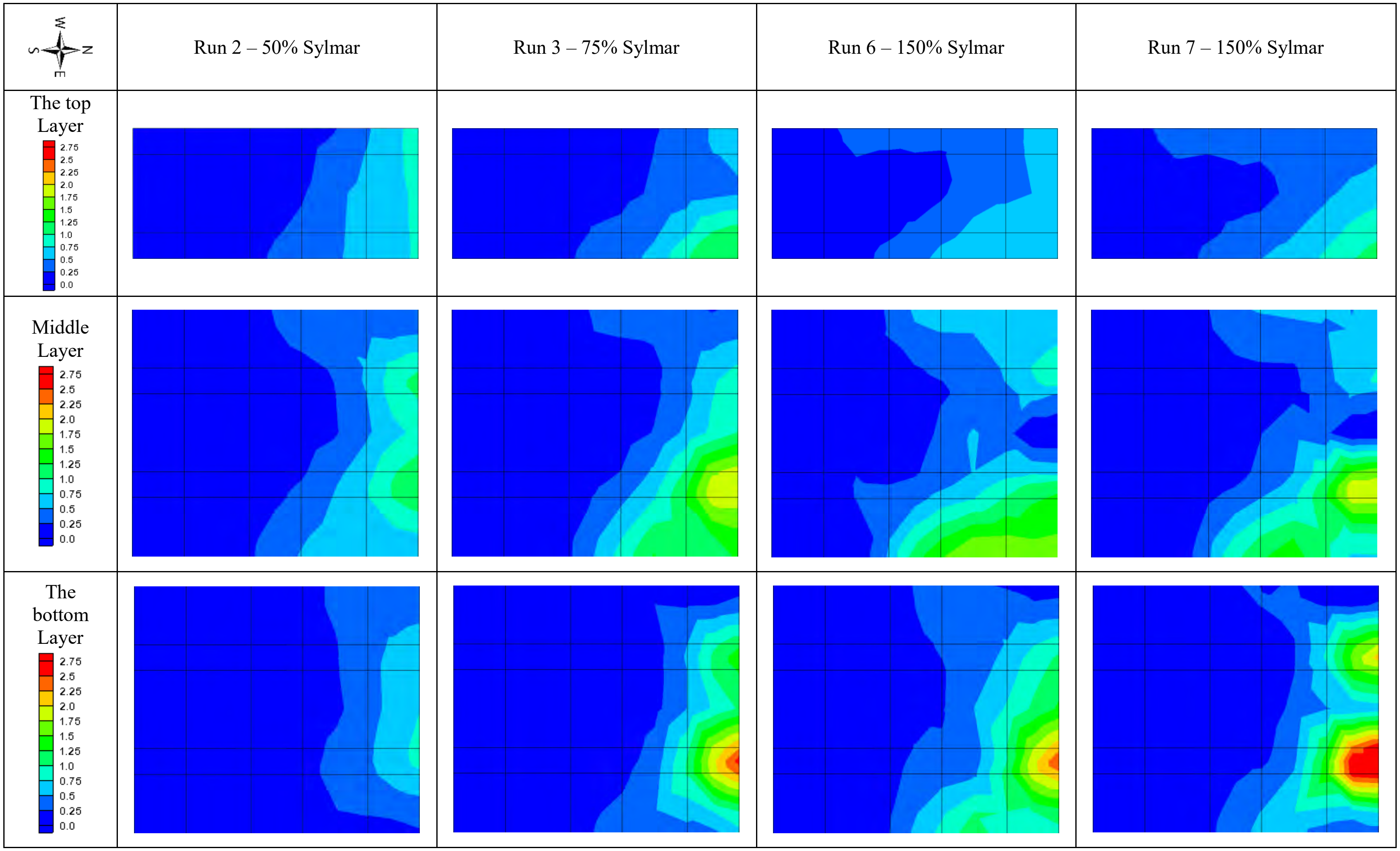

Figure 6-231 Contours of soil maximum accelerations in the transverse direction towards the east for the 0° skew test in terms of g.

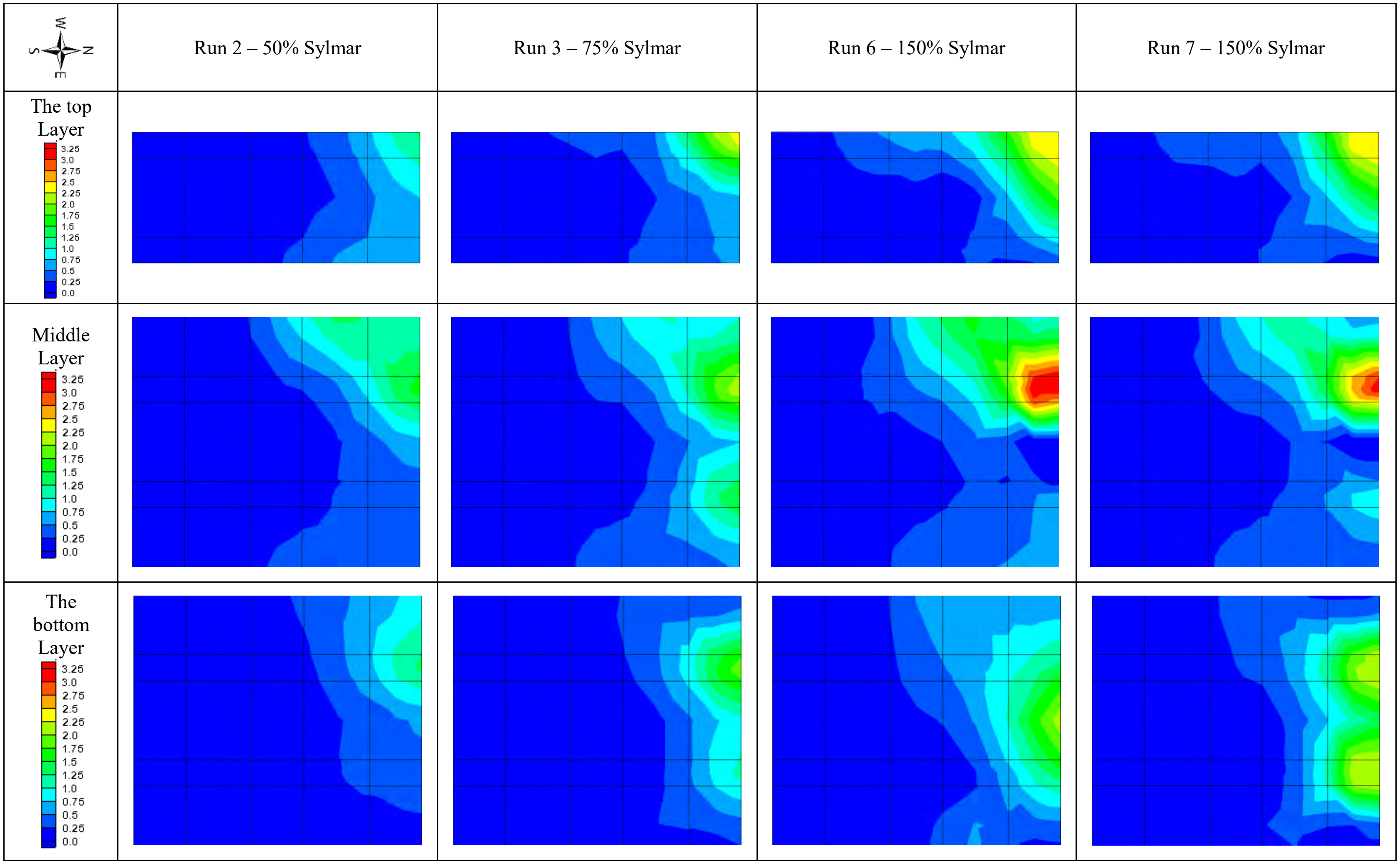

Figure 6-232 Contours of soil maximum accelerations in the transverse direction towards the west for the 0° skew test in terms of g.

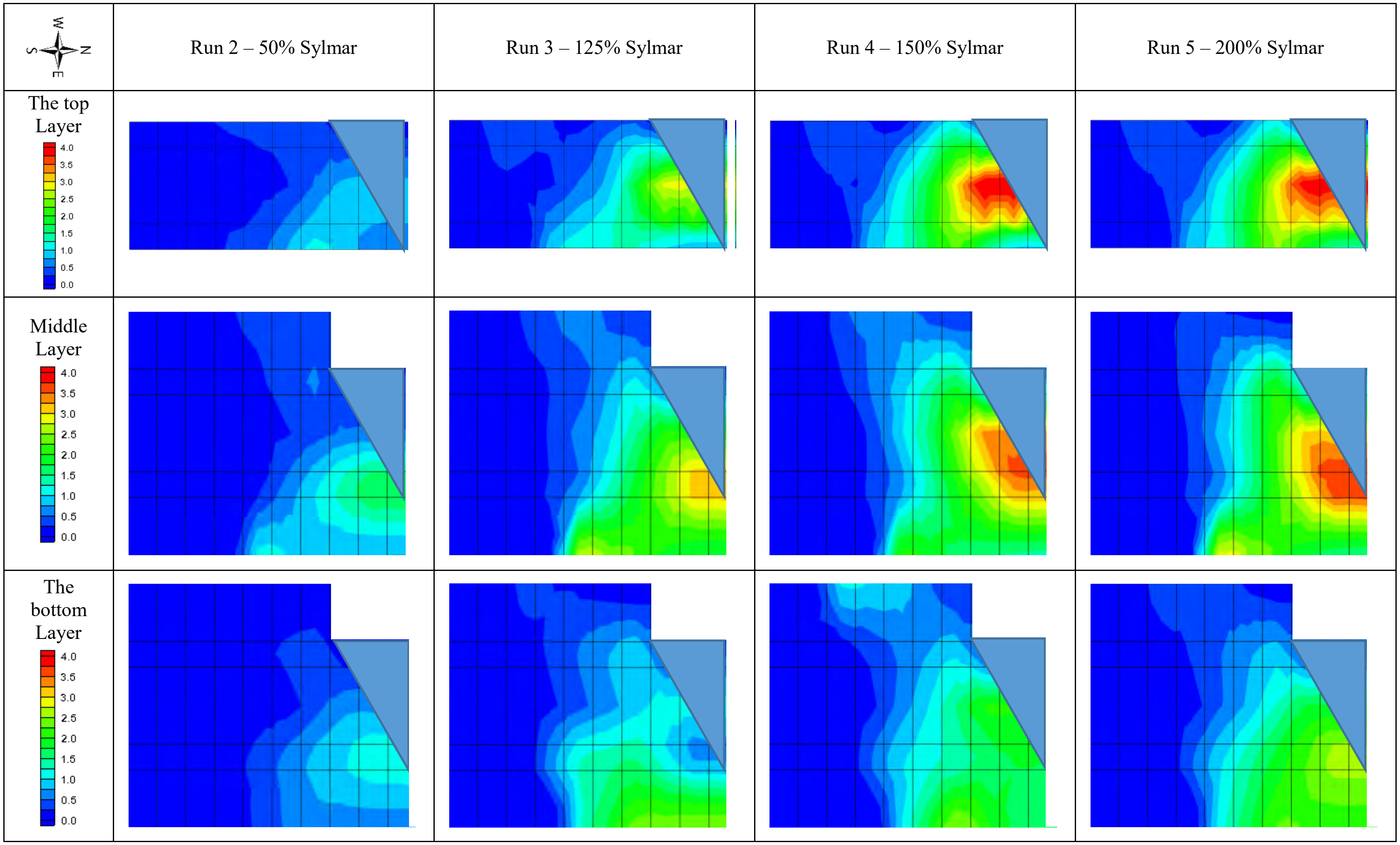

Figure 6-233 Contours of soil maximum accelerations in the transverse direction towards the obtuse corner for the 30° skew test in terms of g.

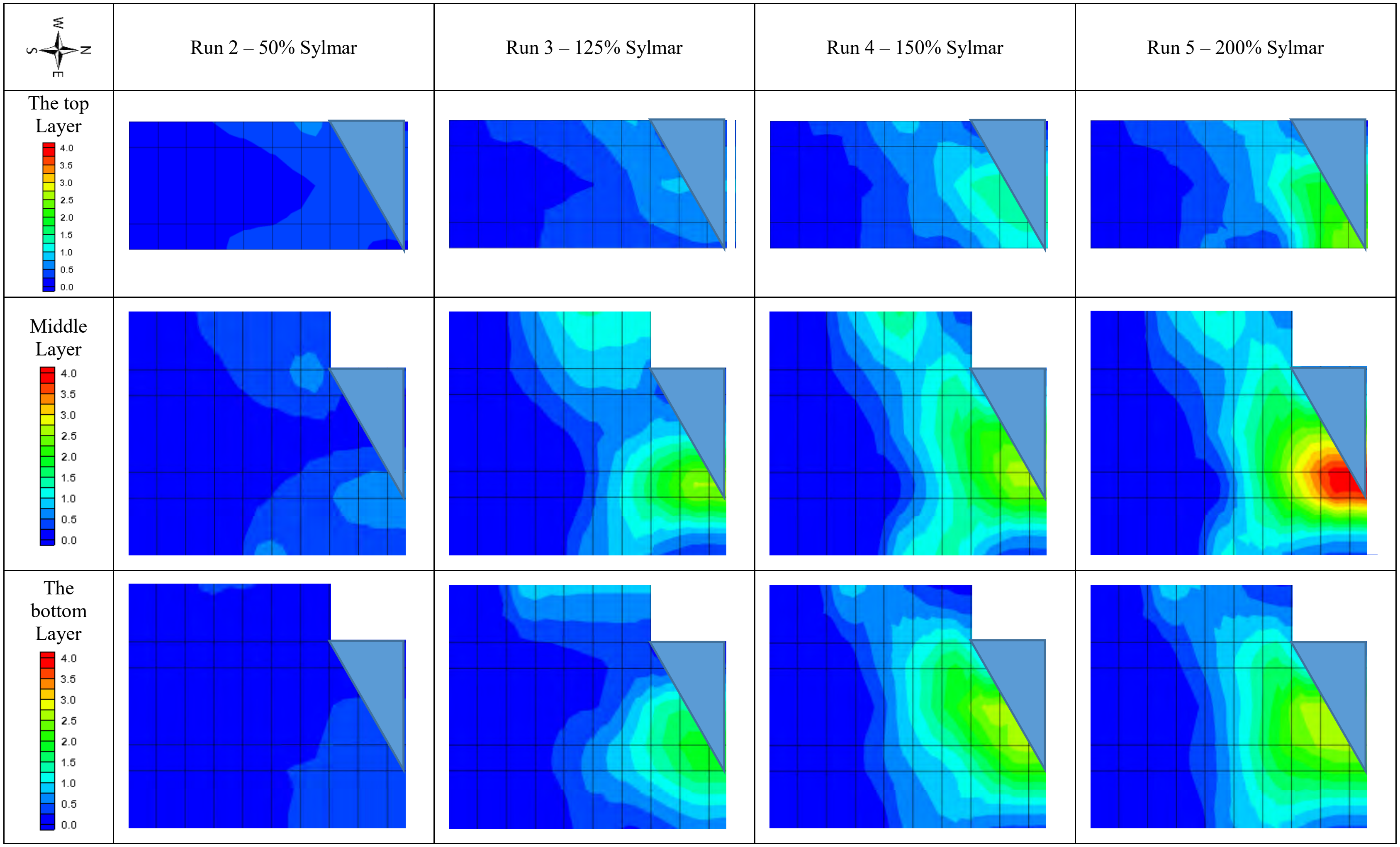

Figure 6-234 Contours of soil maximum accelerations in the transverse direction towards the acute corner for the 30° skew test in terms of g.

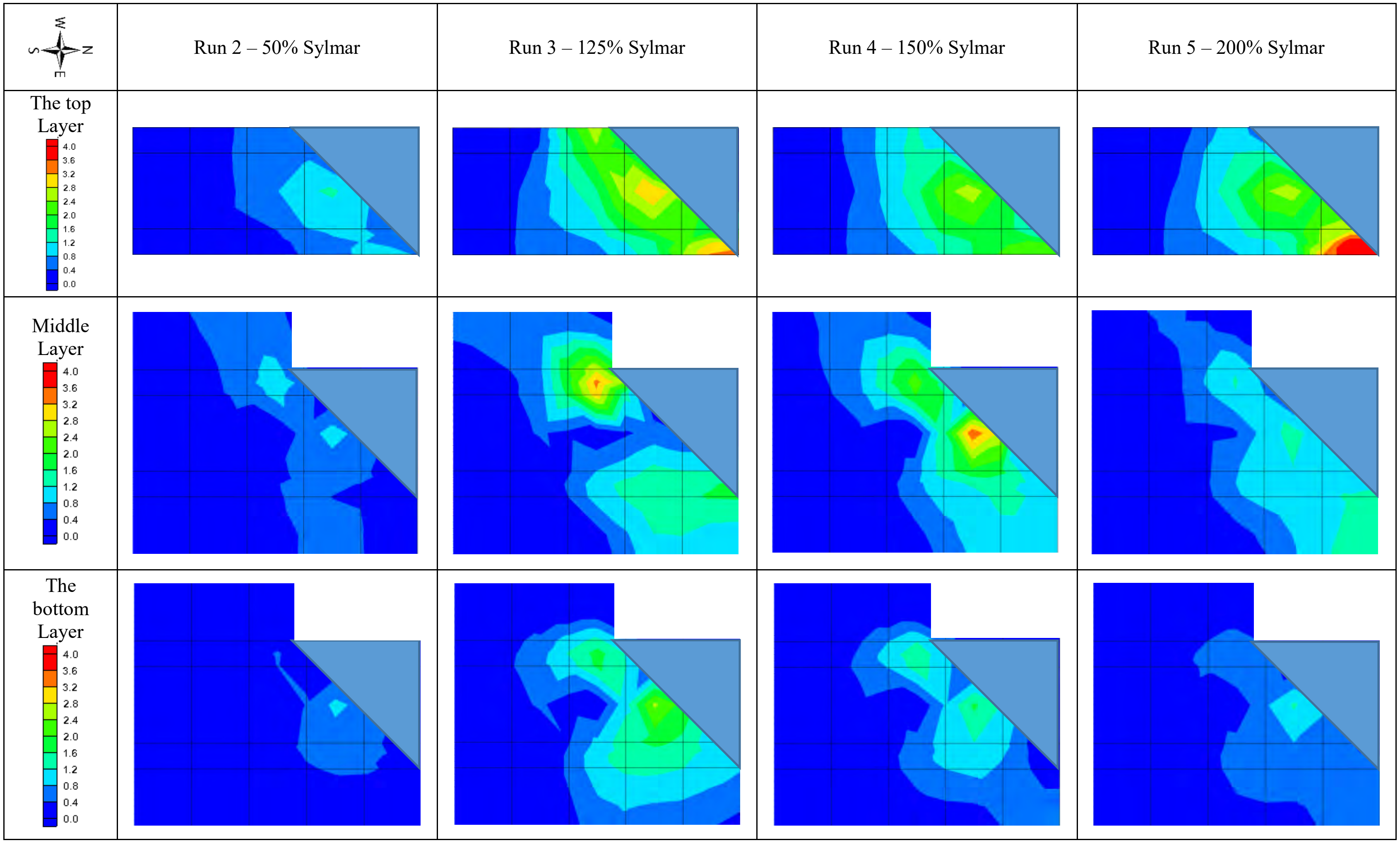

Figure 6-235 Contours of soil maximum accelerations in the transverse direction towards the obtuse corner for the 45° skew test in terms of g.

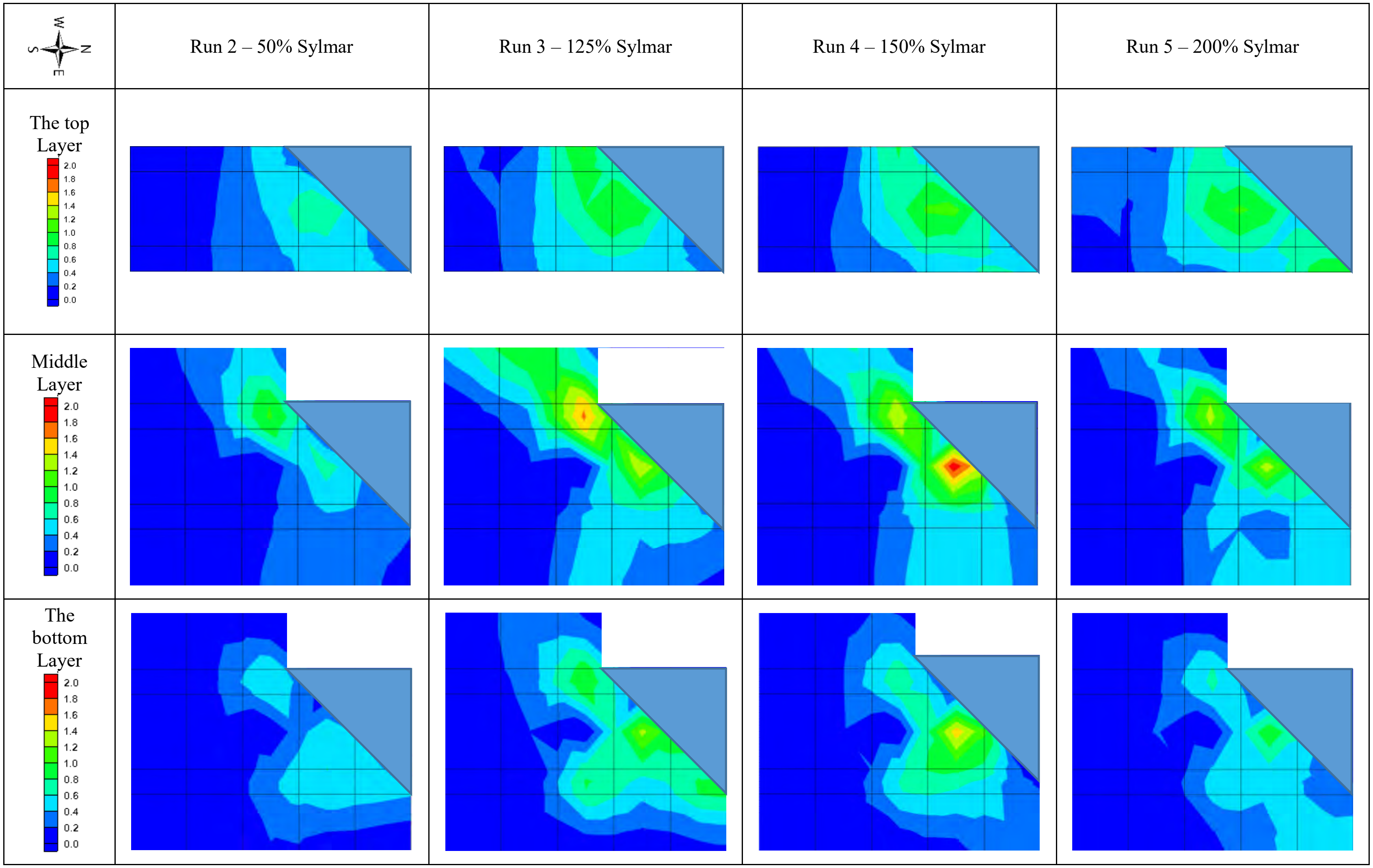

Figure 6-236 Contours of soil maximum accelerations in the transverse direction towards the acute corner for the 45° skew test in terms of g.

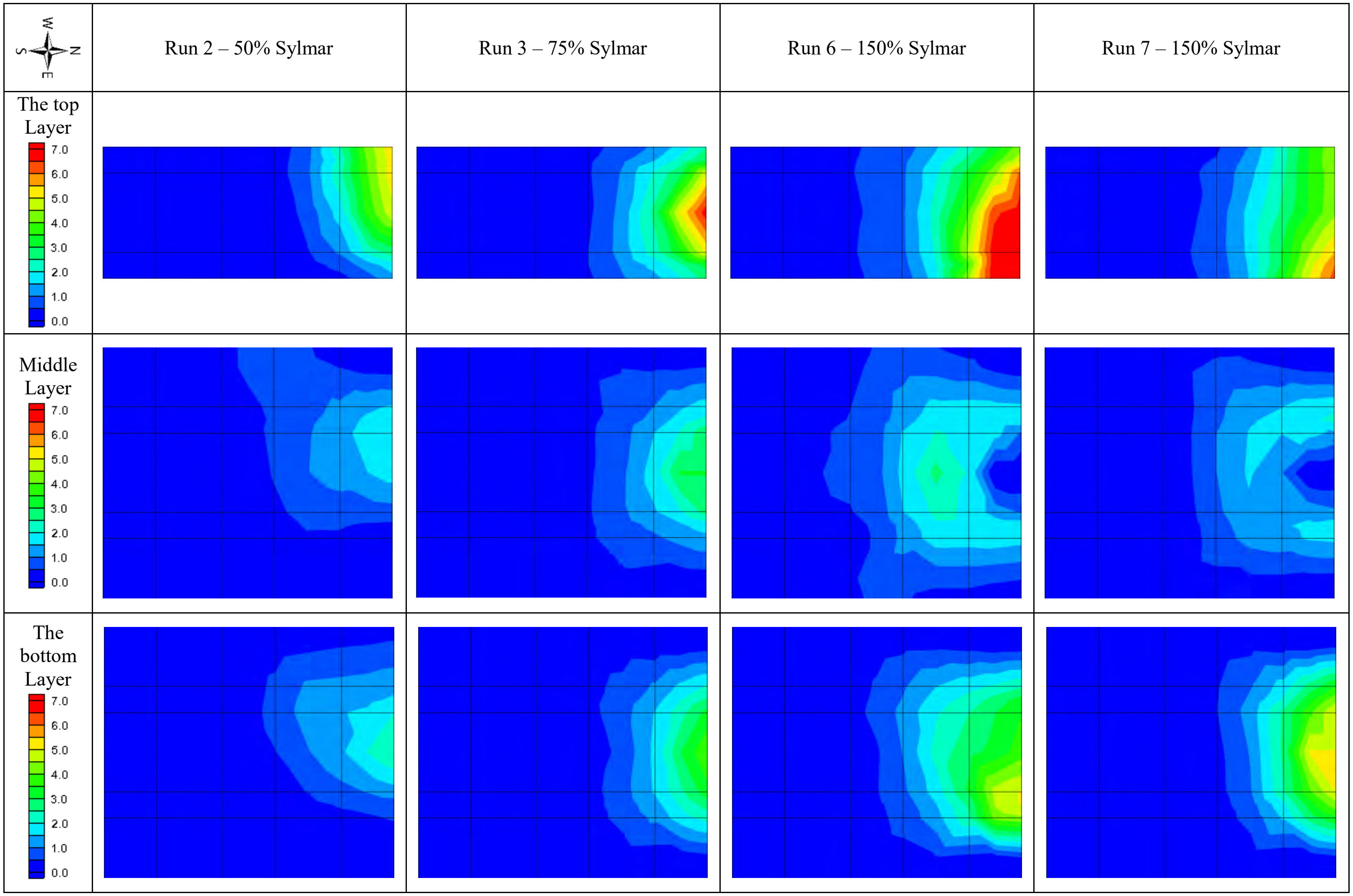

Figure 6-237 Contours of soil maximum upward accelerations for the 0° skew test in terms of g.

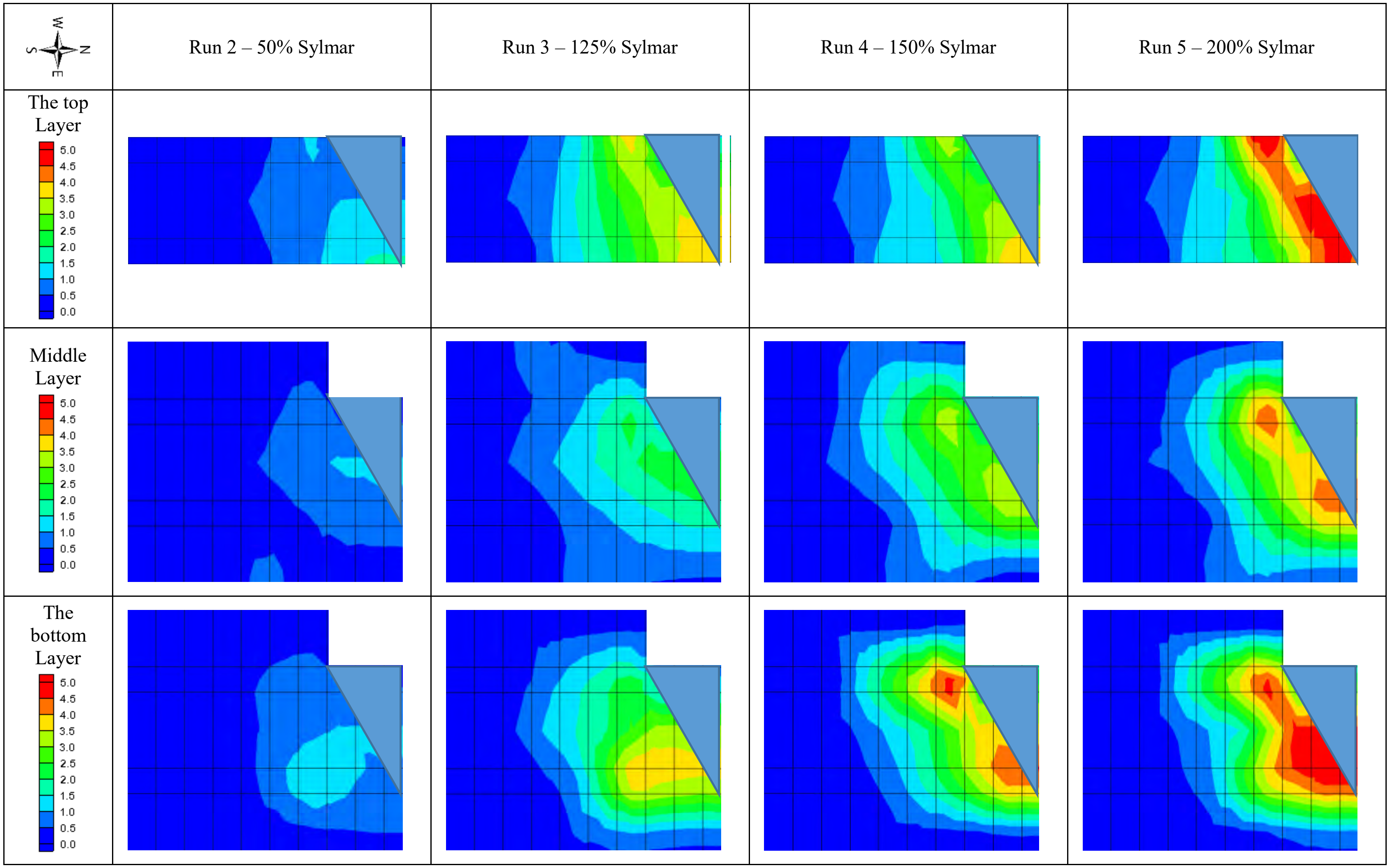

Figure 6-238 Contours of soil maximum upward accelerations for the 30° skew test in terms of g.

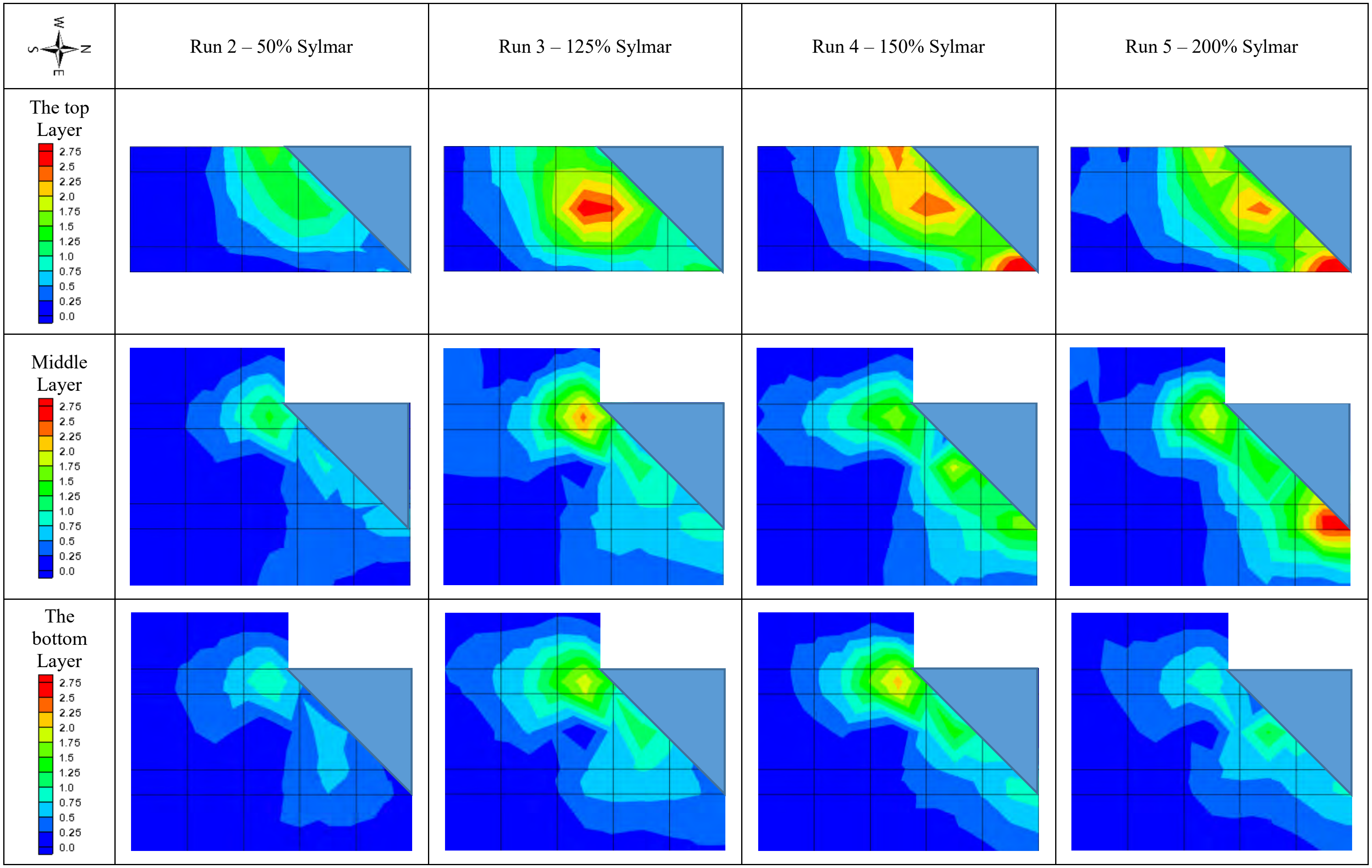

Figure 6-239 Contours of soil maximum upward accelerations for the 45° skew test in terms of g.

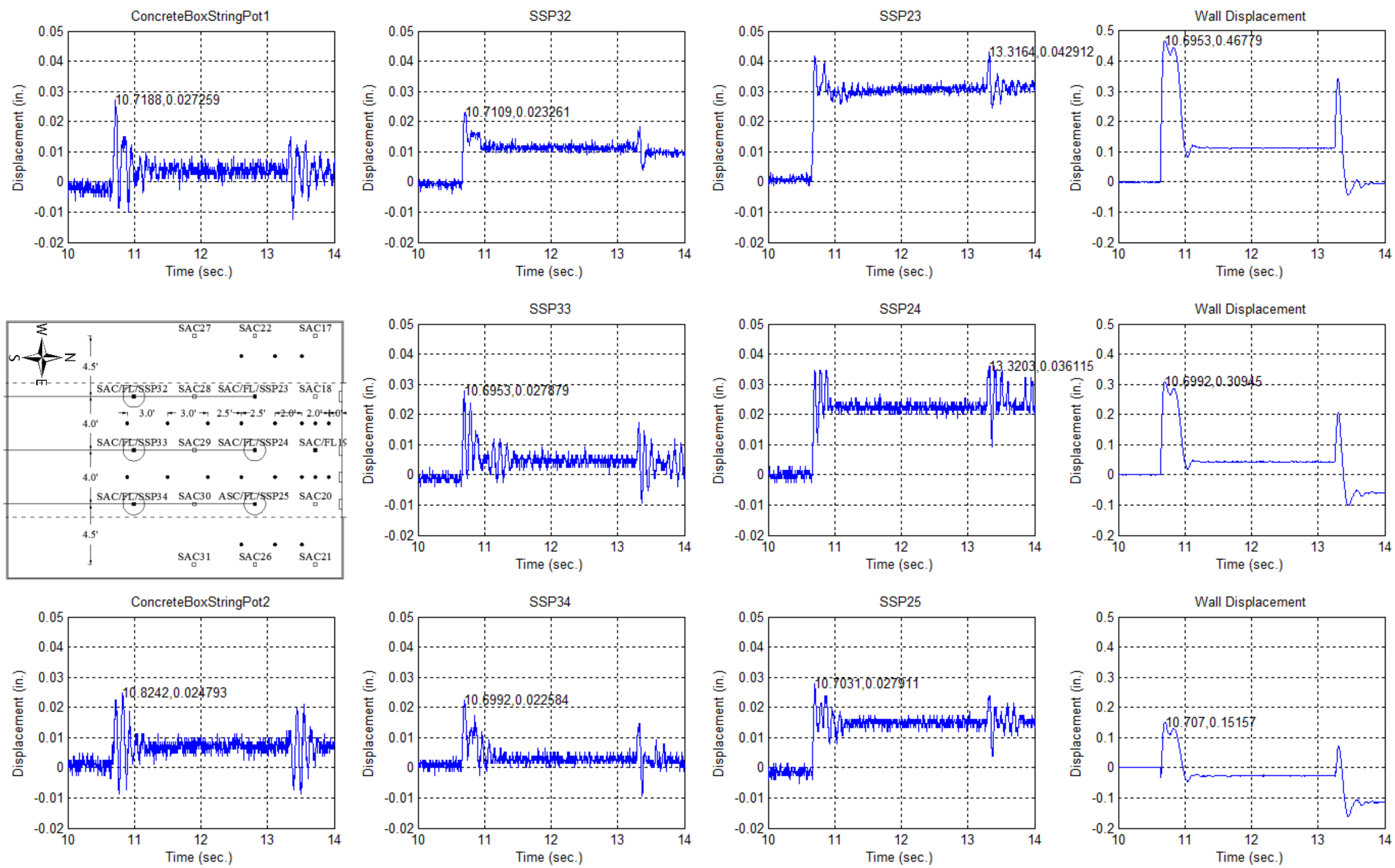

Figure 6-240 Longitudinal soil displacement at the middle layer of the soil for the 0° skew test in Run 2.

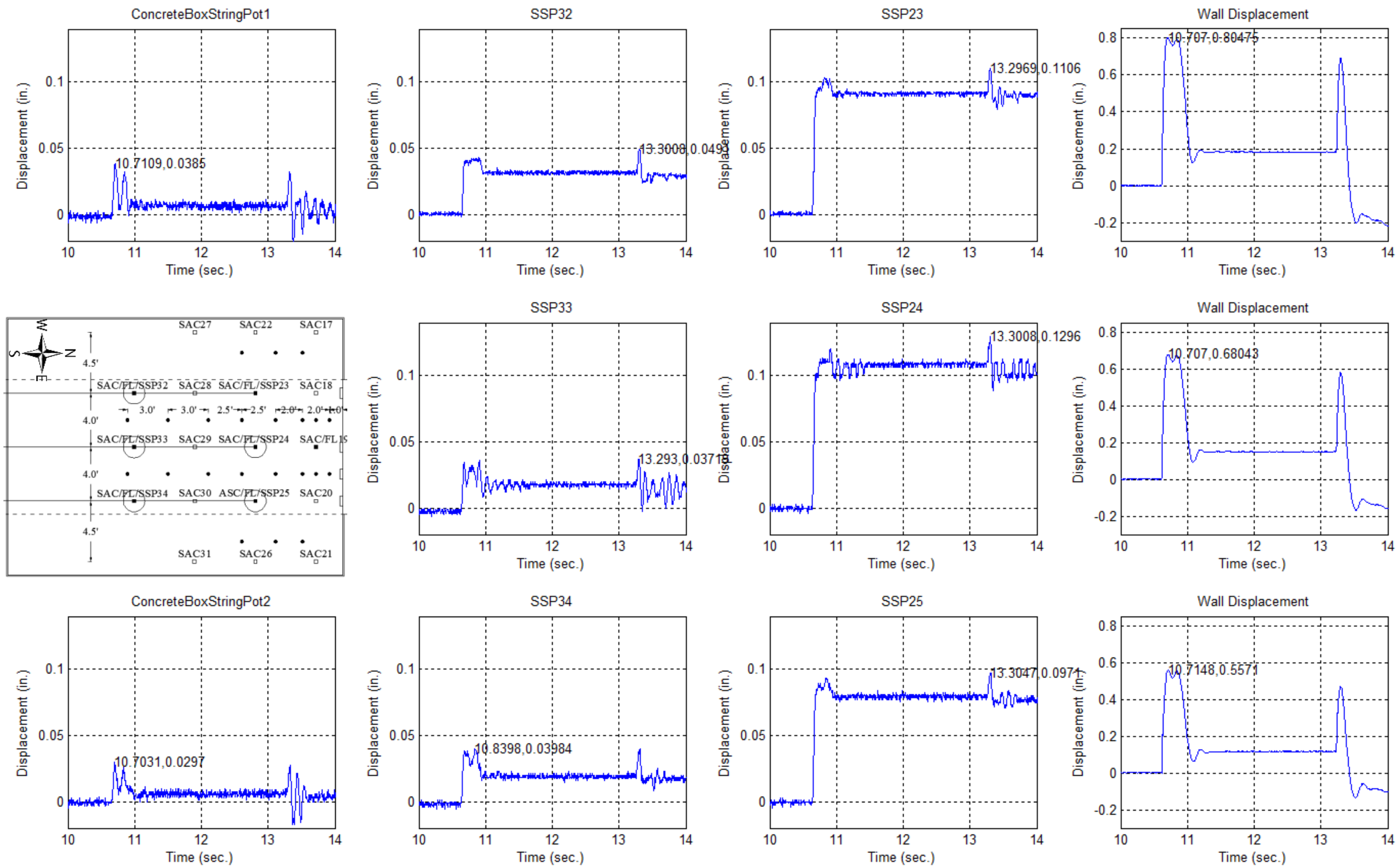

Figure 6-241 Longitudinal soil displacement at the middle layer of the soil for the 0° skew test in Run 3.

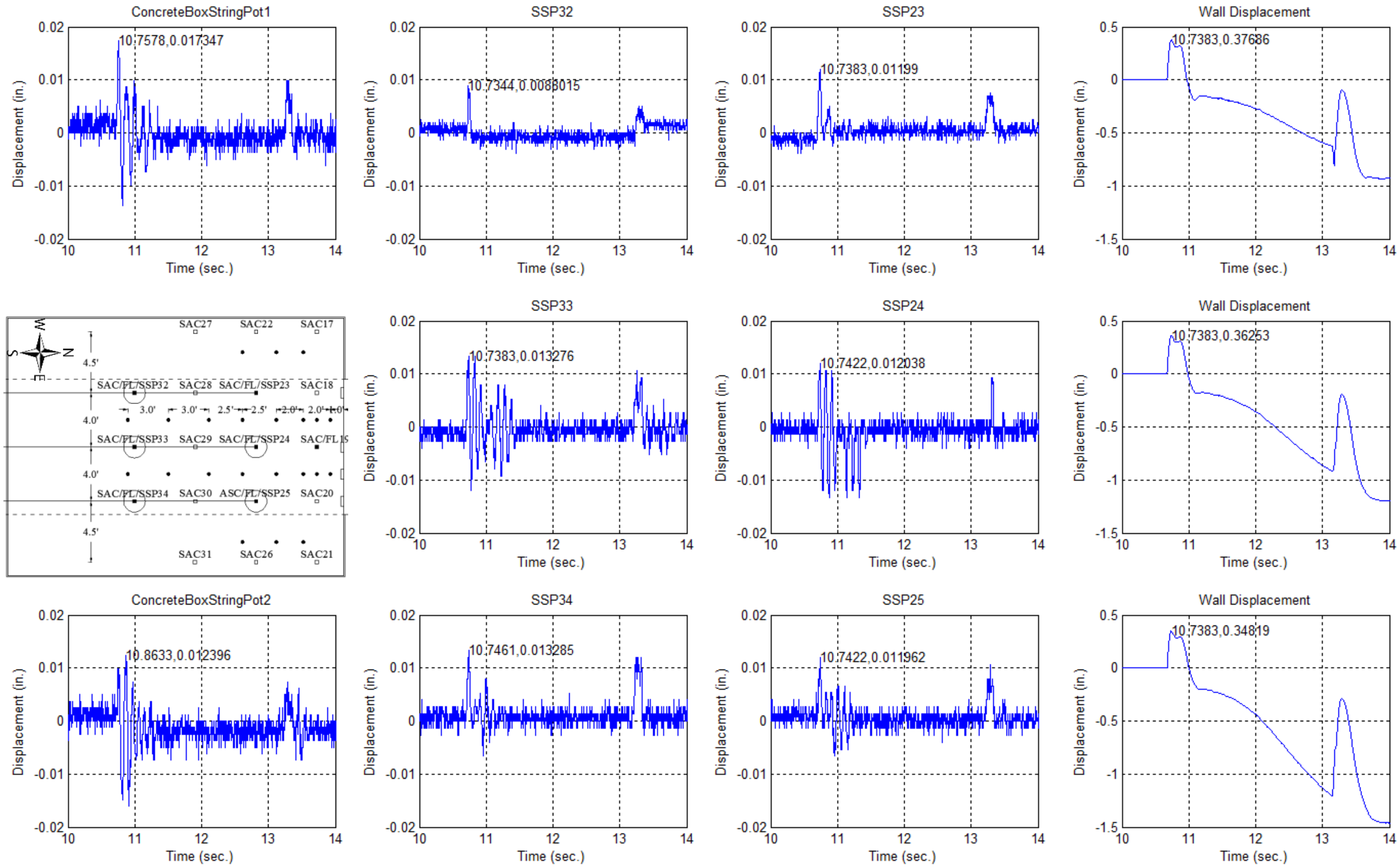

Figure 6-242 Longitudinal soil displacement at the middle layer of the soil for the 0° skew test in Run 4.

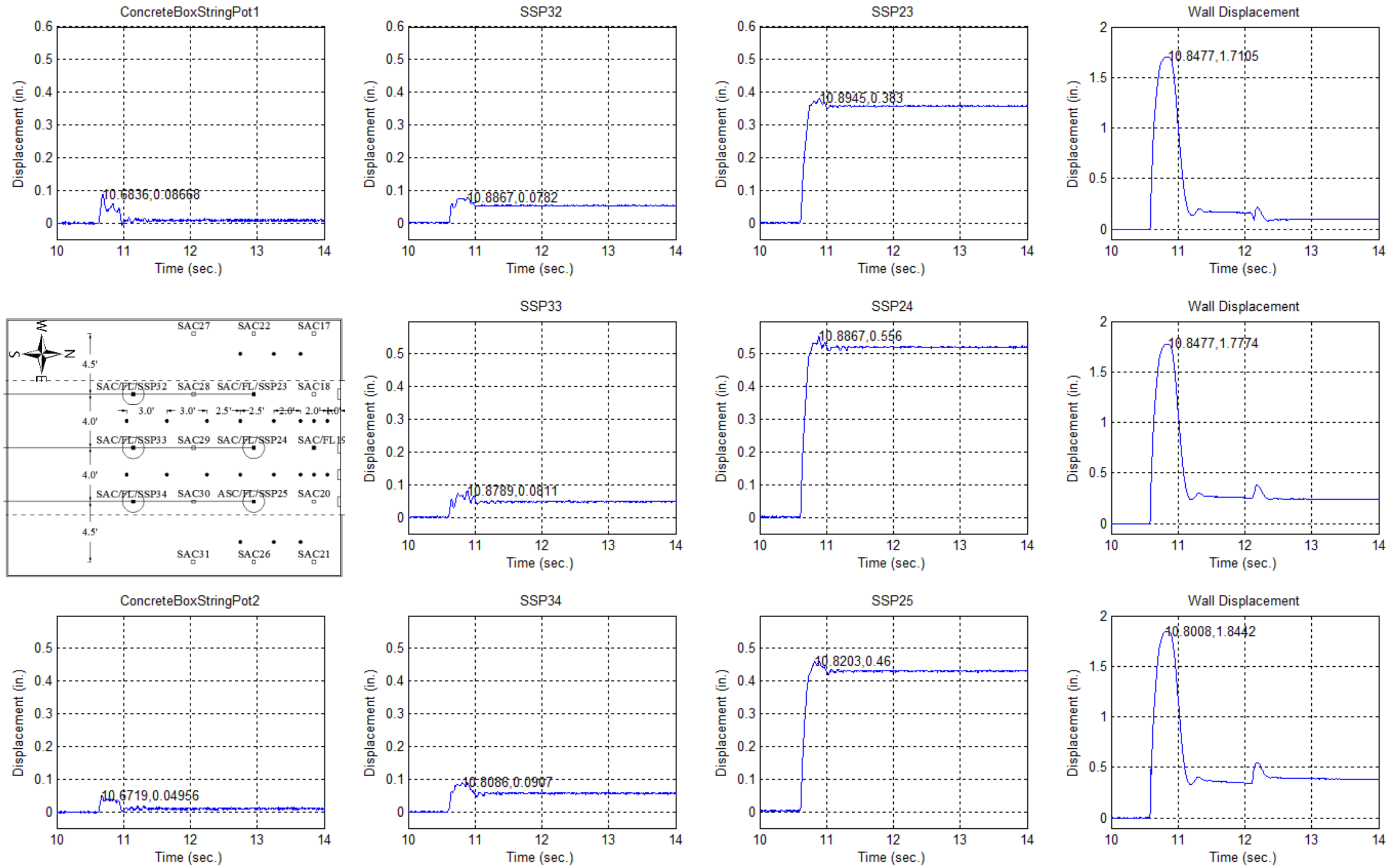

Figure 6-243 Longitudinal soil displacement at the middle layer of the soil for the 0° skew test in Run 6.

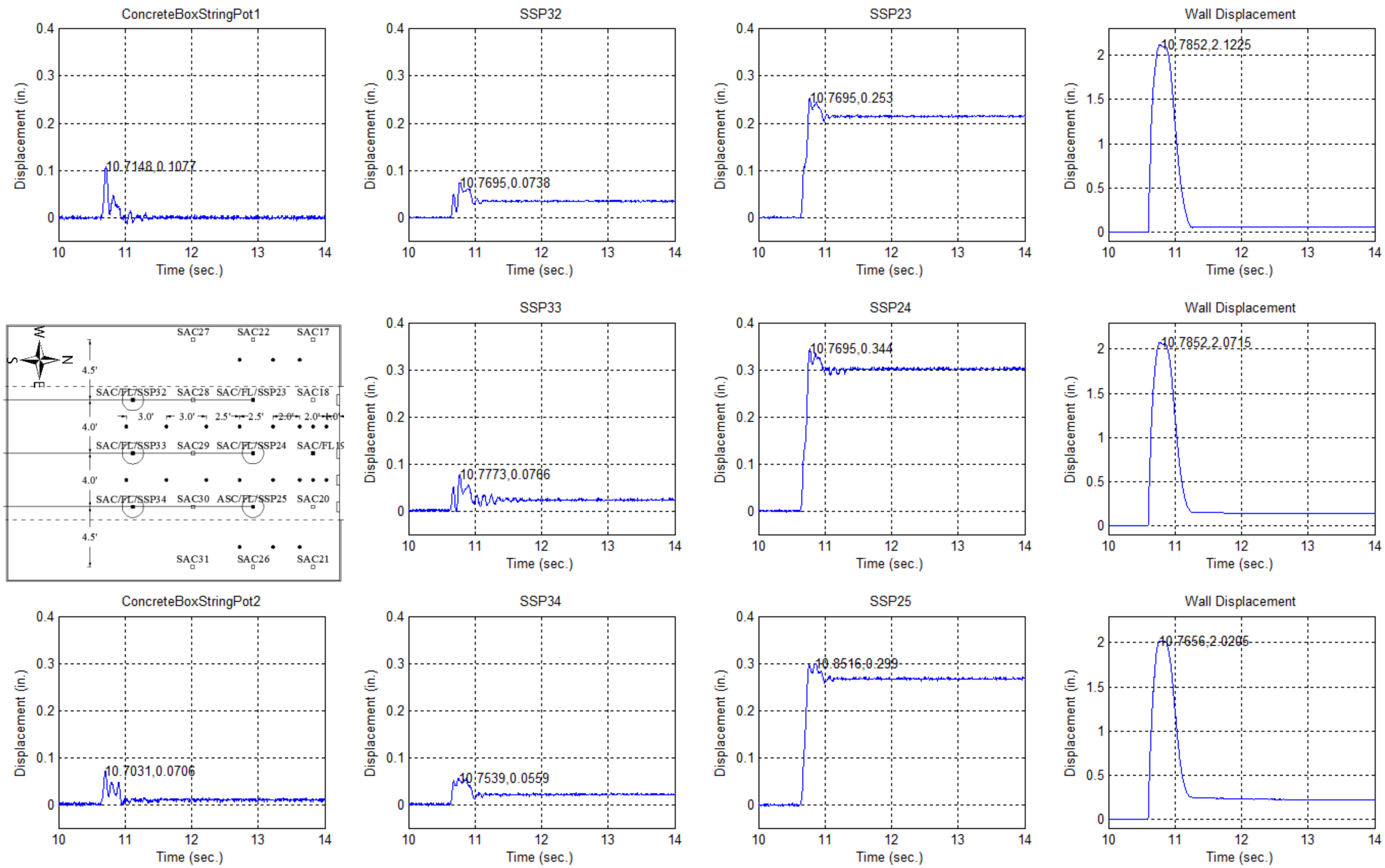

Figure 6-244 Longitudinal soil displacement at the middle layer of the soil for the 0° skew test in Run 7.

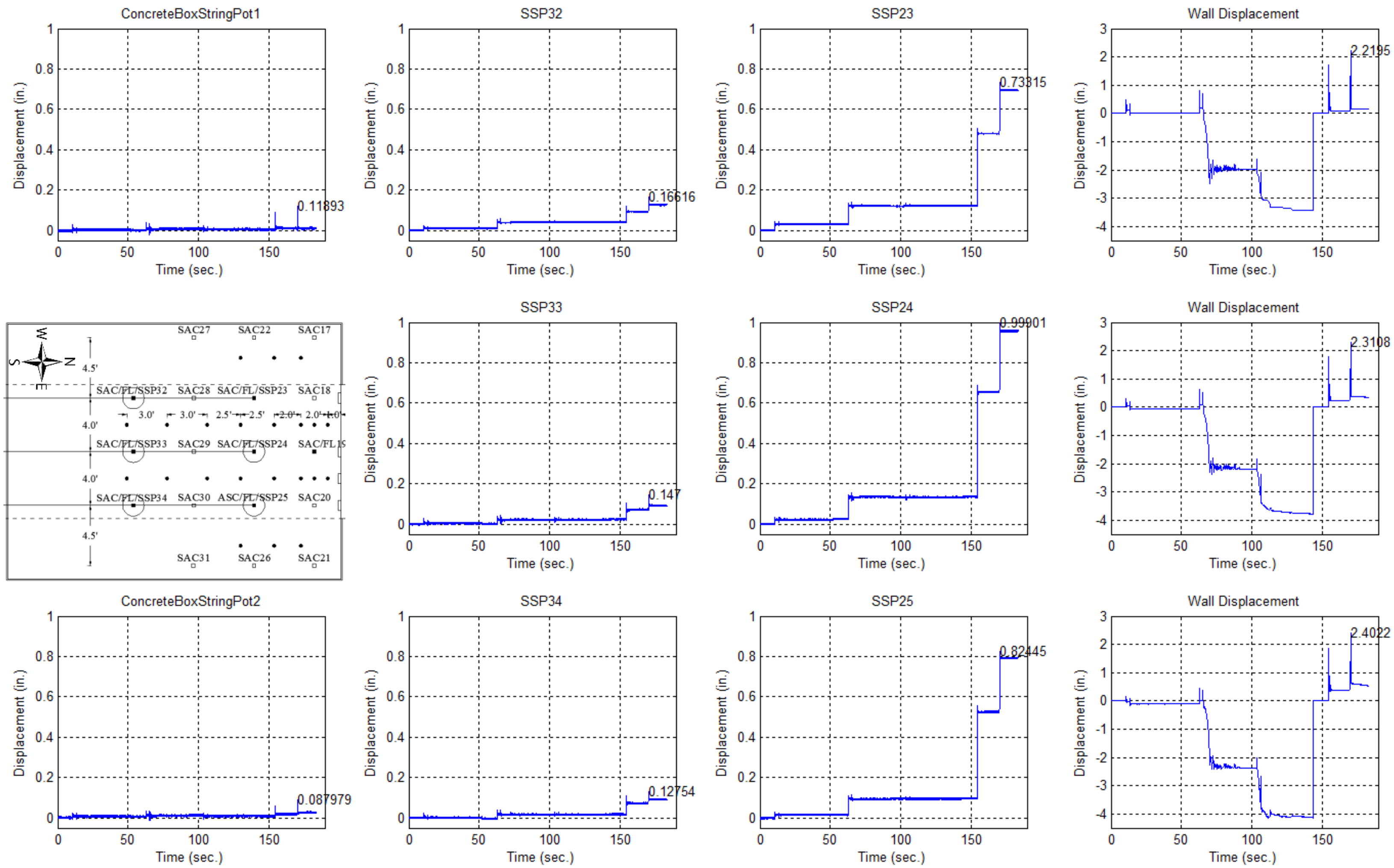

Figure 6-245 Combined longitudinal soil displacement at the middle layer of the soil for the 0° skew test.

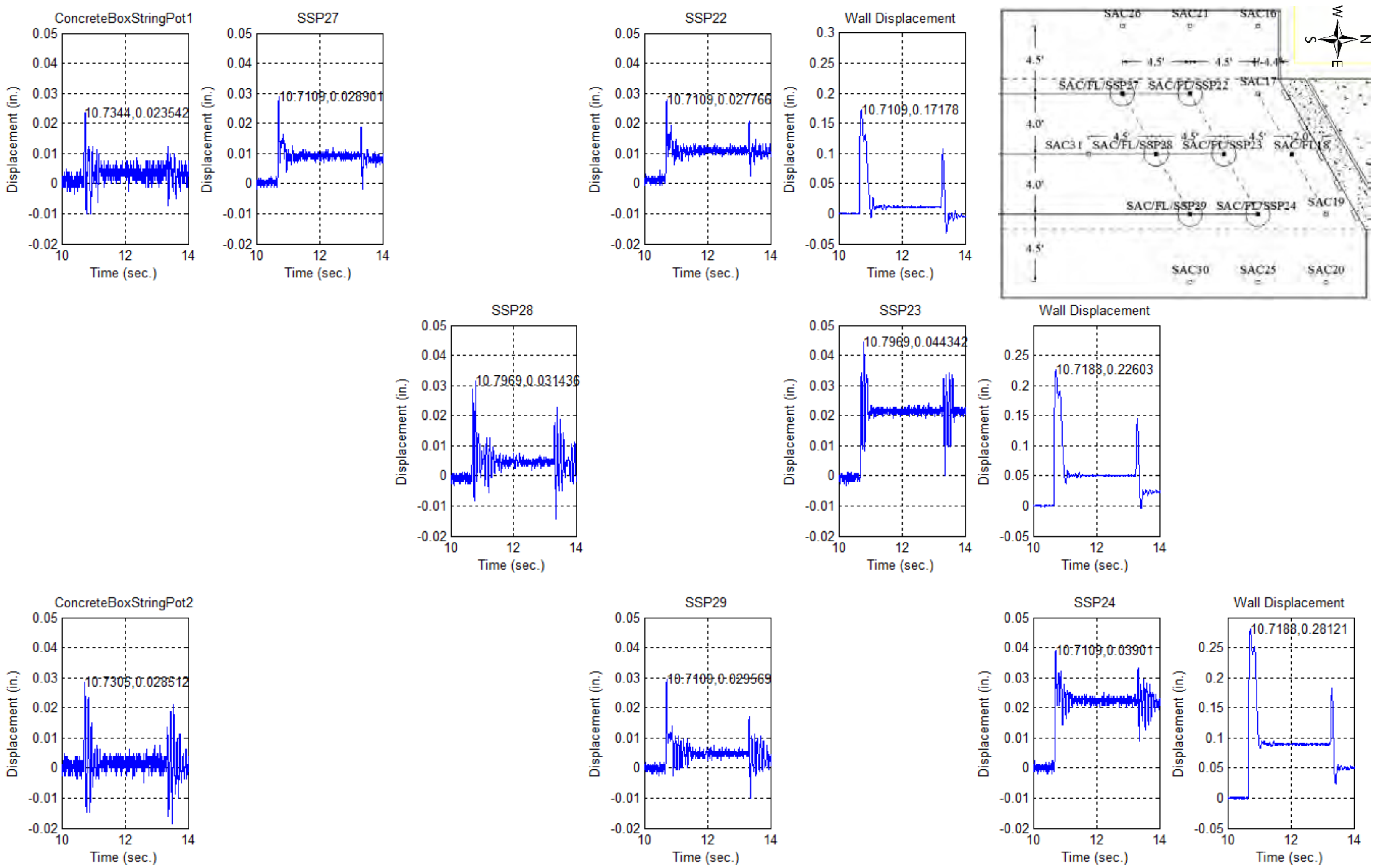

Figure 6-246 Longitudinal soil displacement at the middle layer of the soil for the 30° skew test in Run 2.

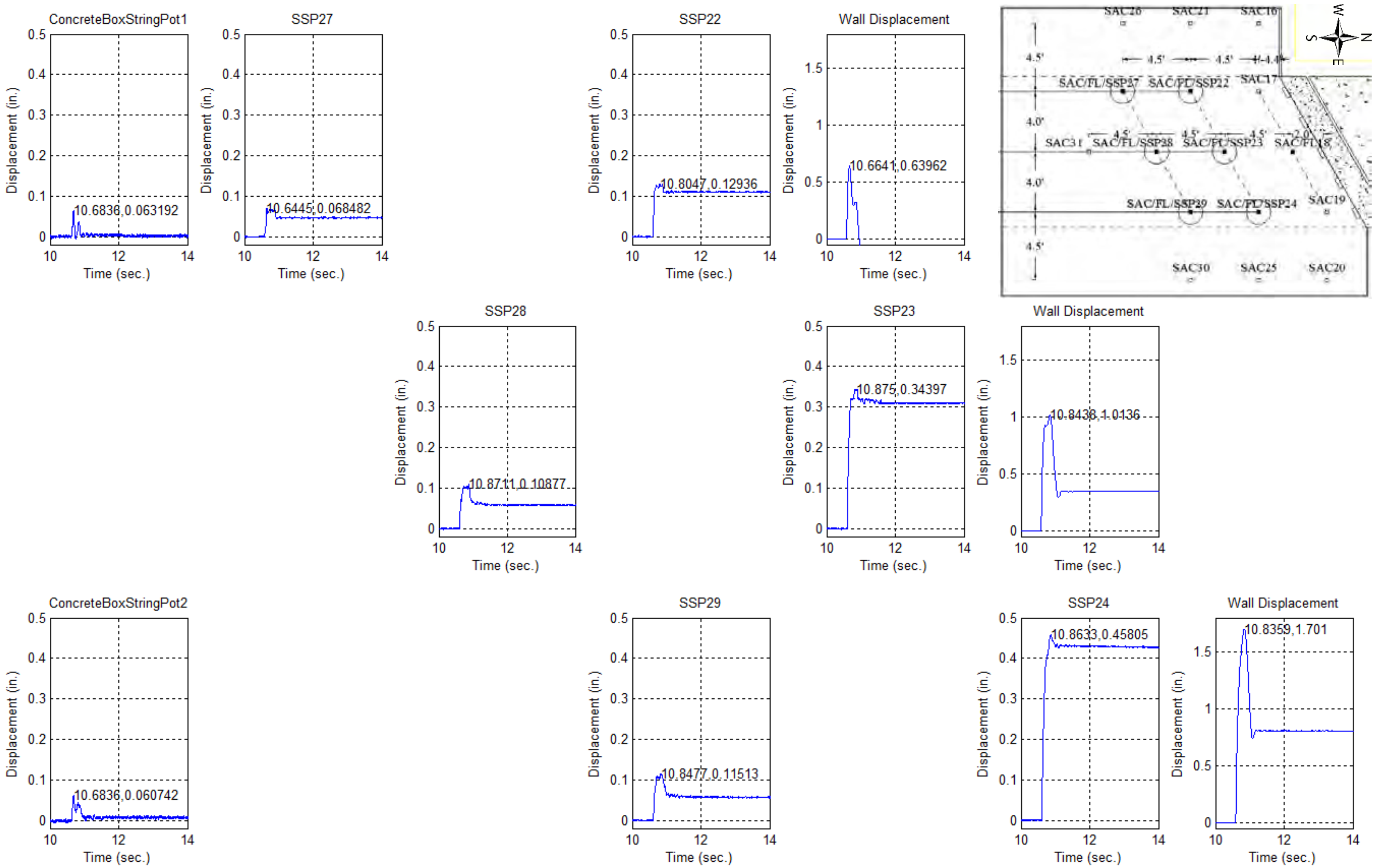

Figure 6-247 Longitudinal soil displacement at the middle layer of the soil for the 30° skew test in Run 3.

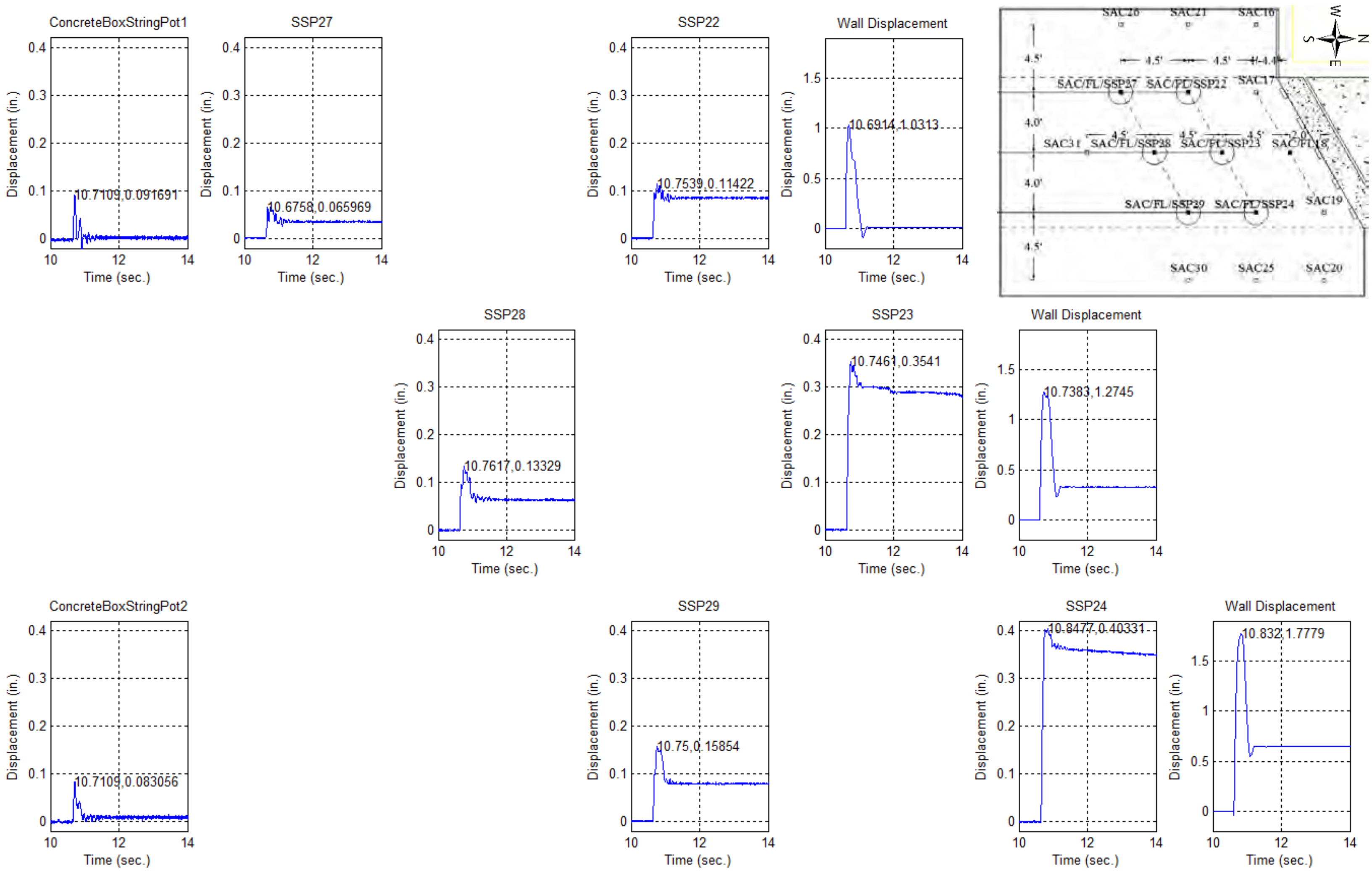

Figure 6-248 Longitudinal soil displacement at the middle layer of the soil for the 30° skew test in Run 4.

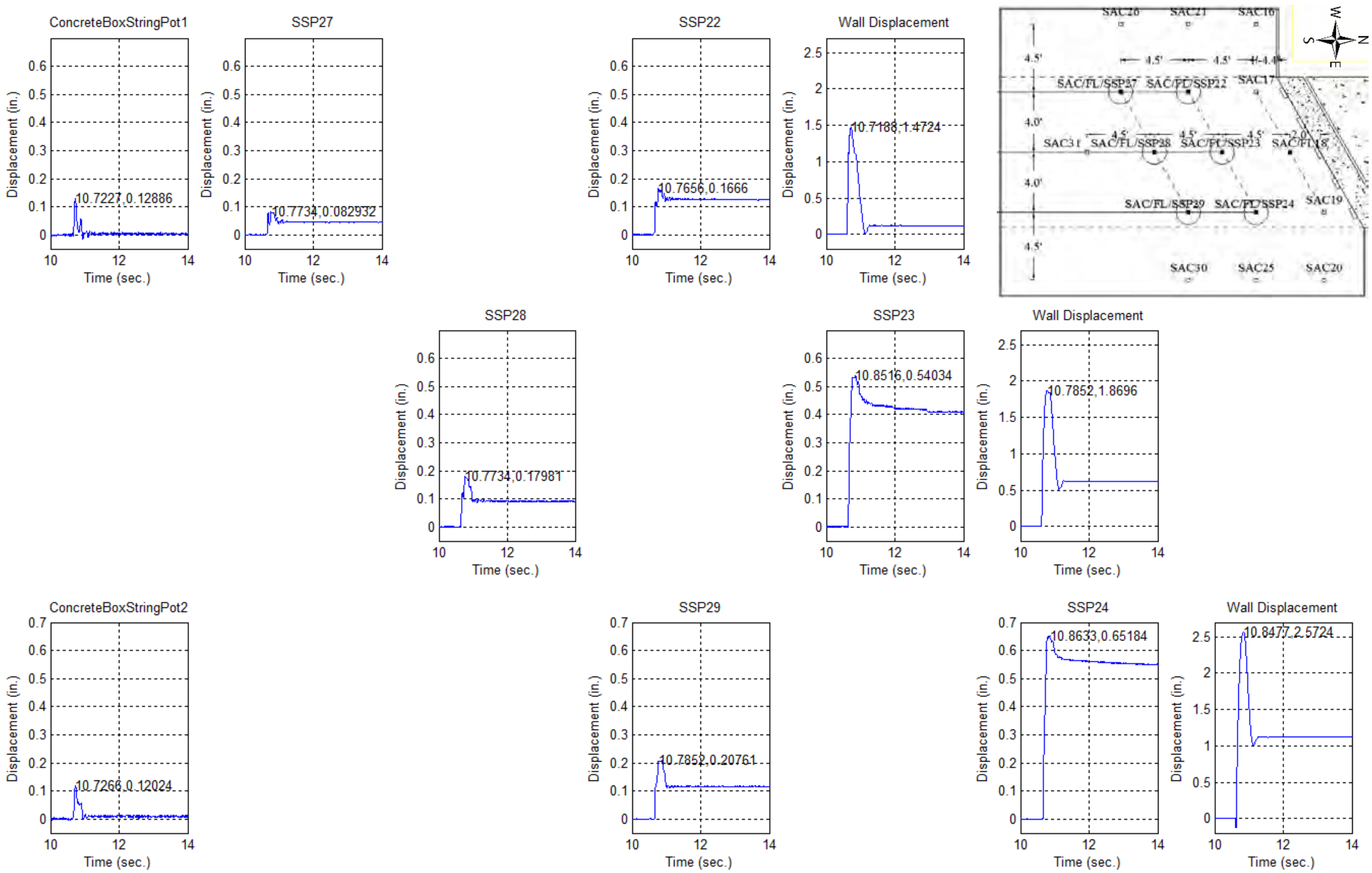

Figure 6-249 Longitudinal soil displacement at the middle layer of the soil for the 30° skew test in Run 5.

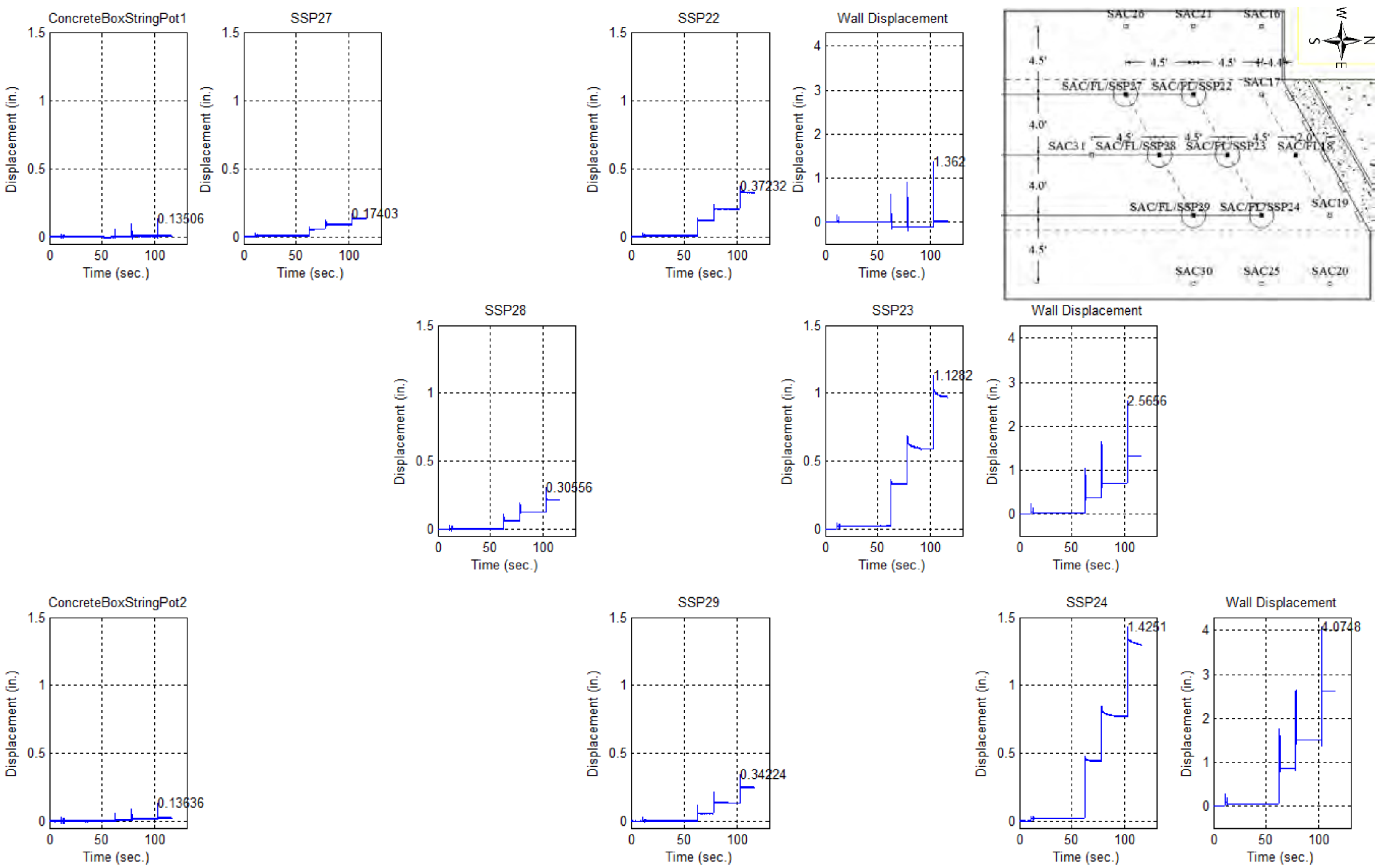

Figure 6-250 Combined longitudinal soil displacement at the middle layer of the soil for the 30° skew test.

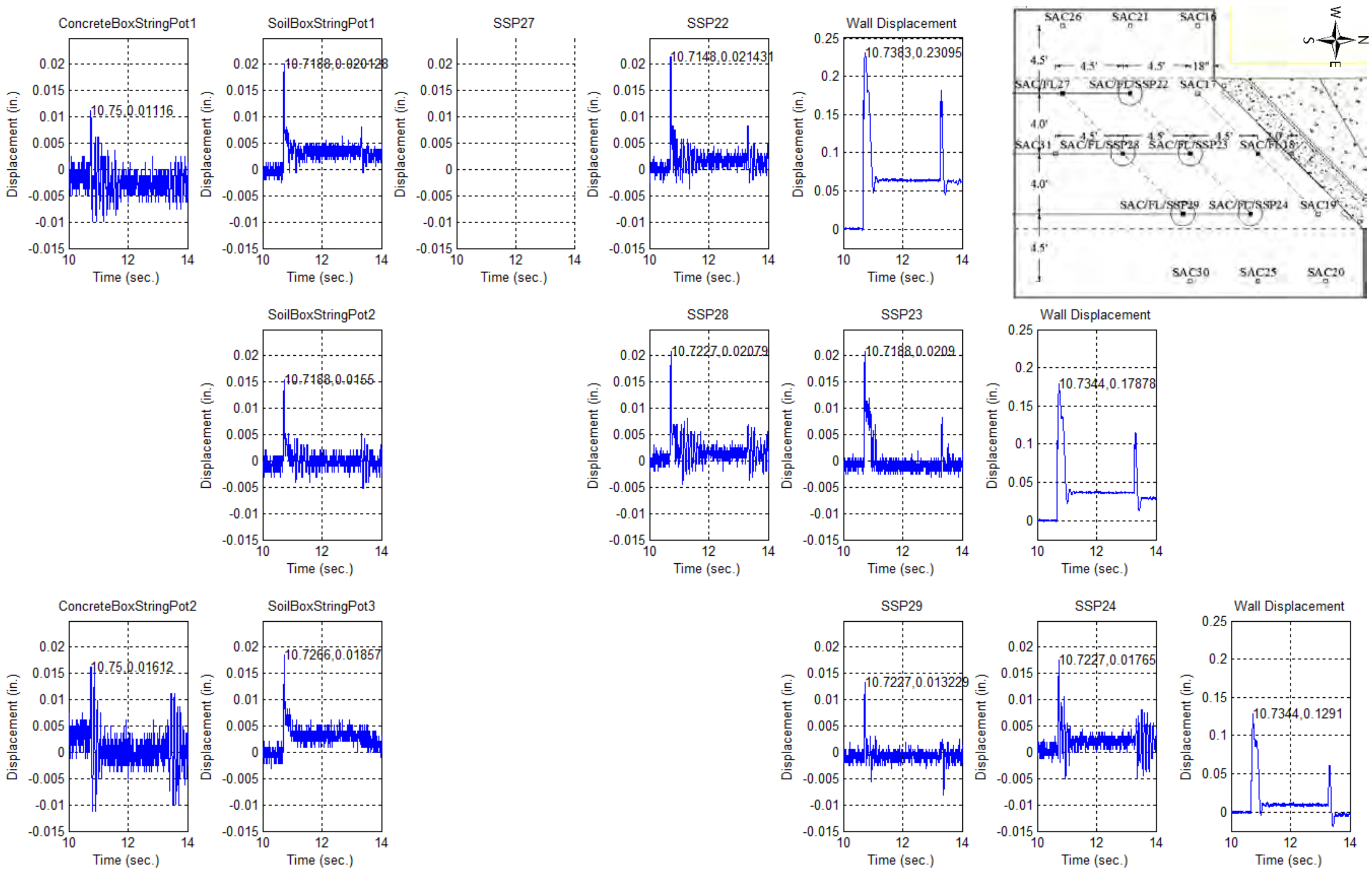

Figure 6-251 Longitudinal soil displacement at the middle layer of the soil for the 45° skew test in Run 2.

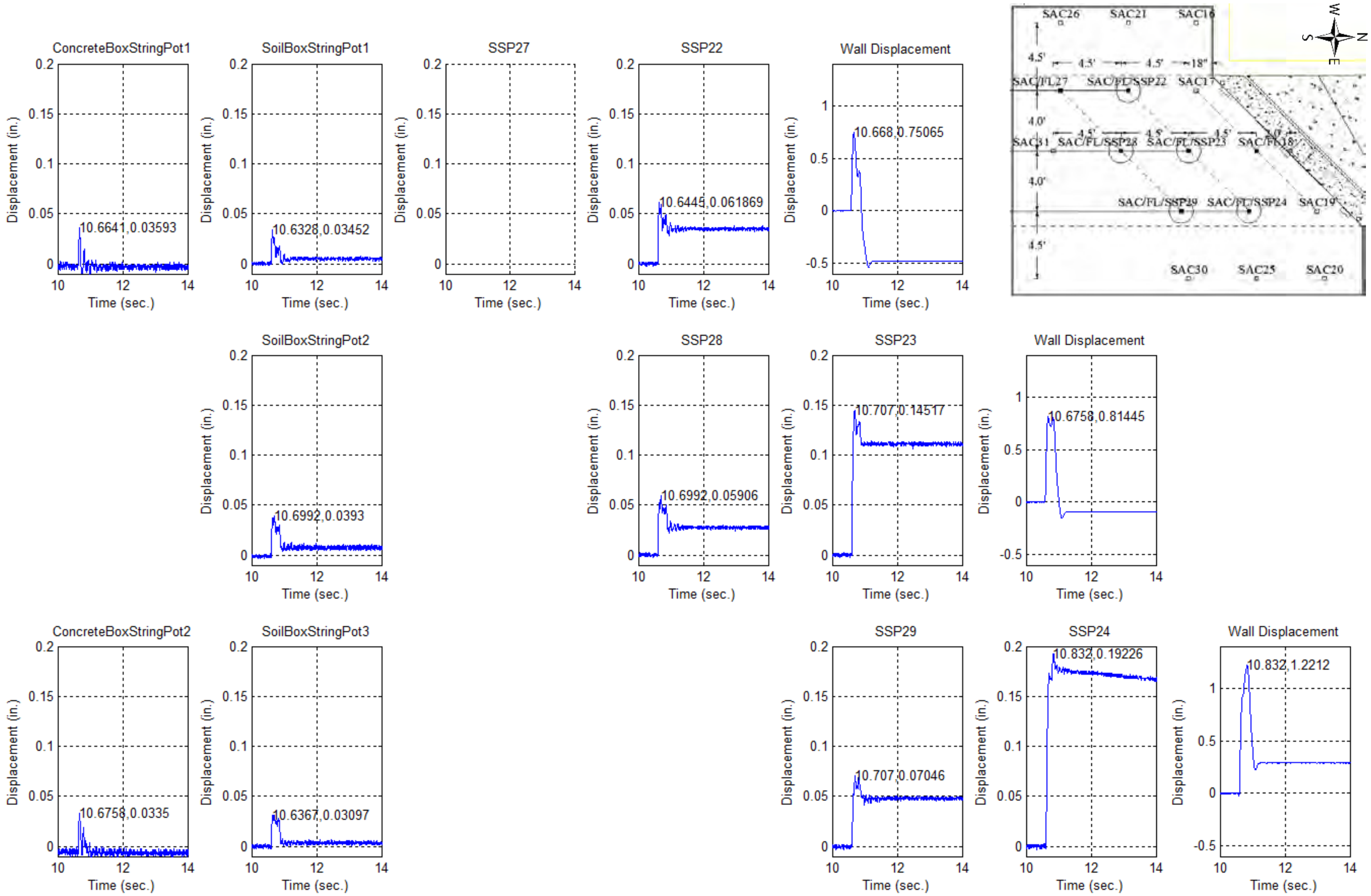

Figure 6-252 Longitudinal soil displacement at the middle layer of the soil for the 45° skew test in Run 3.

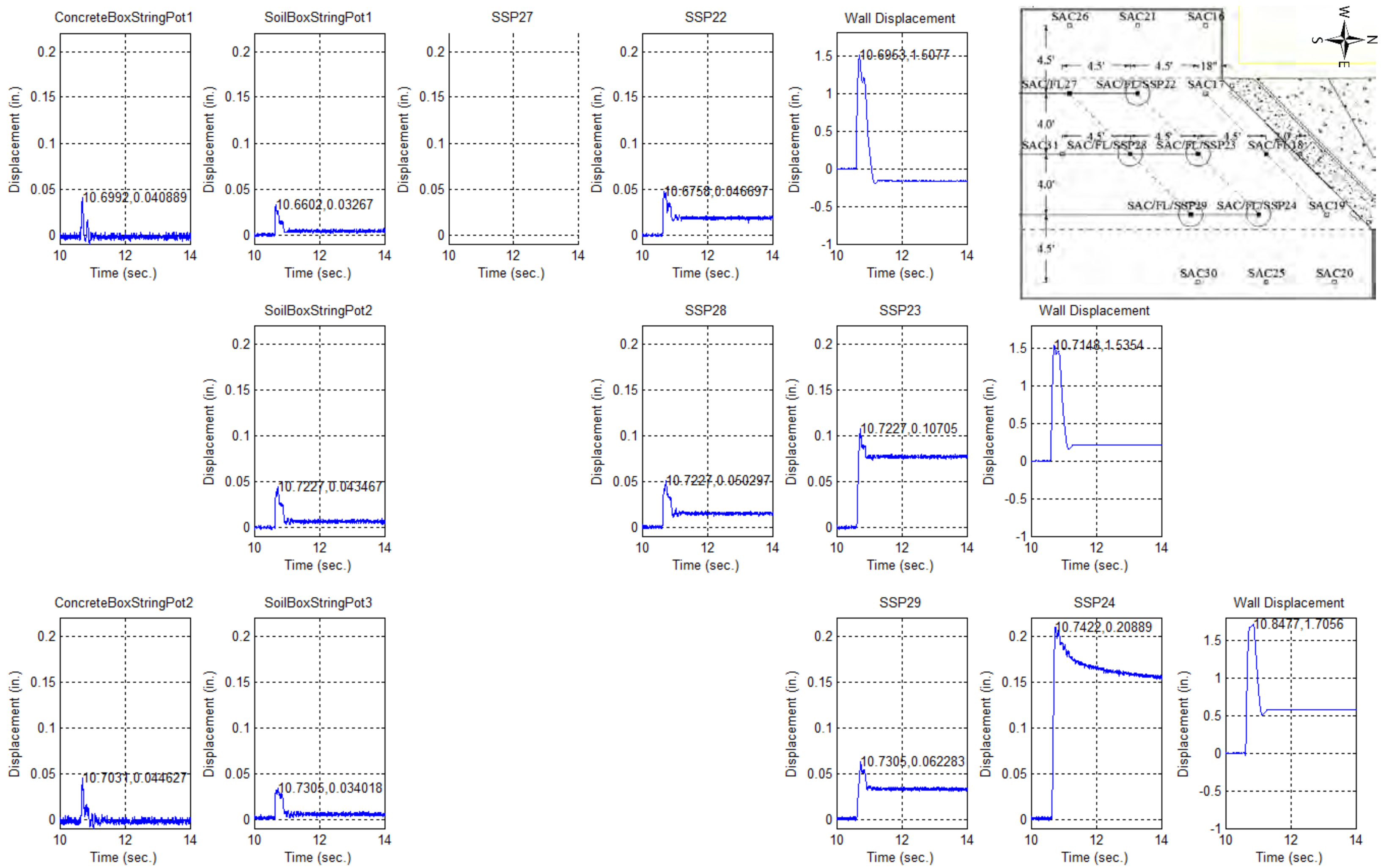

Figure 6-253 Longitudinal soil displacement at the middle layer of the soil for the 45° skew test in Run 4.

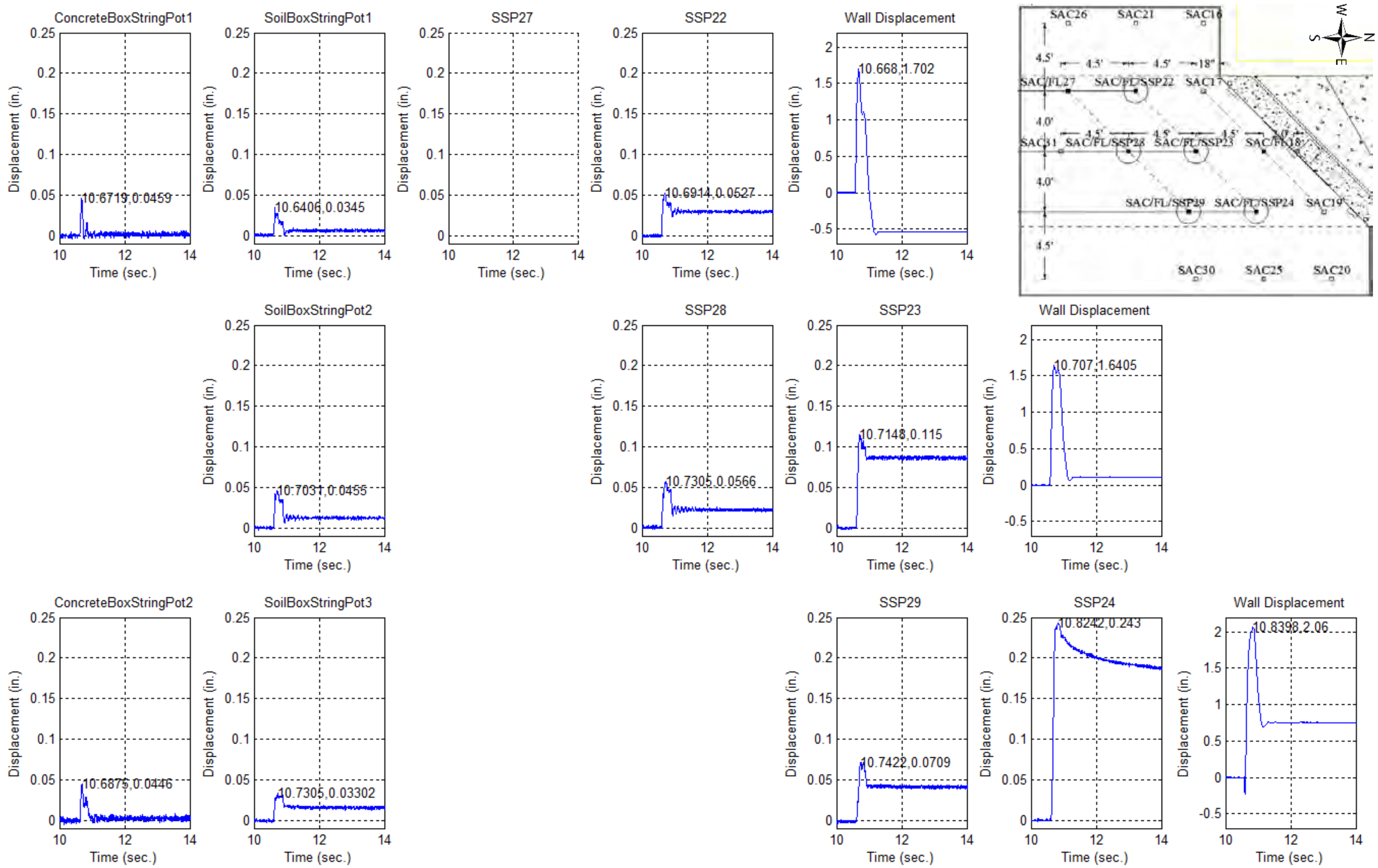

Figure 6-254 Longitudinal soil displacement at the middle layer of the soil for the 45° skew in Run 5.

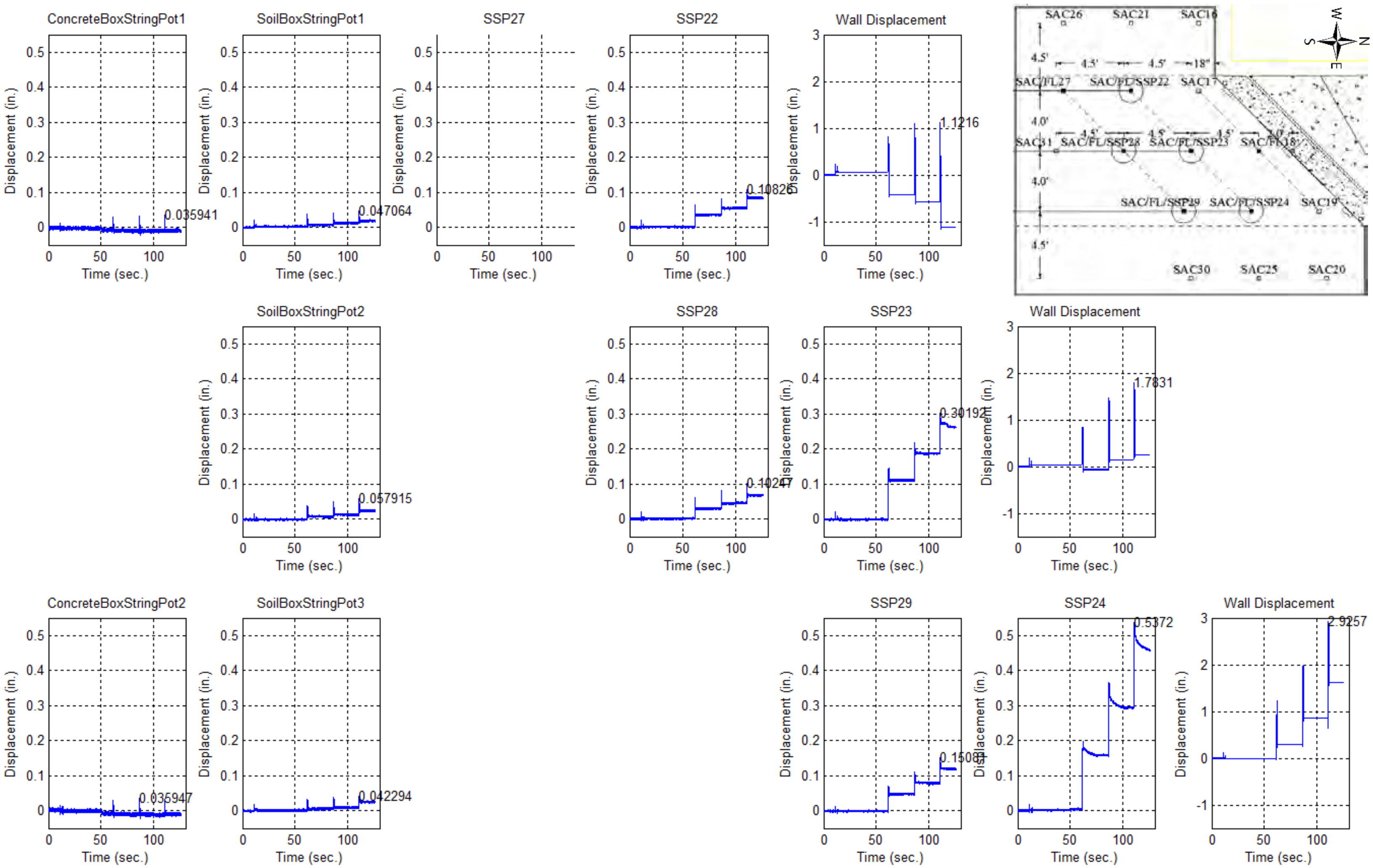

Figure 6-255 Combined longitudinal soil displacement at the middle layer of the soil for the 45° skew test.

Marked Columns: West side of the backwall	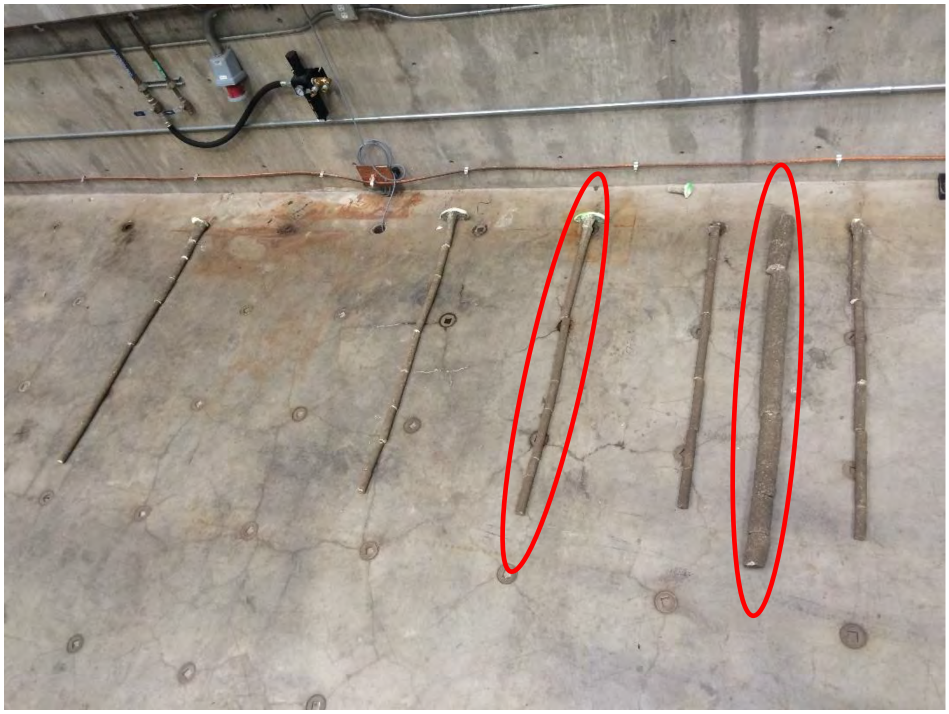
Marked Columns: East side of the backwall	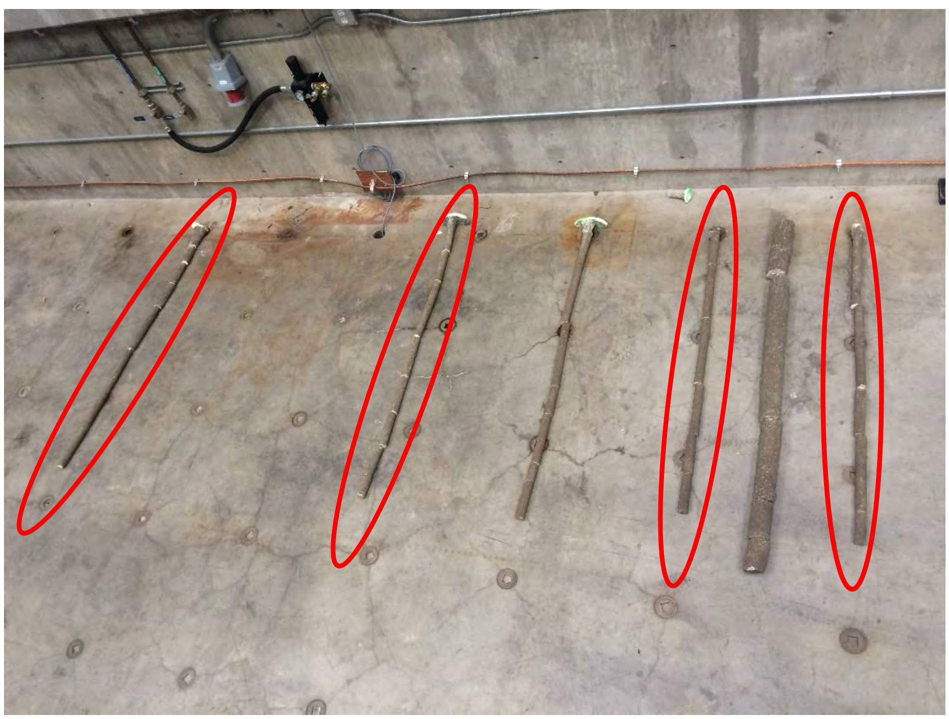

Figure 6-256 Gypsum columns excavated from the backfill soil for the 0° skew test.

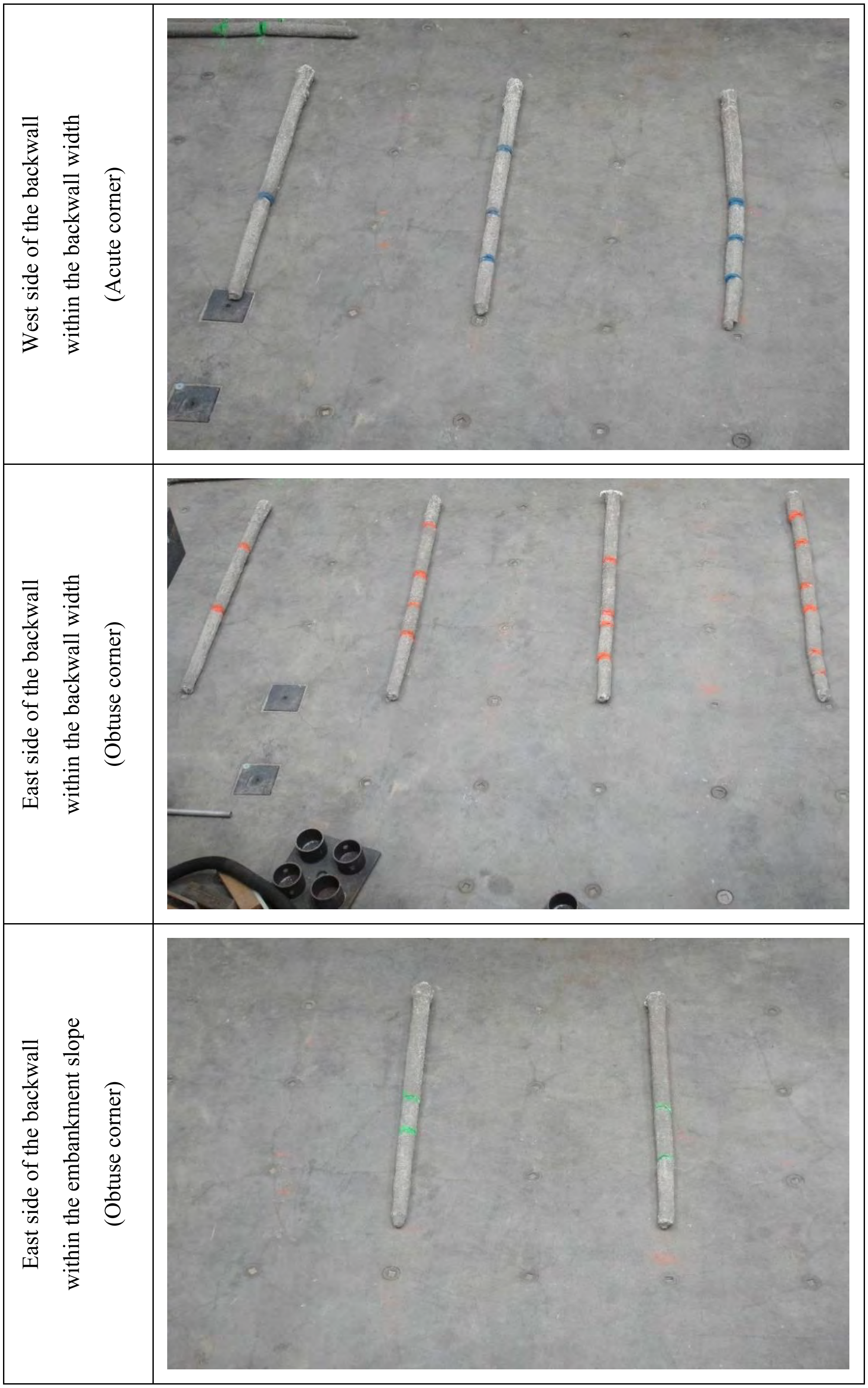

Figure 6-257 Gypsum columns excavated from the backfill soil for the 30° skew test.

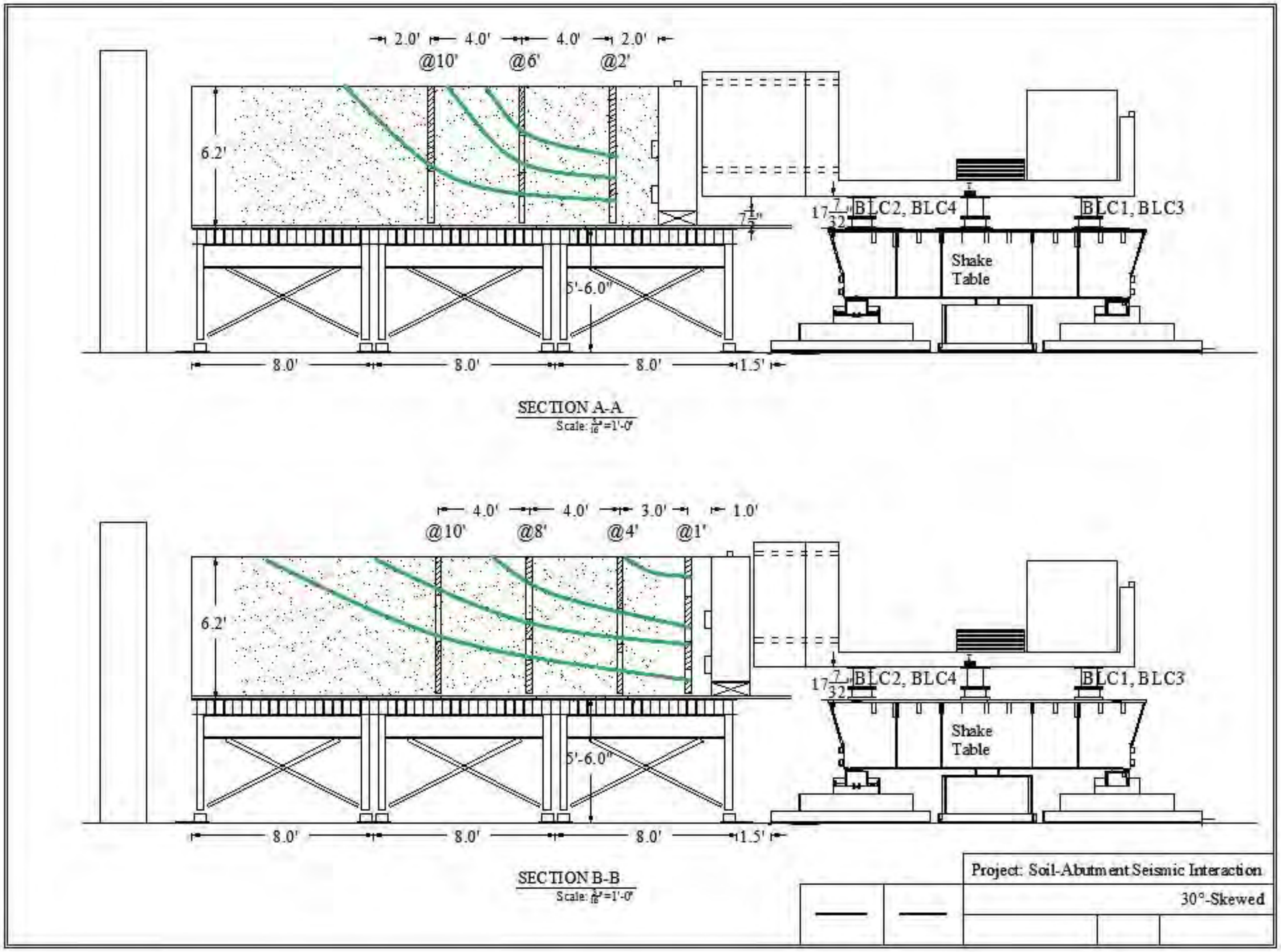

Figure 6-258 Asymptotic failure planes from the excavated gypsum columns for the 30° skew test.

Figure 6-259 Colored sand columns excavated from the acute corner for the 30° skew test.

Figure 6-260 Colored sand columns excavated from the obtuse corner for the 30° skew test.

West side of the backwall within the backwall width (Acute corner)	
East side of the backwall within the backwall width (Obtuse corner)	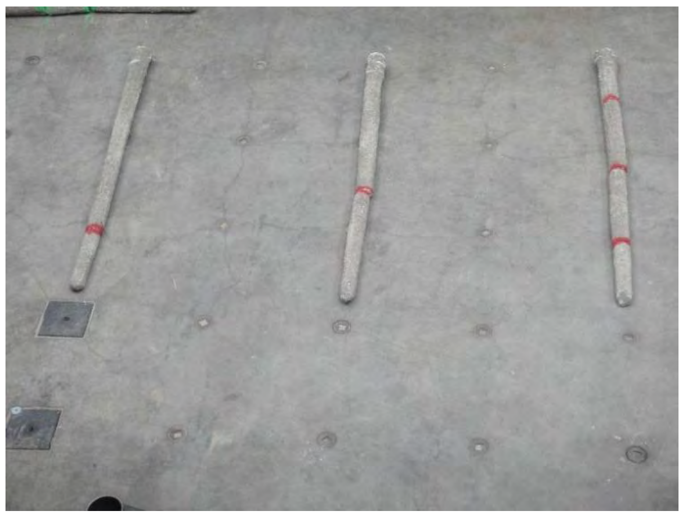
East side of the backwall within the embankment slope (Obtuse corner)	

Figure 6-261 Gypsum columns excavated from the backfill soil for the 45° skew test.

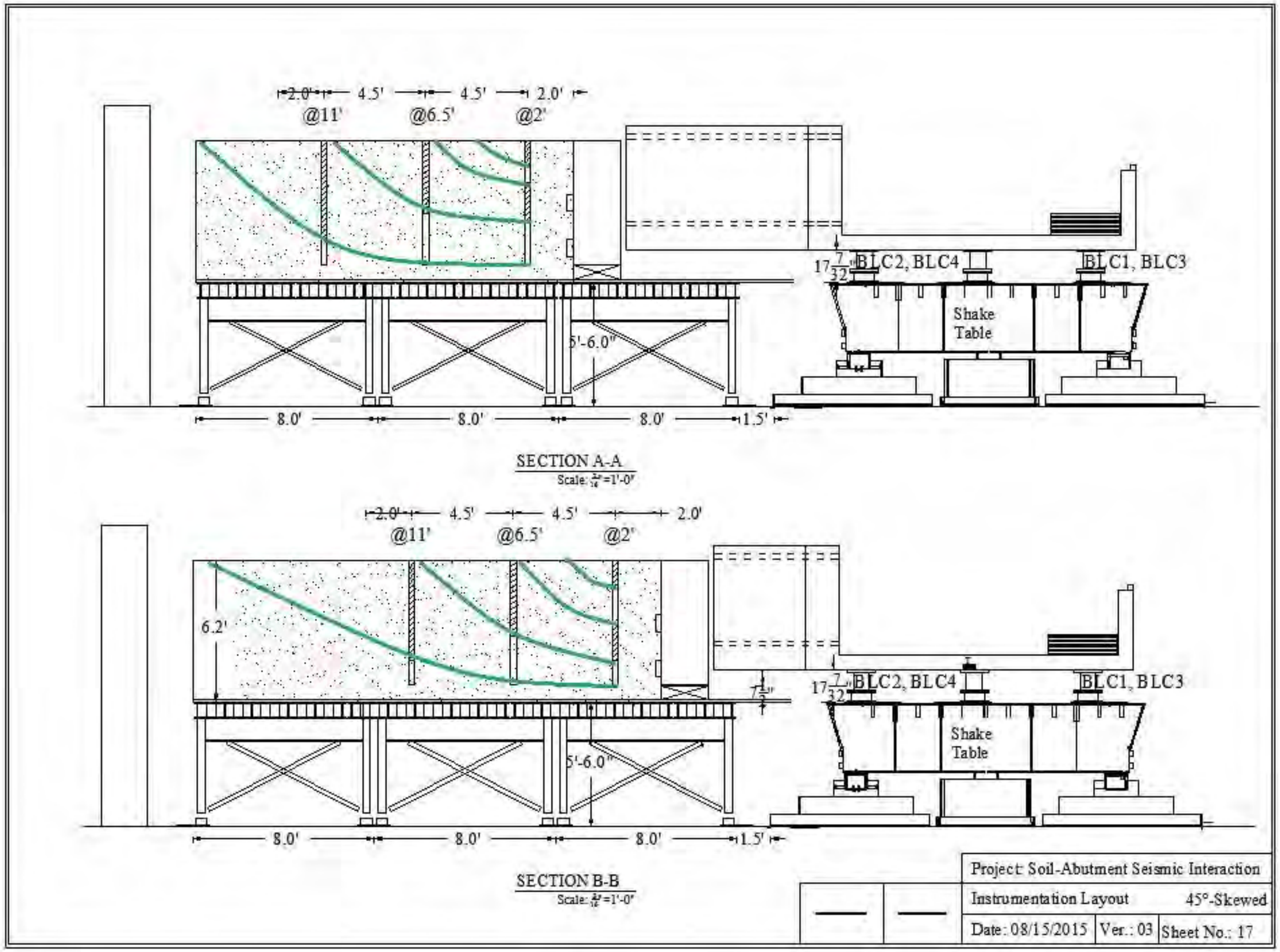

Figure 6-262 Asymptotic failure planes from the excavated gypsum columns for the 45° skew test.

Figure 6-263 Colored sand columns excavated from the acute corner for the 45° skew test.

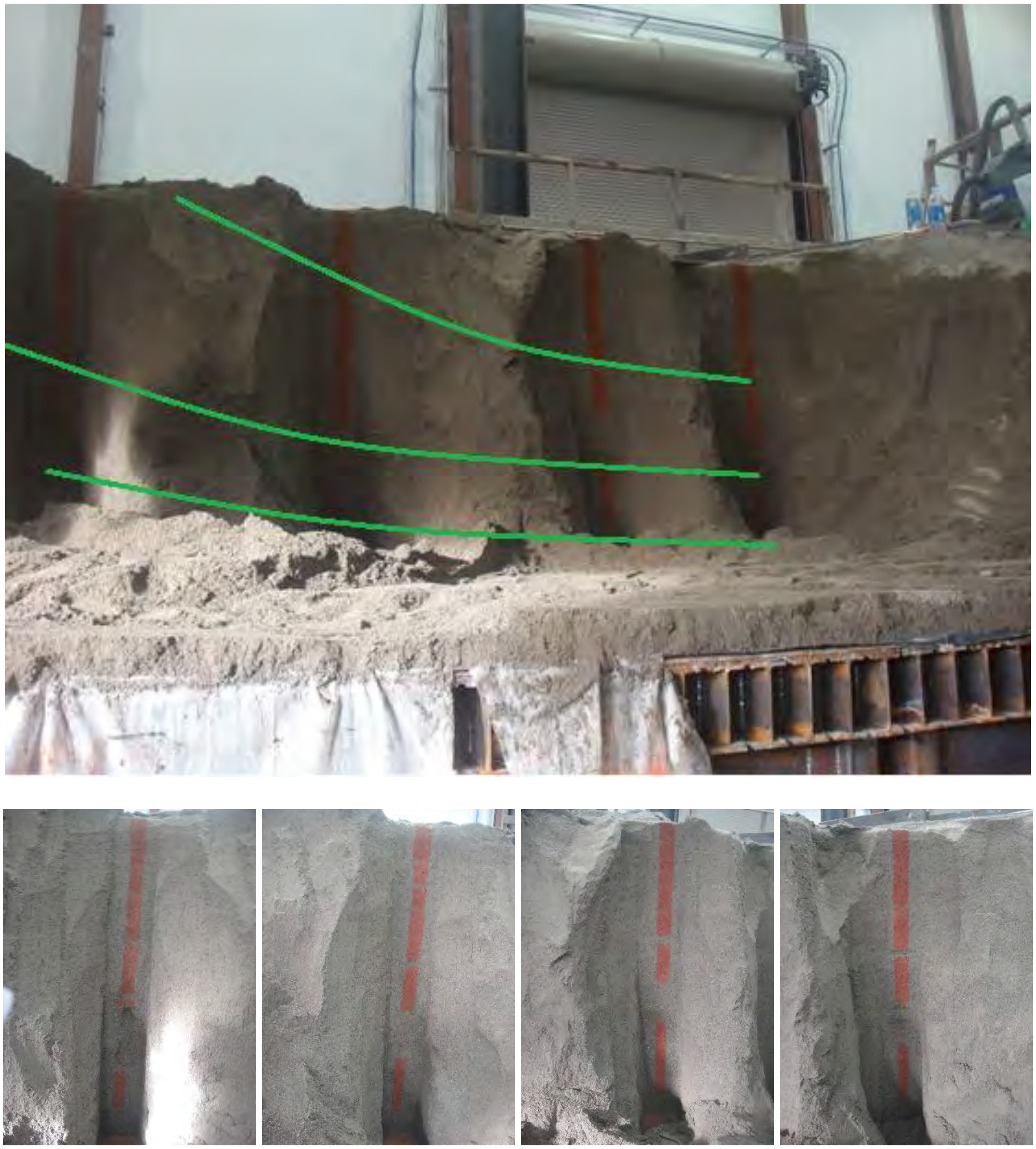

Figure 6-264 Colored sand columns excavated from the obtuse corner for the 45° skew test.

Figure 6-265 Colored sand columns excavated from the embankment slope at the obtuse corner for the 45° skew test.

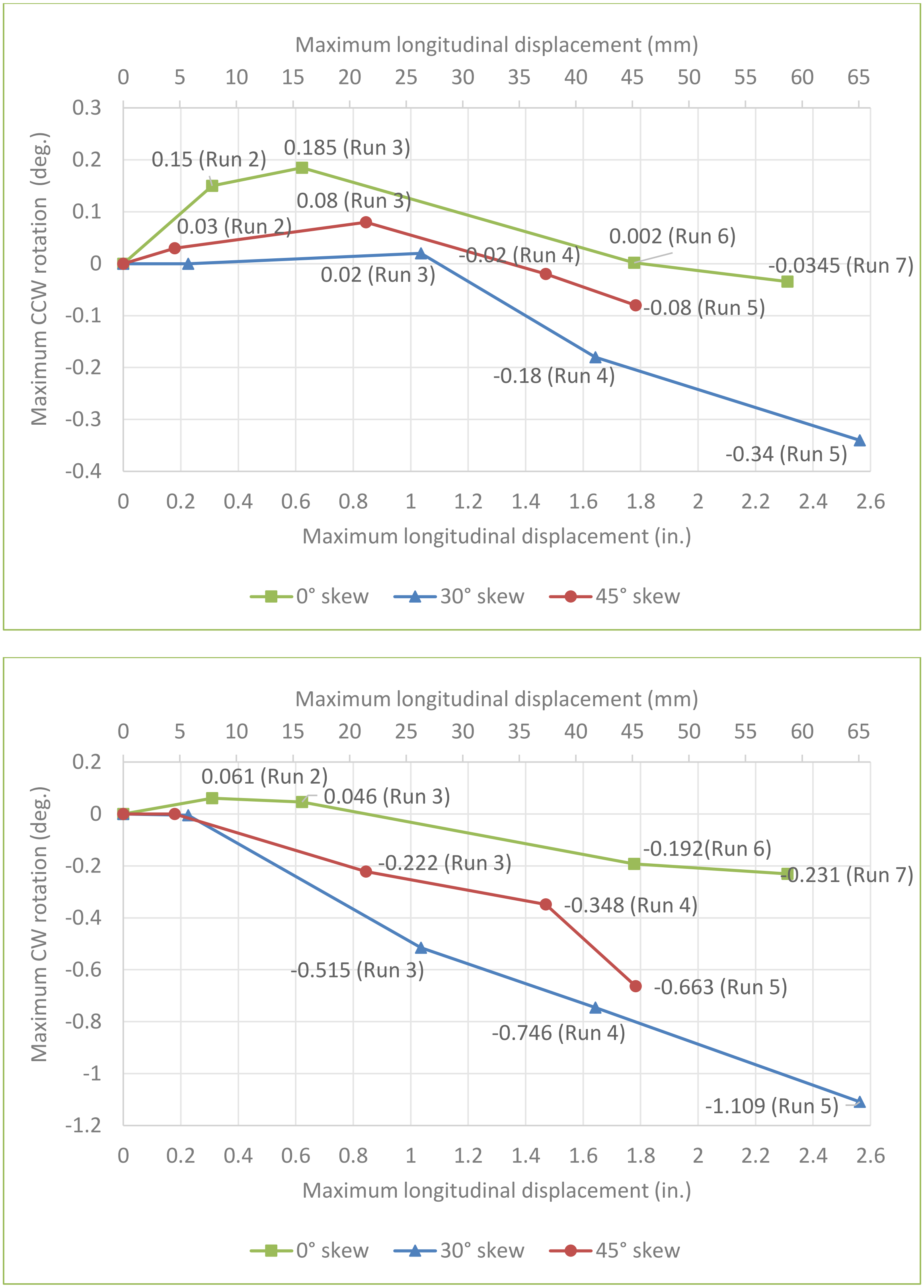

Figure 7-1 Skew angle effect on the backwall maximum combined rotations.

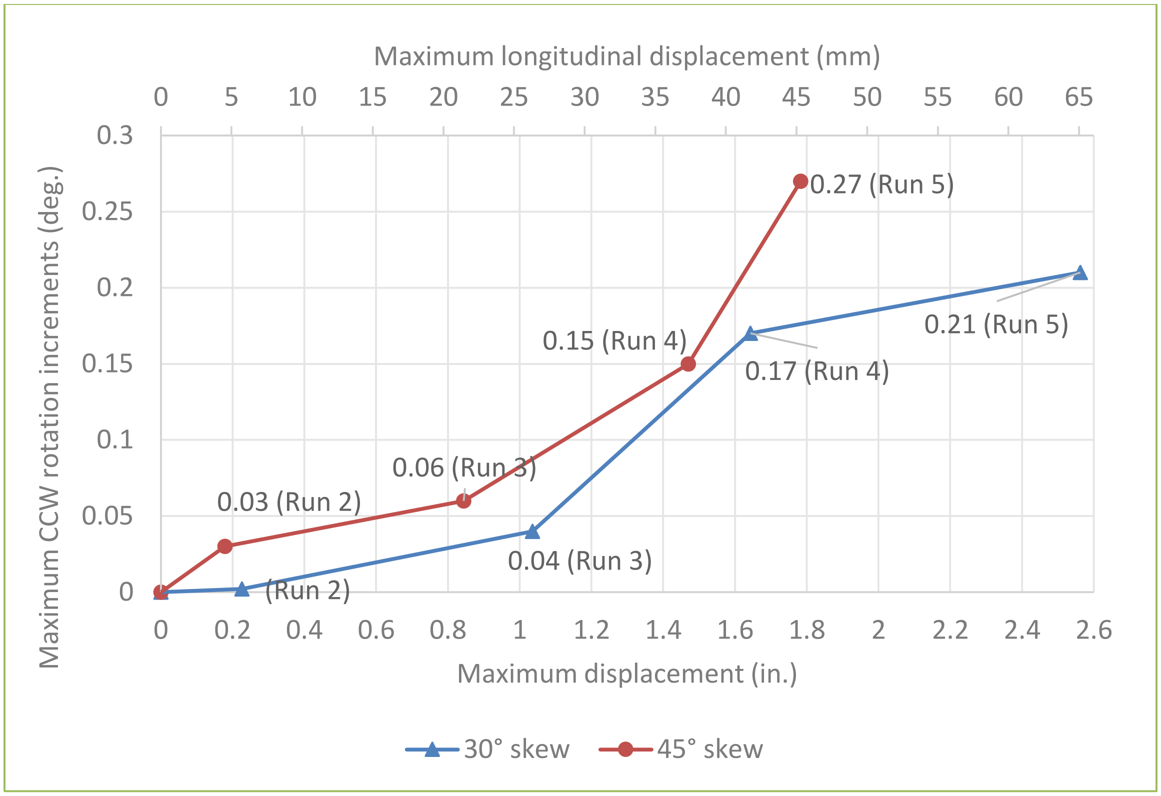

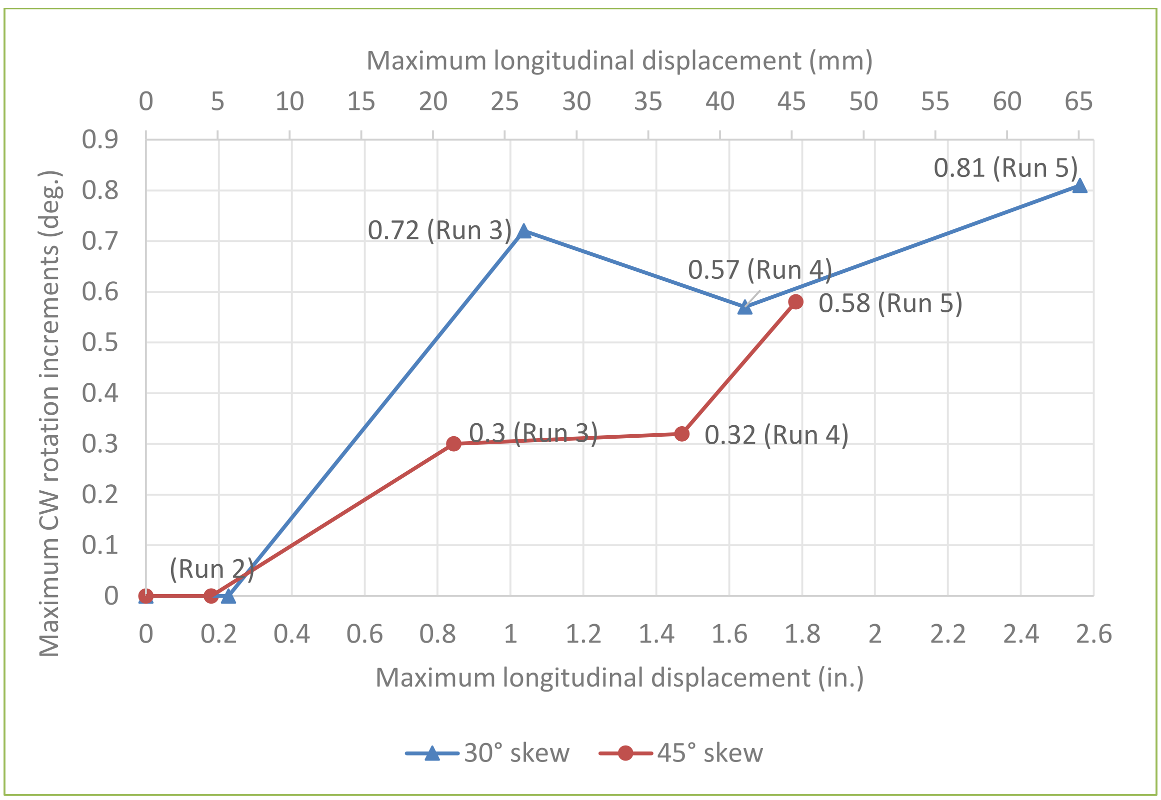

Figure 7-2 Skew angle effect on backwall maximum rotation increments (Top: CCW; Bot: CW).

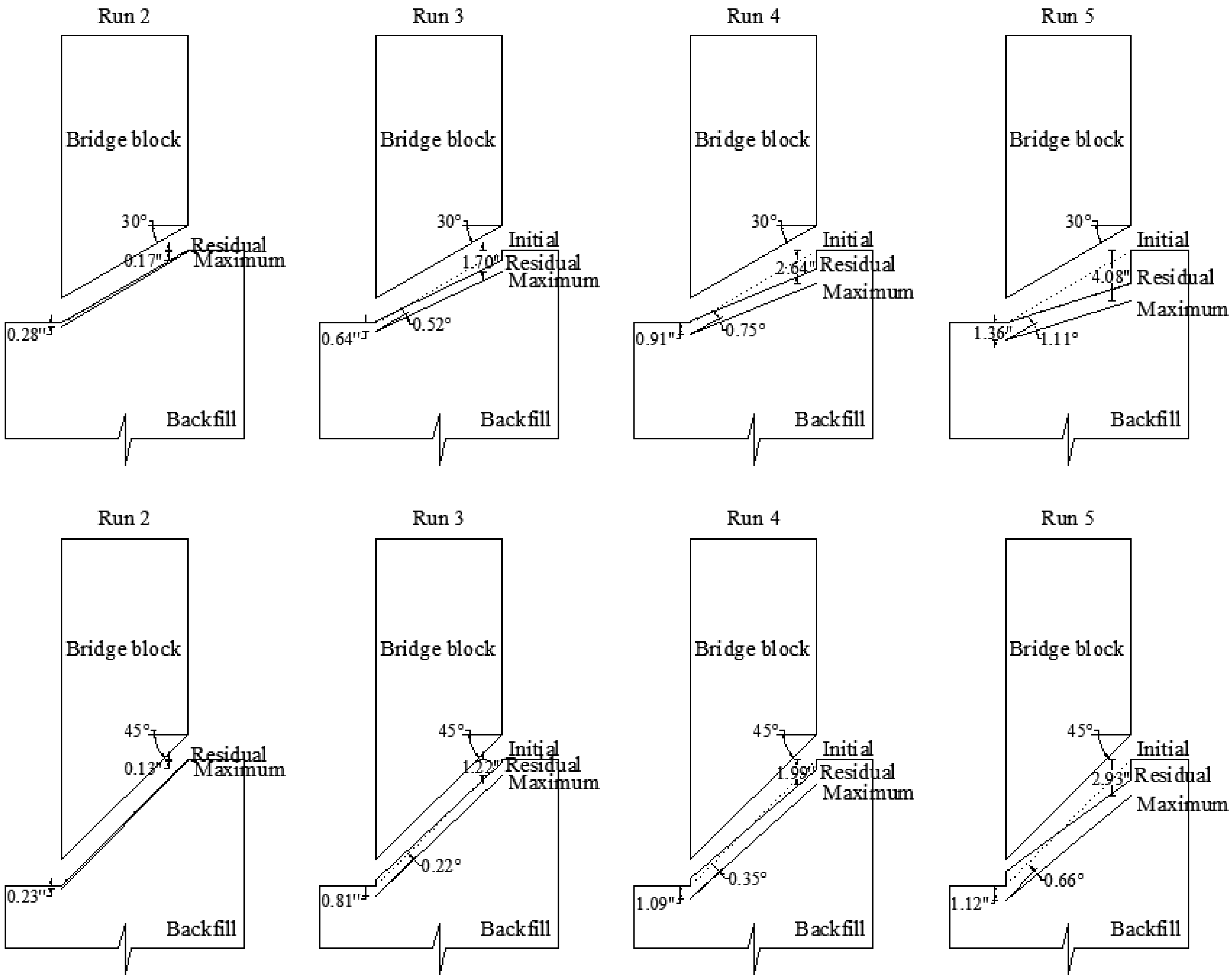

Figure 7-3 Backwall maximum CW rotations and residual positions.

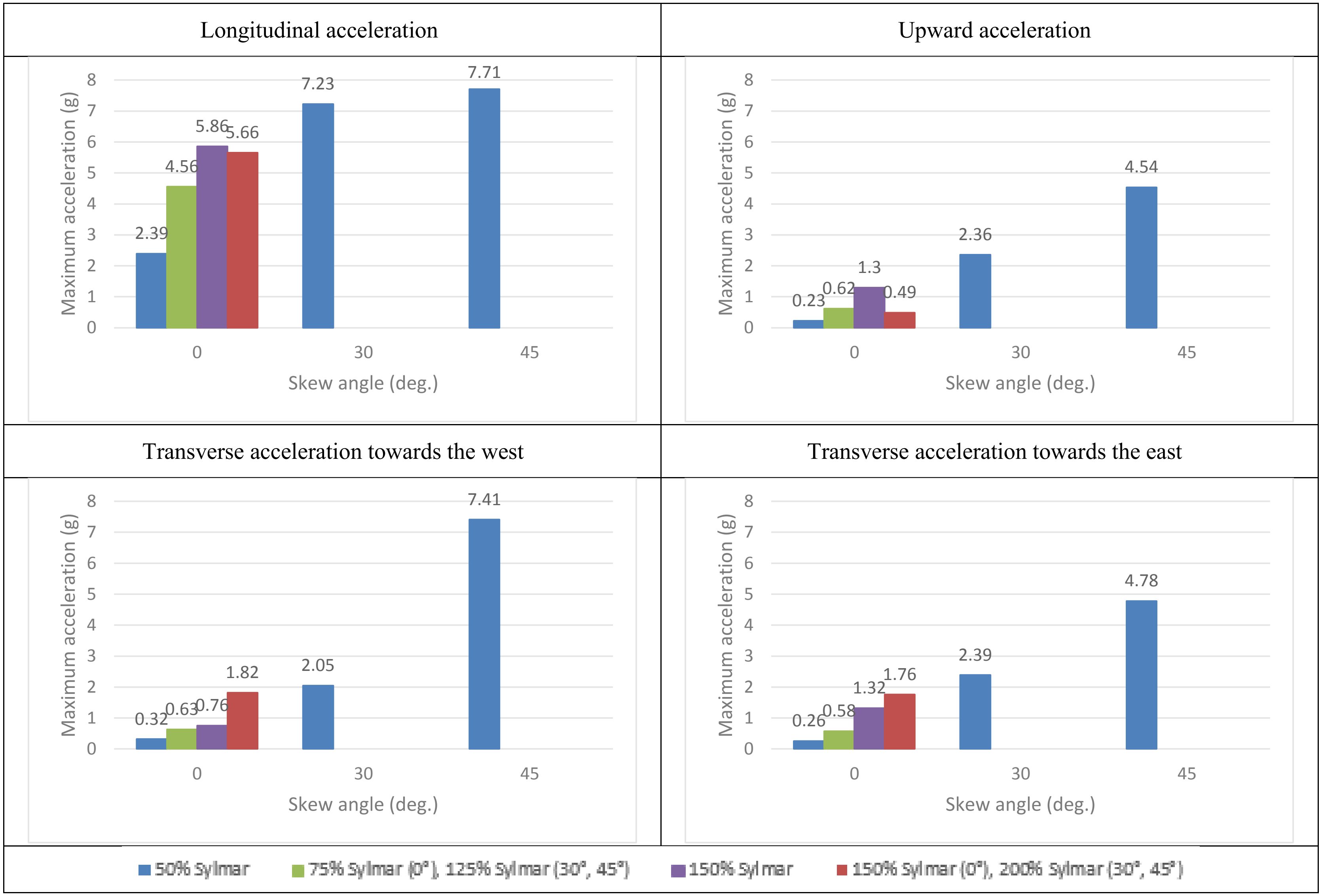

Figure 7-4 Skew angle effect on the maximum average accelerations of the backwall.

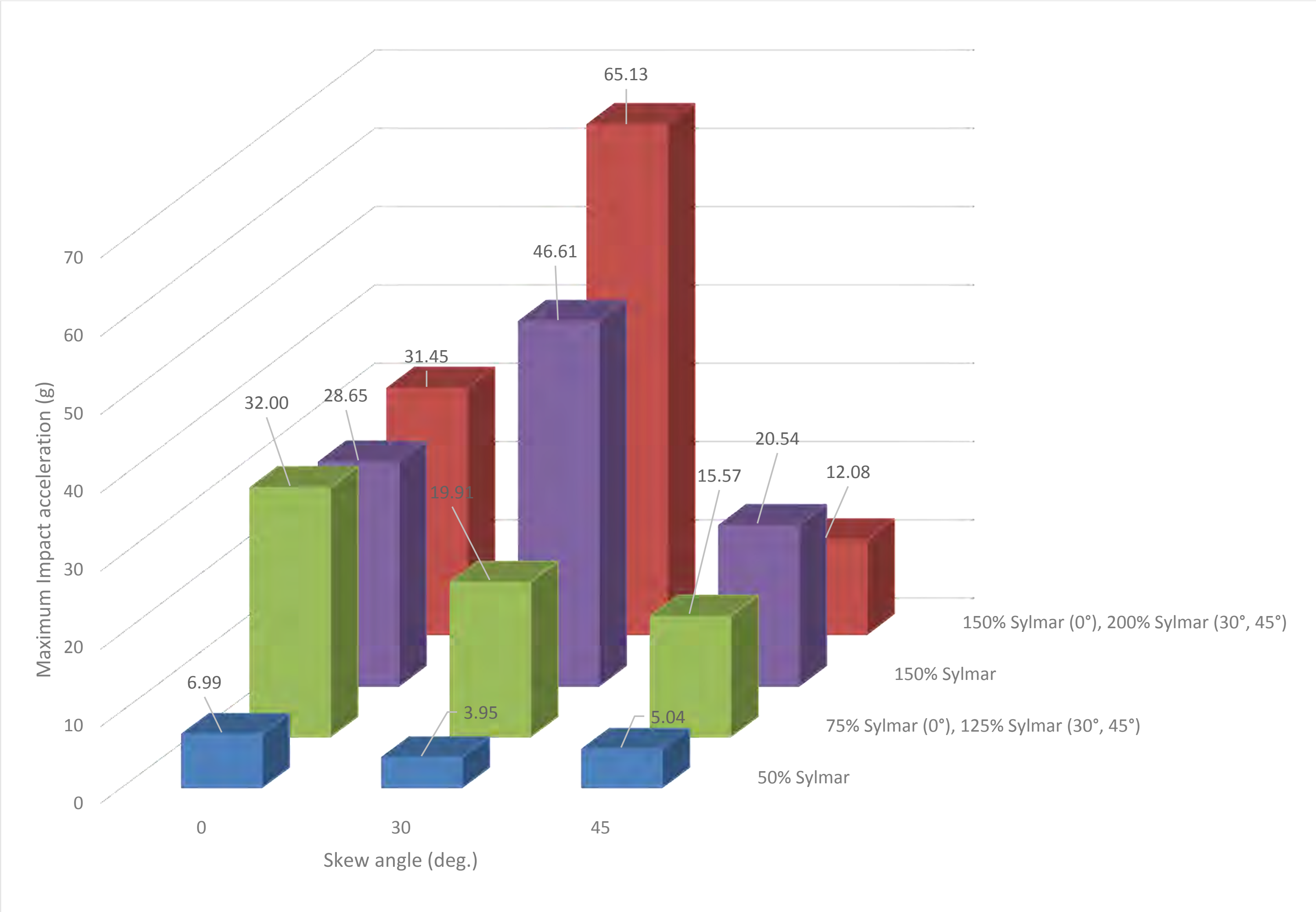

Figure 7-5 Skew angle effect on the maximum average impact accelertions on the backwall.

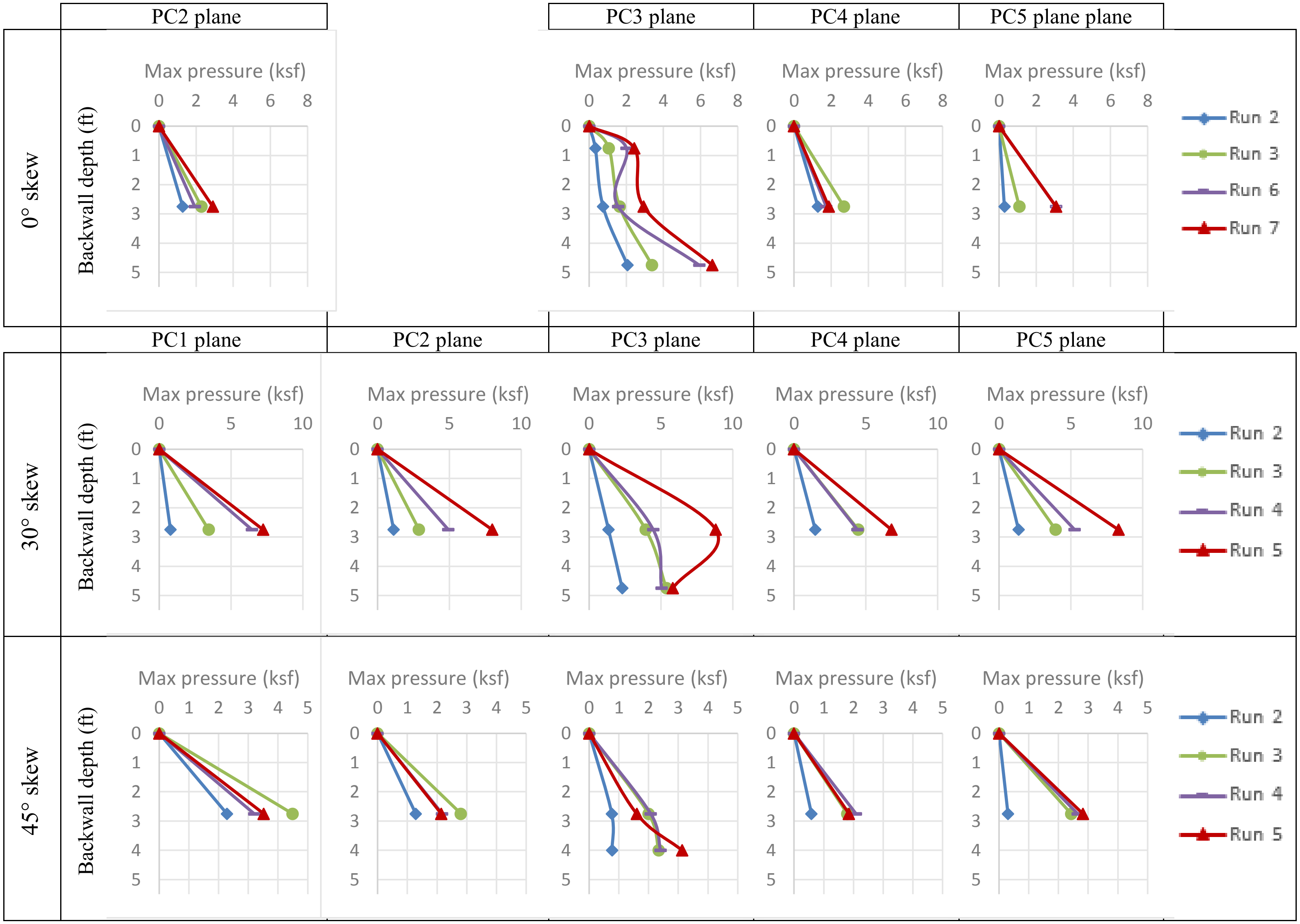

Figure 7-6 The maximum soil pressure distributions along the backwall height.

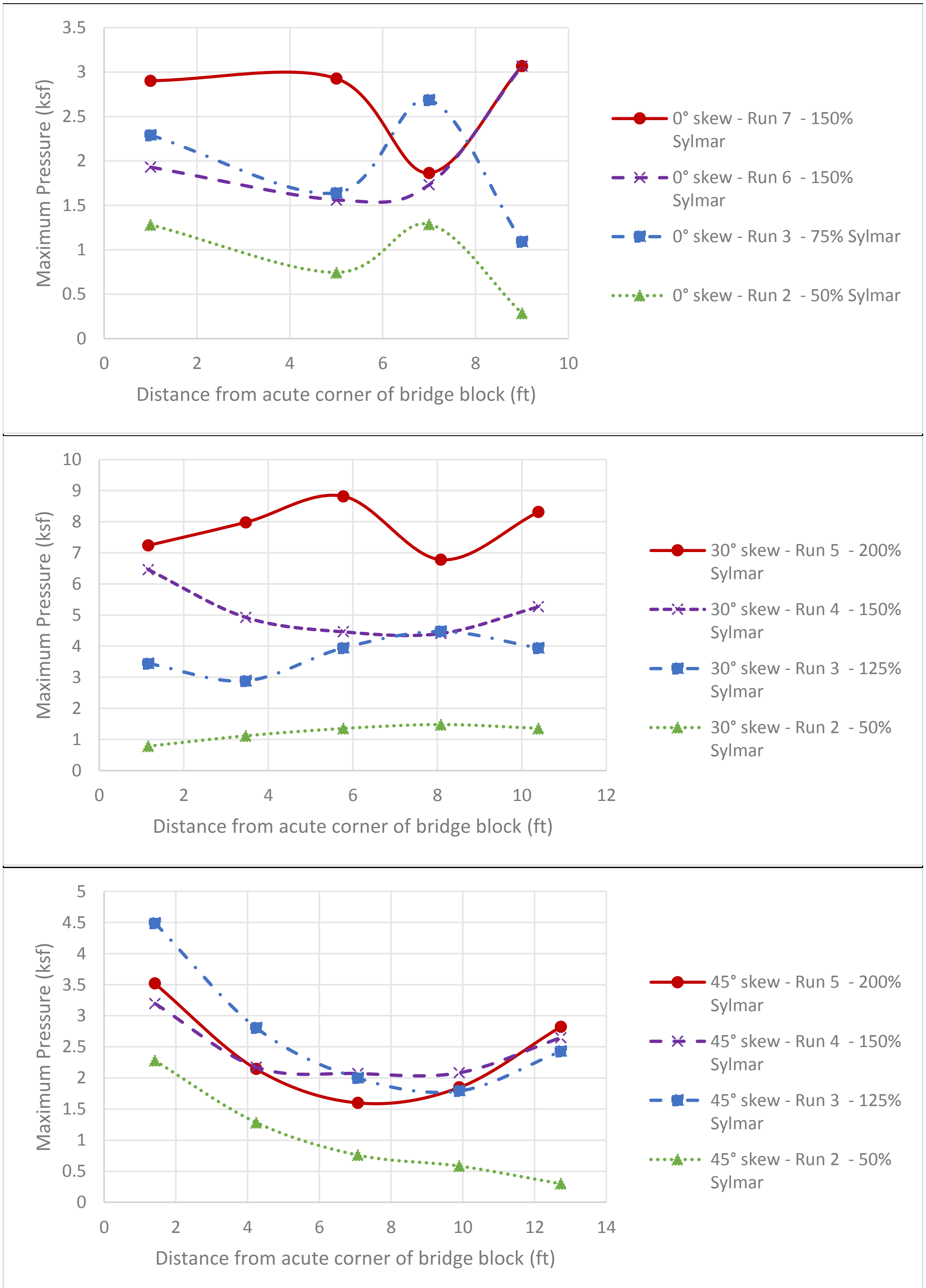

Figure 7-7 The maximum soil pressure distributions along the backwall width.

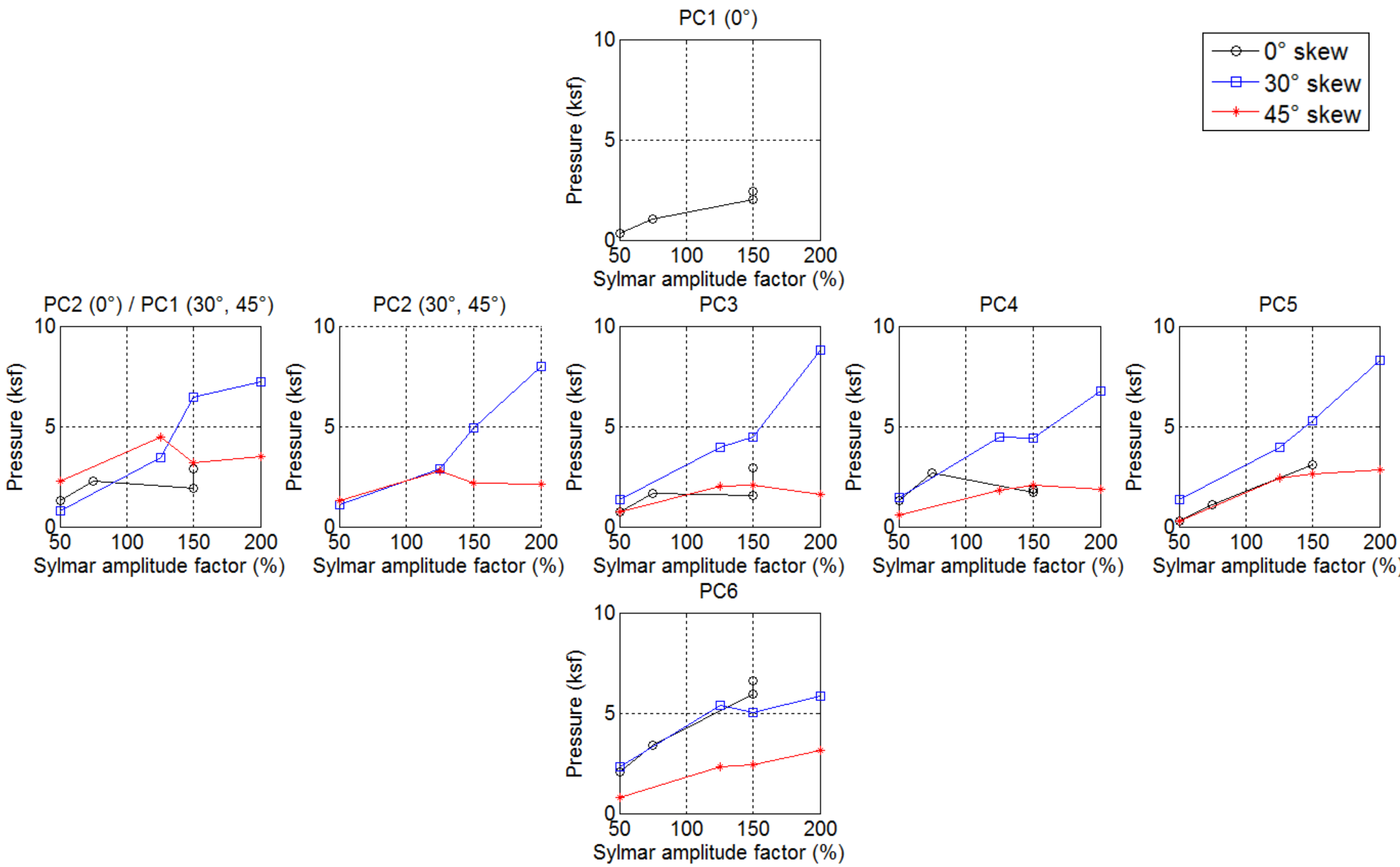

Figure 7-8 Skew angle effect on the maximum soil pressures.

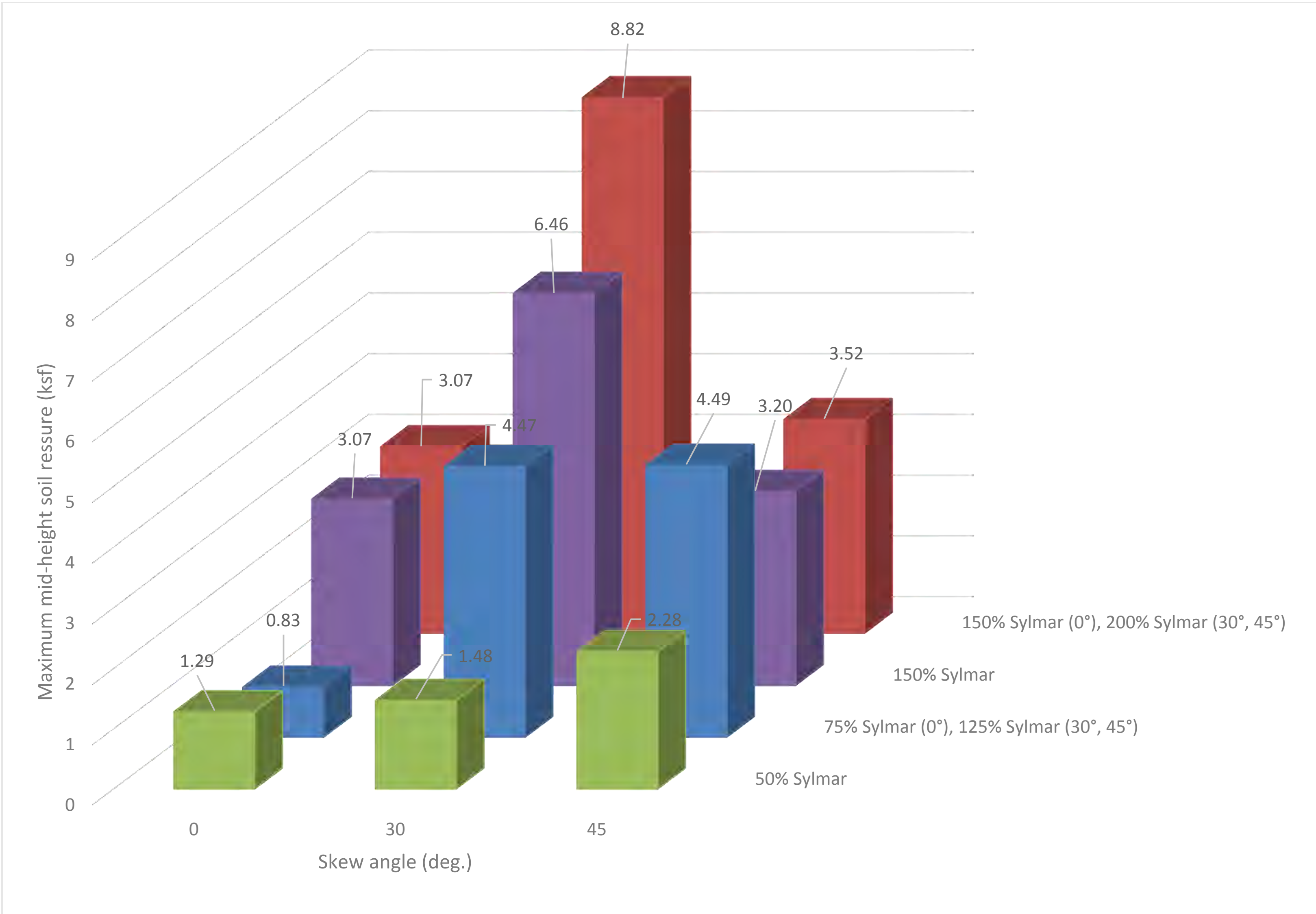

Figure 7-9 Skew angle effect on the maximum soil mid-height pressures.

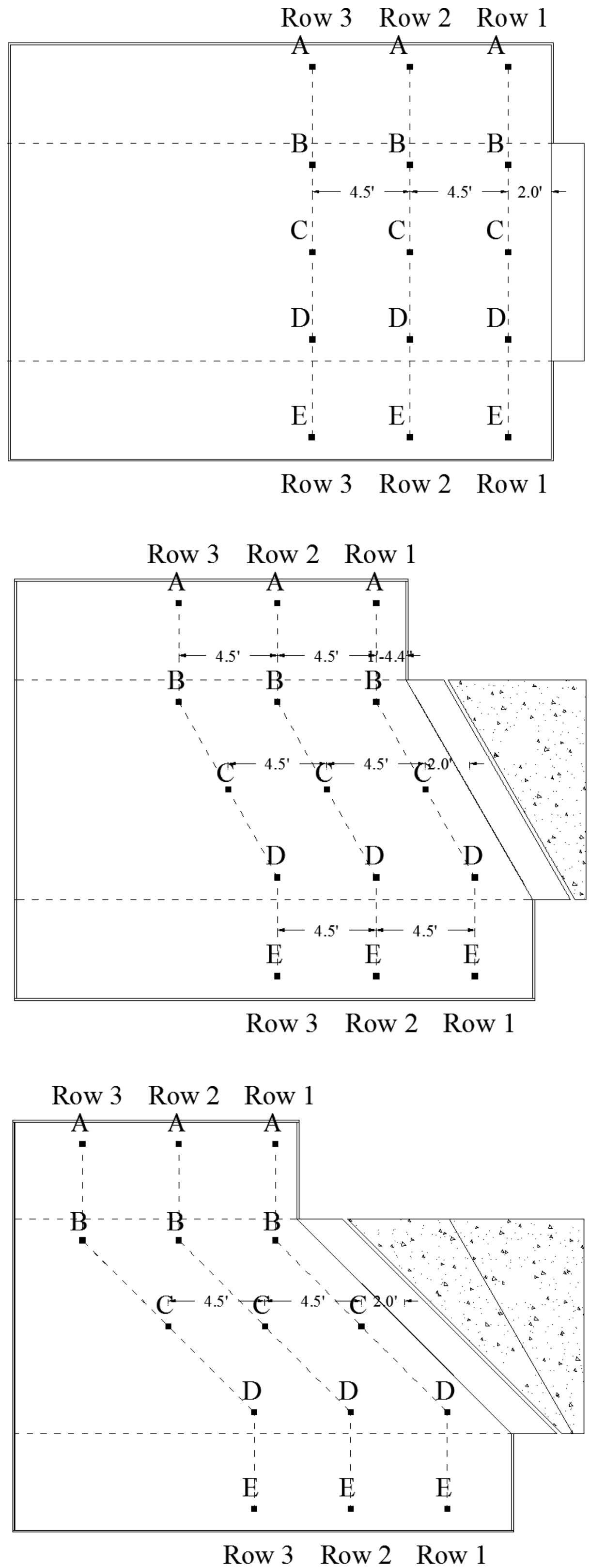

Figure 7-10 Definition of points along the backfill width.

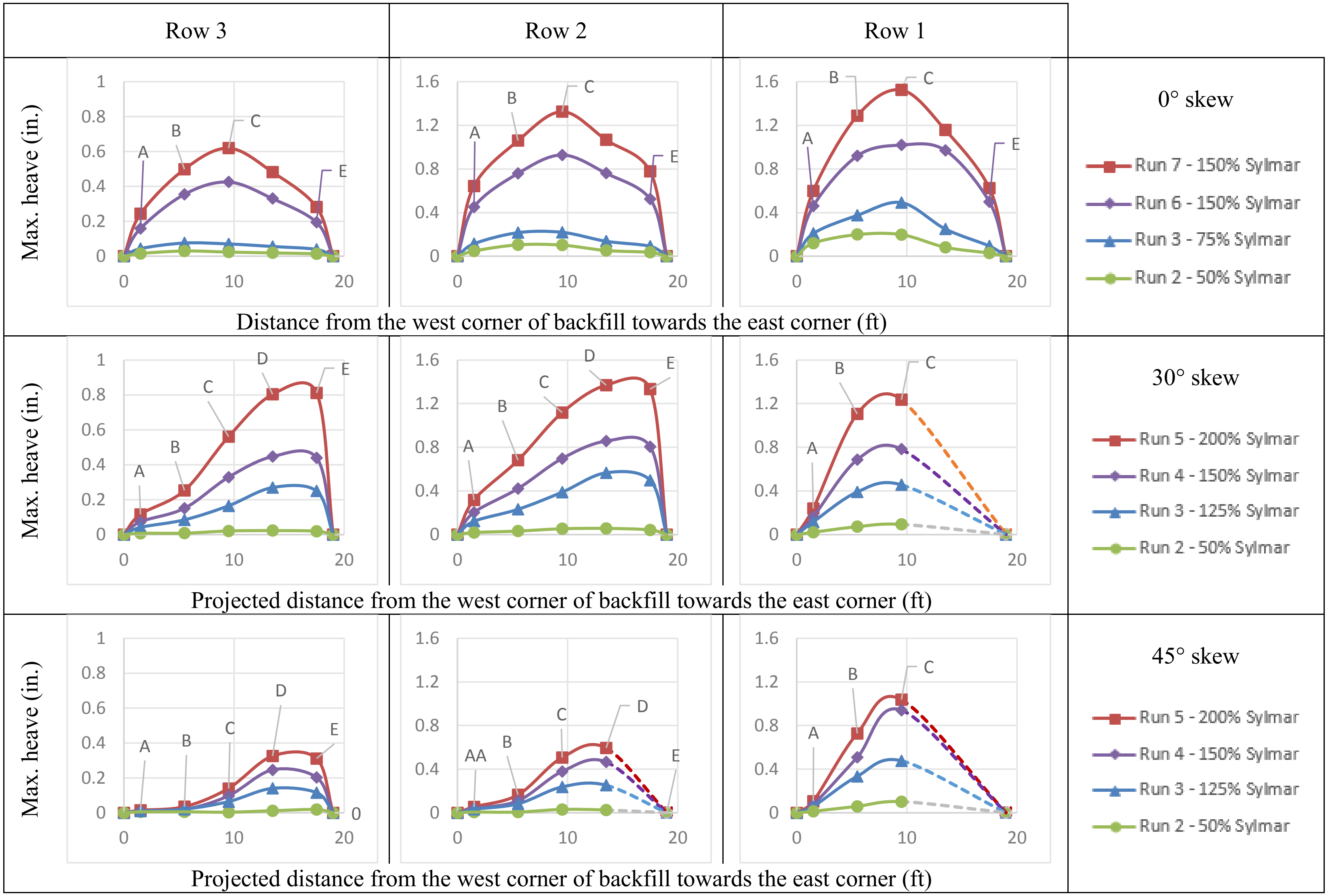

Figure 7-11 The maximum soil surface heave distributions along the backfill width.

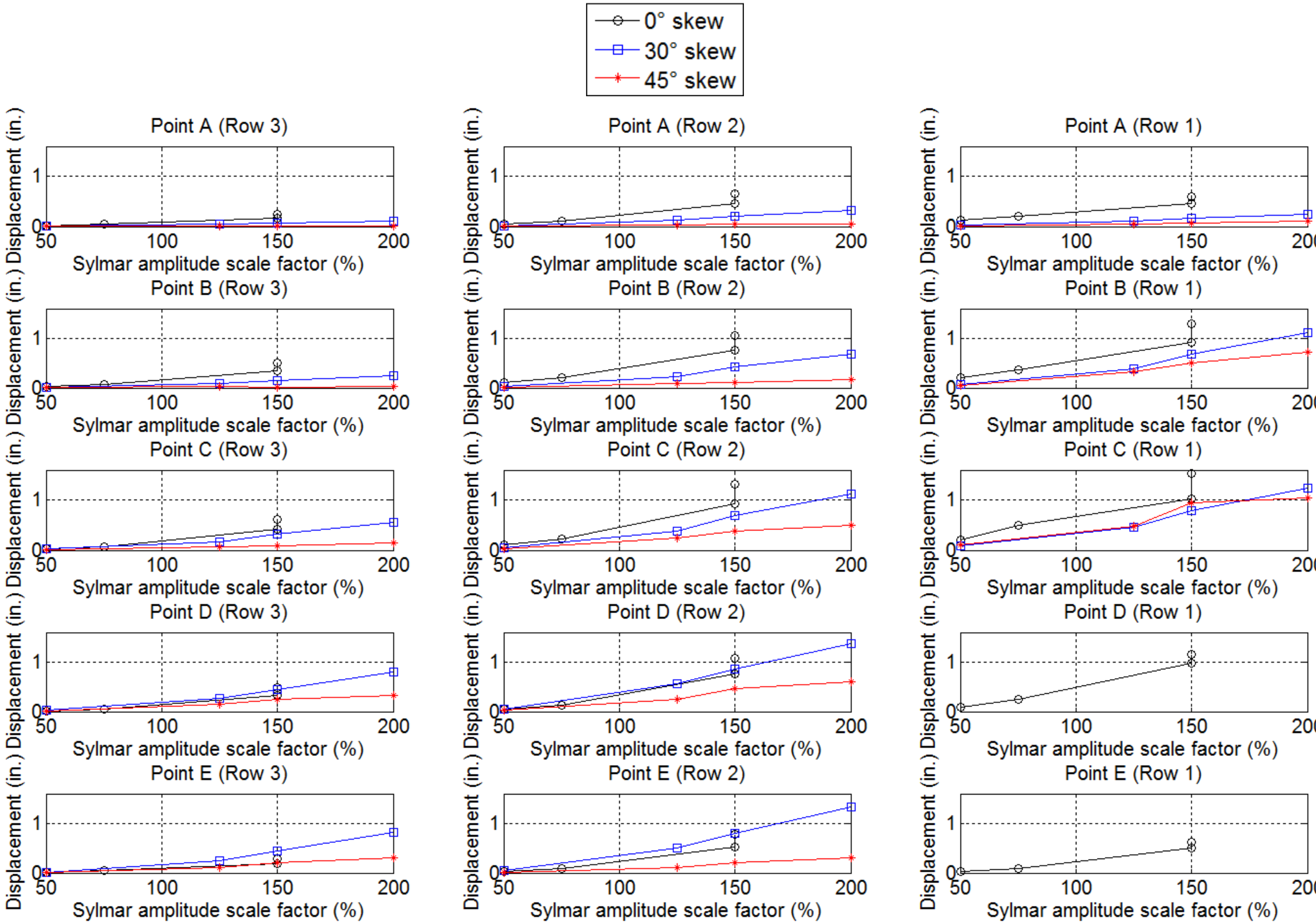

Figure 7-12 Skew angle effect on the maximum soil surface heaves at different points.

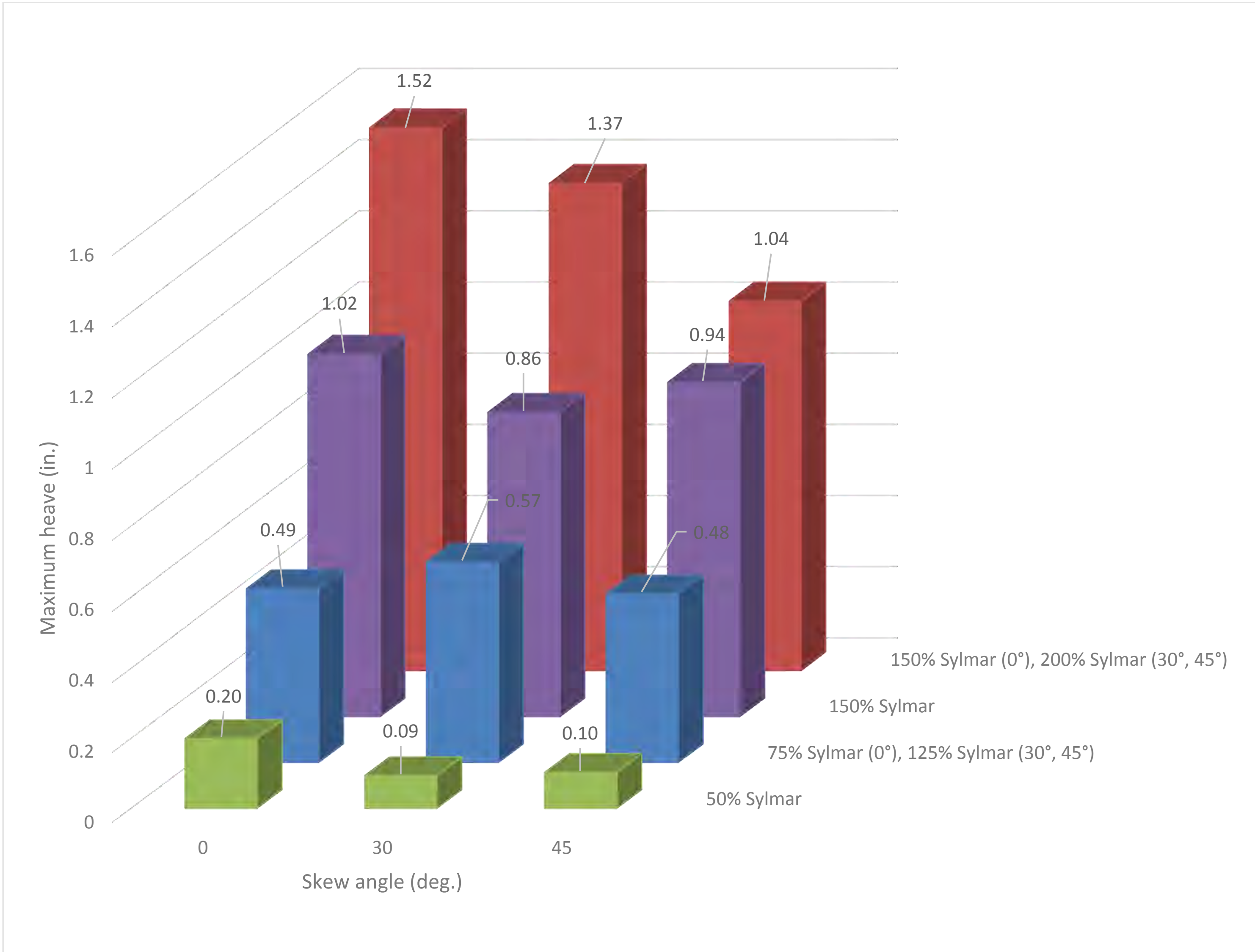

Figure 7-13 Skew angle effect on the maximum soil surface heaves.

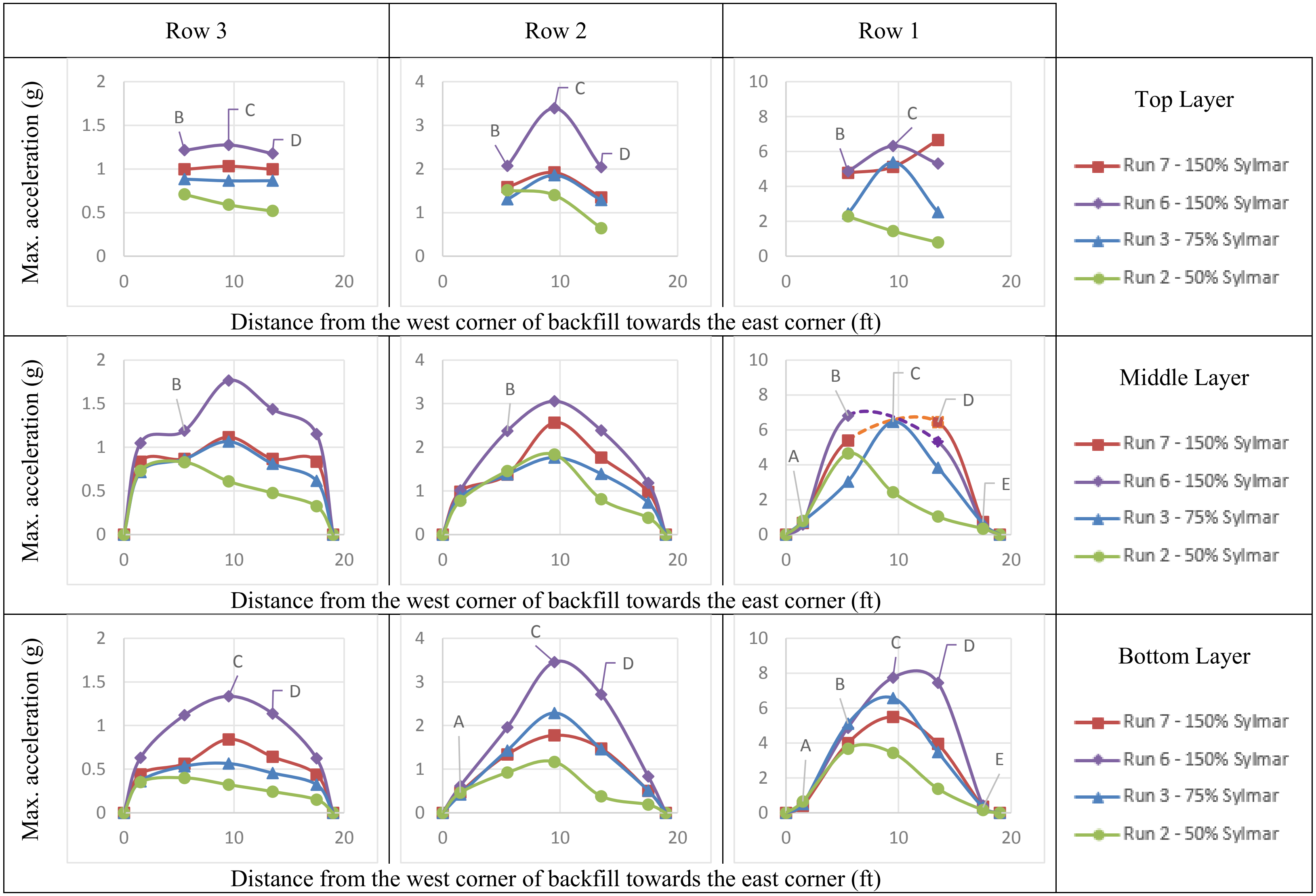

Figure 7-14 Distribution of the maximum longitudinal soil accelerations for the 0° skew test.

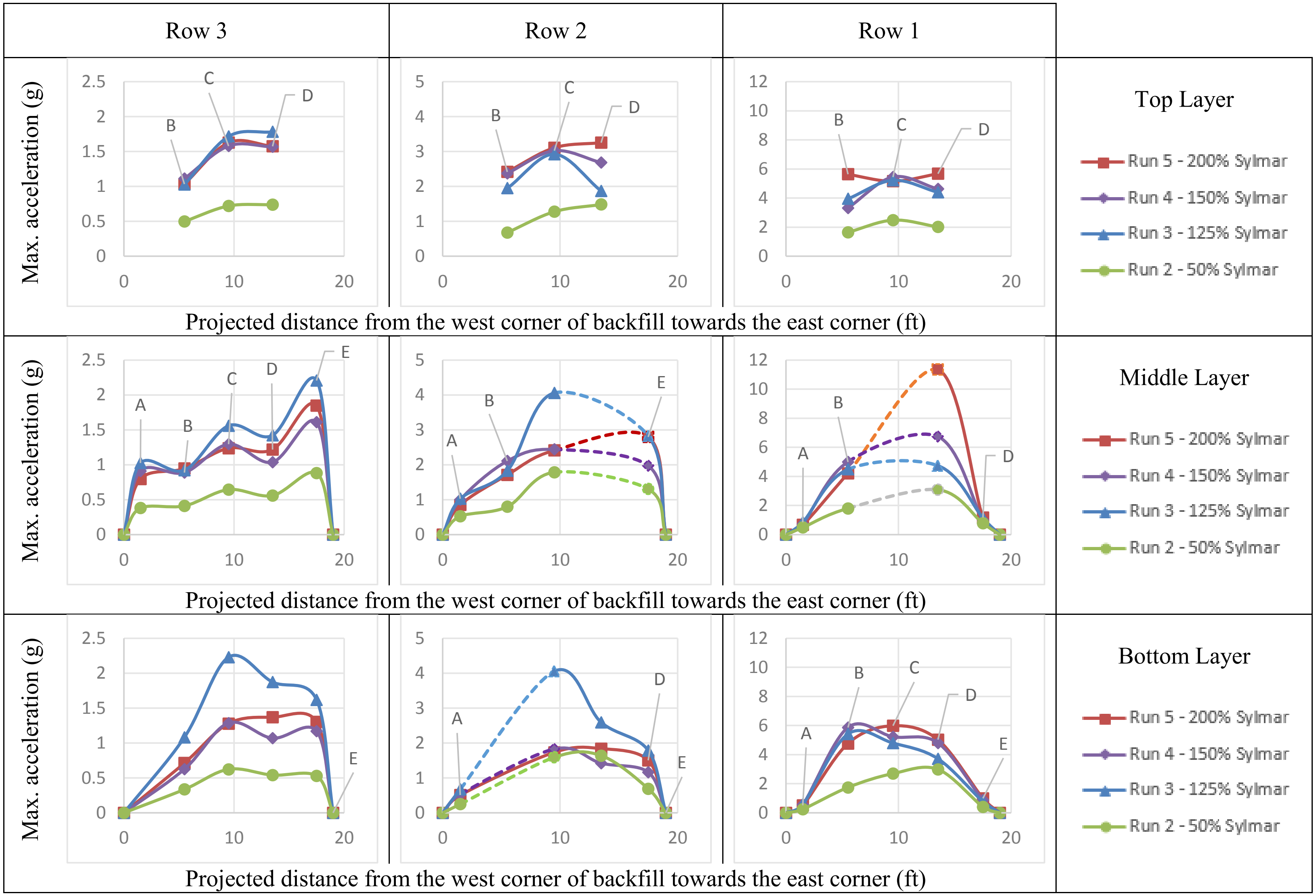

Figure 7-15 Distribution of the maximum longitudinal soil accelerations for the 30° skew test.

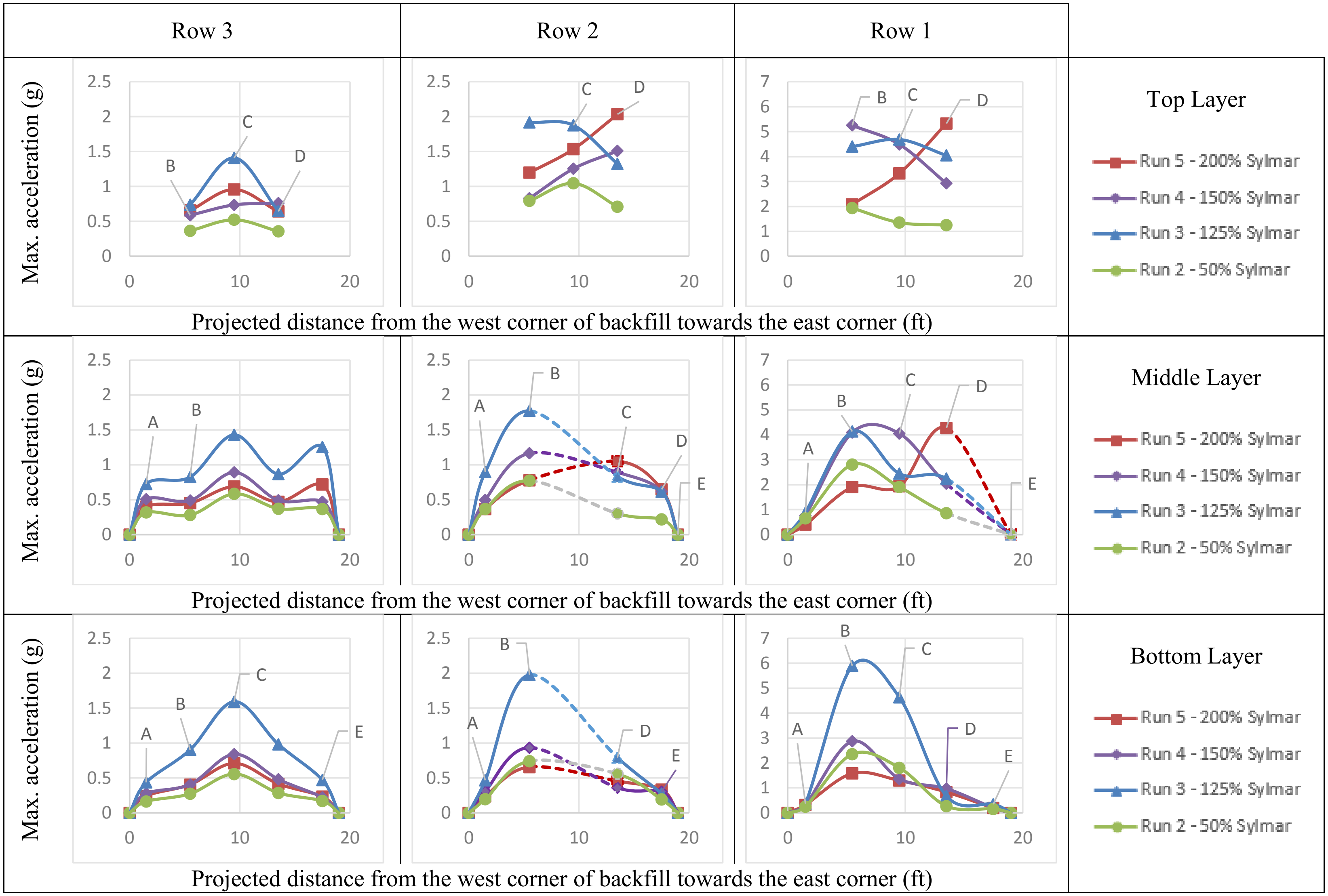

Figure 7-16 Distribution of the maximum longitudinal soil accelerations for the 45° skew test.

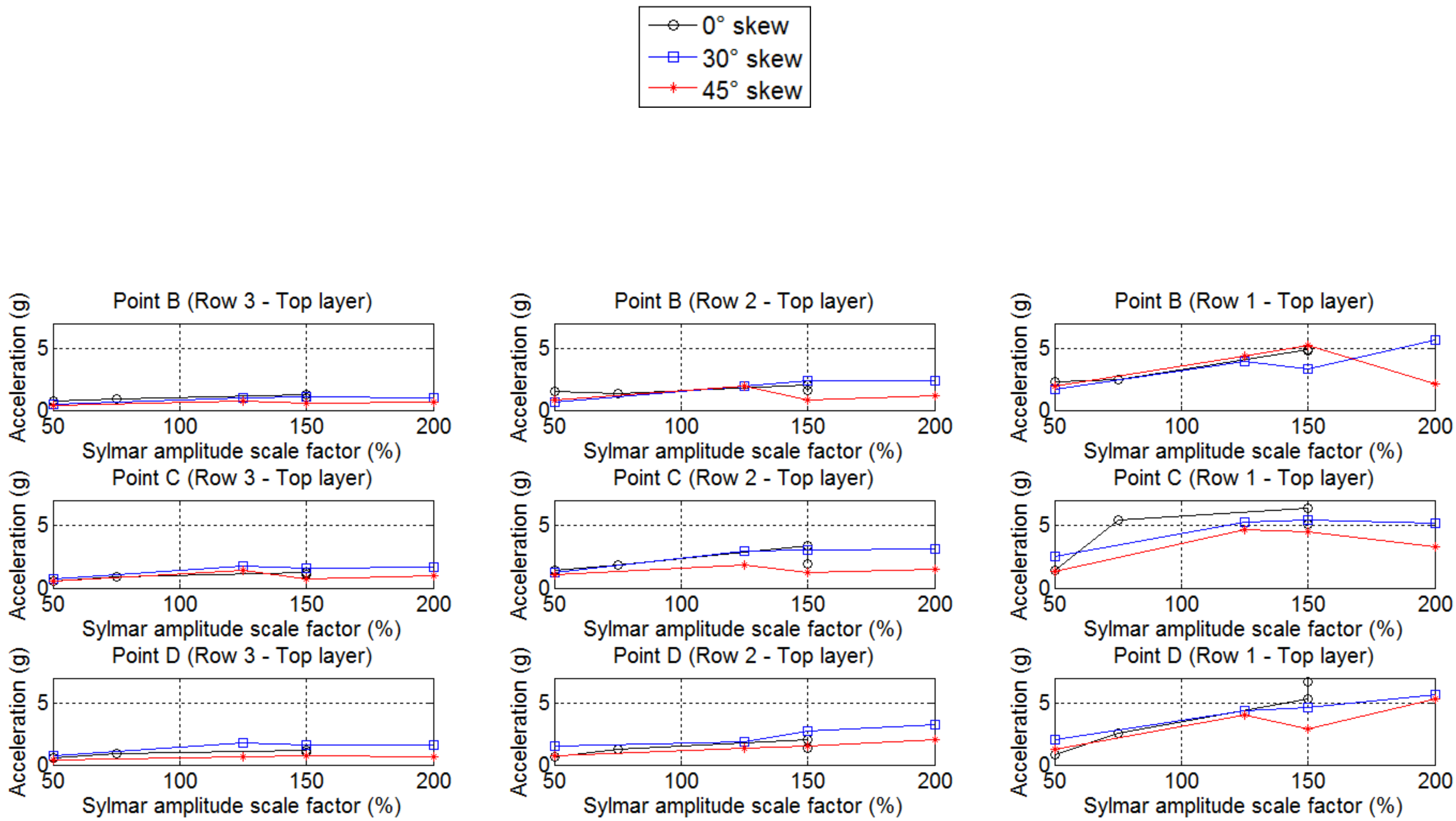

Figure 7-17 Skew angle effect on the maximum longitudinal soil accelerations in the top layer.

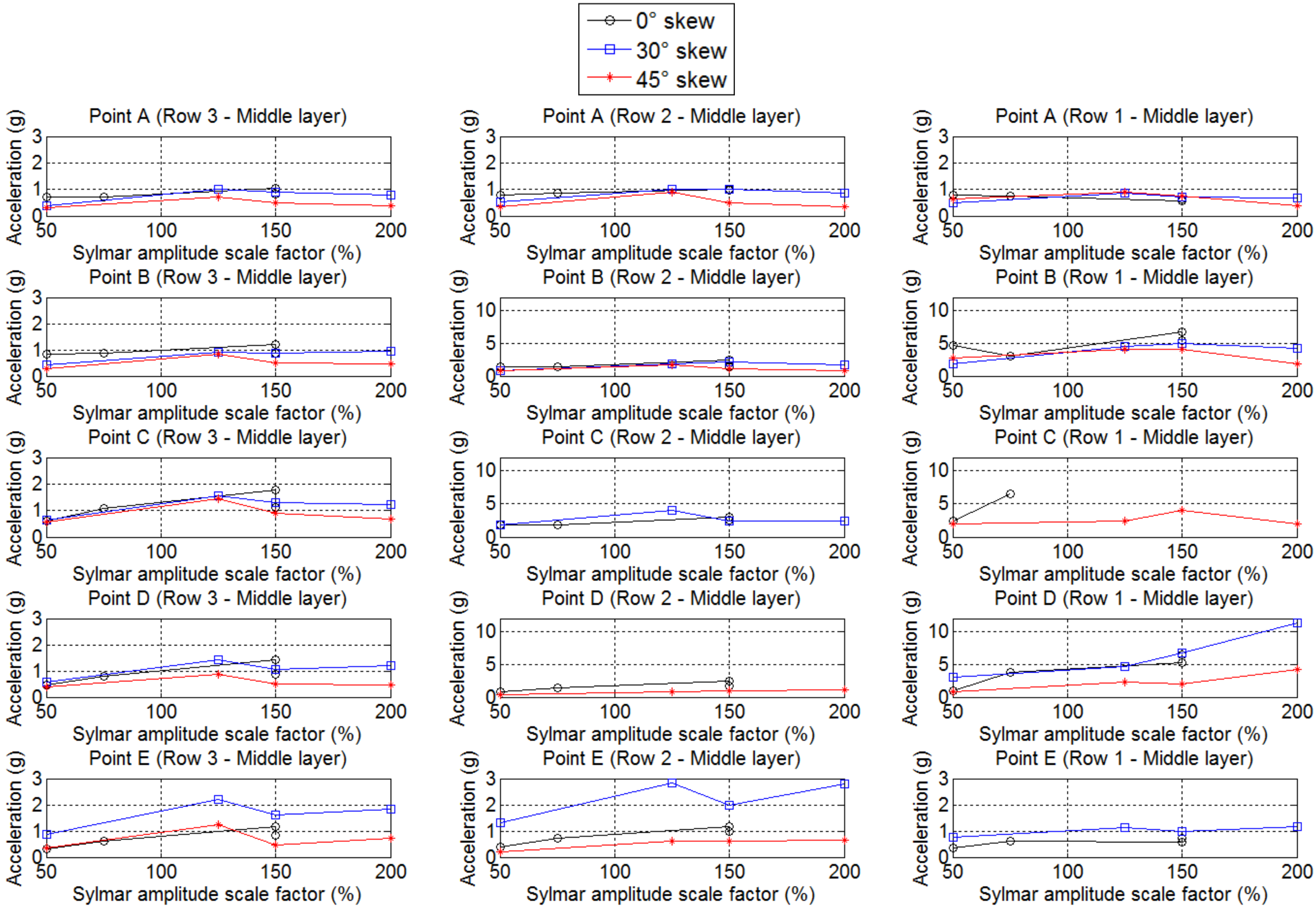

Figure 7-18 Skew angle effect on the maximum longitudinal soil accelerations in the middle layer.

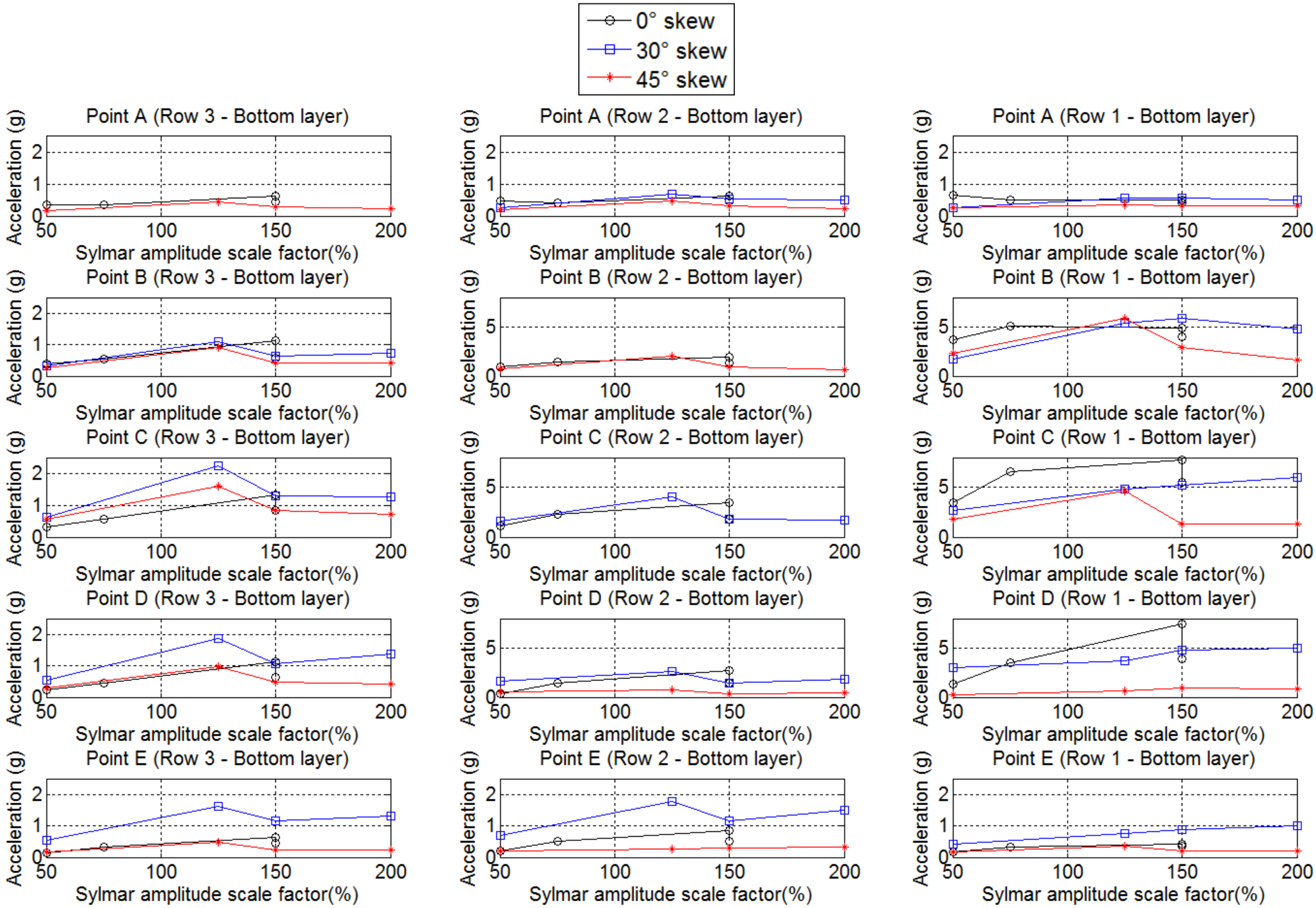

Figure 7-19 Skew angle effect on the maximum longitudinal soil accelerations in the bottom layer.

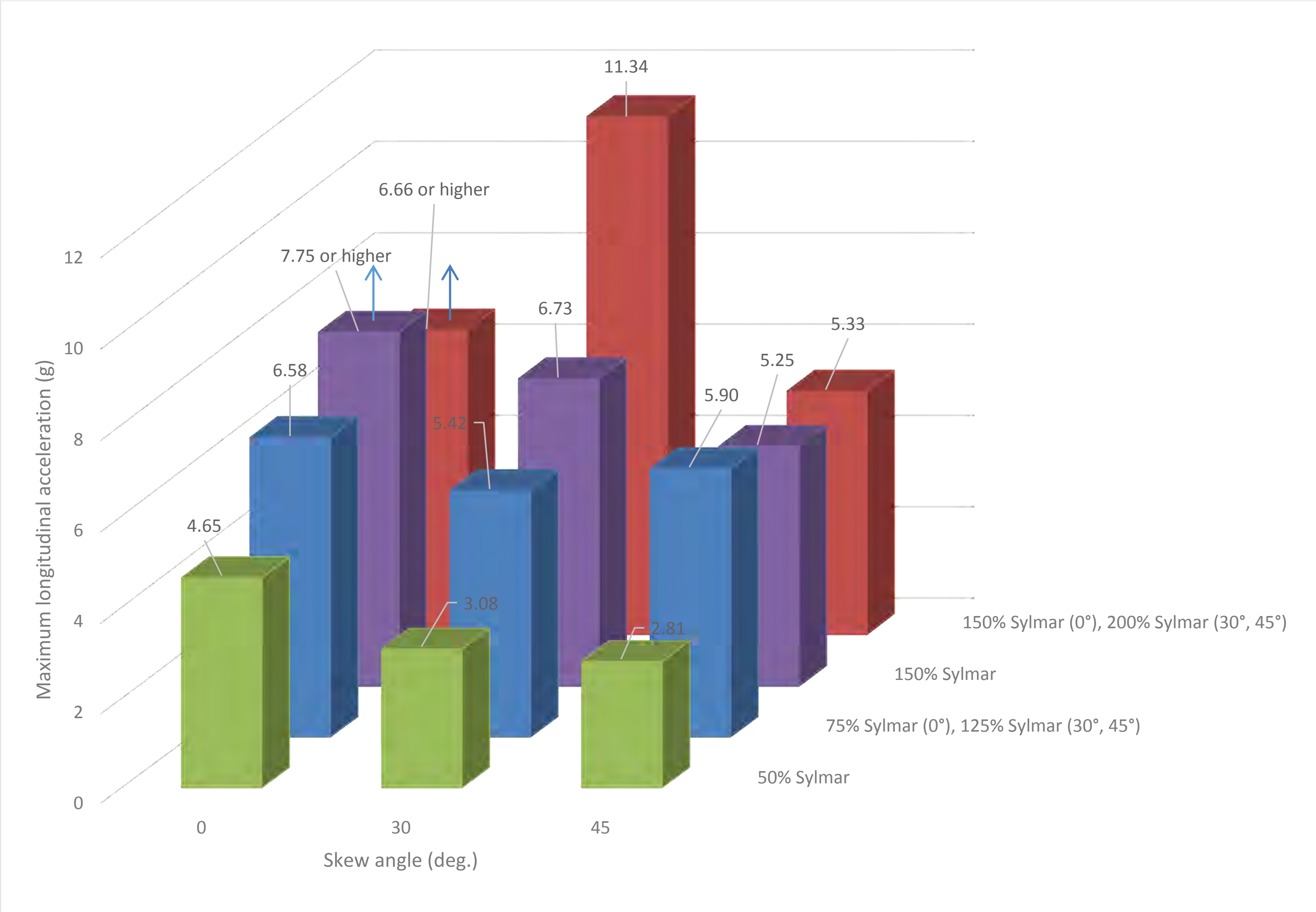

Figure 7-20 Skew angle effect on the maximum longitudinal soil accelerations.

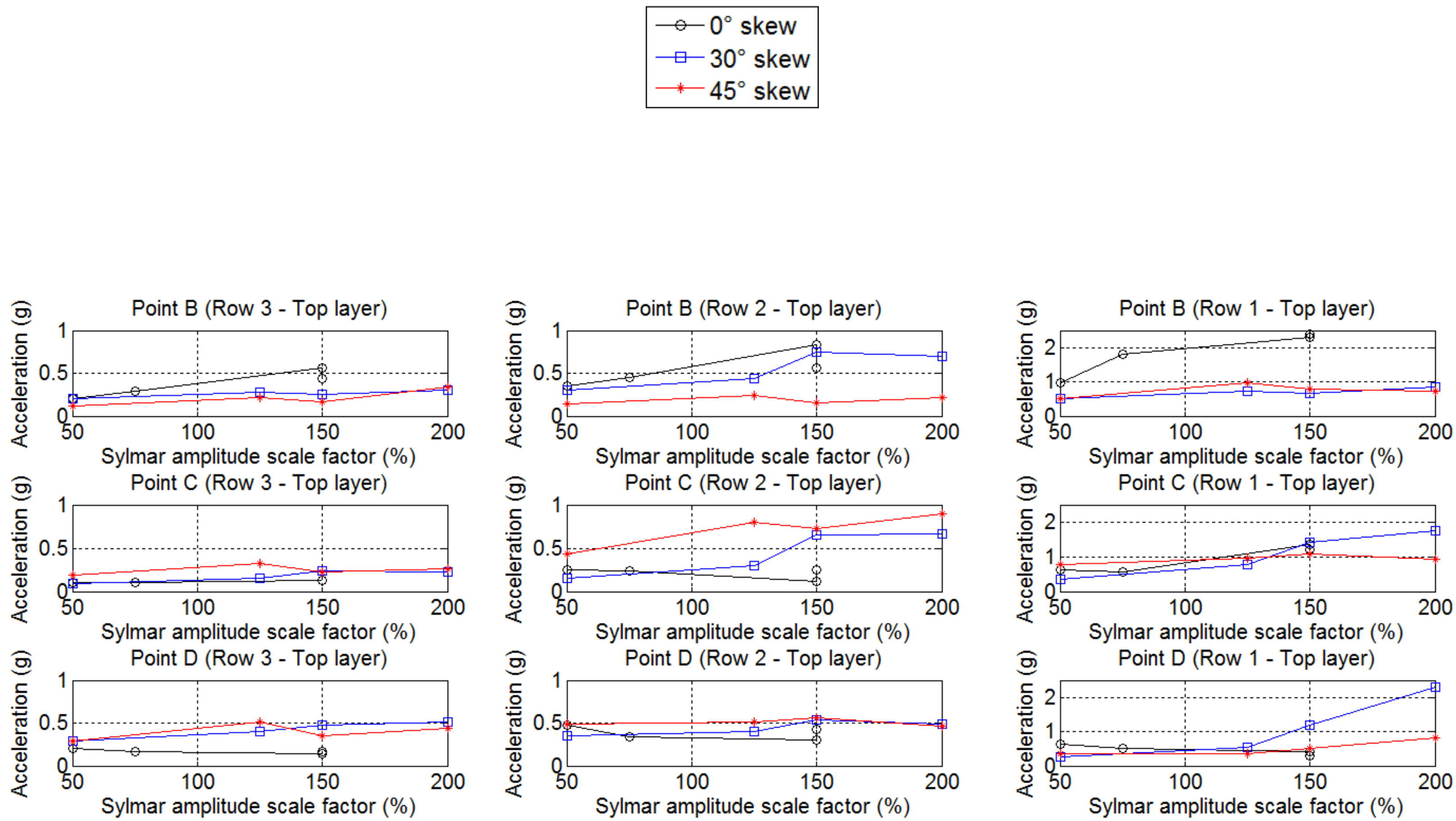

Figure 7-21 Skew angle effect on the maximum transverse (towards the west) soil accelerations in the top layer.

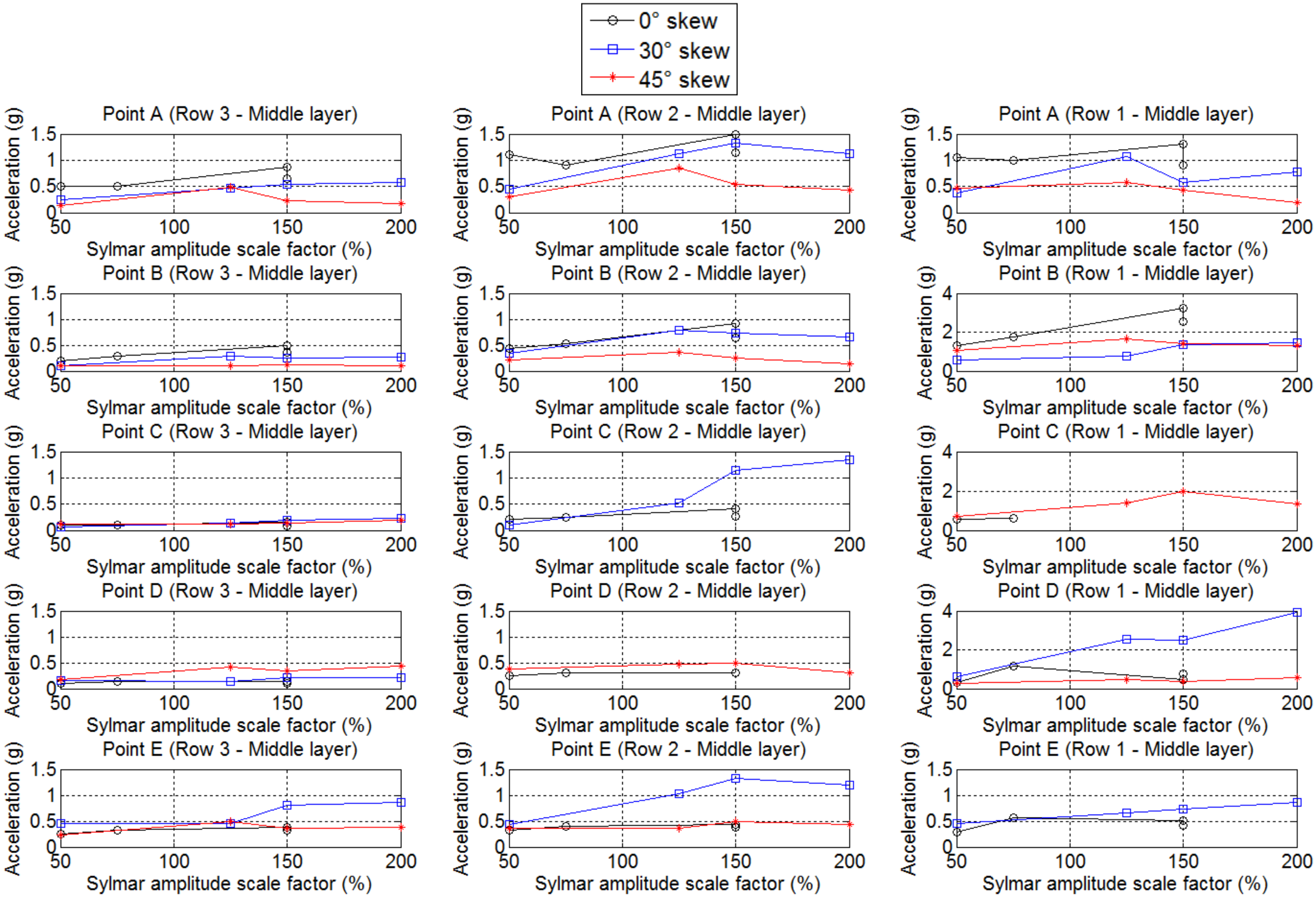

Figure 7-22 Skew angle effect on the maximum transverse (towards the west) soil accelerations in the middle layer.

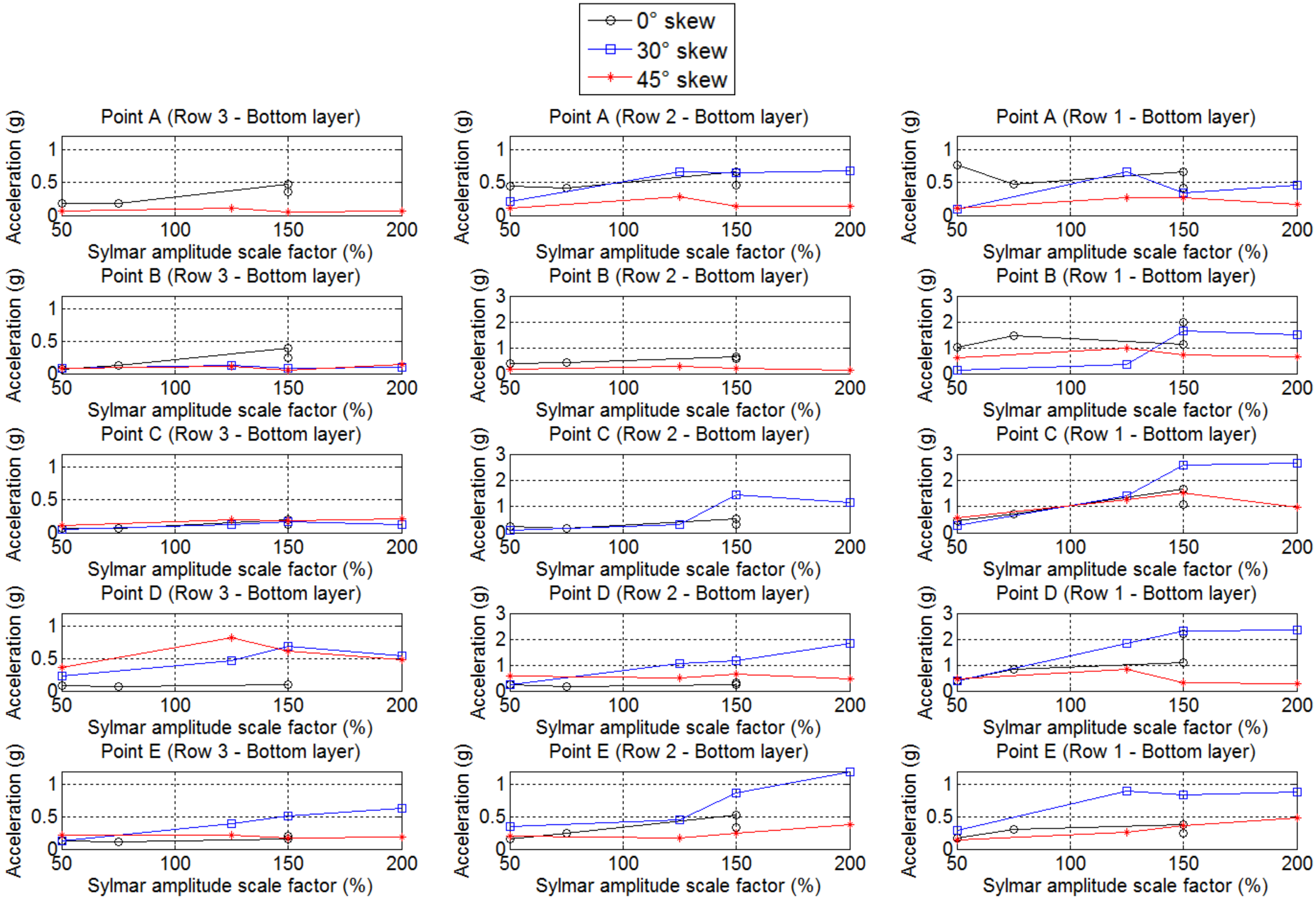

Figure 7-23 Skew angle effect on the maximum transverse (towards the west) soil accelerations in the bottom layer.

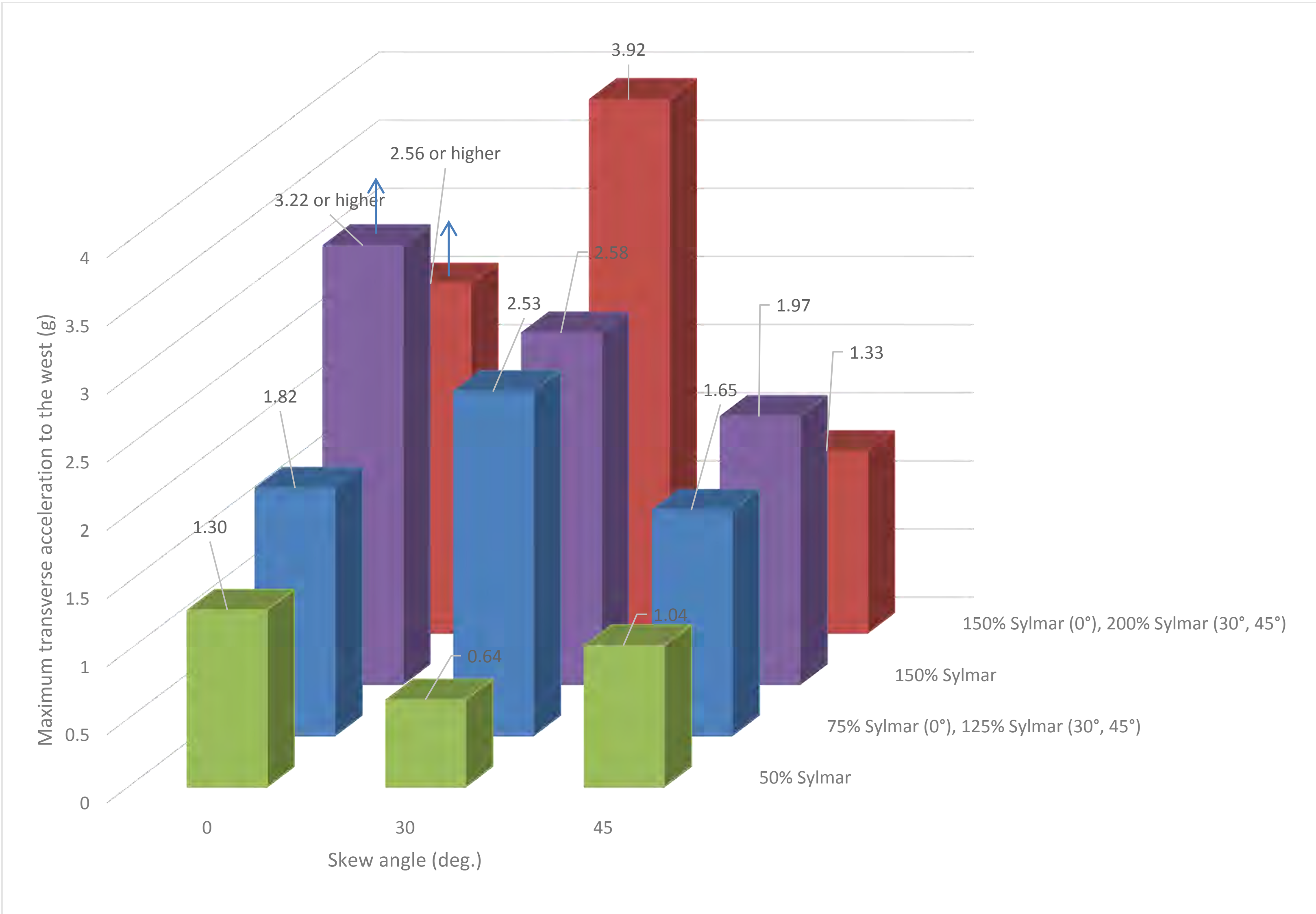

Figure 7-24 Skew angle effect on the maximum transverse (towards the west) soil accelerations.

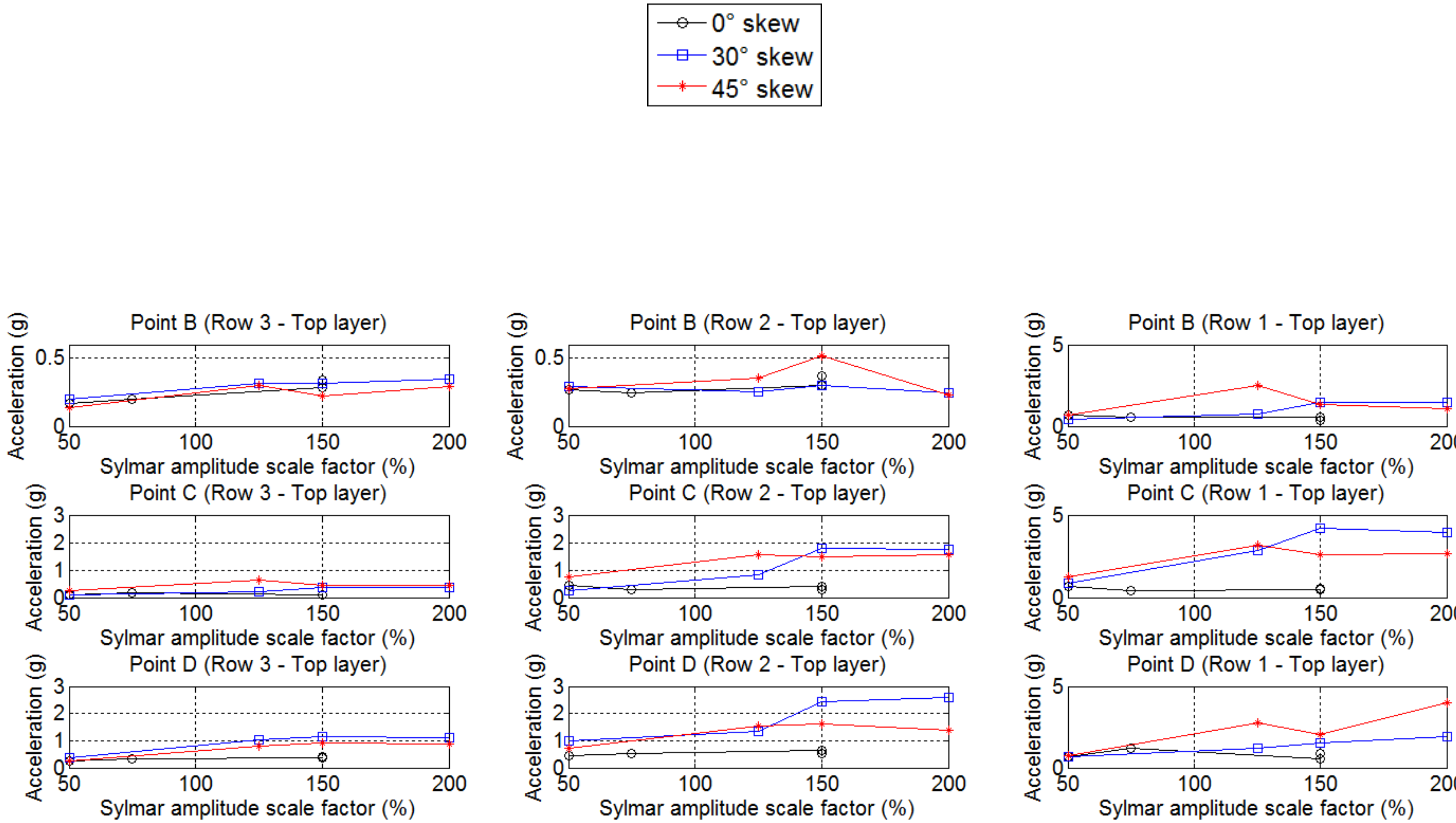

Figure 7-25 Skew angle effect on the maximum transverse (towards the east) soil accelerations in the top layer.

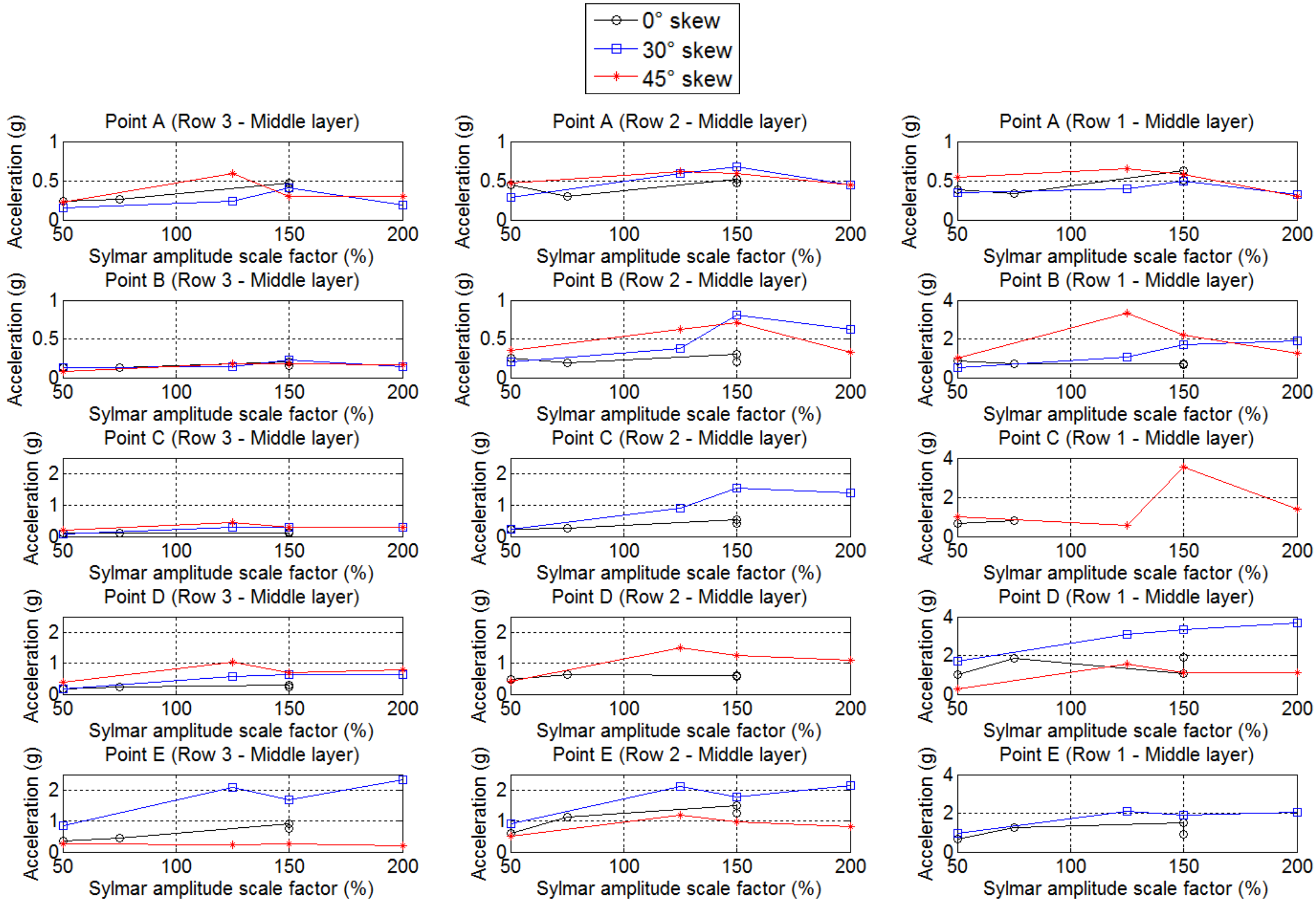

Figure 7-26 Skew angle effect on the maximum transverse (towards the east) soil accelerations in the middle layer.

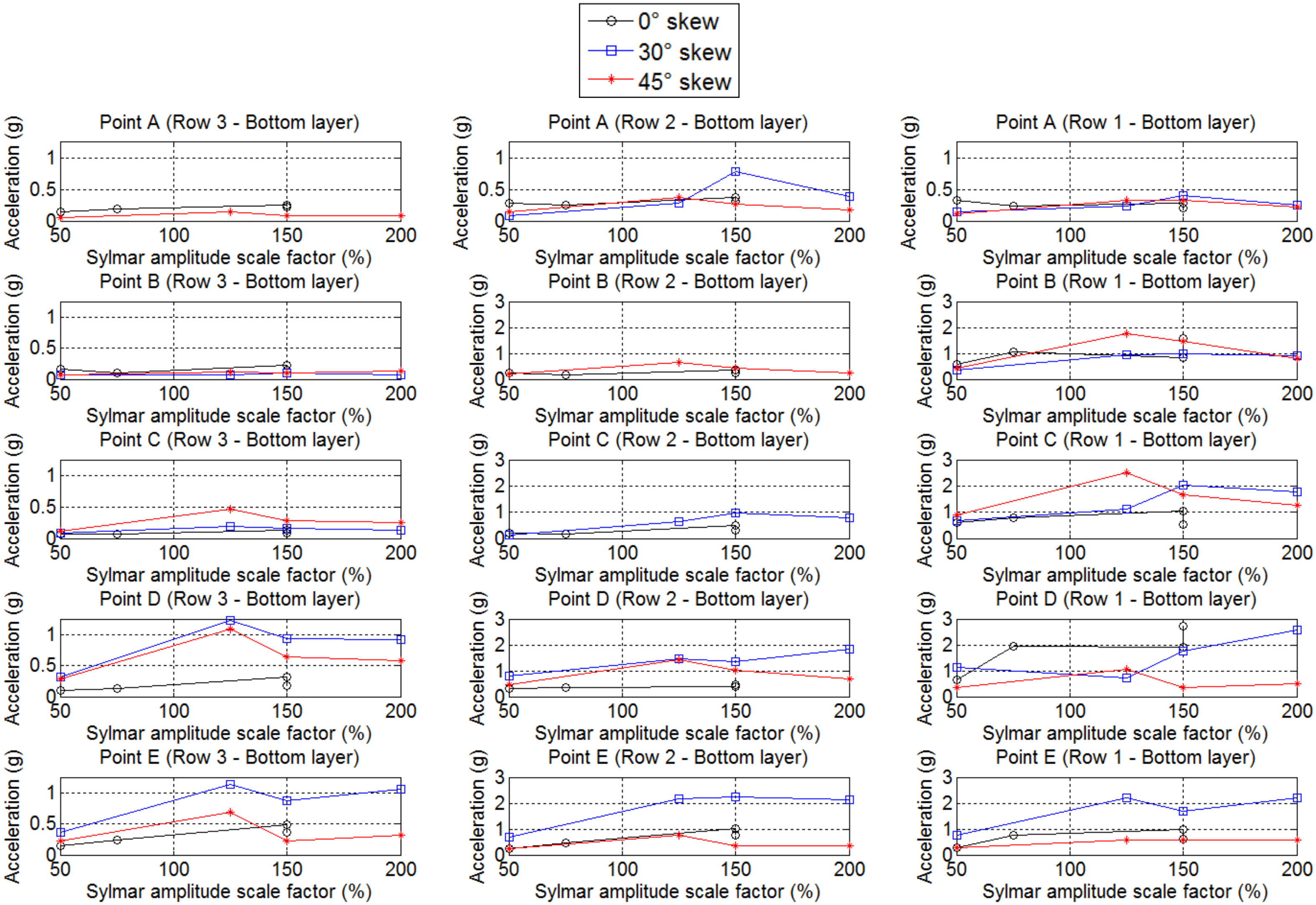

Figure 7-27 Skew angle effect on the maximum transverse (towards the east) soil accelerations in the bottom layer.

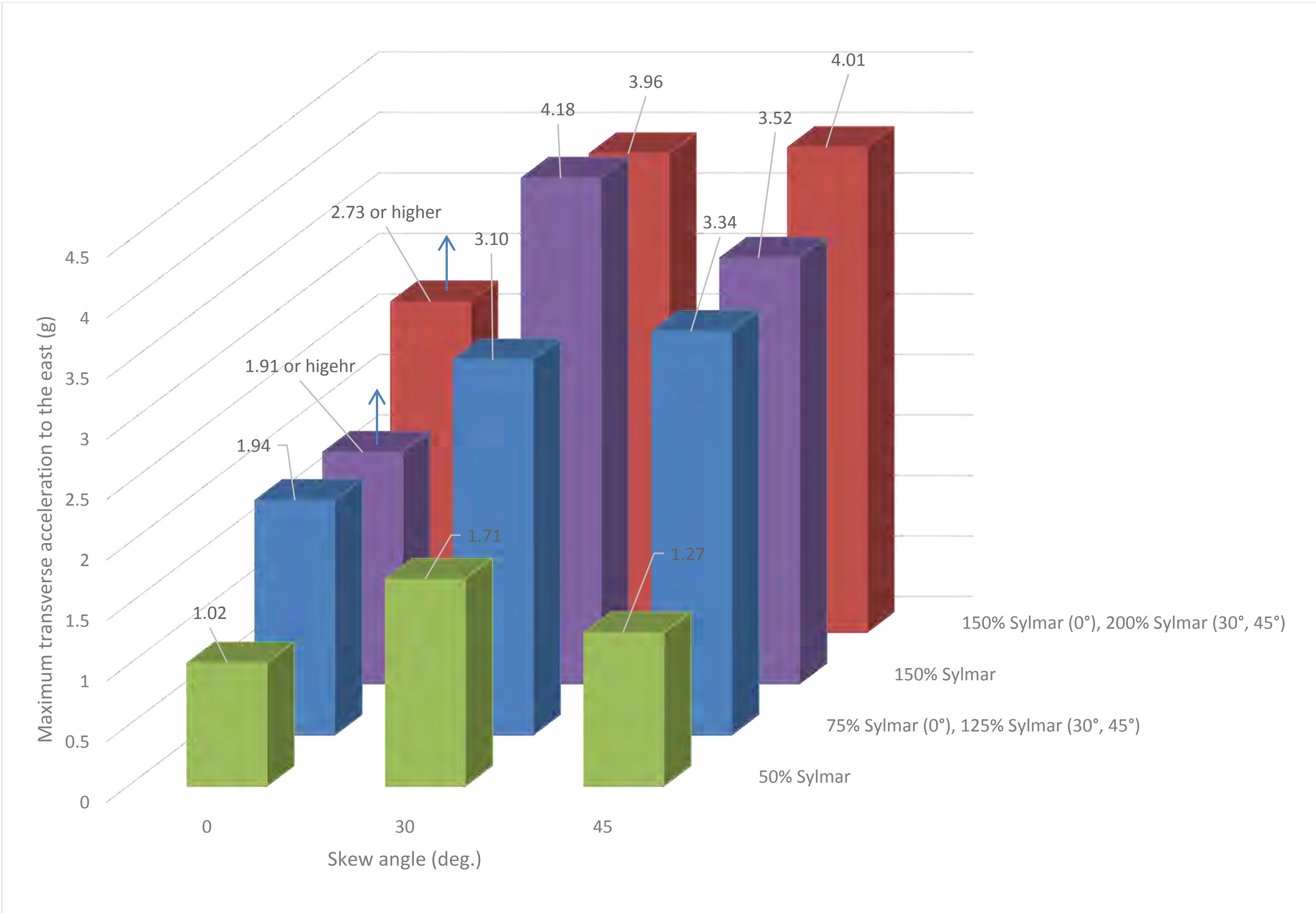

Figure 7-28 Skew angle effect on the maximum transverse (towards the east) soil accelerations.

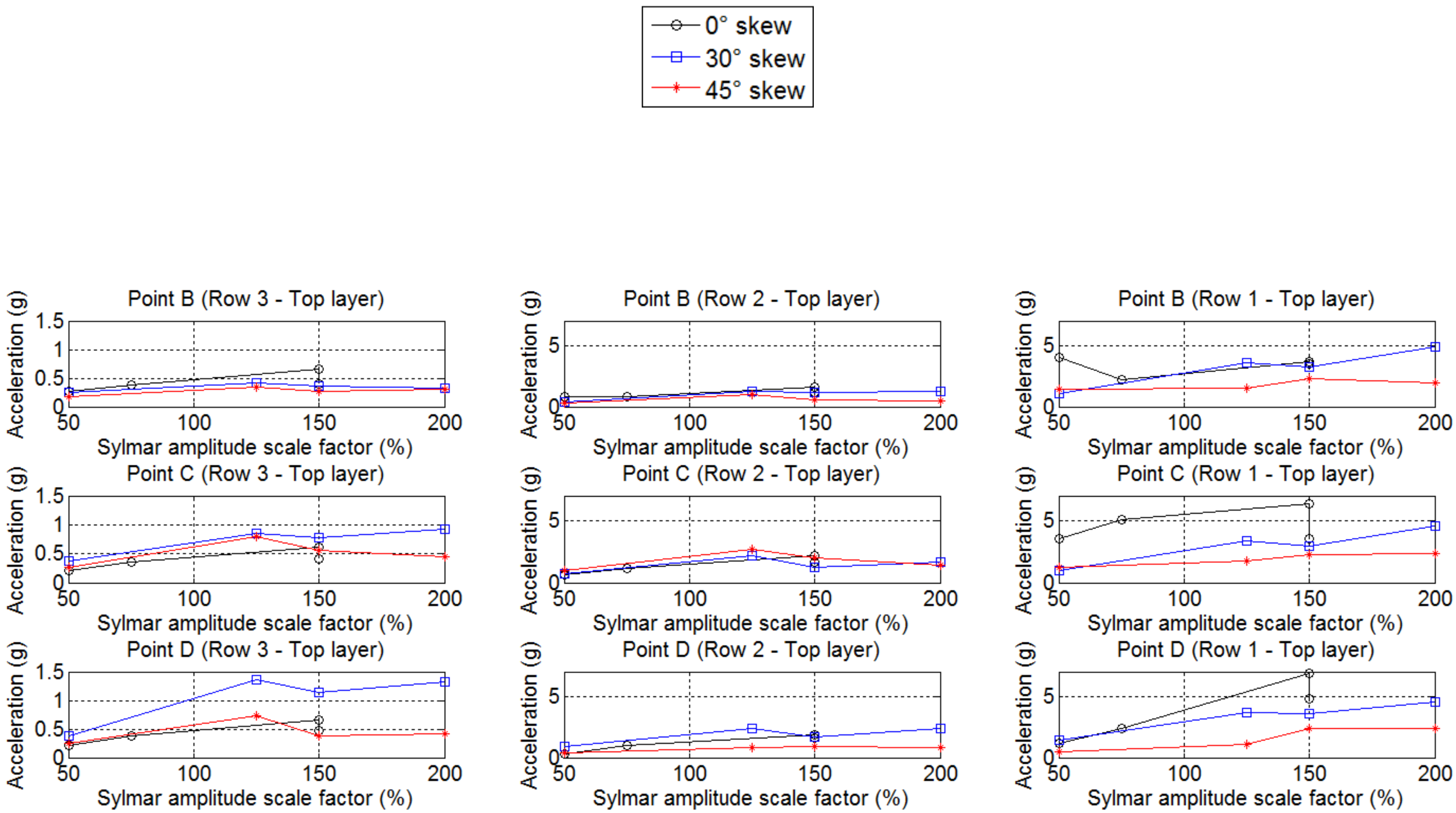

Figure 7-29 Skew angle effect on the maximum vertical (upward) soil accelerations in the top layer.

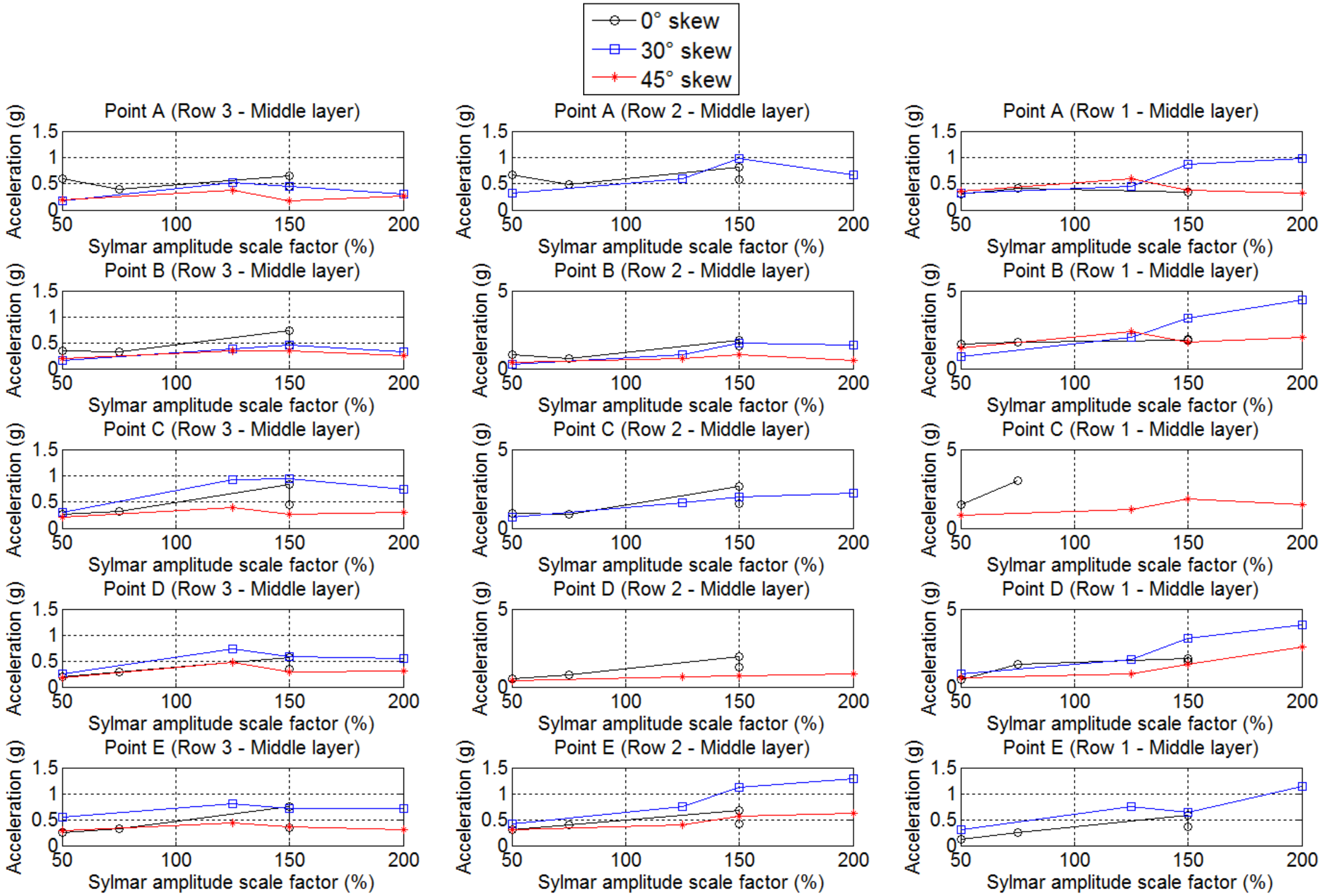

Figure 7-30 Skew angle effect on the maximum vertical (upward) soil accelerations in the middle layer.

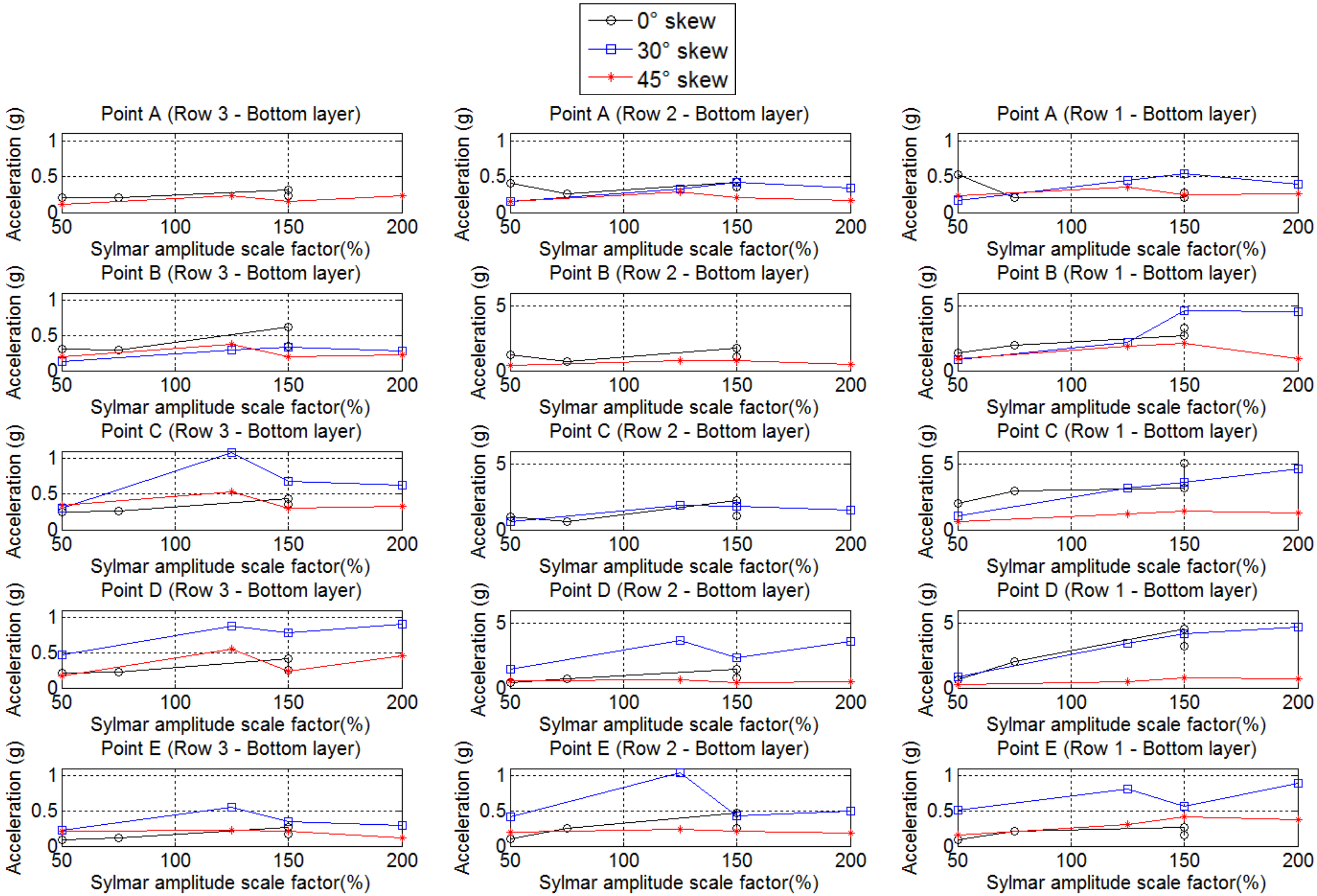

Figure 7-31 Skew angle effect on the maximum vertical (upward) soil accelerations in the bottom layer.

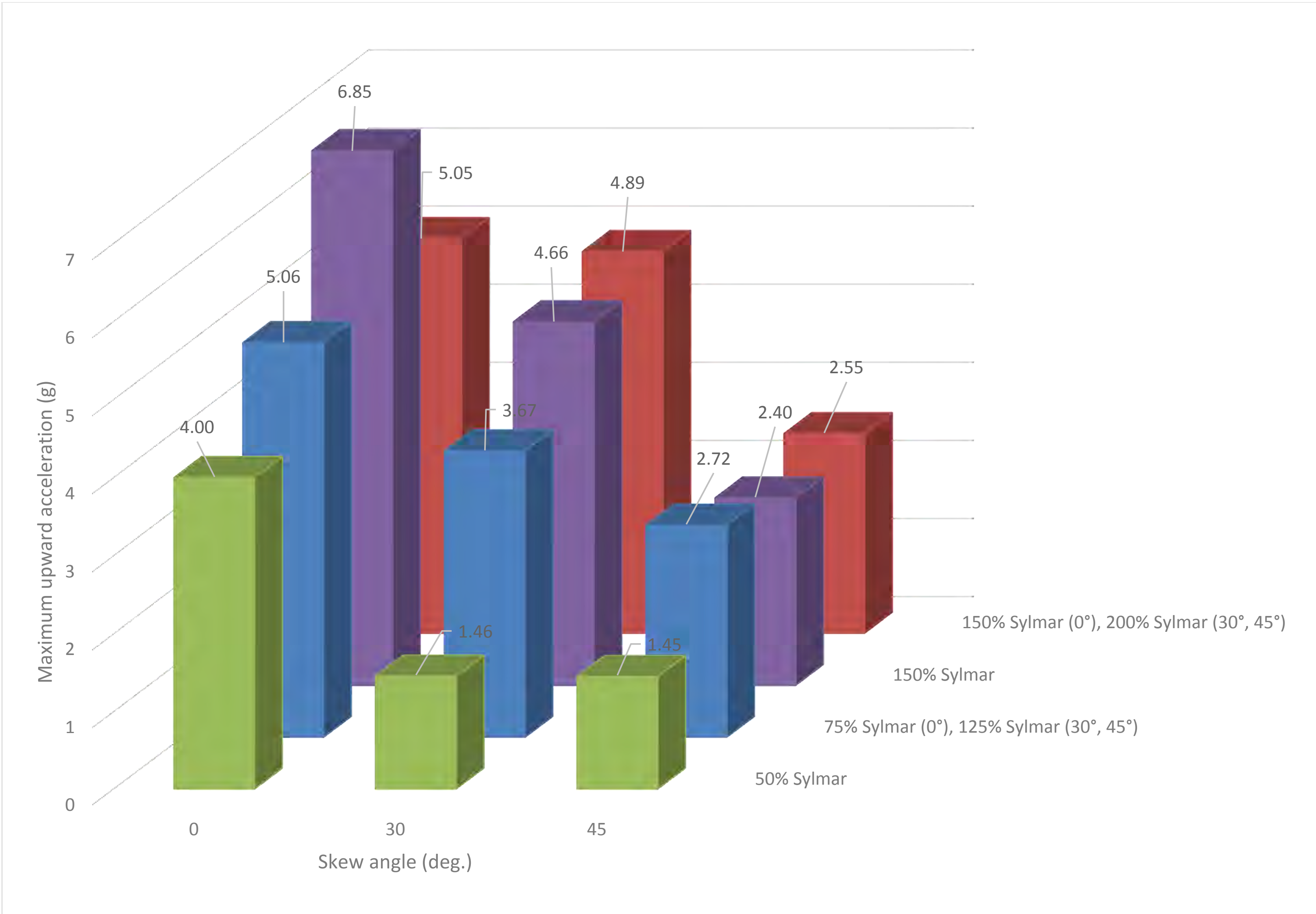

Figure 7-32 Skew angle effect on the maximum vertical (upward) soil accelerations.

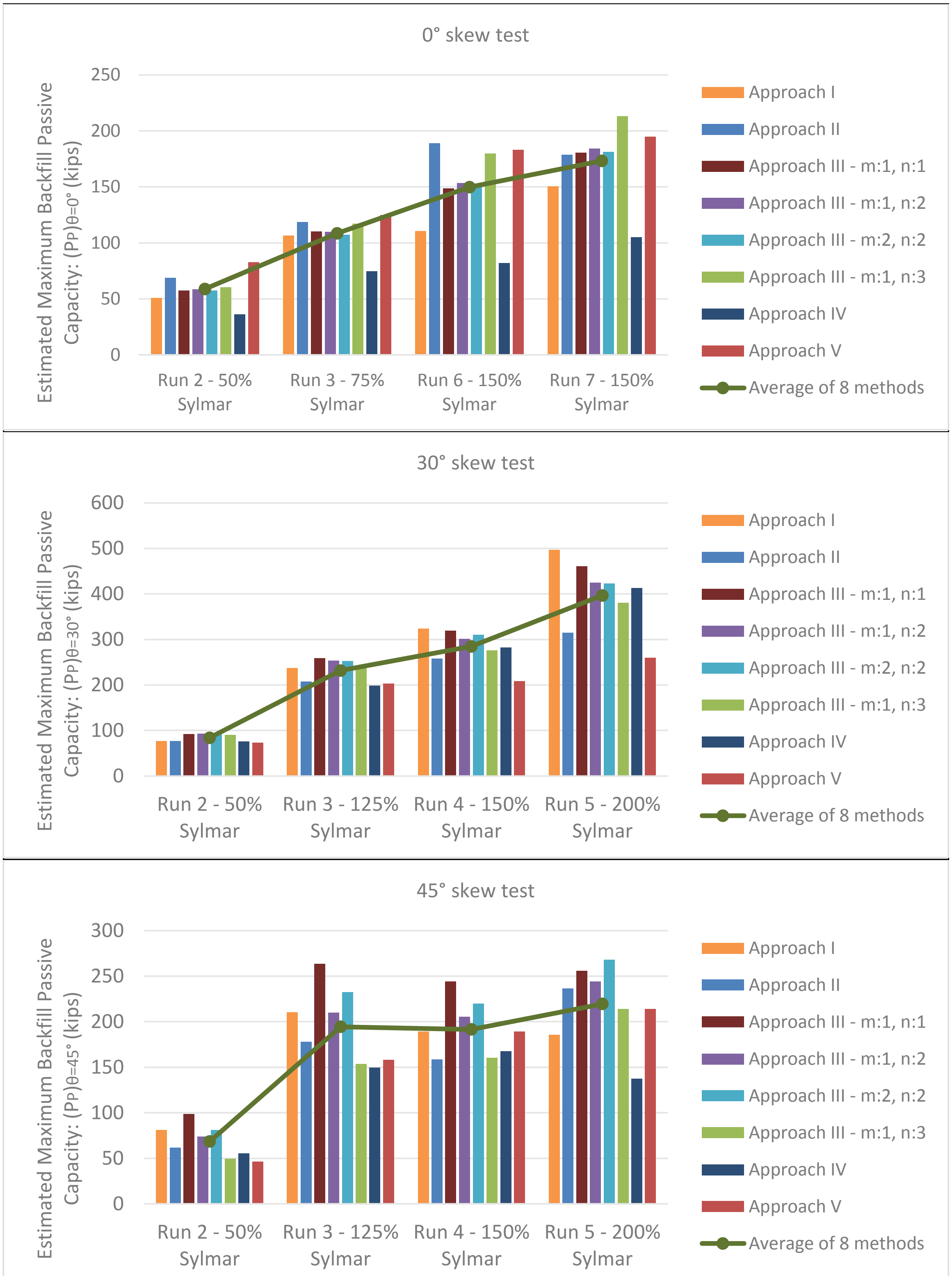

Figure 7-33 Estimated maximum backfill passive capacity.

Run 2 – 50%	Run 3 – 75%
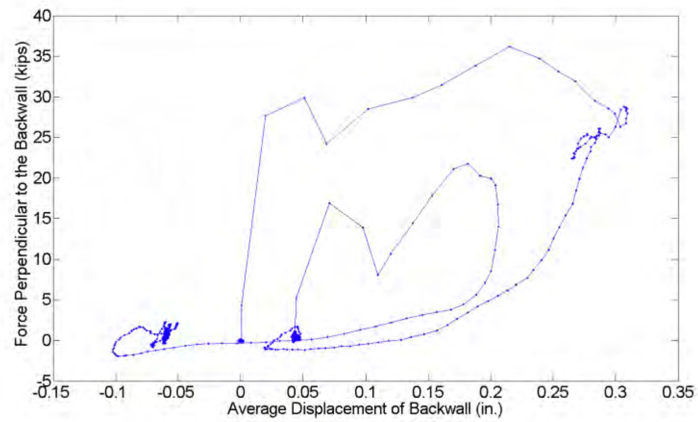	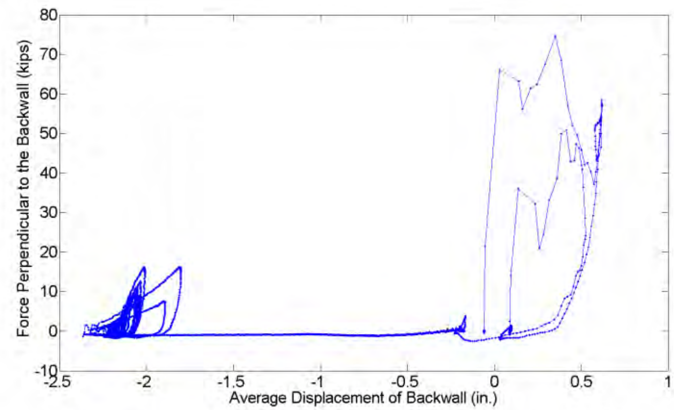
Run 6 – 150%	**Run 7 – 150%**
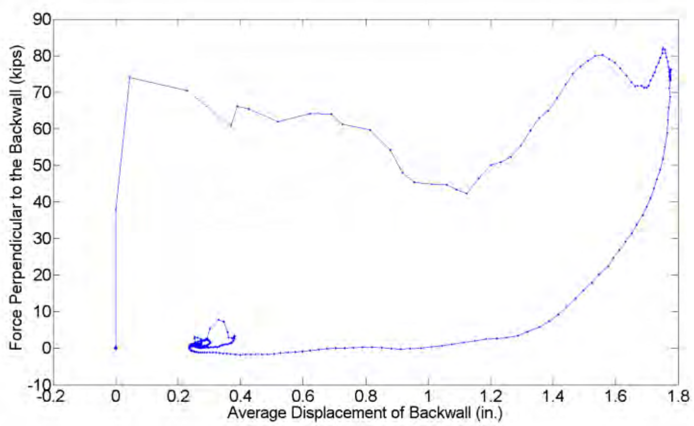	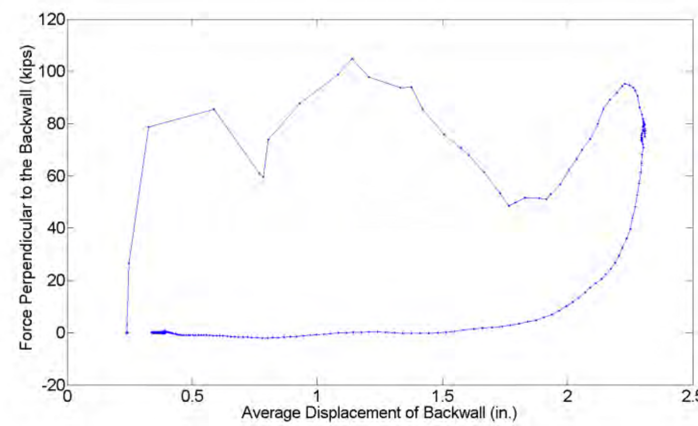

Figure 7-34 Backfill force-displacement (approach IV) for the 0° skew test.

Run 2 – 50%	Run 3 – 125%
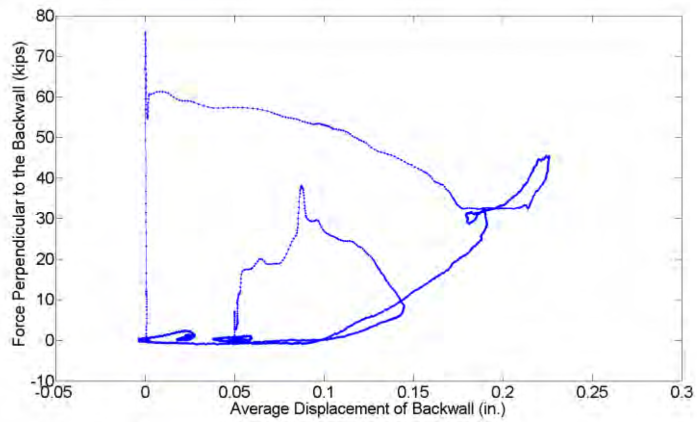	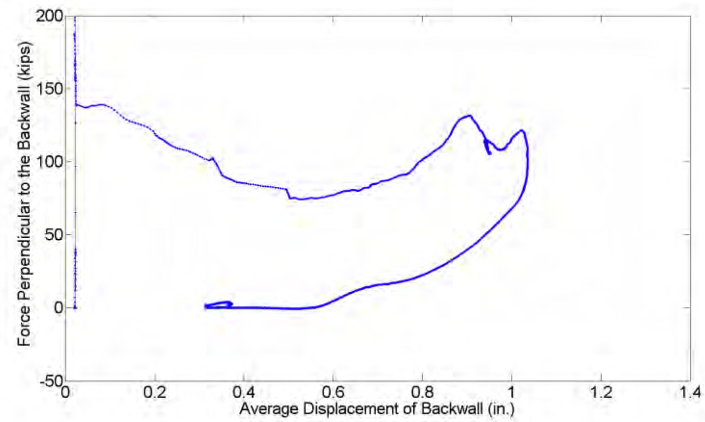
Run 4 – 150%	**Run 5 – 200%**
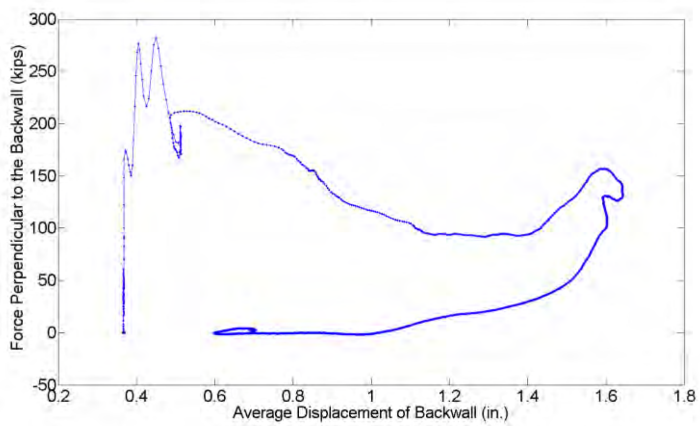	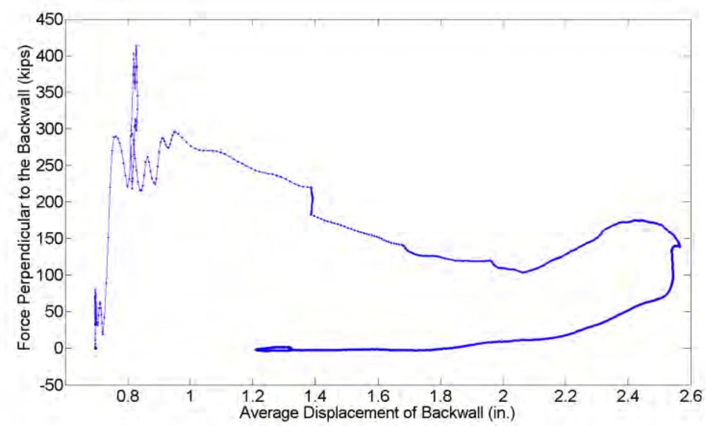

Figure 7-35 Backfill force-displacement (approach IV) for the 30° skew test.

Run 2 – 50%	Run 3 – 125%

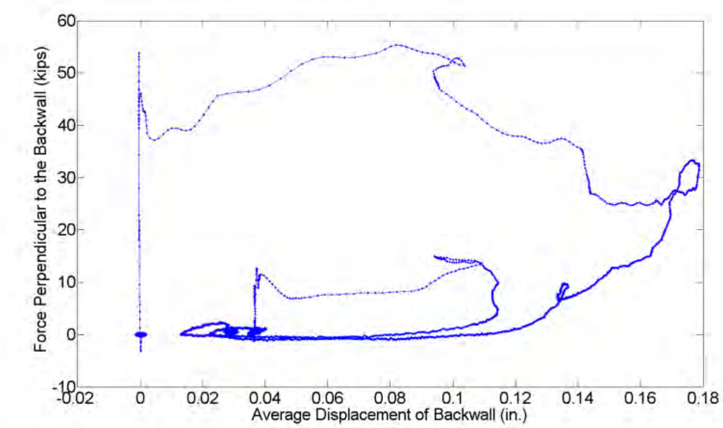

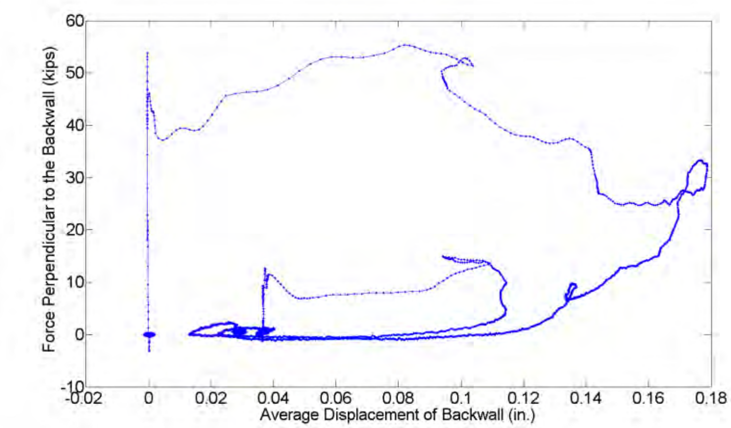

Run 4 – 150%	Run 5 – 200%

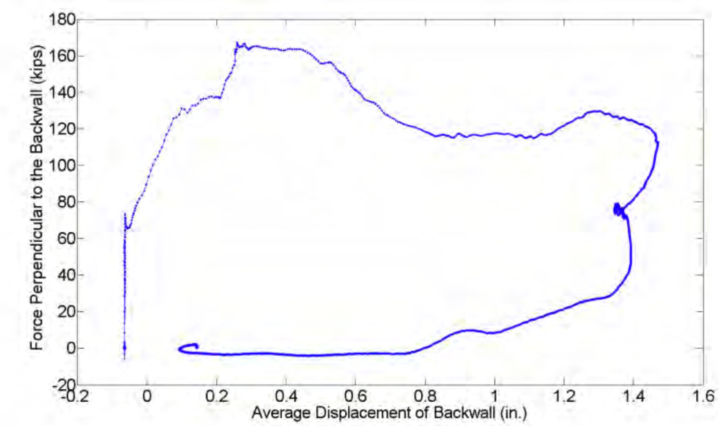

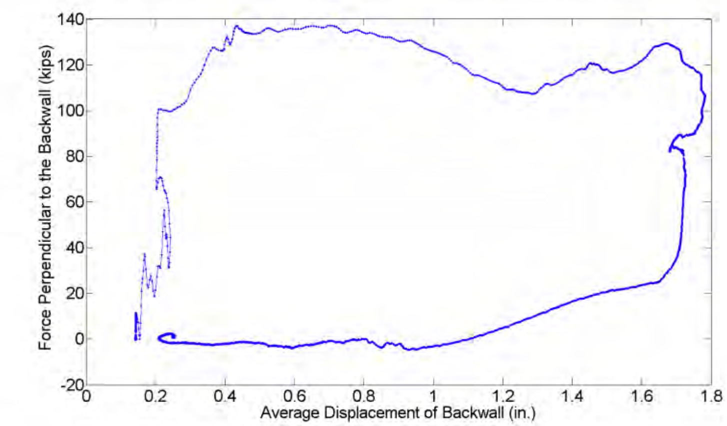

Figure 7-36 Backfill force-displacement (approach IV) for the 45° skew test.

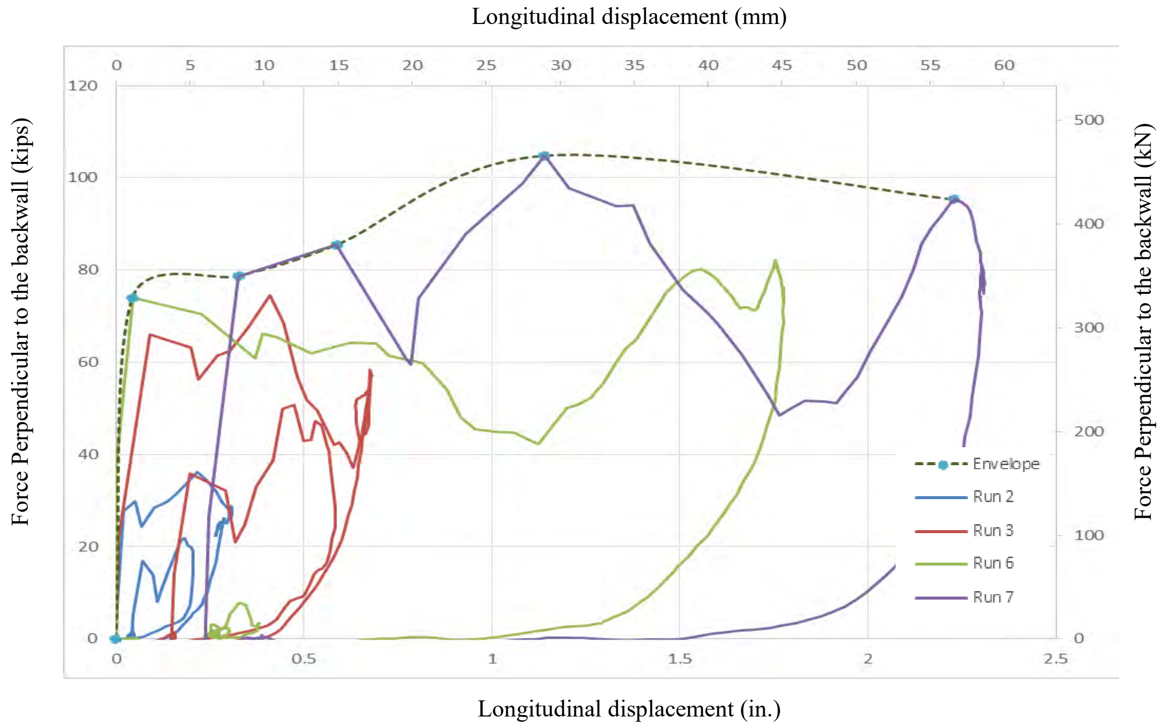

Figure 7-37 Backfill force-displacement envelope (approach IV) for the 0° skew test.

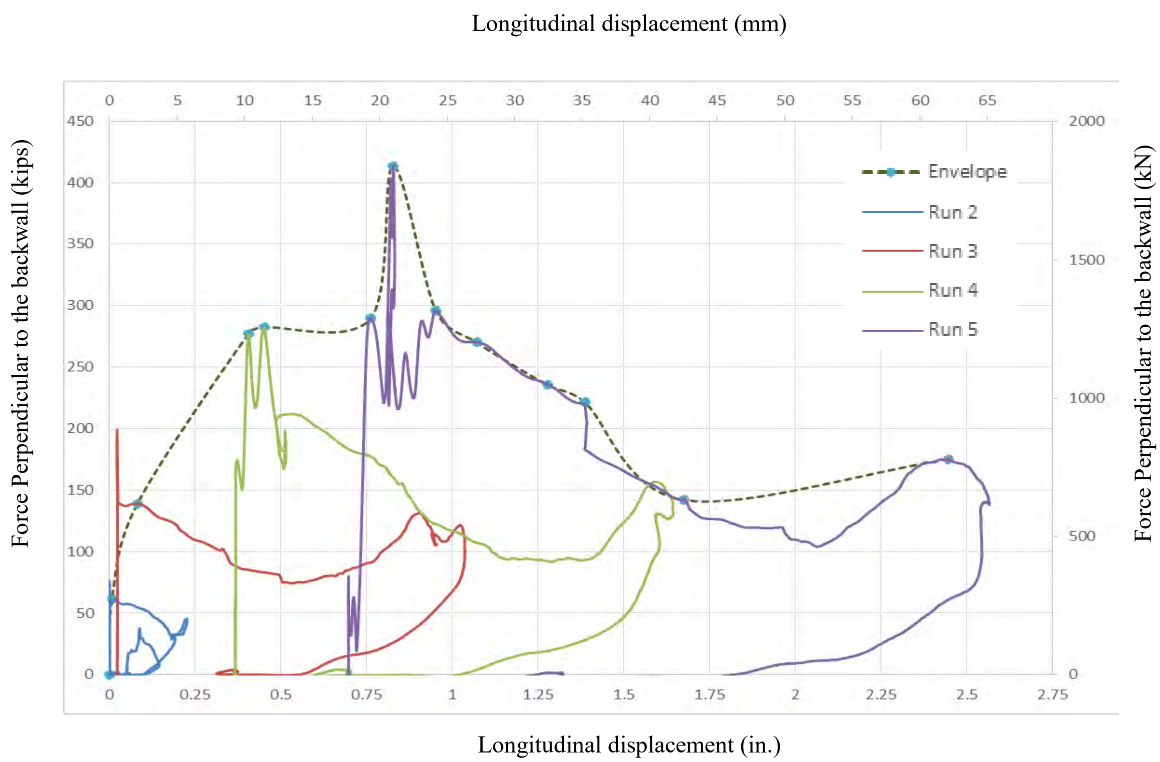

Figure 7-38 Backfill force-displacement envelope (approach IV) for the 30° skew test.

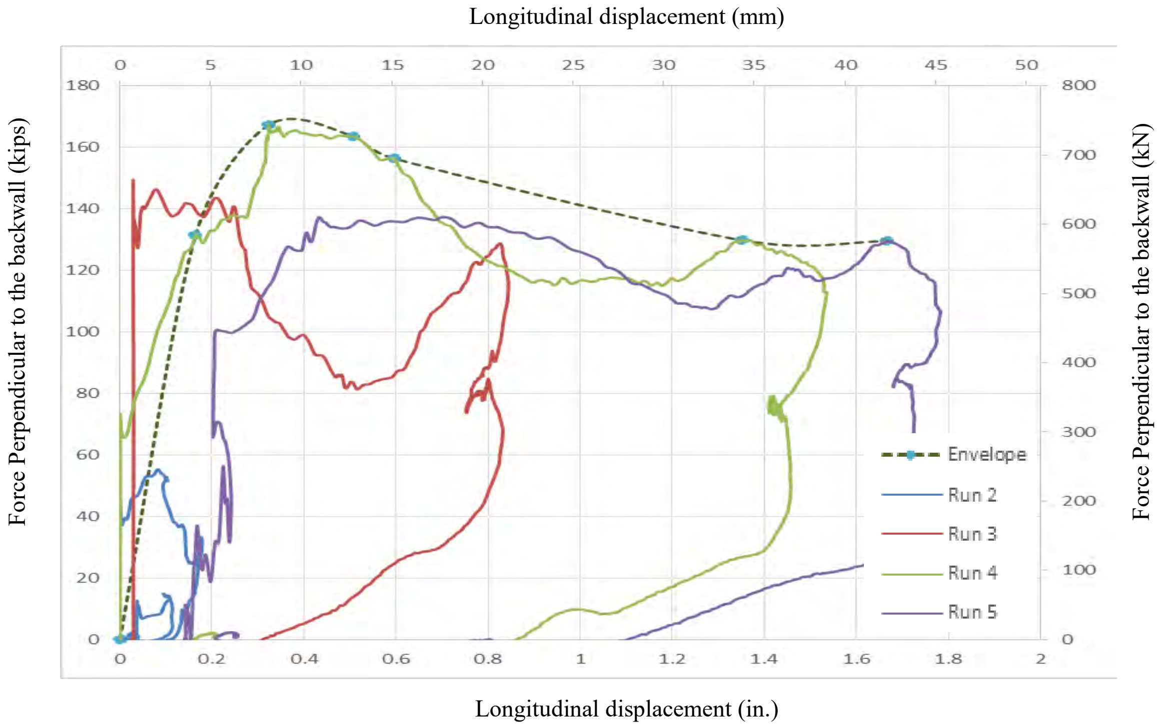

Figure 7-39 Backfill force-displacement envelope (approach IV) for the 45° skew test.

Run 2 – 50%	Run 3 – 75%
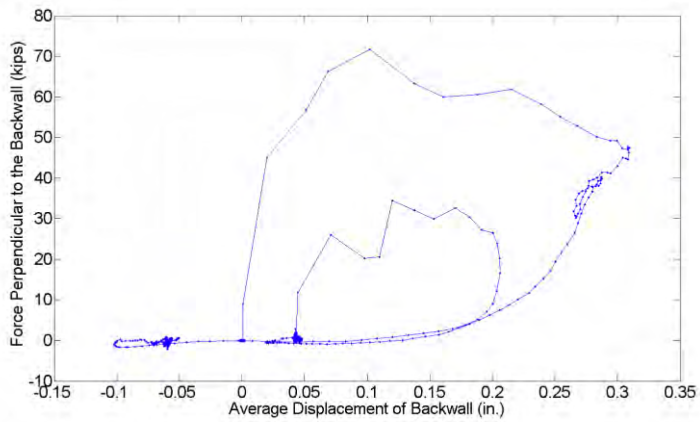	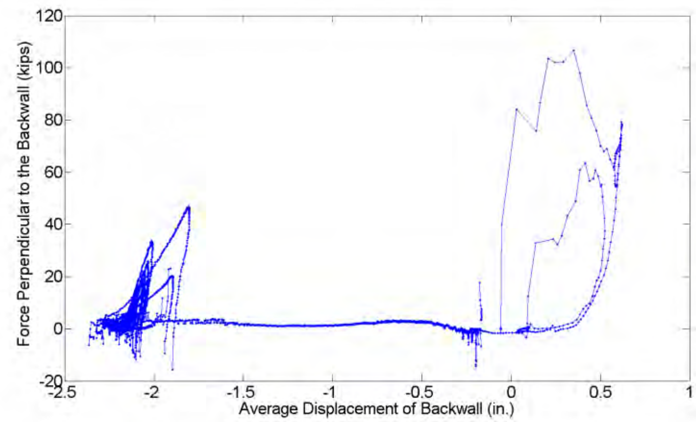
Run 6 – 150%	**Run 7 – 150%**
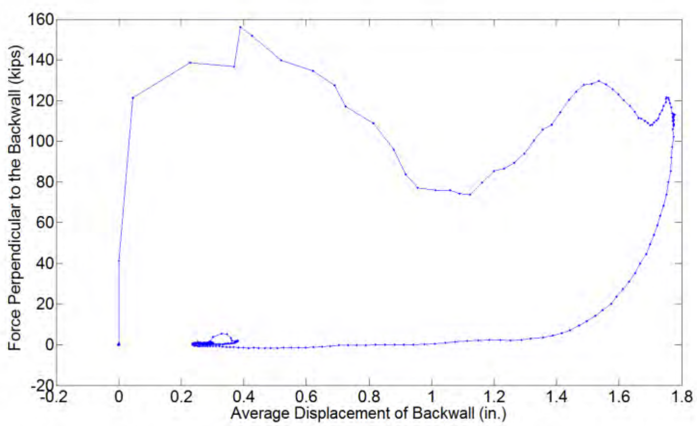	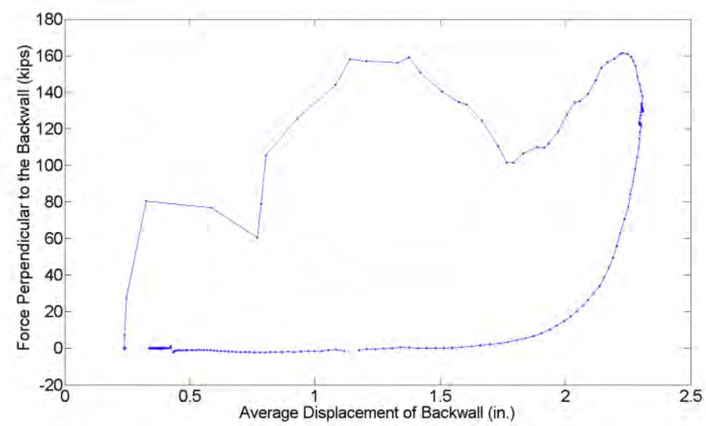

Figure 7-40 Backfill force-displacement (approach V) for the 0° skew test.

Run 2 – 50%	Run 3 – 125%

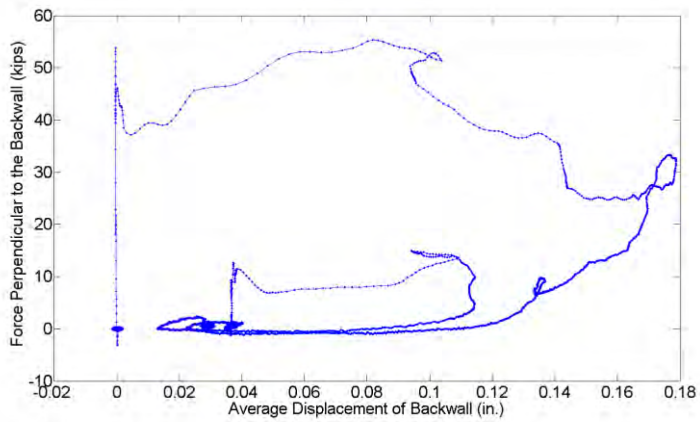

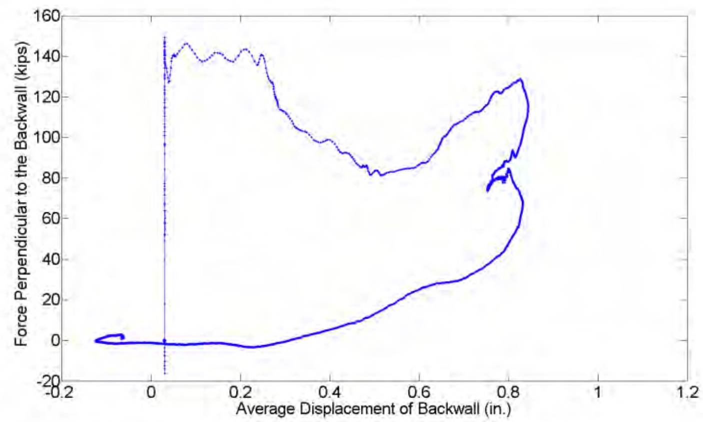

Run 4 – 150%	Run 5 – 200%

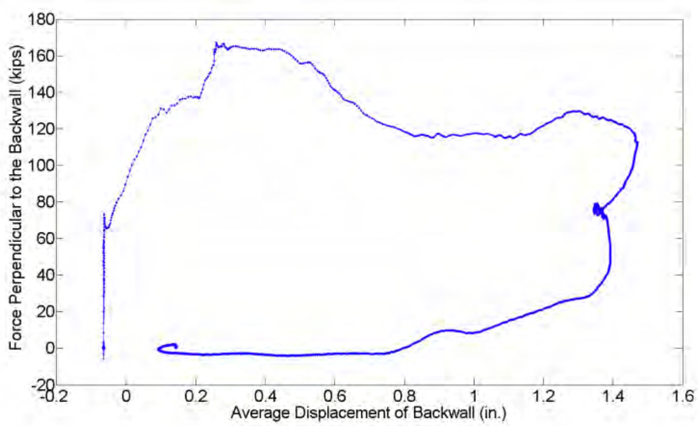

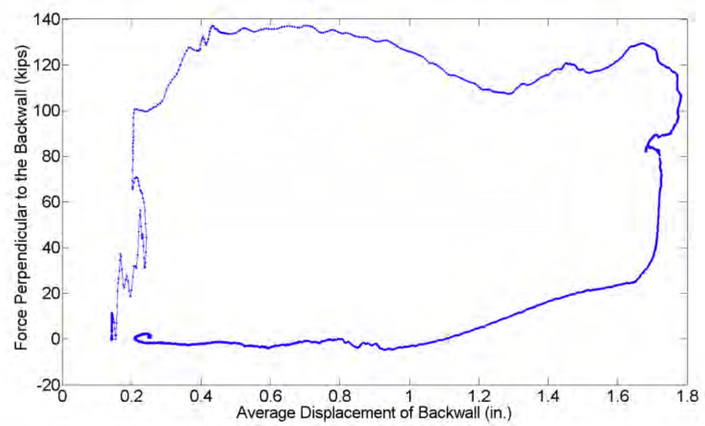

Figure 7-41 Backfill force-displacement (approach V) for the 30° skew test.

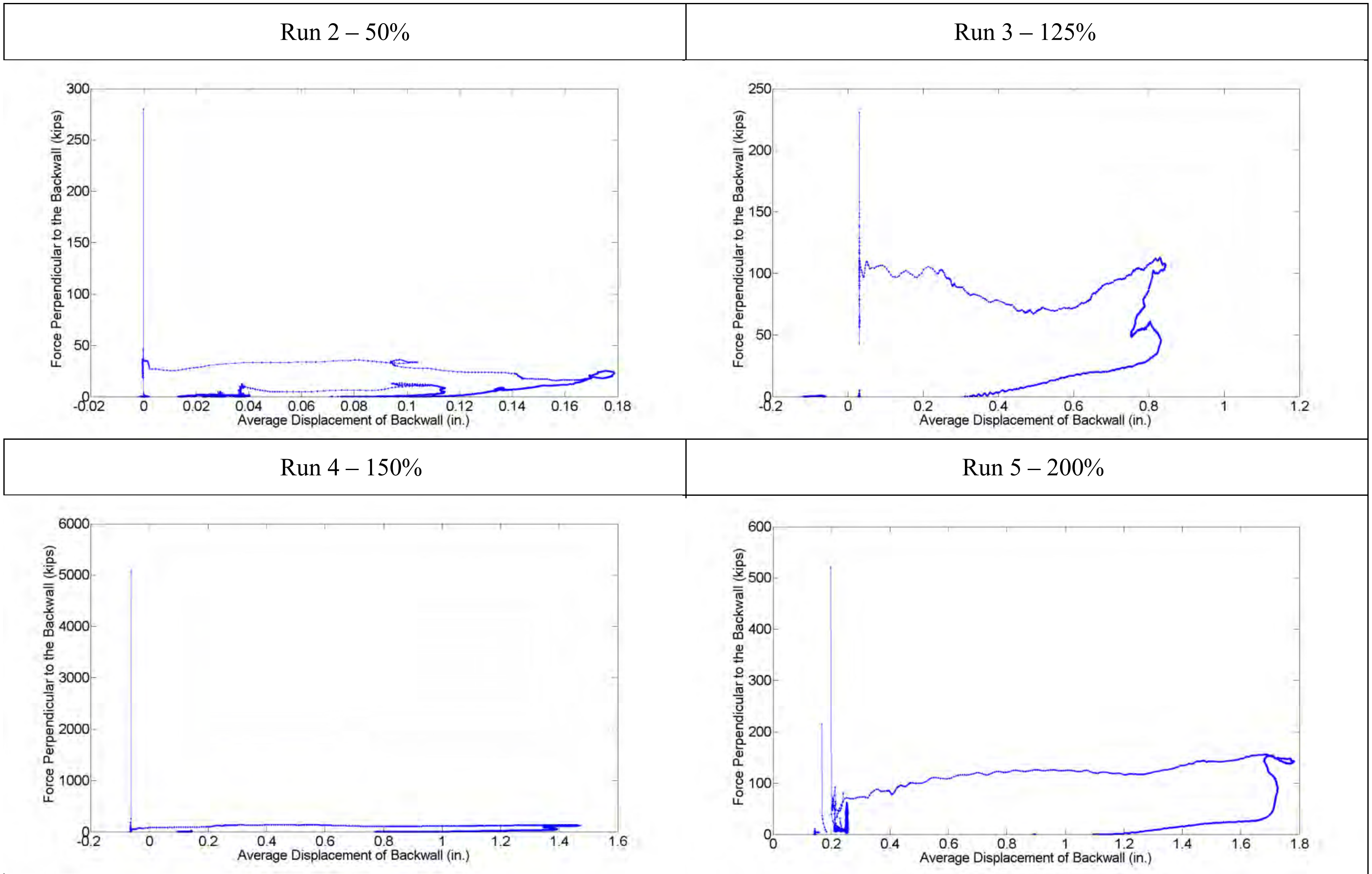

Figure 7-42 Backfill force-displacement (approach IV) for the 45° skew test.

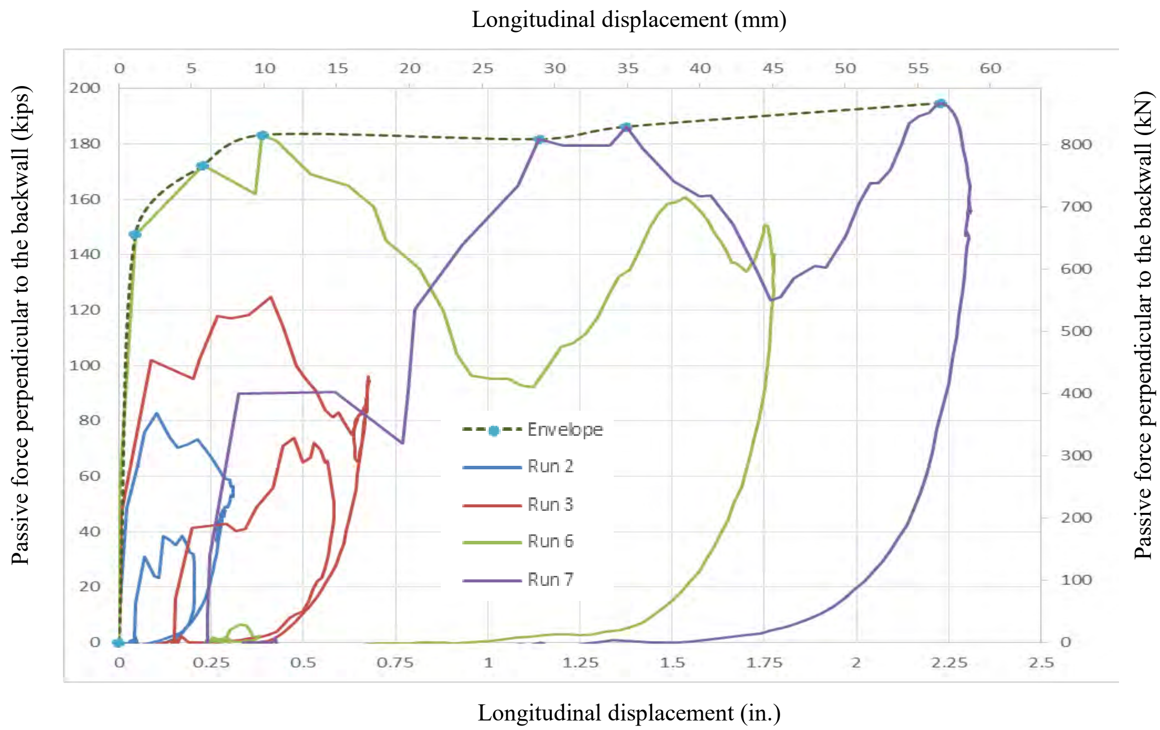

Figure 7-43 Backfill force-displacement envelope (approach V) for the 0° skew test.

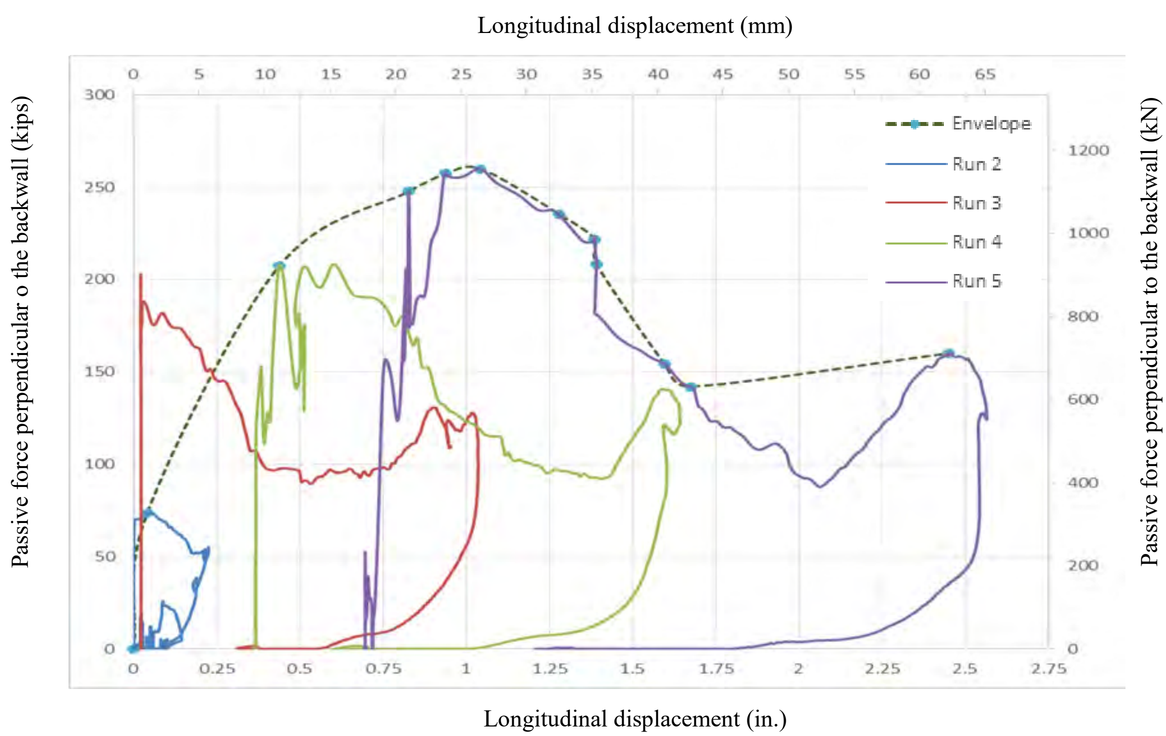

Figure 7-44 Backfill force-displacement envelope (approach V) for the 30° skew test.

Longitudinal displacement (mm)

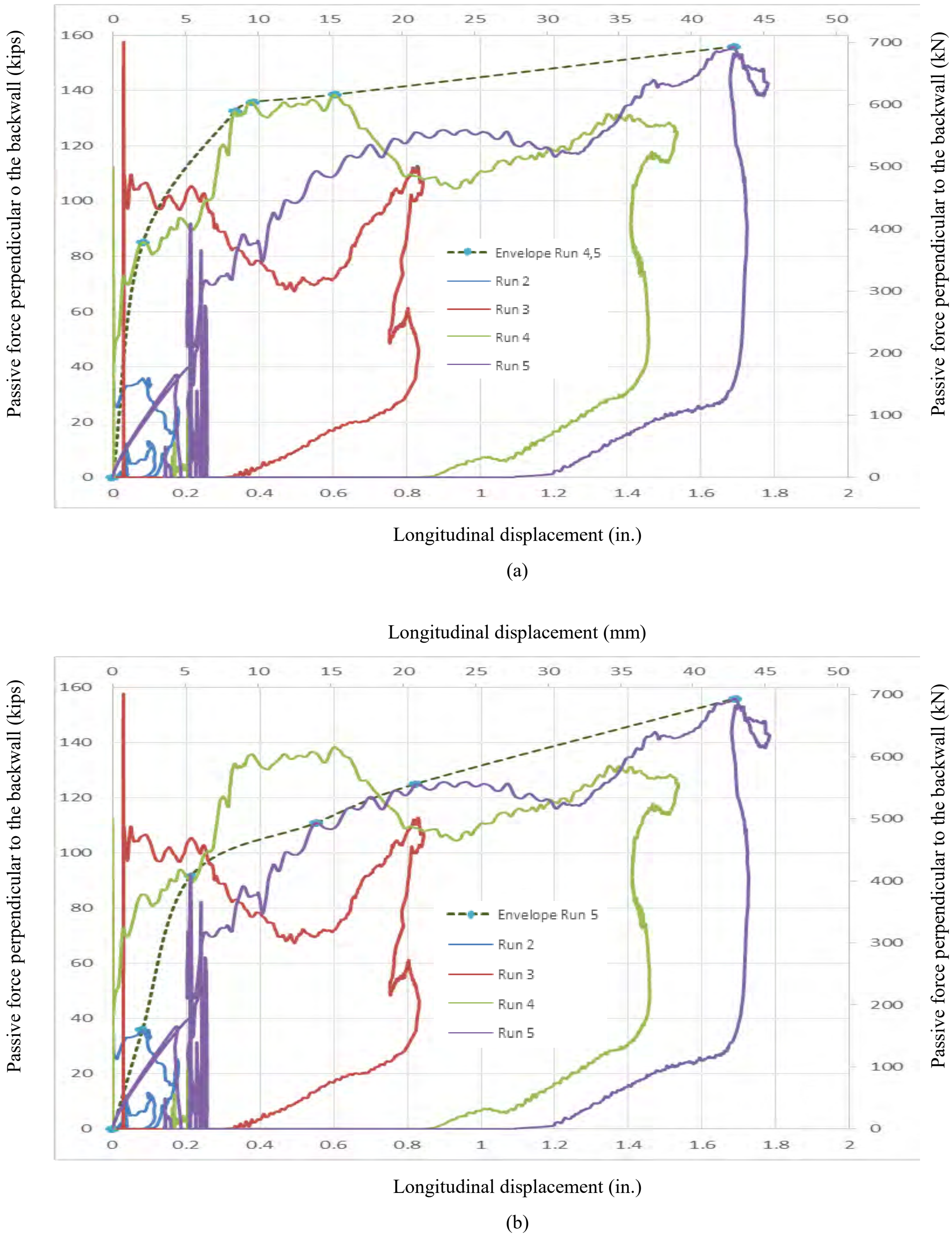

Figure 7-45 Backfill force-displacement envelope (approach IV) for the 45° skew test: (a) Run 4 and 5, and (b) Run 5 only.

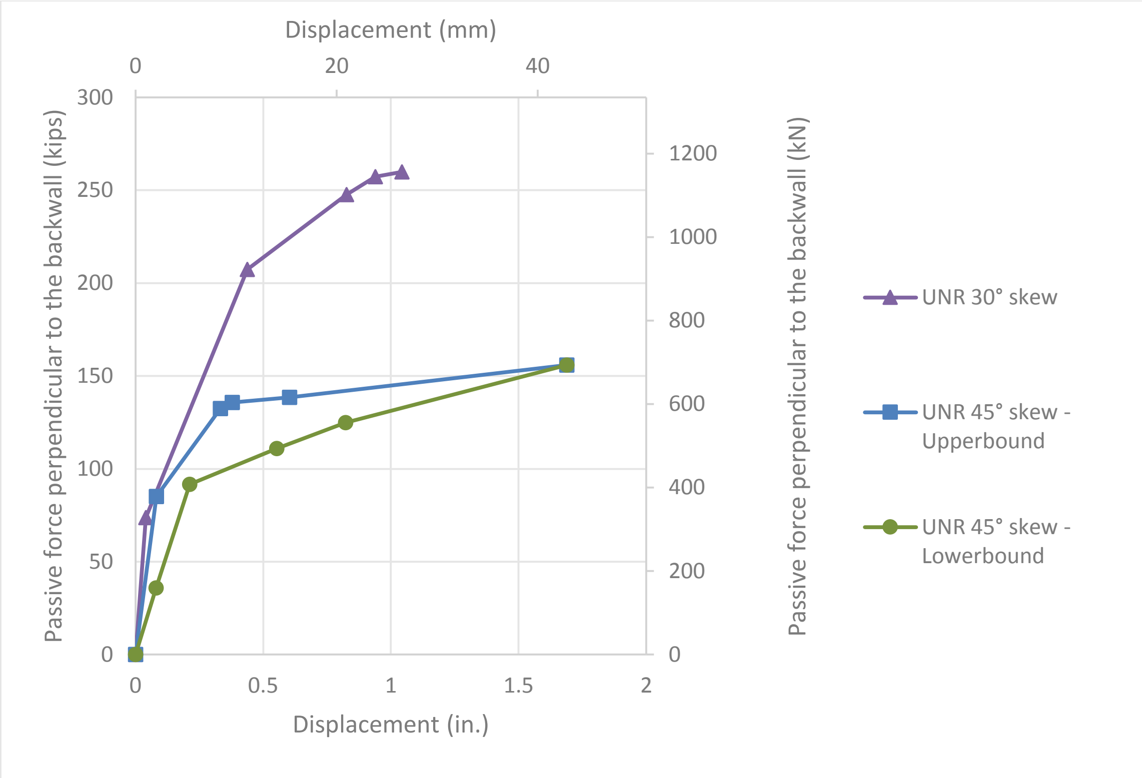

Figure 7-46 Comparison of UNR force-displacement envelopes (approach V).

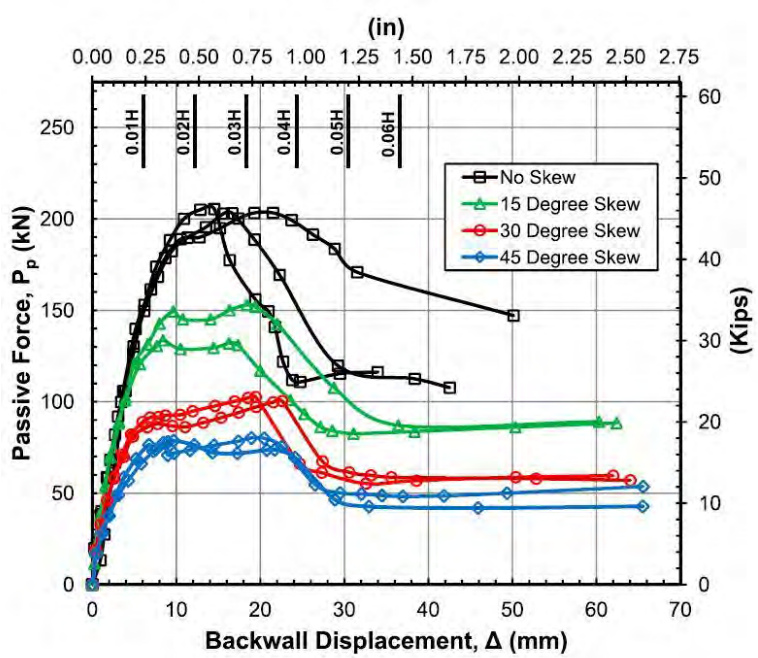

Figure 7-47 Passive capacity curves of BYU lab test for w/H=2 (Jessee, 2012; Rollins & Jessee, 2013).

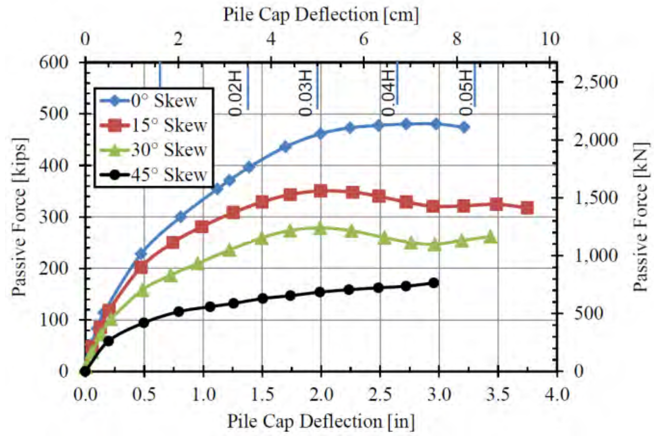

Figure 7-48 Lateral force-displacement relationship of BYU field test for w/H=2 (Marsh, 2013; Marsh et al., 2013).

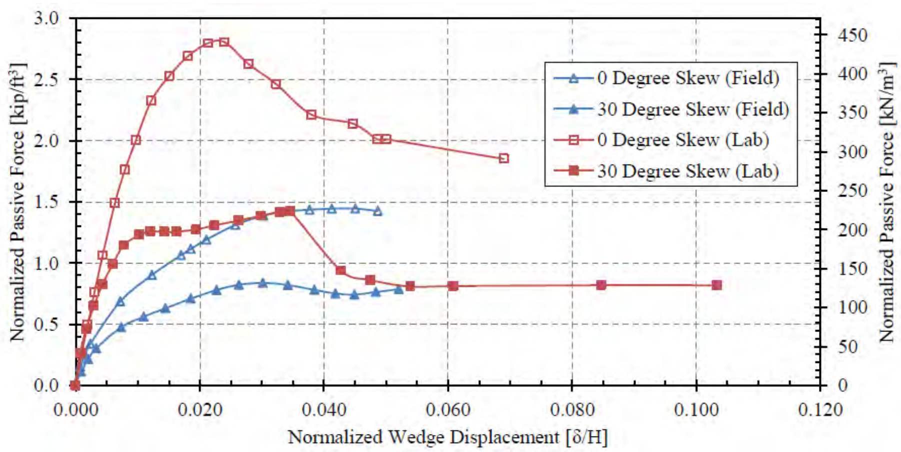

Figure 7-49 Lateral force-displacement relationship of BYU lab and field tests for w/H=2 (Marsh et al., 2012; Marsh et al., 2013).

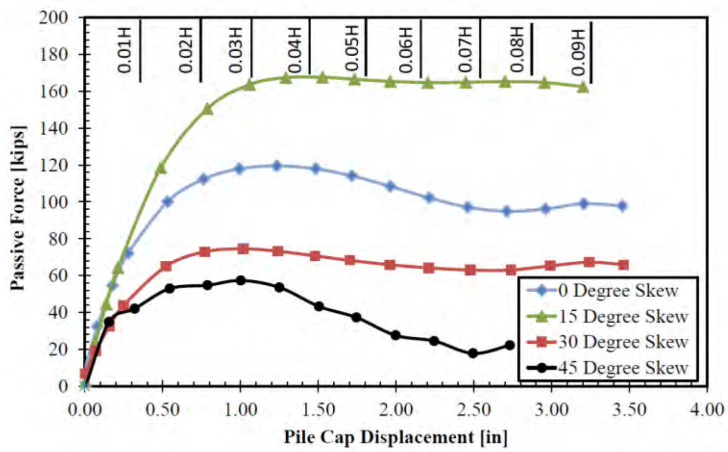

Figure 7-50 Lateral force-displacement relationship of BYU field test for w/H=3.7 (Palmer, 2013).

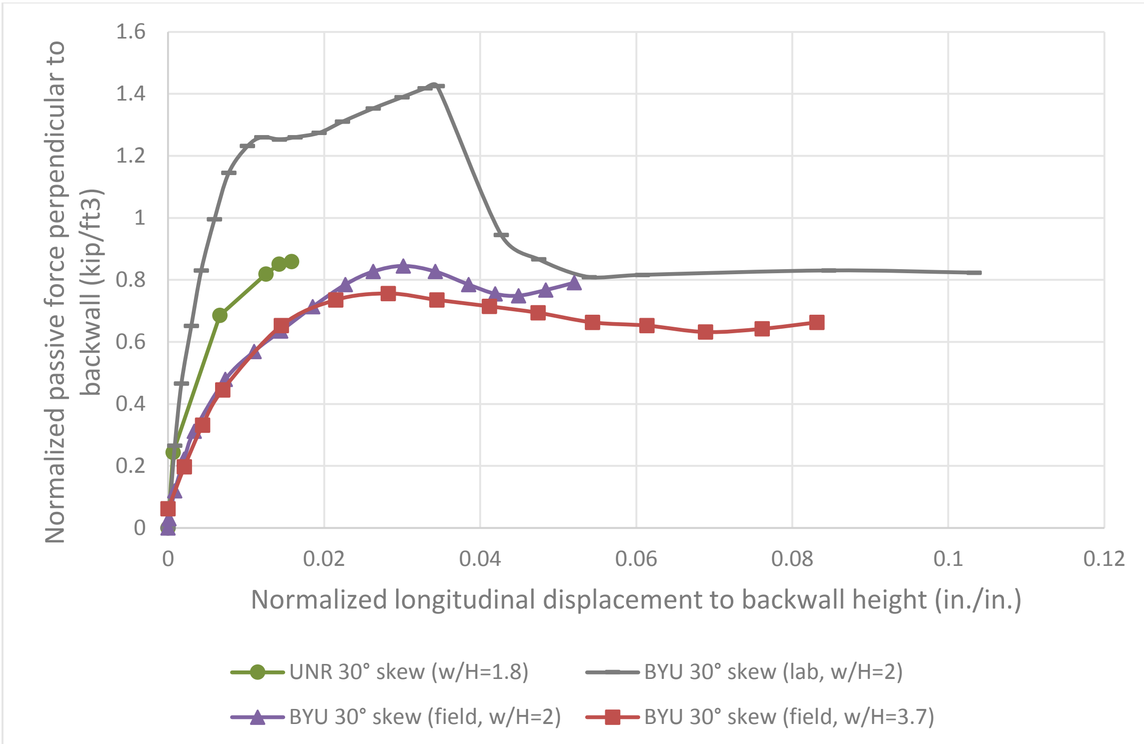

Figure 7-51 Lateral force-displacement relationship of UNR and BYU for the 30° skew test.

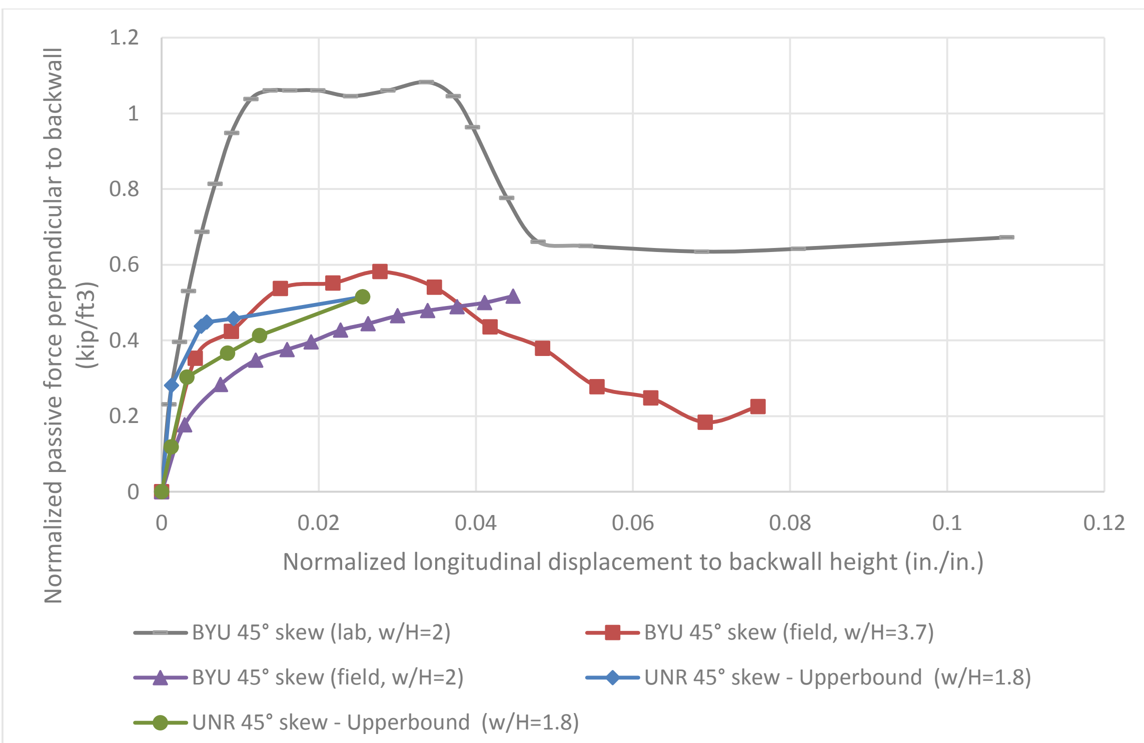

Figure 7-52 Lateral force-displacement relationship of UNR and BYU for the 45° skew test.

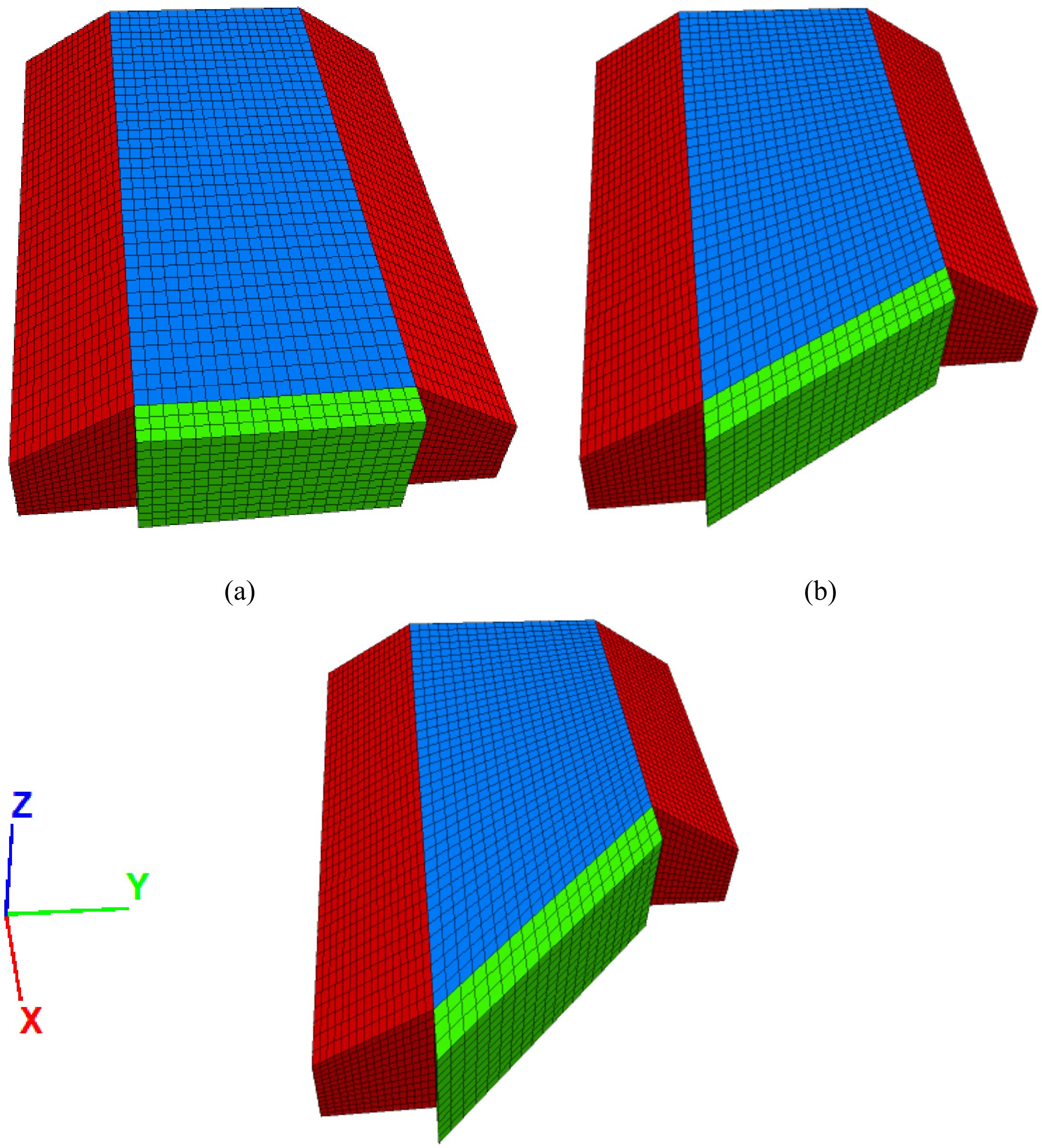

(a) (b)

(c)

Figure 8-1 FLAC3D model: (a) 0° skew, (b) 30° skew, and (c) 45° skew.

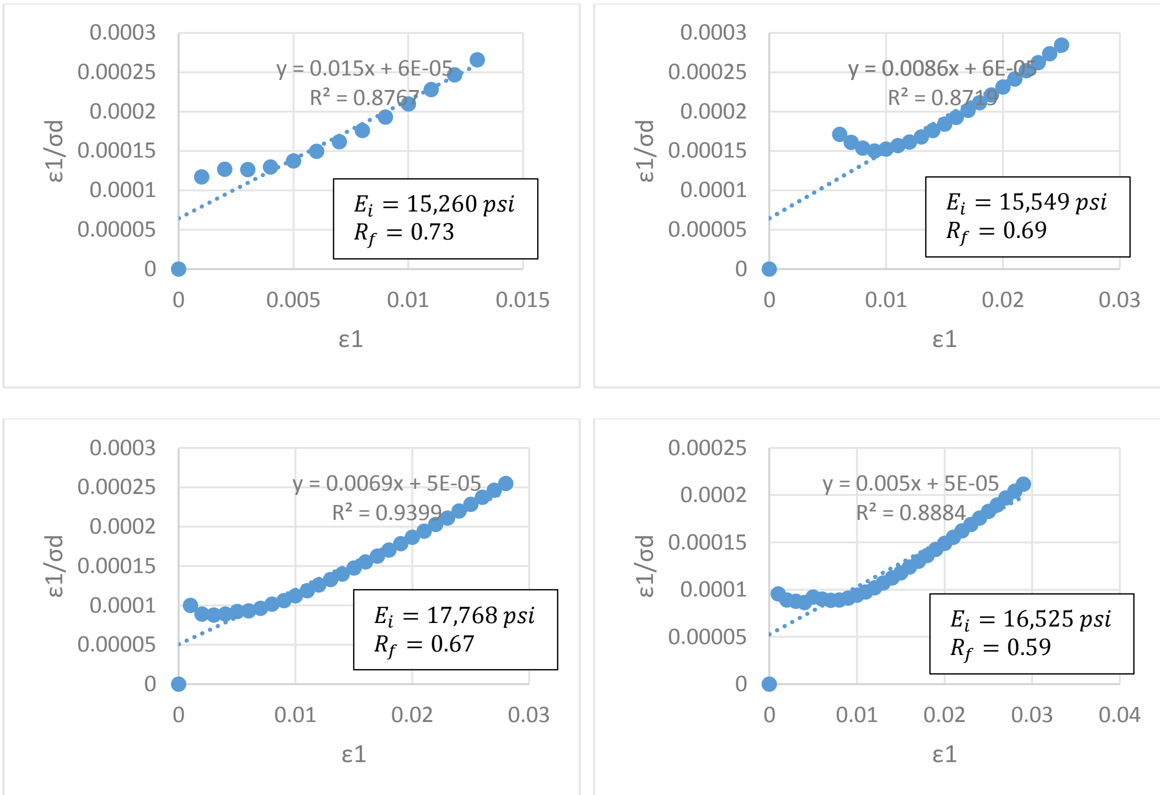

Figure 8-2 Duncan model parameters (E_i and R_f).

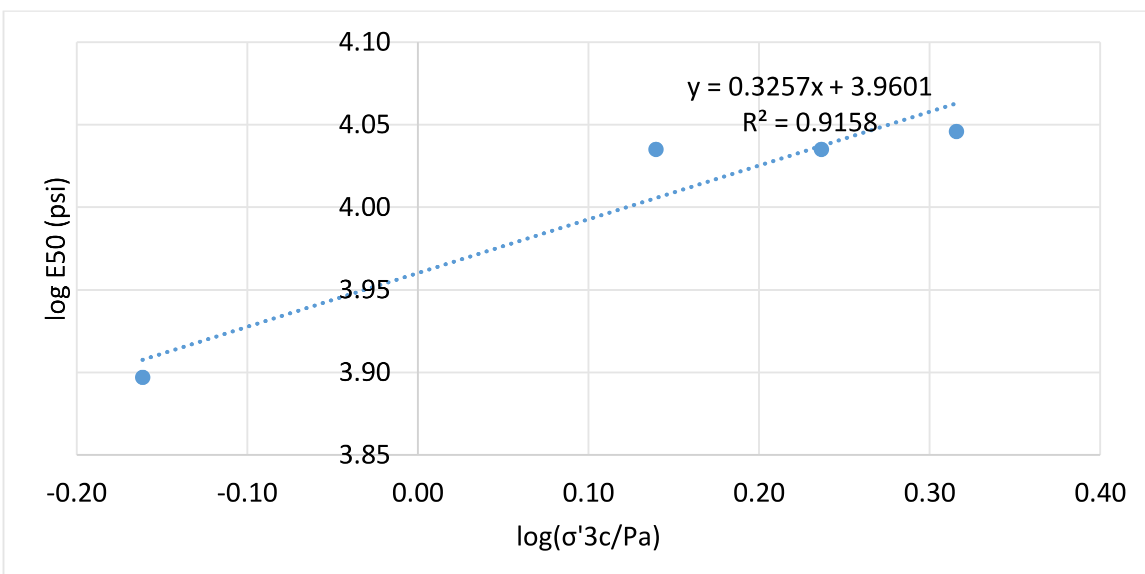

Figure 8-3 Duncan model parameters ($\log E_{50}^{ref}$ and n).

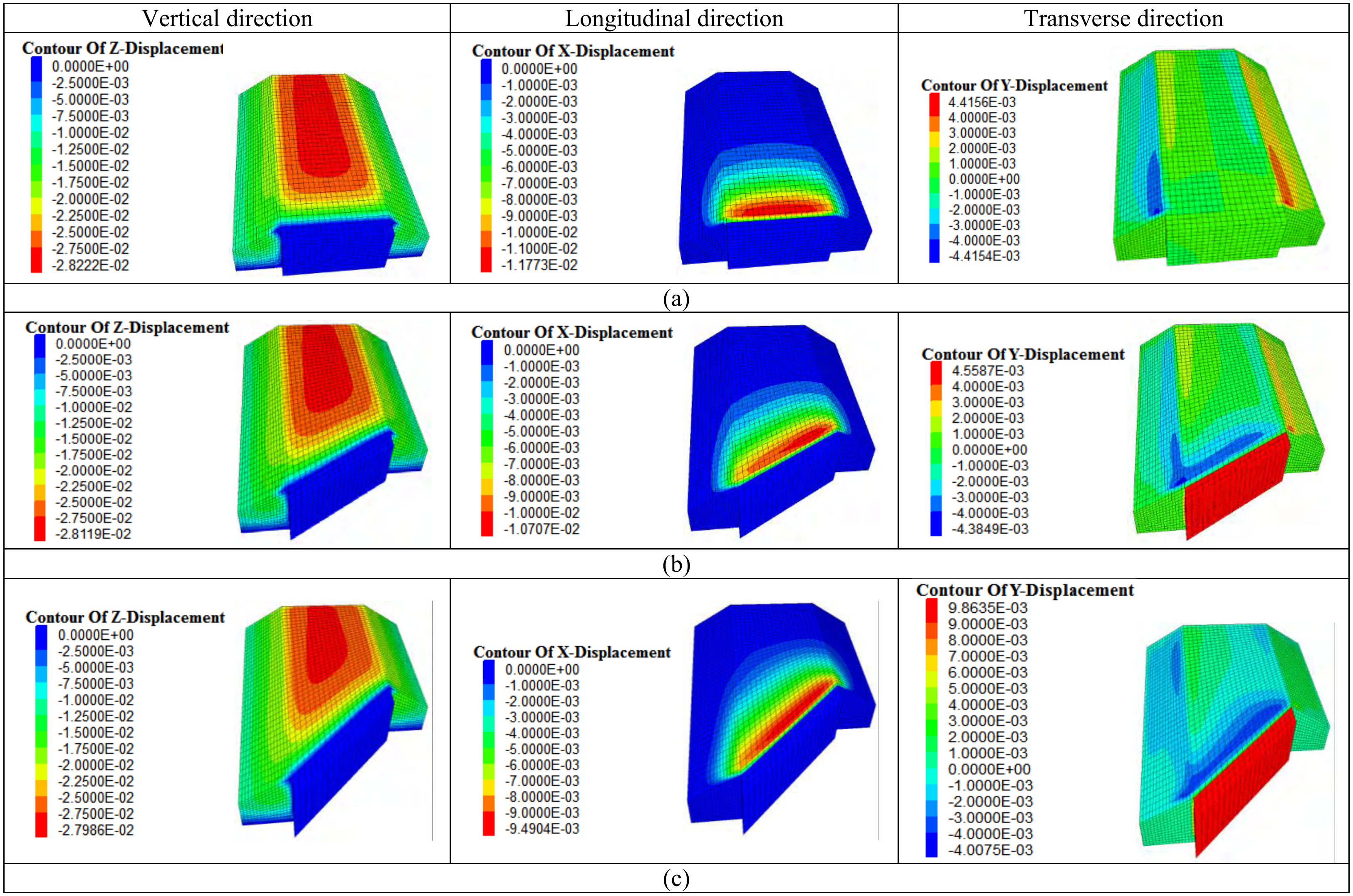

Figure 8-4 Displacements contours under gravity loading: (a) 0° skew, (b) 30° skew, and (c) 45° skew.

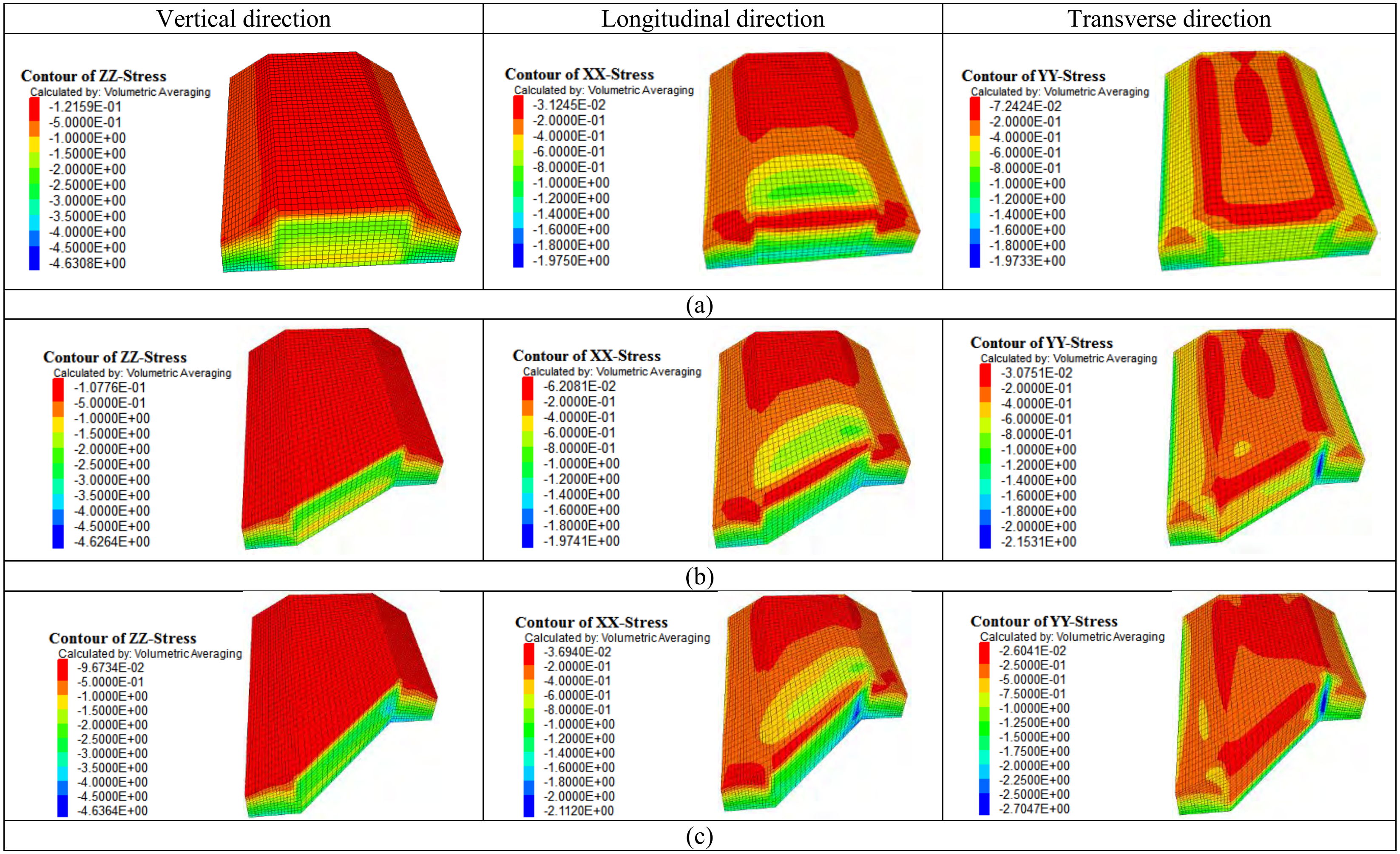

Figure 8-5 Stress contours under gravity loading: (a) 0° skew, (b) 30° skew, and (c) 45° skew.

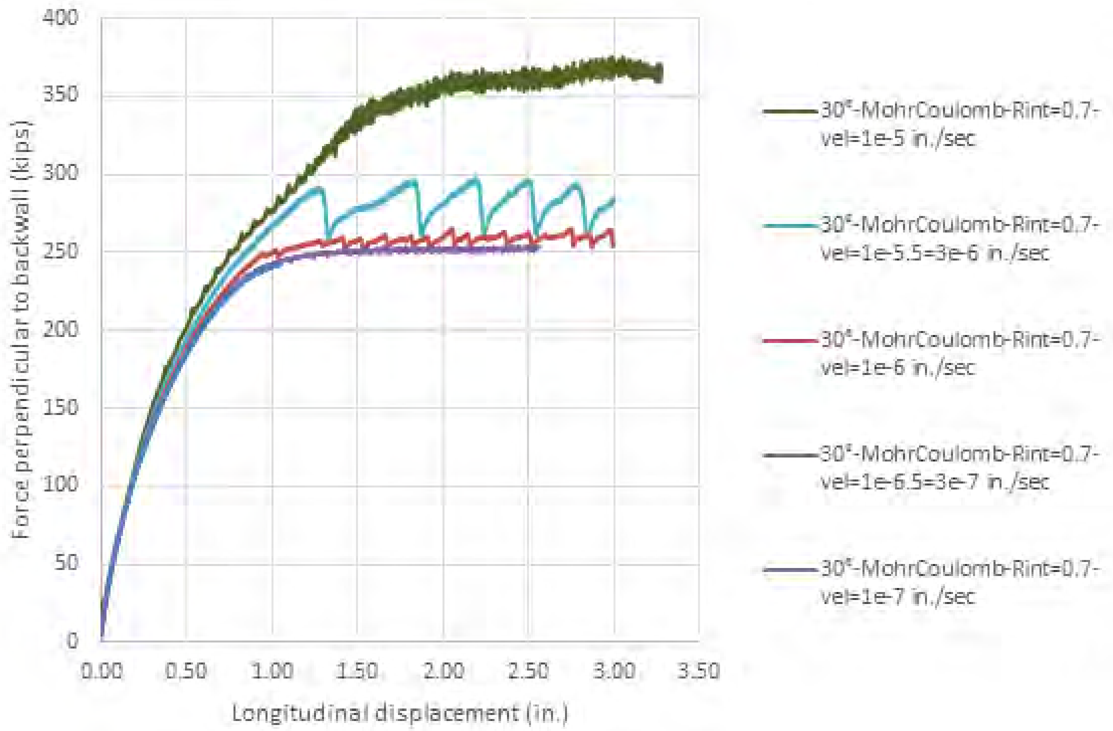

Figure 8-6 Effect of applied velocity on force-displacement relationship.

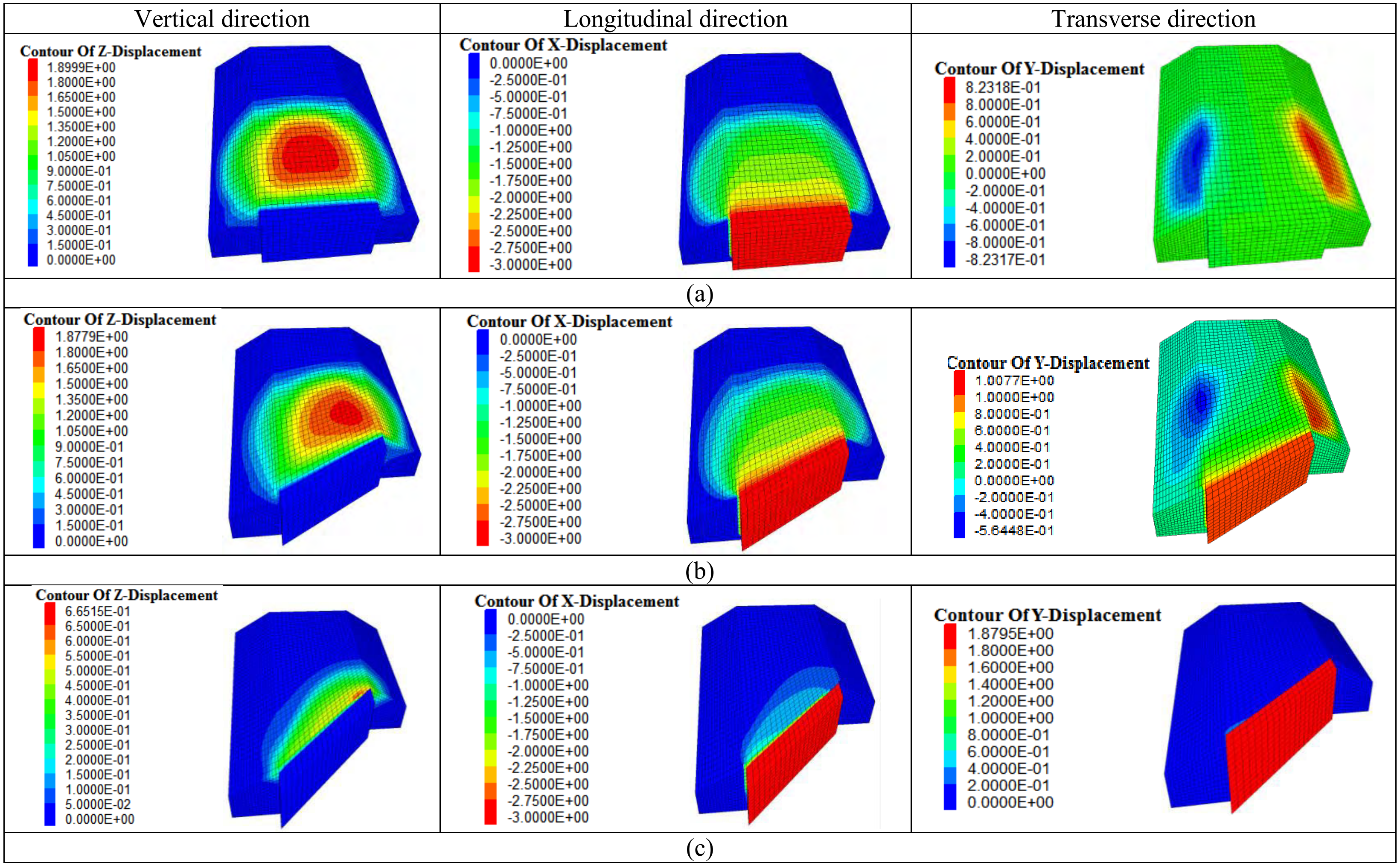

Figure 8-7 Displacements contours under uniform displacement loading: (a) 0° skew, (b) 30° skew, and (c) 45° skew.

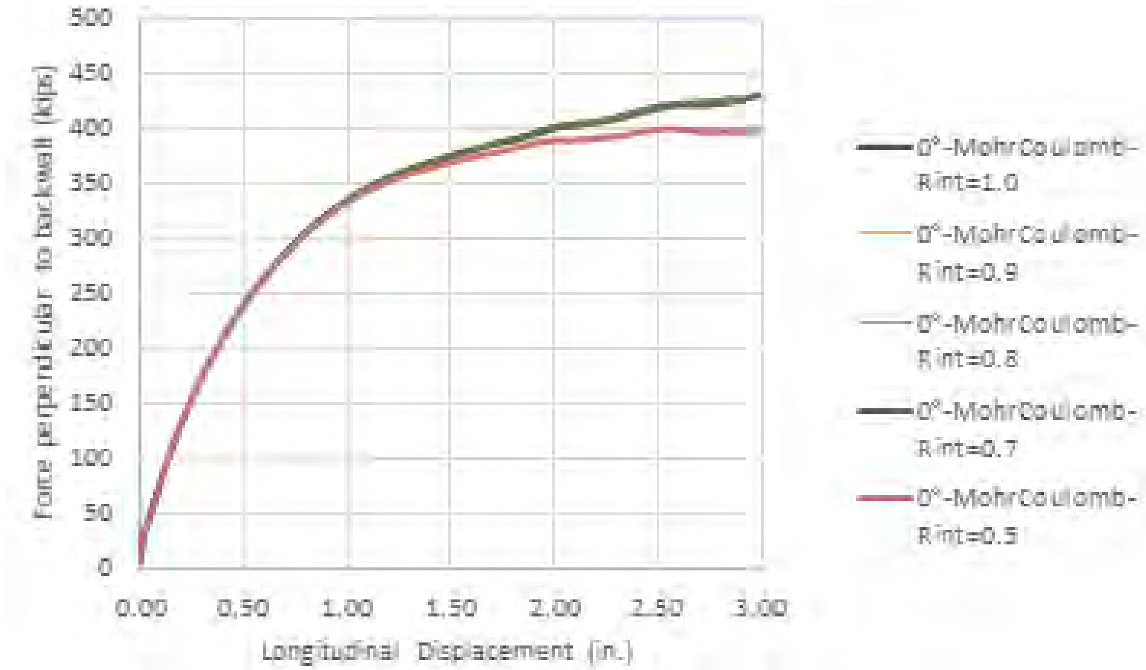

Figure 8-8 Force-displacement results under uniform displacement loading in the 0° skew model.

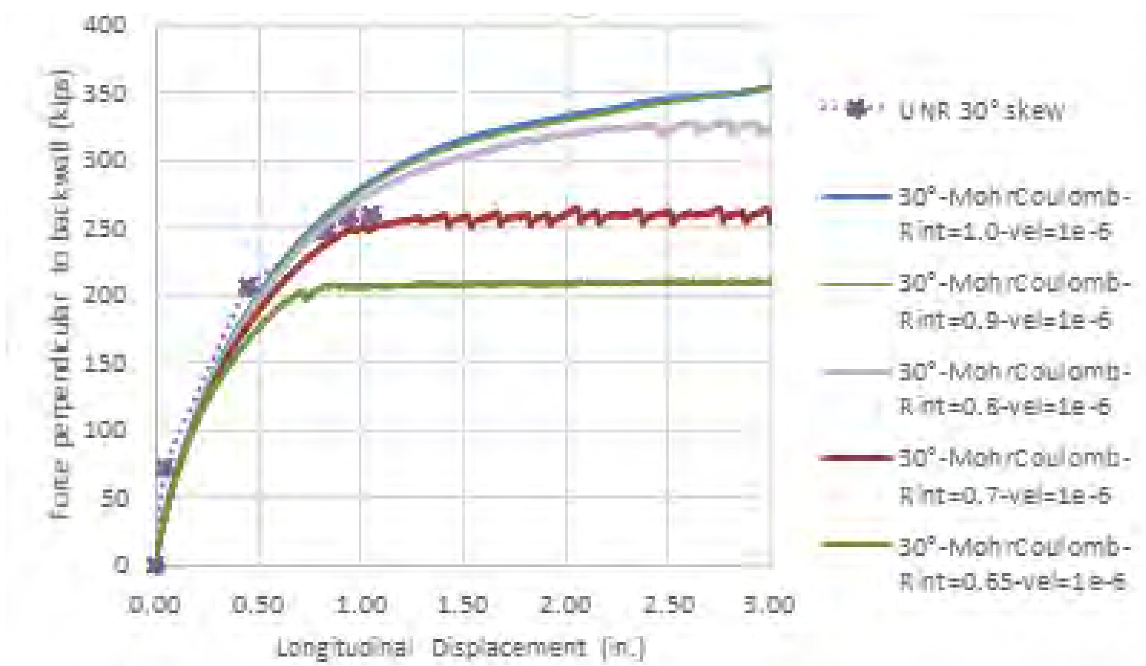

Figure 8-9 Force-displacement results under uniform displacement loading in the 30° skew model.

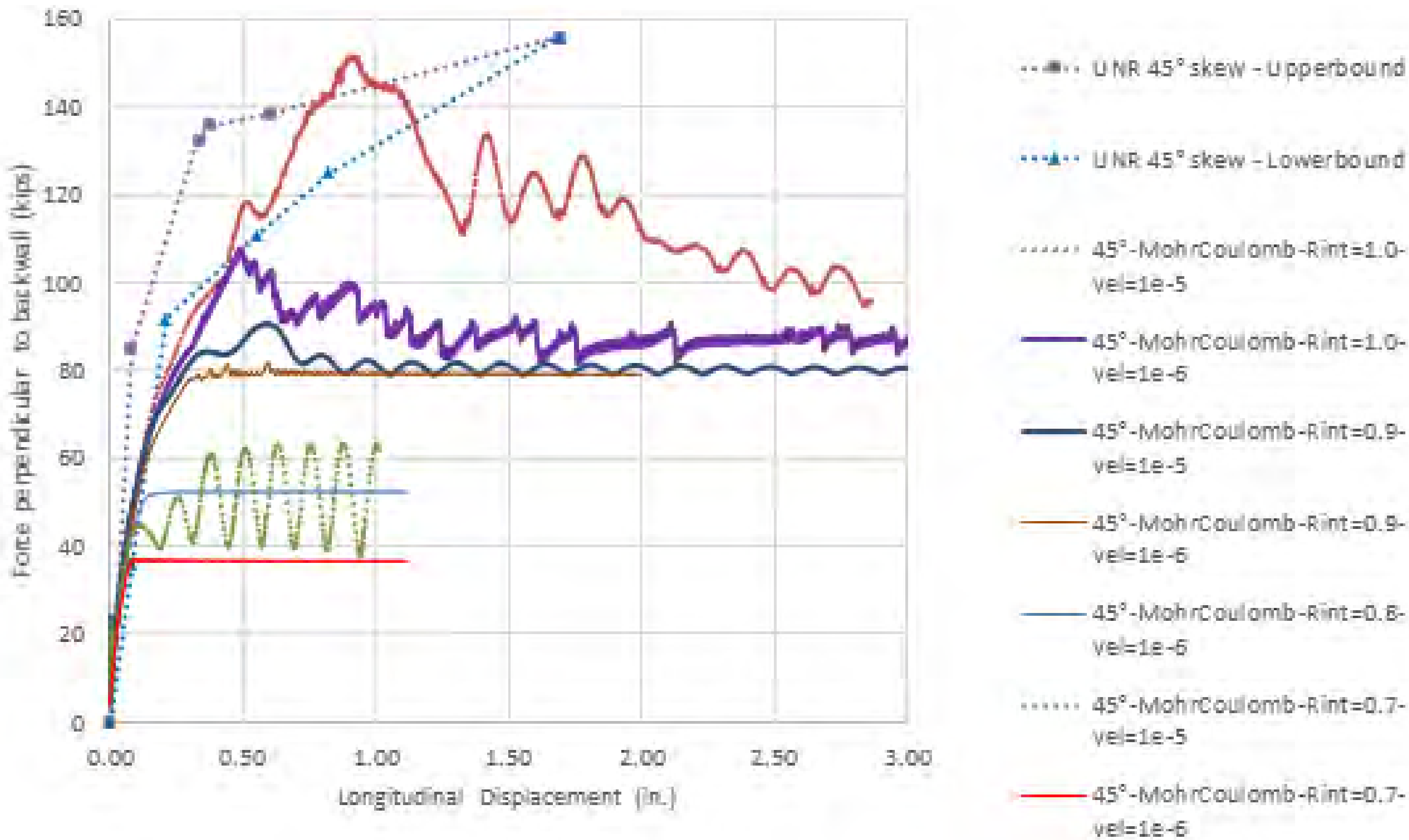

Figure 8-10 Force-displacement relationship under uniform displacement loading in the 45° skew model.

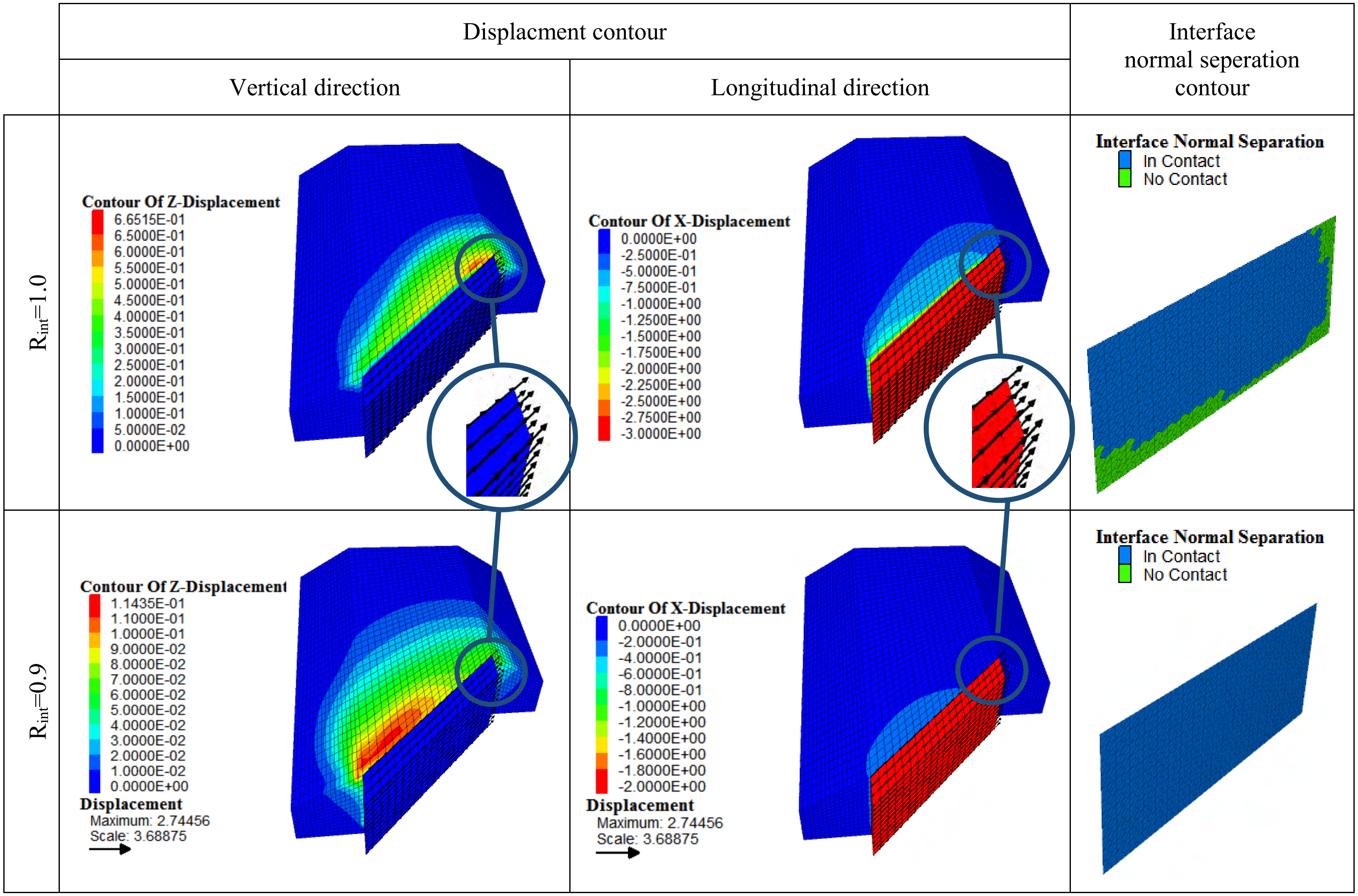

Figure 8-11 Displacement contours under uniform displacement loading in the 45° skew model.

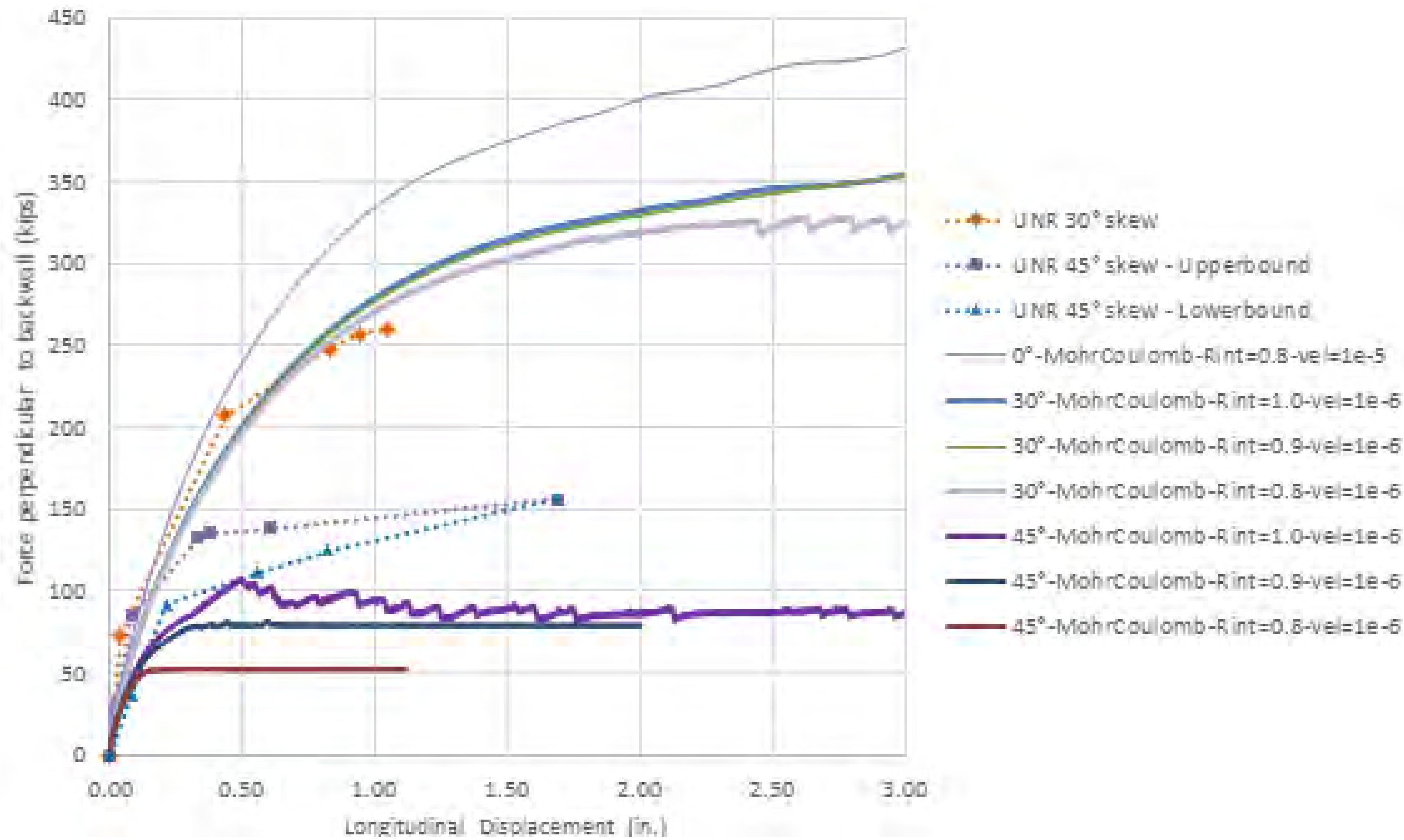

Figure 8-12 Force-displacement relationships under uniform displacement loading.

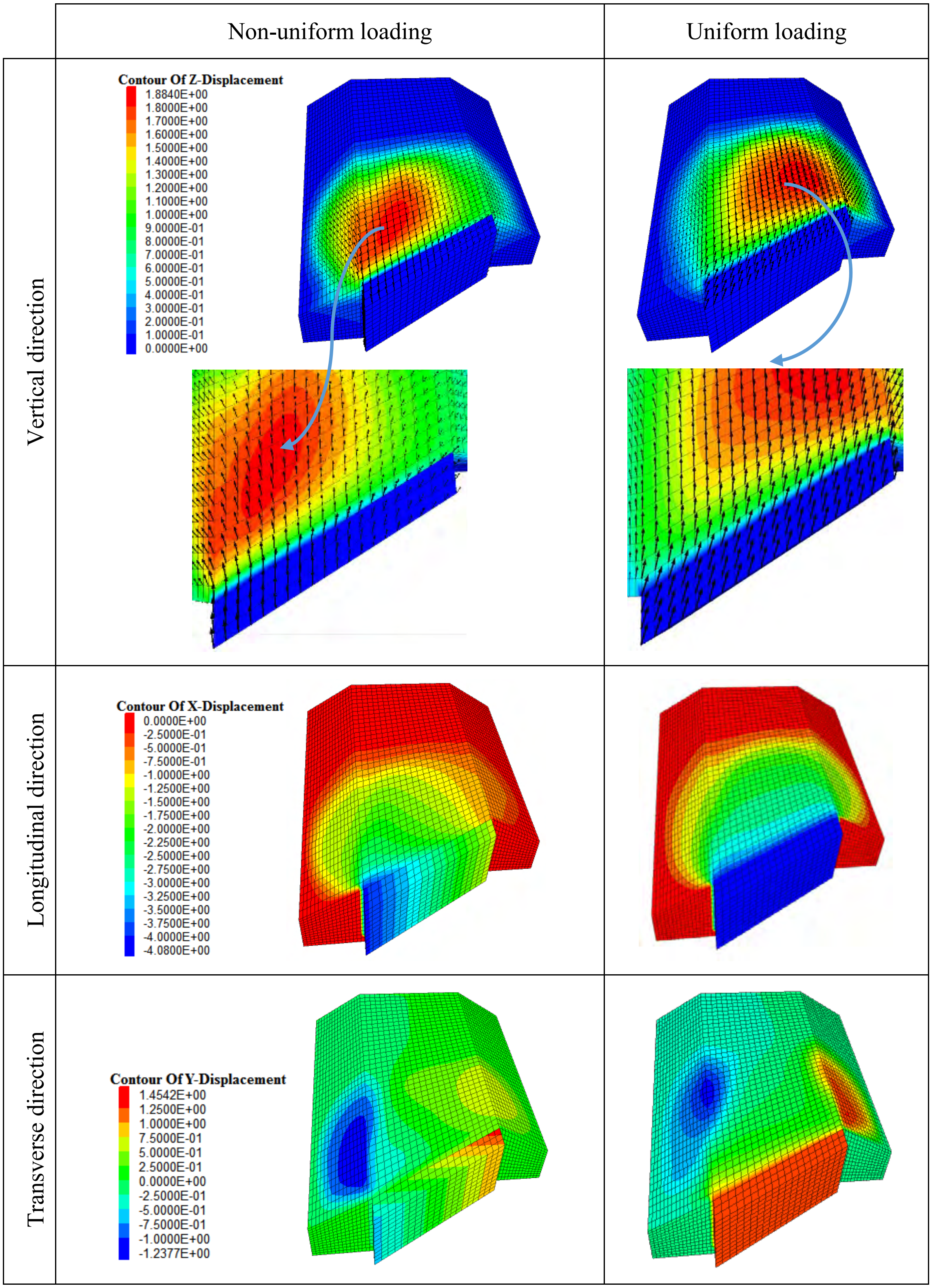

Figure 8-13 Displacement contours under non-uniform displacement loading in the 30° skew model.

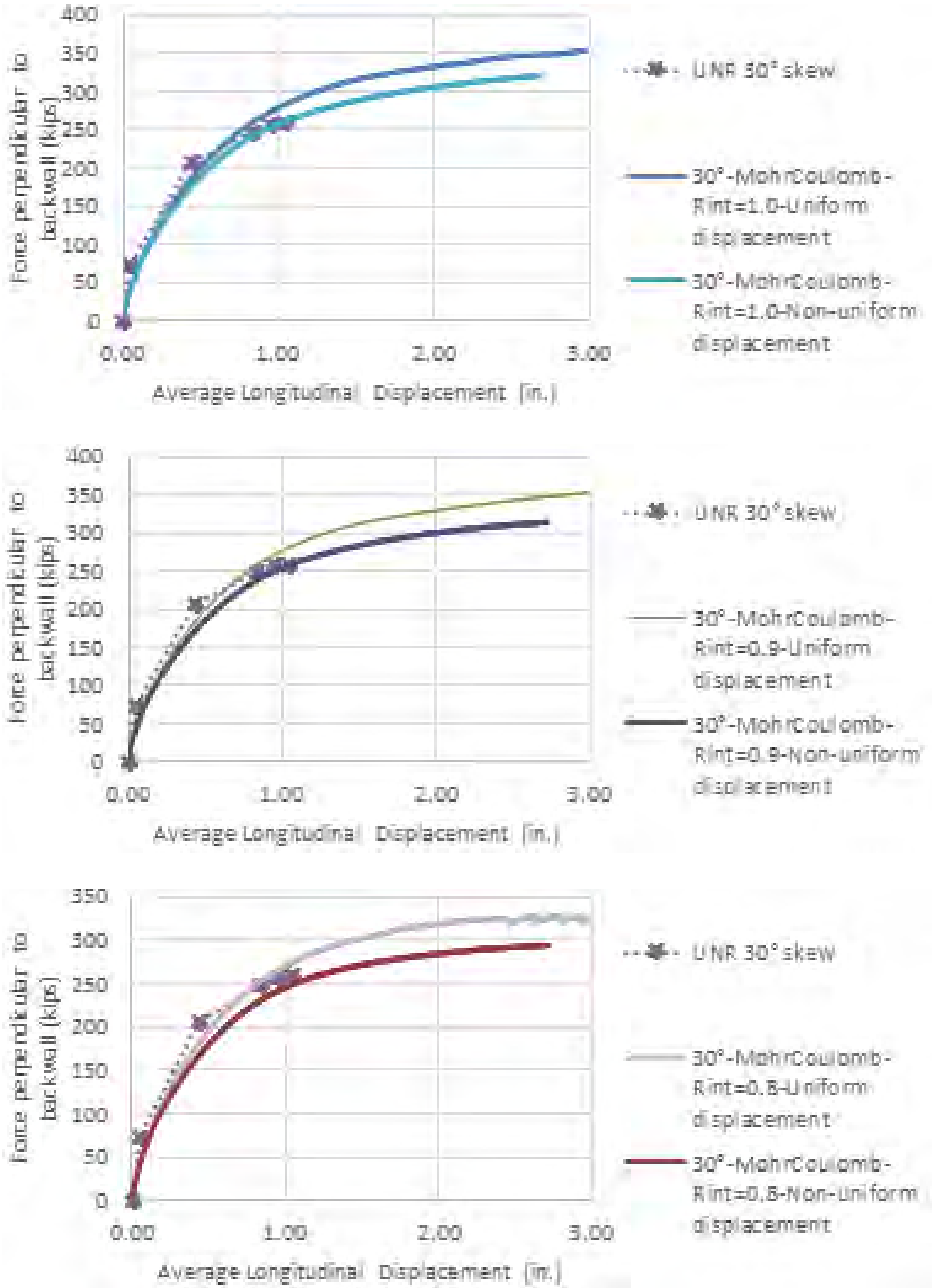

(a)

(b)

(c)

Figure 8-14 Effect of non-uniform displacement loading on force-displacement results: (a) R=1.0, (b) R=0.9, and (c) R=0.8.

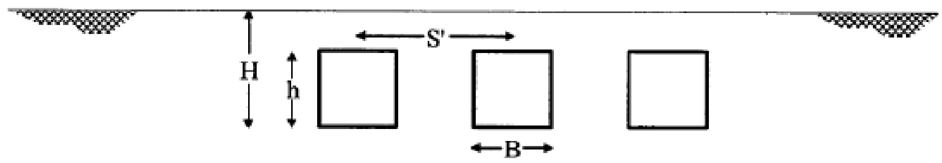

Figure 8-15 Brinch Hansen (1996) 3D factor parameters.

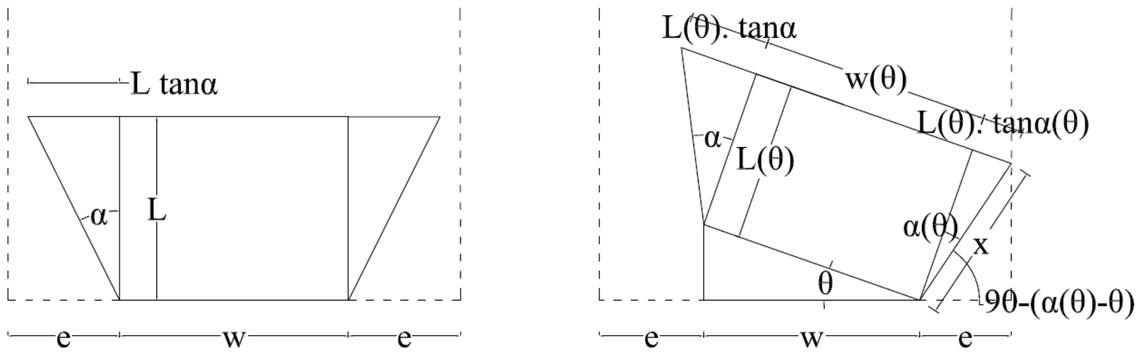

Figure 8-16 Skewed 3D wedge parameters.

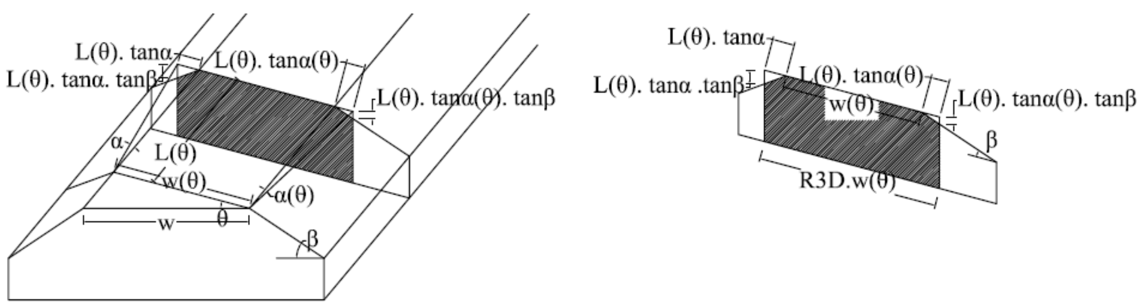

Figure 8-17 Skewed 3D wedge cross section.

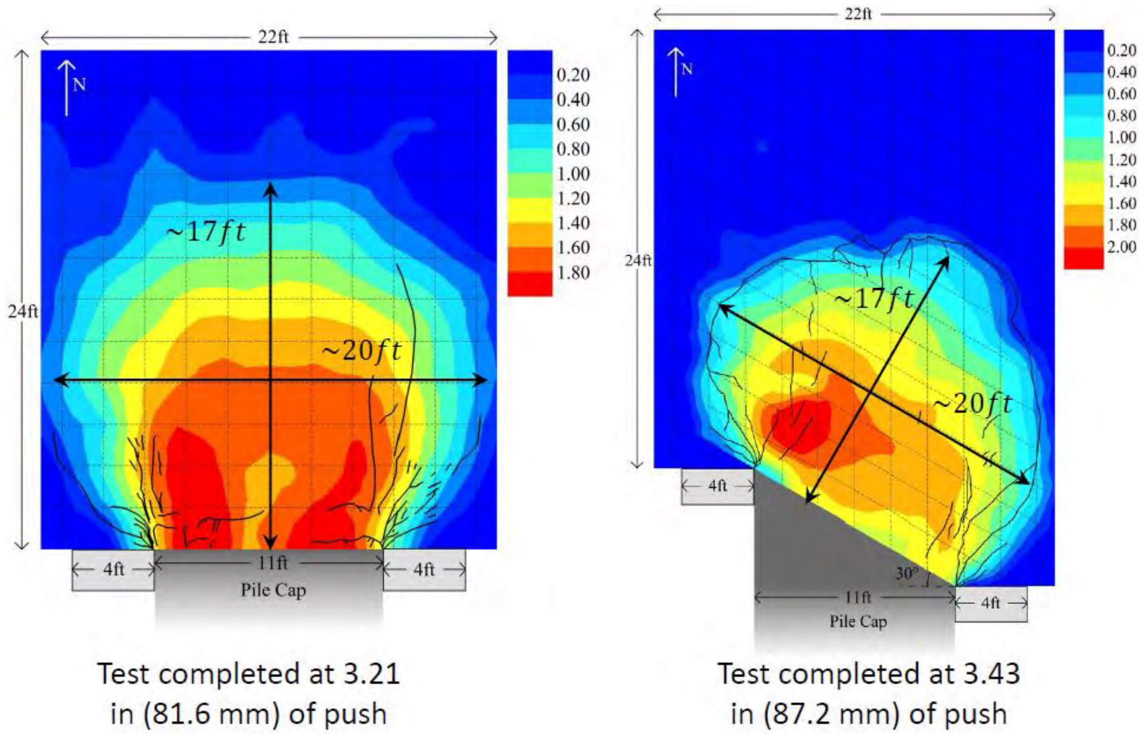

Figure 8-18 Heave contours in BYU test (Marsh et al., 2013).

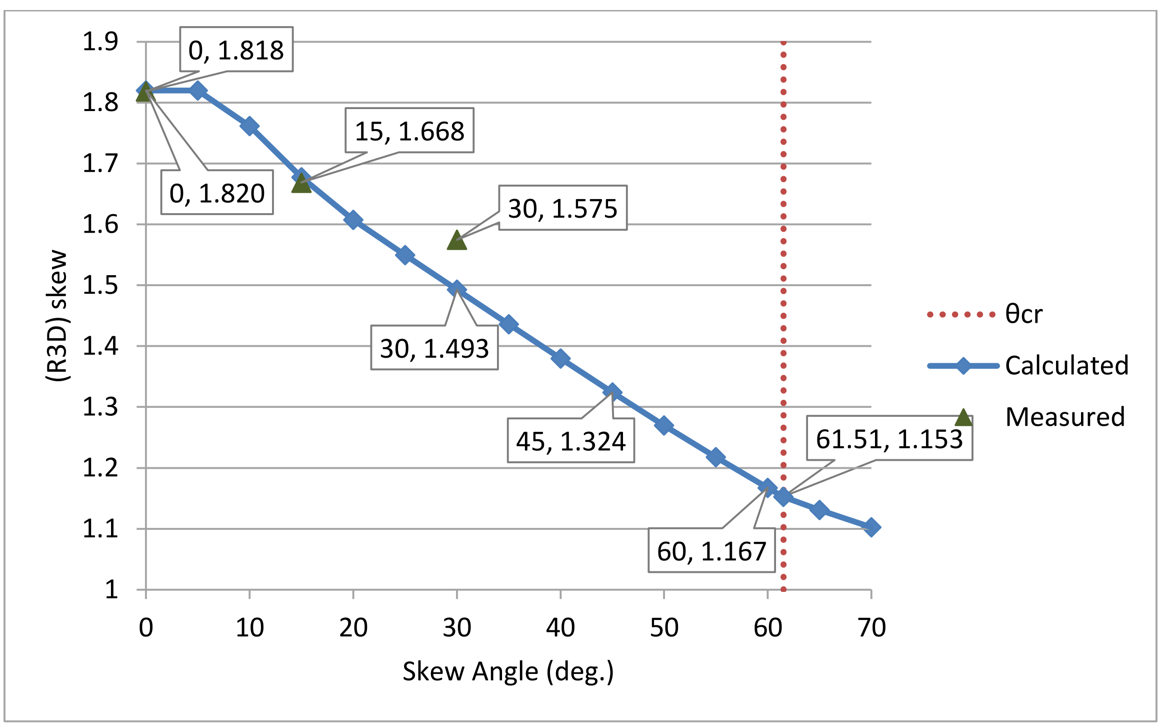

Figure 8-19 Skewed 3D factor for BYU test (Marsh et al., 2013).

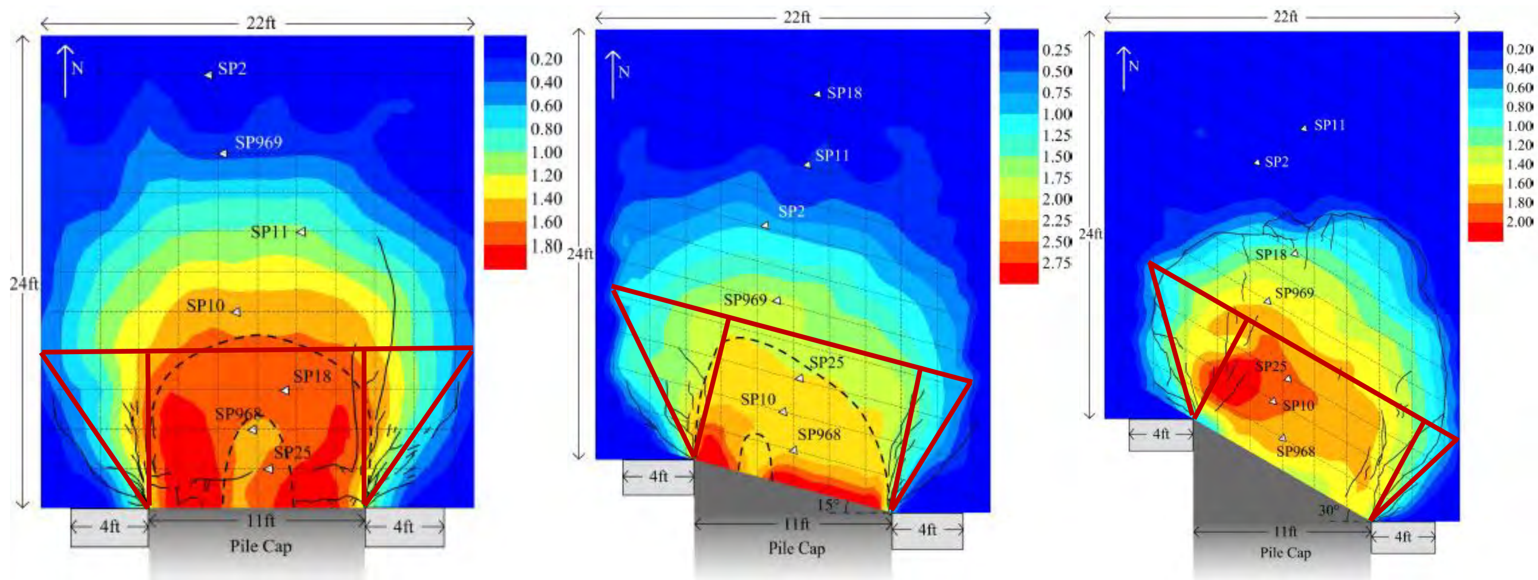

(a)

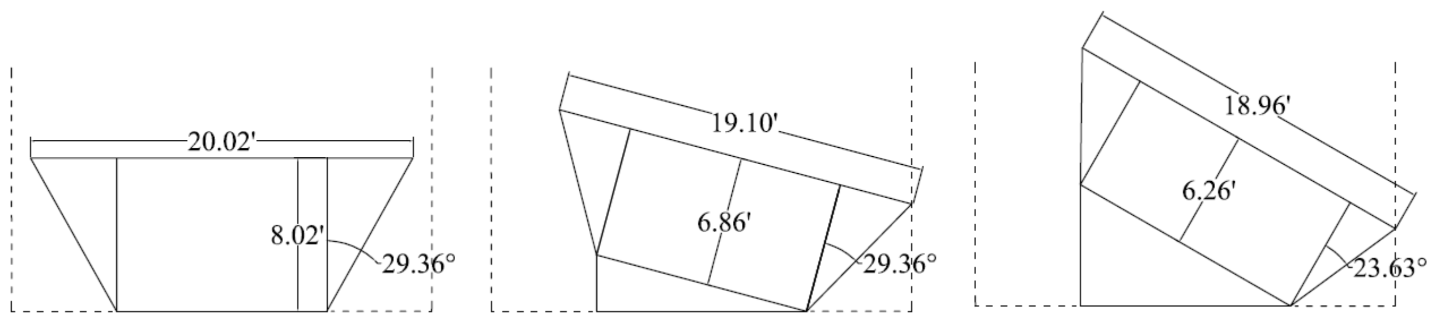

(b)

Figure 8-20 Skewed 3D wedge geometry in BYU test (Marsh et al., 2013): (a) measured, and (b) calculated.

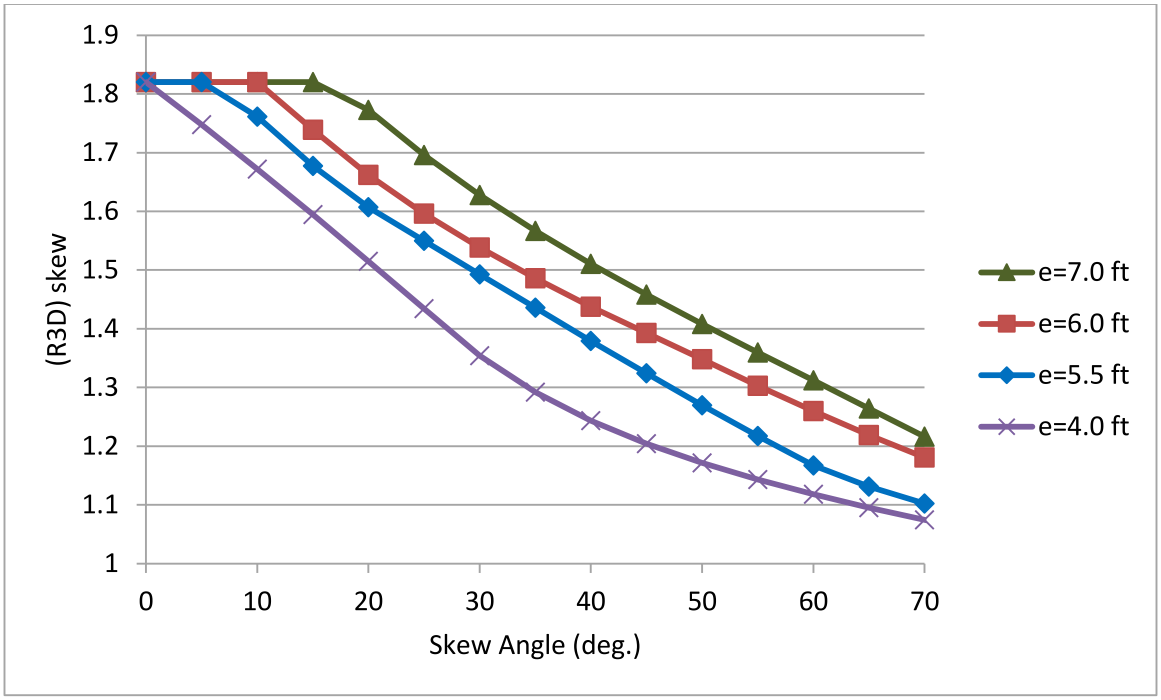

Figure 8-21 Effect of backfill extension on 3D factor for BYU test (Marsh et al., 2013).

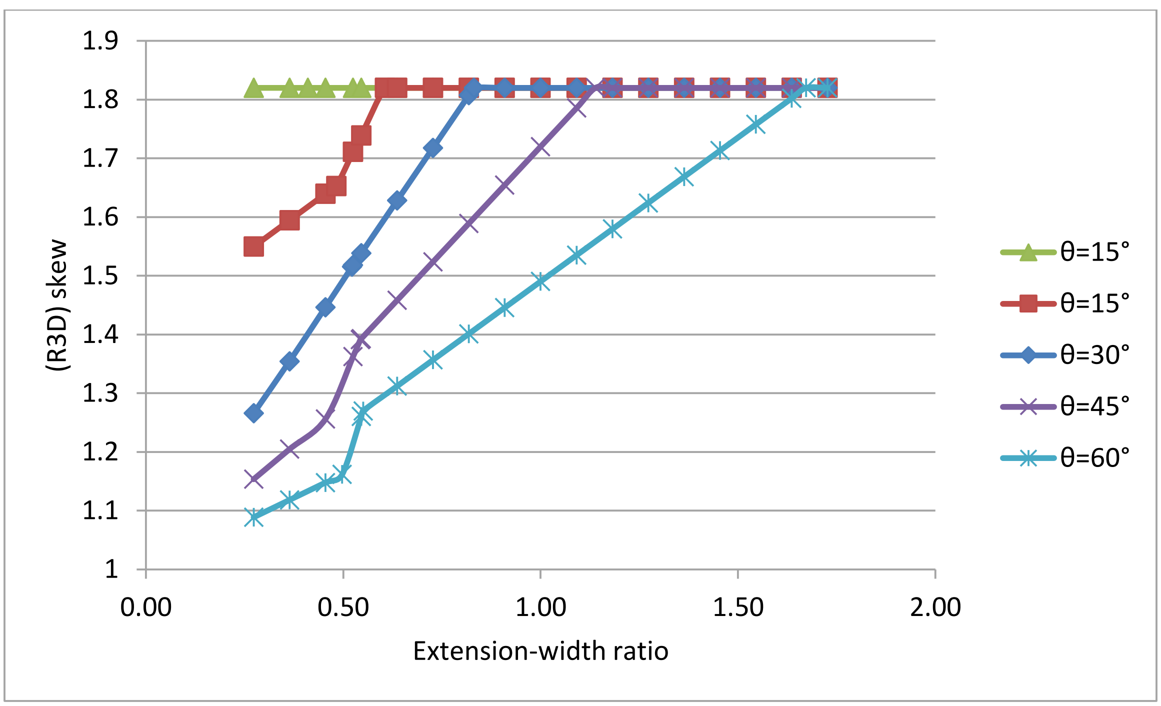

Figure 8-22 Effect of backfill extension to backwall projected width on 3D factor for BYU test (Marsh et al., 2013).

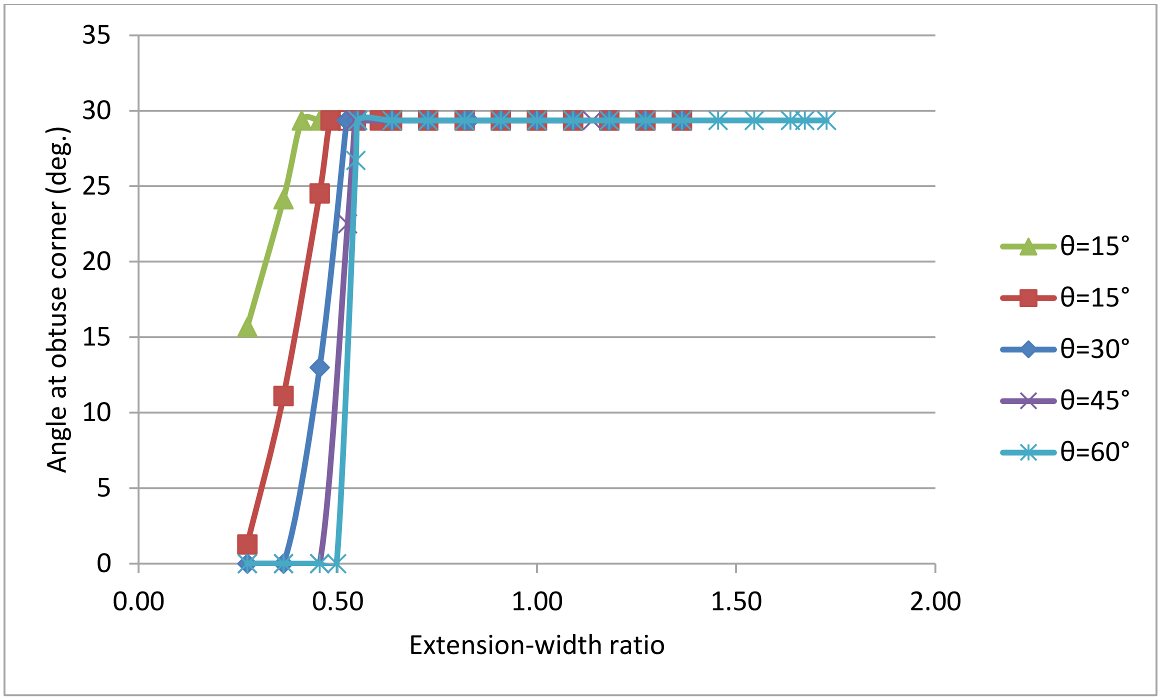

Figure 8-23 Effect of backfill extension to backwall projected width on obtuse corner spread angle.

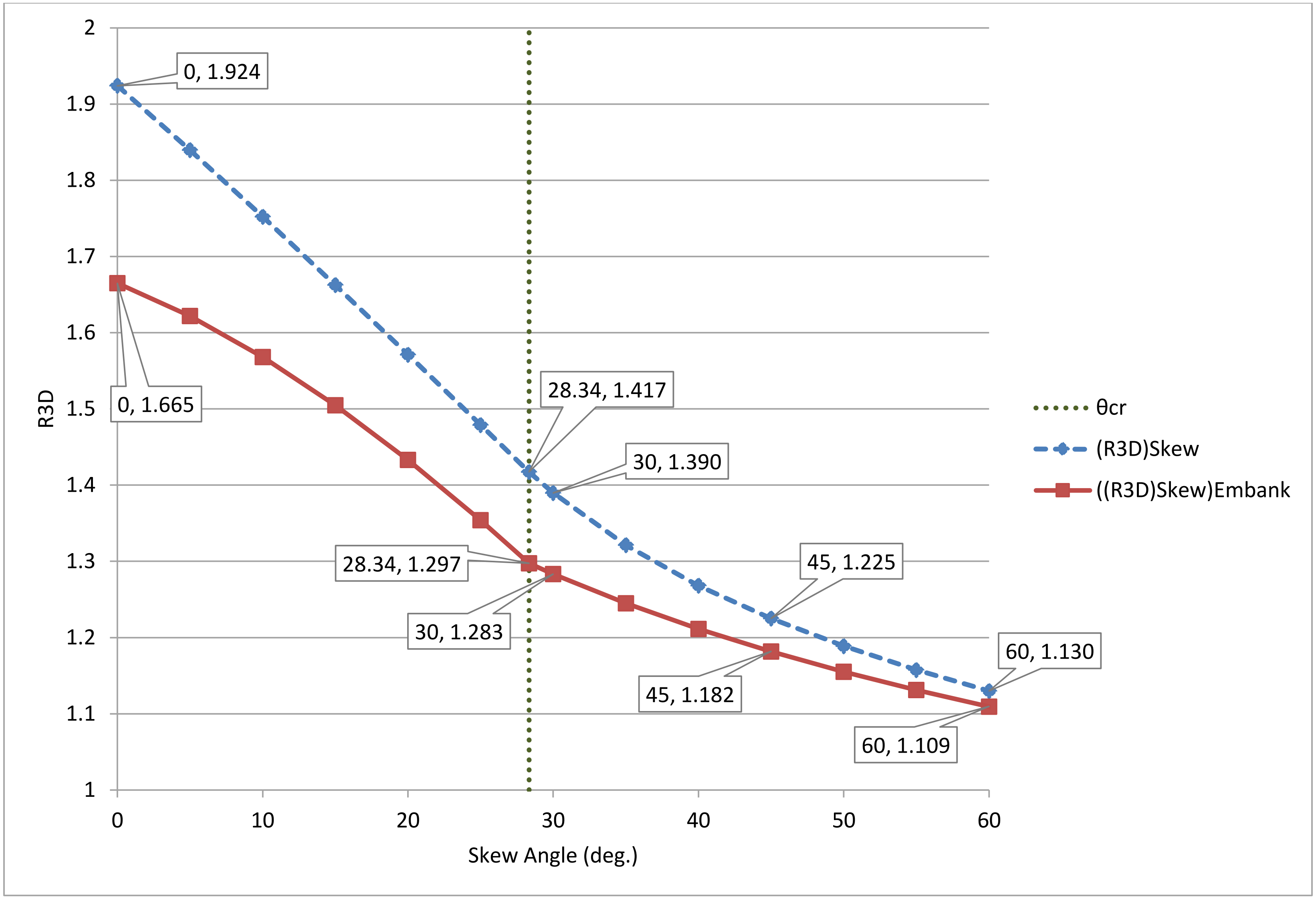

Figure 8-24 Skewed 3D factors for UNR test.

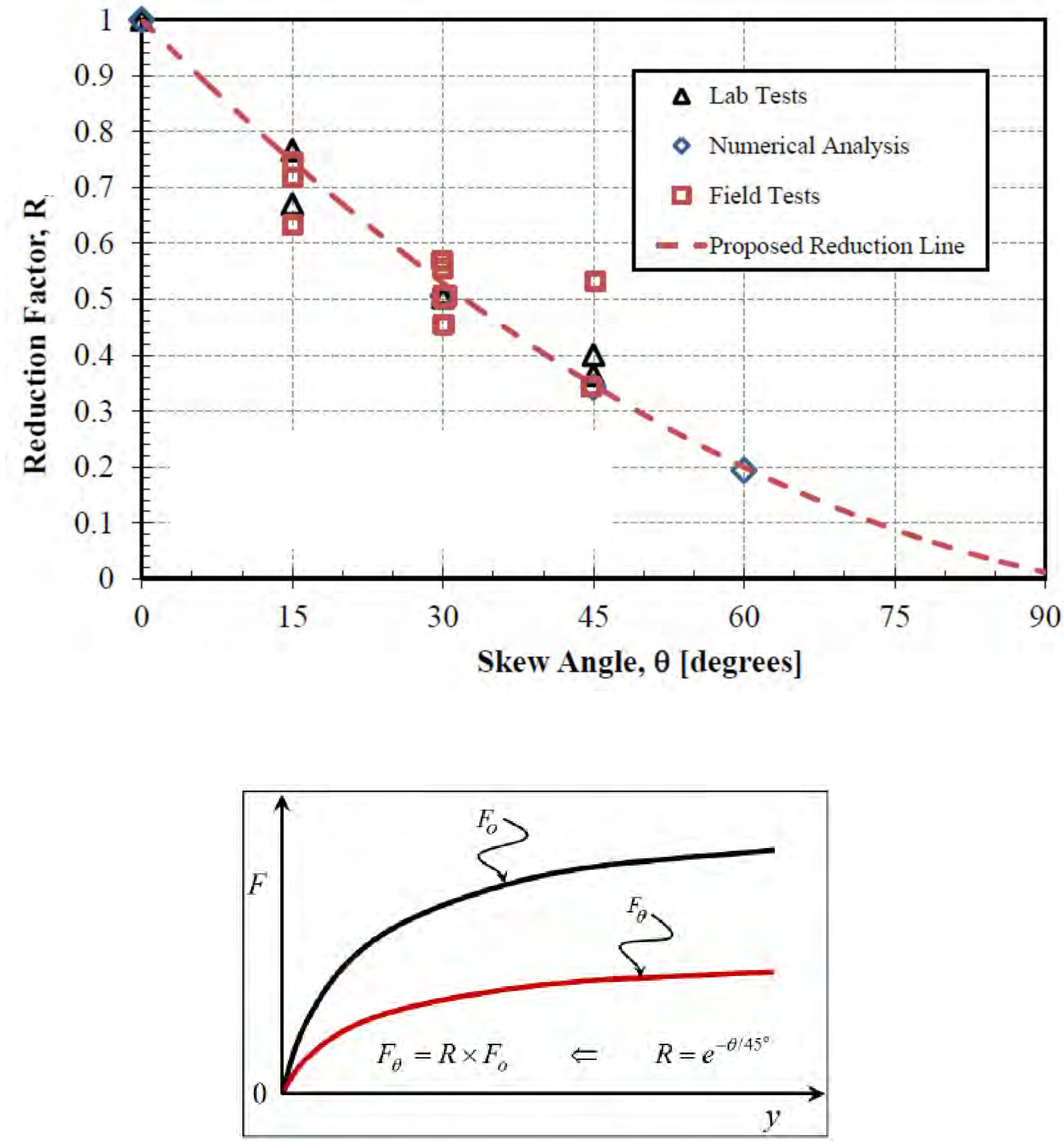

Figure 8-25 Skew reduction factor of backbone curve (Shamsabadi & Rollins, 2014).

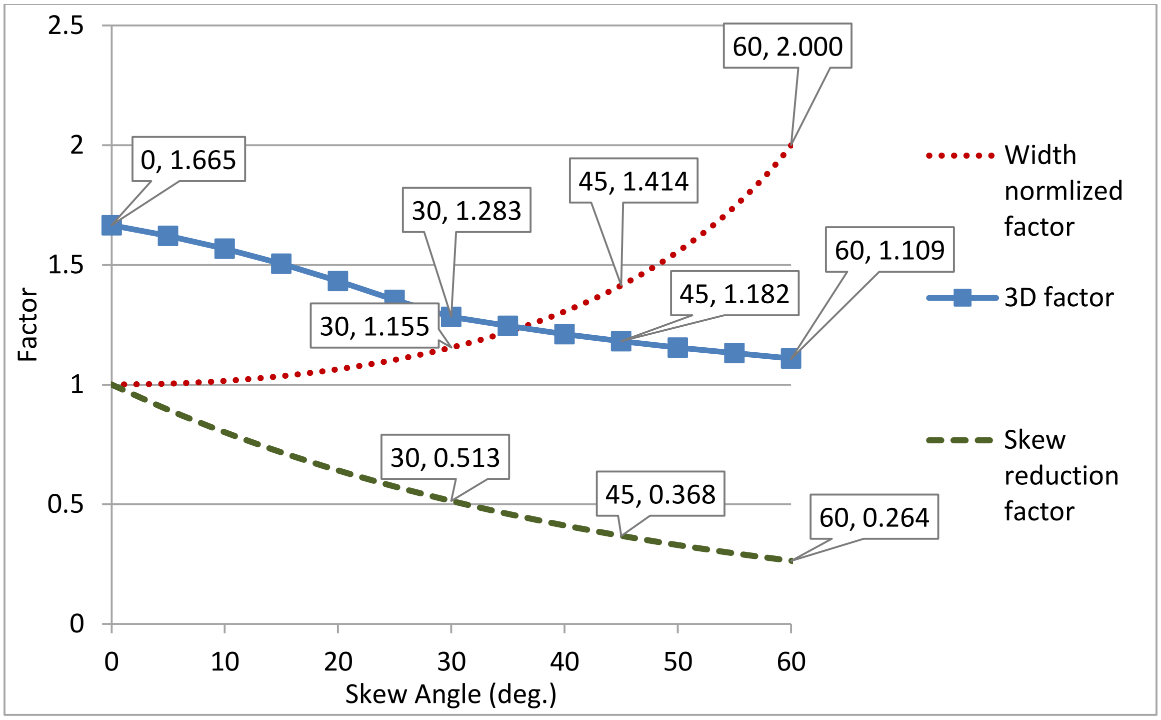

(a)

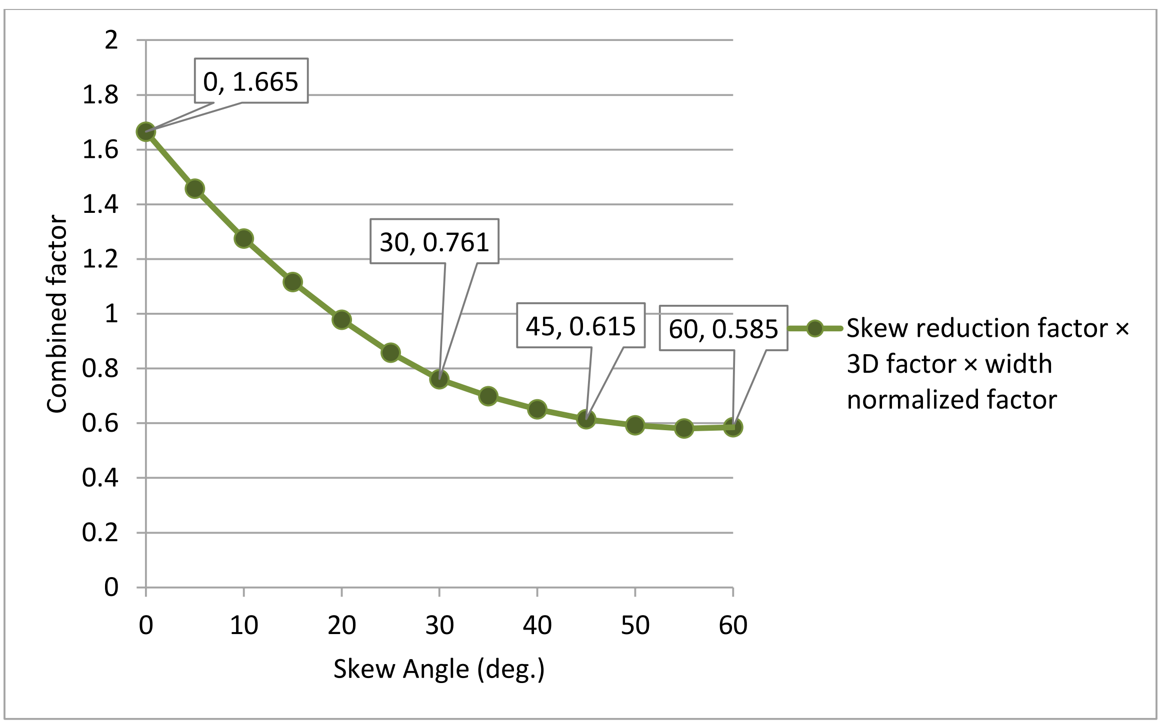

(b)

Figure 8-26 Passive capacity factors of UNR test: (a) single effect, and (b) combined effect.

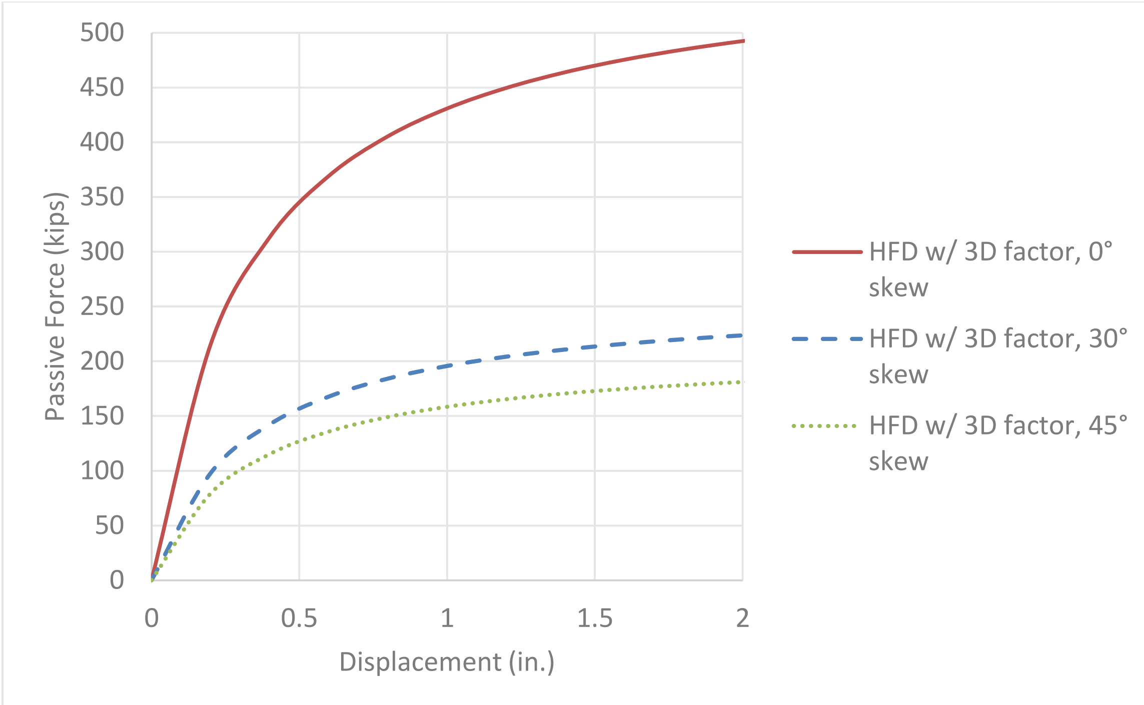

Figure 8-27 HFD relationships for UNR test.

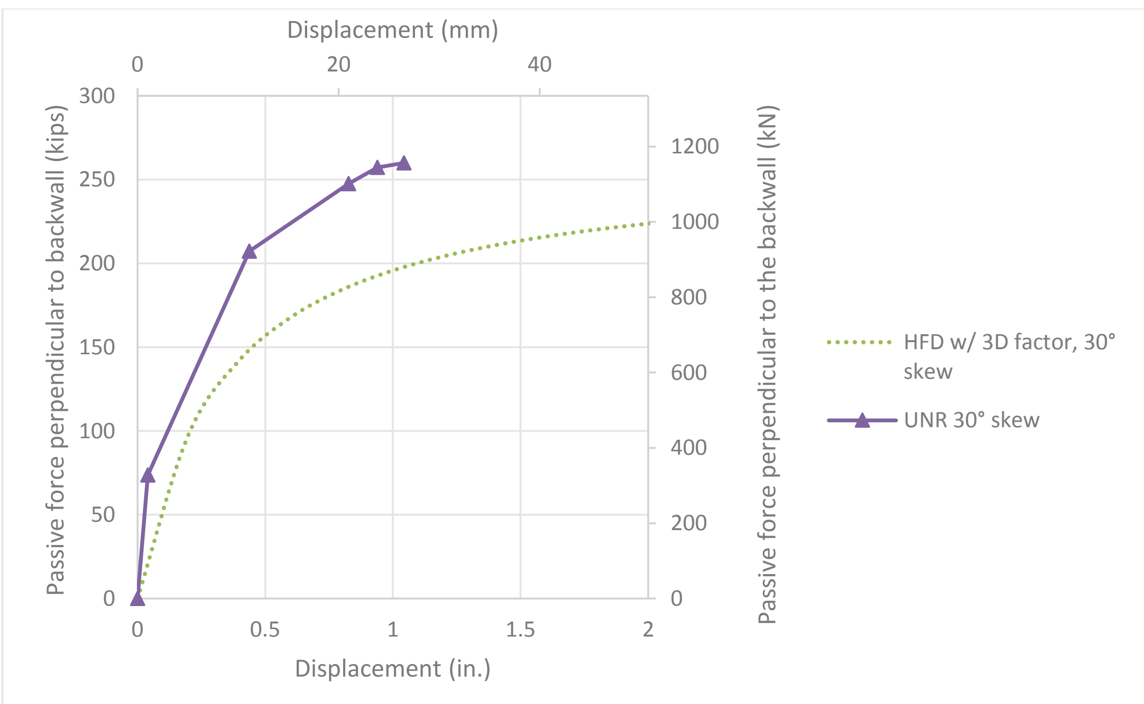

Figure 8-28 HFD relationship compared with UNR test data (30° skew).

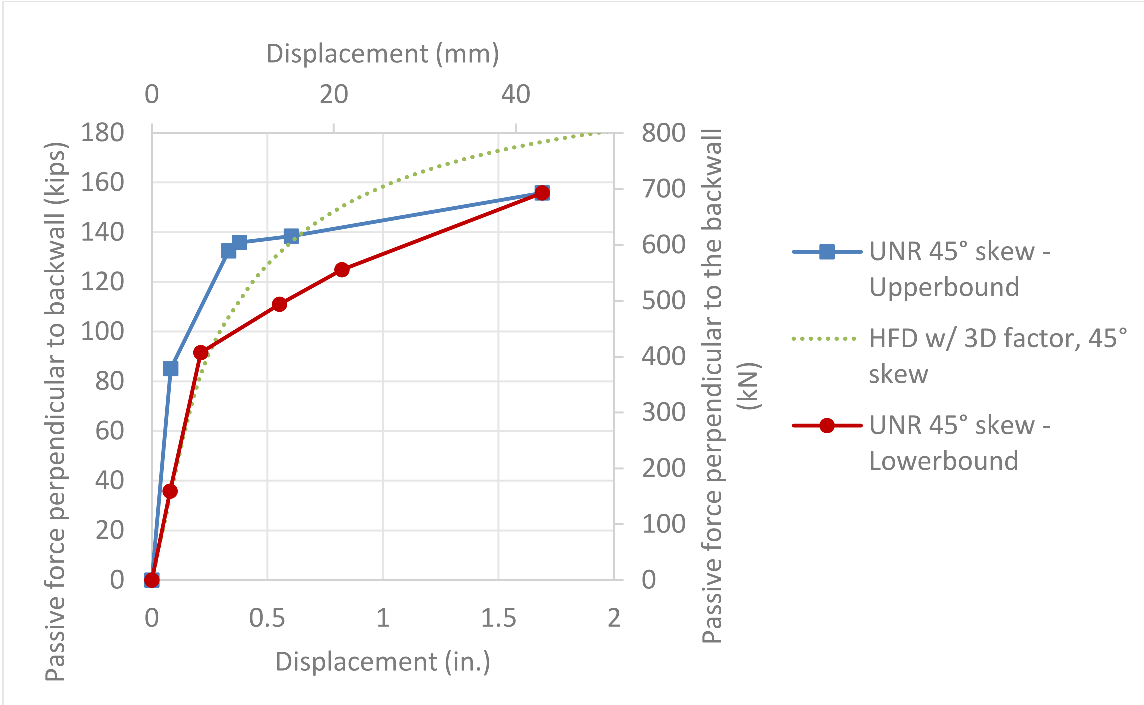

Figure 8-29 HFD relationship compared with UNR test data (45° skew).

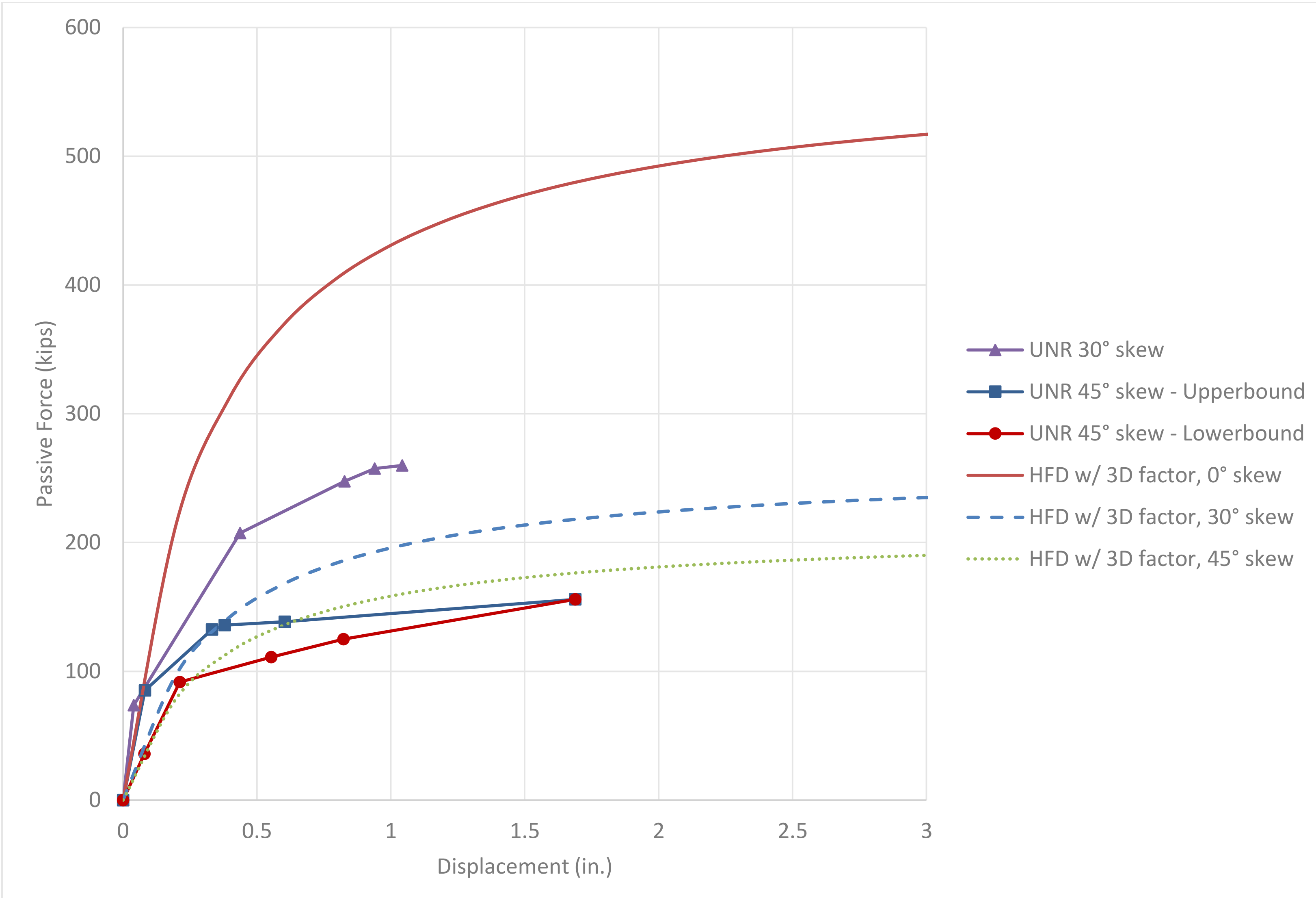

Figure 8-30 HFD relationships compared with UNR test data.

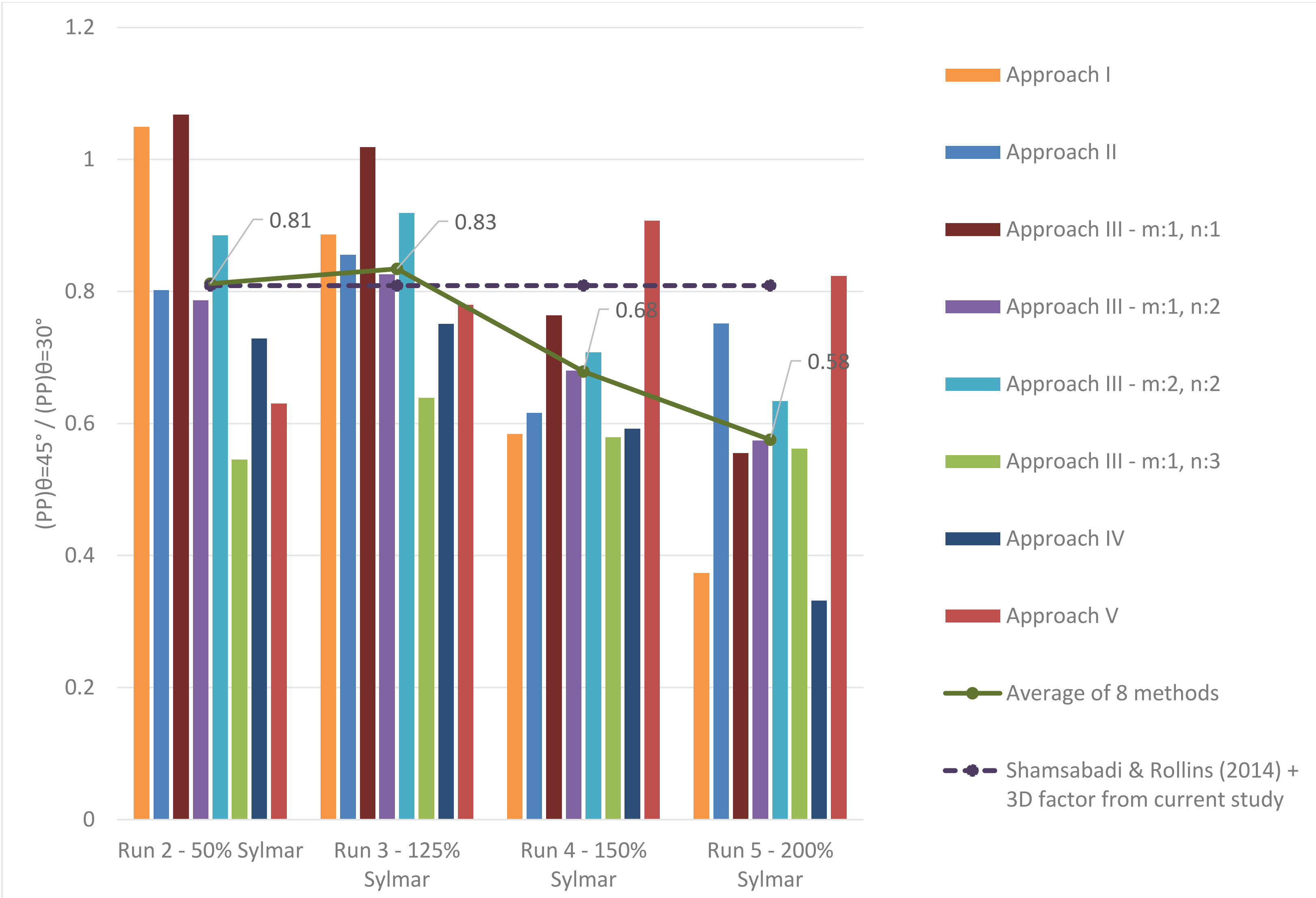

Figure 8-31 Measured force ratio between 30° and 45° skew tests.

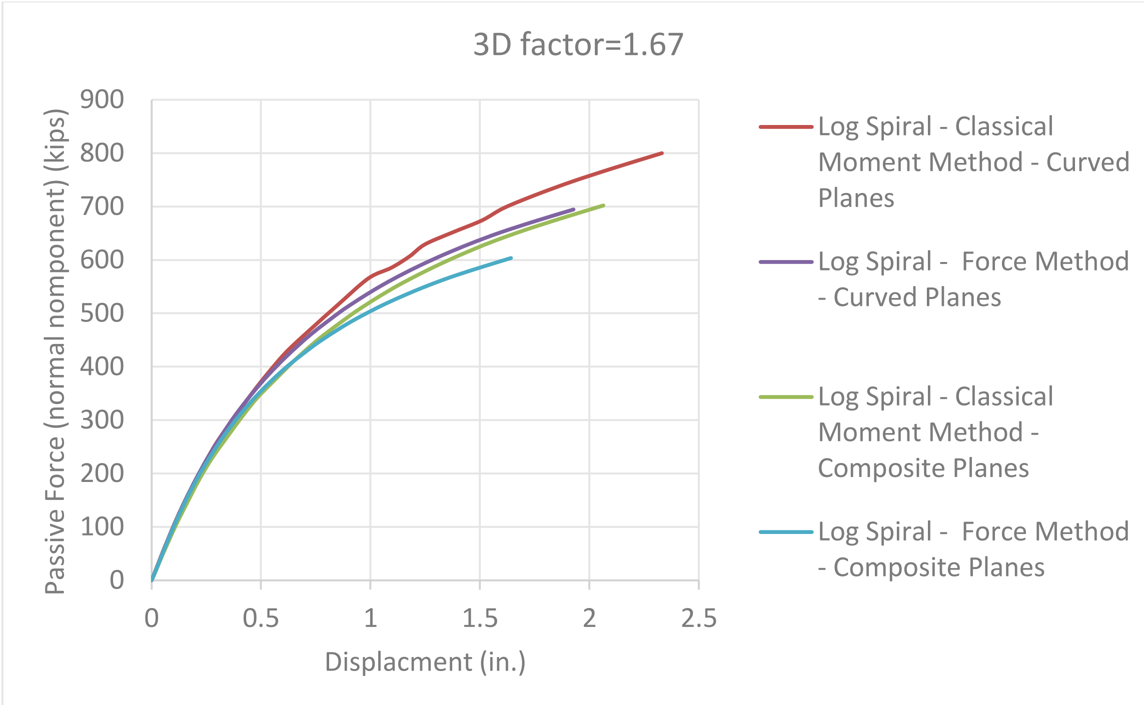

Figure 8-32 S-LSH force-displacement for UNR test (0° skew).

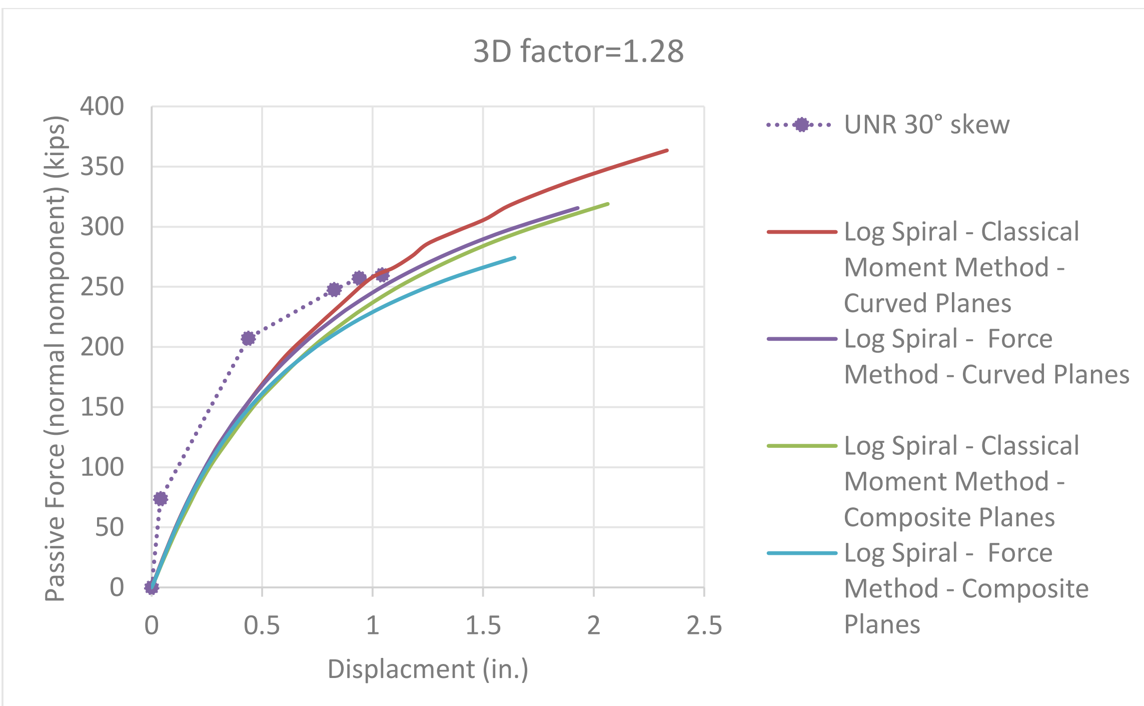

Figure 8-33 S-LSH force-displacement for UNR test (30° skew).

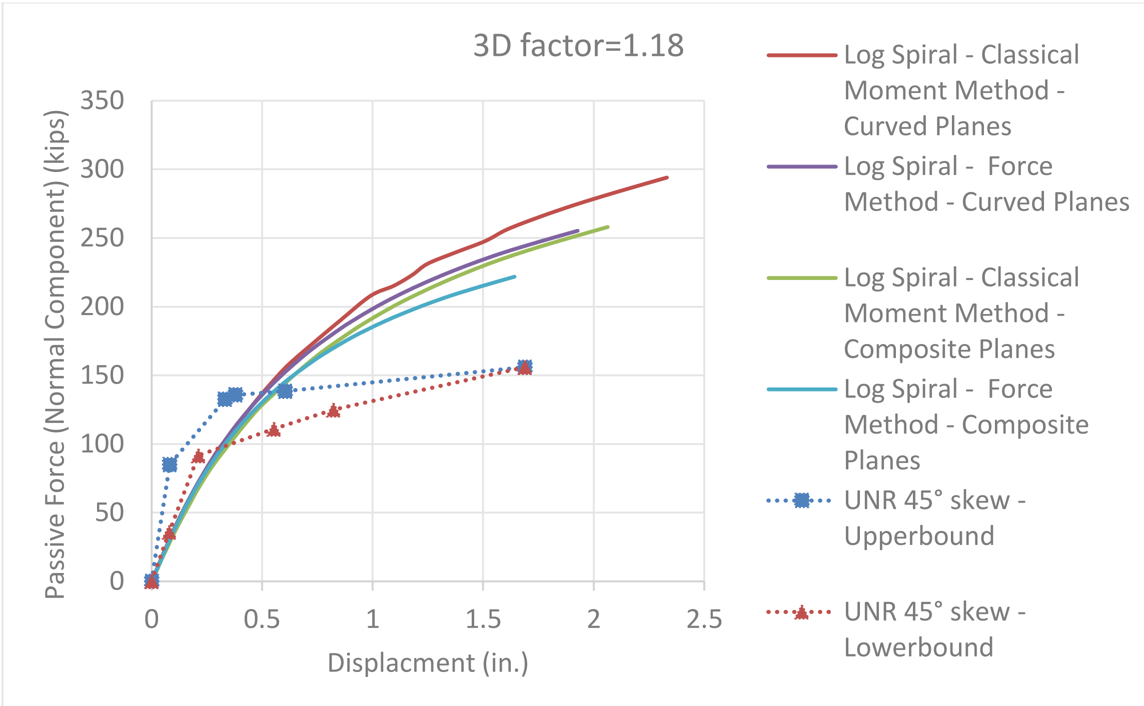

Figure 8-34 S-LSH force-displacement for UNR test (45° skew).

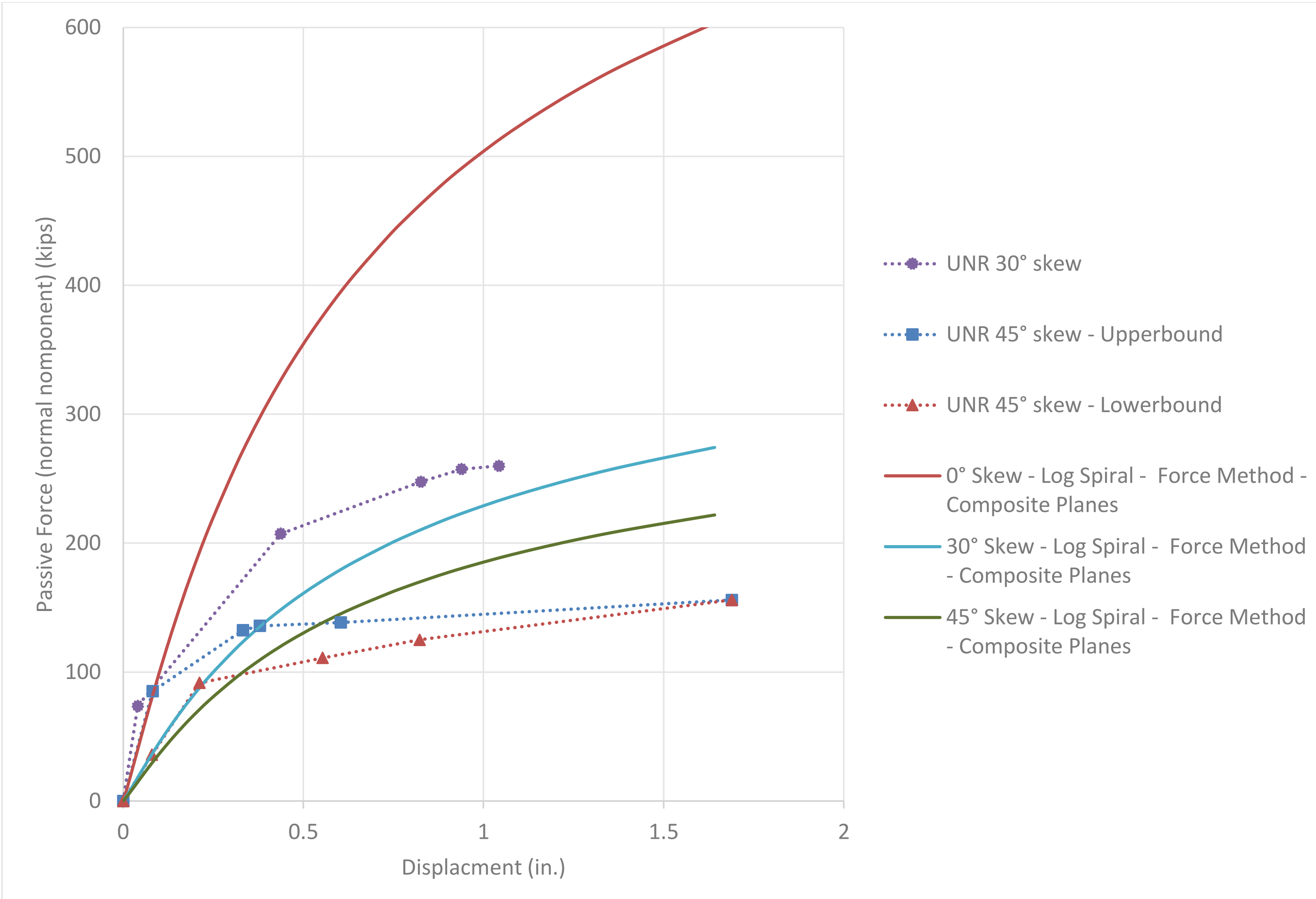

Figure 8-35 S-LSH force-displacement for UNR test.

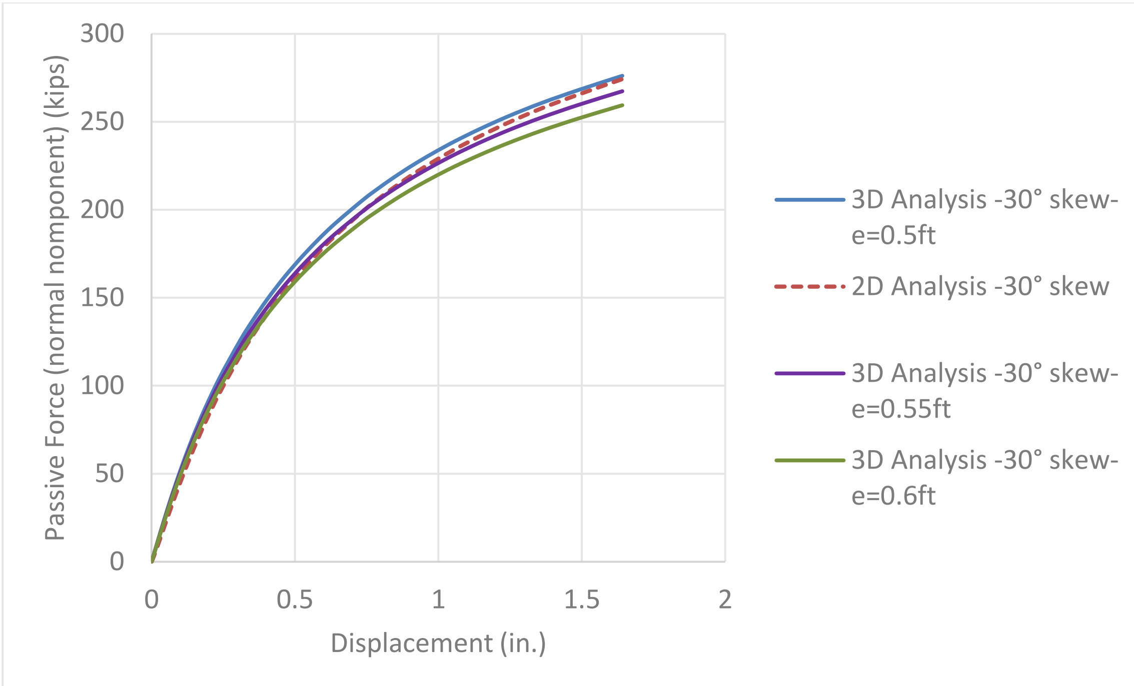

Figure 8-36 S-LSH force-displacement curves for 30° skew UNR abutment (2D and 3D analyses).

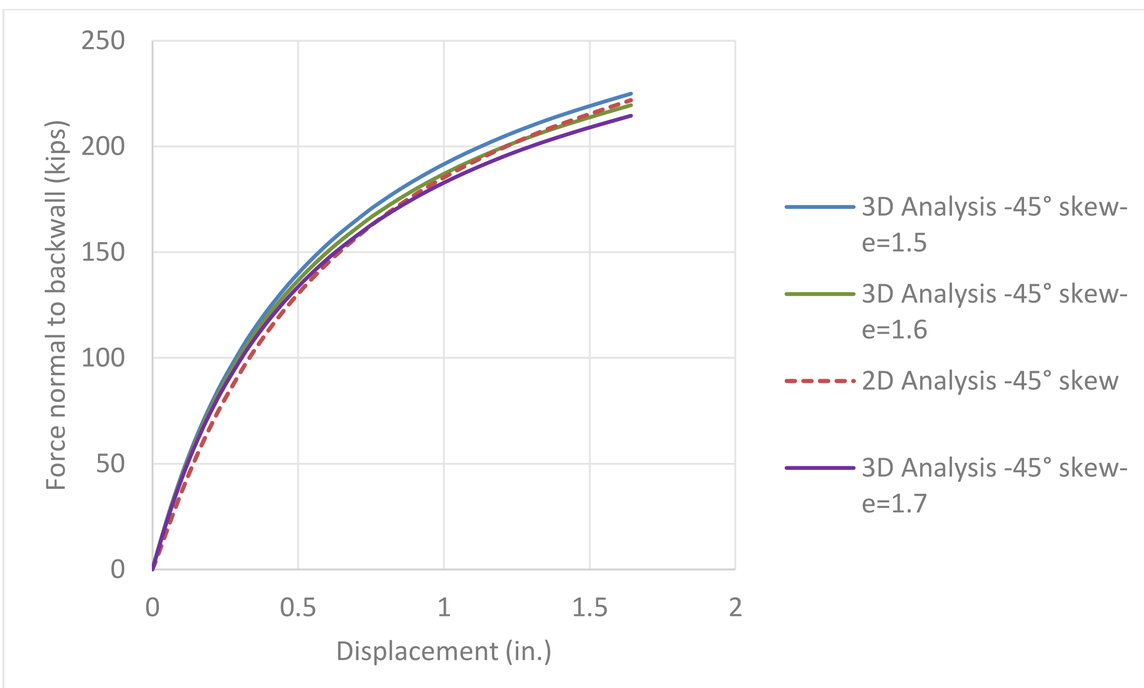

Figure 8-37 S-LSH force-displacement curves for 45° skew UNR abutment (2D and 3D analyses).

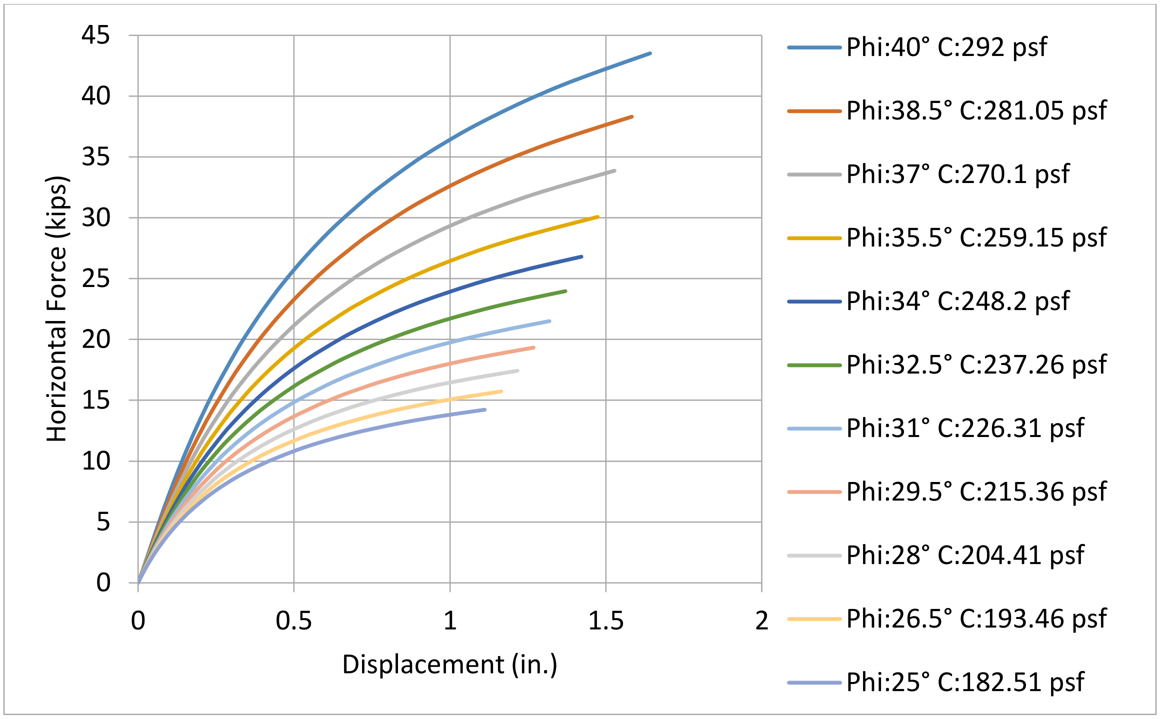

Figure 8-38 S-LSH force-displacement curves for 30° skew UNR abutment (3D analysis).

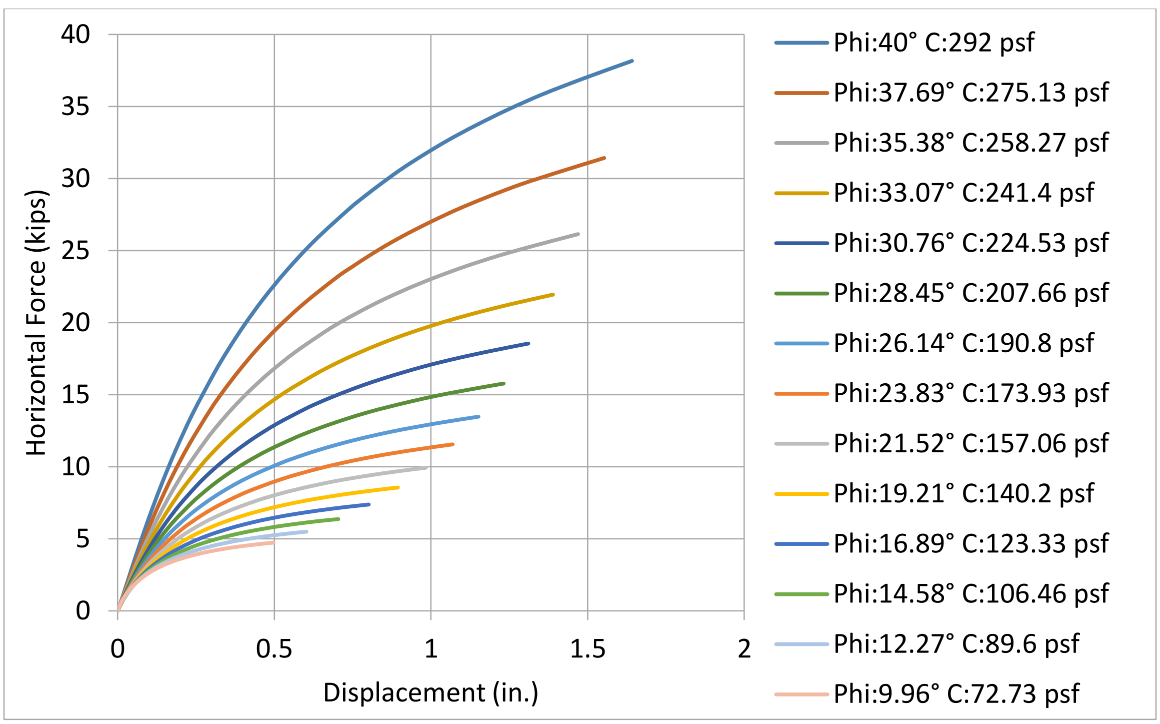

Figure 8-39 S-LSH force-displacement curves for 45° skew UNR abutment (3D analysis).

APPENDIX A. Bridge Block and Backwall Drawings

This appendix presents the detail drawings of the bridge block (including the main block and the skewed wedges) and the backwalls of the test models described in Chapter 5.

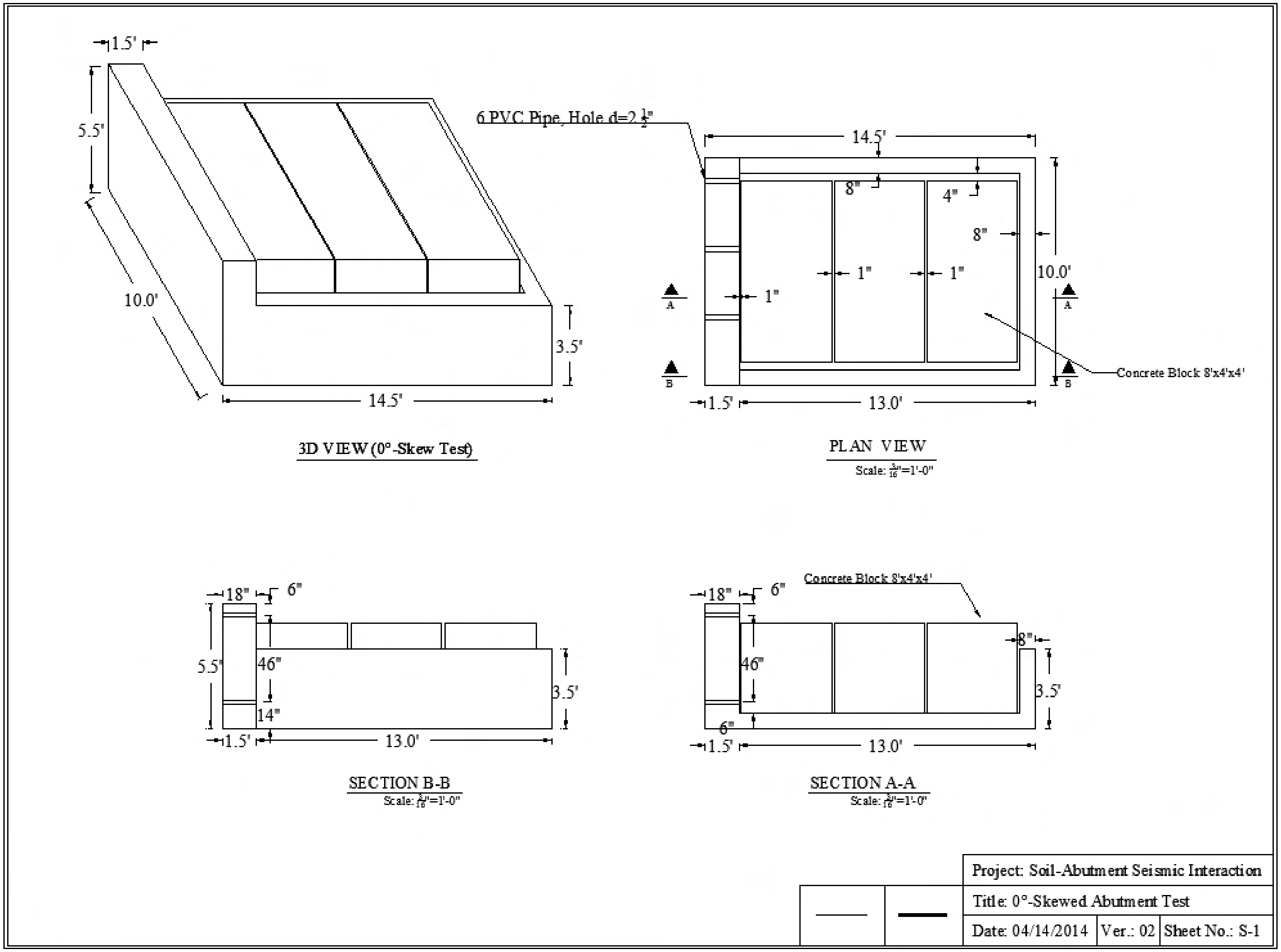

Figure A-1 Bridge block in the 0° skew test.

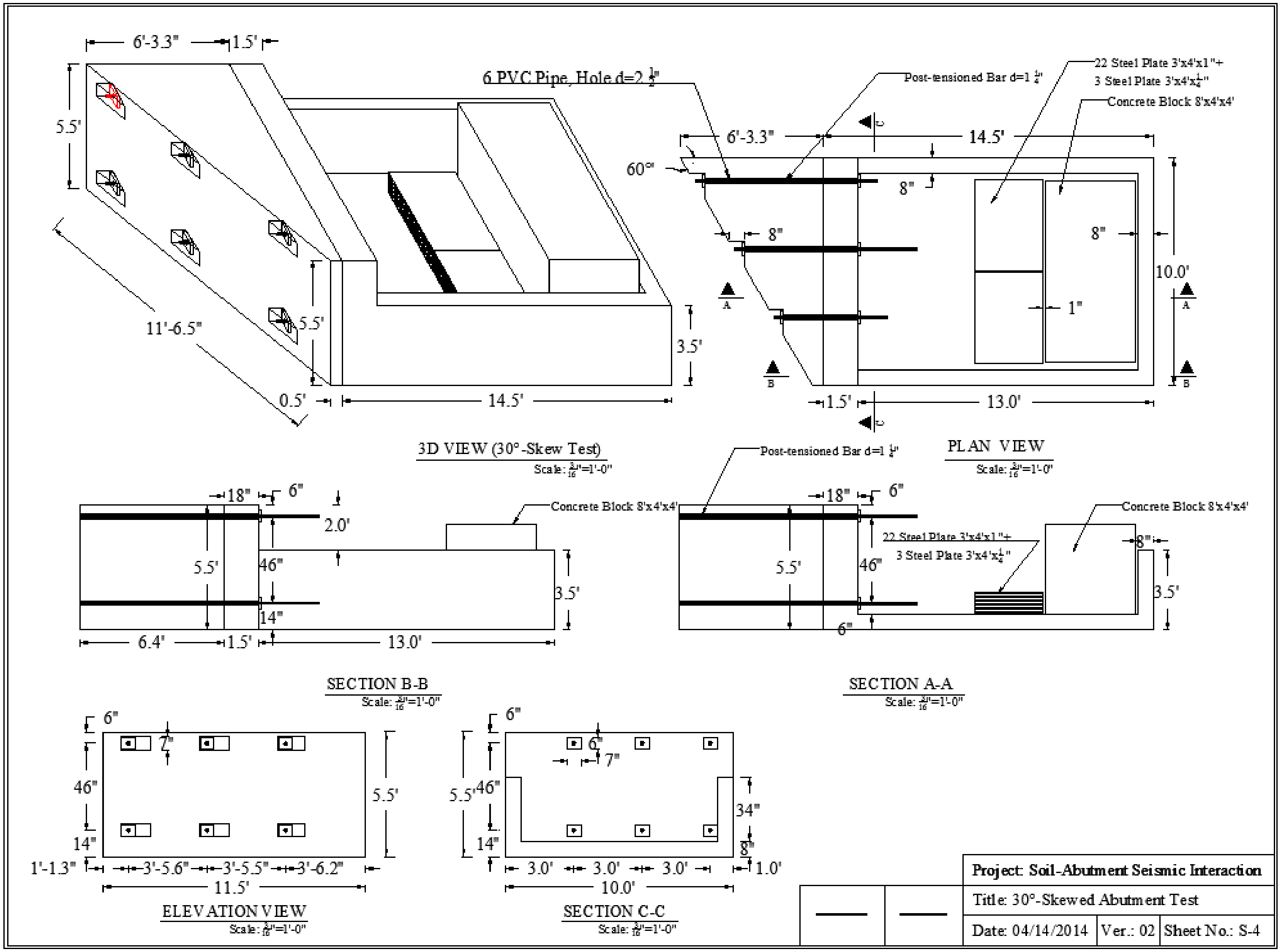

Figure A-2 Bridge block in the 30° skew test.

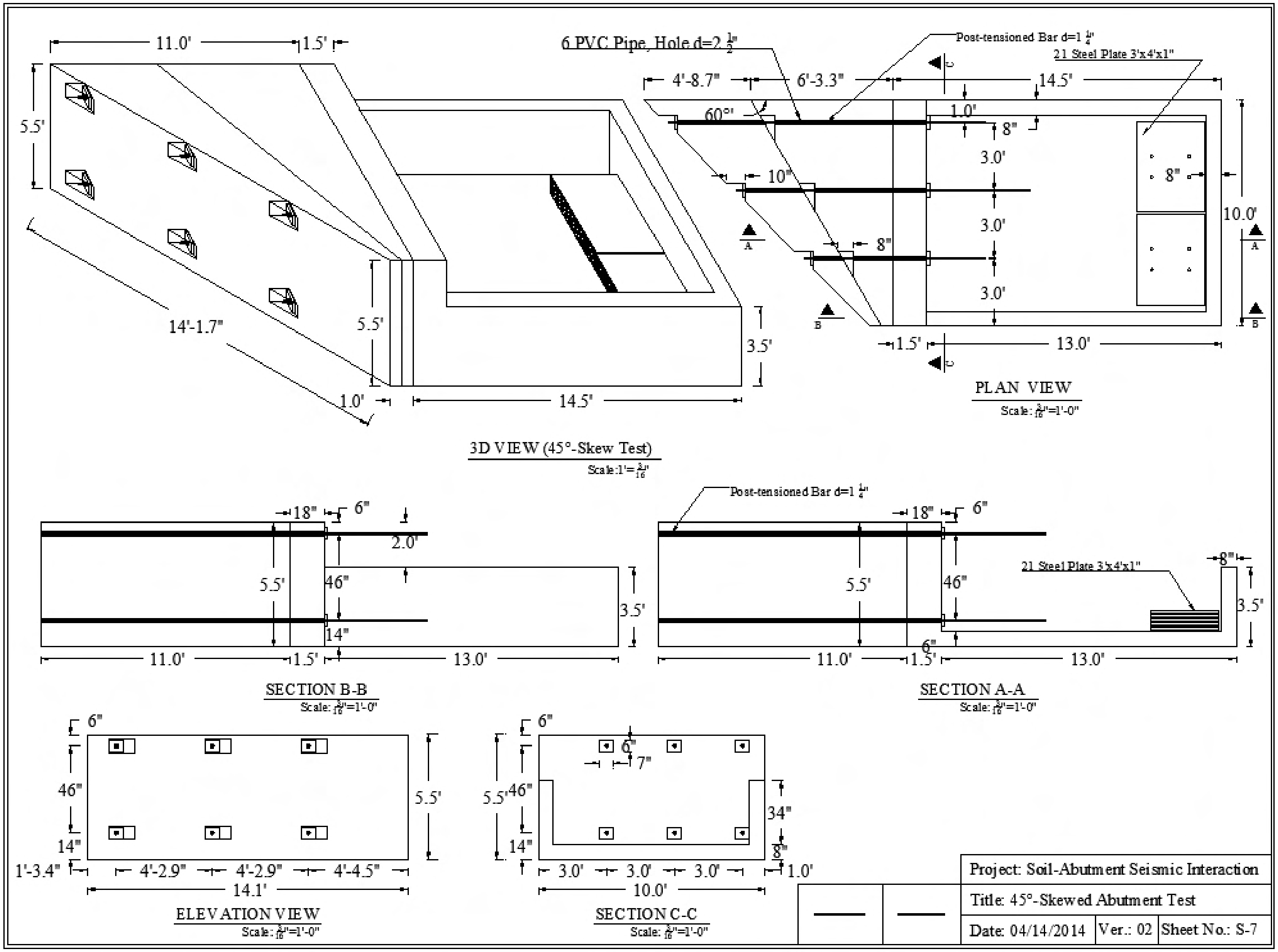

Figure A-3 Bridge block in the 45° skew test.

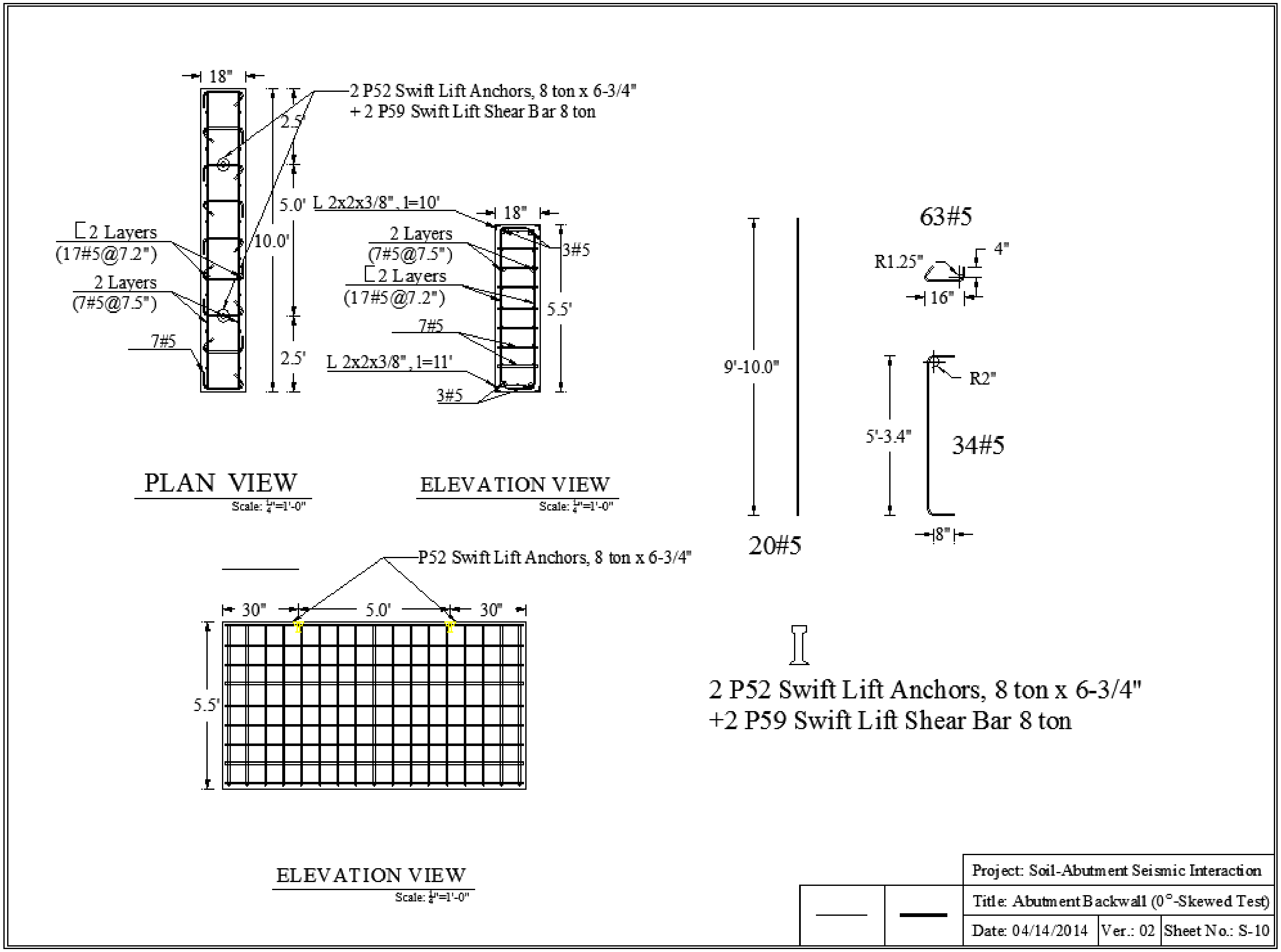

Figure A-4 Abutment wall in the 0° skew test.

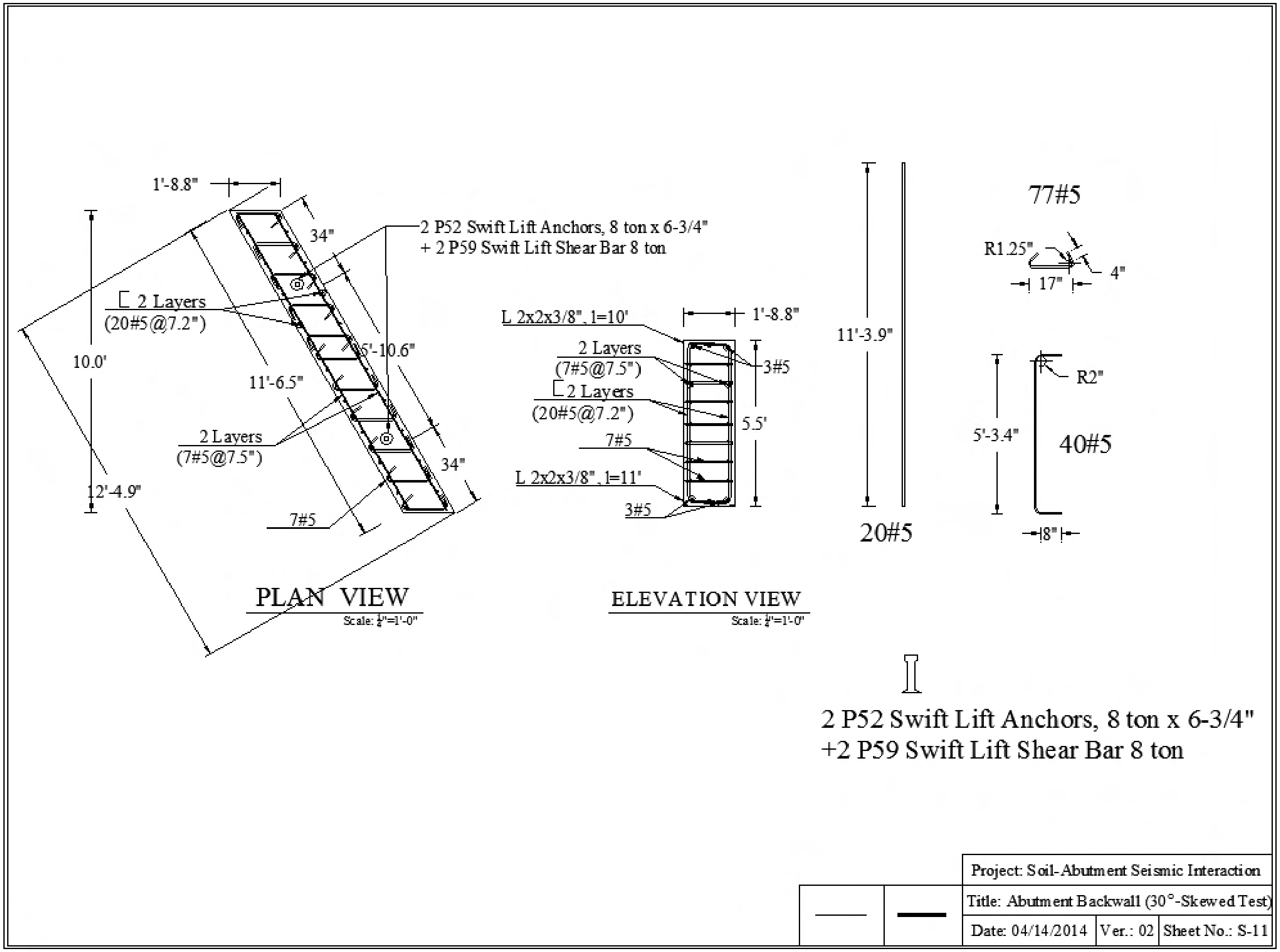

Figure A-5 Abutment wall in the 30° skew test.

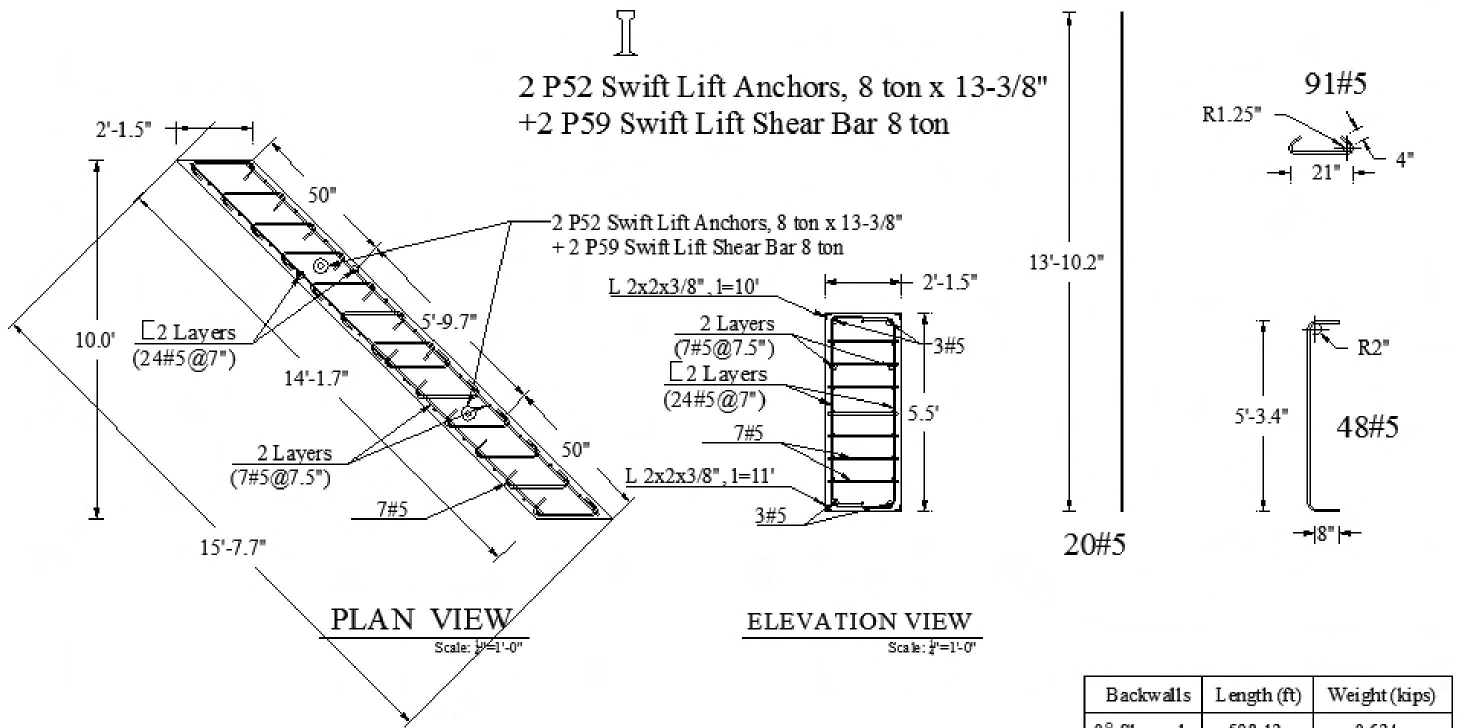

Backwalls	Length (ft)	Weight (kips)
0°-Skewed	598.12	0.624
30°-Skewed	693.15	0.723
45°-Skewed	887.26	0.925
		2.272

Project: Soil-Abutment Seismic Interaction
Title: Abutment Backwall (45°-Skewed Test)
Date: 04/14/2014 | Ver.: 02 | Sheet No.: S-12

Figure A-6 Abutment wall in the 45° skew test.

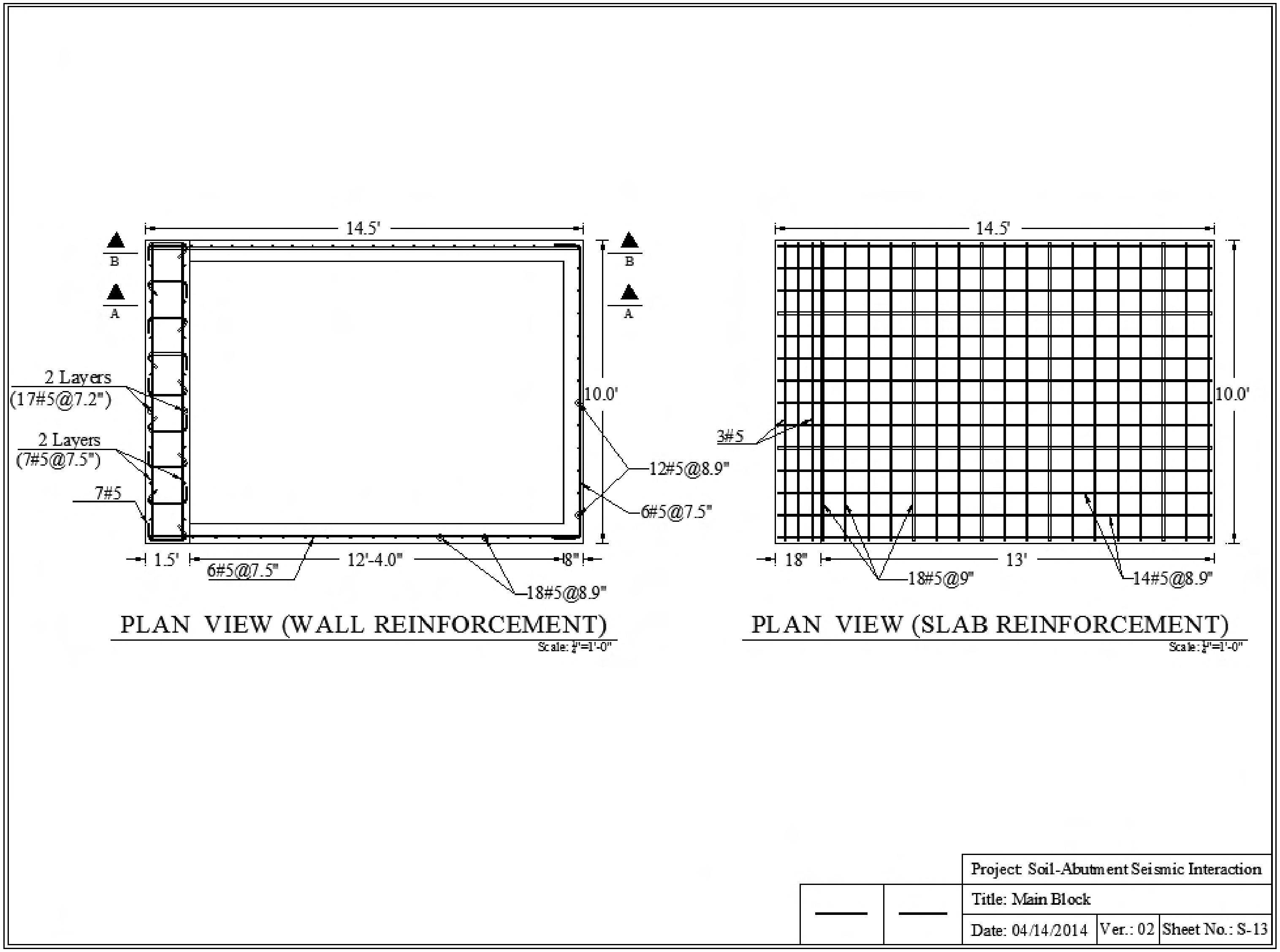

Figure A-7 Main bridge block (plan view).

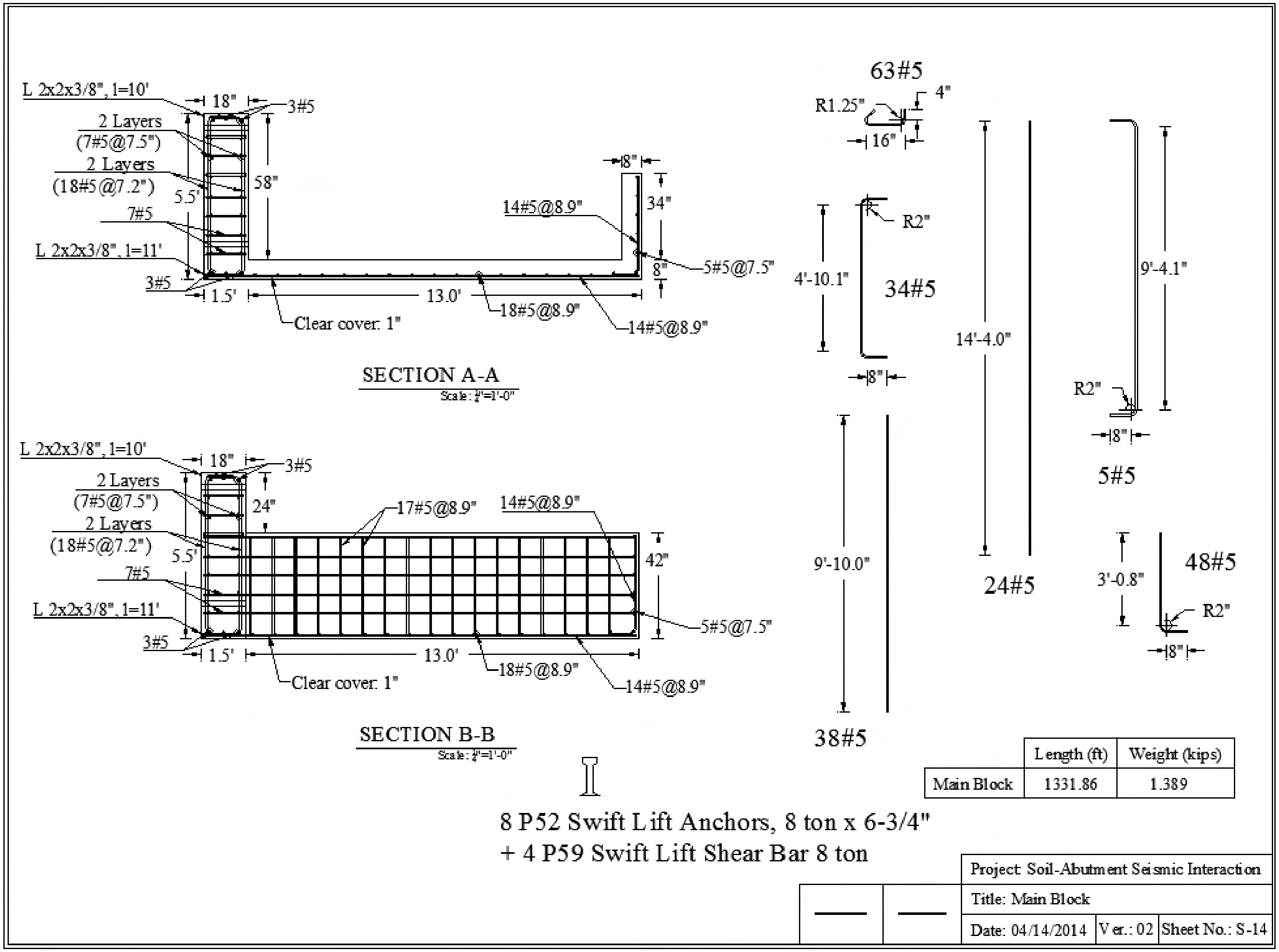

	Length (ft)	Weight (kips)
Main Block	1331.86	1.389

Figure A-8 Main bridge block (elevation view).

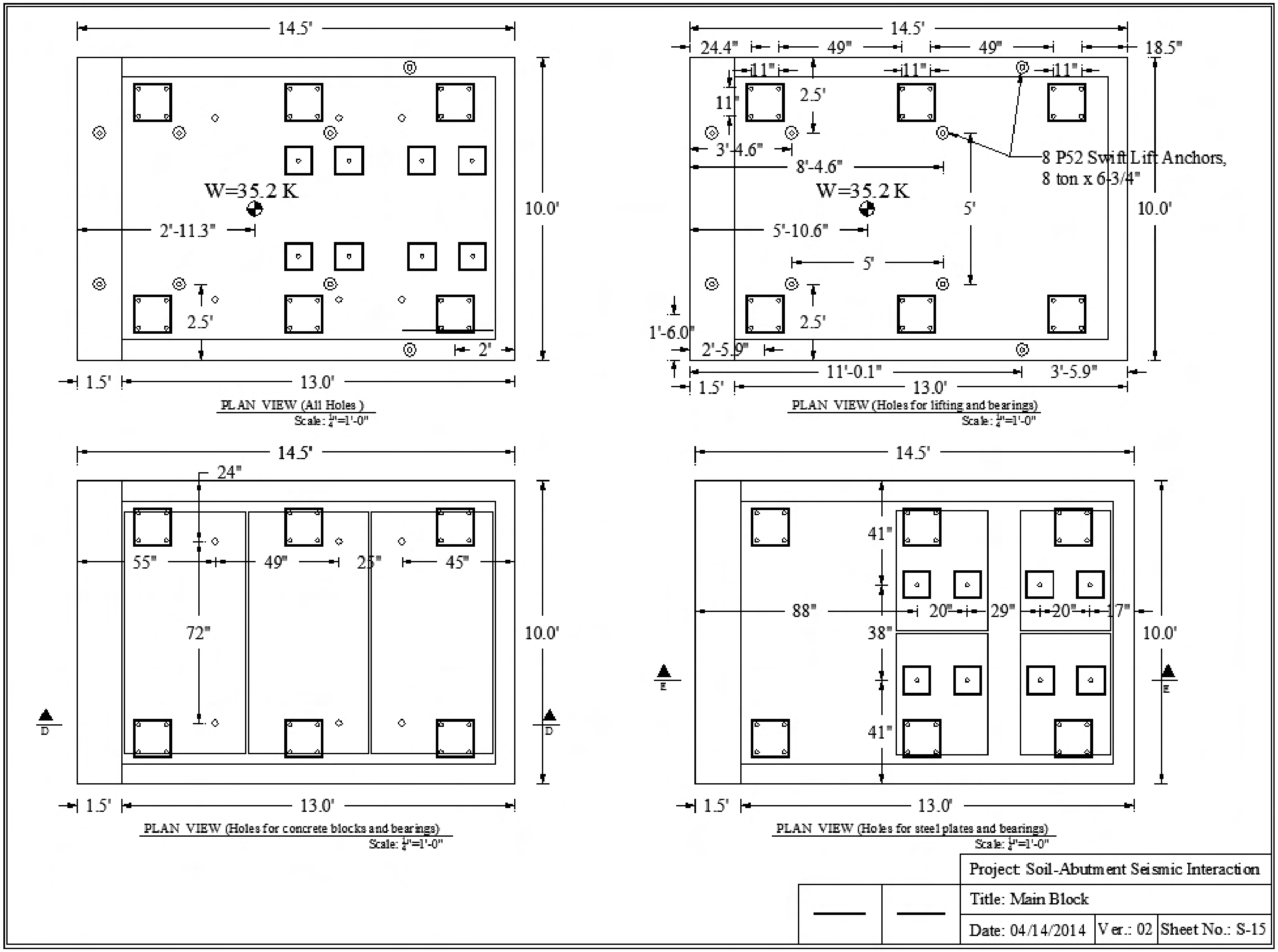

Figure A-9 Main bridge block (plan view of connections).

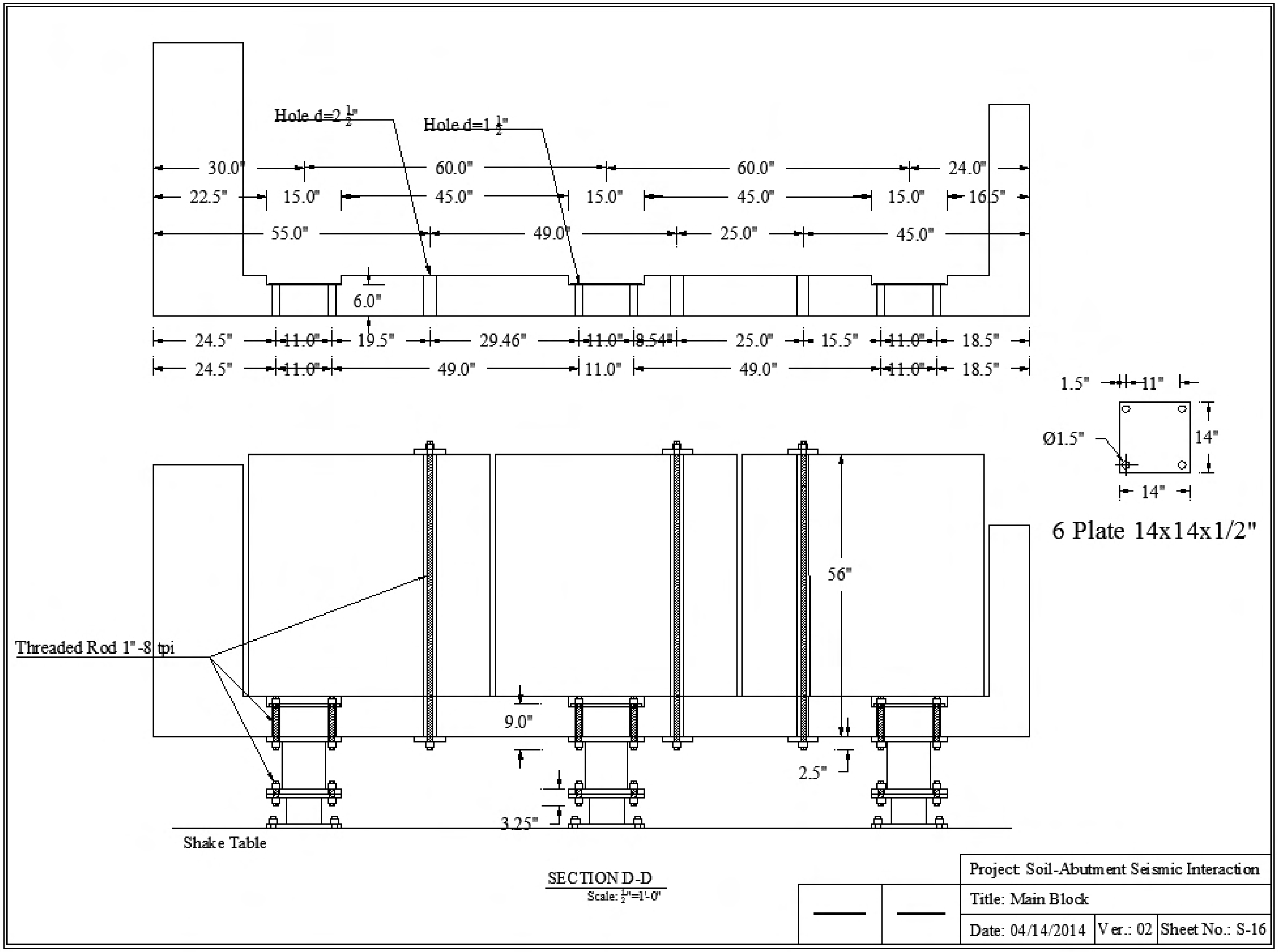

Figure A-10 Main bridge block (elevation view of concrete block connections).

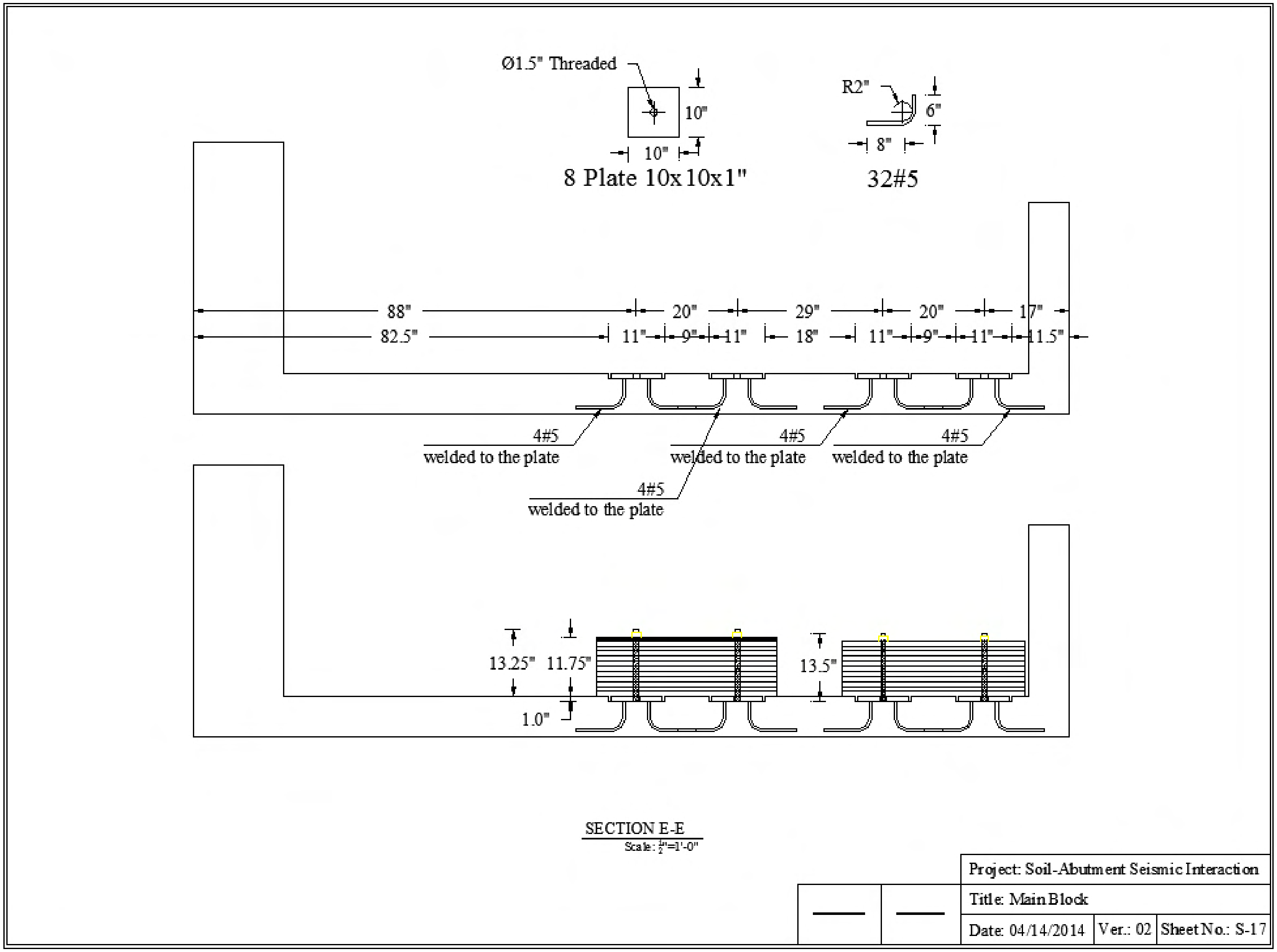

Figure A-11 Main bridge block (elevation view of steel plate connections).

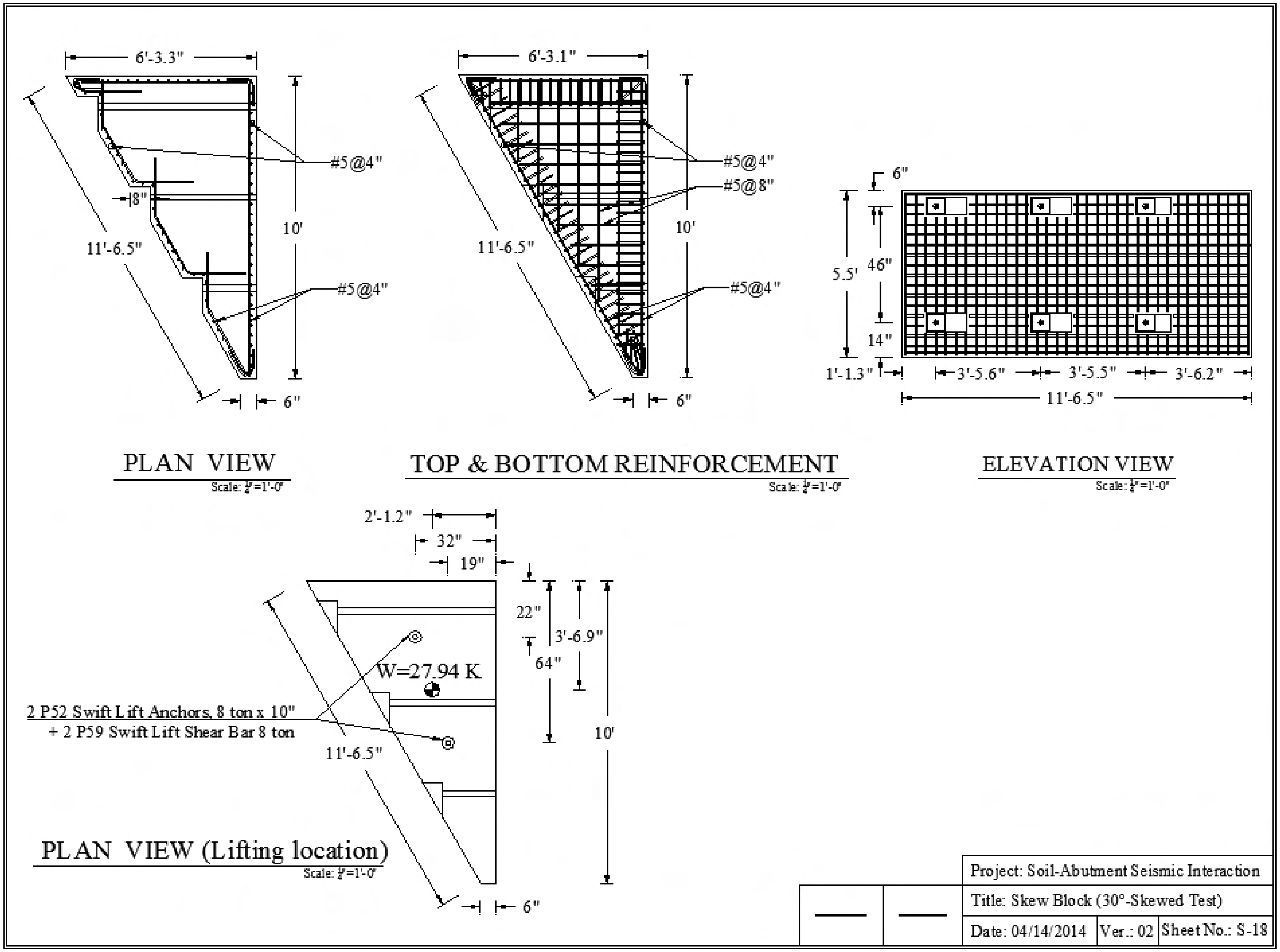

Figure A-12 Skewed wedge in the 30° skew test.

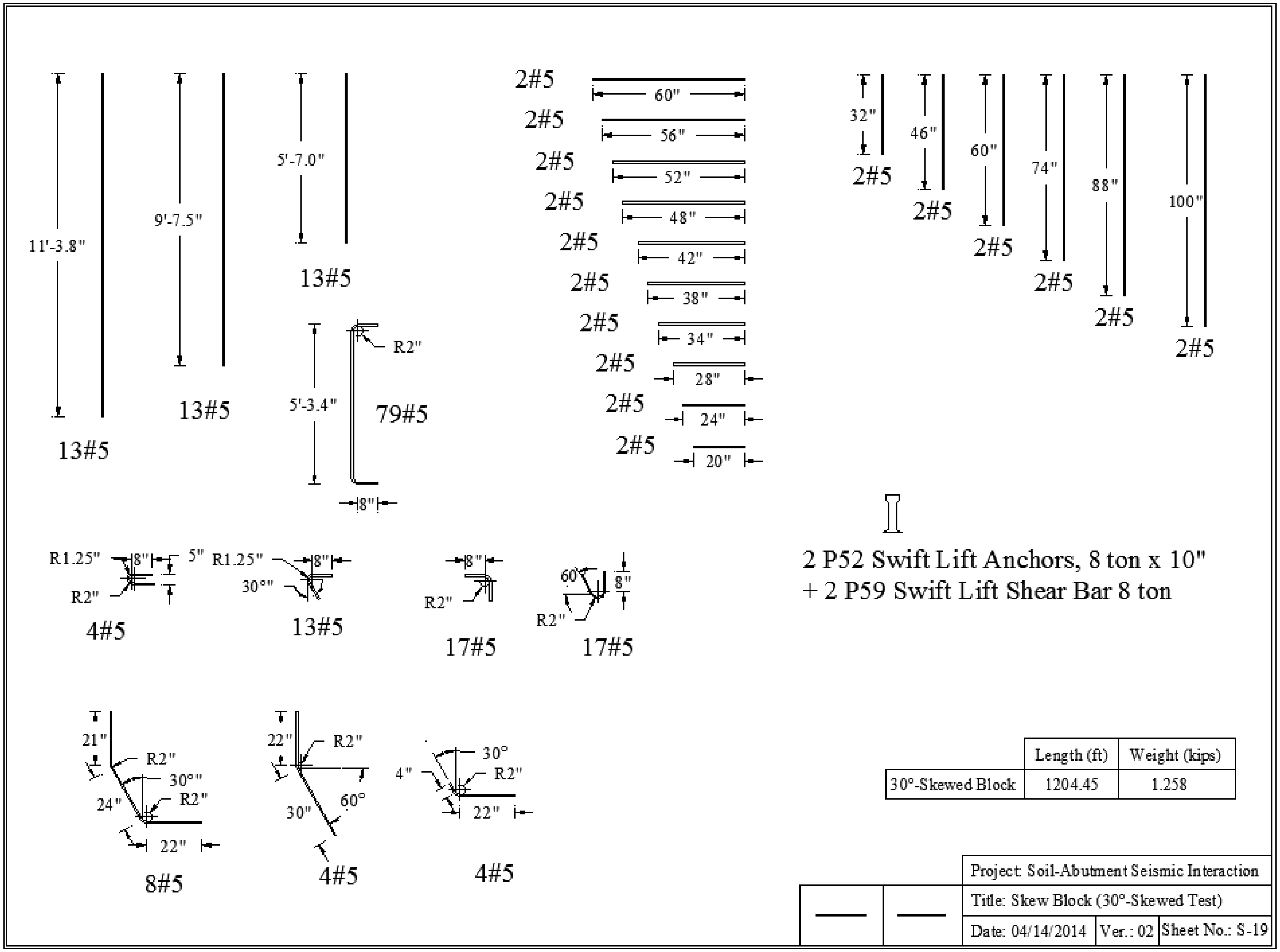

Figure A-13 Reinforcement details of 30° skewed wedge.

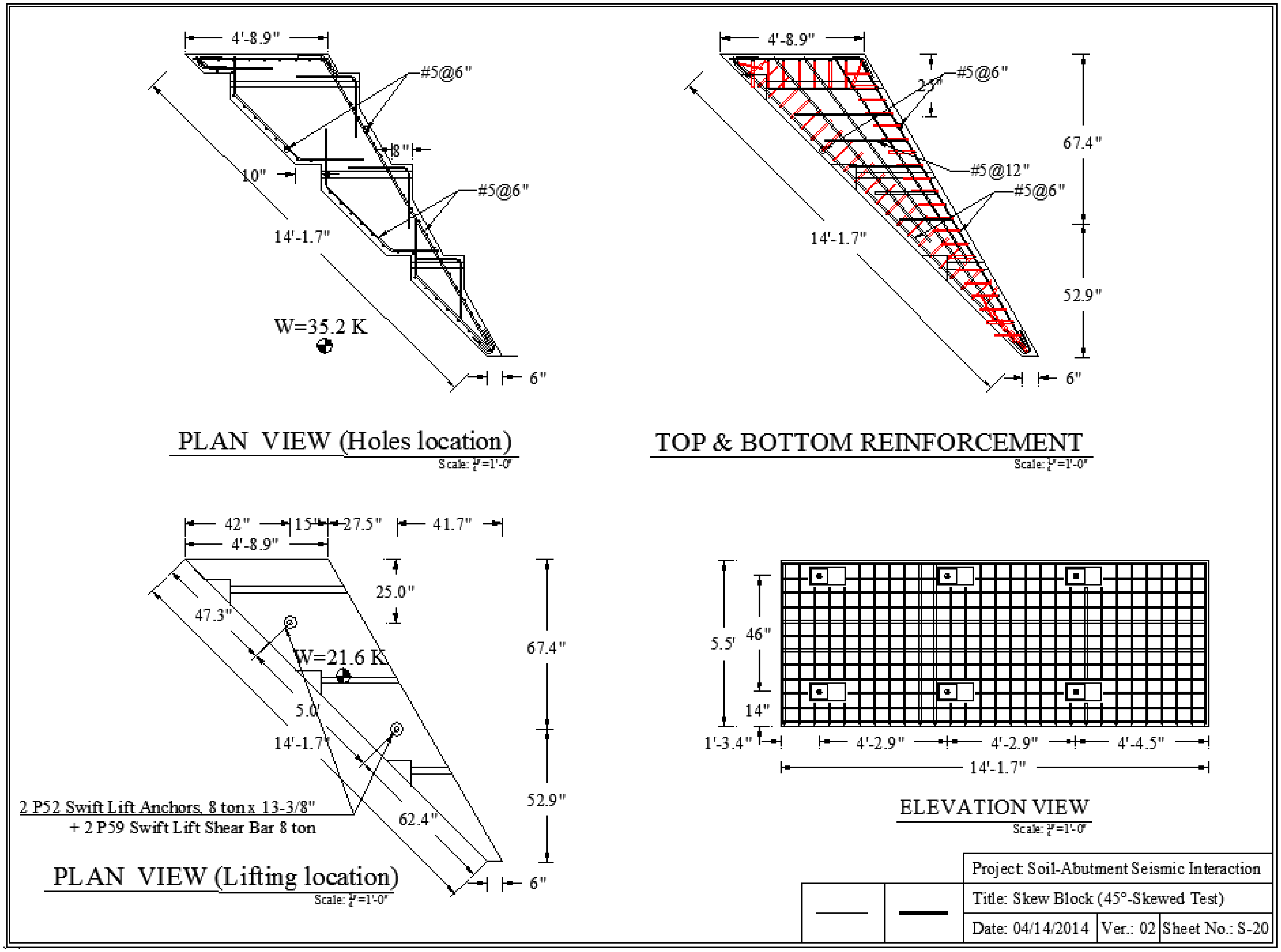

Figure A-14 Skewed wedge in the 45° skew test.

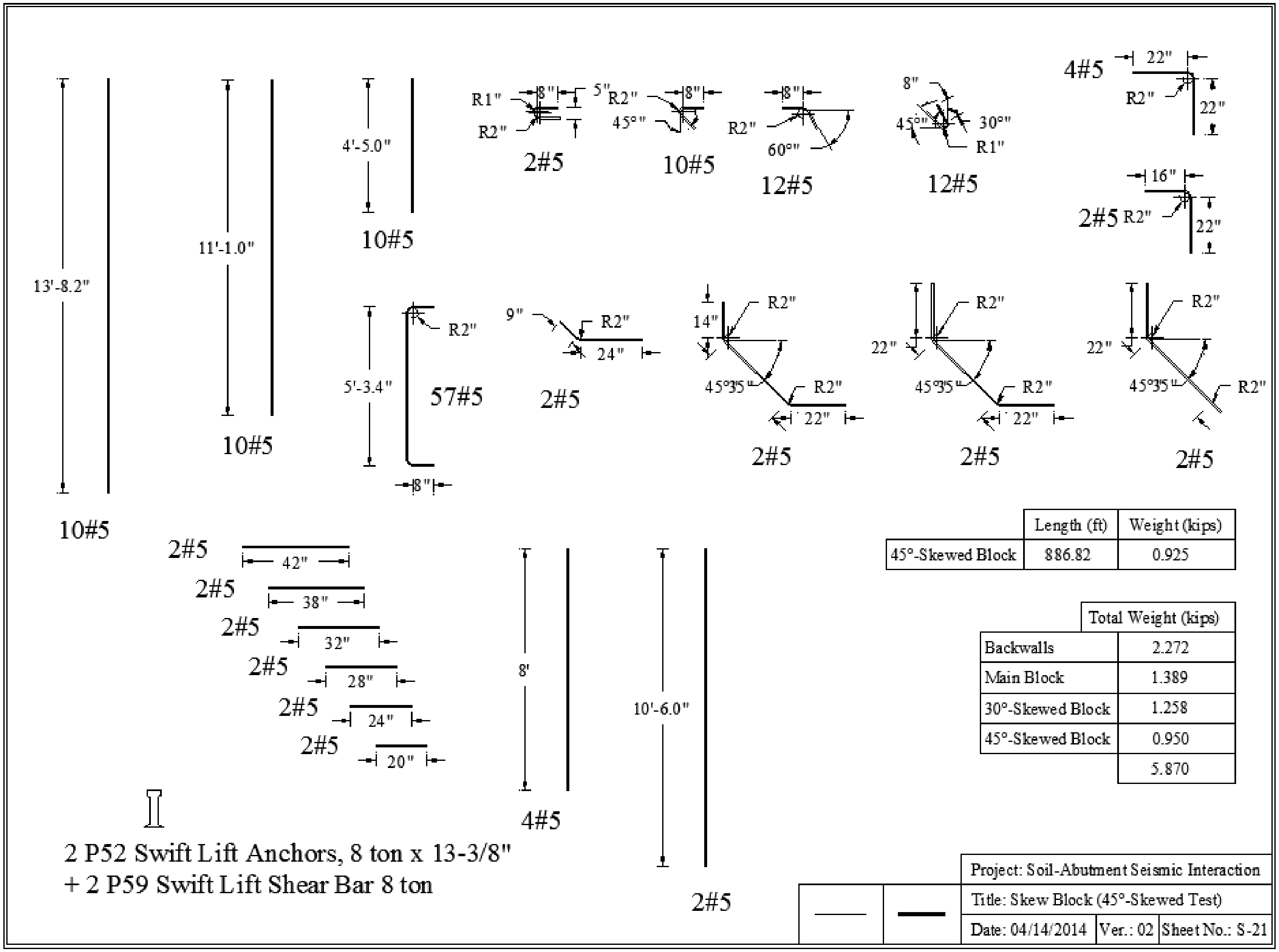

	Length (ft)	Weight (kips)
45°-Skewed Block	886.82	0.925

	Total Weight (kips)
Backwalls	2.272
Main Block	1.389
30°-Skewed Block	1.258
45°-Skewed Block	0.950
	5.870

Figure A-15 Reinforcement details of 45° skewed wedge.

APPENDIX B. Soil Tests

B.1. Introduction

This appendix provides information about the basic properties and strength parameters of the soil that was used in the shake table test of the current study. Results from Atterberg Limit, Sieve Analysis, Proctor Compaction, Direct Shear and Triaxial tests conducted on five different types of soil are presented. The first soil was Crusher Fines material from Lockwood, Nevada with about 10% fine materials and a maximum dry density of 130 pcf. The second soil was Natural Sand from Lockwood, Nevada with maximum dry density of 101.7 pcf. The third soil was ConSand material from Lockwood, Nevada with about 3% fine content and a maximum dry density of 112.1 pcf. The fourth soil was Lohanton Pit Sand with about 1% fine materials and a maximum dry density of 107.4 pcf. The fifth soil was Paiute Pit sand with about 2% fine content and a maximum dry density of 107 pcf.

The Paiute Pit sand was used in the test model as an engineered backfill behind the abutment and was conditioned at optimum water content and compacted in 8-in. lifts to a relative compaction of 95% of maximum dry density of the Standard Proctor Compaction. Direct shear and triaxial tests were carried out on specimens constructed to the same target density and water content.

B.2. Description of Tests

B.2.1. Sieve Analysis

A sieve analysis (ASTM D-422) test on a representative sample of each soil was done and compared with the Caltrans specifications.

B.2.2. Atterberg Limit Test

Tests to determine the liquid and plastic limits were conducted on -#40 sieve material and in accordance with ASTM D-4318. The relationship between the water content and blow count was plotted to find the liquid limit. The plastic limit test was also conducted three times to find the corresponding value.

B.2.3. Proctor Compaction Test

The Standard Proctor (ASTM D-698) and Modified Proctor (ASTM D-1557) tests were done to determine the maximum dry density and the optimum water content for each soil.

B.2.4. Direct Shear Test

Direct shear test was used to determine the shear strength parameters of the soil. Tests were done on circular shear boxes with a diameter of 2.5 in. and a height of 1.0 in. or on square shear boxes with a width of 4 in. and a height of one in. The size of shear box limited the soil fraction that could be tested, according to ASTM D3080. Thus, the soil had to be sieved through sieve #10. As a result, a fraction of soil, which particles sizes were larger than 2 mm, was not included in the test. Samples were prepared at 95% relative compaction and the corresponding optimum moisture content. Figure B-1 shows the sample preparation and direct shear test set up at UNR.

At least three tests at different normal stresses were conducted on the submerged samples using the Humboldt computer controlled direct shear device at UNR. The measured shear stresses and normal stresses at the points of peak and residual stresses were used to find the corresponding shear strength parameters. Figure B-2 shows the typical failure modes of the direct shear test samples.

B.2.5. Triaxial Test

Consolidated Drained (CD) triaxial tests were conducted using a Geocomp computer controlled triaxial system at UNR. The samples were prepared in a mold with an approximate diameter of 2.8 in. and height of 6 in., while the entire material fraction was used. Samples were compacted in ¼-in. or ½-in. layers to obtain a relative compaction of 95% at their optimum moisture content. Sample preparation and test set up are shown in Figure B-3. The tests were at least conducted at three different confining pressures.

Figure B-4 shows the typical failure modes of soil samples under the CD triaxial test. One CD traixial test was also conducted on Crusher Fines material at Nevada Department of Transportation (NDOT) laboratory as a bench mark and to verify the Geocomp device results. Figure B-5 shows the NDOT triaxial test set up and the sheared sample after the test.

B.3. Crusher Fines Sand

B.3.1. Sieve Analysis, Atterberg Limit, Classification, and Compaction Results

Figure B-6 shows a picture of Crusher Fines material. The results of a sieve analysis test on a representative sample are presented in Table B-1 and Figure B-7 along with Caltrans specifications for comparison. The percentage of the fines passing -#200 is 9.8%. The results of Atterberg limits are presented in Table B-2. According to Unified Soil Classification System (USDS), this soil is classified as SP-SC (poorly graded sand with clay, or silty clay). According to AASHTO classification system, this soil is classified as A-1-b (0). The maximum dry density was assessed to be about 130 pcf at an optimum water content of 10% for the standard test and about 134 pcf at an optimum water content of 8% for the modified test.

B.3.2. Direct Shear Test Results

Due to the shear box size, 46% of the soil fraction, which particles sizes were larger than 2 mm, was not included in the test. The measured shear stress versus normal stress of the specimens is shown in Figure B-8. The peak friction angle and cohesion of the sieved material were found to be 39º and 5.51 psi and the residual friction angle and cohesion were determined to be 34º and 1.43 psi, respectively.

B.3.3. Triaxial Test Results

The corresponding Mohr's circles and the p'-q relationship are presented in Figure B-9 and Figure B-10. The shear strength parameters of friction angle and cohesion were found to be 44.3º and 12.35 psi, respectively.

B.4. Natural Sand

B.4.1. Classification and Compaction Results

Figure B-11 shows a picture of Natural Sand material. According to USDS, this soil is classified as SP (poorly graded sand). According to AASHTO classification system, this soil is classified as A-1-b. The maximum dry density was assessed to be about 101.7 pcf at an optimum water content of 17.5% for the standard proctor test.

B.4.2. Direct Shear Test Results

Due to the shear box size, a low fraction of soil, which particles sizes were larger than 2 mm, was not included in the test. The measured shear stress versus the normal stress of the specimens is shown in Figure B-12. The peak friction angle and cohesion of the sieved material were found to be 28.9º and 1.53 psi (221 psf) and the residual friction angle and cohesion were determined to be 20.7º and 2 psi (287 psf), respectively. The direct shear tests were relatively representative of the whole material. Therefore, triaxial tests were not done on this soil since the measured shear strength parameters were not satisfying the required values.

B.5. ConSand

B.5.1. Sieve Analysis, Classification, and Compaction Results

Figure B-13 shows a picture of ConSand material. The results of a sieve analysis test on a representative sample are presented in Table B-3 and Figure B-14 along with Caltrans specifications for comparison. The percentage of the fines passing -#200 is 3.1%. According to USDS, this soil is classified as SP (poorly graded sand). According to AASHTO classification system, this soil is classified as A-1-b. The maximum dry density was assessed to be about 112.1 pcf at an optimum water content of 16.3% for the standard proctor test.

B.5.2. Direct Shear Test Results

Due to the shear box size, about 23% of the soil fraction, which particles sizes were larger than 2 mm, was not included in the test. The measured shear stress versus the normal stress of the specimens is shown in Figure B-15. The peak friction angle and cohesion of the sieved material were found to be 36.3º and 3.51 psi (505 psf) and the residual friction angle and cohesion were determined to be 23º and 2.66 psi (383 psf), respectively.

B.5.3. Triaxial Test Results

The corresponding Mohr's circles and the p'-q relationship are presented in Figure B-16. The shear strength parameters of friction angle and cohesion were found to be 37.2º and 3.39 psi (488 psf), respectively.

B.6. Lohanton Pit Sand

B.6.1. Sieve Analysis, Classification, and Compaction Results

Figure B-17 shows a picture of Lohanton Pit sand material. The results of a sieve analysis test on a representative sample are presented in Table B-4 and Figure B-18 along with Caltrans specifications for comparison. The percentage of the fines passing -#200 is 1.1%. According to USDS, this soil is classified as SP (poorly graded sand). According to AASHTO classification system, this soil is classified as A-1-b. The maximum dry density was assessed to be about 107.4 pcf at an optimum water content of 12.3% for the standard proctor test.

B.6.2. Direct Shear Test Results

Due to the shear box size, about 1/4th of the soil fraction, which particles sizes were larger than 2 mm, was not included in the test. The measured shear stress versus the normal stress of the specimens is shown in Figure B-19. The peak friction angle and cohesion of the sieved material were found to be 34.8º and 0.71 psi (103 psf).

B.6.3. Triaxial Test Results

The corresponding Mohr's circles and the p'-q relationship are presented in Figure B-20. The shear strength parameters of friction angle and cohesion were found to be 37.2º and 3.39 psi (488 psf), respectively.

B.7. Paiute Pit Sand

B.7.1. Sieve Analysis, Classification, and Compaction Results

Figure B-21 shows a picture of Paiute Pit sand material. The results of a sieve analysis test on a representative sample are presented in Table B-5 and Figure B-22 along with Caltrans specifications for comparison. The percentage of the fines passing -#200 is 1.9%. According to USDS, this soil is classified as SP (poorly graded sand). According to AASHTO classification system, this soil is classified as A-1-b. The maximum dry density was assessed to be about 107 pcf at an optimum water content of 10% for the standard proctor test.

B.7.2. Direct Shear Test Results

Due to the shear box size, about 20% of the soil fraction, which particles sizes were larger than 2 mm, was not included in the test. The measured shear stress the normal stress of the specimens is shown in Figure B-23. The peak friction angle and cohesion of the sieved material were found to be 34.3º and 1.31 psi (188 psf) and the residual friction angle and cohesion were determined to be 24.2º and 1.40 psi (202 psf), respectively.

B.7.3. Triaxial Test Results

The corresponding Mohr's circles and the p'-q relationship are presented in Figure B-24. The shear strength parameters of friction angle and cohesion were found to be 40.4º and 2.03 psi (292 psf), respectively.

B.8. Summary and Conclusion

The results of Sieve Analysis, Atterberg Limit, Proctor Compaction, Direct Shear, and Triaxial tests were presented for five different types of soil including Crusher fines, Natural Sand, ConSand, Lohanton Pit sand, and Paiute Pit sand. A summary of test results on all the chosen soil material is presented in Table B-6. For the sake of comparison, Table B-7 provides some information about the properties of the soil that was used in the previous abutment tests.

Among the several types of soil tested, the Paiute Pit sand was proposed as the backfill material for the current experimental study. The soil contains about 2% fines with a maximum dry unit weight of about 107 pcf at an optimum water content of 10%. Results from the direct shear and triaxial tests indicate that the average friction angle and cohesion are approximately 40º and 300 psf, respectively. It was thus concluded that the soil properties conformed to Caltrans requirements of gradation and shear strength parameters to represent an engineered backfill to be used in the current study.

Table B-1 Sieve analysis results of Crusher Fines.

Sieve #	Sieve Size (mm)	Mass Passing (%)	Caltrans Spec. (%)	
3/8"	9.5	100.0	Lower	Upper
#4	4.75	93.9	35	100
#8	2.36	62.8	-	-
#10	2	54.1	-	-
#16	1.18	36.7	-	-
#30	0.6	23.1	20	100
#40	0.425	19.4		
#50	0.3	16.4		
#100	0.15	12.5		
#200	0.075	9.8		
Pan	Pan	0.0		

Table B-2 Atterberg limits for -#40 for Lockwood Crusher Fines

Liquid Limit	26.11%
Plastic Limit	21.02%
Plasticity Index	5.09%

Table B-3 Sieve analysis results of ConSand.

Sieve #	Sieve Size (mm)	Mass Passing (%)	Caltrans Spec. (%)	
3/8"	9.5	100.0	Lower	Upper
#4	4.75	99.8	35	100
#8	2.36	82.1	-	-
#10	2	76.7	-	-
#16	1.18	59.3	-	-
#30	0.6	40.5	20	100
#40	0.425	30.5		
#50	0.3	19.7		
#100	0.15	7.0		
#200	0.075	3.1		
Pan	Pan	0.0		

Table B-4 Sieve analysis results of Lohanton Pit sand.

Sieve #	Sieve Size (mm)	Mass Passing (%)	Caltrans Spec. (%)	
3/8"	9.5	100.0	Lower	Upper
#4	4.75	97.0	35	100
#8	2.36	90.0	-	-
#16	1.18	74.0	-	-
#30	0.6	45.0	-	-
#50	0.3	16.0	20	100
#100	0.15	3.0		
#200	0.075	1.1		
Pan	Pan	0.0		

Table B-5 Sieve analysis results of Paiute Pit sand.

Sieve #	Sieve Size (mm)	Mass Passing (%)	Caltrans Spec. (%)	
3/8"	9.5	100.0	Lower	Upper
#4	4.75	99.0	35	100
#8	2.36	87.0	-	-
#16	1.18	72.0	-	-
#30	0.6	49.0	-	-
#50	0.3	22.0	20	100
#100	0.15	6.0		
#200	0.075	1.9		
Pan	Pan	0.0		

Table B-6 Summary of soil test results.

	$\gamma_{d\ max}$ (pcf)	w_{opt} (%)	Direct Shear Test on Sieved#10		CD Triaxial Test (* test on sieved#4)	
			c psi (psf)	Φ (deg)	c psi (psf)	Φ (deg)
Crusher Fines	130	10	5.51 (793)	39.0	12.53 (1804)	44.3
Natural Sand	101.7	17.2	1.53 (221)	28.9	-	-
ConSand	112.1	16.3	3.51 (505)	36.0	5.06 (729)	44.3
Lohanton Pit Sand	107.4	12.3	0.71 (103)	34.8	3.39 (488)*	37.2*
Paiute Pit Sand	107.0	10	1.31 (188)	34.3	2.03 (292)*	40.4*

Table B-7 Summary of soil properties in previous abutment tests.

	γd_{max} (pcf)	w_{opt} (%)	Fines (%)	Test	c (psf)	Φ (deg)	Remarks
BYU Rollins and Cole (2006)	105	17.1	1.3	In-situ direct shear	0.0	39	Clean Sand
	108	16.8	44.7		570	27	Silty Sand
	128	9.5	19.9		79	34	Fine Gravel
	137	7.2	11.7		150	40	Corse Gravel
UCLA Stewart et (2007) Lemnitzer et al. (2009)	127	9	≈10	Triaxial	300-500	39-40	Silty Sand
UCSD Bozorgzadeh (2007) Bozorgzadeh et al. (2008)	126	10.5	35-40	Triaxial	1000	28	Clayey Sand
	127	8.6	25-30		600	34.5	Silty Sand
BYU Rollins et al. (2008) Rollins et al. (2010)	111	11	<5	Direct Shear (Rel. comp. 96% @ 8% w.c.)	39 (grad. 1)	0 (grad. 1)	Clean Sand (Dry density not sensitive to moisture content) c=0, Φ=40.5º was assumed
					43.3 (grad. 2)	0 (grad. 2)	
UCSD Wilson and Elgamal (2008) Wilson (2009) Wilson and Elgamal (2010)	129	8.5	≈7	Direct Shear	292	48	Silty Sand
				Triaxial		44	
BYU Rollins and Jesse (2013) Jesse and Rollins (2013)	113.5	13	<5	Direct Shear	70-140	46	Clean Sand (Dry density not sensitive to moisture content)
BYU Marsh et al. (2013)	111.5	7.1	<5	Direct Shear	96.3	41	Clean Sand (9% moisture content was used in the field compaction)

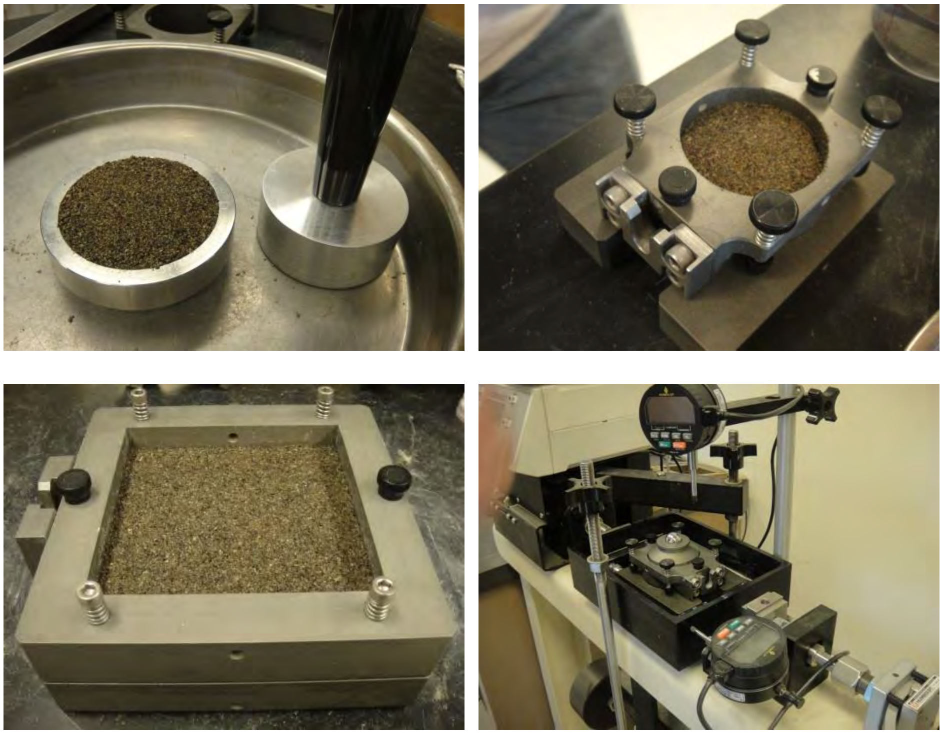

Figure B-1 Sample preparation and direct shear test set up.

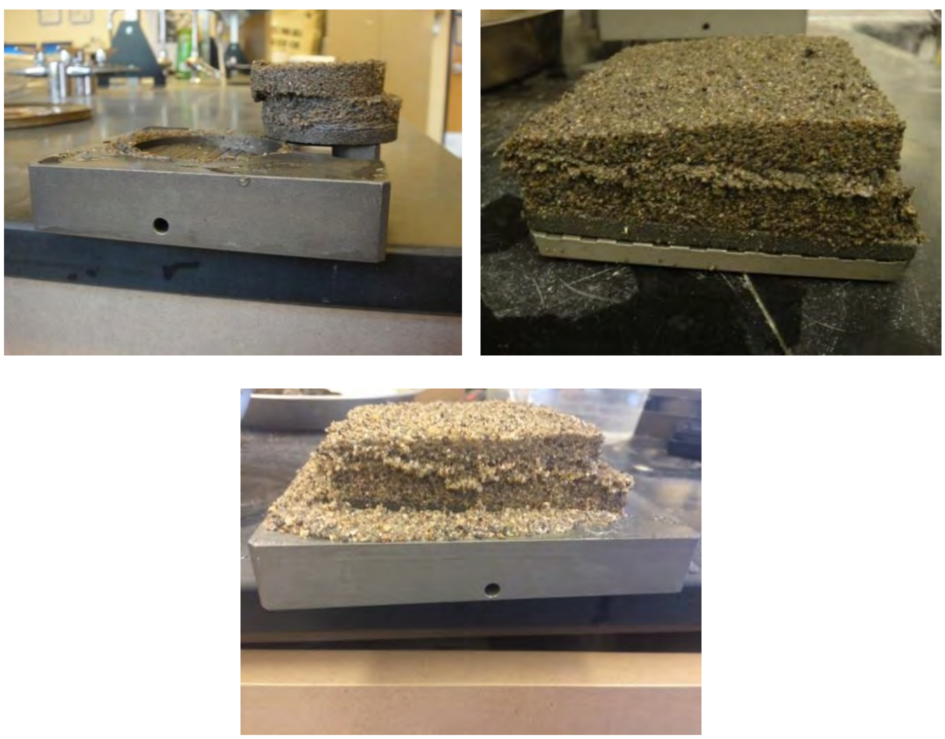

Figure B-2 Failure modes of direct shear test samples.

Figure B-3 Sample preparation and test set up of triaxial test at UNR.

Figure B-4 Failure modes of triaxial test samples.

Figure B-5 NDOT triaxial test set up and the failed Crusher Fines sample.

Figure B-6 Crusher Fines material.

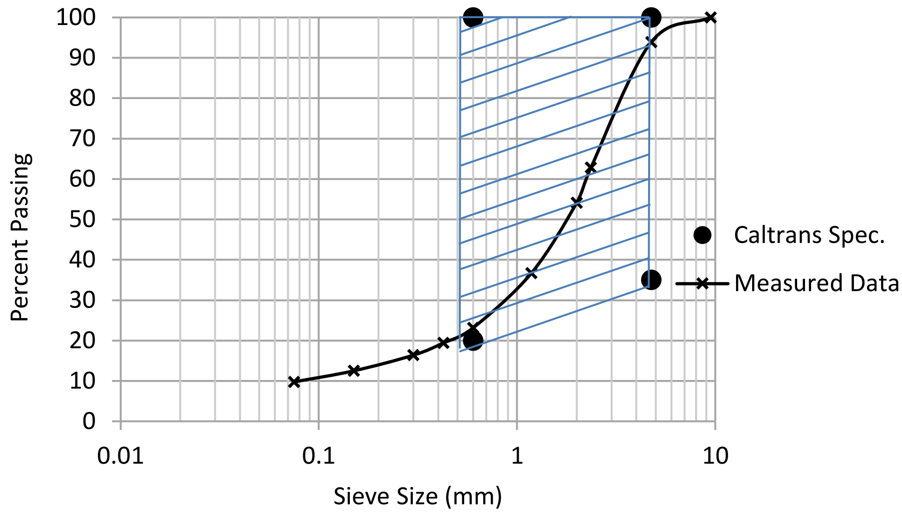

Figure B-7 Sieve analysis results of Crusher Fines.

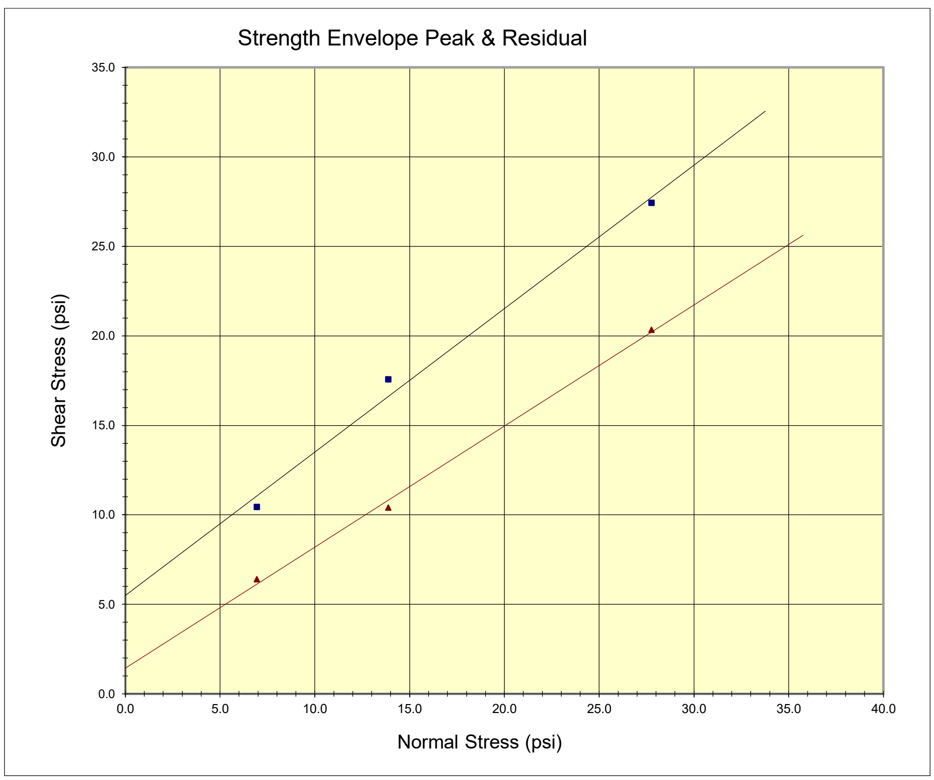

Figure B-8 Direct shear test results of the sieved Crusher Fines.

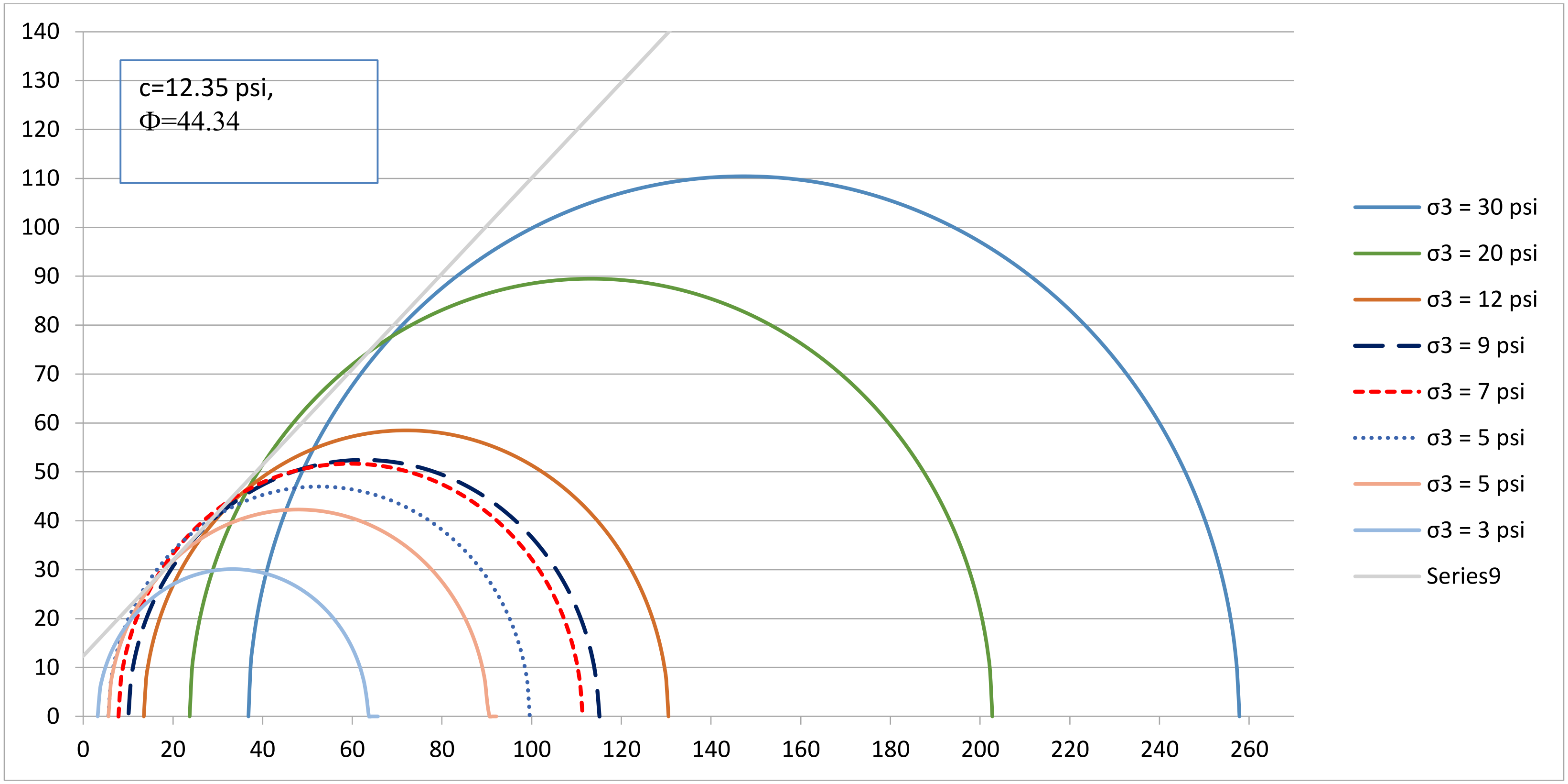

Figure B-9 Mohr's circles of CD triaxial tests on Crusher Fines.

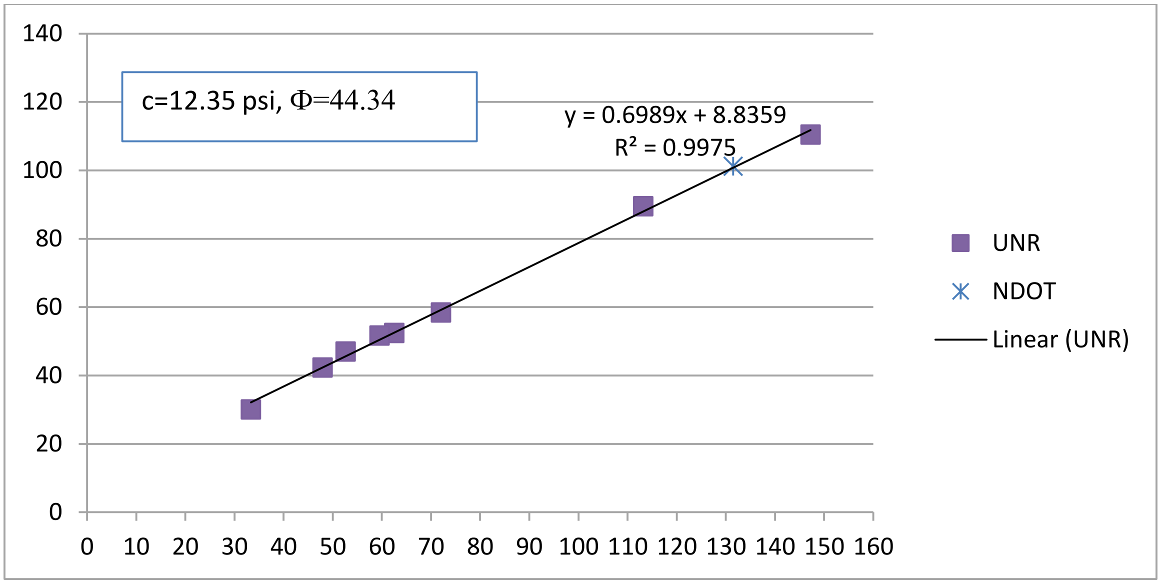

Figure B-10 p'-q relationship of CD triaxial test samples of Crusher Fines.

Figure B-11 Natural Sand material.

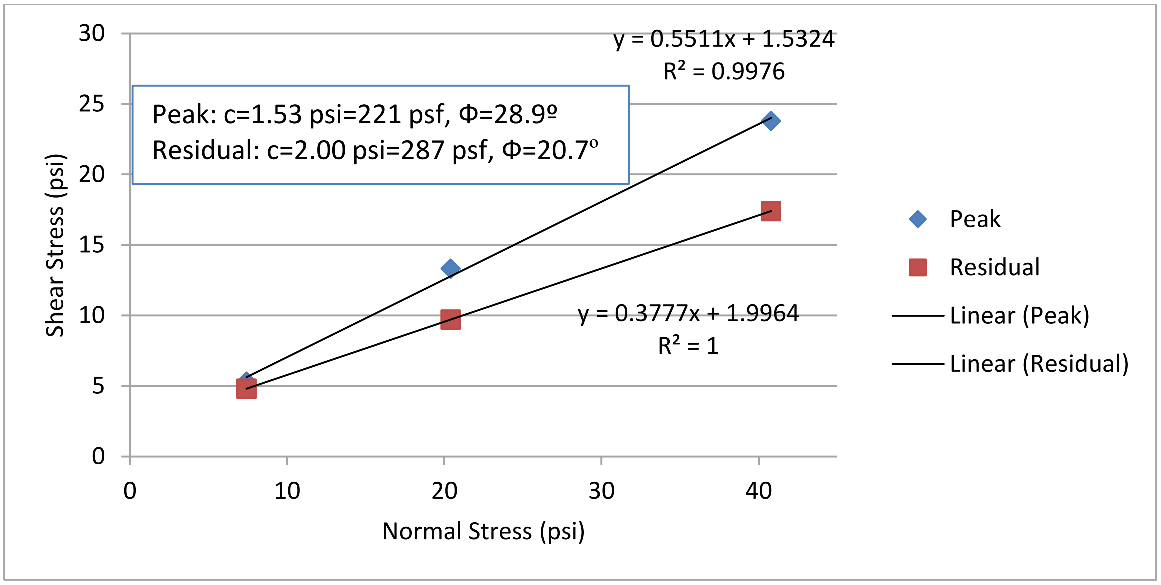

Figure B-12 Direct shear test results on the sieved Natural Sand.

Figure B-13 ConSand material.

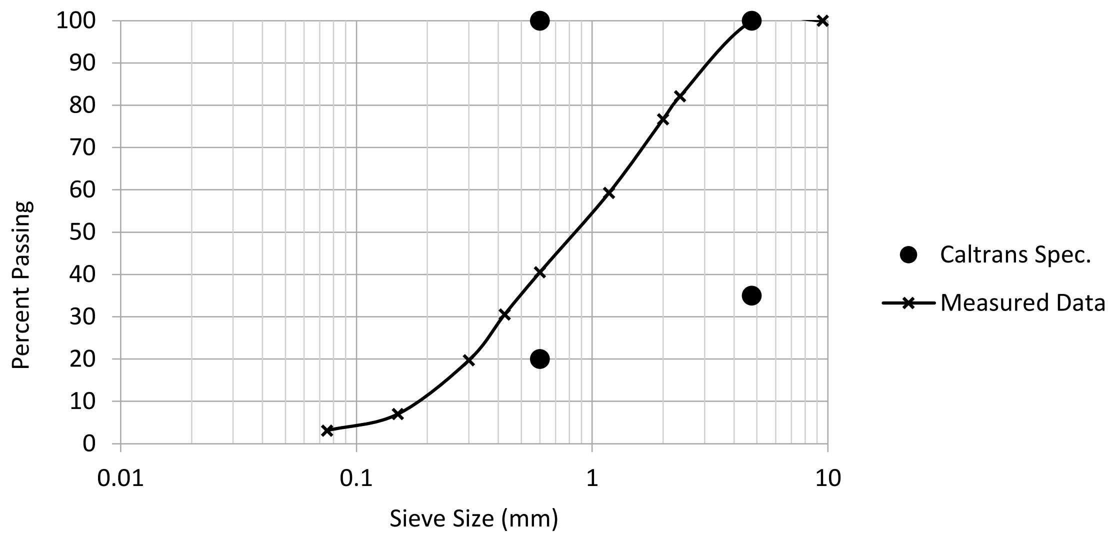

Figure B-14 Sieve analysis results of ConSand.

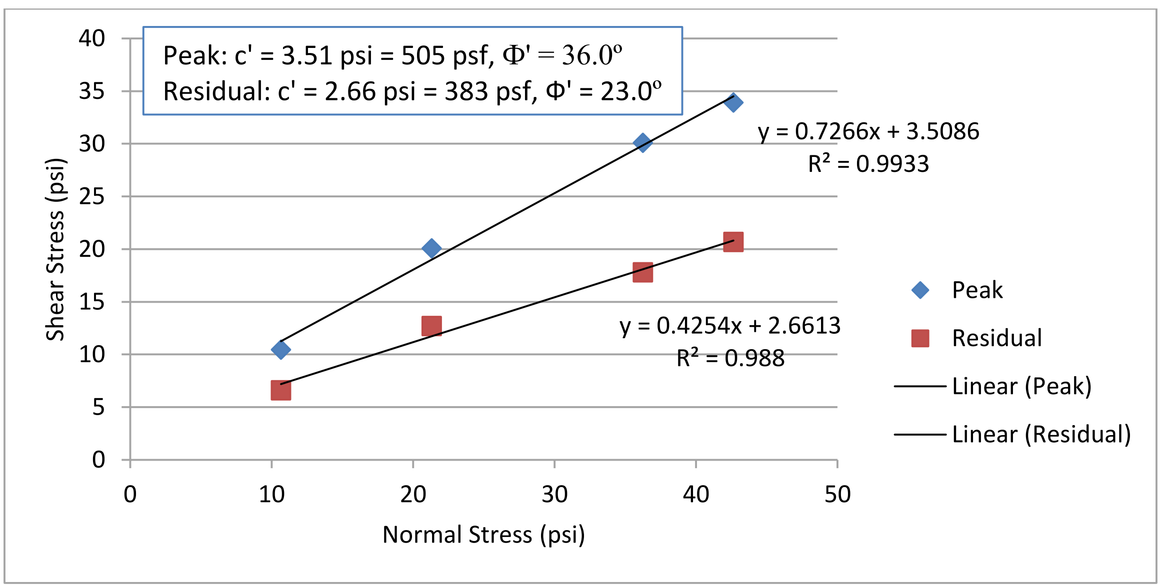

Figure B-15 Direct shear test results of the sieved ConSand.

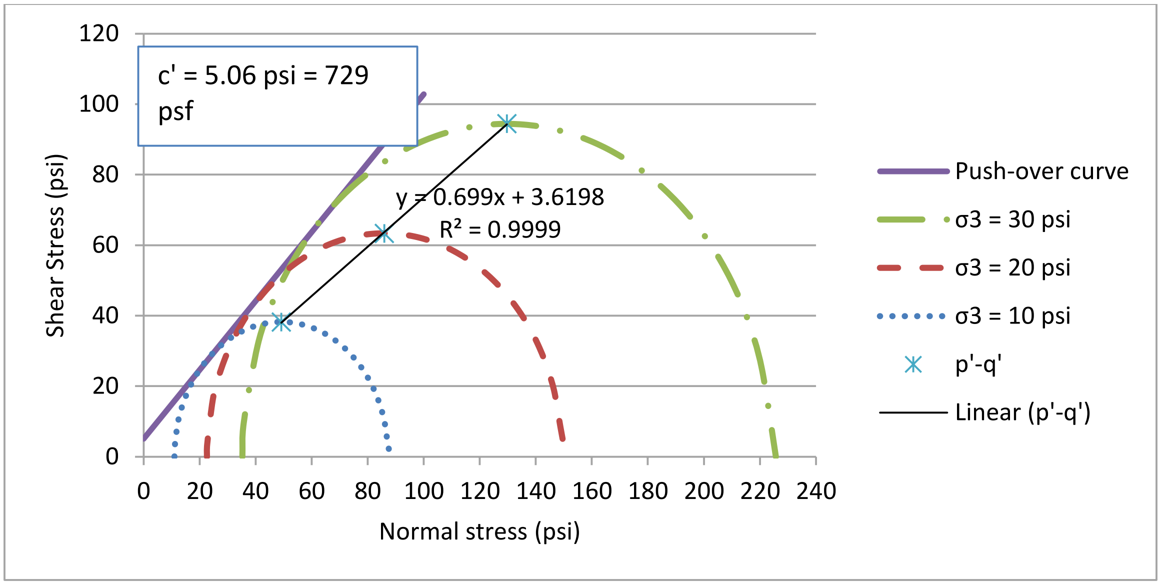

Figure B-16 Mohr’s circles of CD triaxial tests on ConSand.

Figure B-17 Lohanton Pit sand material.

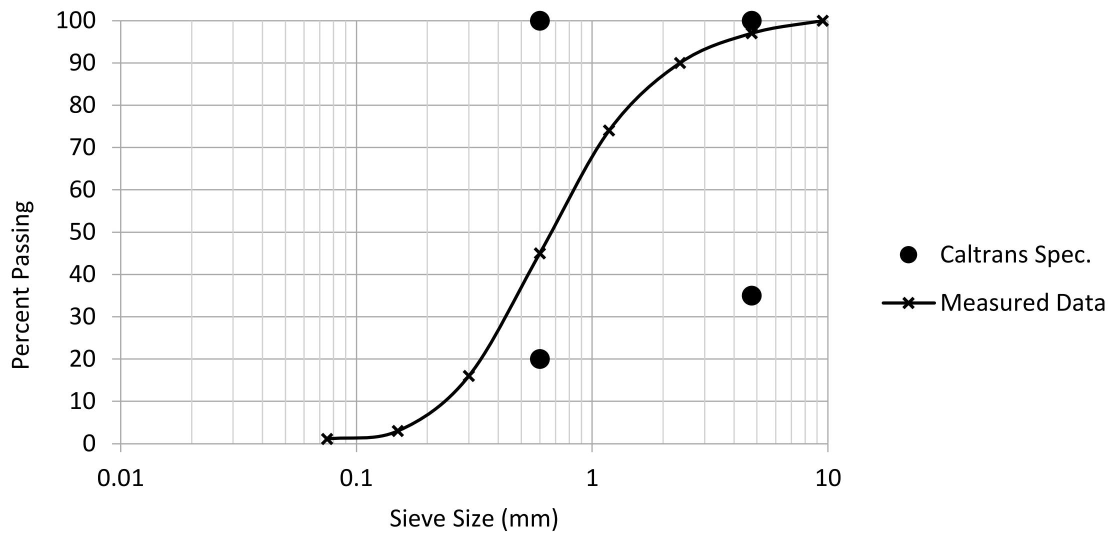

Figure B-18 Sieve analysis results of Lohanton Pit sand.

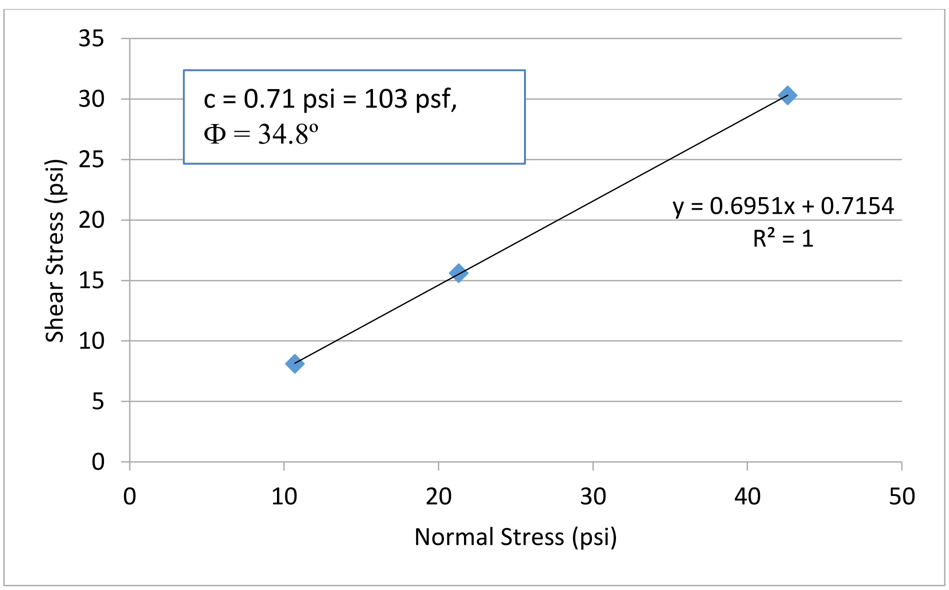

Figure B-19 Direct shear test results of the sieved Lohanton Pit sand.

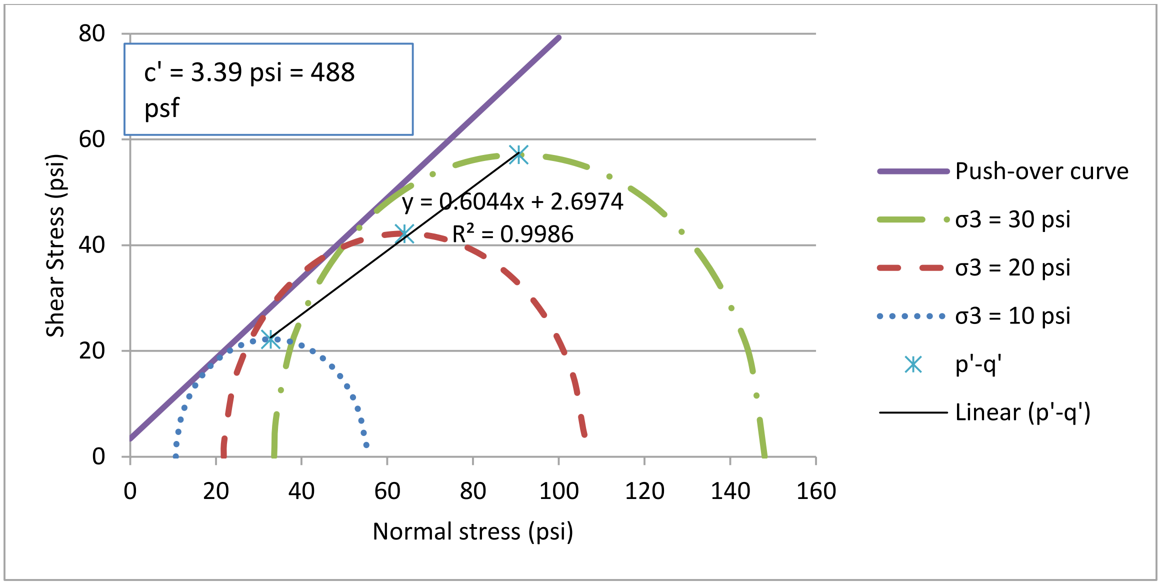

Figure B-20 Mohr's circles of CD triaxial tests on Lohanton Pit sand.

Figure B-21 Paiute Pit sand material.

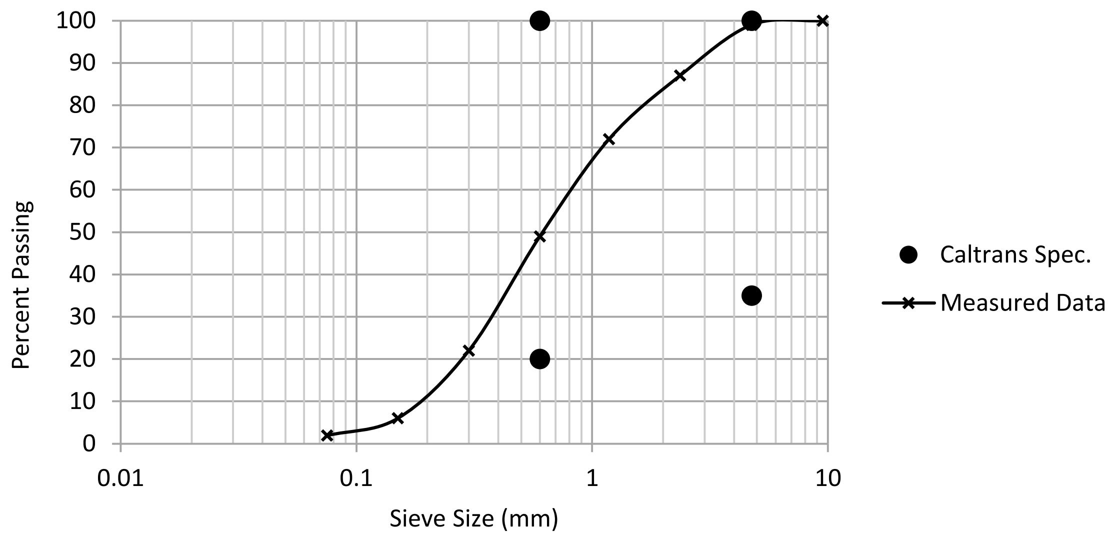

Figure B-22 Sieve analysis results of Paiute Pit sand.

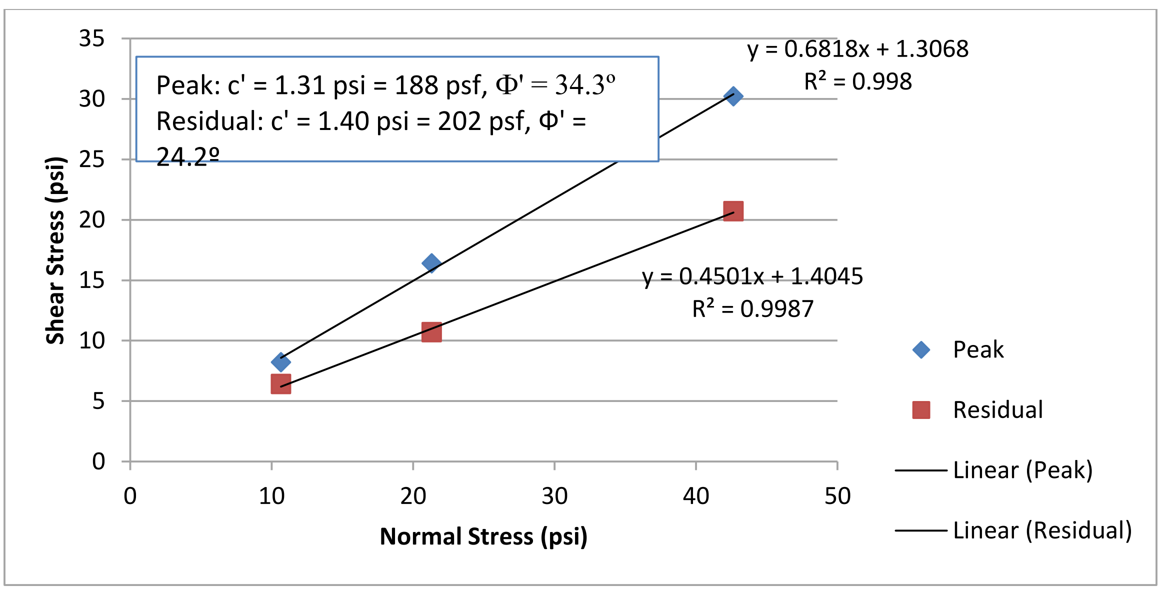

Figure B-23 Direct shear test results of the sieved Paiute Pit sand.

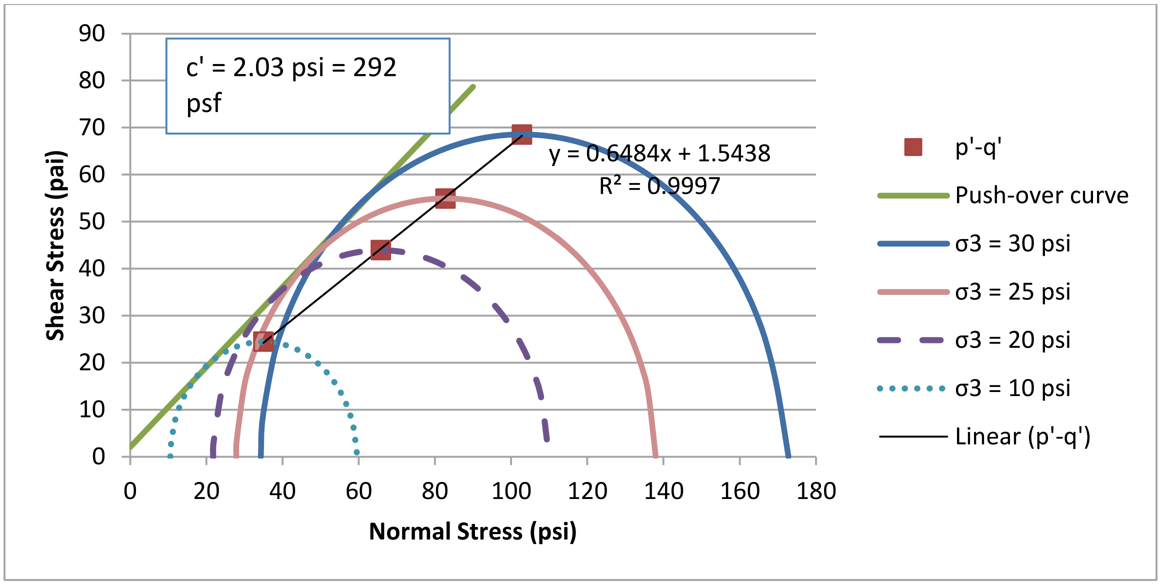

Figure B-24 Mohr's circles of CD triaxial tests on Paiute Pit sand.

APPENDIX C. Soil Box Design

C.1. Introduction

This appendix presents design details of the test model soil box described in Chapter 5 including the shear studs connecting the base plywood to the steel supports, and the wooden studs supporting the soil box.

C.2. Base Plywood Shear Studs

- 2" pipe sleeves (l=8-5/16")
- Tightening HSS 2"x1/8" or HSS 2"x1/4" in the sleeve with shims
- Coefficient of friction between wood and steel: 0.2-0.6=0.2

$$V_n = F_{cr} A_g / 2$$

$$F_{cr} = \frac{1.6E}{\sqrt{\frac{L_v}{D}\left(\frac{D}{t}\right)^{\frac{5}{4}}}} \leq 0.6F_y$$

$$F_{cr} = \frac{0.78E}{\left(\frac{D}{t}\right)^{\frac{3}{2}}} \leq 0.6F_y$$

For HSS 2"×1/8": $F_{cr} = \frac{0.78(29000)}{\left(\frac{2}{0.125}\right)^{\frac{3}{2}}} = 353.44$ ksi > 30 ksi $\rightarrow F_{cr} = 30$ ksi

$$\rightarrow V_n = \frac{30\left(\pi/4\left(2^2 - 1.75^2\right)\right)}{2} = 11 \text{ kips}$$

$$\gamma = 1.1\gamma_{d\max} = 1.1(107) = 118 \text{ pcf}$$

$$\rightarrow W = \frac{118(115)(27)}{1000} = 365 \text{ kips} \rightarrow \mu W = 0.2(365) = 73 \text{ kips}$$

Soil Passive Capacity: $(8ksf)(5.5ft)(10ft) = 440$ kips

Additional Shear: $440 - 73 = 367$ kips

Number of Shear Studs: $\frac{367}{11} \cong 33 \rightarrow$ choose 36

C.3. Soil Box Wooden Studs

__Design Loads:__

$$h = 6.8ft$$

$$\gamma = 1.1\gamma_{d\max} = 1.1(107) = 118 \text{ pcf}$$

$$k_0 = 1 - \sin\phi = 1 - \sin 40° = 0.36$$

$$\sigma_h = k_0\gamma h = (0.36)(118)(6.8) = 290 \text{ psf}$$

$(\sigma_h)_{factored} = 1.75 k_0 \gamma h = 1.75(0.36)(118)(6.8) \approx 500$ psf (dynamic effect)

For each stud at 2-ft spacing: $(\sigma_h)_{factored} = 2 \times 500 = 1{,}000$ lb/ft $= 1.0$ kip/ft

$V_{\max} = 1.21$ kips (See Figure C-1 and Figure C-2)

$M_{\max} = 7.1$ kip.in (See Figure C-1 and Figure C-2)

Shear Capacity:

$$V_r' = \frac{2}{3} F_v' b d_n$$

$F_v' = F_v C_D C_M C_t C_i K_F \phi \lambda$ (NDS Table 4.3.1)

Reference Design Value of Shear: $F_v = 180$ psi (NDS Supplement Table 4A)

Load Duration Factor (ASD only): $C_D = 1.0$ (NDS Table 2.3.2)

Wet Service Factor: $C_M = 1.0$ (NDS Supplement Table 4A)

Temperature Factor: $C_t = 1.0$ (NDS Table 2.3.3)

Incising Factor: $C_i = 1.0$ (NDS Section 4.3.8)

Format Conversion Factor (LRFD only): $K_F = 2.88$ (NDS Table 4.3.1)

Resistance Factor (LRFD only): $\phi = 0.75$ (NDS Table 4.3.1)

Time Effect Factor (LRFD only): $\lambda = 0.6$ (NDS Table N3)

ASD: $F_v' = 180(1.0)(1.0)(1.0) = 180$ kips

$V_r' = \frac{2}{3} F_v' b d_n = \frac{2}{3}(180)(3.5)(3.5) = 1{,}470$ lbs $= 1.5$ kips > $V_{\max} = 1.2$ kips

Flexural Capacity:

$$M' = F_b' . S$$

$F_b' = F_b C_D C_M C_t C_L C_F C_{fu} C_i C_r K_F \phi \lambda$ (NDS Table 4.3.1)

Reference Design Value of Bending: $F_b = 900$ psi (NDS Supplement Table 4A)

Load Duration Factor (ASD only): $C_D = 1.0$ (NDS Table 2.3.2)

Wet Service Factor: $C_M = 1.0$ (NDS Supplement Table 4A)

Temperature Factor: $C_t = 1.0$ (NDS Table 2.3.3)

Beam Stability Factor: $C_L = 1.0$ (NDS Section 3.3.3)

Size Factor: $C_F = 1.5$ (NDS Supplement Table 4A)

Flat Use Factor: $C_{fu} = 1.0$ (NDS Supplement Table 4A)

Incising Factor: $C_i = 1.0$ (NDS Section 4.3.8)

Repetitive Member Factor: $C_r = 1.15$ (NDS Section 4.3.9)

Format Conversion Factor (LRFD only): $K_F = 2.54$ (NDS Table 4.3.1)

Resistance Factor (LRFD only): $\phi = 0.85$ (NDS Table 4.3.1)

Time Effect Factor (LRFD only): $\lambda = 0.6$ (NDS Table N3)

ASD: $F_b' = 900(1.0)(1.0)(1.0)(1.0)(1.5)(1.0)(1.0)(1.15) = 1{,}552$ psi

$$M' = (1{,}552)\left(\frac{3.5 \times 3.5^2}{6}\right) = 11{,}090 \text{ lb.in} = 11.1 \text{ kip.in} > M_{max} = 7.1 \text{ kip.in}$$

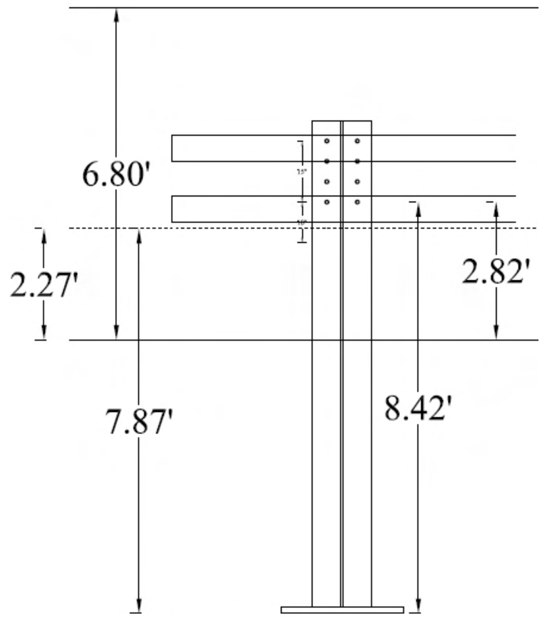

Figure C-1 Lateral support of soil box at east side.

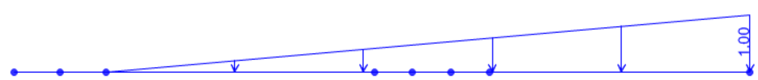

(a)

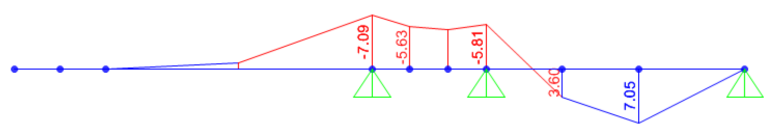

(b)

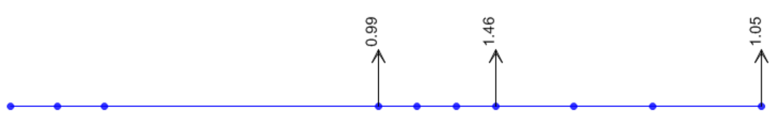

(c)

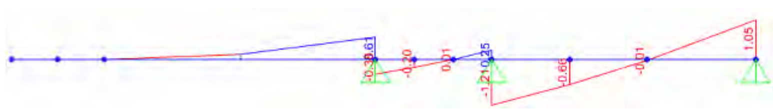

(d)

Figure C-2 Design loading of soil box studs: (a) Loading (kip/ft), (b) Moment (kip.in), (c) Reaction force (kips), and (d) Shear (kips)

APPENDIX D. LVDTs Reference Frame Drawings

This appendix presents the detail drawings of the reference frames of the soil surface LVDTs described in Chapter 5.

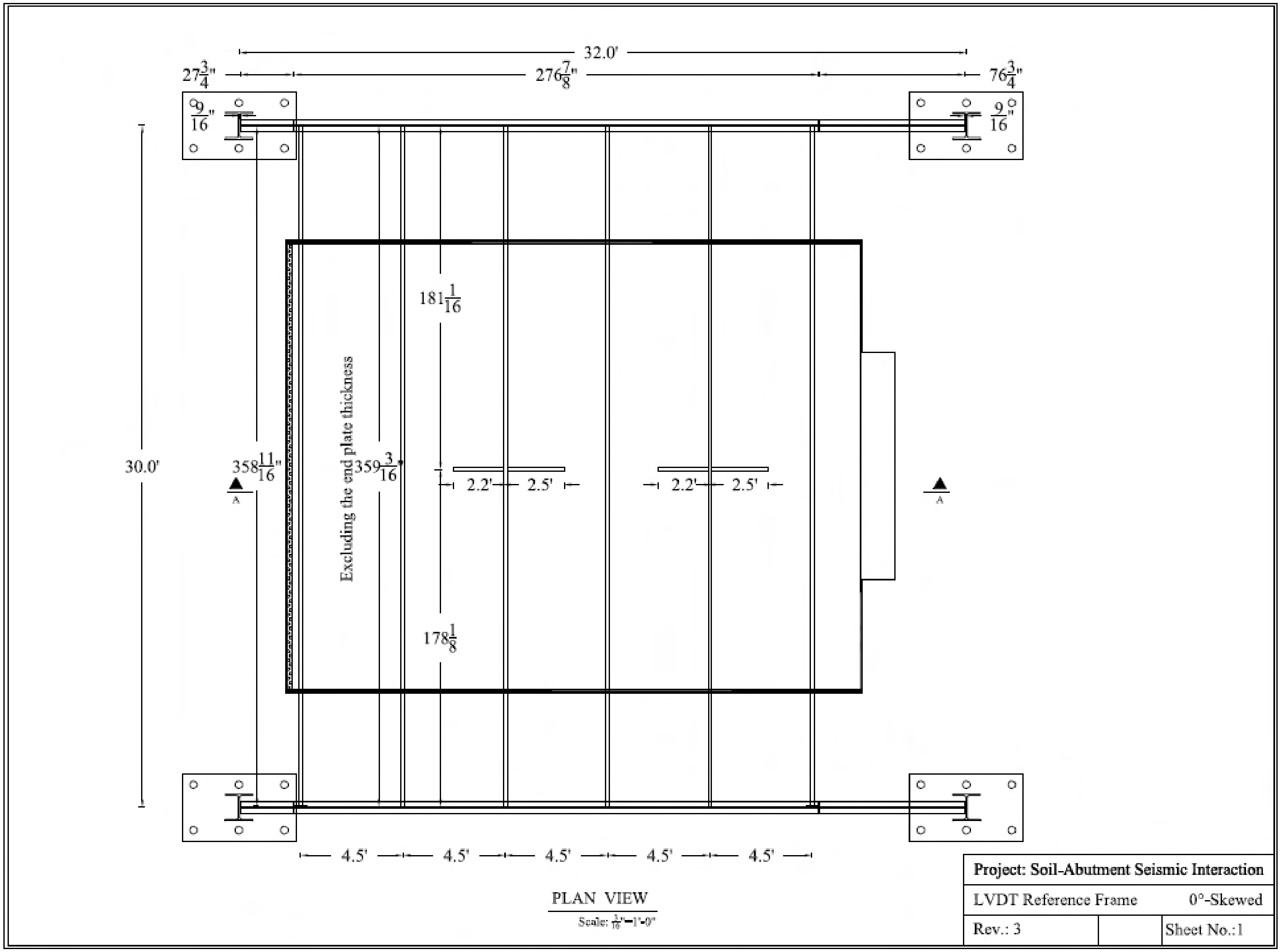

Figure D-1 LVDT reference frame in the 0° skew test (plan view).

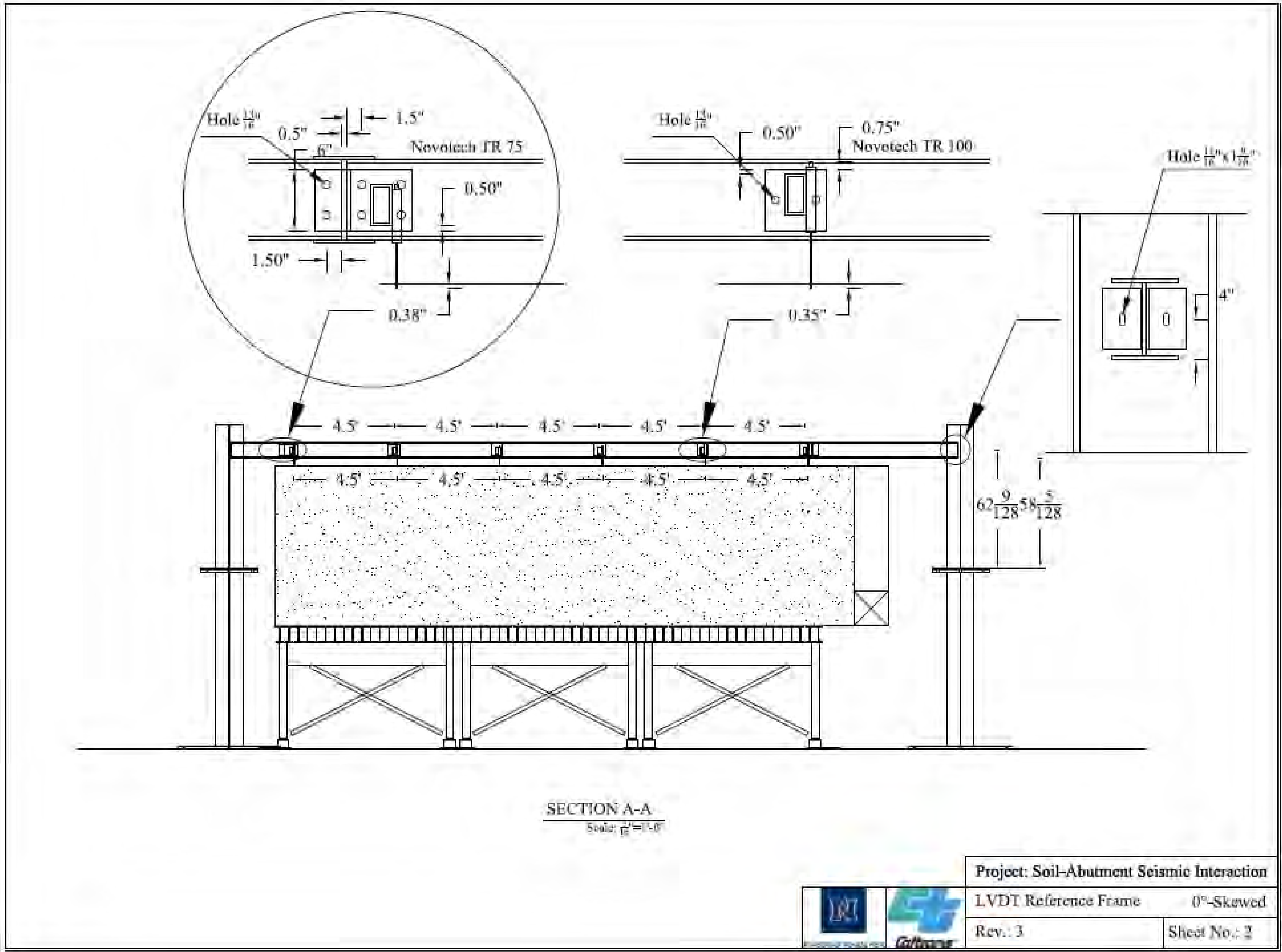

Figure D-2 LVDT reference frame in the 0° skew test (elevation view).

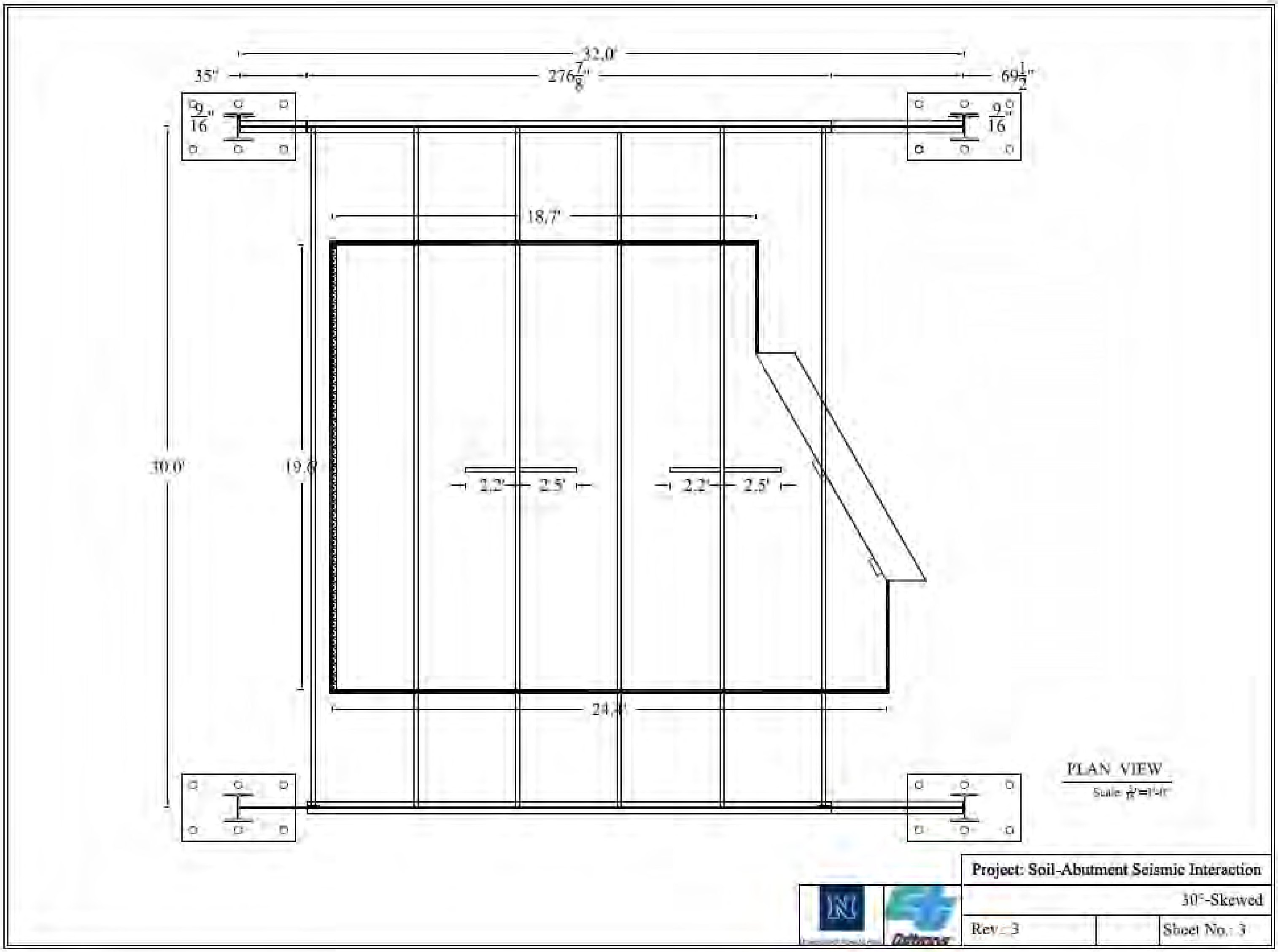

Figure D-3 LVDT reference frame in the 30° skew test (plan view).

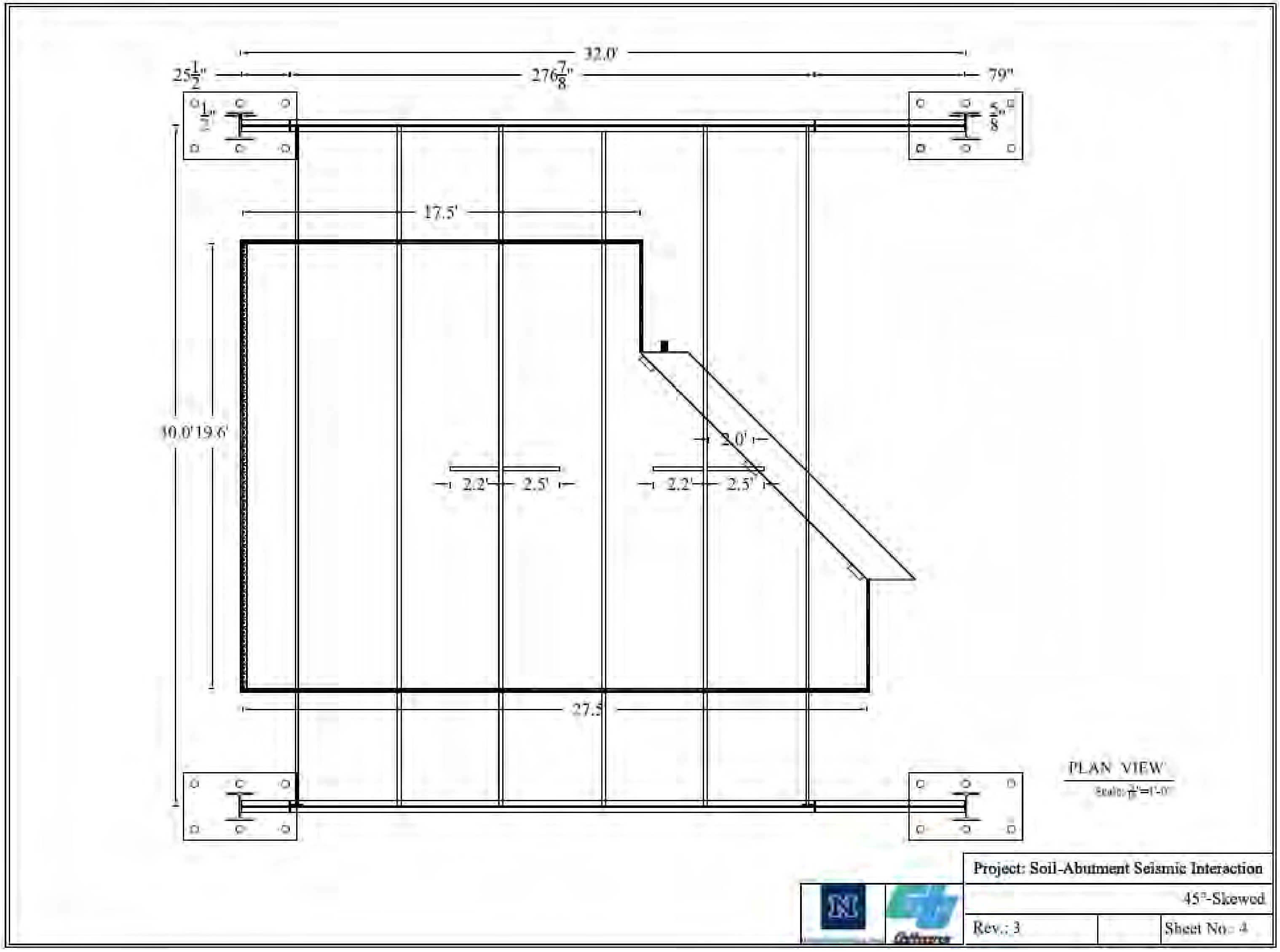

Figure D-4 LVDT reference frame in the 45° skew test (plan view).

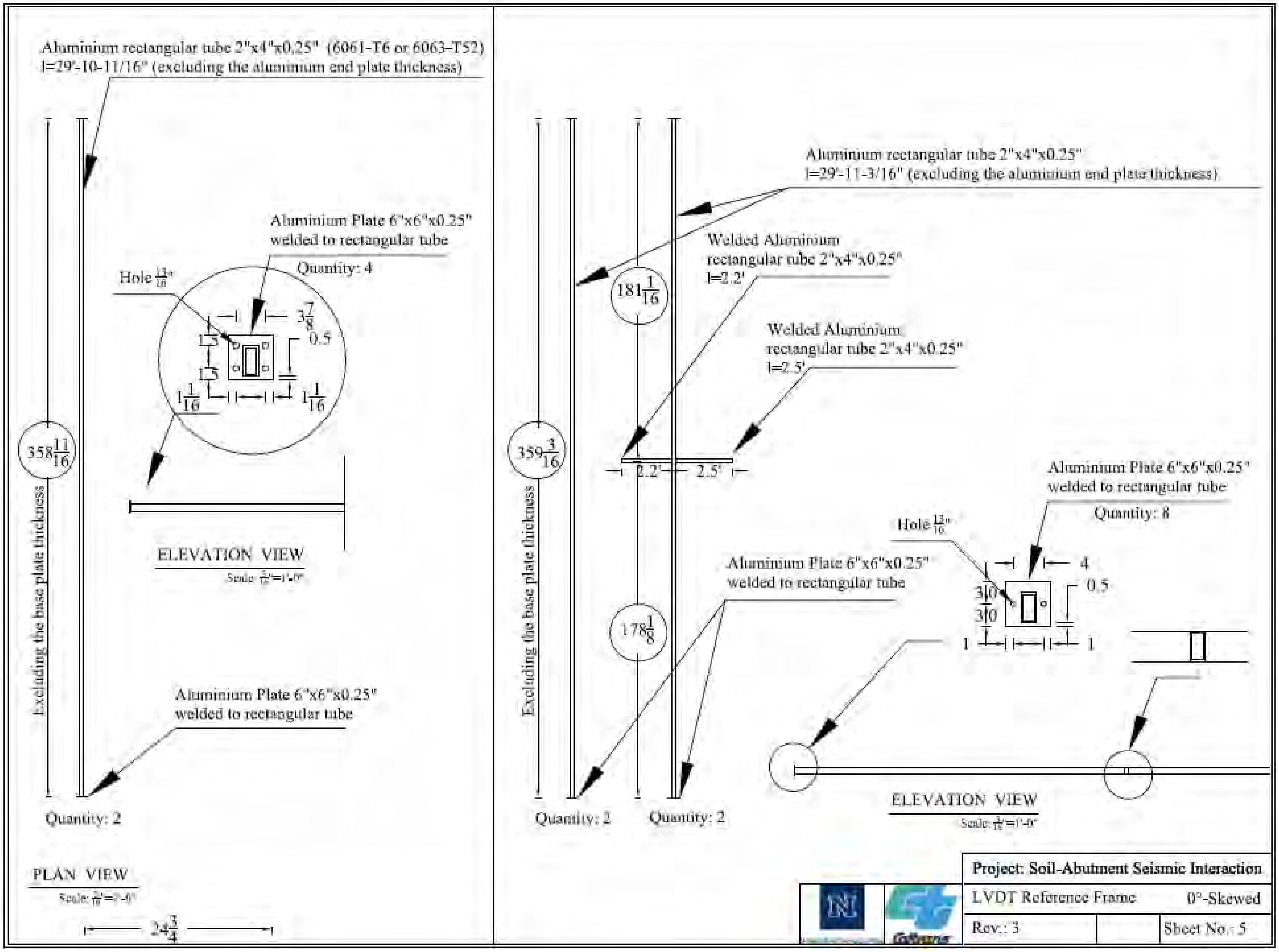

Figure D-5 LVDT reference frame (aluminum beam details).

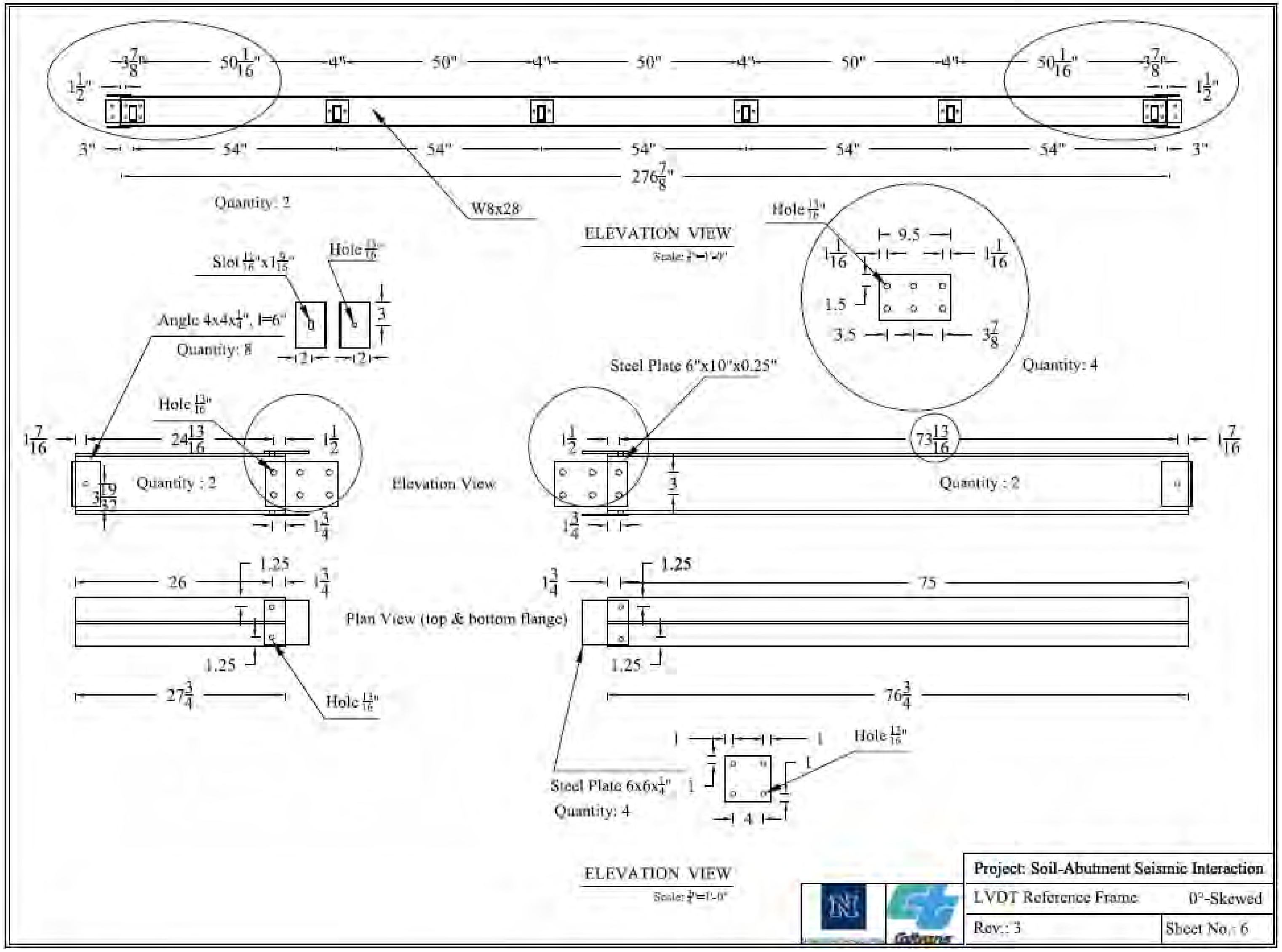

Figure D-6 LVDT reference frame (steel beam details in the 0° skew test).

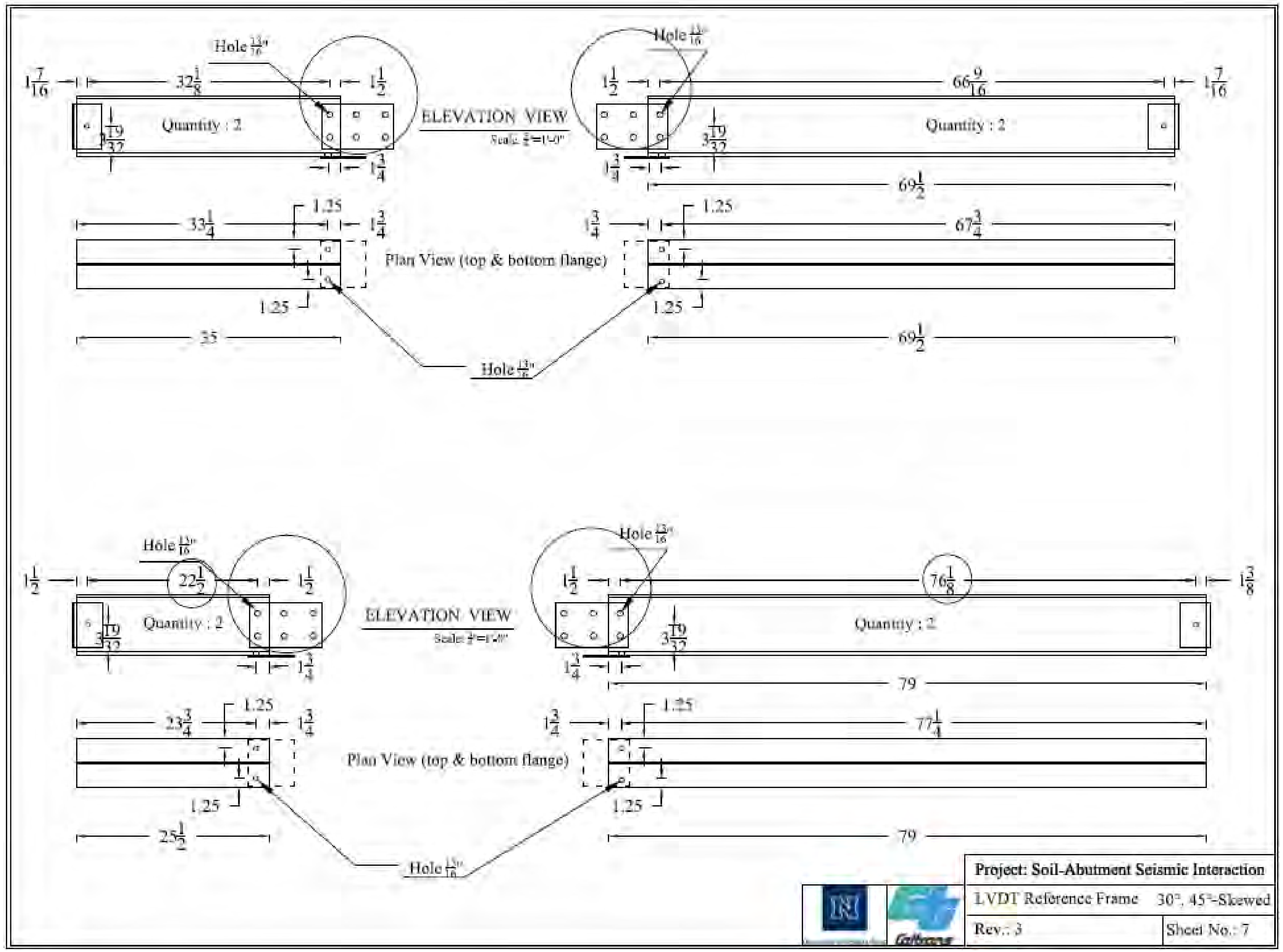

Figure D-7 LVDT reference frame (steel beam details in the 30° and 45° skew tests).

APPENDIX E. Natural Period of Bridge Block

Details of estimating natural period of the bridge block is presented in this appendix based on the data measured by the bridge block accelerometers under the white noise motions.

Two methods were used to determine the fundamental frequency of the bridge block. The Fast Fourier Transform (FFT) spectra of longitudinal acceleration measured by the four accelerometers were calculated in the first method. A transfer function equal to the ratio of the response of the bridge block accelerometers to the base acceleration of shake table was determined in the second method using “tfestimate” function in MATLAB program. The frequency corresponding to the maximum peak was selected as the fundamental frequency of the bridge block in both methods. The results of the FFT spectra of the bridge block accelerations are shown in the figures.

WN1

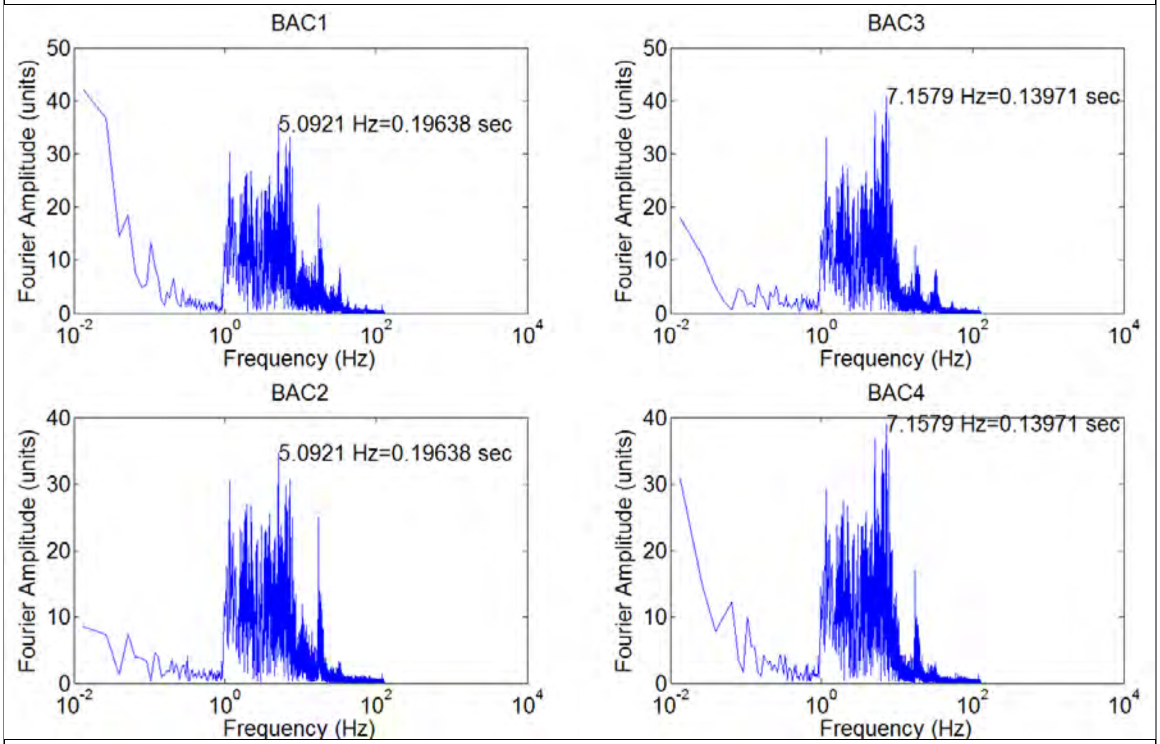

WN2

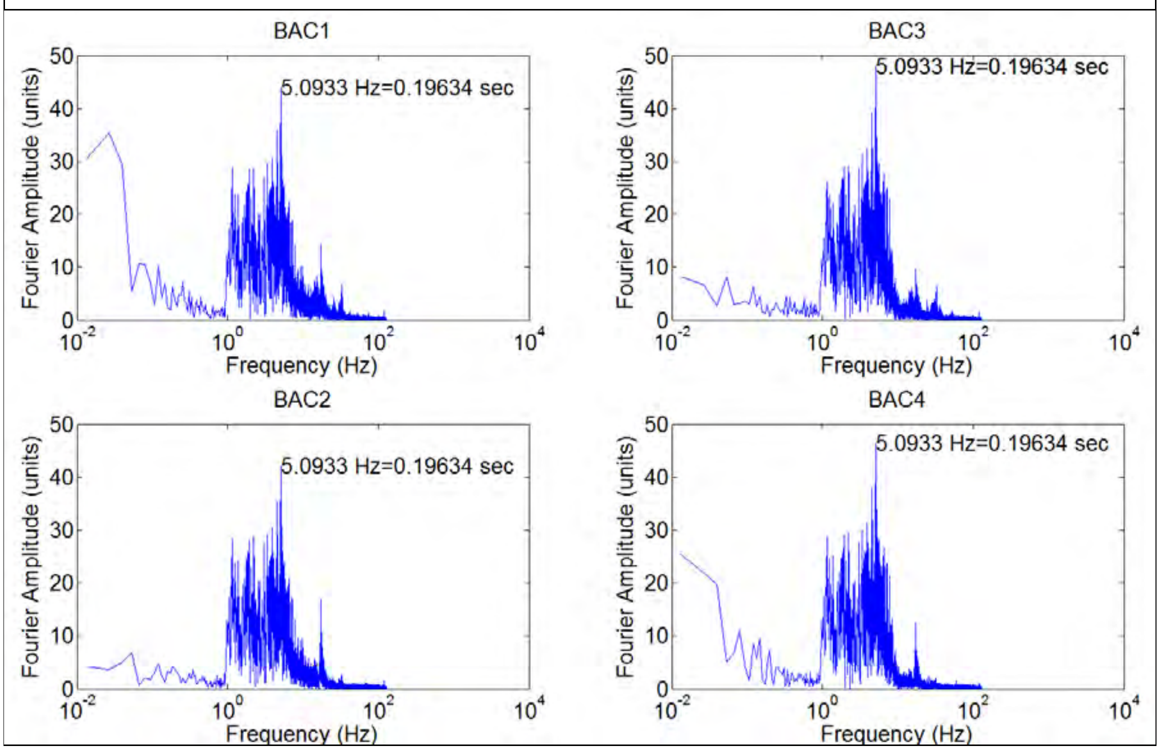

Figure E-1 FFT spectra of the bridge block accelerations in the 0° skew test.

WN3

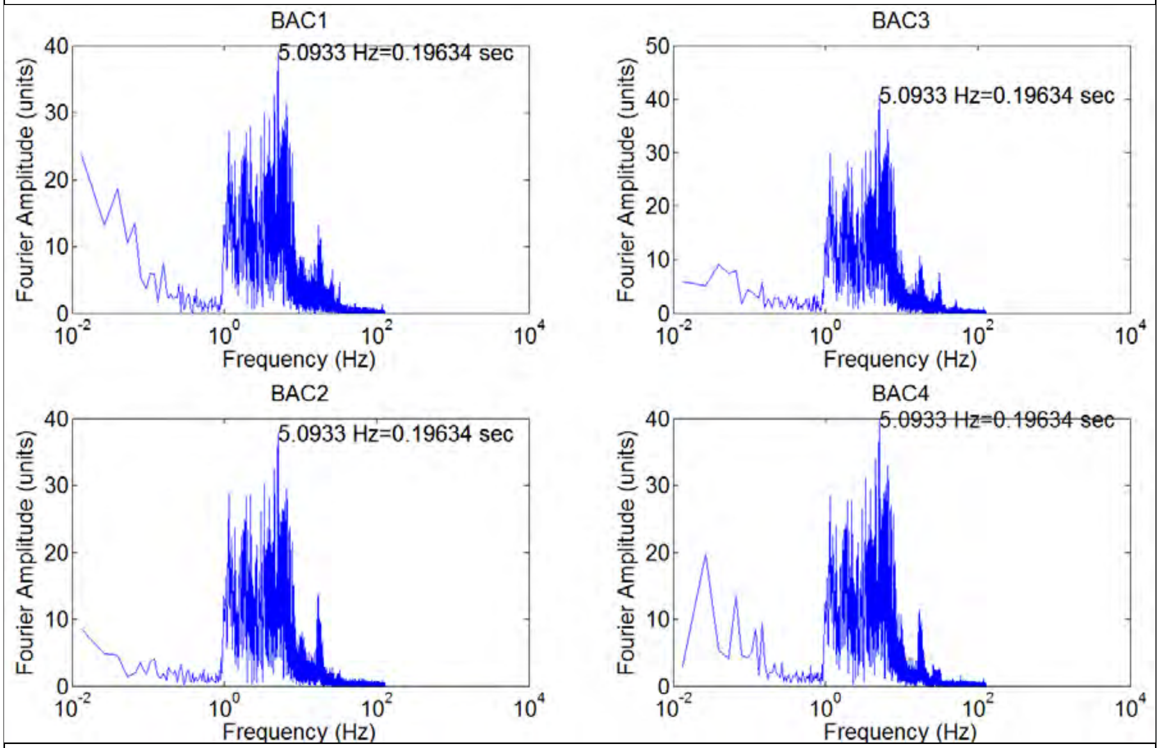

WN4

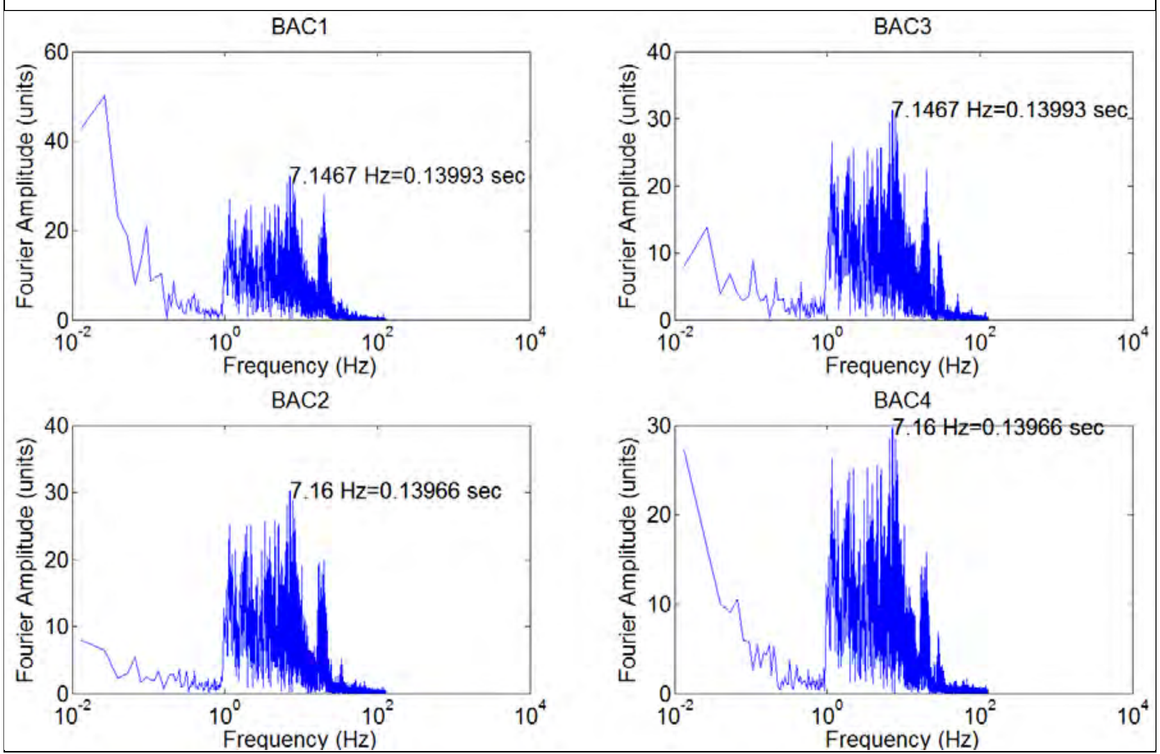

Figure E-2 FFT spectra of the bridge block accelerations in the 0° skew test.

WN6

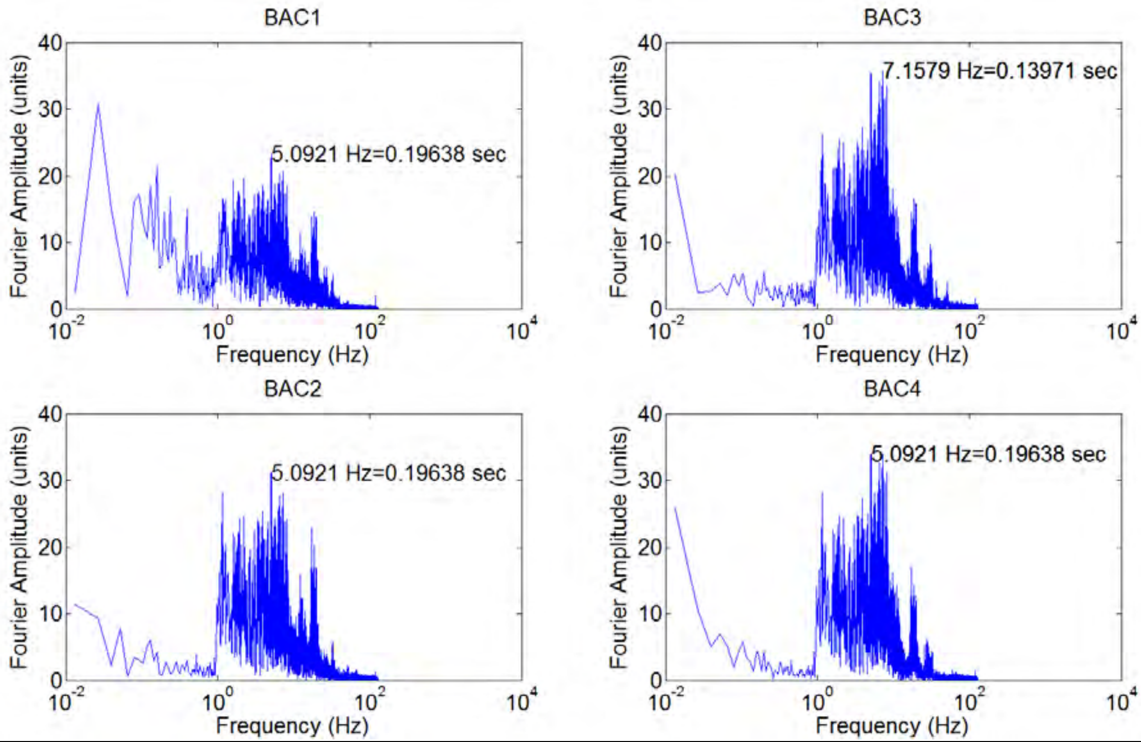

WN7

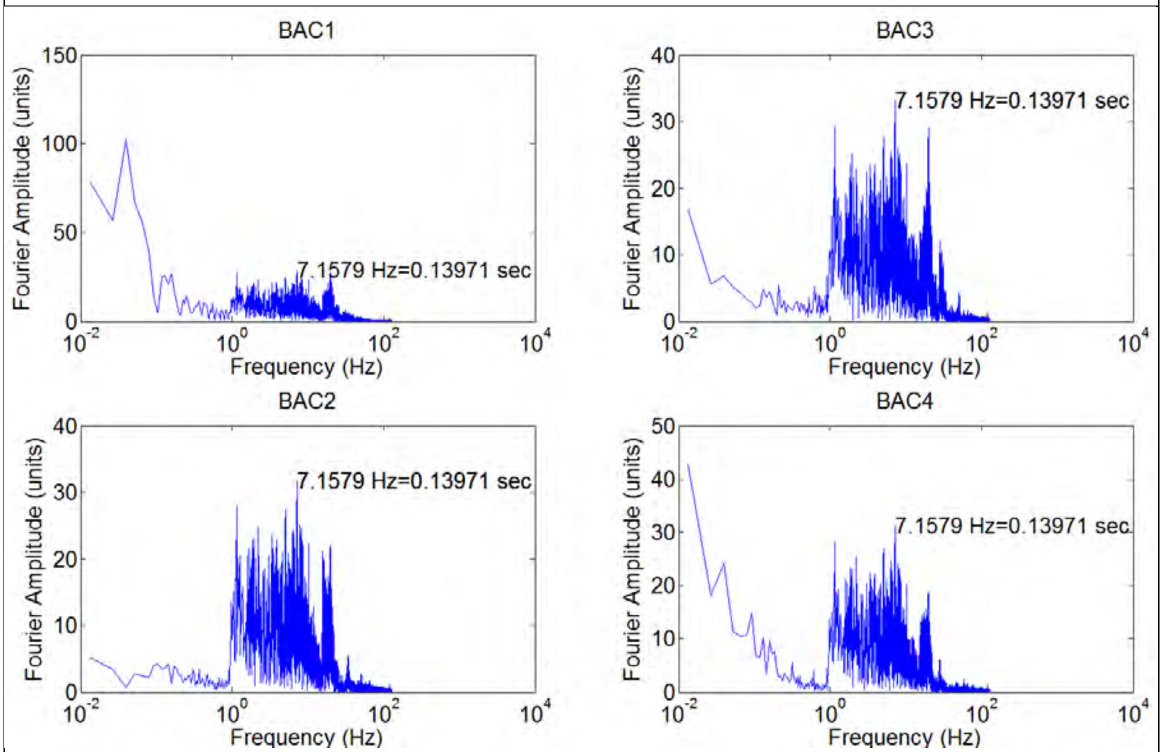

Figure E-3 FFT spectra of the bridge block accelerations in the 0° skew test.

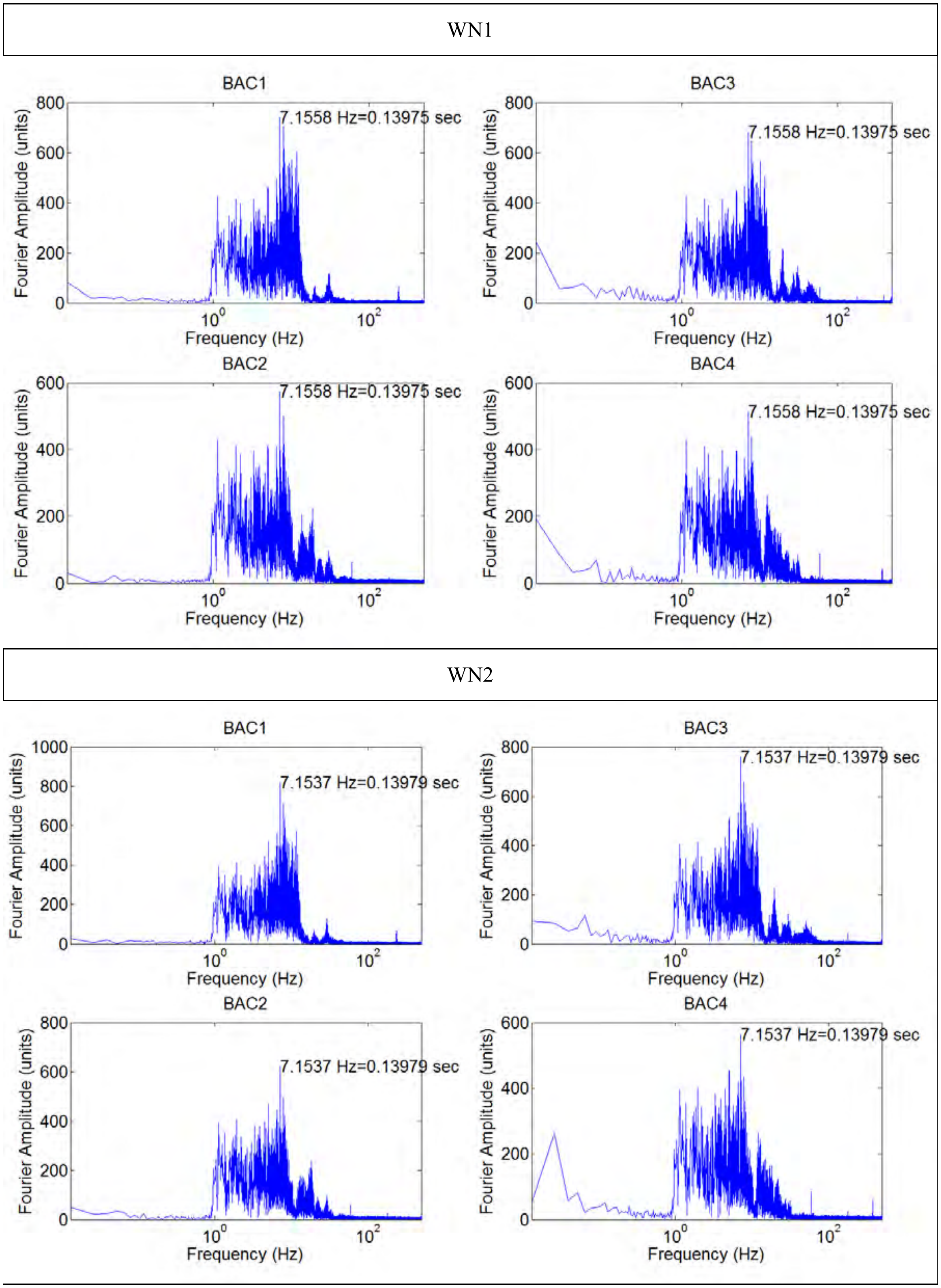

Figure E-4 FFT spectra of the bridge block accelerations in the 30° skew test.

WN3

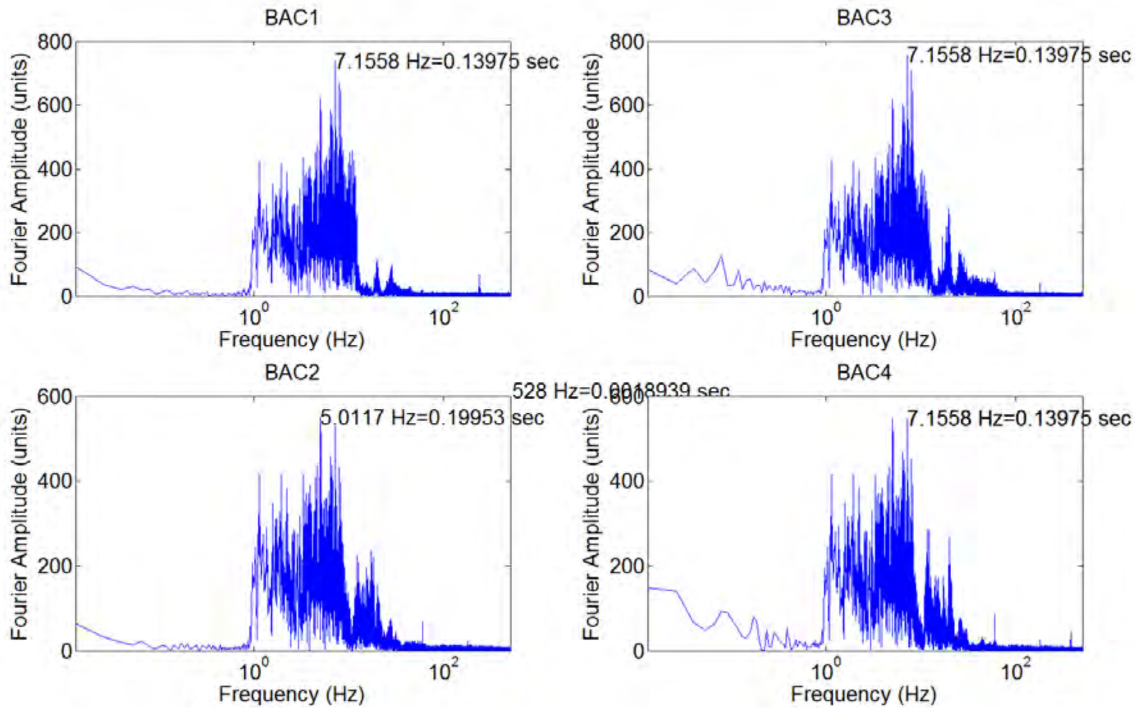

WN4

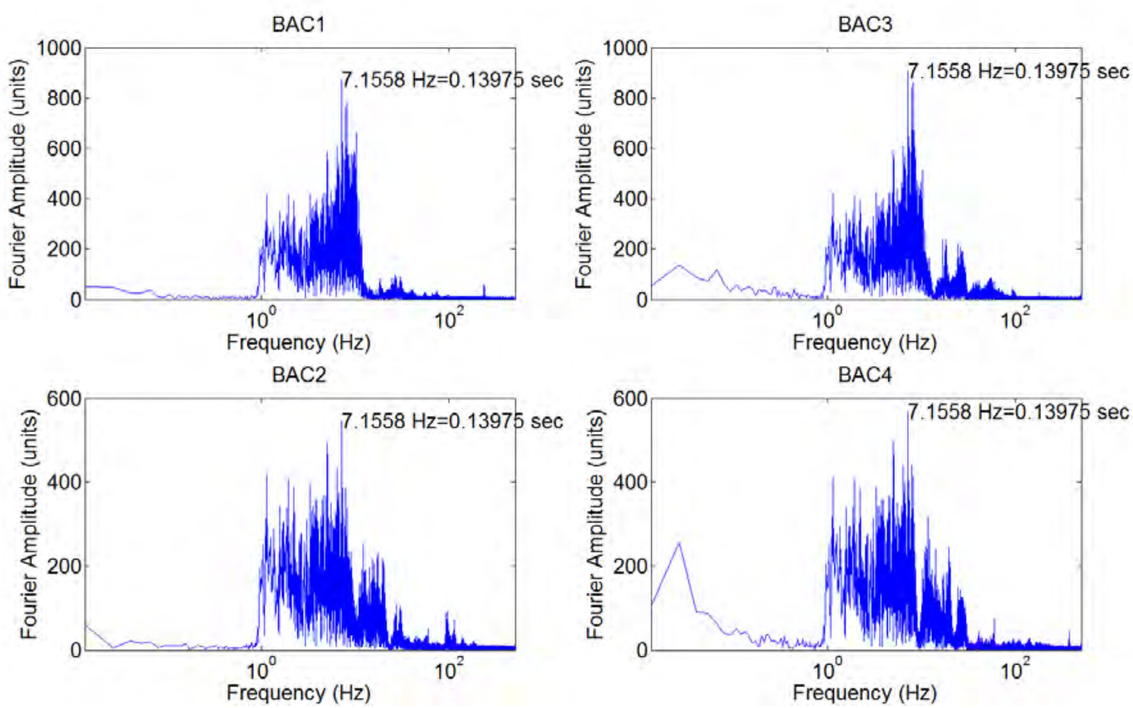

Figure E-5 FFT spectra of the bridge block accelerations in the 30° skew test.

WN5

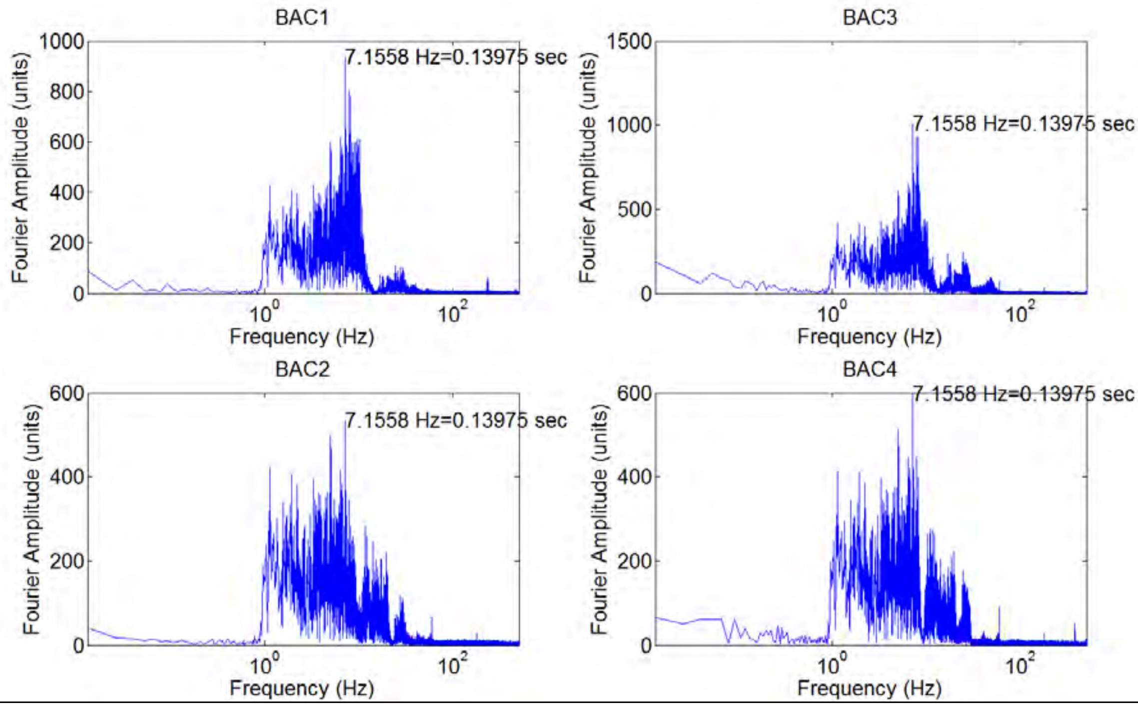

WN6

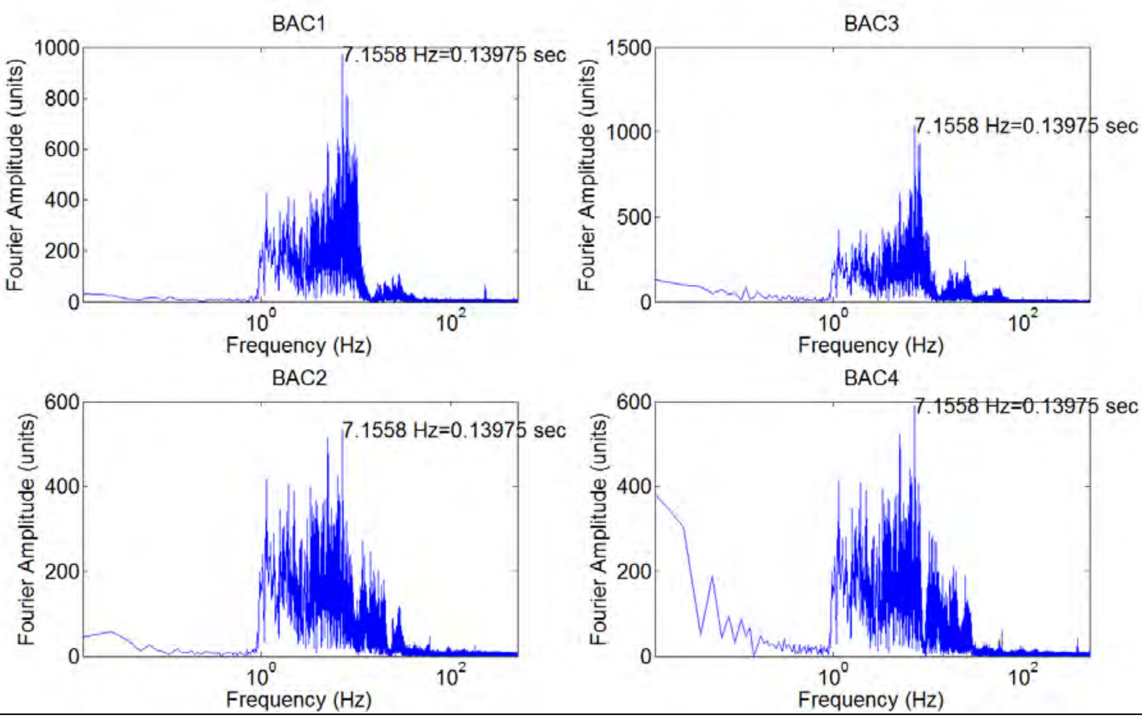

Figure E-6 FFT spectra of the bridge block accelerations in the 30° skew test.

WN1

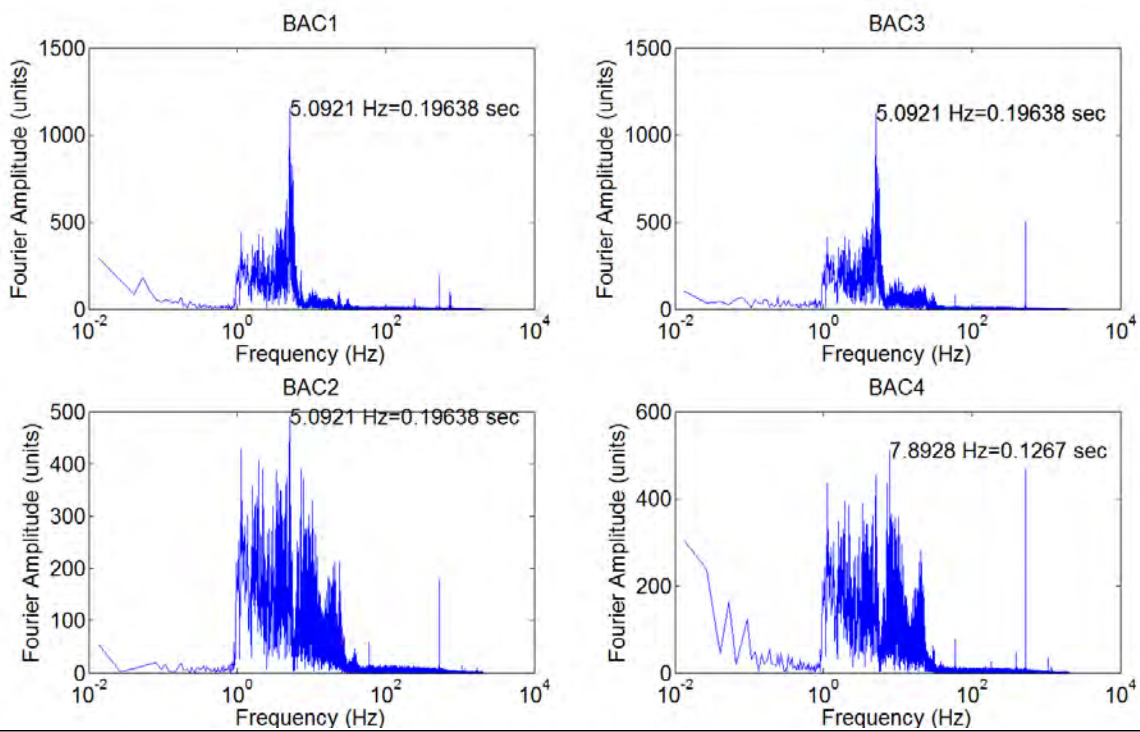

WN2

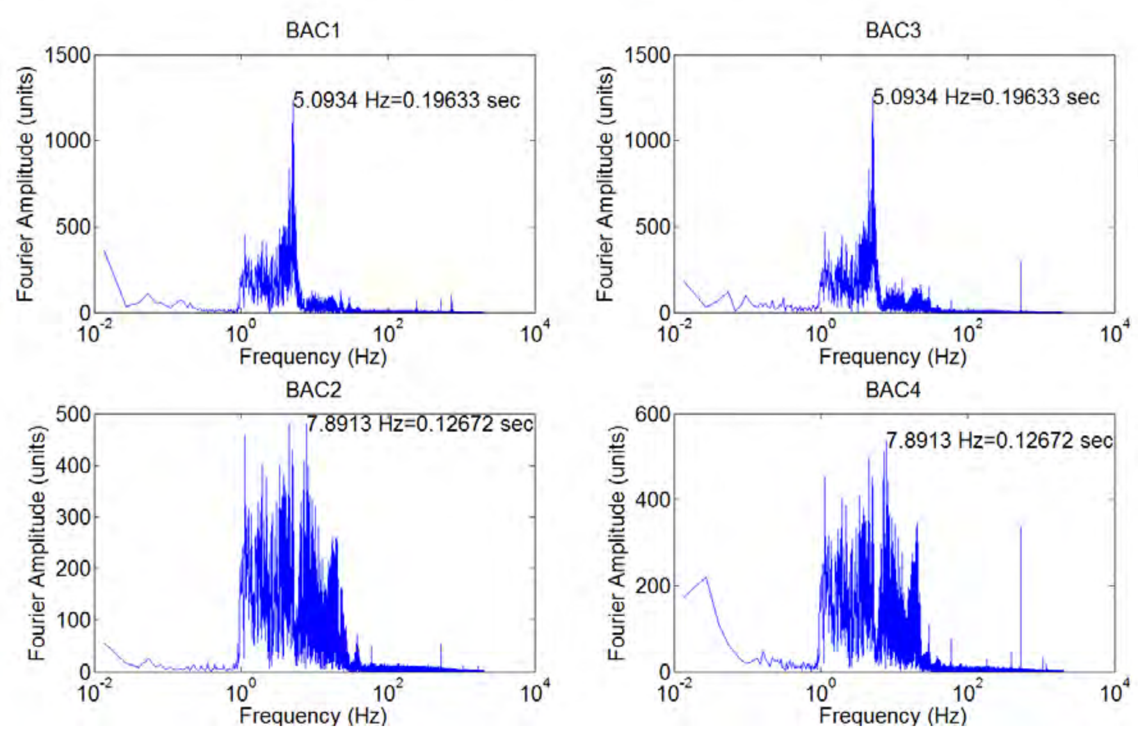

Figure E-7 FFT spectra of the bridge block accelerations in the 45° skew test.

WN3

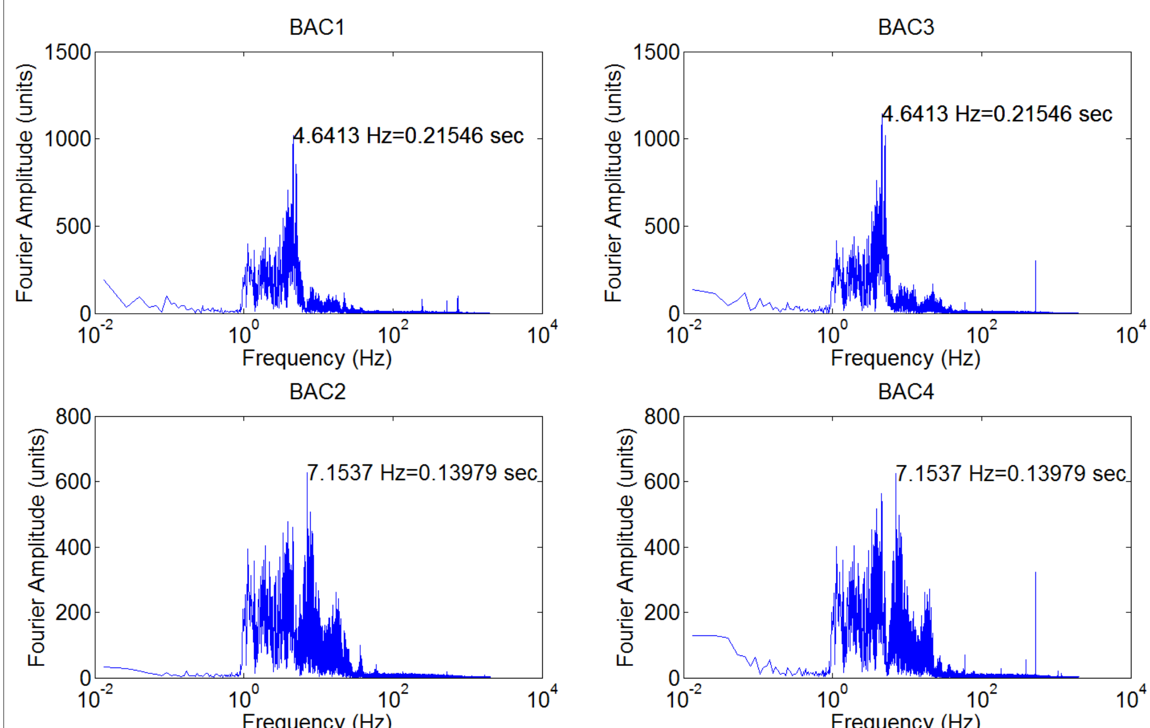

WN4

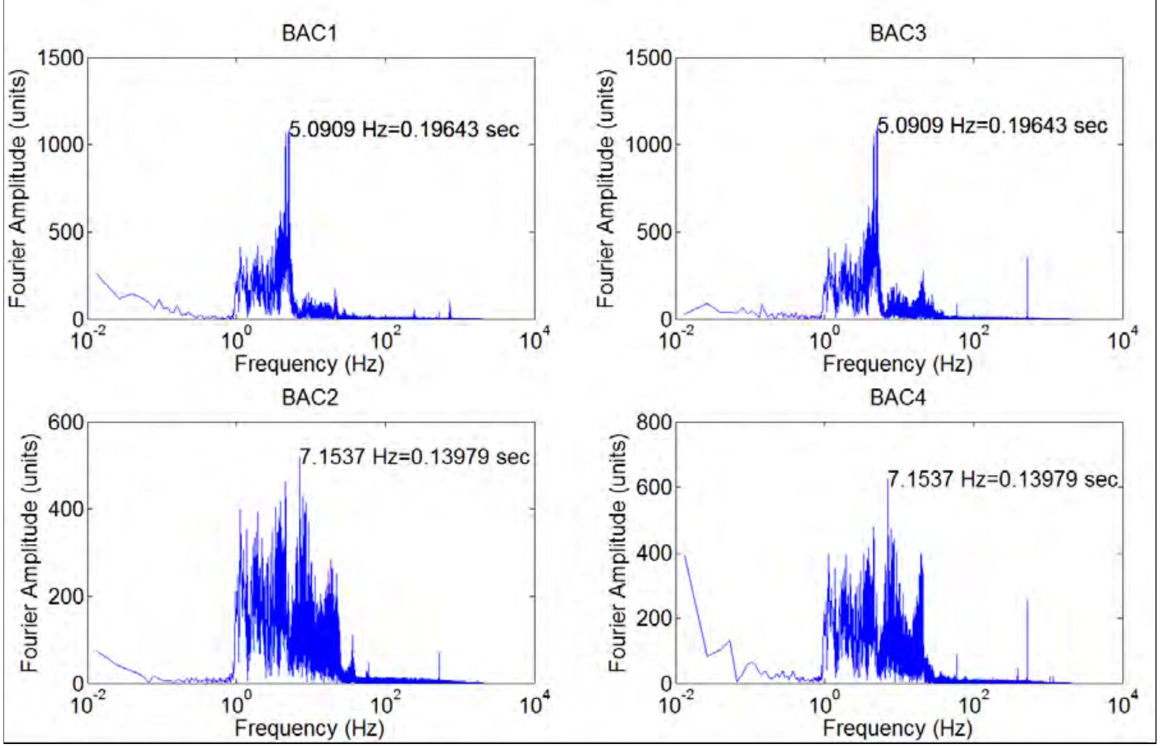

Figure E-8 FFT spectra of the bridge block accelerations in the 45° skew test.

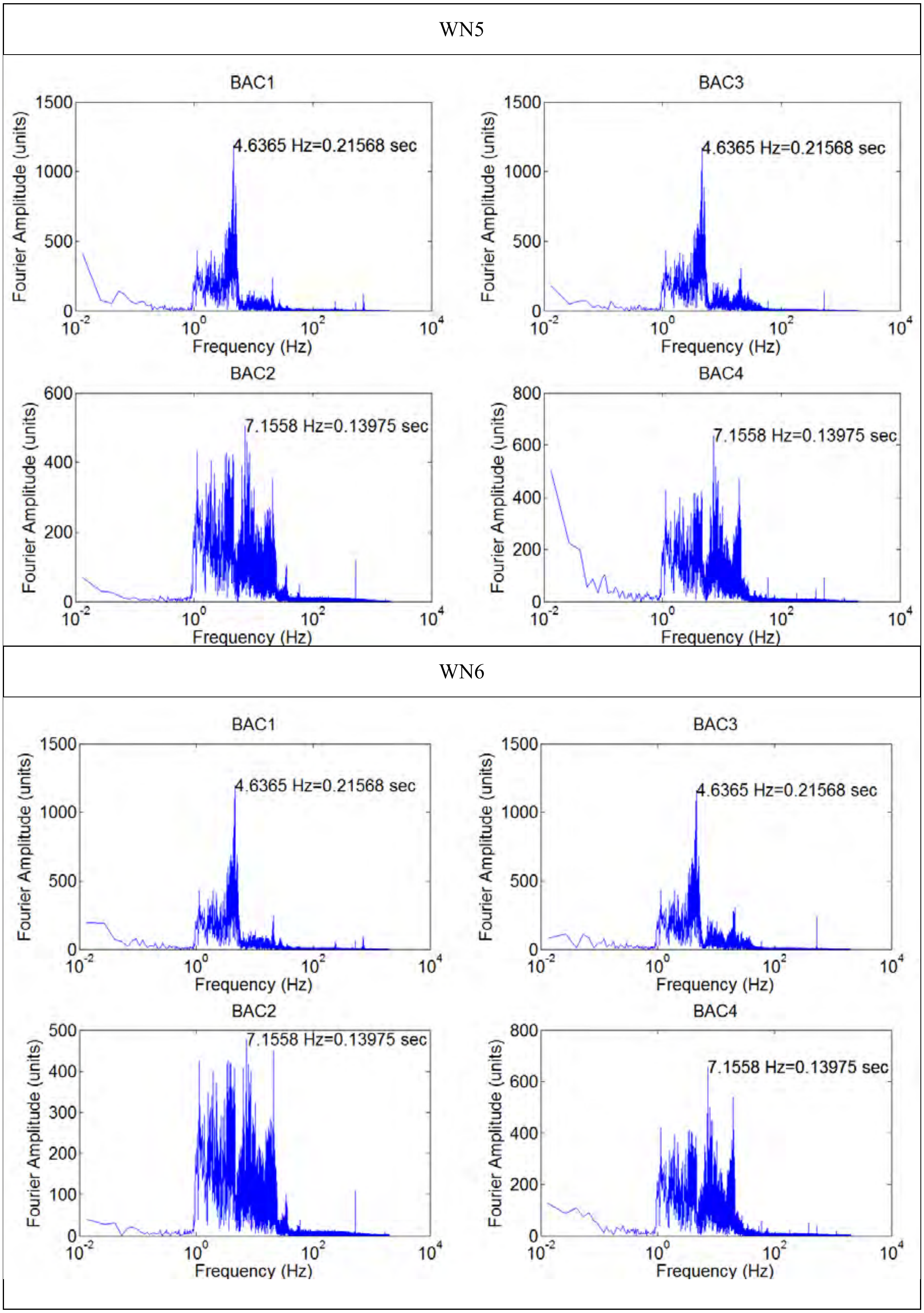

Figure E-9 FFT spectra of the bridge block accelerations in the 45° skew test.

APPENDIX F. Soil Acceleration Histories

Experimental data measured by each accelerometer in the longitudinal, transverse, and vertical directions at different locations inside the backfill soil are presented in this appendix. Each figure shows the measured acceleration in one specific direction at the top, middle and bottom layers of the backfill soil. Positive direction of the longitudinal, transverse, and vertical accelerations is towards the backfill soil, towards the west (acute corner of the bridge in skewed case), and upwards, respectively, throughout this appendix. Additional interpretation of these data is available in Section 6.7.6 of Chapter 6.

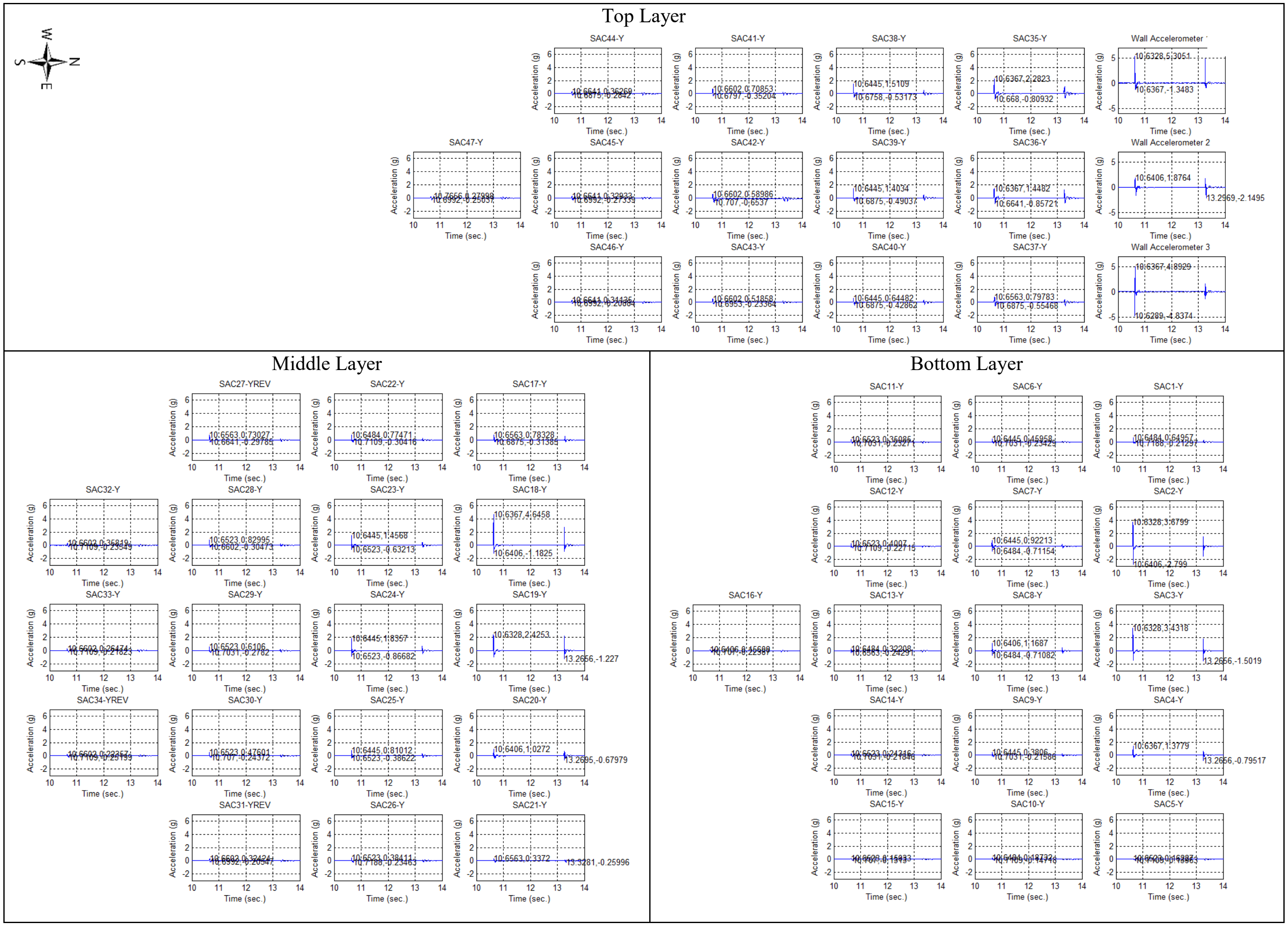

Figure F-1 Longitudinal acceleration of backfill soil for the 0° skew test in Run 2.

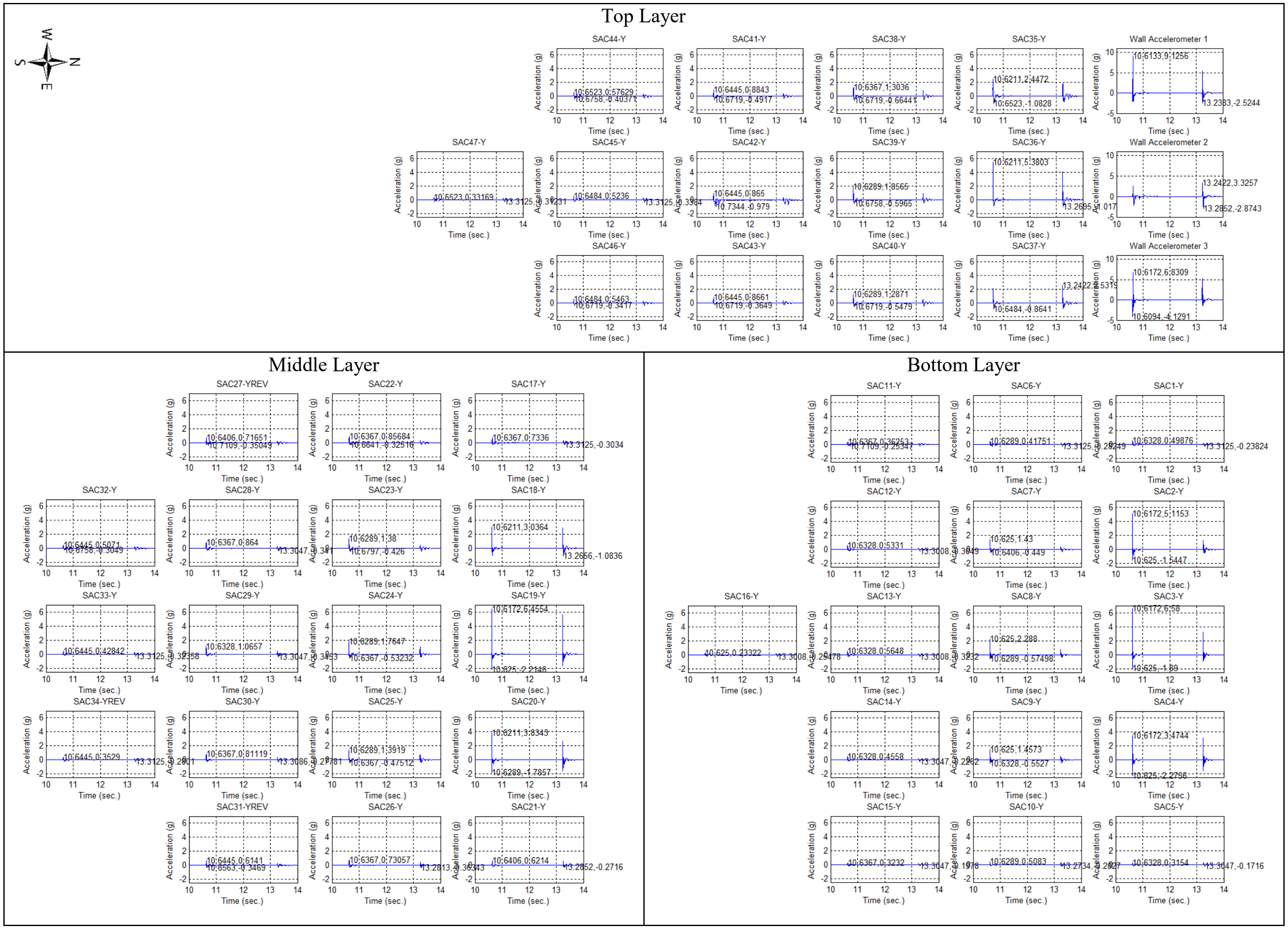

Figure F-2 Longitudinal acceleration of backfill soil for the 0° skew test in Run 3.

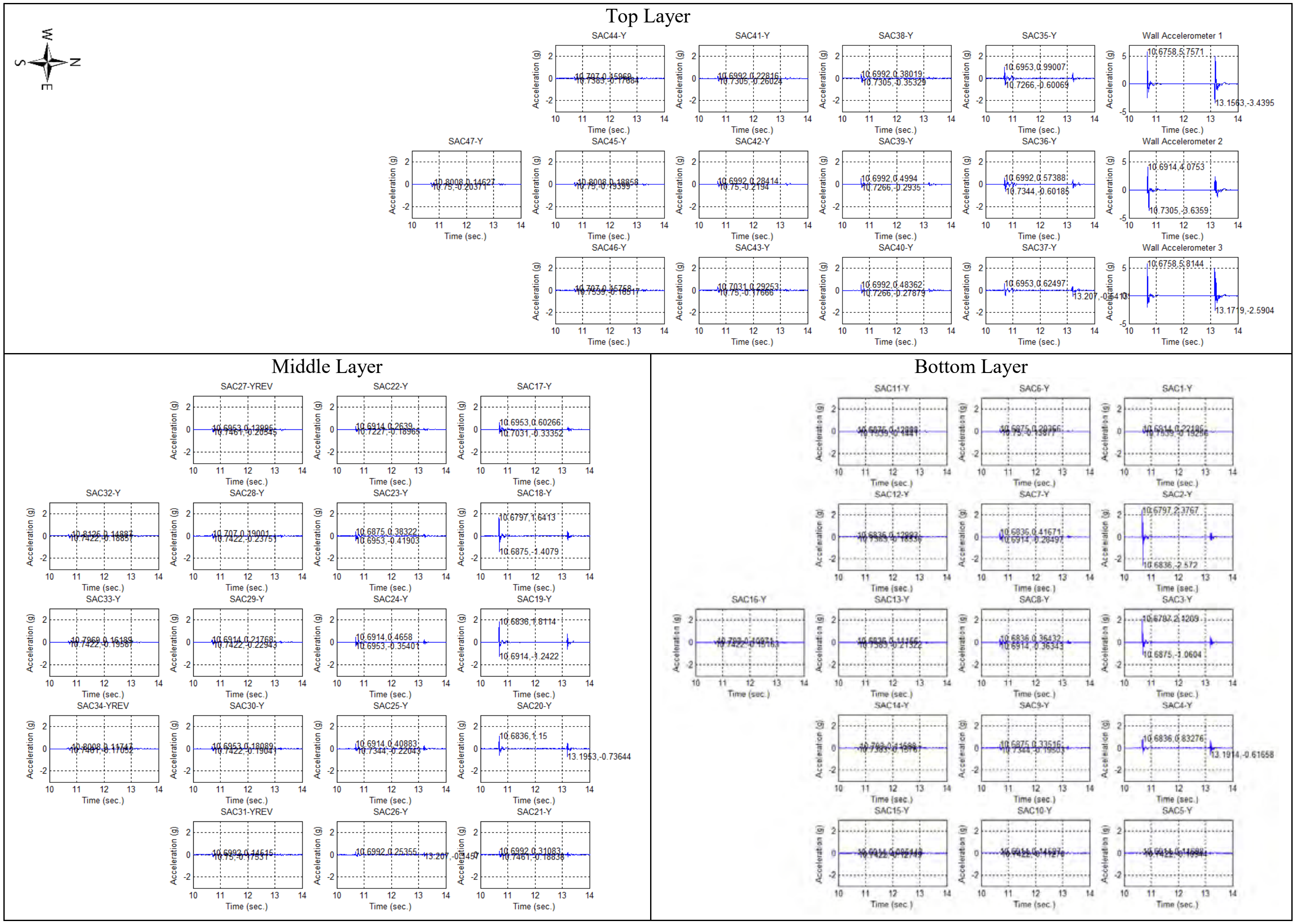

Figure F-3 Longitudinal acceleration of backfill soil for the 0° skew test in Run 4.

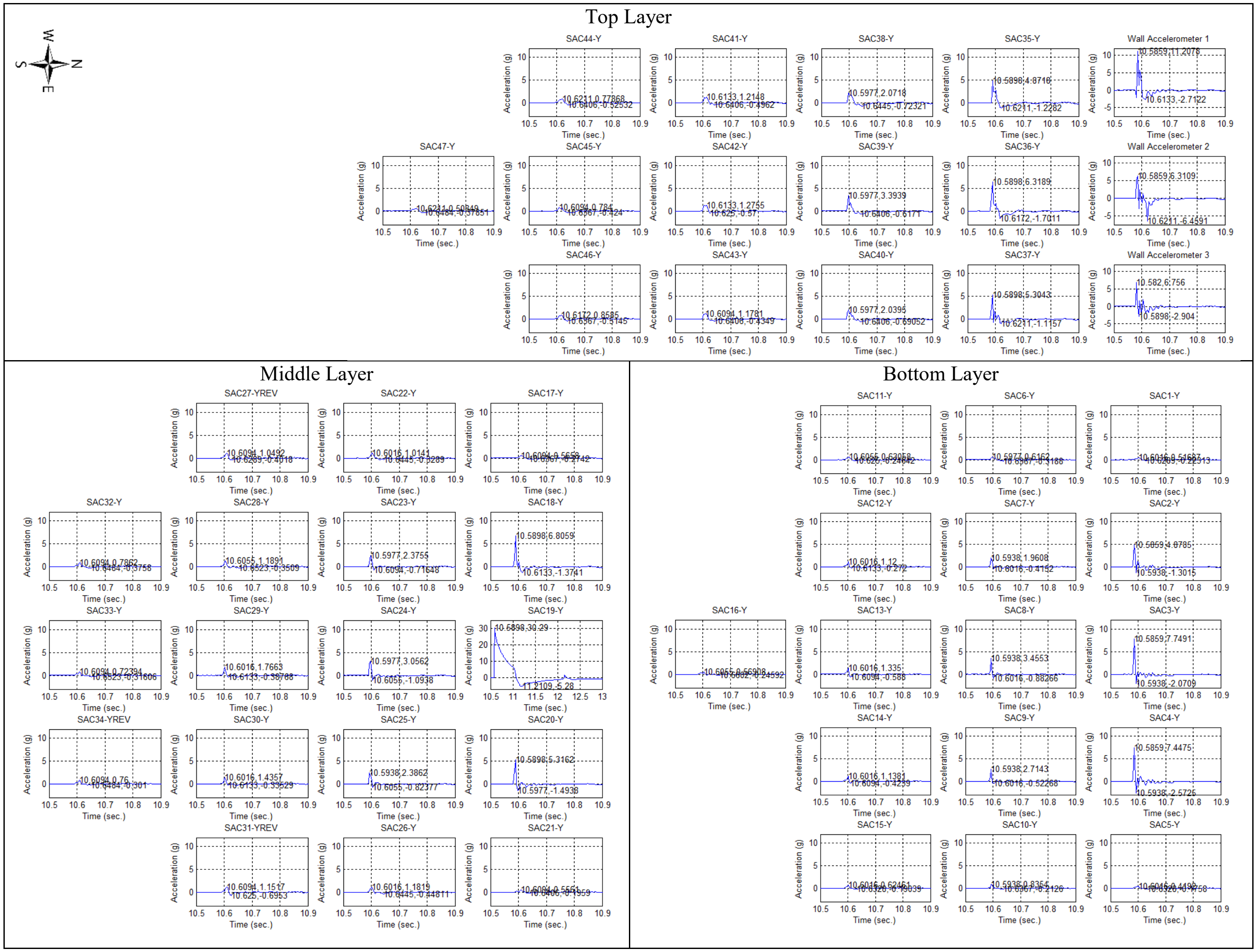

Figure F-4 Longitudinal acceleration of backfill soil for the 0° skew test in Run 6.

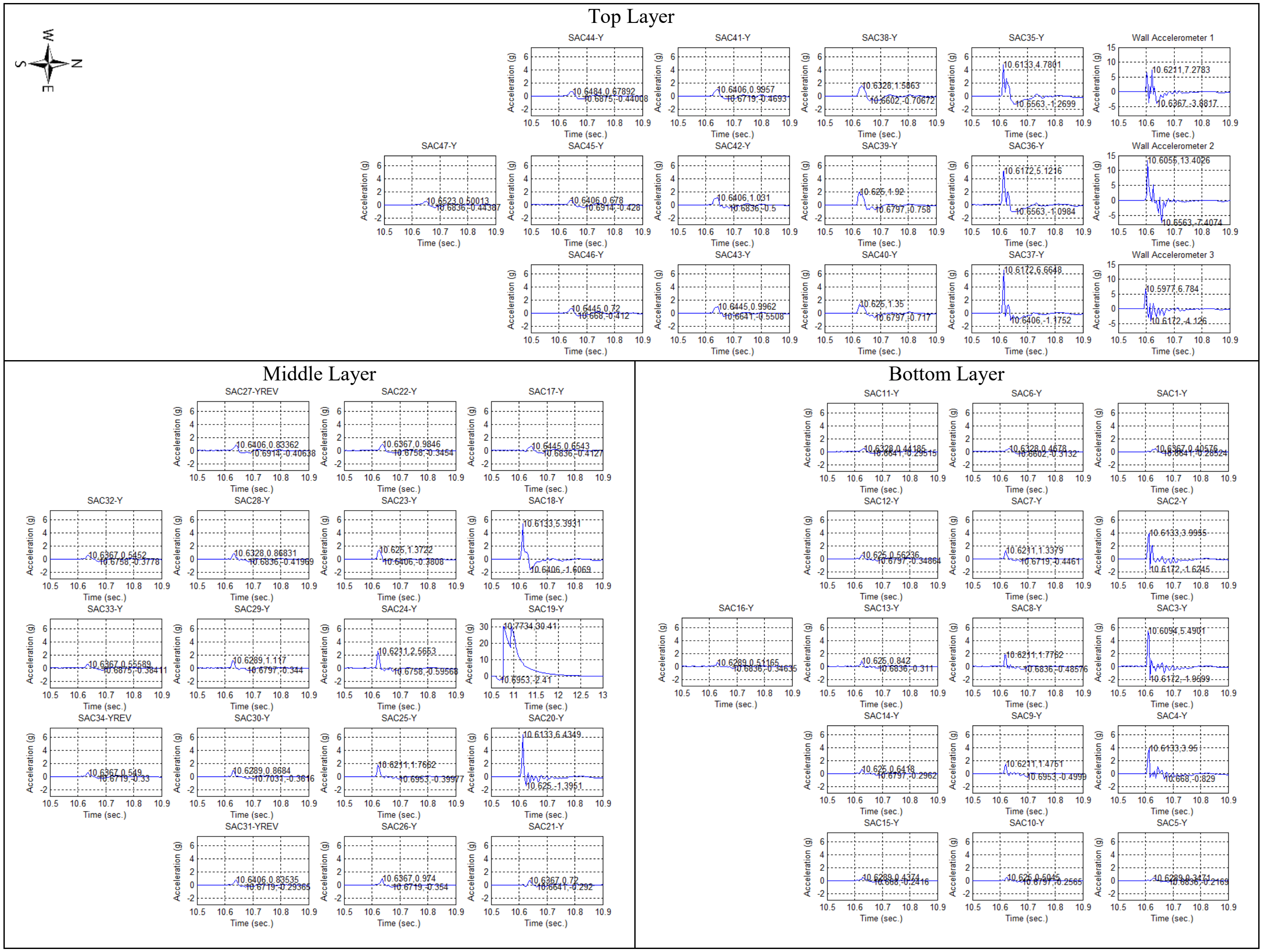

Figure F-5 Longitudinal acceleration of backfill soil for the 0° skew test in Run 7.

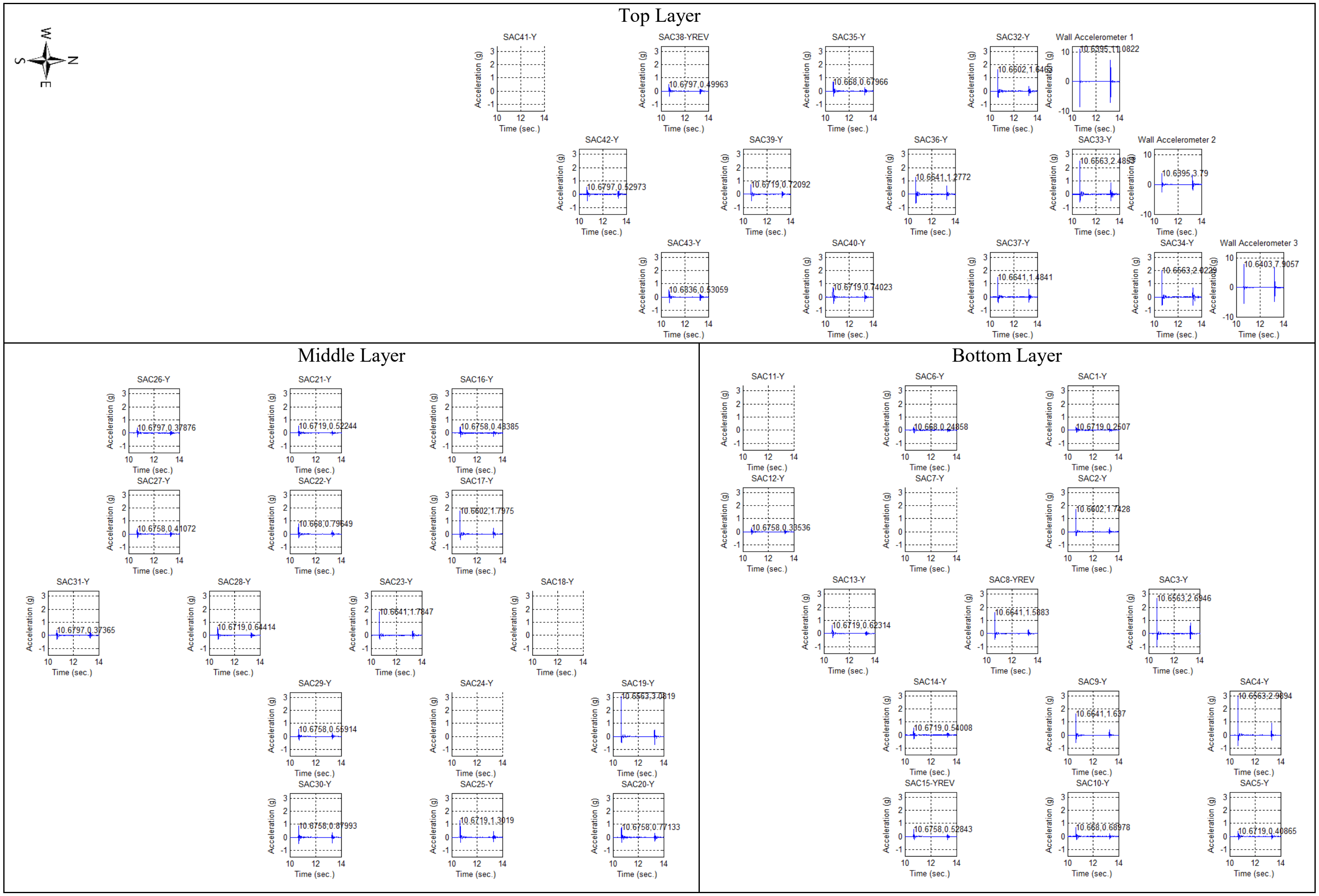

Figure F-6 Longitudinal acceleration of backfill soil for the 30° skew test in Run 2.

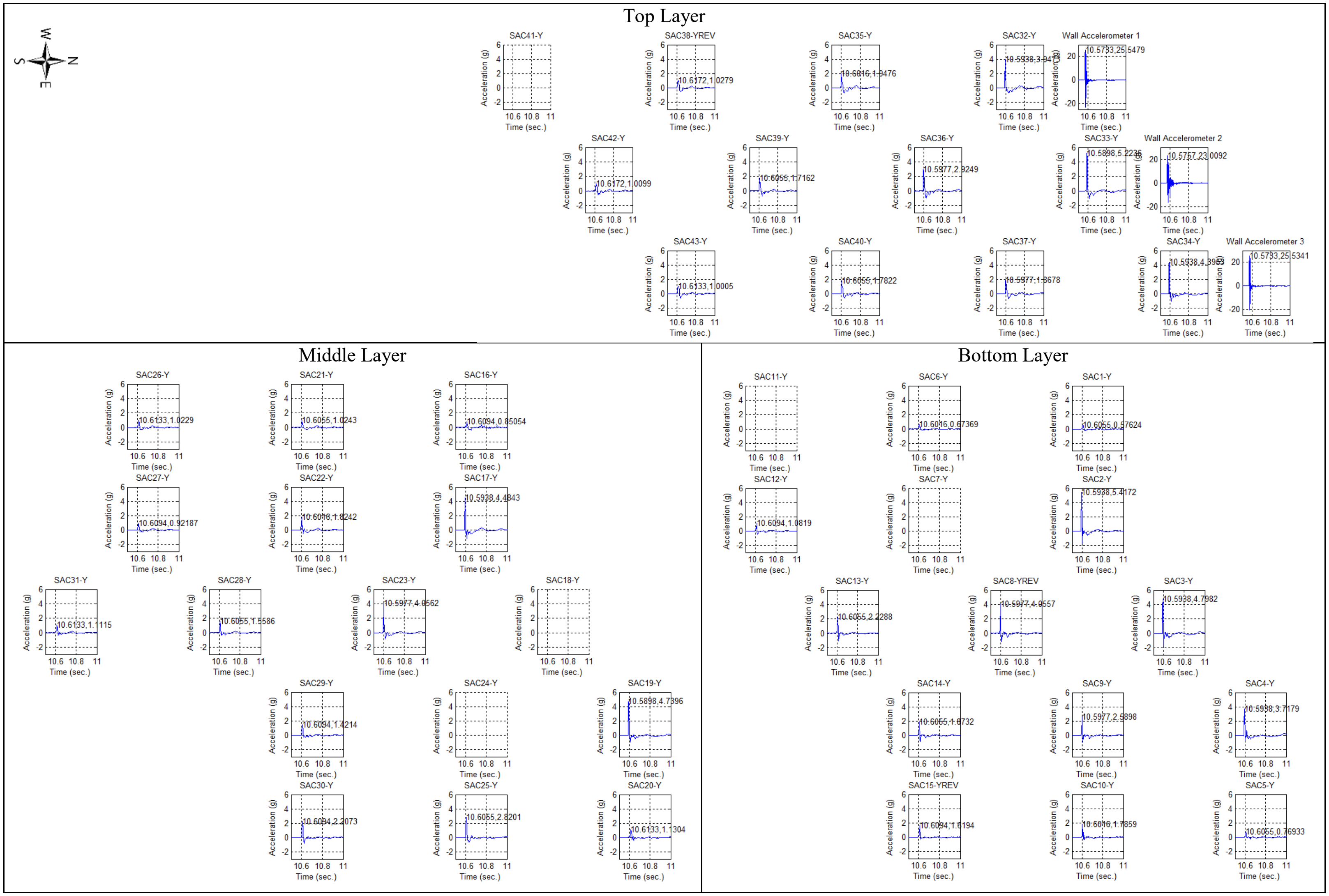

Figure F-7 Longitudinal acceleration of backfill soil for the 30° skew test in Run 3.

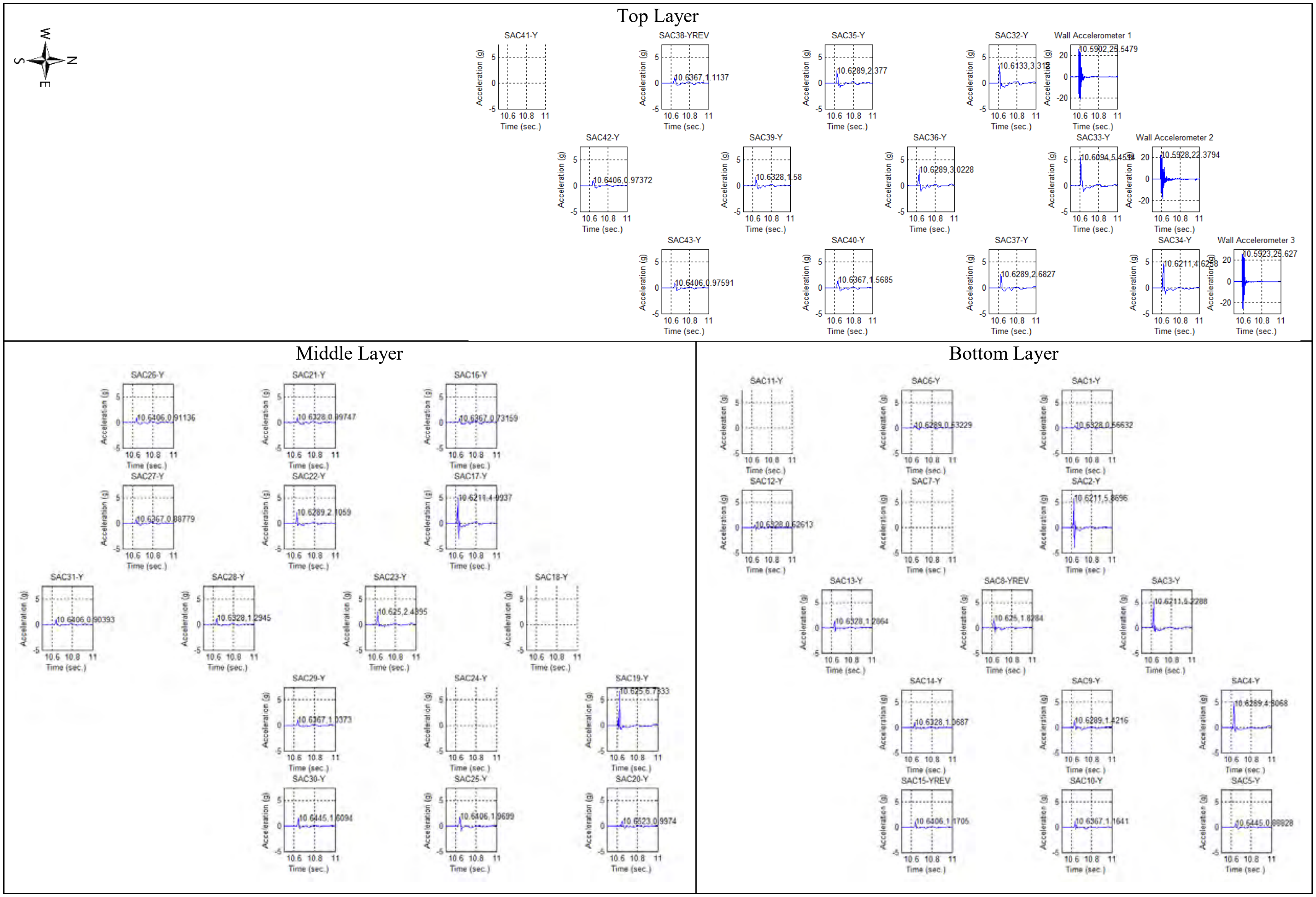

Figure F-8 Longitudinal acceleration of backfill soil for the 30° skew test in Run 4.

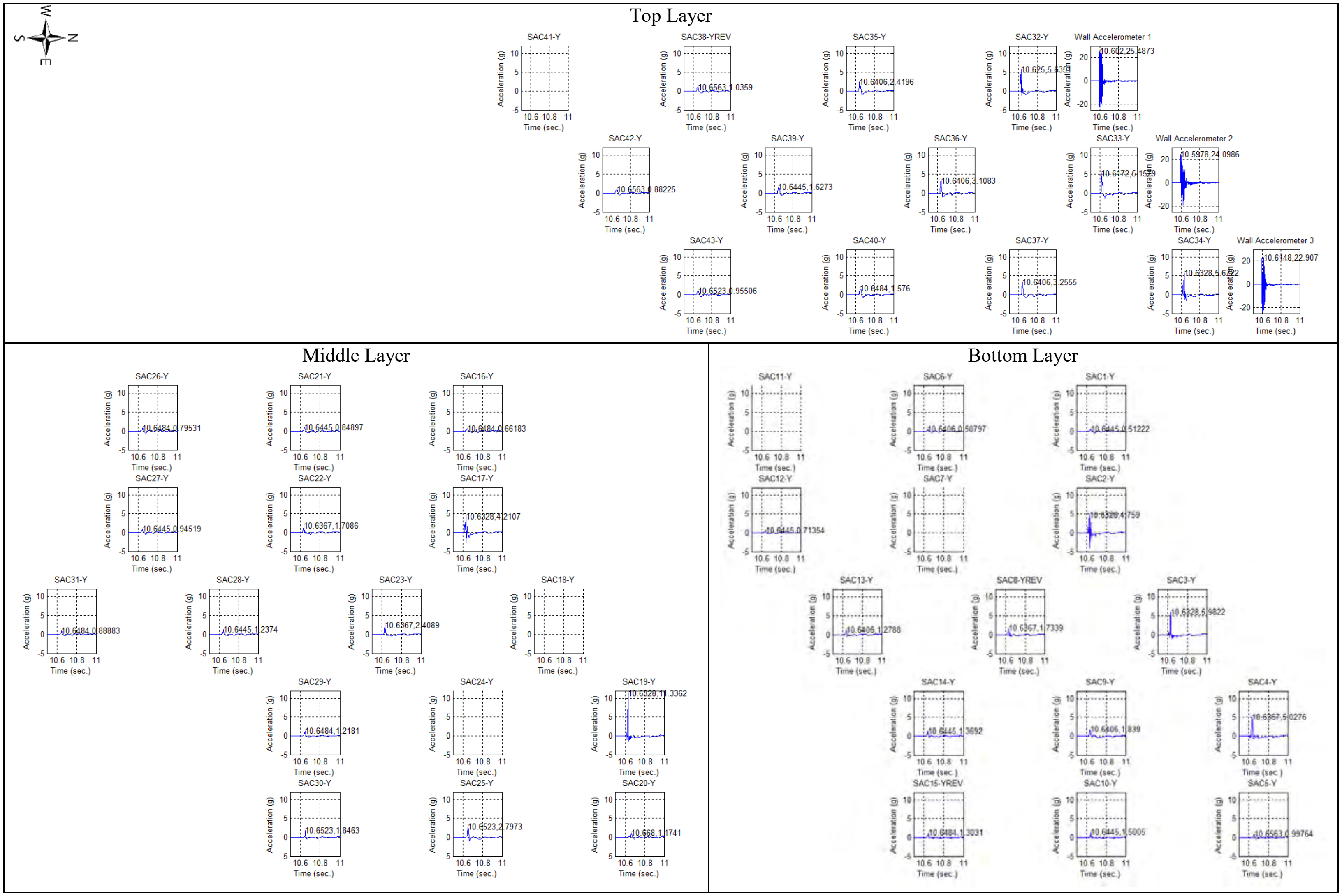

Figure F-9 Longitudinal acceleration of backfill soil for the 30° skew test in Run 5.

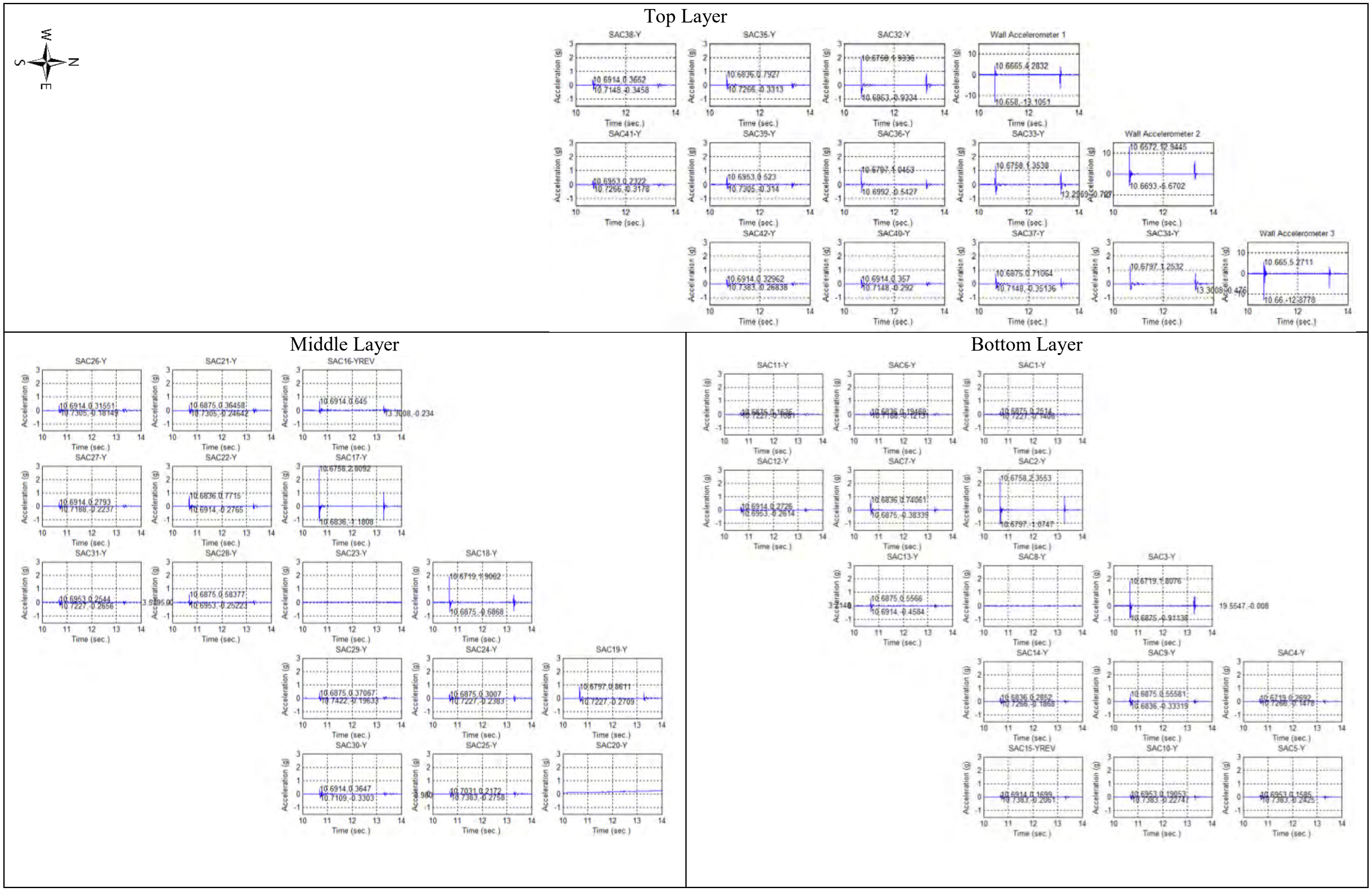

Figure F-10 Longitudinal acceleration of backfill soil for the 45° skew test in Run 2.

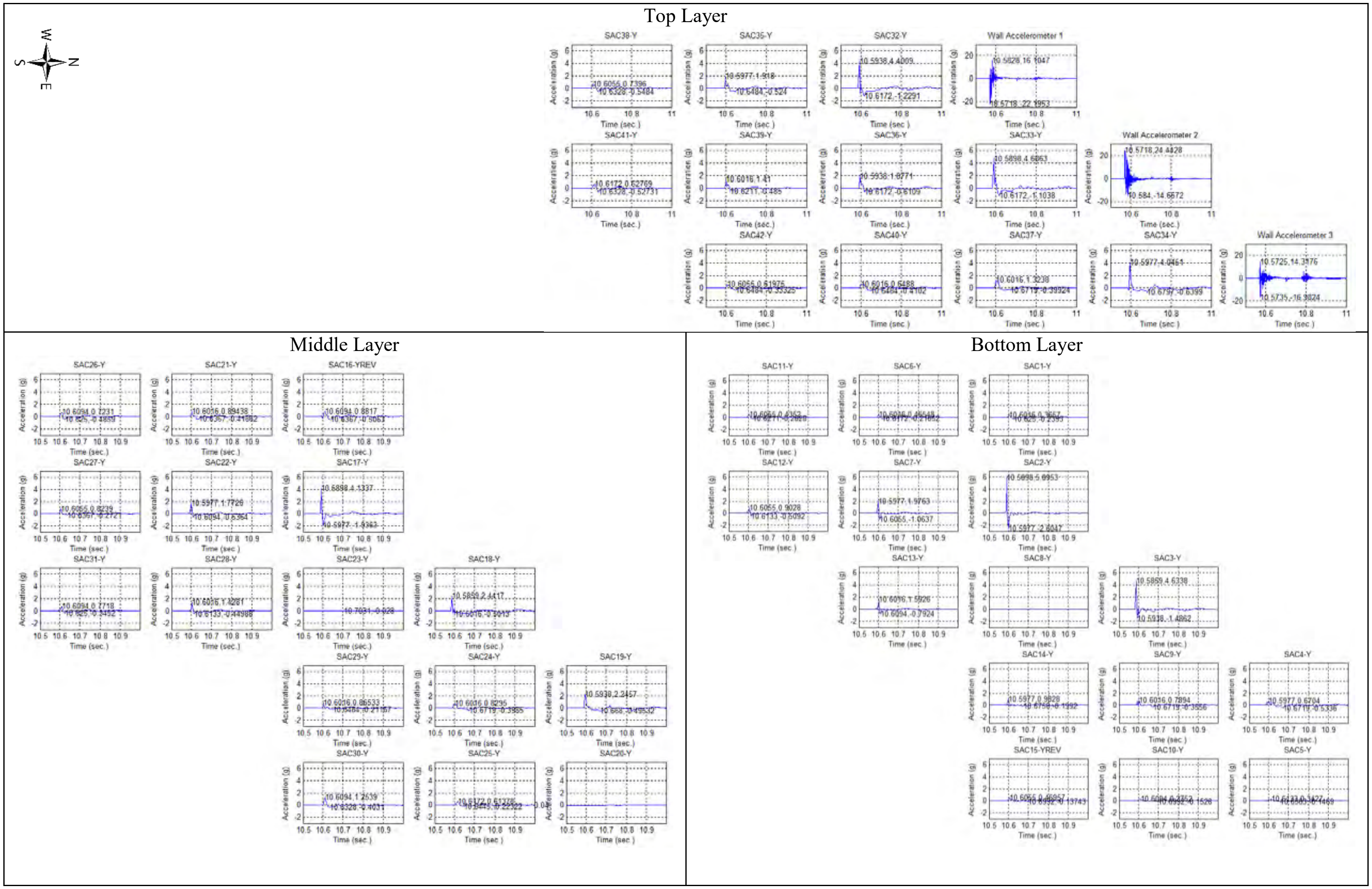

Figure F-11 Longitudinal acceleration of backfill soil for the 45° skew test in Run 3.

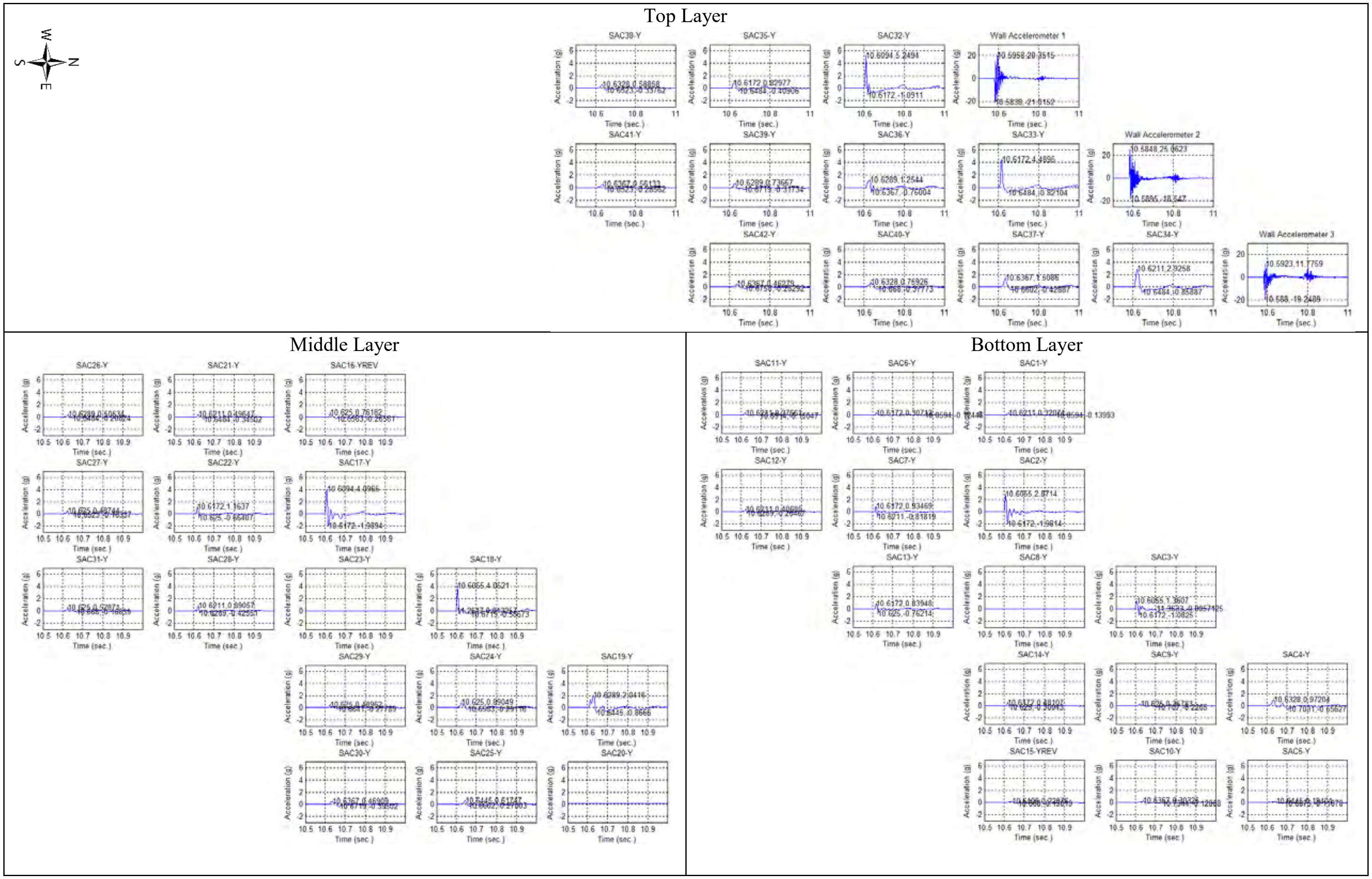

Figure F-12 Longitudinal acceleration of backfill soil for the 45° skew test in Run 4.

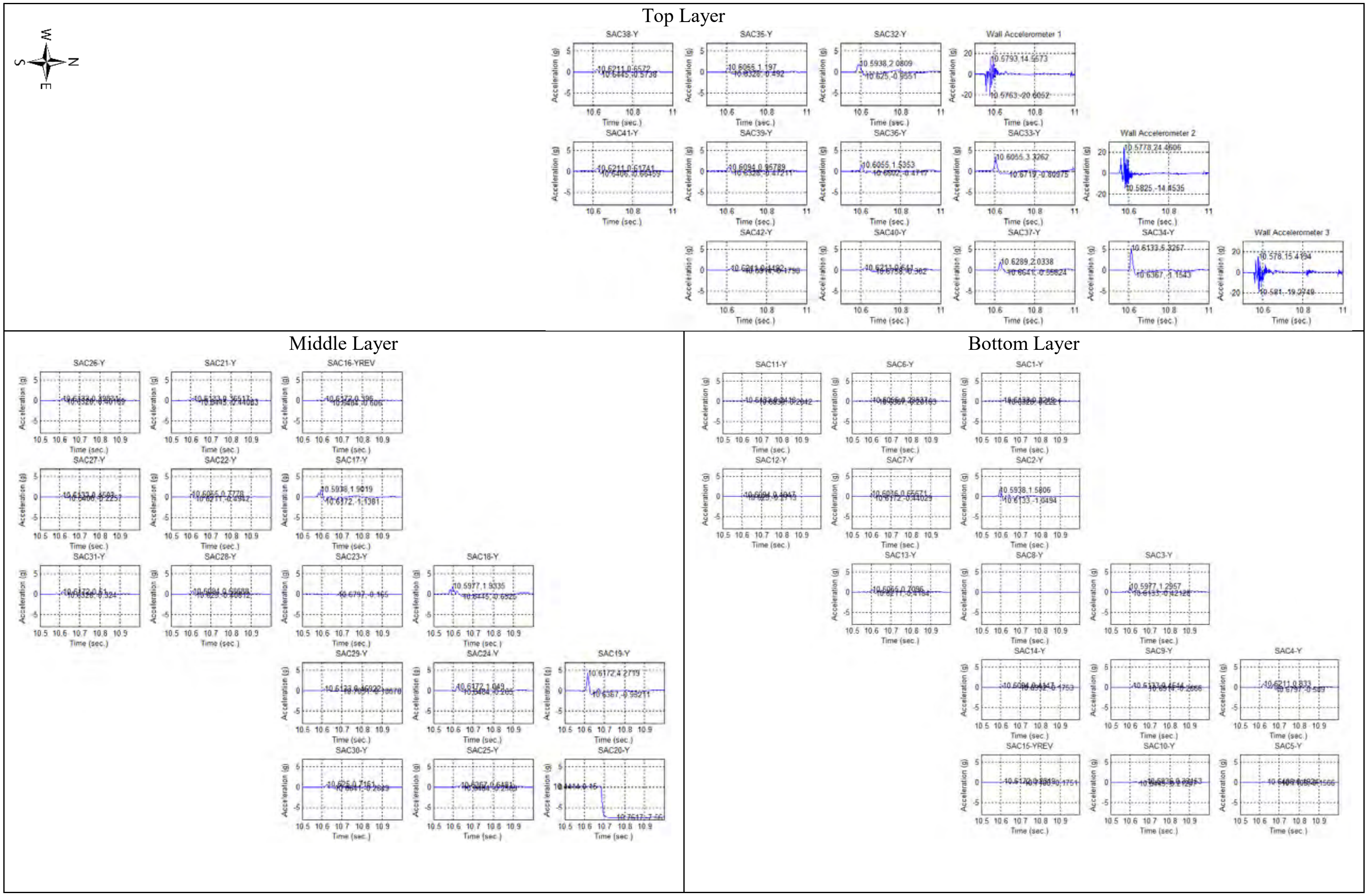

Figure F-13 Longitudinal acceleration of backfill soil for the 45° skew test in Run 5.

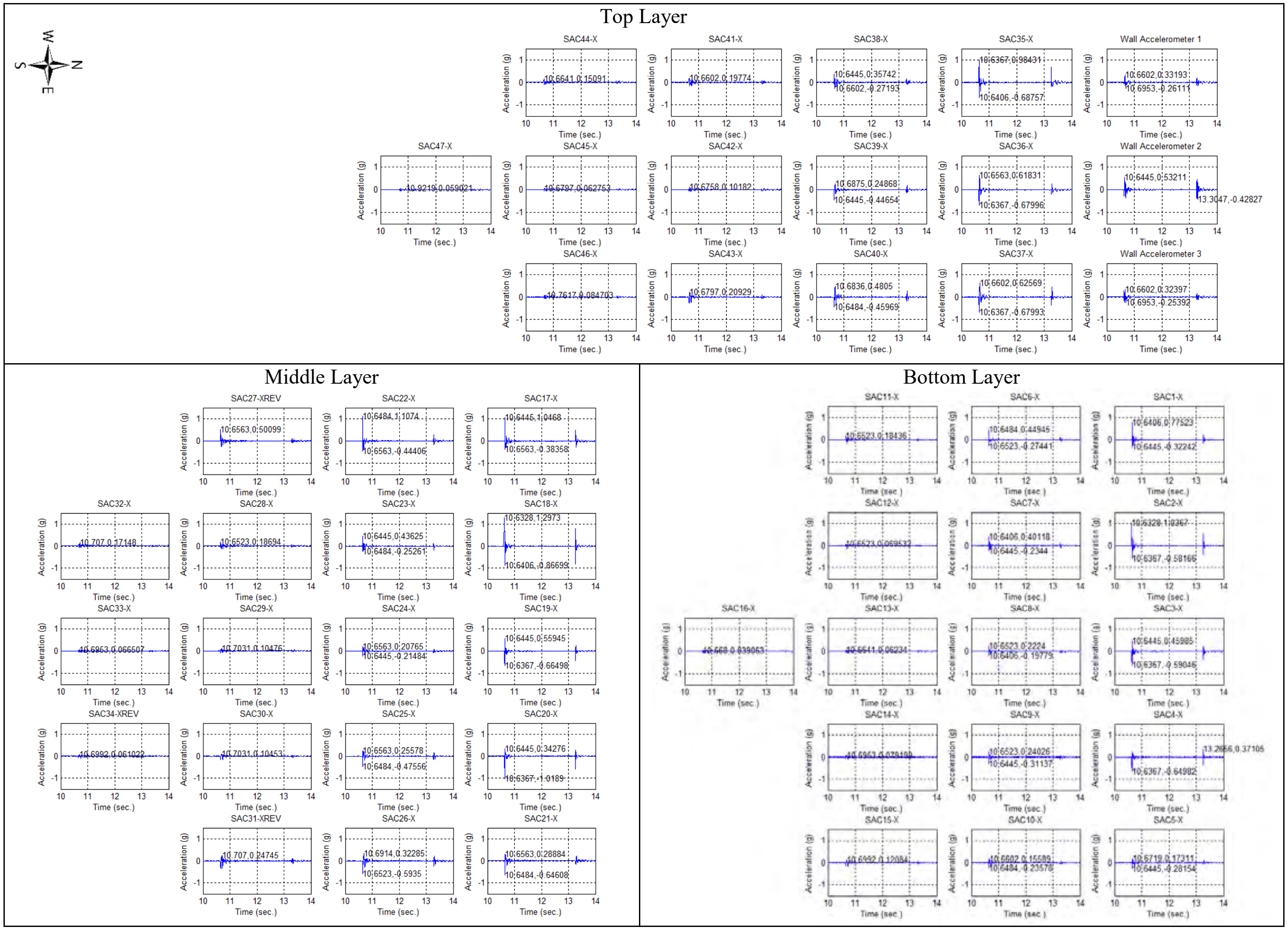

Figure F-14 Transverse acceleration of backfill soil for the 0° skew test in Run 2.

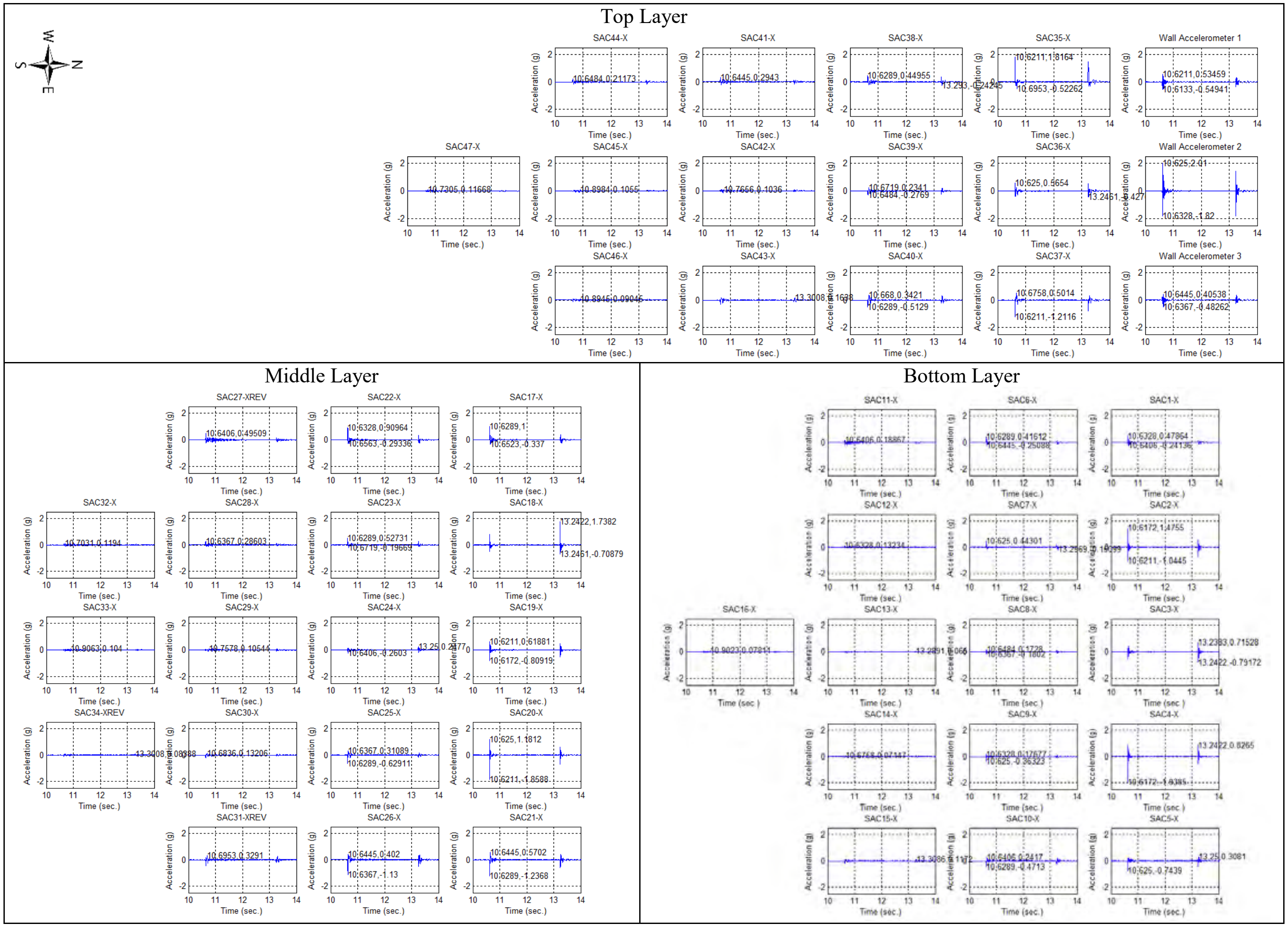

Figure F-15 Transverse acceleration of backfill soil for the 0° skew test in Run 3.

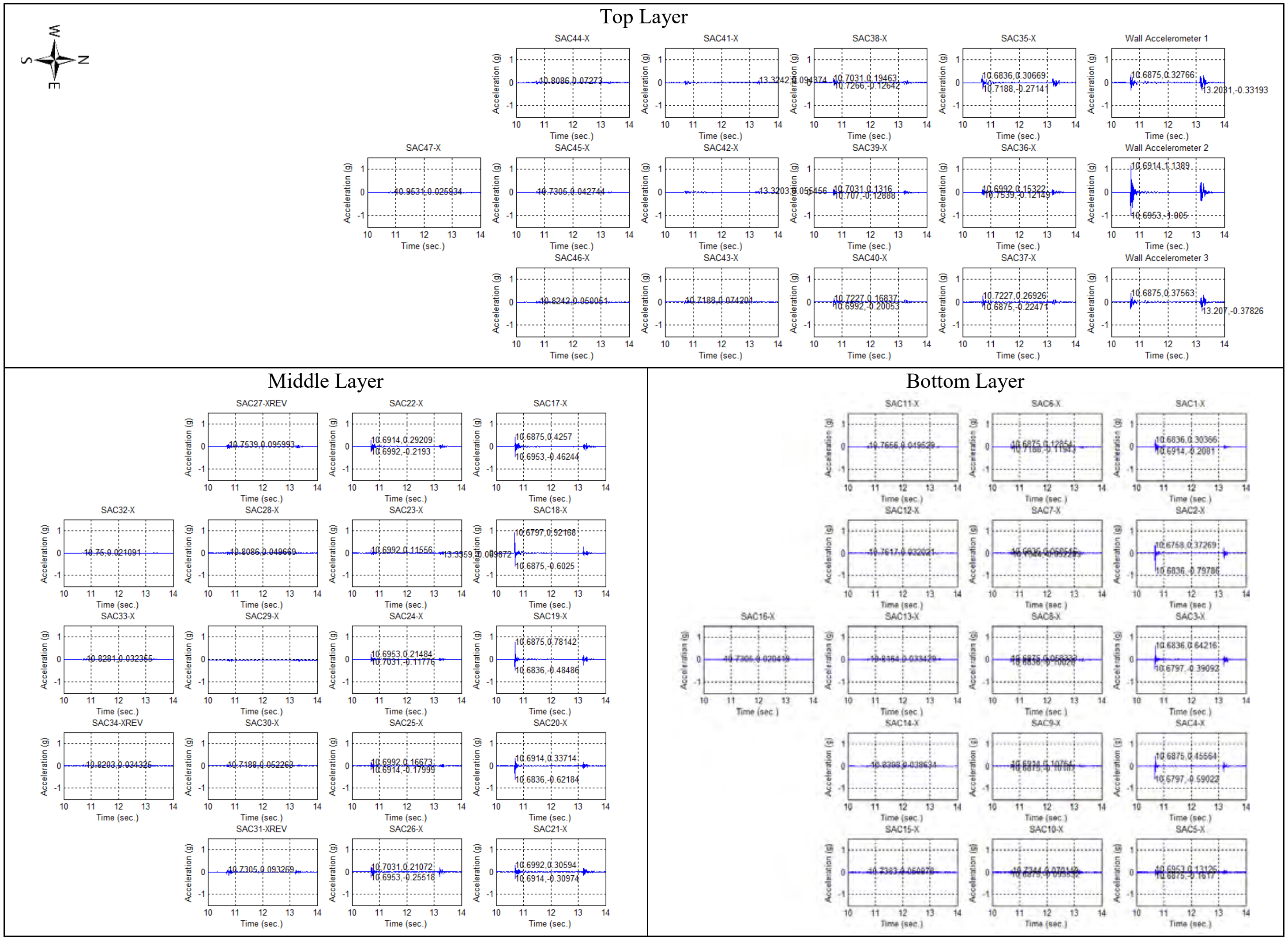

Figure F-16 Transverse acceleration of backfill soil for the 0° skew test in Run 4.

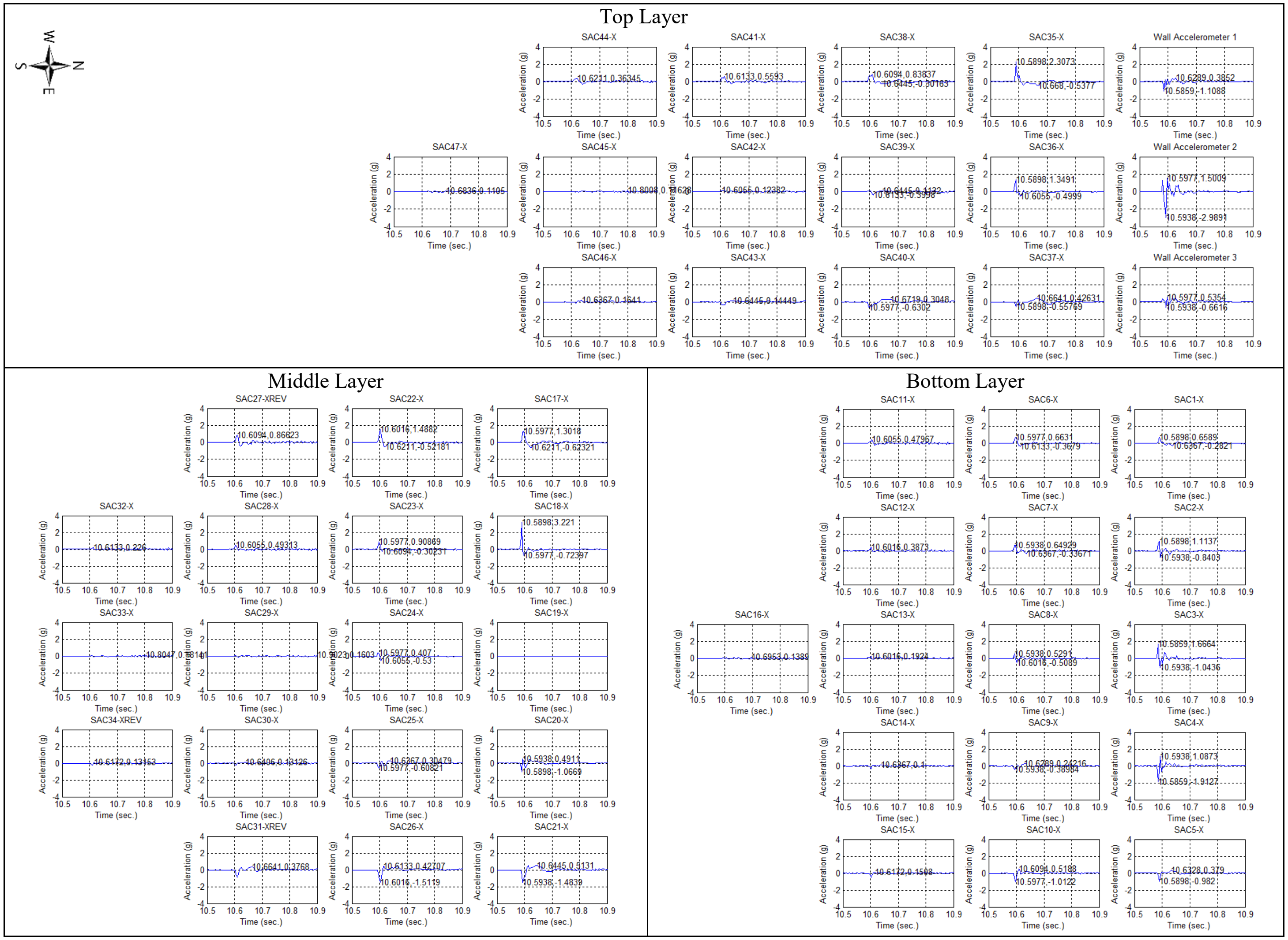

Figure F-17 Transverse acceleration of backfill soil for the 0° skew test in Run 6.

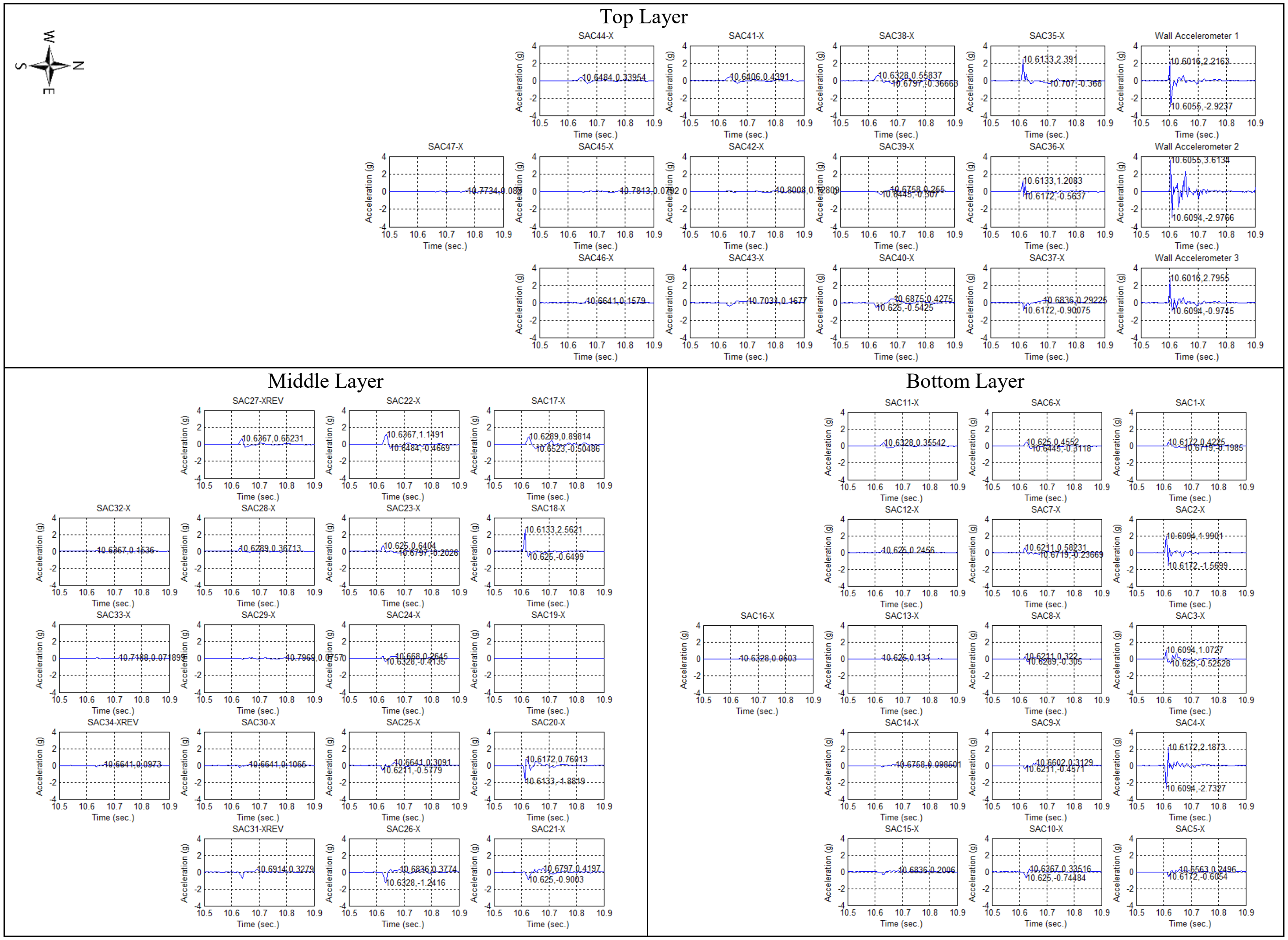

Figure F-18 Transverse acceleration of backfill soil for the 0° skew test in Run 7.

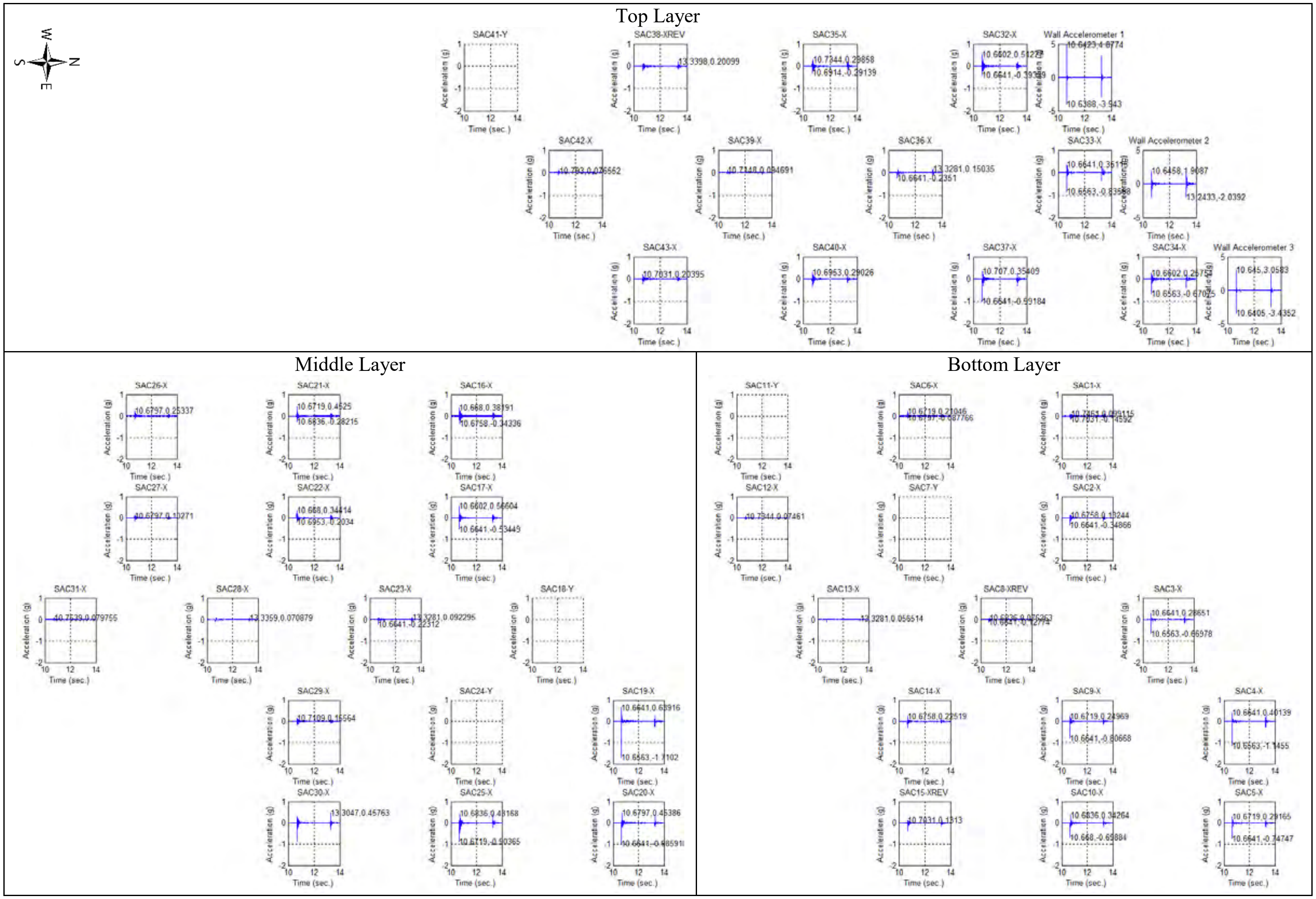

Figure F-19 Transverse acceleration of backfill soil for the 30° skew test in Run 2.

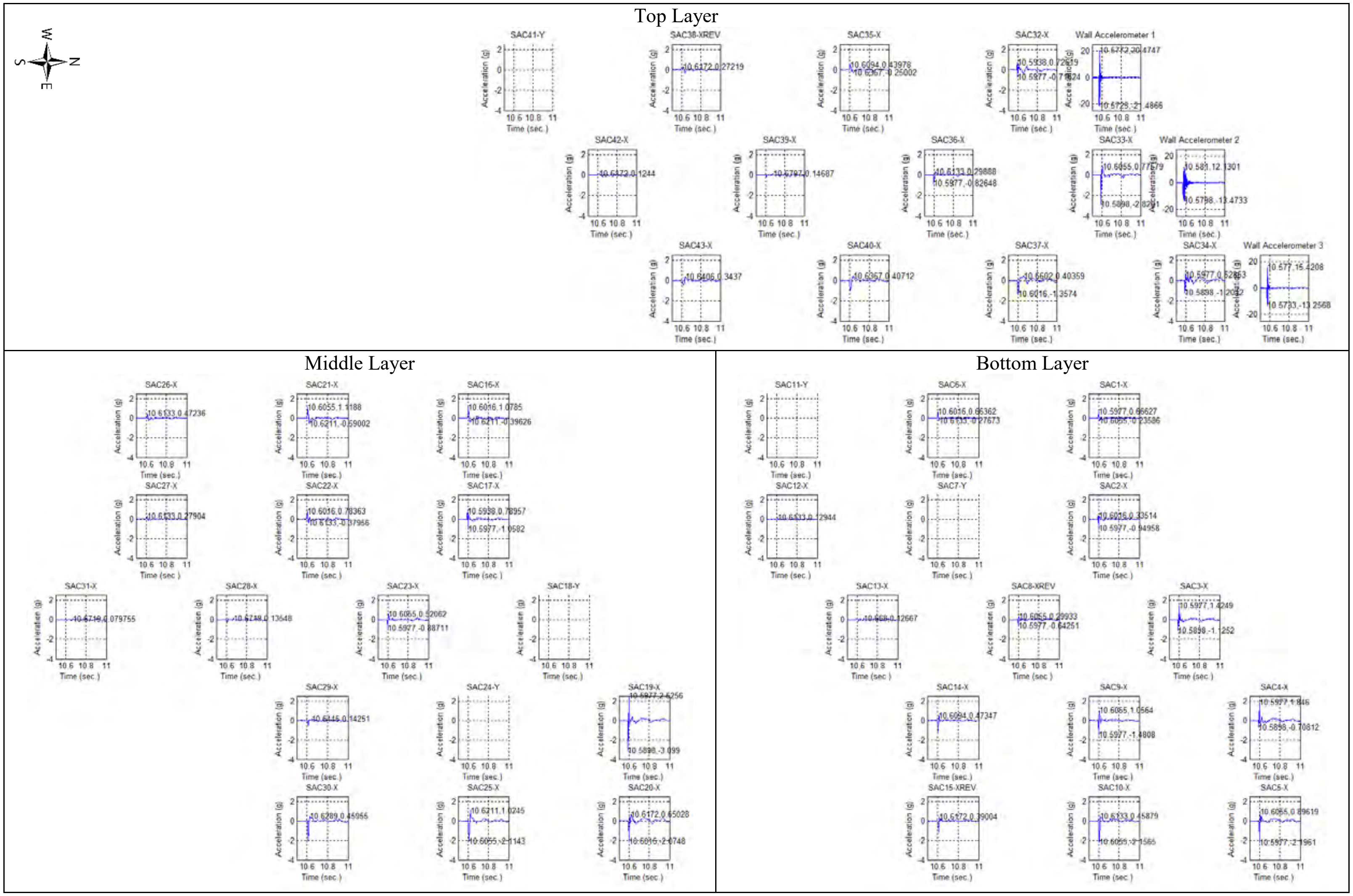

Figure F-20 Transverse acceleration of backfill soil for the 30° skew test in Run 3.

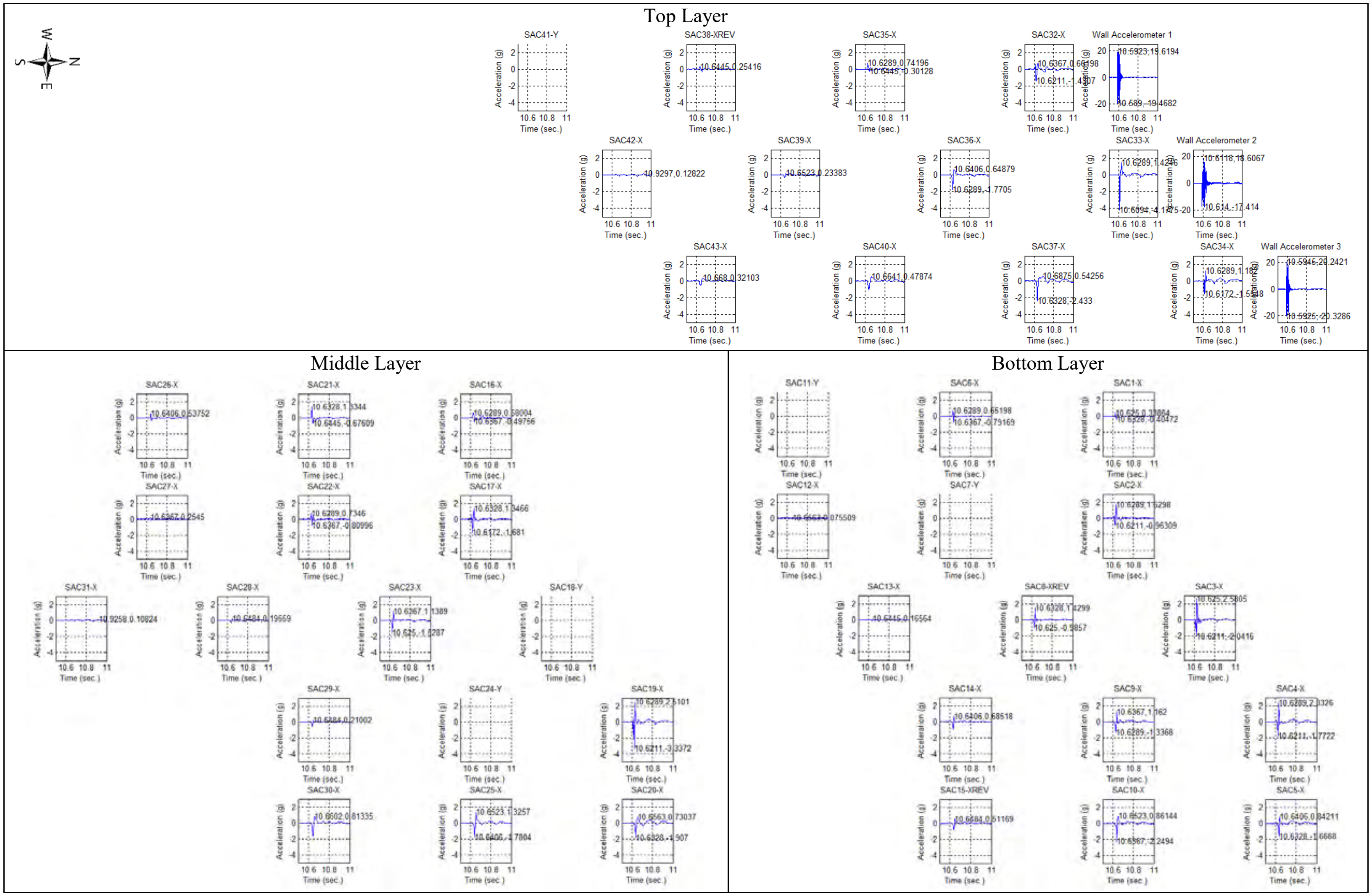

Figure F-21 Transverse acceleration of backfill soil for the 30° skew test in Run 4.

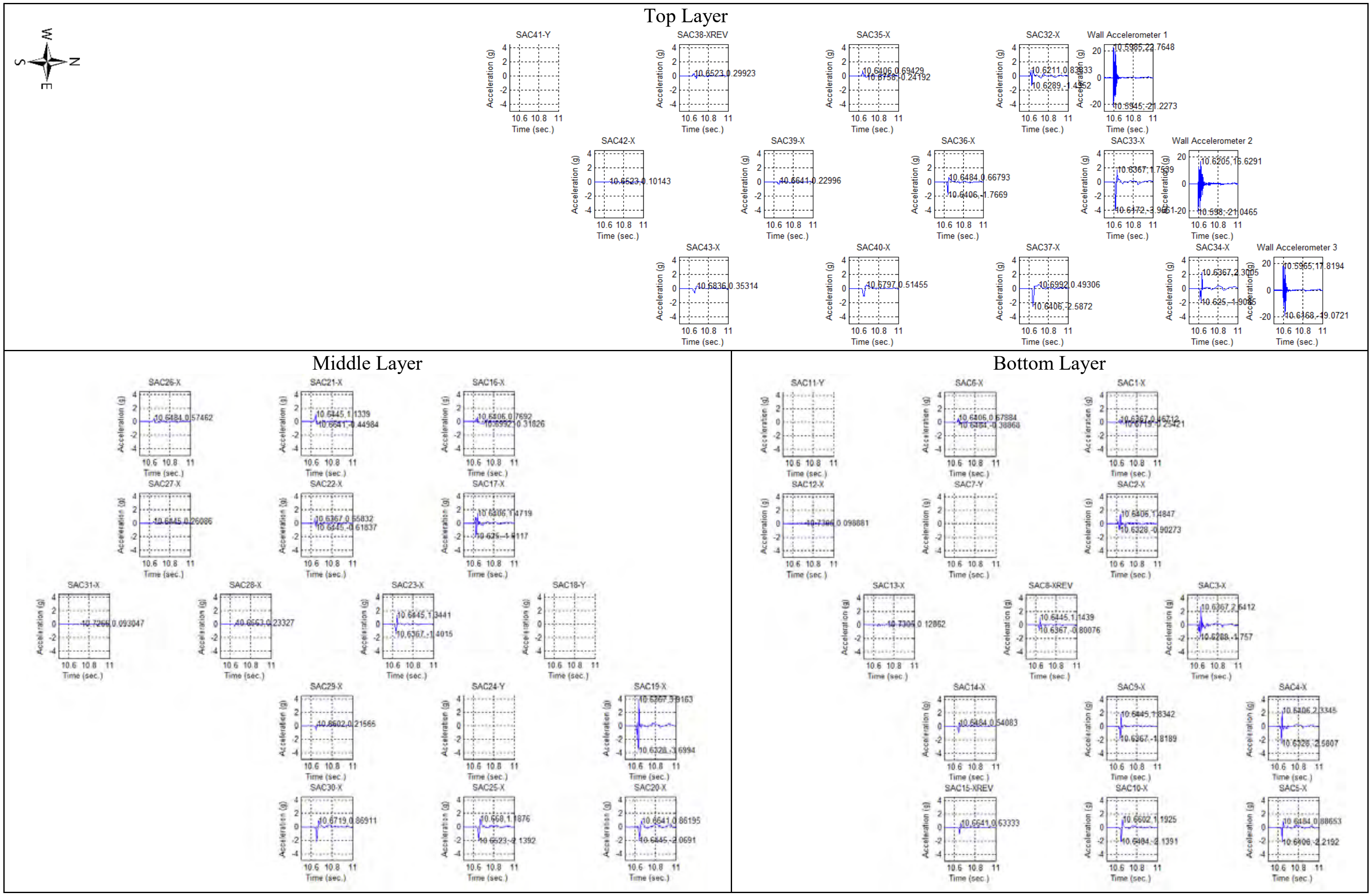

Figure F-22 Transverse acceleration of backfill soil for the 30° skew test in Run 5.

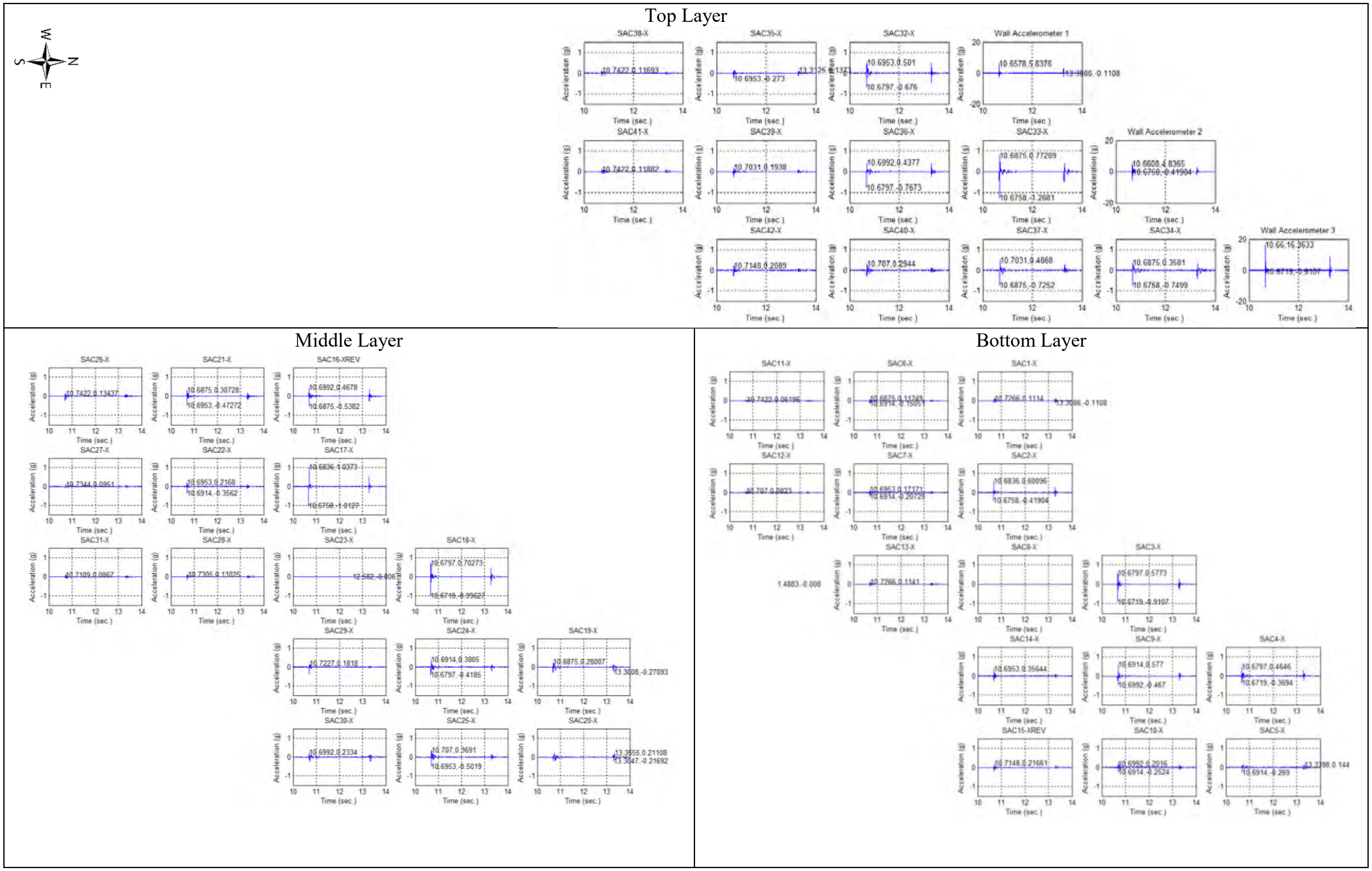

Figure F-23 Transverse acceleration of backfill soil for the 45° skew test in Run 2.

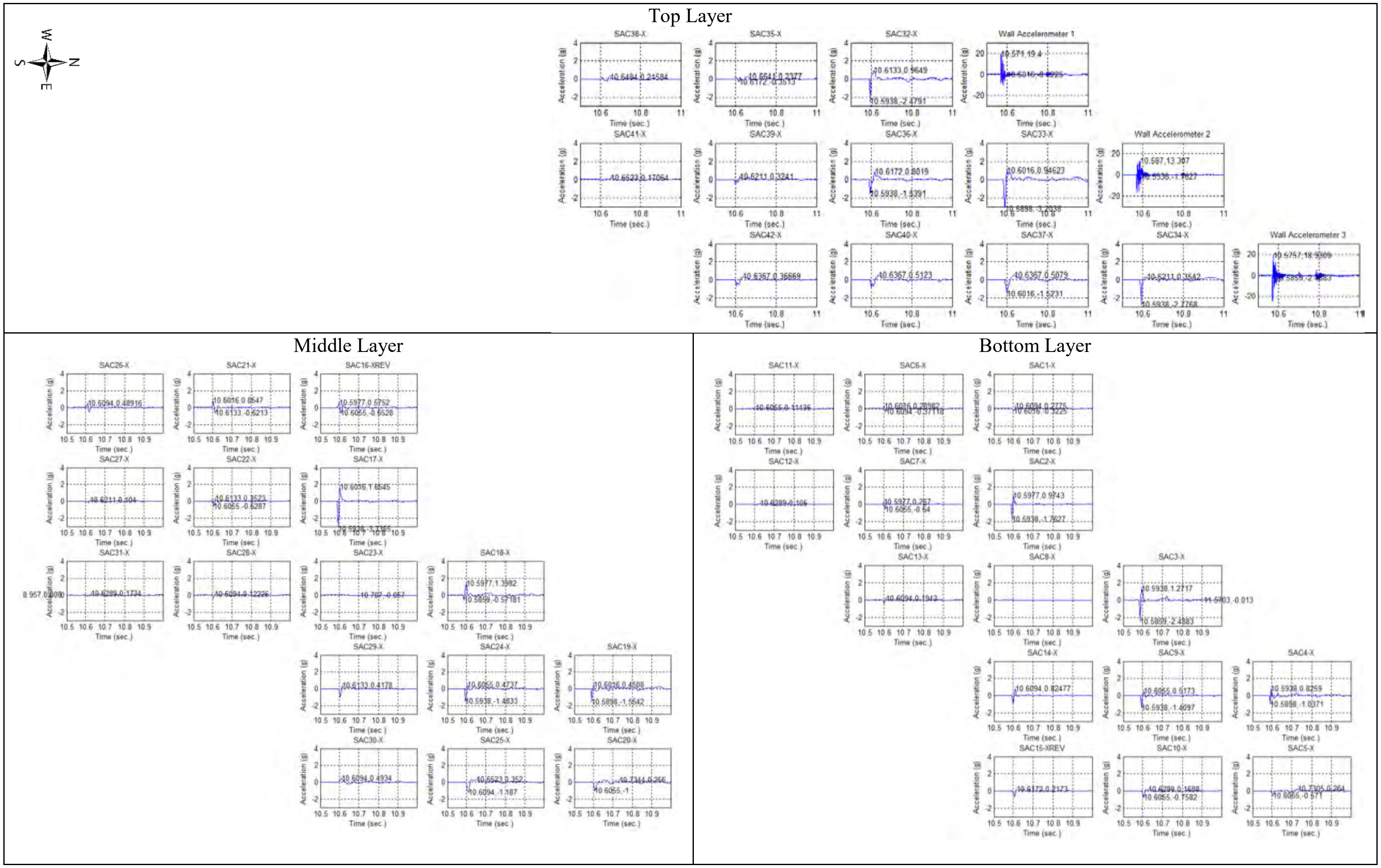

Figure F-24 Transverse acceleration of backfill soil for the 45° skew test in Run 3.

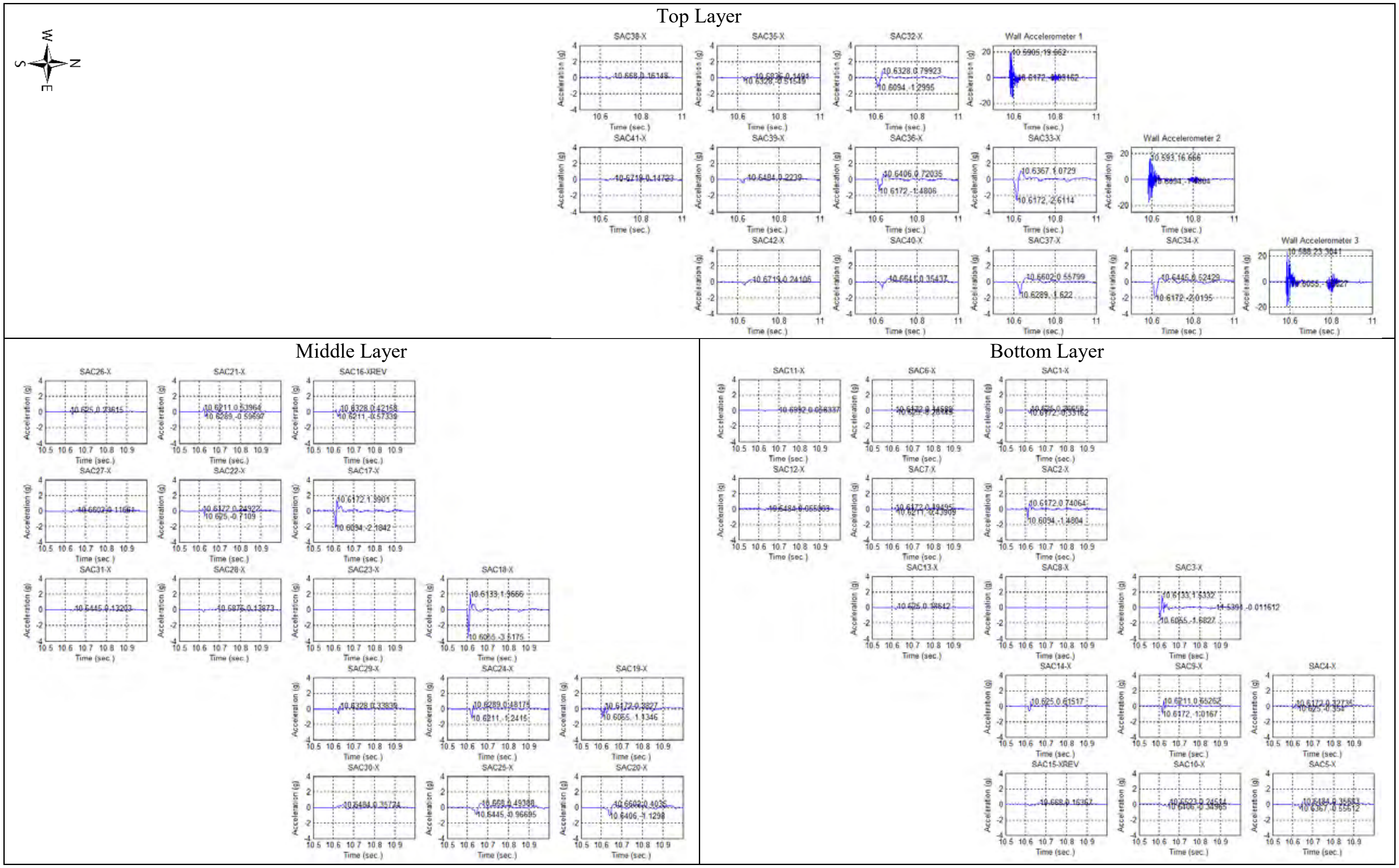

Figure F-25 Transverse acceleration of backfill soil for the 45° skew test in Run 4.

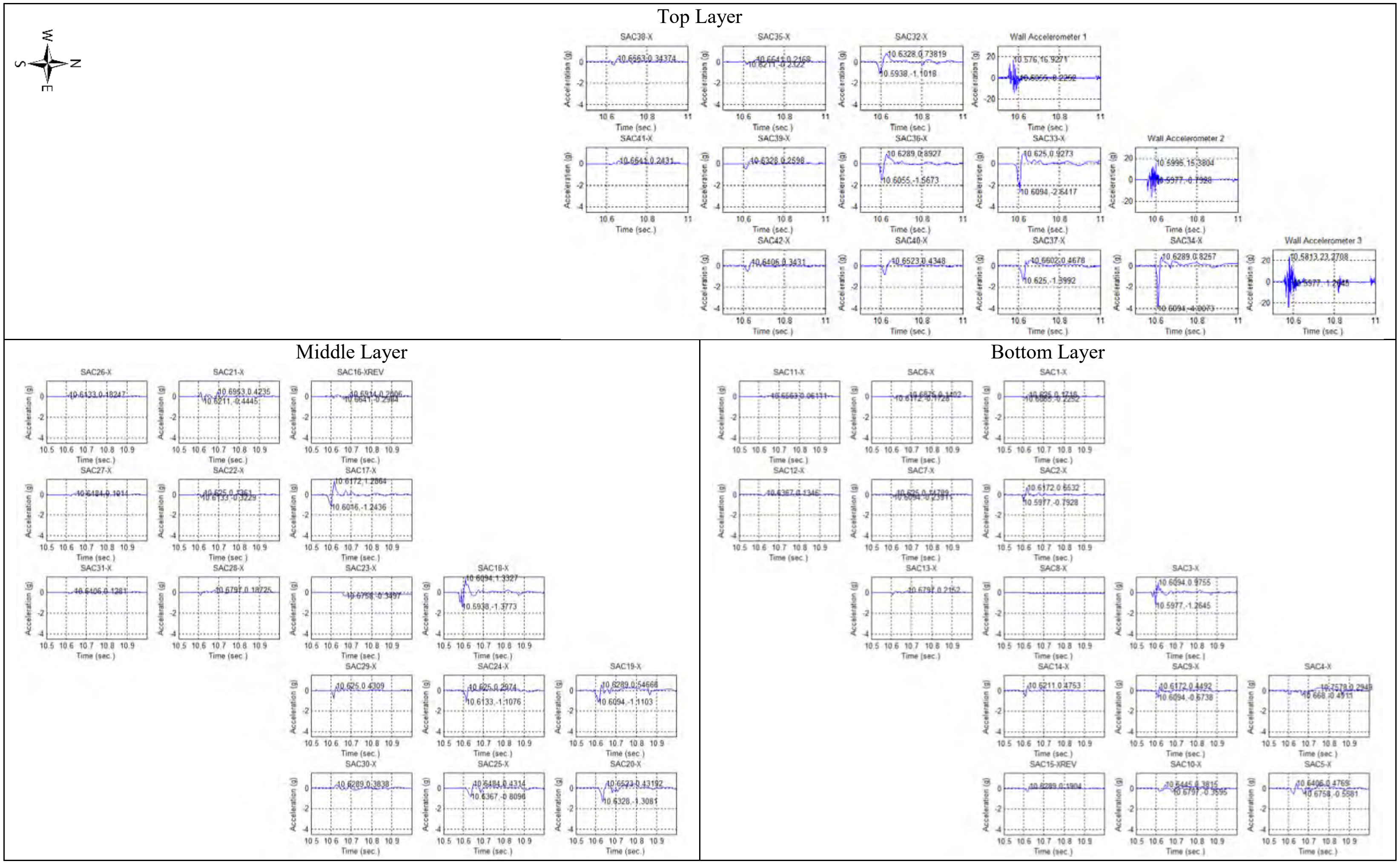

Figure F-26 Transverse acceleration of backfill soil for the 45° skew test in Run 5.

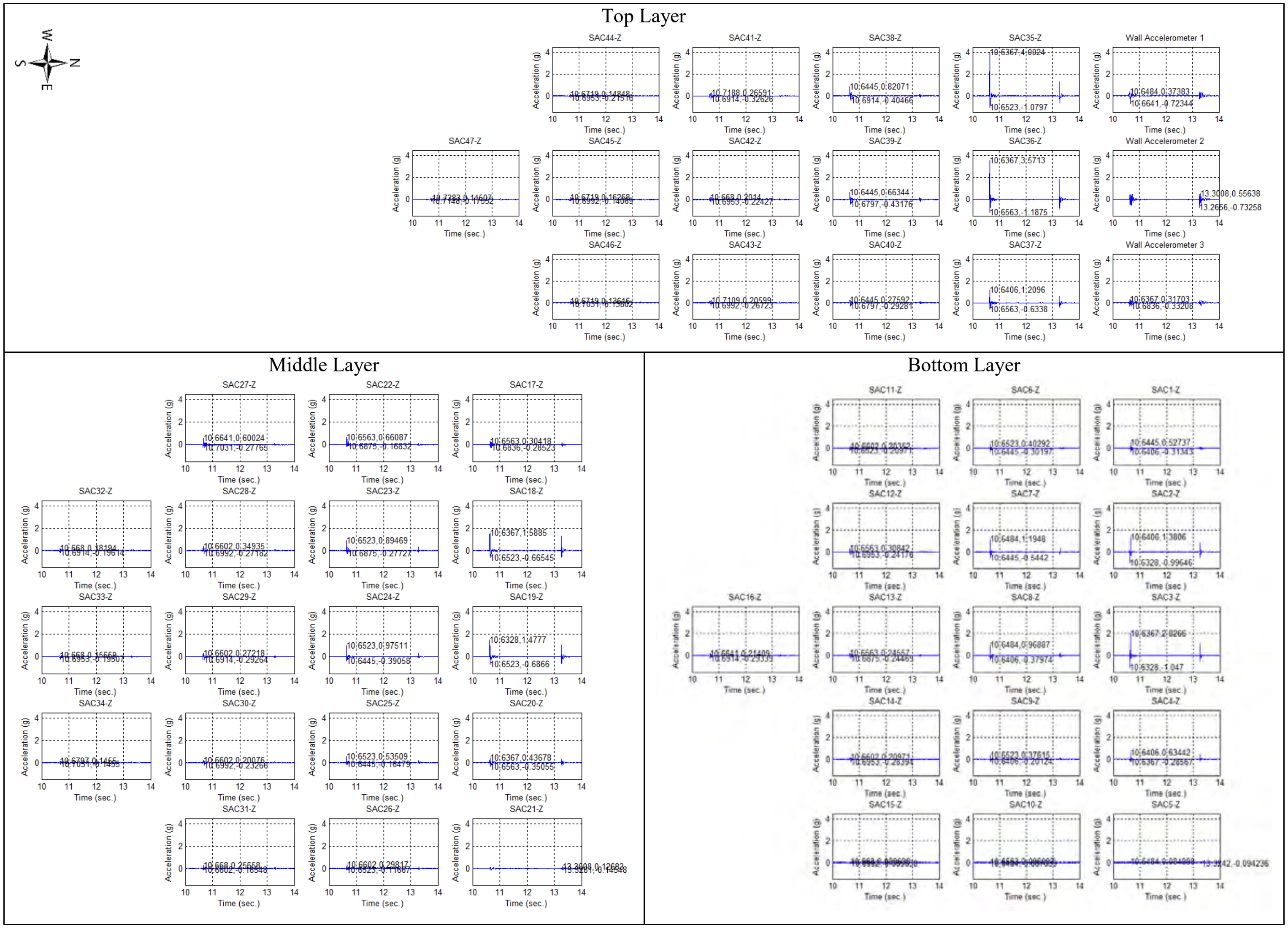

Figure F-27 Vertical acceleration of backfill soil for the 0° skew test in Run 2.

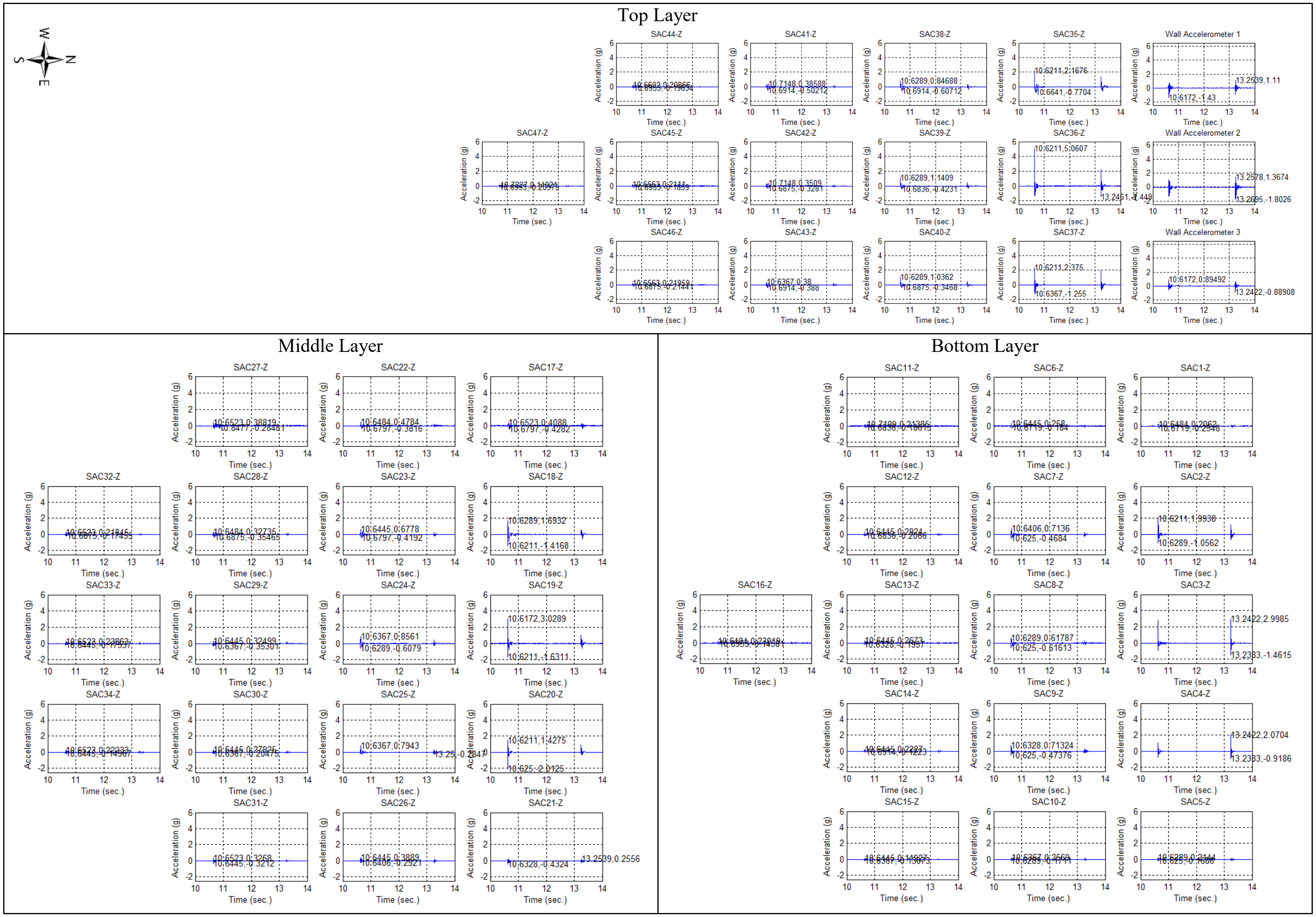

Figure F-28 Vertical acceleration of backfill soil for the 0° skew test in Run 3.

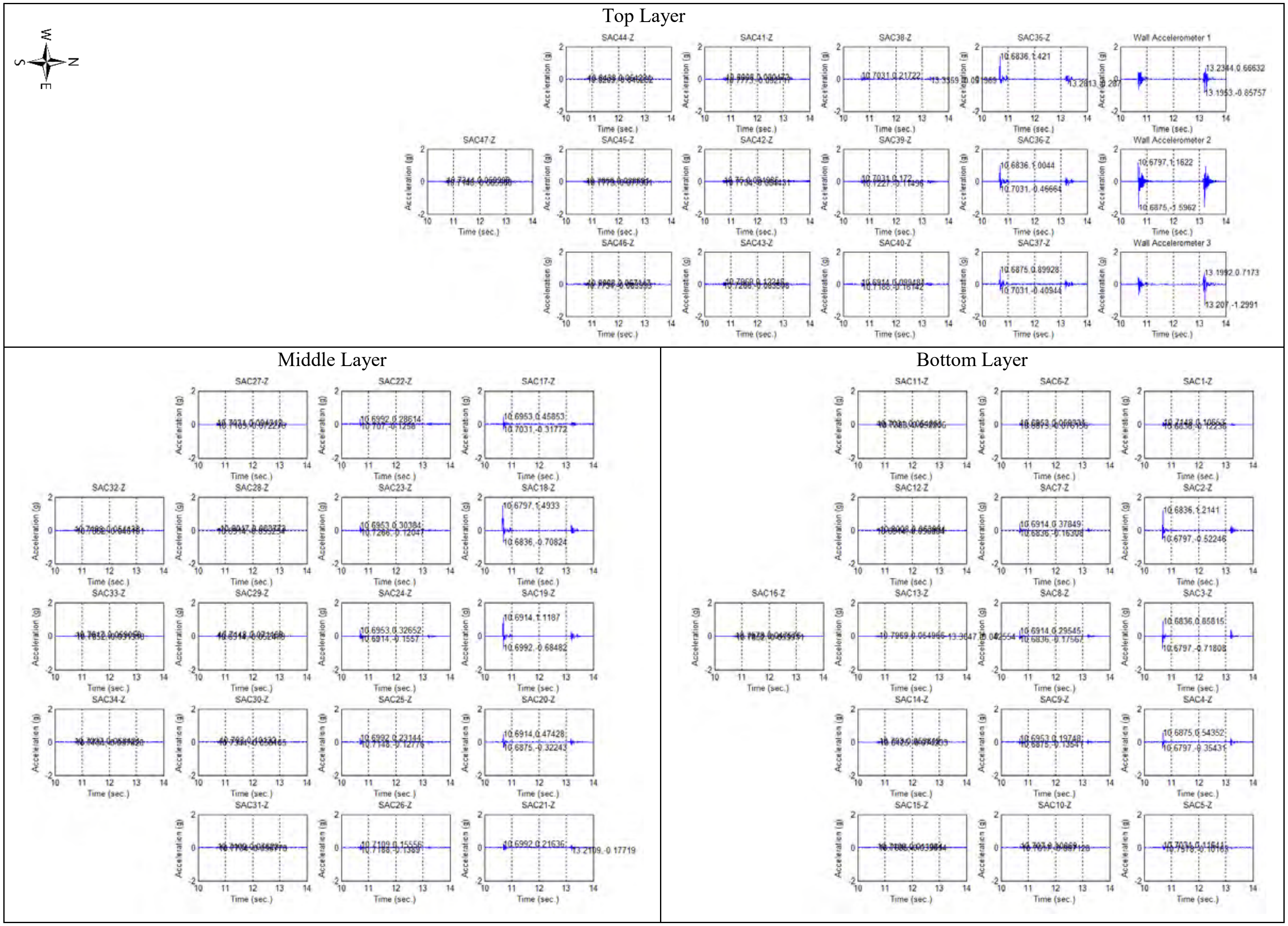

Figure F-29 Vertical acceleration of backfill soil for the 0° skew test in Run 4.

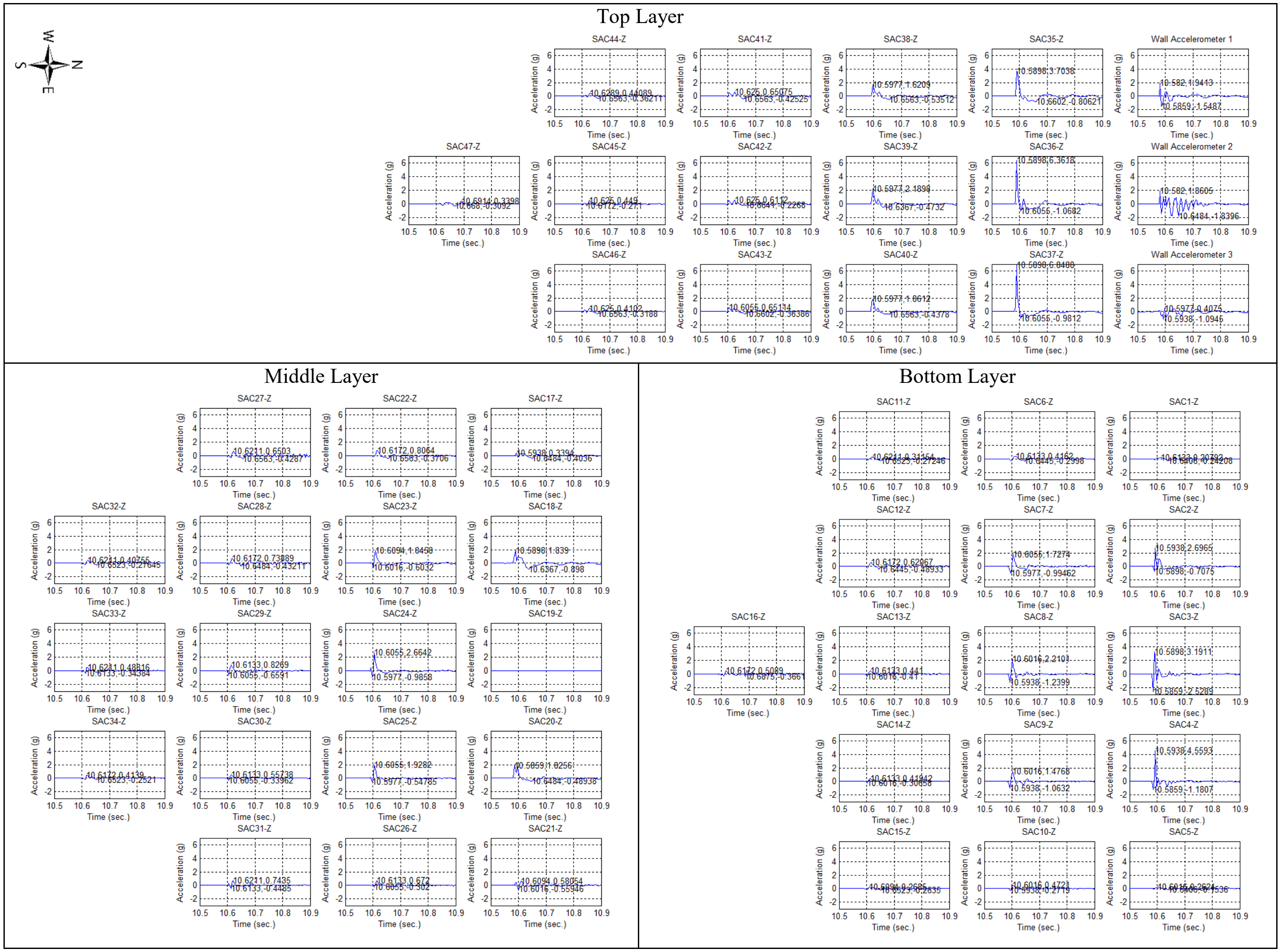

Figure F-30 Vertical acceleration of backfill soil for the 0° skew test in Run 6.

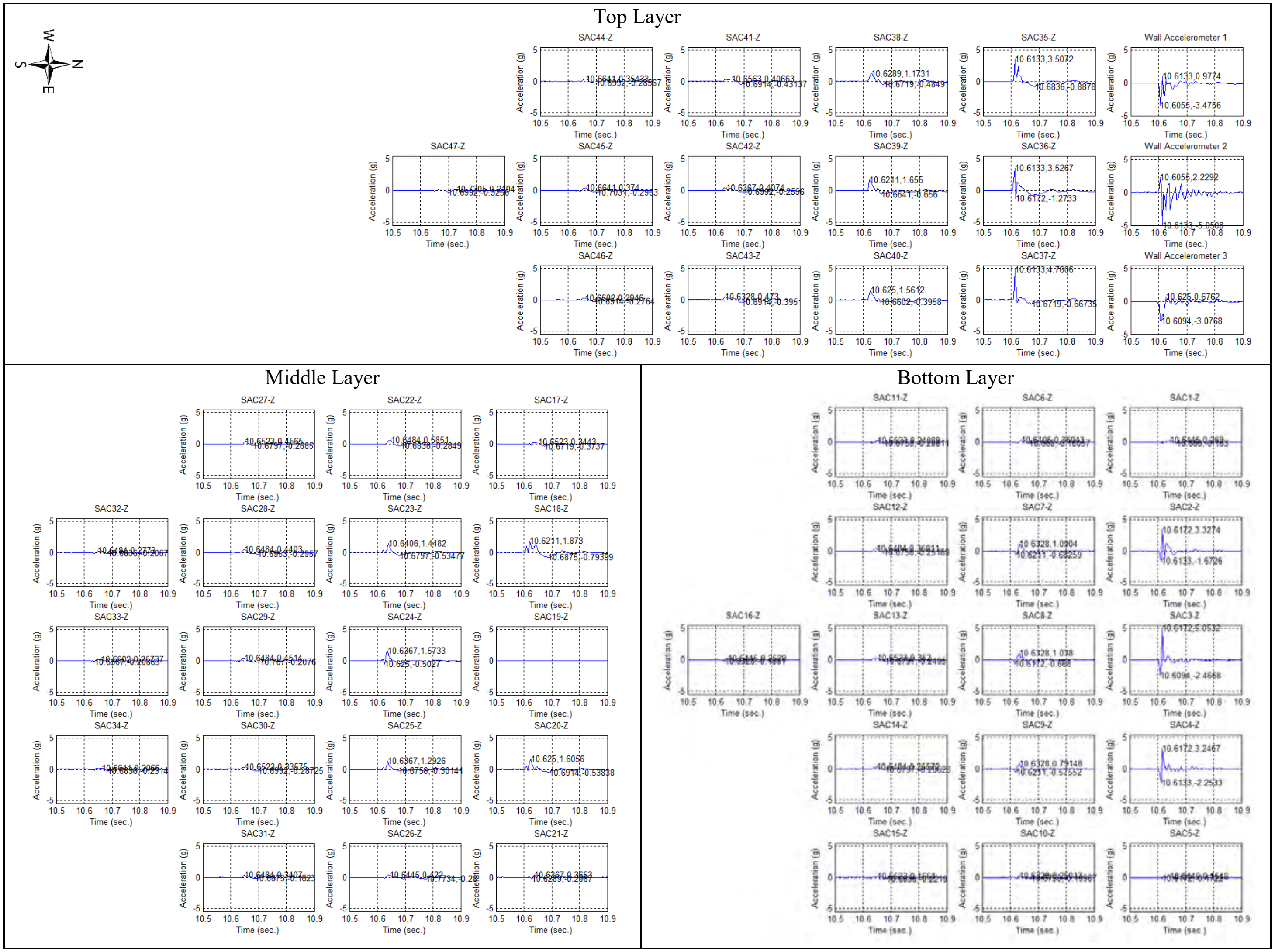

Figure F-31 Vertical acceleration of backfill soil for the 0° skew test in Run 7.

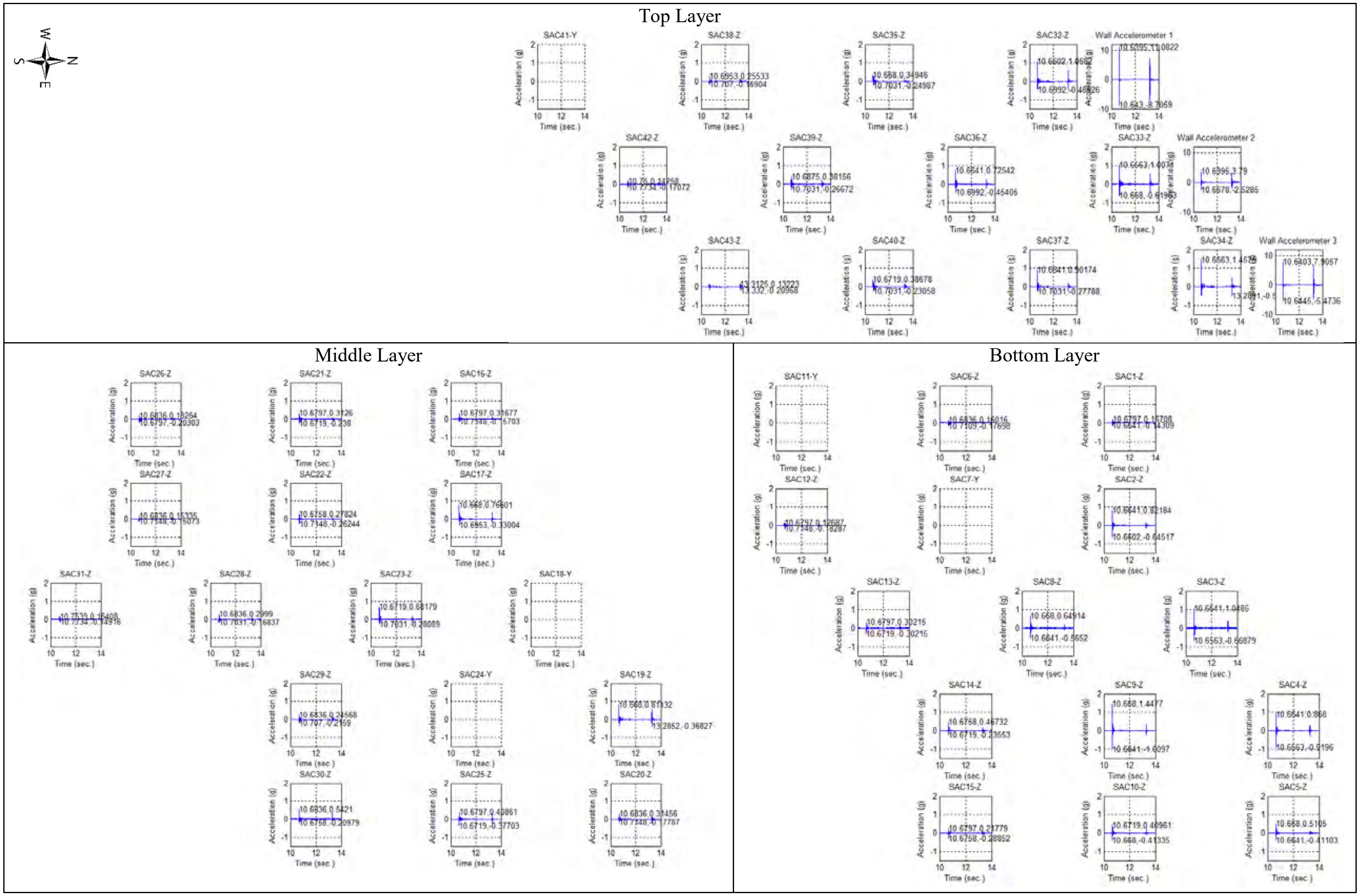

Figure F-32 Vertical acceleration of backfill soil for the 30° skew test in Run 2.

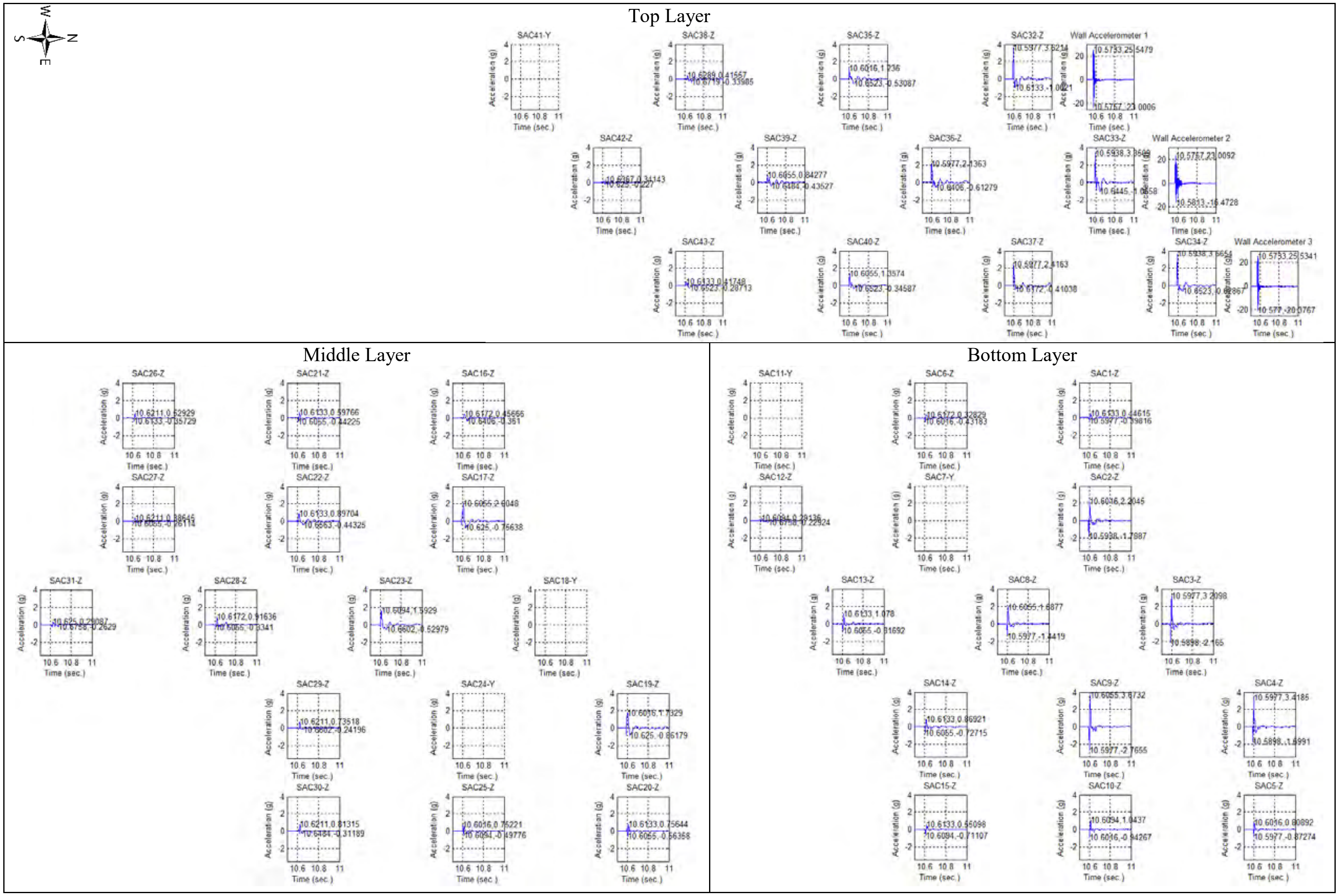

Figure F-33 Vertical acceleration of backfill soil for the 30° skew test in Run 3.

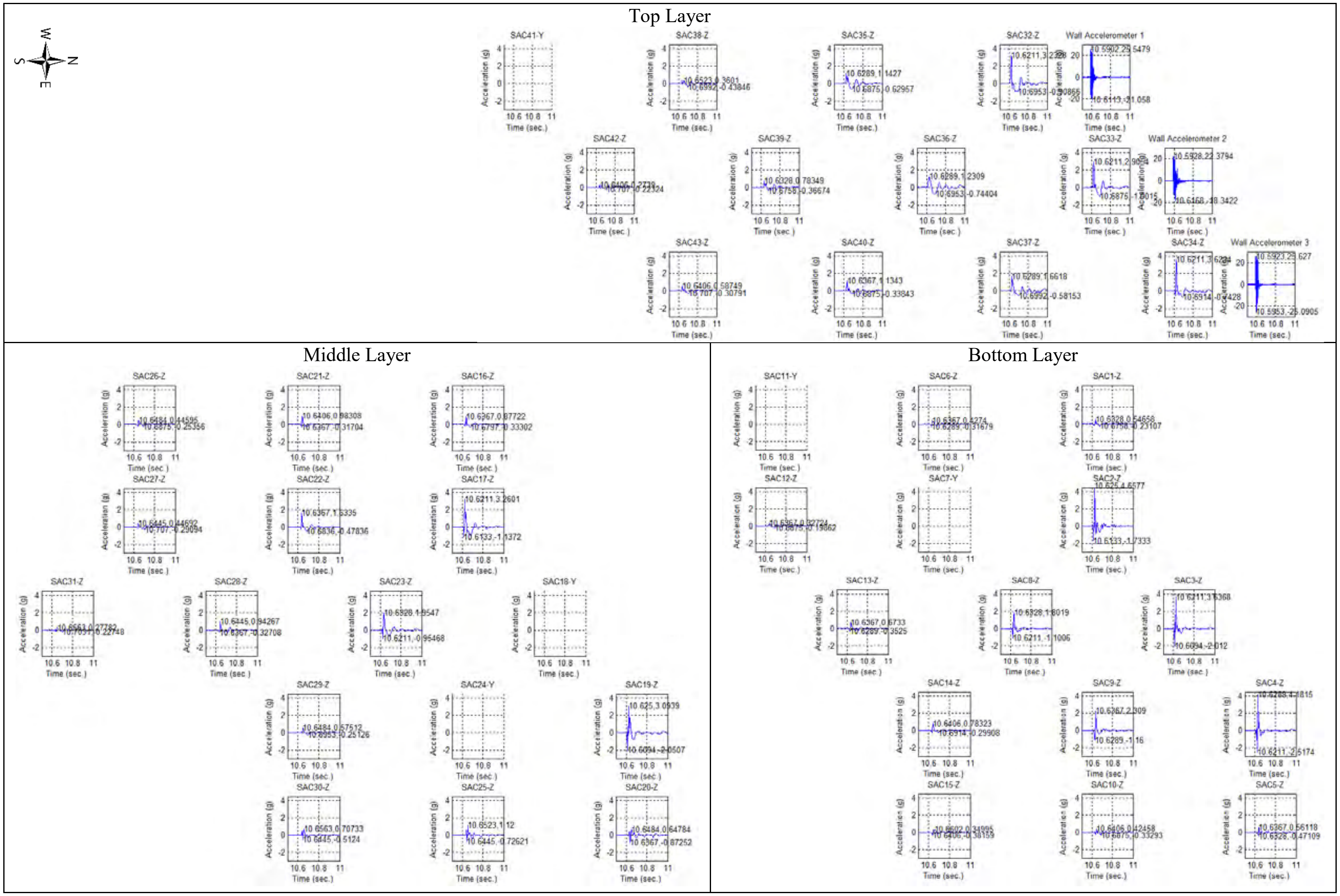

Figure F-34 Vertical acceleration of backfill soil for the 30° skew test in Run 4.

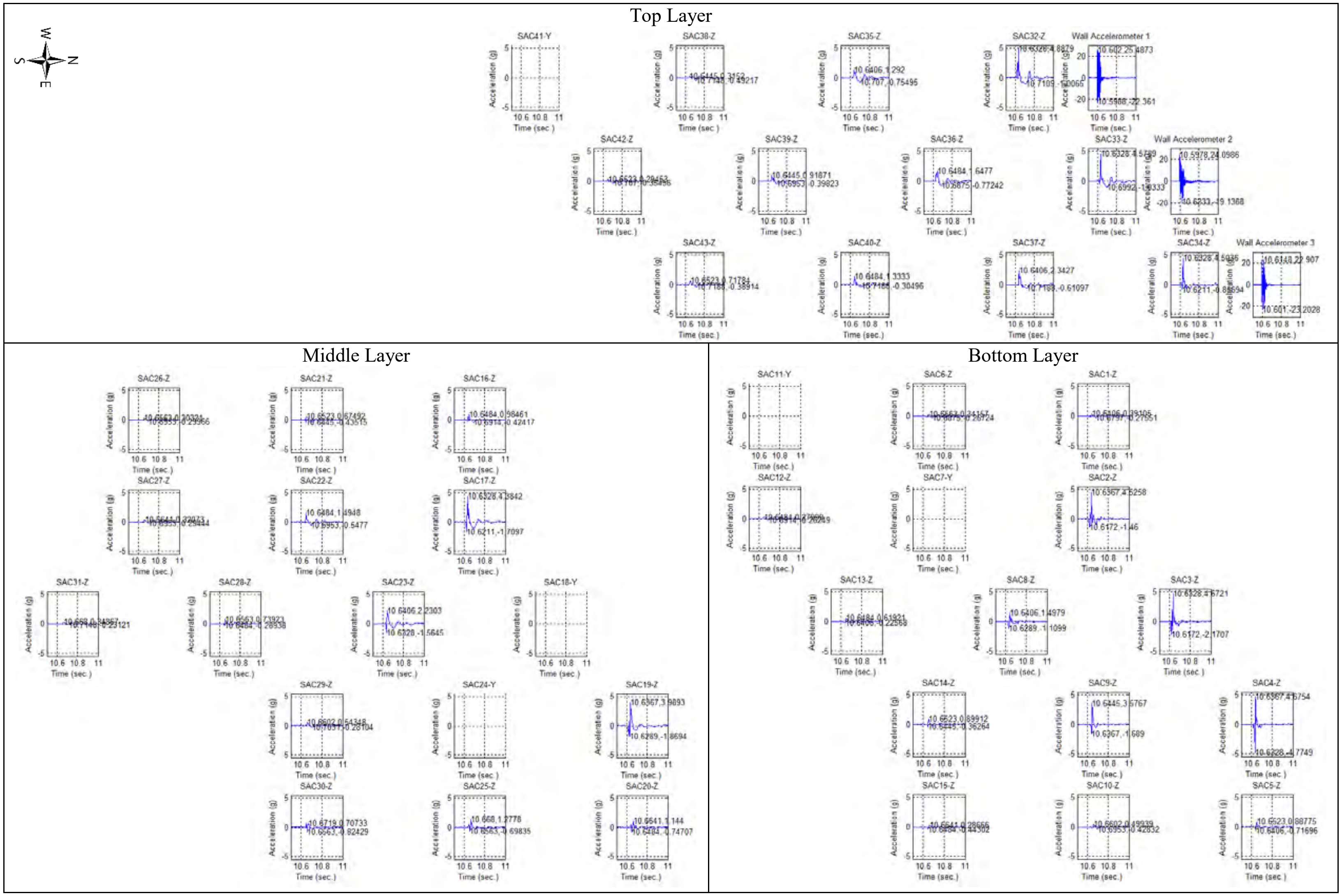

Figure F-35 Vertical acceleration of backfill soil for the 30° skew test in Run 5.

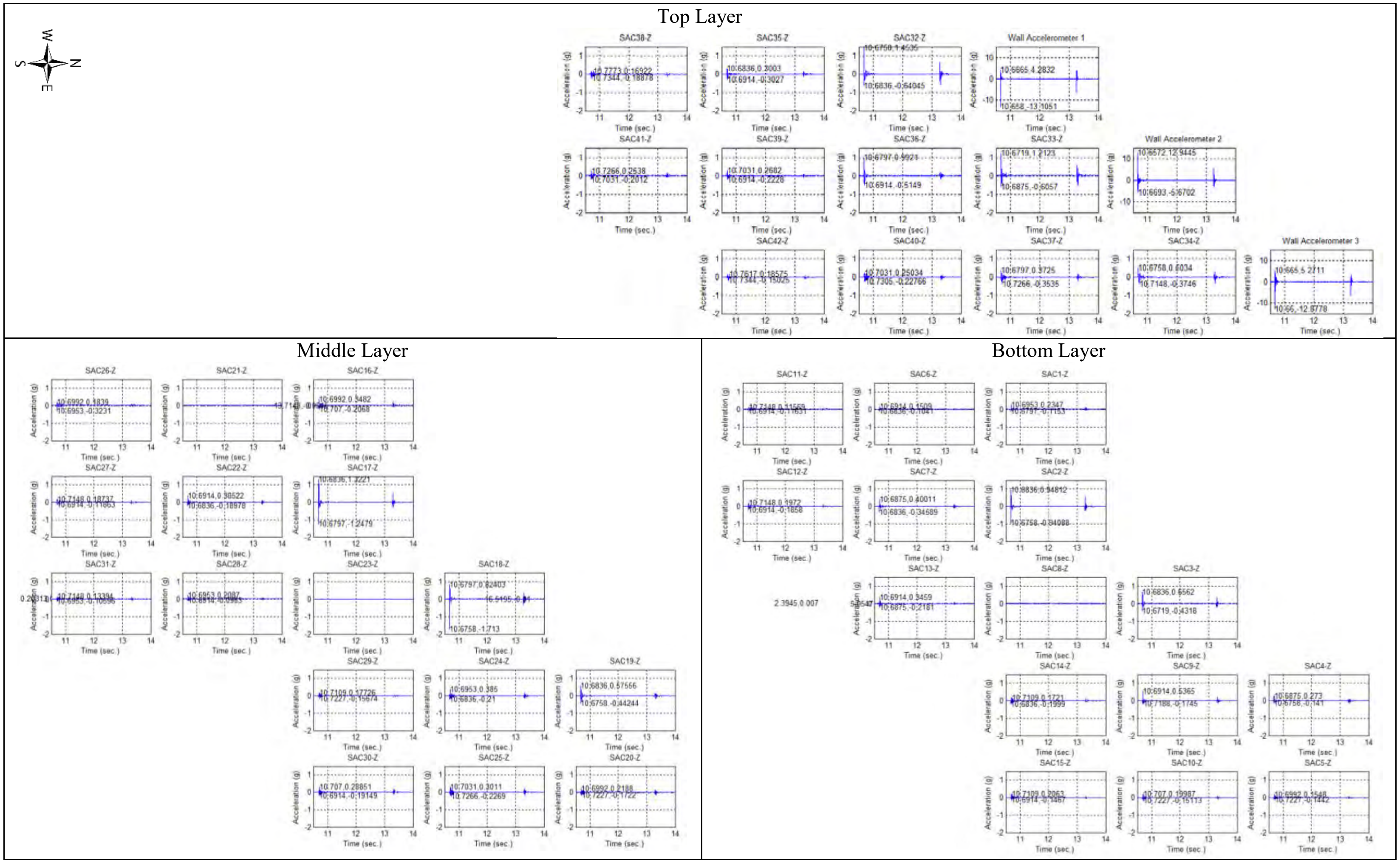

Figure F-36 Vertical acceleration of backfill soil for the 45° skew test in Run 2.

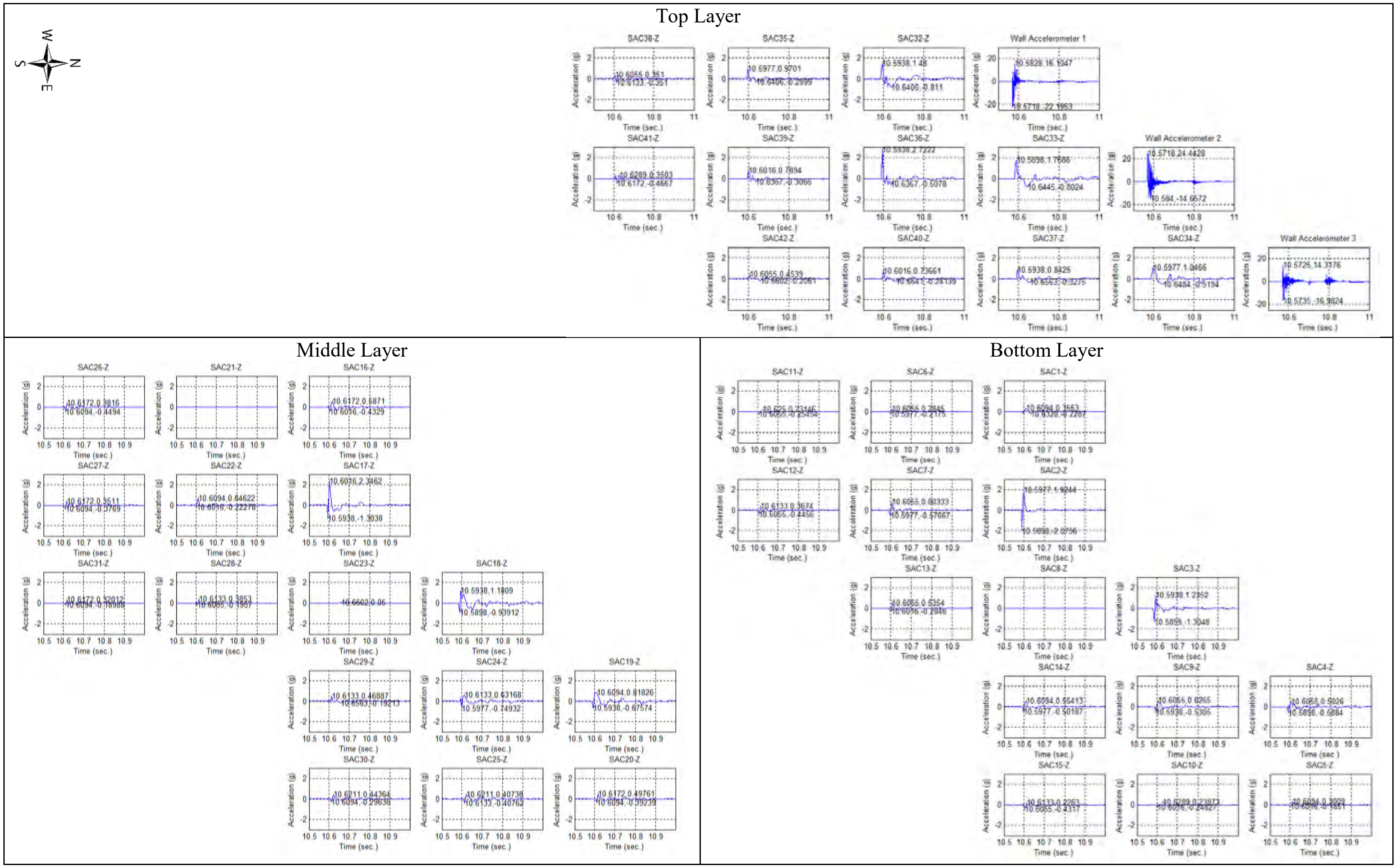

Figure F-37 Vertical acceleration of backfill soil for the 45° skew test in Run 3.

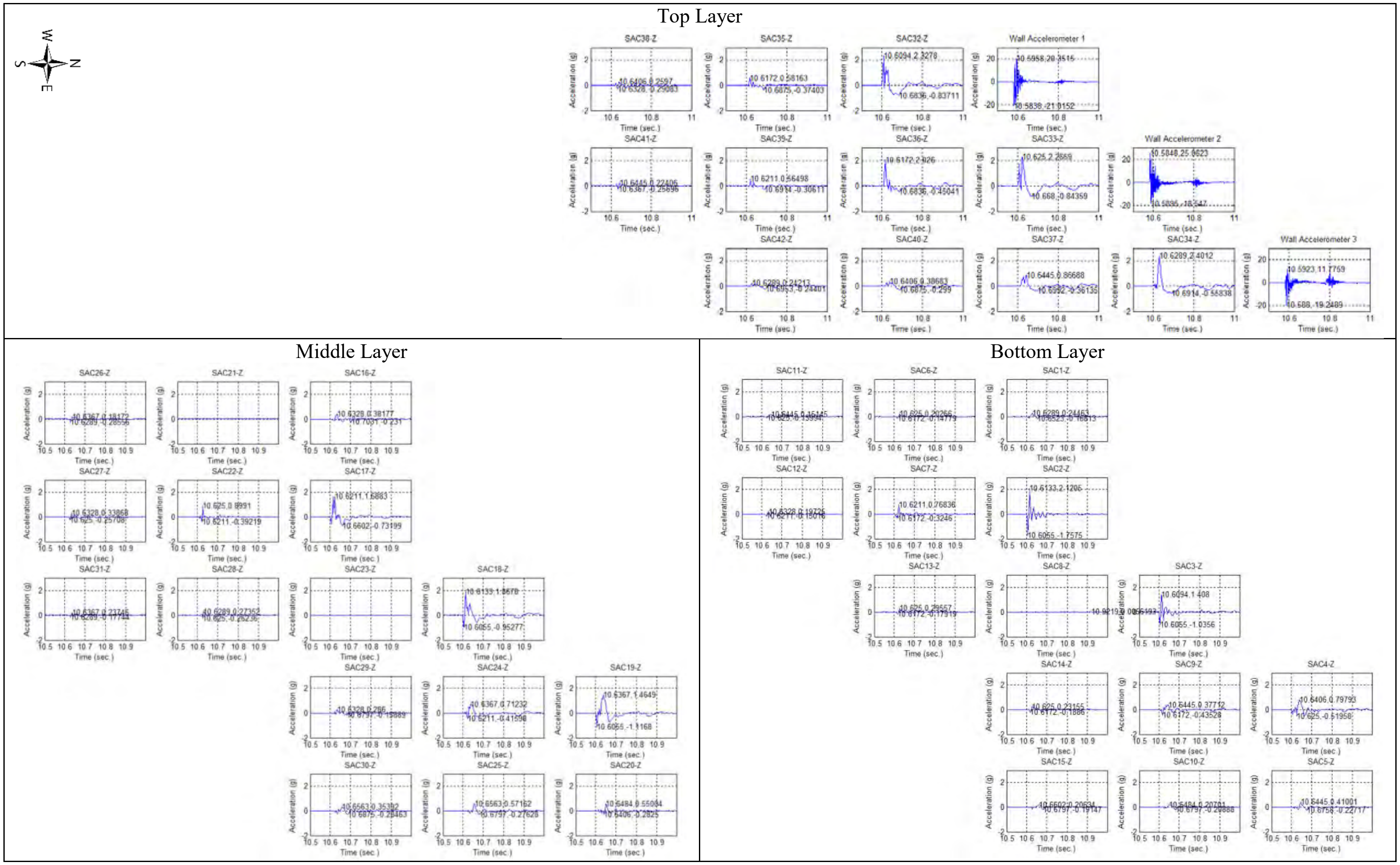

Figure F-38 Vertical acceleration of backfill soil for the 45° skew test in Run 4.

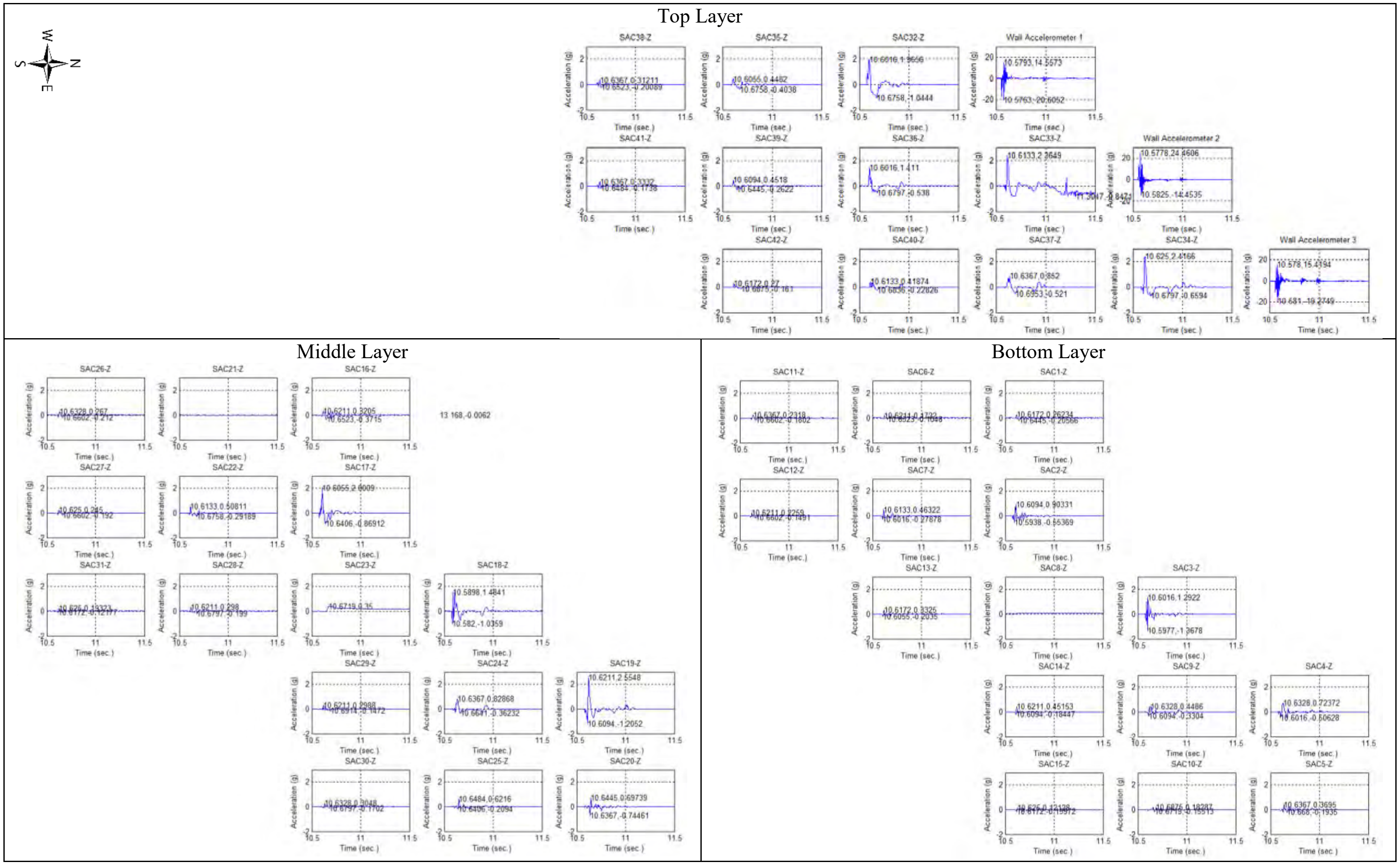

Figure F-39 Vertical acceleration of backfill soil for the 45° skew test in Run 5.

APPENDIX G. Estimation of Maximum Soil Pressure Distribution and Passive Force Histories

Estimation of the maximum soil pressure distribution and passive force histories are presented in this appendix based on the data measured by the earth pressure cells.

Figure G-1 to Figure G-12 show the estimated soil pressure distribution along the backwall height based on Approach I, Approach II, Approach III (combination a, b, and d) as described in Chapter 7. The 3D fitted polynomial for the combination b of Approach III are also depicted for the 30° and 45° skew cases.

The estimated passive force histories are shown in Figure G-13 to Figure G-18 based on Approach IV and in Figure G-19 to Figure G-24 based on Approach V. Interpretation of these data is available in Section 7.3 of Chapter 7.

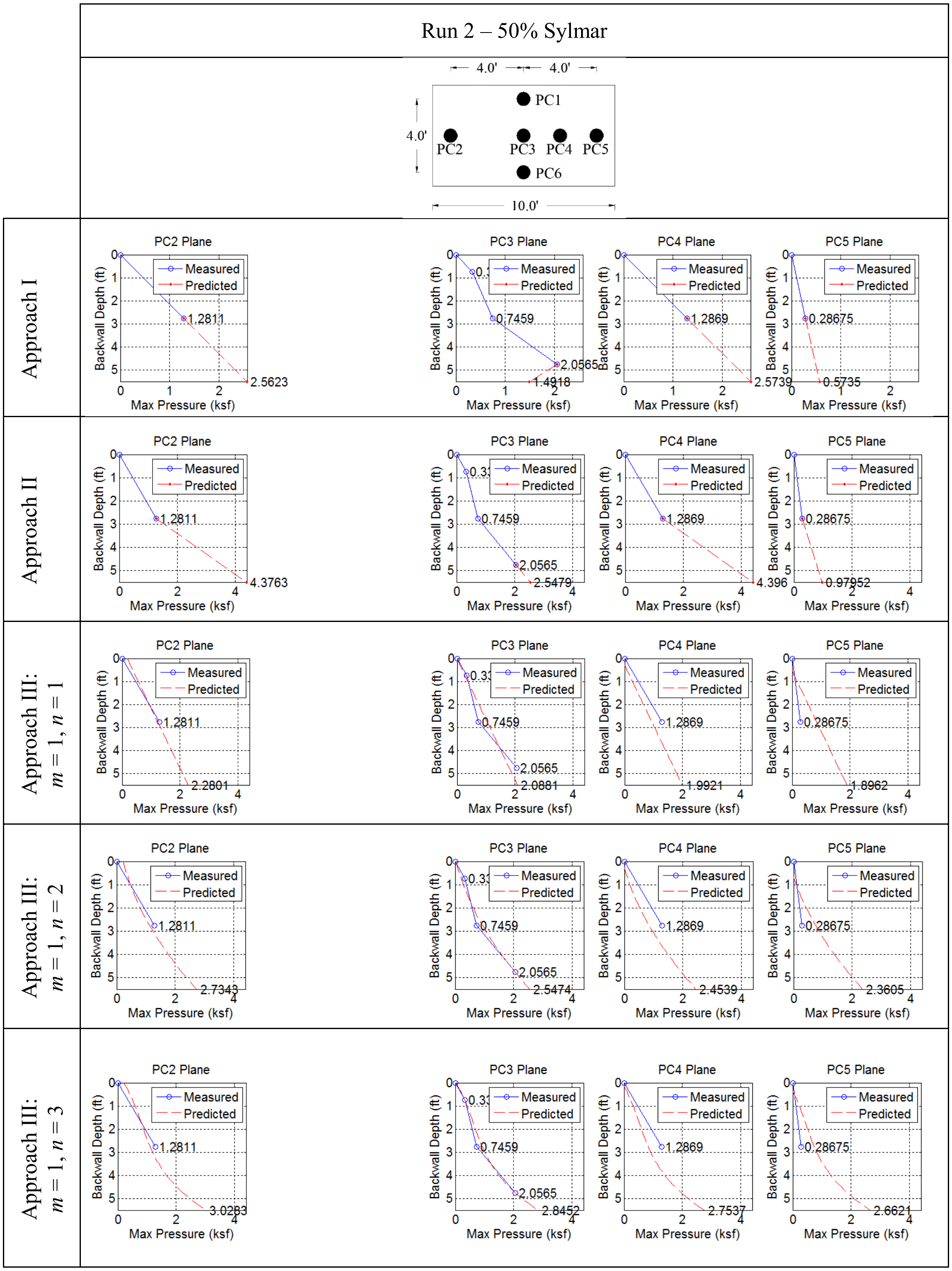

Figure G-1 The maximum soil pressure distribution for the 0° skew test in Run 2.

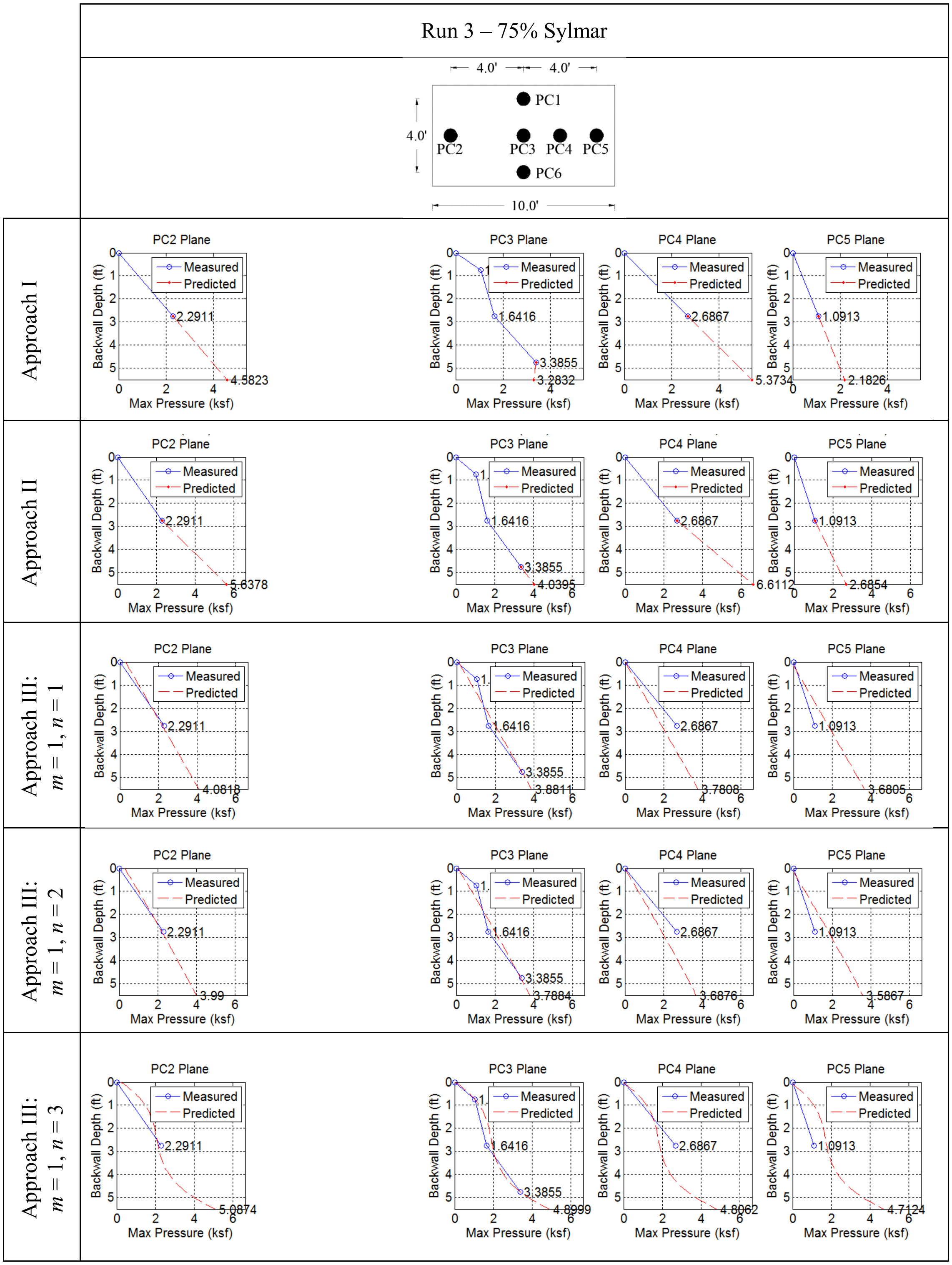

Figure G-2 The maximum soil pressure distribution for the 0° skew test in Run 3.

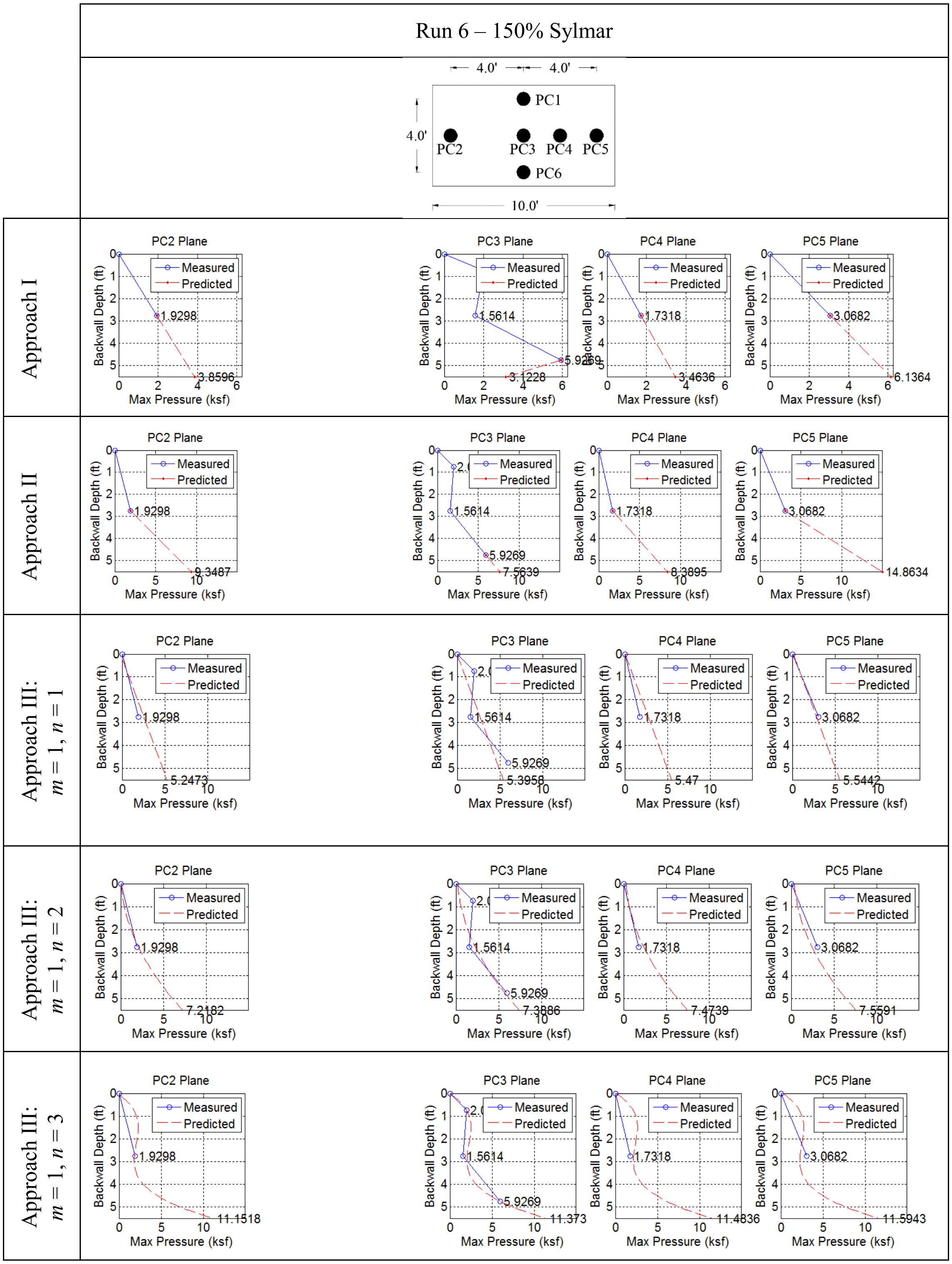

Figure G-3 The maximum soil pressure distribution for the 0° skew test in Run 6.

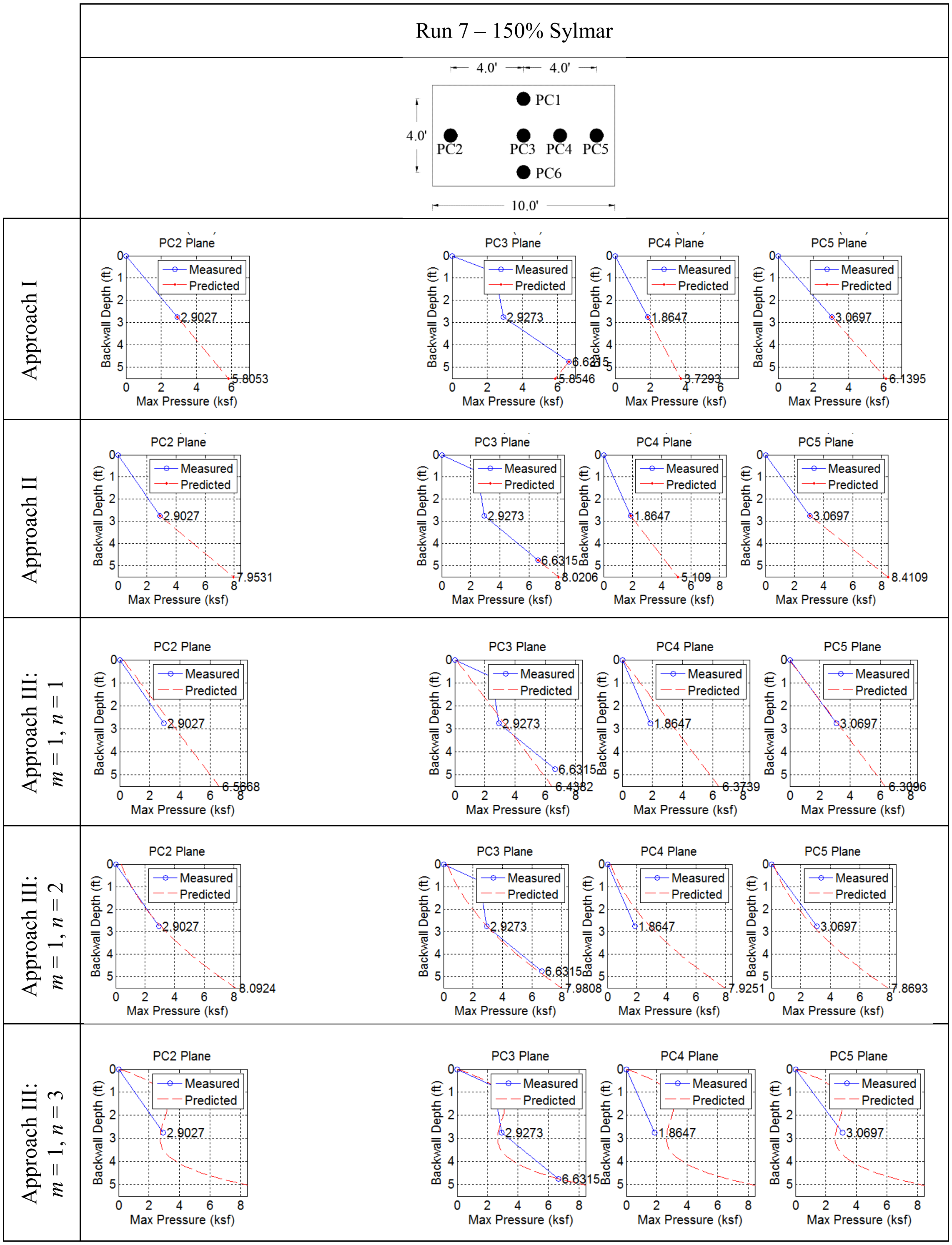

Figure G-4 The maximum soil pressure distribution for the 0° skew test in Run 7.

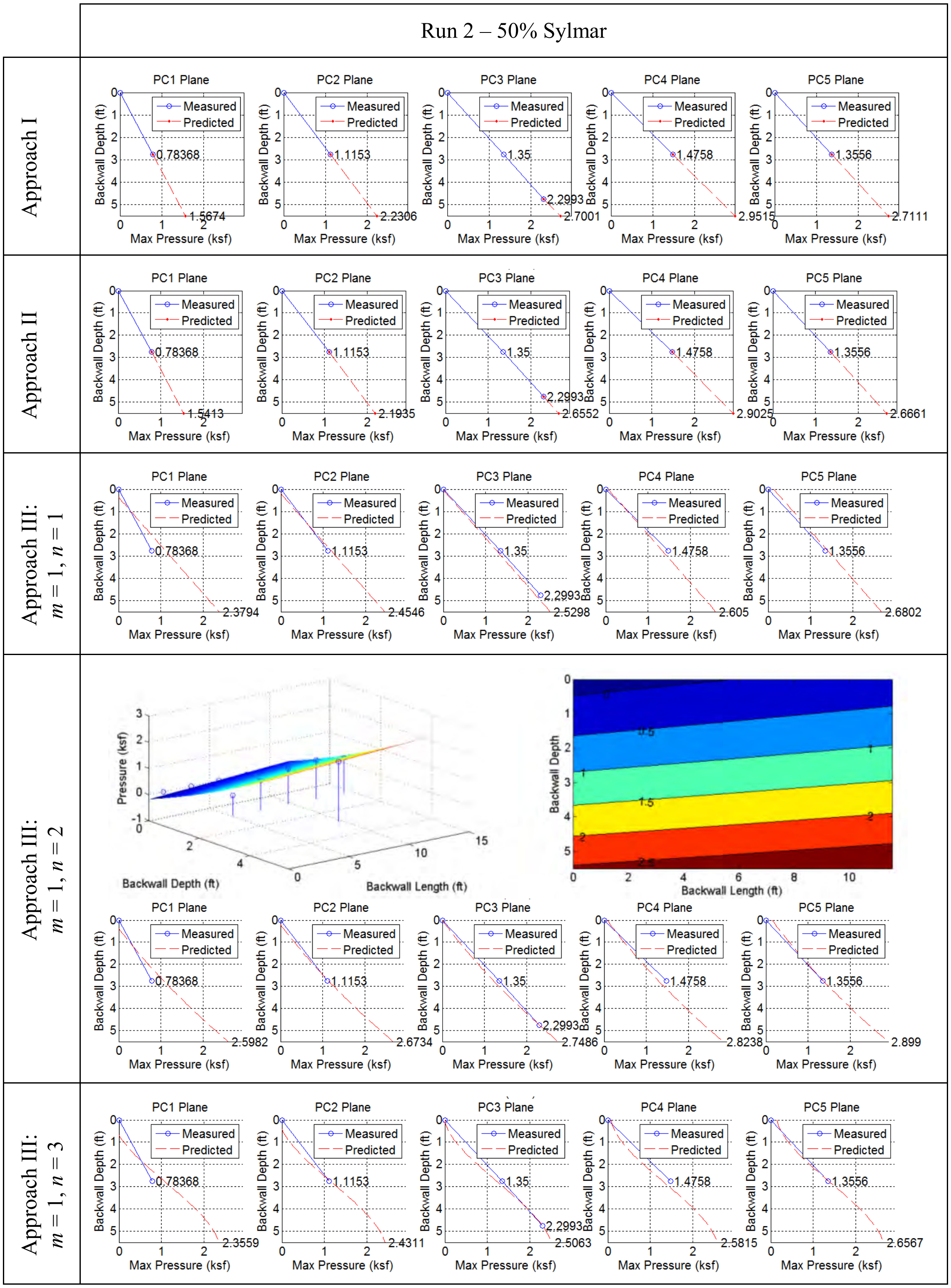

Figure G-5 The maximum soil pressure distribution for the 30° skew test in Run 2.

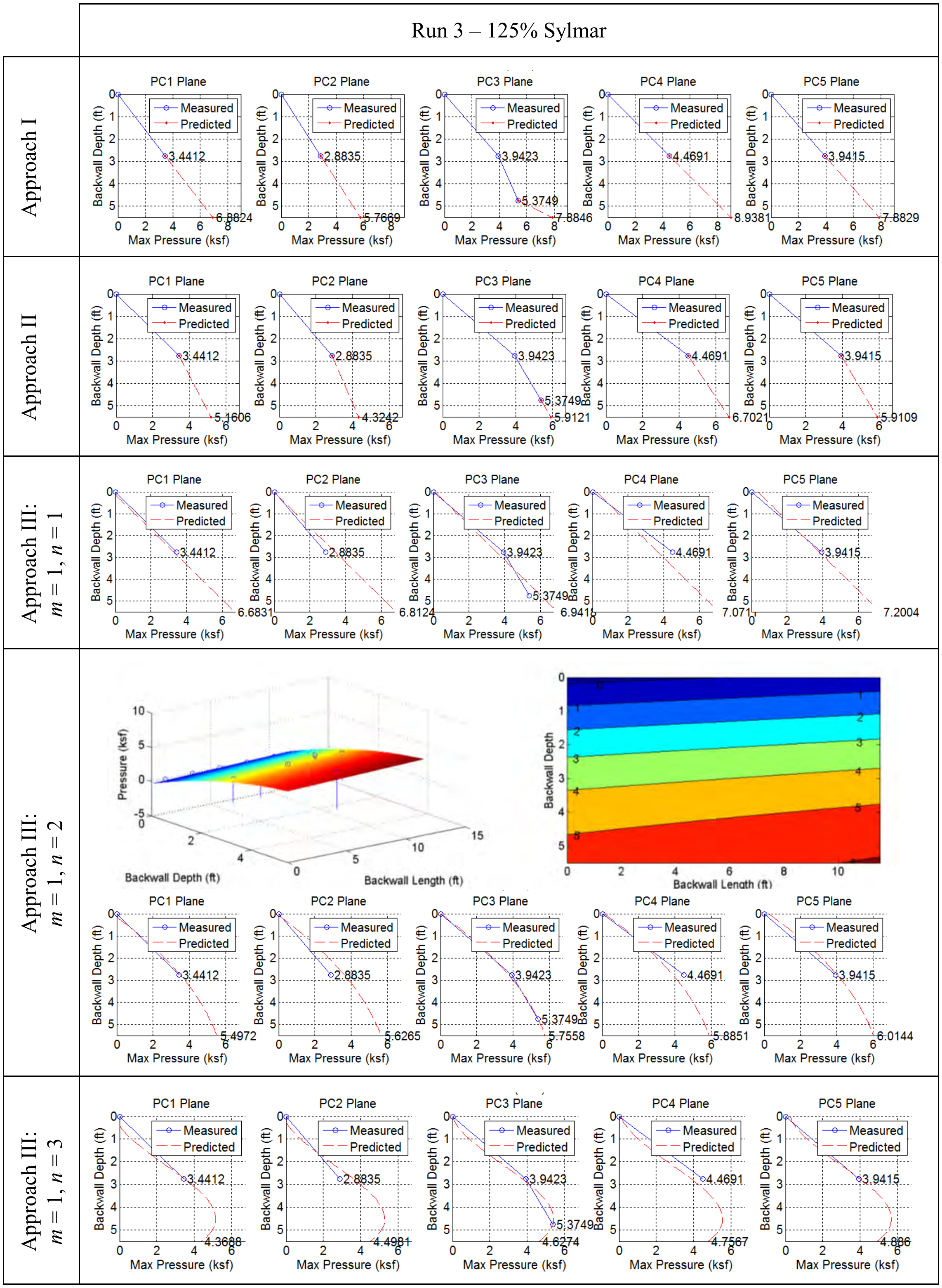

Figure G-6 The maximum soil pressure distribution for the 30° skew test in Run 3.

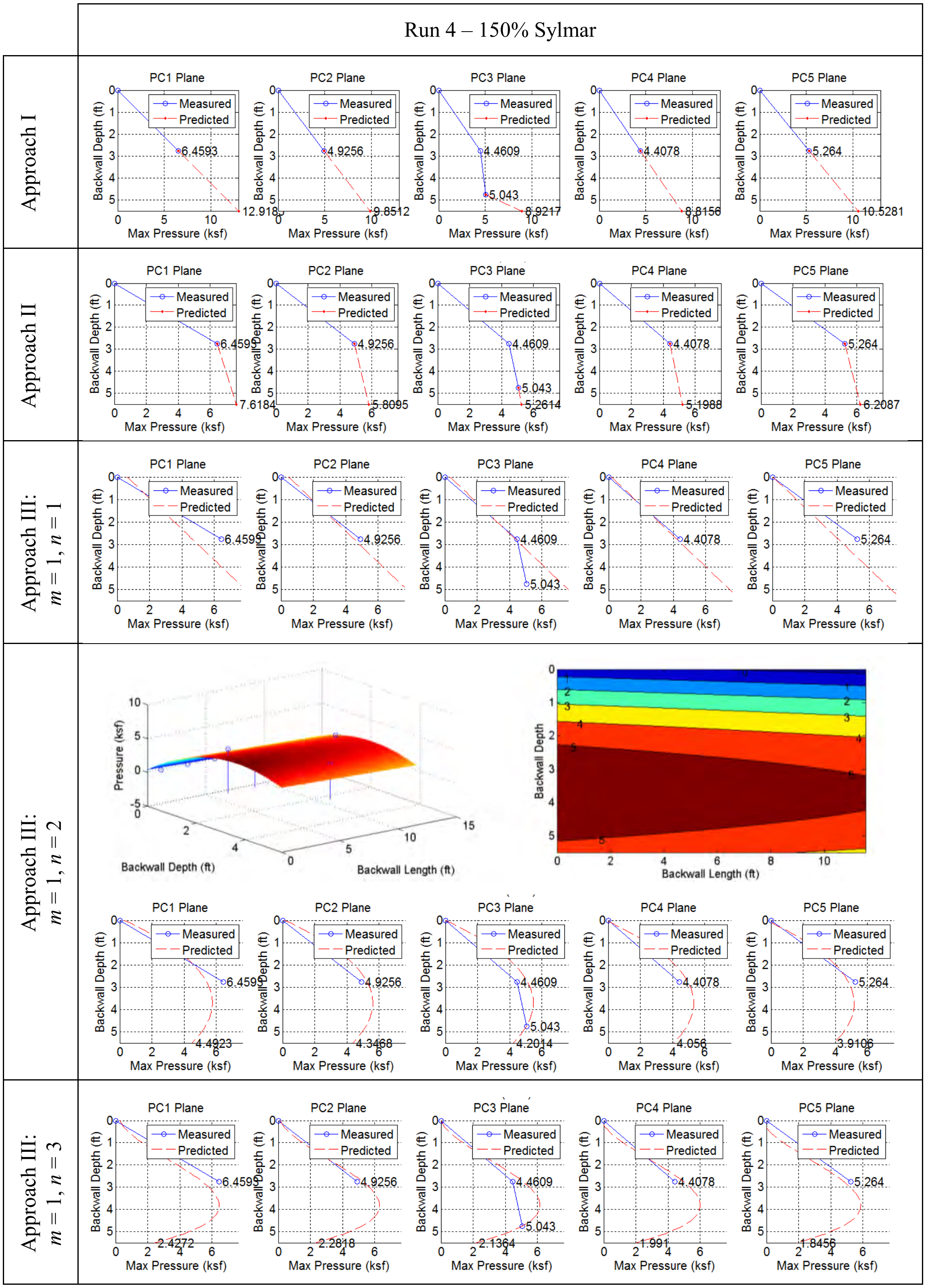

Figure G-7 The maximum soil pressure distribution for the 30° skew test in Run 4.

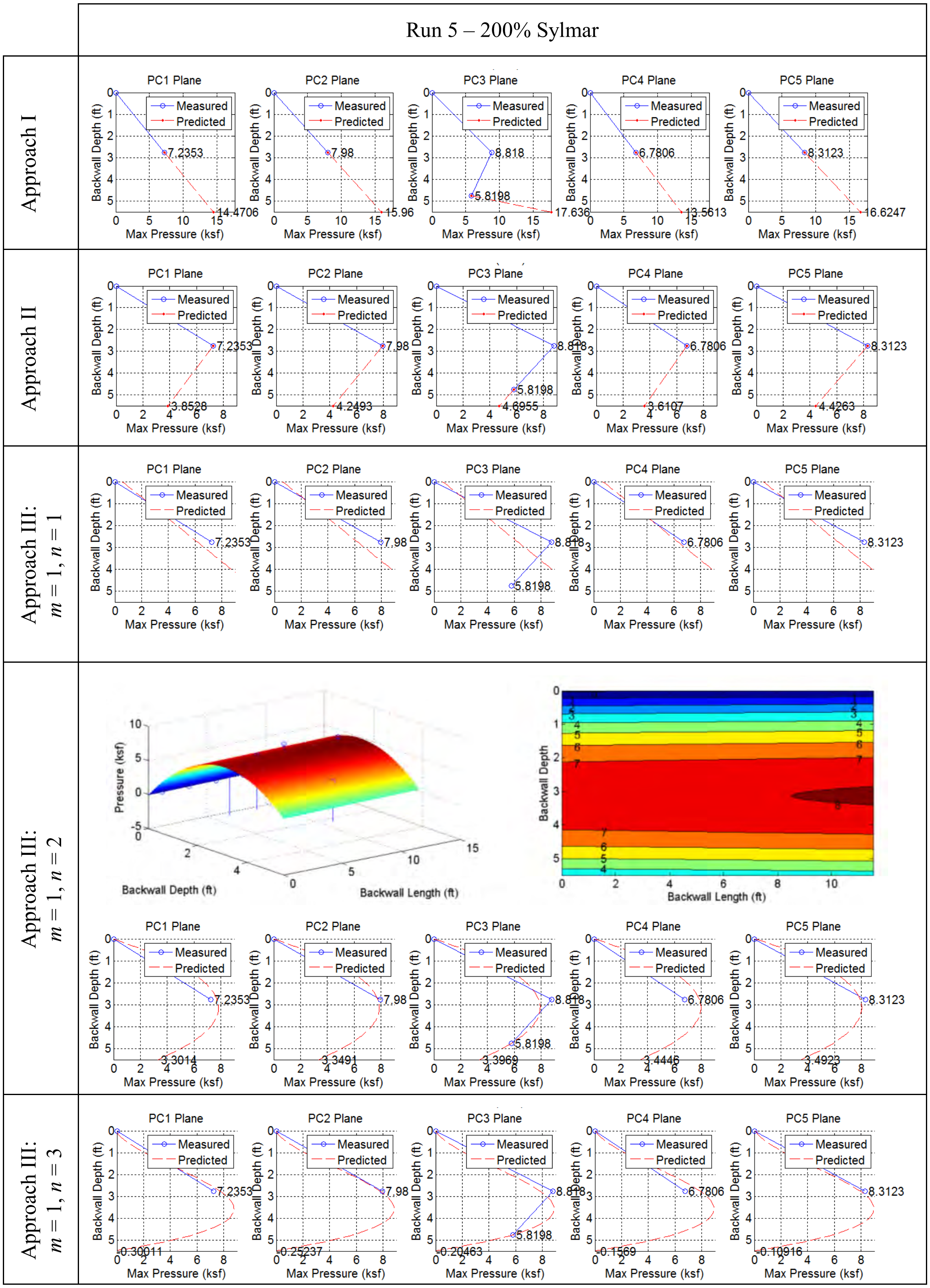

Figure G-8 The maximum soil pressure distribution for the 30° skew test in Run 5.

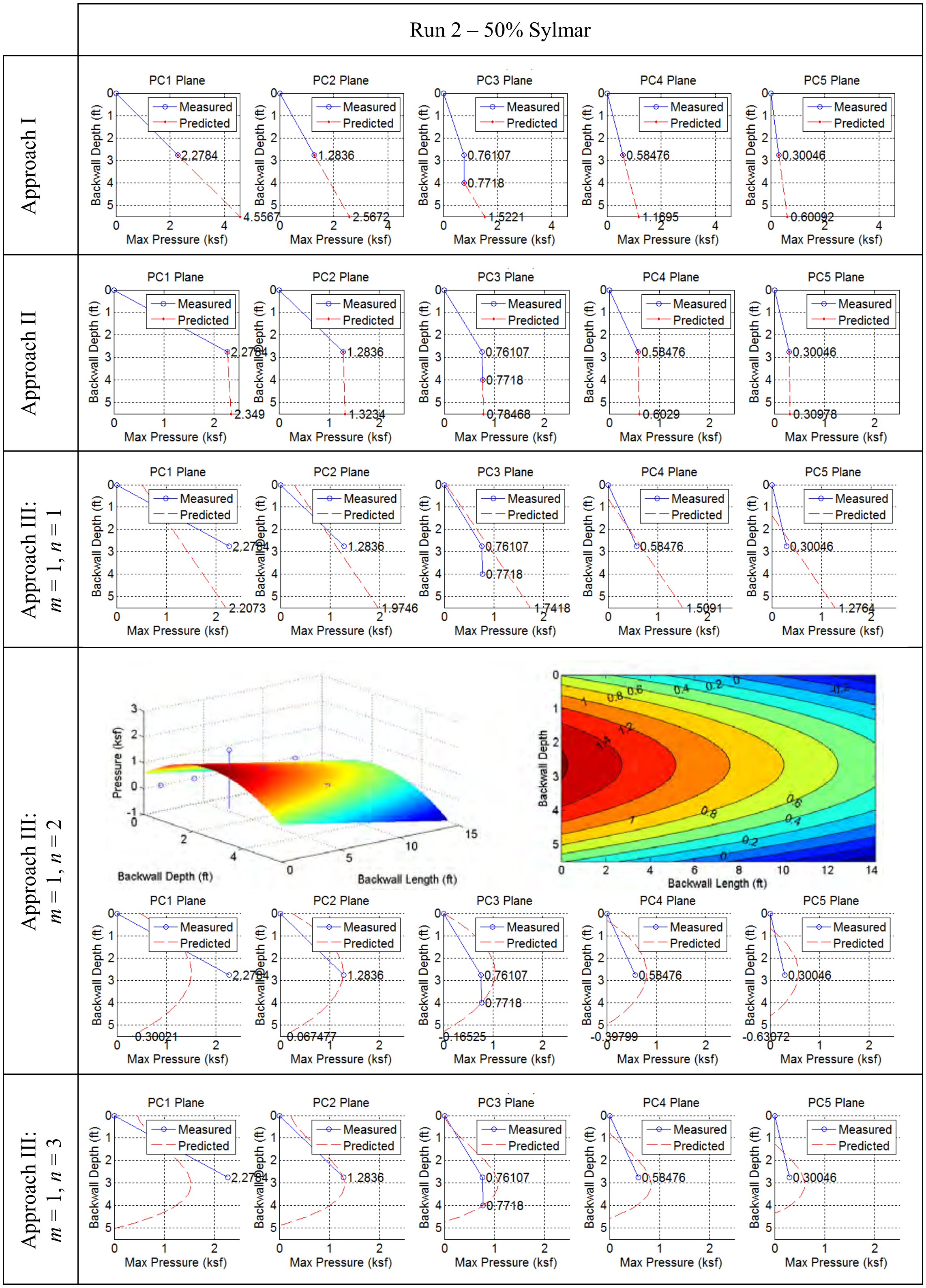

Figure G-9 The maximum soil pressure distribution for the 45° skew test in Run 2.

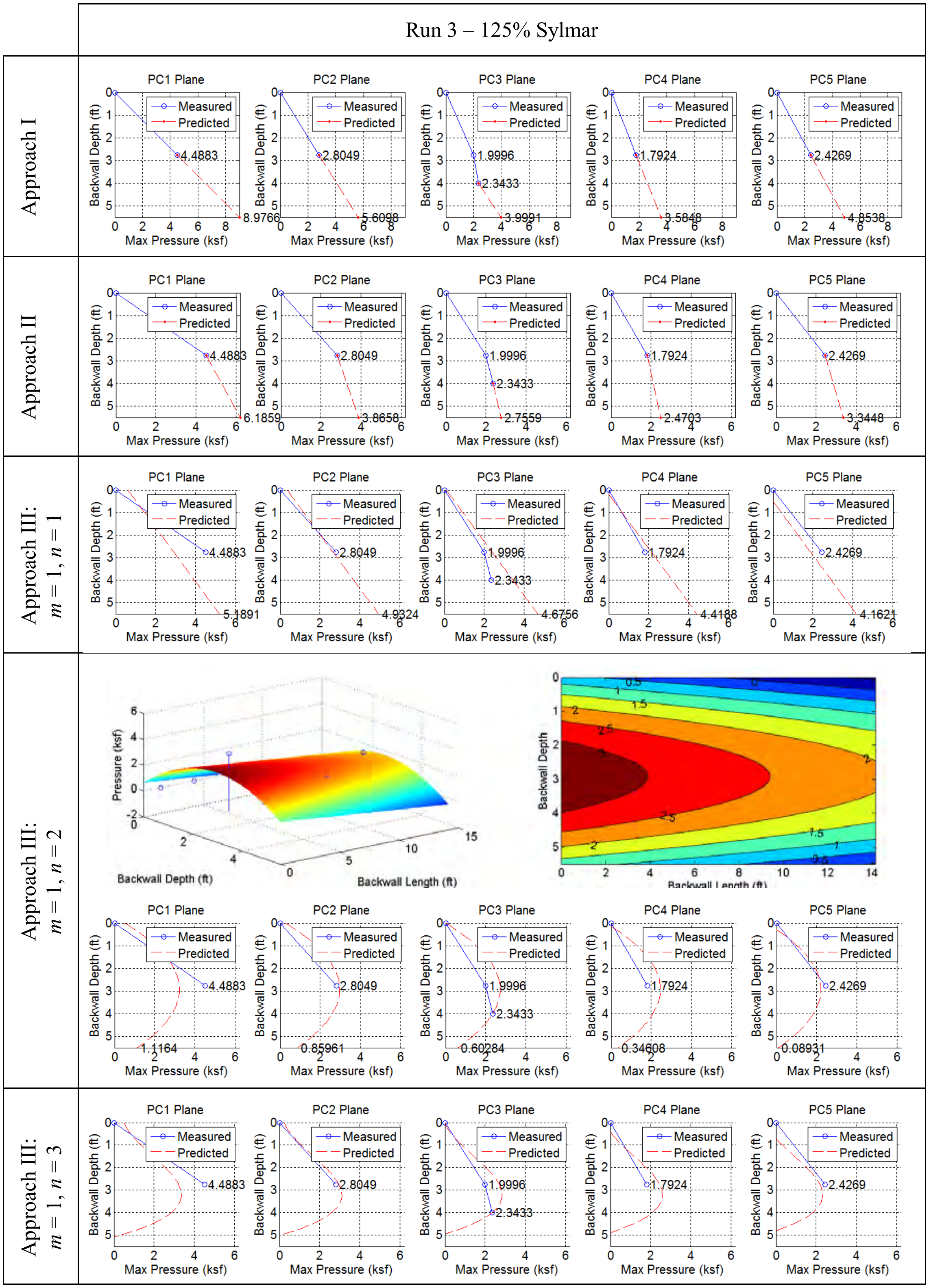

Figure G-10 The maximum soil pressure distribution the 45° skew test in Run 3.

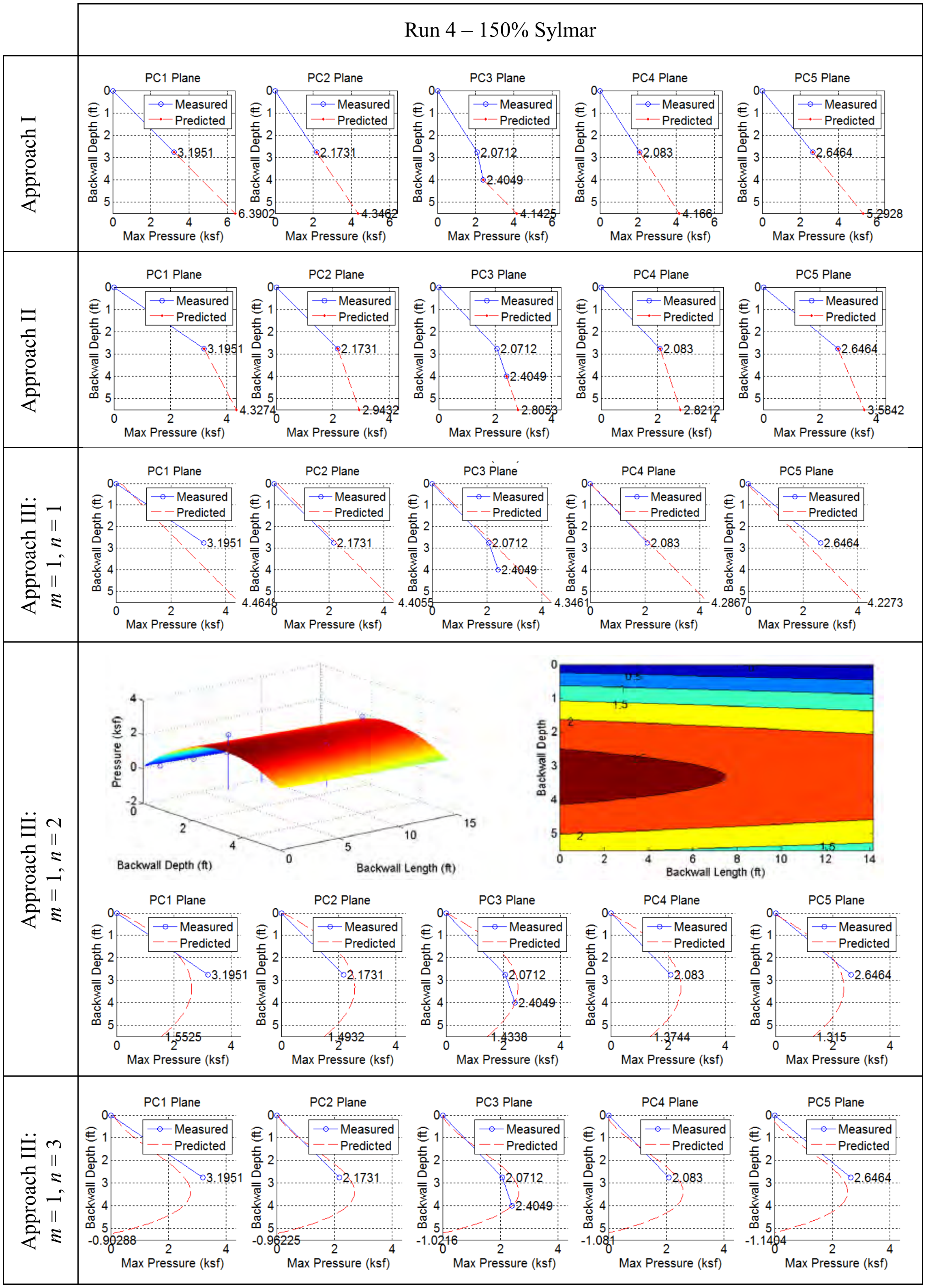

Figure G-11 The maximum soil pressure distribution for the 45° skew test in Run 4.

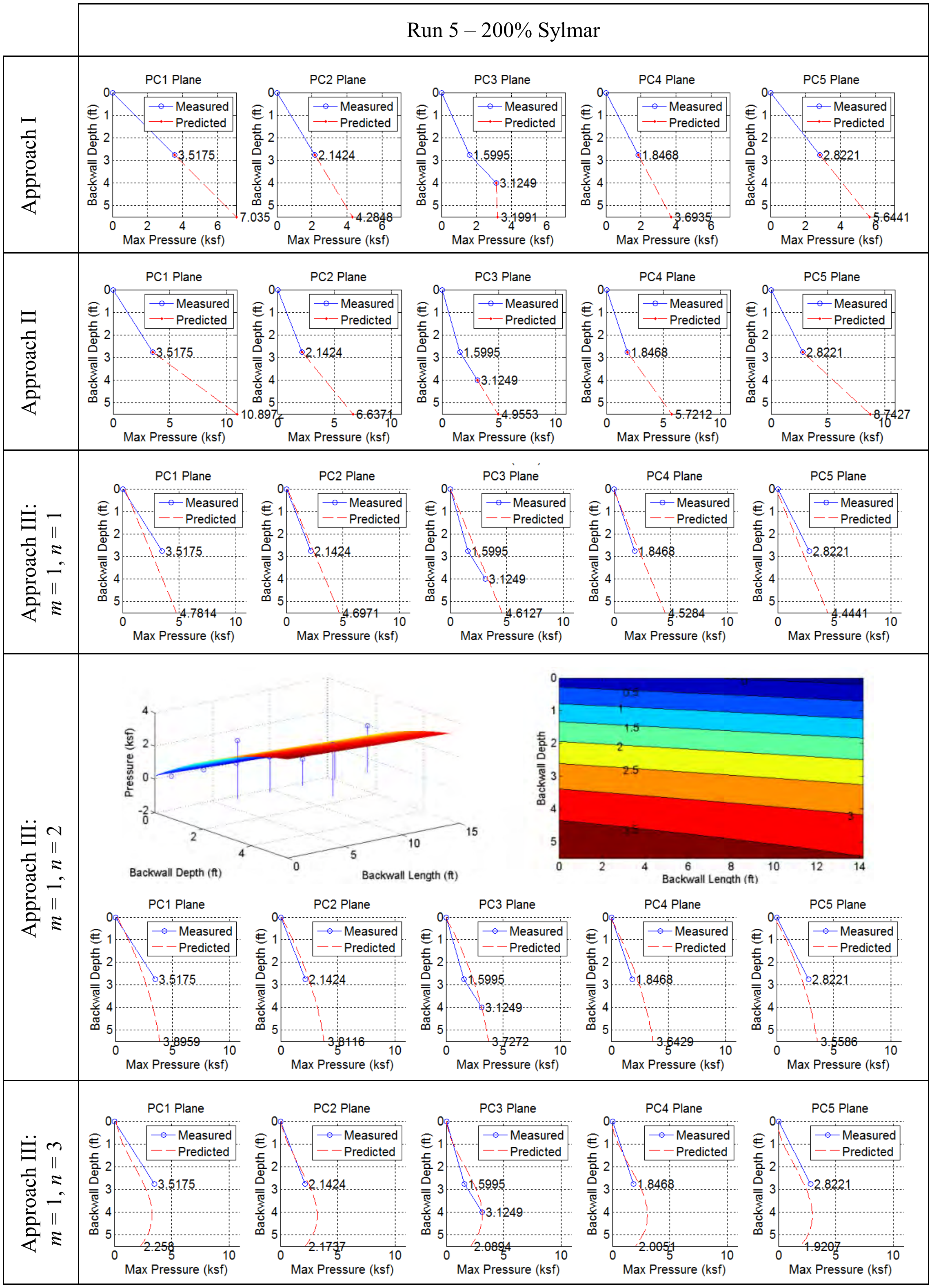

Figure G-12 The maximum soil pressure distribution for the 45° skew test in Run 5.

Run 2 – 50% Sylmar

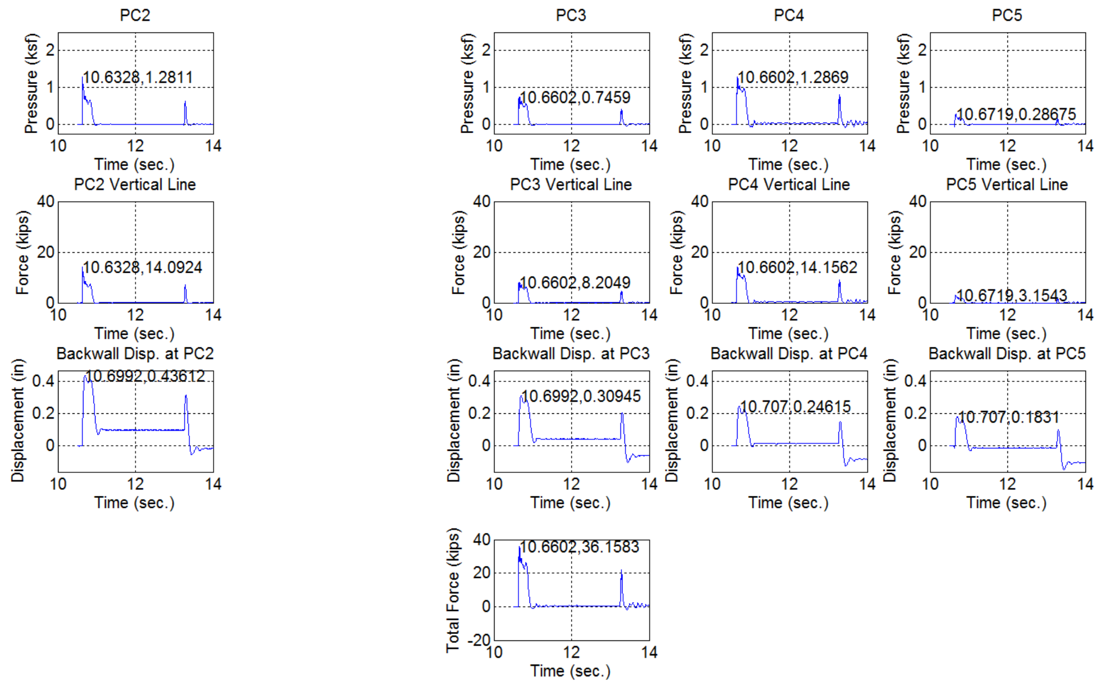

Run 3 – 75% Sylmar

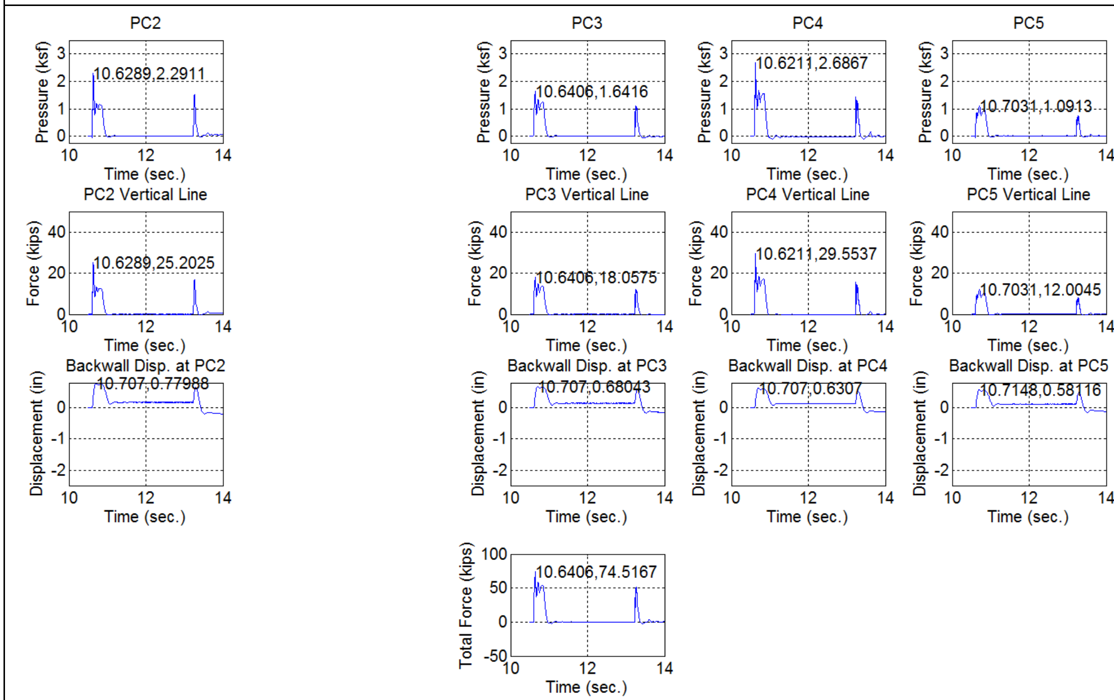

Figure G-13 Passive force histories based on approach IV for the 0° skew test in Run 2 and 3.

Run 6 – 150% Sylmar

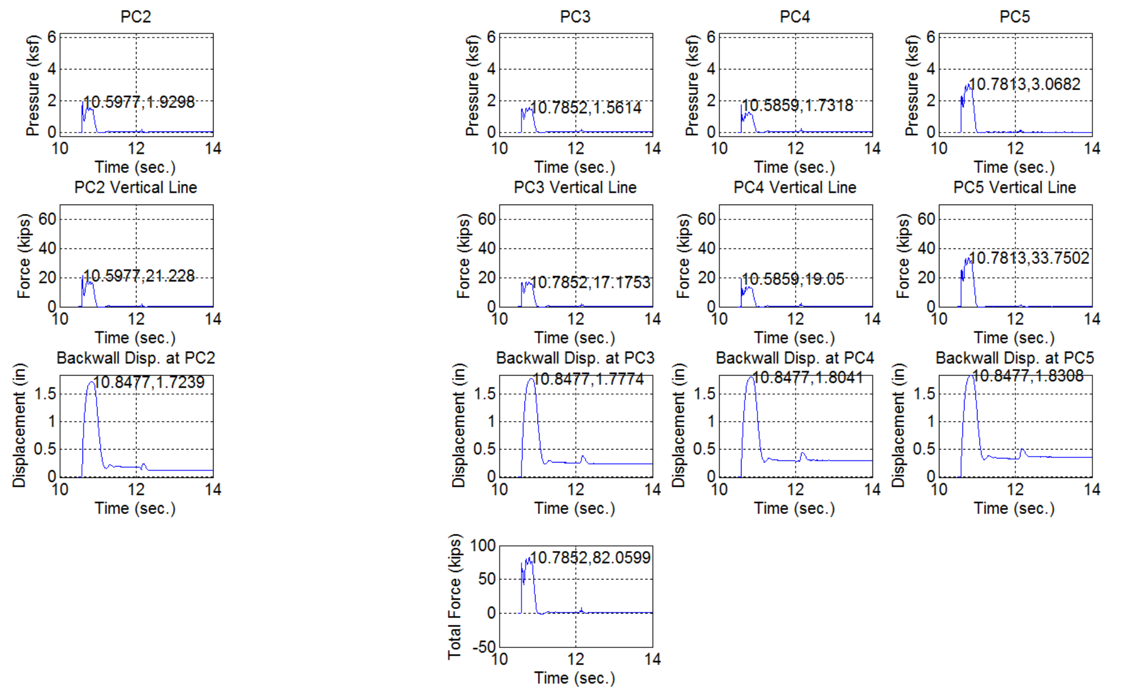

Run 7 – 150% Sylmar

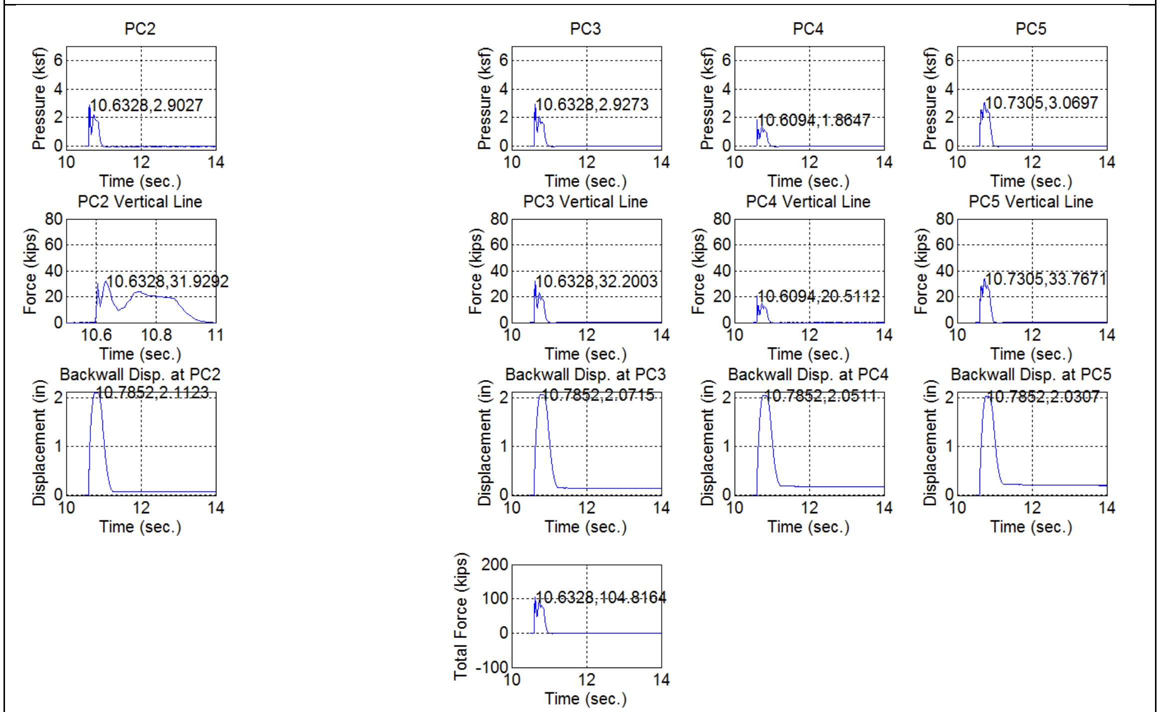

Figure G-14 Passive force histories based on approach IV for the 0° skew test in Run 6 and 7.

Run 2 – 50% Sylmar

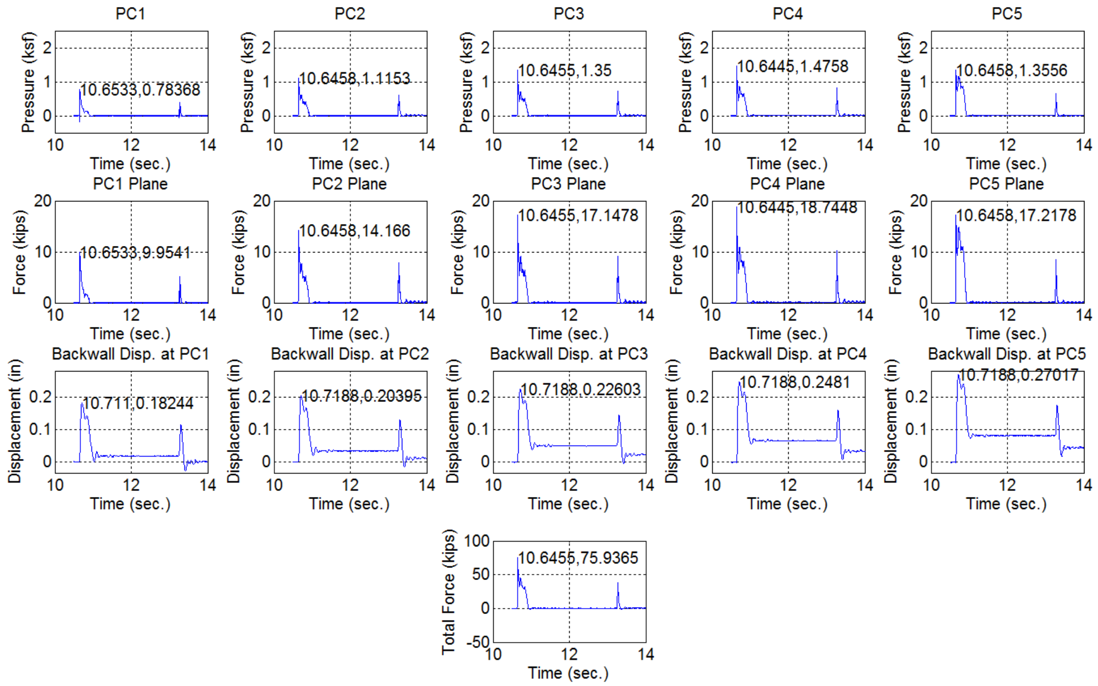

Run 3 – 125% Sylmar

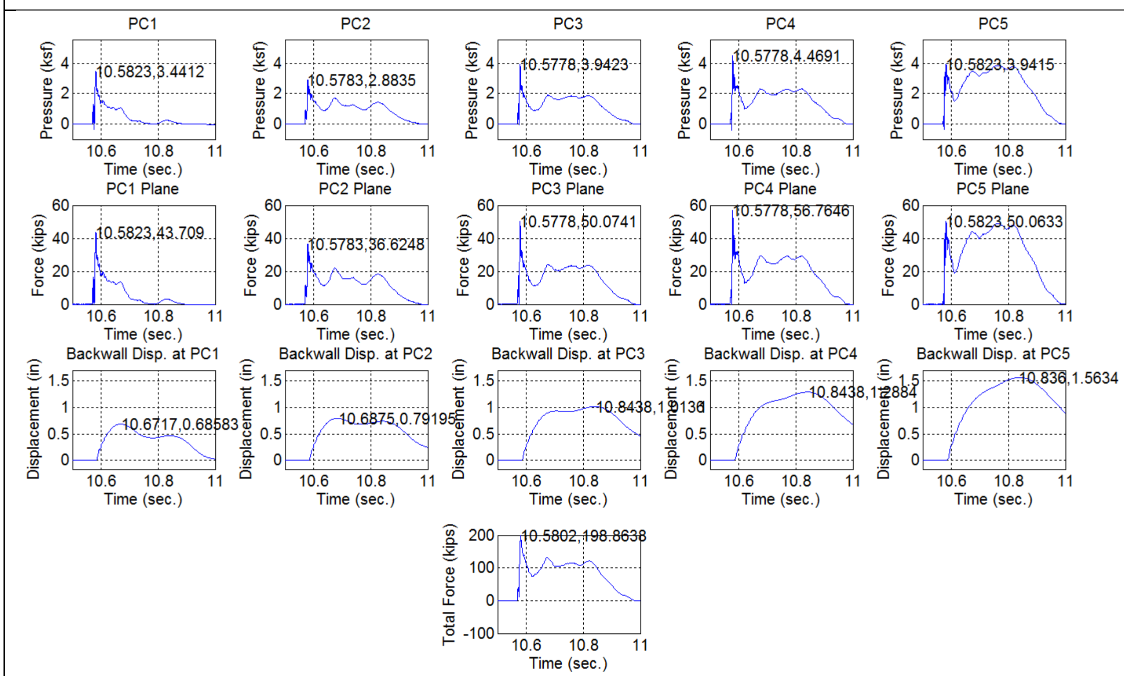

Figure G-15 Passive force histories based on approach IV for the 30° skew test in Run 2 and 3.

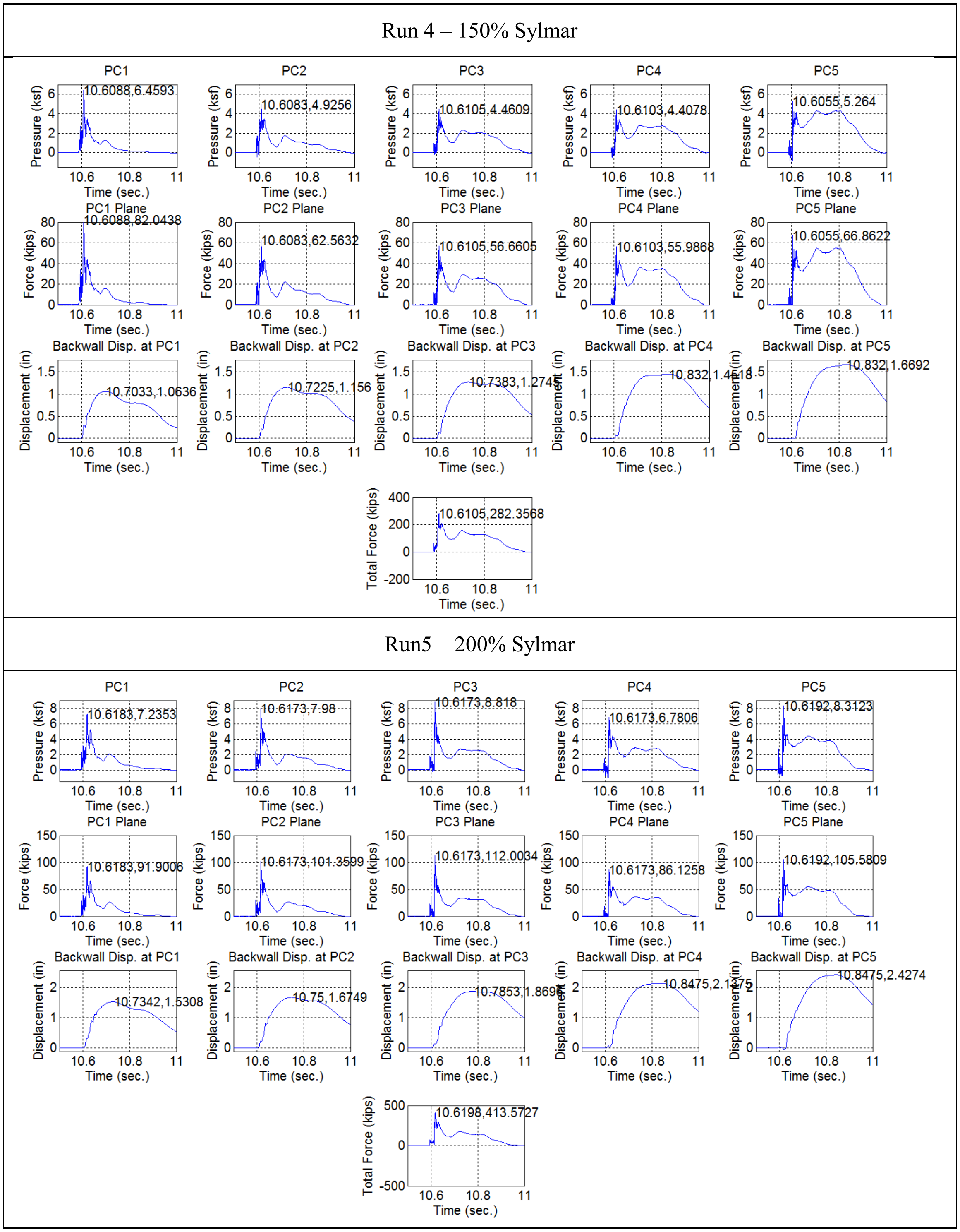

Figure G-16 Passive force histories based on approach IV for the 30° skew test in Run 4 and 5.

Run 2 – 50% Sylmar

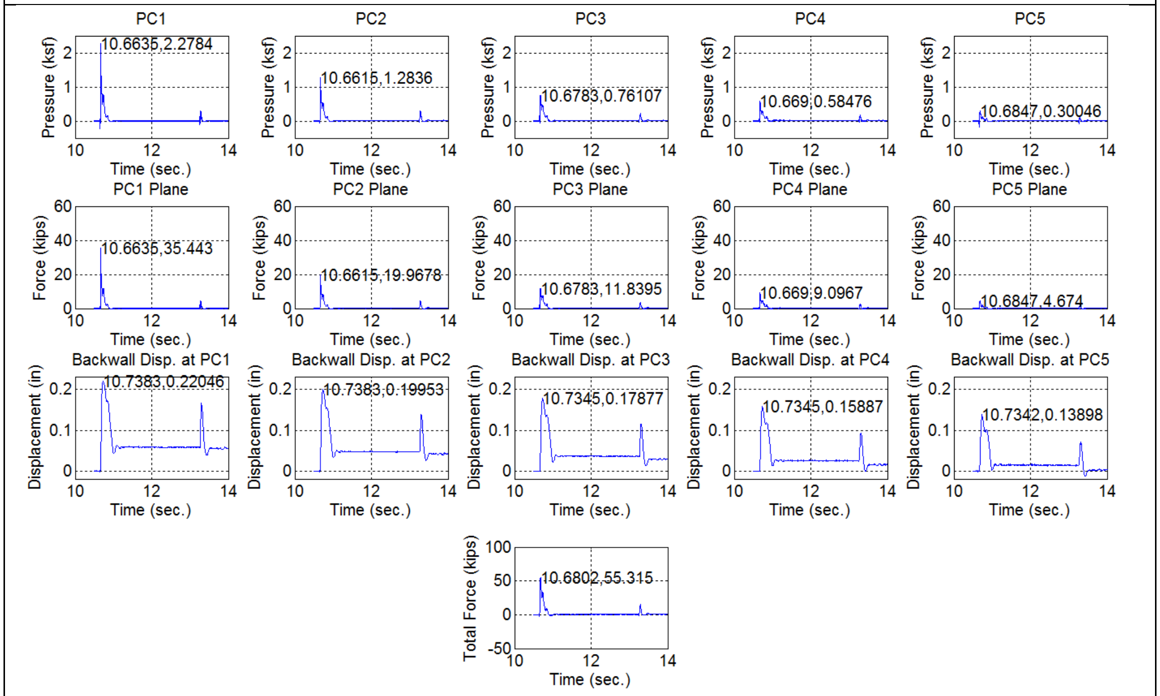

Run 3 – 75% Sylmar

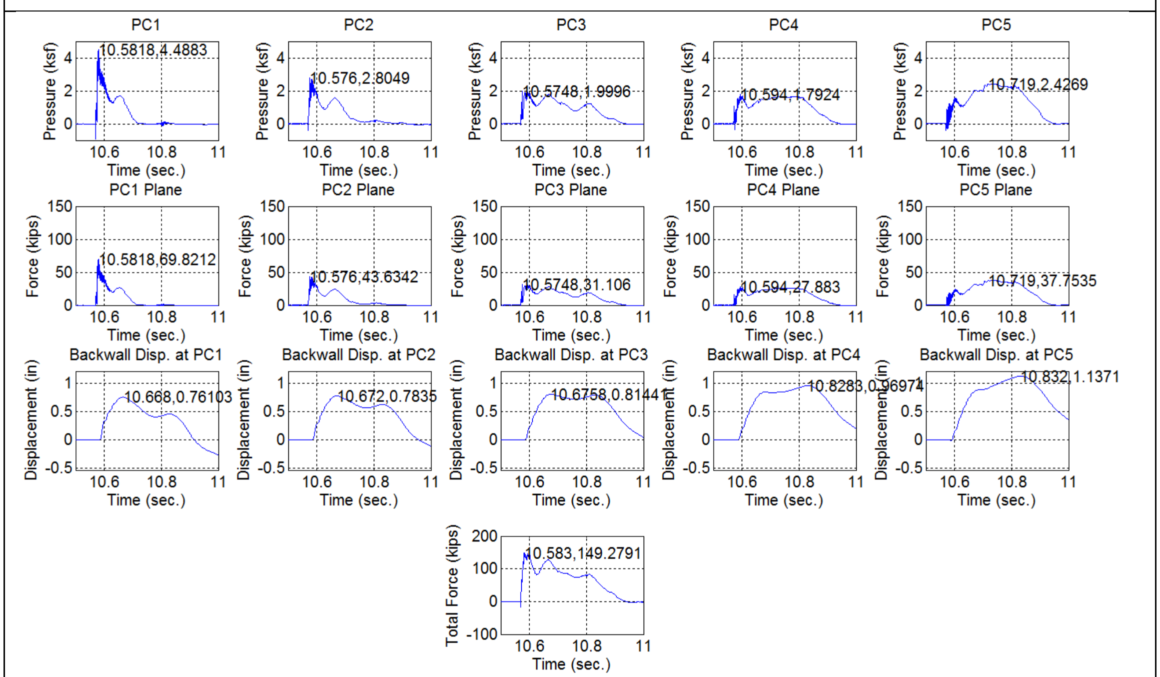

Figure G-17 Passive force histories based on approach IV for the 45° skew test in Run 2 and 3.

Run 4 – 150% Sylmar

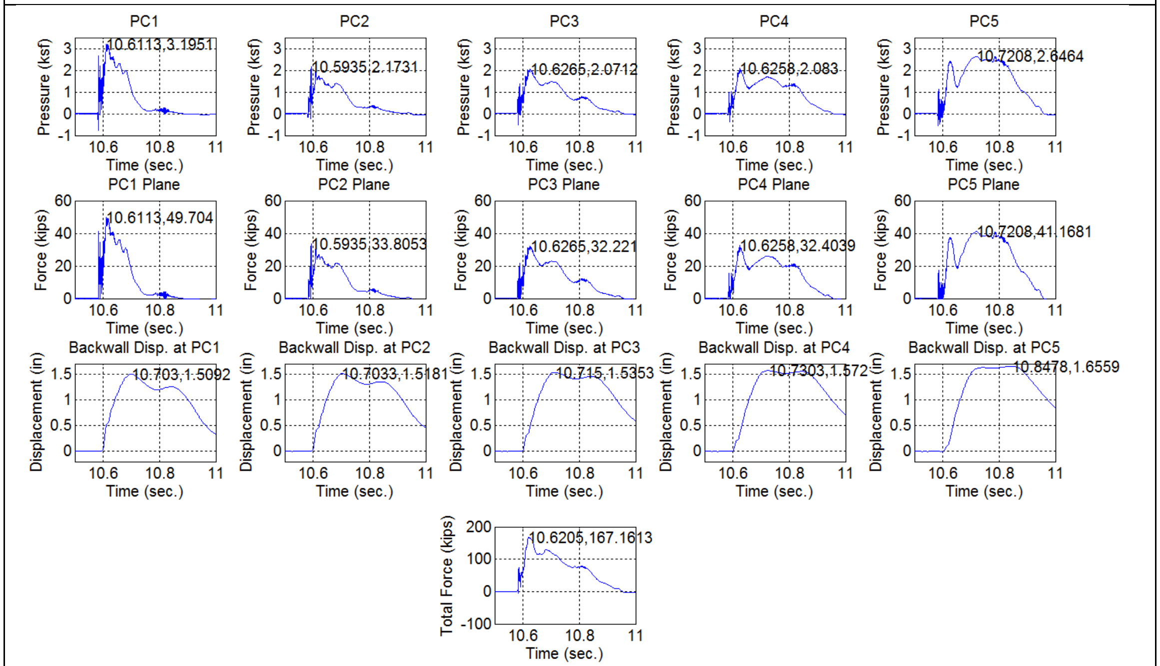

Run5 – 200% Sylmar

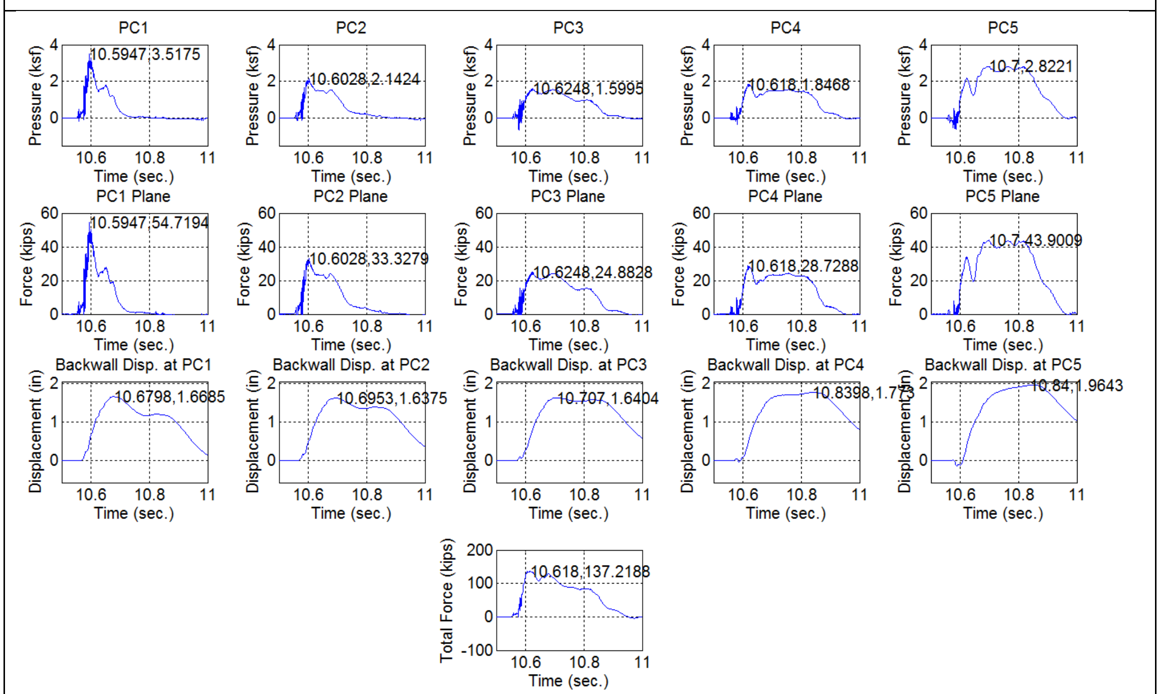

Figure G-18 Passive force histories based on approach IV for the 45° skew test in Run 4 and 5.

Run 2 – 50% Sylmar

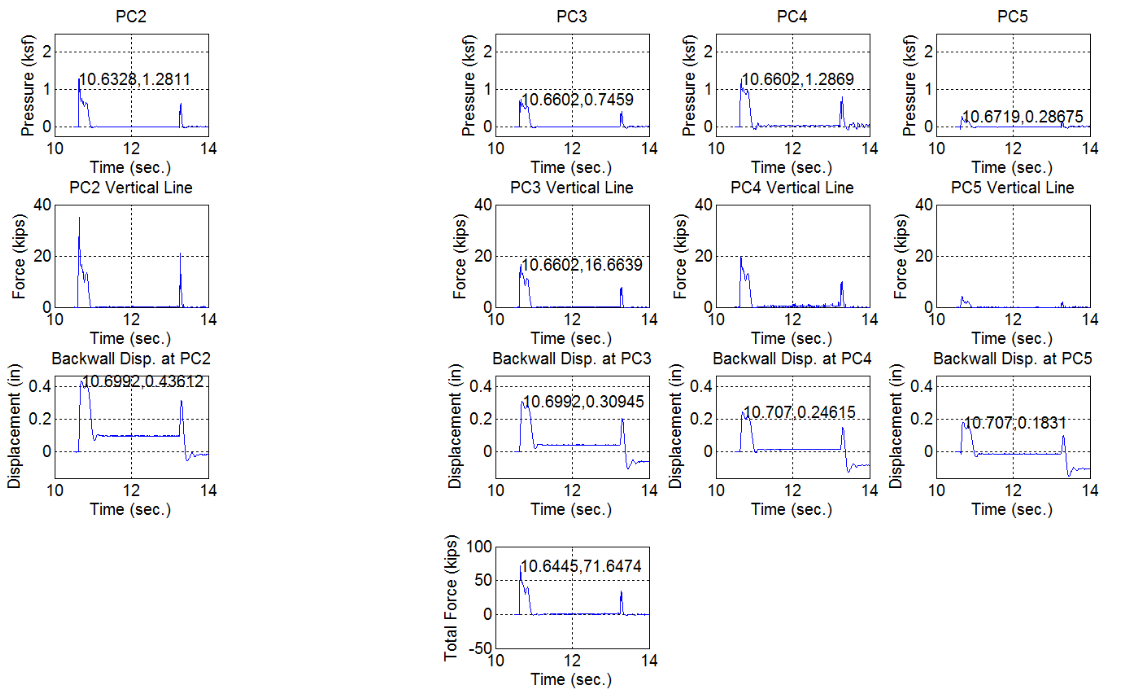

Run 3 – 75% Sylmar

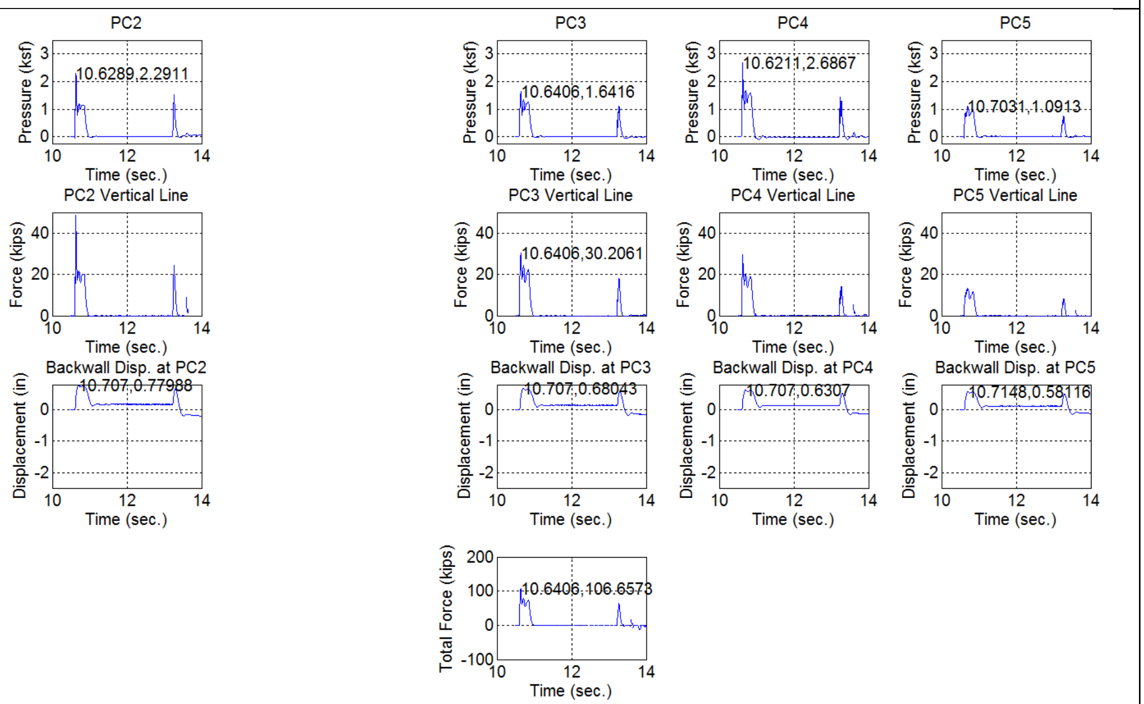

Figure G-19 Passive force histories based on approach V for the 0° skew test in Run 2 and 3.

Run 6 – 150% Sylmar

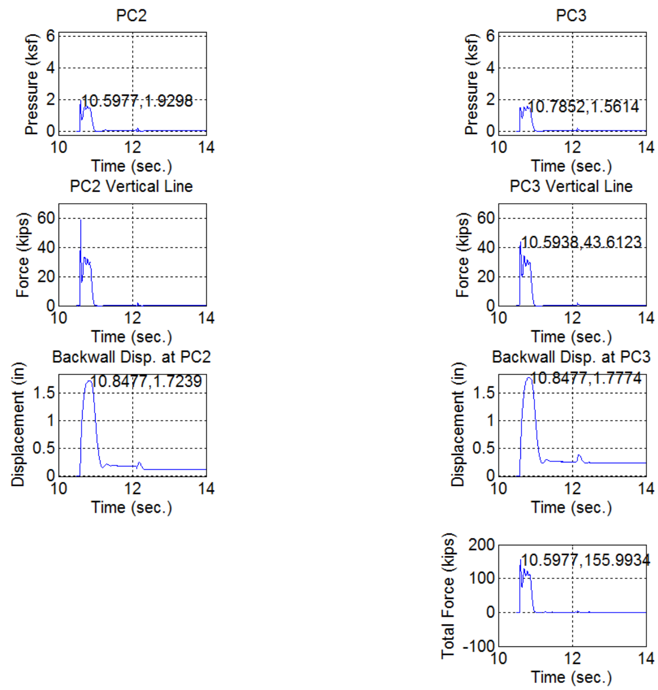

Run 7 – 150% Sylmar

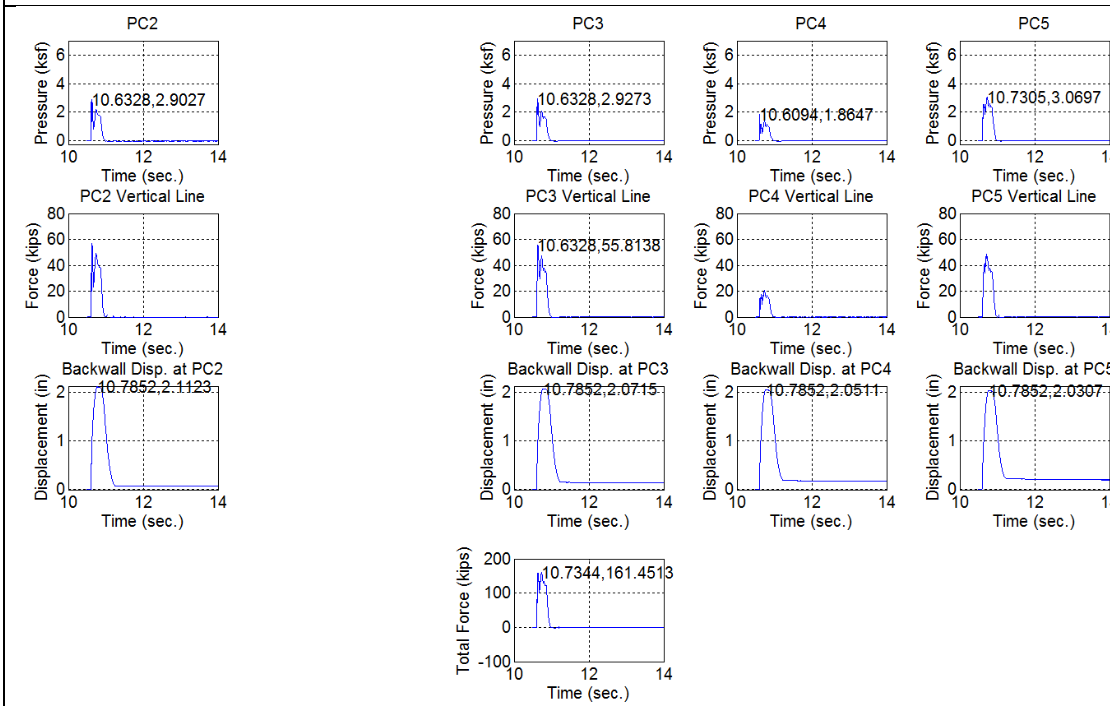

Figure G-20 Passive force histories based on approach V for the 0° skew test in Run 6 and 7.

Run 2 – 50% Sylmar

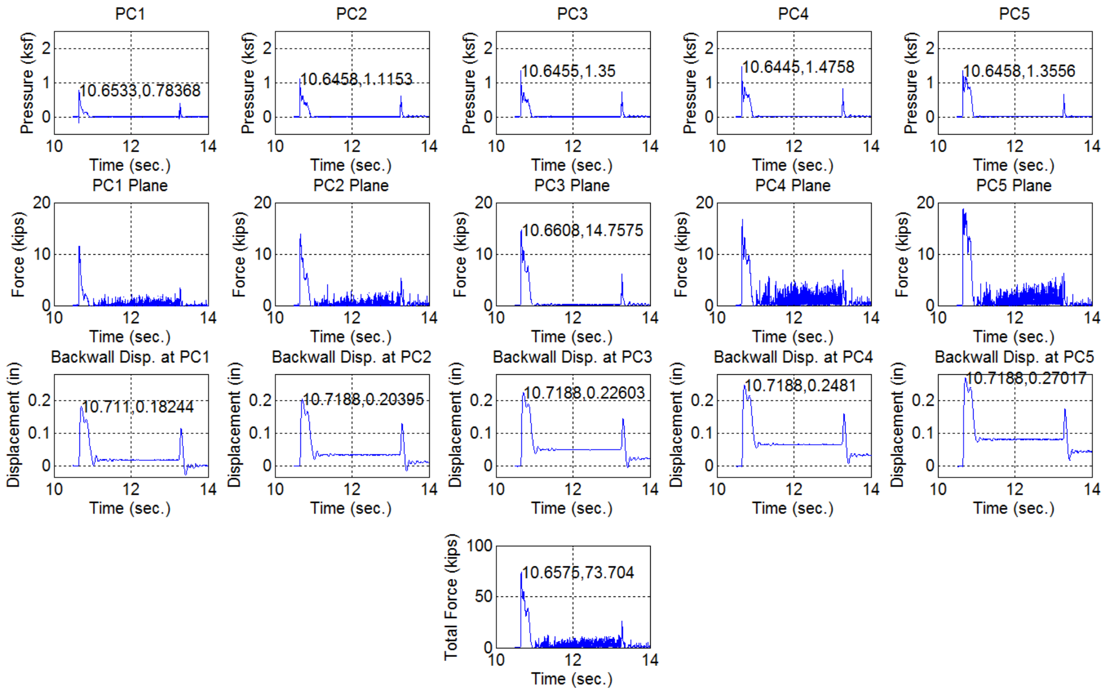

Run 3 – 125% Sylmar

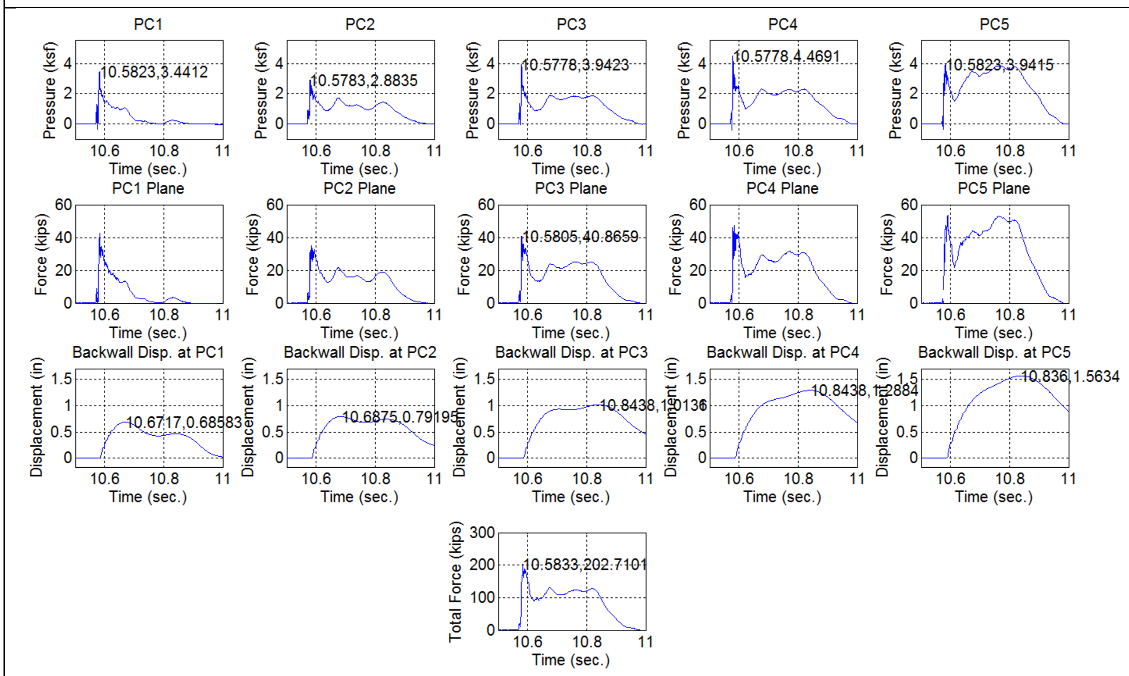

Figure G-21 Passive force histories based on approach V for the 30° skew test in Run 2 and 3.

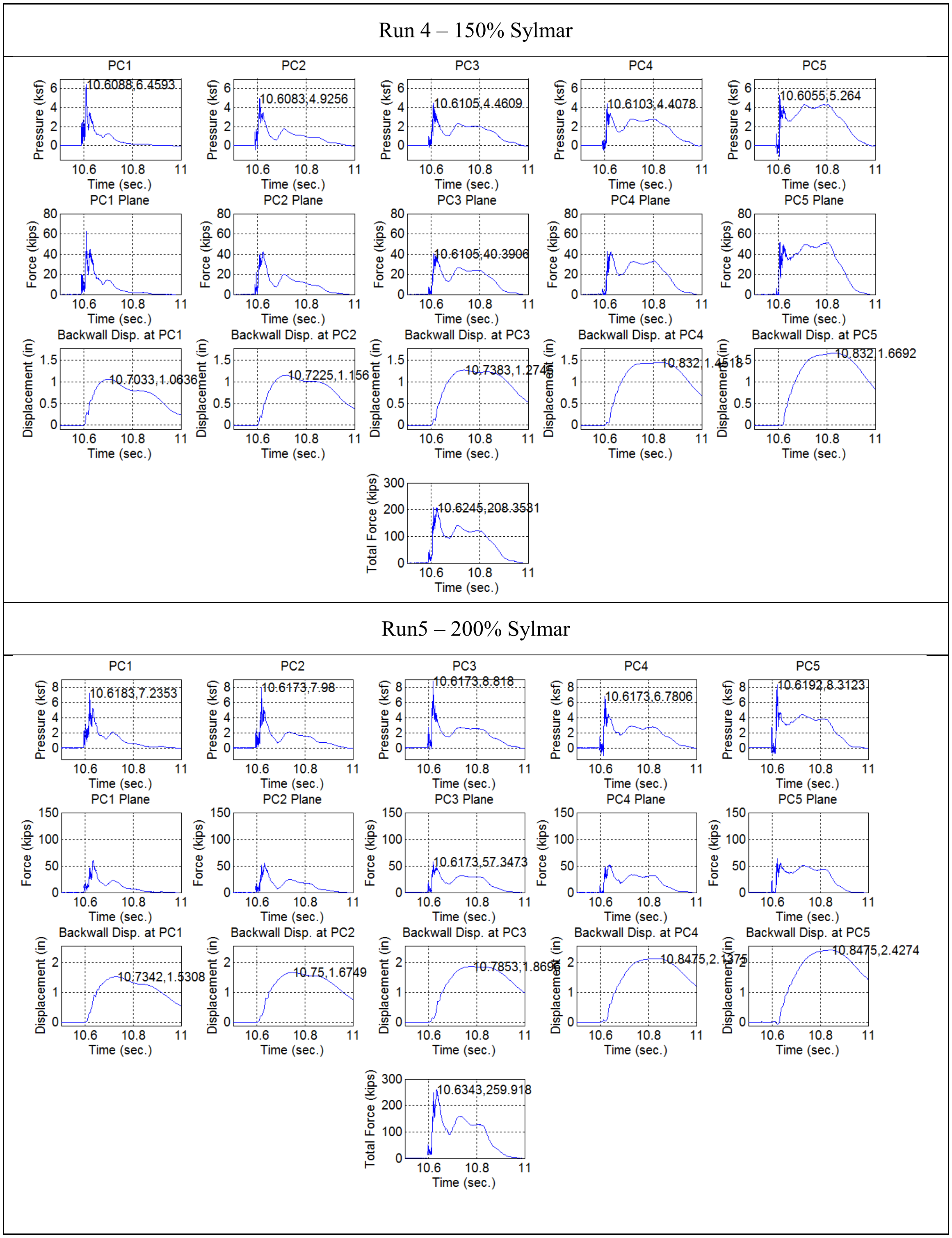

Figure G-22 Passive force histories based on approach V for the 30° skew test in Run 4 and 5.

Run 2 – 50% Sylmar

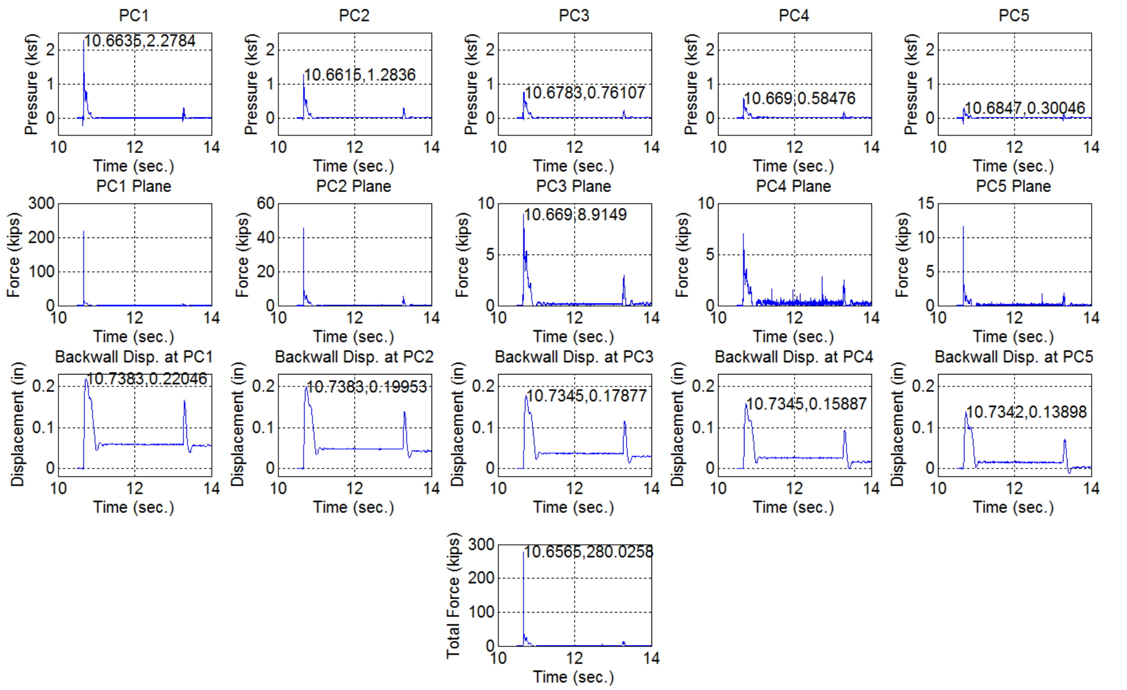

Run 3 – 125% Sylmar

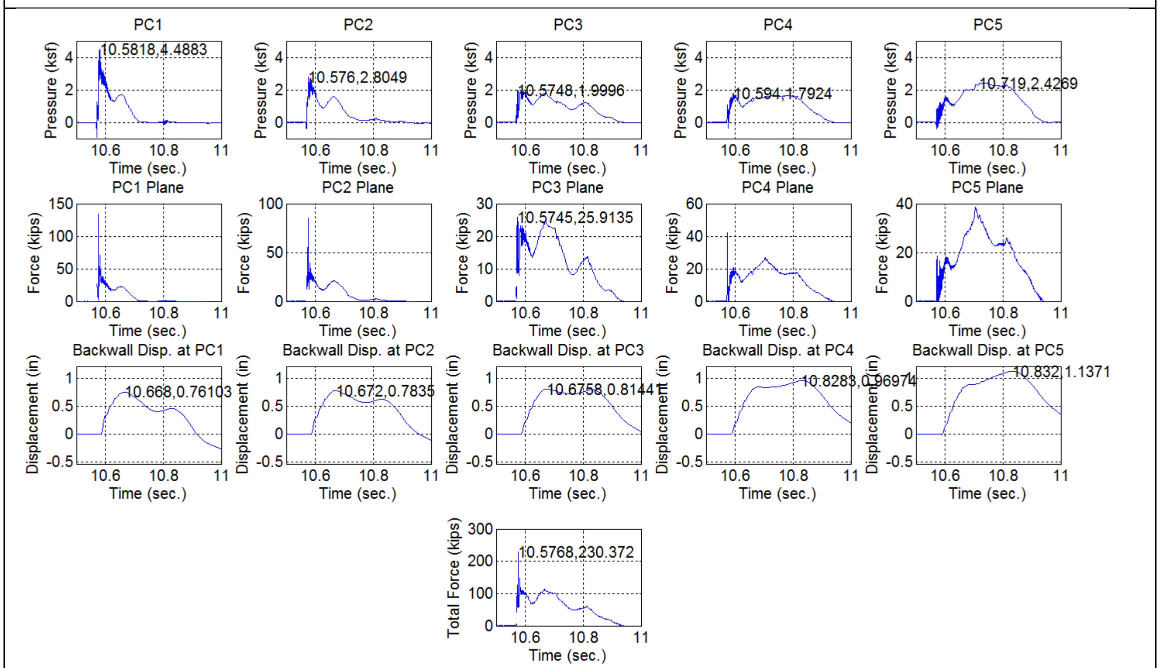

Figure G-23 Passive force histories based on approach V for the 45° skew test in Run 2 and 3.

Run 4 – 150% Sylmar

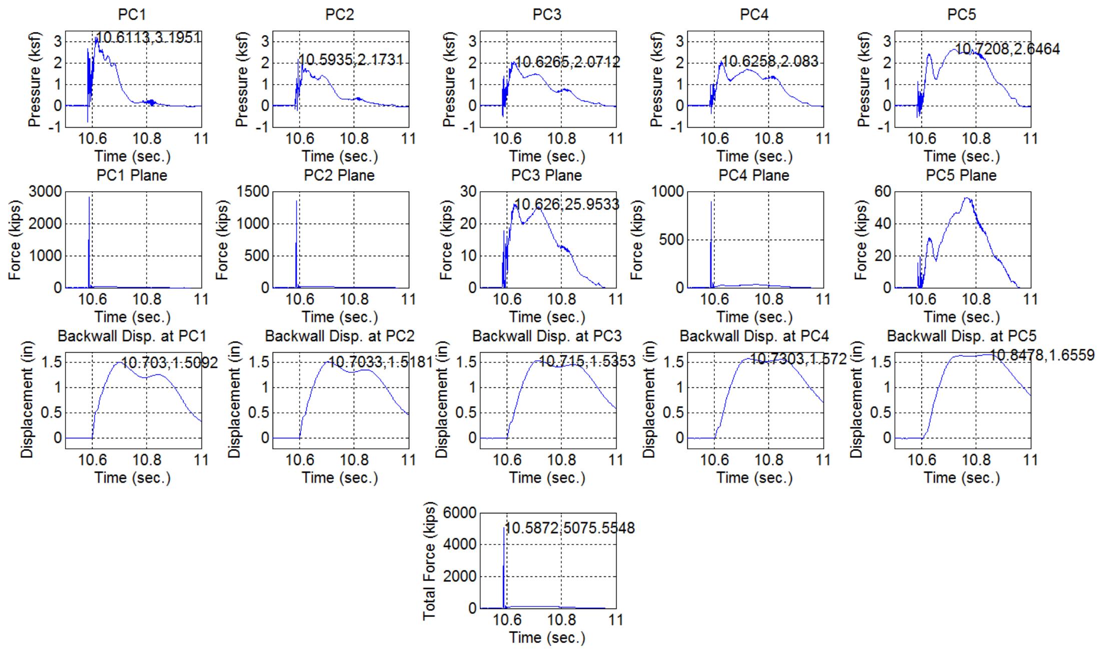

Run5 – 200% Sylmar

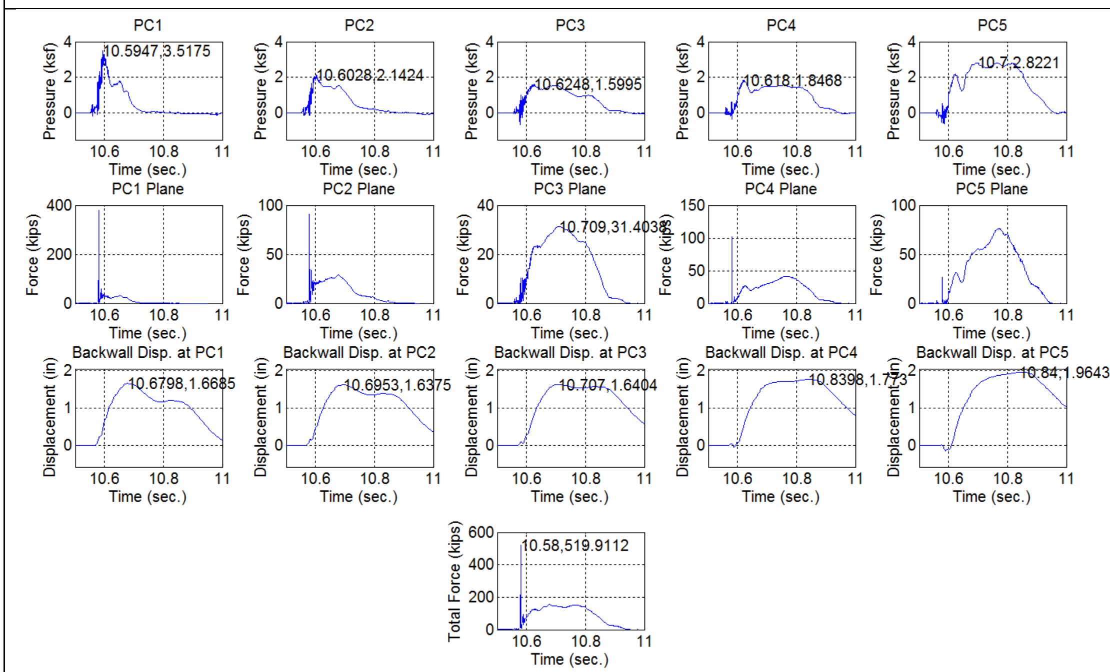

Figure G-24 Passive force histories based on approach V for the 45° skew test in Run 4 and 5.

LIST OF CCEER PUBLICATIONS

Report No. Publication

CCEER-84-1 Saiidi, M., and R. Lawver, "User's Manual for LZAK-C64, A Computer Program to Implement the Q-Model on Commodore 64," Civil Engineering Department, Report No. CCEER-84-1, University of Nevada, Reno, January 1984.

CCEER-84-1 Douglas, B., Norris, G., Saiidi, M., Dodd, L., Richardson, J. and Reid, W., "Simple Bridge Models for Earthquakes and Test Data," Civil Engineering Department, Report No. CCEER-84-1 Reprint, University of Nevada, Reno, January 1984.

CCEER-84-2 Douglas, B. and T. Iwasaki, "Proceedings of the First USA-Japan Bridge Engineering Workshop," held at the Public Works Research Institute, Tsukuba, Japan, Civil Engineering Department, Report No. CCEER-84-2, University of Nevada, Reno, April 1984.

CCEER-84-3 Saiidi, M., J. Hart, and B. Douglas, "Inelastic Static and Dynamic Analysis of Short R/C Bridges Subjected to Lateral Loads," Civil Engineering Department, Report No. CCEER-84-3, University of Nevada, Reno, July 1984.

CCEER-84-4 Douglas, B., "A Proposed Plan for a National Bridge Engineering Laboratory," Civil Engineering Department, Report No. CCEER-84-4, University of Nevada, Reno, December 1984.

CCEER-85-1 Norris, G. and P. Abdollaholiaee, "Laterally Loaded Pile Response: Studies with the Strain Wedge Model," Civil Engineering Department, Report No. CCEER-85-1, University of Nevada, Reno, April 1985.

CCEER-86-1 Ghusn, G. and M. Saiidi, "A Simple Hysteretic Element for Biaxial Bending of R/C in NEABS-86," Civil Engineering Department, Report No. CCEER-86-1, University of Nevada, Reno, July 1986.

CCEER-86-2 Saiidi, M., R. Lawver, and J. Hart, "User's Manual of ISADAB and SIBA, Computer Programs for Nonlinear Transverse Analysis of Highway Bridges Subjected to Static and Dynamic Lateral Loads," Civil Engineering Department, Report No. CCEER-86-2, University of Nevada, Reno, September 1986.

CCEER-87-1 Siddharthan, R., "Dynamic Effective Stress Response of Surface and Embedded Footings in Sand," Civil Engineering Department, Report No. CCEER-86-2, University of Nevada, Reno, June 1987.

CCEER-87-2 Norris, G. and R. Sack, "Lateral and Rotational Stiffness of Pile Groups for Seismic Analysis of Highway Bridges," Civil Engineering Department, Report No. CCEER-87-2, University of Nevada, Reno, June 1987.

CCEER-88-1 Orie, J. and M. Saiidi, "A Preliminary Study of One-Way Reinforced Concrete Pier Hinges Subjected to Shear and Flexure," Civil Engineering Department, Report No. CCEER-88-1, University of Nevada, Reno, January 1988.

CCEER-88-2 Orie, D., M. Saiidi, and B. Douglas, "A Micro-CAD System for Seismic Design of Regular Highway Bridges," Civil Engineering Department, Report No. CCEER-88-2, University of Nevada, Reno, June 1988.

CCEER-88-3 Orie, D. and M. Saiidi, "User's Manual for Micro-SARB, a Microcomputer Program for Seismic Analysis of Regular Highway Bridges," Civil Engineering Department, Report

No. CCEER-88-3, University of Nevada, Reno, October 1988.

CCEER-89-1 Douglas, B., M. Saiidi, R. Hayes, and G. Holcomb, “A Comprehensive Study of the Loads and Pressures Exerted on Wall Forms by the Placement of Concrete,” Civil Engineering Department, Report No. CCEER-89-1, University of Nevada, Reno, February 1989.

CCEER-89-2 Richardson, J. and B. Douglas, “Dynamic Response Analysis of the Dominion Road Bridge Test Data,” Civil Engineering Department, Report No. CCEER-89-2, University of Nevada, Reno, March 1989.

CCEER-89-2 Vrontinos, S., M. Saiidi, and B. Douglas, “A Simple Model to Predict the Ultimate Response of R/C Beams with Concrete Overlays,” Civil Engineering Department, Report NO. CCEER-89-2, University of Nevada, Reno, June 1989.

CCEER-89-3 Ebrahimpour, A. and P. Jagadish, “Statistical Modeling of Bridge Traffic Loads - A Case Study,” Civil Engineering Department, Report No. CCEER-89-3, University of Nevada, Reno, December 1989.

CCEER-89-4 Shields, J. and M. Saiidi, “Direct Field Measurement of Prestress Losses in Box Girder Bridges,” Civil Engineering Department, Report No. CCEER-89-4, University of Nevada, Reno, December 1989.

CCEER-90-1 Saiidi, M., E. Maragakis, G. Ghusn, Y. Jiang, and D. Schwartz, “Survey and Evaluation of Nevada's Transportation Infrastructure, Task 7.2 - Highway Bridges, Final Report,” Civil Engineering Department, Report No. CCEER 90-1, University of Nevada, Reno, October 1990.

CCEER-90-2 Abdel-Ghaffar, S., E. Maragakis, and M. Saiidi, “Analysis of the Response of Reinforced Concrete Structures During the Whittier Earthquake 1987,” Civil Engineering Department, Report No. CCEER 90-2, University of Nevada, Reno, October 1990.

CCEER-91-1 Saiidi, M., E. Hwang, E. Maragakis, and B. Douglas, “Dynamic Testing and the Analysis of the Flamingo Road Interchange,” Civil Engineering Department, Report No. CCEER-91-1, University of Nevada, Reno, February 1991.

CCEER-91-2 Norris, G., R. Siddharthan, Z. Zafir, S. Abdel-Ghaffar, and P. Gowda, “Soil-Foundation-Structure Behavior at the Oakland Outer Harbor Wharf,” Civil Engineering Department, Report No. CCEER-91-2, University of Nevada, Reno, July 1991.

CCEER-91-3 Norris, G., “Seismic Lateral and Rotational Pile Foundation Stiffnesses at Cypress,” Civil Engineering Department, Report No. CCEER-91-3, University of Nevada, Reno, August 1991.

CCEER-91-4 O'Connor, D. and M. Saiidi, “A Study of Protective Overlays for Highway Bridge Decks in Nevada, with Emphasis on Polyester-Styrene Polymer Concrete,” Civil Engineering Department, Report No. CCEER-91-4, University of Nevada, Reno, October 1991.

CCEER-91-5 O'Connor, D.N. and M. Saiidi, “Laboratory Studies of Polyester-Styrene Polymer Concrete Engineering Properties,” Civil Engineering Department, Report No. CCEER-91-5, University of Nevada, Reno, November 1991.

CCEER-92-1 Straw, D.L. and M. Saiidi, “Scale Model Testing of One-Way Reinforced Concrete Pier Hinges Subject to Combined Axial Force, Shear and Flexure,” edited by D.N. O'Connor, Civil Engineering Department, Report No. CCEER-92-1, University of Nevada, Reno, March 1992.

CCEER-92-2 Wehbe, N., M. Saiidi, and F. Gordaninejad, “Basic Behavior of Composite Sections Made of Concrete Slabs and Graphite Epoxy Beams,” Civil Engineering Department, Report No. CCEER-92-2, University of Nevada, Reno, August 1992.

CCEER-92-3 Saiidi, M. and E. Hutchens, “A Study of Prestress Changes in A Post-Tensioned Bridge During the First 30 Months,” Civil Engineering Department, Report No. CCEER-92-3, University of Nevada, Reno, April 1992.

CCEER-92-4 Saiidi, M., B. Douglas, S. Feng, E. Hwang, and E. Maragakis, “Effects of Axial Force on Frequency of Prestressed Concrete Bridges,” Civil Engineering Department, Report No. CCEER-92-4, University of Nevada, Reno, August 1992.

CCEER-92-5 Siddharthan, R., and Z. Zafir, “Response of Layered Deposits to Traveling Surface Pressure Waves,” Civil Engineering Department, Report No. CCEER-92-5, University of Nevada, Reno, September 1992.

CCEER-92-6 Norris, G., and Z. Zafir, “Liquefaction and Residual Strength of Loose Sands from Drained Triaxial Tests,” Civil Engineering Department, Report No. CCEER-92-6, University of Nevada, Reno, September 1992.

CCEER-92-6-A Norris, G., Siddharthan, R., Zafir, Z. and Madhu, R. “Liquefaction and Residual Strength of Sands from Drained Triaxial Tests,” Civil Engineering Department, Report No. CCEER-92-6-A, University of Nevada, Reno, September 1992.

CCEER-92-7 Douglas, B., “Some Thoughts Regarding the Improvement of the University of Nevada, Reno's National Academic Standing,” Civil Engineering Department, Report No. CCEER-92-7, University of Nevada, Reno, September 1992.

CCEER-92-8 Saiidi, M., E. Maragakis, and S. Feng, “An Evaluation of the Current Caltrans Seismic Restrainer Design Method,” Civil Engineering Department, Report No. CCEER-92-8, University of Nevada, Reno, October 1992.

CCEER-92-9 O'Connor, D., M. Saiidi, and E. Maragakis, “Effect of Hinge Restrainers on the Response of the Madrone Drive Undercrossing During the Loma Prieta Earthquake,” Civil Engineering Department, Report No. CCEER-92-9, University of Nevada, Reno, February 1993.

CCEER-92-10 O'Connor, D., and M. Saiidi, “Laboratory Studies of Polyester Concrete: Compressive Strength at Elevated Temperatures and Following Temperature Cycling, Bond Strength to Portland Cement Concrete, and Modulus of Elasticity,” Civil Engineering Department, Report No. CCEER-92-10, University of Nevada, Reno, February 1993.

CCEER-92-11 Wehbe, N., M. Saiidi, and D. O'Connor, “Economic Impact of Passage of Spent Fuel Traffic on Two Bridges in Northeast Nevada,” Civil Engineering Department, Report No. CCEER-92-11, University of Nevada, Reno, December 1992.

CCEER-93-1 Jiang, Y., and M. Saiidi, “Behavior, Design, and Retrofit of Reinforced Concrete One-way Bridge Column Hinges,” edited by D. O'Connor, Civil Engineering Department, Report No. CCEER-93-1, University of Nevada, Reno, March 1993.

CCEER-93-2 Abdel-Ghaffar, S., E. Maragakis, and M. Saiidi, “Evaluation of the Response of the Aptos Creek Bridge During the 1989 Loma Prieta Earthquake,” Civil Engineering Department, Report No. CCEER-93-2, University of Nevada, Reno, June 1993.

CCEER-93-3 Sanders, D.H., B.M. Douglas, and T.L. Martin, “Seismic Retrofit Prioritization of Nevada Bridges,” Civil Engineering Department, Report No. CCEER-93-3, University of

Nevada, Reno, July 1993.

CCEER-93-4 Abdel-Ghaffar, S., E. Maragakis, and M. Saiidi, “Performance of Hinge Restrainers in the Huntington Avenue Overhead During the 1989 Loma Prieta Earthquake,” Civil Engineering Department, Report No. CCEER-93-4, University of Nevada, Reno, June 1993.

CCEER-93-5 Maragakis, E., M. Saiidi, S. Feng, and L. Flournoy, “Effects of Hinge Restrainers on the Response of the San Gregorio Bridge during the Loma Prieta Earthquake,” (in final preparation) Civil Engineering Department, Report No. CCEER-93-5, University of Nevada, Reno.

CCEER-93-6 Saiidi, M., E. Maragakis, S. Abdel-Ghaffar, S. Feng, and D. O'Connor, “Response of Bridge Hinge Restrainers during Earthquakes -Field Performance, Analysis, and Design,” Civil Engineering Department, Report No. CCEER-93-6, University of Nevada, Reno, May 1993.

CCEER-93-7 Wehbe, N., Saiidi, M., Maragakis, E., and Sanders, D., “Adequacy of Three Highway Structures in Southern Nevada for Spent Fuel Transportation,” Civil Engineering Department, Report No. CCEER-93-7, University of Nevada, Reno, August 1993.

CCEER-93-8 Roybal, J., Sanders, D.H., and Maragakis, E., “Vulnerability Assessment of Masonry in the Reno-Carson City Urban Corridor,” Civil Engineering Department, Report No. CCEER-93-8, University of Nevada, Reno, May 1993.

CCEER-93-9 Zafir, Z. and Siddharthan, R., “MOVLOAD: A Program to Determine the Behavior of Nonlinear Horizontally Layered Medium Under Moving Load,” Civil Engineering Department, Report No. CCEER-93-9, University of Nevada, Reno, August 1993.

CCEER-93-10 O'Connor, D.N., Saiidi, M., and Maragakis, E.A., “A Study of Bridge Column Seismic Damage Susceptibility at the Interstate 80/U.S. 395 Interchange in Reno, Nevada,” Civil Engineering Department, Report No. CCEER-93-10, University of Nevada, Reno, October 1993.

CCEER-94-1 Maragakis, E., B. Douglas, and E. Abdelwahed, “Preliminary Dynamic Analysis of a Railroad Bridge,” Report CCEER-94-1, January 1994.

CCEER-94-2 Douglas, B.M., Maragakis, E.A., and Feng, S., “Stiffness Evaluation of Pile Foundation of Cazenovia Creek Overpass,” Civil Engineering Department, Report No. CCEER-94-2, University of Nevada, Reno, March 1994.

CCEER-94-3 Douglas, B.M., Maragakis, E.A., and Feng, S., “Summary of Pretest Analysis of Cazenovia Creek Bridge,” Civil Engineering Department, Report No. CCEER-94-3, University of Nevada, Reno, April 1994.

CCEER-94-4 Norris, G.M., Madhu, R., Valceschini, R., and Ashour, M., “Liquefaction and Residual Strength of Loose Sands from Drained Triaxial Tests,” Report 2, Vol. 1&2, Civil Engineering Department, Report No. CCEER-94-4, University of Nevada, Reno, August 1994.

CCEER-94-5 Saiidi, M., Hutchens, E., and Gardella, D., “Prestress Losses in a Post-Tensioned R/C Box Girder Bridge in Southern Nevada,” Civil Engineering Department, CCEER-94-5, University of Nevada, Reno, August 1994.

CCEER-95-1 Siddharthan, R., El-Gamal, M., and Maragakis, E.A., “Nonlinear Bridge Abutment , Verification, and Design Curves,” Civil Engineering Department, CCEER-95-1, University of Nevada, Reno, January 1995.

CCEER-95-2 Ashour, M. and Norris, G., "Liquefaction and Undrained Response Evaluation of Sands from Drained Formulation," Civil Engineering Department, Report No. CCEER-95-2, University of Nevada, Reno, February 1995.

CCEER-95-3 Wehbe, N., Saiidi, M., Sanders, D. and Douglas, B., "Ductility of Rectangular Reinforced Concrete Bridge Columns with Moderate Confinement," Civil Engineering Department, Report No. CCEER-95-3, University of Nevada, Reno, July 1995.

CCEER-95-4 Martin, T.., Saiidi, M. and Sanders, D., "Seismic Retrofit of Column-Pier Cap Connections in Bridges in Northern Nevada," Civil Engineering Department, Report No. CCEER-95-4, University of Nevada, Reno, August 1995.

CCEER-95-5 Darwish, I., Saiidi, M. and Sanders, D., "Experimental Study of Seismic Susceptibility Column-Footing Connections in Bridges in Northern Nevada," Civil Engineering Department, Report No. CCEER-95-5, University of Nevada, Reno, September 1995.

CCEER-95-6 Griffin, G., Saiidi, M. and Maragakis, E., "Nonlinear Seismic Response of Isolated Bridges and Effects of Pier Ductility Demand," Civil Engineering Department, Report No. CCEER-95-6, University of Nevada, Reno, November 1995.

CCEER-95-7 Acharya, S.., Saiidi, M. and Sanders, D., "Seismic Retrofit of Bridge Footings and Column-Footing Connections," Civil Engineering Department, Report No. CCEER-95-7, University of Nevada, Reno, November 1995.

CCEER-95-8 Maragakis, E., Douglas, B., and Sandirasegaram, U., "Full-Scale Field Resonance Tests of a Railway Bridge," A Report to the Association of American Railroads, Civil Engineering Department, Report No. CCEER-95-8, University of Nevada, Reno, December 1995.

CCEER-95-9 Douglas, B., Maragakis, E. and Feng, S., "System Identification Studies on Cazenovia Creek Overpass," Report for the National Center for Earthquake Engineering Research, Civil Engineering Department, Report No. CCEER-95-9, University of Nevada, Reno, October 1995.

CCEER-96-1 El-Gamal, M.E. and Siddharthan, R.V., "Programs to Computer Translational Stiffness of Seat-Type Bridge Abutment," Civil Engineering Department, Report No. CCEER-96-1, University of Nevada, Reno, March 1996.

CCEER-96-2 Labia, Y., Saiidi, M. and Douglas, B., "Evaluation and Repair of Full-Scale Prestressed Concrete Box Girders," A Report to the National Science Foundation, Research Grant CMS-9201908, Civil Engineering Department, Report No. CCEER-96-2, University of Nevada, Reno, May 1996.

CCEER-96-3 Darwish, I., Saiidi, M. and Sanders, D., "Seismic Retrofit of R/C Oblong Tapered Bridge Columns with Inadequate Bar Anchorage in Columns and Footings," A Report to the Nevada Department of Transportation, Civil Engineering Department, Report No. CCEER-96-3, University of Nevada, Reno, May 1996.

CCEER-96-4 Ashour, M., Pilling, R., Norris, G. and Perez, H., "The Prediction of Lateral Load Behavior of Single Piles and Pile Groups Using the Strain Wedge Model," A Report to the California Department of Transportation, Civil Engineering Department, Report No. CCEER-96-4, University of Nevada, Reno, June 1996.

CCEER-97-1-A Rimal, P. and Itani, A. "Sensitivity Analysis of Fatigue Evaluations of Steel Bridges," Center for Earthquake Research, Department of Civil Engineering, University of Nevada, Reno, Nevada Report No. CCEER-97-1-A, September, 1997.

CCEER-97-1-B Maragakis, E., Douglas, B., and Sandirasegaram, U. "Full-Scale Field Resonance Tests of a Railway Bridge," A Report to the Association of American Railroads, Civil Engineering Department, University of Nevada, Reno, May, 1996.

CCEER-97-2 Wehbe, N., Saiidi, M., and D. Sanders, "Effect of Confinement and Flares on the Seismic Performance of Reinforced Concrete Bridge Columns," Civil Engineering Department, Report No. CCEER-97-2, University of Nevada, Reno, September 1997.

CCEER-97-3 Darwish, I., M. Saiidi, G. Norris, and E. Maragakis, "Determination of In-Situ Footing Stiffness Using Full-Scale Dynamic Field Testing," A Report to the Nevada Department of Transportation, Structural Design Division, Carson City, Nevada, Report No. CCEER-97-3, University of Nevada, Reno, October 1997.

CCEER-97-4-A Itani, A. "Cyclic Behavior of Richmond-San Rafael Tower Links," Center for Civil Engineering Earthquake Research, Department of Civil Engineering, University of Nevada, Reno, Nevada, Report No. CCEER-97-4, August 1997.

CCEER-97-4-B Wehbe, N., and M. Saiidi, "User's Manual for RCMC v. 1.2 : A Computer Program for Moment-Curvature Analysis of Confined and Unconfined Reinforced Concrete Sections," Center for Civil Engineering Earthquake Research, Department of Civil Engineering, University of Nevada, Reno, Nevada, Report No. CCEER-97-4, November, 1997.

CCEER-97-5 Isakovic, T., M. Saiidi, and A. Itani, "Influence of new Bridge Configurations on Seismic Performance," Department of Civil Engineering, University of Nevada, Reno, Report No. CCEER-97-5, September, 1997.

CCEER-98-1 Itani, A., Vesco, T. and Dietrich, A., "Cyclic Behavior of "as Built" Laced Members With End Gusset Plates on the San Francisco Bay Bridge," Center for Civil Engineering Earthquake Research, Department of Civil Engineering, University of Nevada, Reno, Nevada Report No. CCEER-98-1, March, 1998.

CCEER-98-2 G. Norris and M. Ashour, "Liquefaction and Undrained Response Evaluation of Sands from Drained Formulation," Center for Civil Engineering Earthquake Research, Department of Civil Engineering, University of Nevada, Reno, Nevada, Report No. CCEER-98-2, May, 1998.

CCEER-98-3 Qingbin, Chen, B. M. Douglas, E. Maragakis, and I. G. Buckle, "Extraction of Nonlinear Hysteretic Properties of Seismically Isolated Bridges from Quick-Release Field Tests," Center for Civil Engineering Earthquake Research, Department of Civil Engineering, University of Nevada, Reno, Nevada, Report No. CCEER-98-3, June, 1998.

CCEER-98-4 Maragakis, E., B. M. Douglas, and C. Qingbin, "Full-Scale Field Capacity Tests of a Railway Bridge," Center for Civil Engineering Earthquake Research, Department of Civil Engineering, University of Nevada, Reno, Nevada, Report No. CCEER-98-4, June, 1998.

CCEER-98-5 Itani, A., Douglas, B., and Woodgate, J., "Cyclic Behavior of Richmond-San Rafael Retrofitted Tower Leg," Center for Civil Engineering Earthquake Research, Department of Civil Engineering, University of Nevada, Reno. Report No. CCEER-98-5, June 1998

CCEER-98-6 Moore, R., Saiidi, M., and Itani, A., "Seismic Behavior of New Bridges with Skew and Curvature," Center for Civil Engineering Earthquake Research, Department of Civil Engineering, University of Nevada, Reno. Report No. CCEER-98-6, October, 1998.

CCEER-98-7 Itani, A and Dietrich, A, "Cyclic Behavior of Double Gusset Plate Connections," Center for Civil Engineering Earthquake Research, Department of Civil Engineering, University of Nevada, Reno, Nevada, Report No. CCEER-98-5, December, 1998.

CCEER-99-1 Caywood, C., M. Saiidi, and D. Sanders, "Seismic Retrofit of Flared Bridge Columns with Steel Jackets," Civil Engineering Department, University of Nevada, Reno, Report No. CCEER-99-1, February 1999.

CCEER-99-2 Mangoba, N., M. Mayberry, and M. Saiidi, "Prestress Loss in Four Box Girder Bridges in Northern Nevada," Civil Engineering Department, University of Nevada, Reno, Report No. CCEER-99-2, March 1999.

CCEER-99-3 Abo-Shadi, N., M. Saiidi, and D. Sanders, "Seismic Response of Bridge Pier Walls in the Weak Direction," Civil Engineering Department, University of Nevada, Reno, Report No. CCEER-99-3, April 1999.

CCEER-99-4 Buzick, A., and M. Saiidi, "Shear Strength and Shear Fatigue Behavior of Full-Scale Prestressed Concrete Box Girders," Civil Engineering Department, University of Nevada, Reno, Report No. CCEER-99-4, April 1999.

CCEER-99-5 Randall, M., M. Saiidi, E. Maragakis and T. Isakovic, "Restrainer Design Procedures For Multi-Span Simply-Supported Bridges," Civil Engineering Department, University of Nevada, Reno, Report No. CCEER-99-5, April 1999.

CCEER-99-6 Wehbe, N. and M. Saiidi, "User's Manual for RCMC v. 1.2, A Computer Program for Moment-Curvature Analysis of Confined and Unconfined Reinforced Concrete Sections," Civil Engineering Department, University of Nevada, Reno, Report No. CCEER-99-6, May 1999.

CCEER-99-7 Burda, J. and A. Itani, "Studies of Seismic Behavior of Steel Base Plates," Civil Engineering Department, University of Nevada, Reno, Report No. CCEER-99-7, May 1999.

CCEER-99-8 Ashour, M. and G. Norris, "Refinement of the Strain Wedge Model Program," Civil Engineering Department, University of Nevada, Reno, Report No. CCEER-99-8, March 1999.

CCEER-99-9 Dietrich, A., and A. Itani, "Cyclic Behavior of Laced and Perforated Steel Members on the San Francisco-Oakland Bay Bridge," Civil Engineering Department, University, Reno, Report No. CCEER-99-9, December 1999.

CCEER 99-10 Itani, A., A. Dietrich, "Cyclic Behavior of Built Up Steel Members and their Connections," Civil Engineering Department, University of Nevada, Reno, Report No. CCEER-99-10, December 1999.

CCEER 99-10-A Itani, A., E. Maragakis and P. He, "Fatigue Behavior of Riveted Open Deck Railroad Bridge Girders," Civil Engineering Department, University of Nevada, Reno, Report No. CCEER-99-10-A, August 1999.

CCEER 99-11 Itani, A., J. Woodgate, "Axial and Rotational Ductility of Built Up Structural Steel Members," Civil Engineering Department, University of Nevada, Reno, Report No. CCEER-99-11, December 1999.

CCEER-99-12 Sgambelluri, M., Sanders, D.H., and Saiidi, M.S., "Behavior of One-Way Reinforced Concrete Bridge Column Hinges in the Weak Direction," Department of Civil Engineering, University of Nevada, Reno, Report No. CCEER-99-12, December 1999.

CCEER-99-13 Laplace, P., Sanders, D.H., Douglas, B, and Saiidi, M, “Shake Table Testing of Flexure Dominated Reinforced Concrete Bridge Columns”, Department of Civil Engineering, University of Nevada, Reno, Report No. CCEER-99-13, December 1999.

CCEER-99-14 Ahmad M. Itani, Jose A. Zepeda, and Elizabeth A. Ware “Cyclic Behavior of Steel Moment Frame Connections for the Moscone Center Expansion,” Department of Civil Engineering, University of Nevada, Reno, Report No. CCEER-99-14, December 1999.

CCEER 00-1 Ashour, M., and Norris, G. “Undrained Lateral Pile and Pile Group Response in Saturated Sand,” Civil Engineering Department, University of Nevada, Reno, Report No. CCEER-00-1, May 1999. January 2000.

CCEER 00-2 Saiidi, M. and Wehbe, N., “A Comparison of Confinement Requirements in Different Codes for Rectangular, Circular, and Double-Spiral RC Bridge Columns,” Civil Engineering Department, University of Nevada, Reno, Report No. CCEER-00-2, January 2000.

CCEER 00-3 McElhaney, B., M. Saiidi, and D. Sanders, “Shake Table Testing of Flared Bridge Columns With Steel Jacket Retrofit,” Civil Engineering Department, University of Nevada, Reno, Report No. CCEER-00-3, January 2000.

CCEER 00-4 Martinovic, F., M. Saiidi, D. Sanders, and F. Gordaninejad, “Dynamic Testing of Non-Prismatic Reinforced Concrete Bridge Columns Retrofitted with FRP Jackets,” Civil Engineering Department, University of Nevada, Reno, Report No. CCEER-00-4, January 2000.

CCEER 00-5 Itani, A., and M. Saiidi, “Seismic Evaluation of Steel Joints for UCLA Center for Health Science Westwood Replacement Hospital,” Civil Engineering Department, University of Nevada, Reno, Report No. CCEER-00-5, February 2000.

CCEER 00-6 Will, J. and D. Sanders, “High Performance Concrete Using Nevada Aggregates,” Civil Engineering Department, University of Nevada, Reno, Report No. CCEER-00-6, May 2000.

CCEER 00-7 French, C., and M. Saiidi, “A Comparison of Static and Dynamic Performance of Models of Flared Bridge Columns,” Civil Engineering Department, University of Nevada, Reno, Report No. CCEER-00-7, October 2000.

CCEER 00-8 Itani, A., H. Sedarat, “Seismic Analysis of the AISI LRFD Design Example of Steel Highway Bridges,” Civil Engineering Department, University of Nevada, Reno, Report No. CCEER 00-08, November 2000.

CCEER 00-9 Moore, J., D. Sanders, and M. Saiidi, “Shake Table Testing of 1960’s Two Column Bent with Hinges Bases,” Civil Engineering Department, University of Nevada, Reno, Report No. CCEER 00-09, December 2000.

CCEER 00-10 Asthana, M., D. Sanders, and M. Saiidi, “One-Way Reinforced Concrete Bridge Column Hinges in the Weak Direction,” Civil Engineering Department, University of Nevada, Reno, Report No. CCEER 00-10, April 2001.

CCEER 01-1 Ah Sha, H., D. Sanders, M. Saiidi, “Early Age Shrinkage and Cracking of Nevada Concrete Bridge Decks,” Civil Engineering Department, University of Nevada, Reno, Report No. CCEER 01-01, May 2001.

CCEER 01-2 Ashour, M. and G. Norris, “Pile Group program for Full Material Modeling a Progressive

Failure," Civil Engineering Department, University of Nevada, Reno, Report No. CCEER 01-02, July 2001.

CCEER 01-3 Itani, A., C. Lanaud, and P. Dusicka, "Non-Linear Finite Element Analysis of Built-Up Shear Links," Civil Engineering Department, University of Nevada, Reno, Report No. CCEER 01-03, July 2001.

CCEER 01-4 Saiidi, M., J. Mortensen, and F. Martinovic, "Analysis and Retrofit of Fixed Flared Columns with Glass Fiber-Reinforced Plastic Jacketing," Civil Engineering Department, University of Nevada, Reno, Report No. CCEER 01-4, August 2001

CCEER 01-5 Not Published

CCEER 01-6 Laplace, P., D. Sanders, and M. Saiidi, "Experimental Study and Analysis of Retrofitted Flexure and Shear Dominated Circular Reinforced Concrete Bridge Columns Subjected to Shake Table Excitation," Civil Engineering Department, University of Nevada, Reno, Report No. CCEER 01-6, June 2001.

CCEER 01-7 Reppi, F., and D. Sanders, "Removal and Replacement of Cast-in-Place, Post-tensioned, Box Girder Bridge," Civil Engineering Department, University of Nevada, Reno, Report No. CCEER 01-7, December 2001.

CCEER 02-1 Pulido, C., M. Saiidi, D. Sanders, and A. Itani, "Seismic Performance and Retrofitting of Reinforced Concrete Bridge Bents," Civil Engineering Department, University of Nevada, Reno, Report No. CCEER 02-1, January 2002.

CCEER 02-2 Yang, Q., M. Saiidi, H. Wang, and A. Itani, "Influence of Ground Motion Incoherency on Earthquake Response of Multi-Support Structures," Civil Engineering Department, University of Nevada, Reno, Report No. CCEER 02-2, May 2002.

CCEER 02-3 M. Saiidi, B. Gopalakrishnan, E. Reinhardt, and R. Siddharthan, "A Preliminary Study of Shake Table Response of A Two-Column Bridge Bent on Flexible Footings," Civil Engineering Department, University of Nevada, Reno, Report No. CCEER 02-03, June 2002.

CCEER 02-4 Not Published

CCEER 02-5 Banghart, A., Sanders, D., Saiidi, M., "Evaluation of Concrete Mixes for Filling the Steel Arches in the Galena Creek Bridge," Civil Engineering Department, University of Nevada, Reno, Report No. CCEER 02-05, June 2002.

CCEER 02-6 Dusicka, P., Itani, A., Buckle, I. G., "Cyclic Behavior of Shear Links and Tower Shaft Assembly of San Francisco – Oakland Bay Bridge Tower," Civil Engineering Department, University of Nevada, Reno, Report No. CCEER 02-06, July 2002.

CCEER 02-7 Mortensen, J., and M. Saiidi, "A Performance-Based Design Method for Confinement in Circular Columns," Civil Engineering Department, University of Nevada, Reno, Report No. CCEER 02-07, November 2002.

CCEER 03-1 Wehbe, N., and M. Saiidi, "User's manual for SPMC v. 1.0 : A Computer Program for Moment-Curvature Analysis of Reinforced Concrete Sections with Interlocking Spirals," Center for Civil Engineering Earthquake Research, Department of Civil Engineering, University of Nevada, Reno, Nevada, Report No. CCEER-03-1, May, 2003.

CCEER 03-2 Wehbe, N., and M. Saiidi, "User's manual for RCMC v. 2.0 : A Computer Program for Moment-Curvature Analysis of Confined and Unconfined Reinforced Concrete Sections," Center for Civil Engineering Earthquake Research, Department of Civil Engineering, University of Nevada, Reno, Nevada, Report No. CCEER-03-2, June, 2003.

CCEER 03-3 Nada, H., D. Sanders, and M. Saiidi, "Seismic Performance of RC Bridge Frames with Architectural-Flared Columns," Civil Engineering Department, University of Nevada, Reno, Report No. CCEER 03-3, January 2003.

CCEER 03-4 Reinhardt, E., M. Saiidi, and R. Siddharthan, "Seismic Performance of a CFRP/ Concrete Bridge Bent on Flexible Footings," Civil Engineering Department, University of Nevada, Reno, Report No. CCEER 03-4, August 2003.

CCEER 03-5 Johnson, N., M. Saiidi, A. Itani, and S. Ladkany, "Seismic Retrofit of Octagonal Columns with Pedestal and One-Way Hinge at the Base," Center for Civil Engineering Earthquake Research, Department of Civil Engineering, University of Nevada, Reno, Nevada, and Report No. CCEER-03-5, August 2003.

CCEER 03-6 Mortensen, C., M. Saiidi, and S. Ladkany, "Creep and Shrinkage Losses in Highly Variable Climates," Center for Civil Engineering Earthquake Research, Department of Civil Engineering, University of Nevada, Reno, Report No. CCEER-03-6, September 2003.

CCEER 03- 7 Ayoub, C., M. Saiidi, and A. Itani, "A Study of Shape-Memory-Alloy-Reinforced Beams and Cubes," Center for Civil Engineering Earthquake Research, Department of Civil Engineering, University of Nevada, Reno, Nevada, Report No. CCEER-03-7, October 2003.

CCEER 03-8 Chandane, S., D. Sanders, and M. Saiidi, "Static and Dynamic Performance of RC Bridge Bents with Architectural-Flared Columns," Center for Civil Engineering Earthquake Research, Department of Civil Engineering, University of Nevada, Reno, Nevada, Report No. CCEER-03-8, November 2003.

CCEER 04-1 Olaegbe, C., and Saiidi, M., "Effect of Loading History on Shake Table Performance of A Two-Column Bent with Infill Wall," Center for Civil Engineering Earthquake Research, Department of Civil Engineering, University of Nevada, Reno, Nevada, Report No. CCEER-04-1, January 2004.

CCEER 04-2 Johnson, R., Maragakis, E., Saiidi, M., and DesRoches, R., "Experimental Evaluation of Seismic Performance of SMA Bridge Restrainers," Center for Civil Engineering Earthquake Research, Department of Civil Engineering, University of Nevada, Reno, Nevada, Report No. CCEER-04-2, February 2004.

CCEER 04-3 Moustafa, K., Sanders, D., and Saiidi, M., "Impact of Aspect Ratio on Two-Column Bent Seismic Performance," Center for Civil Engineering Earthquake Research, Department of Civil Engineering, University of Nevada, Reno, Nevada, Report No. CCEER-04-3, February 2004.

CCEER 04-4 Maragakis, E., Saiidi, M., Sanchez-Camargo, F., and Elfass, S., "Seismic Performance of Bridge Restrainers At In-Span Hinges," Center for Civil Engineering Earthquake Research, Department of Civil Engineering, University of Nevada, Reno, Nevada, Report No. CCEER-04-4, March 2004.

CCEER 04-5 Ashour, M., Norris, G. and Elfass, S., "Analysis of Laterally Loaded Long or Intermediate Drilled Shafts of Small or Large Diameter in Layered Soil," Center for Civil Engineering Earthquake Research, Department of Civil Engineering, University of Nevada, Reno, Nevada, Report No. CCEER-04-5, June 2004.

CCEER 04-6 Correal, J., Saiidi, M. and Sanders, D., "Seismic Performance of RC Bridge Columns Reinforced with Two Interlocking Spirals," Center for Civil Engineering Earthquake Research, Department of Civil Engineering, University of Nevada, Reno, Nevada, Report No. CCEER-04-6, August 2004.

CCEER 04-7 Dusicka, P., Itani, A. and Buckle, I., "Cyclic Response and Low Cycle Fatigue Characteristics of Plate Steels," Center for Civil Engineering Earthquake Research, Department of Civil Engineering, University of Nevada, Reno, Nevada, Report No. CCEER-04-7, November 2004.

CCEER 04-8 Dusicka, P., Itani, A. and Buckle, I., "Built-up Shear Links as Energy Dissipaters for Seismic Protection of Bridges," Center for Civil Engineering Earthquake Research, Department of Civil Engineering, University of Nevada, Reno, Nevada, Report No. CCEER-04-8, November 2004.

CCEER 04-9 Sureshkumar, K., Saiidi, S., Itani, A. and Ladkany, S., "Seismic Retrofit of Two-Column Bents with Diamond Shape Columns," Center for Civil Engineering Earthquake Research, Department of Civil Engineering, University of Nevada, Reno, Nevada, Report No. CCEER-04-9, November 2004.

CCEER 05-1 Wang, H. and Saiidi, S., "A Study of RC Columns with Shape Memory Alloy and Engineered Cementitious Composites," Center for Civil Engineering Earthquake Research, Department of Civil Engineering, University of Nevada, Reno, Nevada, Report No. CCEER-05-1, January 2005.

CCEER 05-2 Johnson, R., Saiidi, S. and Maragakis, E., "A Study of Fiber Reinforced Plastics for Seismic Bridge Restrainers," Center for Civil Engineering Earthquake Research, Department of Civil Engineering, University of Nevada, Reno, Nevada, Report No. CCEER-05-2, January 2005.

CCEER 05-3 Carden, L.P., Itani, A.M., Buckle, I.G, "Seismic Load Path in Steel Girder Bridge Superstructures," Center for Civil Engineering Earthquake Research, Department of Civil Engineering, University of Nevada, Reno, Nevada, Report No. CCEER-05-3, January 2005.

CCEER 05-4 Carden, L.P., Itani, A.M., Buckle, I.G, "Seismic Performance of Steel Girder Bridge Superstructures with Ductile End Cross Frames and Seismic Isolation," Center for Civil Engineering Earthquake Research, Department of Civil Engineering, University of Nevada, Reno, Nevada, Report No. CCEER-05-4, January 2005.

CCEER 05-5 Goodwin, E., Maragakis, M., Itani, A. and Luo, S., "Experimental Evaluation of the Seismic Performance of Hospital Piping Subassemblies," Center for Civil Engineering Earthquake Research, Department of Civil Engineering, University of Nevada, Reno, Nevada, Report No. CCEER-05-5, February 2005.

CCEER 05-6 Zadeh M. S., Saiidi, S, Itani, A. and Ladkany, S., "Seismic Vulnerability Evaluation and Retrofit Design of Las Vegas Downtown Viaduct," Center for Civil Engineering Earthquake Research, Department of Civil Engineering, University of Nevada, Reno, Nevada, Report No. CCEER-05-6, February 2005.

CCEER 05-7 Phan, V., Saiidi, S. and Anderson, J., "Near Fault (Near Field) Ground Motion Effects on Reinforced Concrete Bridge Columns," Center for Civil Engineering Earthquake Research, Department of Civil Engineering, University of Nevada, Reno, Nevada, Report No. CCEER-05-7, August 2005.

CCEER 05-8 Carden, L., Itani, A. and Laplace, P., "Performance of Steel Props at the UNR Fire Science Academy subjected to Repeated Fire," Center for Civil Engineering Earthquake Research, Department of Civil Engineering, University of Nevada, Reno, Nevada, Report No. CCEER-05-8, August 2005.

CCEER 05-9 Yamashita, R. and Sanders, D., "Shake Table Testing and an Analytical Study of Unbonded Prestressed Hollow Concrete Column Constructed with Precast Segments," Center for Civil Engineering Earthquake Research, Department of Civil Engineering, University of Nevada, Reno, Nevada, Report No. CCEER-05-9, August 2005.

CCEER 05-10 Not Published

CCEER 05-11 Carden, L., Itani., A., and Peckan, G., "Recommendations for the Design of Beams and Posts in Bridge Falsework," Center for Civil Engineering Earthquake Research, Department of Civil Engineering, University of Nevada, Reno, Nevada, Report No. CCEER-05-11, October 2005.

CCEER 06-01 Cheng, Z., Saiidi, M., and Sanders, D., "Development of a Seismic Design Method for Reinforced Concrete Two-Way Bridge Column Hinges," Center for Civil Engineering Earthquake Research, Department of Civil Engineering, University of Nevada, Reno, Nevada, Report No. CCEER-06-01, February 2006.

CCEER 06-02 Johnson, N., Saiidi, M., and Sanders, D., "Large-Scale Experimental and Analytical Studies of a Two-Span Reinforced Concrete Bridge System," Center for Civil Engineering Earthquake Research, Department of Civil Engineering, University of Nevada, Reno, Nevada, Report No. CCEER-06-02, March 2006.

CCEER 06-03 Saiidi, M., Ghasemi, H. and Tiras, A., "Seismic Design and Retrofit of Highway Bridges," Proceedings, Second US-Turkey Workshop, Center for Civil Engineering Earthquake Research, Department of Civil Engineering, University of Nevada, Reno, Nevada, Report No. CCEER-06-03, May 2006.

CCEER 07-01 O'Brien, M., Saiidi, M. and Sadrossadat-Zadeh, M., "A Study of Concrete Bridge Columns Using Innovative Materials Subjected to Cyclic Loading," Center for Civil Engineering Earthquake Research, Department of Civil Engineering, University of Nevada, Reno, Nevada, Report No. CCEER-07-01, January 2007.

CCEER 07-02 Sadrossadat-Zadeh, M. and Saiidi, M., "Effect of Strain rate on Stress-Strain Properties and Yield Propagation in Steel Reinforcing Bars," Center for Civil Engineering Earthquake Research, Department of Civil Engineering, University of Nevada, Reno, Nevada, Report No. CCEER-07-02, January 2007.

CCEER 07-03 Sadrossadat-Zadeh, M. and Saiidi, M., "Analytical Study of NEESR-SG 4-Span Bridge Model Using OpenSees," Center for Civil Engineering Earthquake Research, Department of Civil Engineering, University of Nevada, Reno, Nevada, Report No. CCEER-07-03, January 2007.

CCEER 07-04 Nelson, R., Saiidi, M. and Zadeh, S., "Experimental Evaluation of Performance of Conventional Bridge Systems," Center for Civil Engineering Earthquake Research, Department of Civil Engineering, University of Nevada, Reno, Nevada, Report No. CCEER-07-04, October 2007.

CCEER 07-05 Bahen, N. and Sanders, D., “Strut-and-Tie Modeling for Disturbed Regions in Structural Concrete Members with Emphasis on Deep Beams,” Center for Civil Engineering Earthquake Research, Department of Civil Engineering, University of Nevada, Reno, Nevada, Report No. CCEER-07-05, December 2007.

CCEER 07-06 Choi, H., Saiidi, M. and Somerville, P., “Effects of Near-Fault Ground Motion and Fault-Rupture on the Seismic Response of Reinforced Concrete Bridges,” Center for Civil Engineering Earthquake Research, Department of Civil Engineering, University of Nevada, Reno, Nevada, Report No. CCEER-07-06, December 2007.

CCEER 07-07 Ashour M. and Norris, G., “Report and User Manual on Strain Wedge Model Computer Program for Files and Large Diameter Shafts with LRFD Procedure,” Center for Civil Engineering Earthquake Research, Department of Civil Engineering, University of Nevada, Reno, Nevada, Report No. CCEER-07-07, October 2007.

CCEER 08-01 Doyle, K. and Saiidi, M., “Seismic Response of Telescopic Pipe Pin Connections,” Center for Civil Engineering Earthquake Research, Department of Civil Engineering, University of Nevada, Reno, Nevada, Report No. CCEER-08-01, February 2008.

CCEER 08-02 Taylor, M. and Sanders, D., “Seismic Time History Analysis and Instrumentation of the Galena Creek Bridge,” Center for Civil Engineering Earthquake Research, Department of Civil Engineering, University of Nevada, Reno, Nevada, Report No. CCEER-08-02, April 2008.

CCEER 08-03 Abdel-Mohti, A. and Pekcan, G., “Seismic Response Assessment and Recommendations for the Design of Skewed Post-Tensioned Concrete Box-Girder Highway Bridges,” Center for Civil Engineering Earthquake Research, Department of Civil and Environmental Engineering, University of Nevada, Reno, Nevada, Report No. CCEER-08-03, September 2008.

CCEER 08-04 Saiidi, M., Ghasemi, H. and Hook, J., “Long Term Bridge Performance Monitoring, Assessment & Management,” Proceedings, FHWA/NSF Workshop on Future Directions,” Center for Civil Engineering Earthquake Research, Department of Civil and Environmental Engineering, University of Nevada, Reno, Nevada, Report No. CCEER 08-04, September 2008.

CCEER 09-01 Brown, A., and Saiidi, M., “Investigation of Near-Fault Ground Motion Effects on Substandard Bridge Columns and Bents,” Center for Civil Engineering Earthquake Research, Department of Civil and Environmental Engineering, University of Nevada, Reno, Nevada, Report No. CCEER-09-01, July 2009.

CCEER 09-02 Linke, C., Pekcan, G., and Itani, A., “Detailing of Seismically Resilient Special Truss Moment Frames,” Center for Civil Engineering Earthquake Research, Department of Civil and Environmental Engineering, University of Nevada, Reno, Nevada, Report No. CCEER-09-02, August 2009.

CCEER 09-03 Hillis, D., and Saiidi, M., “Design, Construction, and Nonlinear Dynamic Analysis of Three Bridge Bents Used in a Bridge System Test,” Center for Civil Engineering Earthquake Research, Department of Civil and Environmental Engineering, University of Nevada, Reno, Nevada, Report No. CCEER-09-03, August 2009.

CCEER 09-04 Bahrami, H., Itani, A., and Buckle, I., “Guidelines for the Seismic Design of Ductile End Cross Frames in Steel Girder Bridge Superstructures,” Center for Civil Engineering Earthquake Research, Department of Civil and Environmental Engineering, University of Nevada, Reno, Nevada, Report No. CCEER-09-04, September 2so009.

CCEER 10-01 Zaghi, A. E., and Saiidi, M., “Seismic Design of Pipe-Pin Connections in Concrete Bridges,” Center for Civil Engineering Earthquake Research, Department of Civil and Environmental Engineering, University of Nevada, Reno, Nevada, Report No. CCEER-10-01, January 2010.

CCEER 10-02 Pooranampillai, S., Elfass, S., and Norris, G., “Laboratory Study to Assess Load Capacity Increase of Drilled Shafts through Post Grouting,” Center for Civil Engineering Earthquake Research, Department of Civil and Environmental Engineering, University of Nevada, Reno, Nevada, Report No. CCEER-10-02, January 2010.

CCEER 10-03 Itani, A., Grubb, M., and Monzon, E, “Proposed Seismic Provisions and Commentary for Steel Plate Girder Superstructures,” Center for Civil Engineering Earthquake Research, Department of Civil and Environmental Engineering, University of Nevada, Reno, Nevada, Report No. CCEER-10-03, June 2010.

CCEER 10-04 Cruz-Noguez, C., Saiidi, M., “Experimental and Analytical Seismic Studies of a Four-Span Bridge System with Innovative Materials,” Center for Civil Engineering Earthquake Research, Department of Civil and Environmental Engineering, University of Nevada, Reno, Nevada, Report No. CCEER-10-04, September 2010.

CCEER 10-05 Vosooghi, A., Saiidi, M., “Post-Earthquake Evaluation and Emergency Repair of Damaged RC Bridge Columns Using CFRP Materials,” Center for Civil Engineering Earthquake Research, Department of Civil and Environmental Engineering, University of Nevada, Reno, Nevada, Report No. CCEER-10-05, September 2010.

CCEER 10-06 Ayoub, M., Sanders, D., “Testing of Pile Extension Connections to Slab Bridges,” Center for Civil Engineering Earthquake Research, Department of Civil and Environmental Engineering, University of Nevada, Reno, Nevada, Report No. CCEER-10-06, October 2010.

CCEER 10-07 Builes-Mejia, J. C. and Itani, A., “Stability of Bridge Column Rebar Cages during Construction,” Center for Civil Engineering Earthquake Research, Department of Civil and Environmental Engineering, University of Nevada, Reno, Nevada, Report No. CCEER-10-07, November 2010.

CCEER 10-08 Monzon, E.V., “Seismic Performance of Steel Plate Girder Bridges with Integral Abutments,” Center for Civil Engineering Earthquake Research, Department of Civil and Environmental Engineering, University of Nevada, Reno, Nevada, Report No. CCEER-10-08, November 2010.

CCEER 11-01 Motaref, S., Saiidi, M., and Sanders, D., “Seismic Response of Precast Bridge Columns with Energy Dissipating Joints,” Center for Civil Engineering Earthquake Research, Department of Civil and Environmental Engineering, University of Nevada, Reno, Nevada, Report No. CCEER-11-01, May 2011.

CCEER 11-02 Harrison, N. and Sanders, D., “Preliminary Seismic Analysis and Design of Reinforced Concrete Bridge Columns for Curved Bridge Experiments,” Center for Civil Engineering Earthquake Research, Department of Civil and Environmental Engineering, University of Nevada, Reno, Nevada, Report No. CCEER-11-02, May 2011.

CCEER 11-03 Vallejera, J. and Sanders, D., "Instrumentation and Monitoring the Galena Creek Bridge," Center for Civil Engineering Earthquake Research, Department of Civil and Environmental Engineering, University of Nevada, Reno, Nevada, Report No. CCEER-11-03, September 2011.

CCEER 11-04 Levi, M., Sanders, D., and Buckle, I., "Seismic Response of Columns in Horizontally Curved Bridges," Center for Civil Engineering Earthquake Research, Department of Civil and Environmental Engineering, University of Nevada, Reno, Nevada, Report No. CCEER-11-04, December 2011.

CCEER 12-01 Saiidi, M., "NSF International Workshop on Bridges of the Future – Wide Spread Implementation of Innovation," Center for Civil Engineering Earthquake Research, Department of Civil and Environmental Engineering, University of Nevada, Reno, Nevada, Report No. CCEER-12-01, January 2012.

CCEER 12-02 Larkin, A.S., Sanders, D., and Saiidi, M., "Unbonded Prestressed Columns for Earthquake Resistance," Center for Civil Engineering Earthquake Research, Department of Civil and Environmental Engineering, University of Nevada, Reno, Nevada, Report No. CCEER-12-02, January 2012.

CCEER 12-03 Arias-Acosta, J. G., Sanders, D., "Seismic Performance of Circular and Interlocking Spirals RC Bridge Columns under Bidirectional Shake Table Loading Part 1," Center for Civil Engineering Earthquake Research, Department of Civil and Environmental Engineering, University of Nevada, Reno, Nevada, Report No. CCEER-12-03, September 2012.

CCEER 12-04 Cukrov, M.E., Sanders, D., "Seismic Performance of Prestressed Pile-To-Bent Cap Connections," Center for Civil Engineering Earthquake Research, Department of Civil and Environmental Engineering, University of Nevada, Reno, Nevada, Report No. CCEER-12-04, September 2012.

CCEER 13-01 Carr, T. and Sanders, D., "Instrumentation and Dynamic Characterization of the Galena Creek Bridge," Center for Civil Engineering Earthquake Research, Department of Civil and Environmental Engineering, University of Nevada, Reno, Nevada, Report No. CCEER-13-01, January 2013.

CCEER 13-02 Vosooghi, A. and Buckle, I., "Evaluation of the Performance of a Conventional Four-Span Bridge During Shake Table Tests," Center for Civil Engineering Earthquake Research, Department of Civil and Environmental Engineering, University of Nevada, Reno, Nevada, Report No. CCEER-13-02, January 2013.

CCEER 13-03 Amirihormozaki, E. and Pekcan, G., "Analytical Fragility Curves for Horizontally Curved Steel Girder Highway Bridges," Center for Civil Engineering Earthquake Research, Department of Civil and Environmental Engineering, University of Nevada, Reno, Nevada, Report No. CCEER-13-03, February 2013.

CCEER 13-04 Almer, K. and Sanders, D., "Longitudinal Seismic Performance of Precast Bridge Girders Integrally Connected to a Cast-in-Place Bentcap," Center for Civil Engineering Earthquake Research, Department of Civil and Environmental Engineering, University of Nevada, Reno, Nevada, Report No. CCEER-13-04, April 2013.

CCEER 13-05 Monzon, E.V., Itani, A.I., and Buckle, I.G., "Seismic Modeling and Analysis of Curved Steel Plate Girder Bridges," Center for Civil Engineering Earthquake Research, Department of Civil and Environmental Engineering, University of Nevada, Reno, Nevada, Report No. CCEER-13-05, April 2013.

CCEER 13-06 Monzon, E.V., Buckle, I.G., and Itani, A.I., "Seismic Performance of Curved Steel Plate Girder Bridges with Seismic Isolation," Center for Civil Engineering Earthquake Research, Department of Civil and Environmental Engineering, University of Nevada, Reno, Nevada, Report No. CCEER-13-06, April 2013.

CCEER 13-07 Monzon, E.V., Buckle, I.G., and Itani, A.I., "Seismic Response of Isolated Bridge Superstructure to Incoherent Ground Motions," Center for Civil Engineering Earthquake Research, Department of Civil and Environmental Engineering, University of Nevada, Reno, Nevada, Report No. CCEER-13-07, April 2013.

CCEER 13-08 Haber, Z.B., Saiidi, M.S., and Sanders, D.H., "Precast Column-Footing Connections for Accelerated Bridge Construction in Seismic Zones," Center for Civil Engineering Earthquake Research, Department of Civil and Environmental Engineering, University of Nevada, Reno, Nevada, Report No. CCEER-13-08, April 2013.

CCEER 13-09 Ryan, K.L., Coria, C.B., and Dao, N.D., "Large Scale Earthquake Simulation of a Hybrid Lead Rubber Isolation System Designed under Nuclear Seismicity Considerations," Center for Civil Engineering Earthquake Research, Department of Civil and Environmental Engineering, University of Nevada, Reno, Nevada, Report No. CCEER-13-09, April 2013.

CCEER 13-10 Wibowo, H., Sanford, D.M., Buckle, I.G., and Sanders, D.H., "The Effect of Live Load on the Seismic Response of Bridges," Center for Civil Engineering Earthquake Research, Department of Civil and Environmental Engineering, University of Nevada, Reno, Nevada, Report No. CCEER-13-10, May 2013.

CCEER 13-11 Sanford, D.M., Wibowo, H., Buckle, I.G., and Sanders, D.H., "Preliminary Experimental Study on the Effect of Live Load on the Seismic Response of Highway Bridges," Center for Civil Engineering Earthquake Research, Department of Civil and Environmental Engineering, University of Nevada, Reno, Nevada, Report No. CCEER-13-11, May 2013.

CCEER 13-12 Saad, A.S., Sanders, D.H., and Buckle, I.G., "Assessment of Foundation Rocking Behavior in Reducing the Seismic Demand on Horizontally Curved Bridges," Center for Civil Engineering Earthquake Research, Department of Civil and Environmental Engineering, University of Nevada, Reno, Nevada, Report No. CCEER-13-12, June 2013.

CCEER 13-13 Ardakani, S.M.S. and Saiidi, M.S., "Design of Reinforced Concrete Bridge Columns for Near-Fault Earthquakes," Center for Civil Engineering Earthquake Research, Department of Civil and Environmental Engineering, University of Nevada, Reno, Nevada, Report No. CCEER-13-13, July 2013.

CCEER 13-14 Wei, C. and Buckle, I., "Seismic Analysis and Response of Highway Bridges with Hybrid Isolation," Center for Civil Engineering Earthquake Research, Department of Civil and Environmental Engineering, University of Nevada, Reno, Nevada, Report No. CCEER-13-14, August 2013.

CCEER 13-15 Wibowo, H., Buckle, I.G., and Sanders, D.H., "Experimental and Analytical Investigations on the Effects of Live Load on the Seismic Performance of a Highway Bridge," Center for Civil Engineering Earthquake Research, Department of Civil and Environmental Engineering, University of Nevada, Reno, Nevada, Report No. CCEER-13-15, August 2013.

CCEER 13-16 Itani, A.M., Monzon, E.V., Grubb, M., and Amirihormozaki, E. “Seismic Design and Nonlinear Evaluation of Steel I-Girder Bridges with Ductile End Cross-Frames,” Center for Civil Engineering Earthquake Research, Department of Civil and Environmental Engineering, University of Nevada, Reno, Nevada, Report No. CCEER-13-16, September 2013.

CCEER 13-17 Kavianipour, F. and Saiidi, M.S., “Experimental and Analytical Seismic Studies of a Four-span Bridge System with Composite Piers,” Center for Civil Engineering Earthquake Research, Department of Civil and Environmental Engineering, University of Nevada, Reno, Nevada, Report No. CCEER-13-17, September 2013.

CCEER 13-18 Mohebbi, A., Ryan, K., and Sanders, D., “Seismic Response of a Highway Bridge with Structural Fuses for Seismic Protection of Piers,” Center for Civil Engineering Earthquake Research, Department of Civil and Environmental Engineering, University of Nevada, Reno, Nevada, Report No. CCEER-13-18, December 2013.

CCEER 13-19 Guzman Pujols, Jean C., Ryan, K.L., “Development of Generalized Fragility Functions for Seismic Induced Content Disruption,” Center for Civil Engineering Earthquake Research, Department of Civil and Environmental Engineering, University of Nevada, Reno, Nevada, Report No. CCEER-13-19, December 2013.

CCEER 14-01 Salem, M. M. A., Pekcan, G., and Itani, A., “Seismic Response Control Of Structures Using Semi-Active and Passive Variable Stiffness Devices,” Center for Civil Engineering Earthquake Research, Department of Civil and Environmental Engineering, University of Nevada, Reno, Nevada, Report No. CCEER-14-01, May 2014.

CCEER 14-02 Saini, A. and Saiidi, M., “Performance-Based Probabilistic Damage Control Approach for Seismic Design of Bridge Columns,” Center For Civil Engineering Earthquake Research, Department Of Civil and Environmental Engineering, University of Nevada, Reno, Nevada, Report No. CCEER-14-02, May 2014.

CCEER 14-03 Saini, A. and Saiidi, M., “Post Earthquake Damage Repair of Various Reinforced Concrete Bridge Components,” Center For Civil Engineering Earthquake Research, Department Of Civil and Environmental Engineering, University of Nevada, Reno, Nevada, Report No. CCEER-14-03, May 2014.

CCEER 14-04 Monzon, E.V., Itani, A.M., and Grubb, M.A., “Nonlinear Evaluation of the Proposed Seismic Design Procedure for Steel Bridges with Ductile End Cross Frames,” Center For Civil Engineering Earthquake Research, Department Of Civil and Environmental Engineering, University of Nevada, Reno, Nevada, Report No. CCEER-14-04, July 2014.

CCEER 14-05 Nakashoji, B. and Saiidi, M.S., “Seismic Performance of Square Nickel-Titanium Reinforced ECC Columns with Headed Couplers,” Center For Civil Engineering Earthquake Research, Department Of Civil and Environmental Engineering, University of Nevada, Reno, Nevada, Report No. CCEER-14-05, July 2014.

CCEER 14-06 Tazarv, M. and Saiidi, M.S., “Next Generation of Bridge Columns for Accelerated Bridge Construction in High Seismic Zones,” Center For Civil Engineering Earthquake Research, Department Of Civil and Environmental Engineering, University of Nevada, Reno, Nevada, Report No. CCEER-14-06, August 2014.

CCEER 14-07 Mehrsoroush, A. and Saiidi, M.S., “Experimental and Analytical Seismic Studies of Bridge Piers with Innovative Pipe Pin Column-Footing Connections and Precast Cap Beams,” Center For Civil Engineering Earthquake Research, Department Of Civil and Environmental Engineering, University of Nevada, Reno, Nevada, Report No. CCEER-14-07, December 2014.

CCEER 15-01 Dao, N.D. and Ryan, K.L., “Seismic Response of a Full-scale 5-story Steel Frame Building Isolated by Triple Pendulum Bearings under 3D Excitations,” Center For Civil Engineering Earthquake Research, Department Of Civil and Environmental Engineering, University of Nevada, Reno, Nevada, Report No. CCEER-15-01, January 2015.

CCEER 15-02 Allen, B.M. and Sanders, D.H., “Post-Tensioning Duct Air Pressure Testing Effects on Web Cracking,” Center For Civil Engineering Earthquake Research, Department Of Civil and Environmental Engineering, University of Nevada, Reno, Nevada, Report No. CCEER-15-02, January 2015.

CCEER 15-03 Akl, A. and Saiidi, M.S., “Time-Dependent Deflection of In-Span Hinges in Prestressed Concrete Box Girder Bridges,” Center For Civil Engineering Earthquake Research, Department Of Civil and Environmental Engineering, University of Nevada, Reno, Nevada, Report No. CCEER-15-03, May 2015.

CCEER 15-04 Zargar Shotorbani, H. and Ryan, K., “Analytical and Experimental Study of Gap Damper System to Limit Seismic Isolator Displacements in Extreme Earthquakes,” Center For Civil Engineering Earthquake Research, Department Of Civil and Environmental Engineering, University of Nevada, Reno, Nevada, Report No. CCEER-15-04, June 2015.

CCEER 15-05 Wieser, J., Maragakis, E.M., and Buckle, I., “Experimental and Analytical Investigation of Seismic Bridge-Abutment Interaction in a Curved Highway Bridge,” Center For Civil Engineering Earthquake Research, Department Of Civil and Environmental Engineering, University of Nevada, Reno, Nevada, Report No. CCEER-15-05, July 2015.

CCEER 15-06 Tazarv, M. and Saiidi, M.S., “Design and Construction of Precast Bent Caps with Pocket Connections for High Seismic Regions,” Center For Civil Engineering Earthquake Research, Department Of Civil and Environmental Engineering, University of Nevada, Reno, Nevada, Report No. CCEER-15-06, August 2015.

CCEER 15-07 Tazarv, M. and Saiidi, M.S., “Design and Construction of Bridge Columns Incorporating Mechanical Bar Splices in Plastic Hinge Zones,” Center For Civil Engineering Earthquake Research, Department Of Civil and Environmental Engineering, University of Nevada, Reno, Nevada, Report No. CCEER-15-07, August 2015.

CCEER 15-08 Sarraf Shirazi, R., Pekcan, G., and Itani, A.M., “Seismic Response and Analytical Fragility Functions for Curved Concrete Box-Girder Bridges,” Center For Civil Engineering Earthquake Research, Department Of Civil and Environmental Engineering, University of Nevada, Reno, Nevada, Report No. CCEER-15-08, December 2015.

CCEER 15-09 Coria, C.B., Ryan, K.L., and Dao, N.D., “Response of Lead Rubber Bearings in a Hybrid Isolation System During a Large Scale Shaking Experiment of an Isolated Building,” Center For Civil Engineering Earthquake Research, Department Of Civil and Environmental Engineering, University of Nevada, Reno, Nevada, Report No. CCEER-15-09, December 2015.

CCEER 16-01 Mehraein, M and Saiidi, M.S., “Seismic Performance of Bridge Column-Pile-Shaft Pin Connections for Application in Accelerated Bridge Construction,” Center For Civil Engineering Earthquake Research, Department Of Civil and Environmental Engineering, University of Nevada, Reno, Nevada, Report No. CCEER-16-01, May 2016.

CCEER 16-02 Varela Fontecha, S. and Saiidi, M.S., “Resilient Earthquake-Resistant Bridges Designed For Disassembly,” Center For Civil Engineering Earthquake Research, Department Of

Civil and Environmental Engineering, University of Nevada, Reno, Nevada, Report No. CCEER-16-02, May 2016.

CCEER 16-03 Mantawy, I. M, and Sanders, D. H., “Assessment of an Earthquake Resilient Bridge with Pretensioned, Rocking Columns,” Center For Civil Engineering Earthquake Research, Department Of Civil and Environmental Engineering, University of Nevada, Reno, Nevada, Report No. CCEER-16-03, May 2016.

CCEER 16-04 Mohammed, M, Biasi, G., and Sanders, D., “Post-earthquake Assessment of Nevada Bridges using ShakeMap/ShakeCast,” Center For Civil Engineering Earthquake Research, Department Of Civil and Environmental Engineering, University of Nevada, Reno, Nevada, Report No. CCEER-16-04, May 2016.

CCEER 16-05 Jones, J, Ryan, K., and Saiidi, M, “Toward Successful Implementation of Prefabricated Deck Panels to Accelerate the Bridge Construction Process,” Center For Civil Engineering Earthquake Research, Department Of Civil and Environmental Engineering, University of Nevada, Reno, Nevada, Report No. CCEER-16-05, August 2016.

CCEER 16-06 Mehrsoroush, A. and Saiidi, M., “Probabilistic Seismic Damage Assessment for Sub-standard Bridge Columns,” Center For Civil Engineering Earthquake Research, Department Of Civil and Environmental Engineering, University of Nevada, Reno, Nevada, Report No. CCEER-16-06, November 2016.

CCEER 16-07 Nielsen, T., Maree, A., and Sanders, D., “Experimental Investigation into the Long-Term Seismic Performance of Dry Storage Casks,” Center For Civil Engineering Earthquake Research, Department Of Civil and Environmental Engineering, University of Nevada, Reno, Nevada, Report No. CCEER-16-07, December 2016.

CCEER 16-08 Wu, S., Buckle, I., and Itani, A., “Effect of Skew on Seismic Performance of Bridges with Seat-Type Abutments,” Center For Civil Engineering Earthquake Research, Department Of Civil and Environmental Engineering, University of Nevada, Reno, Nevada, Report No. CCEER-16-08, December 2016.

CCEER 16-09 Mohammed, M., and Sanders, D., “Effect of Earthquake Duration on Reinforced Concrete Bridge Columns,” Center For Civil Engineering Earthquake Research, Department Of Civil and Environmental Engineering, University of Nevada, Reno, Nevada, Report No. CCEER-16-09, December 2016.

CCEER 16-10 Guzman Pujols, J., and Ryan, K., “Slab Vibration and Horizontal-Vertical Coupling in the Seismic Response of Irregular Base-Isolated and Conventional Buildings,” Center For Civil Engineering Earthquake Research, Department Of Civil and Environmental Engineering, University of Nevada, Reno, Nevada, Report No. CCEER-16-10, December 2016.

CCEER 17-01 White, L., Ryan, K., and Buckle, I., “Thermal Gradients in Southwestern United States and the Effect on Bridge Bearing Loads,” Center For Civil Engineering Earthquake Research, Department Of Civil and Environmental Engineering, University of Nevada, Reno, Nevada, Report No. CCEER-17-01, May 2017.

CCEER 17-02 Mohebbi, A., Saiidi, M., and Itani, A., “Development and Seismic Evaluation of Pier Systems w/Pocket Connections, CFRP Tendons, and ECC/UHPC Columns,” Center For Civil Engineering Earthquake Research, Department Of Civil and Environmental Engineering, University of Nevada, Reno, Nevada, Report No. CCEER-17-02, May 2017.

CCEER 17-03 Mehrsoroush, A., Saiidi, M., and Ryan, K., "Development of Earthquake-resistant Precast Pier Systems for Accelerated Bridge Construction in Nevada," Center For Civil Engineering Earthquake Research, Department Of Civil and Environmental Engineering, University of Nevada, Reno, Nevada, Report No. CCEER-17-03, June 2017.

CCEER 17-04 Abdollahi, B., Saiidi, M., Siddharthan, R., and Elfass, S., "Shake Table Studies of Soil-Abutment-Structure Interaction in Skewed Bridges," Center For Civil Engineering Earthquake Research, Department Of Civil and Environmental Engineering, University of Nevada, Reno, Nevada, Report No. CCEER-17-04, July 2017.